

# VHCF7

## Seventh International Conference on Very High Cycle Fatigue

JULY 3-5, 2017, DRESDEN, GERMANY

Editors: M. Zimmermann, H.-J. Christ



SIEGENER WERKSTOFFKUNDLICHE BERICHTE | BAND 14/2017  
HERAUSGEBER: PROF. DR.-ING. HABIL. H.-J. CHRIST





**DVM**

German Association for  
Materials Research and Testing e.V.

**VHCF7**

**Seventh International Conference  
on Very High Cycle Fatigue**

July 3-5, 2017, Dresden, Germany

**Editors: *M. Zimmermann, H.-J. Christ***



Bibliografische Information der Deutschen Nationalbibliothek  
Die Deutsche Nationalbibliothek verzeichnet diese Publikation in der Deutschen  
Nationalbibliografie; detaillierte bibliografische Daten sind im Internet über  
<http://dnb.d-nb.de> abrufbar.

Zugl.: Siegen, Univ., 2017

Herausgeber:

Prof. Dr.-Ing. habil. H.-J. Christ  
Lehrstuhl für Materialkunde und  
Werkstoffprüfung  
Institut für Werkstofftechnik  
Paul-Bonatz-Str. 9-11  
Universität Siegen  
D-57068 Siegen

Prof. Dr.-Ing. M. Zimmermann  
TU Dresden Institute of Materials Science and  
Fraunhofer IWS Institut für Werkstoff- und  
Strahltechnik, Dresden

© Copyright H.-J. Christ 2017

© Copyright Lehrstuhl für Materialkunde und Werkstoffprüfung,  
Universität Siegen 2017

Alle Rechte vorbehalten, auch das des auszugsweisen Nachdruckes,  
der auszugsweisen oder vollständigen Wiedergabe, der Speicherung  
in Datenverarbeitungsanlagen und das der Übersetzung.

Als Manuskript gedruckt. Printed in Germany.

urn:nbn:de:hbz:467-11701  
ISSN 2193-5114

## **Executive Chairs**

*M. Zimmermann*, TU Dresden Institute of Materials Science

and Fraunhofer IWS Institut für Werkstoff- und Strahltechnik, Dresden, DE

*H.-J. Christ*, Universität Siegen Institute of Materials Technology, Siegen, DE

## **Organizing Committee**

*M. Zimmermann*

*H.-J. Christ*

*M. Bacher-Höchst*

*C. Eberl*

*D. Eifler*

*H. W. Höppel*

*M. Sander*

## **Scientific Committee**

*F. Ballani*

*F. Balle*

*T. Beck*

*H. Biermann*

*E. Bitzek*

*T. Bläß*

*C. Boller*

*B. Clausen*

*B. Fiedler*

*M. Gude*

*A. Hartmaier*

*P. Horst*

*E. Kaufmann*

*E. Kerscher*

*U. Krupp*

*K.-H. Lang*

*U. Pietsch*

*B. Pyttel*

*R. Rolfes*

*M. Sinapius*

*W. Trojahn*

*A. Weidner*

*D. Weygand*

*P. Wierach*

*H.-W. Zoch*

## **International Advisory Committee**

*S. Beretta*

*C. Berger*

*J. Bergström*

*G. C. Chai*

*V. Favier*

*M. de Freitas*

*G. Härkegard*

*Y. Hong*

*L. Kunz*

*H. Mayer*

*H. Mughrabi*

*Y. Murakami*

*T. Nakamura*

*A. Navarro*

*T. Palin-Luc*

*O. Pierron*

*T. Pollock*

*H. Proudhon*

*M. Quaresimin*

*R. O. Ritchie*

*T. Sakai*

*A. Shanyavskiy*

*C. Sonsino*

*S. Stanzl-Tschegg*

*Q. Wang*

## **Organization**

VHCF7 is organized by DVM German Association for Materials Research and Testing  
Schloßstr. 48, 12165 Berlin, DE

Phone: +49 30 811 30 66 Fax: +49 30 811 93 59

E-Mail: [dvm@dvm-berlin.de](mailto:dvm@dvm-berlin.de) [www.dvm-berlin.de](http://www.dvm-berlin.de)



## **VHCF7 Preface**

On behalf of the German Association for Materials Research and Testing (DVM) we would like to welcome all participants to

## **VHCF7**

### **Seventh International Conference on Very High Cycle Fatigue**

July 3 to 5, 2017, Dresden, Germany

The Seventh International Conference on Very High Cycle Fatigue resumes the successful series of previous conferences starting with VHCF1 1998 in Paris (FR) followed by VHCF2 2001 in Vienna (AT), VHCF3 2004 in Kyoto/Kusatsu (JP), VHCF4 2007 in Ann Arbor (US), VHCF5 2011 in Berlin (Germany) and VHCF6 2014 in Chengdu (China).

Today the fatigue behavior of materials for number of loading cycles surpassing the classical fatigue limit has become a question of major interest. More and more components are subjected to load scenarios with numbers of loading cycles up to  $10^8$  or even beyond, a range which is either called gigacycle or ultrahigh cycle fatigue, but most often is referred to as Very High Cycle Fatigue (VHCF). A survey on publications focusing on VHCF on behalf of the 6th international conference in 2014 by Wang and Khan revealed that VHCF has the highest impact in the domain of fatigue publications. Topics such as damage mechanisms, crack initiation and fatigue crack growth behavior are still of major interest as are recent and future trends in the experimental techniques related to VHCF studies. While in the past research findings were mainly focused on metallic materials, the scope of research has meanwhile strongly broadened taking all classes of materials into consideration. In particular, the material group of composites has drawn significant attention. Moreover, the development of simulation models to predict damage accumulation in the VHCF regime and the application of statistical methods to describe VHCF-specific fatigue life variation have become a matter of intensive research activities. With an increasing number of experimentally obtained as well as simulated VHCF data, the question of reliable fatigue life prediction models based on probabilistic models can now be dealt with on a sound basis. Several coordinated nation-wide research programs, such as e.g. the German Research Foundation funded priority program "Infinite Life" have contributed to an explosive increase in new findings and insights into VHCF, justifying high expectations in a lively discussion of latest scientific issues as well as application driven matters.

In the tradition of the earlier VHCF conferences, the objective of the conference is to provide a worldwide platform for scientific communication, discussion and activities for all those interested in both fundamental aspects and practical applications. The conference comprises invited plenary lectures by outstanding international scientists, invited talks, contributed oral presentations and posters to the scientific topics focusing on

- practically all metallic material groups (ferrous materials, non-ferrous materials such as Al, Mg, Ti, Ni, etc.),
- composites and advanced materials and materials for micro electro mechanical systems (MEMS),
- latest developments regarding experimental techniques in high frequency testing as well as damage detection methods
- computational simulation models to predict VHCF behavior and
- statistically based fatigue life prediction models.

On behalf of the Scientific Committee and the Conference Organizers we are very glad to welcome you in Dresden, the Capital of Saxony. We wish to thank all the authors, session chairs, members of the committees and numerous others who gave their important contributions to this conference and are looking forward to a successful and fruitful scientific exchange.

Dresden, July 2017

*Martina Zimmermann*  
*Hans-Jürgen Christ*

## **VHCF7 Welcome Address by the President of DVM**

On behalf of the German Association for Materials Research and Testing (DVM) I want to give all delegates a very warm welcome to

### **VHCF7 Seventh International Conference on Very High Cycle Fatigue**

The VHCF series started in 1998 with VHCF1 in Paris further events took place in 2001 (VHCF2, Vienna, Austria), 2004 (VHCF3, Kyoto/Kusatsu, Japan), 2007 (VHCF4, Ann Arbor, USA), 2011 (VHCF5, Berlin, Germany), 2014 (VHCF6, Chengdu, China) and now 2017 again in Germany in Dresden.

VHCF7 is hosting over 110 engineers and scientists from 16 nations worldwide, who are working in the field of Very High Cycle Fatigue. We are proud to have the opportunity to welcoming you all again in Germany and we will do our best that this conference will also be well remembered in your global VHCF community.

Especially for the selection and arrangement of all scientific contributions – the essentials of the conference - we want to thank the chairpersons of VHCF7, Martina Zimmermann and Hans-Jürgen Christ, as well as all the members of the Organizing Committee, the Scientific Committee and the International Advisory Committee.

VHCF7 is supported moreover by a range of distinguished national and international associations and committees.

DGM Deutsche Gesellschaft für Materialkunde e.V. (DE)  
ESIS European Structural Integrity Society  
FEMS Federation of European Materials Societies  
IGF Gruppo Italiana Frattura (IT)  
ICF International Congress on Fracture  
JSMS The Society of Materials Science (JP)  
SF2M Société Française de Métallurgie et de Matériaux (FR)  
TMS The Minerals, Metals & Materials Society (US)  
WAW Wissenschaftlicher Arbeitskreis e.V. der Universitäts-Professoren der Werkstofftechnik (DE)

Our thanks go to them for promotion and publication of this conference and its topics.

We also highly appreciate the support of Fraunhofer IWS Dresden, IABG Dresden and IMA Materialforschung und Anwendungstechnik Dresden. All management aspects have been handled by our DVM-Office in Berlin. Sincere thanks to you all for your outstanding work.

On behalf of the DVM board and the whole VHCF7 team I am wishing you all a very successful conference with three really inspiring days in Dresden.

Prof. Dr.-Ing. Hans-Albert Richard, University of Paderborn  
DVM President



## Tribute

On occasion of VHCF7 Seventh International Conference on Very High Cycle Fatigue in Dresden, July 03-05, 2017, DVM German Association for Materials Research and Testing takes pride in awarding the



**DVM Honorary Membership** on

***Professor J. Wayne Jones***

University of Michigan, Materials Science and Engineering, Ann Arbor, MI, US

Since 1987, the DVM Honorary Membership is awarded to foreign scientists for outstanding achievements concerning the technical and scientific cooperation with Germany in the field of materials research and testing. The Honorary Membership is usually awarded during an international DVM conference.

A list of all DVM Honorary Members as well as other laureates of DVM awards can be found on the DVM website, [www.dvm-berlin.de](http://www.dvm-berlin.de).





# Contents

## PLENARY LECTURES

<b>EFFECTS OF SURFACE DEFECTS/NOTCHES ON VERY-HIGH-CYCLE FATIGUE BEHAVIOR OF A STRUCTURAL STEEL</b> .....	2
Y. Hong , Q. Jiang , C. Sun	
<b>FROM DEFECTS TO MICROSTRUCTURE NEIGHBORHOODS: A REVIEW OF ULTRASONIC FATIGUE STUDIES AT THE UNIVERSITY OF MICHIGAN</b> .....	3
W. Jones, J. Allison, T. Pollock, C. Torbet, S. Daly	
<b>FATIGUE BEHAVIOR OF TWO-PHASE TITANIUM ALLOY IN VHCF REGIME</b> .....	4
A. Nikitin, A. Shanyavskiy, T. Palin-Luc	
<b>FATIGUE TESTING OF CARBON FIBRE REINFORCED EPOXY BASED COMPOSITES AT ULTRASONIC FREQUENCIES AND DAMAGE MONITORING UNDER VHCF LOADING</b> .....	13
F. Balle, D. Weibel, D. Backe	
<b>PRISMS: AN INTEGRATED PREDICTIVE MULTI-SCALE CAPABILITY FOR PREDICTING VERY HIGH CYCLE FATIGUE BEHAVIOR OF METALS</b> .....	22
J. Allison	

## FUNDAMENTALS, PHYSICS AND MECHANISMS MECHANISMS OF CRACK INITIATION

<b>ON THE FATIGUE CRACK INITIATION AT SUBSURFACE INCLUSION AND MATRIX (INVITED)</b> .....	24
G. Chai	
<b>INFLUENCE OF LOADING TYPE ON FRACTURE BEHAVIOR OF HIGH STRENGTH STEEL UNDER VERY HIGH CYCLE FATIGUE</b> .....	25
Y. Sandaiji, E. Tamura	
<b>SELF-HEATING AND DISSIPATION STUDY FOR STEELS WITH DIFFERENT CARBON CONTENTS IN THE GIGACYCLE FATIGUE DOMAIN</b> .....	31
X. Pu, I. Ranc-Darbord, J. Petit, D. Wagner	

<b>FATIGUE CHARACTERISTICS INCLUDING VERY HIGH CYCLE REGION OF LOW ALLOY STEEL FOR SOLID TYPE CRANCSHAFT .....</b>	<b>38</b>
T. Ikegami, R. Yakura, M. Matsuda, T. Sakai, A. Ueno	
<b>VHCF BEHAVIOUR OF INCONEL718 UNDER SYMMETRIC TENSION COMPRESSION AT ROOM TEMPERATURE.....</b>	<b>45</b>
M.X. Zhao, O. Polit, E. Valot, T. Palin-Luc, V. Bonnard	
<b>TORSIONAL AND AXIAL VHCF PROPERTIES OF SPRING STEEL AT DIFFERENT LOAD RATIOS.....</b>	<b>51</b>
H. Mayer, U. Karr, Y. Sandaiji, E. Tamura	
<b>FORMATION MECHANISM OF FINE GRANULAR AREA (FGA) AROUND INTERIOR INCLUSION AT CRACK INITIATION SITE IN VERY HIGH CYCLE FATIGUE .....</b>	<b>57</b>
T. Sakai, N. Oguma, A. Nakagawa, S. Tsutsumi, O. Naimark, M. Bannikov	
<b>FRACTURE MECHANICS CONSIDERATION OF INTERIOR FRACTURE ORIGIN WITHOUT INCLUSION UNDER ROTATING BENDING IN VERY HIGH CYCLE FATIGUE.....</b>	<b>63</b>
N. Oguma, Y. Nakahashi, T. Sakai	
<b>SCALING ANALYSIS OF FINE GRANULAR AREA (FGA) AROUND INTERIOR INCLUSION AT CRACK INITIATION SITE IN VERY HIGH CYCLE FATIGUE.....</b>	<b>69</b>
M. Bannikov, O. Naimark, T. Sakai, N. Oguma	
<b>A GENERAL STATISTICAL MODEL FOR THE DESCRIPTION OF THE HYDROGEN ASSISTED CRACK INITIATION IN THE VHCF REGIME .....</b>	<b>75</b>
D.S. Paolino, A. Tridello, G. Chiandussi, M. Rossetto	
<b>PROBABILISTIC MODEL ON STATISTICAL FATIGUE PROPERTY IN VERY HIGH CYCLE REGIME BASED ON DISTRIBUTIONS OF SIZE AND LOCATION OF INTERIOR INCLUSIONS .....</b>	<b>81</b>
Y. Nakamura, T. Sakai, D. G. Harlo, N. Oguma, M. Nakajima, A. Nakagawa	
<b>EVALUATION OF THREE-DIMENSIONAL MICROSTRUCTURAL EFFECTS ON DAMAGE EVOLUTION DURING VHCF LOADING OF A DUPLEX STAINLESS STEEL – MECHANISMS OF DAMAGE EVOLUTION AND CORRESPONDING FATIGUE LIFE.....</b>	<b>87</b>
A. Giertler, N. Heilemann, B. Dönges, H.-J. Christ, U. Krupp	
<b>LATTICE TILT AND SUBDIVISION OF GRAINS DURING CRACK FORMATION IN VHCF DUPLEX STAINLESS STEEL USING MICROBEAM X-RAY LAUE DIFFRACTION .....</b>	<b>93</b>
A. Abboud, B. Dönges, M. Shokr, A. Tosson, J-S. Micha, R. Hartmann, L. Strüder, H.-J. Christ, U. Pietsch	
<b>FATIGUE PROPERTIES OF CFRP CROSS-PLY LAMINATES WITH TAILORED FEW-LAYER GRAPHENE ENHANCEMENT .....</b>	<b>99</b>
C. Leopold, A. Schetle, J. Kosmann, G. Just, I. Koch, M. Gude, B. Fiedler	

**FUNDAMENTALS, PHYSICS AND MECHANISMS**  
**NONPROPAGATING CRACKS, GROWTH OF SHORT AND LONG CRACKS AND**  
**MECHANISMS OF DAMAGE ACCUMULATION**

<b>THE SIGNIFICANCE OF MICROSTRUCTURE INHOMOGENEITIES DURING VHCF OF TEMPERED MARTENSITIC STEEL (INVITED) .....</b>	<b>106</b>
U. Krupp, A. Giertler, K. Koschella	
<b>A PHYSICALLY BASED CONSTITUTIVE EQUATION TO CHARACTERIZE S-N FATIGUE BEHAVIOR IN VERY HIGH CYCLE FATIGUE .....</b>	<b>113</b>
K. S. R. Chandran	
<b>CHARACTERIZATION OF CRACK INITIATION AND CRACK GROWTH IN THE VHCF REGIME ON THE BASIS OF NONLINEAR MATERIAL BEHAVIOUR IN COMPARISON TO OPTICAL INVESTIGATIONS FOR TWO ALUMINUM ALLOYS .....</b>	<b>119</b>
T. Kirsten, F. Bülbül, T. Stein, M. Wicke, H.-J. Christ, A. Brückner-Foit, M. Zimmermann	
<b>MEASUREMENT OF INTERNAL FATIGUE CRACK GROWTH RATE OF TI-6AL-4V BY USING HIGH-RESOLUTION X-RAY CT .....</b>	<b>125</b>
F. Yoshinaka, T. Nakamura, D. Shiozawa, Y. Nakai, K. Uesugi	
<b>TORSIONAL FATIGUE PROPERTIES OF 17-4PH STAINLESS STEEL IN THE VHCF REGIME.....</b>	<b>130</b>
B.M. Schönbauer, H. Mayer, K. Yanase, M. Endo	
<b>HCF AND VHCF STRENGTH OF SPRING STEEL WITH SMALL SCRATCHES .....</b>	<b>136</b>
Y. Nishimura, M. Endo, K. Yanase, Y. Ikeda, Y. Tanaka, N. Miyamoto, S. Miyakawa	
<b>NONLINEAR AND SCALING PHENOMENA OF DAMAGE ACCUMULATION, CRACK INITIATION AND PROPAGATION IN VHCF .....</b>	<b>142</b>
O. Naimark, T. Palin-Luc	
<b>A PHYSICALLY BASED CONSTITUTIVE EQUATION FOR FATIGUE CRACK GROWTH IN METALS.....</b>	<b>148</b>
K. S. R. Chandran	
<b>STAGES OF FATIGUE DAMAGE OF PLAIN CARBON STEELS AT THE TRANSITION FROM THE HIGH CYCLE FATIGUE TO THE VERY HIGH CYCLE FATIGUE REGIME .....</b>	<b>154</b>
J. Bach, M. Göken, H. W. Höppel	
<b>EVALUATION OF THREE-DIMENSIONAL MICROSTRUCTURAL EFFECTS ON DAMAGE EVOLUTION DURING VHCF LOADING OF DUPLEX STAINLESS STEEL – MICROSTRUCTURE-SENSITIVE FATIGUE LIFE ASSESSMENT .....</b>	<b>160</b>
B. Dönges, C.-P. Fritzen, H.-J. Christ	

**FUNDAMENTALS, PHYSICS AND MECHANISMS**  
**INFLUENCE OF MICROSTRUCTURE AND DEFECTS**

<b>DATA ACQUISITION FOR VERY HIGH CYCLE FATIGUE OF NON-FERROUS METALLIC MATERIALS BASED ON THE COLLABORATIVE RESEARCH IN JSMS</b> <b>1st report: outline of round-robin experiments on aluminum die casting, beta titanium and wrought magnesium alloys (INVITED)</b> .....	167
T. Nakamura, A. Ueno, T. Matsumura, K. Masaki, H. Oguma, H. Akebono, T. Kakiuchi, S. Kikuchi, Y. Nakamura, T. Nishida, T. Ogawa, N. Oguma, T. Sakai, Y. Shimamura, K. Shiozawa, Y. Uematsu	
<b>FATIGUE BEHAVIOR IN METASTABLE STAINLESS STEEL DURING VERY HIGH CYCLE FATIGUE USING A STEPWISE LOADING METHOD</b> .....	174
G. Chai, L. Ewenz, K. Persson, J. Bergström, C. Burman, M. Zimmermann	
<b>FEM ANALYSES OF STRESS DISTRIBUTIONS AROUND INCLUSIONS AT INTERIOR CRACK INITIATION SITE IN VERY HIGH CYCLE FATIGUE</b> .....	180
T. Sakai, R. Fincato, S. Tsutsumi, M. Sano, D.S. Paolino, T. Miyoshi, N. Oguma, A. Nakagawa	
<b>DEVELOPMENT OF NITRIDED 18NI MARAGING STEEL TO OPTIMISE THE VERY HIGH CYCLE FATIGUE PROPERTIES</b> .....	186
U. Karr, B. Pennings, D. Tran, H. Mayer	
<b>MICROSTRUCTURE, MEAN STRESS AND NOTCH INFLUENCE ON FATIGUE STRENGTH AND INITIATION OF THREE BAR STEEL GRADES IN THE VERY HIGH CYCLE FATIGUE REGIME</b> .....	192
M. Sadek, J. Bergström, N. Hallbäck, C. Burman, R. Elvira, B. Escauriaza	
<b>DATA ACQUISITION FOR VERY HIGH CYCLE FATIGUE OF NON-FERROUS METALLIC MATERIALS BASED ON THE COLLABORATIVE RESEARCH IN JSM</b> <b>2nd report: Effects of loading type, test environment, surface treatment and casting defects on VHCF properties of ADC12 aluminum die-casting alloy</b> .....	198
A. Ueno, T. Matsamura, K. Masaki, T. Ogawa, K. Shiozawa, Y. Nakamura, T. Nishida	
<b>DATA ACQUISITION FOR VERY HIGH CYCLE FATIGUE OF NON-FERROUS METALLIC MATERIALS BASED ON THE COLLABORATIVE RESEARCH IN JSMS</b> <b>3rd Report: Effects of loading type and test frequency on VHCF properties of beta Ti22V4Al alloy</b> .....	204
H. Oguma, T. Nakamura, A. Ueno, T. Matsumura, K. Masaki, H. Akebono, Y. Uematsu, N. Oguma, T. Kakiuchi, Y. Shimamura, Y. Nakamura	
<b>DATA ACQUISITION FOR VERY HIGH CYCLE FATIGUE OF NON-FERROUS METALLIC MATERIALS BASED ON THE COLLABORATIVE RESEARCH IN JSMS</b> <b>4th report: basic research of VHCF properties of extruded magnesium alloy under rotary bending loading</b> .....	210
K. Masaki, T. Matsamura, H. Akebono, T. Kakiuchi, Y. Nakamura, Y. Uematsu	
<b>S-N BEHAVIOUR OF COPPER AT VHCF LOADING</b> .....	216
S. E. Stanzl-Tschegg, A. Perlega, M. Meischel, B. Schönbauer	

**INFLUENCE OF MICROSTRUCTURAL CHARACTERISTICS ON THE VHCF BEHAVIOR OF THE ALUMINUM CAST ALLOY EN AC-ALSi7MG0.3** .....222  
S. Knorre, J. Tenkamp, U. Krupp, W. Michels, F. Walther

**INFLUENCE OF HYBRIDISATION BY SELECTIVE LASER MELTING ON THE VERY HIGH CYCLE FATIGUE BEHAVIOUR OF ALUMINIUM ALLOYS** .....228  
S. Siddique, M. Awd, F. Walther

## **PARAMETERS**

**VARIABLE AMPLITUDE LOADING OF 17-4PH STAINLESS STEEL IN THE VHCF REGIME (INVITED)**.....235  
B.M. Schönbauer, M. Fitzka, U. Karr, H. Mayer

**ENVIRONMENTAL INFLUENCES ON THE NEAR THRESHOLD FATIGUE CRACK GROWTH OF WROUGHT MAGNESIUM ALLOY AZ61 HP** .....242  
U. Karr, B.M. Schönbauer, A. Stich, H. Mayer

**VERY HIGH CYCLE FATIGUE BEHAVIOR OF METASTABLE AUSTENITIC STEEL X6CRNINB1810 AT 300°C** .....248  
M. Smaga, A. Sorich, D. Eifler, T. Beck

**RELATIONSHIP BETWEEN TEMPERATURE PROPERTY AND LOADING FREQUENCY OF ROTATING BENDING FATIGUE TESTING MACHINE OF CANTILEVER TYPE** .....254  
T. Yamamoto, B. Lian, K. Gotoh

**GIGACYCLE FATIGUE PROPERTIES OF A TURBINE ENGINE BLADE TITANIUM ALLOY Ti811 AT ELEVATED TEMPERATURE** .....260  
K Yang, J.K. Li, C He, Y.J. Liu, H Zhang, Q.Y. Wang

**MICROSTRUCTURAL TIME LAPSE DAMAGE QUANTIFICATION IN GFRP DURING HIGH CYCLE TENSION-TENSION FATIGUE USING STEREOLOGY** .....266  
S. Bhattacharya, A. Tewari, A. Guha, P. Potluri

**NONLINEARITIES BASED INVERSE APPROACH FOR THE CHARACTERISATION OF THE DAMAGE EVALUATION PROCESS IN VERY HIGH CYCLE FATIGUED CFRP SPECIMENS** .....272  
C. Boller, R. S. Venkat, P. Starke, B. Müller, T. Heckel, D. Gohlke, G. Bruno

**INFLUENCE OF R-RATIO ON THE FATIGUE BEHAVIOR OF Ti6Al4V IN THE VERY HIGH CYCLE FATIGUE REGIME** .....278  
S. Heinz, F. Ritz, T. Beck, D. Eifler

**INFLUENCE OF MEAN STRESS AND NOTCHES ON THE VHCF-BEHAVIOR OF A MARTENSITIC STEEL FOR LOW-PRESSURE STEAM TURBINE BLADES**.....284  
F. Ritz, T. Beck

<b>COAXING EFFECT OF MAGNESIUM ALLOYS UNDER ROTATING BENDING IN VERY HIGH CYCLE REGIME .....</b>	<b>290</b>
Y. Nakamura, T. Kasuya, T. Shimizu	
<b>DEVELOPMENT OF A NEW SURFACE MODIFICATION TECHNIQUE: SCANNING CYCLIC PRESS AND ITS APPLICATION FOR THE IMPROVEMENT OF FATIGUE LIFE OF MAGNESIUM ALLOY AZ31 .....</b>	<b>296</b>
N. Fujimura, T. Nakamura, T. Wajima	
<b>INFLUENCE OF HYBRID SURFACE MODIFICATION ON VERY HIGH CYCLE FATIGUE STRENGTH OF VARIOUS STEEL MATERIALS .....</b>	<b>302</b>
K. Nambu, N. Egami	
<b>EXPERIMENTAL INVESTIGATION OF FREQUENCY EFFECT ON FATIGUE CRACK PROPAGATION ON 3 STEELS: DUAL PHASE (DP1180), COMPLEX PHASE (CP1000) AND MULTI-PHASE (M800HY) .....</b>	<b>308</b>
M. Ouarabi, K. Gillner, T. Palin-Luc, S. Muenstermann, O. Polit	
 <b><u>EXPERIMENTAL METHODS</u></b>	
<b>DESIGN AND INSTRUMENTATION OF AN AXIAL/TORSION DEVICE WORKING AT ULTRASONIC FREQUENCIES FOR VHCF TESTING (INVITED).....</b>	<b>315</b>
M. de Freitas, P. Costa, M. Vieira, A.M.R. Ribeiro, L. Reis	
<b>METHODOLOGY FOR SPECIMEN DESIGN AT ULTRASONIC FREQUENCIES IN AXIAL/TORSION FATIGUE LOADINGS FOR VHCF .....</b>	<b>322</b>
P. Rodrigues da Costa, M. Vieira, M. Freitas, A. Ribeiro, L. Reis	
<b>HIGH-FREQUENCY RESONANCE-REGULATED TESTING DEVICE FOR VERY HIGH CYCLE AXIAL FATIGUE TESTING OF LARGE-SCALE CAST IRON AND STEEL SPECIMENS .....</b>	<b>328</b>
P. Schaumann, A. Alt, J. Kulikowski, L. Radulovic, S. Steppeler	
<b>ON THE USE OF THERMOGRAPHIC TECHNIQUE TO DETERMINE THE FATIGUE LIMIT OF A COLD DRAWN CARBON STEEL .....</b>	<b>334</b>
C.F.C. Bandeira, P.P. Kenedi, J.T.P. Castro, M.A. Meggiolaro	
<b>A FIRST PROPOSAL OF A NEW HIGH FREQUENCY TESTING METHOD FOR HIGH STRENGTH STEELS UNDER TENSION / COMPRESSION LOADING IN THE VHCF REGIME .....</b>	<b>340</b>
I. Milošević, G. Winter, F. Grün, M. Kober	
<b>AN INNOVATIVE TESTING TECHNIQUE FOR ASSESSING THE VHCF RESPONSE OF ADHESIVELY BONDED JOINTS .....</b>	<b>345</b>
D.S. Paolino, L. Goglio, A. Tridello, G. Chiandussi, M. Rossetto	
<b>ULTRASONIC FATIGUE TESTING OF THIN NITINOL SHEETS IN THE VHCF REGIME .....</b>	<b>351</b>
M. Fitzka, D. Catoor, M. Reiterer, H. Mayer	
<b>ACCELERATED FRETTING FATIGUE TESTING BY USING ULTRASONIC FATIGUE TESTING MACHINE WITH A CLAMPING CONTACT PAD...</b>	<b>357</b>
Y. Shimamura, T. Izumikawa, H. Ishii, K. Tohgo, T. Fujii, T. Yagasaki, S. Sumida	

<b>INFINITE LIFE OF FIBRE REINFORCED PLASTICS (FRP) INVESTIGATED WITH X-RAY-REFRACTION-TOPOGRAPHY FOR NON-DESTRUCTIVE EVALUATION OF MICRO-STRUCTURAL DEGRADATION PROCESSES IN-SITU CYCLIC FATIGUE LOADING</b> .....	362
V. Trappe, A. Müller, S. Hickmann	
<b>INVESTIGATION OF THE RESPONSE OF DUAL-PHASE STEELS SUBMITTED TO 20 KHZ AND LOW FREQUENCY FATIGUE LOADINGS</b> .....	368
N. Torabian, V. Favier, J. Dirrenberger, F. Adamski, S. Ziaei-Rad, N. Ranc	
<b>INVESTIGATION OF THE FATIGUE BEHAVIOR OF CARBON FIBER REINFORCED PLASTICS DUE TO MICRO-DAMAGE AND EFFECTS OF THE MICRO-DAMAGE ON THE PLY STRENGTHS IN THE VERY HIGH CYCLE FATIGUE REGIME</b> .....	374
Ch. Hopmann, J. Marder, F. Becker	
 <b><u>APPLICATION</u></b>	
<b>PROBABILISTIC MODEL FOR VHCF DATA ASSESSMENT (INVITED)</b> .....	381
A. Fernández Canteli, M. Muniz Calvente, P. Brita, E. Castillo	
<b>STOCHASTIC MODELS FOR THE FATIGUE LIFETIME OF PARTICLE- OR FIBRE-REINFORCED METAL MATRIX COMPOSITES IN THE VHCF REGIME AND RELATED STATISTICAL METHODS</b> .....	382
M. Baaske, F. Ballani	
<b>EVALUATION OF MULTIPLE-FLAW FAILURE OF BEARING STEEL 52100 IN THE VHCF REGIME AND DESCRIPTION OF THE SINGLE-FLAW BEHAVIOUR</b> ....	388
K. Burkart, B. Clausen, H.-W. Zoch	
<b>DEVELOPMENT OF A PROBABILISTIC MODEL FOR THE PREDICTION OF FATIGUE LIFE IN THE VERY HIGH CYCLE FATIGUE (VHCF) RANGE BASED ON MICROSTRUCTURAL PROPERTIES</b> .....	394
M. Zimmermann, A. Kolyshkin, E. Kaufmann, H.-J. Christ	
<b>INCREMENTAL DAMAGE CALCULATION FOR VHCF UNDER NONPROPORTIONAL MULTIAXIAL LOADING</b> .....	400
M.A. Meggiolaro, J.T.P. Castro, H. Wu	
<b>ULTRASONIC VHCF TESTS ON AISI H13 STEEL WITH TWO DIFFERENT INCLUSION CONTENT: ASSESSMENT OF SIZE EFFECTS WITH GAUSSIAN SPECIMENS</b> .....	406
A. Tridello, D.S. Paolino, G. Chiandussi, M. Rossetto	
<b>INTRINSIC DISSIPATION ASSESSMENT DURING VERY HIGH CYCLE FATIGUE TESTS ON PURE COPPER</b> .....	412
S. Yang, N. Ranc, E. Monteiro, J. Dirrenberger	
<b>SIMULATION OF DAMAGE BEHAVIOR IN GFRPS IN THE VERY HIGH CYCLE REGIME</b> .....	418
H. Madhusoodanan, E.L. Jansen, R. Rolfes	



<b>MODELLING STRATEGY FOR MICROCRACKING IN OFF-AXIS PLIES IN CFRP-LAMINATES UNDER MONOTONIC AND FATIGUE LOADING UP TO THE VHCF-REGIME</b> .....	424
G. Just, I. Koch, C. Leopold, M. Gude, B. Fiedler	

<b>STRESS LEVEL INFLUENCE ON VHCF REGIME FOR IN-SERVICE FAILED TITANIUM BLADES</b> .....	430
A.A. Shanyavskiy, A. Nikitin, M. Soldatenkova	

## **MATERIALS DATABASES AND ITS APPLICATION AND NUMERICAL MODELLING**

<b>EXPANSION OF JSMS DATABASE ON FATIGUE STRENGTH OF METALLIC MATERIALS AS TO INCLUDE VHCF DATA (INVITED)</b> .....	437
T. Sakai, A. Sakaida, A. Ueno, K. Okada, Y. Nakamura, K. Hanaki, K. Mukoyama, N. Oguma, T. Nakamura, T. Matsumura, M. Nakagawa, H. Oguma, Y. Shimamura	

<b>SIMULATION OF THE CYCLIC DEFORMATION BEHAVIOR OF AUSTENITIC STAINLESS STEELS BELOW THE VHCF STRENGTH</b> .....	446
P.-M. Hilgendorff, A. Grigorescu, M. Zimmermann, C.-P. Fritzen, H.-J. Christ	

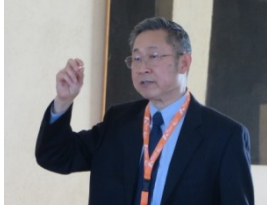
<b>ELASTIC-PLASTIC SIMULATIONS ON CRACK CLOSURE BEHAVIOR IN VHCF REGIME</b> .....	452
C. Stäcker, M. Sander	

<b>ASSESSMENT OF A LOCAL STRESS-STRAIN BASED FATIGUE CRACK GROWTH MODEL IN HIGH CYCLE FATIGUE</b> .....	458
D. Bang, A. Ince	

<b>OPTIMIZATION OF A GIGACYCLIC TORSIONAL FATIGUE SYSTEM FOR HIGH STRENGTH MATERIALS TESTING</b> .....	468
J. Petit, Z. Jiang, O. Polit	



# **Plenary Lectures**



## **Youshi Hong**

Youshi Hong is a Professor of the Institute of Mechanics (IMECH), Chinese Academy of Sciences (CAS). He was the Director of IMECH-CAS between 1998 and 2006. He is Editor-in-Chief for “Fatigue & Fracture of Engineering Materials & Structures (FFEMS)”; and Associate Editor-in-Chief for “Science China – Physics, Mechanics & Astronomy”.

His research fields are mechanical behavior of materials, fracture mechanics and structure mechanics. His main research achievements are related to: high-cycle and very-high-cycle fatigue behavior of metallic materials; effects of second phase particles on deformation, fracture and stress corrosion cracking of steels; analyses of stress intensity factors and plastic zone sizes for notch-cracks and fatigue crack growth from a circular notch under biaxial stress; mechanism and modeling of collective damage evolution process of initiation and propagation for short fatigue cracks; and mechanical behavior of submicron/nanometer crystalline metallic materials. He has published 290 papers in academic journals and conference proceedings, and has obtained 13 Chinese patents. He received a First Grade Award of Natural Science of CAS in 1996, and received a National Second Grade Award of Natural Science in 2013.

### **EFFECTS OF SURFACE DEFECTS/NOTCHES ON VERY-HIGH-CYCLE FATIGUE BEHAVIOR OF A STRUCTURAL STEEL**

**Y. Hong**, Q. Jiang, C. Sun

LNM, Institute of Mechanics, Chinese Academy of Sciences, Beijing, China

Surface defects/notches of materials have remarkable influence on the behavior of crack initiation and early growth for very-high-cycle fatigue (VHCF). Thus, the mechanism of crack initiation and early growth for VHCF induced by surface defects/notches is an important topic requiring further research. In this paper, we performed fatigue tests with rotary bending method on specimens with different types of surface defects/notches for a structural steel, such that to investigate the effects of surface defects/notches on the behavior of crack initiation and early growth for VHCF. The S-N data show the degradation of fatigue strength due to the existence of surface defects/notches, which is described by relevant models. The observations via SEM and TEM on the region of crack initiation and early growth demonstrate the detailed microstructure morphologies and selected area X-ray diffraction patterns, which reveal the micro-mechanism of crack initiation and early growth for VHCF with the effects of surface defects/notches. The results are compared with the case without surface defects/notches.



### **J. Wayne Jones**

Arthur F. Thurnau Professor  
Department of Materials Science and Engineering, College of Engineering  
University of Michigan

J. Wayne Jones, Arthur F. Thurnau Professor, professor of Materials Science and Engineering, College of Engineering. Jones received a BS degree in engineering physics from Western Kentucky University in 1971 and a PhD in materials science from Vanderbilt University in 1977. He joined the UM faculty in 1978. He was named a Thurnau Professor in 2004. His research has focused on understanding structure-mechanical property relationships in advanced metal alloys for automotive and aerospace applications. He has published widely on the mechanisms of materials degradation associated with cyclic stressing and high temperature exposure in automotive and aerospace materials. He is noted for research on the application of ultrasonic fatigue techniques to the study of damage mechanisms in the very high cycle fatigue regime. He served as Associate Dean for Undergraduate Education in the College of Engineering from 1996 to 2001 and as interim chair of MSE in 1992. From 2008 to 2013 he was associate director of the ADVANCE Program at UM. He has served on the boards of directors of professional materials societies and in 1999 he served as the president of The Minerals, Metals and Materials Society (TMS). He was elected a fellow of ASM International in 2000. He received the College of Engineering's 1938E award in 1983 and the UM's Harold H. Johnson Diversity Award in 2007. In 2010 he received ASM International's Alfred Easton White Distinguished Teacher Award, the society's highest honor for materials science teaching excellence.

## **FROM DEFECTS TO MICROSTRUCTURE NEIGHBORHOODS: A REVIEW OF ULTRASONIC FATIGUE STUDIES AT THE UNIVERSITY OF MICHIGAN**

**W. Jones**<sup>1</sup>, J. Allison<sup>1</sup>, T. Pollock<sup>2</sup>, Torbet<sup>2</sup>, S. Daly<sup>3</sup>

<sup>1</sup>University of Michigan, Department of Materials Science and Engineering - Ann Arbor, United States

<sup>2</sup>University of California Santa Barbara, Materials Department - Santa Barbara, United States

<sup>3</sup>University of California Santa Barbara, Mechanical Engineering - Santa Barbara, United States

Fatigue lifetimes in the very high cycle fatigue (VHCF) regime are controlled by fatigue crack initiation and, in some cases, small fatigue crack growth behavior. A fundamental aspect of this behavior is that a hierarchy of microstructure features can be identified that directly influences fatigue life through their influence on initiation and small fatigue crack growth behavior. In many commercial alloys features such as porosity or inclusions are critical. In other advanced alloys where such features are minimized microstructural variability and the characteristics of specific microstructural neighborhoods become the dominant influence on fatigue life. This presentation reviews research over the past fifteen years at the University of Michigan that has used ultrasonic fatigue methodologies to investigate the influence of microstructure on fatigue behavior in the VHCF regime for a wide range of structural alloys. Alloys examined using ultrasonic fatigue include cast aluminum alloys, wrought magnesium alloys, titanium alloys and nickel base superalloys. Emphasis will be placed on how the research findings from this broad range of alloys can inform alloy design and fatigue life prediction.



## Thierry Palin-Luc

Company: Arts et Metiers ParisTech

Affiliation: Institute of Mechanics and Mechanical Engineering

Responsibilities and Research Interests:

Deputy Director of the Institute of Mechanics and Mechanical Engineering (I2M) in Bordeaux

Research interests:

-Multiaxial fatigue of materials and structures both in LCF, HCF and VHCF regime with a special interest in VHCF.

-Relation between fatigue strength of components and manufacturing process. Transferability of fatigue

data from the lab to real component

Publications, seminars:

Thierry Palin-Luc is the author or co-authors of more than 40 papers in international journals and more than 70 communications in international conferences, 3 chapters of books.

Awards:

1997: Best PhD thesis in Mechanics by the French Society for Mechanics

## FATIGUE BEHAVIOR OF TWO-PHASE TITANIUM ALLOYS IN VHCF REGIME

**A. Nikitin**<sup>1,2</sup>, A. Shanyavskiy<sup>2,3</sup>, T. Palin-Luc<sup>4</sup>

<sup>1</sup>ICAD-Russian Academy of Science, Moscow, Russia

<sup>2</sup>MAI – National Research University, Moscow, Russia

<sup>3</sup>Aviaregister, Moscow, Russia

<sup>4</sup>Arts et Metiers ParisTech Institute of Mechanics and Mechanical Engineering, Talence Cedex, France

This paper is focused on the problem of crack initiation in two-phase titanium alloy VT3-1 (similar to Ti-6Al-4V) under different loading types including tension-compression, tension-tension and torsion. Fatigue tests were performed on this Ti-alloy produced by two different techniques: forging and extrusion. All the tests were carried out on ultrasonic fatigue testing machine [1] working at 20 kHz in continuous regime with constant amplitude loading. The 'run out' limit for all the fatigue tests was not less than  $10^9$  cycles. After the fatigue test all the broken specimens were observed by scanning electron microscopy (SEM).

It was found that both (forged and extruded) materials show a permanent decreasing of the fatigue strength versus the number of cycles. It was reported as for axial loading [2, 3] as well for torsion loads [2, 4, 5]. However, the crack initiation mechanisms are not the same for forged and extruded titanium alloy. In the case of axial tests on forged VT3-1 the fatigue crack can initiate as from agglomeration of alpha-platelets, as well from individual alpha-platelet. Moreover, borders of macroscopically large microstructural elements with similarly orientated alpha-platelets ('macro-zones') have a significant influence on crack initiation mechanism in the forged alloy. In the case of extruded VT3-1 the critical feature of microstructure is an agglomeration of alpha-platelets.

The study of the mean stress effect on the VHCF behavior of VT3-1 has shown an important influence of macroscopically large microstructural element borders on crack initiation mechanism. The presence of large microstructural elements reduces the VHCF resistance of the forged Ti-alloy. The extruded material does not exhibit 'macro-zones' and the mean normal stress effect on its fatigue strength can be estimated by using Gerber's parabola.

Axial tensile results were compared with ultrasonic torsion results in order to investigate an effect of the loading type on the VHCF behavior and crack initiation mechanisms in forged and extruded VT3-1. Some similarities in crack initiation and propagation scenarios were outlined between tensile and torsion loads.

# FATIGUE BEHAVIOR OF TWO-PHASE TITANIUM ALLOY IN VHCF REGIME

A. Nikitin <sup>1,2)</sup>, A. Shanyavskiy <sup>3)</sup>, T. Palin-Luc <sup>4)</sup>

<sup>1)</sup> MAI – National Research University, Volokolamskoe, 4, Moscow, Russia

<sup>2)</sup> ICAD, 2<sup>nd</sup> Brestskaya, 18/19, Moscow, Russia

<sup>3)</sup> Aviation Register, Sheremetievo-1, PO Box 54, Chimlovskiy state, Russia

<sup>4)</sup> Arts et Metiers ParisTech, I2M, CNRS, Esplanade des Arts et Metiers, Talence, France

## ABSTRACT

This paper is focused on fatigue crack initiation and early growth in two-phase titanium alloy VT3-1 (similar to Ti-6Al-4V) under VHCF loads. The material was produced by two different processes: forging and extrusion. Each kind of material was investigated under three different loading types (push-pull, pull-pull and fully reversed torsion). Fracture surfaces of the tested specimens were analyzed by scanning electron microscopy (SEM) for getting information on crack initiation sites and surrounded fracture surface zones. The results of such analysis were compared with microstructure of the titanium alloy for establishing a crack initiation and early crack growth mechanisms. It was found that crack initiation in this alloy is caused by single or an agglomeration (“cluster”) of alpha-platelets. Under fully reversed tension the fatigue life seems to depend on the geometry of alpha-platelets clusters whereas under tension loading such dependence was not observed. However, materials with larger alpha-platelets clusters (macro-zones) have a lower VHCF resistance. The comparison of tension and torsion VHCF test results show a higher slope of the S-N curve under torsion than under tension for both forged and extruded titanium alloys. Nonetheless, some similarities in crack initiation and propagation scenarios were outlined between tension and torsion loadings.

## KEYWORDS

Crack initiation mechanism, Ultrasonic torsion, Titanium alloy, Microstructure

## INTRODUCTION

The problem of fatigue resistance in aeronautic industry is very important [1]. Some elements of turbojet engine can experience many cyclic loads at high frequency (vibrations) [2]. Acting for a long time they could load the material in the gigacycle regime. The problem of VHCF resistance of structural aeronautic materials is not a simple task due to complex interaction between VHCF strength of materials and their microstructure. As it is well known, crack initiation in gigacycle regime is related to the accumulation of micro-plasticity at microstructural defects [3]. The aeronautic titanium alloys are typically assumed as defect free materials. Nonetheless, it was experimentally shown that subsurface crack initiation may occur in such materials after  $10^8$  cycles or more [4]. The crack initiation in this case is related to microstructural features of the alloy such as individual alpha-platelets or its agglomeration (“clusters”). The analysis of fracture surfaces in titanium alloys has shows that a more common mechanism of subsurface crack initiation is faceted fracture [5]. Regardless that many research groups have observed fractured facets in titanium alloys [5-10] a common explanation for its formation is still under discussion. This is also due to the fact that morphologies of fracture facets are different. Some authors have observed single fractured

facet at the crack initiation site [9, 11] while others show multi facets fracture [5]. Sometimes the fractured facet exhibits a perfectly smooth fracture plane while sometimes a kind of relief can be observed on fractured facet surface [5]. These different features of facet morphology lead to different interpretation of crack initiation mechanisms. The flat facet formation is supposed to be due to cleavage or quasi-cleavage fracture of alpha grains that is similar to the mechanism observed in HCF regime [12]. The quasi-cleavage fracture is explaining by high strain incompatibility between phases in two phase titanium alloys. The rough morphology of facets is formed due to cyclic slip activity within alpha grains [11, 12]. It is important to note that there is no information about the material (i.e. the phase) where both smooth and rough facet formations were found. Therefore a technological process could affect dominant crack initiation mechanisms. In order to study a possible effect of production process the material for present tests was obtained by two different procedures: forging and extrusion. Addition of titanium alloy to fractured surface crack and strain incompatibility could also lead to unusual fatigue behavior under mean stress [12, 13]. In order to study the effect of mean stress in the VHCF regime, some tests on the VT3-1 titanium alloy were performed with two different loading ratios. Moreover, there are just a few results on the same titanium alloy subjected to different loading types. In practice some components of turbojet engine, such as blades, could experience different loadings types and R ratios. For example the blade can be subjected to high frequency vibration superimposed on static centrifuge force leading to positive loading ratio. Another possible loading type is torsion due to non uniform and not stationary distribution of air pressure on the blade. Therefore, the study of loading type and R ratio on fatigue crack initiation and early growth in aeronautic titanium alloy is an important problem. This paper is focused on the investigation of the fatigue strength of a two-phase titanium alloy in VHCF regime under different loading types and R ratios.

## MATERIAL, EXPERIMENTAL PROCEDURE AND RESULTS

### Material

The investigated material is the alpha-beta titanium alloy, VT3-1, that is commonly used for aeronautic applications in Russia. Its standard chemical composition is presented in Table 1. The main alloying elements are aluminum, molybdenum and chromium.

Table 1: Chemical composition of VT3-1 titanium alloy (%w)

Fe	C	Si	Cr	Mo	N	Al	Zr	O	H
0.2 - 0.7	< 0.1	0.15 - 0.4	0.8 - 2	2 - 3	< 0.05	5.5 - 7	< 0.5	< 0.15	< 0.015

For this study, the VT3-1 titanium alloy was produced by two different technological processes: forging and extrusion. The forged VT3-1 specimens were machined from a real compressor disk of the turbojet engine D30 that is usually installed on Tupolev 154 aircraft. The disk was in service on a Tu-154 aircraft for 6,000 flights before VHCF tests. This period is a regular lifetime for such elements guaranteed by the company. After the in-service the turbine disk was replaced by a new one and subjected to non-destructive analysis for fatigue crack detection. No notable degradation of the material (fatigue cracks, localized plasticity or defectiveness) was detected after these 6,000 flights. The extruded titanium alloy was produced as cylindrical bars with an external diameter of 10 mm. Extruded titanium alloy was treated for having a needle like microstructure that was similar to the forged VT3-1 alloy. The microstructures of both forged and extruded VT3-1 titanium alloys are illustrated in fig. 1.



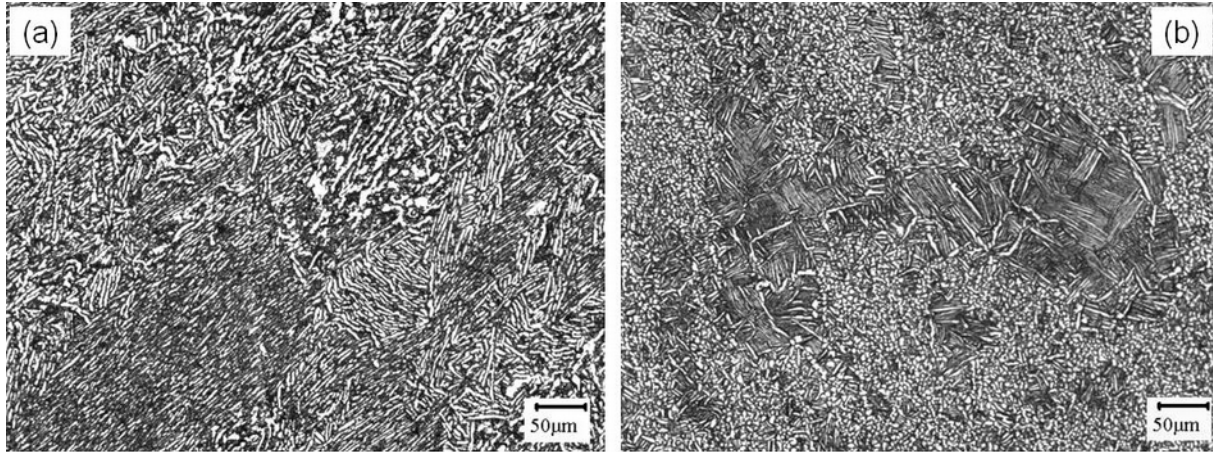


Fig.1: Microstructure of (a) forged and (b) extruded VT3-1 titanium alloys after etching.

The microstructure of these titanium alloys contains elongated alpha-platelets separated by very thin beta phase. These alpha-platelets are bigger in forged titanium alloy than in extruded one. The microhardness of extruded VT3-1 is slightly higher than the microhardness of the forged titanium alloy: 373 HV<sub>500</sub> and 364 HV<sub>500</sub> respectively.

### Test conditions and results

Fatigue tests were performed with an ultrasonic fatigue testing system at 20 kHz in laboratory air. Hourglass specimens were used for both tensile and torsion tests, details are given in [4, 7]. Fatigue tests were either stopped automatically when the resonance frequency dropped below 19.5 kHz or manually, when the fatigue life becomes greater than 10<sup>9</sup> cycles. The results of the tension fatigue tests under fully reversed loading (R=-1) for forged and extruded VT3-1 titanium alloys are shown in figure 2.

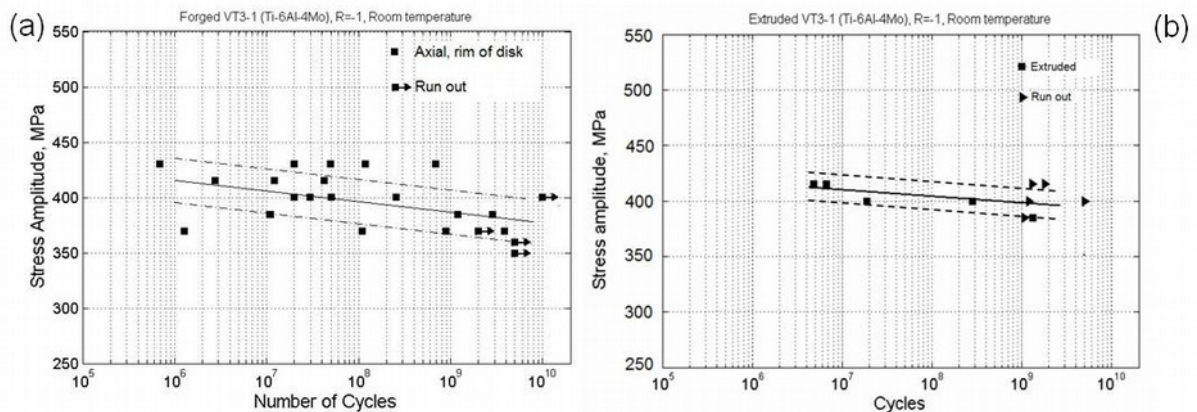


Fig. 2: Results of VHCF tests under tension (R=-1) for (a) forged and (b) extruded VT3-1 titanium alloys.

The S-N curve for the forged VT3-1 is characterized by a large scatter of fatigue life, fig.2a. Such spread of fatigue data is not uncommon for two-phase titanium alloy and was already reported for Ti-6Al-4V alloy [5, 6]. The fatigue strength of the extruded titanium alloy is slightly higher than for the forged VT3-1. However when considering the scatter of the fatigue data one can say that under fully reversed tension the fatigue strength is the same. Both S-N curves have a clear decreasing tendency. The scatter of the fatigue life is higher for forged

VT3-1 than for the other alloy. This can achieve three orders of magnitude at certain stress levels. Unlike results of push-pull tests, the results of tension tests with positive mean stress are quite different for forged and extruded titanium alloys, figure 3.

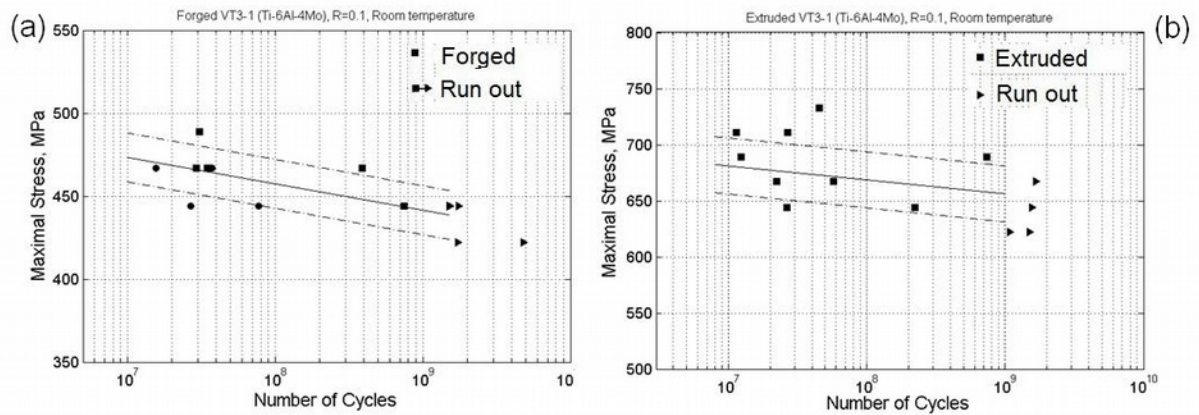


Fig. 3: Results of pull-pull VHCF tests ( $R=0.1$ ) for (a) forged and (b) extruded VT3-1 titanium alloys.

Under tension ( $R=0.1$ ), the VHCF strength of the extruded titanium alloy is higher compared to the forged one. The resistance of the forged titanium alloy against VHCF with positive mean stress is very low and cannot be correctly assessed neither by Gerber, nor Goodman models. The slope of the S-N curves is lower under tension with positive mean stress than under fully-reversed tension. However, under torsion this conclusion is not valid. Indeed, the results of torsion tests in VHCF regime, illustrated in figure 4, show the higher slope of the S-N curve between all the obtained results.

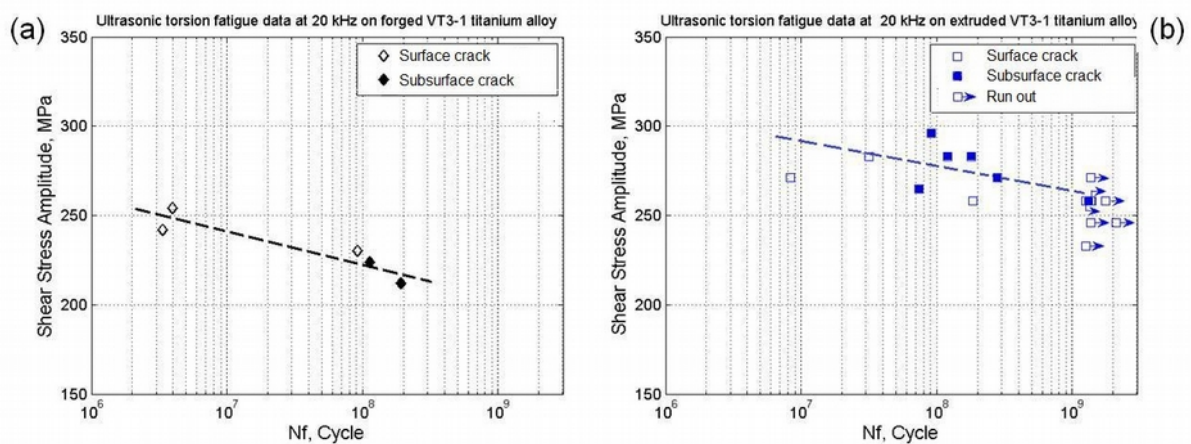


Fig. 4: Results of torsion ( $R=-1$ ) in VHCF regime for (a) forged and (b) extruded VT3-1 titanium alloys [7].

In order to compare the results of torsion and tension tests the Von-Mises equivalent stress amplitude were calculated. A similar comparison was already done in HCF regime [14]. In the case of HCF result the Von-Mises equivalent stresses gave a good agreement between tension and torsion fatigue results. In the case of VHCF these calculations gives a good agreement between tension and torsion data for the forged VT3-1. But for the extruded one the Von-Mises equivalent stress amplitudes in torsion are always higher than that under tension.



## Fracture surfaces

SEM analysis of the fracture surfaces on forged and extruded VT3-1 titanium alloy has shown subsurface crack initiation for both kinds of Ti-alloys. Moreover, subsurface crack initiation was observed for all the studied loading types including torsion. Examples of subsurface crack initiations under tension and torsion loadings are shown in figure 5.

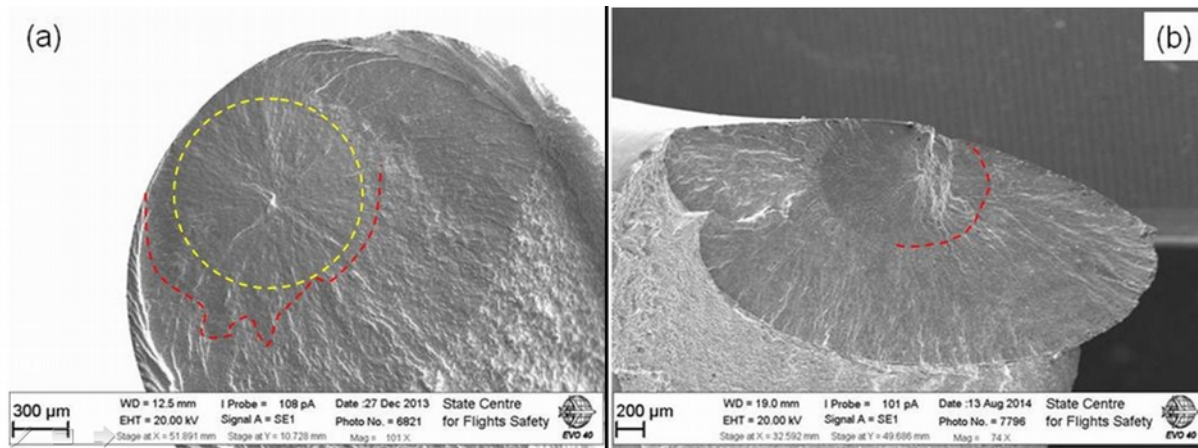


**Fig 5:** Subsurface crack initiations under (a) tension (R=-1) and (b) torsion (R=-1) loadings in VHCF regime.

Detailed analysis on crack initiation site has shown different types of subsurface crack initiation. In the case of forged titanium alloy both flat and rough fractured facets were found under tension loads. In the case of extruded VT3-1 the crack initiation is related to the fracture of alpha-phase platelets agglomeration. Therefore there is no evidence of flat facet fractures. Similar crack initiation from agglomerations of alpha-grains was observed in forged titanium alloy. However the typical size of alpha-grains within these agglomerations is different for forged and extruded alloys. In the case of extruded VT3-1 the alpha-platelets are extremely thin (less than 1 micrometer in width) while in the case of forged alloy the alpha-grains within agglomeration are large. Thin alpha-platelets are also observed in forged titanium alloy, but they mainly forms large zones (up to 1 millimeter) that are known in literature as 'macro-zones' [15]. In both cases the crack initiation site is located in the bulk of the material. At the center of the fatigue crack no inclusion was observed, but a broken microstructural element can be seen. In the case of torsion load such microstructural element is less recognizable because of fracture surface destruction due to crack lips friction (wear). The crack initiation site is surrounded by a zone that is optically darker (red dashed line on Fig.5). This zone limits a subsurface stage of fatigue crack propagation. The morphology of this zone is smoother than the relief of the next bright zone.

## DISCUSSION

The analysis of the S-N curves for the two Ti-alloys under the different loadings has shown a permanent decrease of the VHCF strength versus the number of cycles, Fig. 2 – Fig. 4. But these slopes are not the same for the different loading types. The higher slopes is under torsion. S-N curves slopes for the extruded VT3-1 are slightly lower than for the forged titanium alloy. The VHCF strength of the extruded alloy is higher than that of the forged one. This can be explained by its higher mechanical resistance under monotonic quasi-static loading: the ultimate tensile strength (UTS) of the extruded VT3-1 is 1100 MPa against 980 MPa for the forged one. Forged titanium alloy has a large scatter of fatigue life According to [8] the large scatter of fatigue life is usually observed in Ti-alloys under stress levels

corresponding to the transition in crack initiation mechanisms from surface to subsurface. In the case of VT3-1 titanium alloy the large scatter is observed for subsurface crack initiation only. All the fatigue data beyond  $10^7$  cycles, fig.2a, show subsurface crack initiations. The analysis of the fracture surfaces has shown that the morphology of subsurface crack initiation sites is quite varying. Behind fractured facets the crack initiation from alpha-grain agglomerations, 'macro-zone' borders and primary beta-phase grains were found. The crack initiation is located at different distances from the specimen surface but there is no correlation between internal location and fatigue life. Similar result was already reported for titanium alloys [9]. However, a correlation between fatigue life and crack initiation mechanism in forged VT3-1 can be outlined. It was found that internal crack initiation is caused by different features of microstructure such as agglomerations of coarse alpha-platelets, large macro-zones and single facets. The crack initiation from macro-zones borders and agglomerations lead to shorter fatigue life compared to the crack initiation from single facets. This result is well correlated with results of [10] where these authors state the fatigue life dependence from alpha-grain size. They observed that larger alpha-grain size of titanium alloy lead to shorter fatigue life. The size of agglomerations and macro-zones in forged VT3-1 is larger than single facet.

Regarding the difference of UTS it seems surprising that approximately the same VHCF strength is observed under fully-reversed tension. However, the analysis of the fracture surfaces of extruded VT3-1 has shown strong heterogeneities of microstructure (figure 6) that were always observed at the crack initiation site. These heterogeneities are agglomerations of ultra thin alpha-platelets that were formed within primary beta phase grains. The presence of such features in the microstructure of the extruded VT3-1 significantly decreases the VHCF resistance of this alloy. The microstructure of forged VT3-1 is represented by different types of alpha-platelets agglomerations from rough alpha-platelets grouped in areas about 20 – 50 micrometers to thin alpha-platelets grouped in macro-zones of several hundreds of micrometers. The high variability of agglomeration sizes and typology lead to large scatter of experimental VHCF results. In the two cases the key parameter is the type of alpha-platelets agglomeration.

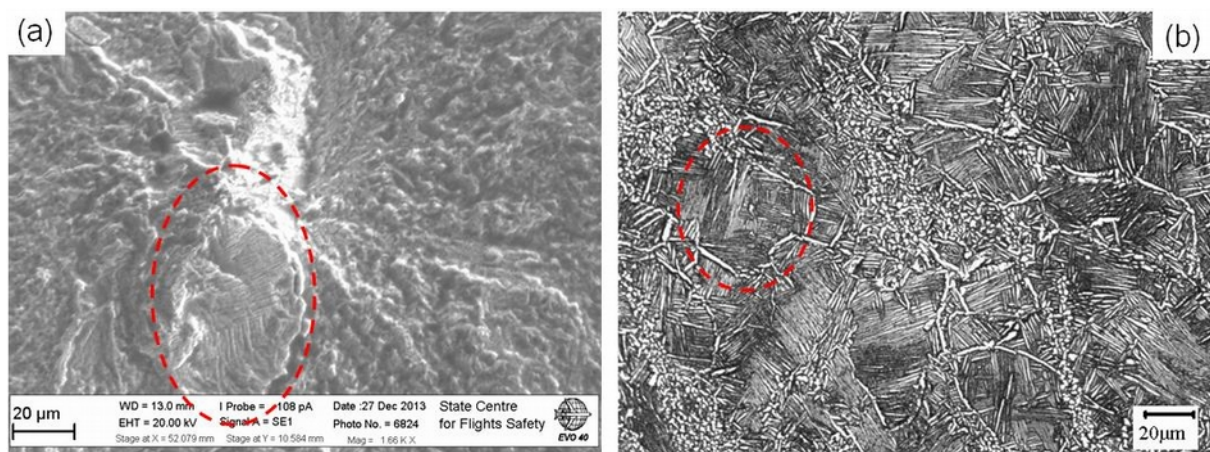


**Fig. 6:** Heterogeneity of microstructure in extruded VT3-1 titanium alloy: (a) on fracture surface after tension fatigue test in VHCF regime, (b) on micro section after polishing and etching.

Under positive mean tensile stress, the fatigue resistance of the forged titanium alloy in VHCF regime has an important drop. Similar result of stress ratio effect was also reported for forged titanium alloy Ti-6Al-4V under high cycle fatigue (HCF) loading [11]. According to [11] the experimental data for forged material were found below the Goodman line for loading

ratios from  $R=0.05$  to  $R=0.7$ . The study of the fracture surfaces has shown an important role of material texture in crack initiation. The drop of fatigue resistance under positive loading ratios is explained by cleavage of T-textured alpha grains. The experimental data for VT3-1 titanium alloy under VHCF loading were also found significantly below the Goodman line for  $R=0.1$  while the fatigue results for extruded VT3-1 alloy were found between the Gerber and Goodman lines. An important decrease of the VHCF resistance under positive static tensile force can be explained by large macro-zones that are typical for forged titanium alloy. The fatigue crack initiation sites in this case were found at the macro-zones borders. These borders are barriers for dislocation movement that lead to dislocation accumulation and consequently play the role of fatigue crack initiation trigger.

The analysis of torsion crack fracture surface has shown a significant destruction of the pattern due to crack lips wearing. This does not allow us to investigate in details the crack initiation site. Therefore it is impossible to detect fractured facets under VHCF torsion. Comparison of fracture surfaces obtained under tensile and torsion VHCF loadings has shown some similarities in patterns morphology. In both cases the fatigue crack can nucleate at the specimen surface, as well as in the bulk of the material. In the case of subsurface crack initiation several fatigue crack propagation zones can be clearly outlined. The crack initiation site is surrounded by optically darker area, Fig. 5, that has a very clear border. The darker color can be explained by smoother fracture surface morphology. The drastically change of color is observed where / when fatigue crack turns from subsurface to surface propagation, that is when the environment start to play a role in the crack growth. Typically, the developed surface crack should have a higher stress intensity factor (SIF) range. Therefore, the fracture surface morphology change is related to change in SIF range, and, consequently, in crack growth rate. The same color change was observed for crack under tension and torsion. SIF calculation at the transition line (dashed red line in Fig. 5) gives more or less the same result for both tensile and torsion fatigue cracks. Thus, based on the analysis of tension and torsion fracture surface and SIF calculations at the border transition it can be outlined some similarities in crack initiation and propagation scenarios for tension and torsion loadings in VHCF regime.

## **CONCLUSION AND PROSPECTS**

The results of VHCF tests on forged and extruded VT3-1 titanium alloy has shown that both surface and subsurface crack initiation can be observed in this alloy whatever the technological process and loading type (tension or torsion). The subsurface crack initiation in this alpha-beta titanium alloy is related to the agglomeration of alpha-platelets. The key parameters in this case are the size and typology of these agglomerations. It has been shown that the agglomeration of ultra thin alpha-platelets in extruded titanium alloy can lead to significant decrease of the VHCF resistance under fully-reversed tension. In the case of tests with positive tensile mean stress a critical parameter of the microstructure is macro-zone. The fatigue strength of forged VT3-1 titanium alloy under tension  $R=0.1$  has a significant drop (compared to the extruded one). The fatigue crack initiates at the macro-zone borders in such case. The analysis of the fracture surfaces obtained under tension and torsion VHCF loadings has shown similarities in their fracture pattern morphology with a clear transition from subsurface to surface crack propagation stages. The calculation of the SIF range at the transition crack front gives close results. These results show a similarity in crack evolution scenarios under tension and torsion loadings in VHCF regime. Other investigations should be done under higher R ratio to confirm this conclusion.

## ACKNOWLEDGEMENT

A part of this work was realized with the support of the Russian Scientific Foundation, project No. 16-19-10376.

## REFERENCES

- [1] M.R. Bache, A review of dwell sensitivity fatigue in titanium alloy: the role of microstructure, texture and operating conditions, 2003, *Int. J. Fatigue*, 25, pp. 1079 - 1087 .
- [2] A. Shanyavskiy, Very-high cycle fatigue of in-service air engine blades, compressor and turbine, *Science China*, 2014, vol. 57, issue 1, pp. 19 – 29.
- [3] C. Bathias, P.C. Paris, *Gigacycle fatigue in mechanical practice*, 2004, Dekker, New-York, 328 p.
- [4] A. Nikitin, T. Palin-Luc, A. Shanyavskiy, Crack initiation in VHCF regime on forged titanium alloy under tensile and torsion loading modes, 2016, *International Journal of Fatigue*, Vol.93, Part 2, pp. 318 – 325.
- [5] J. Everaerts, B. Verlinden, M. Wevers, Internal crack initiation in drawn Ti-6Al-4V wires, *Material science and technology*, 2016, Vol. 32, Issue 16, pp. 1639 – 1645.
- [6] Y. Furuya and E. Takeuchi, Gigacycle fatigue properties of Ti-6Al-4V alloy under tensile mean stress, 2014, *Mater. Sci. Eng. A-Struct. Mater. Prop. Microstruct. Process* pp. 598, 135-140.
- [7] A. Nikitin, T. Palin-Luc, A. Shanyavskiy, C. Bathias, Comparison of crack path in a forged and extruded aeronautical titanium alloy loaded in torsion in the gigacycle fatigue regime, 2016, *Engineering Fracture Mechanics*, Vol. 167, pp. 259 – 272.
- [8] H. Yokoyama, O. Umezawa, K. Nagai and T. Suzuki, Distribution of internal crack initiation sites in high cycle fatigue for titanium alloy, 1997, *ISIS Int.*, 37 (12), 1237 – 1244.
- [9] S.K. Jha, C.J. Szczepanski, P.J. Golden, W.J. Porter and R. John, Characterization of fatigue crack initiation facets in relation to lifetime variability in Ti-6Al-4V, *Int. J. Fatigue*, 2012, 48, pp. 248 – 257.
- [10] J. Everaerts, B. Verlinden, M. Wevers, The influence of alpha grain size on internal fatigue crack initiation in drawn Ti-6Al-4V wires, 2016, *Procedia Structural Integrity*, Vol.2, pp.1055 – 1062.
- [11] S.G. Ivanova, R.R. Biederman, R.D. Sisson, Investigation of fatigue crack initiation in Ti-6Al-4V during tensile-tensile fatigue, 2002, *Journal of Materials Engineering and Performance* 11(2) pp. 226-231.
- [12] D.F. Nael, P.A. Blenkinsop, Internal crack origin in alpha-beta titanium alloy, 1976, *Acta Metal*, 24, pp 59 – 63.
- [13] A.M. Freudenthal, New aspects of fatigue and fracture mechanics, *Engineering Fracture Mechanics*, 1974, 8 (6), pp. 775 – 93.
- [14] C. M. Sonsino, H. Kaufmann, V. Grubisic, Transferability of material data for the example of a randomly loaded truck stub axle, SAE Tech. paper series, 970708, (1997), pp. 1-22.
- [15] K. LeBiavant, S. Pommier and C. Prioul (2003) Local texture and fatigue crack initiation in Ti-6Al-4V titanium alloy, *Fatigue Fract. Engng Mater Struct.* vol.25, pp. 527-545

**Corresponding authors:** nikitin\_alex@bk.ru and thierry.palin-luc@ensam



**Frank Balle**

holds an assistant professorship for Hybrid Materials Engineering at the University of Kaiserslautern (Germany) since 2015. His main research topics are focused on research and scientific application of power ultrasonics for engineering materials, especially joining and accelerated fatigue testing of composites and hybrid joints. Furthermore he focuses on the characterization of monotonic and cyclic properties (LCF to VHCF) in cross correlation with the microstructure of light alloys and polymer-based as well as metal-matrix-composites. Balle holds a diploma in mechanical engineering (Dipl.-Ing.) and a PhD (Dr.-Ing.) in materials science and engineering. 2011 and 2012 he worked several months at the Oak Ridge National Laboratory (TN, USA) as visiting scientist in the advanced microscopy lab. He has organized several international symposia in the field of high power ultrasonics concerning ultrasonic welding and ultrasonic fatigue of advanced materials by the help of The Minerals, Metals and Materials Society (TMS, USA). Furthermore Prof. Balle is associate editor of the international journal "Ultrasonics" (Elsevier) since 2011 and guest editor of 3 special issues on ultrasonic fatigue and joining (JOM, Adv. Eng. Mat., Ultrasonics).

## **FATIGUE TESTING OF CARBON FIBER REINFORCED POLYMER COMPOSITES AT ULTRASONIC FREQUENCIES AND DAMAGE MONITORING UNDER VHCF LOADING**

**F. Balle**<sup>1</sup>, D. Backe<sup>2</sup>, D. Weibel<sup>1</sup>

<sup>1</sup>University of Kaiserslautern Institute of Materials Science and Engineering (WKK), Kaiserslautern, Germany

<sup>2</sup>PFW Aerospace GmbH, Speyer, Germany

Carbon fiber reinforced polymers (CFRP) are increasingly used for high performance applications such as aircraft structures which are often subjected to more than  $10^8$  loading cycles during their operation time of up to 30 years. To utilize the full mechanical performance of CFRP for lightweight applications, the very high cycle fatigue (VHCF) behavior has to be well understood. To realize fundamental investigations in the VHCF regime in an economic reasonable time period a novel and patented ultrasonic fatigue testing system for polymer composites was developed. This unique system enables cyclic three-point bending at a frequency of 20 kHz and experiments up to  $10^9$  loading cycles in only twelve days without unacceptable internal heating of the polymer due to alternating pulse and pause sequences and the advantages of testing in resonance. The main principle as well as the specific VHCF geometry for fatigue testing of composites at 20 kHz will be explained. All ultrasonic fatigue experiments were monitored by IR thermography, high resolution force measurements as well as displacement control via Laser Doppler Vibrometry. The VHCF behavior up to  $10^9$  cycles has been studied for two polymer composites: a carbon fiber twill 2/2 fabric reinforced polyphenylene sulfide (CF-PPS) and a carbon fiber satin fabric reinforced epoxy resin (CF-EP). Lifetime-oriented investigations showed a significant decrease of the bearable stress amplitudes of CF-PPS in the range between  $10^6$  and  $10^9$  loading cycles. Based on light optical and scanning electron microscopy the fatigue damage mechanisms of CF-PPS in the VHCF regime from first fiber-matrix debonding up to meta- and finally macro-delaminations were characterized in detail. The fatigue damage development in the specimen's volume was investigated by X-ray computed tomography as well as X-ray refraction measurements. The ultrasonically fatigued thermoset composites (CF-EP) showed a significantly different VHCF behavior in comparison to the investigated thermoplastic composites (CF-PPS): No fiber-matrix debonding or transversal cracks were present on the specimen edges, but a sudden specimen failure along with carbon fiber breakage have been observed and will be discussed during the talk at VHCF 7.



# **FATIGUE TESTING OF CARBON FIBRE REINFORCED EPOXY BASED COMPOSITES AT ULTRASONIC FREQUENCIES AND DAMAGE MONITORING UNDER VHCF LOADING**

F. Balle<sup>1)</sup>, D. Weibel<sup>1)</sup>, D. Backe<sup>2)</sup>

<sup>1)</sup> Institute of Materials Science and Engineering (WKK), Hybrid Materials Engineering Group, University of Kaiserslautern, P.O. Box 3049, 67653 Kaiserslautern (Germany)

<sup>2)</sup> PFW Aerospace GmbH, Am Neuen Rheinhafen 10, 67346 Speyer (Germany)

## **ABSTRACT**

The increasing use of carbon fibre reinforced polymers in lightweight structures which are subjected to more than  $10^8$  loading cycles leads to the demand of a precise knowledge of the fatigue behaviour and the corresponding failure mechanisms in the very high cycle fatigue range. To realise fundamental investigations in the very high cycle fatigue regime in an economic reasonable time, a novel and patented ultrasonic testing facility for polymer composites was developed. This unique system enables cyclic three-point bending tests at a frequency of 20 kHz and fatigue experiments up to  $10^9$  loading cycles in less than twelve days. To avoid critical internal heating of the fatigue specimen as well as to ensure suitable fatigue testing conditions, the experiments are performed in resonance and in pulse-pause control. Furthermore, the fatigue specimens are monitored by IR thermography, high-resolution force measurements and displacement control via Laser Doppler vibrometry. In the present work, the fatigue behaviour within the very high cycle fatigue range of carbon fibre 4-H satin fabric reinforced epoxy resin was characterised by light optical and SEM investigations during interruptions of constant amplitude tests. Lifetime-oriented investigations showed a significant decrease of the bearable stress amplitudes of the epoxy composite in the range between  $10^7$  and  $10^9$  loading cycles. Based on phenomenological investigations, two different characteristic fatigue damage mechanisms for the thermoset matrix composite could be determined.

## **KEYWORDS**

Carbon fabric reinforced epoxy, cyclic three-point bending, ultrasonic fatigue testing, polymer composites, damage evolution, failure mechanisms, VHCF of composites

## **INTRODUCTION**

To utilize the full mechanical potential of carbon fibre reinforced polymers (CFRP) for cyclically loaded lightweight applications, it is mandatory to understand the fatigue behaviour and the occurring failure mechanisms. To reach very high numbers of cycles ( $> 10^9$ ) very long test periods are necessary by the use of conventional testing systems due to their test frequencies in the range of 5 to 150 Hz for composites. Consequently, the very high cycle fatigue (VHCF) behaviour of CFRP is insufficiently characterised so far. For instance, a single VHCF experiment up to  $10^9$  cycles at a testing frequency of 5 Hz would take at least 6.3 years. At present, only a few data of the VHCF behaviour of CFRP obtained by long-term experiments with testing frequencies in the range of 0.1 to 157 Hz are available [1-4]. To avoid excessively long testing periods for fatigue investigations of CFRP, there is great potential of utilising high-frequency operating testing facilities such as ultrasonic testing facilities (UTF) for metals [5]. However, the significant increase of the testing frequency is often discussed as a criterion for



exclusion in case of high-frequency fatigue testing due to overcritical heating of the fatigue specimen. Nevertheless, first VHCF investigations of composites concerning the fatigue crack growth of glass-fibre-aluminium laminates (GLARE) have been carried out up to  $10^8$  cycles by the use of an ultrasonic resonance device working with a frequency of 21 kHz and a load ratio of  $R = 1$  [6].

To obtain comprehensive knowledge about the fatigue behaviour as well as the failure mechanisms of CFRP in the VHCF regime in an economic reasonable testing period, a novel UTF for cyclic three-point bending has been developed at the Institute of Materials Science and Engineering (WKK), University of Kaiserslautern. Regarding the concerns of overcritical heating, the feasibility of ultrasonic fatigue testing for CFRP was finally achieved by pulse-pause sequences and resonant-based testing. The UTF works with a testing frequency of 20 kHz and online monitoring by infrared thermography, high-resolution force measurements and displacement control via 1D Laser Doppler vibrometry. Further details of the used UTF are given in Ref. [7]. To validate the oscillation behaviour of the fatigue specimens as well as the load amplitudes, calibration measurements were performed by a 3D Scanning-Laser-Vibrometer (3D-SLV).

The chosen material in this present work is a carbon fibre 4-H satin fabric reinforced epoxy resin (CF-EP) with a quasi-isotropic layup. Cyclic bending tests with a constant stress amplitude were supplemented by detailed microscopy as well as the change in specimen stiffness due to VHCF loading.

## SPECIMEN, MATERIAL AND TESTING PROCEDURE

### Material and specimen design for VHCF testing

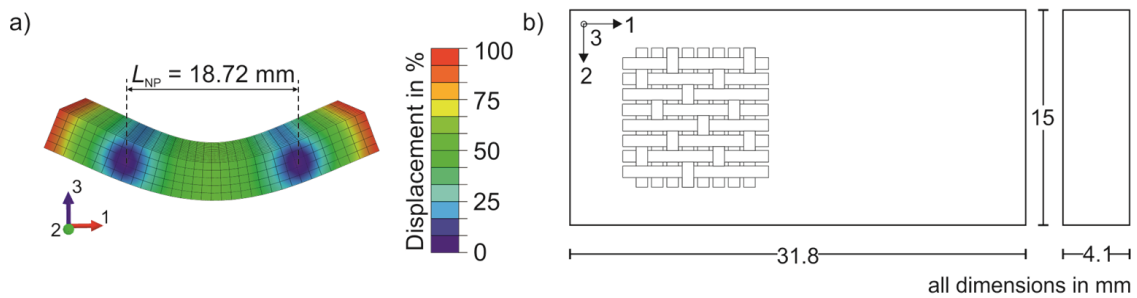
The composite investigated within this work is a commercial carbon fibre 4-H satin fabric reinforced epoxy Hexcel M18/1 prepreg, laminated and cured by Airbus Helicopters (Ottobrunn, Germany). The chosen epoxy matrix has a glass transition temperature of  $T_g \approx 196$  °C. The used 4-H satin fabric has an area weight of 200 g/m<sup>2</sup>. Selected material properties of the aircraft qualified epoxy polymer reinforced by a quasi-isotropic 16 ply layup are summarized in Table 1.

Table 1: Selected material properties of CF-EP

Fibre volume content	55 %	Young's modulus in GPa	$E_{11}$	40.0
Mass density in g/m <sup>3</sup>	1.5		$E_{22}$	40.8
Ultimate tensile strength in MPa	<i>11-dir.</i>	Shear modulus in GPa	$E_{33}$	4.5*
	<i>22-dir.</i>		$G_{12}$	15.0
Flexural strength in MPa	<i>11-dir.</i>	$G_{13}$	8.5	
	<i>22-dir.</i>	$G_{23}$	8.2	
Shear strength in MPa	<i>12-dir.</i>	Poisson's ratio	$\nu_{12}$	0.20
	<i>13-dir.</i>		$\nu_{13}$	0.05*
	<i>23-dir.</i>		$\nu_{23}$	0.05*

\* Values estimated based on literature [8] and reference material

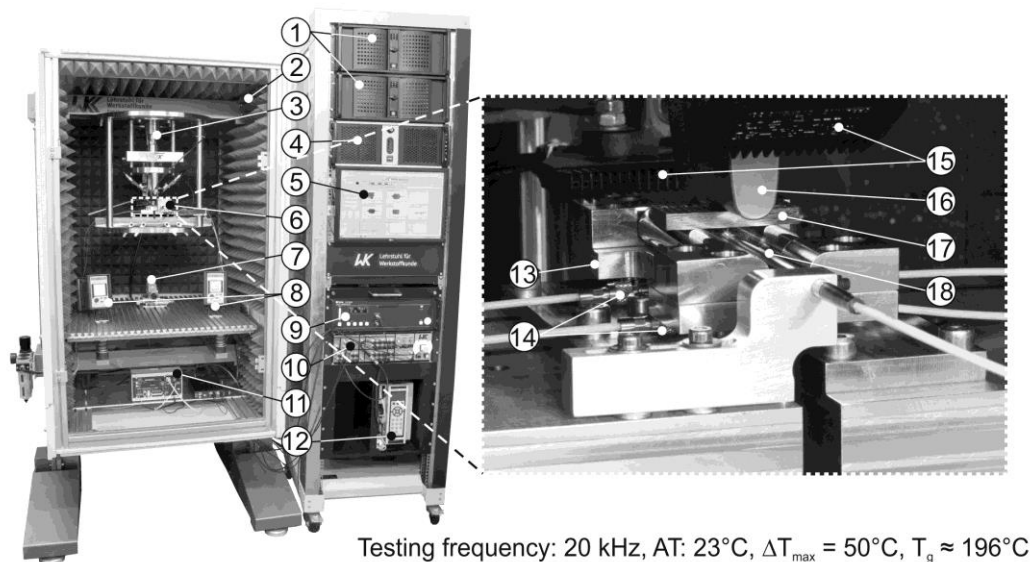
The material-specific specimen design was determined via modal analysis by fitting the frequency of its first bending eigenmode to the final testing frequency (Fig. 1a). The elastic constants required for the FEM-simulations using ABAQUS CAE were determined in a comprehensive study. Furthermore, the thickness of the CF-EP specimen was pre-set by the ply count to 4.1 mm, leaving the fit of the bending eigenmode by adjusting width and length of the CFRP specimen. The final dimensions are given in Fig. 1b.



**Fig. 1:** Specimen geometry for the investigated CF-EP: a) Simulation using ABAQUS CAE, b) Resulting specimen geometry for VHCF experiments at 20 kHz

### Testing procedure for CFRP at 20 kHz

All presented fatigue experiments have been carried out using a novel ultrasonic fatigue testing facility for cyclic three-point bending. To generate the ultrasonic mechanical oscillation, the UTF uses the inverse piezoelectric effect. As the specimen is not a friction-locked part of the testing facility, the total load of the specimen consists of a monotonic preload to ensure permanent contact between the specimen and the loading device on the one hand as well as of a superimposed cyclic oscillation on the other hand. The experiments have been arranged in pulse-pause mode to avoid critical internal heating of the CFRP specimens during the ultrasonic pulses with a frequency of 20 kHz. The resulting effective test frequency at a pulse-pause ratio of 1:20 was  $\sim 1$  kHz. Hence, the facility is capable of performing  $10^9$  loading cycles in about 12 days. Additionally, the specimens have been permanently cooled with dry compressed air. The online monitoring of the CFRP specimens was realised by 1D Laser-Doppler vibrometry, IR-thermography and piezoelectric force sensors. The setup of the patented [9] testing system is shown in Fig. 2 [10].



- |                                |                             |                                 |
|--------------------------------|-----------------------------|---------------------------------|
| 1: Real-Time-systems           | 7: LDV-sensor               | 13: Shoulders                   |
| 2: Convection chamber          | 8: Charge amplifier         | 14: Piezoelectric force sensors |
| 3: Ultrasonic resonance system | 9: LDV-controller           | 15: Specimen cooling            |
| 4: Windows-system (Host)       | 10: Junction box            | 16: Loading device              |
| 5: User interface              | 11: Controller conf. sensor | 17: CF-PPS-specimen             |
| 6: IR-thermocamera             | 12: Digital US-generator    | 18: Confocal sensor             |

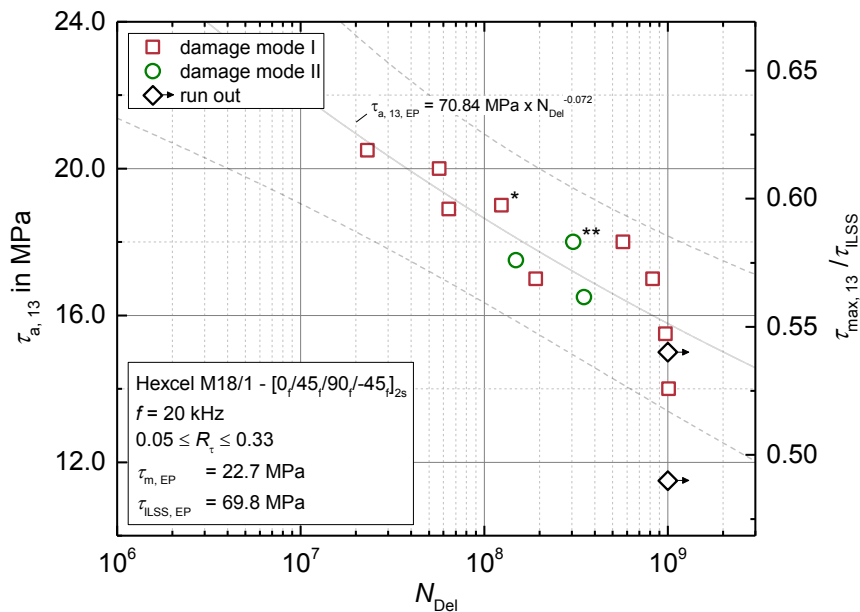
**Fig. 2:** UTF for cyclic three-point bending of CF-EP at 20 kHz testing frequency [10]

The high testing frequency as well as the data acquisition with a recording rate of 500 kHz and the online data processing required a robust process control ensured by a real time environment and a specifically developed LabVIEW procedure. Further monitoring was realised by the power-time function of the ultrasonic generator, the so called dissipated energy, the eigenfrequency of the specimen calculated based on the Laser-Doppler vibrometry data as well as the thermogram of the infrared camera. These parameters also operate as abort criteria for the VHCF experiment for predefined critical values.

## EXPERIMENTAL RESULTS

### Constant amplitude tests

The fatigue behaviour of CF-EP up to  $10^9$  loading cycles has been investigated in cyclic three-point bending tests at constant load amplitudes and a final testing frequency of 20.26 kHz. To characterise the fatigue mechanisms and the damage development microscopically, the constant amplitude tests (CAT) were supplemented by interrupted CAT. No significant difference in specimen lifetime between interrupted CAT and conventional CAT could be detected. The lifetime-oriented results of the fatigue experiments are summarized in Fig. 3. The shear stress amplitudes in 13-direction and the corresponding ratio of the maximum cyclic shear stress to the monotonic interlaminar shear strength (ILSS) are plotted versus the number of cycles to delamination  $N_{Del}$ .



The results show an exponential decrease of the bearable shear stress amplitude over the number of cycles to delamination, appropriately fitted by a power law, given in Fig. 3. A 95 % prediction interval marked by dashed lines depicts a significant variance of the measured data of CF-EP caused by the difficulties of defining consistent abort criteria and  $N_{Del}$ -criteria, respectively. The VHCF behaviour of CF-EP is characterised by two primary modes of damage: Damage mode I and II. Therefore, a suitable  $N_{Del}$ -criterion was defined either by a reconstruction of the monitoring parameters due to insufficient sensitivity of abort values or by overcritical heating and microscopic verification of macro-delaminations. Both damage modes are accordingly marked in Fig. 3. No fatigue damage was observed at the specimen's surface for the run outs at lowest cyclic amplitudes. In summary, there seems to be no infinite life for the investigated material for the applied fatigue loading conditions. Nevertheless, the fatigue shear strength for the thermoset CF-EP at  $10^9$  cycles could be determined to  $\tau_{a, 13, EP} = 15.7$  MPa corresponding to more than 50 % of the ultimate monotonic shear strength.

### Microscopic analysis of failure mechanisms for VHCF loading

For the characterisation of the fatigue failure mechanisms as well as the damage progress during VHCF loading, light optical and SEM investigations were performed. The investigations have been carried out before starting the VHCF experiment, during CAT interruptions, in case of specimen failure at  $N_{Del}$  or after reaching  $10^9$  cycles. The failure mechanisms as well as the damage development of the chosen laminate were characterised by different fatigue damage modes with either “sudden death” failure in the bottom specimen area or fatigue failure in the shear deformation dominated areas, respectively. The fatigue characteristics observed for damage mode I are shown in Fig. 4a, corresponding to the marked specimen (\*) in Fig. 3, and Fig. 4b by means of a light optical overview of the specimen's edge surface at  $N_{Del}$  as well as a SEM micrograph of an actual fracture surface.

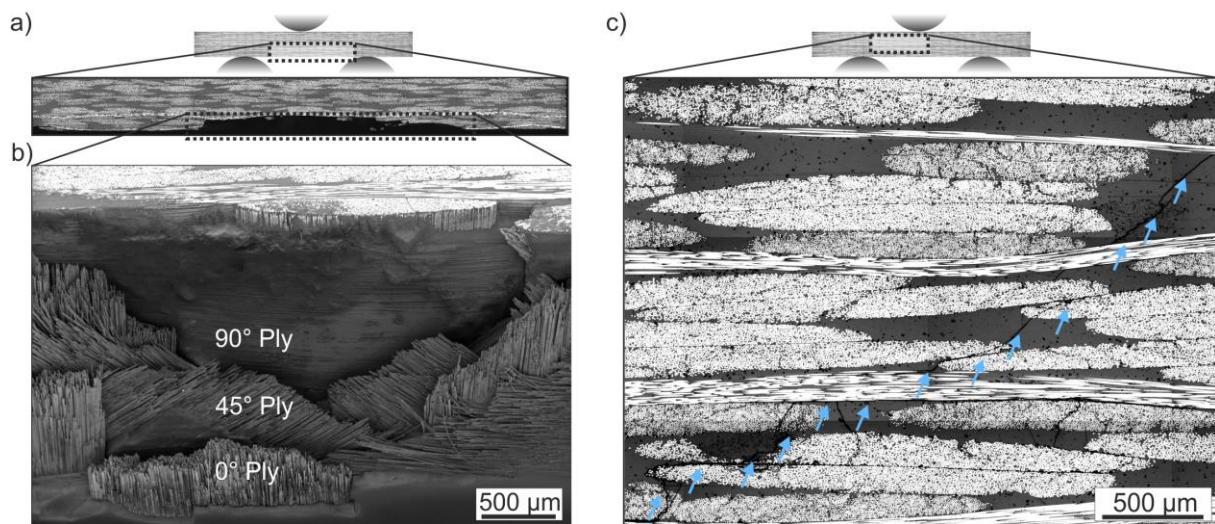


**Fig. 4:** Microscopic fatigue damage characterisation: a) Sudden fatigue failure of CF-EP – damage mode I (\*); b) Detail of delamination area (tilted micrograph); c) shear stress dominated failure – damage mode II (\*\*)

No progressive fatigue damage was determined for damage mode I, neither during CAT interruptions nor by monitoring parameters. Instead, the fatigue behaviour is characterised by a sudden specimen failure along with fracture of specimen fragments at specific areas like the bottom middle of the specimen. The damage initiation reproducibly occurs in between the 90° ply and the 45° ply, see Fig. 4b, corresponding to high local stress gradients as a result of the

layup and the applied cyclic three-point bending. Furthermore, the layup of CF-EP induces additional stresses due to the free edge effect. For damage mode II, specimen failure in terms of macro-delaminations induced by cyclic shear stresses between the loading device and the shoulder unit was determined for 25 % of the experiments with finite lifetime, also illustrated exemplarily in Fig. 4c by means of the marked specimen (\*\*\*) in Fig. 3. Damage mode II is characterised by intra- and interlaminar cracks in the areas of highest shear stresses at 45° within resin-rich regions, 90° and 45° rovings. For low and high cycle fatigue loading the corresponding fatigue-induced damage progresses nearly over the entire lifetime for CFRP starting from the first cycles. In contrast to the knowledge described in literature, the examined damage mode II for CF-EP shows similar states but starting at approx. 80 % of  $N_{Del}$  and progressing with far superior velocity. No fibre-matrix debonding was present on the specimen's edges. The fatigue damage did develop with micro-/meta-delaminations growing to macro-delaminations across several plies with a significant increase in surface temperature due to internal friction as well as the loss of specimen stiffness. Both damage modes indicate excellent fibre-matrix interface properties due to the broad absence of fibre-matrix debonding, which is confirmed by the cohesive fracture surface, see Fig. 4b. The sudden specimen failure in case of damage mode I and the fast damage progression in case of damage mode II subsequent to the fatigue induced crack initiation are indicating brittle material behaviour of the epoxy matrix in case of VHCF loading at ultrasonic frequencies.

**Stiffness degradation**

Additionally to microscopy, the stiffness degradation for several specimen has been measured ex-situ during the interrupted CATs. The measured residual stiffness values were referred to the initial stiffness  $S_0$  determined before each VHCF experiment. The normalized specimen stiffness  $S/S_0$  versus the normalized number of cycles to delamination  $N/N_{Del}$  for CF-EP is plotted in Fig. 5.

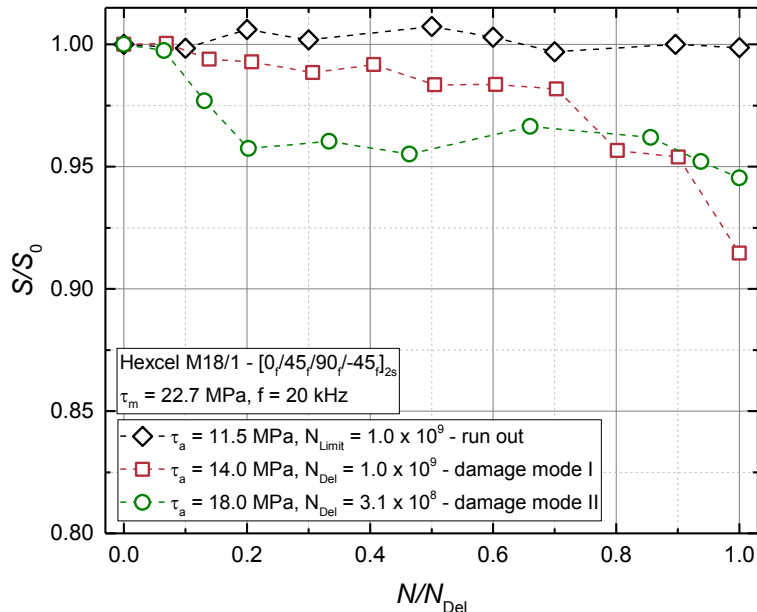


Fig. 5: Stiffness degradation vs. lifetime for selected CF-EP specimen under VHCF loading

Each data point represents the mean value out of five measurements. The standard deviation is not plotted due to high consistency within the repeated measurements. The data showed versatile stiffness degradation for the different damage modes and a run out. While the specimen with lowest shear stress amplitude reveals no considerable loss in stiffness, damage



mode I is characterised by a slight degradation of about 2 % up to 70 % of  $N_{Del}$  and a subsequent loss of another 2 – 3 % in the range of 70 % - 80 % of  $N_{Del}$  followed by the characteristic sudden specimen failure at the end of the lifetime. Damage mode II is characterised by an initial stiffness degradation of about 3.5 % up to 65 % of  $N_{Del}$  with subsequent damage progression in terms of meta delaminations starting at about 80 % of  $N_{Del}$  and followed by macro delaminations. The initial stiffness degradation is caused by a transversal crack in the bottom area of highest tensile stresses. So this kind of crack is not significant for damage mode II as it remains stable after reaching the bending induced boundary tensile stress value for further crack growth. Additionally, the transversal crack is not located in the area of shear stress induced delaminations.

## CONCLUDING REMARKS

The VHCF behaviour of a carbon fibre 4-H satin fabric reinforced epoxy resin was systematically investigated up to  $10^9$  loading cycles at a testing frequency of 20 kHz. To perform the VHCF experiments in an economically reasonable time period, a ultrasonic fatigue testing facility for cyclic three-point bending was developed and used for the investigations. Pulse and pause sequences with a ratio of 1:20 as well as permanent specimen monitoring by IR thermography ensured the reliability of the used UTF. The effective test frequency of ~1 kHz enables fatigue experiments up to  $10^9$  cycles in only 12 days. The material specific specimen design was determined via modal analysis by fitting the frequency of the first bending mode to the testing frequency. 3D scanning laser vibrometry measurements have been carried out in preparation of the experiments to confirm the calculated oscillation mode at the working frequency of 20 kHz and for analysing the exact tensile and shear strain distribution. Constant amplitude tests were performed at low shear stress amplitudes and positive stress ratios up to the ultimate number of  $10^9$  cycles. The bearable shear stress amplitudes showed an exponential decrease over the number of cycles to delamination  $N_{Del}$ . No infinite life for the investigated epoxy-based composite could be determined under the applied loading conditions. Nevertheless, a fatigue shear strength at  $10^9$  cycles for CF-EP of  $T_{a, 13, EP} = 15.7$  MPa was evaluated from lifetime-oriented investigations. The microscopic investigations of the CF-EP specimens revealed two different damage modes, characterised by sudden specimen failures in representative areas with high local stresses or by shear stress induced macro-delaminations. The analysis of the change in specimen stiffness during the interrupted VHCF tests showed a comprehensive progress with regard to the damage mode.

## ACKNOWLEDGMENTS

The authors would like to thank the German Research Foundation (DFG) for the financial support in framework of the priority program (SPP) 1466 – Infinite Life (BA 4073/2-2).

## REFERENCES

- [1] S. A. Michel, R. Kieselbach and H. J. Martens: 'Fatigue strength of carbon fibre composites up to the gigacycle regime (gigacycle-composites)', *Int. J. Fatigue*, 2006, 28, 3, 261-270.
- [2] A. Hosoi, N. Sato, Y. Kusumoto, K. Fujiwara and H. Kawada: 'High-cycle fatigue characteristics of quasi-isotropic CFRP laminates over  $10^8$  cycles (initiation and propagation of delamination considering interaction with transverse cracks)', *Int. J. Fatigue*, 2010, 32, 1, 29-36.

- [3] M. Gude, W. Hufenbach, I. Koch, R. Koschickow, K. Schulte and J. Knoll: 'Fatigue testing of carbon fibre reinforced polymers under VHCF loading', Proc. Mater. Sci., 2013, 2, 18 24.
- [4] T. K. Yoshi and T. O. Fujii: 'Stiffness reduction of woven CFRP and CFRTP spring under ultra high cyclic fatigue for vibration conveyor', Adv. Mater. Research, 2010, 123 125, 217 220.
- [5] S. Heinz, F. Balle, G. Wagner and D. Eifler: 'Innovative ultrasonic testing facility for fatigue experiments in the VHCF regime', Mater. Test., 2012, 11 12, 750 755.
- [6] M. Papakyriacou, J. Schijve and S. Stanzl-Tschegg: 'Fatigue crack growth behavior of fibre-metal laminate GLARE-1 and metal laminate 7475 with different blunt notches', Fatigue Fract. Eng. M., 1997, 20, 11, 1573 1584.
- [7] D. Backe, F. Balle and D. Eifler: 'Fatigue testing of CFRP in the very high cycle fatigue (VHCF) regime at ultrasonic frequencies', Comp. Sci. Technol., 2015, 106, 93 99.
- [8] G. W. Ehrenstein: 'Polymeric materials structure - properties – applications', 2001, Munich, Hanser.
- [9] F. Balle, D. Backe and D. Eifler: 'Prüfvorrichtung und Verfahren zur Beurteilung des Ermüdungsverhaltens eines Prüflings', Institute of Materials Science and Engineering, University of Kaiserslautern, DE 10 2012 110 811 B4 2014.12.04, 04 December 2014.
- [10] D. Backe and F. Balle: 'Ultrasonic fatigue and microstructural characterization of carbon fiber fabric reinforced polyphenylene sulfide in the very high cycle fatigue regime', Comp. Sci. Technol., 2016, 126, 115 121.
- [11] D. Backe: 'Ultraschallermüdung und Schädigungsverhalten von C-Faser-Gewebe verstärktem Polyphenylensulfid im Bereich sehr hoher Lastspielzahlen', Institute of Materials Science and Engineering, University of Kaiserslautern, Dissertation 2015.

**Corresponding author:** Frank Balle, balle@mv.uni-kl.de



**John E. Allison**

Professor of Materials Science and Engineering at The University of Michigan where he is Director of the Center for PRedictive Integrated Structural Materials Science (PRISMS). His research interests are in microstructural evolution and mechanical behavior of light alloys (Al, Mg, Ti), fatigue of metals and the myriad topics that encompass the discipline of Integrated Computational Materials Engineering (ICME). He joined the UM faculty in September 2010. Prior to that he was a Senior Technical Leader at Ford Research and Advanced Engineering, Ford Motor Company in Dearborn, Michigan, where he was employed for 27 years. At Ford he led teams developing Integrated Computational Materials Engineering (ICME) methods, advanced CAE tools and light metals technology for automotive applications. He served as Vice-Chair of the influential National Academies Study on "ICME: A Transformational Discipline for Improved Competitiveness and National Security". He has over 177 publications and 5 patents. Professor Allison received his PhD in Metallurgical Engineering and Materials Science from Carnegie-Mellon University, his MS in Metallurgical Engineering from The Ohio State University and his BS in Engineering Mechanics from the US Air Force Academy. Dr. Allison was the 2002 President of The Minerals, Metals and Materials Society (TMS) and is a member of the National Academy of Engineering, a Fellow of TMS and ASM and a past-member of the US National Materials Advisory Board.

## **PRISMS: AN INTEGRATED PREDICTIVE MULTI-SCALE CAPABILITY FOR PREDICTING VERY HIGH CYCLE FATIGUE BEHAVIOR OF METALS**

**J. Allison**

University of Michigan Materials Science and Engineering, Ann Arbor, United States

The Center for PRedictive Integrated Structural Materials Science (PRISMS) is a major Materials Genome Initiative effort creating a unique scientific framework for accelerated predictive materials science and Integrated Computational Materials Engineering (ICME). There are three key elements of this framework. This first is a suite of high performance, open-source integrated multi-scale computational tools for predicting microstructural evolution and mechanical behavior of structural metals. The second is The Materials Commons, a knowledge repository and virtual collaboration space for curating, archiving and disseminating information from experiments and computations. The third element of the PRISMS framework is set of integrated scientific "Use Cases" in which these computational methods are tightly linked with advanced experimental methods to demonstrate the ability of the PRISMS framework for improving our predictive understanding of magnesium alloys, in particular precipitate evolution and the influence of microstructure on monotonic and cyclic mechanical behavior. Developing advanced computational and experimental tools for characterizing and predicting the VHCF response of metals is an important demonstrator for the PRISMS Center. This talk will review our progress in simulating VHCF and the microstructures and tensile properties which have a significant influence on VHCF. In addition, this talk will review how the Materials Commons can be used by the global VHCF community to be more effective and contribute to the "Big Data" revolution.



**Fundamentals, physics and mechanisms**  
**Mechanisms of crack initiation**

## **INVITED**



### **Guocai Chai**

is the global group chief expert at Sandvik group and an adjunct professor in Engineering Materials at Linköping University, Sweden. His main research areas are material development and characterization, mainly focusing the correlations between microstructures and properties such as strength, deformation, toughness, fatigue and fracture, and creep, and multiscale material modeling. He graduated at University of Science and Technology, Beijing in 1982, and got PhD at Stockholm University in 1994, and then worked as a postdoc at Windsor University, Canada. He joined Sandvik in 1997, and has parallel been working as an assoc. and then adjunct professor at Linköping University from 2006. He has published more than 196 papers, two books, two monographs and three chapters/overviews in three books, and delivered more than 42 plenary, keynote and invited lectures at different international conferences. He has been awarded many patents. He is the member of the scientific committee for six international conferences. He received the Howard F. Taylor Award of the American Foundryman's Society in 1992. He was the nominee for the "Kami Prize" between 2012-2015, and the Wilhelm Haglund Medal 2015 and 2016. He is the board member of Swedish Society for Materials, the board member for Swedish steel producers' association, Jernkontoret TO 41, steel development and applications, the management committee member, MCM, of ECCC (European creep collaboration committee), and the technical advisor/expert member of the EU Research Funding for Coal and Steel – TGS6-Physical metallurgy and design of new generic steel grades. He has been invited as an international independent expert as a project reviewer for EU and other 6 countries.

## **ON THE FATIGUE CRACK INITIATION AT SUBSURFACE INCLUSION AND MATRIX**

### **G. Chai**

Sandvik Materials Technology R&D center, Sandviken, Sweden

Two types of fatigue crack initiation origins in metallic materials after very high cycle fatigue have usually been observed. One is that fatigue crack initiation starts at subsurface inclusion or defect, another is that fatigue crack initiation starts at subsurface matrix. This paper provides an analysis on the fatigue crack initiation mechanisms in a nickel base alloy and some steels using micro plasticity and material mechanics. The fatigue behaviors from damage to crack initiation for these two cases were studied. For fatigue crack initiation at subsurface inclusion, the stress concentration can cause cyclic plastic deformation near the inclusion and lead to the following two consequences: intrusion and extrusion at the internal free surface near the inclusion and the grain fragmentation. The former can lead to damage and eventually crack initiation; the later can cause the formation fine grained area. High plastic strain localization and cyclic plastic deformation will lead to dislocation annihilation and formation of vacancies or nano pores at the dislocation subcell boundary, which is early stage of fatigue crack initiation. For fatigue crack initiation at subsurface matrix, the results show that cyclic plastic deformation can occur very locally even with an applied stress that is much lower than the yield strength. Local impingement and interaction between slip bands and grain or twin boundaries can lead to the fatigue damage. The crystallographic properties, Schmid factors and orientations of grain and boundaries play very important roles to the fatigue damage. Subsurface fatigue crack initiation in the matrix is one of very high cycle fatigue mechanisms.

# INFLUENCE OF LOADING TYPE ON FRACTURE BEHAVIOR OF HIGH STRENGTH STEEL UNDER VERY HIGH CYCLE FATIGUE

Y. Sandaiji, E. Tamura  
Materials Research Laboratory, KOBE STEEL LTD, 1-5-5 Takatsukadai,  
Nishi-ku, Kobe, Hyogo, 651-2271, Japan

## ABSTRACT

In high-strength steel, inclusion-initiated fracture is known to occur in very high-cycle fatigue (VHCF) region; however, the fracture behavior under cyclic shear stress has not been elucidated yet. In this study, ultrasonic torsional fatigue test and ultrasonic axial fatigue test were performed on a high carbon chromium steel to compare the fracture behaviors. The influence of load type on VHCF characteristics was also examined. Both the torsional and axial fatigue tests resulted in fracture originated from inclusions, and an optically dark area (ODA) was observed in the vicinity of each fracture origin; however, no difference in load type was recognized in the relationship between the  $\Delta K$  value, obtained from the inclusion size and ODA size, and number of cycles. Nevertheless, there is a difference in the kind of inclusions at the origin. It has been found that, in the case of the torsional fatigue test, the inclusions elongated in the rolling direction tend to cause the fracture.

## KEYWORDS

Cyclic torsion, cyclic tension, very high cycle fatigue, bearing steel, internal fracture

## INTRODUCTION

In the VHCF regime beyond  $10^7$  cycles, fatigue cracks tend to initiate from internal non-metallic inclusions in high strength steel and numerous studies have been carried out in attempts to clarify the mechanism [1]. In the VHCF, most of fatigue life is spent on crack propagating [2], which forms characteristic fracture surface called ODA and so on, around inclusion. However, the mechanisms of internal crack initiation and the propagation are not well understood yet. It is also known that important car-engine parts, such as coil spring and bearing, is applied very high number of cyclic shear stress and sometimes the fatigue fracture, which is initiated from an inclusion, occurred. Therefore it is necessary to clarify the mechanism of the fracture under cyclic shear stress, but there is almost no study because it is difficult to conduct fatigue test beyond  $10^8 - 10^9$  cycles with conventional torsional fatigue testing machine in realistic time. Recently, a torsional-load type ultrasonic fatigue machine which can apply cyclic shear stress has been developed [3]-[4], and the study of inclusion initiated fracture under shear stress in the VHCF has started. Xue *et al.* [4] performed an ultrasonic axial fatigue test and an ultrasonic torsional fatigue test to the same high strength steel and found that the type of inclusion at the fracture origin is different, i.e. the axial load type is  $\text{CaO-Al}_2\text{O}_3$  and the torsional load type is MnS. In a previous investigation[5], crack

initiation behaviors are different depending on inclusion type, i. e. in a case of the initiation from oxide type inclusion, it propagates in a mode I manner, in a case that the crack initiates from MnS inclusion, it initiates and propagates in shear mode at first, then branches and propagates in a mode I manner. These result may mean that the influence of inclusion type is different depending on the load type. In this investigation, an ultrasonic axial fatigue test and an ultrasonic torsional fatigue test were conducted to same bearing steel and the fracture behaviors were compared to investigate the influence of loading type on fracture behavior under VHCF.

## MATERIAL AND METHOD

A high carbon chromium steel was used in this study. The chemical composition, which is based on bearing steel JIS-SUJ2, is summarized in Table 1. An ingot was melted in air to increase oxide inclusion and hot-forged to bar ( $\phi 65$ ). The material was spheroidizing annealed and rough-machined, then the heat-treated as follows; oil quenching from 1123K for 20min, then tempering at 438K for 150 min. The microstructure is martensite structure and the Vickers hardness was 698. Lots of spherical inclusion, expected oxiside inclusion, were found on the mirror-polished surface. After heat treatment, the material were machined to the specimen shape shown in Fig. 1. For torsional fatigue test, the dumbbell-shaped specimen was used as well as the hourglass-shape specimen to increase risk volume, which was applied 90% stress of maximum stress. It was  $2.85\text{mm}^3$  and  $8.71\text{mm}^3$  for the hourglass-shape specimen and the dumbbell-shape specimen respectively. The risk volume of axial fatigue specimen was  $33.7\text{mm}^3$ . These specimens were sampled as the direction of sample axis become parallel to forging direction. Every specimen was mirror-polished and given additional compression residual stress by shot-peening to prevent surface-initiation fracture. As shown in Fig. 2, the compressive residual stress in the  $45^\circ$  direction of the specimen axis was measured by X-ray diffraction from the surface to  $300\mu\text{m}$  depth with electro polishing. The compressive residual stress at the surface was about 500 MPa, this increased to about 1200MPa at  $20\mu\text{m}$  depth, and then decreased to about 125MPa at  $300\mu\text{m}$  depth.

C	Si	Mn	S	Cr	Al	N	O	Fe
0.95	0.25	0.33	0.0015	1.47	0.019	0.033	0.0048	balance

Table 1: Chemical compositions (mass%)

Torsional fatigue test as well as axial fatigue test were conducted with ultra sonic torsional fatigue test machine (Shimadzu USF-2000T) and ultrasonic axial fatigue machine (Shimadzu USF-2000) under fully reversed torsional and axial loading condition respectively and the frequency was 20kHz. The specimens were cooled with compressive dry air during testing. Cyclic loads were applied intermittently to keep the temperature of specimen under  $50^\circ\text{C}$ . Fracture surface was observed by scanning electron microscope (SEM) and optical microscope (OM). When an inclusion was found at fracture origin, the kind of inclusion was identified by energy dispersive X-ray spectroscopy (EDX). Inclusion size  $\sqrt{\text{area}_{inc}}$  and ODA size  $\sqrt{\text{area}_{ODA}}$  were calculated using actual area which is measured from SEM image and OM image using image analysis software.

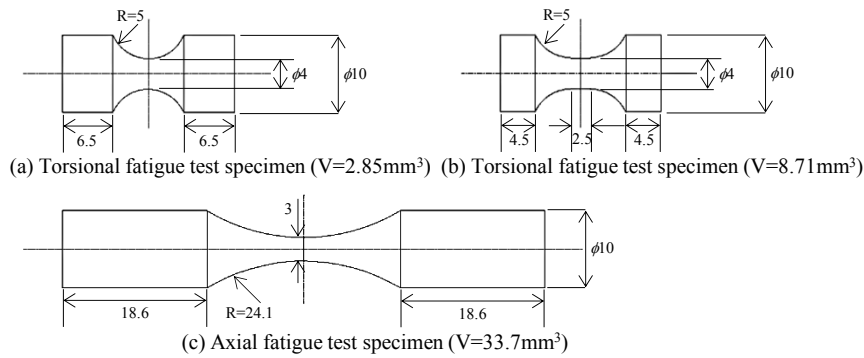


Fig. 1: Specimen shapes for ultrasonic fatigue test

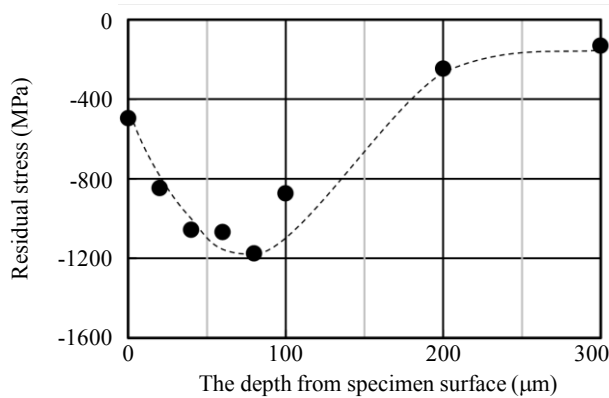


Fig. 2: Distribution of residual stress

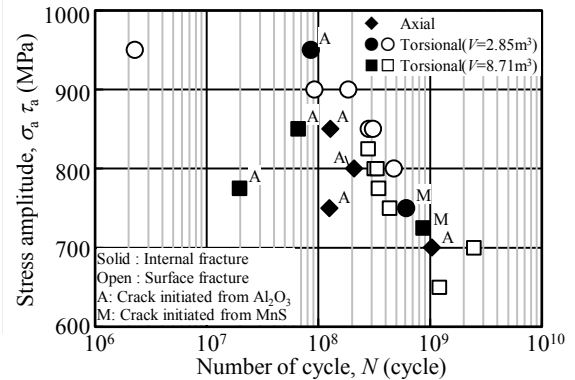


Fig. 3: Fatigue test results

## RESULTS AND DISCUSSION

Fig. 3 shows the result of fatigue tests. As the result of fracture surface observation mentioned later, open plots and solid plots mean surface fracture and internal fracture respectively. Additional note means the kind of inclusion, i. e. "A" and "M" denotes  $\text{Al}_2\text{O}_3$  type inclusion and MnS type inclusion respectively. In torsional fatigue test, the fatigue life was increased with decreasing shear stress amplitude and both of surface fracture and internal fracture were occurred. Sakanaka et al. conducted ultrasonic torsional fatigue test between  $10^5 \sim 10^9$  cycles with bearing steel without shot-peening, no internal fracture was found [3]. In this study, it is supposed that internal fracture was occurred due to increasing inclusion by air-melting and surface strengthening by shot-peening. The S-N curves of the dumbbell-shaped specimen and the hourglass-shape specimen were almost same, excluded the plot of  $\tau_a=775\text{MPa}$  around  $N=2 \times 10^7$  cycles which was fractured from huge inclusion, the influence of risk volume was not found. So since here, the results of both torsional specimen shapes were handled without distinction. On the other hand, the fatigue life of axial fatigue test was also increased with decreasing stress amplitude and only internal fractures were found.

Fig. 4 shows overview of fractured torsional specimen. Under torsional loading, the fracture surface was formed on the direction of  $45^\circ$  to specimen axis which is perpendicular to the direction of maximum principle stress, so it is considered the fatigue crack was propagated in mode I manner. Fig. 5 shows SEM images and OM images of fracture origins. An inclusion was found at all internal fracture origin and ODA was also found around inclusion, excluded the specimen fractured  $\tau_a=775\text{MPa}$  around  $N=2 \times 10^7$  cycles. When a crack propagates in shear mode, a smooth fracture surface is formed by abrasion. However no smooth fracture surface was found but the ODA was found as well as axial fatigue test. Therefore it is also

considered the crack was propagated in a manner of mode I. On the other hand, under axial loading, the fatigue crack was propagated in a manner of mode I and ODA was also found.

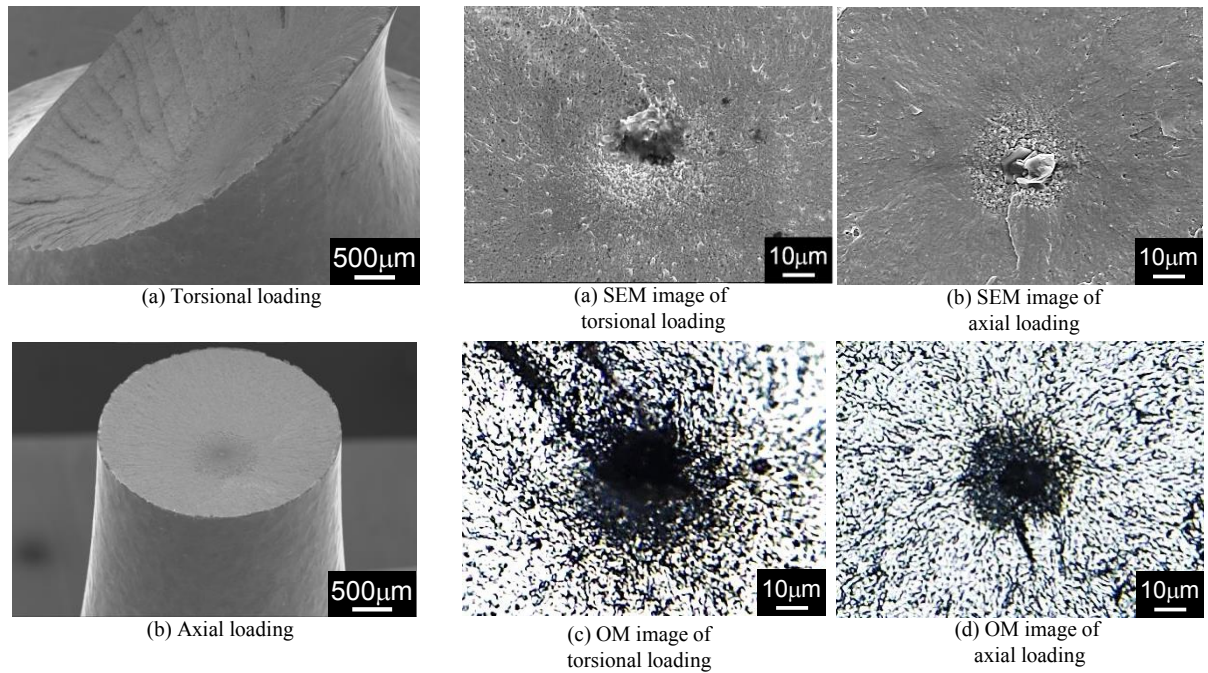


Fig. 4: Fractured surface

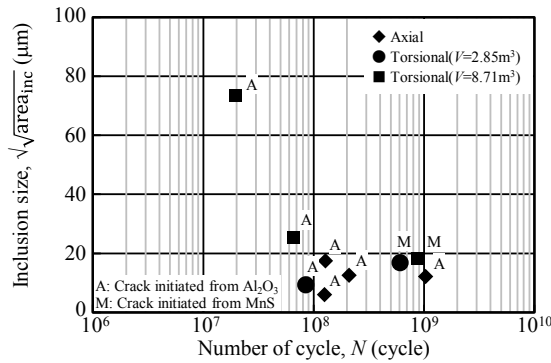


Fig. 6  $\sqrt{\text{area}_{inc}}$  and  $N$  relationship

Fig. 5: Fracture origin

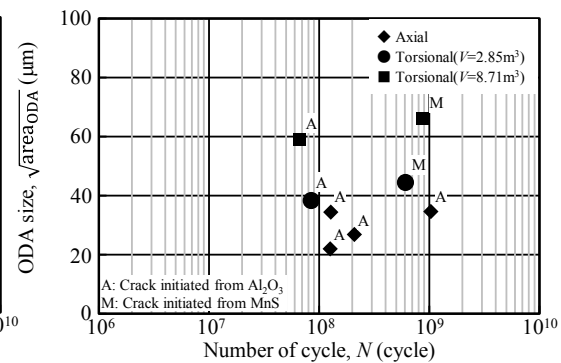


Fig. 7  $\sqrt{\text{area}_{ODA}}$  and  $N$  relationship

Fig. 6 shows the relationship between inclusion size  $\sqrt{\text{area}_{inc}}$  and number of cycles. Inclusion sizes at fracture origin were  $\sqrt{\text{area}_{inc}} = 10 \sim 80 \mu\text{m}$  for torsional fatigue test and  $\sqrt{\text{area}_{inc}} = 5 \sim 20 \mu\text{m}$  for axial fatigue test. Over  $10^8$  cycle region, there is no clear dependency between  $\sqrt{\text{area}_{inc}}$  and number of cycles. Fig. 7 shows the relationship between ODA size  $\sqrt{\text{area}_{ODA}}$  and number of cycles. The ODA sizes were  $\sqrt{\text{area}_{ODA}} = 30 \sim 60 \mu\text{m}$  and  $\sqrt{\text{area}_{ODA}} = 20 \sim 40 \mu\text{m}$  for torsional loading and axial loading respectively, but clear dependency between  $\sqrt{\text{area}_{ODA}}$  and number of cycles were not found.

As shown in Fig. 3, under axial loading, all fracture origin were  $\text{Al}_2\text{O}_3$  type inclusion, but MnS type inclusions were also found on half of fractured specimens. In previous investigation [5], it was found that a crack propagates in a manner of mode I from the beginning when it initiates from  $\text{Al}_2\text{O}_3$  type inclusions. But when a crack initiates from MnS type inclusion, it initiates in shear mode at first and it branches and propagates in a manner of mode I. In this

case the shear crack was initiated from the inside of MnS type inclusion, therefore it is supposed that the projection area of inclusion to the plane of maximum shear stress becomes larger than its to the plane of maximum principle stress then a crack was initiated in shear mode. In this study, those specimens were sampled as the direction of specimen axis became parallel to forging direction then MnS type inclusion was elongated to the direction of maximum shear stress. Therefore some MnS type inclusion became the origin under torsional loading. In contrast, under axial loading, the projection area of MnS type inclusion becomes smaller to the plane of maximum principle stress, and then the MnS type inclusion didn't become the origin.

To considering the influence of loading type to crack propagation, the relationship between number of cycle and stress intensity factor range  $\Delta K_{inc}$  and  $\Delta K_{ODA}$ , which were calculated with inclusion size and ODA size respectively, were compared. The stress intensity factor range can be calculated using Eq. (1) developed by Murakami [6]:

$$\Delta K_I = \Delta\sigma \cdot \alpha \cdot \sqrt{\pi \sqrt{area}} \quad (1)$$

where  $\Delta\sigma$  is the tensile stress range  $\alpha$  is 0.50 for internal cracks. Only tensile part of the applied stress is assumed to be effective. As mentioned above, fatigue crack was propagated by the maximum principal stress  $\sigma_{pr}$  under torsional loading, the effective stress amplitude  $\sigma_{pr,eff,a}$  was calculated as follows considering stress gradient:

$$\sigma_{pr,a} = \tau_a \quad (2)$$

$$\sigma_{pr,eff,a} = \tau_a \cdot (1 - D/R) \quad (3)$$

$\tau_a$  is maximum shear stress amplitude at specimen surface,  $D$  is the position of the fracture origin in respect to the specimen surface and  $R$  is radius of specimen.

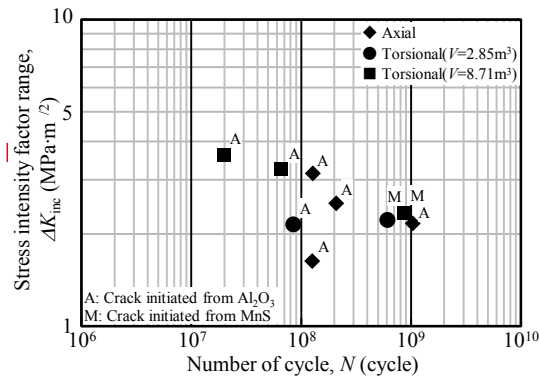


Fig. 8:  $\Delta K_{inc}$  and  $N$  relationship

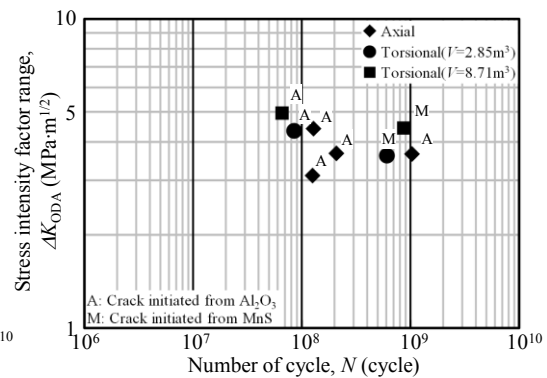


Fig. 9:  $\Delta K_{ODA}$  and  $N$  relationship

As shown in Fig. 9,  $\Delta K_{inc}$  decreased as fatigue life increased and didn't have a tendency to converge to constant at least by  $10^9$  cycles under both of axial loading and torsional loading. On the other hand, as shown in Fig. 10,  $\Delta K_{ODA}$  was about 3~5MPa $m^{1/2}$  and almost constant with respect to the fatigue life. Both relationships didn't depend on the type of inclusion. These tendencies and the  $\Delta K_{ODA}$  value agree to those observed under axial loading and previous studies [5]. Those results suggest that fatigue crack propagates in a manner of mode I forming ODA even if under torsional loading and when  $\Delta K$  reached constant value, i.e.  $\Delta K_{ODA}$ , it transits to the normal crack propagation without forming ODA.

Hence when internal crack initiates from inclusion under torsional loading, the initiation behaviour could be influenced by inclusion shape. These are two type of behaviour, in case of shear crack initiation and tensile crack initiation, and in both case, crack propagates in a manner of mode I forming ODA around inclusion and then it change the behaviour to normal crack propagation when its  $\Delta K$  reached  $\Delta K_{ODA}$ . Ishida *et al.* reported almost all fatigue life was spent to crack propagation with ODA forming. It is supposed that it is also dominant under torsional loading. Therefore it is important to obtain the material design method to prevent the crack propagation with forming ODA by clarifying the relationship between crack and microstructure. Furthermore there is still possibility that inclusion property, such as hardness or adhesion to matrix, could affect the fatigue life before crack initiation. Thus more investigation is needed to clarify the fatigue fracture mechanism under torsional loading.

## CONCLUSION

Torsional fatigue test and axial fatigue test until VHCF were conducted using ultrasonic fatigue test with same high carbon chromium steel. The following conclusions may be drawn:

- I. In case of crack initiation under torsional loading, crack initiation from elongated inclusion, such as MnS type inclusion, could be occurred as well as  $Al_2O_3$  type inclusion.
- II. Crack propagates in a manner of mode I with forming ODA at first even if under torsional loading and it transits normal crack propagation when it reaches  $\Delta K_{ODA}$ .
- III.  $\Delta K_{ODA}$  values under torsional loading and axial loading are almost same because both crack propagation could be occurred in a manner of mode I.

## REFERENCES

- [1] Y. Murakami, T. Nemoto, T. Ueda, Factors influencing the mechanism of superlong fatigue failure in steels, *Fatigue Fract. Engng. Mater. Struct.*, 22 (1999) 581-590.
- [2] W. Ishida, T. Yamamoto, S. Kaneda, T. Ogawa, Fatigue strength and internal crack growth behavior of strength steel under variable amplitude in very high cycle regime, *Trans. J. Soc. Mech. Eng. A* 78 (2012) 23-33.
- [3] N. Sakanaka, Y. Matsubara, Y. Shimamura, H. Ishii, Rapid evaluation of shear fatigue properties of rolling bearing steels for lifespans up to the Gigacycle range, *NTN Technical review* 79 (2011) 104-110.
- [4] Q. Xue, C. bathias, Crack path in torsional loading in very high cycle fatigue regime, *Eng. Fract. Mech.*, 77 (2010) 1866-1873..
- [5] Y. Sandaiji, E. Tamura, T. Tsuchida, Influence of inclusion type on internal fatigue fracture under cyclic shear stress, *Proc. Mat. Sci.*, 3 (2014) 894-899.
- [6] Y. Murakami, *Metal Fatigue: Effects of Small Defects and Nonmetallic Inclusions*, Elsevier Science Ltd. , Kidlington, Oxford, UK, 2002.

**Corresponding author:** sandaiji.yusuke@kobelco.com



# SELF-HEATING AND DISSIPATION STUDY FOR STEELS WITH DIFFERENT CARBON CONTENTS IN THE GIGACYCLE FATIGUE DOMAIN

X. Pu, I. Ranc-Darbord, J. Petit, D. Wagner

University Paris Nanterre, LEME laboratory, 50 rue de Sèvres, 92410 VILLE D'AVRAY, France

## ABSTRACT

When a plastic deformation occurs in a metallic material subjected to a mechanical loading, the major part of the provided mechanical energy is transformed into heat, which results from heat sources related to the intrinsic dissipation. In fatigue tests the first damages appearance on the specimen surface is the Persistent Slips Bands (PSB) occurrence, which has been correlated to the heat sources and dissipation for a body cubic centered  $\alpha$ -iron [1].

In this paper, tests are performed on plate specimens in the VHCF domain using piezoelectric fatigue machine working at 20 kHz on an  $\alpha$ -iron (0.008% carbon) and steels with different carbon contents (0.12 wt% for C12 steel and 0.65 wt% for C65 steel). The thermal conductivity of each material has been measured by the transient plane source method. During the fatigue tests, the temperature recording is achieved by an infrared camera. From the temperature recording, the intrinsic dissipation is calculated using a 1D expression of the heat diffusion equation, taking into account the different thermal conductivities. Observations through a Scanning Electron Microscope on the specimen fracture surfaces are related to stage I of crack initiation for each material.

## KEYWORDS

Very High Cycle Fatigue, Armco Iron, Steels, Crack Initiation, Self-heating, Conductivity, Dissipation

## INTRODUCTION

Cyclic loading in a material results into damage, crack initiation and propagation stage. These stages were studied on an  $\alpha$ -iron by C. Wang [2] in the VHCF domain using an infrared camera (IR) to record the temperature field on the specimen surface during the tests. Indeed, when the plastic deformation occurs in a metallic material subjected to a mechanical loading, the major part of the provided mechanical energy is transformed into heat which results from heat sources related to the intrinsic dissipation [1].

The objective of this study is to perform tensile and fatigue (in the VHCF domain) tests on an  $\alpha$ -iron and steels with different carbon contents (0.12 wt% and 0.65 wt%). The temperature field on the specimen surface was recorded during the tests. For the fatigue tests, the intrinsic dissipation is calculated using a 1D expression of the heat diffusion equation taking into account the different thermal conductivities of  $\alpha$ -iron and steels. Scanning Electron Microscope observations of the fracture surfaces complete the results.

## MATERIALS

The studied materials are a polycrystalline  $\alpha$ -iron and two steels. The carbon content is 0.008 wt% ( $\alpha$ -iron), 0.12 wt% (C12 steel) and 0.65 wt% (C65 steel). The microstructure is ferrite with equiaxed grains for  $\alpha$ -iron and proeutectoid ferrite-pearlite for the steels whose contents are given in Table 1. In these steels, the pearlite is lamellar and formed of alternate ferrite lamellas (88 wt%) and cementite  $\text{Fe}_3\text{C}$  lamellas (12 wt%).

Material	Proeutectoid ferrite (wt%)	Pearlite (wt%)	$k$ ( $\text{W}\cdot\text{m}^{-1}\cdot\text{K}^{-1}$ )
$\alpha$ -iron	100	0	76.9
C12	87	13	60.7
C65	16	84	42.3

**Table 1:** Proeutectoid ferrite/pearlite contents and thermal conductivity results

The thermal conductivity  $k$  of each material has been measured by the transient plane source method. The method and results details are given in [3]. Table 1 gives the obtained values for  $\alpha$ -iron and steels. In pure metals, the thermal conductivity is mainly due to the free electrons-phonons (quasi-particles coming from the lattice vibration) collisions. With the carbon content increasing, the thermal conductivity strongly decreases. This result has been attributed to the pearlite content increasing and more precisely to the cementite  $\text{Fe}_3\text{C}$  which has no free electron which modifies the electron mean free path.

## EXPERIMENTAL PROCEDURE

The tensile tests were performed at a strain rate of 10 mm/min on a mechanical tensile machine. The specimens have 1 mm thickness, 50 mm initial length and 12 mm width.

The fatigue tests were performed using a piezoelectric fatigue machine designed by C. Bathias and co-workers [4]. To facilitate the surface temperature measurements using an IR camera, a 1 mm flat specimen was used for fatigue testing [2]. The resonance system was tuned to work at 20 kHz and consisted of the specimen, special attachments and the piezoelectric fatigue machine. The cyclic loading was tension-compression at a stress ratio  $R_\sigma = -1$ . All the fatigue tests were carried out without cooling. In order to record the temperature field on their surface, the specimens were covered with a strongly emissive black paint, and the IR camera acquisition frequency was 3.75 Hz. These tests consisted of a series of cyclic loadings for the same specimen with increasing stress amplitude. For each stress amplitude, a fatigue test was carried out up to  $2.5 \times 10^7$  cycles and then interrupted. After the specimen is cooled down to the room temperature, another next loading step starts.

## EXPERIMENTAL RESULTS

### Tensile tests

Fig. 1 gives the conventional tensile curves for the 3 materials. From these uniaxial tensile tests, the tensile mechanical properties were deduced, as shown in Table. 2.

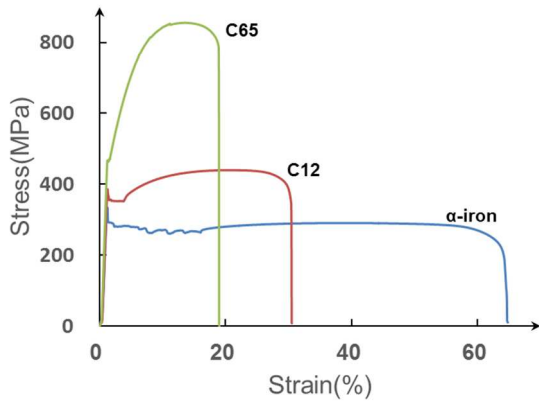


Fig. 1 Conventional tensile stress-strain curves measured for  $\alpha$ -iron, C12 and C65

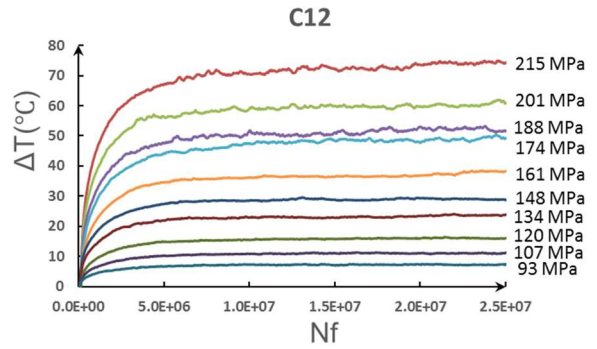


Fig. 2: Temperature evolutions during interrupted tests

Material	Lower yield stress (MPa)	Upper yield stress (MPa)	Ultimate tensile stress (MPa)	Strain at fracture (%)
$\alpha$ -iron	288	368	320	64.4
C12	357	392	446	30.5
C65	467	470	860	19

Table 2: Tensile tests results

### Fatigue tests

The temperature evolutions measured in the center of the specimen during the interrupted tests are given in Fig. 2 for the C12 steel as an example. At the beginning of the fatigue test, the temperature increases and then stabilizes. As reported previously [5], the higher the stress amplitude level, the higher the temperature on the surface.

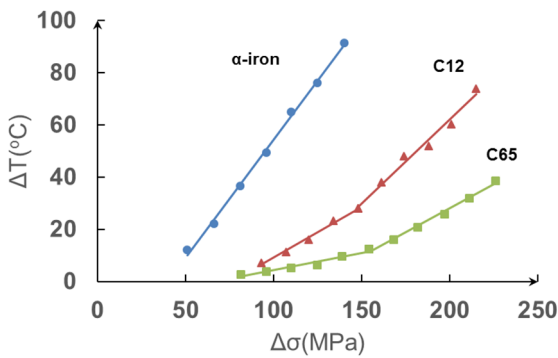


Fig. 3: Temperature evolution with stress amplitude

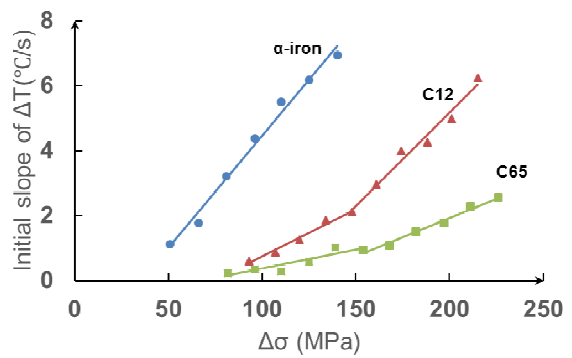


Fig. 4: The temperature slope at the beginning

Fig. 3 summarizes the evolution of the  $\Delta T$ , equal to  $T - T_0$ , with  $T_0$  initial temperature (taken at  $2.5 \times 10^7$  cycles) with the stress amplitude during interrupted tests. We can see clearly that the  $\alpha$ -iron has the strongest ability of self-heating, followed well below by C12 and C65 steels, the self-heating of C12 being higher than the C65 one. For the  $\alpha$ -iron, it seems there is only one

behavior whatever the stress amplitude, whereas for C12 and C65 steels, 2 slopes appear. Below 150 MPa of stress amplitude, the slope is lowest than above 150 MPa. In order to analyze deeply the temperature curves, we have calculated the slope of the temperature increase at the beginning (Fig. 4). As in Fig. 3, the evolution with stress amplitude of the initial slope of the temperature variation (Fig. 4) is different for  $\alpha$ -iron and steels. For  $\alpha$ -iron, the results are lined up together, whereas for the steels, 2 behaviors appear with the stress amplitude increase, and the change occurs at about 150 MPa. The slope of equilibrium stage (from  $1 \times 10^7$  cycles to  $2.5 \times 10^7$  cycles) has also been calculated. For each material, this slope is very weak or even zero and the temperature is stabilized (for these stress amplitudes).

## Scanning Electron Microscope

Fracture surface observations of the crack initiation stage are shown in Fig. 5a ( $\alpha$ -iron) and 5b (C12 steel). As previously reported [2], the crack initiation stage for  $\alpha$ -iron shows the ferrite grains trace and their size can be retrieved. Intergranular, transgranular and mixed fracture surfaces are present. Details of crack initiation mechanism (related to the Persistent Slips Bands) have been already published [6]. For the C12 (Fig. 5b, as an example) and C65, the fracture surface is flatter and the ferrite grain trace is less visible. In the identified ferrite grains, intergranular, transgranular and mixed fracture surfaces can also be noticed.

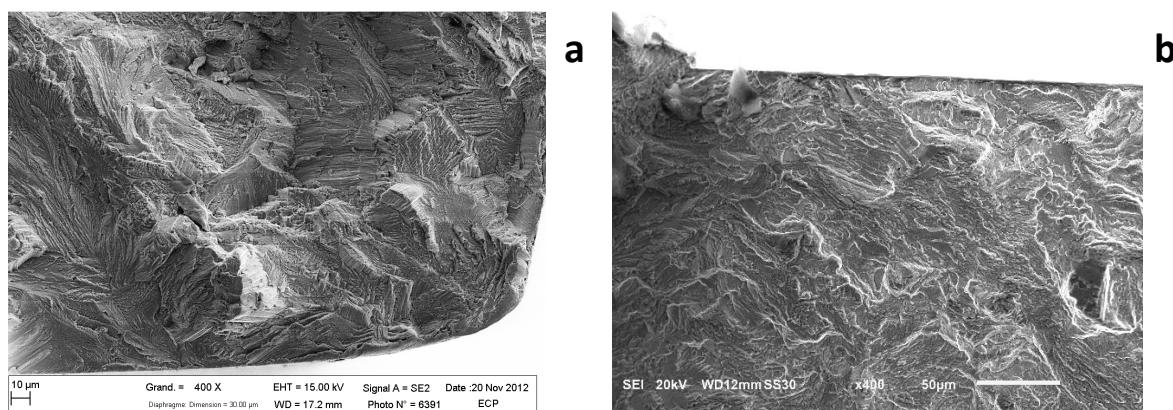


Fig. 5a) Fracture surface of  $\alpha$ -iron [2]; b) Fracture surface of C12 steel

## DISCUSSION

### Normalized results

Fig. 6 and 7 are the temperature evolution at  $2.5 \times 10^7$  cycles and the slope of the temperature increase at the beginning of the test evolution with the stress amplitude normalized by the upper yield stress  $\bar{\sigma}_{upper}$ . The results are not very different from Fig. 3 and 4. As expected, the difference between the 3 materials is reduced.

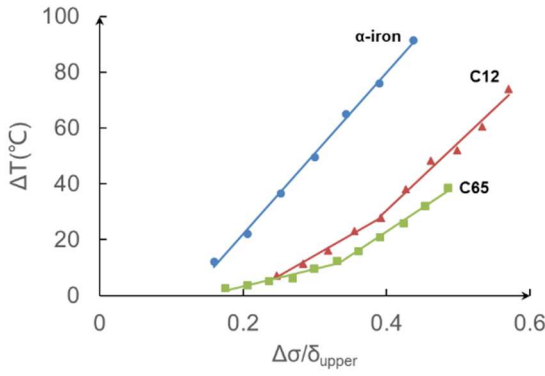


Fig. 6 Temperature evolution versus the normalized stress amplitude

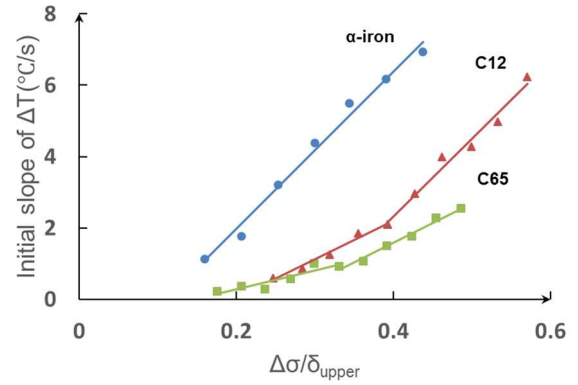


Fig. 7 Slope of the temperature increase at the beginning versus the normalized stress amplitude

### Intrinsic dissipation

The assumptions proposed by Boulanger et al. [7] are followed to estimate the intrinsic dissipation from the thermal imaging: constant thermophysical properties of material during the test, no coupling between microstructure and temperature and negligible convective terms in the particulate derivative. The heat equation is then written as:

$$\rho C \dot{T} + \text{div}(\vec{q}) = S_{the} + d_1 + r$$

where  $\rho$  is the mass density,  $C$  the specific heat,  $\dot{T}$  denotes the local temperature time derivative,  $\vec{q} = -k \overrightarrow{\text{grad}}(T)$  (with  $k$  the thermal conductivity) the conduction heat flux,  $S_{the}$  represents the thermoelastic source,  $d_1$  the intrinsic dissipation and  $r$  the external volume heat supply. The detailed calculation of  $d_1$  has been developed in [1], assuming isothermal cross-sections of the sample.

The intrinsic dissipation evolution for each material with the stress amplitude and the normalized stress amplitude are given Figs. 8 and 9. The heat sources are always higher for the  $\alpha$ -iron than for steels.

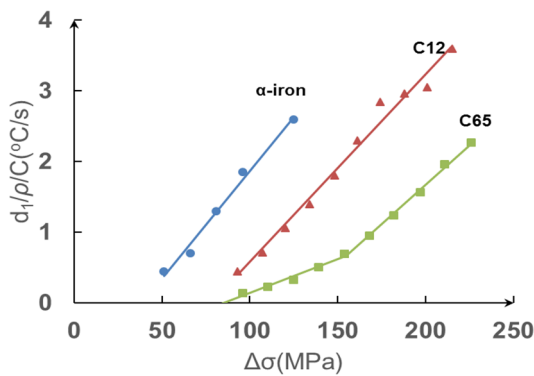


Fig. 8 Intrinsic dissipation evolution with stress amplitude

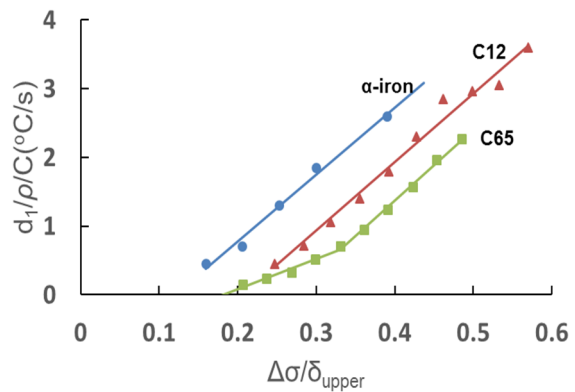


Fig. 9 Intrinsic dissipation evolution with normalized stress amplitude

## Comparison of the three materials

Two parts must be considered: on one side, the stabilized state given by the  $\Delta T$  and the  $d_1$  measured at  $2.5 \times 10^7$  cycles, and on the other side, the  $\Delta T$  initial slope at the beginning of the test.

The  $\Delta T$  (normalized or not, Fig. 3 and 6) measured at  $2.5 \times 10^7$  cycles (i.e. at the temperature stabilization), and the intrinsic dissipation  $d_1$  (Fig. 8 and 9) is much higher for  $\alpha$ -iron than for C12 and C65 steels. This behavior is firstly in relationship with the microstructure. The dislocation gliding is mainly in ferrite grains, so it is normal that the heat sources are more important for the  $\alpha$ -iron with 100% ferrite than for C12 (87% ferrite) and C65 (16% ferrite). When the percent of proeutectoid ferrite increases, more grains are correctly oriented and prone to dislocations gliding. Moreover, the more important interstitial solute contents (carbon and/or nitrogen) in C12 and C65 are obstacles to the dislocation gliding which reduce also the dissipation and the heat sources. The observations of the fracture surface by SEM show that the ferrite grains trace is less obvious in C12 (and C65) steel, but in the ferrite grains trace, intergranular, transgranular and mixed fracture surface are observed.

For  $\alpha$ -iron, the fatigue mechanism in the damage stage is governed by the transition temperature  $T_0$ . Below  $T_0$ , at low temperatures and low strains amplitudes, the screw dislocations are nearly immobile due to the increase of the thermal stress [8]. At low temperature, the activation of kinks will be absent leading to a much higher Peierls stress and less mobility. The dislocation gliding occurs mainly by the quasi-reversible gliding of edge dislocations (except on the specimen surface). Multiplication of dislocations is largely suppressed and there is no or little cyclic hardening. Above  $T_0$ , the gliding of screw dislocations increases. So, the behavior depends on the fatigue test temperature. Moreover, the temperature  $T_0$  depends on the strain rate. This  $T_0$  temperature is shifted to higher temperatures at higher strain rates. At a strain rate of  $10^{-4} \text{ s}^{-1}$ , for  $\alpha$ -iron,  $T_0$  lies around room temperature. In the VHCF domain, the strain rate is around 60-80  $\text{s}^{-1}$  for  $\alpha$ -iron and  $T_0$  will increase substantially. The dislocation behavior for the 3 materials in the VHCF regime probably corresponds to the dislocation behavior observed below  $T_0$ , with almost no cyclic hardening. Indeed, the slope of the stabilized stage (from  $1 \times 10^7$  cycles to  $2.5 \times 10^7$  cycles) is nearly zero (Fig. 2). The behavior below  $T_0$  with the gliding of only edge dislocations probably will be the behavior for the 3 materials whatever the stress amplitude. The same  $d_1$  evolution slope with the normalized stress amplitude (Fig. 9) for  $\alpha$ -iron and steels (above  $\Delta\sigma/\bar{\sigma}_{\text{upper}} = \sim 0.35$  for the C65) proves there is only one mechanism which operates. For C12, when considering  $d_1$ , the slope change disappears. Additional fatigue tests are needed at very low stress amplitudes for  $\alpha$ -iron and C12. The stress amplitude threshold for the occurrence of Persistent Slips Bands must be also studied.

At the beginning of the test (Fig. 4 and 7), the mobile dislocation rate measured by the slope of  $\Delta T$  follows the same trend as explained previously. The slope is higher for  $\alpha$ -iron, and the higher the stress amplitude, the higher the mobile dislocation rate. As reported by Mughrabi [8], the cyclic hardening for  $\alpha$ -iron which occurs is limited to the thin surface layer. The very low work hardening rate for C12 and C65 is also due to the proeutectoid ferrite content decrease which reduced the dislocation gliding.

For these levels of stress amplitude, the cyclic work hardening for these materials operates only at the beginning of the test. After  $10^7$  cycles,  $\Delta T$  is stabilized. This part of the curve

corresponds to the balance between the constant heat dissipation sources and the energy loss by conduction inside the specimen and convection and radiation at the specimen surface.

## CONCLUSION

Tensile tests and fatigue tests in the VHCF domain were performed on  $\alpha$ -iron (0.008 wt% carbon) and C12 (0.12 wt% carbon) and C65 (0.65 wt% carbon) steels. During the fatigue tests, the temperature was recorded by IR camera, allowing to calculate the intrinsic dissipation  $d_1$ .

At the beginning of the test, the initial slope of  $\Delta T$  increases with the stress amplitude for the 3 materials. The  $\Delta T$  rate is higher for  $\alpha$ -iron and reduced for the 2 steels due to the pearlite attendance.

In the stabilized domain, the  $\Delta T$  remains constant in agreement with the dislocations gliding behavior of bcc materials below the transition temperature  $T_0$ . The intrinsic dissipation balances with external exchanges, and consequently, no work hardening occurs.

## REFERENCES

- [1] Wang, C.; Blanche, A.; Wagner, D.; Chrysochoos, A.; Bathias C.:  
Dissipative and microstructural effects associated with fatigue crack initiation on an Armco iron  
Int. Journal of Fatigue, 58 (2014), pp. 152-157
- [2] Wang, C.;  
Microplasticité et dissipation en fatigue à très grand nombre de cycles du fer et de l'acier  
PhD Thesis, Paris Ouest University, juin 7, 2013
- [3] Darbord-Ranc, I.; Cedelle, J.; Wagner, D.:  
Influence de différents paramètres sur la conductivité thermique des métaux  
Com. Congrès Société française de Thermique, Toulouse, juin 2016
- [4] Bathias, C.; Paris, P. C.:  
Gigacycle Fatigue in Mechanical Practice  
Marcel Dekker publishing, New York, 2004
- [5] Wagner, D.; Ranc, N.; Bathias C.; Paris P.C.:  
Fatigue crack initiation detection by an infrared thermography method  
Fatigue & Fracture Eng. Mat. & Structures, 33 (2009), pp. 12-21
- [6] Wagner, D.; Wang C.; Huang Z.; Bathias, C.:  
Surface crack initiation mechanism for body centered cubic materials in the gigacycle domain  
Int. Journal of Fatigue, 93-2 (2016), pp. 292-300
- [7] Boulanger, T.; Chrysochoos, A.; Maru, C.; Galtier, A.:  
Calorimetric analysis of dissipative and thermoelastic effects associated with the fatigue behavior of steels  
Int. Journal of Fatigue, 26 (2004), No.3, pp. 221-229
- [8] Mughrabi, H.:  
Cyclic slip irreversibilities and the evolution of fatigue damage  
Met. Mat. Trans A, 40 (2009), No.4, pp. 1257-1279

**Corresponding author:** dwagner@u-paris10.fr

# FATIGUE CHARACTERISTICS INCLUDING VERY HIGH CYCLE REGION OF LOW ALLOY STEEL FOR SOLID TYPE CRANCSHAFT

T. Ikegami<sup>1)</sup>, R. Yakura<sup>1)</sup>, M. Matsuda<sup>1)</sup>, T. Sakai<sup>2)</sup>, A. Ueno<sup>3)</sup>

<sup>1)</sup> Steel Casting & Forging Division, Kobe Steel, Ltd.

2-3-1 Shinhamma, Arai-cho, Takasago, Hyogo, 676-8670, Japan

<sup>2)</sup> Research Organization of Science and Engineering, Ritsumeikan University, 1-1-1 Noji-higashi, Kusatsu, Shiga, 525-8577, Japan

<sup>3)</sup> College of Science and Engineering, Ritsumeikan University, 1-1-1 Noji-higashi, Kusatsu, Shiga, 525-8577, Japan

## ABSTRACT

In this study, the fatigue characteristics of the low alloy steel in the tensile strength level around 1000MPa for solid type crankshaft are investigated. The fatigue tests including very high cycle region using test specimens taken from actual size crankshaft and bar-shaped forging with different cleanliness were conducted. The fatigue fracture occurred from the surface, the inclusions in the surface and internal inclusions under the axial loading, although the fatigue fracture in the  $10^9$  cycles did not occur in this series of the tests. The relationship between the fatigue lives and the nonmetallic inclusion sizes is studied in the aspect of fracture mechanics. It is shown that the fatigue lives of fracture from surface and internal inclusions are evaluated with the inclusion size and the stress intensity factor,  $\Delta K$ . The relationship between the threshold of the stress intensity factor range,  $\Delta K_{th}$  and the nonmetallic inclusion sizes is also studied. This suggests that the fatigue strength from internal inclusions but also inclusions in the surface can be improved through controlling the nonmetallic inclusion to smaller size.

## KEYWORDS

Internal inclusion, Surface inclusion,  $\sqrt{area}$  evaluation, Fatigue strength

## INTRODUCTION

Light weight and compact size design of mechanical products are both important from viewpoints to save the global resources, to improve the energy cost performance, and to realize totally the low carbon society. This trend is also very common in the engineering application of diesel engines in the business area of the ship manufacturing.



Thus, high strength crankshaft of the diesel engine is one of the most important subjects in the ship manufacturing business.

It is well known that fatigue strength is influenced by non-metallic inclusions [1]. Fatigue strength can be improved by reducing the amount and size of non-metallic inclusions. The non-metallic inclusions are mainly sulfide and oxide, the volume fraction of sulfide and oxide depends directly on the sulfur and oxygen content. Therefore, Kobe Steel has developed “super clean steel making process” by vacuum ladle refining furnace that is the way to reduce sulfur and oxygen [2]. Furthermore, since the rotation frequency of the 4-stroke diesel engines is about 300 to 1000 rpm, so total rotation frequency reaches  $10^7$  cycles in about only one month, and  $10^9$  cycles until completion of a life of the four-stroke diesel engines (about 20 years). Nevertheless study cases and knowledge of the very high cycle fatigue properties of low alloy steel used for solid-type crankshafts are not enough [3]. Therefore, in order to confirm long-term reliability of super clean steel, the investigation into very high cycle fatigue property was carried out.

## MATERIAL AND TESTING

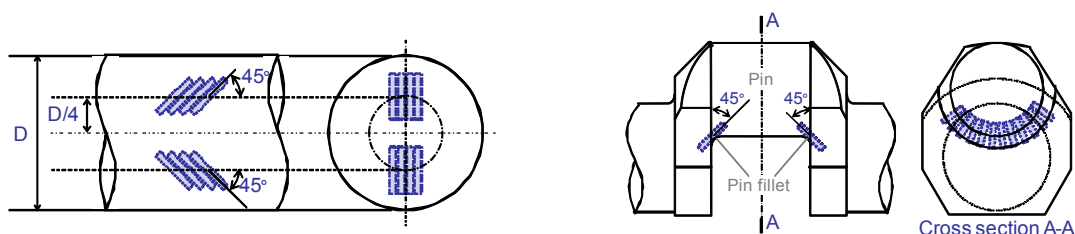
### Material

Fatigue specimens are taken from the ingot with weight of 12~65Ton. The chemical composition is listed in Table 1. Conventional steel and super clean steel are prepared with the control of sulphur, oxgen content ( $S < 20\text{ppm}$ ,  $O < 15\text{ppm}$ ) and the slag composition. These ingots are forged to the bar-shaped forging with the diameter of 450 ~620 mm and the forging ratio is over 3, or RR-forged crankshaft with the pin diameter of 415mm. These materials are heat-treated to be with 800~1100MPa tensile strength.

As shown in Fig.1, the fatigue specimens are taken from 45 degrees to the forging direction at the D/4 position equivalent to the fillet surface region in the case of bar-shaped forging, and from 45 degrees to crankshaft axis at pin-fillet portion in the case of RR-forged crankshaft.

Table1 Target of chemical composition of material

Material	C	Si	Mn	Ni	Cr	Mo	S	O
Max.	0.42	0.25	0.9	1.50	2.00	0.25	<30 ppm	<30 ppm
Min.	0.34		0.65	1.00	1.00	0.23		



(a)shafts

(b)crankshaft

Fig.1 Preparation of specimens

### High cycle fatigue test

The fatigue tests were performed to compare  $10^7$  cycle fatigue strength of super clean steel with conventional steel. Rotating bending fatigue tests and tension and compression fatigue test were performed. In both cases the fatigue test specimens had a parallel part that was 10 mm in diameter and 30 mm in length.

### Very high cycle fatigue test

In order to confirm the very high cycle fatigue property of the super clean steel and the conventional steel, rotating bending cantilevered fatigue test was conducted [4]. The specimens of very high cycle fatigue test with staircase method were taken from a RR-forged crankshaft.

## EXPERIMENTAL RESULT

### The result of fatigue test

Fig. 2 shows the fatigue strength by rotating bending fatigue test of the super clean steels and conventional steels. The fatigue strength of the super clean steel was improved about 10% to the conventional steel.

Fig. 3 shows the fatigue strength by tension compression fatigue test of the super clean steels using and conventional steel. In this test, two types of fracture were observed. Fatigue fracture from the inclusions in the surface occurred under  $10^6$  cycles and from internal inclusions occurred over  $10^6$  cycles. Minimum stress amplitude with failure specimen from the inclusions in the surface is 545MPa for super clean steel, 380MPa for conventional steel. Minimum stress amplitudes with failure specimen from inner inclusion are 545MPa for super clean steel, 380MPa for conventional steel. In both of the fracture types, fatigue strength of super clean steel is higher than of conventional steel.

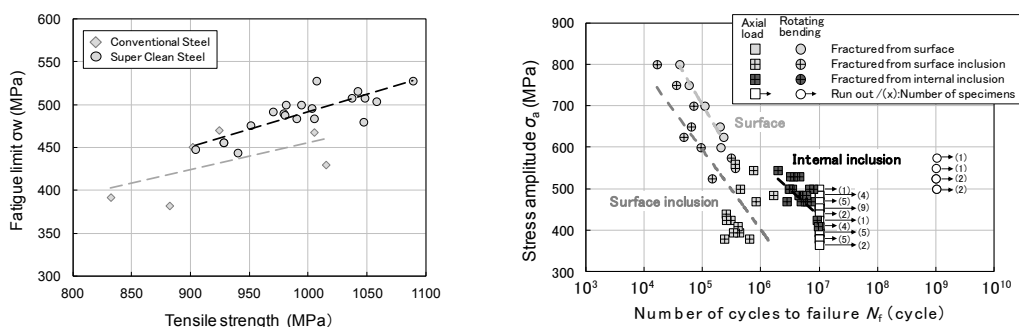


Fig.2 Result of fatigue test

Fig.3 Result of fatigue test

Fig.3 shows very high cycle fatigue test results. In the stress level below the high cycle (<math>10^7</math> cycles) fatigue limit, fatigue fracture did not occur between  $10^7$  to  $10^9$  cycles. It was confirmed that the difference of fatigue strength between the super clean steel and the conventional steel is maintained up to  $10^9$  cycles. These results clarified that the super clean steel has also high fatigue strength and high reliability in very high cycle fatigue region.

### The result of observation of fracture surface

Fig. 4 shows examples of observation of fracture surface. Fractures from the surface, the inclusions in the surface and internal inclusions were observed. In this study, inclusion size of fracture surface of the specimens was  $\sqrt{\text{area}}$  are 20~150 $\mu\text{m}$ .

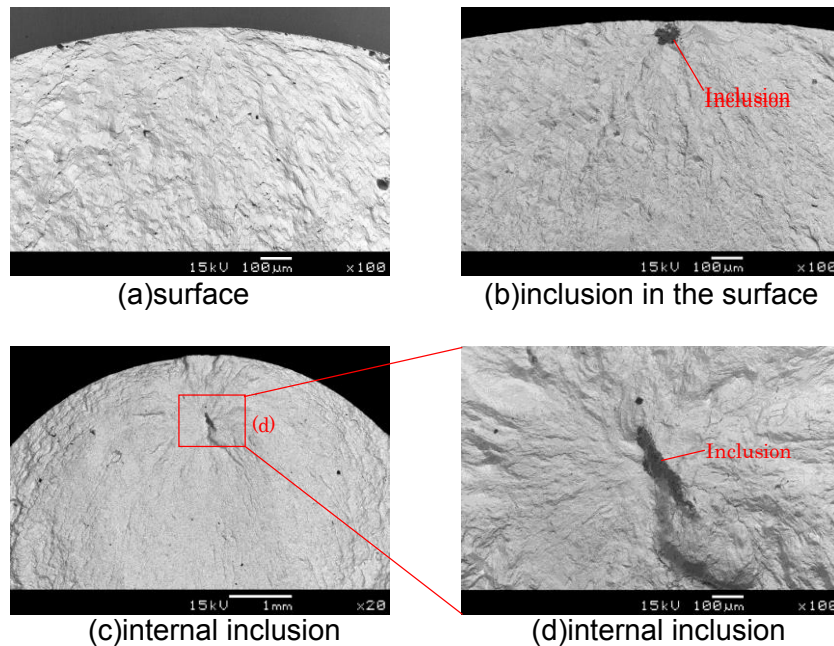


Fig.4 Example of observation results of fracture surface

### EVALUATION OF THE RESULT

According to Fig.3 in each fracture mechanism, surface, inclusions in the surface,

internal inclusions, there can be observed their own S-N curve characteristics. However the possibility of the fracture from internal inclusion over  $10^7$  cycles is unclear yet. To predict very high cycle fatigue properties, the following studies were made.

### Relation between fatigue lives and inclusion size

If the effects of inclusion and crack on fatigue properties are same, initial stress intensity factor is shown as Eq.1 [1]. M in eq.1 means the coefficient of stress intensity factor, and is known as 0.65 for inclusions in the surface, as 0.50 for internal inclusions [1]. The relation between  $\Delta K$  and fatigue lives is known as Eq.2 [3]. Fig.5 shows the relation between  $\Delta K$  and fatigue lives by conducting fatigue test and observation of surface fracture. According to Fig.5,  $\alpha$  is calculated as 25 for fracture from inclusions in the surface, as 44 from internal inclusions, as -0.21 from surface. Fatigue lives can be predicted from any stress amplitude and inclusion size by using above the coefficients in this study.

$$\Delta K = M\sigma_a(\pi\sqrt{area})^{1/2} \quad (1)$$

$$\Delta K = \alpha(N_f/\sqrt{area})^\beta \quad (2)$$

$$\Delta K_{th} = \gamma\sqrt{area}^{1/3} \quad (3)$$

### Relation between fatigue strength and inclusion size

Fig.6 shows the relation between  $\Delta K_{th}$  and inclusion size by conducting rotating bending fatigue test, observation of surface fracture and Eq.1. According to Fig.6 for both of the fractures from inclusions in the surface and internal inclusions,  $\Delta K_{th}$  can be in proportion to  $\sqrt{area}^{1/3}$  and equation 3 was obtained. According to Fig.6 and Eq.3,  $\gamma$  is calculated as 1.05 for fracture from inclusions in the surface, as 0.84 for internal inclusions.

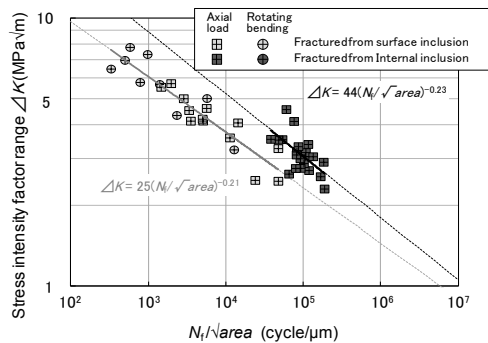


Fig.5 Relation between  $\Delta K$  and  $(N_f/\sqrt{area})$

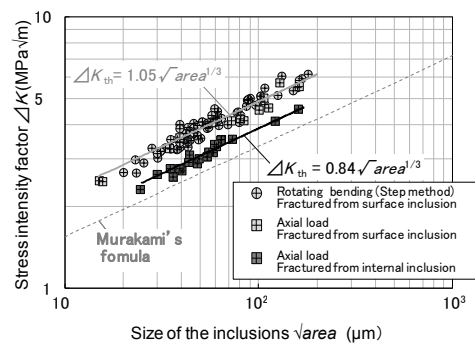


Fig.6 Relation between  $\Delta K_{th}$  and  $\sqrt{area}$

Fig.7 shows the result of predict of number of cycles to failure by Eq.1 and Eq.3. Inclusion size is determined as 20 $\mu$ m for upper limit, as 150 $\mu$ m for lower limit because inclusion sizes on fracture surface in this study were 20~150 $\mu$ m. It is confirmed that most experimental data are between the upper limit and lower limit. So it is assumed that this predicted S-N curve is reasonable in this study. According to Fig.7 if there is same size inclusion at surface and internal area, it is found that fracture doesn't occur from internal inclusion under the fatigue strength of fracture from inclusions in the surface. Moreover, for all S-N curves the intersection of inclined portion and horizontal portion is lower than 10<sup>7</sup> cycles. So it is found that not the fracture from surface inclusions but also the fracture from internal inclusions cannot be occurred in very high cycle region.

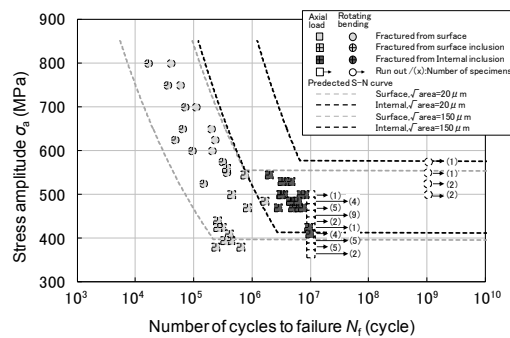


Fig.7 Predicted S-N curves for 40CrMo8

## CONCLUSION

The following conclusions are driven from the results and discussion.

1. According to the results of very high cycle fatigue tests any fracture wasn't be observed in this study.
2. The relations between  $\Delta K$  and fatigue lives, and between  $\Delta K_{th}$  and inclusion size for specimens of fracture from inclusions in the surface and internal inclusions.
3. S-N curves of the specimens of fracture from inclusions in the surface and internal inclusions can be predicted in the inclusion size range from 20~150 $\mu$ m in this study.

## REFERENCES

- 1) Murakami, Y.:  
Fatigue Strength of Metal, Effect of Defects and Non-metallic inclusions, 1993
- 2) Yakura, R.; Shinozaki, T.; Mori, H.; Fujitsuna, M.; Matsuda, M.;

CIMAC Congress (2013), Paper No.442

- 3) Omata, S. et al;  
Marine engineering journal of the Japan Institute of Marine Engineering, Vol.38,  
No.7 (2003), p.55-62
- 4) Kobayashi, H.:  
Fracture Mechanism, 1993

**Corresponding author:** [ikegami.tomonori@kobelco.com](mailto:ikegami.tomonori@kobelco.com)

# VHCF BEHAVIOUR OF INCONEL718 UNDER SYMMETRIC TENSION-COMPRESSION AT ROOM TEMPERATURE

M.X. Zhao<sup>1)</sup>, O. Polit<sup>1)</sup>, E. Valot<sup>1)</sup>, T. Palin-Luc<sup>2)</sup>, V. Bonnard<sup>3)</sup>

<sup>1)</sup> LEME, Universite Paris Nanterre, 50 rue de Sevres, 92410, Ville d'Avray, France

<sup>2)</sup> Arts et Metiers ParisTech, I2M, CNRS, Esplanade des Arts et Metiers, 33405, Talence Cedex, France

<sup>3)</sup> Office National d'Etudes et de Recherches Aeronautiques, 29 avenue de la Division Leclerc, 92322, Chatillon Cedex, France

## ABSTRACT

This work is devoted to the very high cycle fatigue (VHCF) behaviour of nickel based superalloy Inconel 718 under fully reversed tension-compression ( $R=-1$ ) at room temperature. A new record system has been developed to monitor the surface temperature, resonance frequency, displacement at the top and bottom of the specimen in order to investigate the VHCF behaviour of Inconel 718 loaded at 20 kHz. Specimen surface temperature distribution due to self-heating (without cooling) has been obtained for a large range of stress level (100-400 MPa) which is close to practical application. Two sets of results are presented: (i) data acquisition and monitoring during the ultrasonic fatigue test; (ii) self-heating results for different loading levels. These results can be used to improve numerical simulations of the cyclic stress strain state under loading at very high frequency by taking the temperature influence on the material properties into consideration.

## KEYWORDS

Inconel 718, VHCF, Self-heating, Temperature distribution

## INTRODUCTION

With the development of modern industry, many mechanical components have to be designed against VHCF in order to support  $10^9 \sim 10^{10}$  cycles during their lifetime. However, since the 19th century, fatigue strength criteria have been based on experiments up to  $10^7$  cycles. The importance of the fatigue strength and life assessment for an aircraft turbine loaded in VHCF regime can be illustrated by the accident occurred in Los Angeles in 2006 [1]. Most of conventional fatigue testing machines work at a loading frequency lower than 300 Hz. The major advantage of ultrasonic fatigue system at 20 kHz is their ability to reach fatigue limit and threshold crack propagation within a reasonable testing time. The development of ultrasonic fatigue testing method brought advantages not only about the reduced time of experiments but also concerning the clarification of fatigue behavior in very high cycle regime [1,2].

There are very few contributions about VHCF strength for Inconel 718. Chen et al. [3,4] investigated fracture and small crack growth under pull-push mode with a pulse-pause technique, so that the maximum temperature rise was controlled below  $5-8^\circ\text{C}$  during the test.

Shi et al. [5,6] carried out fatigue test on Inconel 718 with different loading frequencies by using ultrasonic axial loading and rotating bending loading under air-cooling to ensure that the specimen temperature was around room temperature during the whole experiment.

This paper is organized as follow: the 1st part presents the experimental setup designed by LEME with data acquisition tools, the 2nd part is dedicated to the design of the specimen and the calibration of the system, while the 3rd part gives data monitored during the ultrasonic fatigue tests and results of self-heating phenomenon.

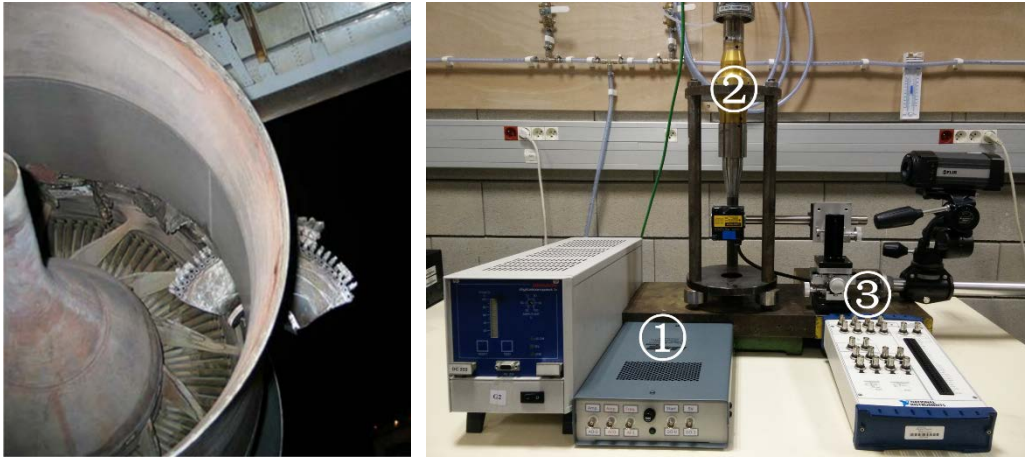


Fig.1: Failure of a turbine disk in Los Angeles engine accident [1]

Fig.2: Ultrasonic VHCF testing equipment

## EXPERIMENTAL SETUP

### VHCF testing equipment at ultrasonic frequency

The VHCF equipment is shown in Fig 2. The major components of this ultrasonic fatigue testing system can be summarized into 3 parts [7]:

1. Control system: National Instrument PCIe card and self-made control program to keep constant the initial parameters all the test long, especially displacement amplitude.
2. Actuation system: generates sinusoidal electrical signal at  $20 \pm 0.5$  kHz, converts the voltage into mechanical displacement, and booster/horn to amplify or reduce the vibration in order to reach the required elastic stress amplitude in the testing section of the specimen.
3. Data acquisition system: record the resonance frequency, surface temperature, displacement at top and bottom of the specimen all the test long.

### Material and specimen design

Inconel 718 is a high strength, corrosion resistant nickel chromium material used from  $-250$  to  $+700^\circ\text{C}$ . It has good tensile resistance, fatigue and creep strength. Therefore, it is used in a wide range of industrial applications, for example the fueled rocket, aircraft component, and disk of gas turbine at room and elevated temperature.



A classic smooth specimen geometry has been designed for having a resonance frequency around 20 kHz. A high stress-amplification coefficient ( $C_s$ ) can be generated by using such hourglass shape. The maximum stress at the resonance frequency is reached in the middle section. The geometry of the specimen has been defined from longitudinal elastic vibration equation [2] or modal analysis using FEM in order to obtain a tension-compression resonance at 20 kHz. The geometry of the specimen is shown in Fig 3a.

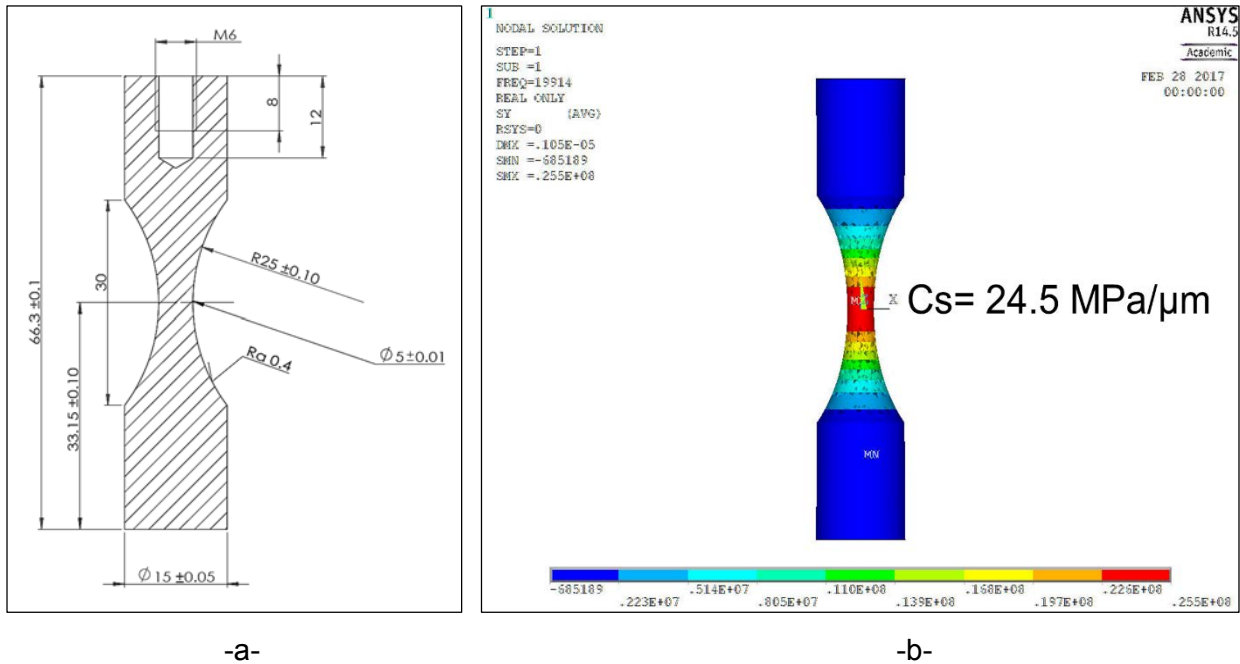


Fig.3: Geometry and stress amplitude from harmonic analysis

### Calibration

The purpose of calibration is to find the relationship between the voltage from the generator and the displacement amplitude of the piezoelectric convertor, as well as the corresponding elastic stress amplitude in the middle section of the specimen. This relation is deduced by harmonic analysis using FEM, considering isotropic material with a linear behaviour. The result is shown in Fig 3b.

### Data acquisition

In order to investigate the VHCF behaviour of Inconel 718, a new record system using LabView<sup>®</sup> has been developed to monitor several parameters continuously during a fatigue test. The monitored parameters are:

- the resonance frequency: signal delivered by Branson ultrasonic generator, and also deduced from the laser displacement sensors, for validation.
- the specimen temperature from the Flir infrared camera.
- the displacements at the top and bottom of the specimen from the Keyence laser sensors.

## RESULTS

The results from an experiment up to  $10^8$  cycles under a load level of 400 MPa are illustrated in Fig 4. The resonance frequency (in black), maximum temperature in the test section of the specimen (in red), wave responses at the top (in green) and at the bottom (in blue) of the specimen have been grouped together using LabView program.

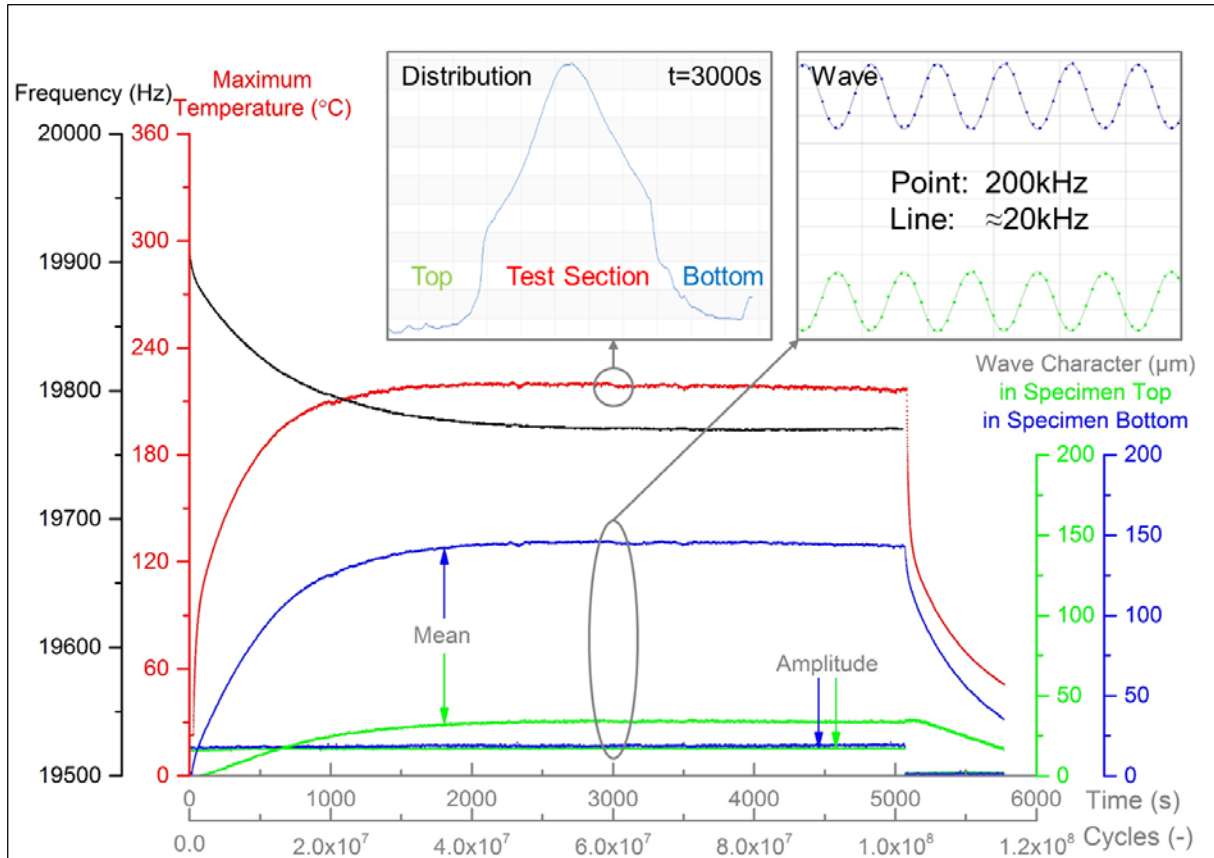


**Fig.4:** Data acquisition during a test at 400 MPa and room temperature without cooling

The maximum temperature of the specimen continuously increases from room temperature to 230°C at the beginning of the experiment, while the resonance frequency decreases, even if the temperature evolution versus time is stabilized after around 2000s. Local thermal stress should be considered because the temperature distribution across the length of the specimen is non uniform (upper left graph in Fig 4). It shows that temperature goes up to 150~200°C in the test section, while only 50°C is obtained in both ends of the specimen. This is in agreement with the elastic stress distribution along the specimen axis.

The wave responses of the top and the bottom ends are analyzed using mean value and amplitude (Fig 4). The amplitude is related to the required elastic stress level and stays nearly constant during the experiment, it seems not to be influenced by the temperature change. This is in agreement with the control system of the piezoelectric converter. The mean value at the top and bottom of the specimen can be analyzed as its elongation due to thermal expansion. It gradually returns to zero after the test. The detailed displacement response after 3000s is also recorded (shown in upper right graph in Fig 4). All the points are recorded by two Keyence high frequency laser sensor at a sampling frequency of 200 kHz. The continuous line is

deduced using Fast Fourier Transform (FFT) which gives the experimental resonance frequency. Excellent conformity is obtained and the opposite phase ensures the expected mode of vibration.

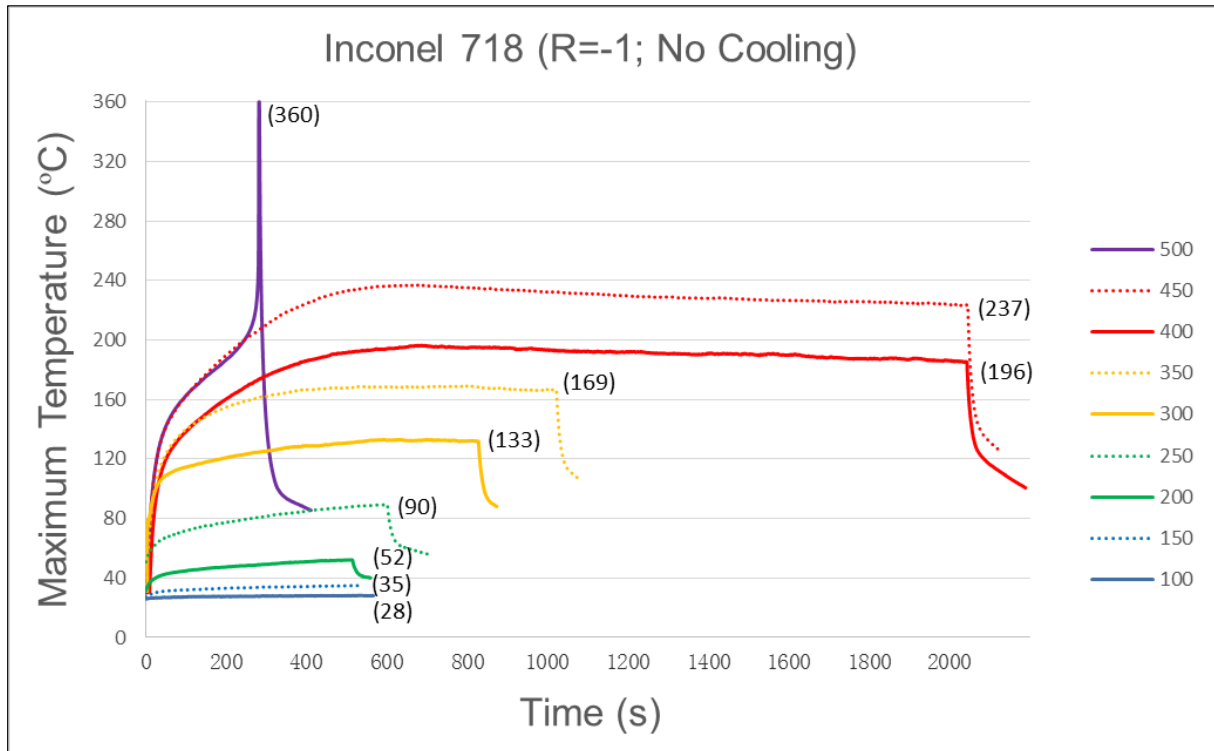


Fig.5: Self-heating under different elastic stress amplitudes at 20 kHz without cooling

The self-heating results at 20 kHz on Inconel 718 under symmetric tension compression ( $R=-1$ ) at room temperature for different stress amplitude (100-500 MPa) are shown in Fig 5. All the curves present the same characteristics: fast increase at the beginning and nearly flat behaviour after, except at 500 MPa. It can be observed that for a low stress amplitude (150 MPa), a stable temperature of 35°C is obtained in the middle section of the specimen, while 200°C is reached for a high stress amplitude (400 MPa). In the specimen, there is a competition between heat generation, conduction from the center section to the ends of the specimen and convection with the surrounding environment. The total balance between these phenomena depends on the load level. The curve related to 500 MPa presents a high temperature of 360°C because the specimen cracked. A quick fractography analysis indicated that there were some surface machining defects on the surface of the reduced section. For this test, the upper limit temperature of Flir A325 infrared camera was reached.

## CONCLUSION AND PROSPECTS

A first set of experiments have been carried out to study the very high cycle fatigue (VHCF) behaviour of Inconel 718 under symmetric tension compression ( $R=-1$ ) at room temperature. The analysis of temperature, frequency, displacements at the top and at the bottom of the specimen have been presented. Furthermore, the self-heating of the specimen has been described for different load levels.

Maximum temperature of the specimen continuously increases from room temperature to 230 °C during the beginning of the experiment, while the resonance frequency decreases. Temperature distribution across the length of the specimen is non uniform. It goes up to 150~200°C in the test section, while only 50°C is obtained in both ends of the specimen. The difference between mean values of the waves at the top and bottom of the specimen increases when temperature grows. It can be analyzed as the elongation of the specimen due to thermal expansion, and returns to zero gradually after the test.

All the curves of self-heating results for different loading present the same characteristics: fast increase at the beginning and nearly flat behaviour after. It can be observed that for low level of stress 150 MPa, a stable temperature of 35°C is obtained in the middle section of the specimen, while 200°C is reached for a high stress level of 400 MPa. The curve related to 500 MPa presents a high temperature over 360°C because the specimen cracked.

This can be used to improve simulation by taking the temperature influence on dynamic modulus, density and thermal stress into consideration. The further objective of this study will be dedicated to S-N curve, fracture analysis and life assessment.

## REFERENCE

- [1] Pineau, A.; Antolovich, S.D.:  
High temperature fatigue of nickel-base superalloys – A review with special emphasis on deformation modes and oxidation  
Engineering Failure Analysis 16 (2009) No.8, pp.2668-2697
- [2] Bathias, C.; Paris, P.C.:  
Gigacycle fatigue in mechanical practice  
CRC Press, New York, 2004
- [3] Chen, Q.; Kawagoishi, N.; Nisitani, H.:  
Evaluation of fatigue crack growth rate and life prediction of Inconel 718 at room and elevated temperatures  
Materials Science and Engineering-A 277 (2000) No.1, pp.250-257
- [4] Chen, Q.; Kawagoishi, N.; Wang, Q.Y.; Yan, N.; Ono, T.:  
Small crack behavior and fracture of nickel-based superalloy under ultrasonic fatigue  
Int. Journal of Fatigue 27 (2005) No.10, pp.1277-1232
- [5] Ma, X.; Duan, Z.; Shi, H.J.; Murai, R.; Yanagisawa, E.:  
Fatigue and fracture behavior of nickel-based superalloy Inconel 718 up to the very high cycle regime  
Journal of Zhejiang University-Science A 11 (2010) No.10, pp.727-737
- [6] Zhang, Y.; Duan, Z.; Shi, H.J.:  
Comparison of the very high cycle fatigue behaviors of INCONEL 718 with different loading frequencies  
Science China Physics, Mechanics and Astronomy 56 (2013) No.3, pp.617-623
- [7] Bathias, C.:  
Piezoelectric fatigue testing machines and devices  
Int. Journal of Fatigue 28 (2006) No.11, pp.1438-1445

**Corresponding author:** Olivier.Polit@u-paris10.fr

# TORSIONAL AND AXIAL VHCF PROPERTIES OF SPRING STEEL AT DIFFERENT LOAD RATIOS

H. Mayer<sup>1)</sup>, U. Karr<sup>1)</sup>, Y. Sandaiji<sup>2)</sup>, E. Tamura<sup>2)</sup>

<sup>1)</sup> Institute of Physics and Material Science, BOKU, Peter-Jordan-Str. 82,  
1190 Vienna, Austria

<sup>2)</sup> Materials Research Laboratory, KOBE STEEL LTD, 1-5-5 Takatsukadai,  
Nishi-ku, Kobe, Hyogo, 651-2271, Japan

## ABSTRACT

High-strength spring steel SWOSC-V with shot-peened surfaces is investigated under cyclic torsional and axial loading at load ratios  $R = -1$ ,  $R = 0.1$  and  $R = 0.35$ . The ultrasonic fatigue testing method is used to measure fatigue data in the HCF and VHCF regime. For both loading conditions, the  $S-N$  curves are shifted towards lower stress amplitudes with increasing load ratio showing a strong mean stress influence. Crack initiation under cyclic torsional loading is preferentially in a direction of maximum shear, at the surface for load ratio  $R = -1$  and in the interior for  $R=0.1$  and  $0.35$ . Initial crack propagation in mode II / mode III continues until it reaches a well-defined stress intensity factor and then changes to mode I. Crack initiation under cyclic axial loading is in the interior, preferentially at inclusions and less frequent in the matrix. Stress amplitudes at limiting lifetimes of  $10^9$  cycles under torsional loading,  $\tau_A$ , and axial loading condition,  $\sigma_A$ , are compared in a Haigh diagram. Ratio of cyclic strength  $\tau_A / \sigma_A$  is close to 1 for all load ratios. Influences of the much larger testing volume in axial loading tests as well as the beneficial influence of shot-peening on cyclic torsional strength serve to explain this high ratio of torsional and axial cyclic strength.

## KEYWORDS

Cyclic torsion, cyclic tension, load ratio, spring steel, very high cycle fatigue, crack initiation, short crack

## INTRODUCTION

Several technical components are predominantly loaded under cyclic torsion. Coil springs, drive shafts or balls and rings in bearings must sustain very high numbers of shear load cycles in service. The VHCF properties under cyclic torsional loading are of great interest therefore. Most VHCF data are, however, available for cyclic tension-compression or cyclic tension loading. This raises the question, if and how torsional loading fatigue properties can be deduced from axial loading behaviour.

In this investigation the cyclic torsion VHCF properties of high-strength spring steel SWOSC-V are investigated at different load ratios. Cyclic tension-compression and cyclic tension tests at the same load ratio serve for comparison. Torsional as well as axial loading fatigue tests are performed using the ultrasonic fatigue testing technique [1]. Crack initiation mechanisms as well as VHCF strength under both loading conditions are compared.

## MATERIAL AND METHOD

The chemical composition of the investigated steel is based on the high-strength spring steel SWOSC-V. Chemical composition of the material is shown in Table 1.

C	Si	Mn	Cr	Al	Fe
0.55	1.50	0.70	0.70	0.003	balance

Table 1: Chemical composition of SWOSC-V

The material is melted by vacuum induction furnace and casted in a special process to increase inclusion size and density. The material is forged, oil quenched and tempered. Static strength properties are summarised in Table 2.

Yield Strength (MPa)	Tensile Strength (MPa)	Elongation (%)	Shear Yield Strength (MPa)	Shear Strength (MPa)	Vickers Hardness (HV)
1645	1866	9	1408	1542	530

Table 2: Mechanical properties of the tested material

Torsional as well as axial loading fatigue tests are performed at load ratios  $R = -1$ ,  $R = 0.1$  and  $R = 0.35$  at cycling frequencies of about 20 kHz. The ultrasonic equipment and details of the experimental procedure used to perform cyclic torsion tests [2] and cyclic tension tests [3] at different load ratios are described previously.

Specimens with a diameter of 4.2 mm in the gage section are used in torsional as well as axial loading experiments. Dumbbell-shaped specimens with a cylindrical gage section of 10 mm length are used in axial loading fatigue tests. The testing volume of these specimens is 140 mm<sup>3</sup>. Specimens with a circular reduction of the cross section in their centre are used in cyclic torsion tests. The hour-glass shape of these specimens as well as the stress gradient due to torsional loading leads to a material volume of 5.1 mm<sup>3</sup> that is subjected to greater than 90% of the nominal stress. All specimens were tested with shot-peened surfaces.

## RESULTS AND DISCUSSION

Figure 1 shows the results of ultrasonic cyclic torsional fatigue experiments.  $S-N$  data are shown on in Fig. 1(a) using different colours for load ratios  $R = -1$ , 0.1 and 0.35. A pronounced influence of the load ratio is visible, i.e.  $S-N$  data are shifted towards lower shear stress amplitudes as the load ratio increases. Different symbols serve to distinguish the crack initiation sites. Crack initiation at internal inclusions is found solely in two of the 20 fractured specimens. Rather, cracks initiate in direction of maximum shear, preferentially at the surface for load ratio  $R = -1$  and exclusively in the interior at load ratios  $R = 0.1$  and 0.35.

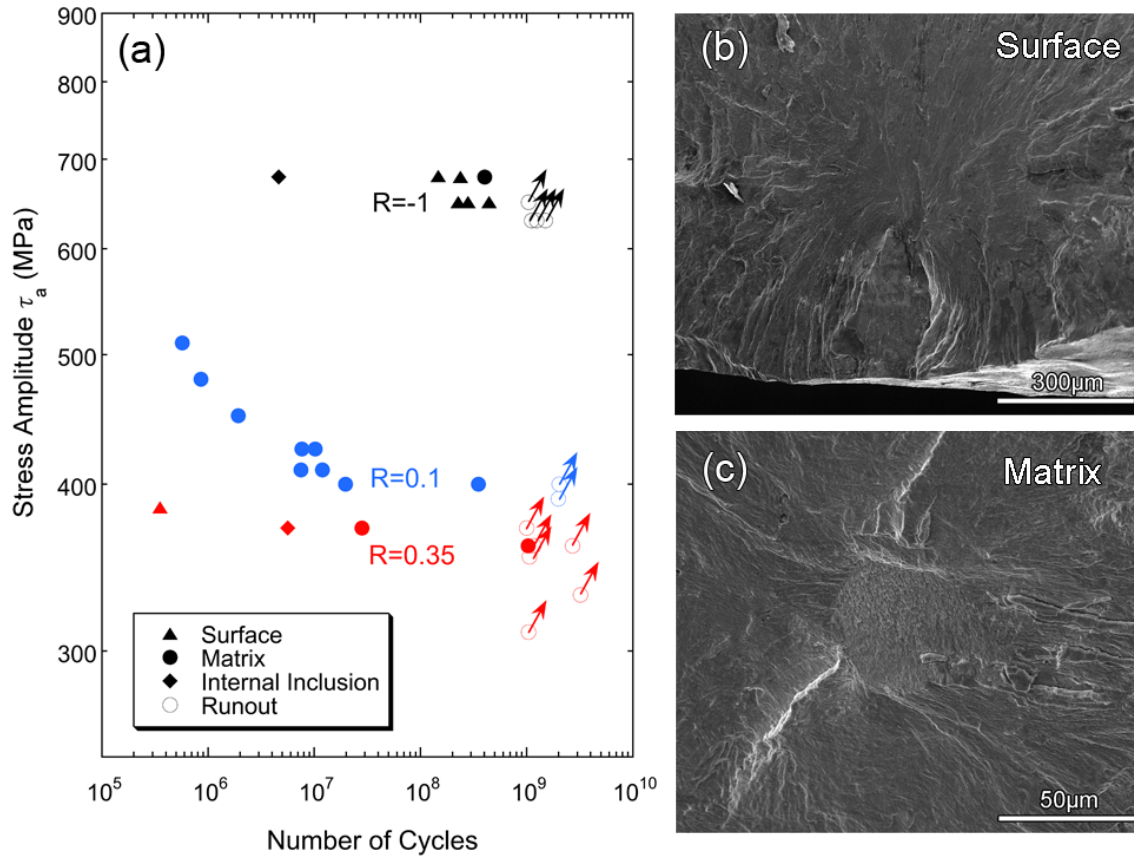


Fig. 1: Cyclic torsional fatigue tests at different load ratios; (a) shows S-N data; (b) shows surface crack initiation ( $\tau_a=650$  MPa,  $R = -1$ ,  $4.4 \times 10^8$  cycles to failure); (c) shows internal crack initiation ( $\tau_a=410$  MPa,  $R = 0.1$ ,  $1.2 \times 10^7$  cycles to failure)

The crack produced by cyclic torsional loading is initiated in one of the directions of maximum shear (parallel or perpendicular to the specimen's longitudinal axis). The initial mode II / mode III crack changes its path to mode I at longer crack lengths. V-shaped initial cracks are formed if the crack starts at the surface whereas internal shear mode fracture shows no distinct shape.

The change from initial shear mode to tensile mode at longer crack lengths can be correlated with a stress intensity factor. The stress intensity factor range  $\Delta K_\tau$  for a crack loaded with cyclic shear stresses can be calculated with Eq. (1), as suggested by Okazaki et al. [4]:

$$\Delta K_\tau = 2\tau_a \cdot \beta \cdot \sqrt{\pi \sqrt{area}} \quad (1)$$

$\Delta K_\tau$  is equal to  $\Delta K_{II}$  or  $\Delta K_{III}$ , whichever is higher for the crack. The size of the crack is considered by the square root of the fractured area,  $\sqrt{area}$ .  $\tau_a$  is the actual shear stress amplitude at the crack initiation site.  $\tau_a$  is the nominal shear stress amplitude for surface crack initiation whereas it is lower for internal crack initiation due to the stress gradient over the cross section. The parameter  $\beta$  is 0.58 for internal cracks and 0.69 for surface cracks.

It is remarkable that the fatigue crack changes from shear mode crack growth (mode II / mode III) to tensile mode crack growth (mode I) at a well defined stress intensity factor range, which is by mean  $5.4 \text{ MPam}^{1/2}$  for load ratio  $R = 0.1$  and internal crack initiation. For



load ratio  $R = -1$  and surface crack initiation the crack path changes when  $\Delta K_t$  reaches about  $22 \text{ MPam}^{1/2}$ .

Figure 2 shows the results of ultrasonic cyclic tension-compression and cyclic tension fatigue tests.  $S-N$  data for load ratio  $R = -1, 0.1$  and  $0.35$  are shown in Fig 2(a). Increasing the load ratio decreases the cyclic stress amplitude the material can sustain. Crack initiation in the VHCF regime is in 67% of the specimens at internal inclusions and in 33% in the matrix without an inclusion. This is a strong difference to cyclic torsional loading, where solely 10% of the fractured specimens showed crack initiation at internal inclusions.

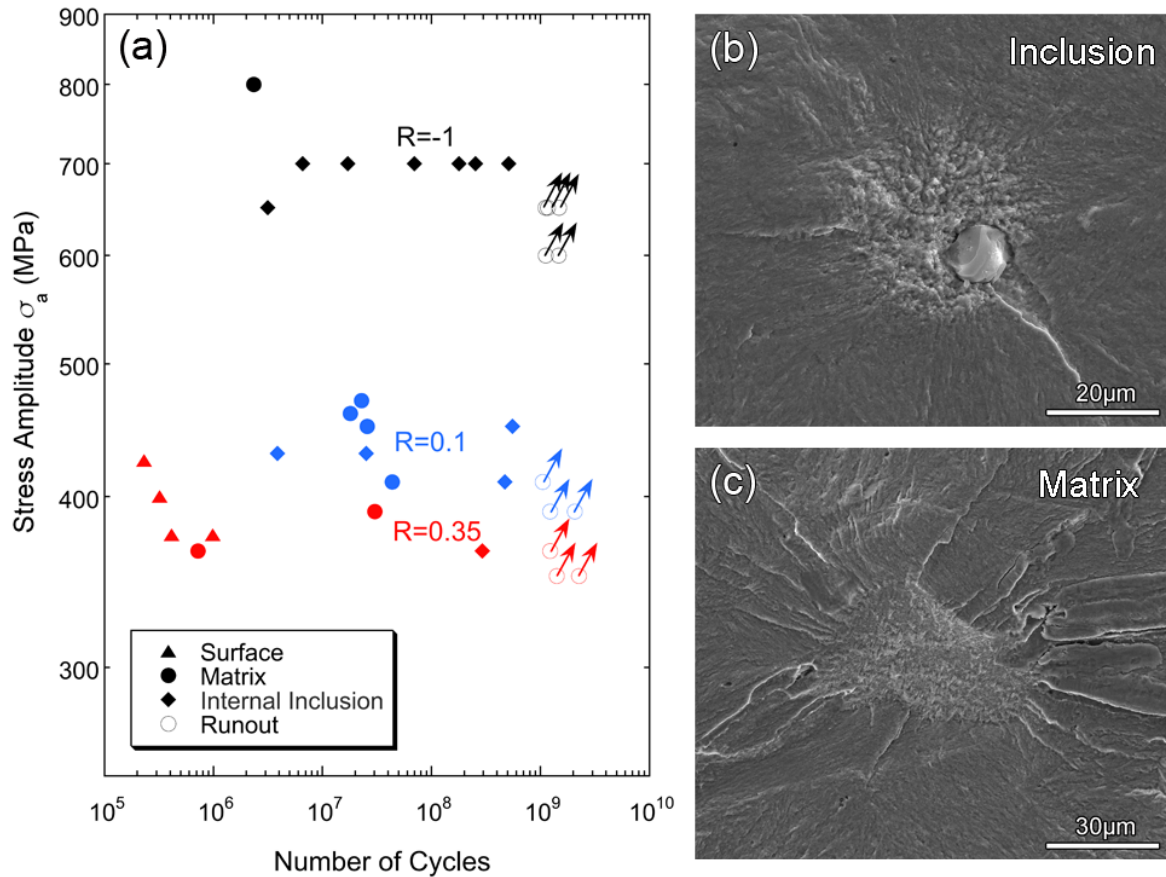


**Fig. 2:** Cyclic tension and tension-compression fatigue tests at different load ratios; (a) shows  $S-N$  data; (b) shows crack initiation at an internal inclusion ( $\sigma_a=700 \text{ MPa}$ ,  $R = -1$ ,  $5.1 \times 10^8$  cycles to failure); (c) shows matrix crack initiation ( $\sigma_a=800 \text{ MPa}$ ,  $R = -1$ ,  $2.3 \times 10^6$  cycles to failure)

Inclusions can be considered as initial cracks and a stress intensity factor range can be calculated using Eq. (2) developed by Murakami [5]:

$$\Delta K_I = 2\sigma_a \cdot \alpha \cdot \sqrt{\pi \sqrt{area}} \quad (2)$$

$\sigma_a$  is the stress amplitude,  $\sqrt{area}$  is the square root of the fractured area,  $\alpha$  is 0.50 for internal and 0.65 for surface cracks.

Larger inclusions and higher stress amplitudes lead to higher stress intensity ranges correlating to shorter lifetimes. A minimum stress intensity range of about  $\Delta K_{inc}=4 \text{ MPam}^{1/2}$  is



necessary for failure in the  $10^9$  cycle regime at load ratio  $R = -1$ . FGAs are visible at inclusions after tension-compression cycling with the size correlating to the stress intensity factor amplitude  $K_{FGA} = \Delta K / 2 = 3.3 \pm 0.4 \text{ MPa}\sqrt{\text{m}}^{1/2}$ , which is somewhat smaller than the often reported value between 4 and 6  $\text{MPa}\sqrt{\text{m}}^{1/2}$  [6].

VHCF strength under cyclic torsional and axial loading is compared in the Haigh diagram shown in Fig. 3(a). The stress amplitudes correspond to 50% fracture probability at  $10^9$  cycles. Cyclic strengths found for both loading conditions are very similar. The ratio of VHCF strength under cyclic torsional loading,  $\tau_A$ , and cyclic axial loading,  $\sigma_A$ , is between 0.98 and 1.01. This ratio is relatively high, however, it is comparable to the result of a previous investigation of a similar shot-peened high-strength spring steel [7]. The high ratio may be explained with the following considerations:

Crack initiation under axial loading condition is mainly at inclusions. Distribution of inclusion sizes is shown in Fig. 3(b): the larger the inclusion size, the lower fatigue lifetime and cyclic strength. Considering the testing volume, which is by a factor of about 27 smaller in cyclic torsional specimens, inclusions large enough to initiate cracks can be rarely found. Therefore, the deterioration of cyclic properties due to inclusions mainly affects the cyclic axial strength, whereas the influence on cyclic torsional strength is less pronounced.

Shot peening is beneficial for the cyclic strength under torsional loading since it impedes surface crack initiation. No effect may be expected for the VHCF strength under axial loading when fatigue cracks are initiated at internal inclusions with or without surface residual stresses. Cracks are formed in the interior after cyclic torsional loading at load ratios  $R = 0.1$  and  $0.35$ . Stresses decrease towards the centre of the specimens for torsional loading due to the stress gradient. Interior crack initiation is on average  $290 \mu\text{m}$  below the surface, where the shear stress is 86% of the nominal shear stress at the surface. This means that the ratio  $\tau_A / \sigma_A$  would be about 0.86 rather than 1, if local rather than nominal stresses are considered.

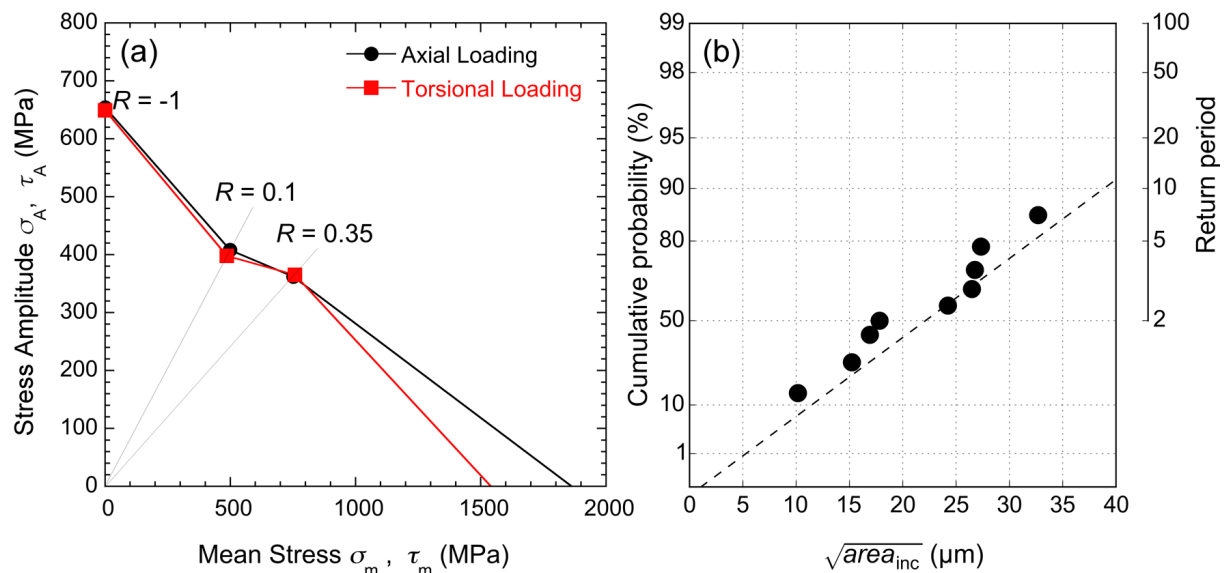


Fig. 3: (a) Haigh diagram of shot-peened SWOSC-V spring steel for torsional and axial loading; (b) cumulative probability of inclusion sizes that initiated cracks in axial loading specimens

## CONCLUSIONS

Cyclic torsional and cyclic axial loading ultrasonic fatigue tests have been performed with high-strength spring steel SWOSC-V. The following conclusions may be drawn:

Fatigue cracks are preferentially initiated in directions of maximum shear under cyclic torsional loading. Surface cracks at load ratio  $R = -1$  and interior cracks at load ratios  $R = 0.1$  and  $0.35$  propagate in mode II / mode III until a well-defined stress intensity factor is reached. Then the crack path changes to mode I. Crack initiations at internal inclusions are rare due to the small testing volume.

Fatigue cracks start in the interior under cyclic axial loading, preferentially at interior inclusions and less frequent in the matrix. FGAs are visible at inclusions after tension-compression cycling.

Both, torsional as well as axial loading, show  $S-N$  curves that are shifted towards lower stress amplitudes with increasing load ratio indicating a strong mean stress sensitivity.

## REFERENCES

- [1] H. Mayer:  
Recent developments in ultrasonic fatigue  
Fatigue & Fracture Eng. Mater. Struct., 39 (2016) pp. 3-29.
- [2] H. Mayer, R. Schuller, U. Karr, D. Irrasch, M. Fitzka, M. Hahn, M. Bacher-Höchst:  
Cyclic torsion very high cycle fatigue of VDSiCr spring steel at different load ratios  
Int. Journal of Fatigue, 70 (2015) pp. 322-327.
- [3] R. Schuller, U. Karr, D. Irrasch, M. Fitzka, M. Hahn, M. Bacher-Höchst, H. Mayer:  
Mean stress sensitivity of spring steel in the very high cycle fatigue regime  
J. Materials Science, 50 (2015) pp. 5514-5523.
- [4] S. Okazaki, H. Matsunaga, T. Ueda, H. Komata, M. Endo:  
A practical expression for evaluating the small shear-mode fatigue crack threshold in bearing steel  
Theoretical & Applied Fracture Mechanics, 73 (2014) pp. 161-169.
- [5] Y. Murakami:  
Metal Fatigue: Effects of Small Defects and Nonmetallic Inclusions  
Elsevier Science Ltd. , Kidlington, Oxford, UK, 2002.
- [6] Y. Hong, Z. Lei, C. Sun, A. Zhao:  
Propensities of crack interior initiation and early growth for very-high-cycle fatigue of high strength steels  
Int. Journal of Fatigue, 58 (2014) pp. 144-151.
- [7] H. Mayer, R. Schuller, U. Karr, M. Fitzka, D. Irrasch, M. Hahn, M. Bacher-Höchst:  
Mean stress sensitivity and crack initiation mechanisms of spring steel for torsional and axial VHCF loading  
Int. Journal of Fatigue, 93 (2016) pp. 309-317.

**Corresponding author:** herwig.mayer@boku.ac.at

# FORMATION MECHANISM OF FINE GRANULAR AREA(FGA) AROUND INTERIOR INCLUSION AT CRACK INITIATION SITE IN VERY HIGH CYCLE FATIGUE

T. Sakai<sup>1)</sup>, N. Oguma<sup>2)</sup>, A. Nakagawa<sup>3)</sup>, S. Tsutsumi<sup>4)</sup>, O. Naimark<sup>5)</sup>, M. Bannikov<sup>5)</sup>,

<sup>1)</sup> Research Organization of Science and Engineering, Ritsumeikan University,  
1-1-1 Noji-higashi, Kusatsu, Shiga, 525-8577 Japan

<sup>2)</sup> Faculty of Engineering, University of Toyama,  
3190 Gofuku, Toyama, 930-8555 Japan

<sup>3)</sup> Industrial Products Company, Hitachi, Ltd.,  
3-18 Nakanoshima 2-chome, Kita-ku, Osaka, 530-0005 Japan

<sup>4)</sup> Joining and Welding Research Institute, Osaka University,  
11-1 Mihagaoka, Ibaraki, Osaka, 567-0047 Japan

<sup>5)</sup> Russian Academy of Sciences, Institute of Continuous Media Mechanics,  
614013, Perm, Russia

## ABSTRACT

In very high cycle fatigue, one can usually observe the fish-eye on the fracture surface and an inclusion is observed at the center of the fish-eye. The fine granular area (FGA) is also found in the vicinity around the inclusion on the fracture surface. The FGA formation mechanism is one of the most important subjects in the very high cycle fatigue. Thus, the authors have attempted to construct the FGA formation model based on the current experimental results obtained by the authors. In this model, FGA formation is interpreted as intermittent micro-debondings and their coalescence during the long sequence of the cyclic loadings.

## KEYWORDS

Very high cycle fatigue, interior inclusion, probabilistic model, fine granular area(FGA), crack growth law

## INTRODUCTION

In cases of high strength steels, the fatigue fracture tends to take place from the interior inclusions introduced in the steel fabrication process in the very high cycle regime. Thus, the fish-eye is usually found on the fracture surface and the inclusion is also observed at the core portion of the fish-eye. Another typical aspect on the fracture is the fact that the fine granular area (FGA) is often found in the vicinity around the inclusion on the fracture surface [1].

Since the FGA formation period occupies more than 90% of the total fatigue life, the FGA formation mechanism is one of the most important subjects in the very high cycle fatigue. Thus, the authors have attempted to construct the FGA formation model to interpret the fatigue fracture process inside of FGA. In this concept, polygonization is caused around the inclusion before any micro-cracking during the long term cyclic loadings. Then, micro-debondings take place along the polygonized layer. Micro-debondings can occur isolatedly, and the debonding probability tends to increase near the inclusion edge at any stage of cyclic loadings.

## TYPICAL ASPECTS OF FRACTURE SURFACES AT CRACK NUCLEATION SITE

Among numerous fatigue test results for high strength steels [1,2], a typical example of the fracture surface in rotating bending is shown in Fig.1(a). A fish-eye is found at the top of the fracture surface, where an inclusion was found at the core portion of the fish-eye. The inclusion depth from the specimen surface is denoted by  $\xi$  in this paper. Fig.1(b) indicates another fracture surface observed at the core portion of the fish-eye, where the fine granular area (FGA) is clearly found in the vicinity around the inclusion. The mark of ① shows inside of the FGA, whereas the other mark of ② indicates outside of the FGA.

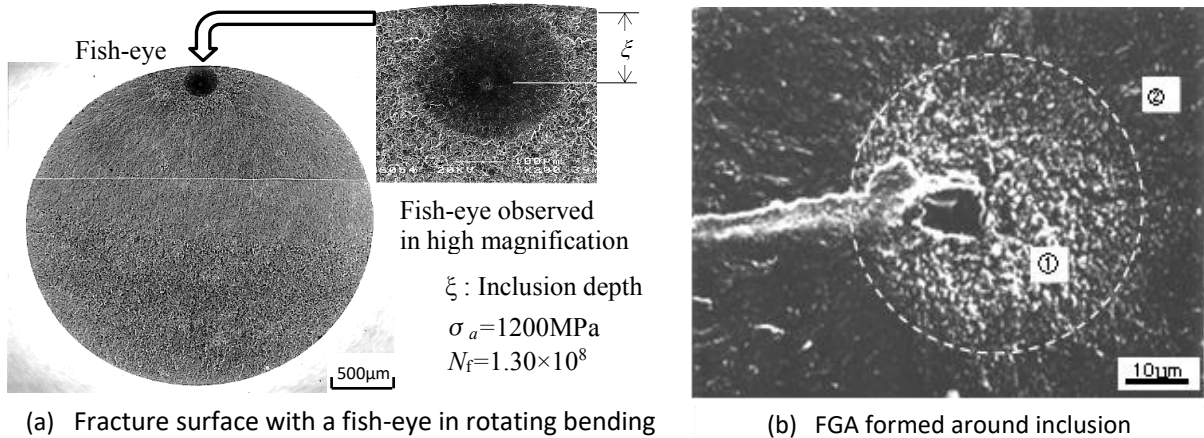


Fig.1: Typical examples of fracture surfaces near crack nucleation site

## REPLACEMENT OF ISOLATED DEBONDINGS BY A PENNY-SHAPED CRACK

Characteristic area of the FGA is divided into a lot of fine cells as shown in Fig.2(a), where seven circumferential areas are arrayed around the inclusion with the diameter of  $2\rho$ . If the value of  $\Delta K$  at the FGA front exceeds the threshold value of  $\Delta K_{th}$ , the crack tends to grow following the Paris' law in each loading cycle. Main aim of this study is the analysis of the crack growth behavior within the FGA. The penny-shaped fine granular layer is formed around the inclusion during the long sequence of cyclic loadings [3].

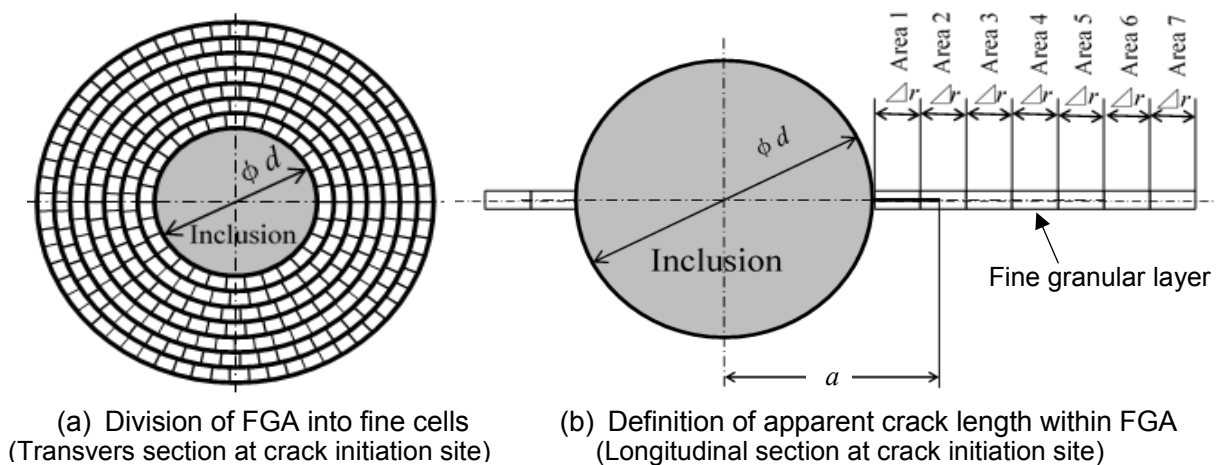


Fig.2: Division of FGA and definition of apparent crack length within FGA.

Here, microscopic debondings begin to take place along the boundary between the fine granular layer and the matrix of the steel at a certain stage of cyclic loadings. If the number of debonded cells is denoted by  $n$  and the total number of polygonised cells by  $n_t$ , the debonding probability,  $P(N)$ , is given by  $n/n_t$ . In addition, the crack length  $a$  which is the radius of the penny-shape crack in Fig.2(b) is given as follows;

$$a = \rho + 7\Delta r \frac{n}{n_t} = \rho + 7\Delta r P(N) \quad (1)$$

Based on this assumption, the isolatedly debonded cells can be replaced by a usual penny-shape crack and the crack growth behavior can be analyzed as the continuous growth of a penny-shape crack. In this paper, the inclusion size is fixed as  $\rho = 5\mu m$  and the step width of each circumferential area is set as  $\Delta r = 1\mu m$ , as reasonable values making reference to the experimental evidence. Since the threshold value of the crack growth is given as  $\Delta K_{th} \cong 5 \text{ MPa} \sqrt{m}$ , the applied stress is calculated as  $\sigma = 1224 \text{ MPa}$  under the condition that the  $\Delta K$  value at the FGA front has to agree with the value of  $\Delta K_{th}$  [1].

### PROBABILISTIC MODELS OF CRACK GROWTH WITHIN FGA

As mentioned previously, the fine granular layer would be formed around the inclusion after a certain number of stress cycles. Fundamental view of the crack growth within the FGA in this study is based on intermittent micro-debondings along the boundary between such a fine granular layer and the matrix of the steel. At a certain stage of the cyclic loadings, a few polygonized cells begin to debond along the boundary.

In this study, three different types of  $P(N)$  are assumed as indicated in Fig.3. In Model 1, the debonding probability  $P(N)$  tends to increase gradually at the early stage of the cyclic loadings. However, this probability tends to decrease at the final stage of the cyclic loading. Thus, the increasing rate of the probability  $P(N)$  gives the highest value at the middle stage. Accordingly, the function of  $P(N)$  reveals “S-shape” as shown by dashed curve in Fig.3. The entire life range to accomplish the FGA is fixed as  $N = 1.3 \times 10^5$  in the present simulation. Of course,  $P(N) = 1$  at  $N = 1.3 \times 10^5$  means the final formation of the FGA.

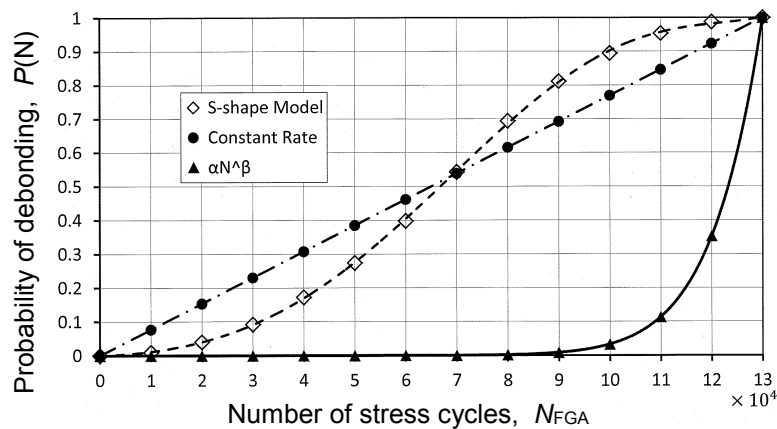


Fig.3: Three different models on the variation of  $P(N)$ .

In model 2, the increasing rate of the debonding probability,  $dP(N)/dN$ , is assumed to be constant as  $dP(N)/dN = 1/1.3 \times 10^5 = 7.69 \times 10^{-6}$ . In this case, the variation of  $P(N)$  is represented by a straight chained line in Fig.3. As model 3, the power law of  $P(N) = \alpha N^\beta$  is

accepted here to represent the crack growth behavior within the FGA. Based on the boundary conditions, parameters  $\alpha$  and  $\beta$  are determined as follows;

$$\alpha = 3.30 \times 10^{-67} \quad \text{and} \quad \beta = 13, \quad (2)$$

respectively. The variation of  $P(N)$  in Model 3 is shown by solid curve in Fig.3.

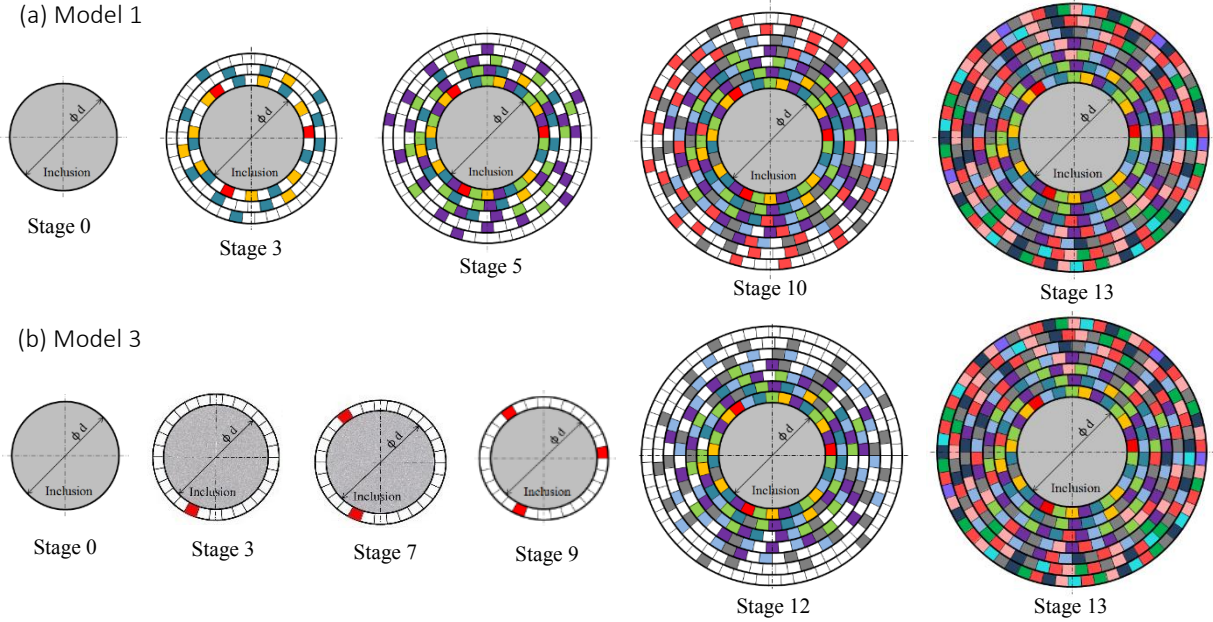


**Fig.4:** Increasing process of debonding probability in Model 1 and Model 3.

For the sake of better understanding, the increasing process of the debonding probability in each of Model 1 and Model 3 is depicted in Fig.4. Each stage number indicates the corresponding stage along the abscissa in Fig.3. In Model 1, the number of debonded cells tends to increase following the dashed curve in Fig.3. However, the number in Model 3 keeps extremely small value during the long term until Stage 10.

## RELATIONSHIPS BETWEEN CRACK GROWTH RATE AND SIF RANGE

Based on the definition in Fig.2(b), the intermittent increasing process of the debonding probability can be replaced into the continuous crack growth behavior for the usual penny-shape crack. By differentiation of Eq.(1), the crack growth rate  $da/dN$  is given as follows;

$$\frac{da}{dN} = 7\Delta r \frac{dP(N)}{dN}. \quad (3)$$

Eq.(3) means that the crack growth rate  $da/dN$  can be analyzed from the increasing rate of the debonding probability  $dP/dN$ . The applied stress in the present simulation is already given as  $\sigma = 1224$  MPa from the fact that the stress intensity factor range at the FGA front agrees with the value of  $\Delta K_{th} \cong 5$  MPa  $\sqrt{m}$ . The value of  $\Delta K$  at the front of the interior defect is evaluated by applying the concept of  $\sqrt{area}$  as follows [4];

$$\Delta K = 0.5\sigma\sqrt{\pi\sqrt{area}} = 0.5\sigma\sqrt{\pi\sqrt{\pi a^2}}. \quad (4)$$

Thus, one can calculate the crack length  $a$ , the crack growth rate  $da/dN$  and the SIF range  $\Delta K$  by Eqs.(1), (3) and (4), respectively.



The relationships between  $da/dN$  and  $\Delta K$  thus obtained are plotted in Fig.5. Symbol of  $\circ$  indicates the experimental data on the large crack obtained for the same steel by Beswick [5]. Based on this figure, the following Paris' law is confirmed

$$\frac{da}{dN} = 2.59 \times 10^{-13} (\Delta K)^{4.91} \quad (5)$$

for the usual size of the crack [6]. Since the threshold value is given as  $\Delta K_{th} \cong 5 \text{ MPa } \sqrt{m}$ , the regression line refracts toward the bottom at the critical value. The refraction point is given as  $\Delta K = 5 \text{ MPa}$  and  $da/dN = 7 \times 10^{-10}$ .

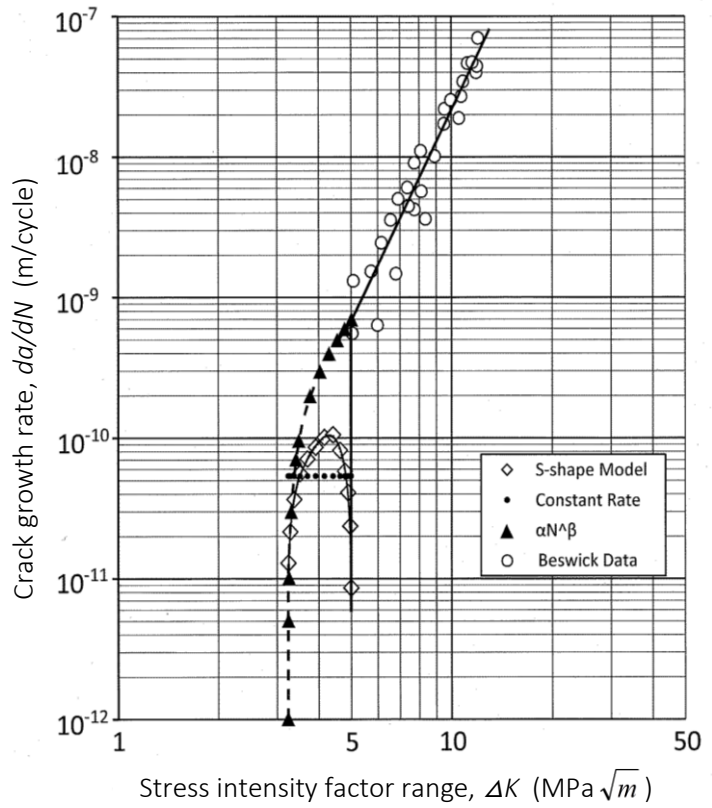


Fig.5: Relationship between crack growth rate and SIF range.

Finally, a particular attention should be paid to the analytical results on the crack growth behavior within the range of the FGA. In Model 1, the crack growth rate tends to increase rapidly at the early stage, but the rate tends to decrease rapidly after the highest rate of  $da/dN \cong 1 \times 10^{-10}$ . Then, after a certain pause, the crack tends to propagate following the Paris' law of Eq.(5). In Model 2, the crack growth rate is constant during the entire period of the crack growth within the FGA. Thus, the analytical results are horizontally plotted at the value of  $da/dN = 5.38 \times 10^{-11} \text{ m/cycle}$  as indicated by small black dots. However, in the case of Model 3, analytical results are appearing along a curve smoothly connected to the regression line of Paris' law. Comparing all the analytical results of Model 1, Model 2 and Model 3 one another, the result in Model 3 is supposed to give the most reasonable one.

## ANALYSIS OF THREE TYPICAL COMPONENTS OF TOTAL FATIGUE LIFE

According to experimental results reported by many researchers[1-3], the fatigue life of the present steel (JIS: SUJ2) is expected to be  $N = 10^8$  at the stress level of  $\sigma = 1224 \text{ MPa}$ . In this case, the crack propagation life to form the fish-eye is calculate by integration of Eq.(5) as follows;

$$N_{fish-eye} = \frac{2}{C(m-2)\pi^{m/2}\Delta\sigma^m} \left\{ a_i^{\frac{2-m}{2}} - a_f^{\frac{2-m}{2}} \right\} = 1.52 \times 10^3 \quad (6)$$

If the analytical results within the FGA in Fig.5 are accepted as the possible crack growth behavior, the fatigue life to form the entire area of the FGA is  $N_{FGA} = 1.3 \times 10^5$  from the debonding probability increasing models in this study. Therefore, the remaining life of the total fatigue life should be occupied for the polygonization (formation of the fine granular layer)

around the inclusion. Then, if the fatigue life causing the polygonization is denoted by  $N_{poly}$ , it is given by

$$N_{poly} = N_t - N_{FGA} - N_{fish-eye} = 10^8 - 1.3 \times 10^5 - 1.52 \times 10^3 = 9.99 \times 10^7. \quad (7)$$

Consequently, it is noted that the fatigue life to produce the fine granular layer without any micro-cracking has to occupy more than 90% of the total fatigue life.

## CONCLUDING REMARKS

- 1) During a long sequence of cyclic loadings, the fine granular layer is formed around the inclusion, after which micro-debondings take place isolatedly along the boundary between the fine granular layer and the matrix of the steel. The apparent crack growth rate can be effectively evaluated from the increasing rate of the micro-debondings.
- 2) Based on comparison of three different models, it was found that the model assuming the power law for the debonding probability increasing rate gives the most reasonable result for the crack growth behavior within the FGA around the interior inclusion.
- 3) Total fatigue life is divided into three typical components of the fine granular layer forming life, the FGA forming life and the fish-eye forming life, respectively. In such life components, the component of the fine granular layer formation occupies more than 90% of the total fatigue life.

## REFERENCES

- [ 1 ] Sakai T.:  
Review and prospects for current studies on very high cycle fatigue of metallic materials for machine structural use  
J. Solid Mech. and Mater Engng, Vol.3, No.3, (2009), pp.425-439
- [ 2 ] Sakai, T.; Sato, Y.; Oguma, N.:  
Characteristic S-N properties of high-carbon-chromium-bearing steel under axial loading in long-life fatigue  
Fatigue Fract. Engng. Mater. Struct., Vol.25, (2002), pp. 765-773
- [ 3 ] Sakai T.; Oguma N.; Morikawa A.: Microscopic and Nanoscopic Observations of Metallurgical Structures around Inclusions at Interior Crack Initiation Site for a Bearing Steel in Very High Cycle Fatigue, Fatigue and Fract. Engng. Mater. Struct., Vol.38, (2015), pp.1305-1314
- [ 4 ] Murakami Y.:  
Metal Fatigue: Effects of Small Defects and Nonmetallic Inclusions  
Elsevier Science Ltd., 2002
- [ 5 ] Beswick J. M.;  
Fracture and Fatigue Crack Propagation Properties of Hardened 52100 Steel,  
Metall. Trans., Vol.20A, (1989), pp.1961-1973
- [ 6 ] Paris P. C.; Erdogan F:  
A Critical Analysis of Crack Propagation Laws,  
Trans., ASME, Series D, Vol.85, No.4, (1963), pp.528-534

**Corresponding author:** sakai@se.ritsumei.ac.jp



# FRACTURE MECHANICS CONSIDERATION OF INTERIOR FRACTURE ORIGIN WITHOUT INCLUSION UNDER ROTATING BENDING IN VERY HIGH CYCLE FATIGUE

N. Oguma<sup>1)</sup>, Y. Nakahashi<sup>2)</sup> and T. Sakai<sup>3)</sup>

<sup>1)</sup> Faculty of Engineering, University of Toyama,  
3190 Gofuku, Toyama, 930-8555 Japan

<sup>2)</sup> Break Design Department, Engineering Division, Hosei Industry Co., Ltd.,  
10 Michigami Kazue-cho, Toyota, Aichi, 470-1293 Japan

<sup>3)</sup> Research Organization of Science and Engineering, Ritsumeikan University,  
1-1-1 Nojihigashi, Kusatsu, Shiga, 525-8577 Japan

## ABSTRACT

In this study, the fatigue property in very high cycle regime for hydrogen-charged specimens of high carbon chromium steel was examined under rotating bending. In the relatively low cycle regime of  $N < 10^6$ , all specimens have failed in the inclusion induced fracture mode. On the other hand, in the regime of  $N > 10^6$ , the fine granular area, FGA, was observed around the inclusion on the fracture surface in some specimens. Furthermore, a certain inclined surface without inclusion was also frequently found at the crack initiation site on the fracture surface. From the three dimensional geometry of the inclined area at the crack initiation site, the inclined area without inclusion are suggested to be formed based on the crystal triple point, CTP, for packet boundaries of martensite in a grain. Fracture mechanics considerations were carried out on these characteristic fracture origin. The stress intensity factor range was calculated by using Murakami's  $\sqrt{area}$  model. The stress intensity factor range at the FGA front,  $\Delta K_{FGA}$ , was within a range from 3.6 to 4.7  $MPa\sqrt{m}$ , whereas the stress intensity factor range at edge of the CTP area,  $\Delta K_{CTP}$ , was from 2.8 to 3.7  $MPa\sqrt{m}$ . In the above calculations, the projected area of the CTP was accepted as the area of  $\sqrt{area}$  model. In addition, the local stress at the CTP area is resolved into parallel and perpendicular stress components with respect to the inclined surface. The stress intensity factor range for each stress component was calculated, and both stress intensity factor ranges were combined with energy release rate model. Based on this procedure, the stress intensity factor range at edge of the CTP area was in good agreement with the corresponding value of FGA.

## KEYWORDS

Hydrogen charged high strength steel, rotating bending, non-inclusion induced fracture, crystal triple point, energy release rate model, stress components

## INTRODUCTION

Various kinds of high strength steels have been used as load carrying components of mechanical structures in the wide variety of the engineering applications. It is well-known that such high strength steels are usually sensitive to environmental factors such as hydrogen and humidity controlling the fracture [1]. Although a lot of researches on hydrogen embrittlement have been reported up to now [2] [3], actual behavior of the hydrogen trapped inside the

material is not sufficiently clear. The authors have carried out the rotating bending fatigue tests for the bearing steel subjected to hydrogen charging. Thus, it was found that the fatigue life became shorter by applying the hydrogen charging. In addition, all fracture origins were interior inclusions and, therefore, any surface induced fracture did not occur [4] [5]. Artificially charged hydrogen may diffuse and release during the long sequence of cyclic loadings. In such a circumstance, there is a possibility that the service life is almost same as that of the specimen without hydrogen charging in the low stress amplitude and long life regime.

The first aim in this study is the accumulation of experimental data causing the fatigue fracture at low stress level in very high cycle regime. Making reference to those data, the authors have found a lot of experimental results, in which no inclusion has observed at the interior crack initiation site. Accordingly, as the second aim of this work, a particular attention was paid to the crack initiation mechanism in the interior fracture mode without any inclusion. As a result, it was found that the crystal triple point (CTP) in the microstructure of the steel played an important role to the crack initiation in the very high cycle fatigue at particularly low stress level.

## EXPERIMENTAL PROCEDURE

### Specimen

The material used in this study was a bearing steel mainly composed of 0.96mass% carbon and 1.45mass% chromium, coded as SUJ2 in Japanese Industrial Standard. Specimens were machined by using a grinder into dimensions shown in Fig.1 after heat treatment. After austenization at 1108K for 40minutes, the specimens were quenched in oil at 353K. Then they were tempered at 453K for 120minutes and cooled in air. Diameter of the critical portion for the hourglass type specimen is 3mm, and the round notch radius is 7mm. The stress concentration factor of this specimen in bending is given as 1.06. The critical portion was finished into a mirror surface in order to remove grinding marks. The average value of hardness was given as 740HV.

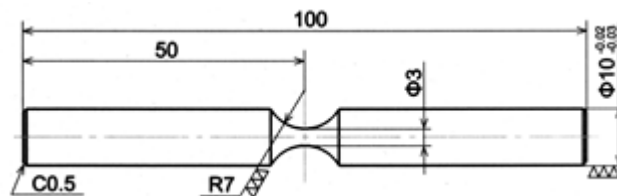


Fig.1: Shape and dimensions of specimen

Hydrogen charge to the specimen was conducted at 323K for 24hours using the immersed method in which 20 mass% ammonium thiocyanate solution was used. After the hydrogen charge, the corrosion layer of the critical portion of the specimen was removed by buffing. All the fatigue tests in this program had started within one and a half hours after hydrogen charging in order to keep the same condition for the hydrogen content.

### Testing

Rotating bending fatigue tests were performed by means of a cantilever-type multi-spindle rotating bending fatigue testing machine in the room atmosphere without any control of temperature and humidity [6]. The rotating speed of the spindle was 4000rpm. Fracture surface and crack origin of each specimen were observed by an SEM.

## EXPERIMENTAL RESULTS

Results of rotating fatigue tests are shown in Fig. 2 together with the duplex S-N curves for hydrogen-uncharged specimens plotted by dashed and solid lines. The hollow circle plots in the figure show the data of the surface inclusion induced fracture, whereas the solid circle pots show the results for the interior inclusion induced fracture. In addition, the semi-solid circle plots show the data indicating the fine granular area, FGA, around the interior inclusion. On the other hand, a lot of plots given by red triangles in the long life region show the data in which inclusion was not confirmed at the crack origin. The percentage of interior fracture origin without inclusion in very high cycle regime was 75%, while the percentage with inclusion was only 25%.

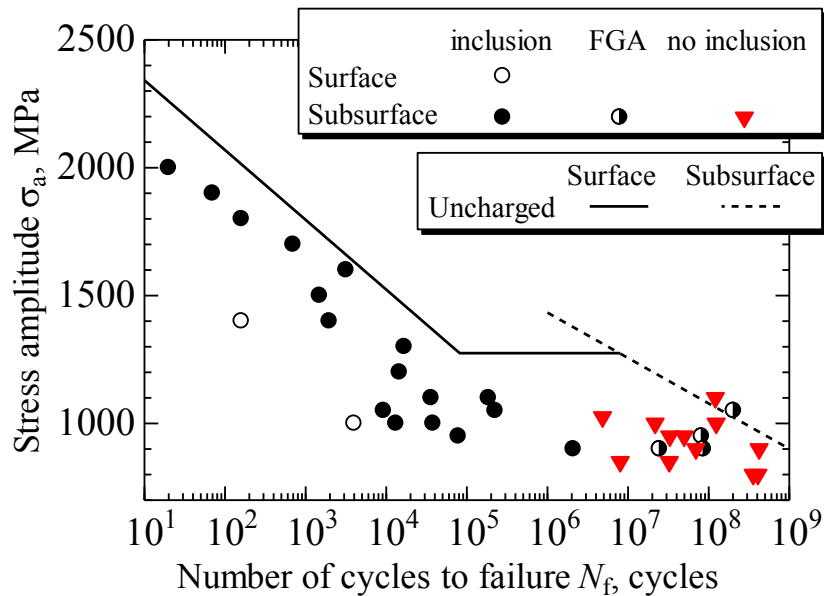
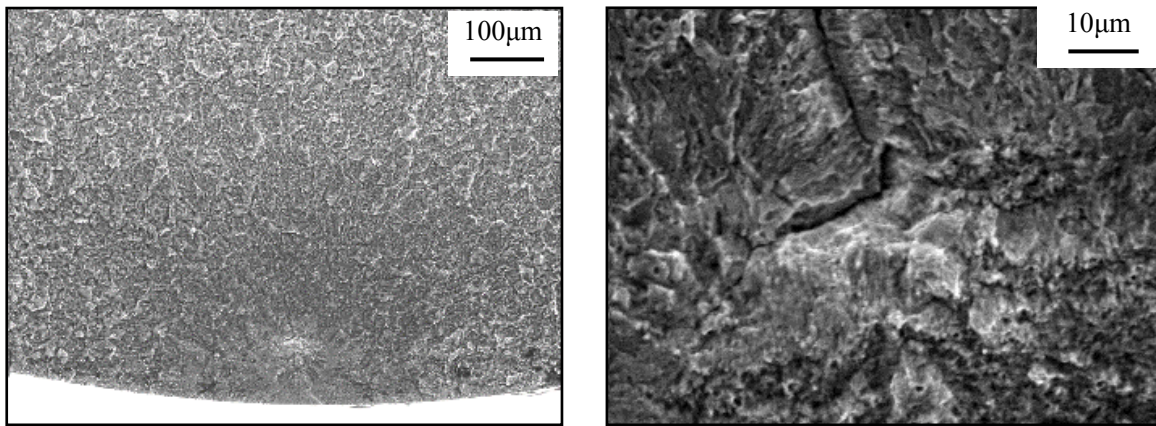


Fig. 2: S-N property of hydrogen charged specimens.

## SEM OBSERVATIONS

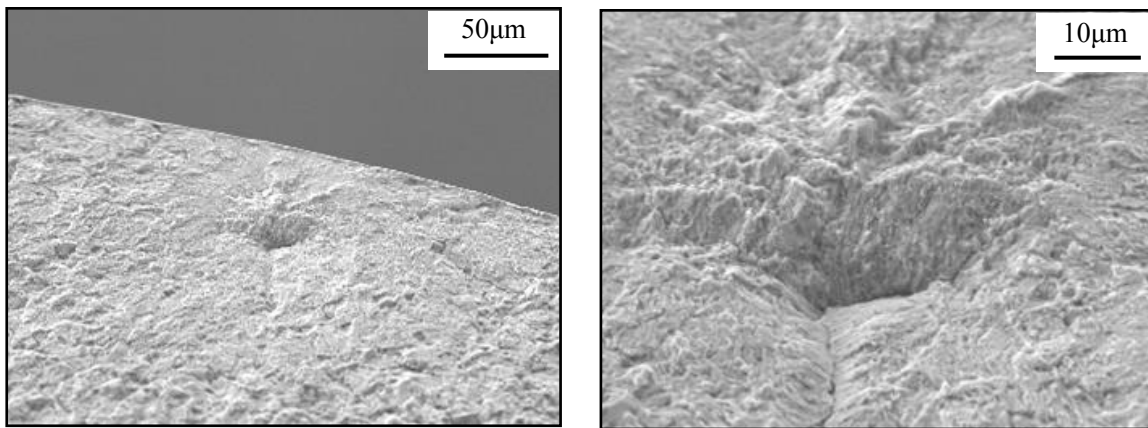
Fig. 3 shows examples of SEM observations of the crack initiation site without inclusion on the fracture surface failed in very high cycles regime ( $\sigma_a=800\text{MPa}$ ,  $N_f=3.56 \times 10^8$  cycles). From the high magnification observation photograph in Fig. 3(b), it is found that there is a clear protrusion at the crack initiation site. Therefore, the opposite fracture surface of the same specimen was observed by FE-SEM. Since the crack initiation site had a slope, the sample was tilted and observed as shown in Fig. 4. From the high magnification observation photograph in Fig. 4(b), the crack would be supposed to take place in the vicinity indicating the characteristic three-dimensional undulation. By paying a particular attention to the three-dimensional aspect at the crack initiation site in a pair of Fig. 3(b) and Fig. 4(b), the packet boundary within martensite grain or the prior austenite grain boundary can work as the crack starter in the very high cycle regime at such a low stress level. However, based on the additional observations, the authors have found following aspects; (1) this area is smaller than the prior austenite grain size, (2) the inclined face is relatively coarse, and (3) precipitation of the spheroidized carbides are less rather than the prior austenite grain boundary. Based on these evidences, it is presumed that the crack initiation site is corresponding to the crystal triple point (hereinafter referred to as CTP) at the martensite packet boundary.



(a) Low magnification

(b) High magnification

**Fig. 3:** SEM observations of the crack initiation site on the fracture surface ( $\sigma_a=800\text{MPa}$ ,  $N_f=3.56 \times 10^8$  cycles).



(a) Low magnification

(b) High magnification

**Fig. 4:** FE-SEM tilted observations of the crack initiation site on the opposite fracture surface of Fig. 3.

## DISCUSSION BASED ON FRACTURE MECHANICS

Fig. 5 shows the relationship between either of the stress intensity factor range at inclusion, FGA or CTP at the crack initiation site and the fatigue life. Meaning of the respective symbols is provided in Fig. 5. The horizontal dotted line in Fig. 5 indicates the threshold stress intensity factor range of the specimen without hydrogen charging. The stress intensity factor range was calculated by the  $\sqrt{areaa}$  model proposed by Murakami [7]. In the case of the CTP origin,  $\sqrt{area_{CTP}}$  was evaluated by the area projected perpendicular to the loading direction. In the long life regime exceeds  $10^6$  cycles, the specimen fails at the inclusion with the FGA and the stress intensity factor range at the FGA is 3.6 to 4.7  $\text{MPa}\sqrt{m}$ . On the other hand, the stress intensity factor range of the CTP is within a range of 2.8 to 3.7  $\text{MPa}\sqrt{m}$ . It is difficult to explain the difference of those values depending on the presence or absence of the inclusion at the crack initiation site.

From this point of view, by using the actual area of the CTP, the stress intensity factor range  $\Delta K_{CTP\sigma_n}$  and  $\Delta K_{CTP\tau}$  were calculated for the respective stress components  $\sigma_n$  and  $\tau$  for the CTP plane. The shape factor for calculating the stress intensity factor range was 0.5 for the

vertical stress component and 0.58 for the shear stress component. The principle of superposition cannot be applied because the stress intensity factor range calculated based on each stress component has different modes. Accordingly, the modified stress intensity factor range of the CTP,  $\Delta K'_{CTP}$ , was calculated by the following equation of an energy release rate model [8].

$$\Delta K'_{CTP} = \sqrt{\Delta K_{CTP\sigma n}^2 + \Delta K_{CTP\tau}^2}. \quad (1)$$

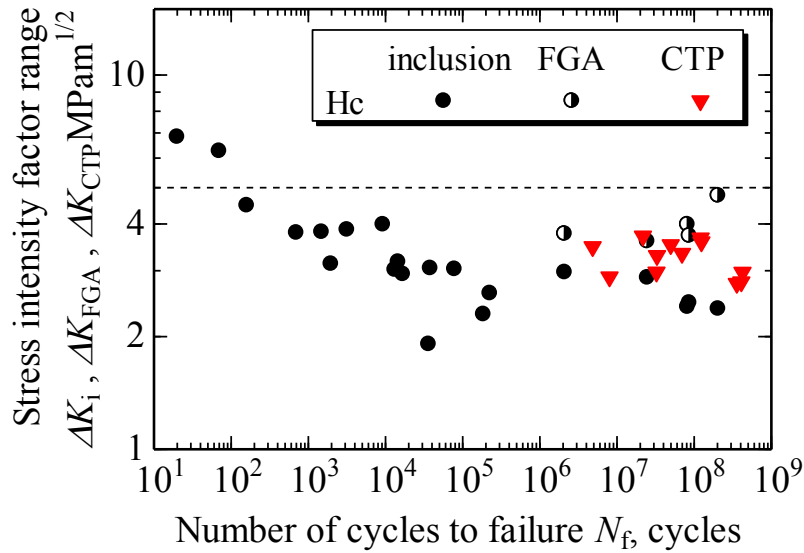


Fig. 5: Relationship between stress intensity factor range and fatigue life.

Values of the modified stress intensity factor range at each of the CTP and the FGA in the very high cycle regime are replotted as functions of the fatigue life in Fig. 6. As can be seen in the figure, the critical stress intensity factor range to restrict the crack growth is almost equal for both fracture modes, which is estimated to be about  $4\text{MPa}\sqrt{m}$ .

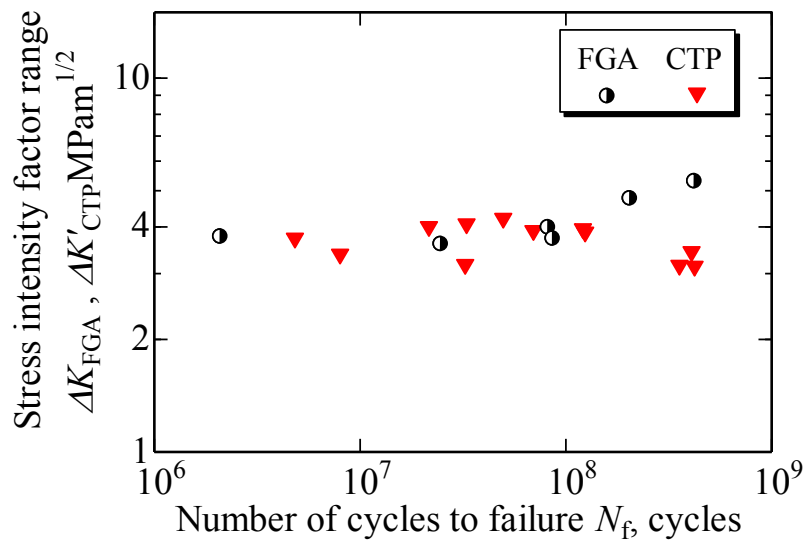


Fig. 6: Relationship between modified stress intensity factor range at the CTP in very high cycle regime and fatigue life.

## CONCLUSIONS

- (1) In fatigue tests for the bearing steel with hydrogen charging, a lot of interior induced fractures without any inclusion were obtained in the very high cycle regime. From the three dimensional geometry at the crack initiation site of the fracture surface, the crack initiation without inclusion is suggested to occur at the crystal triple point, CTP, for packet boundaries of martensite in a grain.
- (2) When the feasibility of the crack initiation due to the inclusion is less than that of the crack initiation at the CTP, the fatigue crack tends to take place preferentially at the CTP. Thus, the competition of the feasibility of each crack initiation mode governs the actual mode of the inclusion-induced crack initiation or the CTP-induced crack initiation.
- (3) If the  $\Delta K$  is evaluated by combination of two different modes of Mode I and Mode II in the CTP crack initiation, the resultant of  $\sqrt{\Delta K_{CTP\sigma n}^2 + \Delta K_{CTP\tau}^2}$  can provide an acceptable value which is well corresponding to the value calculated for the inclusion-induced fracture with the FGA .

## REFERENCES

- [1] Edited by Nakai Y. et al.:  
Strength and Fracture of Materials,  
The Soc. Mat. Sci, Japan, Kyoto, 2011
- [2] Takai K.:  
Hydrogen Existing States in Metals  
Trans. JSME, Vol. 70, No. 696, (2004), pp.1027- 1035
- [3] Murakami Y.; Nagata J.:  
Influence Factor of Fatigue Design in Ultralong Life Regime and Effect of Hydrogen on Fatigue Strength of High Strength Steel  
Trans. JSME, Vol. 70, No. 696, (2004), pp.1093- 1101
- [4] Oguma N.; Sekisugi N.; Kida K.; Otake Y.; Sakai T.:  
Period of Fine Granular Area Formation of Bearing Steel in Very High Cycle Fatigue Regime  
Advanced Materials Research, Vols. 891-892, (2014), pp.434-439
- [5] Oguma N.; Sekisugi N.; Otake Y.; Sakai T.:  
Estimation of Fatigue Limit in Interior Inclusion Induced Fracture Mode for Bearing Steel in Rotating Bending  
Key Engineering Materials, Vol. 664, (2016), pp. 188-198
- [6] Yamamoto T.; Kokubu A.; Sakai T.; Kiyama I.; Nakamura Y.:  
Development and Fundamental Performance of Dual-spindle Rotating Bending Fatigue Testing Machine with Special Device Providing Corrosive Environments  
Proceedings of 5<sup>th</sup> Int. Conf. on Very High Cycle Fatigue, (2011), pp. 439-444
- [7] Murakami Y.:  
Metal Fatigue: Effects of small Defects and Nonmetallic Inclusions  
Elsevier Science Ltd., 2002
- [8] Rhee H.C.; Salama M.M.:  
Mixed-mode stress intensity factor solutions of a warped surface flaw by three-dimensional finite element analysis  
Engineering Fracture Mechanics, Vol. 28, No. 2, (1987), pp.203-209

Corresponding author: oguma@eng.u-toyama.ac.jp

# SCALING ANALYSIS OF FINE GRANULAR AREA (FGA) AROUND INTERIOR INCLUSION AT CRACK INITIATION SITE IN VERY HIGH CYCLE FATIGUE

Mikhail BANNIKOV<sup>1</sup>, Oleg NAIMARK<sup>1</sup>, Tatsuo SAKAI<sup>2</sup> and Noriyasu OGUMA<sup>3</sup>

<sup>1</sup> Institute of Continuous Media Mechanics, Russian Academy of Sciences,  
1 Academician Korolev str., 614013 Perm Russia

<sup>2</sup> Research Organization of Science and Engineering, Ritsumeikan University,  
1-1-1 Noji-higashi, Kusatsu, Shiga, 525-8577 Japan

<sup>3</sup> Faculty of Engineering, University of Toyama, 3190 Gofuku, Toyama, 930-8555 Japan

## ABSTRACT

In the very high cycle regime, the fatigue fracture of high strength steels tends to occur from the interior inclusion and, therefore, a fish-eye is usually observed at the crack initiation site. In addition, the fine granular area (FGA) is often found in the vicinity around the inclusion on the fracture surface. It is reported that the FGA formation period tends to occupy more than 90% of the total fatigue life. Thus, the FGA formation mechanism is one of the most important subjects in the very high cycle fatigue. From this point of view, the authors have attempted to construct the FGA formation model based on the current experimental results obtained by the authors. In this model, FGA formation is interpreted as intermittent micro-debondings and their coalescence during the long sequence of the cyclic loadings.

Structural mechanisms of FGA origin were studied to analyze the defect induced roughness (after interferometer-profiler New View 5000 data) to estimate the spatial scaling invariance in term of the Hurst exponent in this area. Two characteristic cases were analyzed: FGA origin in the presence and without of interior inclusions. Close values of the Hurst exponents in both cases supported the assumption concerning the mechanism of the FGA origin as specific area of damage localization subject to characteristic law of damage kinetics –self-similar blow-up damage kinetics. Blow-up damage kinetics corresponds to the limit case of grain reefing (dislocation free grains) on the size of FGA that is given by the parameter of self-similar solution.

## KEYWORDS

Very high cycle fatigue, Interior inclusion, Fine granular area (FGA), Self-similarity, Crack generation, Crack propagation

## INTRODUCTION

HCF and VHCF are important fundamental and engineering problems for several areas of applications. Catastrophic events caused by failure of gas-turbine motors, high costs of fatigue life-time estimation for constructions and potential cost of development of new constructions initiated perspective conceptions in the area of HCF and VHCF based on the fundamental research in fatigue damage and reliability prediction. The kernel aspects of such programs are development of approaches using the results of fundamental research, modern approaches in the laboratory modeling and structural analysis for the prediction of characteristic stages of fatigue damage and the criticality signs under damage-failure transition. Recently, an increase in the strength properties of structural materials has been achieved by the formation of micro- and nano-crystalline structure. However, traditional methods of testing do not provide an estimate of fatigue life in gigacycle loading conditions ( $10^9$  cycles to failure) leading to the emergence of new techniques based on ultrasonic testing machines like [1] and studying the morphology of the fracture surfaces by modern methods of structural analysis. The effect of microstructure in pure titanium including submicrocrystalline (SMC) and Ti6Al4V alloy was studied in gigacycle fatigue regime and qualitative differences in the mechanisms of fatigue crack initiation in high- and gigacycle fatigue conditions established.



## EXPERIMENTAL CONDITIONS AND MATERIALS

Specimens of iron and pure titanium with different microstructure from original polycrystalline state with grain size of 25  $\mu\text{m}$  to SMC state obtained through equal channel angular extrusion (ECAE) at different conditions: SMC-1 state (annealing at  $T = 450\text{ }^\circ\text{C}$ , 8 passes of ECAE, drawing from 14 to 9 mm at  $T = 200\text{ }^\circ\text{C}$ , the grain size: 100-150 nm) and SMC-2 state (annealing at  $T = 450\text{ }^\circ\text{C}$ , 4 passes of ECAE, the warm rolling from 12 to 8 mm at  $T = 350\text{ }^\circ\text{C}$ , the grain size of 200 nm) and specimens of titanium alloy Ti6Al4V were investigated in high- and gigacycle fatigue regime using the ultrasonic testing machine. In order to establish the scale invariant parameter [2-4] of crack initiation and growth in high- and gigacycle fatigue fracture surfaces of samples were analyzed.

Fatigue tests were carried out on the ultrasonic loading machine Shimadzu USF-2000, which imposes special load conditions due to the geometry of the samples (fig.1). During the experiment, the sample and components of the machine are in resonant oscillations which form a standing wave. In this case peaks of displacement are located on ends of the sample and maximum amplitude of stress is located in the center of sample [4].

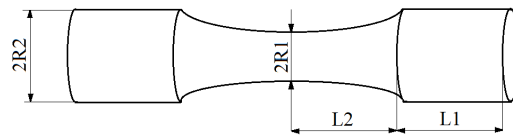


**Fig. 1:** Geometry of specimen. Values of sizes R1, R2, L2, L1 is depends on parameters of material and calculates in formalts at [4].

## RESULTS OF FATIGUE EXPERIMENTS

The result of fatigue tests are shown in the Fig. 2. Fatigue failure of Ti6Al4V after  $10^9$  cycles occurred at stress amplitude 495 MPa. Failure of samples of pure titanium after  $10^9$  loading cycles occurred at 275 MPa stress amplitudes for the initial state and 375 MPa and 340 MPa for the states SMC-1 and SMC-2, respectively. Fatigue life of titanium alloy Ti6Al4V in gigacycle regime corresponds to the data of Bathias [5]. The SMC-1 titanium Ti-Grade 4 with equilibrium grain boundaries exhibits highest fatigue properties compared to the SMC-2 state with non-equilibrium grain boundaries and to the polycrystalline state (grain size of about 25  $\mu\text{m}$ ).

Mechanisms of initiation and propagation of fatigue cracks were investigated by means of qualitative and quantitative analysis of the morphology of fracture surfaces. The results of observation reported in [6] show that during stress cycles several fine subgrains having different crystal orientations are formed in a thin layer (thickness is 400 nm) around non-metallic inclusion. The following mechanism of crack initiation under long cyclic loading was proposed: a fine granular layer caused by the intensive polygonization is gradually formed around the interior inclusion. The number of microdamage centers in this layer gradually increases and some of them coalesce. When damage spread over the entire fine granular layer the crack is finally formed around the interior inclusion. After the crack has grown to a critical size, it propagates in accordance with the Paris law kinetics:

$$\frac{da}{dN} = C(\Delta K)^m, \quad (1)$$

where  $da/dN$  is the fatigue crack growth rate, C and m are empiric constants depending on the material, K is the stress intensity factor. Qualitative analysis was carried out by using optical and electron microscopy of the surface morphology.



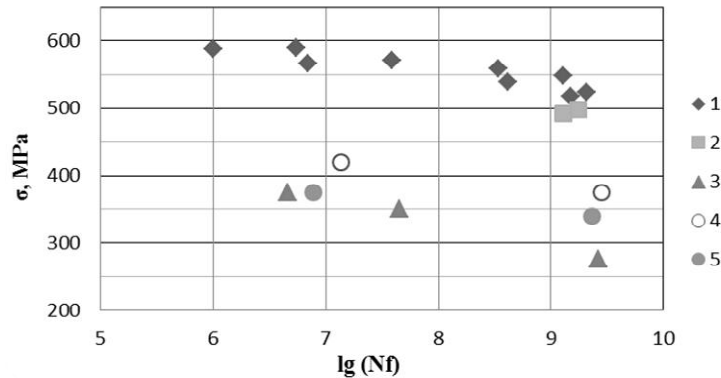


**Fig. 2:** Fatigue curve data for investigated materials:  $\sigma$  – applied mean stress,  $N_f$  – number of cycles to failure. 1 – Ti6Al4V Bathias [5]; 2 – Ti6Al4V; 3 – Ti Grade-4 initial state; 4 – Ti Grade-4 SMC-1 state; 5 – Ti Grade-4 SMC-2 state.

## QUALITY AND QUANTITATIVE ANALYSIS OF FRACTURE SURFACES

Destruction in gigacycle fatigue regime usually forms a characteristic type of fracture surface - "fish-eye"[5-6]. Qualitative analysis by optical microscope allows us to separate zones with different reflectivity. First zone with a radius of 150  $\mu\text{m}$  from the source of crack is very dark, then light and smooth area is followed, which is then replaced by darker area (fig.3).

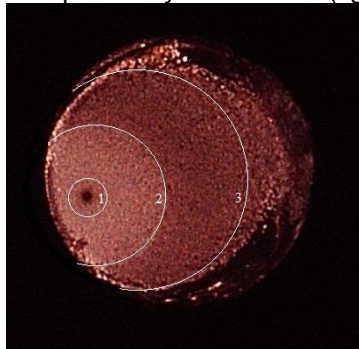


**Fig. 3:** Fracture surface of Ti6Al4V in gigacycle fatigue regime. 1)  $a = 150 \mu\text{m}$ ,  $\Delta K = 6,88 \text{ MPa m}^{1/2} \approx \Delta K_{th}$ ; 2)  $a = 750 \mu\text{m}$ ,  $\Delta K = 21,3 \text{ MPa m}^{1/2}$ ; 3)  $a = 1400 \mu\text{m}$ ,  $\Delta K = 54,1 \text{ MPa m}^{1/2} \approx \Delta K_{1c}$

By substituting the radius of the borders in the formula (2) for the stress intensity factor of radial inner cracks

$$K = 2\sigma\sqrt{a/\pi F[D/(2a)]}, \quad (2)$$

where  $F$  is normalization function,  $D$  is diameter of the sample, these zones can be associated with the stages of crack nucleation and propagation. Radius  $a \sim 150$  microns corresponds to the threshold value of the stress intensity factor  $\Delta K_{th}$  for this material at which the crack begins to grow. In the area between borders of 1 and 2, the crack grows steadily by Paris law (1). Area between boundaries 2 and 3 corresponds to catastrophically fast growth of crack. The value of  $K$  with radius of crack 3 - 1400  $\mu\text{m}$  corresponds to the fracture toughness.

The surface roughness was analysed by interferometer-profiler New View 5010 to establish quantitative characteristics of the fracture surface. Two distinct zones with strongly different roughness were observed: zone I of the size  $\sim 100$ -300  $\mu\text{m}$  diameter, depending on testing material in the vicinity of the crack origin has high fracture surface roughness, which corresponds to the area of defect initiation and accumulation during cyclic loading; zone II that covers rest of the fracture surface is smoother than the first, corresponds to the crack propagation according Paris law (1). These results confirm the crack initiation mechanism described in [6].

To investigate scale-invariant properties of the fracture surface, one-dimensional profiles with different lengths were analyzed using two-dimensional profiles with the interferometer New View data (Fig.4).

The Hurst exponent was defined from the slope of linear portion of the correlation function  $K(r)$  in logarithmic coordinates [3,4,7]:

$$K(r) = \left\langle (z(x+r) - z(x))^2 \right\rangle_x^{1/2} \propto r^H \quad (3)$$

where  $z(x)$  is the relief height, depending on the coordinate  $x$ ; angular brackets denote averaging over  $x$ ,  $H$  is the Hurst exponent. In logarithmic coordinates the slope of the linear plot of this function determines the Hurst exponent. The spatial range of linear part establishes the correlated behaviour of defect induced roughness in the direction of fatigue crack propagation.

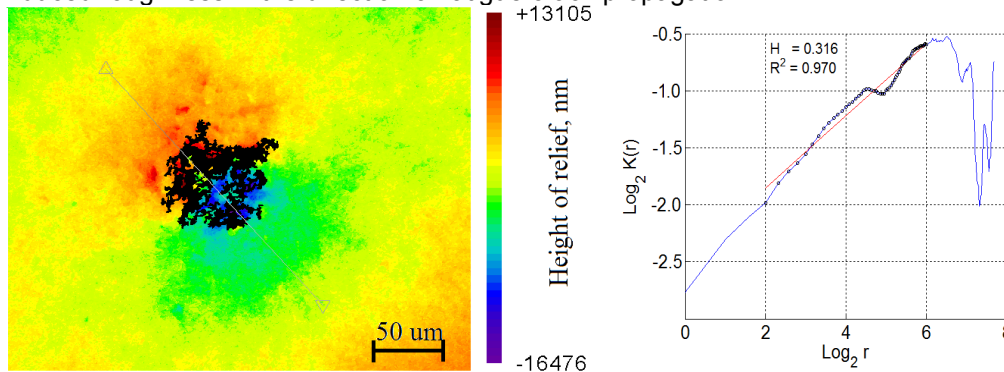


**Fig. 4.** New View colored image of roughness and log-log plot of correlation function  $K(r)$  in FGA. Grey trace show the crack propagation area.

The correlation function (3) calculated from the profiles for both zones has two linear portions with a break on the scale, which corresponds to change in the mechanisms of fracture surface topography. Whereas functions (3) calculated separately for zones 1 and 2 reveal only one linear portion for each zone (Fig. 5).

The gigacycle fatigue cracks for titanium Grade 4 were originated near the surface (70-150  $\mu\text{m}$ ) and the crack hotspot generally could not be detected based on the optical image. The roughness pattern analyzed according to the New View data allows one to differentiate between the zones of crack origination (size  $\sim 100 \mu\text{m}$ ) characterized by roughness invariance and the rest of the crack propagation roughness zone.

In samples of pure titanium Grade-4 under gigacycle fatigue regime of loading the crack was initiated at a depth of 70-150  $\mu\text{m}$  below the surface. Whereas characteristic feature of the fracture surface of such images unlike the alloy Ti6Al4V is the lack of an optical image of any zone boundaries. However, at the height map obtained using profilometer New View 5010 we can observe the characteristic crack initiation zone, which roughness is different from the rest of the zone of crack propagation, its radius is about to 50 microns.

Roughness of fracture surfaces of samples with the surface fatigue crack was also investigated by interferometer New View 5010 and analyzed with correlation function (3). The correlation function detects only one slope across the fracture surface of both near and far from the crack initiation point. The value of the Hurst exponent calculated on linear part of the correlation function corresponds to the fractal dimension of the profile of the crack propagating through Paris law like in second zone in previous case. The accumulation defects zone typical to internal crack initiation is not detected. This shows fundamentally different mechanisms for the fatigue crack initiation in the bulk and on the surface of material.

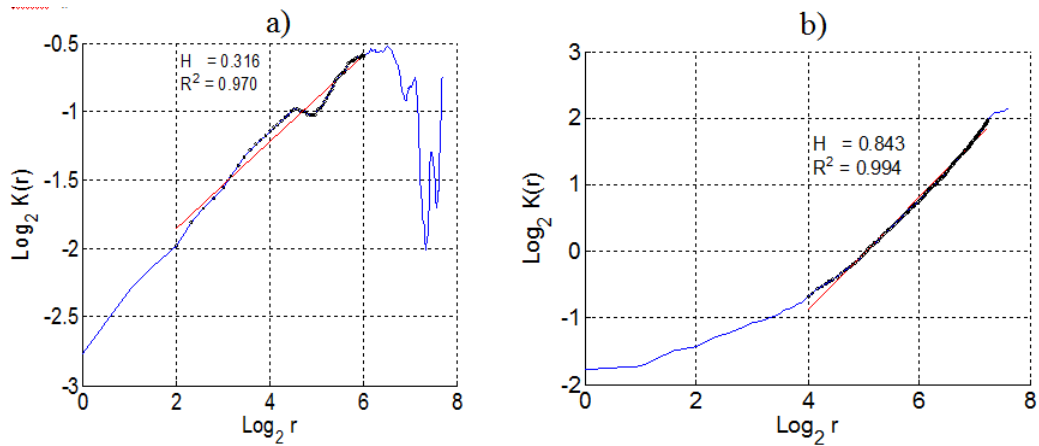


**Fig. 5:** Correlation function built on profiles: a) inside zone 1; b) inside zone 2.

The tests of pure iron samples in air and in contact with the liquid metal were carried out to investigate influence of surfactant on fatigue behavior in VHCF. For the examined material tested in air, there exists the presumed "fatigue limit" of  $3 \cdot 10^9$  cycle loading to fracture with the stress amplitude of 160 MPa. However, the application of a thin layer of liquid gallium alloy on the surface of the sample reduces its fatigue life by more than 2 orders of magnitude:  $6 \cdot 10^6 - 2.3 \cdot 10^7$  cycles to failure.

In the case of ultrasonic loading of the sample interacting with liquid gallium, the fatigue crack was initiated at the sample surface as in the case of operation of the classical cycle fatigue mechanisms. The edges of the cracks indicate that liquid metal penetrates into the crack during fatigue tests. The main role in gigacycle fatigue durability of the material is played by the process of nucleation of the fatigue cracks by [5,6-9], and the process of its propagation in the material takes only 2-5% of the "fatigue life". The fact that at the same level of the stress, fatigue fracture in the material being in contact with liquid metal occurs several orders of loading cycles earlier than in the air indicates that in general, changes in the mechanism of crack initiation occur under the influence of the surfactant.

The analysis of fractured surfaces revealed that the crack in the presence of liquid metal is initiated at the surface of the material. The analysis of the chemical elements using the spectra of electrons reflected from the fracture in the scanning electron microscope allowed us to determine that the liquid metal penetrates into the material to a depth of about 200 microns and resides exclusively in the center of crack initiation. While crack grows further into the material it is not affected by the surfactant. The analysis of fractured surface roughness by profilometer shown same behavior like in conventional high cycle fatigue: only one area with one scale invariance parameter. Thus, we can say that the effect of liquid metal embrittlement is observed only at the stage of fatigue crack initiation, and its propagation deep into the sample is governed by the classical Paris law.

## CONCLUSIONS

The analysis of scale-invariant properties of fracture surface allowed us to establish the qualitative difference in terms of the scale invariance (the Hurst exponent) of the surface roughness for the areas of crack initiation and propagation. The crack initiation area can be identified as the zone with pronounced multiscale defect interaction providing correlated behaviour over characteristic scale. The size of this zone and collective defect growth kinetics were studied in [9] and associated with special type of spatial-temporal defect organization named as collective blow-up mode of defects. The scenarios of crack nucleation (in the bulk of specimen for gigacycle load and at the surface for HCF) reflect qualitative different kinetics of collective behaviour of defects in mentioned regimes caused by typical size of defects and interaction length. However, the scenario of crack propagation under gigacycle regime corresponds to the Paris law that reflects the similarity in the mechanisms of plastic flow at the crack tip that still follows the stress induced singularity in term of the stress intensity factor increment. The effect of liquid-metal embrittlement occurs mainly at the stage of fatigue crack initiation and the process of the crack growth is governed by the classical Paris law. This fact can also be substantiated by the results obtained by [8] under low- and high-cycle fatigue loading regimes, when a decrease in durability (several times) was observed despite the fact that the stage of fatigue crack

initiation under low-cycle fatigue loading is significantly shorter. The property of the surface, as the high power "drain" for defects is significantly reduced in the case when the proximity of the chemical potentials of the solid and surfactant provides "adiabatic" scenario for the process of damage accumulation in the bulk of material.

## ACKNOWLEDGEMENT

This work was supported by grants from RFBR 16-41-590892, 16-48-590534 .

## REFERENCES

- [1] C. Bathias:  
Piezoelectric fatigue testing machines and devices,  
International Journal of Fatigue. 28 (2006) 1438-445.
- [2] G.I. Barenblatt:  
Scaling Phenomena in Fatigue and Fracture,  
International Journal of Fracture. 138(1) (2004) 19-35.
- [3] E. Bouchaud:  
Scaling properties of cracks,  
J. Phys.: Condens. Matter. 9 (1997) 4319–4344.
- [4] V.A. Oborin, M.V. Bannikov, O.B. Naimark, T. Palin-Luc:  
Scale invariance of fatigue crack grow in gigacycle loading,  
Technical Physics Letters. 36(22) (2010) 76-82.
- [5] C. Bathias, P.C. Paris:  
Gigacycle Fatigue in Mechanical Practice,  
Marcel Dekker Publisher Co, 2005.
- [6] T. Sakai:  
Review and Prospects for Current Studies on High Cycle Fatigue of Metallic  
Materials for Machine Structural Use,  
Jour. Solid Mech. and Mat. Eng. 3(3) (2009) 425-439.
- [7] V. Oborin, M. Bannikov, O. Naimark, C. Froustey,  
Long Range Correlation Large Scale Interactions in Ensembles of Defects:  
Estimating Reliability of Aluminum Alloys under Dynamic Cycling and Fatigue  
Loading Conditions,  
Technical Physics Letters. 37(3) (2011) 241–243.
- [8] Naimark O.B., Plekhov O.A., Betekhtin V.I., Kadomtsev A.G., Narykova M.V:  
Kinetics of defect accumulation and duality of the weller curve in gigacycle  
fatigue of metals  
Technical Physics. – 2014. – V 59, Iss 3. – P.398-401.
- [9] Mughrabi H:  
Microstructural fatigue mechanisms: Cyclic slip irreversibility, crack initiation,  
non-linear elastic damage analysis  
Int J Fatigue. – 2013. – V. 57. – P. 2–8.

# A GENERAL STATISTICAL MODEL FOR THE DESCRIPTION OF THE HYDROGEN ASSISTED CRACK INITIATION IN THE VHCF REGIME

D.S. Paolino<sup>1)</sup>, A. Tridello<sup>1)</sup>, G. Chiandussi<sup>1)</sup>, M. Rossetto<sup>1)</sup>

<sup>1)</sup> Department of Mechanical and Aerospace Engineering, Politecnico di Torino, Turin  
10129, Italy

## ABSTRACT

The mechanism of crack initiation from small internal defects is certainly a major point of interest in the Very-High-Cycle Fatigue (VHCF) literature. In particular, the formation mechanism of the so-called 'Fine Granular Area' (FGA) in the vicinity of an initial small defect is currently under investigation. However, it is generally acknowledged in the literature that crack grows within the FGA even if the Stress Intensity Factor (SIF) associated to the initial defect is smaller than the threshold value for crack growth. A number of different theories concerning the crack growth within the FGA have been proposed in the literature. According to the Murakami theory ('hydrogen assisted crack growth'), a crack can grow within the FGA thanks to the assistance of the hydrogen trapped near the initial defect and thereafter it propagates without the hydrogen assistance outside the FGA. Based on this theory, different models have been proposed for the estimation and the prediction of the VHCF response of materials.

The present paper proposes a general statistical model for the estimation of the fatigue limit in the VHCF regime. The proposed model is based on the hydrogen assisted crack growth theory. Starting from a general SIF formulation for the analytical model of the hydrogen assisted crack growth within the FGA, a general expression for the fatigue limit in presence of defects is finally provided.

## KEYWORDS

Effective stress intensity factor range, Stress ratio, Crack growth, Random fatigue limit, Defect size

## 1. INTRODUCTION

The increasing demand for high performance machinery able to sustain significant loads for a very large number of cycles (larger than  $10^8$  cycles) is presently driving the research on the Very-High-Cycle Fatigue (VHCF) response of many metallic materials.

In the last decades, the extensive experimental investigation on VHCF has shown that failures mainly originate from internal defects (inclusions, pores and inhomogeneities) with a typical fish-eye morphology. Within the fish-eye, depending on the defect size and on the applied stress, fracture surfaces may show the so-called Fine Granular Area (FGA) [1] in the vicinity of the internal defect. The FGA (also called Optically Dark Area or ODA by Murakami, Granular Bright Facet or GBF by Shiozawa and Rough Surface Area or RSA by Ochi) is a restricted region, dark at the optical microscope, that plays a key role in the initiation of the VHCF failure, since its formation consumes more than the 98% of the VHCF life. Researchers still dispute about the actual mechanism behind the FGA formation [2], but they unanimously accept that, within the FGA, crack can grow even if the Stress Intensity Factor (SIF) is below the SIF threshold for crack growth.

In the present paper, the reduction of the SIF threshold within the FGA is originally modeled in agreement with the 'hydrogen assisted crack growth' theory proposed by Murakami [3] and also with the different weakening mechanisms discussed in the VHCF literature (i.e., local grain refinement, carbide decohesion, matrix fragmentation or formation of persistent slip bands [2]).

Starting from a very general formulation for the SIF reduction, possible scenarios for crack growth from the initial defect are also identified and described. It is theoretically demonstrated that, depending on the scenario, a VHCF limit may also be present and its final formulation recalls the well-known expression previously proposed by Murakami [3]. An illustrative numerical example, based on experimental data, is finally reported in the paper in order to show the applicability of the proposed model and its potentialities.

## 2. A GENERAL MODEL FOR SIF THRESHOLD WITHIN THE FGA

It is generally acknowledged that crack can grow within the FGA even if the SIF is below the SIF threshold of the material. Regardless of the physical justification for this unexpected experimental evidence, crack growth can occur in the FGA only if a local reduction of the global SIF threshold of the material is accepted.

The following assumptions permit to define a general model for the local reduction of the SIF threshold within the FGA:

1. the global SIF threshold range, referred to as  $\Delta k_{th,g}$ , can be expressed as [3]:

$$\Delta k_{th,g} = c_{th,g}(HV + 120)\sqrt{a_d}^{\alpha_{th,g}}, \quad (1)$$

where  $a_d$  is the projected area of the defect,  $HV$  is the Vickers hardness of the material in the vicinity of the defect and  $c_{th,g} > 0$  and  $0 \leq \alpha_{th,g} < 1/2$  (being  $\alpha_{th,g} = 0$  in case of global SIF threshold range for long cracks) are two material coefficients.

2. the effective SIF range for an internal defect, referred to as  $\Delta k_{d,eff}$ , is given by [3,4]:

$$\Delta k_{d,eff} = 0.5s \left(\frac{1-R}{2}\right)^{-\alpha_d} \sqrt{\pi}\sqrt{a_d}^{1/2} = 0.5s_{eff}\sqrt{\pi}\sqrt{a_d}^{1/2}, \quad (2)$$

where  $s$  is the local stress amplitude at the defect location,  $R$  is the stress ratio,  $s_{eff} = s \left(\frac{1-R}{2}\right)^{-\alpha_d}$  is the effective stress amplitude at the defect location and  $\alpha_d$  is a material parameter that must be estimated from experimental datasets at different stress ratios. According to [3],  $\alpha_d$  only depends on the Vickers hardness of the material and is equal to  $0.226 + HV \times 10^{-4}$ .

3. within the FGA, the local SIF threshold range, referred to as  $\Delta k_{th,l}$ , is defined as:

$$\Delta k_{th,l} = \Delta k_{th,g} - \Delta k_{th,r}, \quad (3)$$

where  $\Delta k_{th,r}$  accounts for the reduction of the SIF threshold range induced by the different weakening mechanisms proposed in the literature [2]: hydrogen embrittlement, local grain refinement, carbide decohesion, matrix fragmentation or formation of persistent slip bands.

4. the SIF threshold reduction has the most general formulation fulfilling the following three basic conditions:

- a. the principle of dimensional homogeneity, for which  $\Delta k_{th,r}$  must be proportional to the effective stress amplitude and to the square-root of the defect size.
- b. the initial condition, for which  $\Delta k_{th,r}$  must be proportional to the square-root of the initial defect size when crack starts growing.
- c. the defect size dependency, for which  $\Delta k_{th,r}$  may depend on the defect size.

According to the conditions a)-c), the easiest and most general formulation for  $\Delta k_{th,r}$  is:

$$\Delta k_{th,r} = c_{th,r}s_{eff}\sqrt{a_{d,0}}^{1/2} \left(\sqrt{a_d}/\sqrt{a_{d,0}}\right)^{\alpha_{th,r}}, \quad (4)$$

where  $a_{d,0}$  is the projected area of the initial defect and  $c_{th,r} \geq 0$  and  $\alpha_{th,r} \leq 0$  (being  $\alpha_{th,r} = 0$  if  $\Delta k_{th,r}$  is a constant value) are two material coefficients that ensure  $0 \leq \Delta k_{th,l} \leq \Delta k_{th,g}$  for any  $\sqrt{a_d}$  value.

5. FGA forms until  $\Delta k_{th,l} < \Delta k_{d,eff} \leq \Delta k_{th,g}$ .

### 3. CRACK GROWTH WITHIN THE FGA

In the VHCF literature [5], the crack growth rate within the FGA is usually modeled with the Paris' law. Three stages can be present in sigmoidal crack growth rate diagrams related to VHCF failures from internal defects (see Fig. 1): the below-threshold region within the FGA (up to  $\Delta k_{th,g}$ ), the steady crack propagation region from the border of the FGA (with effective SIF range equal to  $\Delta k_{th,g}$ ) to the border of the fish-eye (with effective SIF range equal to  $\Delta k_{FiE}$ ), the unsteady crack propagation region beyond the fish-eye border (with effective SIF range larger than  $\Delta k_{FiE}$ ).

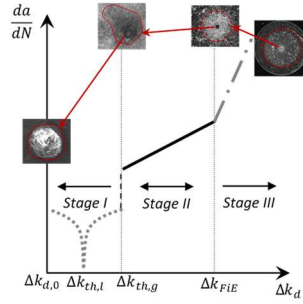


**Fig. 1:** The three stages of crack propagation in a crack growth rate diagram for VHCF failures from internal defects.

In order to model the below-threshold region, the modified Paris' law proposed by [6] and recently considered in [4] is here adopted:

$$\frac{da}{dN} = c_I (\Delta k_{d,eff} - \Delta k_{th,l})^{m_I}, \quad (6)$$

where  $c_I$  and  $m_I$  are the two Paris' constants related to the first propagation stage, from  $\sqrt{a_{d,0}}$  to  $\sqrt{a_{FGA,max}}$ .

From the border of the FGA to the border of the fish-eye (with size  $\sqrt{a_{FiE}}$ ), the crack growth rate is modeled with the conventional Paris' law, in agreement with the literature [5]:

$$\frac{da}{dN} = c_{II} \Delta k_{d,eff}^{m_{II}}, \quad (7)$$

where  $c_{II}$  and  $m_{II}$  are the two Paris' constants related to the second propagation stage, from  $\sqrt{a_{FGA,max}}$  to  $\sqrt{a_{FiE}}$ .

Final fracture may occur when the crack size reaches the border of the fish-eye. In these cases, the third stage of crack propagation is not visible on fracture surfaces and it can be neglected. In some other cases, crack can propagate beyond the fish-eye border until it reaches the border of the final fracture, with size  $\sqrt{a_c}$ . In these cases, a third stage of crack propagation is visible on fracture surfaces and it can be modeled again with the conventional Paris' law [7]:

$$\frac{da}{dN} = c_{III} \Delta k_{d,eff}^{m_{III}}, \quad (8)$$

where  $c_{III}$  and  $m_{III}$  are the two Paris' constants related to the third propagation stage, from  $\sqrt{a_{FiE}}$  to  $\sqrt{a_c}$ .

By taking into account the three stages of propagation, the number of cycles to failure,  $N_f$ , can be expressed as:

$$N_f = N_I + N_{II} + N_{III}, \quad (9)$$

where  $N_I$ ,  $N_{II}$  and  $N_{III}$  are the number of cycles consumed within stages I, II and III, respectively.

Following the procedure usually adopted in the VHCF literature (e.g., [7]),  $N_I$  can be estimated by subtracting, from the experimental  $N_f$ , the number of cycles  $N_{II}$  and  $N_{III}$  obtained through integration of Eqs. (7) and (8). The Paris' constants in Eq. (7) are those typical for surface

cracks in the steady phase of crack growth; whereas, the Paris' constants in Eq. (8) are for surface cracks in the unsteady phase of crack growth, near the final fracture. If the Paris' constants in Eq. (8) are assumed equal to those of Eq. (7), the crack growth rate is underestimated and, consequently,  $N_{III}$  is overestimated. Therefore, it can be concluded that  $N_{I,min} < N_I < N_{I,max}$ , being  $N_{I,min} = N_f - (N_{II} + N_{III})$  and  $N_{I,max} = N_f - N_{II}$ . The difference between  $N_{I,min}$  and  $N_{I,max}$  is generally negligible if  $N_f$  is larger than  $10^8$  cycles. Thus, the average value between  $N_{I,min}$  and  $N_{I,max}$  is a good approximation for  $N_I$  and it can be used for the estimation of the four parameters  $c_I$ ,  $m_I$ ,  $c_{th,r}$  and  $\alpha_{th,r}$ .

#### 4. A GENERAL EXPRESSION FOR THE FATIGUE LIMIT

According to assumption 5) in Section 2, the following four distinct cases may occur:

1.  $\Delta k_{d,eff}(\sqrt{a_{d,0}}) > \Delta k_{th,g}(\sqrt{a_{d,0}})$ : fatigue life is finite and the FGA does not form.
2.  $\Delta k_{th,l}(\sqrt{a_{d,0}}) < \Delta k_{d,eff}(\sqrt{a_{d,0}}) \leq \Delta k_{th,g}(\sqrt{a_{d,0}})$ : fatigue life is finite, the FGA forms and it reaches its maximum extension,  $\sqrt{a_{FGA,max}}$ .
3.  $\Delta k_{th,l}(\sqrt{a_{d,0}}) < \Delta k_{d,eff}(\sqrt{a_{d,0}}) \leq \Delta k_{th,g}(\sqrt{a_{d,0}})$ : fatigue life is infinite, the FGA forms but it does not reach the maximum extension.
4.  $\Delta k_{d,eff}(\sqrt{a_{d,0}}) \leq \Delta k_{th,l}(\sqrt{a_{d,0}})$ : fatigue life is infinite and the FGA does not form.

The transition between case 2) and case 3) discriminates between finite and infinite fatigue life and it occurs when, for a given initial defect size, the stress amplitude equals the material fatigue limit. It can be demonstrated [8] that the material fatigue limit, referred to as  $s_l$ , can be expressed as:

$$s_l = c_{s_l} \frac{c_{th,g}(HV+120)}{\sqrt{a_{d,0}}^{1/2-\alpha_{th,g}}} \left(\frac{1-R}{2}\right)^{\alpha_d}, \quad (10)$$

where  $c_{s_l} = \left(\frac{(1/2-\alpha_{th,g})^{0.5\sqrt{\pi}}}{(\alpha_{th,g}-\alpha_{th,r})c_{th,r}}\right)^{1/2-\alpha_{th,r}} \frac{\alpha_{th,g}-\alpha_{th,r}}{0.5\sqrt{\pi}(1/2-\alpha_{th,r})}$ . Eq. (10) recalls the well-known expression proposed by Murakami [3] and it can be obtained by imposing the condition of tangency between the  $\Delta k_{d,eff}(\sqrt{a_d})$  curve (Eq. (1)) and the  $\Delta k_{th,l}(\sqrt{a_d})$  curve (Eq. (3)).

In order to define the statistical distribution of the fatigue limit, the randomness of the global SIF threshold range and that of the initial defect size must be taken into account.

An approximate  $\alpha$ -th quantile of the fatigue limit, referred to as  $s_{l,\alpha}$ , can be obtained by assuming the rv  $\log_{10}[\sqrt{A_{d,0}}]$  as approximately Normal with mean  $\mu_{\sqrt{A}}$  and standard deviation  $\sigma_{\sqrt{A}}$ . As shown in [8], the error in the approximation is generally negligible and the final  $s_{l,\alpha}$  is given by:

$$s_{l,\alpha} \cong c_{s_l} \frac{c_{th,g}(HV+12)}{10^{(1/2-\alpha_{th,g})\mu_{\sqrt{A}}}} \left(\frac{1-R}{2}\right)^{\alpha_d} 10^{\sqrt{(1/2-\alpha_{th,g})^2 \sigma_{\sqrt{A}}^2 + \sigma_{lK_{th,g}}^2} \Phi_{Gauss}^{-1}(\alpha)}, \quad (11)$$

where  $\Phi_{Gauss}(\cdot)$  denotes a standardized Normal cumulative distribution function and  $\sigma_{lK_{th,g}}$  is the standard deviation of the logarithm of the global SIF threshold range.

#### 5. APPLICATION TO AN EXPERIMENTAL DATASET

In order to show the applicability of the proposed approach, model parameters are fitted to an experimental dataset. Description of dataset and parameter estimation is discussed in [9] and they will not be recalled here for the sake of brevity. Parameter estimates can be used for the estimation of the material fatigue limit, according to Eqs. (10) and (11). Fig. 2a shows the variation of the fatigue limit with respect to the initial defect size (Eq. (10)) together with experimental dataset. Fig. 2b depicts the variation of the percentiles with respect to the stress



ratio (Eq. (11)); the experimental dataset obtained for a stress ratio equal to -1 is also reported in Fig. 2b.

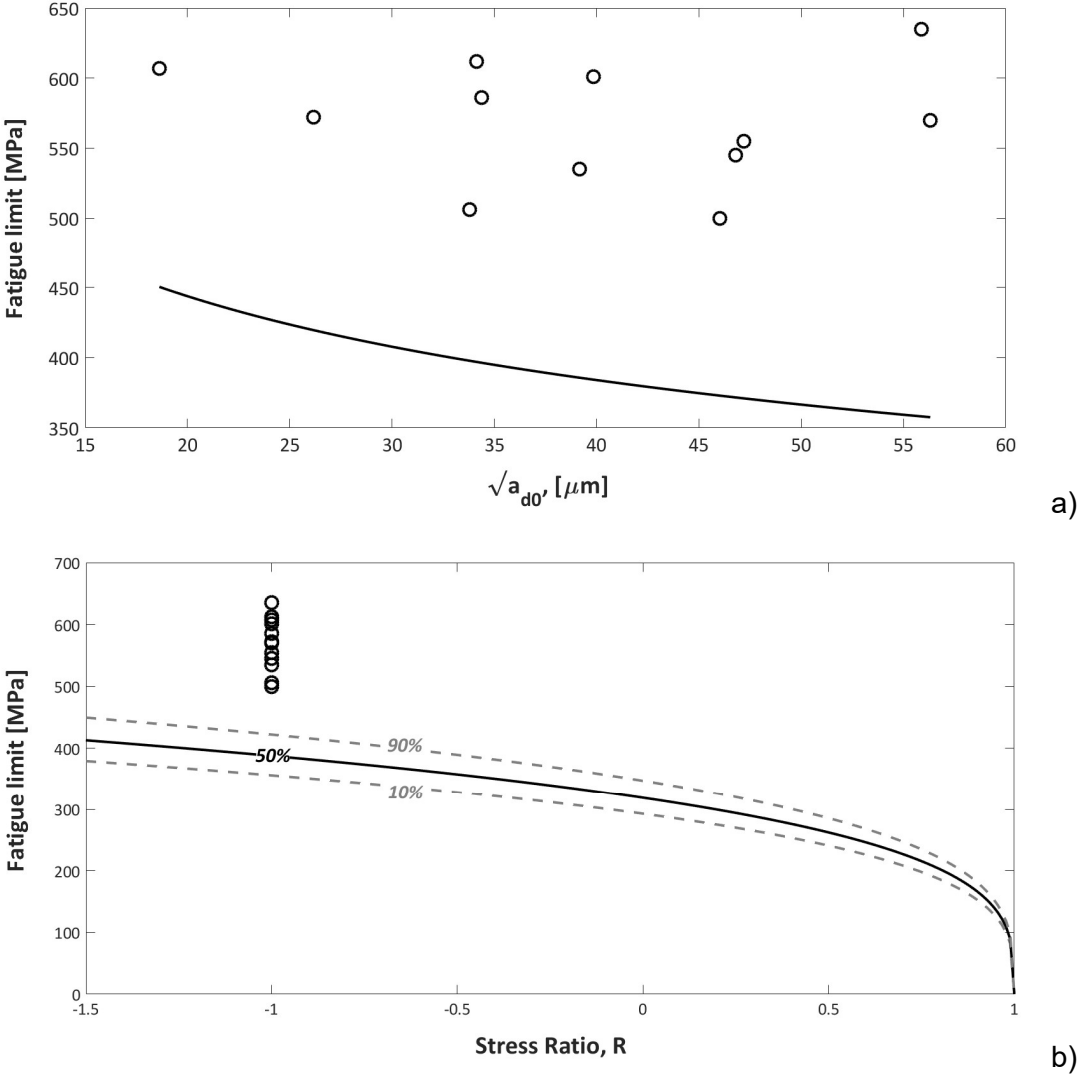


**Fig. 2:** Fatigue limit trends with failure data: a) variation of the median fatigue limit with the initial defect size; b) variation of different percentiles with the stress ratio.

As shown in Fig. 2, all failure data are above the considered percentiles, in agreement with the definition of fatigue limit. It is worth noting that scatter in fatigue limit is mainly dominated by the randomness the initial defect size, since the random variation of the initial defect size is significantly larger than that of the global SIF threshold range (i.e.,  $(1/2 - \alpha_{th,g})\sigma_{\sqrt{A}}/\sigma_{IK_{th,g}} = 76.8$ ).

**CONCLUSIONS**

A simple and general formulation for the reduction of the SIF threshold range in the FGA was proposed in the paper. It was shown that, with the proposed formulation, the different weakening mechanisms involved in the FGA formation can be quantitatively modeled. From

the proposed formulation, a general expression for the fatigue limit and a crack growth rate model for crack propagation from internal defect up to failure were defined. The model was successfully applied to an experimental dataset. The estimated fatigue limit was quite below all failure data. Therefore, percentiles of fatigue limit could be effectively used for a reliable design against VHCF failures.

## REFERENCES

- [ 1 ] Sakai, T.; Sato, Y.; Oguma, N.:  
Characteristic S-N properties of high-carbon-chromium-bearing steel under axial loading in long-life fatigue  
*Fatigue & Fracture of Engineering Materials & Structures* 25 (2002), pp. 765-773
- [ 2 ] Li, Y.D.; Zhang, L.L.; Fei, Y.H.; Liu, X.Y.; Li, M.X.:  
On the formation mechanisms of fine granular area (FGA) on the fracture surface for high strength steels in the VHCF regime  
*International Journal of Fatigue* 82 (2016), pp. 402-410
- [ 3 ] Murakami, Y.:  
Metal fatigue: effects of small defects and nonmetallic inclusions  
Elsevier, Oxford, UK, 2002
- [ 4 ] Sun, C.; Lei, Z.; Hong, Y.:  
Effects of stress ratio on crack growth rate and fatigue strength for high cycle and very-high-cycle fatigue of metallic materials  
*Mechanics of Materials* 69 (2014), pp. 227-236
- [ 5 ] Tanaka, K.; Akiniwa, Y.:  
Fatigue crack propagation behaviour derived from S–N data in very high cycle regime  
*Fatigue & Fracture of Engineering Materials & Structures* 25 (2002), pp. 775-784.
- [ 6 ] Donahue, R.J.; Clark, H.M.; Atanmo, P.; Kumble, R.; McEvily, A.J.:  
Crack opening displacement and the rate of fatigue crack growth  
*International Journal of Fracture Mechanics* 8 (1972), pp. 209-219
- [ 7 ] Su, H.; Liu, X.; Sun, C.; Hong, Y.;  
Nanograin layer formation at crack initiation region for very-high-cycle fatigue of a Ti–6Al–4V alloy  
*Fatigue & Fracture of Engineering Materials & Structures* (in press)
- [ 8 ] Paolino, D.S.; Tridello, A.; Chiandussi, G.; Rossetto, M.;  
S-N curves in the very-high-cycle fatigue regime: statistical modeling based on the hydrogen embrittlement consideration  
*Fatigue & Fracture of Engineering Materials & Structures* 39 (2016), pp. 1319-1336
- [ 9 ] Paolino, D.S.; Tridello, A.; Chiandussi, G.; Rossetto, M.;  
A general model for crack growth from initial defect in Very-High-Cycle Fatigue  
*Procedia Structural Integrity* (in press)

**Corresponding author:** Davide S. Paolino, [davide.paolino@polito.it](mailto:davide.paolino@polito.it)

# PROBABILISTIC MODEL ON STATISTICAL FATIGUE PROPERTY IN VERY HIGH CYCLE REGIME BASED ON DISTRIBUTIONS OF SIZE AND LOCATION OF INTERIOR INCLUSIONS

Y. Nakamura<sup>1)</sup>, T. Sakai<sup>2)</sup>, D. G. Harlow<sup>3)</sup>, N. Oguma<sup>4)</sup>, M. Nakajima<sup>1)</sup>, A. Nakagawa<sup>5)</sup>

<sup>1)</sup> National Institute of Technology, Toyota College,  
2-1 Eisei-cho, Toyota, Aichi, 471-8525 Japan

<sup>2)</sup> Research Organization of Science and Engineering, Ritsumeikan University,  
1-1-1 Noji-higashi, Kusatsu, Shiga, 525-8577 Japan

<sup>3)</sup> Department of Mechanical Engineering and Mechanics, Lehigh University,  
19 Memorial Drive West, Bethlehem, PA 18015-3085 USA

<sup>4)</sup> Faculty of Engineering, University of Toyama,  
3190 Gofuku, Toyama, 930-8555 Japan

<sup>5)</sup> Industrial Products Company, Hitachi, Ltd.,  
3-18 Nakanoshima 2-chome, Kita-ku, Osaka, 530-0005 Japan

## ABSTRACT

In *S-N* diagrams for high strength steels, the duplex *S-N* curves for surface-initiated fracture and interior inclusion-initiated fracture were usually confirmed in the very high cycle regime. This trend is more distinct in the loading type of rotating bending due to the stress distribution. In the case of interior fracture mode, the fish-eye is usually observed on the fracture surface and an inclusion is also observed at the center of the fish-eye. In the present work, the authors have attempted to construct a probabilistic model on the statistical fatigue property in the interior fracture mode based on the distribution characteristics of the location and the size of the interior inclusion at the crack initiation site.

## KEYWORDS

Very high cycle fatigue, interior inclusion, statistical fatigue property, fatigue strength distribution, probabilistic model

## INTRODUCTION

One of the typical aspects of fatigue fracture in the very high cycle regime is the fact that the duplex *S-N* characteristics consisting of the respective *S-N* curves for the surface-initiated fracture and the interior-initiated fracture as reported by many researchers [1-3]. In the case of interior-initiated fracture, an inclusion is usually found at the core portion of the fish-eye formed on the fracture surface. Thus, the interior inclusion at the crack initiation site plays a dominant role to govern the fatigue strength and fatigue life of the specimen.

Fatigue limit of the metallic material is well evaluated by combining the hardness and the concept of  $\sqrt{\text{area}}$  for the defect size proposed by Murakami et al. [4]. Another important factor to control the fatigue is the location of the inclusion, since the stress distribution across the section has a steep slope in rotating bending. Accordingly, the fatigue property of those metallic materials should be analyzed as a function of the size and the location of the interior inclusions.

In the actual metallic materials, both of the size and the location of the inclusions inside the material have particular distributions depending on the fabrication process. From this point of view, the authors have attempted to construct a probabilistic model on the very high cycle fatigue property for the bearing steel of SUJ2 in rotating bending assuming two-parameter Weibull distribution for the inclusion size and random distribution for the inclusion locatiopn.

## EXPERIMENTAL EVIDENCE ON FATIGUE PROPERTY IN VERY HIGH CYCLE REGIME

Fatigue test data for the bearing steel of SUJ2 obtained by Sakai et al. are shown in Fig.1 [1], where the duplex S-N characteristics consisting of the respective S-N curves for the surface-initiated fracture and the interior- initiated fracture are obviously confirmed. Distribution curve attached to the right hand edge of Fig.1 is explained in the later section.

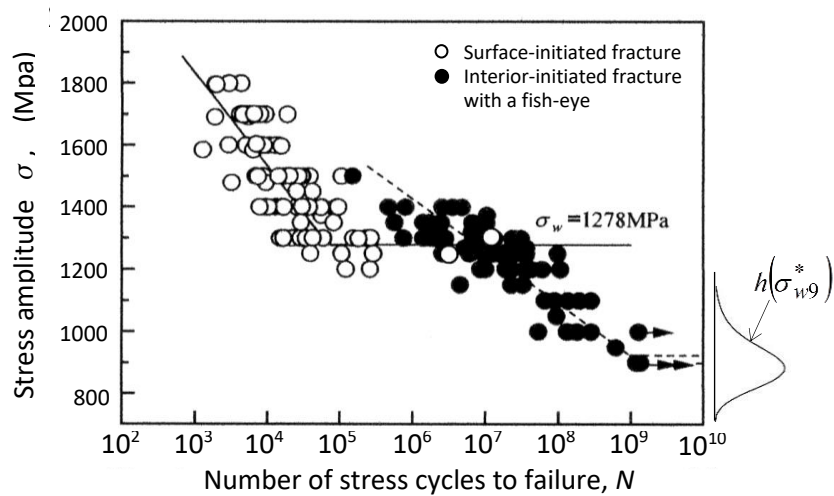


**Fig.1:** Rotating bending S-N characteristics of bearing steel in very high cycle regime

Typical examples of the fracture surfaces in the surface-initiated fracture and the interior-initiated fracture are shown in Fig.2(a)-(c), respectively. Fig.2(a) indicates the fracture surface in the surface-initiated fracture, whereas Fig.2(b) gives the fracture surface in the interior-initiated fracture with a fish-eye. At core portion of the fish-eye, the fine granular area (FGA) was found as shown in Fig.2(c). It was reported that the inclusion depth from the specimen surface,  $\xi$ , is restricted within the range of  $\xi \leq 250\mu\text{m}$  in the case of rotating bending [5].

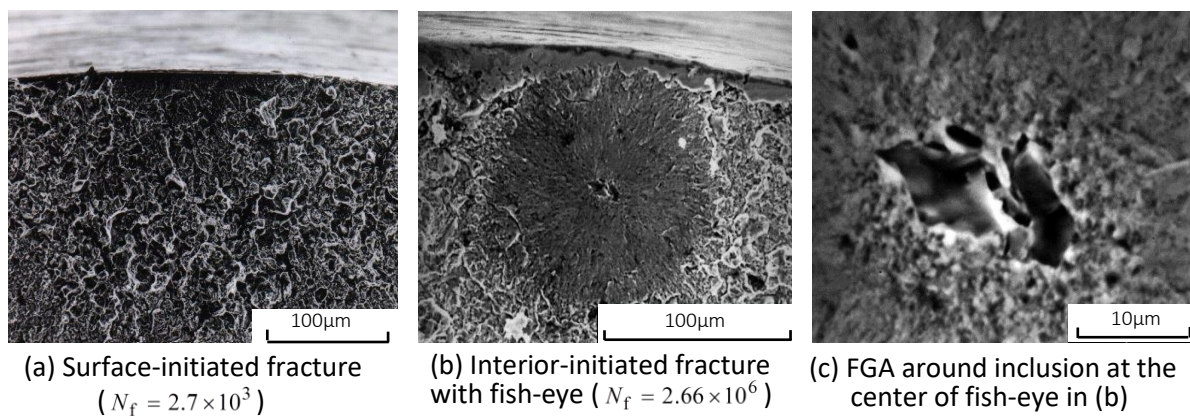


**Fig.2:** Fracture surfaces for the bearing steel (JIS:SUJ2) failed in rotating bending

## EFFECT OF SIZE AND DEPTH OF INCLUSION ON FATIGUE STRENGTH

It is well known that the fatigue limit of the steel with interior defect,  $\sigma_w$ , is given by using a concept of  $\sqrt{area}$  proposed by Murakami as follows[4];  $\sigma_w = 1.56(HV + 120)/(\sqrt{area})^{1/6}$  (1) Although this equation is proposed to evaluate the usual fatigue limit at  $N=10^7$ , this concept is analogously applied to evaluate the fatigue strength at  $N=10^9$  denoted by  $\sigma_{w9}$ . If the area of the defect is replaced by a circle having the same area, we have  $\sqrt{area} = \sqrt{\pi\rho^2}$ . Since the hardness of the SUJ2 steel in this work is  $HV=778$ . Thus, we have

$$\sigma_{w9} = 1.56(778 + 120)/(\sqrt{\pi\rho^2})^{1/6} = 1273\rho^{-1/6} \quad (2)$$

Relationship of Eq.(2) is depicted in Fig.3. If the defect size becomes very small, such a defect has no effect on the fatigue strength. If such a critical size is set as  $\rho = 3\mu m$ , the upper bound of the fatigue strength is given as  $\sigma_{w9} = 1060$  MPa. On the other hand, the fatigue strength of the steel including the large inclusion of  $\rho = 40\mu m$  is given as  $\sigma_{w9} = 689$  MPa.

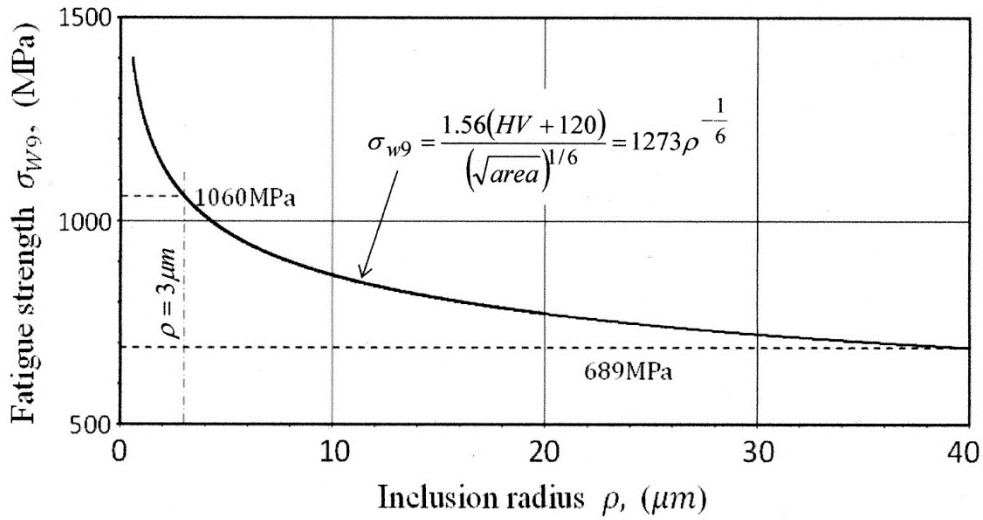


**Fig.3:** Relationship between fatigue strength  $\sigma_{w9}$  and inclusion radius  $\rho$ .

Here, in the case of rotating bending, even if the inclusion size at the crack initiation site is fixed to a certain size, the fatigue strength at  $N=10^9$ ,  $\sigma_{w9}^*$ , is governed by the inclusion depth of  $\xi$  due to the stress distribution across the section of the specimen. As reported in the other paper [5], such a relationship between  $\sigma_{w9}^*$ , and  $\xi$  is represented by the following expression;

$$\sigma_{w9}^* = \frac{r}{r - \xi} \sigma_{w9} = \frac{1.5}{1.5 - \xi} \sigma_{w9} \quad (3)$$

Therefore, substituting Eq.(2) into Eq.(3), one can derive the fatigue strength as follows;

$$\sigma_{w9}^* = \frac{1.5}{1.5 - \xi} \times 1273\rho^{-1/6} = \frac{1910}{1.5 - \xi} \rho^{-1/6} \quad (4)$$

This equation gives the fatigue strength at  $N=10^9$  at any size and depth of the interior inclusion.

## DISTRIBUTION CHARACTERISTICS ON SIZE AND DEPTH OF INCLUSION

At first, distribution pattern of the inclusion size (radius),  $\rho$ , is assumed to be represented by two-parameter Weibull distribution, since the location parameter is thought as  $\rho_{\min} = 0$ . Thus,

we have the following probability density and distribution functions of the inclusion size;

$$f_0(\rho) = \frac{a}{b} \left(\frac{\rho}{b}\right)^{a-1} \exp\left\{-\left(\frac{\rho}{b}\right)^a\right\} \quad (5) \quad \text{and} \quad F_0(\rho) = 1 - \exp\left\{-\left(\frac{\rho}{b}\right)^a\right\}, \quad (6)$$

where  $a$  is shape parameter and  $b$  location parameter, respectively.

Now, if  $n$  of inclusions are included inside the critical volume in the specimen, the largest inclusion is supposed to be the crack starter. Based on this aspect, distribution of the inclusion size at the crack initiation site is given by the distribution of the largest inclusion among total number of the inclusions. By applying the concept of the extreme's distribution [x], we have the probability density function of the largest inclusion size among  $n$  inclusions as follows;

$$f(\rho_n) = n \{F_0(\rho_n)\}^{n-1} \frac{a}{b} \left(\frac{\rho_n}{b}\right)^{a-1} \exp\left\{-\left(\frac{\rho_n}{b}\right)^a\right\}, \quad (7)$$

where  $\rho_n$  means the radius of the largest inclusion among  $n$  of total inclusions.

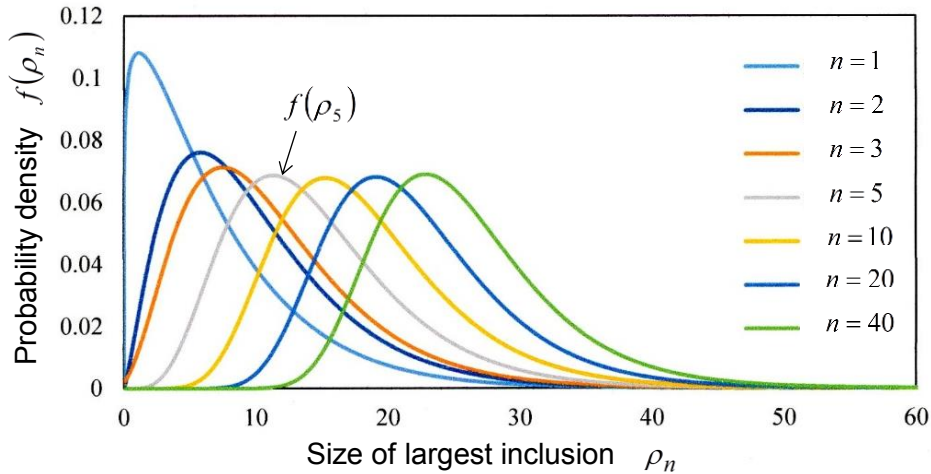


**Fig.4:** Probability density functions of largest inclusion size in  $n$  inclusions.

Assuming  $\rho = 1 \mu m$  at  $F_0 = 0.1$  and  $\rho = 15 \mu m$  at  $F_0 = 0.9$  as reasonable values, Weibull parameters  $a$  and  $b$  are given as  $a = 1.139$  and  $b = 7.214$ , respectively. Probability density functions calculated by Eq.(7) at the total numbers of 2, 3, 5, 10, 20 and 40 are depicted in Fig.4. Analytical result at  $n=1$  gives the original distribution of the inclusion size in the critical volume. It is noted that the average value of each distribution tends to increase with an increase of the number of inclusions included inside the critical volume. Another finding is that the distinct variation cannot be observed in the variance of each distribution.

In the actual configuration of the fatigue specimen in the present study, the critical volume would be supposed to be  $\pi \{r^2 - (r - 0.25)^2\} \times l = 2.16 mm^3$ . In such a situation, the total number of inclusions would be restricted as  $n=3$  or 5, for example. Thus, the number of inclusions is supposed to be  $n=5$  as a reasonable example in this work. Then, the probability density function of the largest inclusion size,  $\rho_5$ , is given by the curve attached an arrow in Fig.4, and the actual value of  $\rho_5$  yields within a range of  $3 \mu m - 40 \mu m$  as indicated by the grey curve.

In the next place, distribution pattern of the inclusion depth from the specimen surface should be analyzed quantitatively. As reported in another paper [5], probability density function of the inclusion depth,  $\xi$ , is given as follows;

$$g(\xi) = \frac{2}{rA} \left(1 - \frac{\xi}{r}\right), [0 \leq \xi \leq \xi_c] \quad (8)$$

where  $r$  is radius of the specimen ( $r=1.5\text{mm}$ ) and  $A=0.3055$ . This probability density function is shown in Fig.5. In case of rotating bending, the inclusion depth is restricted within the range of  $\xi_c \leq 0.25\text{mm}$ . Thus,  $\xi_c$  gives the upper bound of the inclusion depth. It is noted that the probability density of the inclusion depth tend to increase with decrease of the depth.

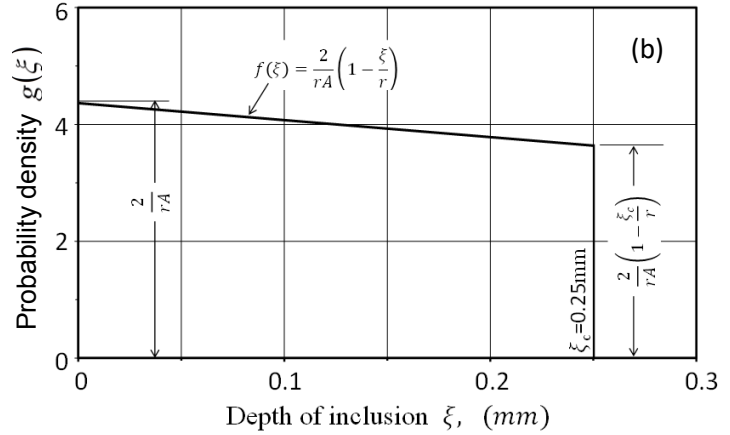


Fig.5: Probability density functions of inclusion depth  $f_0(\xi)$  and  $f(\xi)$ .

### ANALYSIS OF FATIGUE STRENGTH DISTRIBUTION AT $N=10^9$

If size and depth of the interior inclusion are given, the fatigue strength at  $N=10^9$  can be calculated by Eq.(4). However, they have particular distributions as represented by Eqs.(7) and (8). Size and depth of the inclusion have no relation each other, both random variables  $\rho_n$  and  $\xi$  are statistically independent. Then, the joint probability density function  $h(\rho_n, \xi)$  is given by multiplication of the probability density functions of  $f(\rho_n)$  and  $g(\xi)$  as follows;

$$h(\rho_n, \xi) = f(\rho_n) \cdot g(\xi) = n \{F(\rho_n)\}^{n-1} \frac{a}{b} \left(\frac{\rho_n}{b}\right)^{a-1} \exp\left[-\left(\frac{\rho_n}{b}\right)^a\right] \cdot \frac{2}{rA} \left(1 - \frac{\xi}{r}\right) \quad (9)$$

As described previously,  $n=5$ ,  $a=1.139$ ,  $b=7.214$ ,  $r=1.5$  and  $A=0.3055$  in the present work.

Here, when the  $\rho_n - \xi$  plane is finely divided giving the increments of  $\Delta\rho_n$  and  $\Delta\xi$ , probability that the random variables  $\rho_n$  and  $\xi$  are included in any cell of  $\Delta\rho_n \times \Delta\xi$  at the point of  $(\rho_n, \xi)$  provides the probability giving the fatigue strength of  $\sigma_{w9}^*$  of Eq.(4). Thus,

$$P[\rho_n \leq \Delta\rho_n, \xi \leq \Delta\xi] = h(\rho_n, \xi) \Delta\rho_n \Delta\xi = P[\sigma_{w9}^* \in \Delta\sigma_{w9}^*] \quad (10)$$

By repeating such calculations, one can obtain the probability density function  $h_w(\sigma_{w9}^*)$  and the distribution function  $H_w(\sigma_{w9}^*)$  numerically. These functions thus obtained are depicted in Fig.6.

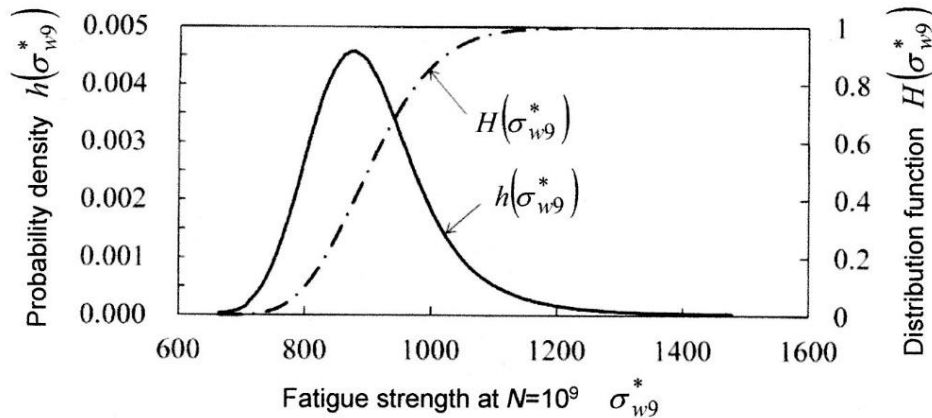


Fig.6: Probability density and distribution functions of fatigue strength.

The probability density function of  $h_w(\sigma_{w9}^*)$  is also plotted at the right hand edge in Fig.1, where the distribution pattern of the fatigue strength,  $\sigma_{w9}^*$ , is well fitted to the statistical aspect of the experimental results.

## CONCLUSIONS

- (1) Relationships between the fatigue strength  $\sigma_{w9}^*$  and either the inclusion size  $\rho$  and the inclusion depth  $\xi$  was quantitatively analyzed, and the fatigue strength is provided by

$$\sigma_{w9}^* = \frac{1.5}{1.5 - \xi} \times 1273 \rho^{-1/6} = \frac{1910}{1.5 - \xi} \rho^{-1/6}.$$

- (2) By connecting the concept of extremes distribution and random distribution, the probability density functions of  $\rho_n$  and  $\xi$  were derived as follows;

$$f(\rho_n) = n \{F_0(\rho_n)\}^{n-1} \frac{a}{b} \left(\frac{\rho_n}{b}\right)^{a-1} \exp\left\{-\left(\frac{\rho_n}{b}\right)^a\right\} \quad \text{and} \quad g(\xi) = \frac{2}{rA} \left(1 - \frac{\xi}{r}\right), \quad [0 \leq \xi \leq \xi_c]$$

- (3) Combining the above distributions on  $\rho_n$  and  $\xi$ , the joint probability density function for them is derived as follows;

$$h(\rho_n, \xi) = n \{F(\rho_n)\}^{n-1} \frac{a}{b} \left(\frac{\rho_n}{b}\right)^{a-1} \exp\left\{-\left(\frac{\rho_n}{b}\right)^a\right\} \cdot \frac{2}{rA} \left(1 - \frac{\xi}{r}\right).$$

The distribution pattern of the fatigue strength at  $N=10^9$  derived from this function is well corresponding to the experimental aspect of the fatigue strength distribution for the bearing steel of SUJ2.

## REFERENCES

- [ 1 ] Sakai T.:  
Review and Prospects for Current Studies on Very High Cycle Fatigue of Metallic Materials for Machine Structural Use  
J. Solid Mech. and Mater Engng, Vol.3, No.3, (2009), pp.425-439
- [ 2 ] Murakami Y., Nomoto T., Ueda T.:  
On the Mechanism of Fatigue Failure in the Superlong Life Regime, Part 1: Influence of Hydrogen Trapped by Inclusions  
Fatigue Fract. Eng. Mater. Struct., Vol.23, (2000), pp. 893-902
- [ 3 ] Sakai T., Oguma N., Morikawa A.:  
Microscopic and Nanoscopic Observations of Metallurgical Structures around Inclusions at Interior Crack Initiation Site for a Bearing Steel in Very High Cycle Fatigue  
Fatigue Fract. Eng. Mater. Struct., Vol.38, (2015), pp.1305-1314
- [ 4 ] Murakami Y.:  
Metal Fatigue: Effects of Small Defects and Nonmetallic Inclusions  
Elsevier Science Ltd., 2002
- [ 5 ] Nakagawa A., Sakai T., Harlow D.G., Oguma N., Nakamura Y., Ueno A., Kikuchi S., Sakaida A.:  
A Probabilistic Model on Crack Initiation Modes of Metallic Materials in Very High Cycle Fatigue  
Procedia Structural Integrity, Vol.2, (2016), pp.1199-1206

**Corresponding author:** nakamura@toyota-ct.ac.jp



# EVALUATION OF THREE-DIMENSIONAL MICROSTRUCTURAL EFFECTS ON DAMAGE EVOLUTION DURING VHCF LOADING OF A DUPLEX STAINLESS STEEL – MECHANISMS OF DAMAGE EVOLUTION AND CORRESPONDING FATIGUE LIFE

A. Giertler<sup>1)</sup>, N. Heilemann<sup>1)</sup>, B. Dönges<sup>2)</sup>, H.-J. Christ<sup>2)</sup>, U. Krupp<sup>1)</sup>

<sup>1)</sup> Institute of Materials Design and Structural Integrity, Faculty of Engineering and Computer Science, University of Applied Sciences Osnabrück, Albrechtstraße 30, 49009 Osnabrück, Germany

<sup>2)</sup> Institute for Materials Technology, University of Siegen, 57068 Siegen, Germany

## ABSTRACT

The present paper is an overview of recent investigations dealing with the fatigue damage in the VHCF regime of duplex stainless steel (DSS, 1.4462, German designation) and super duplex steel (SDSS, 1.4410). The fatigue damage mechanisms have been investigated under vacuum, air and corrosive atmosphere. For the cyclic loading of the fatigue specimens an ultrasonic fatigue testing machine with a testing frequency of  $f = 20000\text{Hz}$  and a stress ratio of  $R = -1$  have been used. The application of light microscopy, thermography and scanning electron microscopy as in-situ techniques, allows the observation of the damage evolution on the electrolytically polished surface of the specimens during the fatigue tests. The investigations show a strong slip band formation within the austenitic phase for the DSS, which leads to crack initiation at the austenitic/ferritic phase boundaries. In comparison to that, crack initiation in SDSS occurs at slip bands within the ferritic phase. The fatigue life of the duplex stainless steels is strongly dominated by the barrier effect of the microstructure surrounding the initially plastified grains.

## KEYWORDS

duplex stainless steel, slip band formation, crack initiation, fatigue limit, corrosion fatigue

## INTRODUCTION

Duplex stainless steels (DSS) combine good mechanical properties with excellent corrosion resistance. Therefore, DSS are widely used for offshore applications, components in the petrochemical industry and in process engineering. In comparison to single-phase stainless steels, DSS exhibit superior mechanical properties, which is governed by the two-phase microstructure arrangement composed of bcc ferrite grains and fcc austenite grains. DSS are materials of VHCF damage type I, i.e., fatigue crack initiation takes place at the surface governed by local plastic deformation within grains or grain patches oriented for easy slip [1,2]. Local plastic deformation manifests itself as slip band formation within austenitic grains of a particular high value of the Schmid factor. The slip bands within the austenitic phase are blocked at the adjacent austenite/ferrite phase boundaries, which leads to a dislocation pile up. Slip band accumulation gives rise to a gradually increasing stress concentration at the phase boundaries, eventually leading to slip transmission and crack initiation. It was found, that in particular austenite/ferrite phase boundaries act as barriers against fatigue crack propagation and their efficiency correlates with the geometrical misorientation between the neighbouring slip systems [3]. It is known that the twist misorientation rather than the tilt misorientation of two adjacent slip systems is determining the barrier efficiency of phase and grain boundaries [4,5].

The damage behaviour of DSS depends substantially on the heat treatment and chemical composition, which influences directly the strength of the individual phases. The addition of nitrogen to SDSS leads to a pronounced solid solution strengthening of the austenite phase and to an increase of the fatigue strength [6,7]. When exposing DSS to temperatures around 475 °C, a spinodal decomposition of the ferrite phase in a Fe-rich matrix phase containing Cr-rich  $\alpha'$  clusters can be observed. The so-called "475 °C embrittlement" leads to a pronounced strength increase of the ferrite grains. The respective increase of the barrier strength of the phase boundaries was shown to increase the HCF strength; however atom probe measurements (APT) revealed a disappearance of the  $\alpha'$  clusters along VHCF slip bands [8].

## EXPERIMENTAL

VHCF damage mechanisms were investigated on the austenitic ferritic duplex stainless steel (DSS) X2CrNiMoN22-5-3 (DIN 1.4462) and the super duplex stainless steel (SDSS) X2CrNiMoN25-7-4 (1.4410). The materials are hot rolled to round bars with a diameter of 25mm. The chemical compositions of the materials are given in Table 1.

Table 1. Chemical composition of the duplex and super duplex stainless steel (wt. %)

steel/ element	Fe	C	Cr	Ni	Mo	Mn	N	P	S	Si
DSS	Bal.	0.02	21.9	5.6	3.1	1.8	0.19	0.02	0.002	0.5
SDSS	Bal.	0.01	25.3	6.5	3.7	0.7	0.3	0.01	0.004	0.2

Consistent test conditions and a homogenous microstructure were achieved by heat treatment for both duplex steels. Cylindrical rods of the DSSs were annealed at 1250°C for 4h, cooled down in the furnace at a cooling rate of 1K/min to 1050°C and then quenched in water. This grain coarsening heat treatment resulted in a microstructure consisting of 50 % austenite and 50 % ferrite, with a mean grain size of 40  $\mu\text{m}$  for the DSS and a mean grain size of 20  $\mu\text{m}$  for the SDSS (see Fig. 1).

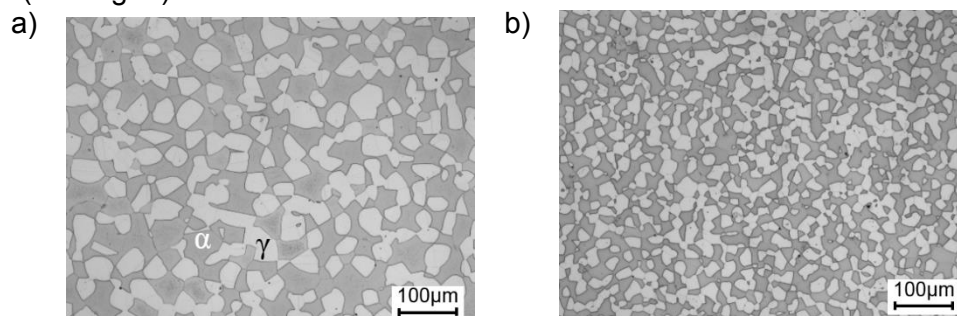


Figure 1: Microstructure of the a) duplex stainless steel (DSS) after grain coarsening and b) super duplex stainless (SDSS) steel as-received consisting of austenite  $\gamma$  (bright) and ferrite  $\alpha$  (dark).

Vickers microhardness measurements revealed hardness values of 304 HV in ferrite and 269 HV in austenite phase in the DSS, and 318 HV in ferrite and 302 HV in austenite phase in the SDSS, respectively. The higher austenite hardness of SDSS is related to a higher content of nitrogen. For the fatigue tests in the VHCF regime an ultrasonic fatigue testing system (BOKU Vienna) was used with a testing frequency of about  $f = 20\text{kHz}$ . The fatigue tests were carried out under laboratory air atmosphere at room temperature with a load ratio of  $R = -1$ . The ultrasonic fatigue testing machine was operated in pulse-pause mode to avoid any sample heating during cyclic loading. Additionally, the fatigue specimens were cooled with compressed

air. Hourglass-shaped, electrolytically polished fatigue specimens were used, containing two opposing shallow notches in the gauge length (notch factor  $k = 1.1$ , Fig. 2c) to allow in-situ observation of VHCF damage by means of light microscopy (Questar and HIROX) and high resolution thermography (Infratec ImageIR 8380 hp). Furthermore, the testing setup was modified for implementation in a high-resolution SEM (Fig. 2b).

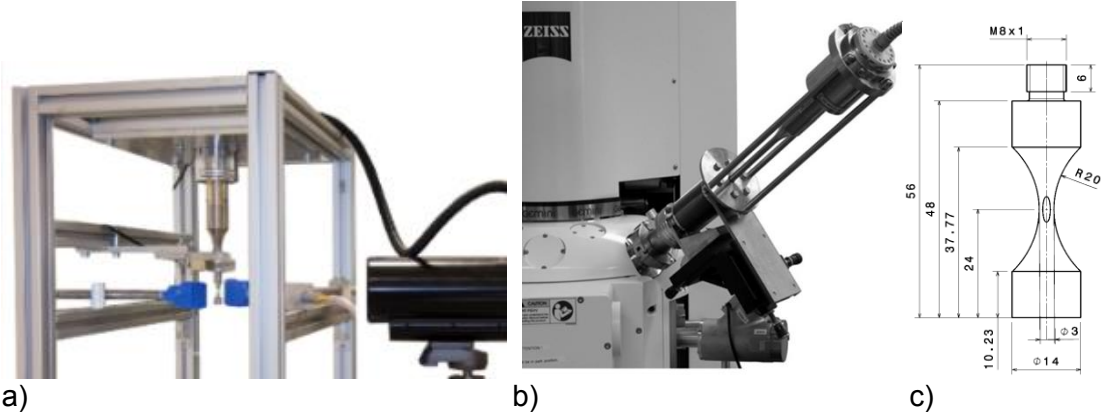


Figure 2: Experimental set-up for in-situ-tests a) using a Questar far field microscope, b) within the SEM and c) specimen geometry with shallow notch.

Fatigue tests under corrosive atmosphere were realized by means of a tailor-made corrosion chamber. The fatigue specimens were exposed to 5 % NaCl solution salt spray. The fatigued specimens are investigated by means of analytical electron scanning microscopy (SEM) in combination with electron backscattered diffraction (EBSD) and focused ion beam (FIB).

**RESULTS**

Figure 3 shows the SN-diagram for the DSS in the as-received and in the embrittled condition. Specimens, which did not fail after  $10^9$  cycles, are declared as run-out samples. Fatigue crack initiation was always observed at the surface of the specimens.

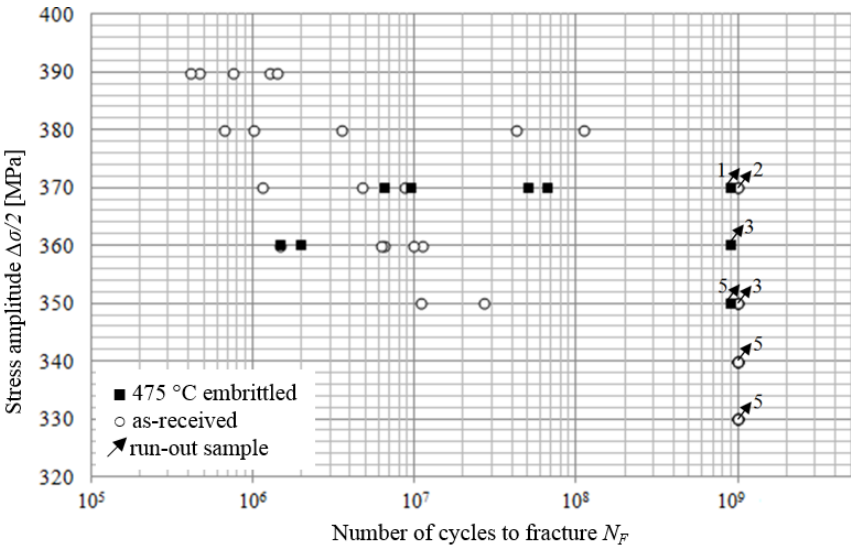
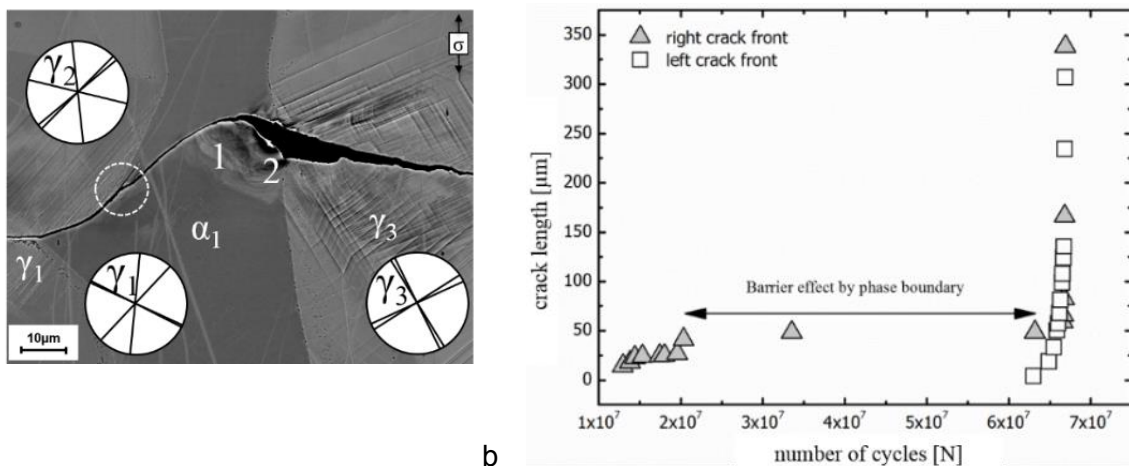


Figure 3: S-N diagram for duplex stainless steel fatigued at 20 kHz with a stress ratio of  $R = -1$  for the as-received compared to 475 °C embrittled specimen.

No failure was observed for a stress amplitude below  $\sigma_a = 340$  MPa. The pronounced scatter of the results in VHCF regime can be related to the influence of the microstructure. By continuous in-situ observation of the surface of the specimens during cyclic loading, an early development of slip bands of gradually increasing density within the austenite phase was observed. The strong dislocation pile-up due to slip band accumulation at the austenite/ferrite phase boundary causes crack initiation usually in ferrite grains. Two mechanisms for crack initiation from the phase boundaries were observed for DSS. Transgranular crack initiation is caused by the accumulated stress concentration by slip band formation within the austenite, which triggers the movement of dislocations and leading to crack initiation in the ferrite phase. Intergranular crack initiation was observed for phase boundaries, where the slip steps within the boundary plane overcome the phase boundary coherence. It is worth mentioning that even for stress amplitudes below  $\sigma_a = 340$  MPa local irreversible plastic slip was identified within the austenite grains. Therefore, one can conclude that local irreversible plastic slip of the DSS has generally to be accepted for fatigue applications also in the VHCF/fatigue limit regime. The key issue is the balance between (i) the amount of accumulated micro strain, (ii) the barrier strength of the respective phase boundaries, and (iii) the fulfilment of the conditions for eventual micro crack initiation.



**Figure 4:** a) SEM micrograph of a duplex stainless steel fatigued at  $\sigma_a=370$  MPa,  $N=6.9 \cdot 10^7$  with marked crack initiation area (white dashed circle) and possible slip traces of  $\{111\}$  planes (white circles) and b) the observed crack length versus the number of cycles.

As an example, Figure 4a shows a micro crack that was initiated at an austenite/ferrite phase boundary. The right crack front was propagating into the adjacent ferrite grain and stopped firstly at an inner phase boundary (1), and secondly in front of the neighbouring austenite grain (2). After the next approximately  $4.7 \cdot 10^7$  cycles, the crack starts spreading in both directions, overcomes the phase boundaries and leads to the final failure. The observation of the crack propagation rate and the crack path by light microscopy, reveals the microstructural barrier effect, cf. Figure 4b. The barrier strength depends on the slip plane misorientation between adjacent grains. The crack growth rate is controlled by the twist angle, because an additional surface within the grain-boundary plane is required for crack growth. The crack propagates on the plane, which shows the smallest difference in tilt and twist angle as compared to the original slip band in the first grain. This is documented by means of the slip trace directions marked in the white circles for the specific grains in Figure 4a. The fatigue behaviour of DSS is determined by the strength of the both phases, austenite and ferrite, respectively. Some samples were embrittled at 475°C, leading to a higher ferrite hardness. The embrittled specimens failed at loads of  $\sigma_a=360$  MPa during the fatigue tests. It was found by means of EBSD measurements that the slip activity seems to be localised to individual  $\{110\}\langle 111 \rangle$  slip systems. The investigation of the fracture surfaces supports this finding by the observation of

a tendency to micro cleavage. Regions with lower Cr content have been found by atom probe tomography (APT) of ferrite slip bands of embrittled run-out samples. This correlates with the high dislocation activity along the slip bands, leading to a disappearance of precipitates during VHCF (cf. [8]). And therefore, give reasons why this effect is not significantly increasing the VHCF life. Contrary to that, an increase in the nitrogen concentration in DSS influences mainly the strength of the austenite phase by solid solution strengthening. In comparison to DSS, crack initiation in SDSS seems to start preferably in austenite grains, since there is less stress relief by slip-band accumulation. Micro cracks within the slip bands form the nuclei for a propagating macro crack.

To investigate the material's response to corrosion fatigue under VHCF conditions, the steels were ultrasonically fatigued in a corrosion chamber using 5% NaCl solution salt spray. The S-N results show a strongly decreasing tendency for the fatigue strength of about 25 to 35% as compared to fatigue in air (cf. [9]). The repeated destruction of the passive layer under cyclic loading at the intrusions and extrusions along the slip band promotes the corrosion attack by the formation of a local electrolytic cell. The investigation of the fracture surfaces by means of high resolution SEM reveals a higher degree of crystalline roughness. A strong tendency to micro cleavage and slip planarity was found on the transgranular fracture surfaces. This is shown in Fig. 5c/d and Fig. 5g/h.

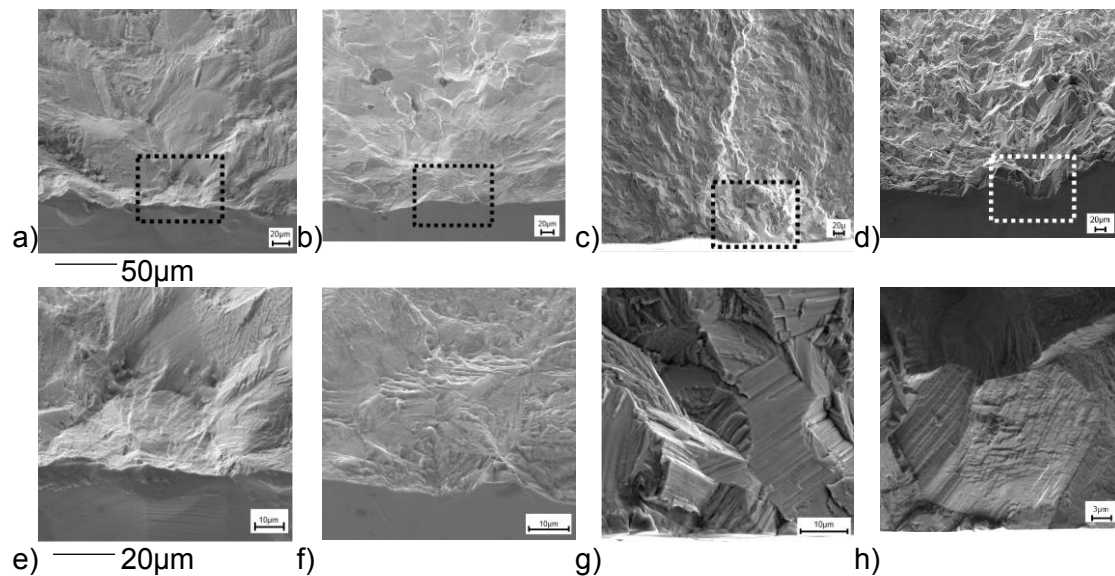


**Figure 5:** Fracture surfaces of both duplex steels at different atmospheres: a) DSS in air; b) DSS in vacuum; c) DSS in salt spray; d) SDSS in salt spray (e-h show the respective fracture surfaces in more detail).

## CONCLUSIONS

To investigate the fatigue mechanism in VHCF region in DSS X2CrNiMoN22-5-3 (1.4462) and SDSS X2CrNiMoN25-7-4 (1.4410), ultrasonic fatigue tests were carried out. The damage evolution during the fatigue tests were observed by means of in-situ monitoring techniques, i.e., light microscopy and scanning electron microscopy. The formation of slip bands at an early state of VHCF loading within the softer fcc austenite phase have been revealed by in-situ monitoring in the SEM. Furthermore, the increasing density of slip bands in the austenite grains leads to a stress concentration in the neighbouring ferrite grains. The impingement of the slip band lines at the austenite ferrite grain boundaries leads to crack initiation. Fatigue cracks are formed either intergranular or transgranularly, depending on the coplanarity of the adjacent slip

systems. Additionally it was found that phase boundaries exhibit a higher barrier strength than grain boundaries. While the efficiency of the microstructural barriers against slip transmission is determined by the twist angle between adjacent grain, the first boundary in front of the initiated crack is determining the existence of a fatigue limit by its effectiveness in blocking the fatigue crack growth. The higher nitrogen content in the fcc austenite for the SDSS leads to a higher fatigue limit as compared to DSS. The 475 °C embrittlement heat treatment, which leads to a strengthening of the bcc ferrite, seems to have a minor effect on an increasing fatigue life in the VHCF regime. Atom probe tomography revealed the disappearance of strengthening chromium-rich precipitates within the slip band areas. The fatigue testing under corrosive atmosphere leads to a strong decrease in fatigue life for both steels, DSS and SDSS, resp. This effect can be attributed to a higher degree of irreversible plastic slip leading into a pronounced slip planarity and a rough fracture surface showing lots of micro-cleavage facets.

## ACKNOWLEDGEMENT

The Deutsche Forschungsgemeinschaft (DFG) is gratefully acknowledged for financial support in the framework of the priority program entitled “Life<sup>∞</sup>: Unendliche Lebensdauer für zyklisch beanspruchte Hochleistungswerkstoffe” (SPP 1466).

## REFERENCES

- [1] H. Mughrabi and C. Wüthrich: ‘Asymmetry of slip and shape changes during cyclic deformation of  $\alpha$ -iron single crystals’, *Philos. Mag.*, 1967, 33, 963-984.
- [2] U. Krupp and I. Alvarez-Armas: ‘Short Fatigue Crack Propagation during Low-Cycle, High Cycle and Very-High-Cycle Fatigue of Duplex Steel – A Unified Approach’, *Int. J. Fatigue*, 2014, 65, 78-85.
- [3] U. Krupp (ed.): ‘Fatigue Crack Propagation in Metals and Alloys’; 2007, Weinheim, Wiley-VCH Verlag.
- [4] T. Zhai, A. J. Wilkinson and J. W. Martin: ‘A crystallographic mechanism for fatigue crack propagation through grain boundaries’, *Acta Mater.*, 2000, 48, 4917-4927.
- [5] M. Marx, W. Schaef and H. Vehoff: ‘Interaction of short cracks with the local microstructure’, *Proc. Eng.*, 2010, 2, 163-171.
- [6] M. Söker, O. Schönfeld, B. Dönges, A. Giertler and U. Krupp: ‘Ermüdungsverhalten von Duplex-Stählen unter Atmosphäreneinfluss’, Tagungsband ‘Werkstoffprüfung 2015’, Bad Neuenahr, Germany, 2015, Deutscher Verband für Materialforschung und -prüfung (DVM), 55-60.
- [7] R. Lillbacka, G. Chai, M. Ekh, P. Liu, E. Johnson and K. Runesson: ‘Cyclic stress–strain behavior and load sharing in duplex stainless steels: Aspects of modeling and experiments’, *Acta Mater.*, 2007, 55, 53-59.
- [8] U. Krupp, A. M. Söker, Giertler, B. Dönges, H.-J. Christ, T. Boll, M. Thuvander: The potential of spinodal ferrite decomposition for increasing the very high cycle fatigue strength of duplex stainless steel, *Intern. J. Fatigue*, 2016, 93, 363.
- [9] T. Waurischk, M. Söker, A. Giertler, N. Schönhoff, M. Galster, B. Dönges, H.-J. Christ, U. Krupp: Slip Band Formation and Crack Initiation during Very High Cycle Fatigue of Duplex Stainless Steel – Part 1: Mechanical Testing and Microstructural Investigations, in: H.H. Christ (ed.) *Fatigue of Materials at Very High Numbers of Loading Cycles, Experimental Techniques - Mechanisms - Modeling and Fatigue Assessment*, Springer, in press

**Corresponding author:** u.krupp@hs-osnabrueck.de

# LATTICE TILT AND SUBDIVISION OF GRAINS DURING CRACK FORMATION IN VHCF DUPLEX STAINLESS STEEL USING MICROBEAM X-RAY LAUE DIFFRACTION

A. Abboud<sup>1)</sup>, B. Dönges<sup>2)</sup>, M. Shokr<sup>1)</sup>, A. Tosson<sup>1)</sup>, J-S. Micha<sup>3)</sup>, R. Hartmann<sup>4)</sup>, L. Strüder<sup>5)</sup>, H.-J. Christ<sup>2)</sup>, U. Pietsch<sup>1)</sup>

<sup>1)</sup> Festkörperphysik, Universität Siegen, D-57068 Siegen, Germany

<sup>2)</sup> Institut für Werkstofftechnik, Universität Siegen, D-57068 Siegen, Germany

<sup>3)</sup> CEA-Grenoble\INAC\SprAM, 17 rue des Martyrs, F-38054 Grenoble Cedex 9, France

<sup>4)</sup> PNSensor GmbH, D-81739 München, Germany

## ABSTRACT

The effects of very high cycle fatigue damage were investigated at the grain level in austenitic-ferritic duplex stainless steel with a mean grain size of 50  $\mu\text{m}$  using a sub-micrometer X-ray Laue diffraction technique. A one-dimensional X-ray scan was performed in the vicinity of a fatigue crack between an austenitic and ferritic grain using a 2D energy dispersive pnCCD. Angular positions, intensities and energies of the Bragg peaks were recorded simultaneously by a single X-ray exposure as a function of measurement position. The diffraction data, show that the austenite grain is made up of two twinned regions (TB) divided by slip band (SB) activated along the most favored  $\{111\}$  slip system oriented by  $45^\circ$  w.r.t. the loading direction. Laue spots outside the SBs show a variation of different spectral and spatial distributions which can be explained by the presence of isolated sub-grains separated by polarized dislocation walls. Our findings support the scenario that dislocations wall formation followed by expansion of the lattice planes is a main phenomenological contributor to the mechanism leading to crack initiation at the grain interface and hence a signal for fatigue failure. The diffraction results are compatible with the optical images and EBSD.

## KEYWORDS

Very high cyclic fatigue, Microbeam X-ray Laue diffraction, Crack Formation,

## INTRODUCTION

Metallic structural materials are usually polycrystalline and show multiphase behavior. They are composed of many grains of mutual orientation and different structure. Many properties of the material, in particular static stiffness and fatigue life time are directly related to the nature of the particular grain-grain interaction. Thus, the boundary between grains of neighbored structural phases can act as barrier for dislocation movement and determine the propagation behavior of micro fatigue cracks and may determine crack intension caused by stress concentration due to the anisotropy of elastic and plastic deformations.

Currently, two main experimental methods are used to characterize inter- and intra-granular interactions, the first is electron backscatter diffraction (EBSD) [1-3] and the second is synchrotron based X-ray Laue diffraction [4-9]. EBSD based method is suitable for surface studies in the nanometer scale, while XRD allows for larger volumes to be sampled ( $\sim 10 \mu\text{m}$  at 20 keV).



Here we apply a new and innovative technique [10] to analyze the fatigue behavior using white beam X-ray Laue diffraction and a 2D energy dispersive pnCCD detector [11]. Simultaneous measurements of the Bragg peaks angle ( $2\theta$ ) and energy in a Laue pattern, allows for crystal structure analysis without any sample rotation in a single shot exposure. The achievable spatial resolution is limited only by the beam size and penetration depth of probing X-rays. Knowing the crystal system, the measured Laue reflections can be assigned to certain grains. Due to structural damage the Laue reflections often show streaking. Using the pnCCD one is able to measure the energy dependence along the streaks and to assign it to the deformation process inside the crystal [10].

In the present paper, we apply the technique to a sample of austenitic-ferritic duplex stainless steel with a mean grain size of  $50\ \mu\text{m}$ . Using a sub micrometer sized X-ray beam we scan across the grain boundary between one austenite and ferrite grain and evaluate the nature of a streaking Bragg peak as function of the distance to the crack. We show that the streaking shows a characteristic pattern changing with the probing position and indicating variation of strain and the formation of sub-grains.

## MATERIAL AND EXPERIMENT

### Setup

The energy-dispersive Laue diffraction (EDLD) experiment has been performed using the micro-beam Laue diffraction setup of the CRG-IF BM32 beamline at ESRF [12]. The primary beam provides polychromatic x-ray photons ranging between 5 to 23 keV. With the help of two Kirkpatrick-Baez mirrors, the beam size was reduced to a spot area of  $(0.5 \times 0.8)\ \mu\text{m}^2$  (FWHM) in the vertical and horizontal direction respectively. The sample was illuminated under an angle of about  $40^\circ$  with respect to the sample surface and the detector was equipped nearly vertically above the sample at a distance of 6.62 cm.

### Sample description

A dog-bone shaped specimen of polycrystalline duplex stainless steel having a circular cross section of 3 mm and a length of 10 cm, Fig. 1. The sample was thinned in the middle to create a weak region. In the process, the sample was hot rolled and then annealed for 4h @  $1250^\circ$  to induce grain coarsening ( $\varnothing$  grain size  $50\ \mu\text{m}$ ) and release residual strains. Next, the DSS cylinder was etched with acid to make the phases visible by microscopy. During these processes, some of the austenitic grains show twinning activities, Fig. 2a. The sample was then deformed in tension with a frequency of 20 kHz up to  $10^9$  cycles.



Fig. 1: A dog-bone shaped Duplex Stainless Steel sample

### XRF AND XRD Measurements

First one has to identify a region of interest on the sample where the EDLD experiment will be performed. The optical microscope images in Fig. 2a show an austenite grain surrounded by a ferrite one, where in the first, a relatively thick slip band system is visibly extruding into the ferrite grain and initiating a micro crack at the border. By recording Laue patterns using a



sub-micrometer X-ray beam in the neighborhood of the crack, one can resolve the crystallographic orientation as well as strain state.

Since Nickel is found with a higher concentration in austenitic phase in comparison to ferritic one, spatially resolved X-ray fluorescence mapping can be used to create a topological map of the surface of the sample. This map is used to determine the position of interest for X-ray analysis. The map shown in Fig. 2b, was recorded with spatial resolution of 5  $\mu\text{m}$  without removing the sample.

The micro crack in the ferrite phase is an example of a fatigue crack that may propagate until a material failure occurs. With a step size of 3  $\mu\text{m}$ , an X-ray scan was performed along the dotted line shown in Fig. 2c, beginning in the ferrite bulk and moving towards the direction of the crack tip, crack base and finally into the austenite phase. The resulting Laue patterns are recorded on a 2D energy dispersive pnCCD detector, and show 2 Laue spots belonging to the ferrite phase Fig. 3a. Due to simultaneous measurement of the Bragg angle and the spectral distribution, the Miller indices of each Laue spot can be calculated to be  $035$  and  $011$ . The changes in the shape and intensity distribution of the Laue spot ( $035$ ) are plotted as a function scan position Fig. 3b.

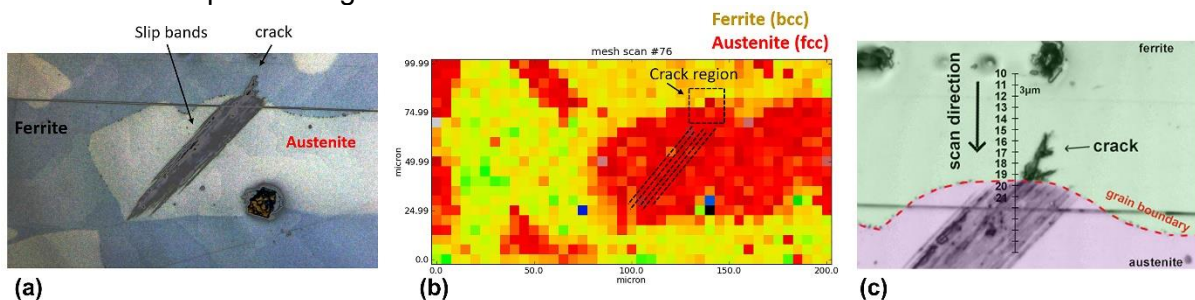


**Fig. 2:** (a) XRF image of the same region of Fig. 2a valuable for monitoring the X-ray beam on the sample. (b) XRF scan of the surface of the sample showing the ferrite phase (yellow/light) and austenite (red/dark) (c) Measurement plane: 10-20 are the X-ray scan positions with a step size of 3 $\mu\text{m}$ .

Starting from a relatively far position with respect to the grain boundary and the visible crack tip, the intensity map at position 10 in Fig. 3b shows a confined high intensity peak (marked as 1) which can be described by a 2D single Gaussian distribution, and a less intense peak (marked as 2). The 2 peaks belong to 2 different crystal grains, the first is the visible ferrite phase and the second is beneath the surface, owing to the  $\sim 10\ \mu\text{m}$  penetration depth of the X-ray beam at 23 keV inside steel. For further analysis, we focus on the first peak.

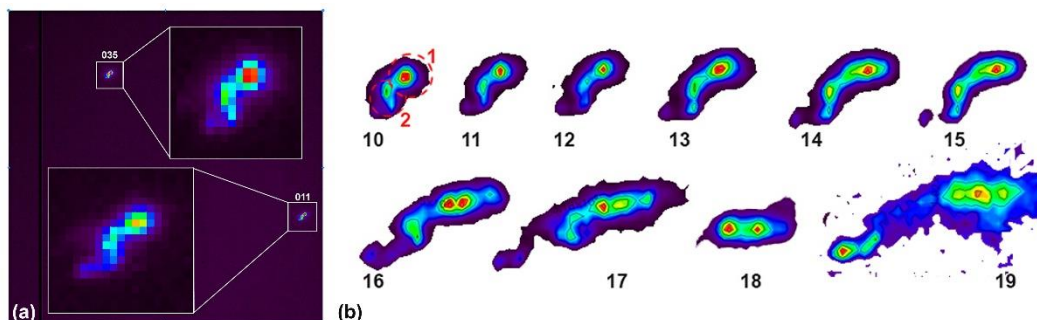


**Fig. 3:** Laue image of the measurement point 10, the two spots are magnified in the boxes. Evolution of the Laue spot 035 seen for different measurement positions 10-19.

Moving closer to the crack tip, a systematic displacement of the Bragg peak compared to position 10 is observed (Fig. 3b and Fig. 4a) which indicates a relative tilt of the lattice planes caused by mesoscale geometrically necessary dislocations (GNDs). An increase in the number of GNDs causes the dislocations to group into walls and sub-grain boundaries known as geometrically necessary boundaries, and causes a continuous lattice curvature redistributing the Bragg peak intensity in a “streak” with a dominant streak axis along the direction of curvature. This describes the state of the Laue spot from positions 13 to 15, where the Bragg peak intensity can no longer be described by a single Gaussian profile. When the angular mis-orientation between the GNBs is sufficiently large, the Bragg streaking becomes discontinuous, explaining the response at the crack. From measurement 16 to 18 the Bragg peak splits into three distinguishable sub-peaks moving away from each other as the X-ray beam reaches the crack base. At position 19, where the X-ray beam is at the grain boundary, the Bragg peak dissipates into a “cloud” like diffused intensity distribution indicating loss of crystallinity due to the high density of dislocations.

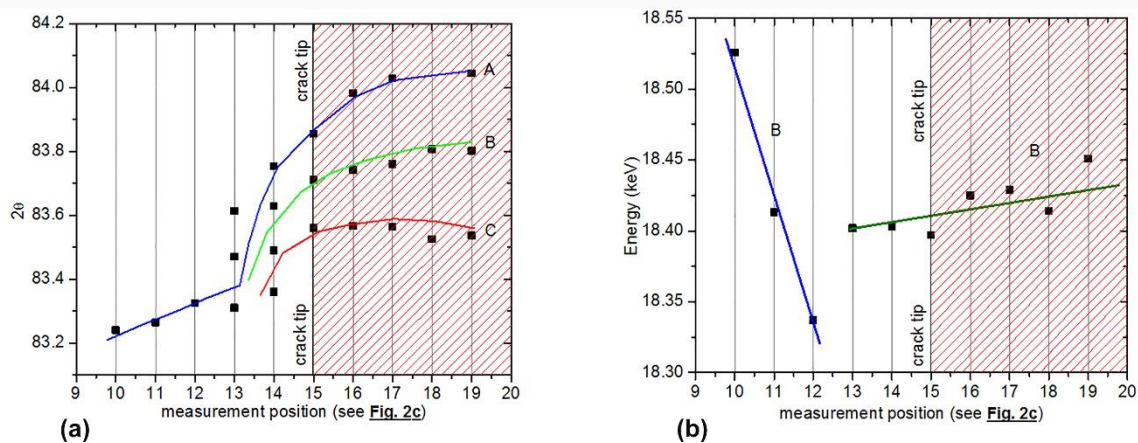


**Fig. 4:** (a) Evolution of Bragg angle ( $2\theta$ ) plotted as function of position within the area of interest. Peak splitting (into 3 Branches) is seen from position 13 on. The crack area starts in the vicinity of position 15 and ends at position 19 (grain interface). In (b) change of Bragg peak energy of peak of highest intensity (Branch B of Fig. 4b is displayed).

These qualitative observations seen in angular position and shape of the Bragg peak can be interpreted quantitatively by plotting the evolution of the Bragg angles and spectral widths of the sub-peaks shown in Fig. 3b as function of the probing position. An increase in the Bragg angle of the order  $\Delta\theta=0.1^\circ$  appears between points 10 and 13, followed by a jump of about  $0.15^\circ$  for the 3 sub-peaks evolving from point 14 on. A relative decrease in the change of the Bragg peak angle is seen in the region of the crack (15 to 19) with  $\Delta\theta<0.05^\circ$ . The strain state of the 035-lattice plane can be determined by the change in the energy of the Bragg peak (Fig. 4b).

The Laue peak energy shows a sharp decrease between measurement position 10 and 12, by  $\Delta E=200\text{eV}$ . This drop in energy can be interpreted by a change in the lattice spacing,  $d$ . Between position 12 and 13 there is a jump in energy by 50 eV indicating release of strain that remains nearly constant throughout the whole crack region.

## DISCUSSION OF RESULTS

Treatment of the sample surface using an etching solvent has revealed a distribution of sub-granular formation, seen as dark and light shadows, in the region surrounding fatigue cracks close to the grain boundary, Fig. 5. On the other hand, previous broad beam X-ray diffraction analysis on DSS [13] revealed splitting in the austenitic grains which was linked to the formation of slip bands. On the other hand; no splitting was visible for the ferrite phase due to the low density of fatigue cracks.

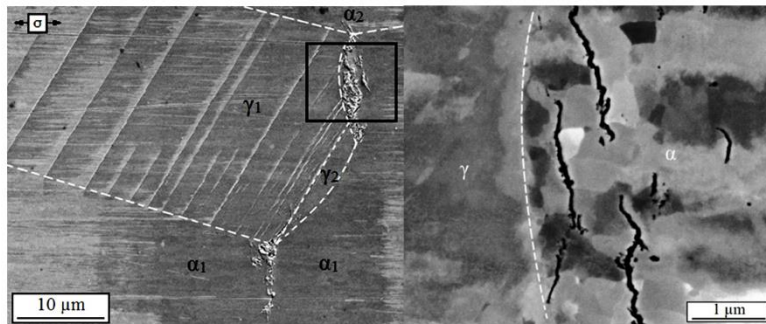


**Fig. 5:** Sub-grain formation seen in the neighborhood of fatigue cracks.

Using a micro-beam X-ray diffraction technique, the fatigue crack can be isolated and probed with high spatial resolution in comparison to the length of the fatigue damage. Our experiment shows two different regions, one with high strain level located at the tip of the crack and one with reduced strain but accompanied by sub grain formation.

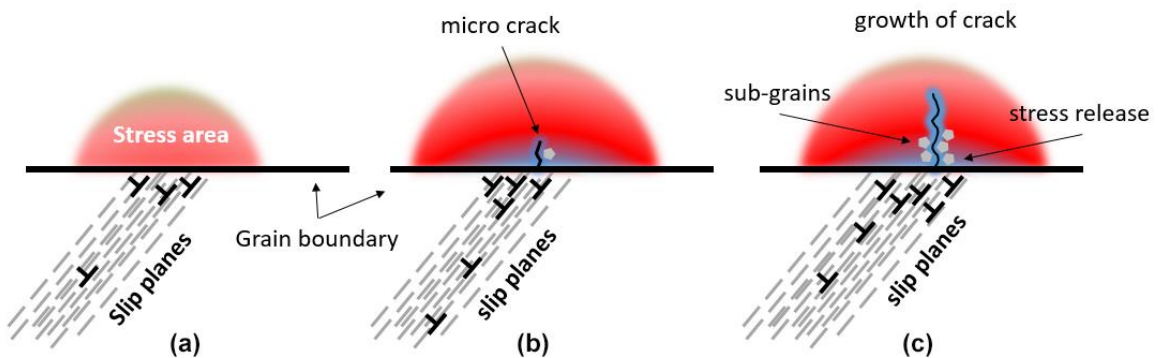


**Fig. 6:** Sketch model of the different stages of crack formation at the boundary between 2 grains. In (a), slip planes (twinning in f.c.c.) cause stress accumulation resulting in a micro crack (b). (c) As the number of cycles increase, the micro crack increases in length and sub grains are formed.

The elastic anisotropy at the boundaries between two grains causes stress concentrations initiated by twin formation in the austenitic grain. In the case of f.c.c. structure, the twin is also a slip plane, this allows for dislocations to glide towards and concentrate at the grain boundary. Within the ferrite grain, the density of dislocations increases causing crystal lattice tilts seen as a change in the Bragg angle. Further increase in the dislocation density, allows for the dislocations to organize in walls separating dislocation free regions and causing the Bragg peaks to streak and eventually to split into sub-grains. This process is accompanied by accumulation of strain, seen as a change in the Bragg peak energy. At one stage, the angular mis-orientation between dislocation walls exceeds a threshold visible as splitting of the Bragg peak into sub-peaks. This phenomenon is well-known and takes place in minerals, for example, where a crystal reduces its free energy by deformation in a process called dynamic recrystallization. Fig. 6 shows a scenario, how one can explain the changes accompanying the crack formation.

Although, this example of a fatigue crack was formed and measured *ex situ*, the dynamics accompanying this process are still hidden. In this paper the formation and subdivision of the duplex structures after the VHCF fatigue became visible by micro-beam white X-ray diffraction proving new information on dislocation arrangement allowing for better understanding of the fatigue process on sub-micron level.

This work was supported by SPP 1466,

## REFERENCES

- [1] Jiang, J.; Britton, B. T.; Wilkinson, A. J.:  
Mapping type III intragranular residual stress distributions in deformed copper polycrystals  
*Acta Mater.* 61 (2013), 5895-5904
- [2] Jiang, J.; Benjamin Britton, T.; Wilkinson, A. J.:  
Evolution of intragranular stresses and dislocation densities during cyclic deformation of polycrystalline copper  
*Acta Mater.* 94 (2015), 193-204
- [3] Plancher, E.; et al.:  
On the Accuracy of Elastic Strain Field Measurements by Laue Microdiffraction and High-Resolution EBSD: a Cross-Validation Experiment  
*Exp. Mech.* 56 (2016), 483-492
- [4] Larson, B. C.; Yang, W.; Ice, G. E.; Budai, J. D.; Tischler, J. Z.:  
Three-dimensional X-ray structural microscopy with submicrometre resolution  
*Nature* 415 (2002), 887-890
- [5] Levine, L. E.; et al.:  
X-ray microbeam measurements of individual dislocation cell elastic strains in deformed single-crystal copper  
*Nature Materials* 5 (2006), 619-622
- [6] Levine, L. E.; Okoro, C.; Xu, R.:  
Full elastic strain and stress tensor measurements from individual dislocation cells in copper through-Si vias  
*IUCrJ* 2 (2015), 635-642
- [7] Ice, G. E.; Barabash, R.:  
Dislocations in Solids vol. 13 ch. 79 (2007), 556
- [8] Petit, J.; et al.:  
Laue-DIC: a new method for improved stress field measurements at the micrometer scale  
*J. Synchrotron Rad.* 22 (2015), 980-994
- [9] Zhang, F. G.; Castelnau, O.; Bornert, M.; Petit, J.; Marijon, J. B.; Plancher, E.:  
Determination of deviatoric elastic strain and lattice orientation by applying digital image correlation to Laue microdiffraction images: the enhanced Laue-DIC method  
*J. Appl. Cryst* 48 (2015), 1805-1817
- [10] Abboud, A.; et al.:  
A new method for polychromatic X-ray  $\mu$ Laue diffraction on a Cu pillar using an energy-dispersive pn-junction charge-coupled device  
*Review of Scientific Instruments* 11(85) (2014)
- [11] Strüder, L. et al.:  
The European Photon Imaging Camera on XMM-Newton: The pn-CCD camera  
*Astronomy and Astrophysics Letters* 368 (2001), L18-L26
- [12] Ulrich, O.; et al.:  
A new white beam x-ray microdiffraction setup on the BM32 beamline at the European Synchrotron Radiation Facility  
*Review of Scientific Instruments*, 82(3) (2011)
- [13] Istomin, K.; Dönges, B.; Schell, N.; Christ, H.J.; Pietsch, U.:  
Analysis of VHCF damage in a duplex stainless steel using hard X-ray diffraction techniques  
*International Journal of Fatigue* 66 (2014), 177-182

**Corresponding author:** ali.abboud@uni-siegen.de

# FATIGUE PROPERTIES OF CFRP CROSS-PLY LAMINATES WITH TAILORED FEW-LAYER GRAPHENE ENHANCEMENT

Christian Leopold<sup>1</sup>, Andreas Schetle<sup>1</sup>, Julia Kosmann<sup>1</sup>, Gordon Just<sup>2</sup>, Ilja Koch<sup>2</sup>,  
Maik Gude<sup>2</sup>, Bodo Fiedler<sup>1\*</sup>

<sup>1</sup>Institute of Polymer Composites, Technical University Hamburg,  
Denickestraße 15, D-21073 Hamburg, Germany

<sup>2</sup>Institute of Lightweight Engineering and Polymer Technology, Technical University Dresden  
Holbeinstraße 3, D-01307 Dresden, Germany

\*presenting author

## ABSTRACT

The influence of graphene nanoparticle modification on damage initiation and propagation in carbon fibre reinforced plastics is investigated in static and cyclic tests using cross-ply laminates. The matrix either in the 0°-layers or in the 90°-layers is modified with few-layer-graphene nanoparticles. In quasi-static tensile tests, a 90°-ply modification exhibits a delay in failure initiation while a 0°-ply modification increases the failure stress, thus exhibiting improved properties compared to the unmodified material. In cyclic tests under alternating loading however, the fatigue lifetime is decreased by the matrix modification, with the largest reduction for the 90°-ply modification. Fractography analysis of the fracture surfaces by scanning electron microscopy reveals differences in the fracture behaviour and a negative influence of the modification under mode I loading.

## KEYWORDS:

Few Layer Graphene, Failure initiation, Matrix cracks, Fractography

## INTRODUCTION

The increasing use of fibre-reinforced plastics (FRP) requires detailed knowledge about failure initiation and propagation within composite laminates. Matrix cracks control the design in layers transverse to loading direction and limit fatigue life in cyclic tests. For achieving higher efficiency and extended in-service life of FRP, especially when used as structural parts, improvement of the fatigue properties of on-going interest. With a carbon nanoparticle modification, increasing mechanical properties of polymers and FRP are reported [1–11]. By incorporating nanoparticles in the matrix, the available additional damage mechanisms enable the material to absorb more energy [7,11].

Since the discovery of graphene [12,13] there is an increasing interest to use it as reinforcing materials in polymers and FRP. Already the addition of small amounts of graphite nanoplatelets or graphene oxide increase the fracture toughness of epoxy matrix significantly [3] and leads to a higher resistance to fatigue crack growth [5,6]. By fractography, different toughening mechanisms such as graphene layer separation, layer shearing and formation of micro voids due to plastic shearing of the matrix are identified [3,11]. In addition to crack pinning, crack deflection and crack branching at the nanoparticles, additional energy is



absorbed by the modified material, leading to a decrease in crack growth rate and thus an increase in fracture toughness [3,14].

One promising approach to increase mechanical properties as well as fatigue life of composite laminate up the very high cycle fatigue regime is thus a modification of the matrix with carbon nanoparticles. However, the influence of carbon nanoparticles on damage initiation and propagation in fatigue loaded composite laminates is yet not fully understood. Furthermore, it was shown in previous investigations, that a nanoparticle modification may have opposing effects when comparing different load cases. For carbon fibre reinforced plastic (CFRP) cross-ply laminates, an increase in fatigue life is achieved with a matrix modification using multi-walled carbon nanotubes (MWCNT) or few layer graphene (FLG) in the tension-tension (t-t) regime [11]. In the tension-compression (t-c) regime however, the nanoparticles have no significant, or in the case of FLG even a negative effect on the fatigue behaviour. Figure 1 shows the influence of a nanoparticle modification with MWCNT and FLG on the fatigue life of CFRP under tensile and alternating loads.

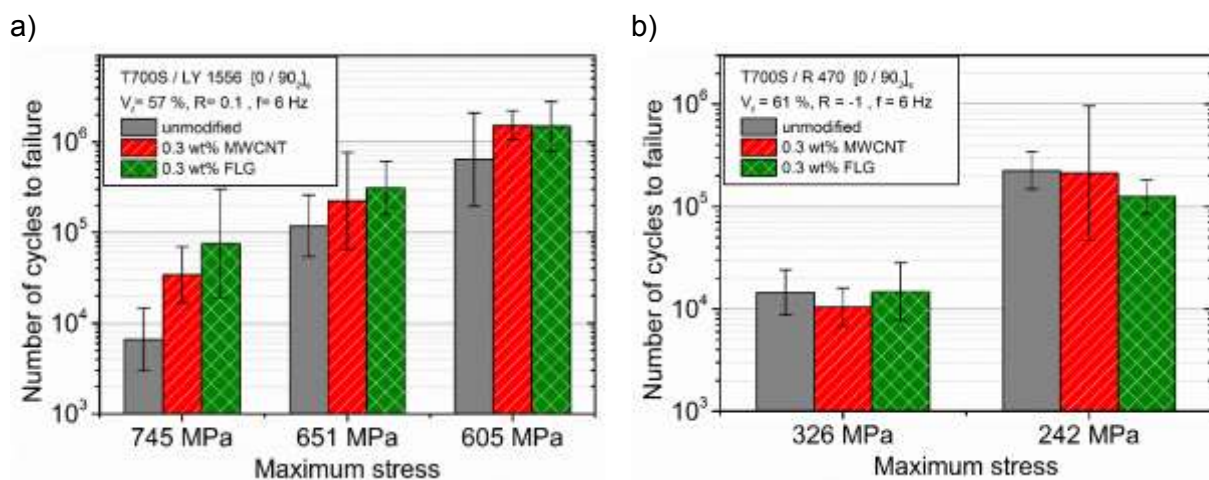


Figure 1: Fatigue life of unmodified and carbon nanoparticle modified CFRP for different load levels a) in the tension-tension regime (from [11]); b) in the tension-compression regime.

The aim of this work is therefore a more detailed investigation of the influence of FLG on the fatigue behaviour of CFRP under alternating loads in the t-c regime. Special focus is set on the effect of the modification in the different layers of cross-ply laminates and the influence of the particles with regard to damage initiation and propagation.

## EXPERIMENTAL

T700S carbon fibres (Toray, Japan) are used with the epoxy prepreg system Ludeko R470 / H471 (Ludeko, Germany) as matrix material. Planar FLG avanGraphene-2 (Avanzare, Spain) are used for nanoparticle modification of the matrix with a filling content of 0.3 wt.% based on the complete matrix system. The FLG particles have less than six layers with a thickness of about 2 nm and lateral dimensions of 5 μm to 25 μm (according to the manufacturer).

The nanoparticles are dispersed in the resin without hardener in a three roll mill (EXAKT Advanced Technologies GmbH 120E). The hardener is added before impregnation of the fibres. The components are degassed for 1 h at 30 °C and then mixed by automated steering in vacuum for 20 min to remove any air inclusions.

Unmodified and FLG modified prepreps are produced with an in-house prepreg machine. The dry carbon fibre roving is impregnated with the unmodified or FLG modified matrix system and wound up on a hexagonal roll. With this method, a unidirectional tape with

straight, aligned fibres of 300 mm width is produced. Nanoparticles are equally dispersed in the matrix between the fibres as is confirmed in transmission light microscopy of thin micro section samples. After B-staging according to the recommendation for this material system, the prepregs are stored at -18 °C until lamination and the following curing process. Cross-ply laminates [0/90<sub>2</sub>]<sub>s</sub> are stacked from the produced prepregs and autoclave cured at 120 °C for 2 h with an applied vacuum of -0.2 bar and an autoclave pressure of 3 bar. From the prepregs, three configurations are laminated:

- Unmodified
- 0°-layers modified with 0.3 wt.% FLG
- 90°-layers modified with 0.3 wt.% FLG

With this approach, the influence of the FLG modification in either the 0°-layers or in the 90°-layers on the mechanical properties and the damage process can be independently determined.

Ultrasonic inspection after curing assures manufacturing quality without any larger voids or delaminations. The fibre volume content is determined according to DIN EN 2564 to be approximately 65 %. Cured laminates are prepared with 50 mm wide and 2 mm thick GFRP/Aluminium end-tabs using 2-component adhesive. Specimens for static and cyclic tensile tests are cut with a diamond saw according to DIN EN ISO 527-4 [15] to length = 250 mm, width = 25 mm and thickness = 2 mm. Specimen edges are polished to minimise edge effects.

Quasi static tensile tests are performed according to DIN EN ISO 527-4 [15] with a universal testing machine type 1474 from Zwick at a cross-head speed of 2 mm/min. Strain is measured with a long-travel extensometer on the specimen surface. Acoustic emission (AE) analysis is used to analyse the damage process. The recording of AE data is carried out with a Micro-II multi-channel acquisition system (MISTRAS, Germany). Two wideband differential (WD) sensors for AE wave detection are fixed on one side of the specimen. The setting of the AE acquisition system is given in Table 1.

Table 1: Setting of the parameters of the AE acquisition system

Parameter	Value
Sampling rate	5 Hz
Preamplifier Gain	20 dB
Threshold	45 dB
HDT	250 µs
HLT	800 µs
PDT	150

Fatigue tests are performed on a servo-hydraulic test machine from Instron/Schenk with alternating loads in the tension-compression regime ( $R = -1$ ) at a frequency of 6 Hz. Two load levels are selected. The higher load level is at 228.8 MPa (23 % mean tensile strength) the lower is at 215 MPa (21.6 % mean tensile strength). The upper load level is selected in the stress range of transverse crack initiation in quasi-static tensile tests, as it is determined with the AE-analysis. The tests are performed at standard conditions of 23 °C and 50 % humidity. Specimens are mounted in an anti-buckling device to prevent global specimen buckling at the compressive loading part.

The fracture surfaces are analysed by scanning electron microscopy (SEM) in order to evaluate the influence of the FLG modification on damage propagation under static and alternating cyclic loads.

## RESULTS AND DISCUSSION

In quasi-static tensile tests, Young's modulus, strain to failure and failure stress are obtained and compared for the three configurations. Using the AE data, the stress at inter fibre failure (IFF) initiation can be determined from an increase in accumulated energy that correlates well with a slight decrease in the slope stress-strain curve. This slope decrease is also referred to as a "knee" and typical for initiation of the first transverse cracks in cross-ply laminates [16].

By modifying either the 0°-layers or the 90°-layers with FLG nanoparticles, Young's modulus increases of about 5.5 %. The strain to failure is not influenced by the nanoparticle modification as it is dominated by the stiff fibres in 0°-direction. Figure 2 shows the stress at IFF initiation and at rupture of the specimen for the three configurations. As can be seen in Figure 2 a), the initiation of IFF is shifted to higher stresses with a modification of the 90°-layers with FLG nanoparticles. This can be explained with nano- or microdamage at the particles such as graphene layer shearing or matrix plastic deformation [3,17]. These types of local damage dissipate energy that is not available for crack initiation or growth. As IFF occurs mainly in the 90°-layers, no significant change is observed for a 0°-layer FLG modification, although the stress at IFF is slightly higher compared to the unmodified specimens. The failure stress is increased with a FLG modification of the 0°-layers, as shown in Figure 2 b). Values for the laminates with 90°-layers modified are in the same range as the unmodified laminates. The higher failure stress for the 0°-layer modification can be attributed to a suppression of delamination growth that is observed during the tests. The 0°-layer modified specimens exhibit a nearly linear stress-strain-behaviour until final failure, whereas for both other configurations load drops and a decreasing slope of the stress-strain curve are observed. These load drops correlate with an abrupt increase in cumulated energy in the AE data and are attributed to delamination initiation and growth or fibre failure. In addition, breakage of fibre bundles in the 0°-layers after single fibre breakage might be reduced due to a better load redistribution via the stiff FLG particles oriented in loading direction between the fibres, resulting in higher tensile stress.

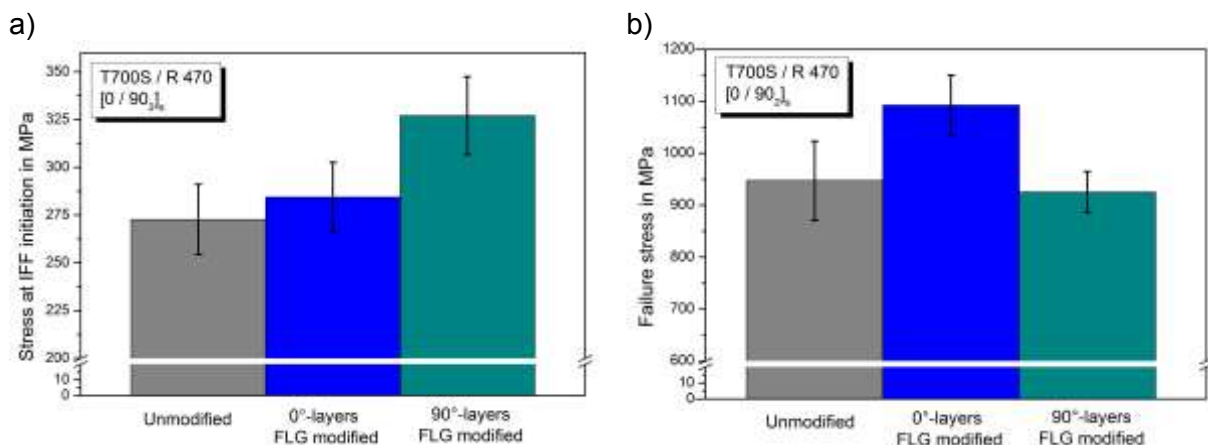


Figure 2: Mechanical properties determined from quasi-static tensile tests: a) stress at failure initiation b) failure stress

These results with regard to the observed damage suppression fit well with the increase in fatigue lifetime under pure tensile loads shown in Figure 1 [11]. With a compressive loading part however, the fatigue life decreases when the matrix in either 0°-layers or 90°-layers is modified with FLG nanoparticles. This is shown in Figure 3, in which the load cycles until failure are given at the two load levels for all three configurations.



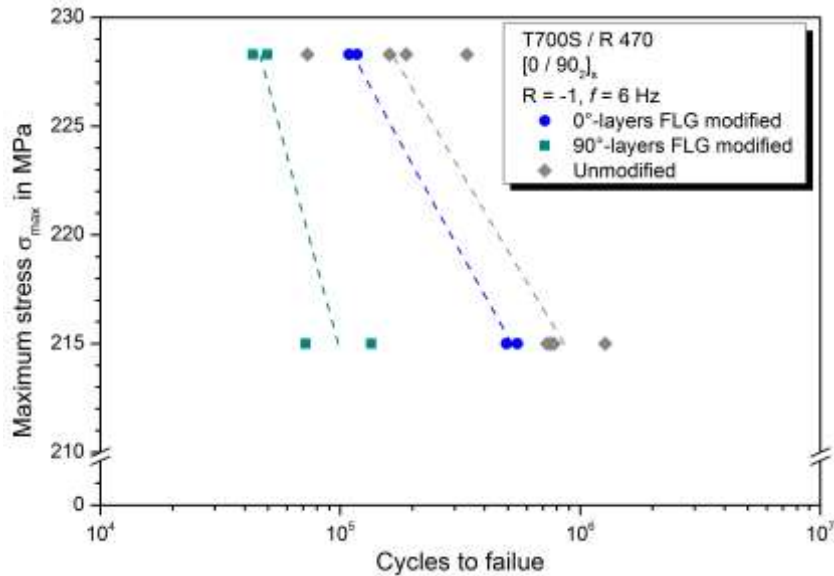


Figure 3: SN-curves of CFRP showing the influence of a matrix modification with FLG nanoparticles in the different layers of cross-ply laminates

A modification of the 90°-layers reduces the cycles to failure for both load levels significantly. Cycles to failure for specimens with the 0°-layers modified are in within the range of the unmodified specimens for the higher load level, but exhibit smaller values for the lower load level. This agrees with observations from Knoll et al. that a modification with FLG nanoparticles in FRP is more promising at higher loading in fatigue tests [11]. The reasons for the inferior fatigue behaviour under alternating loads compared to the unmodified material are investigated using fractography in SEM. It is found that the planar FLG particles between the fibres as well as between the layers are oriented in fibre direction. This may lead to a faster mode I delamination growth during compressive loading and thus results in lower fatigue life. These results agree well with previous investigations on mode I / II fracture toughness of the same material, which showed a decreasing mode I fracture toughness for FLG nanoparticle modified cross-ply laminates [18]. Further investigations with other nanoparticle morphologies and dimension are thus necessary for clarification.

## CONCLUSIONS

With a tailored matrix modification using FLG nanoparticles of either the 90°-layers or the 0°-layers of CFRP cross-ply laminates the influence of these particles with regard to mechanical properties and damage initiation and propagation is investigated under quasi-static tensile and alternating fatigue loading conditions. In tensile tests, the IFF initiation is shifted to higher stresses for a 90°-layer modification, while a 0°-layer modification results in a higher failure stress. This enhancement in mechanical properties shows the potential for increasing fatigue life, at least in the tension-tension regime. In the tension-compression regime, FLG particles may accelerate mode I delamination crack growth when oriented in crack growth direction, leading to the observed decrease in fatigue life.

## ACKNOWLEDGEMENTS

The authors would like to thank Deutsche Forschungsgemeinschaft (DFG) for financial support of this study in the framework of the priority program “Life<sup>∞</sup>” (SPP 1466).

## References

- [1] Bortz DR, Heras EG, Martin-Gullon I. Impressive Fatigue Life and Fracture Toughness Improvements in Graphene Oxide/Epoxy Composites. *Macromolecules* 2011;45(1):238–45.
- [2] Bortz DR, Merino C, Martin-Gullon I. Carbon nanofibers enhance the fracture toughness and fatigue performance of a structural epoxy system. *Composites Science and Technology* 2011;71(1):31–8.
- [3] Chandrasekaran S, Sato N, Tölle F, Mülhaupt R, Fiedler B, Schulte K. Fracture toughness and failure mechanism of graphene based epoxy composites. *Composites Science and Technology* 2014;97:90–9.
- [4] Gojny FH, Wichmann MH, Fiedler B, Schulte K. Influence of different carbon nanotubes on the mechanical properties of epoxy matrix composites – A comparative study. *Composites Science and Technology* 2005;65(15–16):2300–13.
- [5] Rafiee MA, Rafiee J, Srivastava I, Wang Z, Song H, Yu Z et al. Fracture and Fatigue in Graphene Nanocomposites. *Small* 2010;6(2):179–83.
- [6] Rafiee MA, Rafiee J, Wang Z, Song H, Yu Z, Koratkar N. Enhanced Mechanical Properties of Nanocomposites at Low Graphene Content. *ACS Nano* 2009;3(12):3884–90.
- [7] Tang L, Wan Y, Yan D, Pei Y, Zhao L, Li Y et al. The effect of graphene dispersion on the mechanical properties of graphene/epoxy composites. *Carbon* 2013;60:16–27.
- [8] Yavari F, Rafiee MA, Rafiee J, Yu Z, Koratkar N. Dramatic Increase in Fatigue Life in Hierarchical Graphene Composites. *ACS Appl. Mater. Interfaces* 2010;2(10):2738–43.
- [9] Böger L, Sumfleth J, Hedemann H, Schulte K. Improvement of fatigue life by incorporation of nanoparticles in glass fibre reinforced epoxy. *Composites Part A: Applied Science and Manufacturing* 2010;41(10):1419–24.
- [10] Hsieh T, Kinloch AJ, Taylor AC, Kinloch IA. The effect of carbon nanotubes on the fracture toughness and fatigue performance of a thermosetting epoxy polymer. *Journal of Materials Science* 2011;46(23):7525–35.
- [11] Knoll JB, Riecken BT, Kosmann N, Chandrasekaran S, Schulte K, Fiedler B. The effect of carbon nanoparticles on the fatigue performance of carbon fibre reinforced epoxy. *Composites Part A: Applied Science and Manufacturing* 2014;67(0):233–40.
- [12] Novoselov KS, Geim AK, Morozov SV, Jiang D, Zhang Y, Dubonos SV et al. Electric Field Effect in Atomically Thin Carbon Films. *Science* 2004;306(5696):666.
- [13] Geim AK, Novoselov KS. The rise of graphene. *Nat Mater* 2007;6(3):183–91.
- [14] Zaman I, Phan TT, Kuan H, Meng Q, Bao La LT, Luong L et al. Epoxy/graphene platelets nanocomposites with two levels of interface strength. *Polymer* 2011;52(7):1603–11.
- [15] International Organization for Standardization. *Plastics - Determination of tensile properties - Part 4: Test conditions for isotropic and orthotropic fibre-reinforced plastic composites (DIN EN ISO 527-4)*; 1997.
- [16] Garrett KW, Bailey JE. Multiple transverse fracture in 90° cross-ply laminates of a glass fibre-reinforced polyester. *Journal of Materials Science* 1977;12(1):157–68.
- [17] Quaresimin M, Schulte K, Zappalorto M, Chandrasekaran S. Toughening mechanisms in polymer nanocomposites: From experiments to modelling. *Composites Science and Technology* 2016;123:187–204.
- [18] Kosmann J, Leopold C, Schulte K, Fiedler B. Damage initiation and failure mechanisms of carbon nanoparticle modified CFRP up to very high cycle fatigue loading, Hamburg University of Technology: Final report SPP-1466, 2016

**Fundamentals, physics and mechanisms**  
**Nonpropagating cracks, growth of short and**  
**long cracks and mechanisms of Damage**  
**Accumulation**

## **INVITED**



### **Ulrich Krupp**

graduated in Mechanical Engineering in 1994 and received his doctorate degree in Materials Science from the University of Siegen in 1998. From 1997 till 2006 he was employed as group leader 'Materials Fatigue' and senior engineer at the Institute of Materials Technology at the University of Siegen, where he received his habilitation in 2004. In 2001 and 2002 he held a post doc position as Alexander von Humboldt fellow at the University of Pennsylvania in Philadelphia, USA. Since 2006 he is professor for engineering materials at the University of Applied Sciences Osnabrück, where he founded the Institute of Materials Design and Structural Integrity in 2009.

Prof. Krupp published more than 260 articles in peer-reviewed journals and conference proceedings. He is chairman of the working party 'Materials Fatigue' of the DGM (German Materials Society) and chairman of the working party 'Materials Technology' of the VDI (German Society of Engineers). For his outstanding scientific contributions in the field of materials science he received the Masing award of the DGM for in 2005, the Galileo Award of the DGM/DVM and VDEh in 2011, the Konrad Albert Schäfer innovation price in 2015, and the VDI medal of honor in 2017. Since 2015 Prof. Krupp holds the position as an affiliated professor at Chalmers University of Technology.

## **THE SIGNIFICANCE OF MICROSTRUCTURE INHOMOGENEITIES DURING VHCF OF TEMPERED MARTENSITIC STEEL**

**U. Krupp**, A. Giertler, K. Koschella

University of Applied Sciences Osnabrück Institute of Materials Design and Structural Integrity,  
Osnabrück, Germany

Tempered martensitic steels are used for any applications in transport, energy and production technologies that combine high numbers of load cycles with high mechanical load. In series production, maintaining a high degree of microstructure reproducibility is limited. Therefore, the case of VHCF-loaded components, microstructure inhomogeneities can lead to a serious life reduction, since the microstructural blocking of initiated small fatigue cracks might get lost in weak regions.

By means of ultrasonic testing (20000Hz, type BOKU Vienna) and resonance testing (400Hz, type RUMUL Testronic) of a 0.5C-1.25Cr-Mo tempered steel (German designation: 50CrMo4) in combination with high-resolution thermography, the evolution of fatigue damage was monitored throughout the fatigue life. It was found by heat dissipation signals that cyclic plasticity is concentrated within Cr-depleted segregation bands. A closer analysis of these plastic strain concentration sites by using high-resolution scanning electron microscopy (SEM) in combination with automated EBSD (electron back scattered diffraction) reveals that cracks initiate mainly between 60°-misoriented martensite blocks. As long as the cracks are limited to one prior austenite grain they are rather shallow as it was shown by focused ion beam (FIB) milling. For such shallow cracks, the prior austenite grain boundaries act as efficient barriers to fatigue crack propagation and hence, the material exhibits a fatigue limit (here: no fracture at 1 billion of cycles). To correlate the microstructure hierarchy (prior austenite grains size, martensite packet size, and martensite block size), the material was given a defined coarsening heat treatment. By incremental step tests on specimens of the heat-treated materials, the cyclic yield strength vs. prior austenite grain size was determined, allowing the derivation of the cyclic friction stress and the barrier strength. These important microstructural parameters were used to apply a numerical short crack model based on the boundary element method to VHCF of tempered steel.

# THE SIGNIFICANCE OF MICROSTRUCTURE INHOMOGENEITIES DURING VHCF OF TEMPERED MARTENSITIC STEEL

U. Krupp, A. Giertler, K. Koschella

Institute of Materials Design and Structural Integrity, Faculty of Engineering and Computer Science, University of Applied Sciences Osnabrück, Albrechtstraße 30, 49009 Osnabrück, Germany

**KEYWORDS** Martensitic steel, modeling, thermography, FIB, EBSD

## ABSTRACT

By means of high frequency fatigue testing of a 0.5C-1.0Cr-Mo martensitic steel in different tempering conditions, the evolution of fatigue damage was monitored throughout the fatigue life by applying high-resolution thermography. It was found by heat dissipation signals that cyclic plasticity in the medium hardness condition is concentrated within Cr-depleted segregation bands leading to surface crack initiation mainly between 60°-misoriented martensite blocks. As long as the cracks are limited to one prior austenite grain they are rather shallow, as it was shown by FIB milling, and are blocked by prior austenite grain boundaries. In the high strength condition, VHCF cracks initiate internally at non-metallic inclusions. To correlate the hierarchical microstructure features with the fundamental mechanical properties, the material was given a defined coarsening heat treatment. By incremental step tests on specimens of the heat-treated materials, the cyclic yield strength vs. prior austenite grain size was determined, allowing the derivation of the cyclic friction stress and the barrier strength. These important microstructural parameters were used to apply a numerical short crack model based on the boundary element method to VHCF of tempered steel.

## INTRODUCTION

Tempered martensitic steels are used for any applications in transport, energy and production technologies that combine high numbers of load cycles with high mechanical load levels. In series production, maintaining a high degree of microstructure reproducibility is limited. Therefore, in the case of VHCF-loaded components, microstructure inhomogeneities can lead to a serious life reduction, since the blocking of initiated small fatigue cracks might get lost in weak regions. Tempered martensitic steels exhibit a hierarchical microstructure setting [1]; prior fcc austenite grains resulting from the normalization treatment serve as starting point for the diffusion-less martensite formation during quenching. According to [2], the transformation follows the Kurdjumov-Sachs relationship between the fcc austenite grains and the bct martensite laths:  $\{111\}_{\gamma \text{ fcc}} \parallel \{110\}_{\alpha \text{ bct}}$ . The martensite laths, separated either by low-angle or 60° boundaries, are arranged in parallel blocks within packets of similar block orientation. The strength of the martensitic microstructure depends on the degree of tetragonal distortion (due to carbon in supersaturation) and the size of carbide precipitates, and can be adjusted by the tempering temperature and time. In addition to that, the VHCF strength depends on the size of non-metallic inclusions [3] or the local barrier efficiency to withstand the spread of cyclic plasticity (cf. [4]). It has been known from numerous studies on VHCF of high-strength steel that failures at  $10^8$  cycles and more initiate internally at nonmetallic inclusions (VHCF type II behavior). The inclusions are surrounded by a fine granular area (FGA), the size of which becomes larger the lower the applied stress amplitude. The relationship between VHCF life and FGA development can be generally understood on the basis of dislocation accumulation, grain refining and local decrease of the stress intensity threshold for fatigue crack initiation (cf. [5,6]). The mutually interacting loading conditions and microstructure features of martensitic

steels, that determine the crack initiation site, are not fully understood yet and are subject of the present paper.

## EXPERIMENTAL

The VHCF behavior of martensitic steel was studied by means of 0.5C-1.0Cr-Mo tempered steel (German designation: 50CrMo4) that was provided as cylindrical bars and given a normalizing treatment at 860°C for 1h followed by quenching in oil. One set of specimens exhibits an identical prior austenite grain size ( $d=14\mu\text{m}$ ), martensite packet and block size ( $b=0.5\mu\text{m}$ ), but was tempered at two different temperatures, 550°C and 200°C for 1.5h, resulting in hardness of 37HRC and 57HRC, respectively. Another set of specimens was produced using an extended high-temperature treatment prior to normalizing in order to vary the prior austenite grain size and the martensite packet size. To correlate the hierarchic features of the martensitic microstructure with the VHCF properties, the steel was quantitatively analyzed by means of electron back-scattered diffraction (EBSD) in the scanning electron microscope (SEM Zeiss Auriga). Fig. 1 shows the crystallographic orientation distribution of the martensite laths and the prior austenite grains calculated using the variations of the KS orientation relationship (ARPGE: Automatic Reconstruction of Parent Grains from EBSD data, [7]).

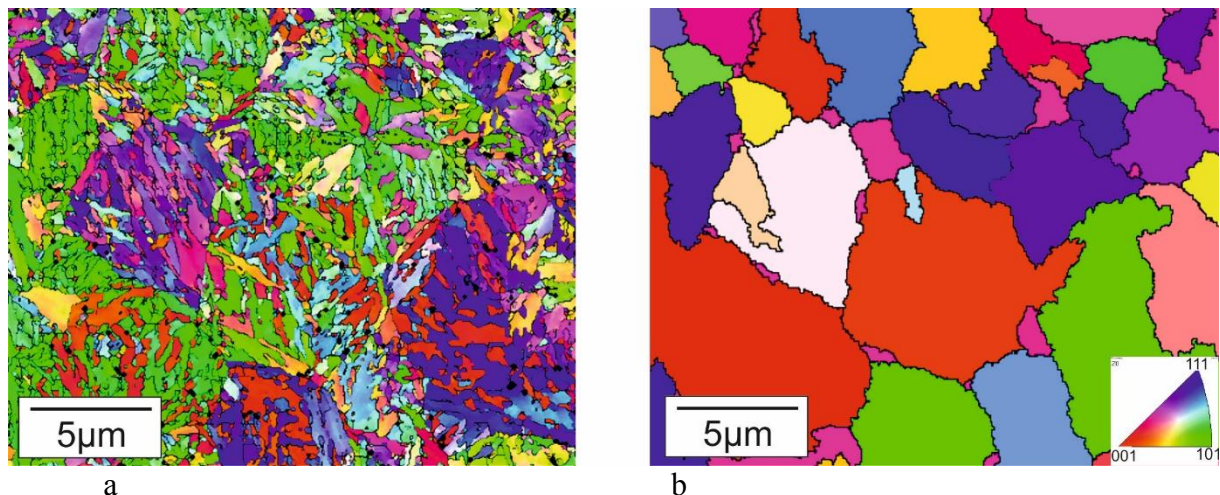


**Figure 1:** (a) EBSD orientation distribution of the martensitic steel 50CrMo4 steel, and (b) automated parent austenite grain reconstruction (inverse pole figure)

VHCF testing was carried out using both, an ultrasonic testing device type BOKU Vienna at  $f=20\text{kHz}$  in pulse-pause mode (100ms pulse followed by 900ms pause leading to an effective testing frequency of  $f=2\text{kHz}$ ), and a resonance testing machine type RUMUL Testronic operating at  $f=95\text{Hz}$  at a stress ratio of  $R=-1$  (fully reversed cycling). Shallow-notched, electropolished specimens were used to allow in-situ damage monitoring using digital microscopy (HIROX) and high-resolution thermography (Infratec Image IR 8380 hp, see Fig. 2a). Furthermore, fatigue damage was characterized by means of scanning electron microscopy in combination with focused ion beam milling (FIB) to gain in-depth information.

## RESULTS AND DISCUSSION

To understand the cyclic damage accumulation throughout millions of load reversals, load increase tests in combination with thermography monitoring were carried out. Cyclic plasticity is localized in Cr depletion bands, manifesting itself by bright areas in the thermogram as shown in the insert in Fig. 2a (cf. [8]). The temperature increase can be correlated with the onset of local plastic deformation, when the remote stress amplitude exceeds approximately  $\sigma_a=400\text{MPa}$  in the 37HRC tempering state. Compared to the results of the Wöhler S-N



experiments, the material's fatigue limit seems to be substantially higher, i.e.,  $\sigma_{FL} \approx 650\text{MPa}$  for testing at 20kHz and  $\sigma_{FL} \approx 480\text{MPa}$  for testing at 95Hz (see Fig. 3a).

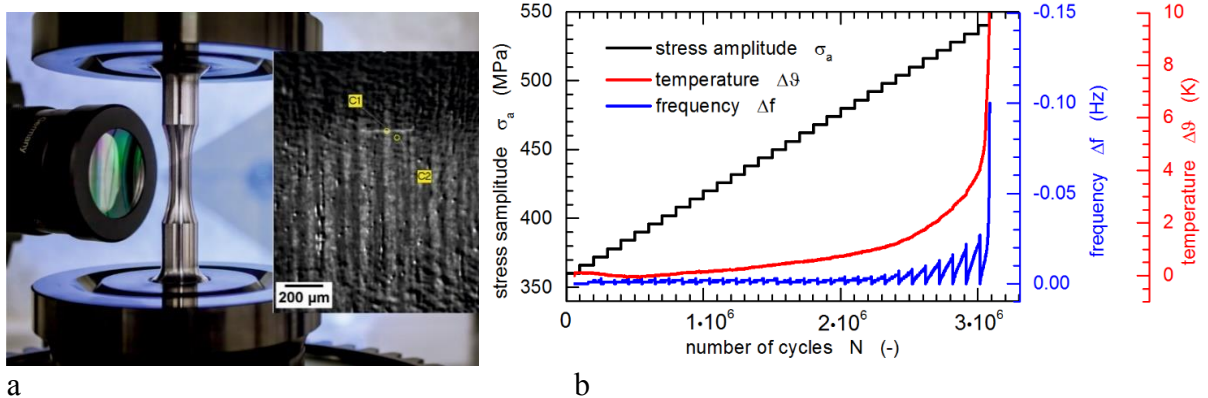


**Figure 2:** VHCF testing in combination with high-resolution thermography: (a) experimental setup and thermogram showing local plasticity as bright bands and the crack initiation (C1) as hot spot; (b) stepwise load increase test and respective specimen response plotted as the change in temperature and resonance frequency

This observation is attributed to a gradual decrease in cyclic plasticity as a consequence of strain hardening and in particular, the presence of microstructural barriers, such as prior austenite grain boundaries and martensite packet boundaries. The obvious frequency effect on the fatigue limit is probably due to the thermal activation of the Peierls energy barrier for plastic slip. While at low strain rates ( $d\varepsilon/dt \approx 0.5\text{s}^{-1}$ ,  $f=95\text{Hz}$ ) the critical shear stress  $\tau_{cr}$  is dominated by mutual interactions between dislocations, the Peierls barrier at high strain rates ( $d\varepsilon/dt \approx 100\text{s}^{-1}$ ,  $f=20\text{kHz}$ ) cannot be fully accommodated by thermal activation at room temperature. Therefore, high strain rates lead to a higher  $\tau_{cr}$  and a higher  $\sigma_{FL}$ , respectively (cf. [9]). Additional experiments to support this hypothesis are subject of ongoing work. In the case of the 37HRC tempering state, no failures were observed beyond  $10^7$  cycles. Therefore, a "real" fatigue limit can be postulated, although run-out samples ( $10^9$  cycles) show small shallow surface cracks (cf. Fig. 4a). However, in the case of the 57HRC tempering state, the same material (with respect to its chemical composition) exhibits a pronounced VHCF type II behavior, i.e., failures beyond  $10^7$  cycles and internal crack initiation at nonmetallic inclusions (cf. Fig. 5a).

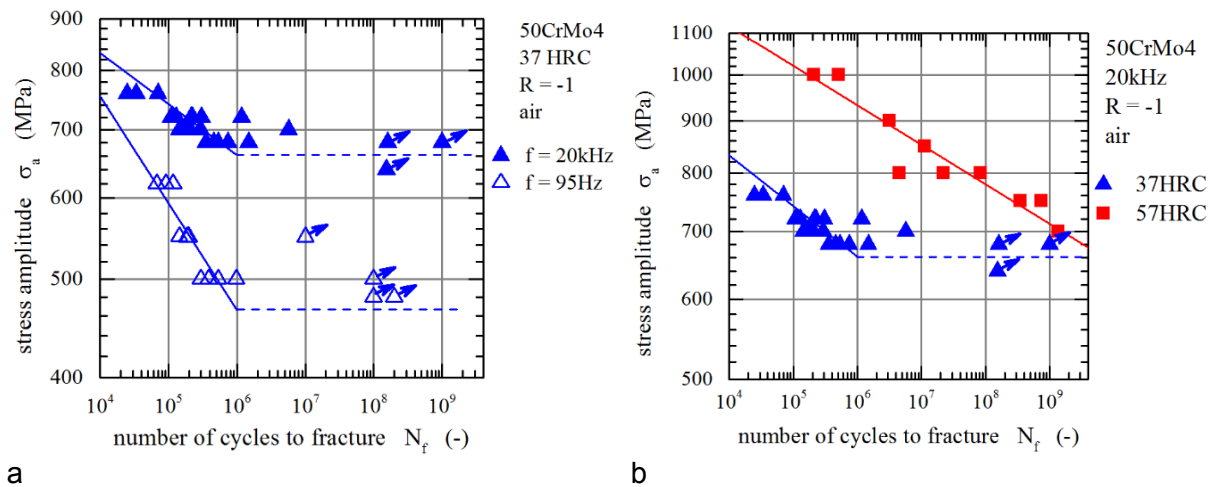


**Figure 3:** Wöhler S-N diagrams showing (a) the different behavior of 37HRC tempered 50CrMo4 steel at 20kHz and 95Hz testing frequency and (b) the different VHCF behavior of 50CrMo4 steel tempered to 37HRC and 55HRC

Fatigue damage sets in by the formation of protrusion bands (similar to slip bands) preferably between  $60^\circ$  misoriented martensite blocks in parallel to the  $\{111\}$  planes of the prior austenite grains (see Fig. 4a). By means of FIB milling perpendicular to the protrusion bands, it was shown that the bands form protrusions due to cyclic slip irreversibility leading to the initiation of microcracks (Fig. 4b).

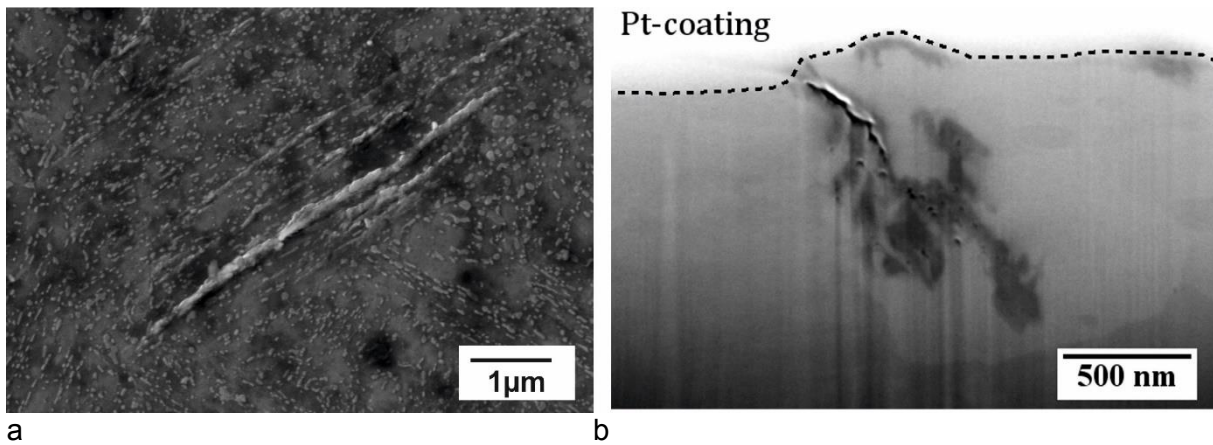


**Figure 4:** Protrusion band formation during VHCF of 50CrMo4 tempered steel (37HRC,  $\sigma_a=640\text{MPa}$ ,  $N=1.5 \cdot 10^8$ ): (a) protrusion bands aligned between martensite blocks (containing small Fe,Cr carbides) and (b) FIB cross section through a protrusion band containing a shallow microcrack

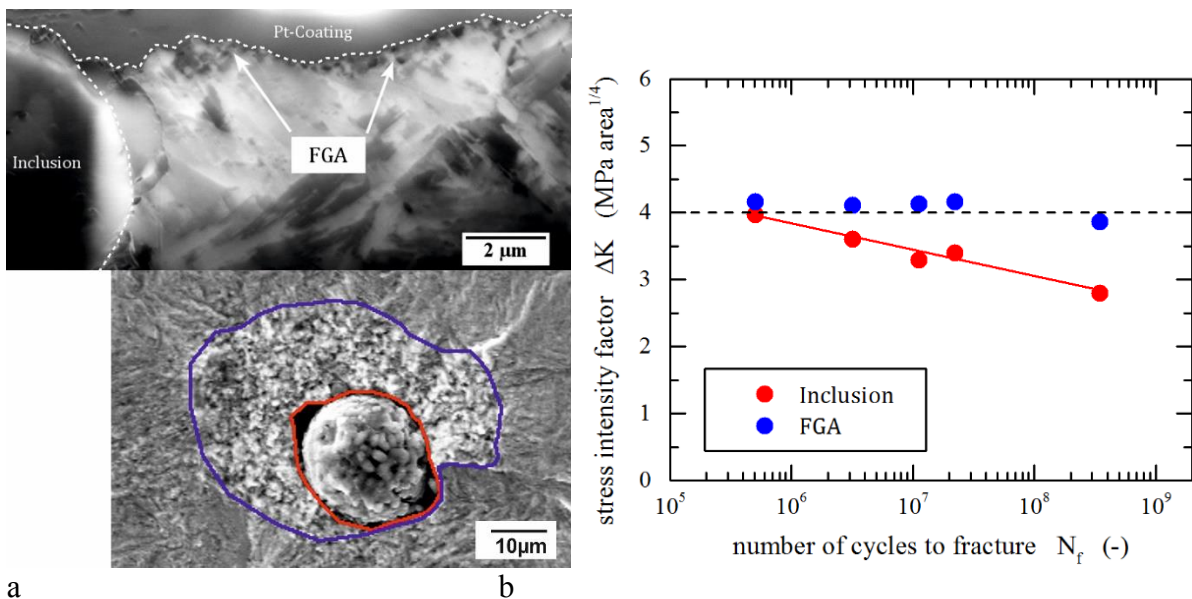


**Figure 5:** Internal VHCF crack initiation at an  $\text{Al}_2\text{O}_3$  inclusion: (a) top view and FIB cross section, and (b) calculated stress intensity factor range at the inclusion and at the respective FGA.

Contrary to that, crack initiation in the 57HRC state was found to occur internally at non-metallic inclusions. According to Fig. 5, a fine-granular area (FGA) was identified, which is attributed to plastic slip accumulation in the vicinity of the inclusion followed by polygonization (due to dislocation patterning). The local drastic reduction in grain size reduces the threshold stress intensity range for crack initiation  $\Delta K_{th, incl.}$ . Therefore, the crack initiation process is driven by the advance of the FGA. Only if the FGA size exceeds the critical length that is required for  $\Delta K > \Delta K_{th}$ , the conditions for initiation and growth of a macroscopic fatigue crack is fulfilled (cf.

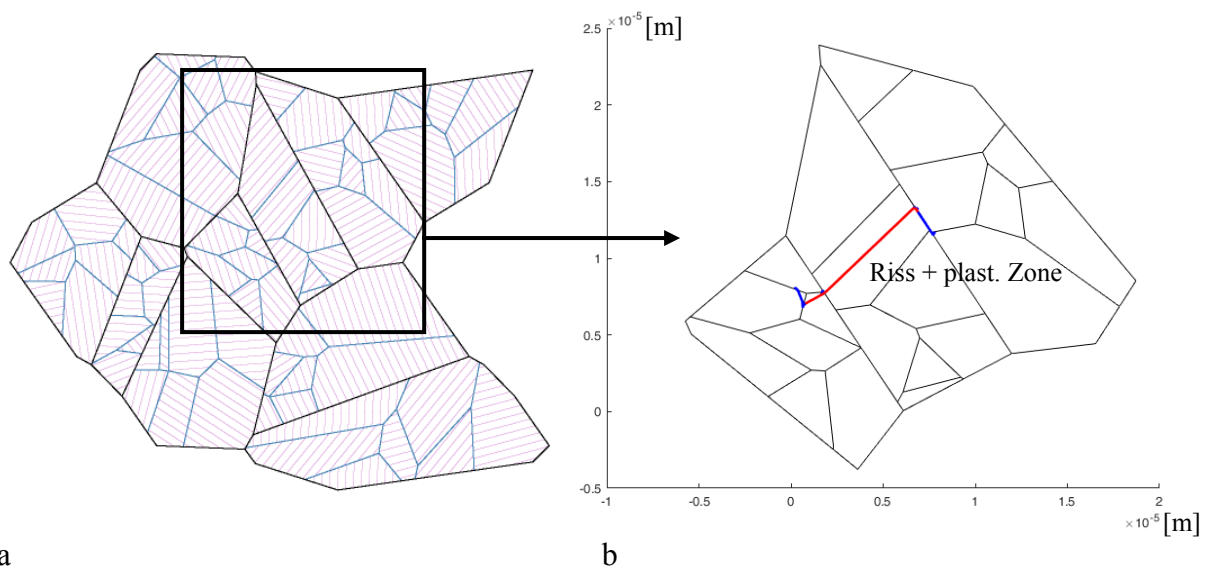


[6]). This concept is supported by the fact that for a given inclusion size the respective stress intensity factor decreases with decreasing remote stress amplitude, being generally below the threshold of  $\Delta K_{th} \approx 4 \text{ MPa m}^{-0.5}$  [10]. The gap between the actual stress intensity range at the inclusion and the macroscopic stress intensity range needs to be overcome by the formation of a FGA, which must be larger the smaller the applied stress amplitude is. This is in agreement with the experimental results presented in Fig. 5b.

The model development is based on the observation that cyclic plasticity is concentrated along protrusion bands between the martensite blocks. According to the above-mentioned hierarchical microstructure, EBSD data (Fig. 1) are extracted and transferred in a simplified arrangement of prior austenite grains, martensite packets and blocks (Fig. 6a). According to earlier work (cf. [11]), plastic slip between the martensite blocks is simulated by the boundary element method (BEM). Therefore, crack advance  $da/dN$  is correlated to the irreversible part (irreversibility factor  $\lambda$ ) of the shear displacement range  $\Delta CTSD$  at the crack tip.

$$\frac{da}{dN} = \lambda \cdot \Delta CTSD \quad (2)$$

An example is shown in Fig. 6b. The blocking effect of the prior austenite and the martensite packet boundaries is implemented by defining a source stress  $\tau_Q$  that needs to be overcome to spread plasticity from the crack-containing grain/packet to the neighboring grain/packet. Beside the microstructure data and  $\tau_Q$  the model requires the critical shear stress to drive dislocations along the protrusion bands  $\tau_c$ . Both, the critical stress and the source stress have been assessed by means of a Hall-Petch analysis, i.e., evaluating the cyclic 0.01%-yield strength ( $R_{p0.01 \text{ cyclic}}$ ) from incremental step tests (IST) as a function of the prior austenite grain size/martensite packet size, which was varied by high-temperature annealing for different durations (cf. [8]).



**a** **b**  
**Figure 6:** Modeling fatigue crack propagation in martensitic steel: (a) synthetic microstructure with prior austenite grains containing martensite packets with martensite blocks (aligned in parallel), (b) simulated microcrack propagation along martensite block boundaries.

## CONCLUSIONS

The VHCF behavior of 0.05C-1.0Cr-Mo martensitic steel was experimentally characterized by means of ultrasonic and resonance testing in combination with high-resolution thermography and scanning electron microscopy. The VHCF failure mechanisms depend strongly on the tempering condition: At 37HRC, only initiation of surface cracks is observed, which are efficiently blocked by microstructural obstacles below a critical stress level. Therefore, the existence of a "real"  $10^7$  cycles fatigue limit is supported. Contrary to that, the 57HRC tempering state leads to higher fatigue strength values that continuously decreases, even beyond  $10^9$  cycles. Above  $10^6$  cycles, the crack initiation site shifts from surface protrusion bands to non-metallic inclusions in combination with a fine granular area, the size of which was shown to depend on the applied stress amplitude. By combining linear elastic fracture mechanics with microstructural fracture mechanics using the boundary element approach, a quantitative evaluation and prediction of the VHCF failure process becomes accessible.

## ACKNOWLEDGEMENT

The financial support by the German Ministry of Education and Research (BMBF) and the Robert Bosch GmbH is gratefully acknowledged.

## REFERENCES

- [1] Z. Nishiyama, Martensite Transformation, Maruzen, Tokyo (1971).
- [2] H. Kitahara, R. Ueji, N. Tsuji, Y. Minamino, Acta Mater. 54 (2006) 1279.
- [3] Y. Murakami, M. Endo, Intl. J. Fatigue 16 (1994) 163.
- [4] U. Krupp, H. Knobbe, H.J. Christ, P. Köster, C.P. Fritzen, Intl. J. Fatigue 32 (2010) 914.
- [5] T. Sakai, JMMP 3 (2009) 425.
- [6] P. Grad, B. Reuscher, A. Brodyanski, M. Kopnarski, E. Kerscher, Scripta Mater. 67 (2012) 838.
- [7] C. Cayron, J. Appl. Cryst. 40 (2007) 1183.
- [8] U. Krupp, A. Giertler, K. Koschella, Engng Fract. Mech., submitted.
- [9] J. Bach, J.J. Möller, M. Göken, E. Bitzek, H.W. Höppel, Intl. J. Fatigue 93 (2016) 281.
- [10] K. Tanaka, Y. Akiniwa, Fat. Frac. Eng. Mat. Struct. 25 (2002) 775.
- [11] B. Künkler, O. Düber, P. Köster, U. Krupp, C.-P. Fritzen, H.-J. Christ, Engng Fract. Mech. 75 (2008) 715.

**Corresponding Author:** u.krupp@hs-osnabrueck.de

# A PHYSICALLY BASED CONSTITUTIVE EQUATION TO CHARACTERIZE S-N FATIGUE BEHAVIOR IN VERY HIGH CYCLE FATIGUE

K. S. Ravi Chandran

Department of Metallurgical Engineering, The University of Utah  
135 South 1460 East Rm. 412, Salt Lake City, UT 84112, USA  
Email: ravi.chandran@utah.edu

## ABSTRACT

A physically based constitutive equation to characterize the very-high-cycle fatigue (VHCF) behavior of structural materials has been formulated on the basis of the macroscopic descriptor of fatigue crack growth. The descriptor is that, at any time during fatigue, the normalized remaining fatigue life is proportional to the normalized remaining uncracked section size of the specimen. A simple functional has been found to express this relationship, universally, in many materials. Integration of this functional and the introduction of physical boundary conditions, leads to a compact constitutive equation for the stress-life (S-N) fatigue behavior. The S-N constitutive equation represents, quite accurately, a large number of HCF and VHCF fatigue data. In particular, the asymptotic approach of the fatigue data toward the physical endurance limit stress in VHCF is accurately characterized by the proposed S-N equation. The constitutive equation also validates the existence of the endurance limit stress in fatigue for homogeneous materials.

## KEYWORDS

S-N curve, constitutive equation, physical model, crack growth, endurance limit, asymptotic behavior, tensile strength, exponential function

## INTRODUCTION

Since Wöhler's first experiments on fatigue, empirical equations such as the Basquin equation or the Coffin-Manson equation has been used to characterize high cycle fatigue (HCF) and low-cycle fatigue (LCF) behavior. These equations generally are power functions of fatigue life. However, S-N fatigue data, when gathered over a very wide range of fatigue cycles, show the sigmoidal behavior with the ends asymptotically approaching the limiting stress values. This behavior cannot be represented by the power-function based empirical equations. The principal reason is the lack of physical models having the ability to accurately describe the fatigue behavior in HCF and VHCF domains. The situation is exacerbated by studies that the claim<sup>1,2</sup> that a low stress limit for infinite specimen survival may not exist, and that the S-N curve is to be expected to continue sloping down with a decrease in the fatigue stress amplitude. The objective of the present work is to show that a constitutive equation for S-N fatigue can be developed from the physical modeling of fatigue failure process. The S-N equation also supports the existence of a physical endurance limit stress in fatigue.

## THE CONSTITUTIVE EQUATION FOR S-N FATIGUE

The physical damage in fatigue begins with the formation of an incipient micro-crack from a persistent-slip-band (PSB), at cyclic stresses above the physical endurance stress limit. The cycles spent in the growth of this micro-crack, through the section of the specimen, is considered as the fatigue life,  $N_f$  at the cyclic stress amplitude. In our recent work<sup>3</sup> it was shown that, any time during fatigue, the normalized remaining fatigue life,  $(1-N/N_f)$ , is

proportional to the normalized remaining uncracked section size,  $(1-a/W)$ , of the fatigue specimen. This relationship was found to be universal and is expressed as

$$1 - \frac{a}{W} = \left(1 - \frac{N}{N_f}\right)^k \quad (1)$$

where  $k$  is the parameter characterizing the crack growth,  $a$  and  $W$  are the crack length and the specimen width, and  $N$  is the number of elapsed fatigue cycles corresponding to the crack length. This functional has been shown to represent the growth behavior of small and large fatigue cracks in many materials<sup>4</sup>.

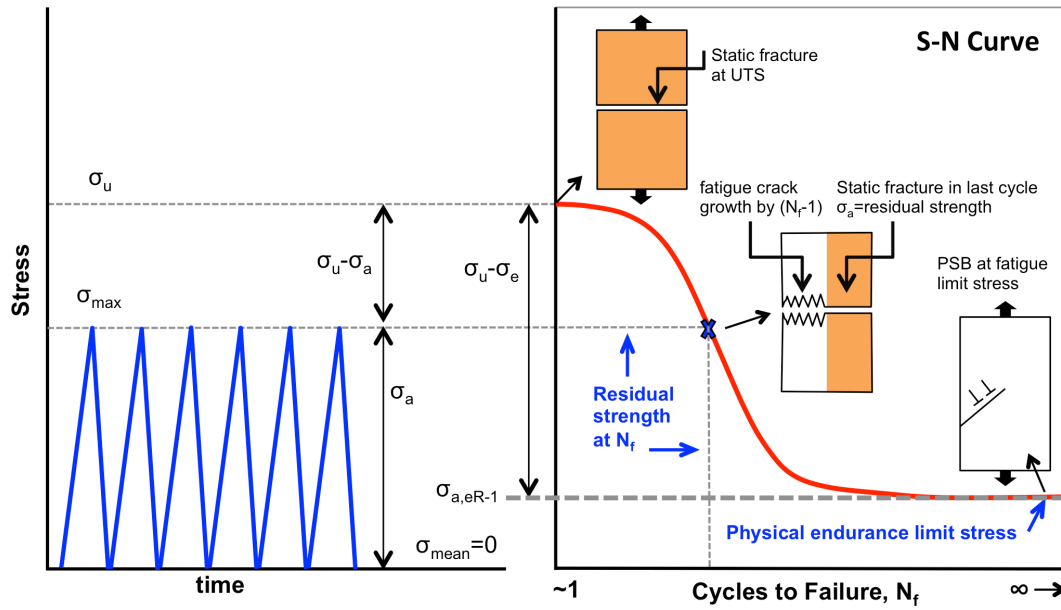


Figure 1. Schematic of the relationship between stress amplitude and fatigue life.

The macroscopic description of fatigue failure, as captured by the functional, can be understood with the help of Figure 1. At the highest possible stress amplitude ( $\sigma_a$ ), which is equal to the tensile strength ( $\sigma_u$ ), the specimen fracture occurs in approximately one cycle. At relatively lower stress amplitudes, but higher than the endurance limit stress ( $\sigma_e$ ), the fatigue fracture occurs by crack growth in  $(N_f-1)$  cycles. The final fracture of the specimen occurs monotonically when the level of stress amplitude reaches the tensile strength level of the remaining ligament. This situation occurs for all stress amplitudes in the range of  $\sigma_u > \sigma_a > \sigma_e$ .

In our previous work<sup>5</sup>, the growth of the micro-crack in fatigue was modeled as a continuous process of increase in cyclic strain energy on the uncracked ligament (net-section), which accelerates the crack growth process. It was then shown<sup>4</sup> that fatigue crack growth in uniformly-stressed fracture mechanics specimens can be expressed as

$$\frac{d\left(\frac{a}{W}\right)}{dN} = A \frac{\sigma_{ae}^\beta}{2E} \left[ \frac{a/W}{1-a/W} \right] \quad (2)$$

where  $A$  is the dimensionality parameter,  $\sigma_{ae}$  is the fatigue stress amplitude at the endurance limit,  $\beta$  is the stress exponent and  $E$  is the elastic modulus. Integration of Eq. (2) with the substitution of Eq. (1), and the imposition of the essential boundary conditions, resulted<sup>4</sup> in a compact constitutive equation for S-N fatigue behavior. The S-N constitutive equation is

$$\left(\frac{\sigma_a - \sigma_e}{\sigma_u - \sigma_e}\right) = \exp\left\{-C_n(N_f)^{m_n}\right\} \quad (3)$$

where  $\sigma_a$ ,  $\sigma_u$  and  $\sigma_e$  are fatigue stress amplitude, tensile strength and endurance limit stress, respectively. The important parameters of the S-N equation are  $C_n$  and  $m_n$  (which characterize the sigmoidal shape of the S-N curve) and the physical boundary conditions,  $\sigma_u$  and  $\sigma_e$  (which determine the asymptotic behavior of the S-N curve at the ends). Equation (1) is the constitutive equation for S-N fatigue behavior at the stress ratio,  $R=0$ .

It is to be noted that the fatigue endurance limit,  $\sigma_e$ , used in Eq. 3 refers to the *physical endurance limit stress*, which either corresponds to the critical stress for slip initiation or to the threshold stress for the growth of a small crack. The common cycle-based definition (that is picking the fatigue strength at  $10^7$  or  $10^8$  cycles) is arbitrary and has no physical basis. Also, the cycles to failure is not an independent variable and a limit definition based on this is not consistent.

Material [Data Ref.]	Test Condition	$\sigma_u^*$ (MPa)	$\sigma_e$ (MPa)	$C_n$	$m_n$
PWA1480 single Xtal [6]	RT/5Hz/Axial/R=-1	280	1237	0.03	0.37
UFG Cu [7]	RT/1Hz-20KHz/Axial/R=-1	387	130	0.05	0.23
Poly Cu [8]	RT/20KHz/Axial/R=-1	230	95	0.015	0.31
A517 Steel [9]	RT/50Hz/Bend/R=-1	820	420	0.0005	0.62
SAE 4130 Steel [10]	RT/30Hz/Axial/R=-1	860	345	0.07	0.3
Cast 319 Al Alloy [11]	RT/40Hz-20KHz/Axial/R=-1	166	38	0.038	0.29
75S-T6 Al Alloy [12]	RT/30Hz/Axial/R=-1	573	123	0.015	0.4
CP Titanium [13]	RT/5-120Hz/Axial/R=-1	460	250	0.002	0.75
Ti-6Al-4V Alloy-1 [13]	RT/5-120HzAxial/R=-1	912	480	0.035	0.33
Ti-6Al-4V Alloy-2 [13]	RT/120Hz/Axial/R=-1	1068	560	0.058	0.29
Rene 88DT Ni Alloy [14]	RT/10Hz-20KHz/Axial/R=-1	1450	560	0.002	0.45
Udimet 500 Ni Alloy [2]	RT/20-20 KHz/Axial/R=-1	968	200	0.17	0.14

\* Average tensile strength; RT=room temperature

Table I. Parameters used for the prediction of S-N Curve

## EXPERIMENTAL VALIDATION

The predicted S-N curves from Eq. (3) are shown in Figures 2 through 4 for various materials including Ni-base alloy single crystals (Figure 2a), pure Cu (Figure 2b), aluminum alloys (Figure 3a) steels (Figure 3b), titanium alloys (Figure 4a) and polycrystalline Ni-base alloys (Figure 4b), along with the respective experimental data. The data are mostly the fatigue data from smooth specimens loaded axially in fully-reversed cycling, with many tests run into VHCF regime. In order to verify the asymptotic behavior of the S-N fatigue curve and the data at the extremes of fatigue life, only high quality S-N data, generated over a wide range of fatigue cycles, are used here. The predicted S-N curves in the figures were generated using Eq. (3) and using the parameters given in Table I.

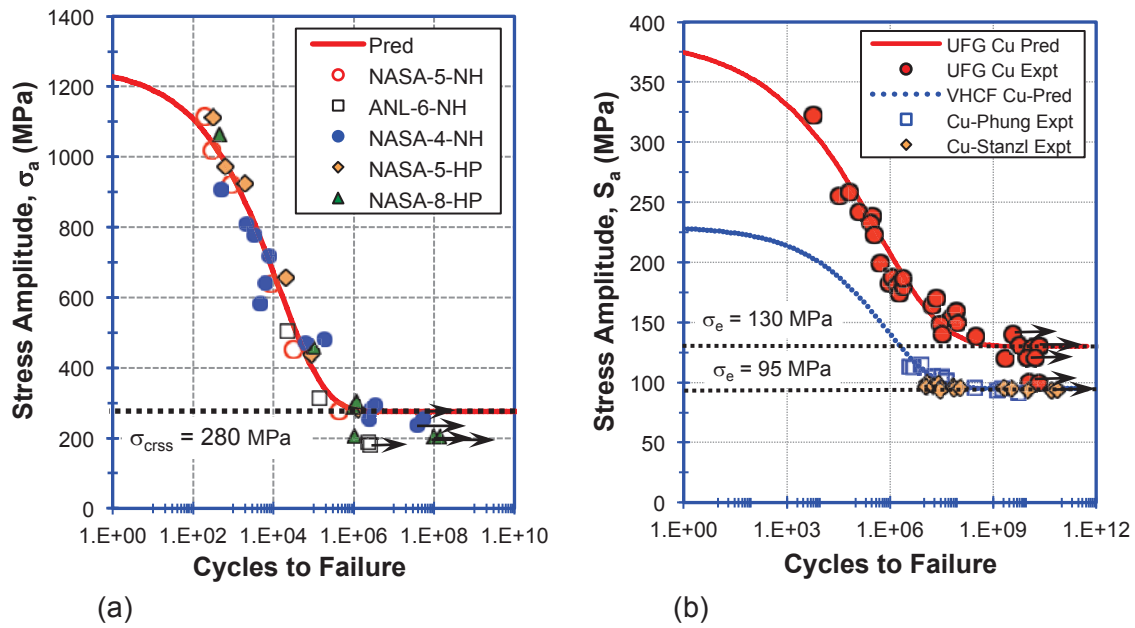


Figure 2. Predicted S-N curves compared with the fatigue data of (a) PWA1480 superalloy single crystal and (b) ultrafine grained copper and polycrystalline Cu tested in VHCF regime.

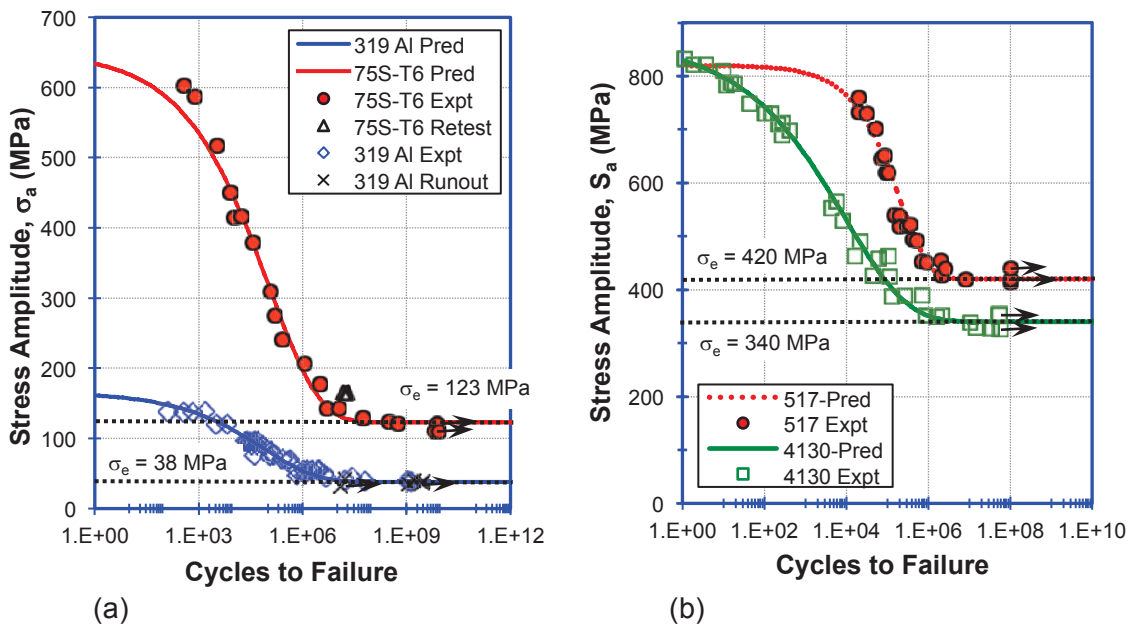


Figure 3. Predicted S-N curves compared with the fatigue data of (a) cast and wrought aluminum alloys and (b) high strength steels.

It can be seen that the S-N curves predicted using Eq. (3) are in very good agreement with the experimental S-N data. Actually, the experimental data in Figures 2-4 show the asymptotic behavior of fatigue life at long lives, especially in the so-called VHCF regime. It is also evident that fatigue data with failure cycles  $>10^7$  are necessary to see the entire S-N behavior, especially the extent of VHCF regime. The present equation also validates the asymptotic nature of fatigue life near the endurance limit—the exponential function (in Eq. 3) approaches zero as  $N_f$  approaches infinity. This means that the stress amplitude,  $\sigma_a$ , is equal to the endurance limit,  $\sigma_e$ , only when  $N_f$  is infinite. This behavior indicates that there is a low

stress limit for infinite specimen survival. Physically, the endurance limit stress is equivalent to the critical resolved shear stress for slip initiation in single crystals or the threshold condition for the propagation of small fatigue cracks in polycrystals. Hence, the asymptotic nature the S-N equation at long fatigue lives is strongly in favor of the existence of a finite endurance stress limit below which fatigue failures will not occur.

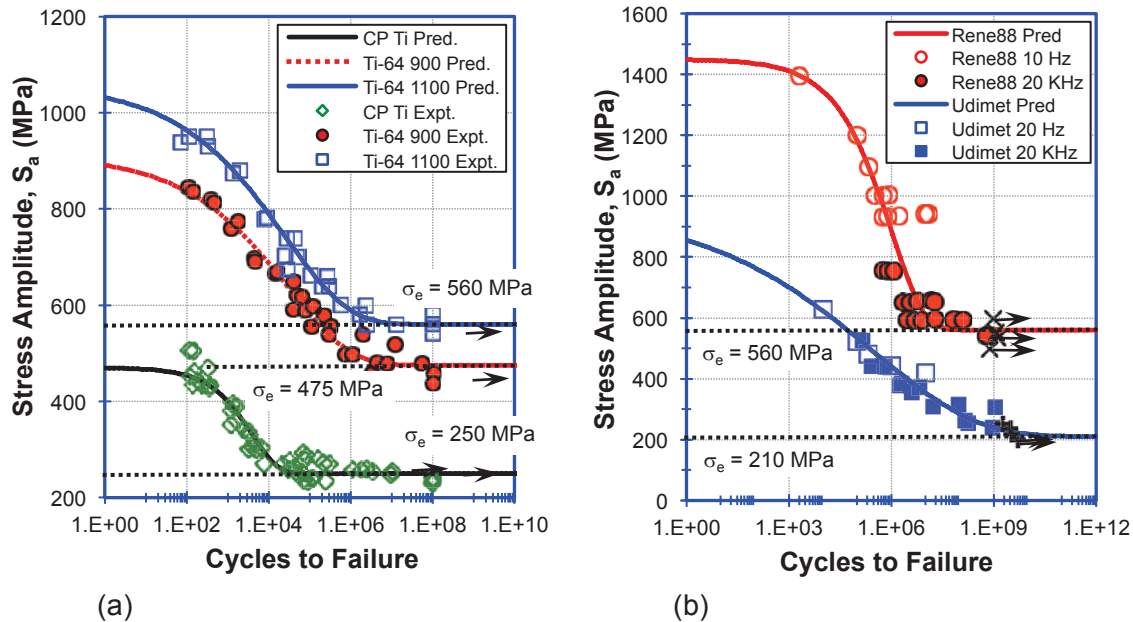


Figure 4. Predicted S-N curves compared with the fatigue data of (a) CP-Ti and Ti-6Al-4V alloys of different tensile strength and (b) polycrystalline Ni-base alloys in VHCF regime.

The present work may help to clarify some confusion about the existence of endurance limit in fatigue below which a specimen may have infinite life. It has recently been suggested<sup>1,2</sup>, based on observation of fatigue failures at  $10^7$ - $10^9$  cycles, that there is no endurance limit in fatigue. This study reported S-N data up to  $10^{10}$  cycles, generated by ultrasonic fatigue testing, with the trends in S-N data depicted as straight lines. It was suggested, probably from the lack of an asymptotic trend in the data at long life, that there is no infinite fatigue life and that fatigue limit, as a material property, does not exist. In light of the present work, this deduction appears to be erroneous. First, the lack of any asymptotic region would suggest that perhaps S-N testing was not done for sufficiently large number of cycles. Secondly, it cannot be argued that the experimental failure life would follow along the downward sloping straight line, as the stress amplitude of fatigue testing is reduced. Such an assumption will lead to intersection of the S-N data with the abscissa at some finite cycles, suggesting finite fatigue life at zero stress, which is not possible.

Materials containing a statistical distribution of defects or having inhomogeneous microstructures may not show the endurance limit condition or the asymptotic nature of the S-N curve at very long fatigue lives (some examples can be found elsewhere<sup>15</sup>). This is because the crack-initiating defect size, in inhomogeneous materials, is a statistical variable between the samples leading to highly variable fatigue failure lives even when a very large number of tests are repeated at the notional endurance limit stress. The principal reason is that identical specimens cannot be produced from inhomogeneous materials to reliably test for the existence of endurance limit stress--each specimen will have its own limit! For such materials, efforts to assess whether there exists a fatigue endurance limit will not be fruitful. However, most commercial materials including that shown in Figure 2-4 are homogenous

enough to produce tight S-N data sets over a wide range of cycles, including the asymptotic trends in the VHCF regime. For each of such materials, it seems that fatigue endurance stress limit, as a unique material property, exists.

## CONCLUSIONS

A physically based constitutive equation for predicting the stress-life (S-N) behavior in fatigue of materials has been developed. The constitutive equation describes quite accurately a large number of S-N fatigue data over a wide range of failure cycles, including the VHCF regime. The equation also exhibits the correct asymptotic end limits, that is, tending to ultimate tensile strength of uncracked specimen at zero fatigue cycle and to physical endurance limit stress at infinite failure cycles. It is also shown that the constitutive equation faithfully reproduces of asymptotic trends in S-N data, including the asymptotic approach of the data toward a physical endurance limit stress.

## REFERENCES

- <sup>1</sup> C. Bathias, L. Drouillac and P. Le Francois. How and why the fatigue S–N curve does not approach a horizontal asymptote. *Int. J. Fat.* 23 (2001) 143-151.
- <sup>2</sup> C. Bathias, There is no infinite fatigue life in metallic materials. *Fat. Fract. Eng. Mater. Struct.* 22 (1999) 559-566.
- <sup>3</sup> K. S. Ravi Chandran. A physically based universal functional to characterize the mechanism of fatigue crack growth in materials. *Scr. Mater.* 107 (2015) 115-118.
- <sup>4</sup> K. S. Ravi Chandran, A physical model and constitutive equations for complete characterization of SN fatigue behavior of metals. *Acta. Mater.* 121 (2016) 85-103.
- <sup>5</sup> K. S. Ravi Chandran, F. Cao and J. C. Newman, Jr. Fatigue crack growth in miniature specimens: The equivalence of  $\Delta K$ -correlation and that based on the change in net-section strain energy density. *Scr. Mater.* 122 (2016): 18-21
- <sup>6</sup> S. Kalluri and M. A. McGaw, Effect of tensile mean stress on fatigue behavior of single crystal and directionally solidified superalloys. NASA Technical Memorandum 103644, Lewis Research Center, Cleveland, OH, USA, pp. 1-15
- <sup>7</sup> L. Kunz. Mechanical properties of copper processed by severe plastic deformation. INTECH Open Access Publisher, 2012.
- <sup>8</sup> N-L. Phung, V. Favier, N. Ranc, F. Vales, and H. Mughrabi. Very high cycle fatigue of copper: Evolution, morphology and locations of surface slip markings. *Int. J. Fat.* 63 (2014) 68-77.
- <sup>9</sup> N. E. Dowling, Introduction and stress based approach. Ch. 9, *Mechanical Behavior of Materials*. Fourth Edition, Chapter 9, 2013, p. 404,
- <sup>10</sup> W. Illg, Fatigue tests on notched and un-notched sheet specimens of 2024-T3 and 7075-T6 aluminum alloys and of SAE 4130 Steel. NACA Technical Note 3866, National Advisory Committee for Aeronautics, Washington, DC 1956.
- <sup>11</sup> M. J. Caton, J. W. Jones, H. Mayer, S. Stanzl-Tschegg, and J. E. Allison, Demonstration of an endurance limit in cast 319 aluminum. *Metall. Mater. Trans.* 34A (2003) 33-41
- <sup>12</sup> T. T. Oberg. When Will It Fail?. *Met. Prog.* 60 (1951) 74-75.
- <sup>13</sup> NIMS Fatigue Data Sheets 95, 101, 103, National Institute of Materials Science, Japan, 2004
- <sup>14</sup> J. Miao, T. M. Pollock, and J. W. Jones. Very high cycle fatigue behavior of nickel-based superalloy René 88DT at 593 C. In VHCF-4, Michigan, USA. 2007, p. 445
- <sup>15</sup> B. Pyttel, D. Schwerdt, and C. Berger. Very high cycle fatigue—Is there a fatigue limit? *Int. J. Fat.* 33 (2011) 49-58.



# CHARACTERIZATION OF CRACK INITIATION AND CRACK GROWTH IN THE VHCF REGIME ON THE BASIS OF NONLINEAR MATERIAL BEHAVIOUR IN COMPARISON TO OPTICAL INVESTIGATIONS FOR TWO ALUMINUM ALLOYS

T. Kirsten<sup>1)</sup>, F. Bülbül<sup>2)</sup>, T. Stein<sup>3)</sup>, M. Wicke<sup>3)</sup>, H.-J. Christ<sup>2)</sup>, A. Brückner-Foit<sup>3)</sup>, M. Zimmermann<sup>1)</sup>

<sup>1)</sup> Institut für Werkstoffwissenschaft, Technische Universität Dresden, 01069 Dresden, Germany

<sup>2)</sup> Institut für Werkstofftechnik, Universität Siegen, 57068 Siegen, Germany

<sup>3)</sup> Institut für Werkstofftechnik, Universität Kassel, 34125 Kassel, Germany

## ABSTRACT

In the present contribution it was investigated to what extent the so-called nonlinearity parameter correlates with the crack propagation in case of very low load amplitudes. Tests were carried out by means of an ultrasonic fatigue testing machine with a resonant frequency of approximately 20 kHz at VHCF-relevant stress levels on two different aluminium alloys, the precipitation-hardening alloy EN AW 6082 and the work-hardening alloy EN AW 5083. Besides the analysis of the nonlinear material behaviour the crack initiation and crack growth at the sample surface were optically recorded with a long-distance microscope. During the in-situ investigation a change in crack growth velocity can be detected. It is assumed that the barrier function of grain boundaries and primary precipitations are the major reason for crack growth retardation despite the fact that the crack is in long crack growth regime. Preliminary results of ongoing investigations could show that this effect of crack growth retardation is reflected in the nonlinearity parameter signal.

## KEYWORDS

Aluminium alloys, crack initiation, crack propagation, nonlinear material behaviour, very high cycle fatigue, ultrasonic fatigue testing

## INTRODUCTION

In previous studies the fatigue crack growth behaviour of metallic materials at low stress amplitudes and therefore high number of load cycles  $N > 10^7$  (very high cycle fatigue – VHCF) was thoroughly investigated. It has been shown that cracks can propagate even below the classical fatigue limit. To investigate the fatigue crack growth under VHCF relevant stress amplitudes high frequency testing equipment such as ultrasonic fatigue testing becomes essential. It allows the examination of long fatigue crack growth at a testing frequency of about 20 kHz. The experiments in this study are based on two aluminium alloys, a precipitation-hardening and a work-hardening one. The aim of the study is to characterize the early and slow fatigue crack propagation in the threshold regime in order to gain insight into the barrier function of microstructural inhomogeneities such as large precipitations or grain boundaries.

Previous studies could show that the crack initiation site for aluminium alloys can move to the subsurface region in the VHCF regime [1]. Therefore, it is less likely to detect the crack initiation and the early crack growth by optical means. Alternative possibilities, such as the

alternate current potential drop system often involve extensive efforts to calibrate the measuring data. A method, which is rarely used concerning fatigue crack growth monitoring, is the acquisition and analysis of the nonlinear material behaviour. It was primarily applied for an ultrasonic fatigue testing system by Kumar et al. [2]. The nonlinear material behaviour is described by the so-called nonlinearity parameter, which is defined by equation (1) with  $c$  denominating the propagation velocity of the ultrasonic wave,  $\omega_0$  the angular frequency of the vibration,  $x$  the distance of propagation and  $a_1$  and  $a_2$  the amplitudes of the first and second harmonics. A detailed description of the nonlinear material behaviour can be found in [3].

$$\beta = \frac{8c^2 \cdot a_2}{\omega_0^2 \cdot x \cdot a_1^2} \quad (1)$$

The ultrasonic fatigue test is based on a longitudinal, sinusoidal ultrasonic wave, which is induced in the sample and reflected at its end. The generated feedback signal is recorded by an inductive displacement transducer. The control unit of the testing system registers the signal directly in form of the nonlinearity parameter. This is based on the principle that a damage caused by cyclic loading can be reflected in the ratio of the higher harmonics. The relative nonlinearity parameter, which can be used as damage indicator after Kumar et al. [4], is calculated with equation (2).

$$\beta_{rel} = \beta - \beta_0 = (A_2 - 2A_1) - (A_2 - 2A_1)_0 \quad (2)$$

Here it is only necessary to record the amplitudes of the fundamental frequency  $A_1$  and the second harmonic  $A_2$  for the damaged and undamaged (initial state) condition.  $\beta_0$  is determined during the first few pulses. While  $A_1$  at around 20 kHz remains unchanged, the second harmonic is very sensitive towards microstructural changes during the test. So the damage caused by fatigue should be detectable by  $\beta_{rel}$  [5]. If it is applicable for aluminium alloys as well was the major purpose of the study presented. In previous studies the nonlinearity parameter was mainly used to distinguish between crack initiation and crack growth phase. The focus on this study was laid on the characterization of the fatigue crack growth and the correlation of  $\beta_{rel}$  and the crack length.

## SPECIMEN, MATERIAL AND TESTING

### Material

In this study the aluminium alloys EN AW 6082 and EN AW 5083 were investigated. Table 1 contains the chemical composition for both alloys.

EN AW 6082 is a precipitation-hardening alloy, whose microstructure is defined by a rolling texture with elongated grains of a length of  $\sim 300 \mu\text{m}$  and a width of  $\sim 50 \mu\text{m}$ . The material is characterized by primary ( $\text{Mg}_2\text{Si}$ ,  $\text{Al}(\text{Si}, \text{Mn}, \text{Fe})$ ) and secondary ( $\text{Mg}_2\text{Si}$ ) precipitations (see Fig. 1a). The alloy was investigated in peak-aged (pa) and overaged (oa) condition. The heat treatment is given in Fig. 1b.

EN AW 5083 is a work hardening alloy, which was investigated in the soft-annealed condition with nearly globular grains (around  $40\text{-}50 \mu\text{m}$ ). The microstructure is defined by the primary precipitations of type  $\text{Mg}_2\text{Si}$  and  $\text{Al}_6(\text{Mn}, \text{Fe})$ , see Fig. 1c.

	Mg	Mn	Si	Fe	Zn	Cu	Cr	Ti	Al
EN AW 6082	0,6-1,2	0,4-1,0	0,7-1,3	0,5	0,2	0,1	0,25	0,1	Bal.
EN AW 5083	4-4,49	0,4-1,0	0,4	0,4	0,25	0,1	0,05-0,25	0,15	Bal.

**Table 1:** Chemical composition (in weight %) of the investigated materials according to Bikar-Aluminium (EN AW 6082) and Hydro (EN AW 5083)

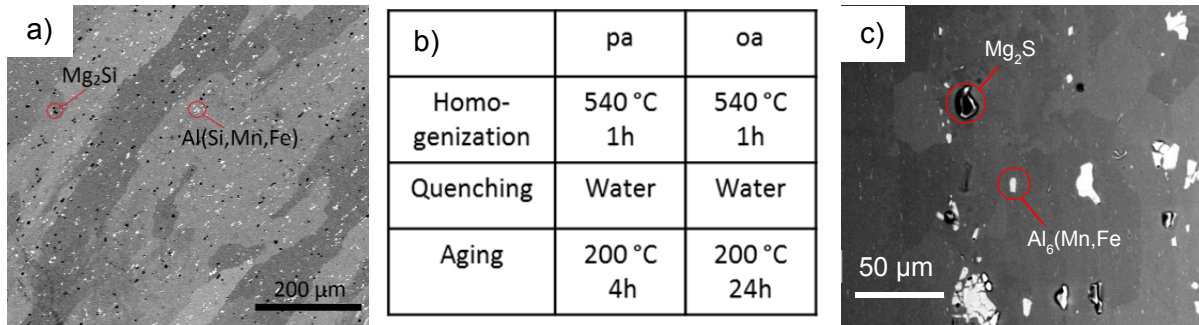


Fig. 1: a) Microstructure with primary precipitations of alloy EN AW 6082 b) precipitation hardening heat treatment and c) microstructure of alloy EN AW 5083.

## Testing

The tests were performed at an ultrasonic fatigue testing system with a resonance frequency of 20 kHz and a load ratio of  $R = -1$ . In front of the ultrasonic fatigue testing system is a long-distance microscope, which has a maximum magnification of 750x and was provided by the workgroup of Prof. Brückner-Foitz from the University of Kassel. The testing area can be seen in Fig. 2a. The samples are hour-glass shaped with a shallow notch in the middle (see Fig. 2b). Furthermore, there was a micro notch inserted on the ground of the shallow notch by means of focused ion beam technology. It acts as a definite crack initiation site for optical crack growth investigations (see Fig. 2c).

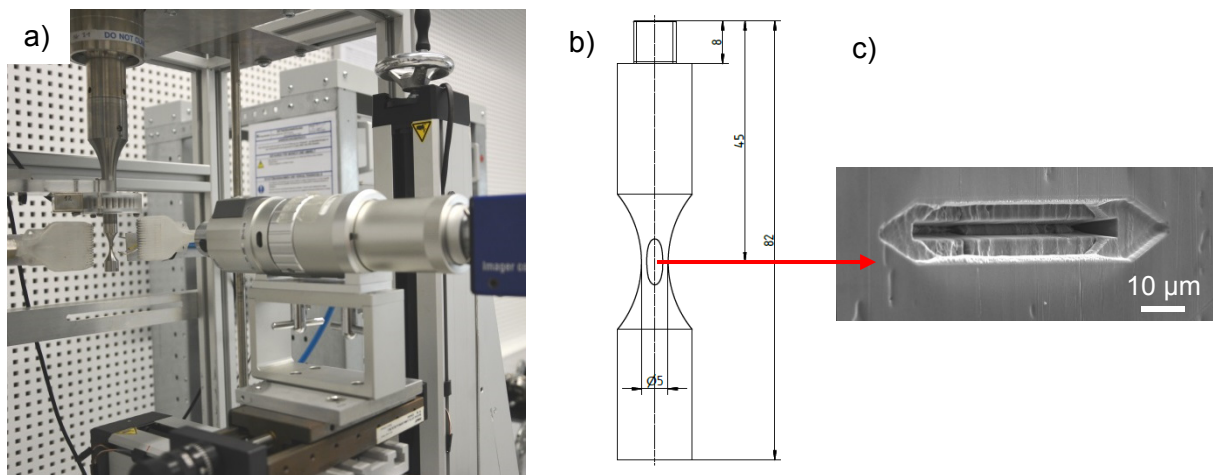


Fig. 2: a) Ultrasonic fatigue testing system (BOKU Vienna) with long-distance microscope in front (Hirox) b) sample geometry with shallow notch and c) FIB notch.

## EXPERIMENTAL RESULTS

Preliminary tests were executed in order to prove if the nonlinearity parameter is suitable to detect the early crack initiation. Fig. 3 shows the nonlinearity parameter at the beginning of the test for the three investigated material conditions. All tests were carried out with samples containing a FIB-notch. The tests were stopped manually when a crack could be seen through the long-distance microscope. For alloy EN AW 6082 there is no significant change of the nonlinearity parameter detectable until break-off. Nevertheless, a crack could easily be detected for both heat treatment conditions for EN AW 6082 with the microscope. According to the literature  $\beta_{rel}$  should be sensitive enough regarding the crack initiation and growth, like Mayer et al. confirmed for the aluminium alloy EN AW 2024-T351[6]. A comparison of the present results to the ones of Mayer et al can be found in [7]. Kumar et al. [3] determined that

the detection of the crack initiation can be difficult because of the variation range of  $\beta_{rel}$  throughout the test. Therefore the use of a  $\lambda$ -rod is recommended. In case of alloy EN AW 6082 the course of  $\beta_{rel}$  is quite stable even without a  $\lambda$ -rod. Until the break-off the variation is only  $\pm 0.03$  dB. Based only on the nonlinear material behaviour it is not possible to detect the crack initiation in these cases.

In contrast, the nonlinearity parameter for alloy EN AW 5083 shows a more distinct change in its course, while the variation range is again quite constant. There is a significant change of 0.25 dB observable right from the beginning of the test. At this point of the test it is not certain, if the decrease of  $\beta_{rel}$  is truly a result of the advancing crack. Another reason could be the hardening of the material during the first load cycles as was observed by Schneider et al. [8] for this alloy. Based on these results one can conclude that a conclusive monitoring of the nonlinear material behaviour regarding the crack initiation and early crack growth depends on the material tested. For alloy 6082 the crack initiation could not be detected, whereas EN AW 5083 shows a change in its nonlinear material behaviour during crack initiation in the VHCF regime.

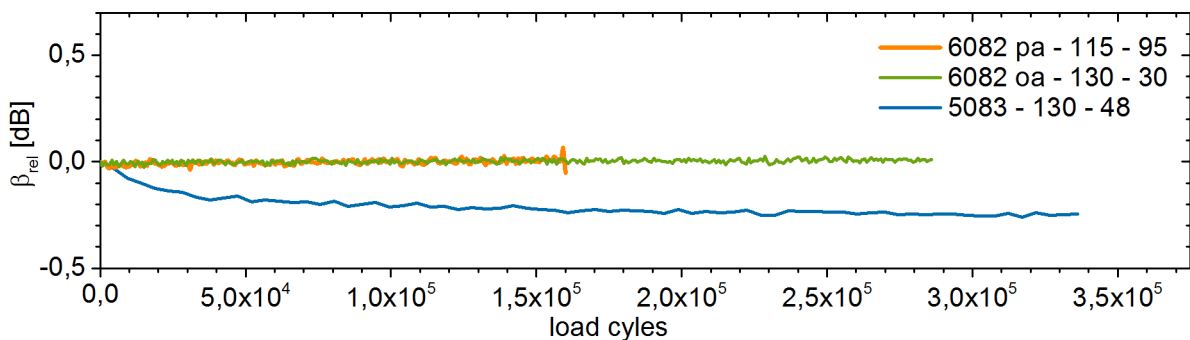


Fig. 3: Nonlinearity parameter at the beginning of the test until manual break-off (nomenclature: alloy - stress amplitude in MPa - crack length at break off in  $\mu\text{m}$ )

In a second step, the focus was on the correlation between nonlinearity parameter and crack growth. Fig. 4 depicts the  $\beta$ -parameter and the crack length as function of the load cycles for the two different alloys, with alloy EN AW 6082 being tested in the peak-aged condition only. Both experiments were investigated under constant stress intensity factor  $\Delta K$ , which was realised by decreasing the stress amplitude accordingly. Kumar et al. [9] and Li et al. [10] already mentioned the dependency of the nonlinearity parameter on the stress amplitude. But the difference of the amplitudes  $A_2 - 2A_1$ , which  $\beta_{rel}$  is based on, should be independent of the stress amplitude assuming the material and experimental conditions remain constant.

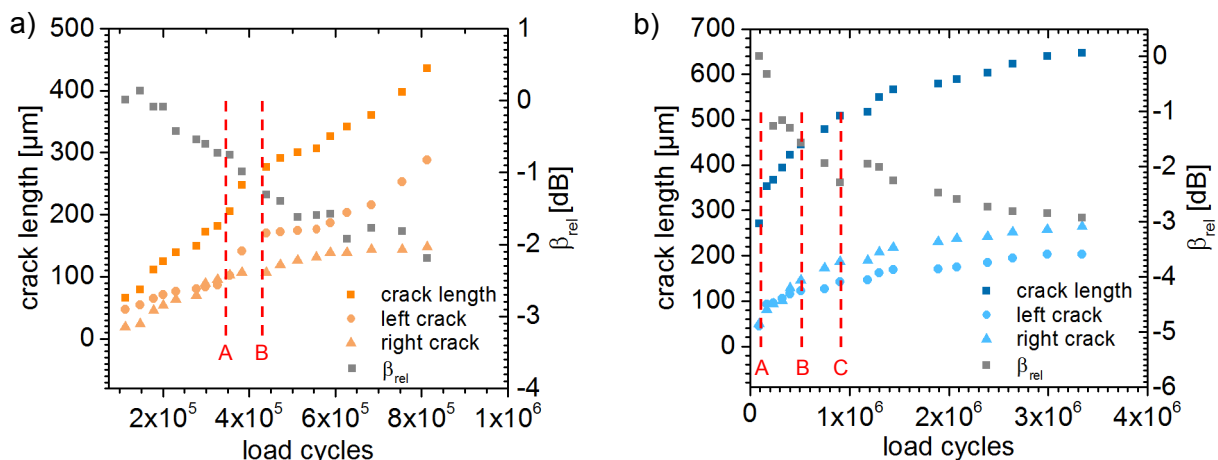
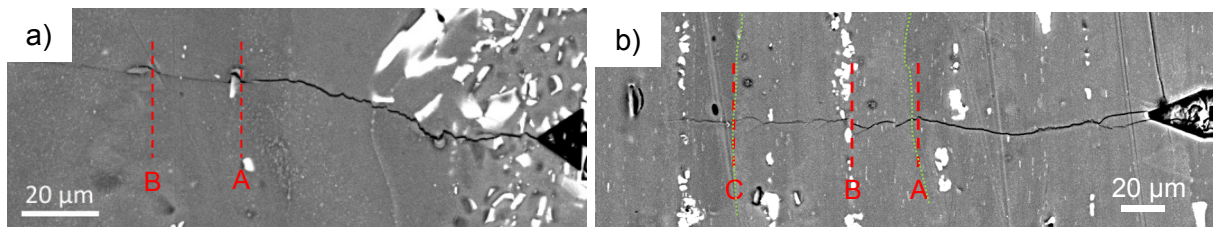


Fig. 4: Fatigue crack growth experiments with constant  $\Delta K$  a) EN AW 6082 pa ( $\Delta K = 1.45 \text{ MPa}\sqrt{\text{m}}$ ) b) EN AW 5083 ( $\Delta K = 1.7 \text{ MPa}\sqrt{\text{m}}$ ).

Fig. 4a contains the results for alloy EN AW 6082 in peak-aged condition. The crack length increases continuously during the test. Similar changes can be observed with a continuously decreasing nonlinearity parameter. This proves that the nonlinearity parameter is a function of the crack length. Comparable results can be observed for alloy EN AW 5083 (Fig. 4b). Here the crack growth velocity remains not constant over the entire test. During the first  $1 \cdot 10^6$  cycles the crack growth rate is around  $10^{-10}$  m/cycles and decreases to  $10^{-11}$  m/cycles at the end of the test. This change is mirrored by the course of the nonlinearity parameter as well. After  $1 \cdot 10^6$  cycles the decrease of  $\beta_{rel}$  is slower.

For some distinctive points in the curves depicted in Fig 4, there is a significant change in the crack growth rate between these points observable, especially when differentiating between left and right side of the crack (left and right side of the micro notch respectively). This can be attributed to the microstructure, as can be seen in Fig. 5. When the crack growth rate decreases, it is in most of the cases caused by primary precipitates or grain boundaries. But it seems that the grain boundaries do not play such an important role for alloy EN AW 6082. In this alloy, crack growth retardation is mainly caused by the ferritic precipitations. Contrarily, in alloy EN AW 5083 grain boundaries can also act as a microstructural barrier.



**Fig. 5:** SEM images of the samples used for the curves depicted in Figure 4 with correlation of crack length to microstructure; a) left crack of Figure 4a; b) left crack of Figure 4b (grain boundaries schematically in green)

Fig. 6 shows the course of the nonlinearity parameter versus the crack length for the tested material conditions. A linear correlation between the two parameters can be seen in all cases, but the slopes are changing, especially between the two different heat treatment conditions of alloy EN AW 6082. The overaged samples exhibit a sharper decrease than the peak-aged ones. The slope of alloy EN AW 5083 is similar to the peak-aged condition. An influence of the test routine can be excluded, because it was left unchanged within the measuring of the data depicted as open or closed symbols. The crack growth rates were in the same range of  $10^{-10}$  m/cycles as well. As a result the different slopes have to be caused by the material condition. A quantitative study is not possible at this state. A possible reason for the different behaviour could be a difference in the plastic zone at the crack tip. Present studies will have to clarify this matter.

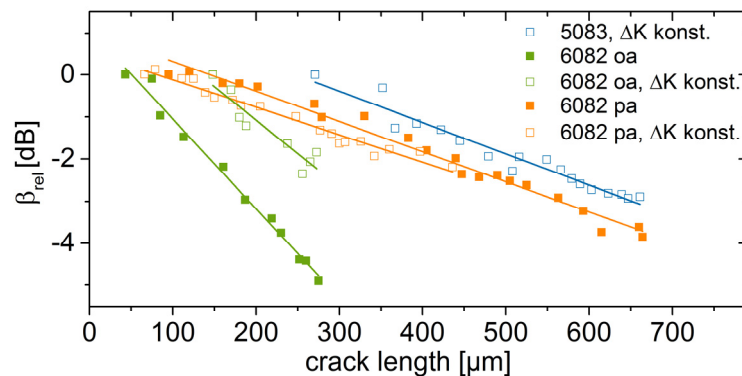


**Fig. 6:** Nonlinearity parameter versus crack length for various material conditions for crack growth rates in the range of  $da/dN \sim 10^{-10}$  m/cycle.

## CONCLUSION

The present investigations had the aim to evaluate the applicability of the nonlinearity parameter in order to describe the crack initiation and growth during ultrasonic fatigue. The experiments show that the crack initiation cannot be detected for sure, but depends on the material. For alloy EN AW 6082 there was no change of the parameter visible for both investigated heat treatment conditions that means the nonlinearity parameter could not be applied for the early fatigue crack detection. However, the parameter changed right from the beginning of the test for alloy EN AW 5083. In case of a change of the nonlinearity parameter, it is not yet clear whether this can be attributed to crack initiation or cyclic hardening/softening and will be the subject of further investigations.

Concerning the crack growth behavior, a good correlation between the nonlinearity parameter and the crack growth rate could be detected. A change in the crack growth rate was clearly mirrored by a significant change of the nonlinearity parameter as well.

## REFERENCES

- [1] J. Bach, H. W. Höppel, M. Prell, M. Göken: Crack Initiation Mechanisms in AA6082 Fatigued in the VHCF-Regime. *International Journal of Fatigue* 60 (2014), pp. 23-27
- [2] A. Kumar, C. J. Torbet, J. W. Jones, T. M. Pollock: Nonlinear Ultrasonics for In Situ Damage Detection during High Frequency Fatigue. *Journal of Applied Physics* 106 (2009) 024904
- [3] M. Zimmermann, B. Langer, A. Grigorescu, H.-J. Christ: In-Situ Charakterisierung der Schädigungsentwicklung während der zyklischen Beanspruchung im VHCF-Bereich mittels „nonlinear ultrasonics“. *Tagungsband Werkstoffprüfung 2011*, pp. 93-98
- [4] A. Kumar, R. R. Adharapurapu, J. W. Jones, T. M. Pollock: In Situ Damage Assessment in a Cast Magnesium Alloy during Very High Cycle Fatigue. *Scripta Materialia* 64 (2011), pp. 65-68
- [5] H. Mayer: Recent developments in ultrasonic fatigue. *Fatigue Fract Engng Mater Struct* 39 (2016), pp. 3-29
- [6] H. Mayer, M. Fitzka, R. Schuller: Constant and Variable Amplitude Ultrasonic Fatigue of 2024-T351 Aluminium Alloy at Different Load Ratios. *Ultrasonics* 53 (2013), pp. 1425-1432
- [7] T. Kirsten, M. Zimmermann, F. Bülbül, H.-J. Christ, T. Stein, A. Brückner-Foit: Charakterisierung der Rissinitiierung und des –wachstums im VHCF-Bereich auf der Basis des nichtlinearen Materialverhaltens am Beispiel einer ausscheidungsgehärteten Aluminiumlegierung. *Tagungsband Werkstoffprüfung 2016*, pp. 71-76
- [8] N. Schneider, J. Bödecker, C. Berger, M. Oechsner: Frequency Effect and Influence of Testing Technique on the Fatigue Behaviour of Quenched and Tempered Steel and Aluminium Alloy. *International Journal of Fatigue* 93 (2016) pp. 224-231
- [9] A. Kumar, C. J. Torbet, T. M. Pollock, J. W. Jones: In situ Characterization of Fatigue Damage Evolution in a Cast Al Alloy via Nonlinear Ultrasonic Measurements. *Acta Materialia* 58 (2010), pp. 2143-2154
- [10] W. Li, H. Cui, W. Wen, X. Su, C. C. Engler-Pinto Jr.: In situ Nonlinear Ultrasonic for Very High Cycle Fatigue Damage Characterization of a Cast Aluminum Alloy. *Materials Science and Engineering A* 645 (2015), pp. 248-254

**Corresponding author:** [tina.kirsten@tu-dresden.de](mailto:tina.kirsten@tu-dresden.de)

# MEASUREMENT OF INTERNAL FATIGUE CRACK GROWTH RATE OF Ti-6Al-4V BY USING HIGH-RESOLUTION X-RAY CT

F. Yoshinaka<sup>1), 2)</sup>, T. Nakamura<sup>3)</sup>, D. Shiozawa<sup>4)</sup>, Y. Nakai<sup>4)</sup>, K. Uesugi<sup>5)</sup>

<sup>1)</sup> Division of Mechanical and Space Engineering, Graduate School of Engineering, Hokkaido University, Kita 13, Nishi 8, Kita-ku, Sapporo, Hokkaido 060-8628, Japan

<sup>2)</sup> Research Fellow of the Japan Society for the Promotion of Science, Japan

<sup>3)</sup> Division of Mechanical and Space Engineering, Faculty of Engineering, Hokkaido University, Kita 13, Nishi 8, Kita-ku, Sapporo, Hokkaido 060-8628, Japan

<sup>4)</sup> Department of Mechanical Engineering, Kobe University, 1-1, Rokkodai-cho, Nada-ku, Kobe, Hyogo 657-8501, Japan

<sup>5)</sup> Japan Synchrotron Radiation Research Institute, 1-1-1, Kouto, Sayo-cho, Sayo-gun, Hyogo 679-5198, Japan

## ABSTRACT

The internal fatigue crack growth rate in Ti-6Al-4V was investigated using high-resolution X-ray CT. The present work was conducted at the SPring-8, one of the world's largest synchrotron radiation facility, located in Japan. The internal crack propagated quite slowly, less than  $10^{-10}$  m/cycle; in contrast, the growth rate significantly increased once the crack reached the specimen surface. The growth rate of the internal crack was compared with those of surface cracks in air and high vacuum to elucidate the internal fracture process in terms of the environment inside the cracks. The rate of the internal crack was lower than that of the surface crack in the air but matched that in the vacuum. This led us to conclude that the low growth rate of the internal crack is due to the vacuum-like environment inside the crack.

## KEYWORDS

Crack growth, titanium alloy, nondestructive inspection, vacuum environment

## INTRODUCTION

( $\alpha+\beta$ ) titanium alloy Ti-6Al-4V is used in various industries including aerospace applications. The excellent fatigue properties allow its use for components subjected to severe cyclic loading. However, fatigue fractures originating from the internal initiation sites have been reported in a very high cycle fatigue regime for this alloy [1]. The growth process of internal cracks has not yet been revealed because they are typically too small to be detected by commonly used non-destructive inspection methods such as X-ray CT.

However, micro computed tomography ( $\mu$ CT) using high brilliance X-rays has become available because of the development of third-generation synchrotron radiation sources [2]. Previous studies have shown the effectiveness of  $\mu$ CT as a high-resolution nondestructive observation method for fatigue cracks in metallic materials [3, 4].

In this study, the internal crack growth in Ti-6Al-4V was observed by using  $\mu$ CT at a large synchrotron radiation facility, SPring-8, in Hyogo, Japan. The internal crack growth rate was obtained from an analysis of the reconstructed images, and the findings are presented from the view point of the environment inside the internal crack.



## EXPERIMENTAL PROCEDURE

### Material and specimen

The material was an ( $\alpha+\beta$ ) titanium alloy, Ti-6Al-4V. The chemical composition of the alloy was as follows (wt %): 6.12 Al, 4.27 V, 0.16 O, 0.002 N, 0.02 C, 0.15 Fe, 0.0029 H, Bal. Ti. The alloy was heat-treated with the following sequence: a solution treatment at 1203 K for 2.6 ks was followed by air cooling and over aging at 978 K for 7.2 ks, followed by air cooling. The microstructure after heat treatment had an ( $\alpha+\beta$ ) dual phase microstructure; the average grain size of each phase was 10  $\mu\text{m}$ . The tensile strength and elongation were 943 MPa and 17%, respectively. An hourglass specimen with a parallel part of  $\phi 1.8 \times 3 \text{ mm}$  was used to ensure a minimal X-ray transmission during  $\mu\text{CT}$ .

### Fatigue test and $\mu\text{CT}$

The experiment entailed the fatigue tests and  $\mu\text{CT}$  be repeatedly conducted at SPring-8. Sinusoidal loadings with a stress ratio  $R = 0.1$  at a frequency  $f = 400 \text{ Hz}$  were applied. The maximum stress was  $\sigma_{\text{max}} = 650 \text{ MPa}$ . Internal fractures were assumed to occur at around  $N_f = 2-3 \times 10^7$  under this condition. The cyclic loadings of  $1.60 \times 10^7$  cycles were applied to the specimen prior to the experiment at SPring-8 in order to reduce the time necessary for the fatigue tests and to observe the internal crack growth up to the final fracture within the available time of the beamline (48 hr).

The experiment was carried out in the second hutch of the medium-length beamline BL20XU at SPring-8. The  $\mu\text{CT}$  system consists of an undulator light source, an optical system, a detector, and a specimen. The optical system consists of a double crystal monochromator (Si 111-111) and a slit. The maximum available X-ray energy is 37.7 keV. A visible-light conversion type X-ray image detector was used. The format of the image was  $2000 \times 1312$  pixels in a  $2 \times 2$  binning mode of a CCD camera (Hamamatsu Photonics K. K., C4880-41S). The final pixel size was 1.5  $\mu\text{m}$ . The specimen was set on a rotating table so that X-rays propagated perpendicularly to the loading axis of the specimen. The  $\mu\text{CT}$  images were created from radiographs obtained by rotating the specimen about the loading axis. The whole parallel part of the specimen ( $\phi 1.8 \times 3 \text{ mm}$ ) was observed.

The  $\mu\text{CT}$  conditions were as follows. The X-ray energy was 37.7 keV. The specimen was rotated about the loading axis from  $0^\circ$  to  $180^\circ$  in steps of  $0.1^\circ$ . At each step, the X-ray intensity was measured by the detector with an exposure time of 0.5 s. The projection number was 1800, and the total scan duration was 15 min. The distance between the specimen and the detector was set to 300 mm to utilize the edge enhancement effect properly [5, 6]. The tensile loading of 1300 N, which corresponds to 78% of the maximum stress of 650 MPa, was applied to the specimen to open the internal cracks using the tensile loading grip developed for this study [6]. A convolution back projection method was used for the reconstruction.

## EXPERIMENTAL RESULTS

Six internal cracks were detected as a result of the first  $\mu\text{CT}$  at  $N = 1.60 \times 10^7$ . Fig. 1(a)–(c) shows examples of the reconstructed longitudinal sections of the internal cracks. The dark line near the center of the images represents the cracks. In the following observations, another three internal cracks were initiated: one crack was detected at  $N = 1.64 \times 10^7$ , and two cracks were detected at  $N = 1.76 \times 10^7$ . A total of nine cracks had initiated up to  $N_f = 1.96 \times 10^7$ , where the crack shown in Fig. 1(a) caused the final fracture that became a fatal crack.



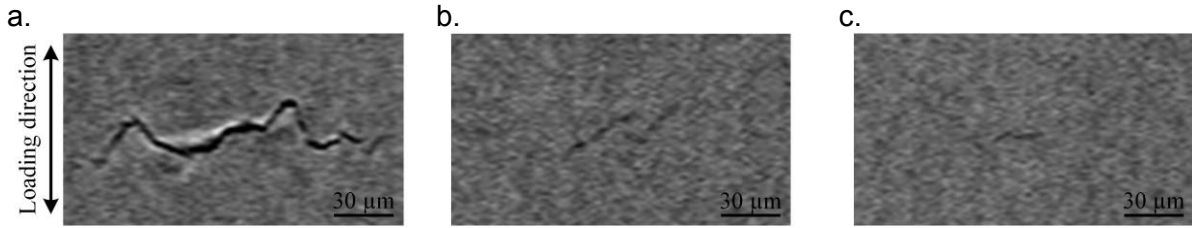


**Fig. 1:** Reconstructed longitudinal sections around the internal cracks

The growth processes of the internal cracks were observed. Most of the cracks did not show any apparent growth during the observation period ( $N = 1.60 \times 10^7 - 1.96 \times 10^7$ ). However, some cracks including the fatal crack propagated widely. In the present work, the growth of the fatal crack was carefully investigated. Fig. 2 shows the 3D reconstructed images of the fatal crack at each cycle. The dashed line indicates the specimen surface. The crack propagated radially outward from the internal initiation site and eventually reached the specimen surface, as shown in Fig. 2(h). Subsequent cyclic loadings of 699 cycles were applied to investigate the growth behavior after the crack reached the specimen surface. The surface crack growth was observed from (h) to (i). The specimen fractured immediately when the subsequent loading was applied after the observation shown in (i). From the above, the number of cycles after the crack reached the specimen surface was no more than order  $10^2$ , and the ratio of the number of cycles in surface crack growth to the total fatigue life was very small.

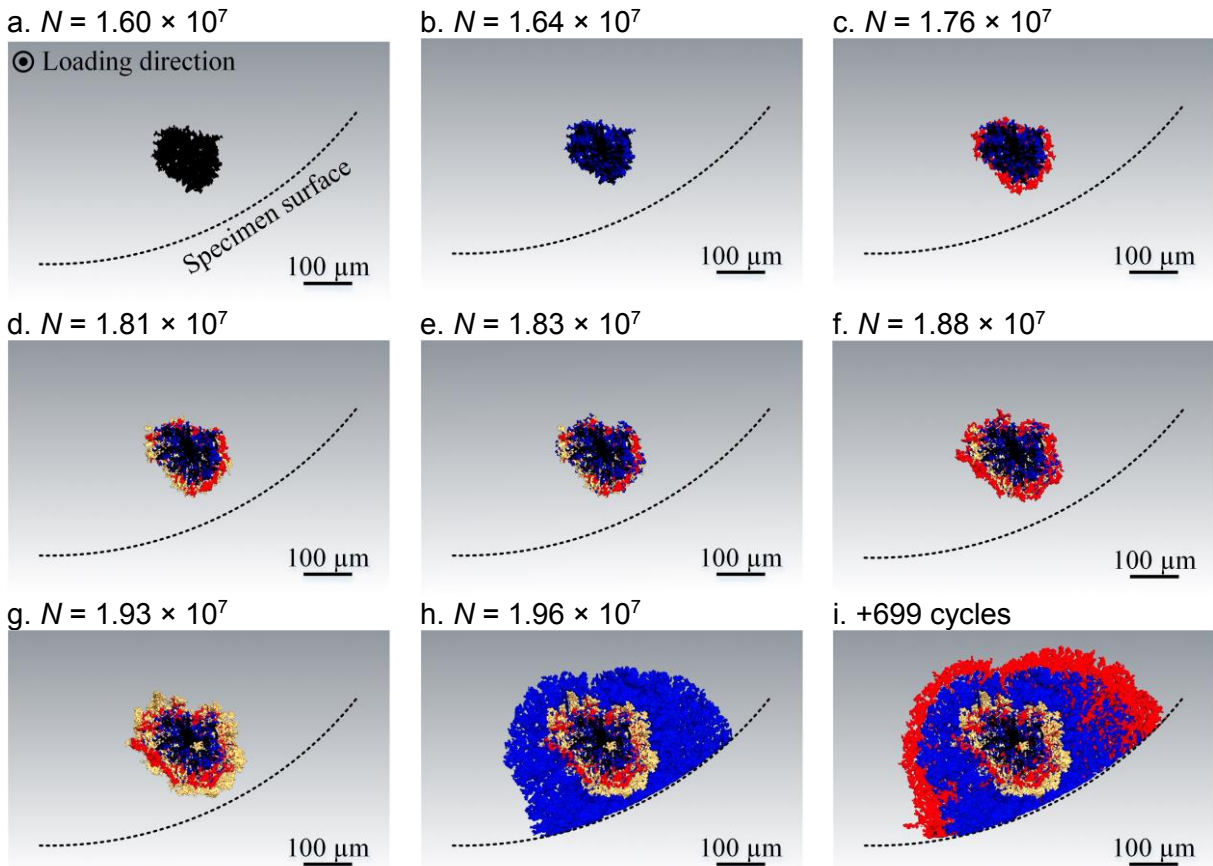


**Fig. 2:** 3D reconstructed images of the fatal crack at each number of cycles

## DISCUSSION

The crack growth rate  $da/dN$  was calculated from the observation results of the crack shown in Fig. 2. The crack was longer in the direction perpendicular to the specimen surface, and the crack growth rate along this direction was obtained. Fig. 3(a) shows the relationship between  $da/dN$  and the stress intensity factor range  $\Delta K$ . The triangles and diamond in the figure represent the results for the internal and surface cracks, respectively.  $\Delta K$  values were calculated using the equation proposed by Murakami et al. [7]. The  $da/dN$  of the internal crack was very small, less than  $10^{-10}$  m/cycle. In contrast, the  $da/dN$  once the crack reached the surface was on the order of  $10^{-8}$  m/cycle and was much larger than that of the internal crack.

The internal crack propagates through a vacuum-like environment that is shut off from the air [8, 9]. Fig. 3(b) shows the relationship between  $da/dN$  and  $\Delta K$  of the surface cracks in the air and vacuum obtained by one of the authors [9]. Circles and squares indicate the results in air and vacuum, respectively. The  $da/dN$  in the air was larger than  $10^{-9}$  m/cycle for a whole  $\Delta K$  regime. In contrast, the  $da/dN$  in the vacuum was less than  $10^{-10}$  m/cycle in the lower  $\Delta K$  regime and was significantly lower than that in the air.

The results of the internal crack were replotted in Fig. 3(b) to elucidate the internal crack growth in terms of the environment inside it and were compared with those of the surface cracks in the air and vacuum. The  $da/dN$  of the internal crack (triangles) was significantly lower than that of surface crack in the air; in contrast, it matched that of the surface crack in the vacuum. This indicates the reason for the low  $da/dN$  of the internal crack is the vacuum-like environment inside the crack.

However, the results once the crack reached the surface (diamond) were of the same order as the surface crack in the air. Namely, the internal crack upon reaching the specimen surface changes its growth behavior to that of a surface initiated crack. These findings indicate that the reason for the growth rates of internal and surface cracks is the difference in environments inside them.

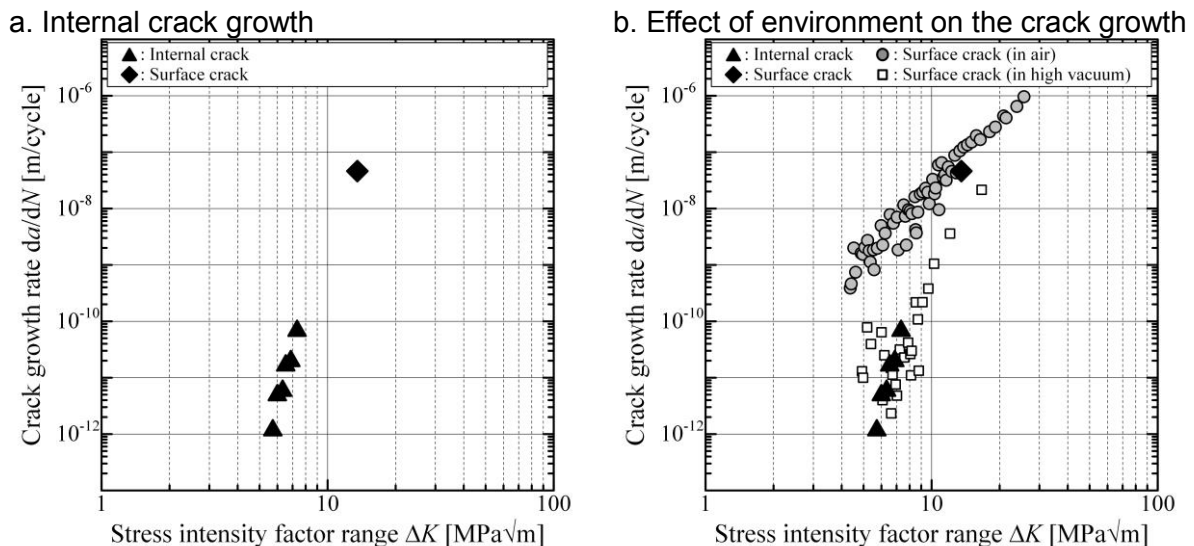


Fig. 3: Relationship between  $da/dN$  and  $\Delta K$

## ACKNOWLEDGEMENTS

The synchrotron radiation experiments were performed at the BL20XU in SPring-8 with the approval of JASRI (Proposal No. 2013A1218 and 2013B1470). The authors acknowledge the support of a Grant-in-Aid for Scientific Research (A) (Grant No. 24246024) and Grant-in-Aid for JSPS Research Fellow (Grant No. 16J01058) from JSPS, Japan.

## REFERENCES

- [1] Neal, DF.; Blenkinsop, PA.:  
Internal Fatigue Origins in  $\alpha$ - $\beta$  Titanium Alloys  
*Acta Mater*, 24 (1976) No. 1, pp. 59–63
- [2] Suzuki, Y.; Yagi, N.; Uesugi, K.:  
X-ray Refraction-enhanced Imaging and a Method for Phase Retrieval for a Simple Object  
*J Synchrotron Radiat*, 9 (2002) No. 3, pp. 160–165
- [3] Toda, H.; Tomizato, F.; Zeismann, F.; Motoyashiki-Besel, Y.; Uesugi, K.; Takeuchi, A.; Suzuki, Y.; Kobayashi, M.; Brueckner-Foit, A.:  
High-resolution Observation of Steel Using X-ray Tomography Technique  
*ISIJ Int*, 52 (2012) No. 3 pp. 516–521
- [4] Marrow, T.J.; Mostafavi, M.; Hashimoto, T.; Thompson, G.E.:  
A Quantitative Three-dimensional in Situ Study of a Short Fatigue Crack in a Magnesium Alloy  
*Int J Fatigue*, 66 (2014) pp. 183–193
- [5] Sera, T.; Uesugi, K.; Yagi, N.:  
Refraction-enhanced Tomography of Mouse and Rabbit Lungs  
*Med Phys*, 32 (2005) No. 9. pp. 2787–2792
- [6] Nakamura, T.; Yoshinaka, F.; Nakayama, S.; Oguma, H.; Shiozawa, D.; Nakai, Y.; Uesugi, K.:  
Detection of Small Internal Fatigue Cracks in Ti-6Al-4V by Using Synchrotron Radiation  $\mu$ CT Imaging  
*Mech Eng Lett*, 2 (2016) pp. 16–00233
- [7] Murakami, Y.; Kodama, S.; Konuma, S.:  
Quantitative Evaluation of Effects of Non-metallic Inclusions on Fatigue Strength of High Strength Steels, I: Basic Fatigue Mechanism and Evaluation of Correlation between the Fatigue Fracture Stress and the Size and Location of Non-metallic Inclusions  
*Int J Fatigue*, 11 (1989) No. 5. pp. 291–298
- [8] Benedetti, M.; Fontanari, V.; Bandini, M.; Savio, E.:  
High- and Very High-cycle Plain Fatigue Resistance of Shot Peened High-strength Aluminum Alloys: the Role of Surface Morphology  
*Int J Fatigue*, 70 (2015) pp. 451–462
- [9] Yoshinaka, F.; Nakamura, T.; Takaku, K.:  
Effects of Vacuum Environment on Small Fatigue Crack Propagation in Ti-6Al-4V  
*Int J Fatigue*, 91 (2016) No. 1. pp. 29–38

**Corresponding author:** yoshinaka@eis.hokudai.ac.jp

# TORSIONAL FATIGUE PROPERTIES OF 17-4PH STAINLESS STEEL IN THE VHCF REGIME

B.M. Schönbauer<sup>1)</sup>, H. Mayer<sup>1)</sup>, K. Yanase<sup>2,3)</sup>, M. Endo<sup>2,3)</sup>

<sup>1)</sup> Institute of Physics and Materials Science, BOKU Vienna, Peter-Jordan-Str. 82, 1190 Vienna, Austria

<sup>2)</sup> Department of Mechanical Engineering, Fukuoka University, 8-19-1 Nanakuma, Jonan-ku, Fukuoka 814-0180, Japan

<sup>3)</sup> Institute of Materials Science and Technology, Fukuoka University, 8-19-1 Nanakuma, Jonan-ku, Fukuoka 814-0180, Japan

## ABSTRACT

The very high cycle fatigue properties of 17-4PH stainless steel under torsional loading condition are studied using ultrasonic testing equipment. The results are compared with torsional tests at conventional frequencies and with uniaxial ultrasonic fatigue tests. Fatigue limits are determined for smooth specimens and for specimens with artificial defects. Ratio of the torsional fatigue limit,  $\tau_{w0}$ , and the tension-compression fatigue limit,  $\sigma_{w0}$ , at a load ratio of  $R = -1$  is about  $1/\sqrt{3}$ , which is in good accordance with the von Mises criterion. In the presence of a defect, however, the ratio of  $\tau_w/\sigma_w$  is close to 1. This suggests that the effect of biaxial stress becomes negligible, and the fatigue behaviour is controlled by the major principal stress. The use of a fracture mechanics approach is found to be appropriate for predicting the fatigue strength in the presence of a defect with small notch root radius.

## KEYWORDS

17-4PH stainless steel, torsional fatigue, very high cycle fatigue, small defects, non-propagating cracks, fatigue limit

## INTRODUCTION

A number of investigations have been performed in the last few years dealing with the influence of intrinsic and artificial defects on the uniaxial fatigue properties of 17-4PH stainless steel [1-3]. It was found that very small defects as non-metallic inclusions with diameters of only a few microns may initiate fatigue cracks, and failure can occur even above  $N = 10^{10}$  load cycles. The fatigue limit in the presence of various types of small surface defects (inclusions, corrosion pits, drilled holes and circumferential notches) was determined. It could be shown that the fatigue limit,  $\sigma_w$ , can be calculated according to the  $\sqrt{area}$  parameter model by Murakami and Endo [4] using the following equation:

$$\sigma_w = \frac{1.43 \cdot (HV + 120)}{(\sqrt{area})^{1/6}} \quad (1)$$

where  $\sqrt{area}$  is the square root of the projection area of a small defect perpendicular to the loading direction (in  $\mu\text{m}$ ),  $HV$  is the Vickers hardness (in  $\text{kgf}/\text{mm}^2$ ) and  $\sigma_w$  is in MPa.

Equation (1) is appropriate to evaluate the fatigue limit of the investigated 17-4PH steel in the presence of small defects with notch root radii,  $\rho$ , less than  $50 \mu\text{m}$  and  $\sqrt{area} \leq 80 \mu\text{m}$ . For larger defect ( $\sqrt{area} > 80 \mu\text{m}$ ), the failure criterion can be expressed by the threshold stress intensity factor range of a long crack (or a large defect),  $\Delta K_{th,lc}$ , as follows:

$$\sigma_w = \frac{\Delta K_{th,lc}/2}{0.65 \cdot \sqrt{\pi \cdot \sqrt{area} \times 10^{-6}}} \quad (2)$$

For a defect with larger notch root radius of  $\rho \geq 50 \mu\text{m}$ , a fracture mechanics approach is not applicable, and the predictions according to Eqs. (1) and (2) become highly conservative. In this case, the fatigue limit is determined by the critical condition for crack initiation, instead of crack propagation. This could be proven due to the absence of non-propagating cracks at the fatigue limit (which were observable for defects with smaller notch root radii) [3].

Recent studies on the torsional fatigue properties [5] reveal that the defect tolerance significantly increases under biaxial loading condition. In contrast to tension-compression loading, defects with  $\sqrt{area} \leq 70 \mu\text{m}$  are non-detrimental since fatigue failure originates from the smooth surface instead of the defect. Furthermore, the sensitivity to notch root radius is less pronounced under torsional loading condition. Drilled holes with diameters of  $100 \mu\text{m}$  ( $\rho = 50 \mu\text{m}$ ) still can be treated with a fracture mechanics approach. But for larger notch root radii ( $\rho \geq 100 \mu\text{m}$ ), the fatigue limit is again determined by the critical condition for crack initiation.

In the present work, torsional fatigue test results in the very high cycle fatigue (VHCF) regime are presented and compared with torsional fatigue tests at conventional frequencies and uniaxial ultrasonic fatigue tests.

## MATERIAL AND EXPERIMENTAL PROCEDURE

Chromium-nickel-copper stainless steel 17-4PH is investigated. The material was precipitation hardened at  $621 \text{ }^\circ\text{C}$  for 4 h (condition H1150). The chemical composition and the mechanical properties are summarised in Table 1 and 2, respectively. For more details on the material, see Ref. [1].

Cr	Ni	Cu	Mn	Si	Nb+Ta	C	P	S
15.57	4.37	3.31	0.49	0.40	0.23	0.033	0.027	0.001

**Table 1:** Chemical composition of 17-4PH (in weight %)

Tensile strength (MPa)	Yield strength (MPa)	Elongation (%)	Reduction of area (%)	Vickers hardness (kgf/mm <sup>2</sup> )
1030	983	21	61	352

**Table 2:** Mechanical properties of 17-4PH

Torsional fatigue tests at 19 kHz were conducted with hourglass and cylindrically shaped specimens as shown in Fig. 1. The surfaces of specimens were ground and electropolished to remove residual stresses.

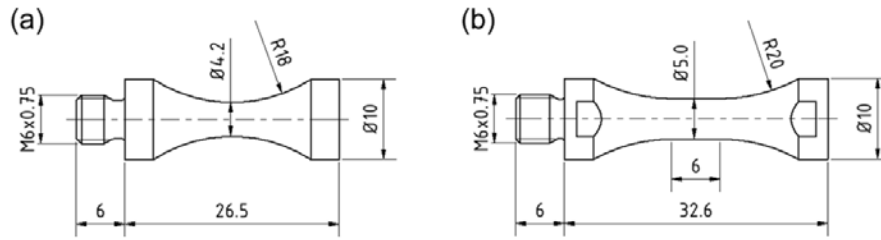


**Fig. 1:** Specimen geometries for ultrasonic fatigue testing with (a) hourglass and (b) cylindrical shape in the gauge length (dimensions in mm)

Ultrasonic fatigue testing equipment developed at BOKU University, Vienna was used which enables VHCF testing under torsional loading condition at different load ratios,  $R$ . Specimens are stimulated to circumferential resonance vibration. At one end of the specimen, the oscillation amplitude is measured with a vibration gauge which is used to control loading in a closed-loop circuit. This leads to an accuracy of  $\pm 1\%$  of the vibration amplitude. A detailed description of the testing equipment can be found in [6].

Both specimen shapes shown in Fig. 1 were used to determine the torsional fatigue limit of smooth specimens. The specimen shape used to determine the fatigue limit under uniaxial ultrasonic fatigue loading can be found in [1]. Torsional test with specimens containing two drilled holes were performed with cylindrically shaped specimens (Fig. 1(b)). The orientation of the 2-hole defects (hole diameter:  $100\ \mu\text{m}$ , hole depth:  $131\ \mu\text{m}$ , distance between hole centres:  $110\ \mu\text{m}$ ) was at an angle of  $45^\circ$  with respect to the specimen axis, i.e. perpendicular to the direction of the major principal stress under torsional loading. The specimens were stress-relief annealed in high vacuum at  $600\ ^\circ\text{C}$  for one hour to remove residual stresses that were potentially generated during drilling.

Previous torsional fatigue test at load frequencies of 25–35 Hz were conducted with round-bar specimens. The diameter in the gauge length of these specimens was between 6 and 10 mm. For more details on specimen shape and experimental procedure, see Ref. [5].

## RESULTS AND DISCUSSION

### Uniaxial and torsional fatigue limit of smooth specimen

The  $S-N$  data received from ultrasonic fatigue tests under tension-compression and torsional loading are summarised in Fig. 2. Additionally, results obtained from low frequency tests are included [5]. The fatigue limit of smooth specimens under fully reversed uniaxial loading,  $\sigma_{w0}$ , determined from test up to  $10^{10}$  cycles can be estimated with the simple equation [7]:

$$\sigma_{w0} = 1.6 \cdot HV \pm 0.1 \cdot HV \quad (3)$$

The ratio between the fatigue limits under uniaxial and torsional loading,  $\sigma_{w0}/\tau_{w0}$ , is in good correlation with the von Mises criterion. The fatigue limit of smooth specimens can be therefore estimated as:

$$\tau_{w0} = \frac{\sigma_{w0}}{\sqrt{3}} = \frac{1.6 \cdot HV}{\sqrt{3}} \quad (4)$$

Fatigue-limit estimations according to Eqs. (3) and (4) are plotted as dashed lines in Fig. 2.

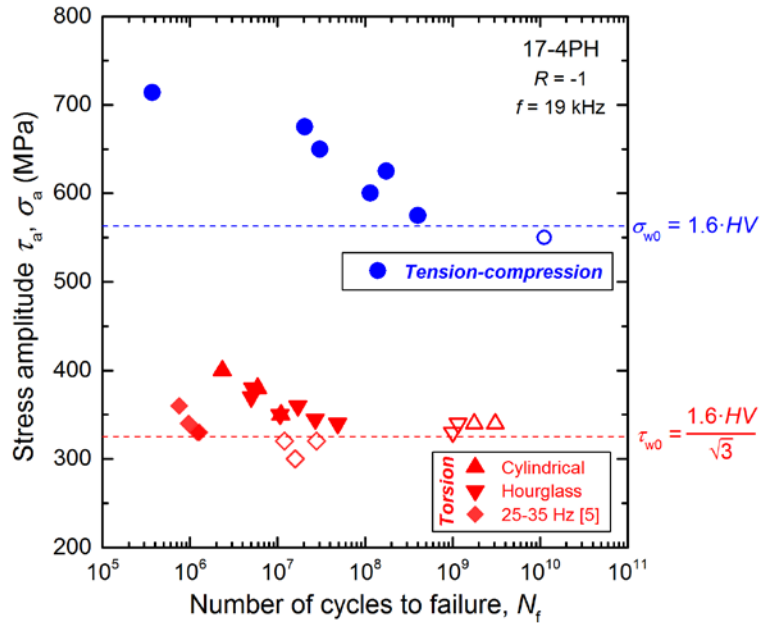


Fig. 2: S-N data for smooth specimens under tension-compression and torsion loading (open symbols indicate run-out specimens)

It is noted that the torsional fatigue limit determined in low-frequency tests coincides to the fatigue limit measured in ultrasonic torsional tests, but lower fatigue lifetimes are measured in the low-frequency experiments. Further investigations are necessary to explain this behaviour. However, the results discussed in the next section rather indicate a size effect than a strain rate effect.

### Torsional fatigue limit in the presence of artificial defects

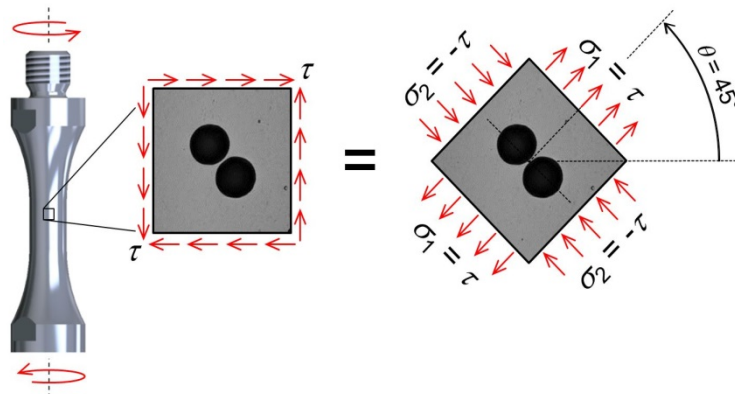
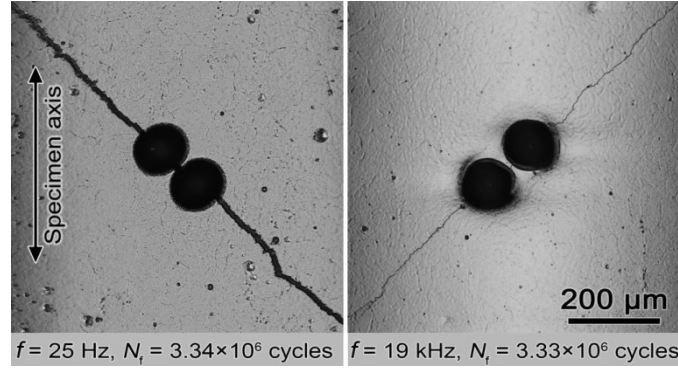
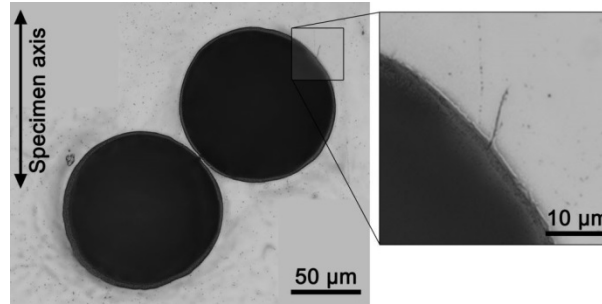


Fig. 3: 2-hole defect on specimen surface and stress transformation to principal stresses

Two ultrasonic torsional fatigue tests were conducted with 2-hole defects as shown in Fig. 3. The first test was performed at a shear stress amplitude of  $\tau_a = 260$  MPa, which is slightly above the fatigue limit of  $\tau_w = 240$  MPa that was determined from prior low-frequency tests [5]. The specimen failed after  $3.33 \times 10^6$  cycles. For comparison: a specimen (containing the same defect) tested at 25 Hz failed at  $3.34 \times 10^6$  cycles. Figure 4 shows the 2-hole defects on the specimen surfaces after testing at both frequencies. The second test was performed at  $\tau_w = 250$  MPa, and the specimen was fatigue loaded for  $2.08 \times 10^9$  cycles. No failure occurred, but a fatigue crack was initiated at the edge of a hole as shown in Fig. 5. These results clearly show that the testing frequency does not influence the fatigue behaviour of the investigated 17-4PH steel in the presence of defects.



**Fig. 4:** 2-hole defects with fatigue cracks after loading at  $\tau_a = 260$  MPa



**Fig. 5:** 2-hole defect with non-propagating short crack after loading at  $\tau_a = 250$  MPa and  $N = 2.08 \times 10^9$  cycles ( $f = 19$  kHz)

The observation of non-propagating cracks at stress amplitudes below  $\tau_w$  indicates that the fatigue limit is determined by the critical condition for crack propagation, but not for crack initiation. This suggests that a fracture mechanics approach can be applied to evaluate the fatigue limit for such kind of defects under torsional loading. As previously shown in [5], the torsional fatigue limit can be evaluated by considering the principal stresses. Under torsional loading, the principal stresses at the specimen surface are given as  $\sigma_1 = \tau$  and  $\sigma_2 = -\tau$  as shown in Fig. 3. Comprehensive tests on the defect tolerance of 17-4PH steel under uniaxial and torsional loading condition [3, 5] reveal that – for the investigated material – only the major principal stress,  $\sigma_1$ , contributes to the accumulation of fatigue damage, while the minor principal stress,  $\sigma_2$ , is negligible. This leads to the assumption that Eqs. (1) and (2) can be also applied to biaxial loading conditions by equating  $\tau_w = \sigma_w$ . For  $\sqrt{area} \leq 80 \mu\text{m}$ , Eq. (1) becomes:

$$\tau_w = \sigma_w = \frac{1.43 \cdot (HV + 120)}{(\sqrt{area})^{1/6}} \quad (5)$$

For larger defect ( $\sqrt{area} > 80 \mu\text{m}$ ), Eq. (2) is extended to:

$$\tau_w = \sigma_w = \frac{\Delta K_{th,lc}/2}{0.65 \cdot \sqrt{\pi \cdot \sqrt{area} \times 10^{-6}}} \quad (6)$$

In Eqs. (5) and (6), the geometry parameter  $\sqrt{area}$  is defined as the square root of the projection area perpendicular to the major principal stress direction. It is noted, that the threshold stress intensity factor range for a long crack,  $\Delta K_{th,lc}$ , is the threshold for Mode I crack propagation. The appearance of Mode I crack propagation during torsional fatigue loading is obvious in Fig. 4.



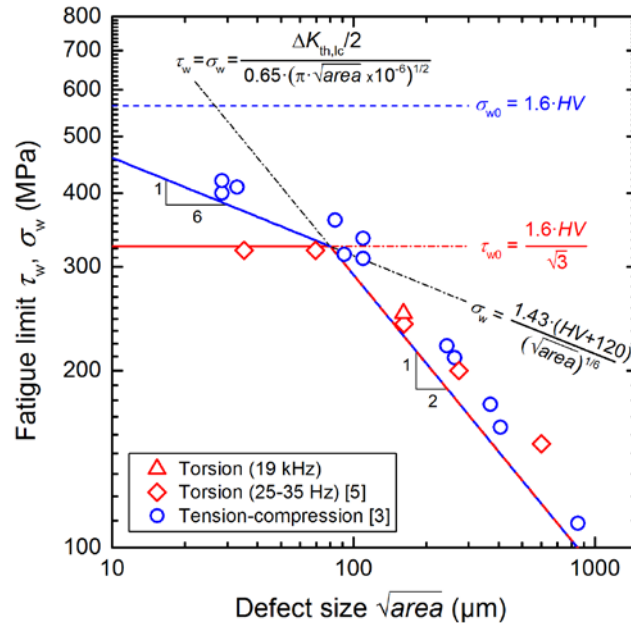


Fig. 6: Relationship between fatigue limit and defect size

The relationship between fatigue limit,  $\tau_w$  and  $\sigma_w$ , and defect size,  $\sqrt{area}$ , is plotted in Fig. 6. Following conclusions can be drawn:

The defect tolerance under torsional loading is significantly higher compared to tension-compression loading. As a consequence, the fatigue limit for defects with  $\sqrt{area} \leq 80 \mu\text{m}$  can be estimated by the fatigue limit of smooth specimens,  $\tau_{w0}$  (Eq. (4)). Eq. (5) becomes therefore inoperative. Under tension-compression loading, the fatigue limit,  $\sigma_w$ , for small defects can be evaluated by Eq. (1). The estimation of  $\sigma_{w0}$  according to Eq. (3) might be considered as an upper bound of the fatigue limit of smooth specimens. For defects with  $\sqrt{area} > 80 \mu\text{m}$ , the threshold stress intensity factor range for Mode I long cracks (Eq. (6)) seems to be appropriate to estimate the fatigue limit for both uniaxial and torsional fatigue loading condition. This demonstrates that the effect of biaxial stress on the surface of specimen is negligible, and the fatigue limit of 17-4PH stainless steel is governed by the major principal stress solely.

## REFERENCES

- [1] Schönbauer, B.M.; Stanzl-Tschegg, S.E.; Perlega, A.; Salzman, R.N.; Rieger, N.F.; Turnbull, A.; Zhou, S.; Lukaszewicz, M.; Gandy, M.: The influence of corrosion pits on the fatigue life of 17-4PH steam turbine blade steel, *Eng Fract Mech* 147 (2015), pp. 158-175
- [2] Schönbauer, B.M.; Yanase, K.; Endo, M.: VHCF properties and fatigue limit prediction of precipitation hardened 17-4PH stainless steel, *Int J Fatigue* 88 (2016), pp. 205-216
- [3] Schönbauer, B.M.; Yanase, K.; Endo, M.: The influence of various types of small defects on the fatigue limit of precipitation-hardened 17-4PH stainless steel, *Theor Appl Fract Mech* 87 (2017), pp. 35-49
- [4] Murakami, Y.; Endo, M.: Effect of hardness and crack geometries on  $\Delta K_{th}$  of small cracks emanating from small defect, in: K.J. Miller, E.R. de Los Rios (Eds.) *The behavior of short fatigue crack*, Mechanical Engineering Publications, London, 1986, pp. 275-293
- [5] Schönbauer, B.M.; Yanase, K.; Endo, M.: Influences of small defects on torsional fatigue limit of 17-4PH stainless steel, *Int J Fatigue* (2017) (in press)
- [6] Mayer, H.: Recent developments in ultrasonic fatigue, *Fatigue Fract Eng M*, 39 (2016), pp. 3-29
- [7] Murakami, Y.: *Metal fatigue; Effects of small defects and nonmetallic inclusions*, Elsevier, 2002

Corresponding author: bernd.schoenbauer@boku.ac.at

# HCF AND VHCF STRENGTH OF SPRING STEEL WITH SMALL SCRATCHES

Yoshiro Nishimura<sup>1)</sup>, Masahiro Endo<sup>2,3)</sup>, Keiji Yanase<sup>2,3)</sup>, Yuichi Ikeda<sup>2)</sup>,  
Yuya Tanaka<sup>2)</sup>, Nobuyuki Miyamoto<sup>1)</sup>, Susumu Miyakawa<sup>1)</sup>

<sup>1)</sup> Materials Eng. R&D Div., DENSO Corporation, Aichi, Japan

<sup>2)</sup> Department of Mechanical Engineering, Fukuoka University, Fukuoka, Japan

<sup>3)</sup> Institute of Materials Science and Engineering, Fukuoka University, Fukuoka, Japan

## ABSTRACT

When the compression coil springs are subjected to high stress, fatigue crack sometimes initiates and propagates from small scratch or defect produced in the manufacturing process. However, there are a limited number of studies on the fatigue behavior of high-strength spring steel in the presence of small scratch. In this study, the fatigue tests were conducted to examine the torsional fatigue behavior of a high-strength spring steel (JIS G 3561, SWOSC-V) in the presence of small scratches. Based on  $\sqrt{area}$  parameter model, the sensitivity of a high-strength spring steel to small scratches was qualitatively and quantitatively examined in HCF and VHCF regimes.

## KEYWORDS

Spring steel, scratch, notch effect, fatigue limit,  $\sqrt{area}$

## INTRODUCTION

These days, a number of components in the automotive vehicles have various types of compression coil springs. Further, because of the strong requirements for weight reduction in automobiles and space saving in the engine components, the use of high-strength spring steel has been increasing [1][2]. When the compression coil springs are subjected to high cyclic stress, fatigue crack sometimes initiates and propagates from small defect or scratch produced in the manufacturing process. Especially, if high-strength spring steel is used in very high cycle fatigue regime, the increased possibility of fatigue fracture from small defect is expected. To improve the fatigue strength of spring steel, the manufacturing process sometimes involves a peeling process to remove defects, an eddy-current test process to detect defects, a nitriding treatment process to enhance surface hardness, or a shot-peening process to introduce compressive residual stress. However, the effects of these processes on fatigue strength are not well-known and there is a limited number of studies on the fatigue behavior of high-strength spring in the presence of small defect in very high cycle fatigue regime.

In practice, the ability to access the effects of small defects, inclusions and inhomogeneities on the uniaxial fatigue strength has grown rapidly over the last decades. However in a wide range of actual engineering applications, the engineering components with complex geometries are usually subjected to multiaxial cyclic loading. In the case of compression coil springs, cyclic torsional stress with mean stress is applied to a wire of spring with defects, the presence of surface-hardened layer and compressive residual stress complicates the evaluation of fatigue strength of compression coil springs. In this study, a series of fatigue tests in high cycle and very high cycle fatigue regime were systematically conducted by using

both a resonance-type torsional fatigue machine and an ultrasonic torsional fatigue machine, at stress ratio,  $R = -1$ . By taking advantage of  $\sqrt{area}$  parameter to represent the effect of small defect [3-8], the fatigue behavior of high-strength spring steel with small scratch was examined in a systematic manner.

## EXPERIMENT

The investigated material was an oil-tempered Si-Cr steel wire used for valve springs (JIS G3561, SWOSC-V). SWOSC-V is a super clean steel, especially intended for the manufacture of valve springs and other springs that require excellent fatigue properties and excellent relaxation properties at moderately high working temperature. Chemical compositions of the investigated material are listed in Table 1. The mechanical properties of the material are controlled through patenting, drawing, and oil-tempering process, and they are shown in Table 2.

C	Si	Mn	Cr	Cu	P	S
0.51 ~ 0.59	1.20 ~ 1.60	0.50 ~ 0.80	0.50 ~ 0.80	~ 0.2	~ 0.025	~ 0.025

**Table 1:** Chemical composition of SWOSC-V (in weight %).

0.2% Proof stress (MPa)	Tensile strength (MPa)	Reduction of area (%)
1400 ~ 1570	1610 ~ 1760	40 ~

**Table 2:** Mechanical properties of SWOSC-V.

Fig. 1 shows the specimens manufactured from the wires with a diameter of 9 mm by turning and grinding process. The center of specimen is finished by using paper-polishing, electro-polishing, and colloidal silica to reduce the roughness and the residual stress on the specimen surface. The residual stress in the axial direction was measured with a X-ray diffraction, and the residual stress of the specimen was within  $\pm 20$  MPa at the specimen surface. By using a micro Vickers hardness tester, the Vickers hardness,  $HV$ , was measured both at cross-section and longitudinal section of a specimen. As a result, the anisotropy on  $HV$  was not observed and  $HV = 533 \text{ kgf/mm}^2$  was obtained. To investigate the effect of scratch on the fatigue properties, a small V-shaped longitudinal notch with various depth (notch-root radius of  $\rho = 15 \pm 5 \mu\text{m}$ ) were introduced at the specimen surface.

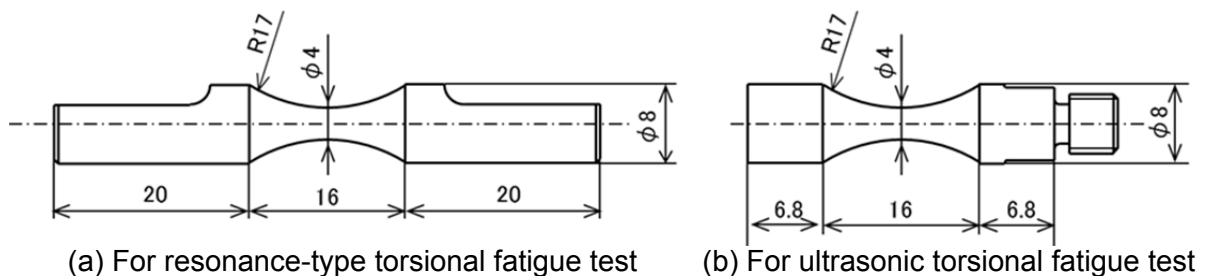


**Figure 1:** Geometries and sizes of test specimens (in mm).

Uniaxial fatigue limit of smooth specimen,  $\sigma_{w0}$ , can be predicted by the following equation [3]:

$$\sigma_{w0} = 1.6HV \quad (1)$$

Here,  $\sigma_{w0}$  is in MPa and  $HV$  is in  $\text{kgf}/\text{mm}^2$ . By substituting  $HV = 533$  in Eq. (1),  $\sigma_{w0} = 853$  MPa is obtained, which is nearly equal to  $\sigma_{w0} = 850$  MPa that is determined by the experiment. The relationship of Eq. (1) holds when fatigue crack mainly initiates from slip bands on the material surface, and Eq. (1) is usually applicable for  $HV < 400$ . On the other hand, when  $HV > 400$ , the defects and inclusions inside the materials frequently influence the initiation of fatigue crack. Namely, uniaxial fatigue limit of high-strength steel becomes sensitive to the presence of defects and inclusions, and fatigue limit can not be properly predicted with Eq. (1). Concerning the investigated material, SWOSC-V, however, fatigue cracks initiates from the surface despite  $HV > 400$ , and fatigue limit is reasonably predicted with Eq. (1). This fact indicates that the size of inclusions in SWOSC-V is significantly small and fatigue limit is controlled by the bulk material property of SWOSC-V (i.e.,  $HV$ ).

Fig. 2 shows the S-N data of smooth specimens. The fatigue limit is defined as the maximum stress amplitude that endured the load cycles of  $N \geq 1.0 \times 10^7$ . In practice, the number of experimental data for torsional fatigue limit of smooth specimen,  $\tau_{w0}$ , is rather limited compared to the data for uniaxial fatigue limit,  $\sigma_{w0}$ . Therefore, based on the available data of  $\tau_{w0}/\sigma_{w0}$ ,  $\tau_{w0}$  is frequently estimated. For steels, it is known that  $\tau_{w0}/\sigma_{w0} = 0.58 \sim 0.72$  [3][8][9]. As shown by a dotted line in Fig. 2, torsional fatigue limit is experimentally determined as  $\tau_{w0} = 661$  MPa from the ultrasonic torsional fatigue test. Accordingly,  $\tau_{w0}/\sigma_{w0}$  is calculated as 0.78 for the investigated material, which is slightly higher than the reported value.

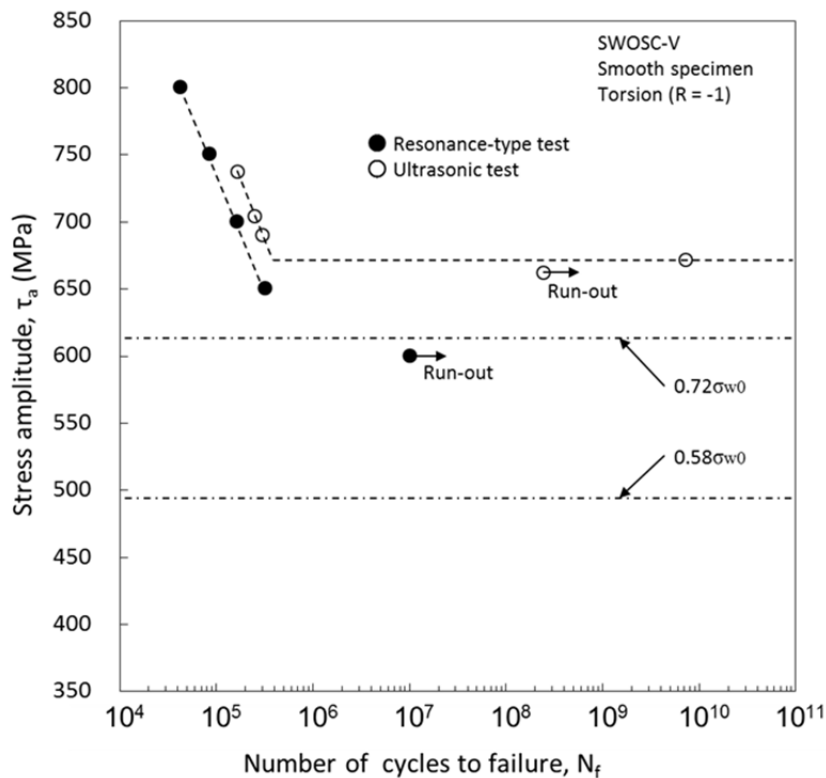


Figure 2: S-N data of smooth specimen.

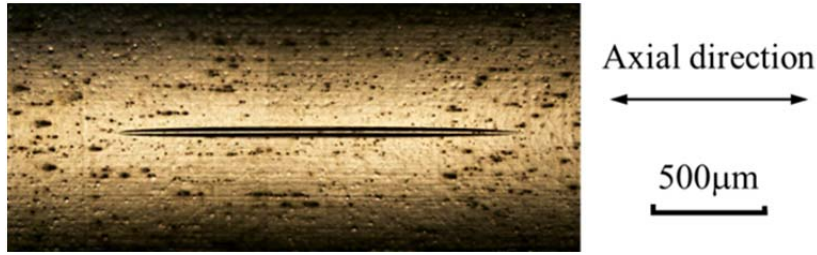
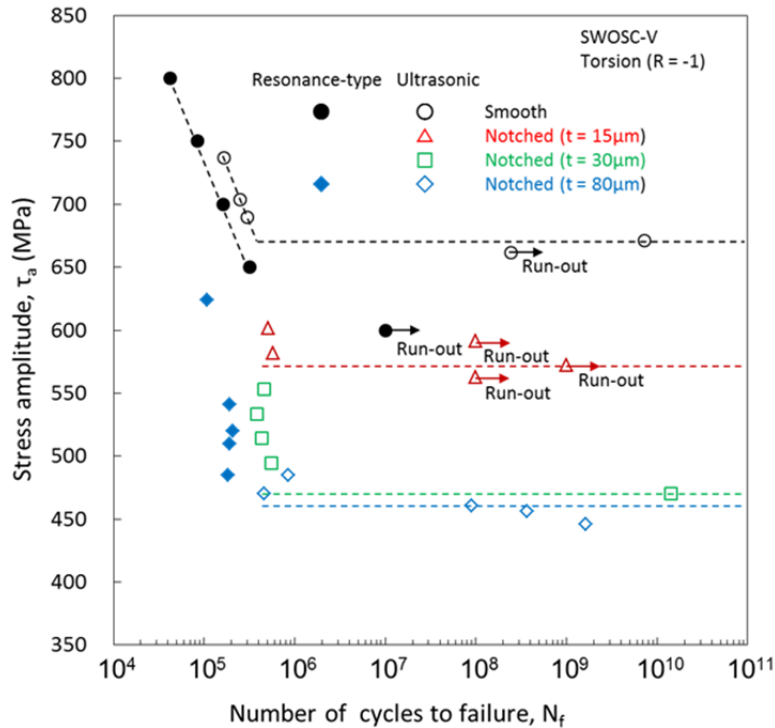


Figure 3: Artificial scratch with notch depth of  $t = 15 \mu\text{m}$

Fig. 3 shows an artificial scratch introduced at the center of specimen by using a special gadget. Electro-polishing was conducted to remove a layer of  $10\sim 15 \mu\text{m}$  thickness at the notch root and the fatigue test was conducted accordingly. Uniaxial fatigue limit with a small circumferential notch can be predicted by the following equation [3]:

$$\sigma_w = \frac{1.43 \cdot (HV+120)}{(\sqrt{\text{area}})^{1/6}}, \quad \text{where } \sqrt{\text{area}} = \sqrt{10} t \quad (2)$$

Here,  $\sqrt{\text{area}}$  (in  $\mu\text{m}$ ) represents the square root of the defect projected onto the plane perpendicular to the loading direction and  $t$  (in  $\mu\text{m}$ ) is the notch depth. As shown by Eq. (2), fatigue limit is governed by the notch depth,  $t$ , not by the notch root radius,  $\rho$ . It is noted that the accuracy of Eq. (2) is within 10 % for a wide variety of steels [3]. For steel specimens in the presence of small defect, it is known that the ratio between torsional and uniaxial fatigue limit,  $\tau_w/\sigma_w$ , is about 0.85. Fig. 4 shows the  $S-N$  data of notched specimens. Based on Fig. 4, torsional fatigue limit is experimentally determined as  $\tau_w = 572 \text{ MPa}$  for  $t = 15 \mu\text{m}$ ,  $\tau_w = 470 \text{ MPa}$  for  $t = 30 \mu\text{m}$  and  $\tau_w = 461 \text{ MPa}$  for  $t = 80 \mu\text{m}$ . Correspondingly, by using Eq. (2),  $\tau_w/\sigma_w$  is calculated as  $1.07 \sim 1.24$  that is much higher than the values of 0.85 [9]. This is a unique characteristic of fatigue behavior with the scratch, and a further study will be conducted to reveal the reason based on the view point of mechanics.



**Figure 4:** S-N data of Notched specimen (Dotted lines represent the respective fatigue limits). It is widely recognized that fatigue limit of notched components is frequently dictated not by crack initiation, but by the critical condition for the propagation of a short crack at the root of a notch. Therefore, the boundary between propagation and non-propagation separates the safe from the potentially unsafe fatigue regime. Fig. 5 shows the propagating cracks observed at the notch root of failed specimen with  $t = 15 \mu\text{m}$ . As shown in Fig. 5, mode II cracks were observed at  $N = 2.0 \times 10^4$  cycles, and mode II cracks were connected with each other at  $N = 5.0 \times 10^4$  cycles. Then mode I cracks were initiated and propagated at  $N = 2.0 \times 10^5 \sim 5.0 \times 10^5$  cycles, and finally the specimen fractured at  $N = 5.1 \times 10^5$  cycles. In other words, mode II cracks initiate at early number of cycles before  $N/N_f = 0.04$ , on the other hand, mode I cracks initiate before  $N/N_f = 0.4$ . This result indicates that the torsional fatigue life mostly devoted to the propagation of mode I fatigue crack.

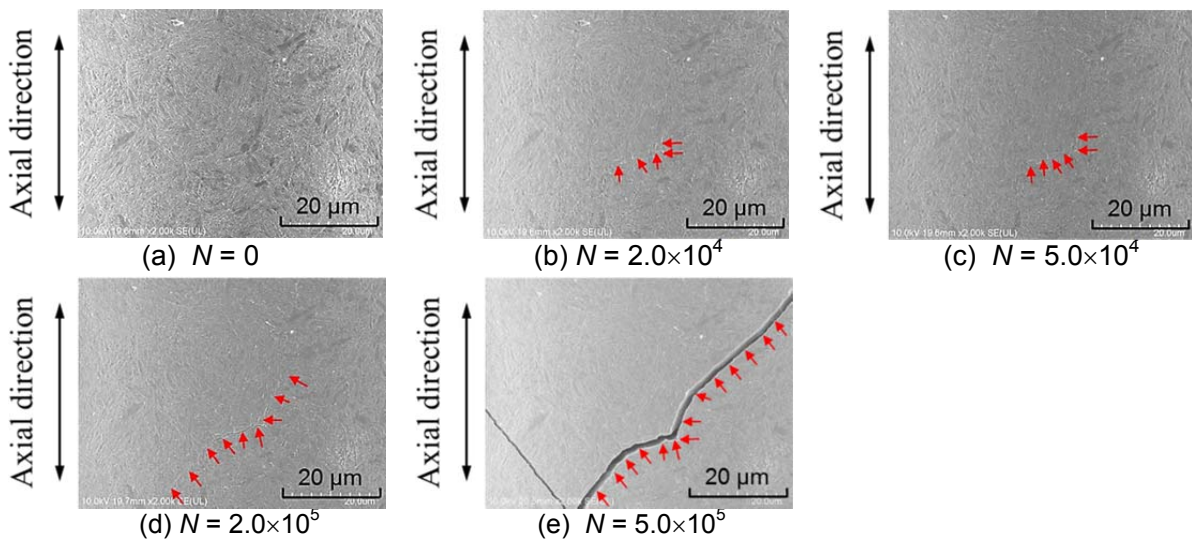


**Figure 5:** Propagating crack observed at the notch root with  $t = 15 \mu\text{m}$ . (Stress amplitude was  $\tau_a = 601 \text{ MPa}$  and fractured at  $N = 5.1 \times 10^5$  cycles)

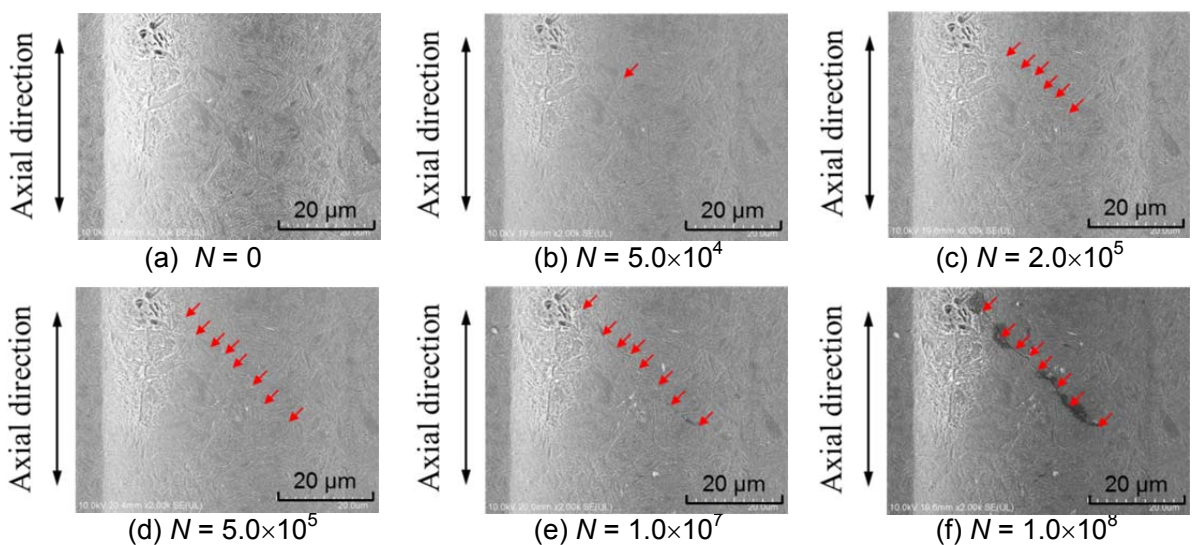


**Figure 6:** Non-propagating cracks observed at the notch root with  $t = 15 \mu\text{m}$  (Stress amplitude was  $\tau_a = 592 \text{ MPa}$  and endured  $N = 1.0 \times 10^8$  cycles)

Fig. 6 shows the non-propagating cracks observed at the notch root of run-out specimen with  $t = 15 \mu\text{m}$ . As shown in Fig. 6, mode II cracks were observed at  $N = 5.0 \times 10^4$  cycles, and mode I cracks were initiated at  $N = 2.0 \times 10^5$  cycles and propagated until  $N = 1.0 \times 10^7$ , and mode I cracks finally stopped the propagation after  $N = 1.0 \times 10^7$  cycles. Namely, non-propagating mode I crack was observed at the notch root. That is to say, this result indicates that torsional fatigue limit is governed by propagation of mode I crack and is the same as for uniaxial fatigue limit.

## CONCLUSIONS

In this study, torsional fatigue tests were conducted to examine torsional fatigue behavior in high cycle and very high cycle fatigue regimes by using different types of machine. To study the effects of small scratch, the small longitudinal notch was carefully introduced at the specimen surface. Compared to uniaxial fatigue, a notable degradation of the torsional fatigue limit was not observed. The present investigation confirms that torsional fatigue limit with small longitudinal notch is governed by the propagation of mode I crack.

## REFERENCES

- [1] N. Ibaragi, Developments in automotive valve spring wire rods (in Japanese), Kobe Steel Engineering Reports, 50(2000), 27-30.
- [2] Y. Akiniwa, S. Stanzi-Tschegg, H. Mayer, M. Wakita, K. Tanaka, Fatigue strength of spring steel under axial and torsional loading in the very high cycle regime, Int. J. Fatigue, 30(2008), 2057-2063.
- [3] Y. Murakami, Metal fatigue: Effects of small defects and nonmetallic inclusions, Elsevier, New York, 2002.
- [4] M. Endo, K. Yanase, Effects of small defects, matrix structures and loading conditions on the fatigue strength of ductile cast irons, Theor. Appl. Fract. Mec., 69(2014), 34-43.
- [5] K. Yanase, M. Endo, Multiaxial high cycle fatigue threshold with small defects and cracks, Eng. Fract. Mech., 123(2014), 182-196.
- [6] B.M. Schönbauer, K. Yanase, M. Endo, VHCF properties and fatigue limit prediction of precipitation hardened 17-4PH stainless steel, Int. J. Fatigue, 88(2016), 205-216.
- [7] B.M. Schönbauer, K. Yanase, M. Endo, The influence of various types of small defects on the fatigue limit of precipitation-hardened 17-4PH stainless steel, Theor. Appl. Fract. Mech., 87(2017), 35-49.
- [8] B.M. Schönbauer, K. Yanase, M. Endo, Influences of small defects on torsional fatigue limit of 17-4PH stainless steel, Int. J. Fatigue (in press).
- [9] M. Endo, The multiaxial fatigue strength of specimens containing small defects, In: Biaxial/Multiaxial Fatigue and FractureESIS Publication 31, Elsevier, Oxford, 2003, 243-264.
- [10] M. Endo, Effects of small defects on the fatigue strength of steel and ductile cast iron under combined axis/torsional loading, In: Small Fatigue Cracks: Mechanics, Mechanisms and Application, 1999, 355-387.
- [11] M. Endo, I. Ishimoto, The fatigue strength of steels containing small holes under out-of-phase combined loading, Int. J. Fatigue, 28(2006), 592-597.
- [12] K. Yanase, A study on the multiaxial fatigue failure criterion with small defects, ASTM Mater. Perform. Charact., 2(2013), 371-390.

**Corresponding author:** YOSHIROU\_NISHIMURA@denso.co.jp

# NONLINEAR AND SCALING PHENOMENA OF DAMAGE ACCUMULATION, CRACK INITIATION AND PROPAGATION IN VHCF

O. Naimark<sup>1)</sup>, T.Palin-Luc<sup>2)</sup>

<sup>1)</sup>Institute of Continuous Media Mechanics UB RAS,  
1 Acad.Korolev str., 614013 Perm Russia

<sup>2)</sup>Univ.Bordeaux, 12M, UMR5295, 351 Cours de la Liberation, 33405 Talence,  
France

## ABSTRACT

Nonlinear multiscale damage kinetics in VHCF is based on statistical field model of collective behavior of defects (slip bands, microshears, microcracks) and representation of defect induced stored energy release in term of damage parameter (defect induced strain). It was shown that damage-failure transition stages can be linked to specific type of criticality in out-of-equilibrium system "solid with defects" - structural-scaling transition. Stages of crack nucleation and propagation are analyzed using the profilometry data from the fracture surface. The scale invariance of fracture surface roughness is established, which allows an explanation of the self-similar nature of fatigue crack kinetics under very high cycle fatigue. Variation of elastic-plastic properties of Armco iron under VHCF is studied using an acoustic resonance method. It is found that the material density decreases during fatigue damage accumulation, with the minimum of the material density in the bulk of the specimen.

## KEYWORDS

Very high cycle fatigue, nonlinear damage-failure kinetics, defect induced transition

## INTRODUCTION

Nonlinear damage kinetics in VHCF based on statistical field model of collective behavior of defects (slip bands, microshears, microcracks) and corresponding representation of defect induced stored energy release in term of damage parameter (defect induced strain) were used for the interpretation of characteristic fracture surface morphology related to self-similar solution for damage localization kinetics (blow-up regimes) and the process zone formation at the crack providing the crack advance. VHCF experiment (Shimadzu USF2000) for conventional, fine grain titanium sample allowed one to establish links of roughness scale invariance with characteristic structural scales and explanation of transformation of the Paris law into the Paris-Herzberg law. Criticality features related to the self-similar damage-failure transition kinetics were used for the definition of VHCF stages and explanation of typical VHCF fracture surface pattern (the fish-eye and FGA areas). It was shown that FGA morphology can be linked to critical grain refining and formation of dislocation free grains providing blow-up damage kinetics and crack initiation. The elastic-plastic properties during fatigue loading were studied for the Armco iron samples at the VHCF post-test using the acoustic resonance method that allowed the estimation of damage induced sample softening. The consequent narrowing of the samples subject to frequency analysis demonstrates the damage localization in the central part of the sample for VHCF load conditions.



## **DAMAGE-FAILURE TRANSITION IN VHCF**

Fatigue damage is traditionally associated with microplastic deformation [1] under cyclic loading that induces various microstructural mechanisms of control of the fatigue life. A qualitative difference of VHCF is the fatigue crack initiation in the material bulk [2]. This radically alters the statement of the problem of fatigue life evaluation and implies the development of new approach, experimental and structural methods for studying fracture stages. Non-local damage kinetics [3] was proposed as the field model of collective behavior of defects (slip bands, microsensors, microcracks) and based on representation of defect induced stored energy release in term of damage parameter (defect induced strain). It was shown that damage-failure transition stages can be linked due metastability of stored energy to specific type of criticality in out-of-equilibrium system "solid with defects", the structural-scaling transition. Defect induced stored energy release kinetics in the presence of non-locality for damage parameter leads to the generation of multiscale collective modes providing the qualitative different mechanisms of structural relaxation: slip bands with autosolitary wave dynamics and blow-up dissipative structures related to the final stage of damage localization and crack initiation. Scenario of structural-scaling transition includes the consequent transition between mentioned types of collective modes that allows the links of characteristic stages of damage-failure transition (fatigue crack initiation and propagation. This "phase field model" provides the interpretation of mechanisms of the "fish-eye" origin as the blow-up damage kinetics over characteristic spatial scale. The replacement of fatigue crack initiation from the near-surface area for HCF regime into the bulk of sample for VHCF has the similarity with the failure scenario in the creep conditions (constant stress), when the stress decrease leads to the replacement of crack initiation area into the bulk of sample [4], that can be not generally linked to the interior inclusions. Mechanism of structural relaxation that is caused by autosolitary wave dynamics of slip band formation allowed the explanation of the power universality of the Paris law for the fatigue crack kinetics for both HCF and VHCF regimes.

## **MATERIAL AND TESTING**

Titanium samples in conventional polycrystalline state (Grade-4, grain size of 25  $\mu\text{m}$ ) and submicrocrystalline (SMC, grain size 100-150 nm) were studied. Fatigue test was carried out on the ultrasonic machine Shimadzu USF-2000, which imposes special loading due to the resonance conditions and formation of a standing wave in the central cross-section of the sample. Failure of titanium samples occurred after  $10^9$  loading cycles at 275 MPa stress amplitudes for the conventional state and 375 MPa for the SMC states. The SMC titanium exhibits more high fatigue properties compared to the titanium with conventional polycrystalline state.

## **MECHASMS AND SCALING ANALYSIS OF FRACTURE SURFACE**

Mechanisms of initiation and propagation of fatigue cracks were investigated by means of qualitative and quantitative study of the morphology of fracture surfaces. Qualitative scenario of fracture can be linked to optical and electron microscopy study of fracture surface, that revealed specific fracture pattern characteristic for VHCF fatigue regime: the origination of the damage localization area as the so-called "fish-eye" zone [1,2]. Optical microscopy allows one to separate zones with different reflectivity: dark Zone 1 with a radius of 150  $\mu\text{m}$  from the crack origin are and light smooth Zone 2, which is then replaced by the rough surface area (Fig. 1).

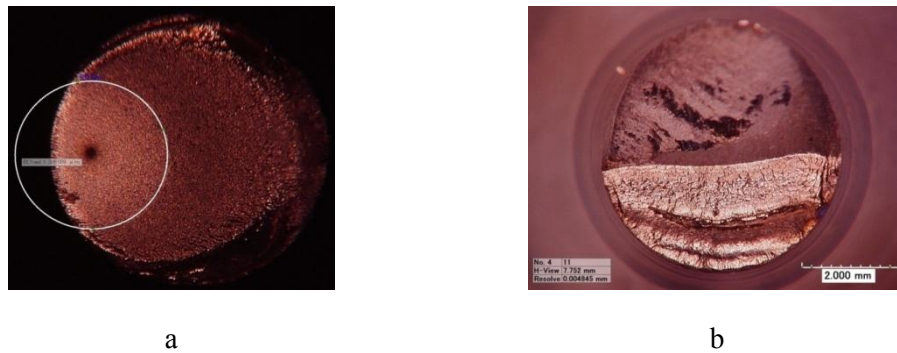


**Fig. 1:** Optical microscope images of fracture surface of Ti: a) crack initiation in the bulk of sample b) crack initiation at the fracture surface

Distinct zones with different roughness were observed (Fig. 2): Zone 1 with the size  $\sim 100\text{--}300\ \mu\text{m}$  (depending on testing material), which corresponds to the area of defect initiation and accumulation during cyclic loading; Zone 2 that is smoother than Zone 1 and corresponds to the crack propagation stage according to the Paris law. These results support mentioned fatigue failure mechanism described by Mughrabi [6].

The surface roughness was analysed by interferometer-profiler New View 5010 to establish quantitative characteristics of the fracture surface in terms of scaling invariants. To investigate the scale-invariant properties of the fracture surface, one-dimensional profiles corresponding to the cross-section of 2D roughness profiles were analyzed using the interferometer New View data.

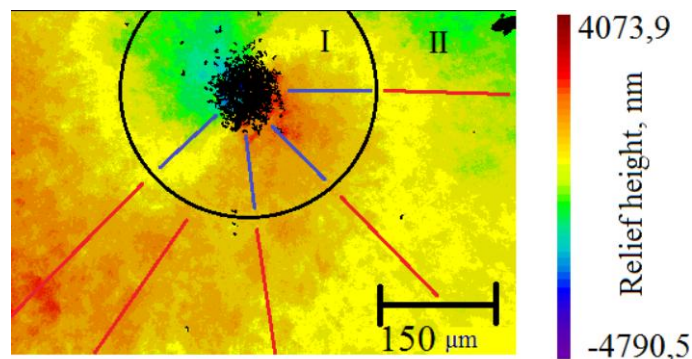


**Fig.2:** 2D collared fracture surface measured by interferometer New View 5010. Zones I and II are the areas of crack initiation and propagation, respectively. Solid lines are cross-sections of surface roughness used for the estimation of scale invariance (the Hurst exponent)

The scale invariance (the Hurst exponent  $H$ ) was defined from the slope of linear portion of the correlation function  $C(r) = \langle (z(x+r) - z(x))^2 \rangle_x^{1/2} \propto r^H$  in log-log coordinates [5], where  $z(x)$  is the relief height at the coordinate  $x$ ; angular brackets denote averaging over  $x$ . The correlation function calculated from the profiles for both zones has two linear portions with a break on the scale, which corresponds to change in the fracture mechanisms. Whereas correlation functions calculated separately for Zones 1 and 2 reveal only one linear portion for each zone (Fig. 3). The roughness pattern analyzed in terms of roughness

invariance allows one to differentiate the zones of crack origination (size  $\sim 100 \mu\text{m}$ ) and the crack propagation zone.

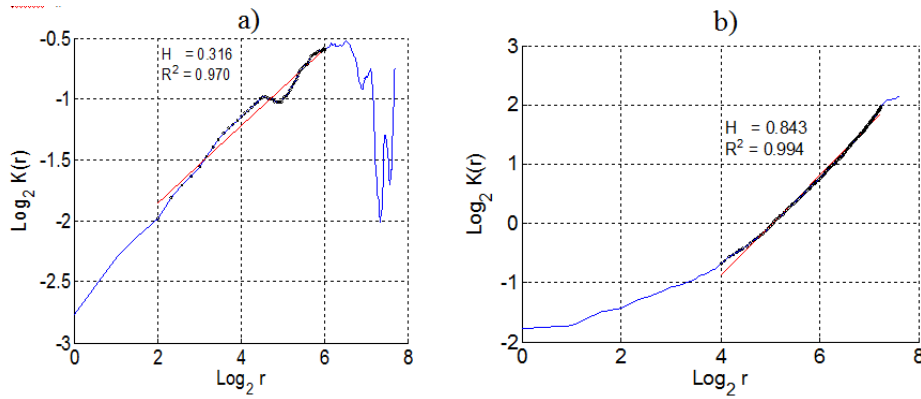


**Fig.3:** Log-log correlation function plots for Zone 1(a) and Zone 2 (b)

The linear branch of correlation function (Fig.3b) determines two characteristic scales  $l_{sc}$  and  $L_{pz}$ , where the defect induced roughness reveals correlated properties and constant value of the scale invariant (the Hurst exponent) [7].

### FATIGUE CRACK KINETICS IN HCF AND VHCF

The power universality of fatigue crack kinetics  $da/dN = A(\Delta K)^m$  in HCF determining the fatigue crack growth rate  $da/dN$  versus stress intensity factor  $\Delta K$  is the subject of intensive experimental and theoretical research. Power-law reflects the self-similar nature of fatigue crack growth due to nonlinear damage accumulation in the crack tip area (process zone) [8]. The link of damage induced self-similarity and structural scaling were studied using characteristic structural scales  $l_{sc}$  and  $L_{pz}$  determining the area of roughness correlated properties for Zone 2 (Fig.3b). To include these scales into the list of variables the fatigue crack kinetics reads

$$\frac{da}{dN} = F(\Delta K, E, l_{sc}, L_{pz}), \quad (1)$$

where  $E$  is Young's modulus, the scale  $l_{sc}$  is the minimum spatial scale in the vicinity of the crack tip on which scale-invariant properties of the fracture surface relief begin to show up,  $L_{pz}$  is the characteristic scale of the process zone at the crack tip. Following the  $\Pi$ -theorem [9] the dimensionless form (1) can be represented as

$$\frac{da}{dN} = l_{sc} \Phi \left( \frac{\Delta K}{E \sqrt{l_{sc}}}, \frac{L_{pz}}{l_{sc}} \right). \quad (2)$$

By evaluating  $\Delta K / (E \sqrt{l_{sc}}) \ll 1$  and  $L_{pz} / l_{sc} \gg 1$ , we can suggest the intermediate asymptotic nature of crack growth kinetics and write (2) in the form

$$\frac{da}{dN} = l_{sc} \left( \frac{\Delta K}{E\sqrt{l_{sc}}} \right)^\alpha \left( \frac{L_{pz}}{l_{sc}} \right)^\beta, \quad (3)$$

where  $\alpha$  and  $\beta$  are exponents determining the intermediate asymptotic kinetics of crack growth in terms of dimensionless variables. To introduce the parameter  $\Delta K_{eff} = \Delta K(L_{pz}/l_{sc})^{\beta/\alpha}$  Eq. (3) can be represented in the form

$$\frac{da}{dN} = l_{sc} \left( \frac{\Delta K_{eff}}{E\sqrt{l_{sc}}} \right)^\alpha. \quad (4)$$

It follows from (4) that at  $L_{pz} \rightarrow l_{sc} \rightarrow b$ , ( $b$  is the value of the Burgers vector)  $\Delta K_{eff} \rightarrow \Delta K$  and fatigue crack kinetics corresponds to the Herzberg form  $da/dN = b(\Delta K/(E\sqrt{b}))^\alpha$  [9]. This result reflects the qualitative difference of crack kinetics under transition from HCF to VHCF when the fatigue crack growth reveals increasing sensitivity to damage evolution at the crack tip area, that is characteristic for damage-failure transition as the critical phenomenon [10].

## ELASTIC-PLASTIC PROPERTIES OF ARMCO IRON DURING VHCF

To determine changes in elastic-plastic properties during fatigue loading, the Armco iron samples are post-test analyzed by the acoustic resonance method with the composite piezoelectric actuator using longitudinal harmonic loading with frequencies of about 100 kHz. The elastic modulus and amplitude-independent decrement are measured in a wide range of strain amplitudes. Rod samples for the acoustic test was machined from initial specimens (30 mm in length and  $d \approx 5$  mm in diameter) that provided the resonance frequency  $f$  of longitudinal oscillations of about 100 kHz. The method used allows an investigation of ultrasound absorption (internal friction) and inelastic (microplastic) properties. Defect induced influence on inelastic properties are obtained from the measurement of the elastic modulus and elastic vibration decrement in a broad range of strain amplitude. It was established the nonlinear amplitude-dependent absorption correlated with the elastic modulus decrease. Experimental data shows that an increasing number of cycles lead to an increase in sample softening due to the damage associated with defects. The consequent mechanical polishing of the samples subject to mentioned frequency analysis demonstrates the damage localization in the central part of the sample for VHCF load conditions.

## CONCLUDING REMARKS

1. Nonlinear damage kinetics based on statistical field model of collective behavior of defects (slip bands, microshears, microcracks) and corresponding representation of defect induced stored energy release in term of damage parameter (defect induced strain) allowed the interpretation of characteristic fracture surface morphology related to self-similar solution for damage localization kinetics (blow-up regimes) and the process zone formation at the crack providing the crack advance.
2. Correlation analysis of defect induced roughness of fracture surface for the titanium samples in conventional and fine grain states subject to VHCF loads established the links of roughness scale invariance with characteristic structural scales and allowed the explanation of transformation of the Paris law of fatigue crack kinetics into the Paris-Herzberg law.

3. Criticality features related to the self-similar damage-failure transition kinetics allowed the interpretation of VHCF stages and explanation of typical VHCF fracture surface pattern (the fish-eye and FGA areas). It was shown that FGA morphology can be linked to critical grain refining and formation of dislocation free grains providing blow-up damage kinetics and crack initiation.
4. Study of elastic-plastic properties during fatigue loading for the Armco iron samples at the VHCF post-test using the acoustic resonance method allowed the estimation of damage induced sample softening. The development of original technique based on the estimation of defect induced softening for the consequent narrowing samples for different stages of VHCF loads supported theoretical prediction of the damage localization in the bulk of samples that can be not associated with interior inclusion.

## REFERENCES

- [1] Bathias C., Paris P.C.:  
Gigacycle Fatigue in Mechanical Practice  
Marcel: Dekker Publisher Co., 2005.
- [2] Mughrabi, H.:  
Specific Features and Mechanisms of Fatigue in the Ultrahigh-Cycle Regime  
Int. J. Fatigue, vol. 28 (2006), pp. 1501–1508
- [3] Naimark O.B.:  
Defect induced transitions as mechanisms of plasticity and failure in multifield continua, in: Advances in multifield theories of continua with substructure ( edited by G.Capriz, P.Mariano) Birkhauser, Boston, 2004, pp.75-114.
- [4] Naimark O.B., Silbershmidt V.V.:  
On the fracture of solids with microcracks  
Eur.J.Mech., A/Solids, vol. 10 (1991), pp.607-619.
- [5] Oborin V., Bannikov M., Naimark O., Palin\_Luc T.  
Scaling invariance of fatigue crack growth in gigacycle loading regime  
Technical Physics Letters, 36(2010), pp.1061–1063
- [6] Mughrabi H.:  
Microstructural Fatigue Mechanisms: Cyclic Slip Irreversibility, Crack Initiation, Non-Linear Elastic Damage Analysis  
Int. J. Fatigue, vol. 57(2013), pp. 2–8.
- [7] Froustey C., Naimark O., Bannikov M., Oborin, V.:  
Microstructure Scaling Properties and Fatigue Resistance of Pre-strained Aluminium Alloys Eur. J. Mech. A. Solids, vol. 29(2010), pp. 1008–1014
- [8] Oborin V., Bannikov M., Naimark O., Froustey C.:  
Long-Range-Correlation Large-Scale Interactions in Ensembles of Defects:  
Estimating Reliability of Aluminium Alloys under Dynamic Cycling and Fatigue Loading  
Tech. Phys. Lett., vol. 37(2011), pp. 241–243
- [9] Bannikov M.V., Naimark O. B., Oborin V.A.:  
Experimental Investigation of Crack Initiation and Propagation in High- and Gigacycle Fatigue in Titanium Alloys by Study of Morphology of Fracture  
Frattura ed Integrità Strutturale, vol. 35(2016), pp. 50–56.
- [10] Naimark O.B.:  
Energy release rate and criticality of multiscale defects kinetics  
Int.J.Fracture, vol.202(2016), pp. 271-279.

# A PHYSICALLY BASED CONSTITUTIVE EQUATION FOR FATIGUE CRACK GROWTH IN METALS

K. S. Ravi Chandran  
Department of Metallurgical Engineering, The University of Utah  
135 South 1460 East Rm. 412, Salt Lake City, UT 84112, USA  
Email: ravi.chandran@utah.edu

## ABSTRACT

A physically based constitutive equation to represent the fatigue crack growth (FCG) behavior of materials under high-cycle fatigue (HCF) is presented in this work. It is shown that the constitutive equation can be deduced, intuitively, from the constitutive equation for stress-life (S-N) fatigue behavior, which is given in a companion paper presented at this conference. Remarkably, the parameters of fatigue crack growth equation are derived from that of S-N constitutive equation, making it possible to invert the S-N curve into the fatigue crack growth curve and vice-versa. The fatigue crack growth equation is shown to describe quite accurately the three-stage behavior, including the asymptotic behavior near threshold and in fast fracture regimes, for several materials. The equations are applicable to a wide range of fatigue crack growth rates and fatigue lives, including that in the VHCF regime.

## KEYWORDS

Fatigue crack growth, S-N curve, constitutive equation, physical model, asymptotic behavior, exponential function, threshold, fast fracture

## INTRODUCTION

Currently, fatigue crack growth behavior (FCG) in high cycle fatigue (HCF) is empirically characterized by the fracture mechanics based Paris' equation<sup>1</sup> and, its modification to account for mean-stress effects, the Foreman equation<sup>2</sup>. These equations have been used widely to characterize fatigue crack growth, but they are not suitable to represent the entire three-stage fatigue crack growth behavior. In addition, these are empirical equations and lack the physical basis. A physical model of the crack growth process is used here to develop a constitutive equation that can represent the three-stage fatigue crack growth behavior.

## THE CONSTITUTIVE EQUATION FOR S-N FATIGUE BEHAVIOR

At stresses above the endurance stress limit, fatigue damage begins with the formation of an incipient micro-crack from a persistent-slip-band (PSB). The growth of this micro-crack, through the specimen, is considered to determine the fatigue life,  $N_f$ . In our previous work<sup>3</sup>, the growth of the micro-crack in fatigue was modeled as a continuous process of increase in cyclic strain energy on the uncracked ligament, which accelerates the crack growth process. In another work<sup>4</sup> it was shown, through a universally applicable functional, that the normalized remaining fatigue life is proportional to the normalized remaining uncracked section size of the fatigue specimen. Integration of the basic crack growth equation with the substitution of functional and the imposition of the essential boundary conditions resulted<sup>5</sup> in a constitutive equation for stress-life (S-N) fatigue behavior. The S-N constitutive equation is

$$\left(\frac{\sigma_a - \sigma_e}{\sigma_u - \sigma_e}\right) = \exp\left\{-C_n (N_f)^{m_n}\right\} \quad (1)$$

where  $\sigma_a$ ,  $\sigma_u$  and  $\sigma_e$  are fatigue stress amplitude, tensile strength and endurance limit stress, respectively. The parameters of the equation are  $C_n$  and  $m_n$  (which determine the shape of the S-N curve) and the physical boundary conditions,  $\sigma_u$  and  $\sigma_e$  (which determine the asymptotic behavior of the S-N curve at the ends). Equation (1) represents the constitutive equation for S-N fatigue behavior at the stress ratio,  $R=0$ .

## FORMULATION OF FATIGUE CRACK GROWTH EQUATION

It is shown here that a fatigue crack growth equation can be deduced, intuitively, from the S-N fatigue equation. Equation (1) can be rearranged by writing the stresses, with “ $\Delta$ ,” as

$$\Delta\sigma(N_f) = \Delta\sigma_e + \{\Delta\sigma_{cf} - \Delta\sigma_e\} \exp\{-C_n(N_f)^{m_n}\} \quad (2)$$

During the fatigue of a smooth specimen, fatigue crack growth occurs throughout the life of the sample by the growth of an incipient micro-crack to final failure. Therefore, each of the stress amplitudes in Eq. (1) can be converted to equivalent fracture mechanics parameters, for the growing fatigue crack, using the following relations:

$$\Delta K = \Delta\sigma\sqrt{\pi a}F \quad \Delta K_{th} = \Delta\sigma_e\sqrt{\pi a}F \quad \& \quad \Delta K_{cf} = \Delta\sigma_{cf}\sqrt{\pi a}F \quad (3)$$

where  $a$  is the crack size and  $F$  is the finite-width correction factor. In writing Eq. (3), we follow the conventions of using  $\Delta K$  for the description of fatigue crack growth behavior of a cracked sample. In fracture mechanics approach to fatigue, the theoretical restrictions on crack size or the plastic zone size, which qualify  $K$  as the linear-elastic stress intensity factor, are often ignored because  $\Delta K$  serves as a useful parameter to correlate fatigue crack growth in a nominally elastic specimen. The interpretation here is that (i) in the limit of zero growth rate, the physical endurance limit stress ( $\Delta\sigma_e$ ) should correspond to the fatigue threshold ( $\Delta K_{th}$ ) of the initial micro-crack and (ii) in the limit of unstable crack growth, the tensile strength ( $\Delta\sigma_{cf} = \sigma_u$  for  $R=0$ ) should correspond to the fracture toughness ( $\Delta K_{cf} = K_c$  for  $R=0$ ). On this basis, the relationships in Eq. (3) are considered to be valid. Multiplying the both sides of the equation (2), by  $\sqrt{\pi a} F(a/W)$ , the S-N equation for the smooth specimen can be converted into the equation for fatigue crack growth:

$$\Delta K(N_f) = \Delta K_{th} + \{\Delta K_{cf} - \Delta K_{th}\} \exp\{-C_n(N_f)^{m_n}\} \quad (4)$$

Equation (4), in this rudimentary form, is actually the descriptor of growth behavior of a fatigue crack, driven by  $\Delta K$ , with the terminal conditions of the growth specified by  $\Delta K_{th}$  and  $\Delta K_{cf}$ . In Eq. (4),  $N_f$  takes the meaning of fatigue life for the growth of a crack through unit length, as discussed below.

The crack in a fatigue specimen grows under increasing  $\Delta K$  or net-section stress, which accelerates the crack. If we consider the situation of local extension of the crack (as specified by the growth rate,  $da/dN$ ), the rate at that point is determined by the  $\Delta K$  or the net-section stress at that time. Weibull<sup>6,7</sup> performed extensive experiments to show that if a constant net-section stress (or constant  $\Delta K$ ) is maintained during fatigue crack growth, by appropriate load reduction, then the fatigue crack grows at a constant rate. This means that for a given  $\Delta K$ , the ‘ $dN$ ’ is the number of failure cycles for fatigue fracture over the crack length, ‘ $da$ ’, which is the growth during a period of constant  $\Delta K$  or net-section stress. Alternatively, the inverse of crack growth rate,  $dN/da$ , is the number of cycles for the advancement of crack by unit length. This can be expressed as

$$\frac{dN}{da} = \left\{ \frac{N_f}{1} \right\} \quad (5)$$

Hence, in equation (4),  $N_f$  on the right side is actually equal to  $dN/da$ , for a given  $\Delta K$  on the left side, because they apply to the extent of local crack growth at that interval. Therefore,

$$\Delta K = \Delta K_{th} + \{ \Delta K_{cf} - \Delta K_{th} \} \exp \left\{ -C_n \left[ \frac{dN}{da} \right]^{m_n} \right\} \quad (6)$$

Rearranging Eq. (6),

$$\frac{da}{dN} = \left\{ \frac{1}{C_n} \right\}^{-\frac{1}{m_n}} \left[ -\ln \left\{ \frac{\Delta K - \Delta K_{th}}{\Delta K_{cf} - \Delta K_{th}} \right\} \right]^{-\frac{1}{m_n}} \quad (7)$$

which can be written in the condensed form as

$$\frac{da}{dN} = \alpha \left[ -\ln \left\{ \frac{\Delta K - \Delta K_{th}}{\Delta K_{cf} - \Delta K_{th}} \right\} \right]^\beta \quad (8)$$

$$\text{Where } \alpha = \left\{ \frac{1}{C_n} \right\}^{-\frac{1}{m_n}} \text{ and } \beta = -\frac{1}{m_n} \quad (9)$$

It can be seen that the constants  $\alpha, \beta$  characterizing fatigue crack growth behavior can be determined from the constants  $C_n$  and  $m_n$  in the S-N constitutive equation (1). Equation (8) is remarkably compact and by choosing appropriate values of  $\Delta K_{th}$  and  $\Delta K_{cf}$ , the three-stage FCG behavior can be reliably represented.

Material	$\sigma_e$ (MPa)	$\sigma_u$ (MPa)	$C_n$	$m_n$	$\Delta K_{th}$ (MPa $\sqrt{m}$ )	$\Delta K_{cf}$ (MPa $\sqrt{m}$ )	$\alpha$	$\beta$
2219-T851	180	455	0.027	0.25	3.4	35	5.3E-7	-4
6061-T6	135	340	0.026	0.25	4.5	50	4.6E-7	-4
Ti-6Al-4V	610	1070	0.037	0.22	3.5	55	3.1E-7	-4.5
Ti-10V-2Fe-3Al	830	1050	0.024	0.28	3.9	95	1.4E-6	-3.6

Table 1. Parameters for the S-N and FCG constitutive equations

## EXPERIMENTAL VALIDATION

The experimental S-N data and the FCG data for several materials are used here to show that the fatigue crack growth data (or curve) can be determined from the S-N data (or curve), using the present approach. Figure 1(a&b) presents the experimental fatigue crack growth data (Bucci<sup>8</sup>) and the experimental S-N data (Kaufman<sup>9</sup>), respectively, for 2219-T851 aluminum alloy. Figure 2(a&b) presents the fatigue crack growth data (Forman<sup>10</sup>) and the S-N fatigue data (Kaufman<sup>9</sup>), respectively for 6061-T6 alloy. For Ti-6Al-4V alloy, the fatigue crack growth data (Okazaki<sup>11</sup>) and the S-N data (Cao et al<sup>12</sup>) are presented in Figure 3a and b, respectively. For Ti-10V-2Fe-3Al beta-titanium alloy, the fatigue crack growth data and the S-N data (both from Jha<sup>13</sup>) are presented in Figure 4a and b, respectively. The S-N data presented here are in terms of maximum stress and they are from R~0 tests. The FCG data presented here are in terms of maximum stress intensity factor and they are for R~0 tests.



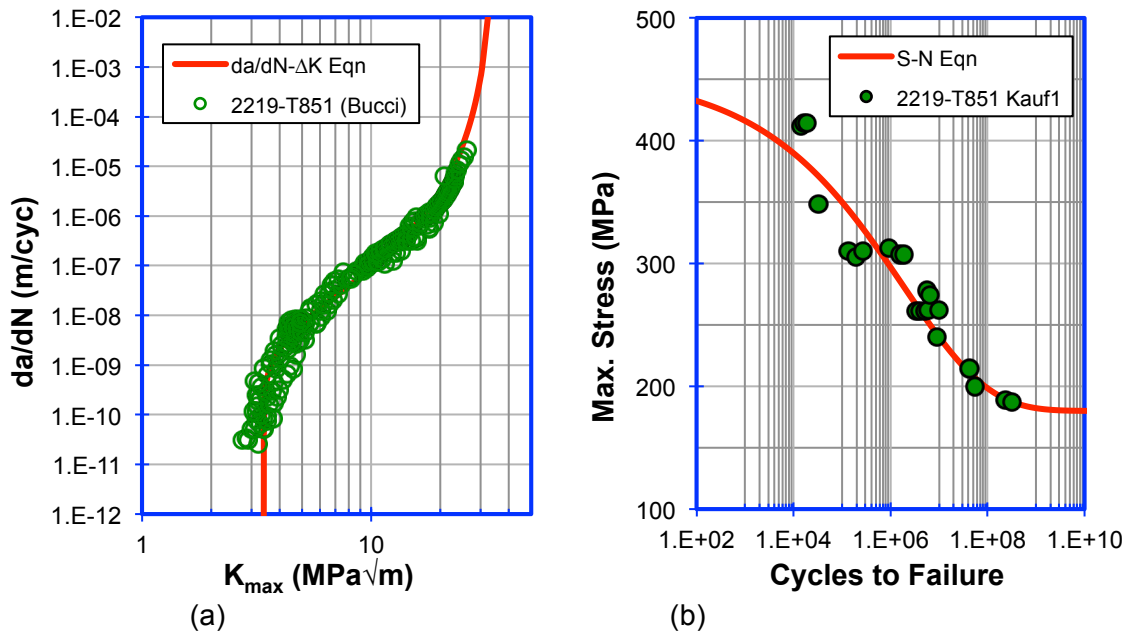


Figure 1. (a) Fatigue crack growth curve (Eq.8) and (b) S-N fatigue curve (Eq.1) for 2219-T851 Al alloy for  $R \sim 0$ , along with the respective experimental data.

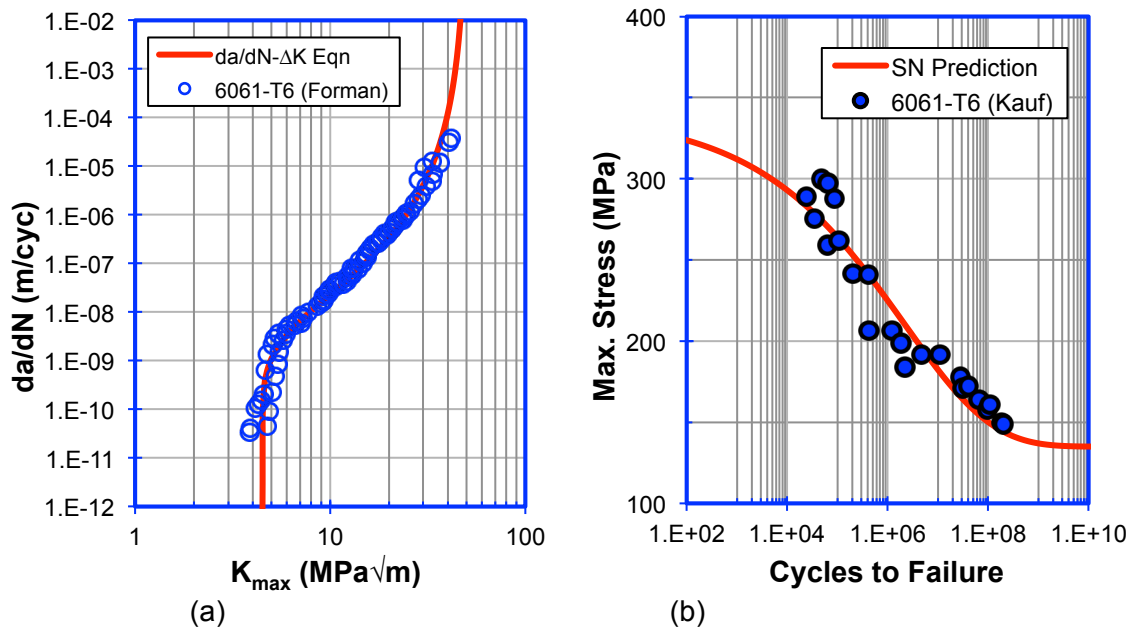


Figure 2. (a) Fatigue crack growth curve (Eq.8) and (b) S-N fatigue curve (Eq.1) for 6061-T6 Al alloy for  $R \sim 0$ . The experimental data for both cases are also shown.

The curves in Figures 1a, 2a, 3a and 4a are from the constitutive equation for FCG, Eq. (8). The curves in Figures 1b, 2b, 3b and 4b are from the S-N constitutive equation, Eq. (1)—these were first generated using the parameters in Table 1. From the  $C_n$  and  $m_n$  values of the S-N curves the corresponding  $\alpha$  and  $\beta$  parameters for FCG curves were calculated using Eq. (9). These values and the  $\Delta K_{th}$  and  $\Delta K_{cf}$  values are given in Table 1. They were used to directly generate the FCG curves shown in Figures 1a, 2a, 3a and 4a.

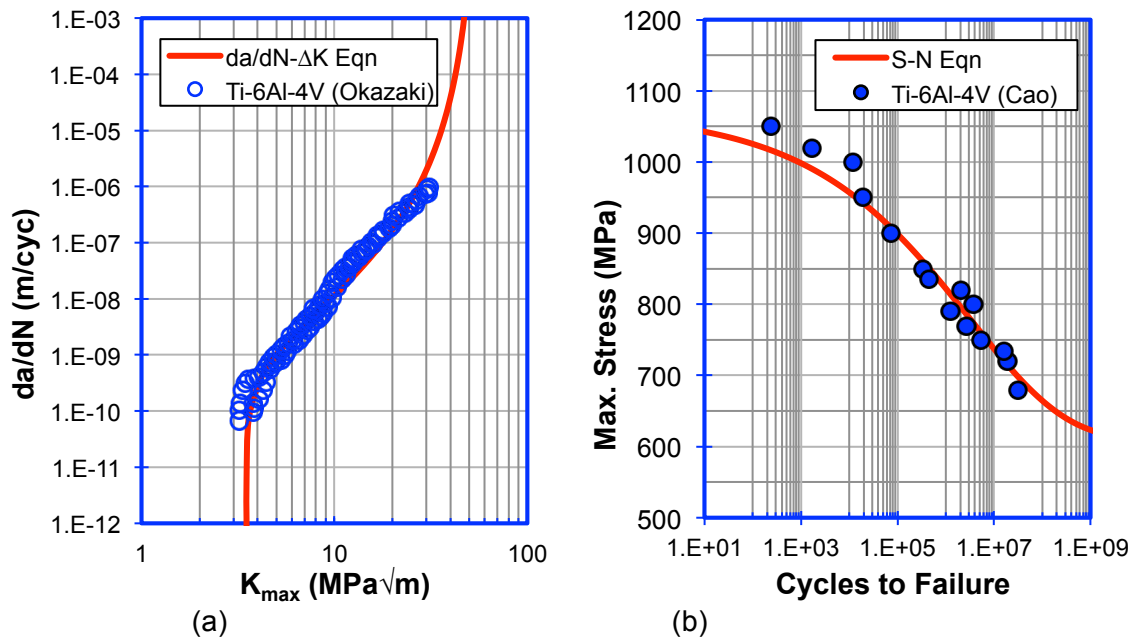


Figure 3. (a) Fatigue crack growth curve (Eq.8) and (b) S-N fatigue curve (Eq.1) for Ti-6Al-4V titanium alloy for  $R\sim 0$ , along with the respective experimental data.

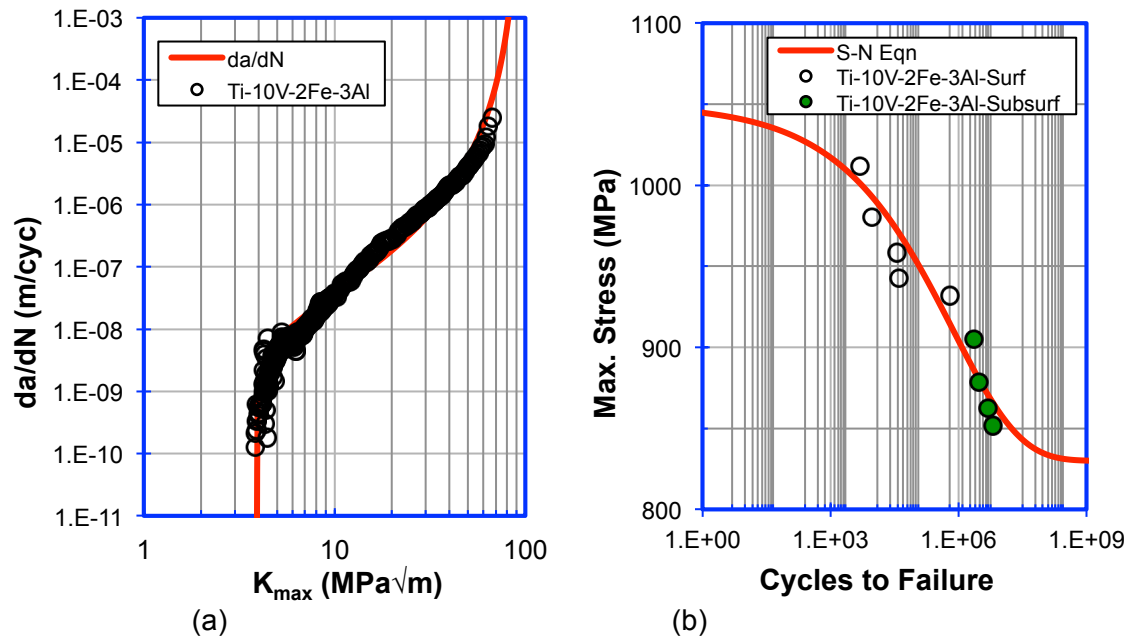


Figure 4. (a) Fatigue crack growth curve (Eq.8) and (b) S-N fatigue curve (Eq.1) for Ti-10V-2Fe-3Al beta titanium alloy for  $R\sim 0$ . The experimental data for both cases are also shown.

It is quite remarkable to see that the parameters of the S-N curve ( $C_n$ ,  $m_n$ ) automatically provide the parameters ( $\alpha$ ,  $\beta$ ) needed for the constitutive equation for fatigue crack growth. This illustrates that the S-N behavior and the fatigue crack growth behavior arise from the same physical foundation. The physical foundation is the growth of an incipient crack at stresses  $> \sigma_e$ , to final failure, and is elaborated in a companion paper at this conference and in Refs. [3]-[5]. This means that the fatigue crack growth behavior can be determined from the S-N behavior. Alternatively, the S-N behavior can be determined from the fatigue crack growth behavior by first determining  $\alpha$  and  $\beta$  from fatigue crack growth data and then

determining from them the values of  $C_n$  and  $m_n$  needed to predict the S-N fatigue behavior. This invertible nature of fatigue phenomenon is intriguing, because the complete three-stage FCG behavior can be obtained by testing a few specimens in a relatively short time, whereas the generation of complete S-N data would take a large number of samples and an enormous amount of time. Most S-N data do not contain many points at stress amplitudes close to tensile strength. Fatigue testing at such high stresses is difficult due to failure in few cycles, and specimen heating, especially when loaded at a relatively high frequency. On the other hand, testing near the asymptotic endurance stress limit might involve cycling for  $10^{10}$  cycles, which will be very time-consuming. However, generation of more data at the extremes of fatigue life will help reinforce the mutual inversion of the S-N fatigue and fatigue crack growth curves, as proposed in this work.

## CONCLUSIONS

It is shown that a physically based constitutive equation to describe the three-stage fatigue crack growth behavior can be obtained from the constitutive equation for S-N fatigue behavior. In fact, the study illustrates the mutual inversion of S-N behavior and the fatigue crack growth behavior from one to the other. Several experimental S-N fatigue data and fatigue crack growth data were used to demonstrate that both constitutive equations represent the fatigue data accurately.

## REFERENCES

- <sup>1</sup> P. C. Paris, M. P. Gomez and W. E. Anderson. A rational analytic theory of fatigue. *The Trend in Engineering*. 13 (1961) 9-14.
- <sup>2</sup> R. G. Forman, V. E. Kearney and R. M. Engle. Numerical analysis of crack propagation in cyclic loaded structures. *J. Bas. Engng. Trans. ASME ser. D* 89 (1967) 459-464.
- <sup>3</sup> K. S. Ravi Chandran, F. Cao and J. C. Newman. Fatigue crack growth in miniature specimens: The equivalence of  $\Delta K$ -correlation and that based on the change in net-section strain energy density. *Scr. Mater.* 122 (2016) 18-21.
- <sup>4</sup> K. S. Ravi Chandran. A physically based universal functional to characterize the mechanism of fatigue crack growth in materials. *Scr. Mater.* 107 (2015) 115-118.
- <sup>5</sup> K. S. Ravi Chandran. A physical model and constitutive equations for complete characterization of SN fatigue behavior of metals. *Acta. Mater.* 121 (2016) 85-103.
- <sup>6</sup> W. Weibull. The effect of size and stress history on fatigue crack initiation and propagation. *Proc. Crack Propagation Symposium, College of Aeronautics, Cranfield, UK, Vol. 2, 1961, pp. 271-286.*
- <sup>7</sup> W. Weibull. A theory of fatigue crack propagation in sheet specimens. *Acta Metall.*, 11 (1963) 745-752.
- <sup>8</sup> R. J. Bucci. Development of a proposed standard for ASTM test method for near threshold fatigue crack growth. In *Fatigue Crack Growth Measurement and Data Analysis. ASTM STP 738, ASTM International, 1981, pp. 5-28.*
- <sup>9</sup> J. G. Kaufman, *Properties of aluminum alloys: fatigue data and the effects of temperature, product form, and processing.* ASM International, 2008.
- <sup>10</sup> R.G. Forman and M. Zanganeh, Fatigue crack growth data for 6061-T6 in NASGRO 7.1
- <sup>11</sup> Y. Okazaki. Comparison of fatigue properties and fatigue crack growth rates of various implantable metals. 5 (2012) 2981-3005.
- <sup>12</sup> F. Cao and K. S. Ravi Chandran. Fatigue performance of powder metallurgy (PM) Ti-6Al-4V Alloy: A critical analysis of current fatigue data and metallurgical approaches for improving fatigue strength. *JOM.* 68, (2016) 735-746.
- <sup>13</sup> S. K. Jha. *Fatigue of Beta Titanium Alloys.* Ph.D. Thesis, Department of Metallurgical Engineering, University of Utah, Salt Lake City, UT, USA. 2001.

# STAGES OF FATIGUE DAMAGE OF PLAIN CARBON STEELS AT THE TRANSITION FROM THE HIGH CYCLE FATIGUE TO THE VERY HIGH CYCLE FATIGUE REGIME

J. Bach, M. Göken and H. W. Höppel\*

Friedrich-Alexander-Universität Erlangen-Nürnberg  
Department of Materials Science and Engineering  
Institute I: General Materials Properties,  
Martensstr. 5, 91058 Erlangen, Germany

**Keywords:** Dissipated energy, fatigue failure, damage detection, plain carbon steels

## Abstract

Fatigue life is a consequence of multistage processes. At the beginning of a fatigue experiment the cyclic deformation behavior is dominated by basic dislocation processes, like strain hardening and softening. During further cycling localization of plastic deformation takes place. Depending on the microstructures strongly localized plastic deformation may lead to trans- or intergranular crack initiation. From these crack nuclei larger fatigue cracks can develop, which finally lead to macroscopic fatigue failure. In order to investigate the influence of different microstructures on relevant deformation and damage mechanisms in the HCF and VHCF-regimes three plain carbon steels with different ferrite to pearlite ratios were investigated. The varying ferrite/pearlite ratios lead to a different deformation behaviour and fatigue lives. C15E and C45E show late fatigue failure after more than  $10^7$  cycles, whereas such late fatigue failure is absent in C60E. To monitor fatigue damage a new method was developed where the change in dissipated energy per fatigue cycle ( $\Delta DEC$ ) is calculated from the ultrasonic generator power input. Using the dissipated energy per cycle different stages of the fatigue life can be distinguished.  $\Delta DEC$  is interpreted to be a measure for the degree of cyclic slip irreversibility as long fatigue damage is absent. The  $\Delta DEC$  method also enables at a very early stage of the fatigue experiment to determine whether late fatigue failure will occur or not. At later stages of the fatigue life, where damage has to be taken into account, the  $\Delta DEC$  method also allows to analyze the early crack initiation and crack propagation stage.

## Introduction

During service many engineering parts are exposed to cyclic loading into the high cycle fatigue (HCF) or to the Very High Cycle fatigue (VHCF) regimes. To insure functionality and safety of these products a profound knowledge of the cyclic behavior in the HCF/VHCF regimes of the used materials is mandatory. According to Mughrabi fatigue failure is a consequence of a multistage process, compare [1]. The different stages can be categorized in basic dislocation and fatigue damage mechanisms. In the HCF- and VHCF-regimes, fatigue life is still mainly determined by the crack initiation stage, i.e. by basic dislocation mechanisms. As it is well known for the LCF-regime and as it was proposed also for the VHCF-regime irreversibility of plastic slip is the relevant quantity which has to be considered [2]. The to and fro of dislocation slip is not always completely reversible, leading to the accumulation of irreversible plastic deformation during each cycle. This

accumulation can lead to the formation of a fatal crack [3, 4]. At the transition from the HCF- to the VHCF-regime plastic deformation becomes gradually less pronounced and strongly localizes at particular sites of the microstructure. However, due to this localization it becomes hard to identify early stages of fatigue damage in the VHCF-regime and to quantify the cyclic slip irreversibility. In this study on steels with different carbon contents a new method was developed which provides a measure for the cyclic slip irreversibility and which also allows to monitor the development of fatigue damage during cycling. Based on this method a prediction whether fatigue failure in the HCF- and VHCF regime or an infinite fatigue life will be obtained is possible.

## Experimental

The steels C60E (SAE 1064), C45E (SAE 1045) and C15E (SAE 1017) were used for this study. To adjust the microstructures of the different steels heat treatments in an argon atmosphere at 900 °C for C60E and C45E and, respectively, at 950 °C for C15E were performed. Afterwards all materials were cooled down with a cooling rate of 10 °C/min. These heat treatments resulted in a ferritic/pearlitic microstructure for all three steels, see Figure 1 a) – c). In addition, C15E was also used in a quenched condition leading to a ferritic microstructure with finely distributed carbide precipitates. The pearlite phase is completely absent in this microstructure, see Figure 1 d).

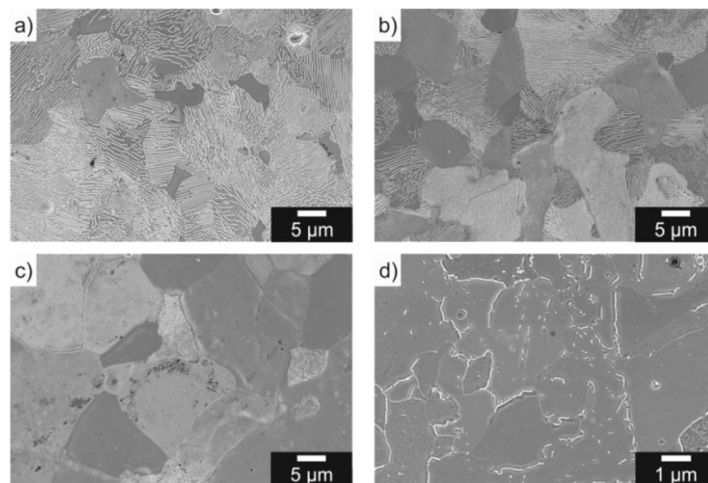


Figure 1: Microstructures of the investigated steels: a) C60E, b) C45E, c) C15E after heat treatment and d) C15E in quenched condition.

For the fatigue tests the ultrasonic fatigue system “UltraFast-WKK-Kaiserslautern” was used. Tests were performed in a pulse-pause mode with a pulse period of 200 ms and 250 ms (depending on the stress amplitude). The pause period varied between 750 ms and 2800 ms. All tests were done at  $R = -1$ . A maximum temperature increase of 10 °C in the undamaged specimens was allowed and controlled by using a pyrometer from Optris GmbH. The specimens were cooled with compressed air. The specimens had a straight gauge length of 11 mm and a diameter of 6 mm. The specimens were ground to 4000 and mechanically polished to 1 μm. For a final step the specimens were electrolytically polished, using the electrolyte A3 from Struers. The polishing voltages and the polishing times were 50 V / 4×3 s (C15E both conditions), 47.5 V / 3×3 s (C45E) and 45 V / 3×3 s (C60E). The polishing temperature was -10 °C. Microstructural investigations were done at a Cross Beam 1540 Esb scanning electron microscope from Zeiss.

## Results and Discussion

The fatigue tests on C15E, C45E and C60E with a ferritic-pearlitic microstructure showed that the fatigue strength increases with increasing pearlite content, see Figure 2. C60E shows only macroscopic fatigue failure below  $10^7$  fatigue cycles, whereas late fatigue failure above  $10^7$  loading cycles can be found for C15E and C45E. This can be related to the closed pearlitic matrix which is found in C60E. In this microstructure isolated ferritic islands are embedded in a pearlitic matrix. The plastic deformation is localized at the isolated ferrite grains. Short cracks initiate at phase boundaries between ferrite and pearlite grains, but below a stress amplitude of 375 MPa the short cracks cannot penetrate into the pearlite matrix. This barrier effect prevents late fatigue failure.

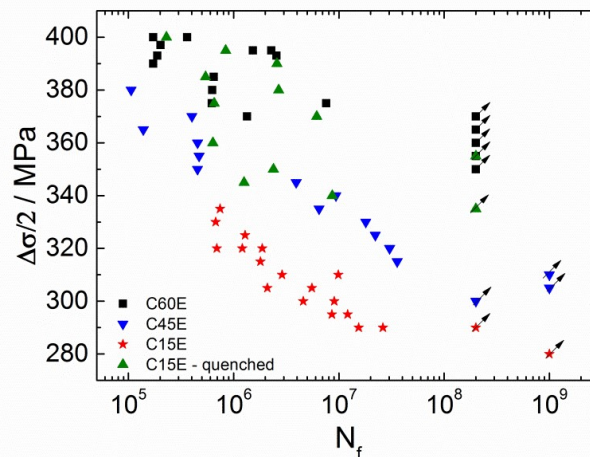


Figure 2: Wöhler-(S-N) diagram for the different steels investigated.

In C15E and C45E, where large purely ferritic areas can be found, cracks initiated at ferrite grain boundaries or on ferrite/pearlite phase boundaries, see Figure 3 a). Those crack nuclei grow in the ferrite phase and cause late macroscopic failure in the VHCF regime above  $10^7$  cycles. In contrast to the C15E in the ferritic-pearlitic condition, the quenched state shows much higher endurable stress amplitudes. In the latter condition pronounced formation of slip bands is observed. Along these slip bands cracks initiated and cause macroscopic fatigue failure, see Figure 3 b). The formation of slip bands is eased in this condition as the quenching leads to a higher amount of solved carbon atoms in the ferrite phase. It is well known that the carbon content essentially influences the slip behavior of dislocation in bcc ferrite [5-8].

For all investigated materials and for both heat treatments in the case of C15E it is revealed that crack initiation stage mainly governs the fatigue life rather than the crack growth stage.

By the use of a modern ultrasonic fatigue system it was possible to develop a new method to monitor the fatigue damage evolution. In this technique the electrical power output, which is needed to produce an ultrasonic fatigue pulse, is monitored. The energy which is dissipated in a fatigue specimen during a fatigue pulse can then be calculated from this measurement. The dissipated energy can be used to describe the damage evolution during a fatigue experiment [9]. There are different processes which cause the dissipation of energy during a fatigue experiment. A typical dissipated energy curve is shown in Figure 4 a). At the beginning of a fatigue experiment transient processes like dynamic hardening or softening cause an increase or decrease in dissipated energy. After these processes a dynamic dislocation equilibrium develops. At this stage

of the fatigue life the dissipation of energy is caused by plastic deformation and the increase of this measure reflects for the irreversibility of plastic deformation. The irreversible plastic deformation accumulates during the cyclic loading and finally leads to crack initiation and the formation of crack nuclei. In contrast to this stage of the experiment where the dissipated energy curve shows a small positive slope, the slope of the curve and the absolute values of the dissipated energy increase strongly after crack initiation. This can be experimentally correlated to the growth of short and at end of experimentally long cracks, compare [10].

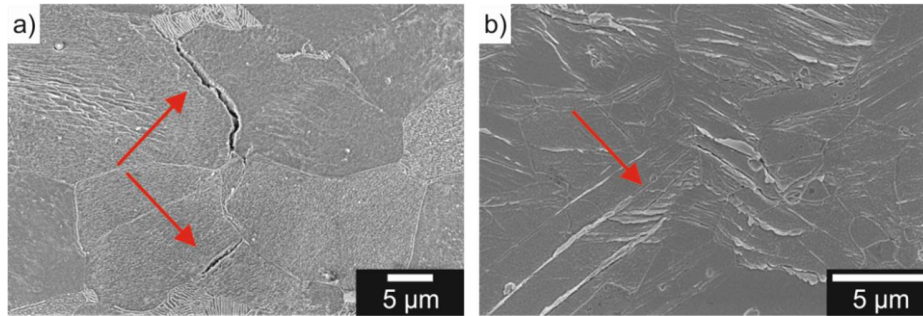


Figure 3: Crack initiation sites in C15E: a) crack initiation on grain boundaries in C15E in the ferritic-pearlitic condition; b) crack initiation in slip bands in C15E in the quenched condition.

By analyzing the different stages of the fatigue life on the basis of the evolution of the dissipated energy it becomes apparent that there is a regime where the dissipated energy increases almost linearly with further cycling. As mentioned above, at this stage of the fatigue life, where transient processes are already completed and crack nuclei do not yet exist, the irreversibility of plastic deformation is prevalent. It becomes also obvious that the fatigue life is mainly governed by this stage [10]. In this stage the small constant slope of the dissipated energy curve, which is further denoted as  $\Delta DEC$ , can be interpreted as a measure for the irreversibility of plastic deformation. To clearly separate from transient deformation effects or from crack initiation effects  $\Delta DEC$  is only determined between 10% and 60 % of the total fatigue life. The obtained  $\Delta DEC$  values depend strongly on the stress amplitude. For higher stress amplitudes the irreversibility will be higher, compare also [2], and thus the fatigue life is shorter. It is also apparent, that in a semi logarithmic plot in which  $\Delta DEC$  is plotted versus the applied stress amplitude,  $\Delta DEC$  values are following an almost linear trend as long as macroscopic failure of the specimens is observed, see Figure 4 b). For all run out specimens a significant deviation from this linear trend is obtained.  $\Delta DEC$  decreases strongly for those specimen where no macroscopic failure is obtained. It is also prevalent that in the case of C45E fatigued at 290 MPa the two specimens with the higher  $\Delta DEC$  values failed whereas the one specimen with the lower  $\Delta DEC$  value survived. Thus, by this analysis, which is based in principal on a change in the fatigue damage mechanism, it is easily possible to determine the transition from fatigue failure to an infinite fatigue life. When the evolution of the  $\Delta DEC$ -values is plotted versus the number of cycles to failure in a double-logarithmic diagram, a linear trend for each material is obtained, Figure 4 c). Due to this correlation fatigue life can be estimated using the following formula:

$$\log N_f = \frac{\log \Delta DEC - c}{d}$$

With: c slope and d intercept for the trend line describing the  $\Delta DEC$ -values over cycles to failure.



As  $\Delta$ DEC can be determined at a very early stage of the fatigue experiment tests can be significantly shortened and run outs can also be easily identified only after a few thousand loading cycles. Comparing the  $\Delta$ DEC values of C15E in the ferritic-pearlitic and quenched conditions it becomes clear that this method is also valid to differentiate between microstructures in chemically identical materials if the dominating damage mechanisms have changed, compare also Figure 3 a) and b).

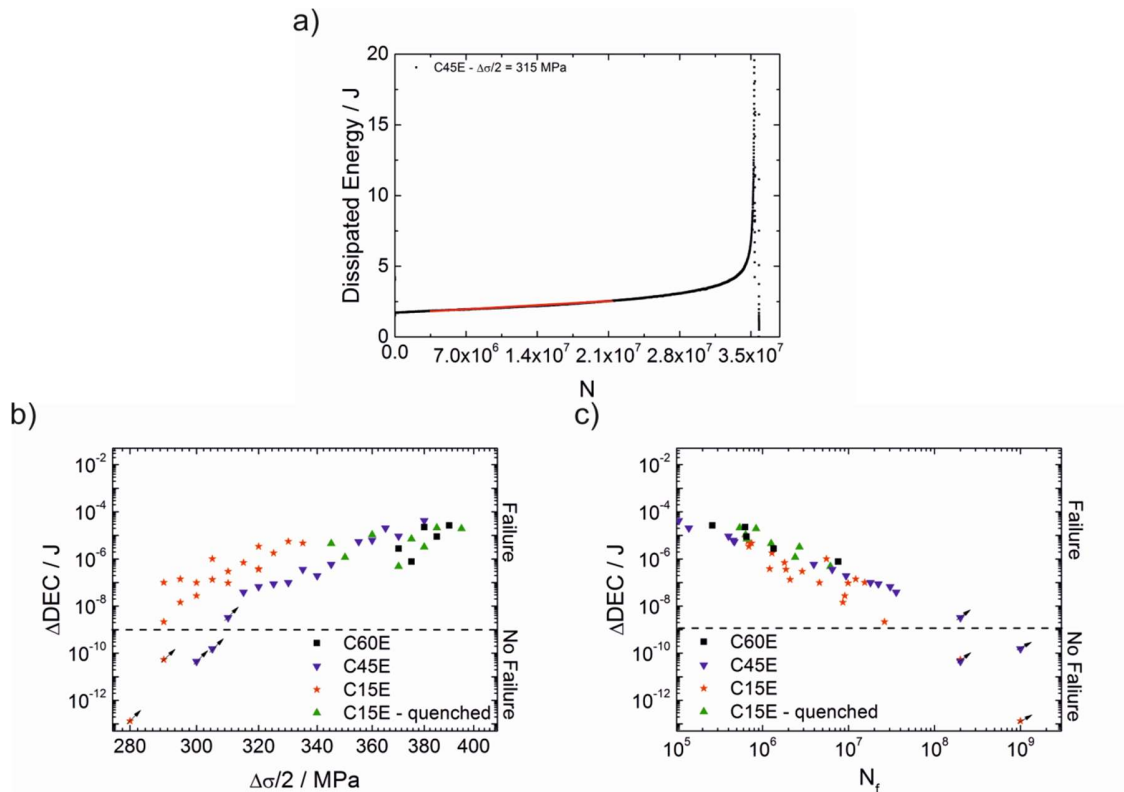


Figure 4: a) Dissipated energy vs. number of cycles for C45E fatigued exemplarily shown for a stress amplitude of 315 MPa. Determination of  $\Delta$ DEC from dissipated energy curve at the red marked regime; b) log  $\Delta$ DEC vs. stress amplitude; c) log  $\Delta$ DEC vs. log  $N_f$ .

The  $\Delta$ DEC can also be used to get first insights to the interaction between microstructure, mechanical loading and cracks or crack nuclei. Run out specimens for C15E (ferrite/pearlite) and C45E show a strong decrease in  $\Delta$ DEC, but the values are still positive. This indicates that irreversible plastic deformation and dislocation movement still takes place in the material, but cannot lead to crack initiation in the investigated fatigue life regime. Run out specimens for C60E and C15E in the quenched condition show a different behavior.  $\Delta$ DEC values in these specimens are negative, see Figure 5 b). The reason for this are dislocation hardening and pile-up effects at phase boundaries. At the beginning of the experiment an increase of dissipated energy to a maximum value is observed. This is caused by an increase in dislocation density. After that maximum a continuous decrease of  $\Delta$ DEC is observed, see Figure 5 a). At the maximum of the curve the dislocation generation and plastic deformation is at a maximum. With further cycling, dislocation slip is increasingly impeded by back stresses that build up during further cycling. It is assumed that these back stresses are due to dislocation pile-up effects at phase boundaries (pearlite phase in C60E and carbides in C15E quenched). This process can proceed until



dislocation generation is completely suppressed and the material deforms only elastically. This would lead to an infinite fatigue life. In contrast to that behavior, the ferritic-pearlitic C15E and C45E run out specimens show low, but still positive  $\Delta$ DEC-values.

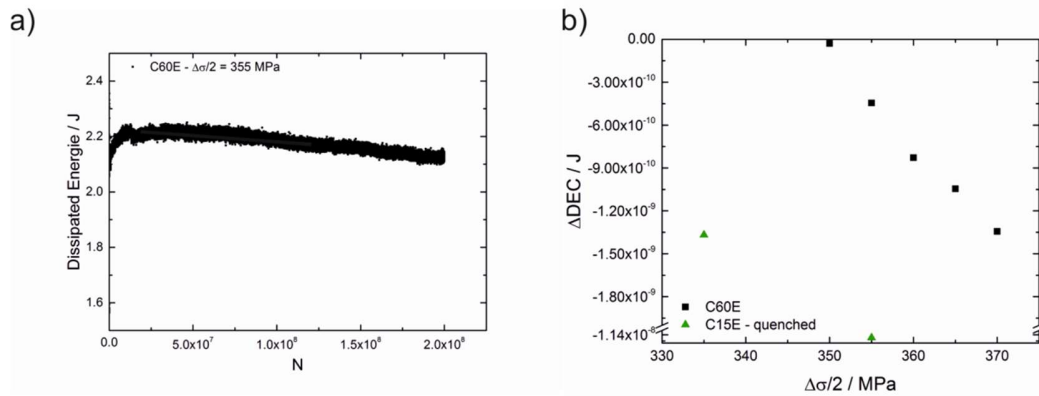


Figure 5: a) Determination of  $\Delta$ DEC in C60E run out with dissipated energy curve; b)  $\Delta$ DEC values for C60E and C15E (quenched) run outs.

From this analysis, it becomes also clear that there is no absolute number of cycles that can be taken to define a “fatigue limit” in the literal sense. In fact, it turns out that such a definition would only be valid for a particular damage mechanism in a material in a defined microstructural condition.

## Acknowledgment

The authors gratefully acknowledge the funding by the German Research Council (DFG) through its priority program “14661 – Infinite life for cyclically loaded high performance materials” and the Cluster of Excellence “Engineering of Advanced Materials”.

## References

- [1] H. Mughrabi. Dislocations in fatigue. In *Dislocations and Properties of Real Materials*, volume 323, pages 244 – 262. The Institute of Metals, 1985.
- [2] H. Mughrabi. On the life-controlling microstructural fatigue mechanisms in ductile metals and alloys in the gigacycle regime. *Fatigue and Fracture of Engineering Materials and Structures*, 22:633–641, 1999.
- [3] H. Mughrabi. Cyclic slip irreversibilities and the evolution of fatigue damage. *METALLURGICAL AND MATERIALS TRANSACTIONS A*, 40A:1257 – 1279, 2009.
- [4] H. Mughrabi. Cyclic strain rate effects in fatigued face-centred and body-centred cubic metals. *Philosophical Magazine*, 93:3821–3834, 2013.
- [5] C. Sommer, H. Mughrabi, and D. Lochner. Influence of temperature and carbon content on the cyclic deformation and fatigue behavior of alpha-iron. part ii: Crack initiation and fatigue life. *Acta Materialia*, 46:1537–1546, 1998.
- [6] C. Sommer, H. Mughrabi, and D. Lochner. Influence of temperature and carbon content on the cyclic deformation and fatigue behavior of iron. part i. cyclic deformation and stress-behaviour. *Acta Materialia*, 46:1527–1536, 1998.
- [7] D. Caillard. Kinetics of dislocations in pure fe. part ii. in situ straining experiments at low temperature. *Acta Materialia*, 58:3504–3515, 2010.
- [8] D. Caillard. An in situ study of hardening and softening of iron by carbon interstitials. *Acta Materialia*, 59:4974–4989, 2011.
- [9] M. Koster, G. Wagner, and D. Eifler. Cyclic deformation behavior of a medium carbon steel in the vhf regime. *Procedia Engineering*, 2:2189 – 2197, 2010.
- [10] J. Bach, J.J. Möller, M. Göken, E. Bitzek, and H.W. Höppel. On the transition from plastic deformation to crack initiation in the high- and very high-cycle fatigue regimes in plain carbon steels. *International Journal of Fatigue*, 93:281 – 291, 2016.

\*Corresponding author: hwe.hoeppel@fau.de

# EVALUATION OF THREE-DIMENSIONAL MICROSTRUCTURAL EFFECTS ON DAMAGE EVOLUTION DURING VHCF LOADING OF DUPLEX STAINLESS STEEL – MICROSTRUCTURE-SENSITIVE FATIGUE LIFE ASSESSMENT

B. Dönges<sup>1,2)</sup>, C.-P. Fritzen<sup>2)</sup>, H.-J. Christ<sup>1)</sup>

<sup>1)</sup>Institut für Werkstofftechnik, Universität Siegen, Paul-Bonatz-Straße 9-11, 57068 Siegen, Germany

<sup>2)</sup>Institut für Mechanik und Regelungstechnik – Mechatronik, Universität Siegen, Paul-Bonatz-Straße 9-11, 57068 Siegen, Germany

## ABSTRACT

High frequency fatigue experiments on duplex stainless steel revealed that the microstructural features of the alloy have a significant influence on the fatigue life at low loading amplitudes. Manufacturing-induced residual stresses as well as anisotropic elasticity of individual grains cause local stress concentrations. Experimental and numerical investigations showed that a three-dimensional consideration is essential for a realistic determination of the stress distribution on the microstructural level. Predominantly on those crystallographic planes of the gamma phase which exhibit high Schmid factors, stress intensifications cause plastic shear in the form of dislocation generation and motion, which are only partially reversible, even under fully reversed loading. The accumulation of the irreversible fraction of this local plastic deformation over many load cycles can cause crack nucleation. Moreover, the propagation of short fatigue cracks, which usually takes place along crystallographic planes in cyclic mode II loading, is determined by the stress distribution on the microstructural level. Such cracks can strongly interact with microstructural barriers, such as grain and phase boundaries, causing a permanent stop of crack propagation under certain circumstances. As an important consequence, duplex stainless steel exhibits a real fatigue limit despite the initiation and formation of small fatigue cracks. A numerical model was developed and is presented for the simulation of fatigue crack nucleation and microstructure-dominated short fatigue crack propagation under consideration of the three-dimensionality of the material microstructure. This model considers the physical processes on the microstructure level in a mechanism-based manner and allows for a quantitative assessment of the resistance of real and synthetic microstructures regarding initiation and propagation of short fatigue cracks under VHCF conditions. A comparison between experimental observations and simulation results shows a high predictive capability.

## KEYWORDS

fatigue crack initiation, short fatigue crack propagation, residual stresses, crystal plasticity

## INTRODUCTION

At relatively low loading amplitudes, the early stages of fatigue, such as crack nucleation and short crack propagation, may determine up to 90 % of the whole fatigue life of a material [1]. The local microstructure can significantly influence the fatigue behaviour due to strong interactions between fatigue cracks and microstructural barriers, such as grain and phase boundaries. Furthermore, the application of traditional fracture mechanics concepts, such as the linear elastic fracture mechanics (LEFM), can cause non-conservative dimensioning of components [2]. Hence, numerous models were created since the end of the twentieth century

in order to describe these early stages of fatigue in a mechanism-based manner. Some of these models are of qualitative nature [3-5], others enable a quantification of the single fatigue stages [6-9]. However, several microstructural features, such as anisotropic elasticity of the material considered or the zig-zag-path of short fatigue cracks due to the different crystallographic orientation of grains, are not considered in these models and thus may result in strong inaccuracy. Hence, a new model for fatigue life assessment of metallic materials is presented in this manuscript, which takes into account crystal plasticity, anisotropic elasticity, first and second order residual stresses, three dimensional grain shapes as well as the mechanisms of fatigue crack nucleation and short fatigue crack propagation. The model is verified by means of a comparison between simulation results and experimental observations. As an ambitious objective of the model, parameter studies shall be made possible, which quantitatively determine the effect of microstructural parameters with respect to crack initiation and propagation revealing the potentialities regarding VHCF resistance improvements of materials.

## EXPERIMENTAL DETAILS

### Material

Austenitic-ferritic duplex stainless steels are often used in applications where high corrosion resistance in combination with high strength is required, such as in off-shore-systems or systems for the chemical and petrochemical industry. The investigated material is the austenitic-ferritic duplex stainless steel 318LN (X2CrNiMo22-5-3). It was delivered as hot rolled and solution annealed bars with a diameter of 25 mm and a fine lamellar microstructure with about 50 vol% austenite and ferrite, respectively. An additional heat treatment was applied in order to ease the experimental investigations by means of grain coarsening. For this purpose the material was additionally annealed at 1250°C for 4 h, cooled to 1050°C within 3 h and quenched in water. The initial volume fraction of both phases was maintained, the mean grain diameter of the austenitic phase was increased to 33  $\mu\text{m}$  and the mean grain diameter of the ferritic phase was increased to 46  $\mu\text{m}$ .

## NUMERICAL DETAILS AND MODEL ASSUMPTIONS

In order to simulate the fatigue behaviour of the investigated duplex stainless steel, the commercial finite element program ABAQUS and a UMAT subroutine for crystal plasticity material behaviour [10] serve as basis. These enable the determination of plastic shear on slip systems of various microstructures as a consequence of cyclic deformation. For this purpose, the microstructures are discretized by means of three dimensional finite elements. Aspects, such as anisotropic elasticity of single grains, crystal plasticity as well as manufacturing induced first and second order residual stresses, are taken into account. According to the dependency between the number of load cycles for fatigue crack initiation and the range of the plastic shear – as analytically derived by Tanaka and Mura [6] and Chan [7] – the accumulated squared range of the plastic shear  $\Delta\gamma_{pl}^2$  is applied as fatigue damage parameter FDP. By reaching a material specific critical value of the fatigue damage parameter  $FDP_{krit}$  the directional elastic constants  $E_{11}$ ,  $E_{12}$  and  $E_{44}$  of the corresponding finite elements are reduced to close to zero. Due to the loss of stiffness, these finite elements do not resist against the applied load and thus together behave like a crack. In order to maintain the force equilibrium of the whole structure, higher stresses have to be present in neighboring finite elements. This can lead to an increased plastic zone and plastic shear in the finite elements at the crack tip. According to the dependency between the crack propagation rate and the range of the crack tip slide displacement [8] – which is in direct relationship with the range of the plastic shear at

the crack tip – the fatigue damage parameter described above is also applied to simulate short fatigue crack propagation. In the proposed model, the simulation of short fatigue crack propagation is a result of the achievement of the critical value of the fatigue damage parameter in finite elements at the crack tip during further simulated load cycles, which results in a loss of the stiffness of the corresponding finite elements.

## RESULTS

Figure 1 shows a SEM image of the surface of a fatigue sample, which contains transgranular crack nuclei. These nuclei were formed at the phase boundary between the austenite grain  $\gamma_1$  and the ferrite grain  $\alpha_1$ .

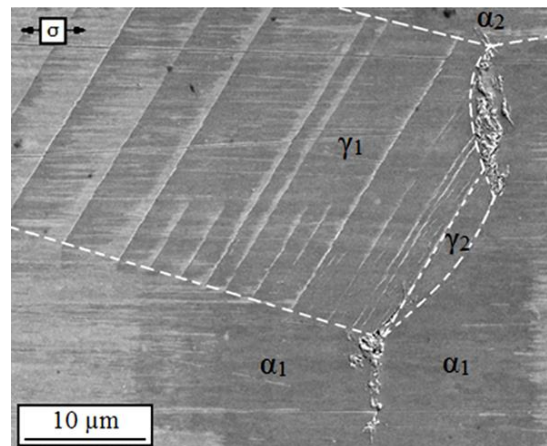
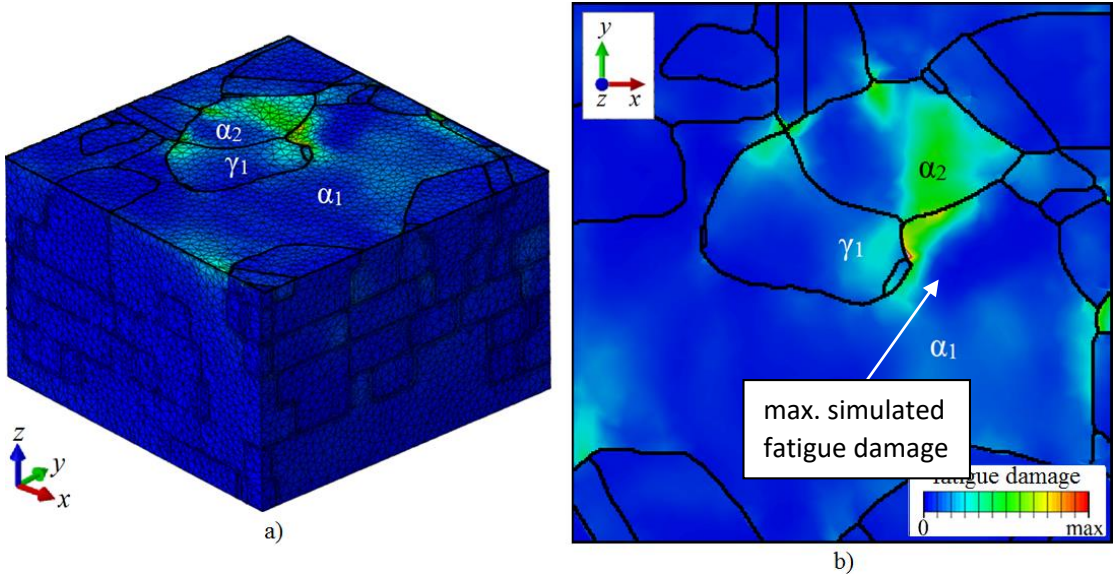


Fig. 1: SE-image of the surface of a VahCF sample; Loading direction: horizontal

Fig. 2 presents a finite element representation of the microstructure shown in Fig. 1. Microstructural information – such as the position of grain and phase boundaries, crystallographic orientations and phase affiliation – were obtained in three dimensions by grinding and polishing the surface of fatigued samples in steps of about 15  $\mu\text{m}$ . An automated EBSD analysis was made before the first and after each further grinding/polishing step. In order to retrieve the exact position of the crack initiation site after each grinding/polishing step, marks were generated by means of focused ion beam (FIB) milling perpendicular to the surface into a depth of about 30  $\mu\text{m}$ . Vickers indents, which were introduced before the first grinding/polishing step at the sample surface, served for measuring the removal depth by means of confocal laser scanning microscopy. The finite element model was created by discretization of the microstructure using tetrahedrons. In order to consider the surrounding of the shown microstructure correctly, a frame consisting of finite elements (not shown here) with elastically isotropic material behaviour ( $E=197$  MPa and  $\nu=0.3$ ) was arranged around the microstructure. The nodes at the left face of the model were fixed in x-direction. One node at the upper left corner of the model was additionally fixed in z-direction and one node at the lower left corner was additionally fixed in z- and y-direction to avoid rigid body motions. Residual stresses due to the manufacturing process of the material were considered by simulating the stress evolution during quenching process from 1050°C (heat treatment temperature) to room temperature. In order to consider second order residual stresses, temperature dependent elastic constants  $E_{11}$ ,  $E_{12}$  and  $E_{44}$ , thermal expansion coefficients  $\alpha$ , microstructural frictional shear stresses of both phases as well as Young's modulus  $E$  for the elastically isotropic frame were considered [11]. Furthermore, first order residual stresses were taken into account by applying a pressure load of 50.2 MPa (tension) at the nodes at the right face of the model and 21 MPa (compression) at the upper and lower face of the model. The simulation of the quenching process was followed by a simulation of cyclic deformation. For

this, a cyclic normal stress amplitude of 365 MPa was applied at the nodes at the right face of the model in x-direction. Fig. 2 shows the distribution of the value of the fatigue damage parameter, which was defined as the cumulative square of the local plastic shear range, after one simulated load cycle under consideration of first and second order residual stresses. The maximum fatigue damage in the whole three-dimensional finite element model was determined at exactly the position, where a crack nuclei generated in the real microstructure.

Figure 3 shows a simplified finite element model with a thickness of 5  $\mu\text{m}$ , which consists of 400 single grains with a diameter of about 40  $\mu\text{m}$ . The model was discretized by tetrahedrons and anisotropic elasticity as well as crystal plasticity were considered. Different crystallographic orientations were taken into account for each grain according to a data set obtained by means of an automated EBSD ganalysis. Finite elements with isotropic elastic material behaviour ( $E=197\text{ MPa}$  and  $\nu=0.3$ ) were defined at the left and right face of the microstructure. The boundary conditions were defined equally to the boundary conditions of the model presented in Fig 2. First and second order residual stresses were considered as described above.



**Fig. 2:** Fatigue damage after one simulated load cycle in the microstructure presented in Fig. 1 under consideration of first and second order residual stresses: a) three-dimensional illustration and b) surface view; Loading direction: horizontal

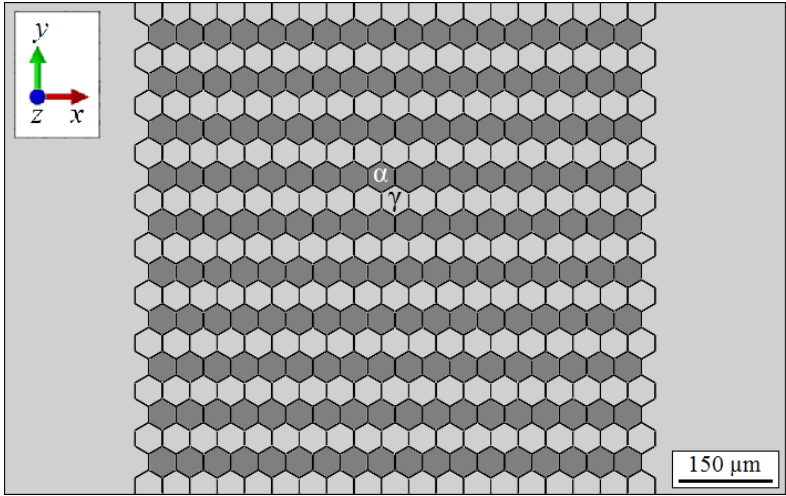


**Fig. 3:** Polycrystalline finite element model for simulation of fatigue crack nucleation and short fatigue crack propagation; Loading direction: Horizontal



The simulation of the quenching process was followed by a simulation of cyclic deformation. For this purpose, a cyclic load with an amplitude of 360 MPa was applied at the nodes of the right face of the model in x direction. The distribution of the simulated local fatigue damage value is presented in Fig. 4 after different load cycles. A transgranular fatigue crack initiated in the ferrite grain  $\alpha_2$  after the 9<sup>th</sup> simulated load cycle. The crack propagated during the further load cycles to the grain boundary with the neighbouring ferrite grain  $\alpha_1$ . The grain boundary did not influence the crack propagation significantly, whereas the phase boundary between the ferrite grain  $\alpha_1$  and the austenite grain  $\gamma_1$  as well as between the ferrite grain  $\alpha_2$  and the austenite grain  $\gamma_6$  blocked the crack propagation for several load cycles. Significant fatigue damage is visible in the austenite grains  $\gamma_1$ ,  $\gamma_5$  and  $\gamma_6$  after the crack tip approached the corresponding grains.

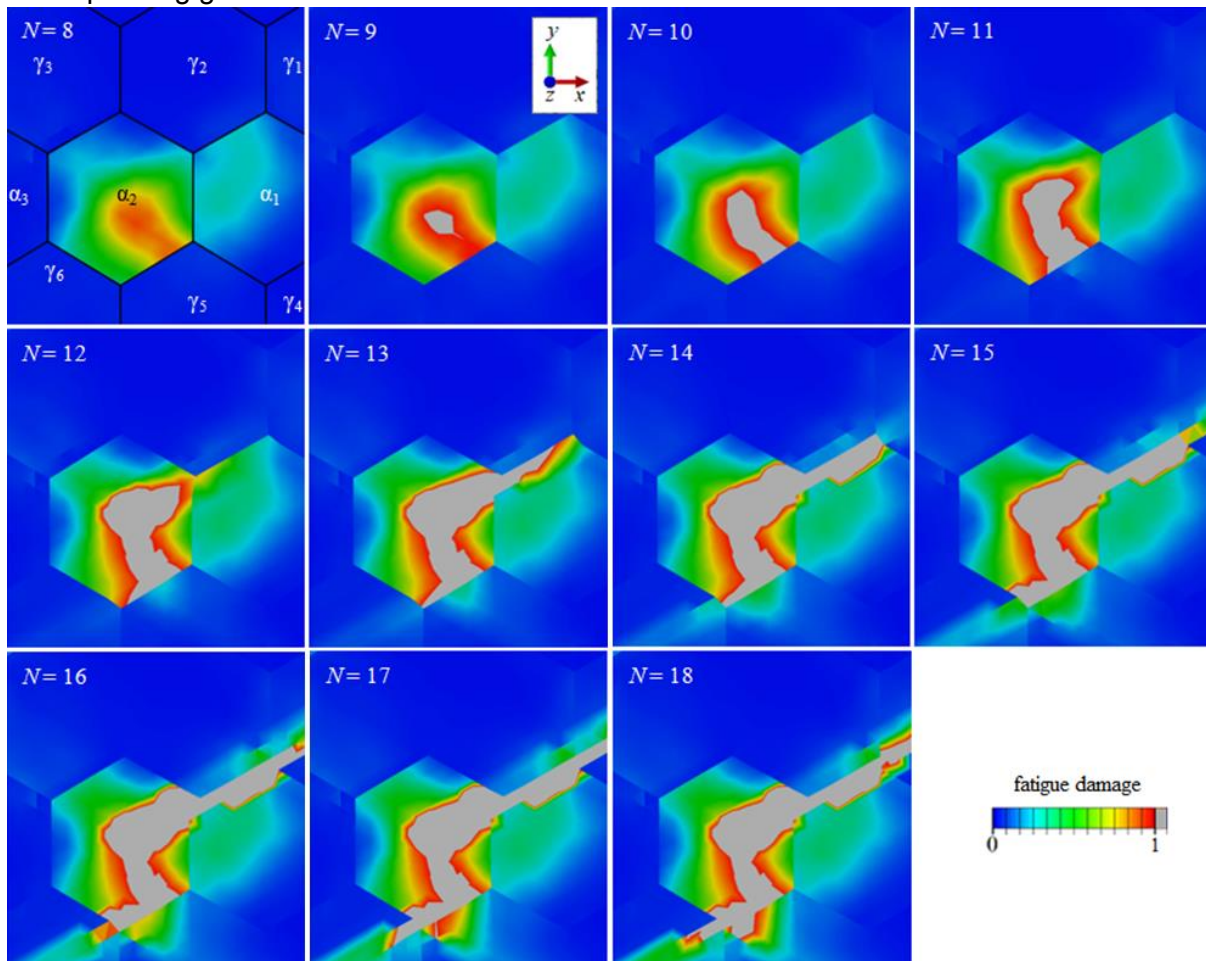


**Fig. 4:** Simulation of fatigue crack initiation and short fatigue crack propagation; Loading direction: horizontal

## CONCLUSIONS

The results of the study presented show that the experimentally identified mechanisms of fatigue crack nucleation and short fatigue crack propagation were successfully implemented into crystal plasticity finite element simulations by applying a fatigue damage parameter according to traditional, mechanism-based fatigue models. Fatigue damage occurs in the proposed model by a loss of stiffness of finite elements when a material specific threshold value of a damage parameter is achieved. Anisotropic elasticity as well as first and second

order residual stresses due to the manufacturing process of the investigated material were taken into account. The proposed model was verified by means of a comparison between simulation results and experimental results. The relevance of the consideration of real three dimensional grain shapes and the microstructure beneath the surface was pointed out. On the basis of this model developed various microstructural parameters can be investigated regarding their influence on the fatigue life of the material and quantitative relationships can be deduced.

## ACKNOWLEDGEMENT

The authors would like to thank Deutsche Forschungsgemeinschaft (DFG) for financial support in the framework of the priority program "life<sup>∞</sup>" (SPP1466).

## REFERENCES

- [ 1 ] Shiozawa, K.; Matsushita, H.: Crack initiation and small fatigue crack growth behaviour of beta Ti-15V-3Cr-3Al-3Sn alloy, Lütjering, G.; Nowack, H. (Eds.): Proceedings of the Sixth International Fatigue Congress, 1996, Berlin, p. 301
- [ 2 ] Suresh, S.; Ritchie, R. O.: Propagation of short fatigue cracks, International Metals Reviews 29 (1984), pp. 445-475
- [ 3 ] Essmann, U.; Gösele, U.; Mughrabi, H.: A model of extrusions and intrusions in fatigued metals - I. Point-defect production and the growth of extrusions, Philosophical Magazine A 44 (1981) pp. 405-426
- [ 4 ] Polák, J.: On the role of point defects in fatigue crack initiation, Materials Science and Engineering 92 (1987), pp. 71-80
- [ 5 ] Wilkinson, A.J.; Roberts, S.G.: A dislocation model for the two critical stress intensities required for threshold fatigue crack propagation, Scripta Materialia 35 (1996), pp. 1365-1371
- [ 6 ] Tanaka, K.; Mura, T.: A dislocation model for fatigue crack initiation, Journal of Applied Mechanics 48 (1981), pp. 97-103
- [ 7 ] Chan, K. S.: A microstructure-based fatigue-crack-initiation model, Metallurgical and Materials Transactions A 34 (2003), pp. 43-58
- [ 8 ] Tanaka, K.; Akiniwa, Y.; Nakai, Y.; Wei, R.P.: Modeling of small fatigue crack growth interacting with grain-boundary, Engineering Fracture Mechanics 24 (1986), pp. 803-819
- [ 9 ] Navarro, A.; de los Rios, E.R.: Short and long fatigue crack-growth: A unified model, Philosophical Magazine A 57 (1988), pp. 15-36
- [ 10 ] Huang, Y.: A user-material subroutine incorporating single crystal plasticity in the ABAQUS finite element program, Diss. Harvard University 1991
- [ 11 ] Dönges, B.; Fritzen, C.P.; Christ, H.J.: Experimental investigation and simulation of the fatigue mechanisms of a duplex stainless steel under HCF and VHCF loading conditions, Key Engineering Materials 664 (2015), pp. 267-274.

**Corresponding author:** [hans-juergen.christ@uni-siegen.de](mailto:hans-juergen.christ@uni-siegen.de)

**Fundamentals, physics and mechanisms**  
**Influence of microstructure defects**



## INVITED



### **Takashi Nakamura**

Division of Mechanical and Space Engineering,  
Faculty of Engineering, Hokkaido University  
Fellow, the Japan Society of Mechanical Engineers

#### AREA OF INTERESTS

- Very high cycle fatigue properties of high strength materials
- Fatigue crack growth in vacuum environment
- Degradation mechanism of polymers in space environment
- Nano-structural refinement of metal surface

#### EXPERIENCES

2007 Professor, Faculty of Engineering, Hokkaido University  
2004 Visiting Professor, Mechanical Engineering, University of Alberta, Canada  
1995 Associate Professor, Faculty of Engineering, Hokkaido University  
1991 Research Associate, Tokyo Institute of Technology  
1986 Moog Japan Ltd.

#### EDUCATIONS

1995 Academic Degree: Doctor of Engineering, Tokyo Institute of Technology  
1986 Master of Engineering, Tokyo Institute of Technology  
1982 Bachelor of Engineering, Tokyo Institute of Technology

#### AWARDS

2012 "Award for outstanding academic contributions", The Society of Material Science, Japan, 2010 "Award for outstanding paper", The Japan Foundry Engineering Society.  
1999 "Encouraging prize for outstanding researches", The Society of Material Science, Japan.

### **DATA ACQUISITION FOR VERY HIGH CYCLE FATIGUE OF NON-FERROUS METALLIC MATERIALS BASED ON THE COLLABORATIVE RESEARCH IN JSMS - 1<sup>ST</sup> REPORT: OUTLINE OF ROUND-ROBIN EXPERIMENTS ON ALUMINUM DIE CASTING, BETA TITANIUM, AND EXTRUDED MAGNESIUM ALLOYS**

**T. Nakamura**<sup>1</sup>, A. Ueno<sup>2</sup>, T. Matsumura<sup>3</sup>, K. Masaki<sup>4</sup>, H. Oguma<sup>5</sup>, H. Akebono<sup>6</sup>, T. Kakiuchi<sup>7</sup>, S. Kikuchi<sup>8</sup>, Y. Nakamura<sup>9</sup>, T. Nishida<sup>10</sup>, T. Ogawa<sup>11</sup>, N. Oguma<sup>12</sup>, T. Sakai<sup>13</sup>, Y. Shimamura<sup>14</sup>, K. Shiozawa<sup>15</sup>, Y. Uematsu<sup>16</sup>

<sup>1</sup>Hokkaido University Division of Mechanical and Space Engineering, Sapporo, Japan

<sup>2</sup>Ritsumeikan University College of Science and Engineering, Kusatsu, Japan

<sup>3</sup>The University of Electro-Communications Department of Mechanical and Intelligent Systems Engineering, Chofu, Japan

<sup>4</sup>National Institute of Technology, Okinawa College Department of Mechanical Systems Engineering, Nago, Japan

<sup>5</sup>National Institute for Materials Science, Tsukuba, Japan

<sup>6</sup>Hiroshima University Division of Materials and Production Engineering, Higashi-Hiroshima, Japan

<sup>7</sup>Gifu University Department of Mechanical Engineering, Gifu, Japan

<sup>8</sup>Kobe University Department of Mechanical Engineering, Kobe, Japan

<sup>9</sup>National Institute of Technology, Toyota College Department of Mechanical Engineering, Toyota, Japan

<sup>10</sup>National Institute of Technology, Numazu College Department of Mechanical Engineering, Numazu, Japan

<sup>11</sup>Aoyama Gakuin University Department of Mechanical Engineering, Sagami, Japan

<sup>12</sup>University of Toyama Department of Mechanical and Intellectual Systems Engineering, Toyama, Japan

<sup>13</sup>Ritsumeikan University Research Organization of Science and Engineering, Kusatsu, Japan

<sup>14</sup>Shizuoka University Department of Mechanical Engineering, Hamamatsu, Japan

<sup>15</sup>Fukui University of Technology Department of Mechanical Engineering, Fukui, Japan

<sup>16</sup>Gifu University, Gifu, Japan

Very High Cycle Fatigue (VHCF) problem is regarded as one of the important issues to be solved in the field of mechanical engineering. Many researches have been conducted on VHCF properties of ferrous metals including high strength steels; however, long life fatigue data of non-ferrous metals are still limited. Based on this situation, a research sub-committee on VHCF was established in the JSMS committee on fatigue of materials to accumulate fatigue data of non-ferrous metallic materials in the regime over  $10^7$  cycles. In order to reveal influential factors on VHCF properties, fatigue tests and fracture surface observations of die-cast aluminum, beta titanium and extruded magnesium alloys have been carried out, and effects of testing conditions including loading types, stress ratios and test frequencies were investigated. Some of the fatigue mechanisms were discussed from a view point of defects and microstructures. The research sub-committee on VHCF consists of three groups targeting die-cast aluminum alloy, beta titanium alloy and extruded magnesium alloys, respectively. Each group will present the results as the second, third, and fourth reports in this conference. This study, the first report, will describe the purposes and the outline of the collaboration work as well as tentative fatigue data and related results.

**DATA ACQUISITION FOR VERY HIGH CYCLE FATIGUE OF  
NON-FERROUS METALLIC MATERIALS BASED ON THE COLLABORATIVE  
RESEARCH IN JSMS**

**1st report: outline of round-robin experiments on  
aluminum die casting, beta titanium, and wrought magnesium alloys**

T. Nakamura<sup>1)</sup>, A. Ueno<sup>2)</sup>, T. Matsumura<sup>3)</sup>, K. Masaki<sup>4)</sup>, H. Oguma<sup>5)</sup>, H. Akebono<sup>6)</sup>,  
T. Kakiuchi<sup>7)</sup>, S. Kikuchi<sup>8)</sup>, Y. Nakamura<sup>9)</sup>, T. Nishida<sup>10)</sup>, T. Ogawa<sup>11)</sup>, N. Oguma<sup>12)</sup>,  
T. Sakai<sup>13)</sup>, Y. Shimamura<sup>14)</sup>, K. Shiozawa<sup>15)</sup>, Y. Uematsu<sup>7)</sup>

- <sup>1)</sup> Division of Mechanical and Space Engineering, Hokkaido University  
Kita 13, Nishi 8, Kita-ku, Sapporo, Hokkaido, 060-8628 Japan
- <sup>2)</sup> College of Science and Engineering, Ritsumeikan University  
1-1-1 Noji-higashi, Kusatsu, Shiga, 525-8577 Japan
- <sup>3)</sup> Department of Mechanical and Intelligent Systems Engineering, The University of  
Electro-Communications, 1-5-1 Chofugaoka, Chofu, Tokyo, 182-8585 Japan
- <sup>4)</sup> Department of Mechanical Systems Engineering, National Institute of  
Technology, Okinawa College, 905 Henoko, Nago, Okinawa, 905-2192 Japan
- <sup>5)</sup> National Institute for Materials Science,  
1-2-1 Sengen, Tsukuba, Ibaraki, 305-0047 Japan
- <sup>6)</sup> Division of Materials and Production Engineering, Hiroshima University,  
1-4-1 Kagamiyama, Higashi-Hiroshima, Hiroshima, 739-8527 Japan
- <sup>7)</sup> Department of Mechanical Engineering, Gifu University,  
1-1 Yanagido, Gifu, 501-1193 Japan
- <sup>8)</sup> Department of Mechanical Engineering, Kobe University,  
1-1 Rokkodai, Nada, Kobe, Hyogo, 657-8501 Japan
- <sup>9)</sup> Department of Mechanical Engineering, National Institute of Technology, Toyota  
College, 2-1 Eisei-cho, Toyota, Aichi, 471-8525 Japan
- <sup>10)</sup> Department of Mechanical Engineering, National Institute of Technology,  
Numazu College, 3600 Ooka, Numazu, Shizuoka, 410-8501 Japan
- <sup>11)</sup> Department of Mechanical Engineering, Aoyama Gakuin University,  
5-10-1 Fuchinobe, Chuo-ku, Sagami-hara, Kanagawa 252-5258, Japan
- <sup>12)</sup> Department of Mechanical and Intellectual Systems Engineering, University of  
Toyama, 3190 Gofuku, Toyama, 930-8555 Japan
- <sup>13)</sup> Research Organization of Science and Engineering, Ritsumeikan University,  
1-1-1 Noji-higashi, Kusatsu, Shiga, 525-8577 Japan
- <sup>14)</sup> Department of Mechanical Engineering, Shizuoka University,  
3-5-1 Johoku, Naka-ku, Hamamatsu, Shizuoka, 432-8561 Japan
- <sup>15)</sup> Department of Mechanical Engineering, Fukui University of Technology,  
3-6-1 Gakuen, Fukui, 910-8505 Japan

**ABSTRACT**

Very High Cycle Fatigue (VHCF) problem is regarded as one of the important issues to be solved in the field of mechanical engineering. Many researches have been conducted on VHCF properties of ferrous metals including high strength steels; however, long life fatigue data of non-ferrous metals are still limited. Based on this situation, a research sub-committee on VHCF was established in the Japan Society of Materials Science (JSMS) committee on fatigue of materials to accumulate VHCF data of non-ferrous metallic materials. To reveal

influential factors on VHCF properties, fatigue tests and fracture surface observations have been carried out, and effects of testing conditions including loading types, stress ratios and test frequencies were investigated. Some of the fatigue mechanisms were discussed from a view point of defects and microstructures. The research sub-committee on VHCF consists of three groups targeting die-cast aluminum alloy, beta titanium alloy and extruded magnesium alloys, respectively. Each group will present the results as the second, third, and fourth reports in this conference. This study, the first report, describes the purposes and the outline of the collaboration work as well as tentative fatigue data.

## **KEYWORDS**

Non-ferrous metal, Die-cast aluminum, Beta titanium, Extruded magnesium, Stress ratio, Stress gradient, Loading frequency, Microstructure

## **INTRODUCTION**

Reliability and safety of structural materials are highly required in modern society where both speeding-up and long service life are key factors for machine development. In addition, the use of high strength and lighter weight materials is getting expanding due to the strong demand for energy and weight savings of machine structures. With this background, very high cycle fatigue (VHCF) of metallic materials has been regarded as an important issue to be solved in the mechanical engineering field. VHCF phenomena has strange characteristics that fracture occurs with internal crack growth over  $10^7$  cycles and its fatigue strength is lower than that caused by surface crack growth. So far, many researches on VHCF have been reported on high strength steel, and several fracture mechanisms of internal fractures were also proposed [1]. VHCF researches of non-ferrous metallic materials; however, are still limited and the mechanisms of the lower fatigue strength due to internal fractures are hardly clarified yet. The use of lighter weight non-ferrous materials enhances weight saving leading to energy saving; therefore, to clarify those VHCF properties is quite necessary for ensuring reliability and safety in a long-term use. In addition, to accumulate quantitative VHCF data of non-ferrous materials can likely propose an unified understanding of the mechanism of VHCF through the comparison with already conducted researches on ferrous materials.

On the other hand, the requirement of fatigue testing machine optimized for VHCF regime as well as huge amount of time and human resources still makes it difficult to obtain reliable fatigue data in the VHCF regime. To conduct a systematic research in this field; therefore, fatigue researchers are preferable to collaborate and exchange information regarding data acquisition methods, accurate fatigue testing methods, analyses techniques etc. With the above as a background, a new research committee “sub-committee for very high cycle fatigue” was established in the JSMS committee on fatigue of materials in 2011. This sub-committee focuses on die-cast aluminum alloys, beta-titanium alloys and extruded magnesium alloys and plans to obtain VHCF data of those materials systematically [2]. The present study explains the purposes and the outline of the corroborative work and introduces a part of tentative results.

## **PURPOSES AND ORGANIZATIONS OF THE COLLABORATIVE WORK**

The research sub-committee on VHCF aims for conducting different two types of researches; the one is the collaborative work on supplied materials under unified experiments, and the other is the individual work proposed by each institution. Main topics of these two researches are as follows.

(1) Collaborative work

- Accumulation of basic S-N diagrams over  $10^7$  in cycles.
- Fracture origin analyses focusing on its size and location.
- Effect of loading type (rotary bending, push-pull, ultrasonic, etc.) on fatigue data.
- Development of the evaluation method of internal fractures.

(2) Individual work proposed by each institution

- Effect of two stage or three stage multiple fatigue loading.
- Effect of stress ratio or mean stress.
- Effect of loading frequency.
- Effect of microstructure and material on crack initiation and propagation processes.
- The mechanism of grain size reduction around the internal fracture origin.

More than 15 institutes as shown in Table 1 have participated in this sub-committee. Members have carried out VHCF fatigue tests according to the above two kinds of topics and have exchanged information about the obtained data. Die-cast aluminum alloy, beta titanium alloy, and extruded magnesium alloy are chosen as experimental materials, and three working groups focusing on each material were established in the sub-committee.

University	Aoyama Gakuin University, The University of Electro-Communications, Fukui University of Technology, Gifu University, Hiroshima University, Hokkaido University, Kobe University, Ritsumeikan University, Shizuoka University, University of Toyama
National Institute of Technology	NIT, Numazu College, NIT, Okinawa College, NIT, Toyota College, NIT, Akashi College
National research Institute	National Institute for Materials Science
Private company	Denso Corporation, Yamamoto Kinzoku, Co. Ltd.

Table 1: Institutes participating the collaborative work

## OUTLINE OF THE EXPERIMENTS AND TENTATIVE RESULTS

This section introduces the experimental procedures and a part of tentative fatigue data collected by each working group on die-cast aluminum alloys, beta titanium alloy, and extruded magnesium alloys. The more detailed information about fatigue data will be presented in the second, third, and fourth reports in this conference.

### Die-cast aluminum alloys

Material used was ADC 12 supplied by Denso corporation. Chemical compositions are: Si:10.7, Cu:2.21, Fe: 0.73, Zn: 0.7, Mn:0.24, Mg: 0.22, Ti: 0.04, Al: Bal (mass %). Mechanical properties are; tensile strength: 310MPa, elongation at break: 1.2%, Vickers hardness: 90.

Rotating bending tests, push-pull tests, and ultrasonic tests were carried out with specimens having a minimum diameter of 3mm to 5mm. Targets of the collaborative work and individual work proposed by each institution are as follows.

- Effects of loading types: 4-axis-type rotating bending, push-pull, and ultrasonic.

- Effects of loading process: Constant amplitude, 2-step loading, multiple repeated 2-step loading, etc.
- Effects of surface finishing: Machining, emery paper grinding with #1000-2000 grit, buffing with 1 $\mu$ m alumina abrasive, burnishing, etc.
- Effects of environment: Air atmosphere, salt water immersion, etc.

Examples of fatigue data obtained by 4-axis-type rotating bending tests are given in Fig. 1. Fig. 1(a) shows the data with specimen finished by buffing and Fig. 1(b) shows the data with that finished by buffing followed by burnishing. In Fig. 1(a), subsurface fracture initiates in cycles over  $10^8$ . The fracture origin of this data was confirmed a micro-shrinkage in the material. In Fig. 1(b), subsurface fractures of buff finished specimen also occurs in VHCF regime. All the burnished specimens failed from subsurface origins in VHCF regime over around  $10^7$  cycles, and no surface fracture was observed. This can likely be occurred by the suppression of surface crack due to the surface modification by burnishing.

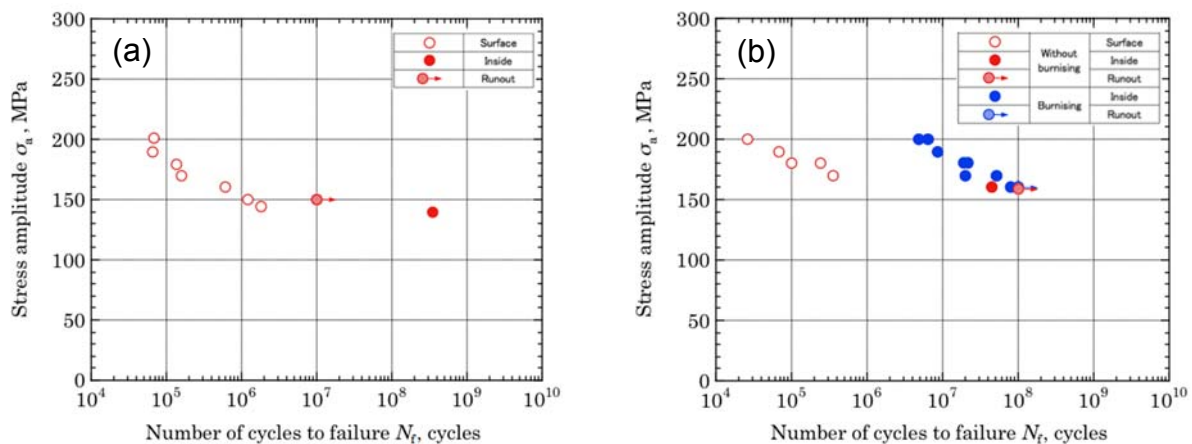


**Fig. 1** S-N diagram of ADC 12 obtained by 4-axis-type rotating bending. (a) shows the results of specimen finished by buffing, and (b) shows the results of finished by both buffing and burnishing.

### Beta titanium alloy

Material used was Ti-22V-4Al (DAT51) supplied by Daido Steel Co., Ltd. Chemical compositions are: Al: 4.15, V: 21.17, Fe: 0.15, C: 0.013, O: 0.14, N: 0.012, H: 0.0124, Ti: Bal. (mass %). Solution treatment for 3.6ks at 1023K followed by water cooling and aging for 14.4ks at 823K followed by air cooling were given to the material. Mechanical properties after the heat treatment are; tensile strength: 1235MPa, elongation at break: 9.3%, Vickers hardness: 327.

Rotating bending tests, push-pull tests, and ultrasonic tests were carried out with specimens having minimum diameter of 4mm. Targets of the collaborative work and individual work proposed by each institution are as follows.

- Effects of loading types: 4-axis-rotating bending, push-pull, and ultrasonic.
- Effects of stress ratio: Negative stress ratio, 0, and positive stress ratio.

Examples of fatigue data obtained by 4-axis-type rotating bending, push-pull, and ultrasonic tests are given in Fig. 2. Regardless of loading types and test frequency, fatigue lives are in the similar band in the S-N diagram. Surface fractures occurred in a relatively short life regime

before  $10^5$  cycles. In contrast, a subsurface fracture initiated at around  $2 \times 10^7$  cycles under 625MPa. Fig. 3 shows an example of fracture surface. A tiny flat area, so called facet, was observed in both surface fractures and subsurface fractures. Different from high strength steel, fatigue crack does not initiate from inclusion but always from microstructure.

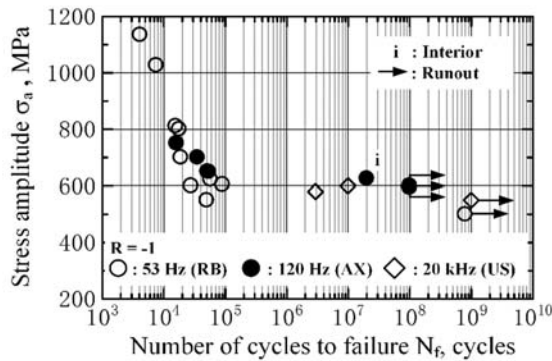


Fig. 2: S-N diagram of Ti-22V-4Al.

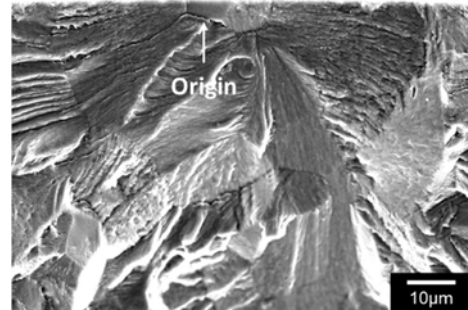


Fig. 3: An example of fracture origin.

Although fatigue data obtained by rotating bending tests generally show higher fatigue strength compared with push-pull tests because of stress gradient, Fig. 2 does not show such an ordinary trend. This is also a matter to be discussed in the collaborative work with accumulating data as well as further analyses including fractography.

### Magnesium alloys

Material used was three kinds of extruded magnesium alloys: JIS AZ31, AZ61, and AZ80. Chemical compositions and mechanical are listed in Table 2. Typical mechanical properties are: tensile strength: 232MPa, elongation at break: 19%, Vickers hardness: 54 for AZ31, tensile strength: 309MPa, elongation at break: 13%, Vickers hardness: 57 for AZ61, and tensile strength: 341MPa, elongation at break: 16%, Vickers hardness: 63 for AZ80.

material	Al	Zn	Mn	Si	Fe	Cu	Ni	Mg
AZ31	3.0	1.1	0.31	0.007	0.002	0.001	0.001	Bal.
AZ61	5.9	0.6	0.28	0.010	0.002	0.002	0.002	Bal.
AZ80	8.1	0.5	0.25	0.038	0.002	0.002	0.001	Bal.

Table 2: Chemical compositions of extruded magnesium alloys.

Rotating bending tests and push-pull tests were carried out in laboratory condition with specimens having minimum diameter of 4mm and 6mm. Surface finishing of the specimens was emery paper grinding (#600 to #2000 grit) in oil immersed condition followed by buffing with alumina abrasive. Targets of the collaborative work and individual work proposed by each institution are as follows.

- Effects of loading types: 4-axis-type rotating bending, push-pull.
- Effects of stress ratio: Negative, zero, and positive stress ratio.
- Effects of specimen size: 4mm diameter and 6mm diameter.

Tentative fatigue data indicate that fatigue strength well reflects the static strength of each material as shown in S-N diagram of AZ31 (Fig. 4) and AZ61 (Fig. 5). According to Fig. 4, push-pull fatigue data show a generally trend that it has a lower strength than rotating bending

fatigue data. Comparing Fig. 4 with Fig. 5, size effect is likely negligible for AZ31 whereas it may exist in AZ61. The reason for this trend should be discussed more deeply with increased number of fatigue tests in our future work. The other data including the results of AZ80 will be introduced in the fourth report in the conference proceedings.

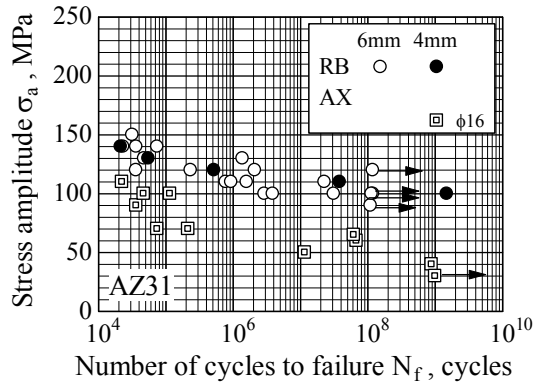


Fig. 4: S-N diagram of AZ31

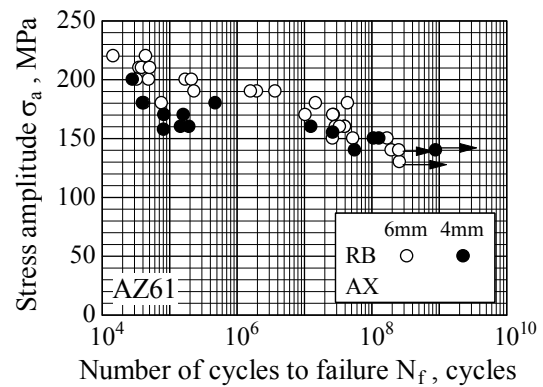


Fig. 5: S-N diagram of AZ61

## CONCLUSION

To clarify the properties of very high cycle fatigue on non-ferrous metallic materials, a research sub-committee was established in the JSMS committee on fatigue of materials, Japan. This committee aims for accumulating very high cycle fatigue data on die-cast aluminium, beta titanium and extruded magnesium alloys based on the two types of researches: the corroborative work on supplied materials under unified experiments and the individual work proposed by each institution. This study explained the purpose of the corroborative work and introduced the tentative results.

## ACKNOWLEDGEMENT

Die-cast aluminium alloys and beta titanium alloys used in this study were offered by Denso Corporation and Daido Steel Co., Ltd., respectively. The authors express sincere appreciation to their considerable supports for this research.

## REFERENCES

- [1] Sakai, T.:  
Review and prospects for current studies on very high cycle fatigue of metallic materials for machine structural use  
Journal of Solid Mechanics and Materials Engineering, Vol. 3, (2009), pp.425-439.
- [2] Akebono, H., Ueno, A., Ogawa, T., Oguma, N., Oguma, H., Kakiuchi, T., Kikuchi, S., Shiozawa, K., Shimamura, Y., Nakajima, M., Nakamura, T., Nakamura, Y., Nishida, T., Masaki, K., and Matsumura, T.:  
An attempt to accumulate very high cycle fatigue data of non-ferrous metal materials  
Proceedings of the 32nd Symposium on Fatigue, JSMS Committee on Fatigue of Materials, (2014), pp.213-217.

**Corresponding author:** nakamut@eng.hokudai.ac.jp

# FATIGUE BEHAVIOR IN METASTABLE STAINLESS STEEL DURING VERY HIGH CYCLE FATIGUE USING A STEPWISE LOADING METHOD

Guocai Chai<sup>1, 2\*</sup>, Lars Ewenz<sup>3</sup>, Katarina Persson<sup>1</sup>, Jens Bergström<sup>5</sup>, Christer Burman<sup>5</sup>, Martina Zimmermann<sup>3, 4</sup>

<sup>1</sup>Strategic Research, Sandvik Materials Technology, SE-811 81 Sandviken, Sweden

<sup>2</sup>Engineering Materials, Linköping University, SE-581 83 Linköping, Sweden

<sup>3</sup>Institut für Werkstoffwissenschaft, TU Dresden, D-01069 Dresden, Germany

<sup>4</sup>Fraunhofer Institut für Werkstoff- und Strahltechnik, D-01277 Dresden, Germany

<sup>5</sup>Universitetsgatan 2, SE-651 88 Karlstad, Sweden

## ABSTRACT

Very high cycle fatigue behaviour in a duplex stainless steel, SAF 2304, has been studied using both one single specimen/load test (OSSLT) and progressive stepwise-load increasing test (PSLIT) up to a total fatigue life of  $10^{10}$  cycles. The results show that the fatigue life is higher using progressive stepwise-load increasing test method with a lower starting stress than one single specimen/load test method with same stress level. Progressive stepwise-load increasing test can be used to predict the fatigue damage process, especially damage rate in individual specimen. In this study, the microstructure in the fatigue tested specimen and fracture surface have been investigated using SEM/EBSD and SEM/ECCI. Besides subsurface crack initiation, surface crack initiation has also been observed even in the VHCF region using PSLIT method. A high stress applied during the final step can be one of the reasons. Austenite to martensite phase transformation in this material during fatigue process has occurred. The initiation mechanism of this martensitic phase transformation and its effect on the fatigue behaviour have been discussed.

**keywords:** Very high cycle fatigue, phase transformation, damage, duplex stainless steels.

## INTRODUCTION

Fatigue behaviours of metals in the VHCF regime have been thoroughly investigated during the last decades. It has been found that fatigue crack initiation in metals can shift from surface defects, subsurface defects and subsurface matrix with decreasing applied stress or increasing fatigue life [1]. This can also lead to the formation of subsurface non-defect fatigue crack origin (SNDFCO) in the VHCF regime [2]. A conventional fatigue testing process to generate an S-N curve uses one single specimen/load test (OSSLT). However, stepwise load increase test or progressive stepwise load increasing test (PSLIT) has also been used to study fatigue and damage behaviour [3]. PSLIT can be used to estimate the endurance limit and to select appropriate stress amplitudes for constant amplitude tests with one single specimen. In this investigation, fatigue deformation and damage behaviour in a duplex stainless steel has been studied using both conventional OSSLT and PSLIT methods. The microstructure in the fatigue tested specimen and fracture surface have been investigated using SEM/EBSD and SEM/ECCI. The purpose is to get a better understanding of the VHCF behaviour in the material using PSLIT.

## MATERIALS AND EXPERIMENTAL PROCEDURES

In this investigation, one austenitic ferritic duplex stainless steel grade, Sandvik SAF 2304, was used. The specimens were taken from a bar material with a diameter of 25 mm, which was in the solution-annealed condition. Table 1 shows its chemical composition and mechanical properties. The material has a much higher yield strength comparing to that of



304/316 type of austenitic steels. Fig. 1 shows the microstructures of the material in the longitudinal direction. It looks like an austenite and ferrite lamellar composite structure (Fig. 1a). Fig. 1b shows a grain structure of the material, which has a rather small grain size.

C	Si	Mn	Cr	Ni	N	Mo	Fe	$\sigma_{YT}$ (MPa)	$\sigma_{UT}$ (MPa)	A (%)
0.010	0.44	0.86	22.6	4.62	0.119	0.08	Bal.	461	692	48.8

**Table 1:** Chemical composition (wt%) and tensile properties of SAF 2304 material used

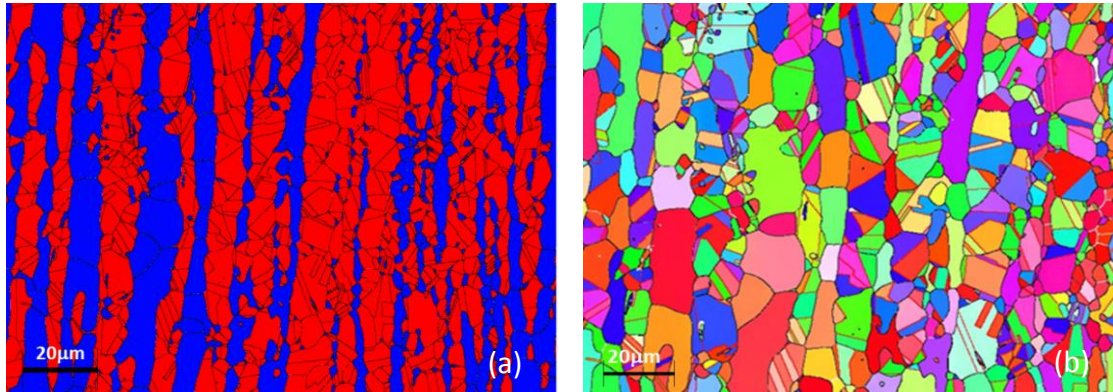


**Fig. 1:** Microstructure of SAF 2304 material used, (a). Phase structure, (b). Grain structure.

Two types of fatigue tests have been carried out. One was performed using an Amsler machine with a stress controlled testing and a frequency of about 140 Hz up to  $2 \times 10^6$  cycles. Another test was performed using an ultrasonic fatigue testing machine with a displacement controlled testing and a frequency of 20 kHz. An hour-glass geometry sample with a diameter of 3 mm was used. A stress ratio of  $R=0.1$  was applied for both tests. For the 20 kHz fatigue testing, a progressive stepwise load increase test (PSLIT) was used. Each load step was 10 MPa with a load cycle step higher than  $10^7$  cycles, stepwise increased until the specimen failed. The origins of fatigue crack initiation were investigated using a scanning electron microscope (SEM). The fatigue pre-initiation damage (dislocation slip bands) and phase transformation were studied using electron back-scattering diffraction (EBSD) technique and electron channelling contrast image (ECCI) technique.

## RESULTS AND DISCUSSION

### Influence of progressive stepwise load increasing test on fatigue life in VHCF region

Fig. 2 shows the S-N curves using one single specimen/load and progressive stepwise-load increasing testing. Three interesting phenomena have been observed. One is that the fatigue life of the material using PSLIT starting with a much lower stress is much higher than that using OSSLT comparing that with same stress level. The second is that depending on loading sequence the difference in total fatigue life using PSLIT is very high (about two orders). A larger cycle step (higher number of cycles) at a lower starting stress may lead to a much higher total fatigue life. Sample 2 and 3 started with a stress of 150MPa, but specimen 2 used a cycle step of  $10^9$  cycles, and sample 3 used a cycle step of  $10^7$  cycles. Consequently, sample 2 has a total fatigue life of  $1.38 \times 10^{10}$  cycles and a final stress of 260MPa, and sample 3 has a fatigue life of  $8.11 \times 10^7$  and a final stress of 250MPa. The third is that a smaller cycle step with same load step can lead to a higher cyclic deformation hardening. Sample 4 and 7 have the same starting stress. Sample 7 used a cycle step of about  $10^8$  cycles and sample 4 has a cycle step starting at  $10^7$  then increasing to  $10^8$  to  $10^9$  cycles. Sample 4 has a total fatigue life of  $1.10 \times 10^{10}$  cycles, but  $2.07 \times 10^9$  cycles for sample 7. Sample 5 shows an extreme condition. The cyclic deformation-hardening rate in this specimen is quite high. The large difference in both fatigue life and cyclic deformation hardening rate in this alloy using PSLIT can be dependent upon cyclic damage rate of

individual specimen and formation of martensite during fatigue testing. They will be discussed in the followings. Sample 1 was only run with a single loading.

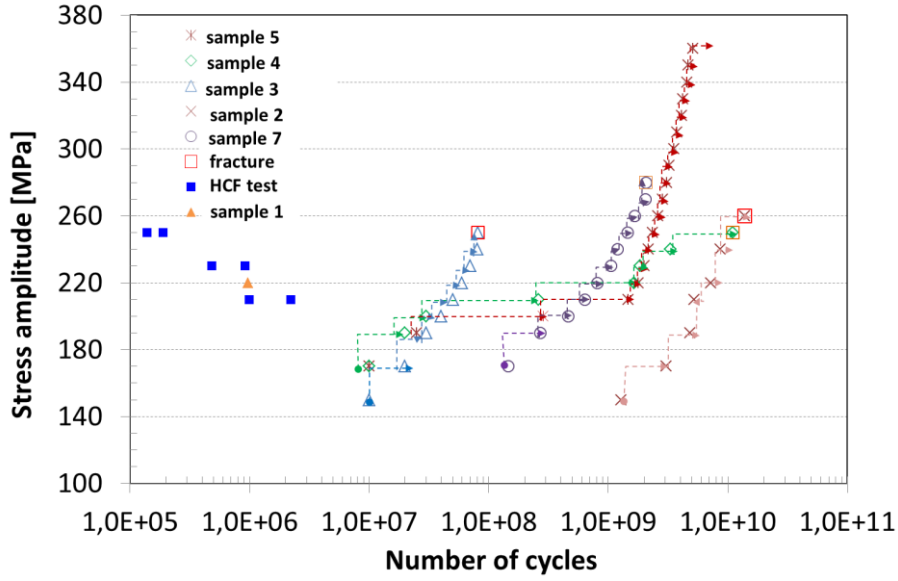


Fig. 2: S-N curves using one single loading (HCF) and accumulated cycles in progressive stepwise-load increasing tests. Sample 1 is only a single loading, and sample 5 is run-out.

### Damage and energy consumption with stepwise load increasing

As know, Miner's rule is usually used to predict accumulated damage in material during fatigue, which is shown as follows.

$$C = \sum_{i=1}^k \frac{n_i}{N_i} \quad \text{or} \quad C = \frac{\sum_{i=1}^k n_i \times \sigma_i}{W_{failure}} \quad (1)$$

where  $n_i$  is the number of cycles accumulated at stress  $\sigma_i$ ,  $N_i$  is the average number of cycles to failure at the  $i_{th}$  stress.  $W_{failure}$  is the critical damage.

In this paper, energy consumption,  $\Delta U$ , instead of the above damage parameter,  $n_i \times \sigma_i$ , is used to describe the fatigue damage process. This is due to the fact that in physics, strain energy is the energy stored by a system undergoing deformation. Fatigue damage is a cyclic plastic deformation process. The fatigue damage should therefore be correlated to the energy consumption during cyclic plastic deformation. For load controlled fatigue testing, plastic deformation mainly occurs during the first cycle, and then mainly elastic strain. In this study, total energy (elastic energy and plastic energy) is used to describe the damage process. The strain energy can be calculated as follows.

$$U = \frac{1}{2} V \sigma, \quad \sigma = E \varepsilon \quad \text{when } \varepsilon \leq \frac{\sigma_Y}{E} \quad \text{and} \quad \sigma = K' \varepsilon_{pl}^{n'} \quad \text{when } \varepsilon \geq \frac{\sigma_Y}{E} \quad (2)$$

where  $E$  is the Young's modulus,  $\varepsilon$  and  $\varepsilon_{pl}$  are the strain and plastic strain,  $V$  is the volume,  $K'$  and  $n'$  are constants. To study the influence of elastic and plastic strain on the fatigue behaviour, the Basquin and Coffin-Manson failure models were also used here.

$$\text{Basquin equation: } \frac{\Delta \varepsilon_{el}}{2} = \frac{\sigma_{f'}}{E} (2N_f)^b, \quad \text{Coffin-Manson equation: } \frac{\Delta \varepsilon_{pl}}{2} = \varepsilon_f' (2N_f)^c \quad (3)$$

The cyclic properties of the present 2304 grade are approximated from the cyclic parameters presented in Table 3, reported in [5].

$\sigma_f'$ , MPa	b	$\varepsilon_f'$	c	$n'$	$K'$ , MPa
728	-0,049	0,038	-0,43	0,114	1057

**Table 3.** Cyclic properties of the SAF 2304 grade, assumed from [5]

Fig. 3a shows the accumulated plastic strain versus total accumulated number of cycles of the samples with PSLIT. It shows an increasing relation for all samples tested, but at different lives. It indicates that the final accumulated damage in individual sample is of the same order amongst the different samples, although the damage rate may differ (e.g. see sample 4). Applying the cyclic properties of Table 3, the experimental results may be inserted in a strain-life diagram and compared against the Basquin and Coffin-Manson equations, Fig. 3b, representing the elastic and plastic damages, respectively. Fig. 3c shows the correlation of fraction of energy consumption in each specimen during each step versus number of cycles. Fraction of energy consumption is defined here as a ratio of energy consumption of each step to the total energy consumption until specimen fails,  $\Delta U_i / \sum \Delta U_i$ . This diagram actually shows the damage rate of each specimen during fatigue process. Specimen 7 has a higher damage rate than specimen 2, and consequently a lower fatigue life. Since all curves show a similar slope, it is therefore believe that the damage mechanism in these specimens during fatigue process is similar, but the damage rate or speed is different. Specimen 3 has a low cycle step of  $10^7$  cycles. It shows a very high damage rate.

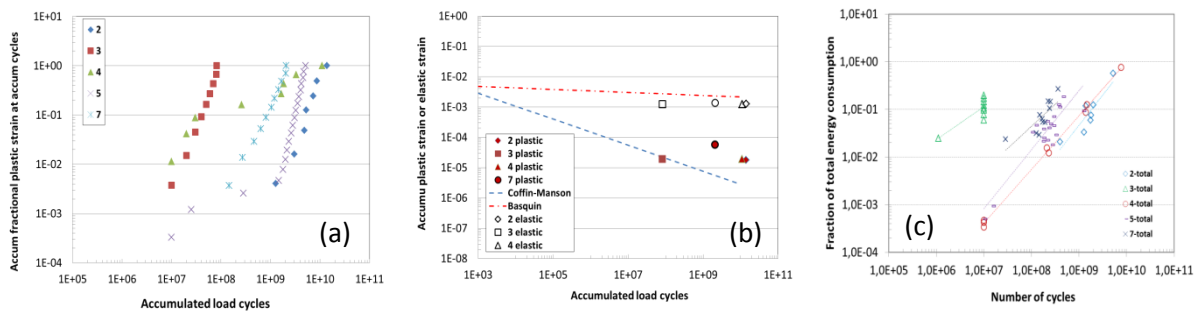


**Fig. 3:** Damage during fatigue, (a). Accumulated plastic strain versus accumulated number of load cycles, (b). Strain-life failure diagram correlating experimental results of individual samples to the Basquin and Coffin-Manson failure models, (c). Fraction of energy consumption of each specimen during each step versus number of cycles.

### Fatigue crack initiation with stepwise load increase

An earlier study shows that fatigue crack initiation at subsurface inclusion in duplex stainless steel can be observed when the fatigue life is higher than  $2 \times 10^8$  cycles [6]. In this study, fatigue crack initiation at subsurface inclusion was only observed in specimen 4, which has a total fatigue life of  $1.10 \times 10^{10}$  cycles at a maximum stress of 250 MPa. A fine grain area, FGA, around the inclusion has formed (Fig. 4a). For other failed specimens, the fatigue crack initiation occurred mainly at surface defects, and no FGA can be observed although they have a total fatigue life longer than  $10^9$  cycles such as specimen 7, which has a total fatigue life of  $2.07 \times 10^9$  cycles (Fig. 4b). One explanation can be that at the last stress applied the stress was now high enough to cause the fatigue crack initiation at the surface defect.

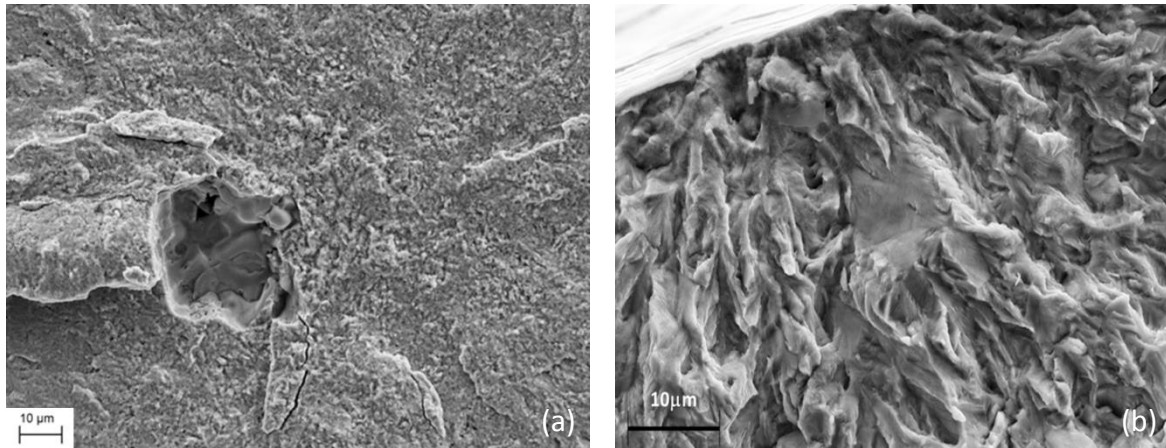


**Fig. 4:** Fatigue crack initiation, (a). Specimen 4, a total fatigue life of  $1.10 \times 10^{10}$  cycles, FGA formed at subsurface inclusion, (b). Specimen 7, a total fatigue life of  $2.07 \times 10^9$  cycles, fatigue crack initiation at surface defect, no FGA can be observed.

### Cyclic deformation induced phase transformation

It has been reported that deformation induced austenite to martensite phase transformation can occur in 2304 type of duplex stainless steel when the material is severely deformed [7]. For high cycle or very high cycle fatigue, it is interesting to know if this phase transformation can occur since the applied stress is usually low. Actually, this does occur as show in Fig. 5 (green phase).

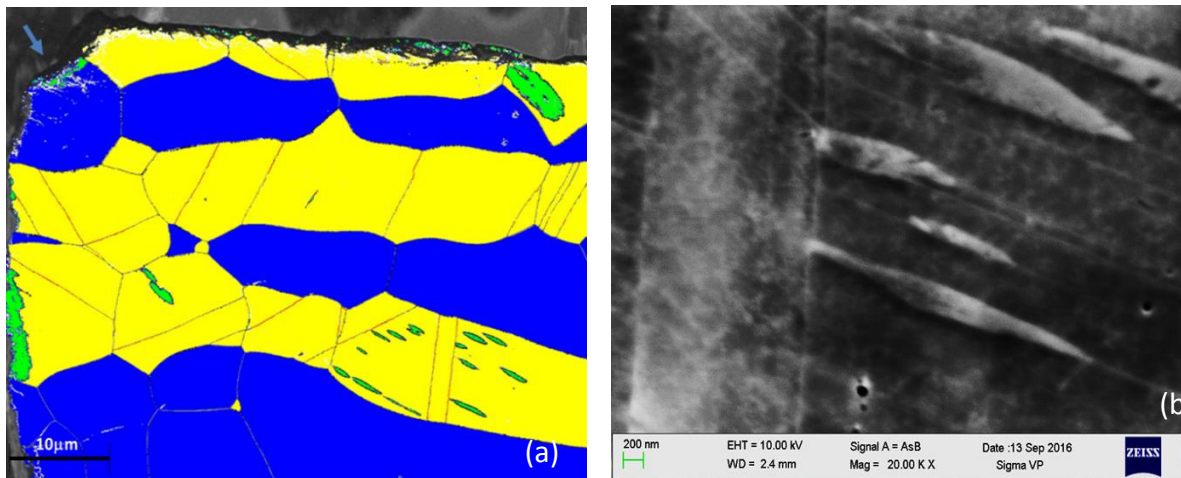


**Fig. 5:** Deformation induced austenite to martensite phase transformation at a stress amplitude of 250 MPa, (a). Formation of martensite, green-martensite, blue-ferrite, yellow-austenite, arrow indicating fatigue crack initiation starting area, (b). Initiation and propagation of martensitic phase during cyclic loading.

Martensitic phase has been observed in the fatigue-tested specimen. They appear near the fracture, but also in the grain inside with a stress amplitude of 250MPa. It has also been found that the amount of deformation martensite increases with crack propagation. This is reasonable since the remaining ligament of the specimen was reduced with crack propagation, which will increase the stress concentration at the crack front and cause a promotion of deformation martensitic phase transformation. Since martensitic phase transformation has a TRIP effect and promotes a further deformation hardening, this can affect fatigue behaviour and cause scatter in fatigue life with different phase transformation in the specimens as shown in Fig. 2. With ECCI technique, it was found that martensite mainly nucleated at the intersection points of different slip bands or between slip bands and grain boundary or twin boundary. The martensite phase then grows or propagates along the slip



bands (see Fig. 5b). Martensitic phase transformation during fatigue was also observed in 304 type of austenitic stainless steel [8].

## CONCLUDING REMARKS

SAF 2304 material shows a higher fatigue life using progressive stepwise-load increasing test than one single specimen/load test at same stress level.

The accumulated plastic strain at failure was of the same order of the different samples, but still the failure cyclic lives could differ of several orders of magnitude. It suggests the failure to be controlled by localized failure mechanisms.

Progressive stepwise-load increasing test can predict the fatigue damage process, especially damage rate in individual specimen.

SAF 2304 material can have austenite to martensite phase transformation during fatigue process, which will affect fatigue behaviour in the material and cause the scatter in the results.

## ACKNOWLEDGEMENTS

This paper is published by permission of Sandvik Materials Technology. Supports of Mr Pasi Kangas and Dr Tom Eriksson are acknowledged.

## REFERENCES

- [1] Mughrabi H.  
On multi-stage fatigue life diagram and relevant life-controlling mechanism in ultra high-cycle fatigue. *Fat. Fract. Eng. Mater Struct*, 2002, 25, pp. 755-764.
- [2] Chai G.  
The formation of subsurface non-defect fatigue crack origins, *International Journal of Fatigue*, 2006, 28, pp. 1533–1539.
- [3] Walther F. and Eifler D.  
Cyclic deformation behaviour of steels and light-metal alloys, *Materials Science and Engineering A* 468-470, 2007, pp. 259-266
- [4] <http://www.weibull.com/hotwire/issue116/hottopics116.htm>.
- [5] Bergengren Y., Larsson M., Melander A., Fatigue properties of stainless sheet steels in air at room temperature, *Materials Science and Technology*, 11, 12, 1995.
- [6] Chai G. Zhou N. Ciurea S. Andersson M. and Lin Peng R.  
Local plasticity exhaustion in a very high cycle fatigue regime. *Scripta Materialia* 66 (2012) 769–772.
- [7] Hedström P.  
Deformation and martensitic phase transformation in stainless steels  
Thesis, Luleå University of Technology, 2007:67/ISSN: 1402-1544.
- [8] Christ H-J. Grigorescu A. Müller-Bollenhagen C. Zimmermann M.  
Metastable Austenitic Stainless Steels and the Effect of Deformation-Induced Phase Transformation on the Fatigue Properties  
<http://www.mb.uni-siegen.de/lmw/veroeffentlichungen/2015/spp1204-buchtext-christ-kap2civ.pdf?m=e>.

**Corresponding author:** [guocai.chai@sandvik.com](mailto:guocai.chai@sandvik.com)

## FEM ANALYSES OF STRESS DISTRIBUTIONS AROUND INCLUSIONS AT INTERIOR CRACK INITIATION SITE IN VERY HIGH CYCLE FATIGUE

T. Sakai<sup>1)</sup>, R. Fincato<sup>2)</sup>, S. Tsutsumi<sup>2)</sup>, M. Sano<sup>2)</sup>, D.S. Paolino<sup>3)</sup>, T. Miyoshi<sup>4)</sup>,  
N. Oguma<sup>5)</sup>, A. Nakagawa<sup>6)</sup>

<sup>1)</sup> Research Organization of Science and Engineering, Ritsumeikan University,  
1-1-1 Noji-higashi, Kusatsu, Shiga, 525-8577 Japan

<sup>2)</sup> Joining and Welding Research Institute, Osaka University,  
11-1 Mihagaoka, Ibaraki, Osaka, 567-0047 Japan

<sup>3)</sup> Department of Mechanical and Aerospace Engineering, Politecnico di Torino,  
Corso Duca degli Abruzzi 24, Turin, 10129 Italy

<sup>4)</sup> Faculty of Management Information, Hannan University,  
5-4-33 Amamihigashi Matsubara, Osaka, 580-8502 Japan

<sup>5)</sup> Faculty of Engineering, University of Toyama,  
3190 Gofuku, Toyama, 930-8555 Japan

<sup>6)</sup> Industrial Products Company, Hitachi, Ltd.,  
3-18 Nakanoshima 2-chome, Kita-ku, Osaka, 530-0005 Japan

### ABSTRACT

In the case of interior fracture mode in very high cycle fatigue, one can usually observe the fish-eye on the fracture surface and an inclusion is also observed at the center of the fish-eye. In addition, the fine granular area (FGA) is often found in the vicinity around the inclusion on the fracture surface. Thus, the stress concentration around the inclusion gives the most important factor to govern the fatigue property for high strength steels in the very high cycle regime. From this point of view, the authors have analyzed 3-D stress distributions around the interior inclusions having various shapes and elastic constants. In the present work, the authors have attempted to review the general aspects on the stress distribution paying a particular attention to the effect of shape and elastic constants of typical inclusions such as  $Al_2O_3$  and MnS observed in the high strength steel.

### KEYWORDS

Very high cycle fatigue, Interior inclusion, Stress concentration, FEM analysis, Stress distribution, Crack initiation

### INTRODUCTION

In high strength steels, very high cycle fatigue (VHCF) failures usually originate from internal inclusions [1, 2]. Therefore, stress distribution around inclusions originating internal failures has a key role in the VHCF response of high strength steels. It is well-known that, depending on the shape and on the elastic properties of the inclusion, different stress concentrations take place along the interface between the nonmetallic inclusion and the steel matrix [3]. From the VHCF viewpoint, the location of the region that experiences the maximum stress concentration can be considered as the most critical point for the internal crack nucleation. Referring to the numerous VHCF fracture surfaces analyzed by the authors [3-6], the critical point for crack nucleation is, in most of the cases, edge of the inclusion orthogonal to the loading direction. In a few cases, crack may nucleate at the top or bottom of the inclusion. In these rare cases,

inclusion is not visible since it is beneath the fracture surface. Thus, experimental evidence shows that, regardless of the inclusion type (oxide, sulphide or nitride) and shape (circular, elliptical or parallelepipedal), in high strength steels subjected to tension-compression or to rotating bending, internal VHCF failures mainly nucleate from points belonging to a plane that intersects the inclusion.

From this point of view, the authors have attempted to review the effect of shape and elastic constant on the stress concentrations around internal inclusions, paying a particular attention to  $\text{Al}_2\text{O}_3$  and MnS inclusions typically observed in high strength steels. Various finite element analyses are performed in order to assess stress distributions around typical inclusions and to find possible explanations for the experimental evidence of VHCF cracks that mainly nucleate from a plane that crosses the inclusion in the present paper.

### TYPICAL EXAMPLES OF FRACTURE SURFACES NEAR CRACK NUCLEATION SITE

The authors have performed numerous fatigue tests on different high strength steels such as SUJ2 steel [4-6], and AISI H13 steel [7,8]) by using self-developed rotating bending [9] and ultrasonic tension-compression testing machines. Fig.1(a) indicates a pair of fracture surfaces obtained in the same specimen. The left hand side shows a photograph of the fracture surface having the inclusion, whereas the right hand side gives the fracture surface pulled out the inclusion. In addition, Fig.1(b) indicates a set of the fracture surface and the cross section along the white line in the left hand photograph. In many cases, fracture surfaces in Fig.1(a) are observed as reported by many researchers [1,4]. However, the authors had also taken the fracture surface without inclusion, but an inclusion was newly observed on the cross section sliced along the white line in the fracture surface. Thus, there can be a few examples of the fracture surface having the inclusion beneath the fracture surface, even if no inclusion is observed on the fracture surface.

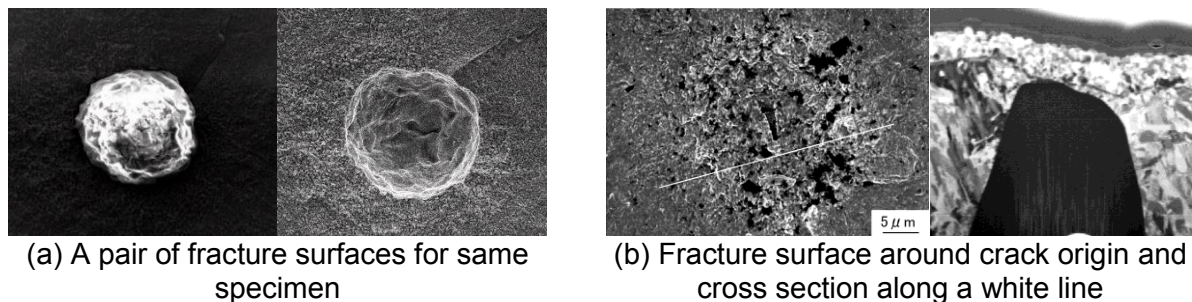


**Fig.1:** Typical examples of fracture surfaces near crack nucleation site

### NUMERICAL ANALYSES

A spherical inclusion, alternatively composed of  $\text{Al}_2\text{O}_3$  or MnS, is modeled within a cylindrical ferritic body with a ratio between the two radii equal to 0.20. The sample is constrained at the base to give a uniaxial stress condition and it is pulled along the y direction up to 100 MPa by a uniformly distributed pressure on top (Fig. 3a). The inclusion material is assumed as isotropic whereas the ferritic matrix is assumed anisotropic. The idea is to investigate the influence of the elastic anisotropy under different Euler angle orientations in terms of stress peak and stress triaxiality around the grain. A preliminary study on pure ferrite was carried out on a cubic sample to define the Young's modulus distribution for different crystal orientations of the cubic structure.

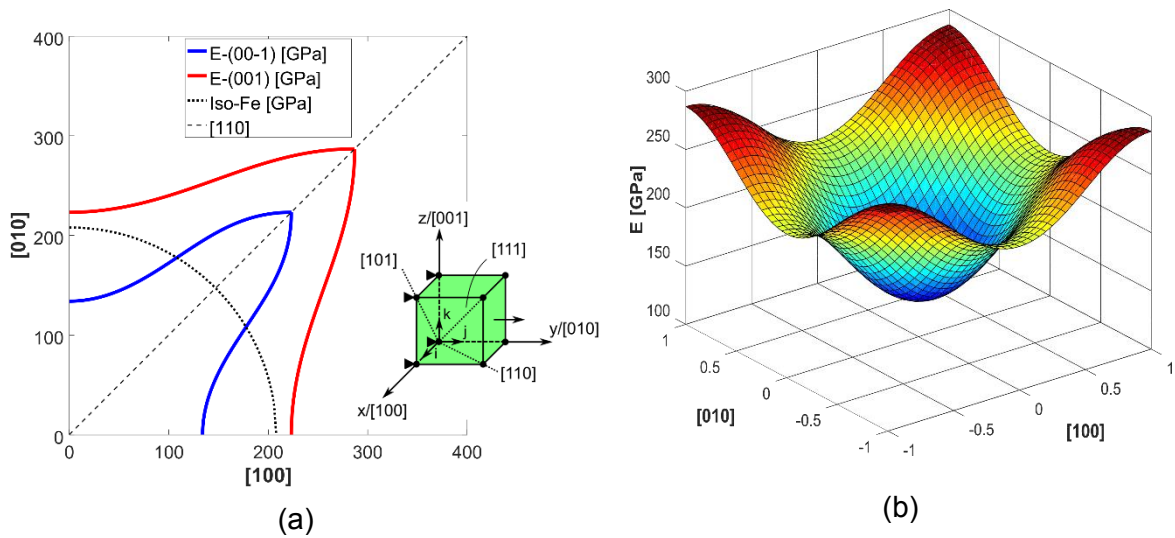


**Fig.2:** (a) (001) and (00 $\bar{1}$ ) cross-sectional views of the Young's modulus; (b) Young's modulus on the (001) plane

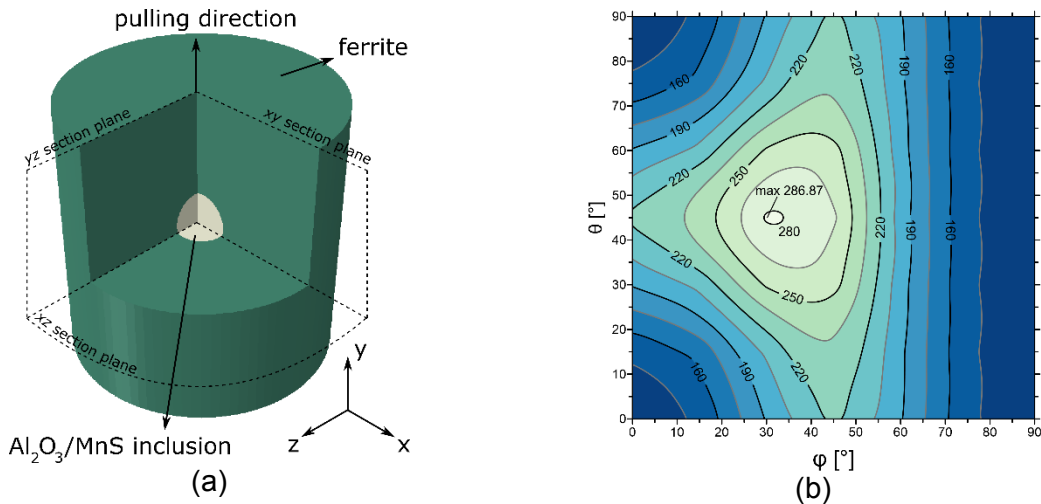


**Fig.3:** (a) sketch of the cylindrical sample with the spherical inclusion; (b) Young's modulus distribution for the cubic sample in Fig 2a for different Euler angles orientations  $(\varphi, \theta, 0^\circ)$ .

The elastic constants assumed accordingly to Tjahjanto *et al.* [10], who investigated the effect of the grain orientation on the retain austenite transformation process for a carbon steel, whereas the homogenized Young's modulus and Poisson's ratio was taken from [11].

The variation of the Young's modulus can be obtained analytically by means of the standard formula proposed by Nye [12]. The results are reported in Fig. 2a with the two cross-sectional  $E$  curves, respectively on the (001) and (00 $\bar{1}$ ) plane, and in Fig. 2b with a 3D view of the elastic potential on the (001) plane. As it can be seen the Young's modulus is maximum along the [111] direction (i.e. cubic diagonal) and is minimum along the [001] one (as well as along the [100] and [010] directions due to symmetry).

The same result can be achieved with finite elements analyses carried out on the cubic sample of Fig. 2a, where the whole base is constrained along the pulling direction  $y$  and only its central node is constrained along  $x$  and  $z$ , realizing a uniaxial tensile test condition. Due to the high symmetry of the bcc configuration, it is possible to consider the variation of only two of the three Euler angles without loss of generality. Starting from the  $(0^\circ, 0^\circ, 0^\circ)$  set, which represents the case where the crystallographic axes are coaxial with the reference system (see Fig. 2a),



the first two Euler angles  $\varphi$  and  $\theta$  were alternatively changed, assuming amplitudes between  $0^\circ$  and  $90^\circ$ , and covering all the mutual combinations. The results are shown in Fig. 3b where the values of  $E$  are reported in GPa. The analytical and numerical  $E$  moduli are reported in Table 1 indicating the crystallographic direction parallel to the  $y$  axis. The numerical values are in good agreement with the analytical ones, with errors that can be considered negligible.

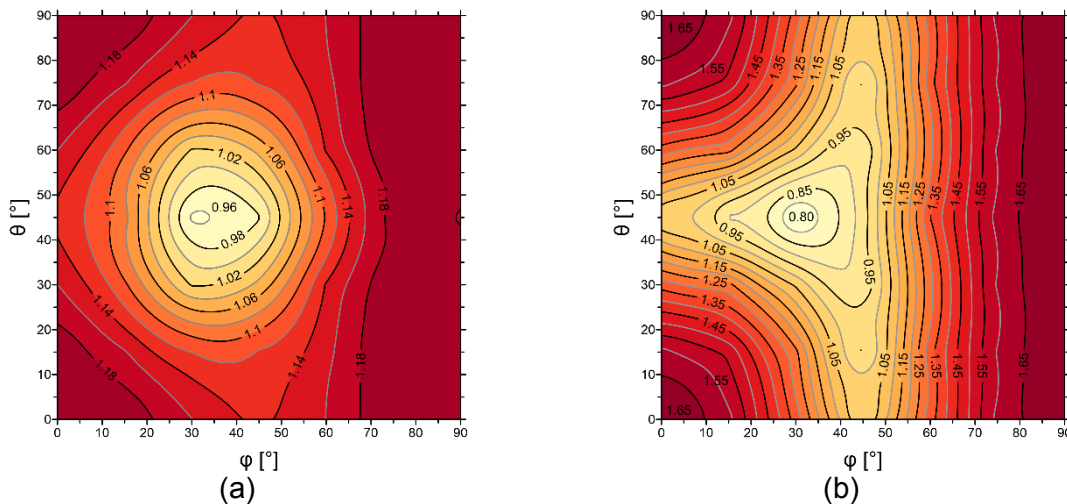
	Analytic E [GPa]	F.E. E [GPa]	Err (%)
[100], [010], [001]	133.98	133.96	0.0164%
[110], [101], [011]	223.21	223.22	0.0072%
[111]	286.89	286.87	0.0067%

**Table 1:** Analytical and numerical values of the Young modulus for different Euler angles.

	E [GPa]	$\nu$
Ferrite (isotropic)	208.0	0.287
$\text{Al}_2\text{O}_3$	389.5	0.25
MnS	138.0	0.3

**Table 2:**  $E$  and  $\nu$  for the isotropic ferrite and the  $\text{Al}_2\text{O}_3$  and MnS inclusions.

The next step was considering a spherical inclusion alternatively harder and softer than the surrounding ferrite. The analyses were conducted via user subroutine for the commercial code Abaqus (ver 6.14-5) meshing the geometry of Fig. 3a with 126144 three-dimensional hexahedral elements with reduced integration (i.e. C3D8R) for a total number of nodes of 135501. The effect of the anisotropy was studied comparing the results carried out for different Euler angles sets against a reference solution, obtained with an homogenized isotropic Young's modulus and Poisson's ratio (see Table 2). The following Fig. 4 displays the Mises stress (Fig. 4a and d) and the stress triaxiality (Fig. 4b and d) peaks normalized against the maximum von Mises stress and stress triaxiality in the isotropic case. The maps in red and green refer respectively to the  $\text{Al}_2\text{O}_3$  and MnS inclusions. Comparing Fig. 3b with Fig 4a and b it is possible to notice an inverse relationship between the Young's modulus and the normalized Mises stress and stress triaxiality: where  $E$  is higher the other two are lower and vice versa. Therefore, a configuration with the crystallographic axis aligned with the pulling direction represents the worst scenario possible for the harder inclusion. In this case the peak values for the stress triaxiality and the Mises stress are localized in two different areas. The first one is generated at the top and bottom of the grain along the  $y$  direction (Fig. 5b) whereas the max Mises stress is located on a circular area around the top of the grain as shown in Fig. 5a.



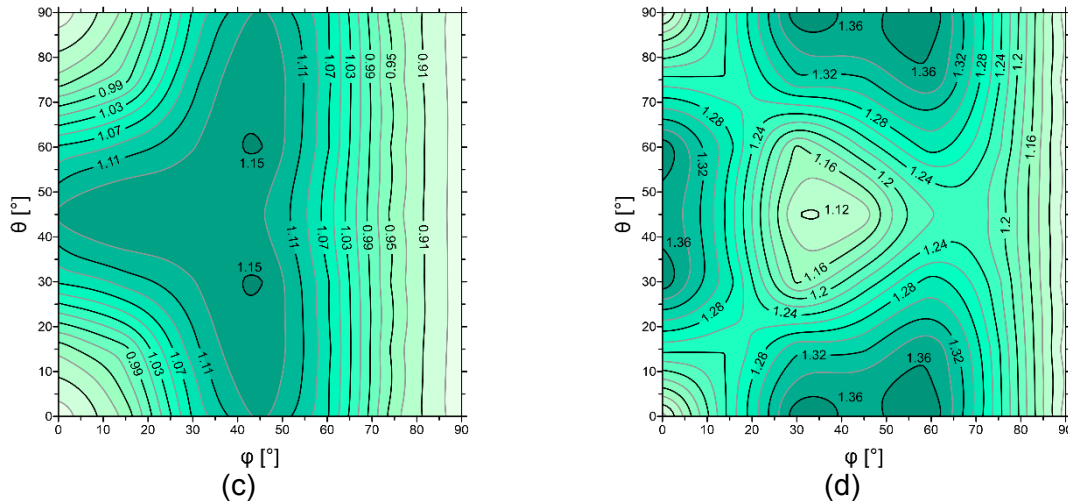


**Fig.4:** (a) and (c)  $\text{MaxMises}_{\text{anisotropic}} / \text{MaxMises}_{\text{isotropic}}$  maps for the  $\text{Al}_2\text{O}_3$  and MnS inclusions, (b) and (d)  $\text{MaxTX}_{\text{anisotropic}} / \text{MaxTX}_{\text{isotropic}}$  maps for the  $\text{Al}_2\text{O}_3$  and MnS inclusions.

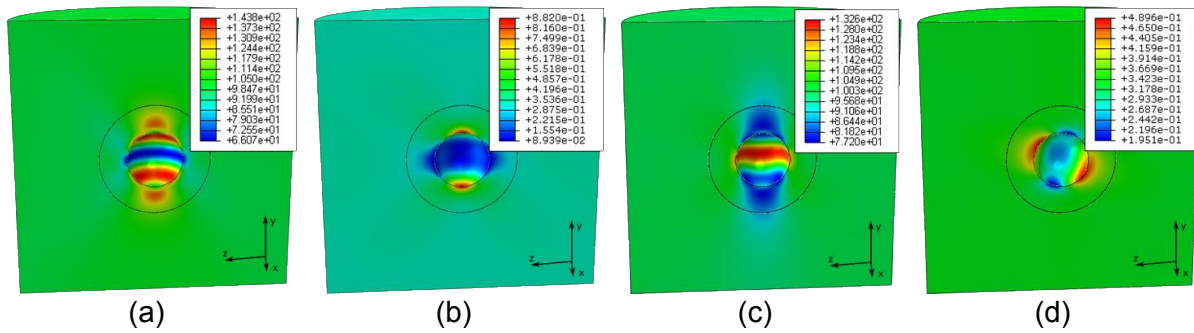


**Fig.5:** (a) and (b) Max Mises stress [MPa] and stress triaxiality contour fields for the  $\text{Al}_2\text{O}_3$  case,  $(0^\circ, 0^\circ, 0^\circ)$  Euler angle set, (c) Max Mises stress contour fields for the MnS case  $(45^\circ, 30^\circ, 0^\circ)$  Euler angles set, (d) stress triaxiality contour fields for the MnS case  $(0^\circ, 30^\circ, 0^\circ)$ .

On the other hand, the investigation on a softer inclusion lead to a different conclusion. The Mises stress shows, more or less, the same distribution of the Young's modulus however the stress triaxiality displays a more complicated pattern, that can may be explained with some instability modes generated during the compression of the softer material. In this last case the max for the Mises stress and the stress triaxiality are obtained in two different combination of the Euler angles:  $(45^\circ, 30^\circ, 0^\circ)$  see Fig. 5c and  $(0^\circ, 30^\circ, 0^\circ)$  see Fig. 5d.

## CONCLUSIONS

The presented in this paper aimed to investigate the stress distribution around a  $\text{Al}_2\text{O}_3$  or MnS spherical inclusion typically observed in high strength steel. Stress peaks are in fact known to be the most important factor to govern the fatigue property in the very high cycle regime. Numerical simulations were conducted on a cylindrical ferritic sample with a spherical inclusion to study the von Mises stress and stress triaxiality concentration under different orientations of the crystallographic structure. Moreover, elastic anisotropy was taken into account for the matrix material to consider an additional factor that may contribute to the individuation of the initial crack formation site. The results show that an initial debonding can take place on the contact surface between the grain and the matrix depending on the crystallographic orientation. It is imagined that, after the initial opening, the crack will proceed along the grain-matrix surface until it reaches the plane orthogonal to the pulling direction. At that point, it will continue to

propagate on that plane. However, a more sophisticated numerical model is needed to catch the proper evolution path of the crack after the initial debonding.

## REFERENCES

- [ 1 ] Sakai T.:  
Review and prospects for current studies on very high cycle fatigue of metallic materials for machine structural use  
J. Solid Mech. and Mater Engng, Vol.3, No.3, (2009), pp.425-439
- [ 2 ] Li, X.S.:  
Effects of inclusions on very high cycle fatigue properties of high strength steels  
Int. Mater. Review 57 (2012), pp. 92-114
- [ 3 ] Pilkey, W.D., Pilkey, D.F.:  
Peterson's stress concentration factors – 3<sup>rd</sup> Edition  
John Wiley & Sons, Hoboken, New Jersey, 2008
- [ 4 ] Sakai, T., Sato, Y. and Oguma, N.:  
Characteristic S-N properties of high-carbon-chromium-bearing steel under axial loading in long-life fatigue  
Fatigue Fract. Engng. Mater. Struct 25 (2002), pp. 765-773
- [ 5 ] Sakai, T., Nakagawa A., Oguma, N., Nakamura, Y., Ueno, A., Kikuchi, S., Sakaida, A.:  
A review on fatigue fracture modes of structural metallic materials in very high cycle regime  
Int. Journal of Fatigue, Vol.93, (2016), pp.339-351
- [ 6 ] Oguma, N., Lian, B., Sakai, T., Watanabe, K., Otake, Y.:  
Long life fatigue fracture induced by interior inclusions for high carbon chromium bearing steels under rotating bending, Journal of ASTM International, Vol.7, No.9, (2010), JAI102540, pp.1-9.
- [ 7 ] Paolino, D.S., Tridello, A., Chiandussi, G., Rossetto, M.:  
S-N curves in the very-high-cycle fatigue regime: statistical modeling based on the hydrogen embrittlement consideration  
Fatigue Fract. Engng. Mater. Struct 39 (2016), pp. 1319-1336
- [ 8 ] Tridello, A.; Paolino, D.S., Chiandussi, G., Rossetto, M.:  
Different inclusion contents in H13 steel: Effects on VHCF response of Gaussian specimens  
Key Engng. Mater. 665 (2016), pp. 49-52
- [ 9 ] Yamamoto, T., Kokubu, A., Sakai, T., Kiyama, I., Nakamura, Y.:  
Development and fundamental performance of dual-spindle rotating bending fatigue testing machine with special device providing corrosive environments  
Proc. of VHCF-5, (2011), pp.439-444
- [ 10 ] Tjahjanto, D.D., Turteltaub, S., Suiker, A.S., van der Zwaag, S.:  
Modelling of the effects of grain orientation on transformation-induced plasticity in multiphase carbon steels  
Modelling Simul. Mater. Sci. Eng., 14(2006), pp.617-636
- [ 11 ] Schmitz, G.J., Prah, U.:  
Integrative computational materials engineering: concepts and application of a modular simulation platform  
Wiley-VCH Verlag GmbH & Co. KGaA, Weinheim, Germany, 2012
- [ 12 ] Nye, J.F.:  
Physical properties of crystals, their representation by tensor and matrices  
Oxford University press, Oxford, 1956

**Corresponding author:** Prof. Tatsuo SAKAI, sakai@se.ritsumei.ac.jp

# DEVELOPMENT OF NITRIDED 18Ni MARAGING STEEL TO OPTIMISE THE VERY HIGH CYCLE FATIGUE PROPERTIES

U. Karr<sup>1)</sup>, B. Pennings<sup>2)</sup>, D. Tran<sup>2)</sup>, H. Mayer<sup>1)</sup>

<sup>1)</sup> Institute of Physics and Materials Science, BOKU, Peter-Jordan-Str. 82, A-1190 Vienna, Austria

<sup>2)</sup> Bosch Transmission Technology, 500 Dr Hub van Doorneweg 120, P.O. Box, NL-5000 AM Tilburg, The Netherlands

## ABSTRACT

The very high cycle fatigue (VHCF) properties of four 18Ni maraging steels are investigated. Ultrasonic fatigue tests are performed on thin sheets with nitrided surfaces at load ratio  $R = 0.1$ . Traditional maraging steel containing Ti (material A) shows crack initiation at TiN-inclusions. The elimination of Ti and the increase of Co content (material B) leads to crack initiation preferentially at  $Al_2O_3$ -inclusions, which are less damaging than TiN-inclusions leading to a higher VHCF strength. A further developed maraging steel (material C) with reduced Co content that is compensated for by alloying with Al showed crack initiation at  $Al_2O_3$ - as well as Zr(N,C)-inclusions. Zr(N,C)-inclusions are more damaging than  $Al_2O_3$ -inclusions and less damaging than TiN-inclusions. The highest VHCF strength was found for a recently developed alloy with increased Al content (material D). Inclusion-initiated fracture as well as surface crack initiation is found for this material.

## KEYWORDS

Maraging steel; Nitriding; Non-metallic inclusion; Ultrasonic fatigue testing; Very high cycle fatigue

## INTRODUCTION

Maraging steels show an exceptional combination of very high mechanical strength and excellent manufacturing properties. Due to the very low carbon content, a relatively soft and tough martensite is yielded by solution annealing or austenitising treatment. Precipitation hardening then leads to the formation of intermetallic compounds resulting in a very high strength. Additionally, nitriding treatment can be applied for surface hardening due to the good nitridability.

These excellent functional properties make maraging steels a potentially attractive material for highly stressed components. Cyclic loads are present in several of the actual applications of maraging steels, such as springs or components of the drive train in vehicles. The numbers of load cycles in these applications can be very high which is why the very high cycle fatigue (VHCF) properties of these materials are of great interest.

## MATERIAL AND METHOD

### Material

Fatigue tests are performed on four 18Ni maraging steels in precipitation hardened condition. Thin sheets with nitrided surfaces are tested. The respective chemical compositions of the four materials are shown in Tab. 1.

	Ni	Co	Mo	Ti	Al	Cr	Fe
Material A	18	9	5	0.5	-	-	balance
Material B	18	16.5	5	-	-	-	balance
Material C	18	5	5	-	1	1	balance
Material D	18	5	5	-	1.5	1	balance

Table 1: Chemical composition of the investigated maraging steels in weight %

Material A is a traditional maraging steel. Ti is eliminated and instead Co content is increased in Material B. The reduction of Co in Material C and D is compensated for by different amounts of aluminium. Tensile strength of all four materials is about 2000 MPa. Vickers hardness is 580 HV<sub>1.0</sub> (material A), 625 HV<sub>1.0</sub> (material B), 560 HV<sub>1.0</sub> (material C) and 615 HV<sub>1.0</sub> (material D), respectively.

### Experimental procedure

The experiments were performed using ultrasonic fatigue testing equipment developed at BOKU University [1]. The method to test thin sheets of high strength steels has been described in detail in a previous work [2]. In brief, rather than vibrating in resonance, the sheet specimens are driven to forced vibrations with a carrier specimen. The carrier specimen serves to introduce static and cyclic loads into the thin sheet specimens and additionally serves to avoid buckling and undesirable bending vibrations. The shape of the specimens used in the present investigation is shown in Fig. 1.

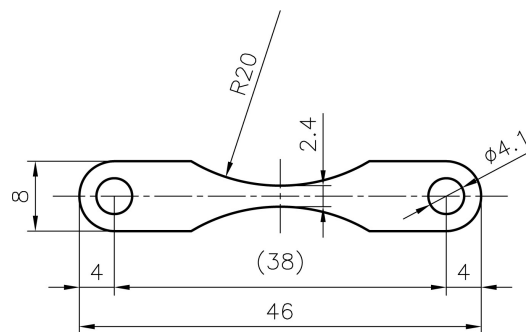


Fig. 1: Sheet specimens used in the ultrasonic fatigue tests (all measures in mm). Thickness of the specimens is 0.35 mm for material A, B and D and 0.435 mm for material C.

Experiments are performed in ambient air at 20 °C and 50% relative humidity. Fractographic investigations are conducted using a scanning electron microscope (SEM). Crack initiating inclusions were analysed using energy dispersive X-ray spectroscopy (EDS).

## RESULTS

VHCF properties of four 18Ni maraging steels have been investigated at load ratio  $R = 0.1$ .  $S-N$  data are shown in Fig. 2. Different symbols are used to denote the crack initiation sites. Lifetimes of fractured specimens are presented versus the respective actual stress amplitude at the crack initiation site. Due to the varying cross section area of the specimens, stresses at the crack initiation sites can be lower than the nominal stress in the centre of the specimen. In order to characterise loading of runout specimens, the nominal stress amplitude is used.

$S-N$  data of material A are shown in Fig. 2(a). Internal crack initiation at a TiN-inclusion is found in 22 of 23 fractured specimens. Fig. 2(b) shows the  $S-N$  data of material B. Crack initiation at an internal aluminate-inclusion is found in 12 of 17 fractured specimens. In three specimens, the crack was initiated internally in the matrix.  $S-N$  data obtained with material C are shown in Fig. 2(c). Of 20 fractured specimens, cracks initiated at an internal aluminate- and Zr(N,C)-inclusion in 5 and 14 specimens, respectively.  $S-N$  data of material D are shown in Fig. 2(d). In 4 specimens, the crack started at an internal aluminate-inclusion. 6 specimens failed from the surface. Surface crack initiation was exclusively found for material D. Specimens showing surface failure tend to fail at higher numbers of cycles than specimens with internal inclusion initiated failures.

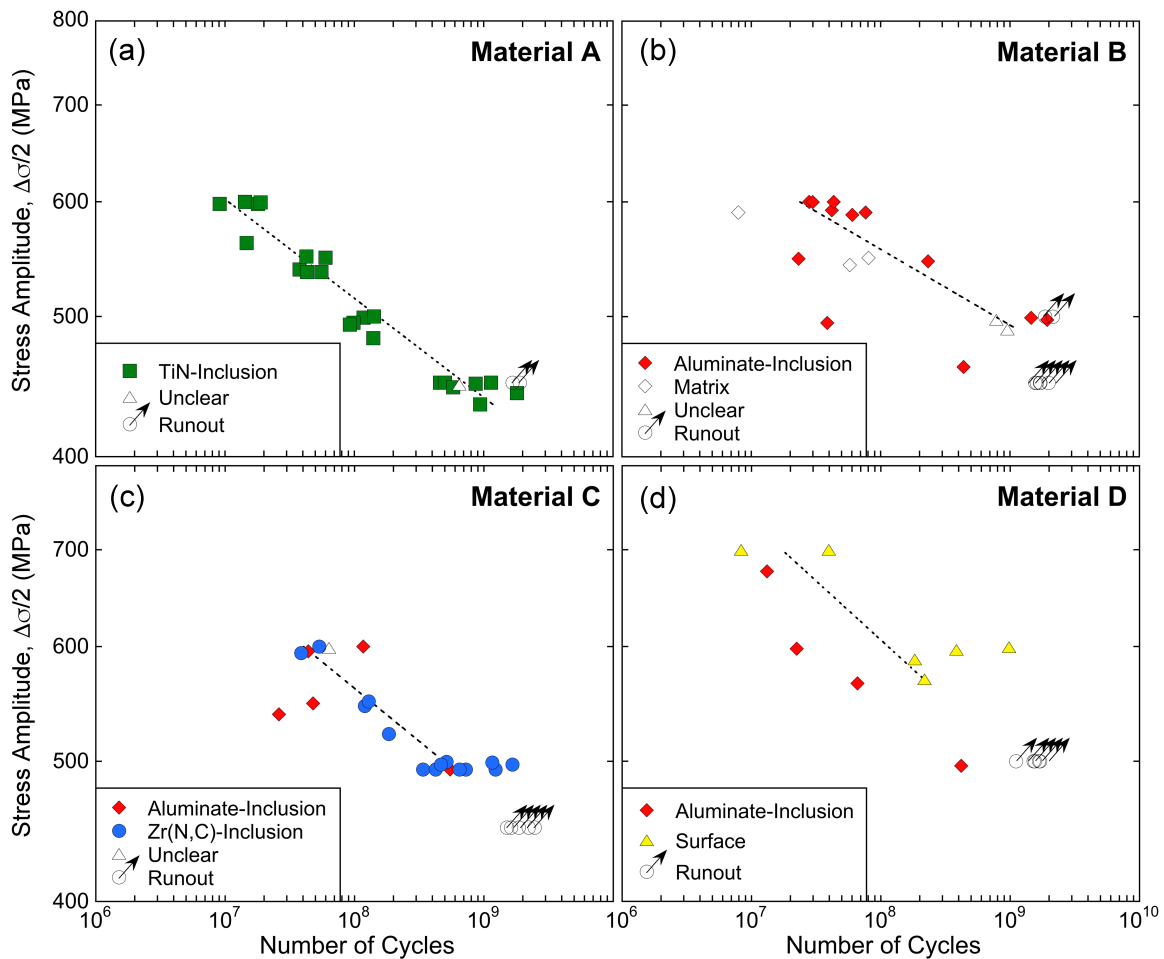


Fig. 2:  $S-N$  data of nitrated 18Ni maraging steel sheets measured at load ratio  $R = 0.1$ : (a) for material A, (b) for material B, (c) for material C and (d) for material D, respectively. Different symbols are used to mark the crack initiation sites

In order to compare the cyclic strength of the investigated materials, the stress amplitude with 50% fracture probability at  $10^8$  cycles can be used. This stress amplitude is 510 MPa for material A and 560 MPa for material B and C, respectively. Material D shows the highest cyclic strength with 610 MPa.

## DISCUSSION

Inclusions are the main source of fatigue cracks in material A, B and C. Solely material D shows surface and internal crack initiation. However, the earliest failures in material D are caused by internal inclusions. This indicates a prominent influence of internal inclusions on the fatigue damage mechanism, the cyclic strength and the fatigue lifetime of the investigated nitrided maraging steels.

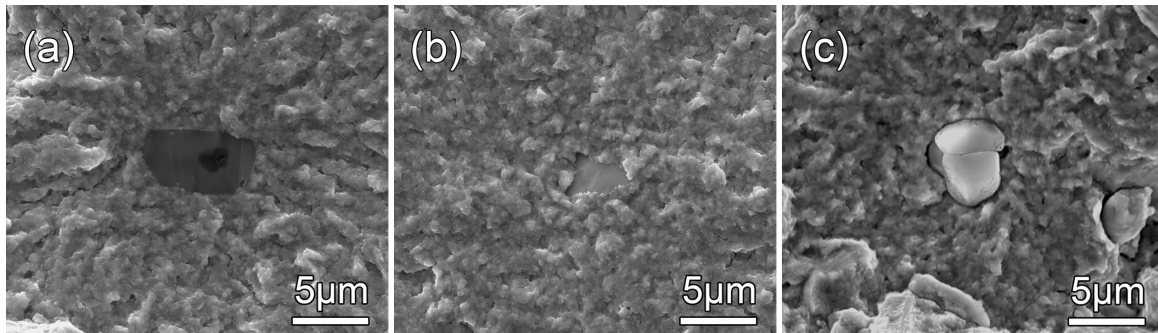


Fig. 3: Crack initiation at (a) TiN-inclusion, (b) Zr(N,C)-inclusion and (c) aluminate-inclusion

Fig. 3 shows examples for the three different crack initiation sites in the VHCF regime. Cracks initiated at broken secondary phase particles (TiN-inclusions and Zr(N,C)-inclusions, see Fig. 3(a) and 3(b), respectively) or at fractured interfaces between particles and matrix (aluminate-inclusions, see Fig.3(c)).

Fatigue lifetimes and cyclic strengths decrease with increasing size of the crack initiating inclusions. Murakami and Endo [3] showed that in presence of a small cavity or a secondary phase particle the endurance limit,  $\sigma_w$ , can be correlated to the square root of the projected area of the inhomogeneity,  $\sqrt{area}$ , as shown in Eq. (1).

$$\sigma_w^6 \cdot \sqrt{area} = C_M \quad (1)$$

The parameter  $C_M$  considers the position of the inhomogeneity (at the surface or in the interior), the Vickers hardness and the load ratio [4].

Eq. (1) suggests that the cyclic stress amplitude,  $\Delta\sigma/2$ , and the square root of the inclusion area,  $\sqrt{area_{INC}}$ , can be combined to the parameter  $\frac{\Delta\sigma}{2} \cdot (\sqrt{area_{INC}})^{\frac{1}{6}}$  that characterises the damage of a fatigue load cycle in presence of an inclusion. The number of cycles to failure,  $N$ , can be presented versus this parameter according to Eq. (2) [5].

$$N = C_A \cdot \left( \frac{\Delta\sigma}{2} \cdot (\sqrt{area_{INC}})^{\frac{1}{6}} \right)^{-n_A} \quad (2)$$

where  $C_A$  and  $n_A$  are material constants.



Fig. 4(a) shows the fatigue lifetimes on the abscissa as a function of  $\frac{\Delta\sigma}{2} \cdot (\sqrt{area_{INC}})^{\frac{1}{6}}$  on the ordinate for the different inclusion types, with stress amplitudes in MPa and  $\sqrt{area_{INC}}$  in  $\mu\text{m}$ . TiN-inclusion are the most and aluminate-inclusions the least damaging among the three.

Another method to consider the influence of cyclic loads and sizes of crack initiating inclusions on fatigue lifetimes is based on a fracture mechanics concept, as suggested by Tanaka and Akiniwa [6]. The crack initiating inclusions are considered as initial cracks. It is assumed that fatigue lifetimes are equal to the number of cycles necessary to propagate the cracks to fracture. The stress intensity range,  $\Delta K$ , of an arbitrarily shaped internal crack can be calculated as suggested by Murakami [4]:

$$\Delta K = 0.5 \cdot \Delta\sigma \cdot \sqrt{\pi \cdot \sqrt{area}} \quad (3)$$

Integrating the growth rates from the starting crack length  $\sqrt{area_{INC}}$  to fracture delivers Eq. (4) [7].

$$\frac{N}{\sqrt{area_{INC}}} = \frac{2}{c_P(n_P-2)} \cdot (\Delta K_{INC})^{-n_P} \quad (4)$$

With this method, the ratio of cycles to failure  $N$  and  $\sqrt{area_{INC}}$  can be correlated to the stress intensity range  $\Delta K_{INC}$  as shown in Fig. 4(b).

The minimum stress intensity range,  $\Delta K_{INC}$  leading to fracture is  $1.2 \text{ MPa}\sqrt{\text{m}}$  for TiN-inclusions,  $1.3 \text{ MPa}\sqrt{\text{m}}$  for Zr(N,C)-inclusions and  $1.8 \text{ MPa}\sqrt{\text{m}}^{1/2}$  for aluminate-inclusions. This confirms the result stated above: TiN-inclusions are more damaging than Zr(N,C)-inclusions and Zr(N,C)-inclusions are more damaging than aluminate-inclusions.

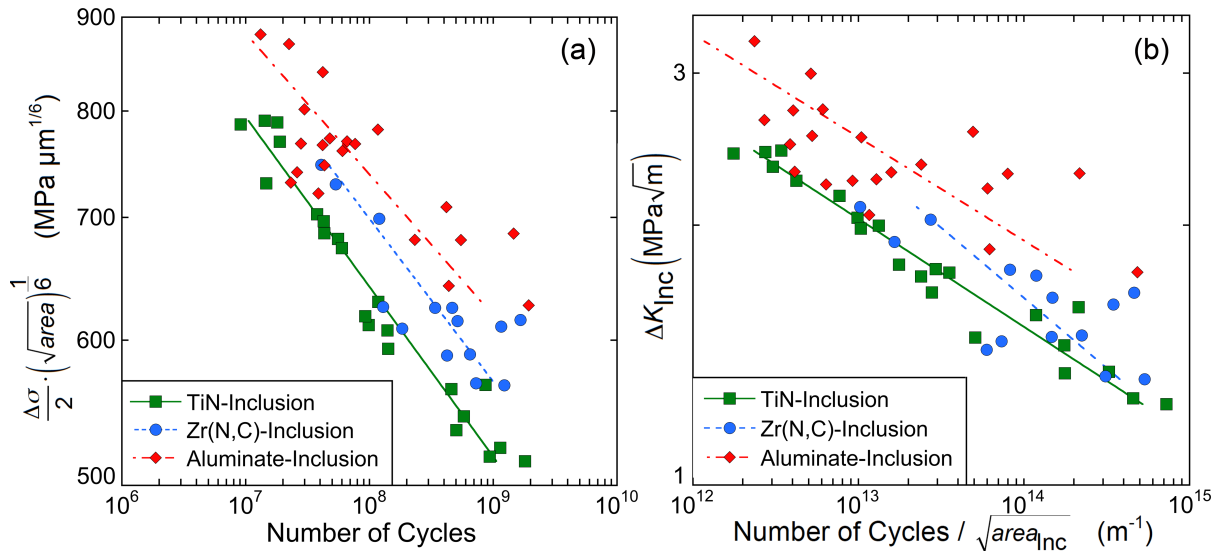


Fig. 4: Fatigue data of specimens with inclusion initiated fracture: (a) Cycles to failure presented as a function of the parameter  $\frac{\Delta\sigma}{2} \cdot (\sqrt{area_{INC}})^{\frac{1}{6}}$  and (b) ratio of cycles to failure and  $\sqrt{area_{INC}}$  presented as a function of the stress intensity range  $\Delta K_{INC}$



## CONCLUSIONS

1. Material A shows the lowest and material D the highest VHCF strength, while material B and C lie in between. The development of maraging steels from material A to D was successful in increasing the VHCF strengths.
2. Fatigue crack initiation at internal inclusions is the most important crack initiating mechanism in the four materials although the sizes of the inclusions  $\sqrt{area_{INC}}$  are very small (between 2 and 10  $\mu\text{m}$ ). Fatigue lifetimes and cyclic strengths decrease with increasing size of the crack initiating inclusion for all inclusion types.
3. TiN-inclusions are found to be most and aluminate-inclusions the least damaging while the detrimental influence of Zr(N,C)-inclusions on the VHCF strength lies in-between.
4. Considering the particles as initial cracks, VHCF failures occurred at minimum stress intensity ranges  $\Delta K_{INC}$  of 1.2  $\text{MPa}\sqrt{\text{m}}$  for TiN-inclusions, 1.3  $\text{MPa}\sqrt{\text{m}}$  for Zr(N,C)-inclusions and 1.8  $\text{MPa}\sqrt{\text{m}}$  for aluminate-inclusions in tests at load ratio  $R = 0.1$ .

## REFERENCES

- [1] H. Mayer:  
Recent developments in ultrasonic fatigue  
Fatigue & Fracture Eng. Mater. Struct., 39 (2016) pp. 3-29.
- [2] U. Karr, R. Schuller, M Fitzka, B. Schönbauer, D. Tran, B. Pennings, H. Mayer:  
Influence of inclusion type on the very high cycle fatigue properties of 18Ni maraging steel  
Journal of Materials Science, 52 (2017) pp. 5954-5967.
- [3] Y. Murakami, M. Endo:  
Effects of hardness and crack geometries on  $\Delta K_{th}$  of small cracks emanating from small defects  
in: K.J.Miller and E.R. de los Rios (Ed.) The behaviour of short fatigue cracks, EGF, Mech. Engng. Pub., London, 1986, pp. 27-293.
- [4] Y. Murakami:  
Metal Fatigue: Effects of small defects and nonmetallic inclusions, Elsevier Science Ltd. , Kidlington, Oxford, UK, 2002.
- [5] H. Mayer, W. Haydn, R. Schuller, S. Issler, B. Furtner, M. Bacher-Höchst:  
Very high cycle fatigue properties of bainitic high-carbon-chromium steel  
Int. Journal of Fatigue, 31 (2009) pp. 242-249.
- [6] K. Tanaka, Y. Akiniwa:  
Fatigue crack propagation behaviour derived from S-N data in very high cycle regime,  
Fatigue & Fracture Eng. Mater. Struct., 25 (2002) pp. 775-784.
- [7] Y. Akiniwa, N. Miyamoto, H. Tsuru, K. Tanaka:  
Notch effect on fatigue strength reduction of bearing steel in the very high cycle regime  
Int. Journal of Fatigue, 28 (2006) pp. 1555-1565.

**Corresponding author:** herwig.mayer@boku.ac.at

# MICROSTRUCTURE, MEAN STRESS AND NOTCH INFLUENCE ON FATIGUE STRENGTH AND INITIATION OF THREE BAR STEEL GRADES IN THE VERY HIGH CYCLE FATIGUE REGIME

**M. Sadek<sup>1</sup>, J. Bergström<sup>1</sup>, N. Hallbäck<sup>1</sup>, C. Burman<sup>1</sup>, R. Elvira<sup>2</sup>, B. Escauriaza<sup>2</sup>**

1) Karlstad University, Department of Engineering and Physics, SE-658 88 Karlstad

2) Department of Development of New Products, SIDENOR I+D, S.A., Barrio Ugarte, s/n E-48970 Basauri, Spain

**keywords:** VHCF, Automotiv steels, SN-curve, Initiation mechanisms

## ABSTRACT

The interest on the VHCF properties of high strength steels has been increasing in the last years and consequently more fatigue testing for the VHCF regime. In the present paper three automotive bar grade steels corresponding to different strength levels and microstructures have been studied with respect to fatigue strength and initiation mechanisms. In addition, effects of mean load and notched geometry have been investigated.

Three bar grades, one micro-alloyed ferritic pearlitic (38MnSiV5, 870 MPa tensile strength), one quenched and tempered martensitic (50CrV4, 1410 MPa tensile strength) and one carburizing (16MnCr5, 1180 MPa core structure tensile strength) grade were employed to reveal characteristic behaviour regarding initiation and fatigue failure mechanisms. A 20 kHz ultrasonic fatigue testing instrument was used to obtain fatigue lives up to and above  $10^9$  load cycles in uniaxial loading. Hour-glass specimens, smooth or notched ( $K_t=1.4$ ), were tested at mean load ratios  $R=-1$  and  $0.1$ . Fatigue strength and SN-diagram data were achieved; initiation was studied using primarily FEG-SEM microscopy.

Different controlling initiating mechanisms were found in the different grades (interior to surface and triple point to inclusion initiation) depending on the different grades and load ratios used. The results are discussed using FEM strength calculations and relevant failure models.

## INTRODUCTION

The very high cycle fatigue (VHCF) properties of steels for automotive components have gained more interest in the last years [1]. With the large variety of different steel alloys and steel conditions being used the mapping of properties are important for the selection of steel alloy and design of components. High strength martensitic bar grades and high strength low alloy steels are frequently used in automotive applications, carburized steels e.g. in gear applications. As a consequence, the number of laboratories installing and using the ultrasonic fatigue testing instrument has been increasing [2]. Several different test specimen geometries are used in fatigue testing depending on the particular test requirements [3, 4]. Common test geometries include smooth and notched specimens, and also different specimen sizes. Stress gradients and effectively stressed volumes can be quite dissimilar, affecting the test outcome. In particular if there is an associated critical defect distribution which initiates failure, these factors need to be considered [5-7]. Of special interest in fatigue

data for engineering purposes is the influence of mean stress, and also the presence of notches in components.

In the present study results of different specimen geometries used in VHCF testing is presented, including hourglass shaped smooth and notched specimens. Stress distributions computed by dynamic FEM calculations display the effect of specimen geometries. Test results of smooth and notched specimens,  $K_t=1.4$ , and with mean stress effect,  $R= 0.1$  and  $R= -1$ , are displayed in S-N diagrams in the life range  $10^6 - 10^9$  load cycles.

## EXPERIMENTALS

### Material description

Three Sidenor steel grades are investigated in this study, and test specimens sampled and prepared from the rolling direction of the  $\varnothing 60$ mm bar steel billet, as with the chemical composition presented in Table 1. 38MnSiV5 is a ferritic-pearlitic micro alloyed steel, in which normal contents of sulphide and oxide inclusions were observed. 50CrV4 is a high strength spring steel, quenched and tempered at 500°C (after specimen manufacturing) achieving the highest tensile strength with tempered martensite found in the microstructure. The 16MnCr5 grade contains a relatively higher content of small sized sulphides and oxides to improve machinability, and was carburized to obtain a martensitic microstructure with a hardened surface layer with 5% retained austenite and a case depth of 0.6 mm.

Table 1. Chemical composition of the three steel grades

Grade	C	Mn	Si	P	S	Cr	Ni	Mo	V	Cu	Al	Sn	Ti
<b>38MnSiV5</b>	0,37	1,46	0,68	0,011	0,050	0,12	0,10	0,03	0,10	0,12	0,014	0,009	0,014
<b>50CrV4</b>	0,52	0,87	0,33	0,009	0,003	1,08	0,09	0,03	0,11	0,15	0,005	0,010	0,002
<b>16MnCr5</b>	0,16	1,10	0,27	0,011	0,021	1,02	0,11	0,03	0,01	0,14	0,021	0,009	0,002

The specimens used were of smooth and notched hourglass geometries designed to run at resonance in a 20 kHz ultrasound fatigue test machine. The specimen net section diameter was 4 mm, the notch depth was 1.0 mm and the notch radius was 2 mm, Figure 2a-b. The test specimens were all prepared to their geometry, then heat treated to final hardness, the 38MnSiV5 and 50CrV4 were subsequently prepared by fine grinding and polishing to final surface finish. The 16MnCr5 was prepared to final surface finish prior to carburizing in order to maintain the carburized layer and surface properties.

Table 2. Mechanical properties (\*Core properties for 16MnCr5)

Grade	Direction	Tensile Strength, (MPa)	Yield Strength, (MPa)	Elongation, A (%)	Area Reduction, Z (%)	Hardness, HV
<b>38MnSiV5</b>	Rolling	867	589	20	55	300
<b>50CrV4</b>	Rolling	1409	1333	13	51	435
<b>16MnCr5*</b>	Rolling	1175	876	9,4	34	365

The mechanical properties of the steel grades are presented in Table 2. However, the mechanical properties of the carburized 16MnCr5-grade are for the core material of the specimens. The carburized hardness profile of these specimens is shown in Figure 1.

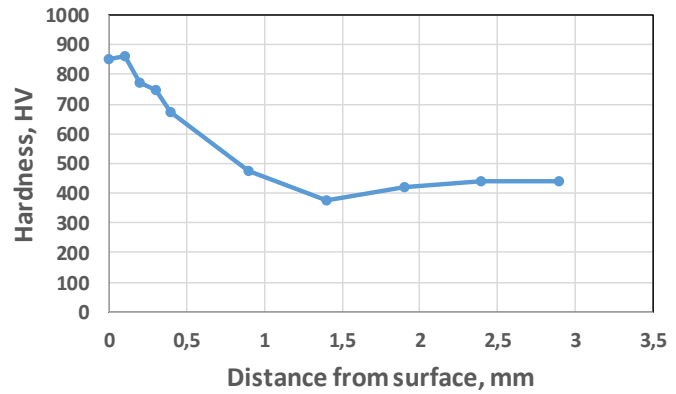


Figure 1. Hardness profile for the carburized 16MnCr5-grade.

## Experimental testing

Hour glass specimens are used in this study with a 4mm mid-section diameter and specimen lengths designed to have a resonance frequency at 20 kHz according to the resonance frequency of the ultrasonic fatigue testing system. The effect of mean load is investigated by using two mean load levels,  $R=-1$  and  $R=0.1$ , as well as the notch effect is studied by preparing notched specimens with notch factor  $K_t=1.4$ . The specimen stresses are computed using dynamic simulations at resonance frequency modelled in FEM software ABAQUS. Specimen geometries and stress distributions with prescribed  $10\mu\text{m}$  displacement at specimen ends are presented in Figure 2c-d.

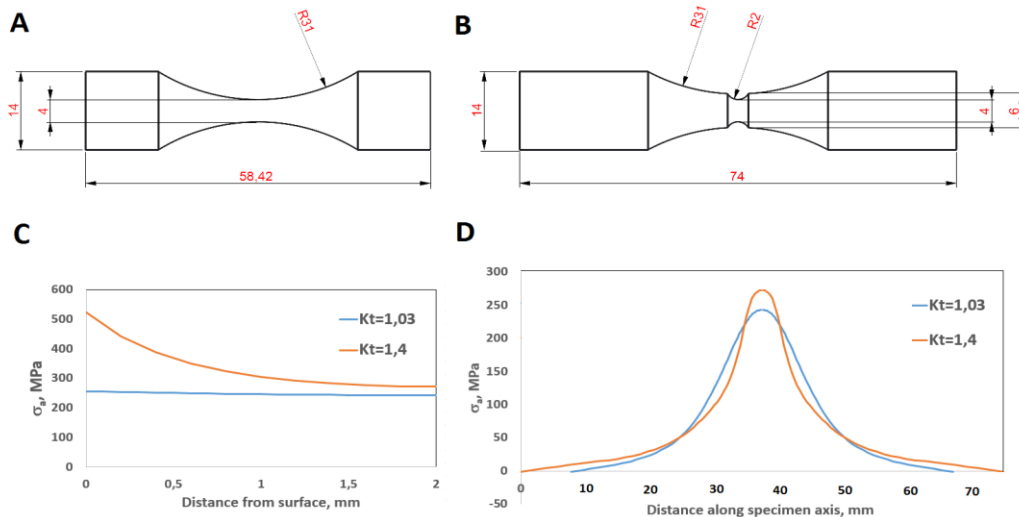


Figure 2. Specimen geometries and longitudinal stress distributions at mid-section and along specimen length.

For each material, loading condition and specimen type, 15 specimens are included in a staircase test to determine the fatigue strength at  $10^8$  cycles. Additional 15 specimens, for each sub group, are then tested at 3 different stress levels to produce data for the SN-curves, in the  $10^6$ - $10^{10}$  cycle regime. Water cooling is used for the  $R=-1$  tests and pressurized air cooling for the  $R=0.1$  tests. Temperature measurement were performed during the  $R=0.1$  tests using a IR thermal imaging camera.

Fractography of the failed specimens was performed using a high resolution FEG-SEM LEO scanning electron microscope. The cause for initiation, defect size, location and chemical content were determined.

### RESULTS

The staircase fatigue testing method with upper limit at  $10^8$  cycles provides the fatigue strength data presented in Table 3.

Table 3. Fatigue strength at  $10^8$  cycles for different loading conditions

Load ratio	Notch factor	38MnSiV5	50CrV4	16MnCr5
R=-1	Kt=1,03	343 MPa	558 MPa	677 MPa
R=0,1	Kt=1,03	258 MPa	543 MPa	402 MPa
R=-1	Kt=1,4	339 MPa	650 MPa	598 MPa

The fatigue strength is expected to decrease with an increased mean load. This effect is clearly seen in the results of the 38MnSiV4- and 16MnCr5-grades, Table 3 and Figures 3-4. However, for the 50CrV4-grade the decrease of the fatigue strength with mean load is not pronounced, hence the position shift between the 50CrV4- and 16MnCr5- grades in Figures 3 and 4. Further, the SN-data clearly reveals a small sensitivity of fatigue strength to the cyclic life in the life range  $10^6$  to  $10^9$  cycles, revealed by the flat appearance of the SN-curves.

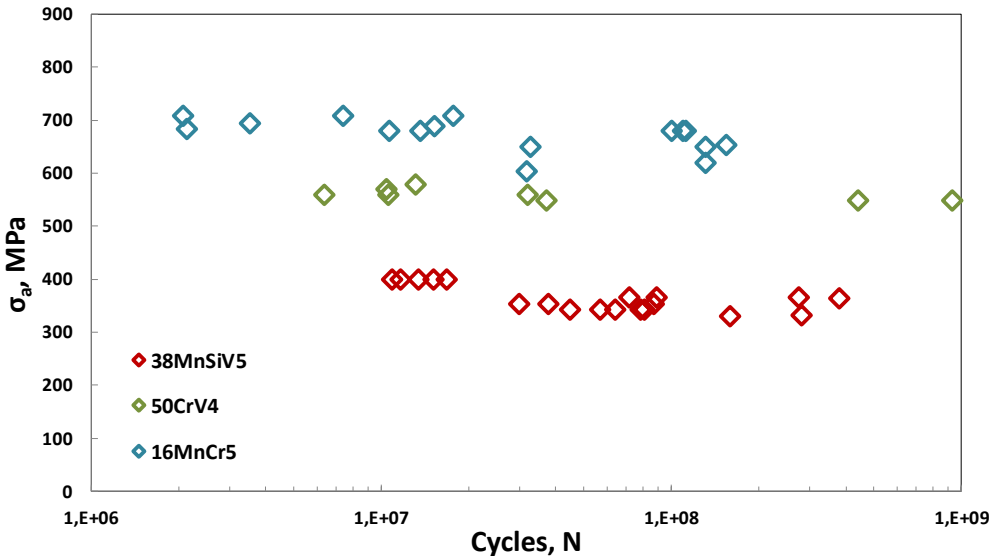


Figure 3. SN-curves for the three steel grades. R=-1 and Kt=1.03.

The SEM study of fracture surfaces supported interpretation of the fatigue test results. Initiation occurred 100% at surface defects in the 50CrV4 smooth specimen at R=-1, while at R=0.1 loading there was 50% interior inclusion initiation and 50% surface defect initiations. In the notched and R=-1 testing there were also mainly surface initiations. As for the 38MnSiV5 grade, the SEM-analysis of the fracture surfaces reveals the effect of the notch as a transition of the initiation sites from approximately 50% interior- and 50% surface-initiations to 100% surface initiations.

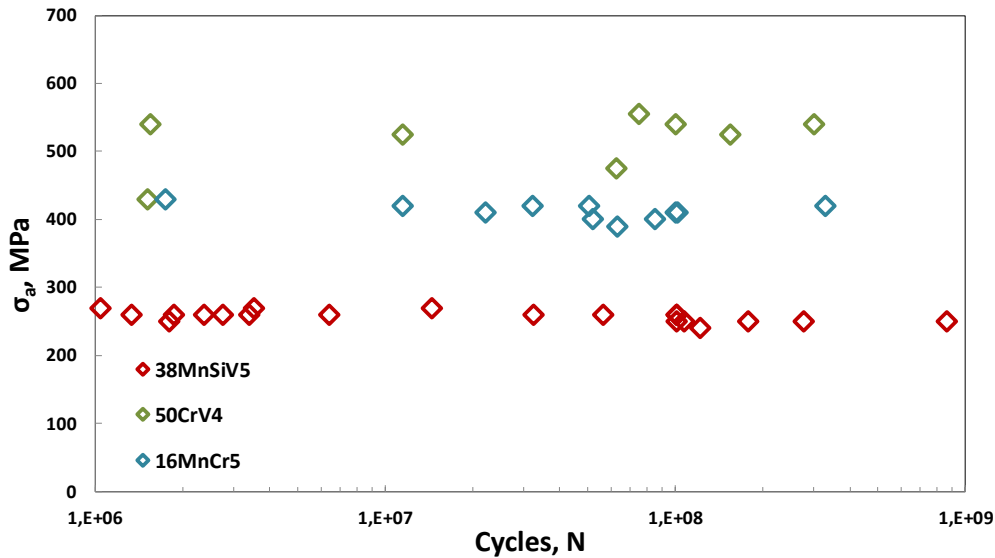


Figure 4. SN-curves for the three steel grades. R=0.1 and Kt=1.03.

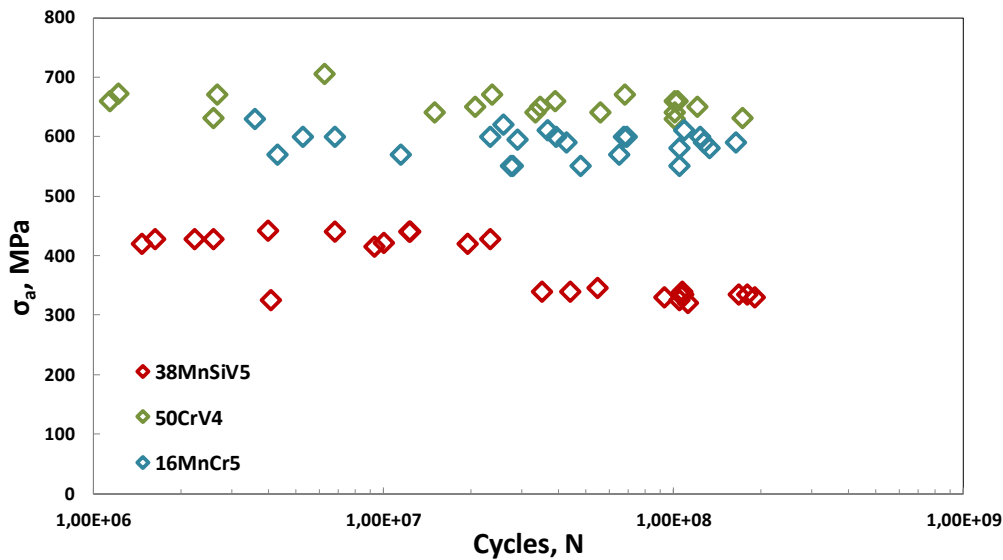


Figure 5. SN-curves for the three steel grades. R=-1 and Kt=1.4.

To ensure there was no overheating in the R=0.1 testing, where water cooling was not possible but where undercooled air was used, the specimen surface temperature was measured during fatigue testing. The measured temperatures were always below 45, 50 and 35 °C for the 38MnSiV5, 50CrV4 and 16MnCr5 grades, respectively.

## DISCUSSION

An increase in the mean load expectedly results in a decrease in the fatigue strength. Table 3 together with Figures 3 and 4, shows that the fatigue strength for the 38MnSiV5- and 16MnCr5-grades decreases with increasing mean stress, i.e. higher R-value. However, the 50CrV4-grade shows only a very small decrease of the fatigue strength. A possible reason is the observed surface defects on the R=-1 specimens causing failure at lower stress levels than expected. For the smooth specimens, Kt=1.03, the initiation sites are expected to be divided between the surface and interior while for the notched specimens, Kt=1.4, all initiation sites should be located at the surface because of the much higher local stresses at the surface, see Figure 2c. The SEM fracture surface-analysis confirms this effect for the

38MnSiV5-grade. However, the 50CrV4 initiation sites were located on the surface, for both  $K_t=1.03$  and  $K_t=1.4$ . Thus, the  $R=-1$  fatigue strength of the 50C4V4 grade is assumed to be reduced from an optimal level due to the surface defects.

An analysis of the notch effect may initially be visualized by the notch factor in fatigue,  $K_f$ , in relation to the geometrical stress concentration  $K_t=1.4$ . The experimental fatigue strengths obtained gives the  $K_f = 1.38, 1.17$  and  $1.54$  for 38MnSiV5, 50CrV4 and 16MnCr5, respectively. It may be interpreted as being reasonable for 38MnSiV5, low because of enhanced influence of inferior surfaces for 50CrV4 and high because of enhanced effect of carburized layer for 16MnCr5.

The  $R=0.1$  tests of the  $K_t=1.03$  specimens are expected to cause the highest elevated temperatures because of the larger, relative to the notched specimens, mid-section volume and the higher maximal stresses. For that reason, the temperature measurements presented above are the highest occurring during these tests, and the 35-50 °C levels are of minor influence.

## CONCLUSIONS

All three investigated bar grades displayed finite fatigue life up to  $10^9$  load cycles, although with a quite flat SN-curve. Both interior and surface failure initiations are occurring depending on presence of initiation defects, local strength (in the carburized case) and stress distribution. The influence of mean loads seems to follow a Goodman relation but with fatigue strength results depending on surface properties. The influence of the notch needs additional analysis to clarify further.

## ACKNOWLEDGEMENTS

The research leading to these results has received funding from the European Union's Research Fund for Coal and Steel (RFCS) research programme under grant agreement no. [RFS-CT-2013-00015 (FREQTIGUE)].

## REFERENCES

1. Bergamo S., Montaudon R., Dumas C., Very high cycle fatigue of automotive materials, Proceedings of VHCF5-Fifth International Conference on Very High Cycle Fatigue, Berlin, 2011.
2. Bathias, C.; Paris, P.C., Gigacycle fatigue in mechanical practice, Marcel Dekker, NY 10016, USA, 2005, p.94.
3. Furuya, Y., Notable size effects on very high cycle fatigue properties of high-strength steel, Materials Science and Engineering A, 528, 2011.
4. Gaenser H.P., Some notes on gradient, volumetric, and weakest link concepts in fatigue, Computational materials science, 44, 2008.
5. Li W.; Sakai T.; Li Q.; Lu L.T.; Wang P., Effect of loading type on fatigue properties of high strength bearing steel in very high cycle regime, Materials Science and Engineering A, 528, 2011.
6. Li W., Sakai T., Li Q., Lu L.T., Wang P., Effect of loading type on fatigue properties of high strength bearing steel in very high cycle regime, Materials Science and Engineering A, 528, 2011.
7. Bergström J., Kazymyrovych V., Burman C., Ekengren J., Test specimen geometry, stress calculation and mean stress in 20kHz testing in the very long fatigue life region, 5th International Conference on Very High Cycle Fatigue, Berlin, July, 2011.

# DATA ACQUISITION FOR VERY HIGH CYCLE FATIGUE OF NON-FERROUS METALLIC MATERIALS BASED ON THE COLLABORATIVE RESEARCH IN JSMS

## - 2nd report: Effects of loading type, test environment, surface treatment and casting defects on VHCF properties of ADC12 aluminum die-casting alloy -

A. UENO<sup>1)</sup>, T. MATSUMURA<sup>2)</sup>, K. MASAKI<sup>3)</sup>, T. OGAWA<sup>4)</sup>,  
K. SHIOZAWA<sup>5)</sup>, Y. NAKAMURA<sup>6)</sup> and T. NISHIDA<sup>7)</sup>

<sup>1)</sup> College of Science and Engineering, Ritsumeikan University,  
1-1-1 Noji-higashi, Kusatsu, Shiga, Japan

<sup>2)</sup> The University of Electro-Communications, 1-5-1 Chofugaoka, Chofu, Tokyo, Japan

<sup>3)</sup> National Institute of Technology, Okinawa College, 905 Henoko, Nago, Okinawa,  
Japan

<sup>4)</sup> Aoyama Gakuin University, 5-10-1 Fuchinobe, Chuo-ku, Sagamihara, Kanagawa,  
Japan

<sup>5)</sup> Fukui University of Technology, 3-6-1 Gakuen, Fukui, Japan

<sup>6)</sup> National Institute of Technology, Toyota College, 2-1 Eisei-cho, Toyota,  
Aichi, Japan

<sup>7)</sup> National Institute of Technology, Numazu College, 3600 Ooka, Numazu, Shizuoka,  
Japan

### ABSTRACT

The very high cycle fatigue (VHCF) fracture has been important problem in the field of mechanical engineering. From this situation, a research sub-committee on VHCF has been established in the Society of Materials Science, Japan (JSMS) and VHCF data of three types of non-ferrous metals, such as die-cast aluminum, magnesium and  $\beta$ -titanium alloys, have been collected by many research organizations in the sub-committee. Our group deal with aluminum die-casting alloy ADC12. An ADC12 alloy is a useful material to reduce a weight of engineering products, but the VHCF data of this material are not many. Therefore, our group member have been carried out experimental works for studying some effects, effects of loading type, test environment, surface treatment and casting defects, on the VHCF properties of ADC12. As a result, it was found that there are some difference of VHCF properties between ADC12 and high-strength steel.

### KEYWORDS

Very high cycle fatigue, Die-casting Al alloy, Rotary bending fatigue, Ultrasonic fatigue, Casting defects

### INTRODUCTION

Very high cycle fatigue (VHCF) fracture has been an important problem in the field of mechanical engineering. Thus, a research sub-committee on VHCF has been established in the Society of Materials Science, Japan [1] and VHCF data on three types of non-ferrous metals —extruded magnesium [2] and  $\beta$ -titanium alloys [3]— have been collected by many research organizations in the sub-committee.

The group dealing with aluminum die-casting alloy consists of 7 institution members. Each institution have been started their research independently. In this paper, interim reports of each institution were briefly introduced.



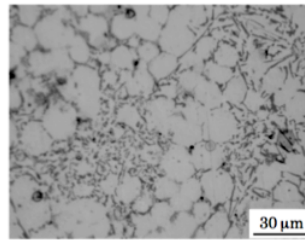
## MATERIAL AND TESTING

### Material

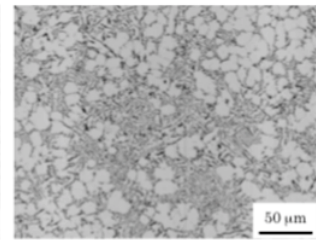
Materials used our group is aluminum die-casting alloy JIS ADC12. This materials are supplied by *DENSO Corporation* as a round bar shape ingot shown in Fig. 1. As a different of manufacturing time, this materials were manufactured in three lots. Fig. 2(a), (b) show an optical micrograph of Lot No.1 and Lot No.2. This ingot have some large casting defects in both thick ends. Although, there are few defects in middle thin region. Therefore, there are no harmful effects of fatigue properties as far as using fatigue specimen having narrow cross section in the middle. The mechanical properties obtained by Lot No.1, No.2 and No.3 were indicated in Table 1.



Fig. 1 Photograph of ingot material



(a) Lot No.1



(b) Lot No.2

Fig. 2 Optical micrographs of microstructure

Lot No.	Young's modulus $E$ , GPa	0.2% Proof stress $\sigma_{0.2}$ , MPa	Tensile strength $\sigma_B$ , MPa	Elongation $\delta$ , %
1	72.8	155.6	289.0	2.0
2	74.6	150.9	328.2	5.5
3	73.6	150.7	298.0	3.0

Table 1 Mechanical properties

### Specimen and testing conditions

**Institution A:** Fig.3(a) and (b) show the shape and size of the specimens for fatigue tests. The surface on center notch of two kinds of specimens was finished with buffing to mirror finish after the polishing with #800 ~ #2000 of emery papers. The rotary bending fatigue tests and the axial-force fatigue tests were carried out at room temperature in air. The testing conditions of the rotary bending fatigue tests were the stress ratio of -1 and the frequency of 3120 rpm. The testing conditions of the axial-force fatigue tests were the stress ratio  $R$  of -1, the frequency  $f$  of 30~50 Hz and the run-out stress cycles of  $1.0 \times 10^7$  cycles.

**Institution B:** Fig.4 showed shape and dimension of fatigue test specimen which was prepared by machining from Lot No.1 and Lot No.2 materials. Center part was mirror-finished by emery paper and buff cloth. Fatigue test were carried out to  $10^8$  cycles with axial loading condition at stress ratio  $R = -1$  in air at room temperature.

**Institution C:** Two types of ultrasonic fatigue tests are performed at 20 kHz under fully reversed loading (stress ratio,  $R = -1$ ) and under the maximum stress,  $\sigma_{max}$ , constant condition in dry (relative humidity,  $RH < 20\%$ ) and humid ( $RH > 90\%$ ) air environments. Shape and dimensions are shown in Fig. 5. The former test uses intermittent loading for 0.1 s followed by stopping for 0.1-0.5 s, and is interrupted at the number of cycles of  $10^8$ . The latter tests are carried out under  $\sigma_{max} = 152, 170, 195$  and  $222$  MPa with the stress amplitude,  $\sigma_a$ , of 50 MPa until  $10^9$  cycles. When the specimens do not break, the  $\sigma_a$  was increased by 20 % under the same  $\sigma_{max}$  conditions. Since

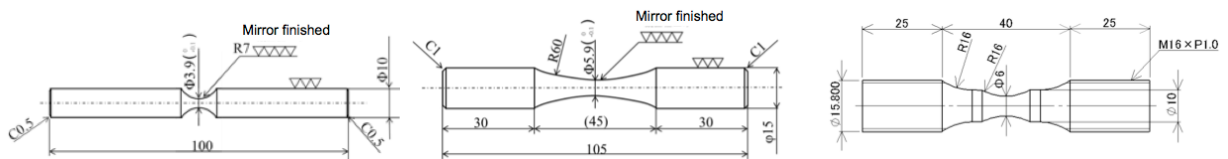
the  $\sigma_a$  is small, the loading and stopping durations are 10 and 1-5 s, respectively.

**Institution D:** Specimen used in this study was same as that shown in Fig. 3(a). Specimen surface was polished by emery paper mesh of #800 after mechanical processing. Fatigue test was carried out using a four-axis cantilever-type rotating bending machine at a frequency of 52.5 Hz under an open environment at room temperature. Repeated two-step loading fatigue test was performed using an apparatus for automatically fluctuating of applied load added to the fatigue testing machine as shown in Fig. 6. An applied loading pattern of this test was illustrated in Fig. 6.

**Institution E:** Fatigue tests were performed using a four-axis cantilever-type rotary bending fatigue testing machine operating at a frequency of 52.5 Hz. 3%NaCl solution was used as a corrosive environment, which was dropped continually onto the minimum cross section of specimen by a pump.

**Institution F:** The surface of the specimens shown in Fig.7 and Fig.8 are paper-polished (#320~#1500). Vanishing processing was given to the surface of the specimen using a ball vanishing tool of diameter 6mm. The plain fatigue tests and fretting fatigue test were carried out using the electromagnetic fatigue testing machine under a stress ratio  $R$  of -1 at frequencies of 150Hz. Fretting was induced by clamping a pair of bridge type pads (Fig.8 right side) onto both sides of the specimen (Fig.8 left side).

**Institution G:** In order to investigate relationship between fatigue strength and defect size, specimen having four artificial drilled holes, whose  $\sqrt{area}$  were ranged from 300  $\mu\text{m}$  to 2000  $\mu\text{m}$ , were used (Fig. 9). Four different size holes were drilled on spiral line with  $90^\circ$  interval. Each hole suffered different bending moment. Specimens were buff-finished with alumina abrasive grain size of 1  $\mu\text{m}$  after the grinding process. Finally, specimen were heat-treated in vacuum at 473 K for two hours to eliminate residual stress. A four-axis cantilever-beam type rotating bending fatigue testing machine, testing frequency of 52.5 Hz, was used in this study.



(a) For rotating bending (b) For axial loading fatigue Fig. 4 Specimen (Institution B)

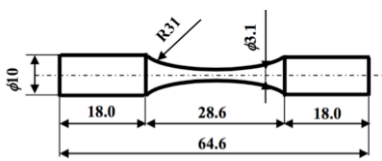


Fig. 5 Specimen (Institution C)

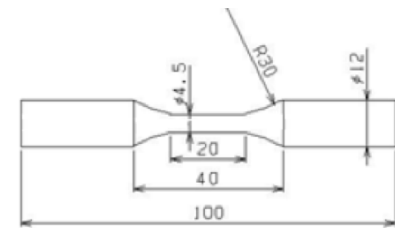


Fig. 7 Specimen (Type 1, Institution F)

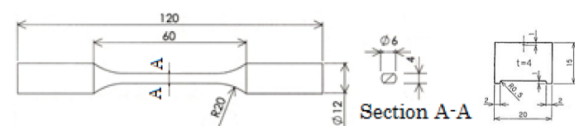


Fig. 8 Specimen (Type 2, Institution F)

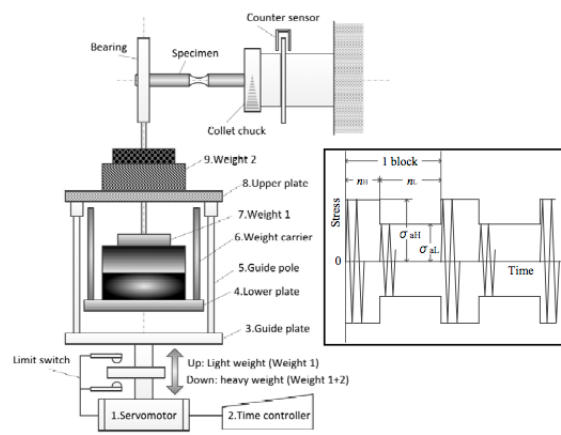


Fig. 6 Testing device (Institution D)

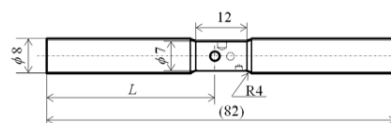


Fig. 9 Specimen (Institution G)

## EXPERIMENTAL RESULT AND DISCUSSION

### Institution A

Figure 10 show the *S-N* curves obtained from the rotary bending fatigue tests and the axial-force fatigue tests. The fatigue strength  $\sigma_w$  at  $1.0 \times 10^7$  cycles for the rotary bending fatigue tests and the axial-force fatigue tests were respectively 160.9MPa, 132.2MPa. As compared to the fatigue strength  $\sigma_w$  of the rotary bending fatigue tests, the fatigue strength  $\sigma_w$  of the axial-force fatigue tests lowered 18%.

### Institution B

Figure 11 showed *S-N* properties of fatigue result obtained by the specimen having no large defect which was confirmed by industrial X-ray computer tomography. There were clear differences between Lot No.1 and Lot No.2. Maximum value of fatigue strength at  $10^8$  cycles of Lot No.1 was about 140 MPa and the value of Lot No.2 was about 110 MPa. There was about 30 MPa difference in those. And fatigue life data between 100 and 150 MPa was very scatter.

### Institution C

Figure 12 represents the *S-N* curves obtained by the ultrasonic fatigue tests. For the  $\sigma_{max}$ -constant tests, the number of cycles to failure,  $N_f$ , is plotted for the  $\sigma_a$ , under which the specimen is broken. The results show a large scatter and the vague effect of *RH* on the fatigue strength. It will be necessary to compare the data with those obtained by the conventional fatigue tests, and to clarify the influence of the very high cyclic frequency, *i.e.* 20 kHz, on the fatigue strength.

### Institution D

*S-N* diagram obtained under the condition of constant stress amplitude is shown in fatigue strength,  $\sigma_w$ , at  $10^7$  cycles is 177.5 MPa. From the experimental result, preset stress amplitude was determined for repeated two-step loading fatigue test. The first stress amplitude,  $\sigma_{aH}$ , that is higher than  $\sigma_w$  is 220 MPa ( $1.24 \sigma_w$ ), and the second stress amplitude,  $\sigma_{aL}$ , set a value of 160 MPa, which is less than  $\sigma_w$  ( $0.901 \sigma_w$ ). Experiments were performed for three cases changed a combination of number of cycles applied under  $\sigma_{aH}$  and  $\sigma_{aL}$  in one block mentioned bellow;

- (1) Case 1: Number of cycles,  $n_L$ , applied under stress amplitude of  $\sigma_{aL}$  is constant of  $3.15 \times 10^6$  in one block, and that under  $\sigma_{aH}$ ,  $n_H$ , is changed to  $3.15 \times 10^3$ ,  $1.575 \times 10^4$  and  $3.15 \times 10^4$ .
- (2) Case 2:  $n_H$  is constant of  $3.15 \times 10^3$  cycles in one block and  $n_L$  is changed from  $1.575 \times 10^4$  to  $1.575 \times 10^6$ .
- (3) Case 3: To discuss an effect of number of cycles  $n_H$  in one block,  $n_H$  is decreased to 83 cycles compared with Case 2 and  $n_L$  is changed from  $3.15 \times 10^3$  to  $5.67 \times 10^5$ .

Fig. 13 shows experimental results obtained from the tests of three cases, as relationship between number of cycles to failure,  $N_{fH}$  ( $= \sum n_H$ ), and  $\sigma_{aH} = 220$  MPa, and also  $N_{fL}$  ( $= \sum n_L$ ) and  $\sigma_{aL} = 160$  MPa. From some discussion, equivalent stress amplitude,  $\sigma_{eq}$ , written by Equation (1) was proposed for evaluation of repeated two-step loading fatigue life.

$$\sigma_{eq} = \left( \frac{\sum n_i \sigma_{ai}^{13.17}}{\sum n_i} \right)^{\frac{1}{13.17}} \quad \dots \quad (1)$$

### Institution E

The *S-N* curves in laboratory air and in 3%NaCl solution are represented in Fig.14, where open and solid marks are the results in laboratory air and in 3%NaCl solution, respectively. The fatigue strength in 3%NaCl solution decreased significantly compared with the results in laboratory air, resulting in the continuous decreasing type *S-N* curve. In laboratory air, fatigue failure was not seen at a stress level of 150 MPa,  $10^9$  cycles, while in 3%NaCl solution failure took place at 40

MPa,  $10^7$  cycles. Fracture surfaces were observed by scanning electron microscope (SEM) after fatigue test. Failure in laboratory air occurred by a single crack initiation and growth, which generated from a casting defect. On the other hand, in 3%NaCl solution, multiple cracks initiated from corrosion pits.

**Institution F**

S-N curves for plain fatigue and fretting fatigue are shown in Fig.15. Plain fatigue and fretting fatigue strength of the specimen with burnishing has been increased compared to that of the untreated specimen.

**Institution G**

Figure 16 shows example of test results using specimens with artificial defects. Four polygonal marks arranged in one line indicate bending stress of each artificial defect suffered different bending moment. Black marks indicate the defect as fracture origin and white marks indicate the defect without fatigue crack after fatigue test. Also, gray marks indicate the defect some fatigue crack initiated. In  $\Delta K-\sqrt{area}$  diagram obtained using specimens having four artificial drilled holes (Fig. 17), we assumed that the  $\Delta K_{th}$  of each size artificial defects were able to define as an average  $\Delta K_{defect}$  value between fractured (black circle) and without crack (white circle) specimen or value between cracked (gray circle) and without crack specimen. After extracting only average  $\Delta K_{defect}$  value, redrawn diagram is shown in Fig. 17. It is found that the inclination of a regression line changed around  $\sqrt{area}$  of about  $1400 \mu m$ . Therefore, following two regression lines were obtained.

For  $\sqrt{area} \leq 1400 \mu m$  :  $\Delta K_{th} = 3.3 \# 10^{-3} (HV + 35)(\sqrt{area})^{1/3}$

For  $\sqrt{area} > 1400 \mu m$  :  $\Delta K_{th} = 3.3 \# 10^{-3} (HV + 420)(\sqrt{area})^{1/6}$

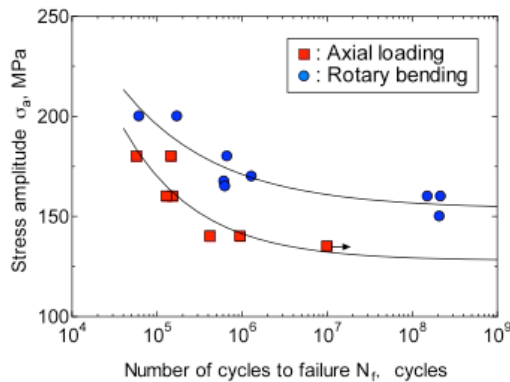


Fig. 10 S-N properties (Institution A)

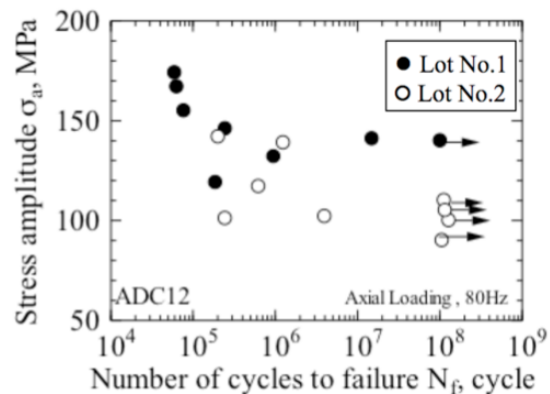


Fig. 11 S-N properties (Institution B)

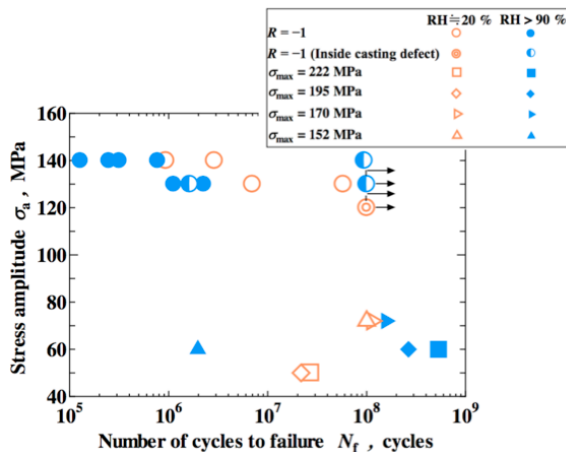


Fig. 12 S-N properties (Institution C)

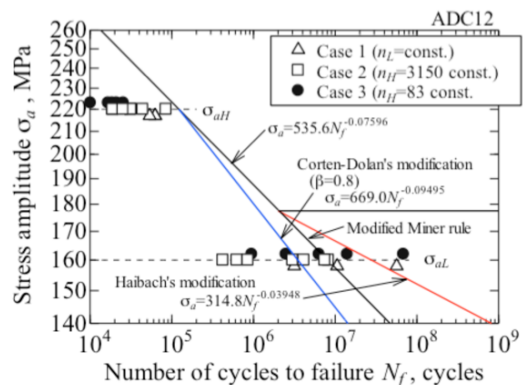


Fig. 13 S-N properties (Institution D)

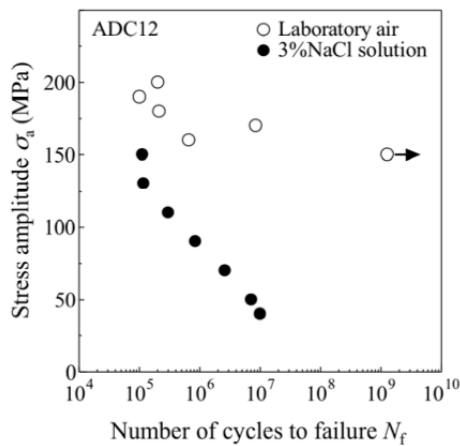


Fig. 14 S-N properties (Institution E)

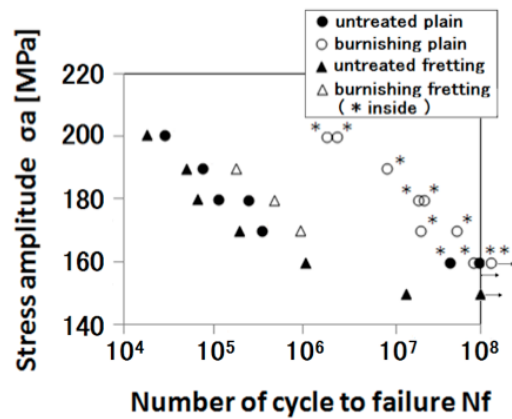


Fig. 15 S-N properties (Institution F)

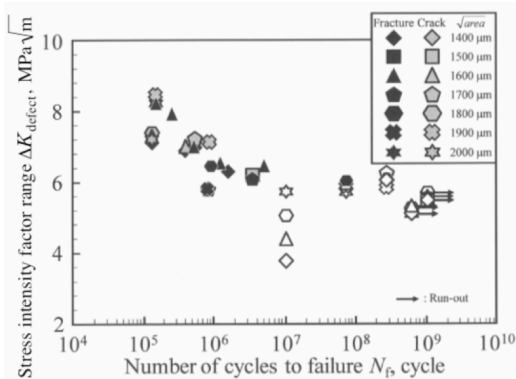


Fig. 16  $\Delta K$ - $N_f$  properties (Institution G)

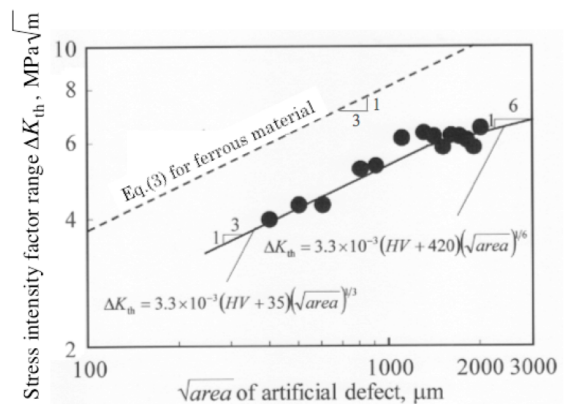


Fig. 17  $\Delta K$ - $\sqrt{areal}$  properties (Institution G)

## SUMMARY

In this paper, interim reports of each institution were briefly introduced. Some institution will continue to study with their individual point of view.

## REFERENCES

- [1] Nakamura, T.; Ueno, A.; Matsumura, T.; Masaki, K.; Oguma, H.; Akebono, H.; Kakiuchi, T.; Kikuchi, S.; Nakamura, Y.; Nishida, T.; Ogawa, T.; Oguma, N.; Sakai, T.; Shimamura, Y.; Shiozawa, K.; Uematsu Y.: Data Acquisition for Very High Cycle Fatigue of Non-ferrous Metallic Materials Based on the Collaborative Research in JSMS -1st report: outline of round-robin experiments on aluminum die casting, beta titanium, and wrought magnesium alloys -, 7th Inter. Conf. on Very High Cycle Fatigue (7th VHCF) (2017).
- [2] Masaki, K.; Matsumura, T.; Akebono, H.; Kakiuchi, T.; Nakamura, Y.; Uematsu, Y.: Data Acquisition for Very High Cycle Fatigue of Non-ferrous Metallic Materials Based on the Collaborative Research in JSMS - 4th report: basic research of VHCF properties of extruded magnesium alloy under rotary bending loading - 7th Inter. Conf. on Very High Cycle Fatigue (7th VHCF) (2017).
- [3] Oguma, H.; Nakamura, T.; Ueno, A.; Matsumura, T.; Masaki, K.; Akebono, H.; Uematsu Y.; Oguma, N.; Kakiuchi, Shimamura, Y.; Nakamura, Y.; Data Acquisition for Very High Cycle Fatigue of Non-ferrous Metallic Materials Based on the Collaborative Research in JSMS - 3rd report: effects of loading type and test frequency on VHCF properties on beta Ti22V4Al -, 7th Inter. Conf. on Very High Cycle Fatigue (7th VHCF) (2017).

Corresponding author: ueno01@fc.ritsumei.ac.jp

# DATA ACQUISITION FOR VERY HIGH CYCLE FATIGUE OF NON-FERROUS METALLIC MATERIALS BASED ON THE COLLABORATIVE RESEARCH IN JSMS

## 3<sup>rd</sup> Report: Effects of loading type and test frequency on VHCF properties of beta Ti22V4Al alloy

H. Oguma<sup>1)</sup>, T. Nakamura<sup>2)</sup>, A. Ueno<sup>3)</sup>, T. Matsumura<sup>4)</sup>, K. Masaki<sup>5)</sup>, H. Akebono<sup>6)</sup>,  
Y. Uematsu<sup>7)</sup>, N. Oguma<sup>8)</sup>, T. Kakiuchi<sup>7)</sup>, Y. Shimamura<sup>9)</sup>, and Y. Nakamura<sup>10)</sup>

<sup>1)</sup> National Institute for Materials Science, Sengen 1-2-1, Tsukuba, Ibaraki,  
305-0047 Japan

<sup>2)</sup> Hokkaido University, Kita 13, Nishi 8, Kita-ku, Sapporo, Hokkaido, 060-8628 Japan

<sup>3)</sup> Ritsumeikan University, 1-1-1 Noji-higashi, Kusatsu, Shiga, 525-8577 Japan

<sup>4)</sup> The University of Electro-Communications, 1-5-1 Chofugaoka, Chofu, Tokyo,  
182-8585 Japan

<sup>5)</sup> National Institute of Technology, Okinawa College, 905 Henoko, Nago, Okinawa,  
905-2192 Japan

<sup>6)</sup> Hiroshima University, 1-4-1 Kagamiyama, Higashi-Hiroshima, Hiroshima,  
739-8527 Japan

<sup>7)</sup> Gifu University, 1-1 Yanagido, Gifu, 501-1193 Japan

<sup>8)</sup> University of Toyama, 3190 Gofuku, Toyama, 930-8555 Japan

<sup>9)</sup> Shizuoka University, 3-5-1 Johoku, Naka-ku, Hamamatsu, Shizuoka,  
432-8561 Japan

<sup>10)</sup> National Institute of Technology, Toyota College, 2-1 Eisei-cho, Toyota, Aichi,  
471-8525 Japan

### ABSTRACT

Very high cycle fatigue (VHCF) is characterized by failures in lower stress levels than common fatigue strength determined by surface fractures, and in that region, the failures occur from sub-surface of materials. There are many studies on VHCF, however, ferrous metals have mainly been investigated. Fatigue test data of non-ferrous metals in very high cycle regime are still limited. Previously, mechanisms of sub-surface crack initiation and growth have been proposed, however, a unified theory of sub-surface fracture in high strength materials remains to be developed. Against such a background, fatigue tests over  $10^7$  cycles were carried out to accumulate fatigue data of non-ferrous materials as a part of the research program conducted by a research sub-committee on VHCF in the Society of Materials Science, Japan (JSMS). One of the tested materials in the research program was beta titanium alloy. Recent years, application of beta titanium alloys have been expanded due to their better producibility and cold workability. This study deals with the effects of loading type and test frequency on very high cycle fatigue properties of beta Ti22V4Al alloy. Three types of testing systems, such as ultrasonic, servo-hydraulic and rotating bending, were used to perform the tests. Obtained fatigue test results will be shown, and fracture surfaces are going to be investigated in detail.

### KEYWORDS

Non-ferrous metal, Loading type, Test frequency, Stress ratio, Fractography, Ti22V4Al, Beta titanium alloy



## INTRODUCTION

High strength materials have been widely used in mechanical structures in recent years. Regarding the materials, very high cycle fatigue (VHCF) becomes an important issue for mechanical engineers [1]. The VHCF is characterized by failures in lower stress levels than common fatigue strength determined by surface fractures, and in that region, the failures occur from sub-surface of materials. Due to the phenomenon, true fatigue strengths of the high strength materials become lower than that expected from the tensile strengths. The VHCF has been observed not only in ferrous materials also in non-ferrous materials such as aluminum and titanium alloys. Fatigue test data of non-ferrous metals in very high cycle regime are still limited. Previously, mechanisms of sub-surface crack initiation and growth have been proposed, however, a unified theory of sub-surface fracture in high strength materials remains to be developed. Therefore, theoretical method of evaluation for strength and fatigue life in very high cycle regime has not been fully established. Against such a background, fatigue tests over  $10^7$  cycles were carried out to accumulate fatigue data of non-ferrous materials as a part of the research program conducted by a research sub-committee on VHCF in the Society of Materials Science, Japan (JSMS). This study deals with the effects of loading type and test frequency on very high cycle fatigue properties of beta Ti22V4Al alloy.

## MATERIAL

Tested materials was beta titanium alloy, Ti22V4Al, and chemical compositions are listed in Table 1. A circular rod with machined surface (D: 18 mm, L: 3000 mm) was underwent the hot forging process. Subsequently, the rod was given solution treatment (1023K, 3.6 ks, Water-cooling) and aging treatment (823K, 14.4 ks, Air-cooling). Microstructure after the heat treatments is shown in Fig. 1. The aging process produces acicular alpha phase, and it is extremely fine. Table 2 contains mechanical properties after the heat treatments.

Al	V	Fe	C	O	N	H	Ti
4.15	21.17	0.15	0.013	0.14	0.012	0.0124	Bal.

**Table 1:** Chemical compositions (in mass %)

Tensile strength [MPa]	0.2% proof strength [MPa]	Elongation [%]	Reduction of area [%]	Hardness [HV]
1235	1154	9.3	21.9	327

**Table 2:** Mechanical properties

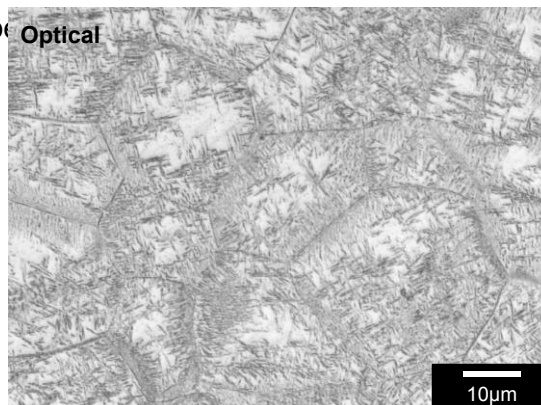


**Fig.1:** Microstructure (Ti22V4Al)

## EFFECT OF LOADING TYPE AND TEST FREQUENCY

Based on fatigue test results obtained from rotating bending (RB), uniaxial servo-hydraulic (AX), and ultrasonic (US) fatigue testing systems, effects of loading type and test frequency are going to be investigated.

### Test conditions

Test specimen with the gauge section of 4mm diameter are used for the fatigue testing. Stress ratio ( $R = \sigma_{\min} / \sigma_{\max}$ ) was  $-1$ , and test frequencies were 50 Hz for RB, 120 Hz for AX, and 20 kHz for US, respectively. All tests were carried out in laboratory air condition.

### Test results

Fatigue test results are summarized in Fig. 2, and the data is arranged by stress amplitude. Fatigue lives distributed in almost the same region regardless of the loading type and test frequency. Surface fractures occurred before  $10^7$  cycles as open marks in the diagram. On the other hand, in the region longer than  $10^7$  cycles, sub-surface fractures were also observed as closed marks. The value of the fatigue limit for this material is about  $\sigma_w = 550$  MPa. Generally, test data obtained in rotating bending tests distribute in the longer life and higher strength than that in uni-axial test. However, in this study, no differences were observed in fatigue life and strength distribution between different loading types. Focusing on the test frequency, fatigue lives of the surface fracture obtained by ultrasonic testing system distributed in longer life region than other testing systems (open triangle marks in Fig. 2). This result indicates that the test frequency effects on the surface fracture.

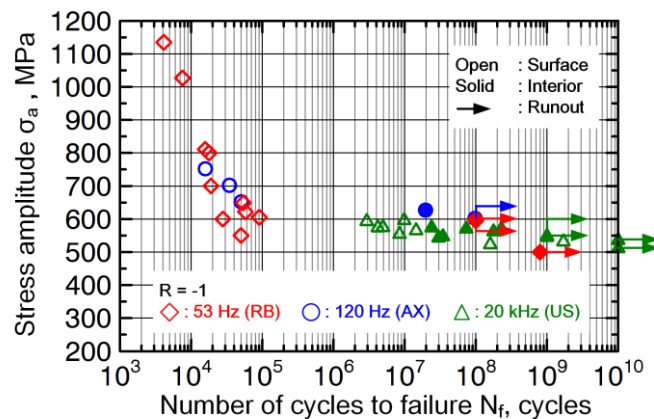


Fig. 2: S-N curves under different loading type and test frequency

### Fracture surface observations

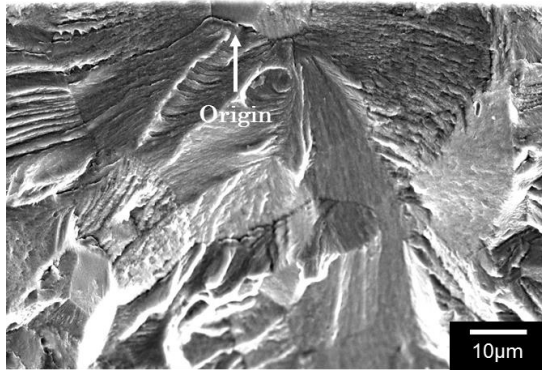
Examples of fracture surfaces around the origins are shown in Fig. 3. Fatigue cracks (both surface and sub-surface crack) propagate from facet, and no inclusions existed at the fracture origin. The size of facet was about 15 to 20  $\mu\text{m}$ . Around the fracture origins, crystallographic pattern was observed. In the case of sub-surface fractures, fine asperities were observed in some cases as shown in Fig. 3b. The fine asperities likely appeared on the fracture surfaces obtained in ultrasonic fatigue testing. To investigate the change of the state during the fatigue test, hardness of the gauge part of the specimen was measured after loading under the condition of  $\sigma_a = 511$  MPa,  $N = 1.0 \times 10^{10}$  cycles. As a result, the hardness of the test specimen was 313 HV near the surface, and 304 HV in the specimen, that is, they



were almost same as the hardness of the as-received material. In the fatigue test results, the effects of test frequency on the fatigue strength did not appear, however, difference of the appearances on the fracture surface was recognized. Therefore, test frequency may effect on the crack propagation mechanism in the material.

a. Surface fracture

$R = -1, f = 120 \text{ Hz}, \sigma_a = 700 \text{ MPa}, N_f = 3.53 \times 10^4$



b. Sub-surface fracture

$R = -1, f = 20 \text{ kHz}, \sigma_a = 570 \text{ MPa}, N_f = 7.33 \times 10^7$

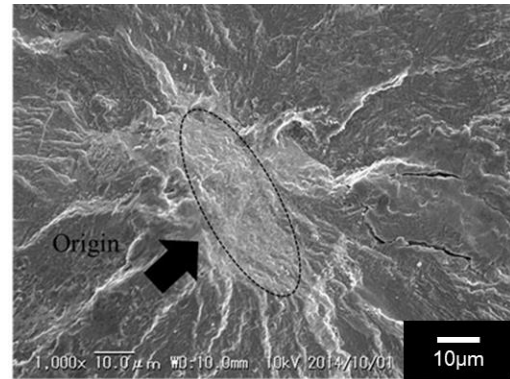


Fig. 3: Fracture surfaces around the origin

## EFFECT OF STRESS RATIOS

### Test conditions

Uniaxial fatigue tests were carried out using uniaxial electro-hydraulic fatigue testing system with hourglass-shaped test specimens. Sinusoidal waveform loads were applied to the specimens. Stress ratios were  $-1, -0.5$  and  $0.1$ . The test frequency was  $120 \text{ Hz}$ , and test environment was laboratory air. Fatigue tests were terminated at  $1.0 \times 10^8$  cycles.

### Test results

Fig. 4 shows the fatigue test results. Square mark indicates the test results under  $R = -1$ , triangle indicates  $R = -0.5$ , and circle indicates  $R = 0.1$ , respectively. Under  $R = -1$ , fatigue lives extremely extended below  $650 \text{ MPa}$ . In shorter life region before  $10^5$  cycles, failure occurred from surface of the material. In long life region around  $2 \times 10^7$  cycles, on the other hand, failure occurred from sub-surface. Under  $R = -0.5$ , fatigue lives became clearly longer when the stress amplitude was smaller than  $\sigma_a = 618 \text{ MPa}$ . In shorter life region until  $10^5$  cycles, surface fractures were observed. Sub-surface fractures occurred longer than  $3 \times 10^6$  cycles. In the case of  $R = 0.1$ , surface fracture occurred at  $\sigma_a = 495 \text{ MPa}$ . Sub-surface fractures occurred below the stress level of  $\sigma_a = 506 \text{ MPa}$ , and this is higher than the stress at which surface fracture occurred. Different from other stress ratio conditions, sub-surface fractures occurred in short life, e.g.  $N_f = 6.5 \times 10^4$  cycles. Sub-surface fractures tend to occur under higher stress ratio or higher mean stress.

The endurance limit diagram is shown in Fig. 5. Each data point indicates the fatigue strength at  $10^8$  cycles. The strength at  $10^8$  cycles was defined as the average of the stress of censored data at  $10^8$  cycles and the minimum stress among the fracture data of sub-surface fractures. The yield limit and constant life curves, such as Gerber line and Modified Goodman's line, are also shown in the diagram. The fatigue strength at  $10^8$  cycles are between the Gerber line and the Modified Goodman's line. According to the Gerber line, the

plots are in the safety area of the diagram, i.e., the fatigue strength in the very high cycle region cannot be estimated using the Gerber line. On the other hand, the Modified Goodman's line provides a conservative estimate. The result indicates that an estimation of the fatigue strength in the very high cycle region by the modified Goodman's diagram is appropriate for this material.

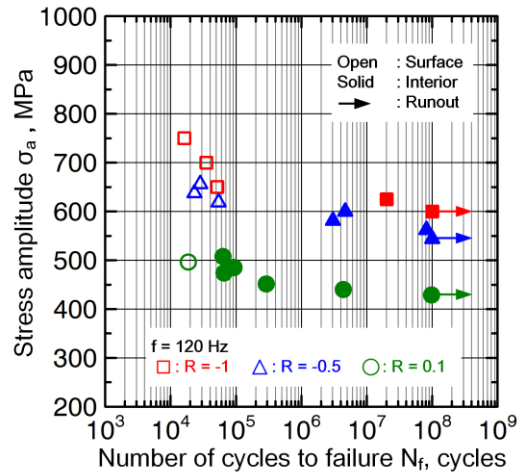


Fig. 4: S-N curves under different stress ratios

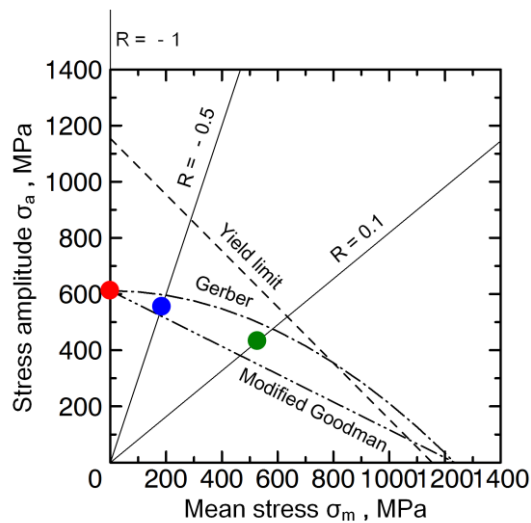
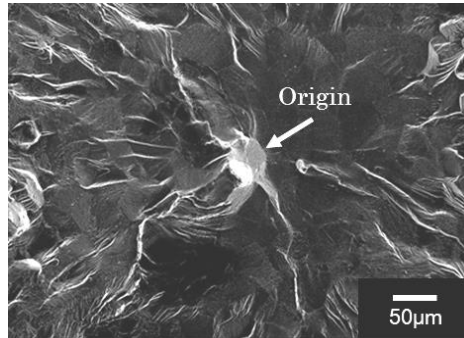


Fig. 5: Endurance limit diagram

### Fracture surface observations

Fracture surface of the sub-surface fracture is shown in Fig. 6. Regardless of stress ratios and fracture types, facet(s) as shown in the figure existed at the fracture origin. Furthermore, there is no clear difference in the fracture surface of initial crack propagation region between stress ratios or fracture types in this study. Facets at the fracture origin were inclined from the maximum principal stress plane. Angles were measured using 3D-observation function in the scanning electron microscope system. As a result, each facet was tilted at 25 to 68 degrees angle, and most of them distributed in 35 to 55 degrees. On the other hand, EBSD analyses for the cross section just below the fracture surface revealed that alpha phase distributed locally at the origin facet as shown in Fig. 7. Consequently, the glide-plane decohesion or cleavage of alpha phase can be responsible for the crack initiation in the material.



Sub-surface fracture,  
 $R = -0.5$ ,  $f = 120$  Hz,  
 $\sigma_a = 581$  MPa,  $N_f = 3.04 \times 10^6$

**Fig. 6:** Fracture surface around the origin

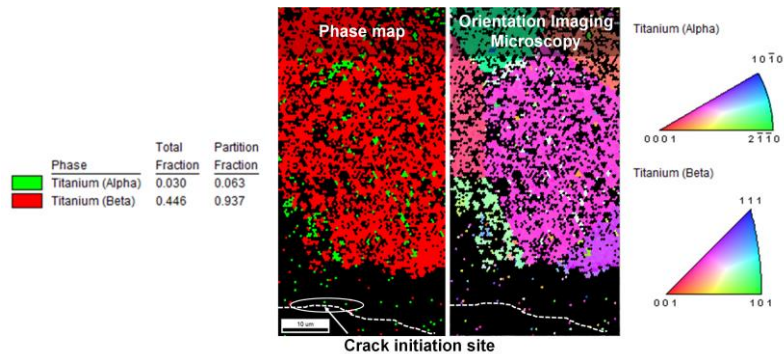


**Fig. 7:** EBSD analysis of the crack initiation site

## SUMMARY AND CONCLUSIONS

The effects of loading type and test frequency on very high cycle fatigue properties of beta Ti22V4Al alloy were investigated as a part of the research program conducted by a research sub-committee on VHCF in JSMS. The major conclusions are summarized as follows:

- (1) Fatigue lives distributed in almost the same region regardless of the loading type and test frequency.
- (2) Sub-surface fractures tend to occur under higher stress ratio or higher mean stress.
- (3) The Modified Goodman's line provides a conservative estimate for this material in the very high cycle region.
- (4) The glide-plane decohesion or cleavage of alpha phase can be responsible for the crack initiation in the material.

## ACKNOWLEDGMENTS

Material for this study was provided by Daido Steel Co., Ltd.

## REFERENCES

- [ 1 ] Sakai, T.:  
 Review and Prospects for Current Studies on Very High Cycle Fatigue of Metallic Materials for Machine Structural Use  
 Journal of Solid Mechanics and Materials Engineering, Vol. 3, No. 3 (2009), pp.425-439

**Corresponding author:** OGUMA.Hiroyuki@nims.go.jp

# DATA ACQUISITION FOR VERY HIGH CYCLE FATIGUE OF NON-FERROUS METALLIC MATERIALS BASED ON THE COLLABORATIVE RESEARCH IN JSMS

## - 4th report: basic research of VHCF properties of extruded magnesium alloy under rotary bending loading -

K. MASAKI<sup>1)</sup>, T. MATSUMURA<sup>2)</sup>, H. AKEBONO<sup>3)</sup>, T. KAKIUCHI<sup>4)</sup>,  
Y. NAKAMURA<sup>5)</sup> and Y. UEMATSU<sup>4)</sup>

<sup>1)</sup> Department of Mechanical Systems Engineering, National Institute of Technology,  
Okinawa College, 905 Henoko, Nago, Okinawa, Japan

<sup>2)</sup> The University of Electro-Communications, 1-5-1 Chofugaoka, Chofu, Tokyo, Japan

<sup>3)</sup> Hiroshima University, 1-4-1 Kagamiyama, Higashi-Hiroshima, Hiroshima, Japan

<sup>4)</sup> Gifu University, 1-1 Yanagido, Gifu, Japan

<sup>5)</sup> National Institute of Technology, Toyota College, 2-1 Eisei-cho, Toyota, Aichi, Japan

### ABSTRACT

A research sub-committee on very high cycle fatigue (VHCF) has been established in the Society of Materials Science, Japan. VHCF data of three types of non-ferrous metals—die-cast aluminium, extruded magnesium and  $\beta$ -titanium alloys—have been collected by many research organizations in the sub-committee, which deals with three types of extruded magnesium alloys, namely, AZ31, AZ61 and AZ80. This study introduces basic VHCF data under rotary bending loading for the mentioned magnesium alloys. The shape of the S-N diagram obtained from fatigue tests differed depending on the material. Only AZ61 clearly demonstrated a step-wise S-N characterization. However, it was classified into the long fatigue life group and short fatigue life group when fatigue tests were conducted using many specimens with the same stress level in other materials. The S-N characterization was discussed from the viewpoints of mechanical strength and fracture surface.

### KEYWORDS

Very high cycle fatigue, Extruded magnesium alloy, S-N data, Rotary bending loading,  
Fatigue life property

### INTRODUCTION

Very high cycle fatigue (VHCF) fracture has been an important problem in the field of mechanical engineering. Thus, a research sub-committee on VHCF has been established in the Society of Materials Science, Japan [1] and VHCF data on three types of non-ferrous metals—die-cast aluminium [2], extruded magnesium and  $\beta$ -titanium alloys [3]—have been collected by many research organizations in the sub-committee. The sub-committee deals with three types of extruded magnesium alloys: AZ31, AZ61 and AZ80, which have been commonly used as structural materials for transportation machinery in recent years. This work deals with the effects of loading type, diameter of specimen, and surface coating on very high cycle fatigue properties. Moreover, the coxing effect has been investigated. This study introduces basic VHCF data under rotary bending loading of all the aforementioned magnesium alloys.

## EXPERIMENTAL PROCEDURE

### Material

For this study, three types of extruded magnesium alloys—AZ31, AZ61 and AZ80—were used, which were provided by Sankyo Tateyama, Inc. Sankyo Material-Company in JAPAN. Chemical compositions of the materials are shown in Table 1 and their manufacturing conditions are shown in Table 2. No thermal treatment was applied to any of the studied materials. Fig.1 shows the microstructure of the materials. AZ31 is a mixed structure of small grain crystals and large grain crystals, whereas the crystal grain sizes of AZ61 and AZ80 were uniform. The average grain sizes of AZ31, AZ61 and AZ80 were 45 $\mu$ m, 17 $\mu$ m and 14 $\mu$ m, respectively. Mechanical properties of the materials are shown in Table 3. AZ80 presented the highest strength among the three materials. The compressive 0.2% proof stress of each material was about half of the respective tensile 0.2% proof stress

### Specimen and fatigue test

High cycle fatigue tests were carried out under cantilever type rotary bending loading in air at room temperature and with a frequency of 4000rpm. Fig. 2 shows the shape and

material	Al	Zn	Mn	Si	Fe	Cu	Ni	Mg
AZ31	3.0	1.1	0.31	0.007	0.002	0.001	0.001	Bal.
AZ61	5.9	0.6	0.28	0.010	0.002	0.002	0.002	Bal.
AZ80	8.1	0.5	0.25	0.038	0.002	0.002	0.001	Bal.

**Table 1:** Chemical composition of materials [wt%].

material	Billet temperature K	Manufacture speed m/min	Bar diameter mm
AZ31	673	5	$\phi$ 13
AZ61	653	2	
AZ80	623	1	

**Table 2:** Manufacturing conditions.

material	$\sigma_{0.2}$ MPa		$\sigma_B$ MPa	$\delta$ %	E GPa	Hv
	Ten.	Com.				
AZ31	197	90	232	19	43	54
AZ61	221	134	309	13	44	57
AZ80	223	168	341	16	46	63

**Table 3:** Mechanical properties of materials.

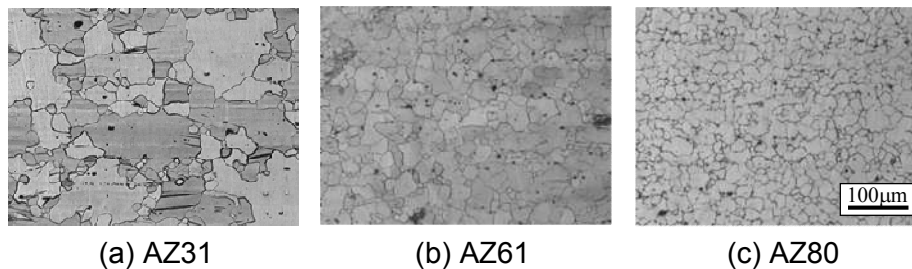


**Fig.1:** Materials microstructure.

dimensions of the fatigue specimen. At first, basic S-N diagrams of all the materials were obtained using the 6mm specimen of Fig.2(a). After the first fatigue test, in order to investigate the fatigue life scattering property under a certain stress amplitude, 5mm of the specimen Fig.2 (b) was machined from the red-dashed frame part of the fatigue-fractured specimen of Fig.2(a). The part of the 5 mm specimen with the minimum diameter was subjected to the fatigue load in the initial fatigue test, but since it was 3% or lower of the set stress, it was considered to hardly have any influence. The surfaces of the central part of all specimens were finished by buffing with an alumina solution after #600 to #2000 wet emery paper polishing with oil. The stress concentration factor for both materials was 1.074. The fracture surfaces were observed by scanning electron microscopy (SEM) to specify the crack initiation sites.

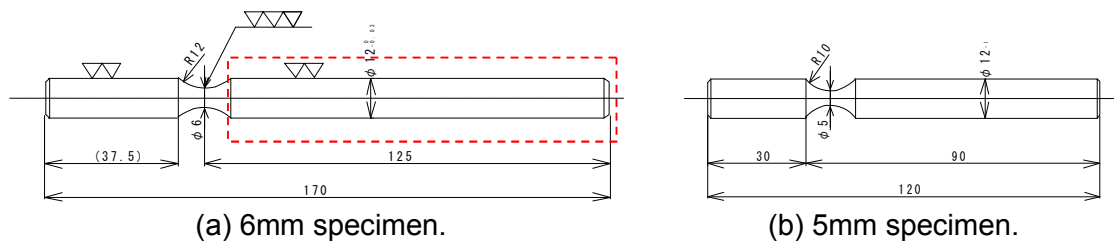


Fig.2: Shape of test specimens (unit: mm).

## RESULTS AND DISCUSSION

### Fatigue results of AZ31

Fig. 3(a) shows the S-N diagram of AZ31 materials. The S-N diagram is a very gentle curve. Fatigue strength for  $10^8$  cycles of AZ31 was about 90MPa, which is the same value as the compressive 0.2% proof stress of the material. Thus, even if the fatigue stress amplitude is lower than the tensile 0.2% proof stress, plastic strain is caused by the compressive stress amplitude. Therefore, the fatigue property of this material is affected by compressive plastic strain. Fatigue life scattering was investigated at two stress amplitude levels of 100MPa and 120MPa. Fig.3(b) shows the Weibull plot of these results. Especially, fatigue life data of 120MPa were divided into long life group and short life group. From this result, the S-N data could be divided into two groups: the shorter fatigue life group of  $10^5$  cycles or fewer and longer life group of  $10^6$  cycles or more. Fig.3(c) shows an example of macroscopic fracture surface. There was no fish-eye fracture pattern in either group. Fig. 4 shows the fracture surface observation result of Fig.3(c) specimens by SEM. The fracture surface of AZ31 was very rough. But there was no

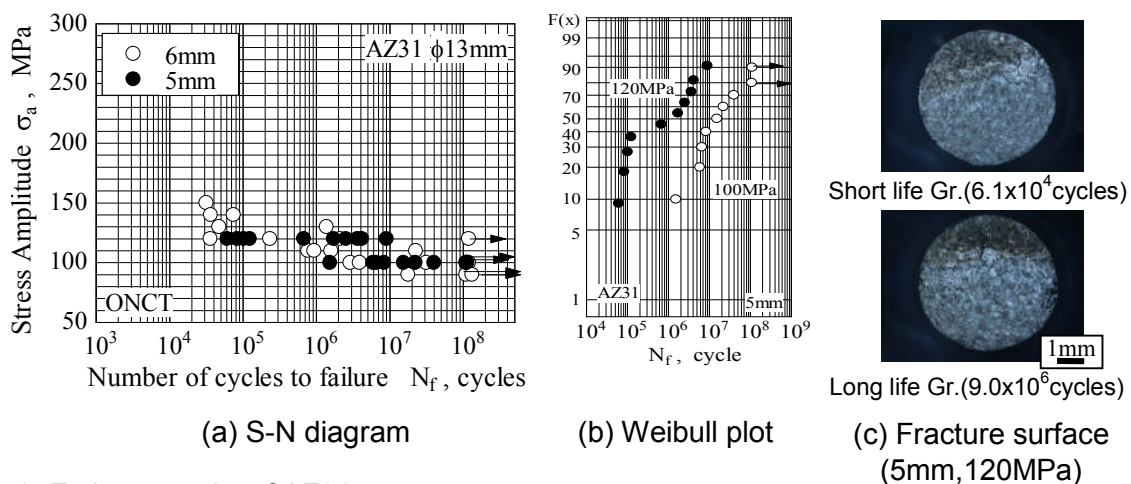


Fig.3: Fatigue results of AZ31.



difference in the fracture surface between the short life group and long life group at this magnification. There were many white stripe patterns in the crystal grain. It was difficult to identify where the fatigue crack initiation point was.

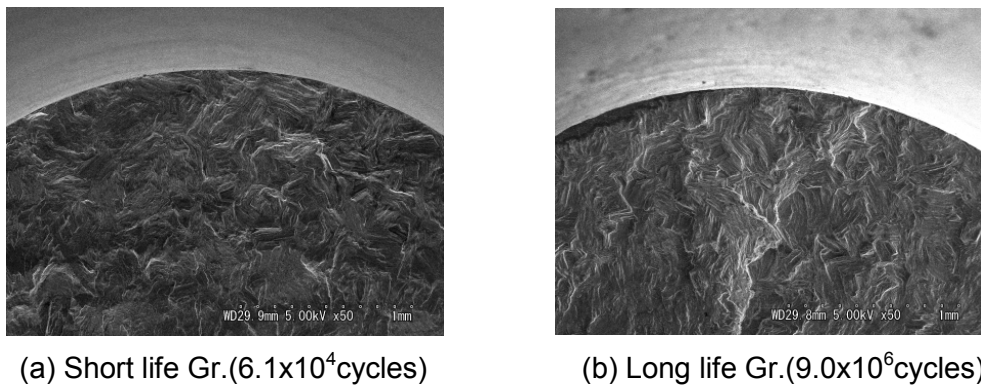


Fig.4: SEM observation results of Fig.3(c) specimens.

### Fatigue results of AZ61

Fig. 5(a) shows the S-N diagram of AZ61 materials. The S-N data of AZ61 was located at a higher stress amplitude level than the data of AZ31 because the tensile strength of AZ61 was higher than that of AZ31. The S-N data was approximated to a two-step diagram with a first step stress level at about 190MPa. Although the fatigue strength at  $10^8$  cycles of AZ61 was about 150MPa, fatigue fracture occurred at  $8 \times 10^8$  cycles under a stress amplitude of 130MPa, the same value as the compressive 0.2% proof stress of the material. Thus, the fatigue properties of this material are also affected by compressive plastic strain. Fatigue life scattering was investigated at two stress amplitude levels: 150MPa and 190MPa. Fig.5(b) shows the Weibull plot of these results. Although the fatigue life data of 150MPa could be approximated to the Weibull distribution, the fatigue life data of 190MPa could not be approximated. Two specimens clearly presented longer fatigue life than the other data. Fig.5(c) shows an example of the macroscopic fracture surface of the short fatigue life group and long fatigue life group. Both fatigue specimens were fractured from surface. Fig.6 shows the fracture surface results of Fig.5(c) specimens according to SEM. The fracture surface morphology of AZ61 presented a flat shape. There seemed to be slight difference in the fracture surfaces shown in Fig.6(a) and Fig.6(b). It seemed that the crack initiation point of long life group specimen was located slightly under the surface. But it was difficult to identify the fatigue crack initiation point.

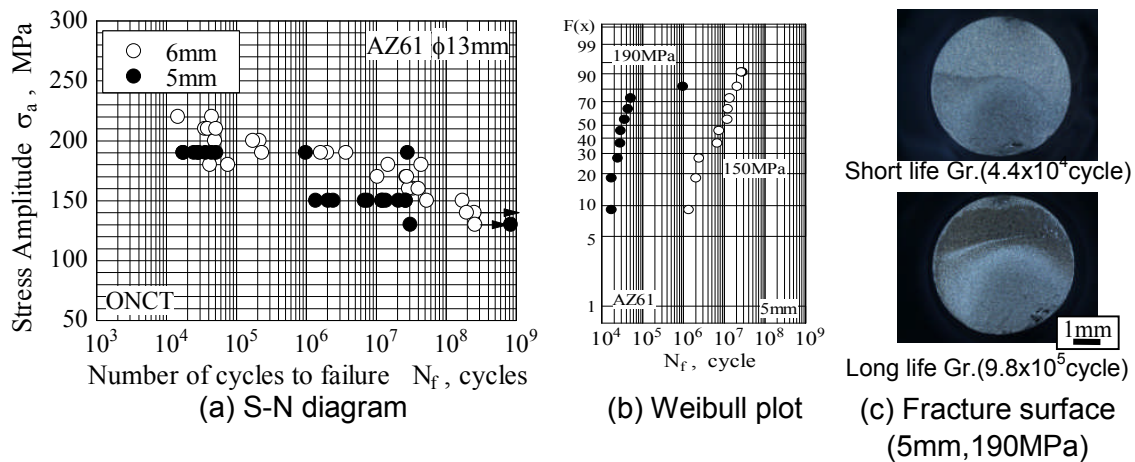
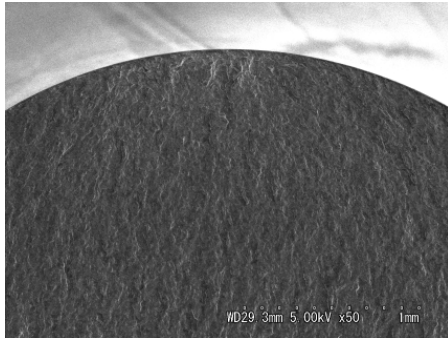
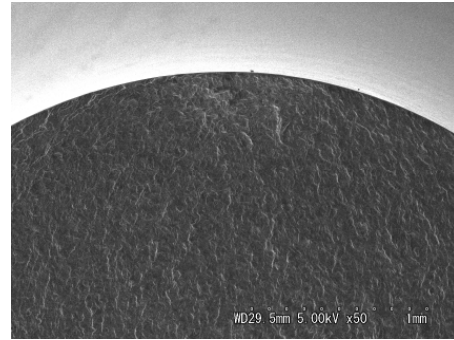


Fig.5: Fatigue results of AZ61.



(a) Short life Gr.( $4.4 \times 10^4$ cycles)

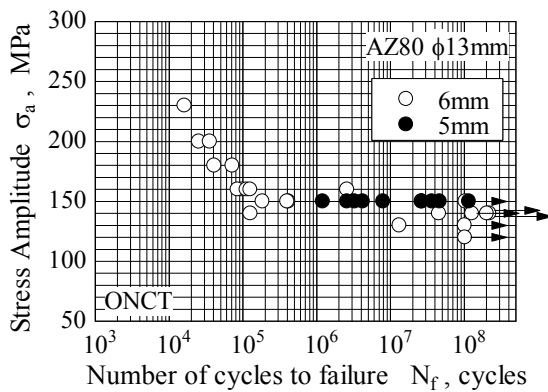


(b) Long life Gr.( $9.8 \times 10^5$ cycles)

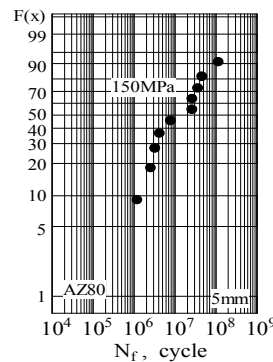
Fig.6: SEM observation results of Fig.5(c) specimens.

### Fatigue results of AZ80

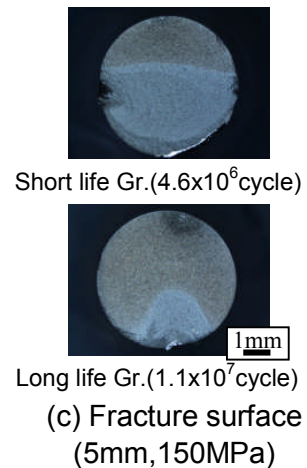
Fig.7(a) shows the S-N diagram of AZ80 materials. The S-N diagram of AZ80 is a simple S-N curve. Fatigue strength at  $10^8$  cycles of AZ80 was about 140MPa. Although the tensile and compressive strengths of AZ80 were higher than the strength of AZ61, fatigue properties of AZ80 were inferior to the properties of AZ61. Only the fatigue strength at  $10^8$  cycles of AZ80 did not correspond to the compressive 0.2% strength of material among the three types of materials. It was expected that the fatigue strength at  $10^8$  cycles of AZ80 is not affected by the compressive plastic strain. Fatigue life scattering was investigated at only the stress amplitude level of 150MPa. Fig.7(b) shows the Weibull plot of the result. Fatigue life data was divided into long life group and short life group. A mixed Weibull distribution was proposed. It could be that the S-N diagram of AZ80 would become a two-step diagram if the fatigue tests were carried out under stress conditions lower than 140MPa. Fig.7(c) shows an example of the macroscopic fracture surface. There was no fish-eye fracture in both groups. Fig.8 shows the fracture surface observation of the result shown in Fig.7(c) specimens by SEM. Fracture surface morphology of AZ80 presented a flat shape. It seems that the crack initiation point of short life group specimen was located slightly under the surface as the long life group of AZ61. On the other hand, crack initiation area of the long life group specimen was coarser than the surrounding area and it seemed that the crack initiation point was located in a deeper position than for the short life group specimen. Nevertheless, it was difficult to identify where the fatigue crack initiation point was.



(a) S-N diagram



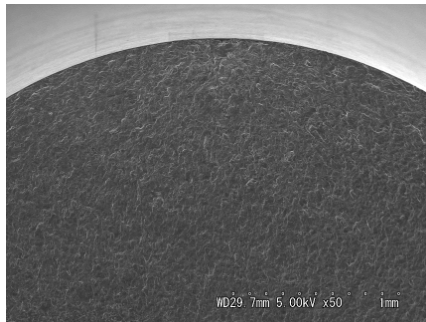
(b) Weibull plot



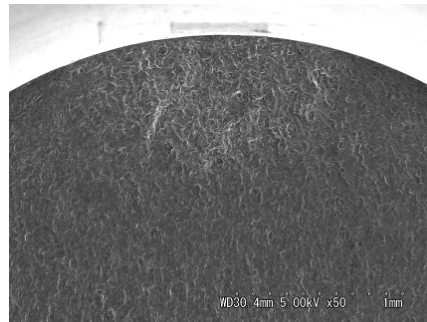
(c) Fracture surface (5mm, 150MPa)

Fig.7: Fatigue results of AZ80.





(a) Short life Gr.( $4.6 \times 10^6$ cycles)



(b) Long life Gr.( $1.1 \times 10^7$ cycles)

**Fig.8:** SEM observation results of Fig.7(c) specimens.

## INTRODUCTION TO OUR RESEARCH

This paper introduces our research on basic rotary bending loading fatigue properties of AZ31, AZ61 and AZ80. This sub-committee is looking into more fatigue properties as shown below.

- ✓ Effect of loading type: axial loading condition, rotary bending loading condition
- ✓ Effect of specimen size: minimum diameter of specimen (4, 5, 6 mm )
- ✓ Effect of surface treatment: peening, coating etc.
- ✓ Coaxing effects

## REFERENCES

- [1] Nakamura, T.; Ueno, A.; Matsumura, T.; Masaki, K.; Oguma, H.; Akebono, H.; Kakiuchi, T.; Kikuchi, S.; Nakamura, Y.; Nishida, T.; Ogawa, T.; Oguma, N.; Sakai, T.; Shimamura, Y.; Shiozawa, K.; Uematsu Y.:  
Data Acquisition for Very High Cycle Fatigue of Non-ferrous Metallic Materials Based on the Collaborative Research in JSMS -1st report: outline of round-robin experiments on aluminum die casting, beta titanium, and wrought magnesium alloys -  
7th Inter. Conf. on Very High Cycle Fatigue (7th VHCF) (2017).
- [2] Ueno, A.; Matsumura, T.; Masaki, K.; Ogawa, T.; Shiozawa, K.; Nakamura, Y.; Nishida, T.:  
Data Acquisition for Very High Cycle Fatigue of Non-ferrous Metallic Materials Based on the Collaborative Research in JSMS - 2nd report: effects of loading type, test environment, surface treatment and casting defects on VHCF properties of ADC12 aluminum die-casting alloy -  
7th Inter. Conf. on Very High Cycle Fatigue (7th VHCF) (2017).
- [3] Oguma, H.; Nakamura, T.; Ueno, A.; Matsumura, T.; Masaki, K.; Akebono, H.; Uematsu Y.; Oguma, N.; Kakiuchi, Shimamura, Y.; Nakamura, Y.;  
Data Acquisition for Very High Cycle Fatigue of Non-ferrous Metallic Materials Based on the Collaborative Research in JSMS - 3rd report: effects of loading type and test frequency on VHCF prpperties on beta Ti22V4Al -  
7th Inter. Conf. on Very High Cycle Fatigue (7th VHCF) (2017).

**Corresponding author:** masaki-k@okinawa-ct.ac.jp

## **S-N BEHAVIOUR OF COPPER AT VHCF LOADING**

S. E. Stanzl-Tschegg<sup>1)</sup>, A. Perlega<sup>1)</sup>, M. Meischel<sup>1)</sup>, B. Schönbauer<sup>1)</sup>

<sup>1)</sup> University of Natural Resources and Life Sciences, BOKU Vienna, Peter Jordan St. 82, 1190 Vienna, Austria

### **ABSTRACT**

*S-N* response of three kinds of polycrystalline copper is reported. New results may explain up-to-date controversial results of different authors. Plastic strains and micro-hardness were measured in this study and their consequences on the *S-N* behaviour are derived. Responsible mechanisms of fatigue damage in the very-high cycle fatigue regime are discussed as well as consequences for life-time predictions.

### **KEYWORDS**

Plastic-strain measurement, VHCF, polycrystalline Cu, *S-N* diagram, Coffin-Manson curves, frequency influence

### **INTRODUCTION**

The existence or non-existence of fatigue limits and of cyclic threshold stress intensity factors for fatigue crack growth became of increasing interest during the last years for several materials. At very high numbers of cycles - typically beyond  $5 \times 10^8$ , failure is observed, which predominantly arises from cracks, being initiated at the surface or in the interior of a specimen. Their formation is strongly influenced by loading mode (uniaxial, constant-amplitude (CA) or variable-amplitude (VA) loading, *R*-ratio etc.), loading amplitudes, microstructure, surface properties of specimens and surface-to-volume ratio.

In an attempt to correlate the fatigue limits with the mechanisms for damage and fracture, experiments were performed with the ultrasonic fatigue testing technique (testing frequency about 19 kHz), which allows obtaining very high numbers of cycles within reasonable testing times. New, partly surprising results on the *S-N* response of polycrystalline copper are reported in this paper. They shed light on up-to-date controversial results of different authors. Relevant cyclic stress and plastic-strain intensity values were measured, and results on the role of material microstructure caused by chemical composition and heat-treatment as well as frequency effects are reported.

### **MATERIAL AND EXPERIMENTAL PROCEDURE**

#### **Material**

Three different variants of polycrystalline copper with different purity and production process were studied. A-Cu is an electrolyte 99.98% copper (DIN 1787/17672/1756), B-Cu is an

electrolytic Cu-ETP (CW004A) of 99.990% purity (DIN E-Cu58/57 (2.0065/60)) [1] and C-Cu is high purity 99.999% copper [3].

All materials were heat-treated in vacuum. A-Cu 750 °C for 75 min, cooled in air, B-Cu 680 °C for 25 min, cooled 300 °C/h in vacuum, C-Cu 650 °C for 60 min, furnace cooled in vacuum. The mechanical properties are summarized in Table 1

Material	Purity (wt.%)	E-Modul. (GPa)	$R_m$ (MPa)	$R_{p,0.2}$ (MPa)	A	MH (HV)	Grain size ( $\mu\text{m}$ )
A-Cu	99.98	130	~200	~130	30	35-70	60
B-Cu	99.990	127.7	~271	~203	~12	~87	39
C-Cu	99.999	120	250	140	30	50	60

**Table 1:** Mechanical properties

Different specimen shapes were chosen for the different types of tests. For the fatigue tests, hourglass shapes with 3 mm diameter in their centre were prepared. With high-purity copper (C-Cu) not only hour shapes were tested but specimens were also machined from rods with 7 mm diameter such that, two opposite flat areas were produced (details see [3]). For the thermoelectric measurements, cylindrical rods with a diameter of 5 mm were used [2]. After machining, all specimens were ground, heat treated and subsequently electrolytically polished.

### Experimental Procedure

It was aimed to realize experimental conditions (especially specimen geometry and surface conditions as well as loading conditions) as similar as possible for the three copper variants and both frequencies.

The fatigue loading experiments at a testing frequency of about 19 kHz were performed with a closed-loop controlled ultrasonic equipment. A vibration gauge serves as feed-back controlling the vibration with an accuracy of  $\pm 1\%$ . The total strain amplitudes are calibrated using a strain gauge in the area of maximum strains. For more details of the ultrasonic testing technique see [4, 5]. Since ultrasound tests are displacement, i.e. total strain controlled, stresses (or loads) cannot be measured directly, but are determined from the measured total strain amplitude  $\Delta\varepsilon_{\text{tot}}/2 = \Delta\varepsilon_{\text{el}}/2 + \Delta\varepsilon_{\text{pl}}/2$ . Subtracting  $\Delta\varepsilon_{\text{pl}}/2$  from  $\Delta\varepsilon_{\text{tot}}/2$ , the elastic part  $\Delta\varepsilon_{\text{el}}/2$  is determined. The axial stress amplitude  $\Delta\sigma/2$  is calculated using Hooke's law:  $\Delta\sigma/2 = E\Delta\varepsilon_{\text{el}}/2$ . In order to minimize the damping heat, pulse-pause sequences are performed and in addition forced air is used [2].

The 20 Hz studies were performed with servo-hydraulic testing equipment under load control. A training procedure was chosen in accordance with former tests [2] for both loading frequencies. The specimens were ramp-loaded in steps of 1 MPa and 5 MPa with a step length of 300 cycles at 20 Hz and  $2.1 \times 10^4$  cycles at 19 kHz. The tests were started at a stress amplitude of 10 MPa in the S-N experiments. As no influence of the step height was observed, this task will not be considered in the following. For more experimental details see [1, 5].

If plastic-strain amplitudes are expected to play a role, they have to be determined indirectly by measuring the damping heat with micro-thermocouples in the ultrasonic tests [2]. For these measurements, the temperature rise during one pulse consisting of  $1.9 \times 10^4$  cycles or less, e.g. 500 cycles at higher total strain amplitudes ( $\Delta\varepsilon_{\text{tot}}/2$  above approximately  $5 \times 10^{-4}$ ) is recorded. The accuracy of measurement is 0.01 °C and the statistical error of the plastic strain amplitudes therefore a few percent. The dissipated energy per cycle  $\Delta W/N$  can be

linked to the plastic strain amplitude  $\Delta\varepsilon_{pl}/2$  using the heat capacity  $c$ , the mass  $m$  and the temperature change per cycle  $\Delta T/N$  [6]:

$$\Delta W/N = c \cdot m \cdot \Delta T/N = c \cdot \rho \cdot V \cdot \Delta T/N \quad (1)$$

with  $\rho$  = mass density. The plastic part of the cyclic strain  $\Delta\varepsilon_{pl}/2$  can be determined by subtracting the elastic portion  $\Delta\varepsilon_{el}/2$  from  $\Delta\varepsilon_{tot}/2$ . Approximating the hysteresis loop's shape by an ellipse, its area  $A$  corresponds to the dissipated energy:

$$A = \Delta W/N = \Delta\varepsilon_{pl} \cdot \Delta\sigma/2 \quad (2)$$

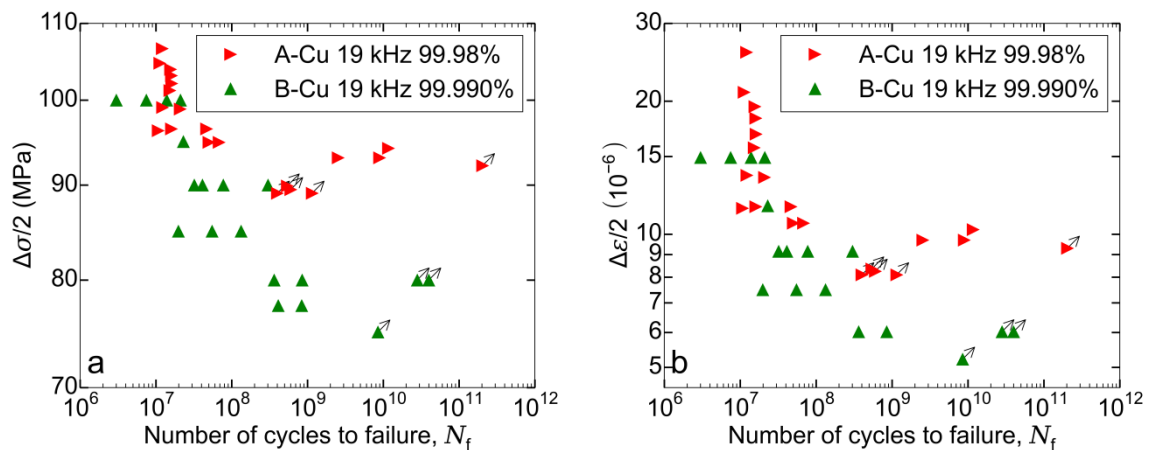
The plastic strain thus is

$$\Delta\varepsilon_{pl} = \frac{1}{2} \cdot \frac{c \cdot \rho \cdot V \cdot \Delta T}{\pi \cdot \Delta\sigma/2 \cdot N} \quad (3)$$

The plastic strain amplitudes were determined at both loading frequencies during the training process and also during the  $S-N$  tests. During the training procedure at 20 Hz,  $\Delta\varepsilon_{pl}/2$  was measured every fifth load step. Beginning with a stress amplitude of 10 MPa, the load was increased in steps of 1 MPa for a defined number of cycles, where the  $\Delta\varepsilon_{pl}/2$  remained constant. Then the load was shut-off. The length of every shut-off period, where  $\Delta\varepsilon_{pl}/2$  was recorded, was five times the step length used in the  $S-N$  tests, namely 1500 cycles. To obtain data on the evolution of the  $\Delta\varepsilon_{pl}/2$  during  $S-N$  testing,  $\Delta\varepsilon_{pl}/2$  was measured for the highest and lowest stress level tested. Data were recorded automatically by the test and motion software of the machine to calculate  $\Delta\varepsilon_{pl}/2$ , single hysteresis loops were used, which can be obtained directly from the machine data, which is in contrast to the ultrasonic-resonance test [1].

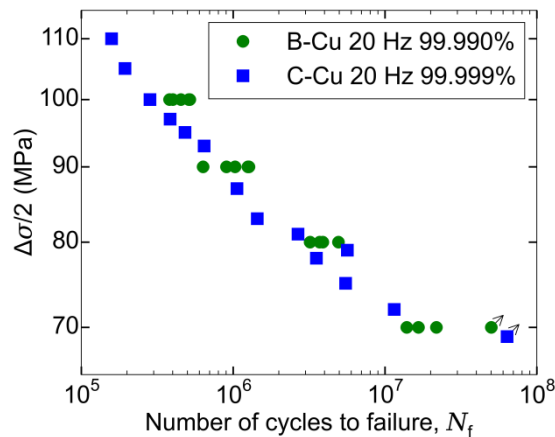
## RESULTS

Fig. 1 shows the material influence on the  $S-N$  curves (a) and Coffin-Manson plots (applied total-strain amplitudes) (b) at the testing frequency of 19 kHz. The two electrolyte copper materials A-Cu (99.98%) and B-Cu (99.990%) were measured. A-Cu was measured by different researchers using different ultrasonic equipment at different times. The good agreement assesses the validity of the results. The VHCF  $S-N$  curve above about  $10^8$  cycles and endurance limit as well as the strain values of A-Cu are much higher [3] compared to B-Cu. Said in other words, the somewhat cleaner 99.990% electrolytic copper breaks much earlier at comparable cyclic-stress and plastic-strain amplitudes.



**Fig. 1:** Strong influence of material properties (two kinds of electrolytic copper) at 19 kHz-loading on fatigue lives. (a)  $S-N$  curves, (b) Coffin-Manson plot

This is in contrast to the low-frequency 20 Hz results which show identical  $S-N$  results (Fig. 2) of C-Cu (high-purity 99.999% Cu) and B-Cu (electrolytic 99.990% Cu) [1].



**Fig. 2:** Almost no influence of material conditions (electrolytic and high-purity copper) on S-N response at 20 Hz loading frequency

Fig. 3 shows the influence of testing frequency (20 Hz and 19 kHz) on the S-N curves and ( $\Delta\epsilon_{pl}$  vs.  $N_f$ )-plots (with the associated plastic strain amplitudes) of the two electrolytic materials, A-Cu and B-Cu [1, 7]. The VHCF S-N curve and endurance limit of the A-Cu are shifted towards higher cyclic stress amplitudes (Fig. 3a) or said in other words to higher numbers of cycles at comparable stress amplitudes. The plastic strain values are much lower (Fig. 3b) [3].

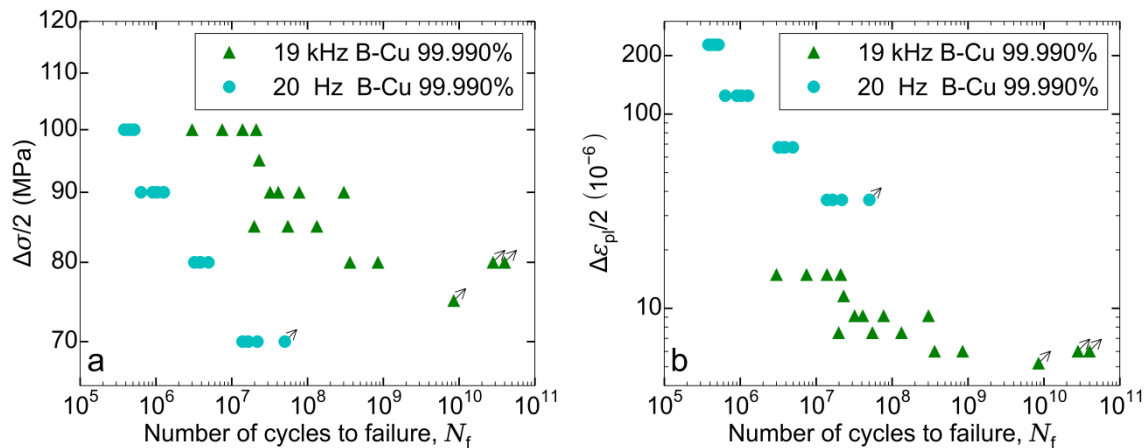


**Fig. 3:** Influence of testing frequency (20 Hz and 19 kHz) on S-N curves and plastic strain amplitudes  $\Delta\epsilon_{pl}/2$  at different numbers of cycles of electrolytic copper B-Cu (99.990% Cu). (a) Larger life-times at 19 kHz, (b) much lower  $\Delta\epsilon_{pl}/2$  at 19 kHz fatigue

In order to interpret the different S-N curves in the ultrasonic-fatigue tests, extensive investigations of the plastic strains were performed as mentioned above and described in detail in [2, 6]. Fig. 4 gives a comparison of the 20 Hz and 19 kHz plastic strain amplitudes vs. the applied total strain amplitudes  $\Delta\epsilon_{tot}/2$  and shows in Fig. 4a that, the plastic strain amplitudes are considerably higher at 20 Hz than at 19 kHz between  $\Delta\epsilon_{tot}/2 \sim 8 \times 10^{-5}$  and  $8 \times 10^{-4}$ .

In addition, Figs. 4a and b demonstrate that, cyclic hardening is the reason for this result. Cycling hardening was determined after each raise of the load level. This is visible in Fig. 4a and can be better identified in Fig. 4b. This plot shows the repeated decrease of  $\Delta\epsilon_{pl}/2$  over the number of cycles at 20 Hz during a training procedure as described above (5 MPa steps). Additional studies were undertaken for an assessment of the mechanical response of cyclic loading at the two frequencies by micro-hardness measurements (9.8 kN load during 15 s).

The results are summarized in a box plot [8] in Fig. 5. They verify that, the mean micro-hardness and thus static strength of 99.990% electrolytic copper is considerably higher than that of the high purity 99.999% copper. For each test series, ten hardness intends were performed and as reference for the non-loading condition of the 19 kHz test, the lower outer specimen part with a diameter of 14 mm served (the diameter of the fatigue loaded inner part was 3 mm diameter). It is suspected that, the higher scatter of the electrolytic-copper results is caused by an inhomogeneity of the microstructure owing to the production process.

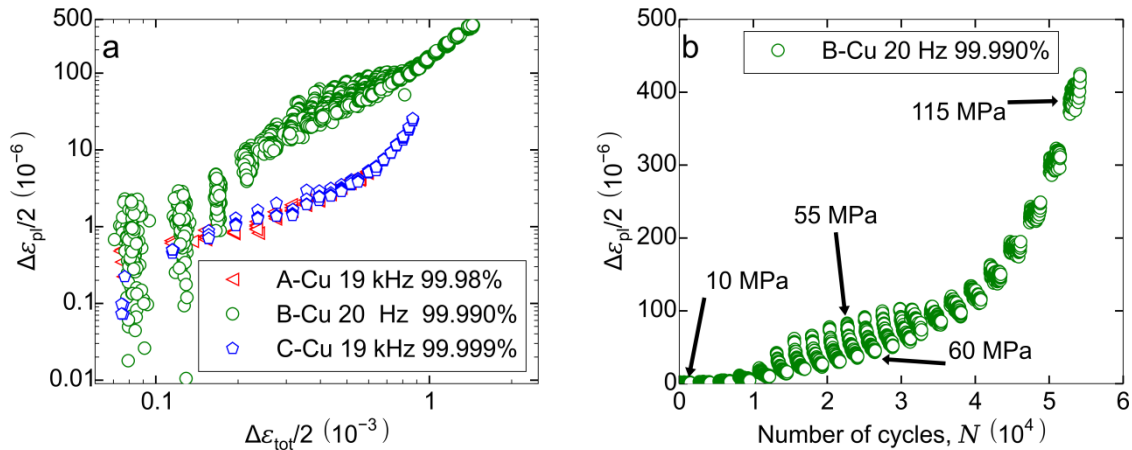


**Fig 4:** Role of frequency (20 Hz and 19 kHz) on plastic strain amplitudes  $\Delta\epsilon_{pl}/2$  at different total strain amplitudes  $\Delta\epsilon_{tot}/2$ . (a) Changes of  $\Delta\epsilon_{pl}/2$  at  $\Delta\epsilon_{tot}/2$  between  $\sim 10^{-4}$  and  $10^{-3}$  in electrolytic and high-purity copper. (b) Strain hardening of electrolytic B-Cu at 20 Hz loading vs. number of cycles.

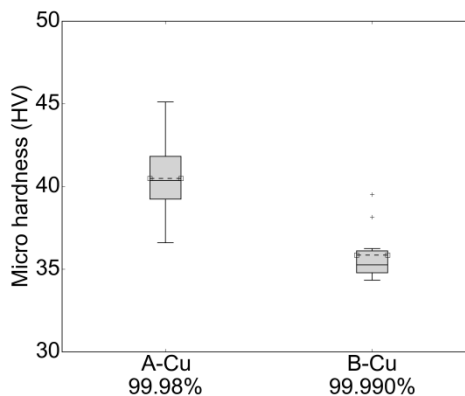


**Fig. 5:** Micro-hardness of two kinds of electrolytic copper (A-Cu and B-Cu) after 19 kHz fatigue loading

## EVALUATION OF RESULTS

The results demonstrate up-to-date unexpected reasons for partly completely different results on life-times such as  $S-N$  curves and endurance limits in the VHCF regime reported by different authors, especially obtained with the ultrasonic-fatigue technique. In many investigations, it was assumed that the high frequency of 19 kHz introduces other micro and nano-structural features than conventional frequencies. It can be assessed, however, that such frequency effects can account for maximal 10% higher  $\Delta\sigma/2$  values if an appropriate testing procedure is applied, especially if sufficient cooling during loading is provided. In

contrast to this, the results of this study demonstrate that the properties of the raw material are mainly responsible for the partly reported different life times, i.e. *S-N* curves of polycrystalline copper.

The results also implicate that all up-to-date procedures of life-time predictions (at constant and variable amplitudes) based solely on physical laws are not in general useful, even if they are restricted to only one metal (copper e.g.). They have to be adapted such that, for example, the different strengthening features of each individual material during the different stages of fatigue loading are introduced considering even processes in the nanometer range. But even such an analysis does not help, if it is based on a general treatment of dislocation arrangements only. Especially in the VHCF regime, only very few parts (grains) of a specimen are affected by changes [9, 10]. Details of the currently active micromechanical response of each individual material condition must be known and only if they are all implemented, prediction of endurance limits might be possible.

## REFERENCES

- [ 1 ] Perlega, A.:  
Influence of Testing Frequency on the Fatigue Properties of Polycrystalline Copper. Master thesis, Technical University Vienna, Austria 2015
- [ 2 ] Stanzl-Tschegg, S. E.; Schönbauer, B.:  
Mechanisms of Strain Localization, Crack Initiation and Fracture of Polycrystalline Copper in the VHCF Regime.  
Int. Journal of Fatigue 32 (2010), pp. 886-893
- [ 3 ] Eichinger, K.:  
Gleiterscheinungen und Rissbildung bei Wechselbeanspruchung von polykristallinem Kupfer. Master thesis, Technical University Vienna, Austria 2009
- [ 4 ] Stanzl, S.:  
A New Experimental Method for Measuring Life Time and Crack Growth of Materials under Multi-stage and Random Loadings.  
Ultrasonics Nov. (1981), pp. 269-272
- [ 5 ] Mayer, H.:  
Recent Developments in Ultrasonic Fatigue  
Fatigue & Fracture of Engineering Materials & Structures 39 (2016) No. 1, pp. 3-29
- [ 6 ] Papakyriacou, M., Mayer, H., Plenk Jr, H., Stanzl-Tschegg, S.:  
Cyclic Plastic Deformation of Tantalum and Niobium at Very High Numbers of Cycles  
Materials Science and Engineering A 325 (2002), pp. 520-524
- [ 7 ] Stanzl-Tschegg, S., Schönbauer, B.:  
PSB Threshold and Fatigue Limit of Polycrystalline Copper in the VHCF Regime  
VHCF4, Michigan, 2007, TMS Warrendale, USA, pp. 15-22 (2007)
- [ 8 ] Perlega, A.:  
Einfluss der Testfrequenz auf das Ermüdungsverhalten von polykristallinem Kupfer  
Institutsseminar IPM, BOKU Vienna, Nov. 19, 2014
- [ 9 ] Lukáš, P., Kunz, L.:  
Specific Features of High-cycle and Ultra-high-cycle Fatigue  
Proc. of the Int. Conf. on Fatigue in the Very High Cycle Fatigue Regime, 2001, ©Institute of Meteorology and Physics, BOKU Univ. f. Bodenkultur, Vienna, pp. 23-33 (2001)
- [ 10 ] Stanzl-Tschegg, S.E., Schönbauer, B.:  
Mechanisms of Strain Localization, Crack Initiation and Fracture of Polycrystalline Copper in the VHCF-Regime  
ECF17, Brno, CR, 2008

Corresponding author: [stefanie.tschegg@boku.ac.at](mailto:stefanie.tschegg@boku.ac.at)

# INFLUENCE OF MICROSTRUCTURAL CHARACTERISTICS ON THE VHCF BEHAVIOR OF THE ALUMINUM CAST ALLOY EN AC-ALSi7Mg0.3

S. Knorre<sup>1</sup>, J. Tenkamp<sup>2</sup>, U. Krupp<sup>1</sup>, W. Michels<sup>1</sup>, F. Walther<sup>2</sup>

<sup>1</sup> University of Applied Sciences Osnabrueck, Faculty of Engineering and Computer Science, Institute of Materials Design and Structural Integrity - Osnabrueck, Germany

<sup>2</sup> TU Dortmund University, Faculty of Mechanical Engineering, Department of Materials Test Engineering (WPT) - Dortmund, Germany

## ABSTRACT

The steady demand for lightweight and fatigue-resistant solutions in several applications, especially in automotive and aerospace industries, requires the extensive use of light alloys. In particular, aluminum cast alloys are promising candidates for highly loaded lightweight components due to their excellent strength-to-weight ratio. Since these alloys contain metallurgical defects, like porosity and precipitates, the knowledge about the relationship between microstructure characteristics and fatigue mechanisms as well as fatigue life of aluminum cast alloys is essential to ensure a safe design for critical components. For this purpose, fatigue tests in the VHCF regime ranging from  $10^6$  to  $10^9$  cycles were performed using the cast alloy EN AC-ALSi7Mg0.3. For this purpose, samples were cast into a steel mold with grain refinement (AlTi5B1), Sr refining and a melt cleaning by nitrogen releasing tablets. An additional HIP treatment was carried out to remove the process-induced porosity. The number of cycles and the location of crack initiation were determined by means of correlated thermographic and fractographic investigations. Due to the absence of inner defects, the eutectic phases act as stress concentrators for fatigue initiation. However, the crack propagation progress was dominated by the eutectic phases as well as grain boundaries to act as efficient barriers to reduce and stop crack advance.

## KEYWORDS

EN AC-ALSi7Mg0.3, aluminum cast alloy, VHCF, fatigue crack initiation, high-resolution thermography

## INTRODUCTION

Modern cast aluminum alloys are suitable for light construction applications, e.g. in automotive and aircraft construction, due to the low density of  $2.7 \text{ g/cm}^3$  and the excellent strength-to-weight ratio. Compared to the widespread aluminum wrought alloys, the use of cast aluminum alloys is limited by metallurgical defects. Therefore, to ensure a safe design for critical components, the knowledge about the influence of microstructure characteristics on fatigue life and mechanisms of aluminum cast alloys is essential.

By means of advanced casting processes, e.g. melt refinement, melt cleaning, and further material post-treatments, e.g. hot isostatic pressing, the remnant porosity in current aluminum cast alloys can be significantly reduced or even removed (cf. [1]). Especially, hot isostatic pressing (HIP) is a common post-processing in automotive industry to remove remnant porosities. Once the porosity is no longer the weakest link of Al cast alloys, microstructure characteristics dominate the fatigue performance. These characteristics include the secondary dendrite arm spacing (SDAS), the grain size as well as the shape and distribution of the silicon particles, and are relevant to ensure a safe design for safety-relevant components made of aluminum cast alloys [1-2]. In the present study, the influence



of microstructural characteristics on the fatigue behavior in the VHCF regime has been characterized by constant amplitude fatigue tests. A new measuring method was evaluated for the detection of crack initiation and progress using high-resolution thermography.

## MATERIAL AND EXPERIMENTAL SETUP

### Material and Microstructure

For testing the fatigue behavior in the VHCF regime, specimens of the cast aluminum alloy EN AC-AISi7Mg0.3 were produced by die casting. The raw material was melted in a resistance furnace with titanium grain refining treatment (using AlTi5B1 additions) and a strontium refining treatment (using AlSr10 additions) before casting it into a steel mould. In order to reduce the porosity, solid and gaseous impurities were flushed out of the melt by nitrogen-emitting tablets. Selected samples were densified by hot isostatic pressing. Finally, the samples were solution heat treated according to a two-stage T6 procedure at 545 °C for one hour and then quenched in water. In addition, the samples were artificially aged at 160 °C for five hours. The chemical composition (Table 1) was analysed by means of spark emission spectroscopy.

Si	Mg	Fe	Mn	Ti	Al
7.5	0.288	0.094	0.0018	0.146	bal.

**Table 1:** Chemical composition of the aluminum cast alloy EN AC-AISi7Mg0.3, in wt.-%

The grain size, the secondary dendrite arm spacing and the formation of the silicon particles have been determined by light microscopy. The grain size was made visible in micrographs by using the electrolytical Barker etching and quantified by line-cutting method. The same line-cutting evaluation procedure was applied to determine the SDAS on polished cross sections. The image processing program ImageJ has been used to evaluate the silicon particle distribution. At first the image has been binarized by ImageJ, in order to establish a limit value for the silicon particle circularity analysis in the next step. In addition to this, X-ray computer tomography (Nikon XT) was used to quantify the effect of hot isostatic pressing on the relative density characteristic microstructures, which are shown in Fig. 1a-c.

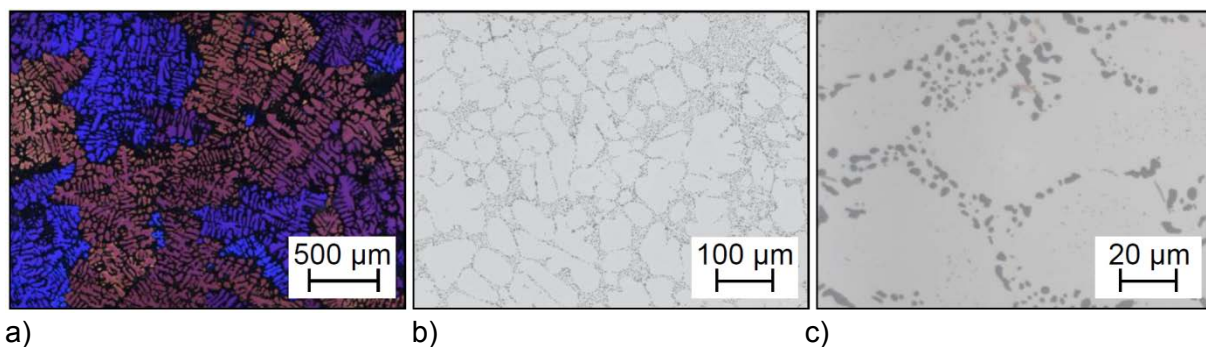


**Fig. 1:** Light micrographs: a) Barker etched (grains), b-c) polished Al dendrites – Al-Si interdendritic eutectic and c) Si precipitates within the Al-Si eutectic.

Grain size [ $\mu\text{m}$ ]	SDAS [ $\mu\text{m}$ ]	Rel. density [%]	Circularity [-]
623 $\pm$ 334	40.5 $\pm$ 7.5	100	0.9

**Table 2:** Microstructure characteristics of the aluminum cast alloy EN AC-AISi7Mg0.3

## Fatigue Testing

To characterize the fatigue behavior in the VHCF regime, specimens for fatigue tests (Fig. 2a) were machined, mechanically ground and polished. The specimens are provided with a shallow notch symmetrically on both sides, which leads to a negligible stress concentration (notch factor  $\alpha_k = 1.1$ ). Preferential fatigue damage is limited to the area of the shallow notch, which is observed in-situ by means of high-resolution thermography in order to detect the crack initiation location, crack initiation time and crack propagation. The polished surface of the shallow notch was aligned to the three-magnifying macro lens of the thermal camera (InfraTec ImageIR 8300) to record the temperature development of the microstructure at the base of the shallow notch during fatigue loading (Fig. 2b). For this purpose, the difference image was observed to clearly identify localized heat development in microstructure, so-called hotspots, and resulting cracks.

For the VHCF tests, an ultrasonic fatigue system (type BOKU Vienna, Fig. 2b) has been used, with which the tests could be carried out in a reasonable time. In this test technique, a sinusoidal ( $f \approx 19.9$  kHz) electric power generated by a frequency generator and amplifier is converted from a piezoelectric crystal into a mechanical oscillation. The oscillation is amplified in its amplitude by a titanium horn (Fig. 2b, pos. 1) and transferred into the fatigue specimen (Fig. 2b, pos. 2). As soon as the exciter frequency coincides with the natural frequency of the fatigue test, the specimen resonates.

The specimen is loaded by a cyclic push-pull loading at a stress ratio of  $R = -1$  in the gauge length. The stress is determined by a strain gauge in the mid-section of the specimen. The desired strain or voltage amplitude, respectively, is calculated using Hooke's law and adjusted via the electrical power provided by the amplifier. The measuring signal of the control loop is supplied by an inductive displacement transducer (Fig. 2b, pos. 3), which detects the displacement of the titanium horn. A further control loop monitors the excitation frequency of the natural frequency of the fatigue specimen during fatigue test. The test frequency changes during the experiment by crack formation and growth, as well as hardening or debonding in the test material. A defined drop in the natural frequency or test frequency, respectively, serves as a shut-off criterion for the test machine.

In order to avoid sample heating, the test was carried out in the pulse-pause mode (200 ms to 800 ms), which led to a reduction of the effective test frequency to 4,000 Hz.

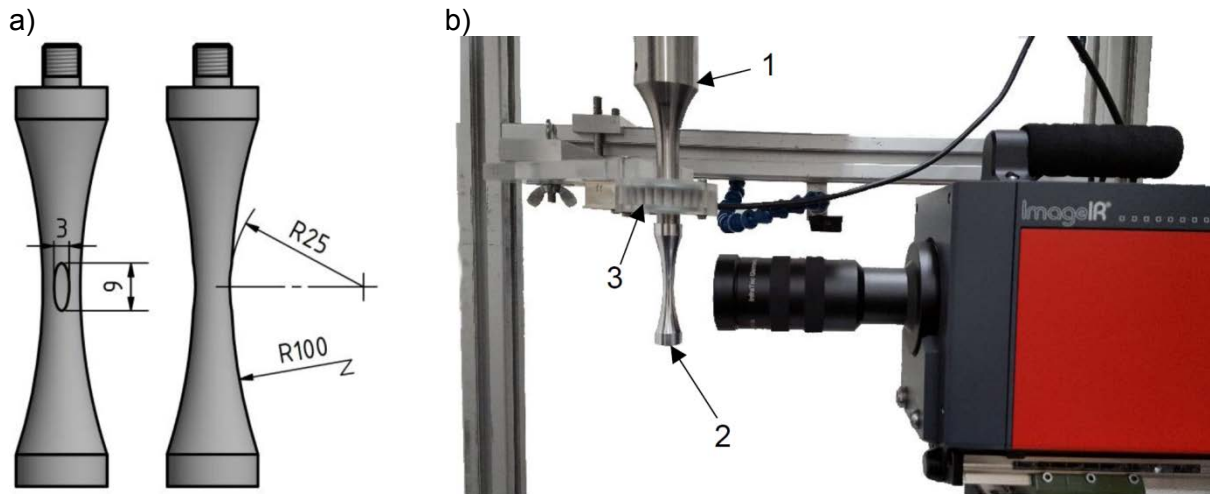


Fig. 2: a) Specimen design with shallow notch ( $R = 25$  mm), b) VHCF testing setup with high-resolution thermal camera

## EXPERIMENTAL RESULTS

The results of the constant amplitude fatigue tests with high-resolution thermography are shown in a S-N curve, Fig. 3. The stress amplitude over the number of cycles to failure is shown in a double-logarithmic manner. As the stress amplitude decreases, higher numbers of cycles to failure are achieved.

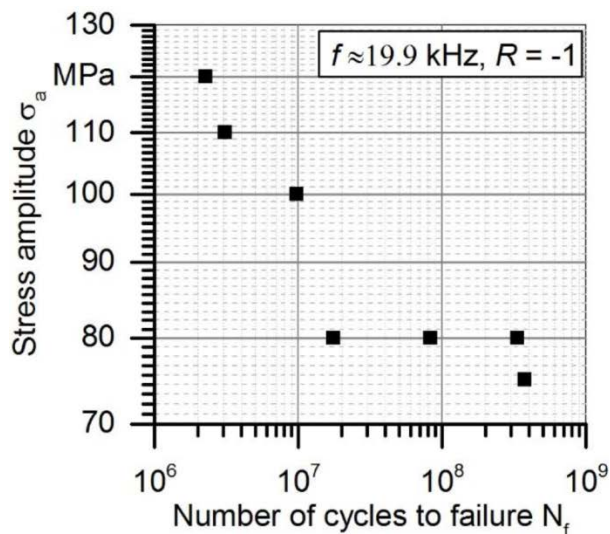


Fig. 3: S-N curve for VHCF regime

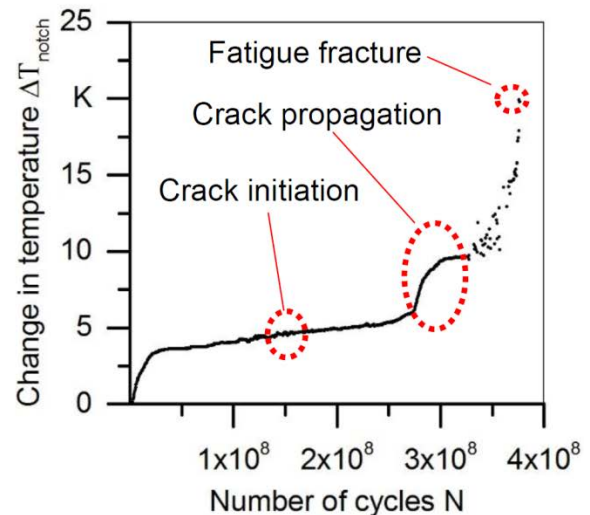


Fig. 4: Experimental results of thermography

As an example, Fig. 4 and Fig. 5 show the results of in-situ high-resolution thermography observation of the shallow notch during the fatigue test with a stress amplitude of  $\sigma_a = 75$  MPa. Fig. 4 shows the temperature development in the region of the shallow notch over the number of cycles. During the linear temperature increase between  $5 \cdot 10^6$  and  $2.75 \cdot 10^8$  cycles, the formation of a hot spot in the  $\alpha$ -Al solid solution was observed at  $1.53 \cdot 10^8$  cycles, Fig. 5a. In the interval between  $2.50 \cdot 10^8$  and  $2.75 \cdot 10^8$  cycles, a slightly higher temperature increase was observed, which is due to the growth of a fatigue crack, Fig. 5b. From  $2.75 \cdot 10^8$  cycles, a sharp temperature increase occurs, which is accompanied with

the fatigue crack growth, Fig. 5c. The plateau in the interval between  $3.0 \cdot 10^8$  and  $3.3 \cdot 10^8$  cycles is associated with less pronounced crack growth. The final failure of the specimen, in which a fatigue crack has formed over the entire width of the shallow notch leads to a significant temperature increase at  $3.3 \cdot 10^8$  cycles, Fig. 5d.

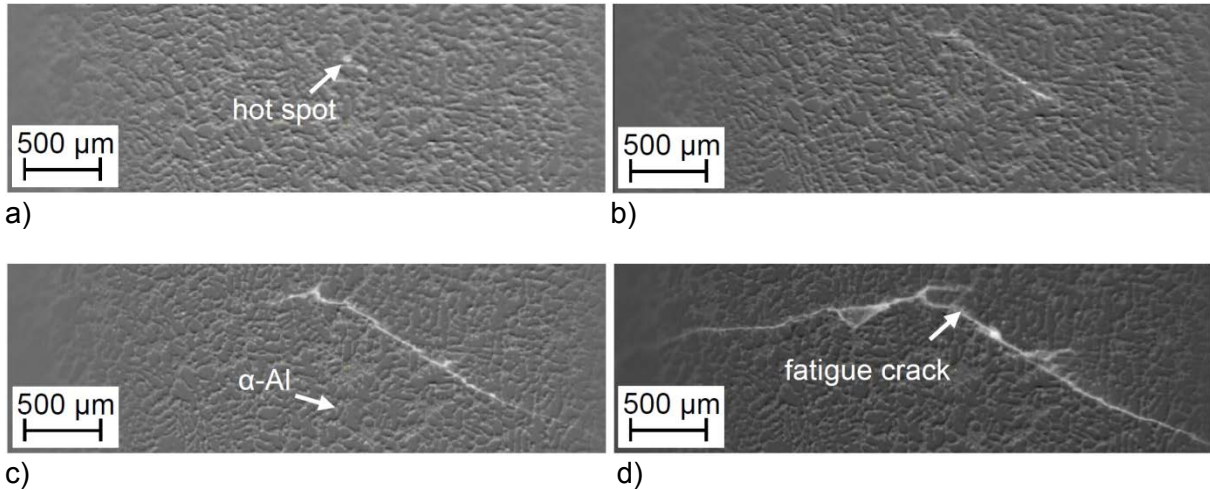
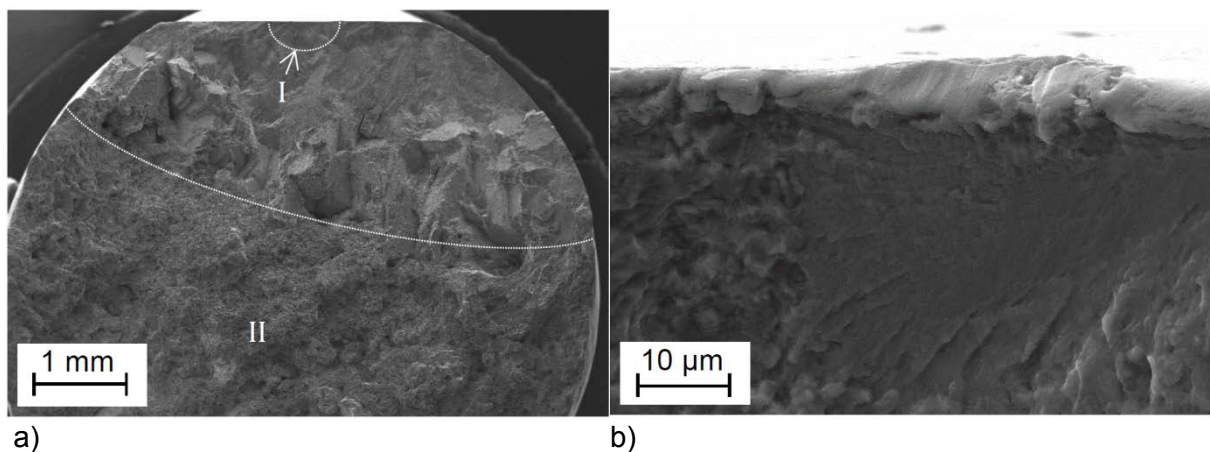
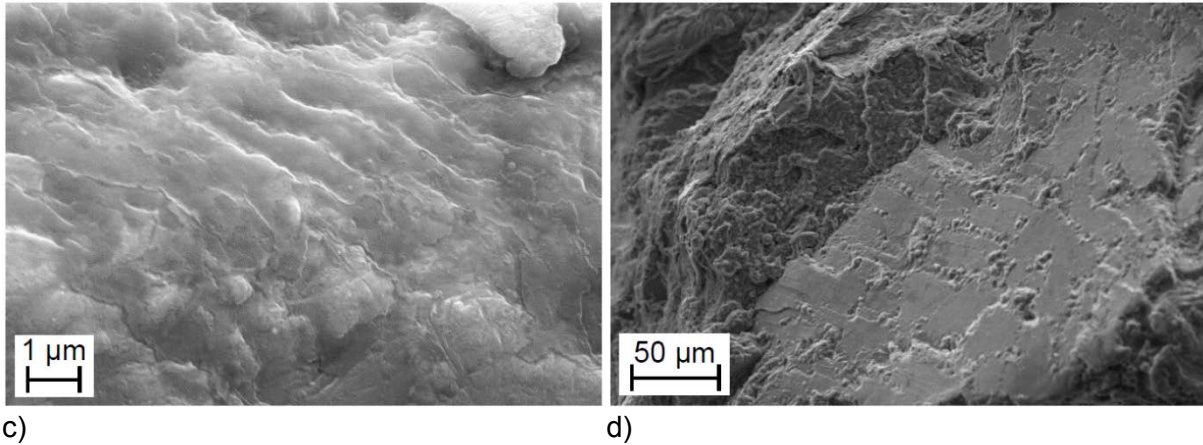


Fig. 5: Constant amplitude VHCF test at  $\sigma_a = 75$  MPa: a) Crack initiation at  $1.53 \cdot 10^8$  cycles, b) crack propagation at  $2.39 \cdot 10^8$  cycles, c) crack propagation at  $3.55 \cdot 10^8$  cycles and d) fracture at  $3.76 \cdot 10^8$  cycles

Fig. 6a-d show the SEM analysis of the fracture surface of a specimen failed after at  $3.3 \cdot 10^8$  cycles. The fracture surface can be divided into two regions. The crack initiation was found to originate from a microcell on the specimen surface in region I. Typical features of this crack initiation site are smooth surfaces, which are caused by planar slip, Fig 5b. Striations and debonded Si particles are visible in the vicinity of the microcell, Fig. 5c (cf. [3]). A characteristic feature of the VHCF fracture surface are micro cleavage facets as shown in Fig. 5d, reflecting mode II crack propagation until the crack turns into ductile rupture (tensile loading after resonant testing) in region II.







**Fig 6:** Characteristic fracture surfaces of a specimen loaded at  $\sigma_a = 80$  MPa: a) overview, b) and c) detailed view of microcell at surface and d) detailed view of the facet-like fracture surface due to single slip in the Al solid solution

## CONCLUDING REMARKS

The results of the fatigue tests in the VHCF regime in combination with in-situ high-resolution thermographic observation of the shallow notches and fractographic investigations reveal that the reduction of porosity causes fatigue crack initiation at microcells. The jagged facet-like structure of the fracture surface indicates mode II crack propagation dominated by single slip limited to the slip systems with the smallest Schmid factor. In this case, the slip bands interact with the eutectic regions, where either the fracture of the silicon particles or their debonding from the surrounding aluminum matrix occurs. The fatigue progress can be described and evaluated in-situ by high-resolution thermography. The thermography allows a distinct identification of the crack initiation and crack propagation phases during fatigue testing.

## ACKNOWLEDGMENT

The authors thank the German Research Foundation (DFG) for the financial support of the research project WA 1672/15-1 and KR 1999/19-1, the company Ohm & Häner Metallwerk GmbH & Co. KG for the supply of the raw material and the company Bodycote GmbH for the hot isostatic pressing of the specimens.

## REFERENCES

- [1] J. Z. Yi, Y.X. Gao, P.D. Lee, T.C. Lindley: Microstructure-based fatigue life prediction for cast A356-T6 aluminum-silicon alloys. *Metallurgical and Materials Transactions* 37B (2006), pp. 301-311
- [2] Q. G. Wang, D. Apelian, D. A. Lados: Fatigue behavior of A356/357 aluminum cast alloys. Part I – Effect of casting defects, *Journal of Light Metals* 1 (2001), pp. 73-84
- [3] C. Nyahumwa, N. R. Green, J. Campbell: Influence of casting technique and hot isostatic pressing on the fatigue of an Al-7Si-Mg alloy. *Metall. Mater. Trans.* 32A (2001), pp. 349358

**Corresponding author:** stephan.knorre@hs-osnabrueck.de

# INFLUENCE OF HYBRIDISATION BY SELECTIVE LASER MELTING ON THE VERY HIGH CYCLE FATIGUE BEHAVIOUR OF ALUMINIUM ALLOYS

S. Siddique, M. Awd, F. Walther  
TU Dortmund University, Department of Materials Test Engineering (WPT),  
Baroper Str. 303, D-44227 Dortmund, Germany

## ABSTRACT

Selective laser melting (SLM) is a novel technique in additive manufacturing which uses laser energy to melt the powder material according to the geometry of the computer aided design (CAD) model provided to the SLM system. The process uses a layer-wise manufacturing process which is specifically suitable for complex geometries and customised parts which otherwise would be costly, and even impossible, to be manufactured using conventional manufacturing processes. This study aims at determining the very high cycle fatigue (VHCF) behaviour of AlSi12 alloy manufactured by SLM process. Two different cooling conditions have been analysed and VHCF characterisation has been carried out until  $1E9$  cycles to determine the effect of SLM processing parameters on the ultrasonic fatigue behaviour of AlSi12 alloy. Additionally, it is investigated to manufacture hybrid Al structures, i.e. combination of conventional and additive manufacturing, which can reduce the costs of manufacturing for several structures. AlSi12 alloy was additively melted over base material to get the optimal joint strength so that an optimal strength and toughness combination can be obtained. The specimens were then tested in the VHCF regime. The results show that by appropriate heat treatment, joint strength of the hybrid specimens as well as their fatigue behaviour can be improved to bring them at par with pure alloys.

## KEYWORDS

Selective laser melting (SLM), AlSi12, porosity, VHCF, hybrid structures

## INTRODUCTION

Selective laser melting (SLM) process, which belongs to the class of metal additive manufacturing (AM) processes, relies on the consolidation of fine powder layers sequentially until a geometry can be obtained. The fusion source is a highly-focused laser beam controlled by state of the art numerical control [1,2]. The process schematic can be envisaged in Fig. 1 [3]. With the extensive freeform fabrication capability of SLM, an opportunity to produce complex parts with intricate geometries has appealed to manufacturers instinctively. The immense advantage is the possibility to get new complex designs to serial production lines in the shortest possible time, thus the product development cycle is significantly reduced [4]. Such capabilities do not imply elimination of conventional manufacturing processes; instead a combined manufacturing strategy is now proposed in which relatively simple part geometries can be obtained by conventional processes while the more intricate part of the component by direct SLM deposition on the conventional part, thus the need for time- and cost-extensive development of special tooling is eliminated. The result is essentially a hybrid manufacturing process which can be envisaged schematically in Fig. 2.

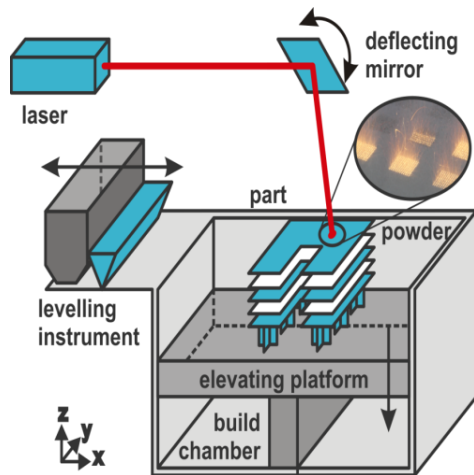


Fig. 1: Schematic of SLM process

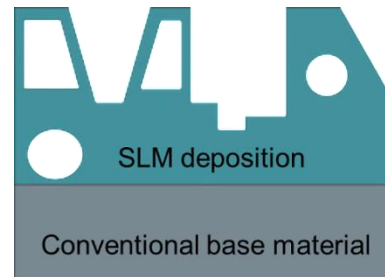


Fig. 2: Envisaged hybridisation concept

The aim of this study is the assessment of cyclic load bearing capabilities of hybrid structures in VHCF regimes. Quasi-static tensile testing was utilized in the initial stage to screen different configurations of the SLM process. Morphology in the fusion zone between SLM and conventional alloys are analysed. Following this stage, fatigue behaviour is investigated via ultrasonic fatigue (USF) system and finite element modelling. In the end, the results conclude about the application of hybrid structures in fatigue applications.

### SPECIMEN MATERIAL AND TESTING

The SLM alloy in this study is chosen to be AlSi12 (commercially Al4047) which is a well-established casting alloy in automotive industry. The Al-Si system depends on a balance of eutectic phase formation and a dispersion strengthening mechanism. The conventional base material is wrought alloy AlZn4.5Mg1 (commercially Al7020) which is a high strength aluminium alloy established in aerospace industry. The preeminent Al-Zn system relies on the nano-dispersion strengthening of post eutectic disintegration towards room temperature which gives the alloy its age hardening potential [5]. Chemical compositions for both alloys are given in Table 1 and Table 2.

Al	Si	Fe	Cu	Mn	Mg
Bal.	12.00	0.80	0.30	0.15	0.10

Table 1: Nominal chemical composition of Al4047

Al	Si	Fe	Cu	Mn	Cr	Mg	Zn	Zr	Ti
Bal.	0.35	0.40	0.20	0.50	0.35	1.40	5.00	0.20	0.25

Table 2: Nominal chemical composition of Al7020

The investigated configurations consist of 4 batches: A, B, C and D as listed in Table 3. Batches A and B are Al4047 alloy configurations processed by SLM. Both of these configurations were subjected to post-process stress relief (SR) at 240°C followed by oven cooling. Batch B was manufactured with base plate heating (BPH) at 200°C during SLM processing. The need for post-process stress relief (SR) for SLM structures have been

demonstrated previously in several studies [6,7]. Batches C and D are hybrid specimens prepared by SLM processing of Al4047 on Al7020 alloy. Batch D was subjected to post-process stress relief heat treatment.

Batch	A	B	C	D
Hybridisation	No	No	Yes	Yes
Material	Al4047	Al4047	Hybrid	Hybrid
Base plate heating (BPH) °C	0	200	0	0
Stress relief (SR) °C	240	240	0	240

Table 3: Study design for structural strength of SLM pure and hybrid structures

Characterisation of the resulting structure was carried out by analysis of microstructure morphology in a scanning electron microscope Tescan Mira XMU. Specimens were first sequentially ground and polished with diamond and oxide suspension, then etched using solutions of NaOH and HNO<sub>3</sub>. Secondly, quasi-static tensile tests followed at Shimadzu AG-100 kN Xplus with a video camera utilized for the strain measurement. Specimen geometry for tensile testing is shown in Fig. 3a.

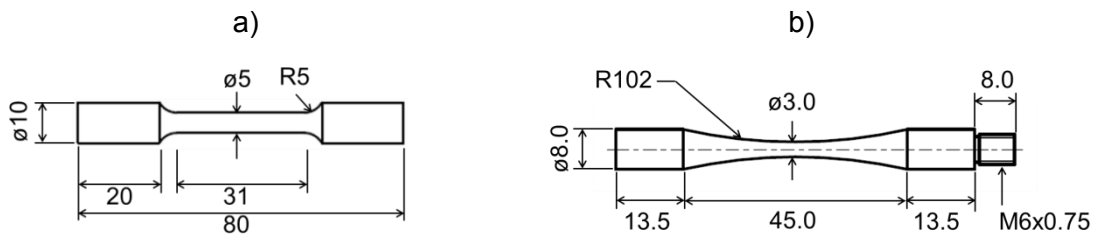


Fig. 3: Technical drawing: a) tensile test specimen, b) VHCF specimen

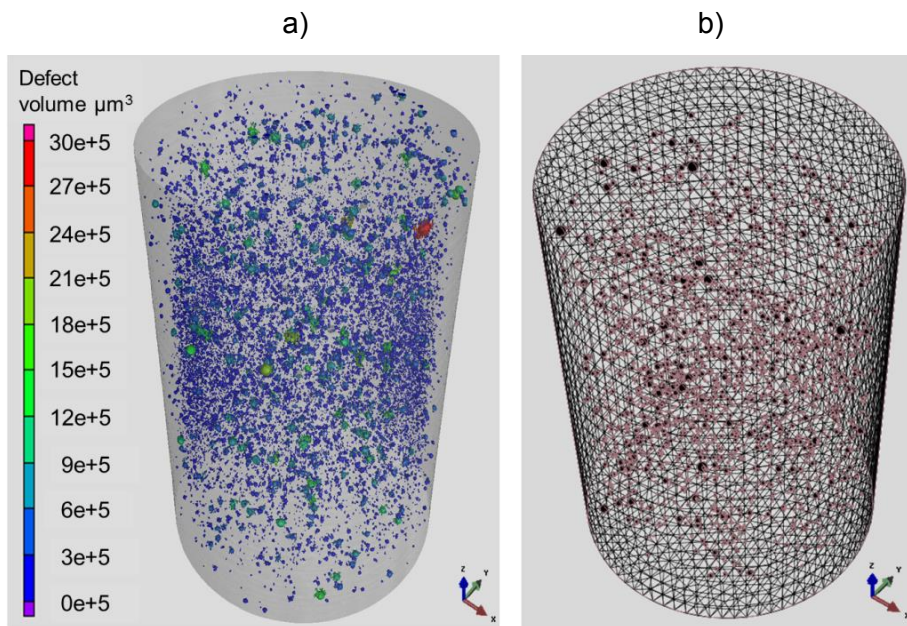


Fig. 4: Representation of defect state of a batch B specimen: a) μ-CT scan, b) corresponding finite element model



An ultrasonic fatigue testing system Shimadzu USF-2000 was utilised for VHCF testing with a frequency of 20 kHz and a fully reversed load spectrum, i.e. load ratio  $R = -1$ . The working principle of this system can be found in detail elsewhere [8]. Specimen geometry for VHCF testing can be seen in Fig. 3b. Finite element modelling of the VHCF behaviour was built relying on  $\mu$ -CT scans in Nikon X TH 160. An exemplary  $\mu$ -CT scan and the corresponding FEM model can be found in Fig. 4.

**RESULTS AND DISCUSSION**

The direct SLM deposition on the conventional material surface did lead to the formation of semi-fusion bond at the boundary interface as seen in Fig. 5. It is a diffusion-driven bonding at the interface evident by the existence of inter-boundary defects in Fig. 5a (exemplary instances pointed by arrows). On the other hand, in Fig. 5b, where post-process heat treatment has been conducted, such interface defects are rarely visible, because of heat treatment promoting continuation of diffusion process started earlier during deposition. Such interface defects can decrease the joint strength which is evident by comparing the total strain at fracture for the batches C and D.

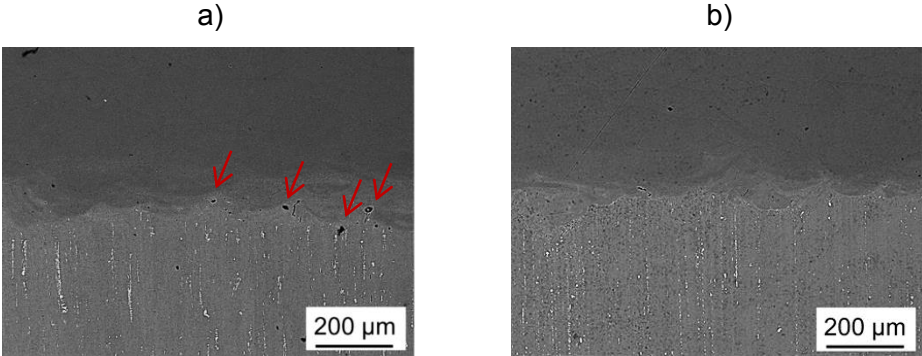


Fig. 5: SEM micrographs of the interface boundary between conventional wrought alloy Al7020 and Al4047: a) batch C, b) batch D

Exemplary stress-strain curves for the batches C and D in Fig. 6 show an increase in total strain from  $4.3 \cdot 10^{-2}$  to  $10.6 \cdot 10^{-2}$ . For the pure alloy Al4047, base plate heating has increased the fracture strain marginally (batch B compared to batch A).

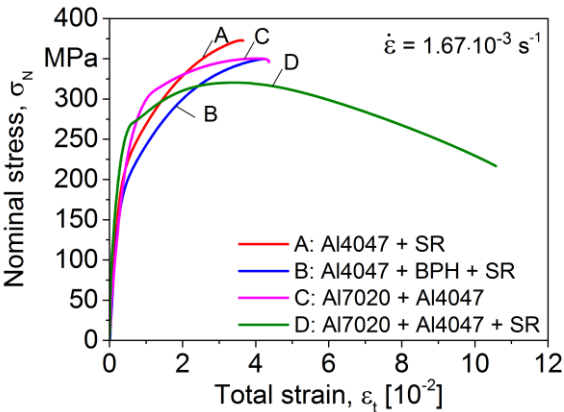


Fig. 6: Effect of base plate heating, hybridisation, and stress relief on stress-strain behaviour

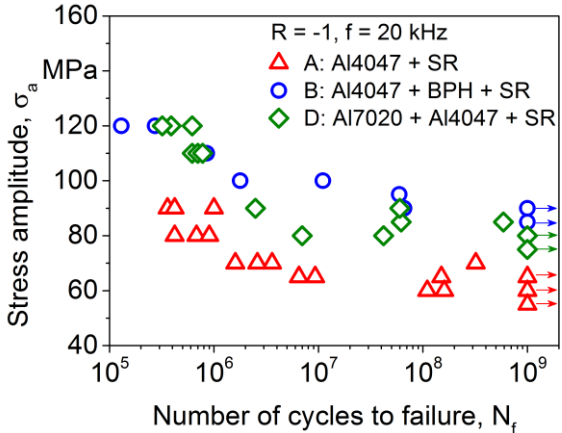


Fig. 7: Woehler curves of batches A, B and D by VHCF testing

Comparing hybrid and non-hybrid alloys after stress relief, the ultimate tensile strength for the hybrid alloy decreased from 370 MPa (batch A) to 320 MPa (batch D); however, the corresponding increase in fracture strain to  $10.6 \cdot 10^{-2}$  is beneficial for the dynamic applications where a combination of strength and toughness is important. Batch C was not regarded for fatigue investigations since it was clear that weakness of interface bond precipitated a premature failure of the specimen.

Fig. 7 summarises the VHCF results of the three batches. Batch A resulted in a fatigue strength of 60.5 MPa; whereas it increased to 88.6 MPa for the base plate heated configuration (batch B). For the hybrid specimens (batch D), it turned out to be 78.3 MPa. Hybrid specimens have consistently higher fatigue life as compared to pure Al4047 alloy. Better joint strength due to post-process stress relief can be a reason for increased fatigue life. Altogether, the expected economic benefit obtained from hybridised structure did nonetheless result in improved performance.

Fatigue life predictions by the FEM<sup>2</sup> (Finite Element Monte-Carlo Modelling) method, developed at WPT TU Dortmund, were conducted for batches B and D. The method which relies on the simulation of fatigue damage process using finite element method is followed by a Monte-Carlo fatigue life integration scheme. It showed good agreement with experimental results. Comparison between computational fatigue life and experimental results can be realised in Fig. 8. The method allows the construction of Woehler curve based on plastic strain measurements in a continuous load increase test. One strong advantage is the freedom out of geometrical constraints, since the scheme can be applied to arbitrary geometries and multi-materials like seen here in the hybrid specimens.

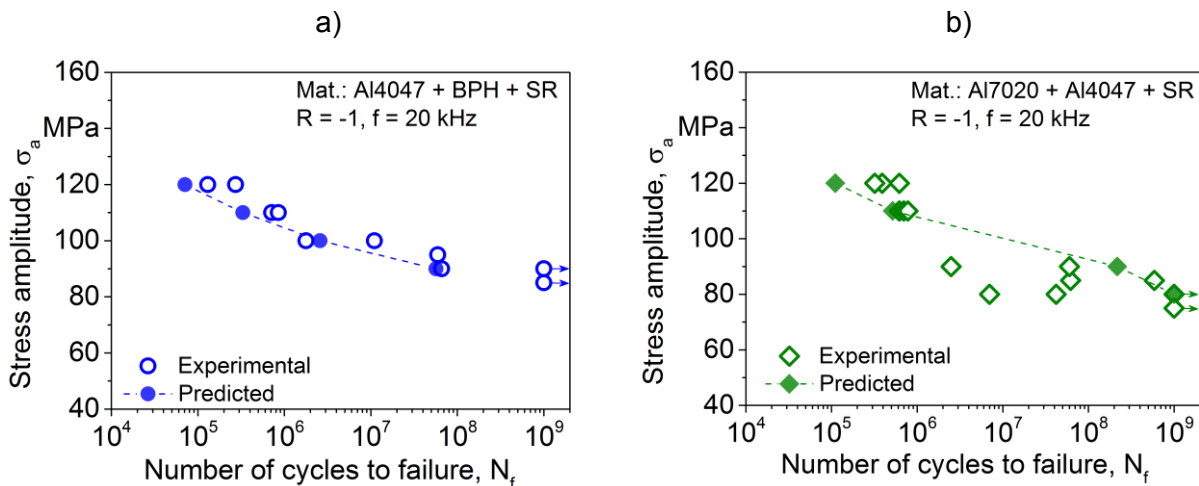


Fig. 8: Comparison between experimental fatigue strength and predicted fatigue strength by the FEM<sup>2</sup> method: a) batch B, b) batch D

## CONCLUSIONS AND OUTLOOK

In this work, the feasibility of producing SLM-conventional hybrid structures has been investigated. The resulting components showed good fatigue performance until VHCF regimes. Base plate heating of the pure alloy Al4047 increased fatigue strength by 46% at  $10^9$  cycles. As-built hybrid specimens resulted in reduced fracture strain due to failure from joint, which was controlled by appropriate post-process heat treatment, by which fracture zone shifted from joint to conventional Al7020 part of the specimen. Modelling of the damage process and the resulting fatigue strength has been proven possible by means of application of the FEM<sup>2</sup> method. This gives a prelude of aspects with design of additively manufactured

hybrid and cellular structures, in which their fatigue strength can be modelled by the newly developed scheme, since experimental fatigue testing of such structures is an immensely challenging task. This should utilise advantages of the FEM<sup>2</sup> method such as geometrically unconstrained prediction and a quite short analysis time. The accuracy of the method should be validated for more material and component conditions as well as different load spectra, such that the method can be reliably applied for structural applications.

## ACKNOWLEDGEMENTS

The authors would like to express special thanks to Eric Wycisk and Prof. Claus Emmelmann from Institute of Laser and System Technologies (iLAS), Hamburg University of Technology (TUHH), for the manufacturing of the investigated specimens. Additionally, authors acknowledge Federal Ministry for Economic Affairs and Energy, Germany for the partial funding of the investigations presented within the frame of the project No. KF2198140CK4 titled “Anwendung der laseradditiven Fertigungstechnologie zur Verarbeitung einer hochfesten Aluminium-Legierung (EN AW-7075) für Luftfahrtanwendungen“.

## REFERENCES

- [1] Frazier WE. Metal additive manufacturing: A review. *Journal of Materials Engineering and Performance* 2014;23(6):1917–28.
- [2] Gu DD, Meiners W, Wissenbach K, Poprawe R. Laser additive manufacturing of metallic components: Materials, processes and mechanisms. *International Materials Reviews* 2012;57(3):133–64.
- [3] Siddique S, Wycisk E, Frieling G, Emmelmann C, Walther F. Microstructural and mechanical properties of selective laser melted Al 4047. *Applied Mechanics and Materials* 2015;752-753:485–90.
- [4] Gibson I, Rosen D, Stucker B. *Additive manufacturing technologies: 3D Printing, Rapid Prototyping, and Direct Digital Manufacturing* 2010; ISBN:978-1-4939-2112-6.
- [5] Sistiaga ML, Mertens R, Vrancken B, Wang X, Van Hooreweder B, Kruth J-P, Van Humbeeck, J. Changing the alloy composition of Al7075 for better processability by selective laser melting. *Journal of Materials Processing Technology* 2016;238:437–45.
- [6] Siddique S, Imran M, Rauer M, Kaloudis M, Wycisk E, Emmelmann C, Walther, F. Computed tomography for characterization of fatigue performance of selective laser melted parts. *Materials & Design* 2015;83:661–9.
- [7] Siddique S, Imran M, Wycisk E, Emmelmann C, Walther F. Influence of process-induced microstructure and imperfections on mechanical properties of AlSi12 processed by selective laser melting. *Journal of Materials Processing Technology* 2015;221:205–13.
- [8] Siddique S, Imran M, Walther F. Very high cycle fatigue and fatigue crack propagation behavior of selective laser melted AlSi12 alloy. *International Journal of Fatigue* 2017; 94(2):246-54.

**Corresponding author:** Shafaqat Siddique [shafaqat.siddique@tu-dortmund.de](mailto:shafaqat.siddique@tu-dortmund.de)

# Parameters

## INVITED



### **Bernd SCHÖNBAUER**

*University of Natural Resources and Life Sciences (BOKU),  
Vienna, Austria*

Bernd Schönbauer is a senior scientist and lecturer at the Institute of Physics and Material Sciences at BOKU, Vienna. He studied Physics at the University of Freiburg and the Technical University of Vienna. In 2014, he received his doctorate on the subject of corrosion-fatigue of steam turbine blade steels from TU Vienna. From 2015 to 2016, he was working as a postdoctoral research fellow at the Institute of Materials Science and Technology, Fukuoka University, Japan.

His current research in the area of VHCF focuses on the torsional fatigue behaviour at different load ratios, variable amplitude loading of steels and environmental influences on fatigue fracture mechanisms. Further interests are defect tolerance under multiaxial loading, role of pitting corrosion on fatigue strength (pit-to-crack transition), hydrogen-embrittlement and application of the ultrasonic fatigue testing technique for a broad variety of test environments.

Dr. Schönbauer's research activities in fatigue and fracture mechanics resulted in numerous publications in academic journals and conference proceedings as well as oral presentations at scientific conferences. He serves as reviewer for various international journals.

### **VARIABLE AMPLITUDE LOADING OF 17-4PH STAINLESS STEEL IN THE VHCF REGIME**

**B. Schönbauer**, M. Fitzka, U. Karr, H. Mayer

BOKU Vienna Institute of Physics and Materials Science, Vienna, Austria

Precipitation-hardening 17-4PH stainless steel was tested under variable amplitude (VA) fatigue loading up to the very high cycle fatigue (VHCF) regime. The tests were performed at load ratio  $R = 0.05$  with ultrasonic fatigue testing equipment at approximately 20 kHz cycling frequency.

In previous studies on the fatigue behavior of 17-4PH stainless steel, several factors such as uniaxial and torsional loading condition, environment, defect tolerance and load ratio were investigated. These tests were performed under constant amplitude (CA) loading, however, in service most technical components are stressed with variable amplitude. Therefore, it is of great technical as well as of scientific interest, how varying stress amplitudes over time influence the mechanisms of fatigue failure and fatigue lifetimes. Ultrasonic VA fatigue tests at constant load ratio are performed to investigate the HCF and VHCF regime within bearable testing times.

Results of VA fatigue tests at  $R = 0.05$  to up to  $10^{10}$  cycles with 17-4PH stainless steel are presented in this study. Damage sums according to Miner's rule are calculated using the actually measured load spectra experienced by the specimens. It is found that the damage sums depend on various influences, such as number of cycles to failure (HCF vs. VHCF) and the location of crack initiation. The mechanisms of fatigue failure in the present VA tests are compared to CA loading under different conditions.

# VARIABLE AMPLITUDE LOADING OF 17-4PH STAINLESS STEEL IN THE VHCF REGIME

B.M. Schönbauer, M. Fitzka, U. Karr, H. Mayer  
Institute of Physics and Materials Science, BOKU Vienna,  
Peter-Jordan-Str. 82, 1190 Vienna, Austria

## ABSTRACT

Precipitation-hardening 17-4PH stainless steel was tested under constant amplitude (CA) and variable amplitude (VA) loading conditions. Experiments were performed with ultrasonic fatigue testing equipment at a constant load ratio of  $R = 0.05$  up to the very high cycle fatigue regime. CA tests did not show a fatigue limit below  $10^{10}$  cycles. Servo-hydraulic CA tests yield similar lifetimes in the high cycle fatigue regime indicating no frequency effect. VA tests with ultrasonic equipment were performed with a Gaussian cumulative frequency distribution of load cycles. Load amplitudes below 30% or 60% of the maximum stress amplitude,  $\sigma_{\max}$ , of the VA sequence were omitted. VA tests with omission level 60% delivered failures at an average damage sum of  $S = 0.25$ . Failures occurred at an average damage sum of  $S = 1.05$  in VA tests with omission level 30%. Low load cycles between 60% and 100% of  $\sigma_{\max}$  are more damaging than considered in a Miner calculation, whereas those between 30% and 60% of  $\sigma_{\max}$  extend the fatigue lifetime.

## KEYWORDS

Variable amplitude loading, damage accumulation, ultrasonic fatigue testing, very high cycle fatigue, 17-4PH stainless steel

## INTRODUCTION

Precipitation-hardening chromium-nickel-copper 17-4PH stainless steel is widely used for applications requiring high strength and good corrosion resistance, such as in the aerospace, chemical, food processing, paper and power industry. In several applications, a very high number of load cycles is accumulated within service life. In the last decades, a number of investigations on the fatigue properties of 17-4PH have been performed, but the vast majority of the experimental work was conducted under constant amplitude (CA) loading. Technical components are, however, often loaded with variable amplitude (VA). Testing the VA fatigue properties is therefore of great practical interest.

Considering in-service loading with lifetimes in the very high cycle fatigue (VHCF) regime, VA load sequences typically contain relatively few high and numerous rather low load amplitudes. It is reasonable to assume that load amplitudes that are far below the cyclic strength of a material will hardly contribute to fatigue damage. Omission of low load cycles shortens the testing time in VA experiments, the more the higher the omission level is chosen. VA experiments with excessive omission levels, on the other hand, do not take their possible influences into account.

In the present work, CA and VA fatigue properties of 17-4PH stainless steel were investigated at a load ratio of  $R = 0.05$ . Ultrasonic CA fatigue tests yielded lifetimes between  $10^5$  and  $10^{10}$  cycles. Additional CA fatigue tests at 20 Hz using servo-hydraulic testing were conducted to investigate a potential strain-rate influence on fatigue lifetimes. VA fatigue tests were performed with ultrasonic fatigue testing equipment. Already three decades ago, first ultrasonic fatigue test with VA at fully reversed loading ( $R = -1$ ) were performed [1]. Recent

development enables VA ultrasonic fatigue tests at constant load ratios other than  $R = -1$  [2]. This method is used to investigate VA lifetimes of more than  $10^{10}$  cycles at  $R = 0.05$ . VA tests with a Gaussian cumulative frequency distribution of load amplitudes are conducted. Fatigue lifetimes are studied in two VA test series, one with an omission level of 30% of the maximum stress amplitude,  $\sigma_{\max}$ , and one series with an omission level of 60% of  $\sigma_{\max}$ .

## MATERIAL AND EXPERIMENTAL PROCEDURE

Chromium-nickel-copper stainless steel 17-4PH is investigated. The material was precipitation hardened at 621 °C for 4 h (condition H1150). Chemical composition and mechanical properties are summarised in Table 1 and 2, respectively. For more details on the material, see Ref. [3].

Cr	Ni	Cu	Mn	Si	Nb+Ta	C	P	S
15.57	4.37	3.31	0.49	0.40	0.23	0.033	0.027	0.001

**Table 1:** Chemical composition of 17-4PH (in weight %)

Tensile strength (MPa)	Yield strength (MPa)	Elongation (%)	Reduction of area (%)	Vickers hardness (kgf/mm <sup>2</sup> )
1030	983	21	61	352

**Table 2:** Mechanical properties of 17-4PH

Fatigue tests at 19 kHz were conducted with dumbbell shaped specimens as shown in Fig. 1. The surfaces of specimens were ground and electropolished. The specimens were additionally stress-relief annealed in high vacuum at 600 °C for one hour to remove residual stresses.

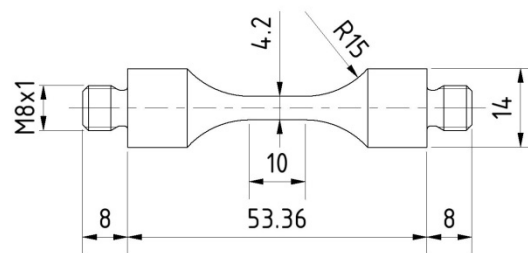


**Fig. 1:** Specimen geometry for ultrasonic fatigue testing (dimensions in mm)

Ultrasonic fatigue testing equipment developed at BOKU University, Vienna was used which enables VHCF testing at different load ratios,  $R$ . Specimens are stimulated to resonance vibration. At one end of the specimen, the oscillation amplitude is measured with a vibration gauge which is used to control loading in a closed-loop circuit. An accuracy of  $\pm 1\%$  of the vibration amplitude is realised. For tests at fully-reversed loading ( $R = -1$ ), only one end of the specimen is fixed to the resonance system, while the other end vibrates freely. In the present investigation, tests at  $R = 0.05$  were executed by mounting the ultrasonic load train into an electromechanical load frame and superimposing forces to the vibration of the specimen. Compressed air cooling as well as pulsed loading were employed to allow carrying off the heat generated by self-heating of the specimen. The lengths of pulses and pauses were chosen according to the applied load amplitude to keep the specimen temperature below 30 °C. More details about the principles of ultrasonic fatigue testing and



related recent developments are provided in [4]. Additionally, constant amplitude fatigue tests at 20 Hz were performed using servo-hydraulic testing equipment.

For CA ultrasonic fatigue testing, the nominal vibration amplitude, as well as the superimposed static mean load, is constant, see Fig. 2(a). During VA ultrasonic fatigue testing at constant load ratio of  $R > -1$ , successive pulses have different nominal vibration amplitudes and associated mean loads. The applied loads follow a pre-determined repeat sequence. The schematic load-time history of a VA ultrasonic fatigue test at  $R = 0.05$  is shown in Fig. 2(b). An appropriate mean load is applied for each pulse according to the nominal vibration amplitude to ensure a constant load ratio. The force is applied in a ramping motion to avoid overshoot and is changed in every pause between two pulses of vibration. It is ensured that the correct preload is reached before the ultrasonic pulse is started. For more details on VA ultrasonic fatigue testing at load ratios of  $R > -1$ , see Ref. [2].

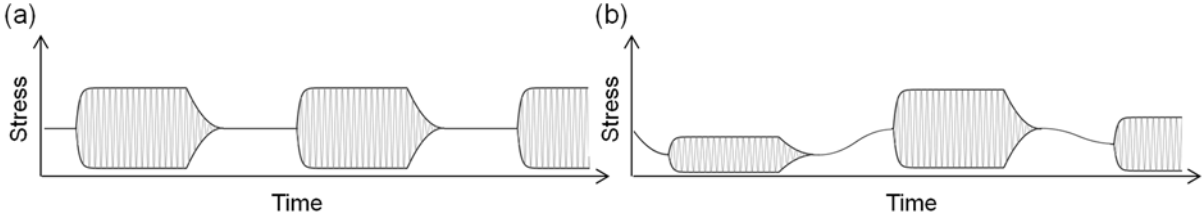


**Fig. 2:** Schematic load-time histories during ultrasonic fatigue testing with (a) CA and (b) VA loading

In the present work, the cumulative frequency distribution of the load cycles during VA ultrasonic fatigue testing follows a Gauss distribution. Two different load collectives with omission levels of 30% and 60% of the maximum cyclic stress,  $\sigma_{max}$ , were used, denoted by VA(30%) and VA(60%) in the following, see Fig. 3. It is noted that these omission levels are related to the nominal stress amplitude rather than to the fatigue limit. The repeat sequence consists of 770 pulses at 27 different stress amplitudes for VA(30%) loading and 155 pulses at 16 different stress amplitudes for VA(60%).

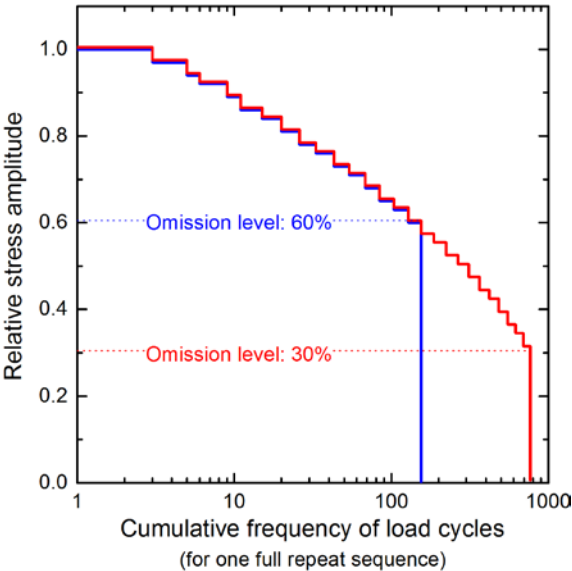


**Fig. 3:** Cumulative frequency distribution of nominal stress amplitude for VA loading with omission levels of 30% and 60%

## RESULTS AND DISCUSSION

The results of ultrasonic fatigue tests under CA and VA loading are summarised in Fig. 4. Under CA loading conditions, data can be clearly distinguished between early fatigue failure with crack initiation at the surface and VHCF failure with internal crack initiation, resulting in a duplex  $S-N$  curve. VA lifetimes at maximum stress amplitude 462.5 MPa are also strongly influenced by the crack initiation location. Specimens with surface crack initiation show much shorter lifetimes than specimens with interior crack initiation.

The three additional CA tests performed with a cyclic frequency of 20 Hz are in good accordance with the ultrasonic fatigue test, see Fig. 4. This suggests that the strain rate does not influence the fatigue lifetimes of the investigated 17-4PH steel.

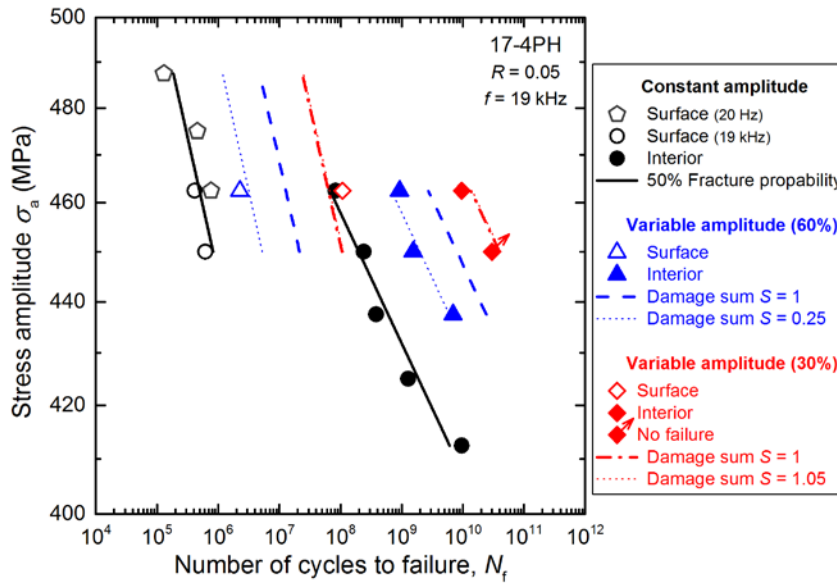


**Fig. 4:** Fatigue lifetimes of 17-4PH measured at load ratio of  $R = 0.05$  under CA loading condition and VA loading conditions with omission levels of 30% and 60%

In Figure 4, data obtained from CA fatigue tests are approximated with straight lines in the double-logarithmic plot, assuming a power law dependency between stress amplitude,  $\sigma_a$ , and number of cycles to failure,  $N_f$ , according to following equation:

$$N_f = c \cdot \sigma_a^{-n} \quad (1)$$

where  $c$  and  $n$  are material constants. With stresses in MPa,  $c = 3.13 \times 10^{55}$  and  $n = 18.69$  for specimens with surface crack initiation, and  $c = 2.37 \times 10^{112}$  and  $n = 39.27$  for specimens with internal crack initiation. These lines are plotted with solid lines in Fig. 4 and represent the mean lifetimes for CA loading.

Damage sums for VA loading are calculated according to linear damage accumulation calculation (Miner calculation) [5, 6]:

$$S = \sum \frac{N_{VA}(\sigma_a)}{N_{CA}(\sigma_a)} \quad (2)$$

$N_{VA}(\sigma_a)$  is the number of load cycles at specific stress amplitude,  $\sigma_a$ , during VA loading, and  $N_{CA}(\sigma_a)$  is the mean lifetime for CA loading at the stress amplitude  $\sigma_a$  determined by Eq. (1). The CA curves are extrapolated to zero stress with the same slope for the purpose of damage accumulation calculation.

The predicted lifetimes for VA(60%) and VA(30%) assuming fracture at a damage sum of  $S = 1$  are plotted in Fig. 4 with dashed and dashed-dotted lines, respectively. By mean, fracture occurred at damage sum of  $S = 0.25 \pm 0.07$  for VA(60%) and  $S = 1.05 \pm 0.45$  for VA(30%). Predicted fatigue lifetimes using these damage sums are plotted with thin dotted lines in Fig. 4.

Figure 5 shows the cumulative frequency distributions of load cycles for three specimens, one tested with CA at  $\sigma_a = 462.5$  MPa and two tested with VA at  $\sigma_{max} = 462.5$  MPa with an omission level of 30% and 60%, respectively. The cumulative frequency distribution of load cycles for the specimen tested with VA(30%) is shifted towards higher numbers of cycles compared with the specimen tested with VA(60%). This is interesting, since the VA(30%) specimen is additionally stressed with a high number of load cycles below 60% of the maximum stress amplitude. These load cycles obviously have beneficial rather than detrimental influences on the fatigue lifetime.

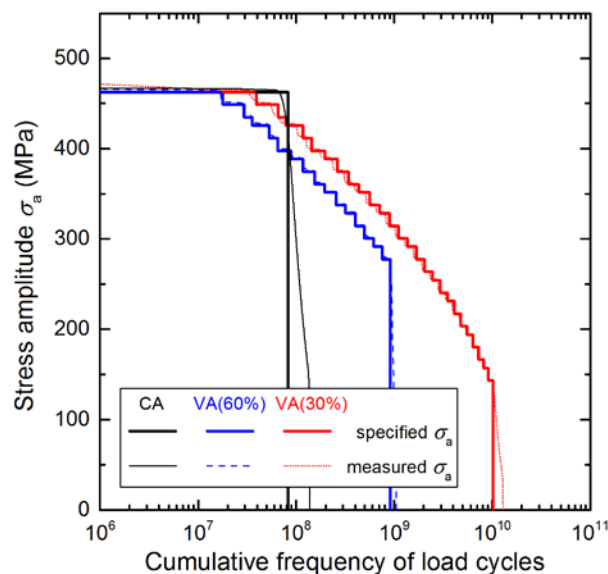


**Fig. 5:** Cumulative frequency distribution of specimens tested with CA of  $\sigma_a = 462.5$  MPa and with VA with maximum stress amplitude of  $\sigma_{max} = 462.5$  MPa and omission level 30% and 60%

The present experiments point to a complex influence of numerous load cycles in a VA load sequence. VA tests with omission level 60% show failures when, on average, a damage sum of  $S = 0.25$  is reached. Low load cycles more severely contribute to fatigue damage than considered in the linear damage accumulation calculation. Experiments with omission level 30% showed failures when, on average, a damage sum of  $S = 1.05$  is reached. This suggests that load cycles in the regime between 30% and 60% of the maximum load amplitude have beneficial influences.

Detrimental as well as beneficial influences of numerous low load cycles have been previously demonstrated in two-step variable amplitude tests with a low carbon steel [7] and a cast aluminium alloy [8]. Low load cycles can accelerate crack propagation and thus reduce the fatigue lifetime. However, they can also increase the threshold for fatigue crack growth and consequently prolong the fatigue lifetime. The rather complex damaging or strengthening effects of low load cycles in VA sequences can hardly be predicted and makes fatigue tests with low omission levels necessary. This points to a great benefit of the ultrasonic VA testing method. The high testing frequency allows VA tests with low amplitude cycles included.

## CONCLUSIONS

Constant amplitude (CA) and variable amplitude (VA) ultrasonic fatigue tests were performed with 17-4PH stainless steel at a load ratio of  $R = 0.05$ . Additional CA servo-hydraulic tests were conducted at 20 Hz. The VA ultrasonic fatigue tests were performed with a cumulative frequency distribution of load amplitudes following a Gauss distribution. Experiments were conducted with omission levels of 30% and 60% of the maximum stress amplitude.

1. Similar fatigue lifetimes were measured in CA tests at 20 Hz and 19 kHz loading frequency. The material does not show strain rate influences on the fatigue lifetime.
2. The material does not show a fatigue limit. Failures were found in CA tests up to  $10^{10}$  cycles. A power law dependency between stress amplitude and number of cycles to failure approximates the measured  $S-N$  data well.
3. VA tests in the VHCF regime with omission level 60% delivered failures at an average damage sum of  $S = 0.25$ . Stress amplitudes between 60% and 100% of maximum stress amplitude are more damaging than considered in a Miner calculation.
4. Tests with omission level 30% led to failure at an average damage sum of  $S = 1.05$ . Numerous low stress amplitudes between 30% and 60% of maximum stress amplitude extend the fatigue lifetime and have beneficial rather than detrimental influences.

## REFERENCES

- [1] Stanzi, S.E.; Tschegg, E.K.; Mayer, H.:  
Lifetime measurements for random loading in the very high cycle fatigue range  
Int J Fatigue, 8 (1986), pp. 195-200
- [2] Mayer, H.; Fitzka, M.; Schuller, R.:  
Variable amplitude loading of Al 2024-T351 at different load ratios using ultrasonic equipment  
Int J Fatigue, 60 (2014), pp. 34-42
- [3] Schönbauer, B.M.; Yanase, K.; Endo, M.:  
VHCF properties and fatigue limit prediction of precipitation hardened 17-4PH stainless steel  
Int J Fatigue, 88 (2016), pp. 205-216
- [4] Mayer, H.:  
Recent developments in ultrasonic fatigue  
Fatigue Fract Eng M, 39 (2016), pp. 3-29
- [5] Palmgren, A.G.:  
Die Lebensdauer von Kugellagern (The Service Life of Ball Bearings)  
VDI-Zeitschrift, 68 (1924), pp. 339-341
- [6] Miner, M.A.:  
Cumulative damage in fatigue  
J Appl Mech Trans ASME, 12 (1945), pp. 159-164
- [7] Mayer, H.:  
Fatigue damage of low amplitude cycles in low carbon steel  
Journal of Materials Science, 44 (2009), pp. 4919-4929
- [8] Mayer, H.; Ede, C.; Allison, J.E.:  
Influence of cyclic loads below endurance limit or threshold stress intensity on fatigue damage in cast aluminium alloy 319-T7  
Int J Fatigue, 27 (2005), pp. 129-141

**Corresponding author:** bernd.schoenbauer@boku.ac.at

# ENVIRONMENTAL INFLUENCES ON THE NEAR THRESHOLD FATIGUE CRACK GROWTH OF WROUGHT MAGNESIUM ALLOY AZ61 HP

U. Karr<sup>1)</sup>, B.M. Schönbauer<sup>1)</sup>, A. Stich<sup>2)</sup>, H. Mayer<sup>1)</sup>

<sup>1)</sup> Institute of Physics and Materials Science, BOKU Vienna,  
Peter Jordan Str. 82, 1190 Vienna, Austria

<sup>2)</sup> AUDI AG, Post Office Box 10 02 20, 85045 Ingolstadt, Germany

## ABSTRACT

S-N tests in the very high cycle fatigue (VHCF) regime and near threshold fatigue crack growth investigations have been performed on wrought magnesium alloy AZ61 hp. Tests have been conducted at ultrasonic frequency and load ratio  $R = -1$ . No endurance limit is found, failures still occurred above  $10^9$  cycles. Fatigue cracks are initiated predominantly at the surface. No inclusions or other imperfections were found at the crack initiations sites. The ratio of VHCF strength and tensile strength is 0.32. Ambient as well as dry air strongly accelerates the near threshold fatigue crack growth compared with vacuum. Threshold stress intensity factor amplitudes are  $1.1 \text{ MPa}\sqrt{\text{m}}$  in ambient air,  $1.2 \text{ MPa}\sqrt{\text{m}}$  in dry air, and  $1.9 \text{ MPa}\sqrt{\text{m}}$  in vacuum. In vacuum, ductile crack growth was found, whereas, in ambient and dry air, brittle, cleavage-like failure was observed as the stress intensity factor amplitude reaches the threshold.

## KEYWORDS

Magnesium alloy; Threshold stress intensity factor; Fatigue crack growth; Corrosion fatigue; Ultrasonic fatigue

## INTRODUCTION

Magnesium alloys being the lightest of the industrial metals feature a high ratio of strength to mass density. This makes magnesium alloys potentially attractive materials for load-bearing applications in transportation industry, for example, where reduction of weight and consequential fuel saving is important. However, magnesium alloys are known to be sensitive to environmental influences, which can significantly deteriorate their mechanical properties.

Fatigue testing is often performed in ambient air, which is a chemically active environment for magnesium alloys. Fatigue tests in wet air with magnesium alloy AZ61 show increased propagation rates compared with dry air in the Paris regime, which points to a corrosive effect of humidity [1-3]. Hydrogen diffusion along the crack wake could be found, and it is concluded that hydrogen embrittlement is the primary effective mechanism that deteriorates the cyclic properties [3]. Ultrasonic fatigue tests in ambient air and in vacuum [4] show, that environmental effects are active also at high testing frequencies: Crack growth rates measured in vacuum were nearly two orders of magnitude lower than in ambient air.

These investigations suggest a strong influence of ambient air on the process of fatigue damage in magnesium alloys, with air humidity being an important chemically active agent. However, the experiments were performed at crack growth rates governing the high cycle fatigue regime, i.e. at crack growth rates above  $10^{-9} \text{ m/cycle}$ . Much lower mean crack growth rates are of significance for the very high cycle fatigue (VHCF) regime.

The present work investigates the influence of ambient air on fatigue crack growth in the near threshold regime of AZ61 hp. Fatigue crack growth rate (FCGR) measurements are performed in vacuum and in ambient air. Additionally, fatigue tests in dry air serve to investigate whether humidity is responsible for the deterioration of cyclic properties in the VHCF regime.

## EXPERIMENTAL PROCEDURE

### Material and Specimens

Testing material was the as-extruded high purity magnesium alloy AZ61 hp. The chemical composition given by weight per cent is: 6.3% Al, 1.0% Zn, 0.2% Mn and balance Mg. Mechanical properties are: Tensile strength of 302 MPa, yield stress of 224 MPa and elongation of 14%.

Specimens were machined from as received, rectangular bars with the specimens' axis parallel to the extrusion direction. The specimen shapes used for ultrasonic fatigue testing and FCGR measurements are shown in Fig. 1. Edges in the centre of the specimens used in S-N tests were rounded and the surfaces were ground with abrasive paper up to grade #600 prior to testing. Specimens used in FCGR measurements were ground with abrasive paper and subsequently polished to obtain a mirror like finish to enable observation of fatigue crack growth on the specimen surface. A single edge notch of 1 mm served for defined crack initiation in FCGR tests.

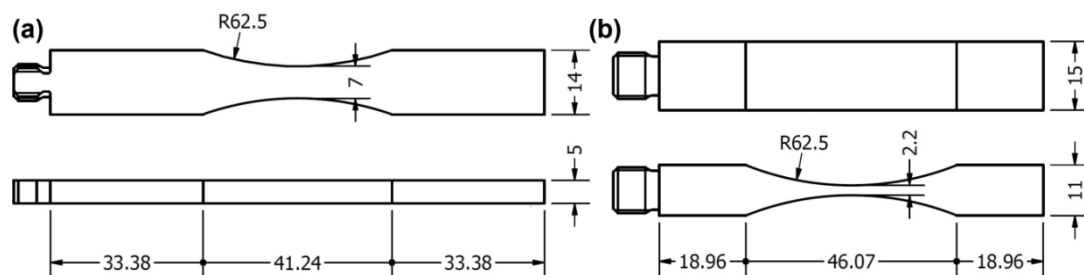


Fig. 1: Specimen shape used for S-N tests (a) and crack growth tests (b)

### Experimental setup

The experiments were performed using ultrasonic fatigue testing equipment developed at BOKU, Vienna [5]. All measurements were performed under fully reversed loading conditions.

S-N investigations were performed in ambient air of 20-22 °C and 50% relative humidity.

FCGR measurements were performed in three different environments: (1) ambient air of 20-22 °C and 50% relative humidity; (2) vacuum of approximately  $1.5 \times 10^{-5}$  mbar and (3) dry air featuring a dew point of -65 °C. Fatigue crack propagation was observed in progress on the surface of the specimens using an optical system with a CCD camera.

The fracture surfaces of the specimens were examined using a scanning electron microscope.

## RESULTS

### Fatigue lifetime measurements in ambient air

S-N data measured in ambient air are shown in Fig. 2(a). Numbers of cycles to failure range from  $10^6$  to  $10^9$ . The material shows no fatigue limit, and failures were found beyond  $10^9$  cycles. 50% probability to survive at  $10^9$  cycles is 98 MPa. The ratio of VHCF strength and tensile strength is 0.32.

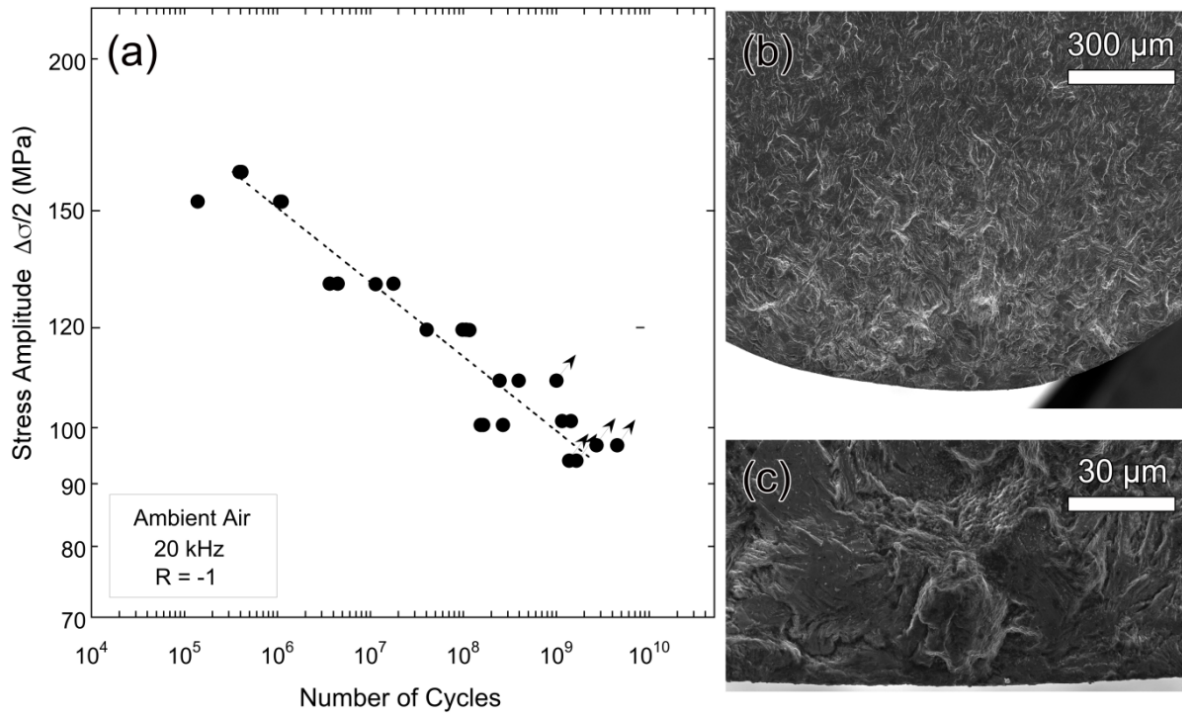


Fig. 2: S-N curve of AZ61 measured in ambient air (a), overview of the fracture surface of a specimen that failed after  $3.9 \times 10^8$  cycles at a stress amplitude  $\Delta\sigma/2 = 110$  MPa (b), crack initiation site of the same specimen at higher magnification (c)

Fatigue cracks of all but two specimens initiated at the surface. An overview of the fracture surface of a specimen that failed in the VHCF regime is shown in Fig. 2(b) and in higher magnification in Fig. 2(c). No inclusions or other imperfections were found at the crack initiation sites.

### Fatigue crack growth measurements in different environments

The results of near threshold FCGR measurements are shown in Fig. 3(a). The investigated FCGRs range from  $10^{-7}$  to  $10^{-13}$  m/cycle corresponding to stress intensity factor amplitudes,  $K_{\text{max}}$ , between 7 and 1  $\text{MPa}\sqrt{\text{m}}$ . It is assumed that the threshold stress intensity factor has been reached if no detectable crack propagation within  $2 \times 10^7$  cycles was observed. The resolution of the used optical system was approximately 10  $\mu\text{m}$ , which enabled observation of crack growth rates below  $5 \times 10^{-13}$  m/cycle.



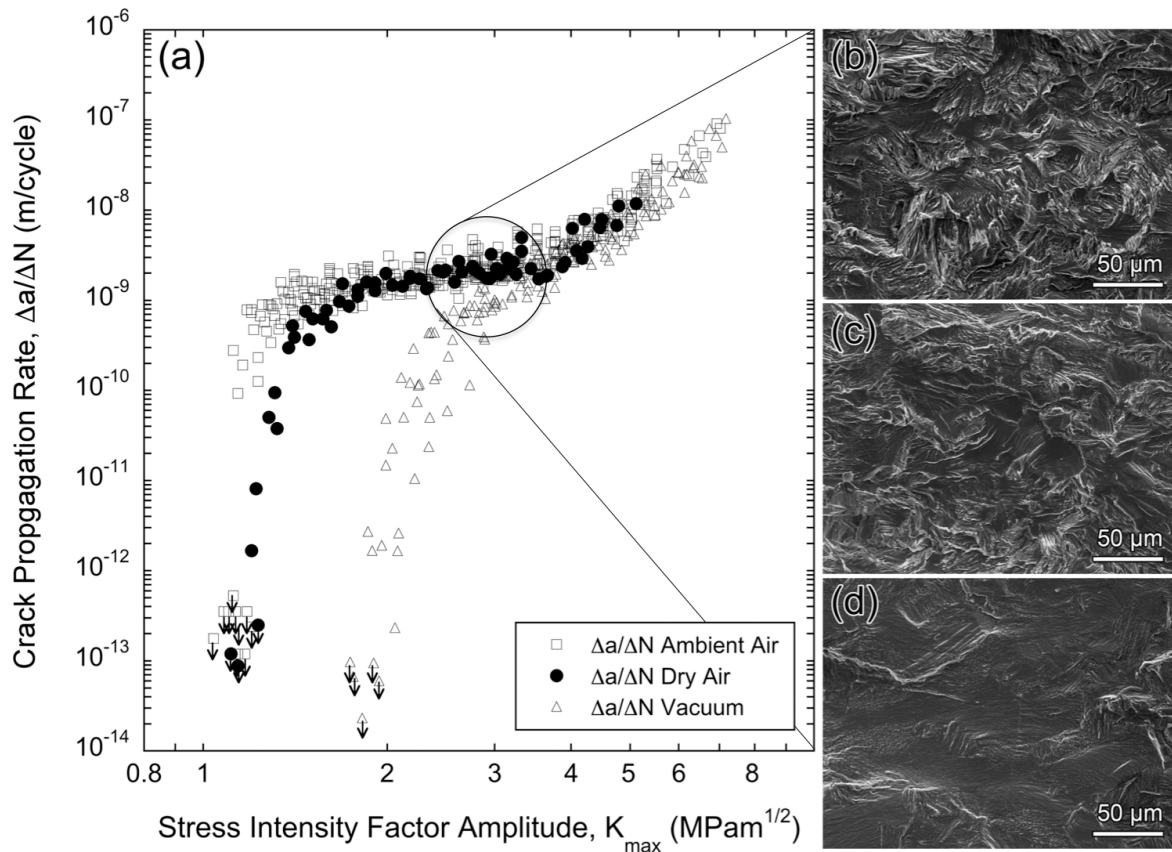


Fig. 3: Fatigue crack growth rates measured in ambient air, dry air and in vacuum (a); fracture surface formed in ambient air (b), in dry air (c) and in vacuum (d) at  $K_{\max} \approx 3 \text{ MPa}\sqrt{\text{m}}$  (crack propagation is from left to right)

The threshold stress intensity factor amplitude,  $K_{\max,th}$ , determined is  $1.1 \text{ MPa}\sqrt{\text{m}}$  in ambient air,  $1.2 \text{ MPa}\sqrt{\text{m}}$  in dry air and  $1.9 \text{ MPa}\sqrt{\text{m}}$  in vacuum. Crack propagation curves in all environments show a change of slope at FCGRs of approximately  $10^{-9} \text{ m/cycle}$ . Crack propagation in vacuum decreases steadily featuring a steepening of slope at crack FCGRs below  $5 \times 10^{-10} \text{ m/cycle}$ . Crack propagation curves in ambient and dry air, on the other hand, show a pronounced flattening of slope resulting in a plateau-like regime of almost constant FCGRs of  $10^{-9} \text{ m/cycle}$ .

Reaching the threshold stress intensity factor amplitude, the FCGR curves deflect sharply, less pronounced in dry than in ambient air, where the curve forms a distinct knee. The observed FCGRs range from  $10^{-7}$  to  $10^{-10} \text{ m/cycle}$  in ambient air and from  $10^{-7}$  to  $10^{-13} \text{ m/cycle}$  in dry air and vacuum. Interestingly, very low crack growth rates (down to  $10^{-12} \text{ m/cycle}$ ) could be observed in dry air and in vacuum but not in ambient air.

### Fractography

A transgranular crack path was found for all environments and for all investigated crack growth rates. At stress intensity factor amplitudes of approximately  $K_{\max} = 3 \text{ MPa}\sqrt{\text{m}}$ , the fracture surfaces obtained in ambient and dry air feature a quasi-cleavage fracture mode (see Figs. 3(b) and 3(c)). Facets in the range of the grain size as well as corrosion products and secondary cracking are visible.

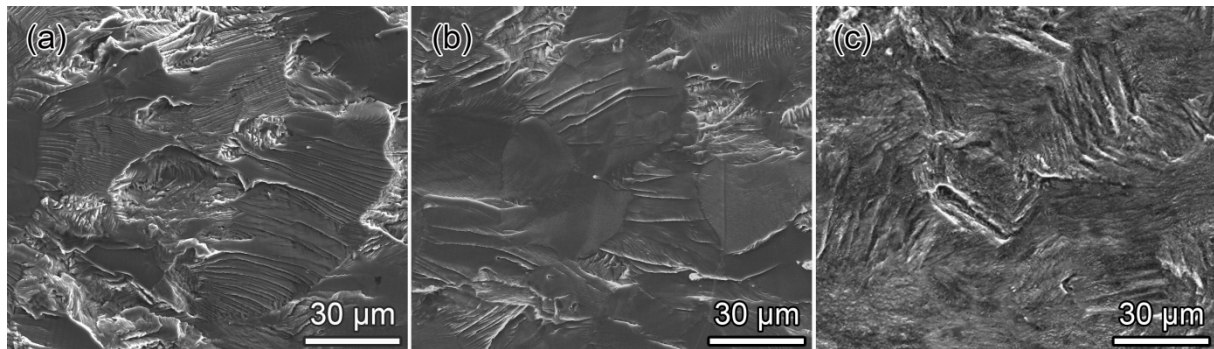


**Fig. 4:** Fracture surfaces obtained at the respective threshold stress intensities factors in ambient air (a), dry air (b) and vacuum (c) (crack propagation is from left to right)

At the threshold stress intensity factor, the size of cleavage facets is considerably increased resulting in a smooth and low-contrast fracture surface, see Figs. 4(a) and 4(b). The morphologies generated in ambient and dry air appear to be essentially similar. However, the fracture surface in ambient air seems to show a higher contrast featuring to a greater extent cleavage steps and areas of tearing topography fracture.

In vacuum, a low-contrast fracture surface can be observed exhibiting areas of fine granular appearance and deformation twins, see Figs. 3(c) and 4(c).

## DISCUSSION

The results show primarily a very strong environmental influence of ambient air on the crack propagation of AZ61 hp. Compared with vacuum, crack growth rates in ambient air are accelerated and  $K_{\max,th}$  is decreased by a factor of 1.7. In vacuum, the fracture mode was ductile whereas in ambient air, a brittle, cleavage-like fracture mode was found featuring cleavage facets that increase in size with decreasing stress intensity factor.

The FCGR curves obtained in dry air are similar with those in ambient air. Furthermore, a brittle, cleavage-like fracture mode is observed, which is well comparable to the results found in ambient air.

The detrimental influences of ambient air on the fatigue properties of magnesium alloys have been reported [2,3]. Using dry air as a reference, previous studies showed, that humidity present in ambient air was an effective agent and concluded that hydrogen embrittlement was likely to be the acting mechanism [1,3]. However, these results were found for FCGRs in the range of  $10^{-6}$  -  $10^{-9}$  m/cycle.

It must be taken into account that the present study concentrates on the threshold regime, where the measured FCGRs can be three orders of magnitude lower. It could be clearly shown from the present experiments in dry air that in the absence of humidity, FCGRs in the near threshold regime are still accelerated and comparable to ambient air. Therefore, it might be concluded that besides humidity additional agents of ambient air are active. Different mechanisms causing material embrittlement are acting depending on the growth rate and the stress intensity factor.

## CONCLUSIONS

Ultrasonic fatigue tests were conducted on wrought magnesium alloy AZ61 hp. S-N tests in the very high cycle fatigue regime and near threshold fatigue crack growth rate measurements were performed in ambient and dry air and in vacuum.

Following conclusions may be drawn:

1. AZ61 hp shows no fatigue limit below  $10^9$  cycles. Mean cyclic strength at  $10^9$  cycles is 32% of the tensile strength of the material.
2. Fatigue crack propagation in ambient and dry air is accelerated compared with vacuum. Threshold stress intensity factor amplitudes were determined as  $K_{\max,th} = 1.1 \text{ MPa}\sqrt{\text{m}}$  in ambient air,  $K_{\max,th} = 1.2 \text{ MPa}\sqrt{\text{m}}$  in dry air and  $K_{\max,th} = 1.9 \text{ MPa}\sqrt{\text{m}}$  in vacuum.
3. Material embrittlement was observed for both ambient and dry air resulting in a quasi-cleavage fracture mode. Embrittlement was found in absence of humidity which means that mechanisms others than hydrogen embrittlement are active in the near threshold regime where crack growth rates are very low.

## ACKNOWLEDGEMENT

The authors wish to thank Dr. Axel Mentler from the Institute of Soil Research, BOKU for his kind support in the experimental set-up of ultrasonic fatigue testing in gaseous environments.

## REFERENCES

- [1] Y. Kobayashi, T. Shibusawa, K. Ishikawa:  
Environmental Effect of Fatigue Crack Propagation of Magnesium Alloy  
Mater. Sci. Eng., A234-236 (1997) pp. 220-222.
- [2] K. Tokaji, M. Nakajima, Y. Uematsu  
Fatigue crack propagation and fracture mechanisms of wrought magnesium alloys in different environments  
Int. Journal of Fatigue, 31 (2009) pp. 1137–1143.
- [3] Y. Uematsu, T. Kakiuchi, M. Nakajima, Y. Nakamura, S. Miyazaki, H. Makino:  
Fatigue crack propagation of AZ61 magnesium alloy under controlled humidity and visualization of hydrogen diffusion along the crack wake  
Int. Journal of Fatigue, 59 (2014) pp. 234-243.
- [4] J.F. Adams, J.E. Allison, J.W. Jones:  
The effects of heat treatment on very high cycle fatigue behavior in hot-rolled WE43 magnesium  
Int. Journal of Fatigue, 93 (2016) pp. 372–386.
- [5] H. Mayer:  
Recent developments in ultrasonic fatigue  
Fatigue & Fracture Eng. Mater. Struct., 39 (2016) pp. 3-29.

**Corresponding author:** herwig.mayer@boku.ac.at

# VERY HIGH CYCLE FATIGUE BEHAVIOR OF METASTABLE AUSTENITIC STEEL X6CrNiNb1810 AT 300°C

<sup>1</sup>M. Smaga, <sup>2</sup>A. Sorich, <sup>1</sup>D. Eifler, <sup>1</sup>T. Beck

<sup>1</sup>Institute of Materials Science and Engineering (WKK), University of Kaiserslautern  
P.O. Box 3049, 67653 Kaiserslautern, Germany

<sup>2</sup>Former employee of WKK

## ABSTRACT

In the present study, specimens of metastable austenitic steel AISI 347 (1.4550, X6CrNiNb1810) were cyclically loaded in a servo-hydraulic fatigue testing system at a frequency of 980 Hz under stress control at a load ratio of  $R = -1$  to study the fatigue behavior in Very High Cycle Fatigue regime at elevated temperature of  $T = 300^\circ\text{C}$  in air. Additionally, the cyclic deformation behavior was investigated using stress-strain hysteresis measurement in fatigue tests at the same temperature with a load frequency of 20 Hz up to the limit cycle number  $N_L = 10^7$ . The results showed, with the stress amplitude decreasing below 165 MPa, a change in the cyclic deformation behavior from cyclic softening to cyclic hardening. Cyclic hardening is driven by deformation induced phase transformation from paramagnetic face-centered cubic  $\gamma$ -austenite to ferromagnetic body-centered cubic  $\alpha'$ -martensite. Measurement of change in magnetic permeability using a Feritscope™ sensor on specimens before and after fatigue testing allowed detection of deformation induced  $\alpha'$ -martensite. The fatigue-related changes in microstructure were characterized by scanning and transmission electron microscopy as well as by X-ray diffraction.

## KEYWORDS

VHCF, austenitic steel, elevated temperature, cyclic deformation behavior,  $\alpha'$ -martensite, phase transformation

## INTRODUCTION

A large number of austenitic Cr-Ni stainless steels are metastable under technically relevant loading conditions [1], i.e. transformation from austenite to  $\alpha'$ - or  $\varepsilon$ -martensite can take place in service. Due to their excellent mechanical and technological properties as well as corrosion resistance, austenitic stainless steels are used for components in nuclear power and chemical plants. In start up and shut down procedures loadings in the Low Cycle Fatigue (LCF) regime occur. Some components additionally undergo high frequency loadings in the Very High Cycle Fatigue (VHCF) regime, induced e.g. by stresses due to fast cyclic thermal fluctuations triggered by fluid dynamic processes [2]. For characterization of the VHCF behavior of metallic and non-metallic materials, typically ultrasonic fatigue systems with a load frequency of 20 kHz are used and experiments are performed at ambient temperature in a pulse-pause sequence. Moreover, some VHCF investigations at elevated temperature are reported in literature [3]. Due to metastability of several austenitic steels, their cyclic deformation behavior is significantly affected by deformation induced formation of martensitic phases and twinning [4]. These microstructural changes are influenced by chemical composition, temperature, strain amplitude and strain rate and can be well interpreted based on the stacking fault energy (SFE) [5]. Furthermore, due to martensite formation and/or twinning, metastable austenitic steels show a "true fatigue limit" in the HCF/VHCF regime [6]. It has been shown in [4-6] that the tendency of deformation induced martensite or twin formation decreases with increasing temperature, due decreasing thermodynamic driving force, i.e. difference of the Gibbs free energies of both phases. Therefore, it is necessary to characterize the fatigue behavior of metastable austenitic steels experimentally at typical operating temperatures, e.g.  $300^\circ\text{C}$ , particularly in the VHCF regime.

## EXPERIMENTAL PROCEDURES AND MATERIAL

Stress controlled fatigue tests with a load ratio  $R = -1$  were performed using two servo-hydraulic systems: (i) for investigations in HCF regime at MTS 100 kN with a load frequency  $f = 20$  Hz and (ii) for investigations in VHCF regime at MTS 25 kN with a load frequency  $f = 980$  Hz at  $300^\circ\text{C}$  in air. The HCF tests allow characterization of cyclic deformation behavior using stress-strain hysteresis measurements. Furthermore, ex-situ magnetic Feritscope™ measurements were performed before and after fatigue tests at ambient temperature. Because of the larger permeability of ferromagnetic ferrite compared to paramagnetic austenite, the material's response to the magnetic induction increases with increasing ferrite content. Feritscope™ measurements are a non-destructive method to measure the relative permeability of a material in the alternating magnetic field of its probe resulting in a ferrite content signal (FE-%), which is influenced by curvature of specimen surface and stress-strain state. To determine the ferromagnetic  $\alpha'$ -martensite content in vol.-% the Feritscope™ signal (FE-%) needs to be multiplied with the factor 1.7 according to [7]. Moreover, X-ray diffraction method with  $\text{Cu-K}\alpha_1$ -radiation at 40 kV acceleration voltage 40 mA current, a scan speed of  $0.002$  °/s and a spot size of  $1.5 \times 1.5$  mm was used for qualitative phase analysis in the near surface layer. To maximize the possibility to detect very small content of  $\alpha'$ -martensite, the diffraction profiles were measured at nine different tilt angles in the range of  $0^\circ \leq \chi \leq 40^\circ$ . The HCF and VHCF specimens were produced from an original nuclear power plant surge pipeline made of the metastable austenitic steel X6CrNiNb1810 with an outside diameter of 330 mm and a wall thickness of 30 mm by turning as well as mechanical and electrical polishing.

C	Cr	Ni	Nb	Ti	Mn	Mo	N	Cu	Si	P	S	V
0.04	17.60	10.64	0.62	0.02	1.83	0.29	0.007	0.06	0.41	0.02	0.007	0.07

Tab. 1: Chemical composition in weight-%

Temperature in °C	$R_{p0.2}$ in MPa	$R_{p1}$ in MPa	UTS in MPa	A in %	$\xi$ in FE-%
300	180	211	357	36	0.00
AT	242	282	569	66	4.41

Tab. 2: Mechanical properties at  $300^\circ\text{C}$  as well as at ambient temperature for reference;  $\xi$  are magnetic Feritscope™ measurements of  $\alpha'$ -martensite

The chemical composition of the investigated Nb-stabilized austenitic stainless steel AISI 347 (1.4550, X6CrNiNb1810) given in Tab. 1 meets the specifications of DIN (German Institute for Standardization) and KTA (German Nuclear Safety Standards Commission). The calculation of the austenite stability parameters e.g.  $M_{030} = 26^\circ\text{C}$  by Angel [4] indicates a metastable state of the test material at ambient temperature. The microstructure of the investigated steel has a mean grain size of  $120 \mu\text{m}$ , and a hardness of  $140 \text{HV}_{10}$ . The results of the monotonic tensile tests are consistent with specification of DIN and KTA. As expected, the yield stress and ultimate tensile strength decrease while elongation to fracture decreases with increasing temperature, see Tab. 2. At ambient temperature  $4.41 \text{ FE-\%}$   $\alpha'$ -martensite (using the mentioned calibration factor  $\alpha' = 7.50 \text{ vol.-%}$ ) were formed after plastic deformation of  $66 \%$ . The  $\alpha'$ -martensite formation starts at a total strain of  $22 \%$ . Magnetic Feritscope™ measurements and micrographs after tensile tests at  $300^\circ\text{C}$  indicated no  $\alpha'$ -martensite fraction [9].

## RESULTS

Figure 1 shows S-N curves of the investigated material at  $300^\circ\text{C}$  in HCF and VHCF regime. It can be seen that a "true fatigue limit" exists. Different specimen geometries were used in the two testing systems mentioned above. The HCF specimens have gauge length with constant diameter of  $7.6 \text{ mm}$  and  $15 \text{ mm}$  length, allowing stress-strain hysteresis measurement for

detailed characterization of cycle deformation behavior (see. Fig. 3). The VHCF specimens feature a slight notch with radius 6 mm in the gauge length with 7 mm diameter in the middle of the specimen and shafts diameter of 10 mm. Note that higher numbers of cycles to failure are measured in VHCF compared to HCF experiments with the same nominal stress amplitude. On the one hand, higher strain rates in VHCF testing tend to reduce dislocation movement and therewith increase of the yield strength of the material. On the other hand, a smaller volume is loaded with maximum stress in the VHCF sample, resulting in higher fatigue life due to statistical size / notch support effects. To clarify both influences, a VHCF specimen was loaded at 20 Hz with a stress amplitude of 180 MPa. The resulting failure at  $N_f = 5 \cdot 10^5$ , i.e. in the same cycle range as VHCF specimens loaded with 980 Hz at this stress amplitude, proves that in the present case specimen geometry has a stronger influence on fatigue life than test frequency. Hence, the shift of the S-N-curve for 980 Hz with respect to the 20 Hz experiments is mainly attributed to statistical size / notch support effects and the influence of frequency is, within the limits investigated here, considered negligible.

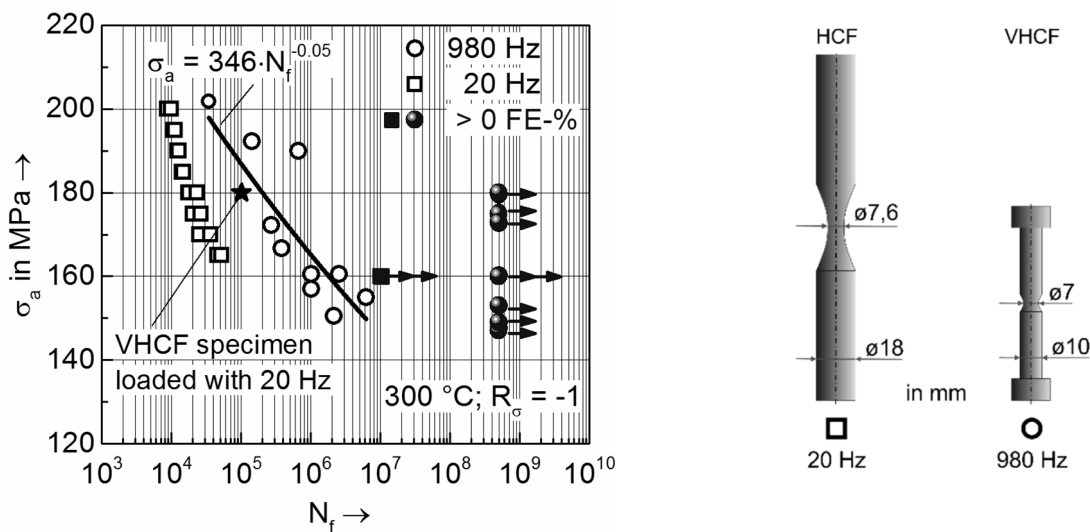


**Fig. 1:** S-N curves in HCF and VHCF regime at 300°C and specimen geometry

Interestingly, two HCF specimens tested at  $\sigma_a = 160$  MPa reached the limit cycle number  $N_L = 10^7$  without failure while at  $\sigma_a = 165$  MPa failure occurred below  $10^5$  cycles. In the VHCF tests a stress amplitude of 160 MPa can lead to both, specimen failure and reaching the limit of  $N_L = 5 \cdot 10^8$  cycles without failure. A similar result is observed at  $\sigma_a = 156$ , 155 and 150 MPa. To study the reasons for this behavior in more detail, Feritscope™ measurements were performed. Measurements at all HCF and VHCF specimens before fatigue testing resulted in  $\xi$  values of 0.00 FE-%, i.e. no  $\alpha'$ -martensite was indicated in the as-received specimens. As mentioned above, all specimens were mechanically and electrolytically polished. Therefore, very small  $\alpha'$ -martensite contents at the specimen surface possibly induced by turning process were removed. Feritscope™ measurements of all samples after fatigue testing revealed only in specimens reaching the limit number of cycles without failure a small content of ferromagnetic  $\alpha'$ -martensite, while no  $\alpha'$ -martensite could be detected in samples which underwent fatigue failure. Figure 2a shows results of Feritscope™ measurements of all samples which reached  $N_L$  without failure. The  $\alpha'$ -martensite content consistently increases with stress amplitude, with a maximum value of  $0.43 \pm 0.05$  FE-%. The standard deviations were calculated from measurements taken at 4 positions in circumferential direction around gauge length. Note that even the max. value of  $\alpha'$ -martensite of 0.73 vol.-% at  $\sigma_a = 180$  MPa, calculated by multiplication of FE-% with factor 1.7 [7], is small and difficult to verify with other non-destructive methods. However,  $\alpha'$ -martensite was also detected in X-ray diffraction measurements, see. Fig. 2b.

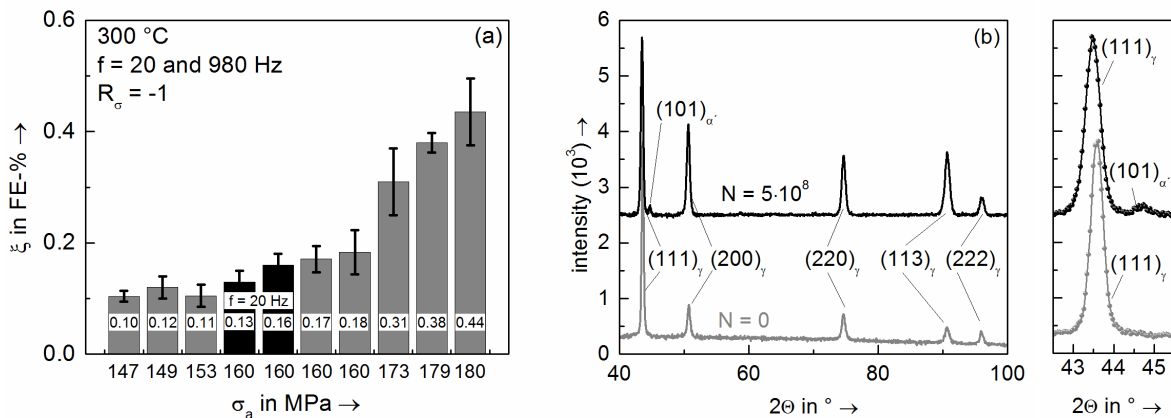


**Fig. 2:**  $\alpha'$ -martensite at the end of fatigue tests measured by Feritscope™ (a) and by X-ray diffraction before and after fatigue test on specimen loaded with 180 MPa (b)

It is known that deformation induced  $\alpha'$ -martensite formation significantly influences the cyclic deformation behavior and leads to cyclic hardening [1, 4, 6, 9]. Figure 3a shows the development of plastic strain amplitude during the fatigue loading of HCF specimens with the frequency  $f = 20$  Hz. At the beginning of the tests, cyclic softening was detected for all stress amplitudes followed by saturation for stress amplitude  $200 \text{ MPa} \leq \sigma_a \leq 165 \text{ MPa}$  and crack growth up to specimen failure. Contrariwise, a stress amplitude of 160 MPa leads after initial softening up to about  $2 \cdot 10^4$  cycles to cyclic hardening until plastic strain amplitude approaches zero, i.e. macroscopically elastic cyclic loading occurred, and, hence,  $N_L$  was reached without failure. Feritscope™ measurements indicated 0.13 FE-% for this specimen and 0.00 FE-% for all tests where fatigue failure occurred. Because stress-strain hysteresis measurement is not possible in tests with  $f = 980$  Hz, an interrupted VHCF test with a stress amplitude of 160 MPa was realized to detect the beginning of  $\alpha'$ -martensite formation. At defined load cycles ex-situ Feritscope™ measurements were performed at ambient temperature. Figure 3b shows no indication of  $\alpha'$ -martensite formation up to  $N = 1 \cdot 10^7$ . The onset of  $\alpha'$ -martensite formation occurred between  $N = 1 \cdot 10^7$  and  $N = 1 \cdot 10^8$ . At  $N = 1 \cdot 10^8$ , saturation is approached at  $\xi = 0.14$  FE-%. Only a slight increase is detected until  $N_L = 5 \cdot 10^8$  is reached without failure.

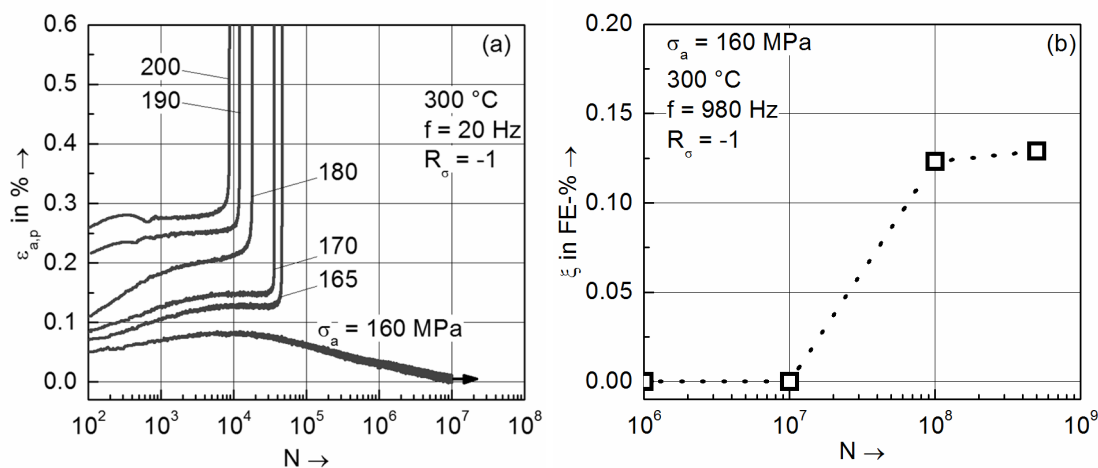


**Fig. 3:** Development of plastic strain amplitude versus number of cycles in HCF regime (a) and development of  $\alpha'$ -martensite in VHCF test with stress amplitude of 160 MPa (b)



In addition to the Feritscope™ measurements, scanning electron microscopy investigations at the same number of cycles were realized in the interrupted VHCF test with  $\sigma_a = 160$  MPa. Figure 4a shows some slip bands with a small micro-crack observed at  $N = 1 \cdot 10^7$ . Further cycling up to  $N = 1 \cdot 10^8$  induced slight changes in the surface relief indicating microcrack growth (Fig. 4b). The same surface area is shown in Fig. 4c at  $N_L = 5 \cdot 10^8$ . Compared with  $N = 1 \cdot 10^8$ , the surface relief did not change significantly and micro-crack growth was stopped. However, evolution of a white dot structure localized along lines (marked by arrows in Fig. 4c) is clearly seen at the specimen surface. To characterize these microstructural features, transmission electron microscopy investigations on focus ion beam (FIB) prepared foils are planned.

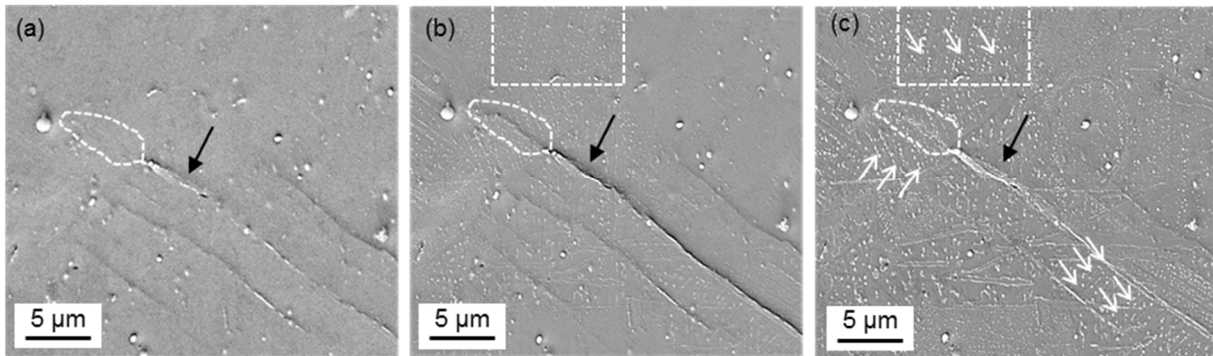


**Fig. 4:** Surface relief from specimen loaded with  $\sigma_a = 160$  MPa at  $N = 1 \cdot 10^7$  (a),  $N = 1 \cdot 10^8$  (b) and  $N = 5 \cdot 10^8$  (c)

## CONCLUSIONS

Considering load amplitude dependent changes in cyclic deformation behavior, it can be assumed that certain loading conditions need to be met to induce  $\alpha'$ -martensite formation at elevated temperature (Fig. 3), but the actual occurrence of this transformation process is also subject to significant scatter (Fig. 1). Generally cyclic deformation mode of face centered cubic materials, represented by typical dislocation structures as schematically summarized in Fig. 5b, is a function of stacking fault energy / temperature and plastic strain amplitude.

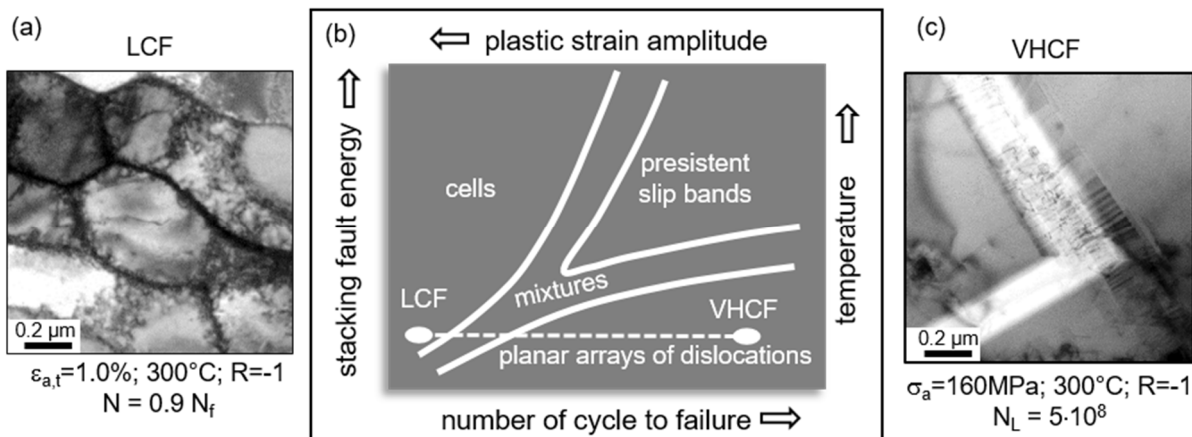


**Fig. 5:** TEM micrograph from a specimen loaded in LCF regime [9] (a), cyclic deformation map according [8] (b) slip bands with stacking faults from specimen loaded in VHCF regime (c); investigated material AISI 347

At 300°C, the investigated metastable austenitic steel AISI 347 showed no  $\alpha'$ -martensite formation in monotonic tensile loading (see. Tab. 2), under LCF [9], HCF as well as VHCF

loading at “higher” loading amplitude (comp. Fig. 1 with Fig. 2). TEM investigations of specimen after LCF and VHCF loading confirm the validity of the dislocation structure map in Fig. 5b. For high load amplitude in LCF regime, dislocation cells can be seen in Fig. 5a. Hence, cyclic deformation at 300°C in LCF/HCF regime is characterized by cross slip of dislocation. Furthermore, due to the small driving force given by the difference of free energies of fcc and bcc phase at 300°C, no  $\alpha'$ -martensite formation occurred in these tests. However, at smaller amplitudes, i.e. in the VHCF regime, planar dislocation glide with formation of typical stacking fault intersections is seen in Fig. 5c. The small plastic deformations in the VHCF regime are confined these structures. Intersection of stacking fault bands, often referred to as  $\varepsilon$ -martensite are nucleation points for body cubic center  $\alpha'$ -martensite formation. The formation of small nuclei of  $\alpha'$ -martensite suppresses further plastic deformation and, consequently results in the “true fatigue limit” in VHCF regime of metastable austenitic steels.

## REFERENCES

- [1] C.-H. Shek:  
Stainless steels, an introduction and their recent developments,  
ISBN: 978-1-60805-305-6.
- [2] O.K. Chopra, W.J. Shack:  
Effect of LWR Coolant Environments on the Fatigue Life of Reactor Materials,  
Final Report, NUREG/CR-6909, ANL-06/08 (2007).
- [3] D. Wagner, F.J. Cavalieri, N. Ranc, C. Bathias:  
High temperature gigacycle fatigue,  
Proceedings VHCF5 (2011) 301-306.
- [4] M. Smaga, F. Walther, D. Eifler:  
Deformation-Induced Martensitic Transformation in Metastable Austenitic Steels,  
Materials Science and Engineering: A 483 (2008), 394-397.
- [5] S. Martin, O. Fabrichnaya, D. Rafaja:  
Prediction of the local deformation mechanisms in metastable austenitic steels from  
the local concentration of the main alloying elements,  
Materials Letters 159 (2015) 484-488.
- [6] A.C. Grigorescu, P.-M. Hilgendorff, M. Zimmermann, C.-P. Fritzen, H.-J. Christ:  
Cyclic deformation behavior of austenitic Cr-Ni-steels in the VHCF regime,  
International Journal of Fatigue 93 (2016), pp. 250-260.
- [7] J. Talonen, P. Aspegren, H. Hänninen:  
Comparison of different methods for measuring strain induced  $\alpha'$ -martensite content  
in austenitic steels,  
Mater. Sci. Technol. 20 (2004) 1506-1512.
- [8] M. Klesnil, P. Lukas:  
Fatigue of metallic materials,  
Materials science monographs; 7, ISBN 0-444-99762-8 (1980).
- [9] A. Sorich, M. Smaga, D. Eifler:  
Influence of load conditions on the cyclic deformation behavior of the austenitic  
stainless steel AISI 347 at ambient temperature and 300 °C,  
Proceedings LCF7 (2013) 33-38.

## ACKNOWLEDGEMENT

The authors thank the Federal Ministry for Economic Affairs and Energy (BMWi), Germany as well as the German Research Foundation (DFG) for the financial support within the CRC 926 “Microscale Morphology of Component Surfaces”. The TEM investigations were performed at the Institute for Surface and Thin Film Analysis (IFOS), Kaiserslautern, Germany.

**Corresponding author:** [smaga@mv.uni-kl.de](mailto:smaga@mv.uni-kl.de)

# RELATIONSHIP BETWEEN TEMPERATURE PROPERTY AND LOADING FREQUENCY OF ROTATING BENDING FATIGUE TESTING MACHINE OF CANTILEVER TYPE

T. YAMAMOTO<sup>1)</sup>, B. LIAN<sup>1)</sup>, K. GOTOH<sup>2)</sup>

<sup>1)</sup>Yamamoto Metal Technos Co., Ltd., Setoguchi 2-4-7, Hirano, Osaka, Japan

<sup>2)</sup>Kyushu University, Motooka 744, Nishi-ku, Fukuoka, Japan

## ABSTRACT

Fatigue property in gigacycle regime is focused as an important subject in recent years. In such a long-life region, a tremendous long period is required to perform the tests. To overcome this difficulty, a part of authors has been developing the new rotating bending fatigue testing machine, which enables to reduce the test period and cost drastically. It was confirmed that the fatigue test dates are consistent with many experimental results obtained by hydraulic tension and compression fatigue testing machines and the rotating bending fatigue test machines of both-handed type known as Ono type. Although it prefers to reduce the fatigue test period as short as possible, the maximum frequency of a rotating bending fatigue test is limited by the standards because of the possibility of local temperature rise in specimen caused by the cyclic plastic work and the heat transfer from fatigue testing machine. Such local temperature rise might affect the fatigue property. However, the appropriate loading frequency limit is unclear because of the difficulty of the temperature measurement in the fracture portion of a specimen precisely during the rotating bending fatigue test. An in-situ temperature measuring technique is proposed to measure the temperature at the fracture portion of the specimen in real time during the fatigue testing, and the validity to determine the loading frequency of a rotating bending fatigue testing machine is discussed in this study.

## KEYWORDS

Maximum loading frequency, Cantilever type rotating bending fatigue testing machine, Temperature measuring, Fracture portion, In-site temperature measuring technique

## INTRODUCTION

The fatigue property in gigacycle regime is focused as an important subject in recent years. For example, it will take too much time to obtain P-S-N curves or S-N curves especially in the regime of very high cycle. In order to shorten the test period, some works have been tried by applying the ultrasonic fatigue test system. In such an ultrasonic fatigue testing, local temperature rise inside the specimen increases so significantly that appropriate temperature control systems are required [2-4]. In addition, the loading frequency is quite higher than the in-service condition of the machines and structures.

Therefore, the high speed fatigue testing machines with mechanical loading system should be developed. In order to shorten the testing period, a part of authors developed a multiplex rotating bending fatigue machine [8-9]. Such a fatigue testing machine can perform the fatigue test on multiple specimens under different load magnitude simultaneously at an appropriate loading frequency

without local temperature increase inside the specimen which might affect the fatigue property and the fracture mechanism. Such a kind of multiplex fatigue testing machine is adopted more and more widely, because the testing condition is quite same with testing performed by the conventional testing machine and the testing result is compatible with the data base of fatigue property which is obtained by the conventional testing machines and usually referred in fatigue testing and safety design of mechanical products [5-6].

On the other hand, many standards for the fatigue tests restrict the loading frequency. For example, Japan Industrial standards JIS Z 2274 for the rotating bending fatigue test is specified in a range of 1000 to 5000 rpm [10]. To obtain effective experimental data, the loading frequency should be limited into a reasonable range, although fatigue testing machine can work very well at a higher frequency. It is considered the local temperature increasing inside the specimen caused by the plastic work during cyclic loading in fatigue test is one of reasons to set a limit of loading frequency. However, the appropriate loading frequency limit is unclear because of the difficulty of the temperature measurement near a fracture portion of a specimen precisely during the rotating bending fatigue test.

In this paper, an in-situ temperature measuring technique is proposed to measure the temperature at the fracture portion of the specimen in real time during the fatigue testing, and the validity of limit loading frequency in the rotating bending fatigue testing machine is discussed.

## DUAL-SPINDLE FATIGUE TESTING MACHINE

In this research, a duplex rotating bend fatigue testing machine developed by a part of authors was applied to perform the fatigue tests. This fatigue testing machine has two spindles and two specimens can be installed at both ends of each spindle. Both spindles are driven by an electric motor. Thus, 4 specimens can be tested simultaneously at a given speed under a given rotating bending load. A photograph (front view) of such a fatigue testing machine is indicated in Fig.1 and a specimen mounted in the chucking parts is shown in Fig.2.



**Fig.1:** Dual-spindle rotating bending fatigue machine YRB300L (front view)



**Fig.2:** Dual-spindle rotating bending fatigue machine YRB300L (chucking parts and specimen)

## IN-SITU TEMPERATURE MEASURING TECHNIQUE

A wireless temperature monitoring system developed by the authors as indicated in Fig.3 [7]. Amplifier, A/D converter, micro-controller, and transmitter are encapsulated in a tool holder. The analog signal produced by the thermocouple is converted to a digital signal and wirelessly and continuously transmitted to a PC through a receiver connected to PC. The temperature history is recorded and monitored on PC in real time. An exchangeable adapter as shown in Fig.4 is adopted to mount such the wireless temperature monitoring tool into the fatigue testing machine.

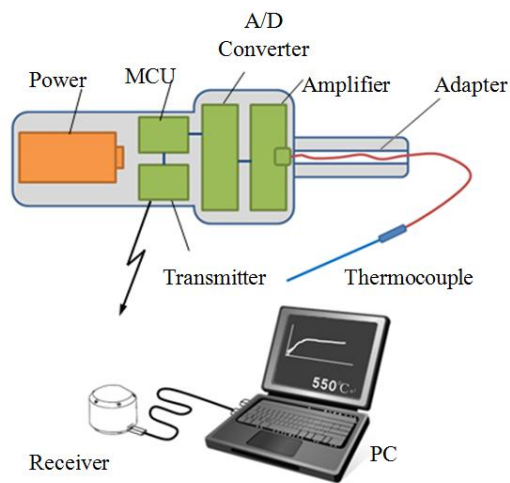


**Fig.3:** Construction of the wireless temperature monitoring system

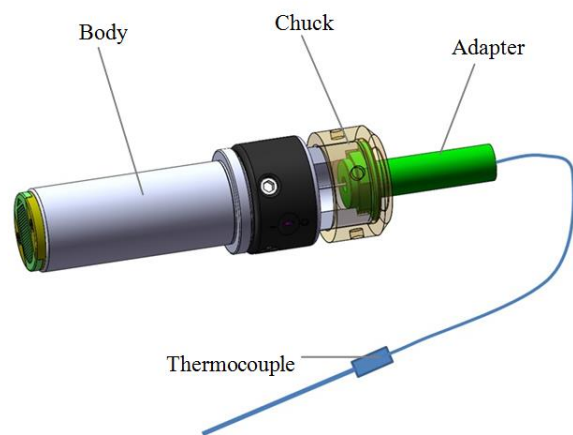


**Fig.4:** Appearance of the wireless temperature monitoring tool

## TEMPERATURE MEASURING METHOD NEAR THE MINIMUM CROSS SECTION OF SPECIMEN

In order to measure the temperature near the minimum cross section of specimen, the developed temperature monitoring system is installed on the other spindle opposite side of the specimen as indicated in Fig.5. A bearing unit is adopted to support the end of temperature monitoring tool to suppress the vibration during the spindle rotating at a high speed. As shown in Fig. 6, a hole with diameter of 0.5mm is prepared at one side of the specimen. A thermocouple (JIS C1605-95, Class 2, K type) is inserted to the center of specimen through the prepared hole and the thermocouple is connected to the temperature monitoring tool through the hollow spindle as indicated in Fig.5.

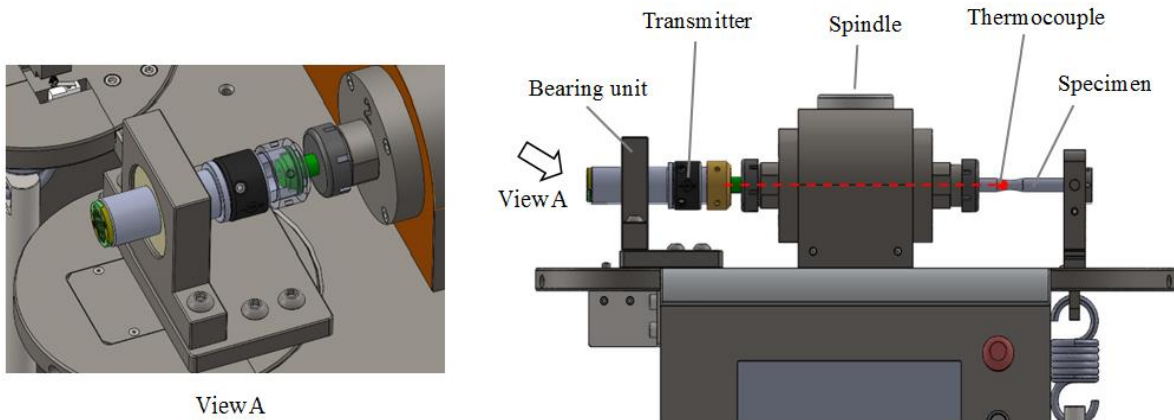


**Fig.5:** Construction of the wireless temperature measuring system

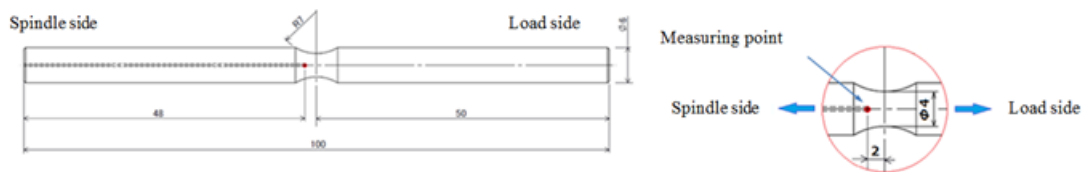


**Fig.6:** Specimen for temperature monitoring

## TEMPERATURE MEASUREMENT RESULTS

The testing conditions are listed in Table 1. Materials used in this study are A6005C (also named as A6N01 in Japan)-T5 aluminum alloy and anti-flammable magnesium alloy AZX611-F. Fatigue specimens were machined into the shape and dimensions indicated in Fig.6. The temperature near the minimum cross section of a specimen was measured during a fatigue test by developed monitoring system as indicated in Fig.5. The stress amplitude loaded on the specimen is 15MPa.

Rotating speed	3000 rpm	5000 rpm	6000 rpm
Material			
A6005C	Condition1	Condition3	Condition5
AZX611	Condition2	Condition4	Condition6

**Table1:** Test conditions

The temperature measured results are shown in Figs.7 and 8. At each rotation speed, the temperature near the minimum cross section of the specimen rose gradually and tended to converge to a constant value for both material. Furthermore, there is a tendency that the amount of temperature increase is large according to the loading speed is higher. However, the maximum temperature increase during the tests is less than 20 degree Celsius for each specimen as shown in Fig.7 and Fig.8. Thus, it was confirmed that the temperature increase during the fatigue tests is not too high to affect the fatigue testing result. Also, same tendencies were confirmed under different load levels such as 80MPa and 148MPa introduced by the authors in the past research [1].

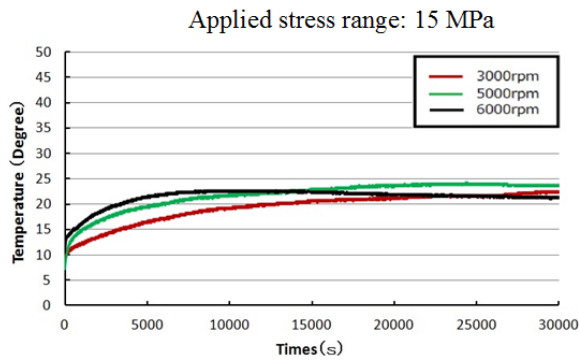


**Fig.7:** Results of temperature monitoring (material: A6005C-T5)

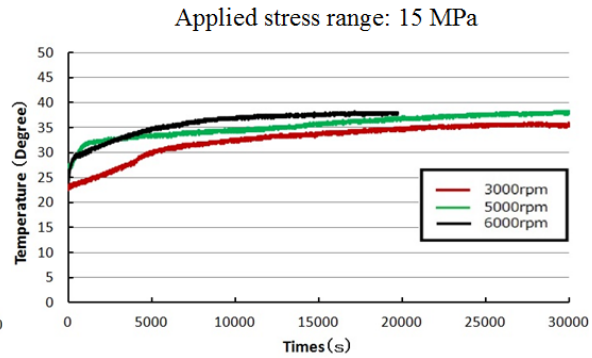


**Fig.8:** Results of temperature monitoring (material: AZX611-F)

### FATIGUE TESTING RESULT UNDER OVER TESTING SPEED LIMIT

Maximum loading frequency is limited below 5000rpm as indicated in the Japanese Industry Standard (JISZ 2274) [10]. Usually the maximum loading frequency is set as nearly 3000rpm [5-6]. In order to investigate the possibility of the enhancement of maximum loading frequency, fatigue test results between the loading frequency 6000 rpm and 3000rpm was compared. It is confirmed that there is no clear gap between the experimental results as indicated in Fig.10. The scatter of fatigue life is in an acceptable range. Referring to the temperature monitoring result indicated in before section, we know that there is no clear temperature increase between them. Thus, it is rational to enhance the maximum loading frequency to 6000rpm for collecting the fatigue data more efficiently.

If the maximum loading frequency is enhanced from 3000rpm to 6000rpm, the fatigue testing period can be shortened to about 120 days in a case of fatigue test in a gigacycle regime.

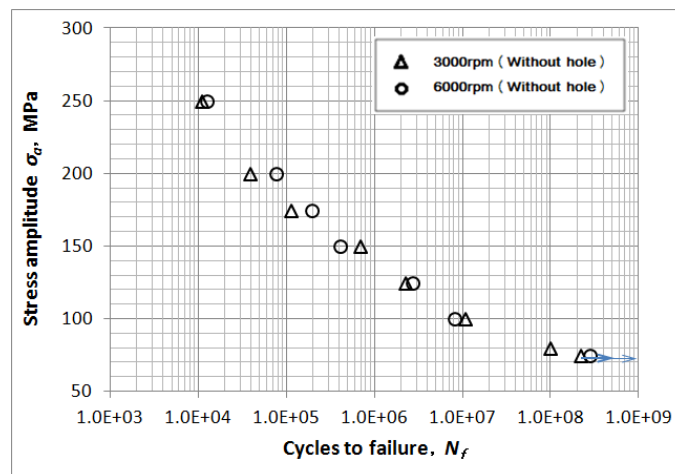


**Fig.10:** Influence of rotating speed on fatigue test results

### CONCLUSIONS

A wireless temperature monitoring system is developed to measure the temperature at the fracture portion of the specimen in real time during the fatigue testing, and the validity to



enhance the loading frequency is discussed. Main conclusions obtained in this study are summarized as follows.

- (1) The temperature increase in vicinity of fracture section of specimen is compared at a loading frequency of 3000rpm which is in the range provided by Japanese Industry Standard (JISZ 2274) and 6000rpm which is over the maximum limit of the loading frequency (5000rpm) provided in JISZ 2274. Although the temperature increase is a little higher at a loading frequency of 6000rpm, there is no clear effect on the fatigue life.
- (2) It is rational to enhance the testing frequency of cantilever rotating bending fatigue test to 6000rpm which is over the limit value of 5000rpm provided in JISZ 2274 for collecting the fatigue data more efficiently.
- (3) The developed wireless temperature monitoring system can be used to measure the temperature of fracture section in a real time during fatigue testing. Thus, it is an effective system to evaluate the loading frequency limit of cantilever rotating bending fatigue test.

## REFERENCES

- [1] Gotoh, K., Nakagome, S. Yamamoto, T. and Enomoto M., Fatigue performance of Light metals (A6005C and AZX611) and their FSW joints, Proceedings of 4th European Conference JOIN-TRANS 2016 on Joining and Construction of Rail Vehicles, (2016)
- [2] Ebara, R., The present situation and future problems in ultrasonic fatigue testing – Mainly reviewed on environmental effects and materials' screening, International Journal of Fatigue, 28, (2006), pp. 1465-1470.
- [3] Ishii, H., Yamada, T., Okada, Y., Very high cycle fatigue strengths of thin sheet metals, Proceedings of VHCF-3, (2004), pp. 420-426.
- [4] Kirchner, H. O. K., Kromp W., Prinz F. B., Trimmel P., Plastic deformation under simultaneous cyclic and unidirectional loading at low and ultrasonic frequencies, Mat. Sci. Eng., 68, (1985), pp. 197-206.
- [5] Sakai, T., Tanaka, N., Okada, K., Furuichi, M., Nishikawa, I., Sugata, A., Statistical Fatigue Properties in Ultra-Long-Life Regime for SCM435 Steels Based on JSMS Database on Fatigue Strength of Metallic Materials, Transactions of the JSME, Part A, (2003), Vol.70, No.696, pp. 2004-2008 (in Japanese).
- [6] Tatsuo SAKAI , Izuru NISHIKAWA, Fundamentals and Recent Topics on Fatigue, V: Databases on Fatigue Strength and Regression Method of S-N Curves, 「Material」 (J. Soc. Mat. Sci., Japan), Vol. 52, No. 6, pp. 709-715, June 2003
- [7] Shindou, M., Matsuda, R., Furuiki, T., Hirogaki, T. and Aoyama, E., Multipoint simultaneous monitoring of end-mill processing temperatures with wireless telegraphic multifunctional tool holder, Transactions of the Abrasive Technology Conference (2015), pp. 359-364 (in Japanese).
- [8] Yamamoto, T., Kokubu, A., Sakai, T., Kiyama, I., and Nakamura, Y., Development and fundamental performance of dual-spindle rotating bending fatigue testing machine with special device providing corrosive environments, VHCF5 (2011)
- [9] Yamamoto, T., Kokubu, A., Sakai, T., and Nakamura, Y., Development and several additional performances of dual-spindle rotating bending fatigue testing machine GIGA QUAD, VHCF6 (2014)
- [10] Yamamoto, T., Lian, B. and Gotoh, K., The study of the heat generation caused by the cyclic plasticity work during rotating bending fatigue test, JSME (2016)

**Corresponding author:** yamakin@mx1.alpha-web.ne.jp

# **GIGACYCLE FATIGUE PROPERTIES OF A TURBINE ENGINE BLADE TITANIUM ALLOY TI811 AT ELEVATED TEMPERATURE**

K Yang<sup>1)</sup>, J.K. Li<sup>1)</sup>, C He<sup>2)</sup>, Y.J. Liu<sup>1)</sup>, H Zhang<sup>1)</sup>, Q.Y. Wang<sup>1,2,\*</sup>

<sup>1)</sup> Failure Mechanics and Engineering Disaster Prevention and Mitigation Key Laboratory of Sichuan Province, College of Architecture and Environment, Sichuan University, Chengdu 610065, PR China

<sup>2)</sup> School of Architecture and Civil Engineering, Chengdu University, Chengdu 610065, PR China

## **ABSTRACT**

An ultrasonic fatigue testing system (20 KHz) equipped with induction heating attachment was employed to study the gigacycle fatigue properties of a turbine engine blade titanium alloy (Ti-8Al-1Mo-1V, named TA11 by Chinese Standard) at ambient temperature (20 °C) and 300 °C under fully reverse loading (stress ratio  $R=-1$ ). With the increase of temperature, the stress-life curve types changed from continuous decline shape to duplex characteristic. Compared with room temperature, very high cycle fatigue (VHCF) strength of the titanium alloy decreased dramatically at high temperature. The interior initiations were only detected at ambient temperature. Fracture surfaces failed at 300 °C showed specific features. Moreover, the mechanism of facet-induced fatigue crack initiation is activated at high temperature.

## **KEYWORDS**

Gigacycle fatigue, titanium alloy, elevated temperature, fatigue strength, fatigue crack initiation

## **1. INTRODUCTION**

Titanium alloys are characterized by high specific strength, fatigue resistance and corrosion resistance, so they are generally used to manufacture blades and disks of advanced turbine engines. Ti811 titanium alloy was developed by America in the 1950's for fabricating advanced aircraft low pressure compressor blades [1], it was exposed to elevated temperatures and high frequency vibration loading at low amplitude levels due to the interaction of air and blades. Larsen et al. [1] has investigated the high cycle fatigue (HCF) behaviors of this alloy, however in-service turbine engine blade failure appeared in the VHCF regime [2] owing to the high frequency vibration loading. The ultrasonic fatigue testing devices with a high loading frequency of 20 KHz have been employed in determining the VHCF performances in view of its high efficiency and economy in recent years.

The application of this alloy raises the question of its fatigue behaviors, especially in the VHCF regime, at elevated temperatures and high frequency

vibration loading. However, so far no relevant study has been reported with respect to the titanium alloy. So in this study, an ultrasonic fatigue testing system that is capable of testing at elevated temperatures was developed to ascertain this issue.

## 2. MATERIAL AND EXPERIMENTAL METHOD

### 2.1 Material

The chemical composition (in % weight) of the titanium alloy (Ti-8Al-1Mo-1V) is: 7.79 Al, 0.98 Mo, 1.00 V, 0.04 Fe, 0.01 C, <0.01 N, 0.006 H, 0.06 O and balance Ti. A double anneal heat treatment process (910 °C for 1 hour, air cooled and 580 °C for 8 hours, air cooled) was applied to the material. Tensile tests were conducted to determine the mechanical properties, and it delivered a Young's modulus of 113.5 GPa, a yield strength of 915 MPa and a tensile strength of 940 MPa.

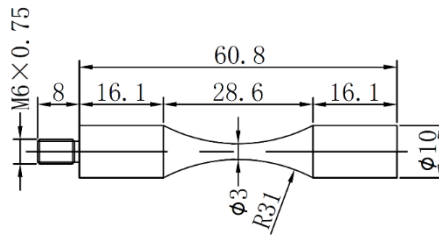


Fig. 1. Specimen geometry (units: mm) for fatigue tests [3].

In order to meet the requirements of ultrasonic fatigue test facilities, the specimens were designed to work at a resonance frequency of 20 KHz in the axial direction. Hour-glass shaped specimens were obtained by machining and final axial-direction mirror polishing as shown in Fig. 1. A diameter of 3 mm at the test section was manufactured for ambient and elevated temperature tests.

### 2.2 Experimental method

In this study, a commercial ultrasonic fatigue test machine was used to investigate the fatigue behaviors at ambient temperature. For the sake of reducing the temperature of the gauge section of specimens resulting from self-heating, a compressed dry air cooling system was equipped. Finally, the surface temperature maintained in the range of 12-16 °C with no pause. Therefore, there was no interruption in the experiment process at ambient temperature.

In order to carry out ultrasonic fatigue tests at elevated temperature, electromagnetic induction heating technology was utilized. An induction coil was equipped in the commercial ultrasonic fatigue test machine. The coil was adjusted in the middle of specimens to heat the test section of specimens at a given temperature. Meanwhile, an infrared camera was applied to monitor and control the temperature. Furthermore, intermittent vibration with a resonance interval of 300 ms per 800 ms was applied to better manage the temperature.

Prior to the experiment, the temperature measured by thermocouples was used to calibrate the emissivity which applied to the infrared camera. In this test, the temperature of 300 °C was chosen due to the operating temperature of the material in low pressure compressor blades. After the fatigue experiments, all fracture surfaces of broken specimens were observed carefully by a scanning electron microscope (SEM).

### 3. RESULTS AND DISCUSSION

#### 3.1 Fatigue strength

Fatigue data regarding stress amplitude versus cycles at room and elevated temperature are shown in Fig. 2. The symbols expressed in square and circle represent the fatigue data at room and high temperature, respectively.

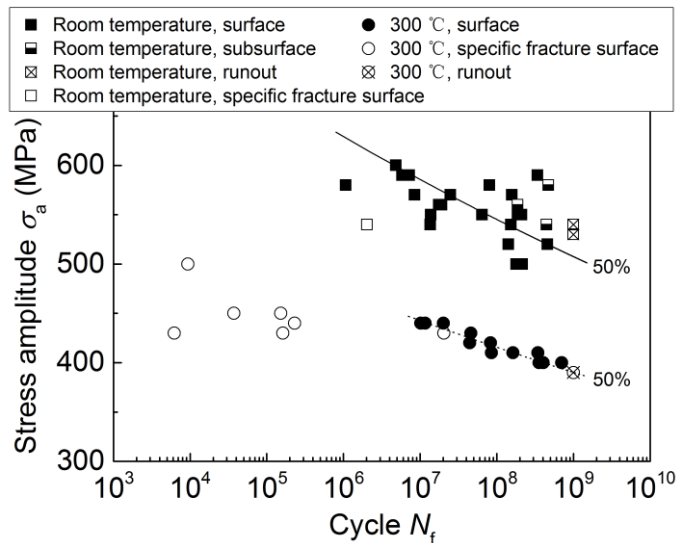


Fig. 2. Fatigue data of the titanium alloy at room and elevated temperature. With the increase of temperature, the  $S-N$  curves turned into a duplex pattern from a continuous declining shape. Moreover, high temperature decreased the fatigue strength dramatically. In order to characterize the degeneration quantitatively, a lognormal distribution with respect to fatigue life was introduced. The solid line denote 50% failure probability of fatigue data at room temperature, and the dash line represent 50% failure probability at elevated temperature in the VHCF regime ( $N_f > 10^7$  cycles). As a result, the fatigue endurance limits at the limiting lifetime of  $10^9$  cycles at room and elevated temperature were determined as 508 and 390 MPa, respectively. The fatigue strength at elevated temperature almost decreased a quarter of the fatigue strength obtained at room temperature. Meanwhile, the fatigue resistance decreased in a nearly uniform tendency with the limiting lifetime increased at room and elevated temperature in the range of VHCF.

### 3.2 Fractography

The fracture surfaces were examined by SEM with the purpose of illuminating the effect of elevated temperature on fatigue failure mechanism of the titanium alloy. As illustrated in Fig. 2, almost all fatigue cracks initiated at the surface except for three fracture surfaces which appeared interior crack initiation, in addition, only one fracture surface emerged special fracture morphology at room temperature. In contrast, no interior crack initiation was detected, and a large amount of fracture surfaces presented special fracture morphology, especially in the LCF and HCF regime, at elevated temperature.

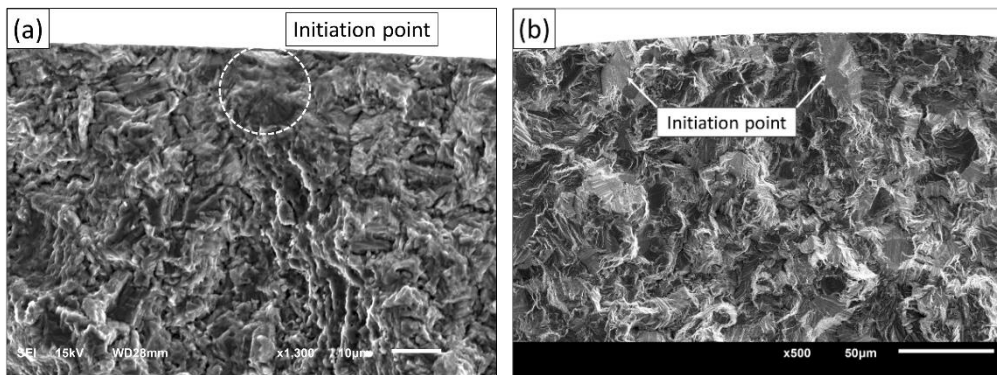


Fig. 3. Typical fracture morphology of the specimens with surface crack initiation at (a) room and (b) elevated temperature. (a)  $\sigma_a=570$  MPa,  $N_f=1.5728 \times 10^8$  cycles; (b)  $\sigma_a=440$  MPa,  $N_f=1.0183 \times 10^7$  cycles.

Fig. 3 shows the fracture morphology of initiation points with surface crack initiation at different temperatures. In general, the fatigue fracture origins of many materials are located in the surface owing to the formation and evolution of persistent slip bands (PSBs) in the HCF regime [4, 5]. However, no PSB was discovered in this tests. The accumulation of irreversible random slips [6] assisted by the lower constraint effect, the possibility of residual manufactured defects [7] and heterogeneity of the microstructure [8] result in inhomogeneously and localised irreversible plastic deformations, and finally lead to surface fatigue crack initiation. On the effect of elevated temperature, the irreversible random slips reached a higher occurrence probability and preferred appearance by means of planar slip (facet) as shown in Fig. 3, it gave rise to the degeneration of fatigue strength essentially.

Fig. 4 illustrates emblematic specific fracture surfaces at elevated temperature. Fig. 4b and c show the high-magnification photographs at the two given regions in Fig. 4a. The planar slips related to crack initiation and radial streaks resulted from crack propagation were not visible in this specific fracture surface, as shown in Fig. 4b and c. The characteristic of intergranular fracture was detected obviously because of the effect of cyclic creep at elevated temperature. The similar intergranular fracture morphology was reported by Shanyavskiy [2] in a failure in-service turbine blade.

Only dimples and shear lips, like the tensile fracture surface without any distinct fatigue features, were discovered in the other specific fracture surface depicted

in Fig. 4d. This fracture aspects are consistent with the fatigued specimens tested under high superimposed mean stresses found by Kovacs et al. [5], its failure process was dominated by cyclic creep. This fracture mode merely occurred in very high stress amplitudes in this experiments. The cyclic creep at elevated temperature governed the deformation and failure of specimens under very high stress amplitudes.

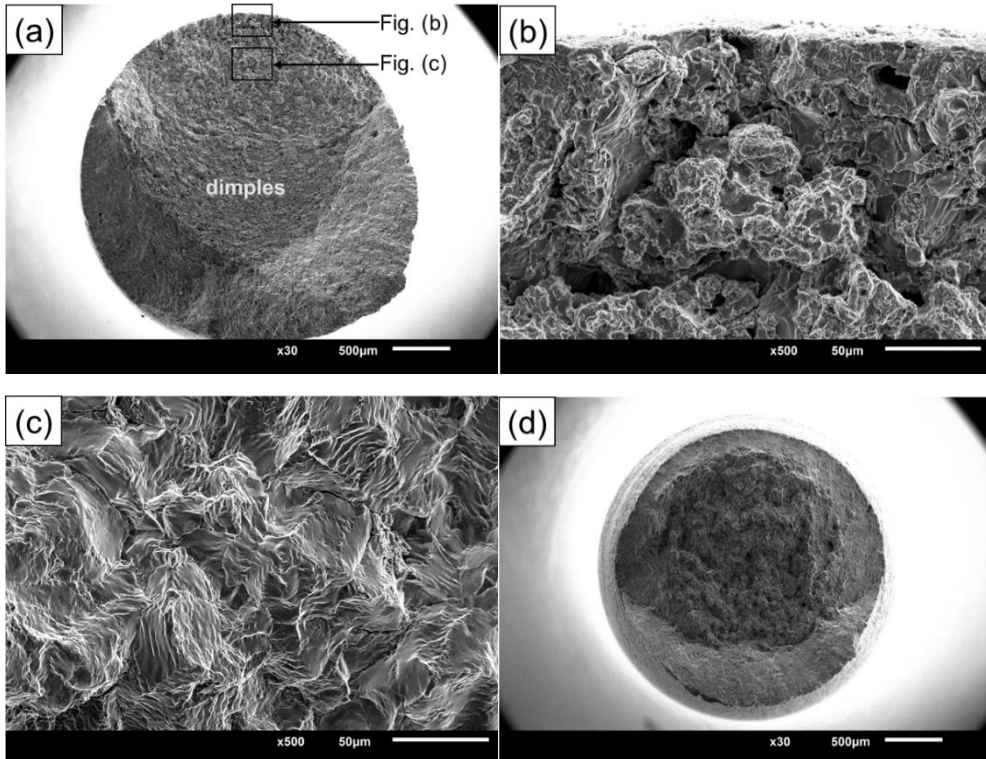


Fig. 4. Typical fracture morphology of the specimens with specific feature at elevated temperature. (a, b and c)  $\sigma_a=430$  MPa,  $N_f=2.0368 \times 10^7$  cycles; (d)  $\sigma_a=450$  MPa,  $N_f=1.52 \times 10^5$  cycles.

Based on the discussion above, the conclusion that the dominance of cyclic creep at elevated temperature on failure process of specimens decreased with the applied stress amplitude levels diminution could be drawn. Meanwhile, the effect of cyclic creep at elevated temperature on fracture strength was prominent in the LCF and HCF regime, as presented in Fig. 2. The competition between two failure modes of cyclic creep-induced and fatigue-induced resulted in the appearance of the platform of  $S-N$  curve in the vicinity of the stress amplitude level of 440 MPa at elevated temperature for this titanium alloy.

#### 4. CONCLUSIONS

This paper investigated the elevated temperature effect on fatigue

behaviors of the titanium alloy by performing ultrasonic fatigue tests. The main conclusions could be drawn as follows: The fatigue strength at elevated temperature almost decreases a quarter of the value at room temperature due to the higher occurrence probability of irreversible random slips and the appearance of planar slip in the VHCF regime. The cyclic creep dominates the failure process at elevated temperature in the LCF and HCF regime, and the dominance decreases with the applied stress amplitude levels reduction. The competition between two failure modes of cyclic creep-induced and fatigue-induced lead to the transformation of *S-N* curve from continuous decline shape to duplex pattern with increased temperatures.

## ACKNOWLEDGMENTS

The authors acknowledge the financial support provided by the National Natural Science Research Foundation of China (No. 11327801, No. 11572057 and No. 11602038).

## REFERENCES

- [1] J.M. Larsen, B.D. Worth, C.G. Annis, F.K. Haake, An assessment of the role of near-threshold crack growth in high-cycle-fatigue life prediction of aerospace titanium alloys under turbine engine spectra, *Int J Fracture*, 80 (1996) 237-255.
- [2] A.A. Shanyavskiy, Fatigue limit - Material property as an opened or closed system? Practical view on the aircraft components failures in GCF area, *Int J Fatigue*, 28 (2006) 1647-1657.
- [3] K. Yang, C. He, Q. Huang, Z.Y. Huang, C. Wang, Q. Wang, Y.J. Liu, B. Zhong, Very high cycle fatigue behaviors of a turbine engine blade alloy at various stress ratios, *Int J Fatigue*, 99, Part 1 (2017) 35-43.
- [4] H. Mughrabi, Specific features and mechanisms of fatigue in the ultrahigh-cycle regime, *Int J Fatigue*, 28 (2006) 1501-1508.
- [5] S. Kovacs, T. Beck, L. Singheiser, Influence of mean stresses on fatigue life and damage of a turbine blade steel in the VHCF-regime, *Int J Fatigue*, 49 (2013) 90-99.
- [6] H. Mughrabi, Microstructural fatigue mechanisms: Cyclic slip irreversibility, crack initiation, non-linear elastic damage analysis, *Int J Fatigue*, 57 (2013) 2-8.
- [7] M.L. Zhu, F.Z. Xuan, Y.N. Du, S.T. Tu, Very high cycle fatigue behavior of a low strength welded joint at moderate temperature, *Int J Fatigue*, 40 (2012) 74-83.
- [8] M. Zimmermann, C. Stocker, H.J. Christ, On the effects of particle strengthening and temperature on the VHCF behavior at high frequency, *Int J Fatigue*, 33 (2011) 42-48.

Corresponding author: Prof. Dr. Qing Yuan Wang  
Fax: +86 02885406919 Phone: +86 02885406919  
E-mail: wangqy@scu.edu.cn



# MICROSTRUCTURAL TIME LAPSE DAMAGE QUANTIFICATION IN GFRP DURING HIGH CYCLE TENSION-TENSION FATIGUE USING STEREOLOGY

S. Bhattacharya<sup>1</sup>, A. Tewari<sup>1,2</sup>, Anirban Guha<sup>1</sup>, P. Potluri<sup>3</sup>

<sup>1</sup>Department of Mechanical Engineering, IIT Bombay, Mumbai, India

<sup>2</sup>National Centre for Aerospace Innovation and Research, IIT Bombay, Mumbai, India

<sup>3</sup>Textile Composites group, Northwest Composite Centre University of Manchester, Manchester, United Kingdom

## Abstract

The progression of damage from initial stages till failure of fiber reinforced polymers has been one of the key aspects of research in the worldwide fatigue community. However, our understanding suffers from a lack of knowledge of quantitative damage evolution as a function of micro-structure. The mathematical framework of stereology offers a huge potential in accurate prediction of damage descriptors, thereby giving a composite damage index. Accordingly, the objective of the research was to provide quantitative characterization of microstructural damage as a function of number of fatigue cycles. For this purpose, unidirectional glass fibre reinforced polymer specimens of 0° fibre orientation were subjected to tension-tension fatigue cycles at 10 Hz for two different R ratios. The fatigue tests were performed at mean stress of forty percent of the tensile strength. The tests were interrupted at 1000, 5000, 10000 and 50000 cycles and the samples were, tested for residual tensile strength. Digital image analysis and detailed stereological measurements in micro-structure were made, and the damage observed was quantified for two damage states, Fiber Matrix De-bonding (FMD) and Fiber Cracking (FC). The number of fiber cracks per unit volume  $N_{V(FC)}$ , and the surface area of fibre-matrix de-bonded surface per unit volume  $[S_{V(FMD)}]$  was estimated from 2D metallographic sections. It was found that both de-bonding and fiber cracking increase monotonically with increase in fatigue cycles. Both  $N_{V(FC)}$  and  $S_{V(FMD)}$  were found to correlate well with the residual strength; however,  $N_{V(FC)}$  showed a larger influence on residual strength than  $S_{V(FMD)}$ .

## KEYWORDS

Glass Fiber Reinforced Polymer (GFRP), Stereology, Fiber Matrix De-bonding (FMD), Fiber Cracking (FC).

## Introduction

Fibre Reinforced Polymers (FRP) are finding application in a diverse range of aero-structural components. Research in composite design methodologies over the last few decades has explored minimization of weight to volume ratio. This has resulted in FRPs being subjected to in-service loads which are close to their static strength and increases the probability of damage due to fatigue.

For fatigue [1-5], the parameters that play a key role are the type of fibre and matrix, stacking sequence of laminates, and the loading conditions (Stress Ratio (R), frequency and boundary conditions). Damage is manifested in the form of matrix cracking, fibre matrix delamination and fibre failure.

Stereology is the technique used to extract quantitative information in 3D from 2D sections. The mathematical framework of stereology [6-8], offers a huge potential in accurate prediction of damage descriptors, thereby giving a composite damage index. It is a robust method in which statistical

inferences can be drawn from plan sections of a solid material. It is important to point out that majority of the studies on polymer composites subjected to fatigue reported in the literature are of qualitative nature. None of the investigations report statistically unbiased estimations of ensemble averaged geometric attributes of fatigue damage, namely fiber-cracks, fibre-matrix de-bonding, matrix cracks in three dimensional microstructural space, relationships of such attributes with the material microstructure and their quantitative linkages to the fatigue crack initiation.

## Manufacturing and Experimentation

The Vacuum Assisted Resin Transfer Molding (VARTM) process was used to manufacture two plates of unidirectional 0 degree orientation  $[0]_{4s}$  having dimensions of 600 mm x 600 x 4 mm as shown in Fig. 1 from E-Glass (Hindoostan Tech.) unidirectional fibre (1200 tex) and having a fabric thickness of 0.36 mm.

The resin system used was epoxy resin Epotec YD 535 LV and hardener TH 7257 from Aditya Birla Chemicals Ltd. This resin system has a pot life of 330 min and a viscosity of 1200 cPs s at 25 °C.

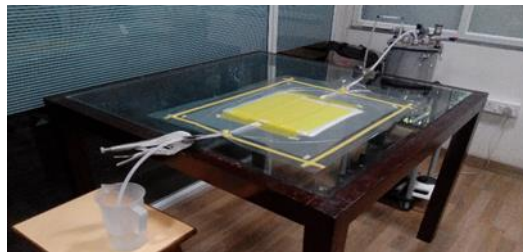


Fig.1. VARTM setup at IIT Bombay

Vacmobile Modular 2S system was used to maintain an absolute vacuum pressure of 15 mbar throughout the infusion process. The epoxy system was degassed for 20 min under vacuum, before commencing the impregnation of resin through the dry fabric. Infusion of the resin was carried out at room temperature, without pre-heating the resin, fabric or mold. The laminate was allowed to cure for 24 hours at room temperature under vacuum and then released. Target fiber volume fraction of composite was 0.6. After curing the material, specimens (210 mm x 19 mm x 4 mm) were obtained by cutting the plate using water jet.

Specimens were subjected to uniaxial tension to obtain ultimate tensile strength using 100 kN capacity universal testing machine (Instron 5982). Ten specimens were loaded in tension until failure to get ultimate tensile strength.

Axial tension-tension fatigue testing of unidirectional GFRP specimens were carried out using fatigue testing machine (Instron 8850) with maximum stress ( $\sigma_{Max}$ ) at 40% of mean ultimate tensile strength, obtained from tension test. Specimens were cyclically loaded at 10 Hz frequency. Stress ratio (R) of 0.1 and 0.3 was used.

To capture the degradation of the GFRPs during different stages of damage initiation, the specimens were loaded to the stress ratios of 0.1 and 0.3 for 1000, 5000, 10000 and 50000 cycles. Ten specimens were tested for each case. Eight of the ten specimens corresponding to each number of cycles was tested to find residual strength of the composite. The remaining two samples were used for microscopic observation.

Five specimens, one untested and four fatigue loaded at different number of cycles, were used for microscopic observation. Each specimen was cut in such a way as to get three different sections, namely, plan (P), longitudinal (L) and cross-section(C). Specimens were cut using diamond saw to obtain three pieces, one for each section. These pieces were cold mounted and then polished using polishing machine to obtain surface roughness less than 1  $\mu\text{m}$ .

## Research Methodology

Stereology has been used to quantify fibre cracks and fibre matrix de-bonding from 2D sections of micro-structures. The entire calculation has been done using open source image processing software, Image J.

Fiber/matrix de-bonding area can be estimated in a micrograph having de-bonding. This is performed by superimposing an array of grid lines on an image and counting the number of intersections of lines and de-bonding. This is defined by

$$S_{V(DB)} = 2 (I_L)$$

where  $S_{V(DB)}$  is the de-bonding area per unit volume in  $(\mu\text{m})^{-1}$ .  $I_L$  is the average number of intersection points per unit length of test lines.

Fiber cracks per unit area include cracks at centre and missing portions of fiber. They can be estimated by counting the number of cracks in an image and it is defined by

$$N_{A(FC)} = N_F/A$$

where  $N_F$  is the number of fiber cracks and  $A$  is the area of micrograph in  $\mu\text{m}^2$ .

Number per unit volume of fibre cracks  $N_{V(FC)}$  is given by the relation

$$N_{V(FC)} = N_{A(FC)} / \bar{r}_H$$

where  $\bar{r}_H$  is caliper diameter. In the case of unidirectional glass fibres, it is equal to 1.57 times the radius of fibres.

## Results and Discussion

Damage progression in Unidirectional GFRP during tension-tension fatigue loading is listed in four stages.

Stage 1 : 1000 cycles: GFRP without any damage or damage due to manufacturing defects.

Stage 2: 5000 cycles: initial fiber breakage as the local failure strain is exceeded.

Stage 3: 10000 cycles: the broken fibers from stage 2, getting de-bonded from the matrix.

Stage 4: 50000 cycles: fibers surrounding the broken fibers taking more load and in turn failing consecutively.

All the above stages can be seen in Fig 2B as the number of fatigue cycles are increased. Since unidirectional (UD) laminates are subjected to unidirectional tension, no damages can be seen in the cross-sectional view of microstructures (Fig 2A).

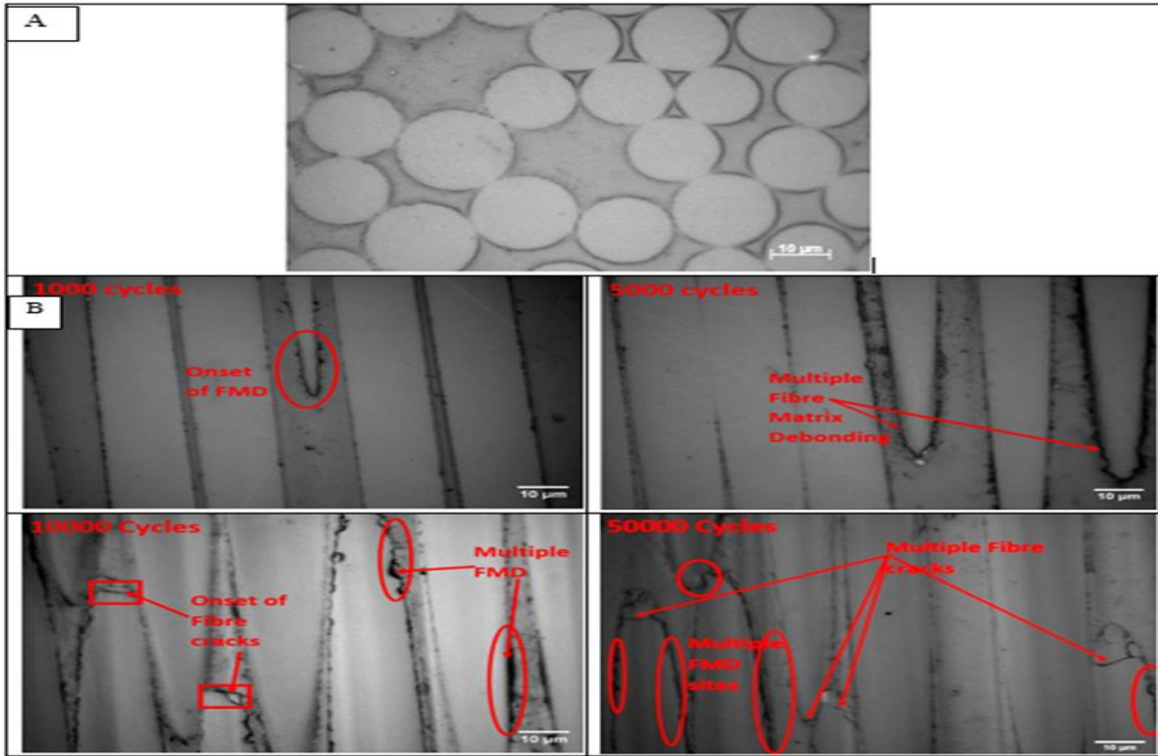


Fig 2A. Cross section of UD fibers

Fig 2B. Micro-structural damage progression with increasing number of fatigue cycles

Thirty random micrographs were used for each case and their average was taken. Surface area per unit volume of fiber matrix de-bonding versus number of cycles is shown in Fig 3a. Both fibre-matrix de-bonding (FMD) and fibre cracking increase with fatigue cycles. However, these two phenomena appear to be independent. The number of fiber matrix de-bonded interfaces has increased with number of fatigue cycles. The instances of FMD has been found to be lower for  $R = 0.3$  as compared to  $R = 0.1$ .

The number of fibre cracks per unit volume shows a steady increase (Fig 3.b) with increased number of fatigue cycles. Also the fibre crack density is more for  $R = 0.1$  as compared to  $R = 0.3$ .

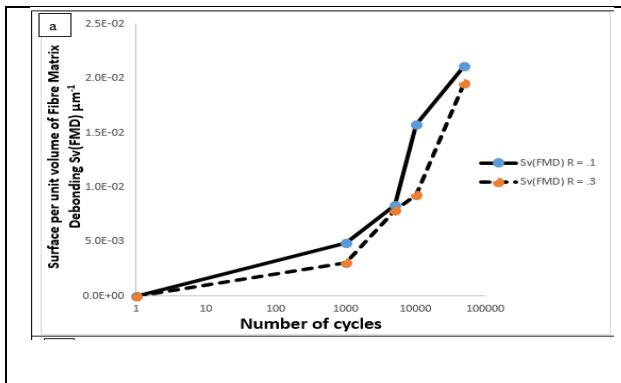


Fig 3a.  $S_{V(FMD)}$  vs Number of cycles

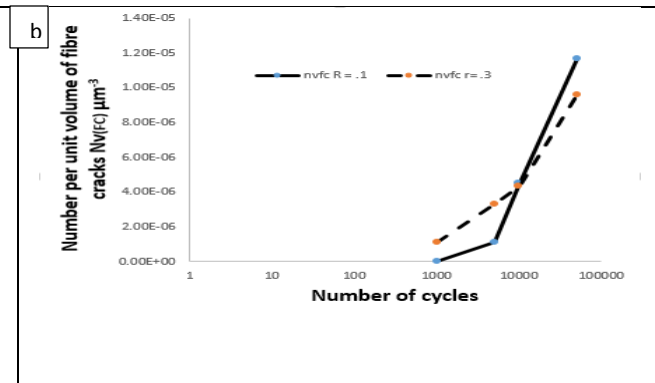


Fig 3b.  $N_{V(FC)}$  vs Number of cycles

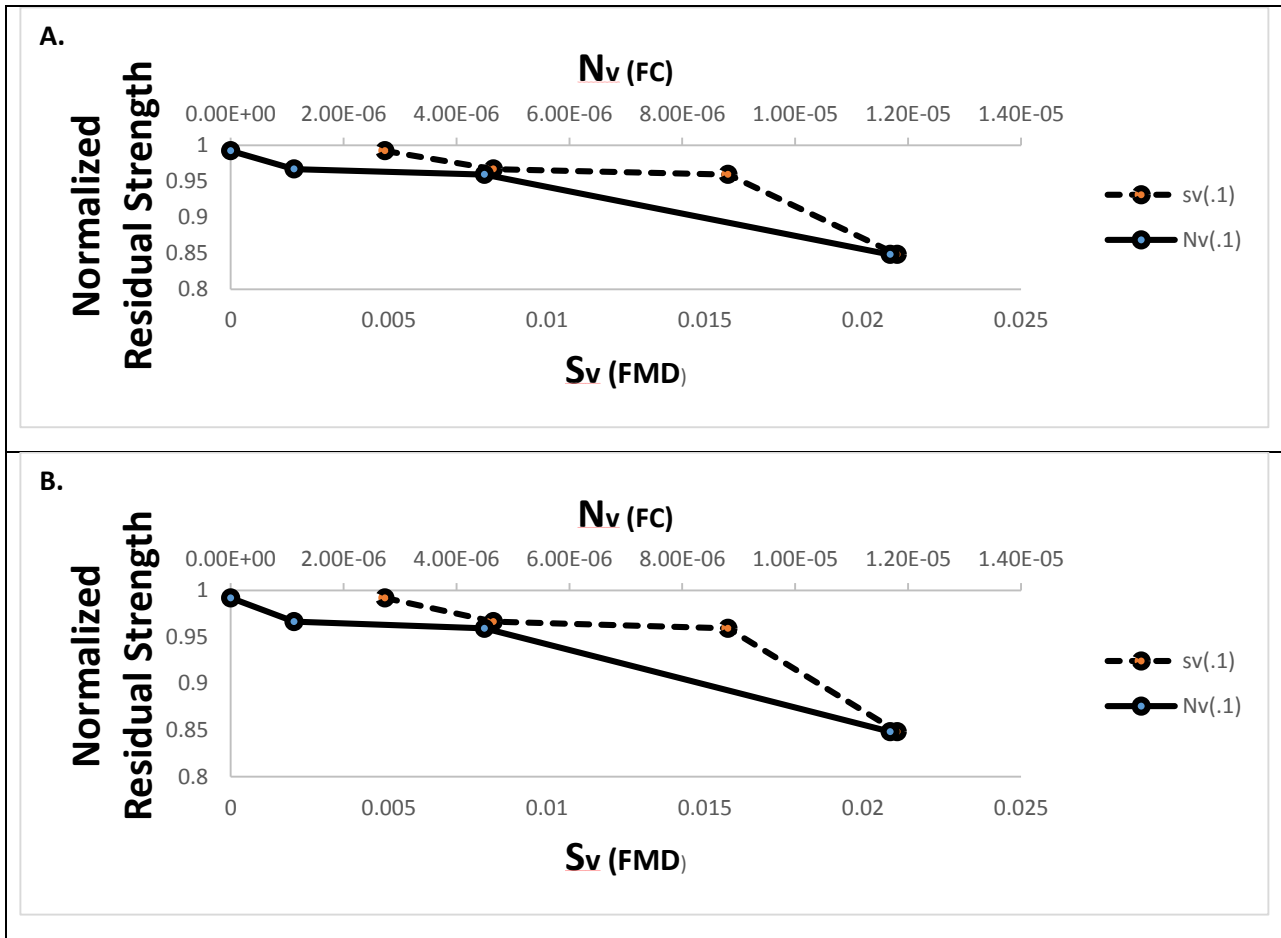


Fig 4. Normalized Residual Strength vs  $S_v$  and  $N_v$  A)  $R = .1$  B)  $R = .3$

As it can be seen from Fig 4, normalized residual strength for  $R = 0.1$ , shows a steep fall from 10000 cycles to 50000 cycles, which coincides with an exponential increase in  $N_{v(FC)}$  during this period. However, for  $R = 0.3$ , the fall in residual strength is only about five percent till 10000 cycles, followed by a steep drop of twenty percent while progressing from 10000 to 50000 cycles.

Correlation ( $R^2 = 0.99$ ) of stereological property with residual strength					
Stereological Property		$S_{v(FMD)}$ co-eff.	$N_{v(FC)}$ co-eff.	Highest Contributor	%Contribution
UD	$R = .3$	0.13	0.27	$N_v(fc)$	66.7
UD	$R = .1$	0.23	0.35	$N_v(fc)$	60.3

Table 1. Correlation of Residual strength with stereological parameters

From Table 1, it can be understood that  $N_{v(FC)}$  has a greater influence on residual strength as compared to  $S_{v(FMD)}$  for both the load ratios in unidirectional composites.

## Conclusions

This paper reports a reliable methodology for fatigue life and damage modeling of Glass Fiber Reinforced Polymers (GFRPs). The process does not compromise the essential nature of the fatigue process. The number of experiments required is within reasonable limits. The quantitative measures of damage postulated in this paper, have been correlated with the property degradation. This gives an adequate foundation for estimating the life and residual tensile properties of structural components made from GFRPs after fatigue. Future work in this area will explore various combinations of fiber orientations and stacking sequences. The trends observed are expected to aid in designing better GFRPs.

## Acknowledgement

The authors gratefully acknowledge the support provided for this work by the National Centre for Aerospace Innovation and Research (NCAIR), IIT Bombay, a Department of Science and Technology, Government of India, The Boeing Company and IIT Bombay collaboration.

## References

- [1] Anastasios P. Vassilopoulos, Thomas Keller. "Fatigue of fiber-reinforced composite" Springer 2011.
- [2] Joris Degrieck, Wim Van Paepegem. "Fatigue damage modeling of fiber-reinforced composite materials: Review".
- [3] Bryan Harris "Fatigue of composites: Science and technology of the fatigue response of fiber-reinforced plastics". CRC press 2003.
- [4] J. Aghazadeh Mohandesi, B. Majidi. "Fatigue damage accumulation in carbon/epoxy laminated composites". *Materials and Design* 2009, 30: 1950–1956.
- [5] H. Mao, S. Mahadevan. "Fatigue damage modeling of composite materials". *Composite Structures* 2002, 58: 405–410.
- [6] John Summerscales. "Microstructural characterization of fibre-reinforced composites". CRC Press 1998.
- [7] Adrian Baddeley, Eva B. Vedel Jensen. "Stereology for Statisticians". Chapman & Hall/CRC 2005.
- [8] E.R. Weibel. "Stereological Methods, 1. Practical Methods for Biological Morphometry". Academic Press, London, 19

swarnendu.bhattacharya@iitb.ac.in

# NONLINEARITIES BASED INVERSE APPROACH FOR THE CHARACTERISATION OF THE DAMAGE EVALUATION PROCESS IN VERY HIGH CYCLE FATIGUED CFRP SPECIMENS

C. Boller<sup>1</sup>, R. Sridaran Venkat<sup>1</sup>, P. Starke<sup>1</sup>, B. Müller<sup>2</sup>, T. Heckel<sup>2</sup>, D. Gohlke<sup>2</sup>,  
G. Bruno<sup>2</sup>

<sup>1</sup>Chair of NDT & Quality Assurance (LZfPQ), Saarland University, Saarbrücken/Germany

<sup>2</sup>Federal Institute for Materials Research and Testing (BAM), Berlin/Germany

## ABSTRACT

This paper focuses on the aspect on how damage evolution processes in composite materials and structures including matrix fracture, delamination, fibre-matrix debonding, and fibre fracture can be detected by taking advantage of the material's inherent mechanical properties. These properties can be described on the basis of non-linear mechanical phenomena measurable as an inert frequency response signal. The approach is proposed as a means for residual life structural assessment specifically in the context of VHCF.

## KEYWORDS

Composite materials, damage, non-destructive testing, fatigue, non-linear vibration, structural simulation

## INTRODUCTION

Composite materials such as CFRP are exposed to fatigue loading as many other materials are which also includes VHCF. The resulting damaging mechanisms are various and do include matrix fracture, delamination, fibre-matrix debonding and fibre fracture, to just name a few. Degradation of those composite materials needs to be measured by some relevant means where the question is open on how to get this done most efficiently. Established means by doing this is certainly the use of X-ray based computed tomography. However, the effort for doing this may be extremely high and is also limited in terms of size and not to forget cost. Ultrasonic based acoustic methods are an alternative, where again classical ultrasound may be the primary choice. However, if the damages to be detected are fairly small in size then easily transducers have to be used which operate at relatively high frequencies, making the analysis again costly in the end.

An alternative is to look into the vibrational behaviour of materials and here specifically the different vibrational modes in terms of the eigenfrequencies or also being called the eigenmodes of those. Every mechanical system has eigenmodes and this virtually at all scales. It is therefore not just the eigenmodes of the component considered which can be observed but rather also those being generated through the damage mechanisms such as those mentioned above. These may result in some complex vibrational signals being worth to be analysed.



## VHCF TESTING AND CHARACTERISATION OF CFRP COUPONS

In a recently completed project jointly performed with the Institute of Materials Science and Engineering (WKK) of the University of Kaiserslautern/Germany small coupon specimens of the type shown in Fig. 1 have been tested at WKK under VHCF conditions, where further details can be found in [1]. The material used was a commercial carbon fibre reinforced polyphenylsulfide (CF-PPS) of 4.06 mm in thickness, which was cut into bars of 33.5 mm in length and 15 mm in width. The specimens were exposed to a 3-point bending fatigue load applied at frequencies up to 20 kHz.

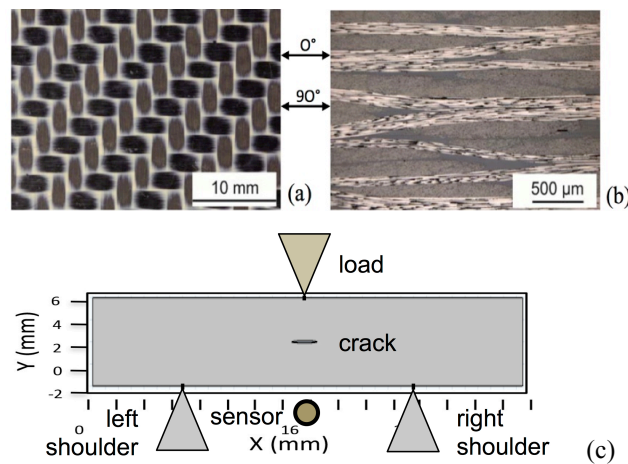


**Fig. 1** a) Light micrographs of the examined CFRP material; b) cross section image showing the 0° and 90° oriented and matrix material; c) 3-point bending experimental setup

Following the observations reported in [1] damages of the character of fibre-matrix-debonding and transversal cracking followed by micro, meta and macro delaminations have been observed which have been summarised under the expression of 'crack densities' and have been carefully analysed. Following this analysis it has been observed that fibre-matrix-debonding has been developing at the onset of fatigue loading while delaminations mainly emerged at 40% and beyond the specimens' fatigue life.

What damage is considered to be needs to be defined. Every material and specifically composite has voids or any other imperfections which are part of the material's pristine condition. To get a feeling of this behaviour some of the specimens were analysed using X-ray computed tomography with an X-ray energy of 60 kV and 150  $\mu$ A as well as a voxel size of 9.5  $\mu$ m without pre-filtering. 500  $\times$  1600  $\times$  1800 voxels of the field of view (FOV) comply with a volume of 4.800  $\times$  15.200  $\times$  17.100  $\mu$ m. Fig. 2 shows the results for the pristine and the damaged condition of a specimen. For the undamaged condition (Fig. 2 left) a large amount of micro-imperfections and micro-cracks can be observed, however, no delaminations, while for the damaged conditions delaminations have been identified (Fig. 2 right). Similar images (Fig. 3) have been obtained through ultrasonic scanning based on immersion testing with the  $\varnothing$  25 mm transducer of 25 MHz centre frequency. It can be observed that different smaller

delaminations seem to gradually merge having most likely started at different of the micro-imperfections observed in the pristine condition.

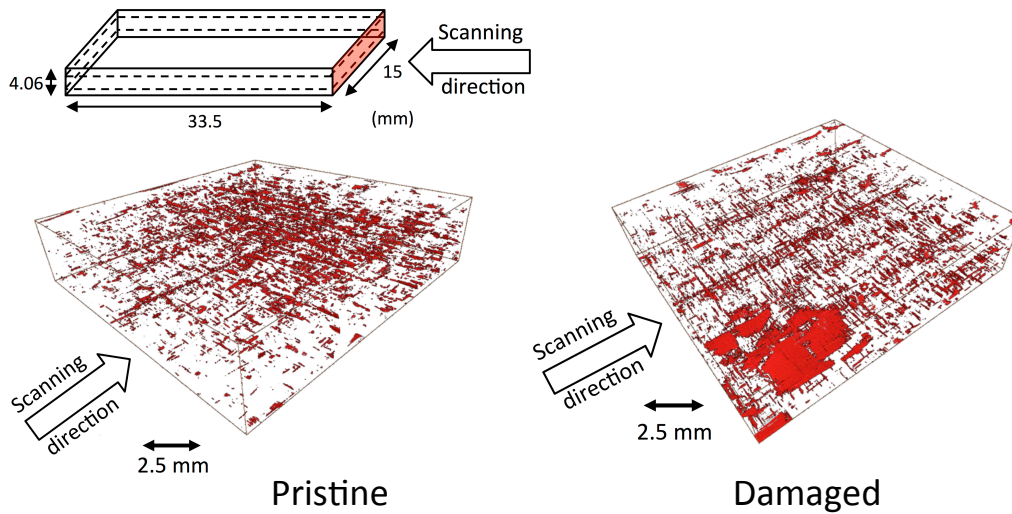


Fig. 2 CT image of pristine composite specimen analysed

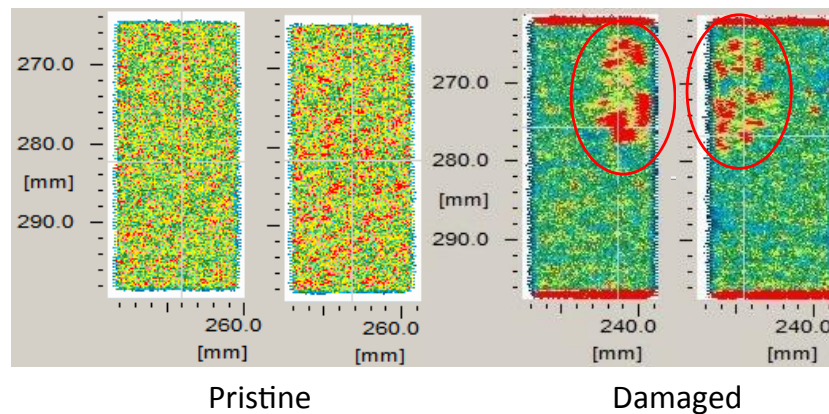


Fig. 3 Ultrasonic scans taken from the top and bottom side of the specimen

### NON-LINEAR CHARACTERISTICS IN DAMAGED CFRP

A material may also be characterised based on its vibrational modes. If a delaminated specimen is brought into vibration it may represent different mechanical systems with different vibrational modes. Fig. 4 shows the model of the delaminated specimen as discussed before. Two cases can at least be considered here: a) the delamination is open (Fig. 4b) and b) the delamination is closed (Fig. 4c). Each case may generate a different eigenfrequency and it can be thought that this difference also applies for the higher vibrational modes.

If a frequency spectrum is determined from the specimens described above then a result is obtained as shown in Fig. 5 below. Besides the 20 kHz frequency, which has been generated due to the VHCF actuation, there is a larger number of higher harmonic frequencies, which are implied by the specimen itself as well as possible manufacturing related imperfections. As soon as those imperfections gradually grow the intensities of their induced eigenfrequencies grow as well in amplitude as can be seen from the right hand figure in Fig. 5. Another effect is that the eigenfrequency due

to the increasing delamination will gradually reduce, which is another effect observed from the disparity between experiment and simulation in the right hand figure of Fig. 5. To explain this disparity a series of simulations has been performed where the (through) delamination was placed at a location similar to where the delaminations were observed in the experiments shown in Figs 2 and 3 and where the delamination size was gradually increased from 1 to 6 mm in length. The results of this are shown in Fig. 6 below. It can indeed be observed that with increasing delamination length the amplitude of the higher harmonic signal increases as well and that the eigenfrequency moves to lower frequencies. With respect to the disparity addressed in Fig. 5 (right) it must therefore be concluded, that the damage occurred in the experiment must have been larger than what had been assumed in the simulation.

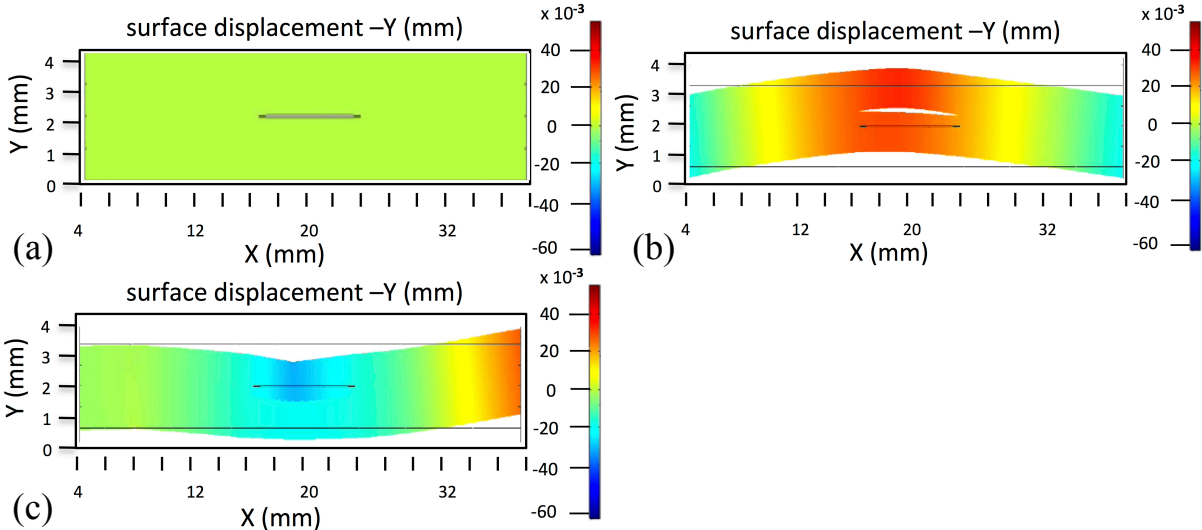


Fig. 4 Simulation of delaminated specimen: a) Neutral position; b) delamination open; c) delamination closed

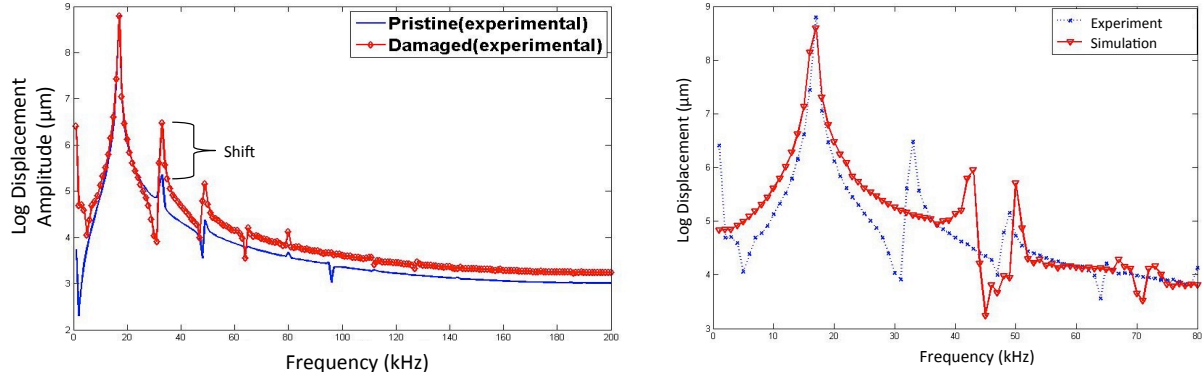


Fig. 5 Higher harmonic vibrational response of composite specimen: comparison between pristine and damaged specimen (left) and comparison between experiment and damaged specimen (right)

**SIMULATION BASED DAMAGE PLOTS FOR STRUCTURAL ASSESSMENT**

The ability to simulate the vibrational behaviour of a delaminated composite material and even structure may lead to the idea to generate damage plots in terms of a data-base that can be used as look-up tables. An example for the specimen considered here is shown in Fig. 7. The 3D-plot considers the delamination size, the location of

the delamination in terms of the position from the left edge and a frequency function. The frequency function is basically a parameter derived from the frequency response such as the FFT-plot where a selection of such parameters is provided in [2].

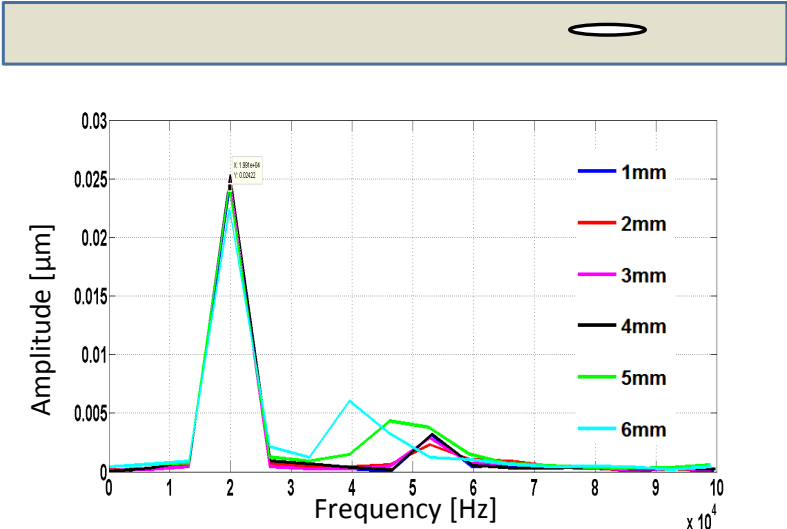


Fig. 6 Fast Fourier transform (FFT) plot obtained from FE simulations performed for composite specimen with an increasing size of a delamination located towards the right hand end of the specimen

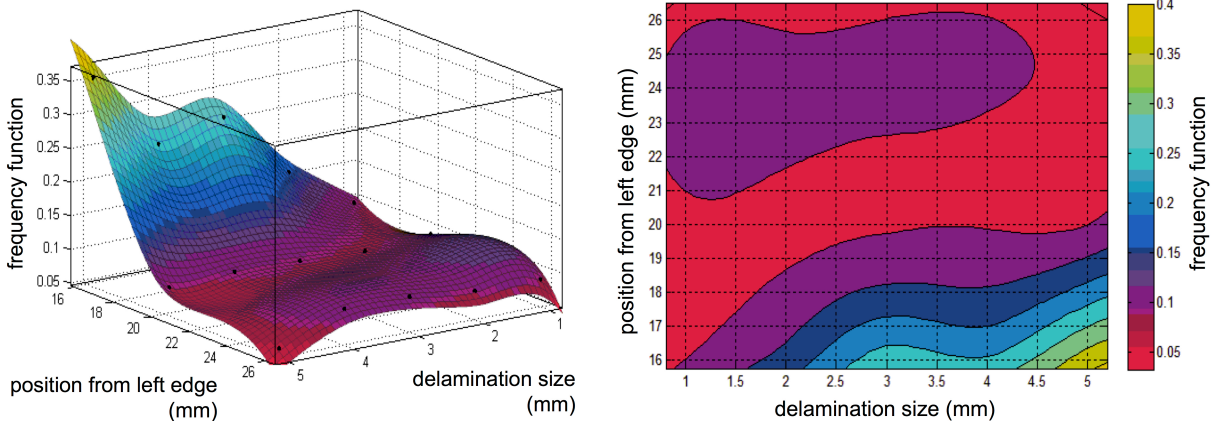


Fig. 7 Simulated frequency response as a function of size and location of a delamination in 3-point bent VHCF specimen

The ability to generate such frequency response plots may allow the degree and location of a delamination to be determined from the frequency response measured. This could therefore become a first approach in terms of assessing damaged structures also under VHCF conditions regarding their degree of damage when applying such an inverse problem approach. The way that could be done is schematically shown in Fig. 8.

**CONCLUSION**

Discussing fatigue damage within the frame of composite materials and structures is a valid point nowadays. This also includes VHCF induced damage. As damage in composite materials accumulates in a non-linear way similar to metals, prognostics

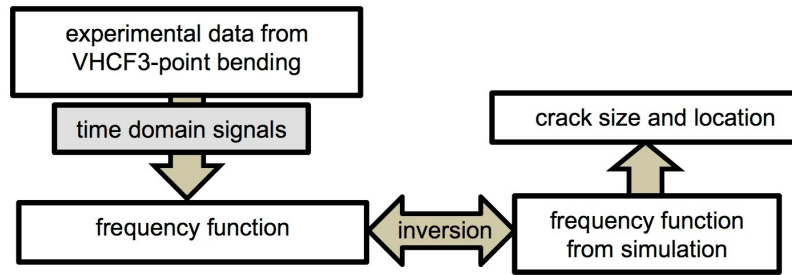


Fig. 8 Inverse problem approach to determine delamination location and size of the VHCF damaged specimen

become difficult, specifically in view of the fact that this non-linearity may even scatter substantially. However, in case the damage tolerance principle should be applied even in composite material structures such that a further light weight potential could be taken advantage of from those materials, then a monitoring principle needs to be implemented that allows monitoring to be performed at a fairly continuous basis. A basis for such a principle may have been laid down with the steps described above. If a sensor or better monitoring system could be implemented into the composite structure considered, which would be able to measure a respective frequency response, then the response signal could be used to determine the structure's damage condition based on a look-up database having been determined beforehand through simulation. What has been shown here for a simple coupon specimen could be possibly extended to real composite structures where the damage tolerance principle could be built in and the resulting inspection performed in the sense of structural health monitoring. The application of such an approach in the context of VHCF may have a further flavour in that regard that the structure may be actuated by the inert high frequency load, that would also generate the higher harmonic vibrations induced by some damage resulting from the structure's degradation.

## ACKNOWLEDGEMENTS

The authors would like to thank Deutsche Forschungsgemeinschaft for financial support of this study in the framework of the priority program "Life<sup>∞</sup>" (SPP 1466).

## REFERENCES

- [1] Backe D., Balle F.: Ultrasonic fatigue and microstructural characterization of carbon fiber fabric reinforced polyphenylene sulfide in the very high cycle fatigue regime; *Composites Science & Technol.*, **126** (2016) pp. 115-121
- [2] Sridaran Venkat R., Starke P., Boller C.: Acoustics Based Assessment of a Composite Material Under Very High Cycle Fatigue Loading; to appear in H.-J. Christ (Ed.): Final Report of Priority Programme SPP 1466, Springer (2017)

**Corresponding author:** c.boller@mx.uni-saarland.de



# INFLUENCE OF R-RATIO ON THE FATIGUE BEHAVIOR OF Ti6Al4V IN THE VERY HIGH CYCLE FATIGUE REGIME

<sup>2)</sup>S. Heinz, <sup>1)</sup>F. Ritz, <sup>1)</sup>T. Beck, <sup>1)</sup>D. Eifler

<sup>1)</sup>Institute of Materials Science and Engineering (WKK), University of Kaiserslautern, P.O. Box 3049, 67653 Kaiserslautern, Germany

<sup>2)</sup>Hydac Technology GmbH, 66280 Sulzbach, Germany

## ABSTRACT

The influence of R-ratio on the fatigue properties of Ti6Al4V was investigated in the VHCF regime with an ultrasonic testing facility of the type "UltraFAST-WKK-Kaiserslautern" (UFK). The UFK allows to control process parameters such as displacement amplitude and power of the ultrasonic generator. The generator power or the temperature are well suited to describe the cyclic deformation behavior at 20 kHz. At R=-1 a multi slope  $S, N_f$  -curve, which can be divided into four ranges, was observed. In the range  $-1 \leq R \leq 0.3$ , a change from surface to subsurface crack initiation occurs in the VHCF regime. With R-values increasing from -1 to 0.3 the tolerable stress amplitude for run-out specimens decreases significantly from  $\sigma_a = 400$  MPa to  $\sigma_a = 235$  MPa. Microscopic investigations indicate that local inhomogeneities in the  $\alpha$ - and  $\beta$ -phase distribution are responsible for subsurface crack initiation in the VHCF regime. For the investigated R-values the fracture surfaces show the typical fish eye structure with a rough optical dark area (ODA) in their center surrounded by a smoother circular area. The size of the ODAs increases with decreasing stress amplitude and increases with increasing number of cycles to failure.

## KEYWORDS

VHCF, Ti6Al4V, R-ratio, cyclic deformation behavior, crack initiation

## INTRODUCTION

Due to attractive properties, i.e. high specific strength and excellent corrosion resistance, titanium alloys are widely used in aerospace application. Compressor blades / disks undergo more than 10 million cycles induced by vibration and/or inhomogenous flow fields and, hence are operated in the Very High Cycle Fatigue (VHCF) regime. Recent investigations show that the stress amplitudes tolerable for Ti6Al4V decrease significantly in the VHCF regime, if  $10^7$  cycles are exceeded [1-3]. Furthermore, a change in the failure mechanisms from surface to subsurface crack initiation as well as grain refinement was observed [3, 4, 9]. To realize  $10^{10}$  cycles and more in an acceptable time, ultrasonic fatigue testing systems, operated at frequencies of about 20 kHz, were developed [5]. At the Institute of Material Science and Engineering of TU Kaiserslautern (WKK), Germany, ultrasonic fatigue tests are performed using the in-house-developed test system "UltraFAST-WKK-Kaiserslautern" (UFK) [3]. In this investigation single step tests (SST) in the range  $-1 \leq R \leq 0.3$  were carried out to evaluate the influence of R on the fatigue behavior of Ti6Al4V in the VHCF regime.

## EXPERIMENTAL PROCEDURES

### Material and specimen design

The fatigue tests were carried out at the  $\alpha + \beta$  titanium alloy Ti6Al4V with the chemical composition 6.45 Al, 4.1 V, 0.01 C, 0.05 Fe, 0.16 O, 0.01 N (weight %) and balance Ti. The

mechanical properties determined in tensile tests according to DIN EN ISO 6892 are given in Table 1.

E in GPa	UTS in MPa	R <sub>p0.2</sub> in MPa	A in %	HV30
103	1010	920	17.5	308

Table 1: Monotonic properties of Ti6Al4V

The SEM micrograph in Fig. 1a shows a cross-section of the Ti6Al4V alloy with about 25 volume % fine grained bcc  $\beta$ -phase embedded in the equiaxed hcp  $\alpha$ -phase.

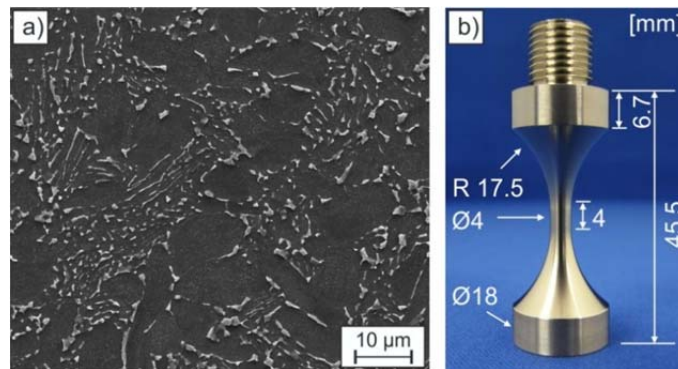


Fig. 1: a) SEM micrograph of the cross-section of the investigated Ti6Al4V, b) Ti6Al4V specimen used for ultrasonic fatigue tests

The specimen design for the ultrasonic fatigue tests is shown in Fig. 1b. The specimen has a gauge length of 4 mm with a diameter of 4 mm. Elastic finite element method (FEM) simulations were used to design a specimen with an eigenfrequency of 20 kHz and sufficiently high stress amplitudes. Additionally, strain gauge measurement and 3D laser scanning vibrometry were used to validate the calculated stress amplitudes.

### Ultrasonic testing facility

An ultrasonic testing facility type “UltraFAST-Kaiserslautern” (U FK), in Fig. 2 was used to investigate the VHCF-behavior of Ti6Al4V.

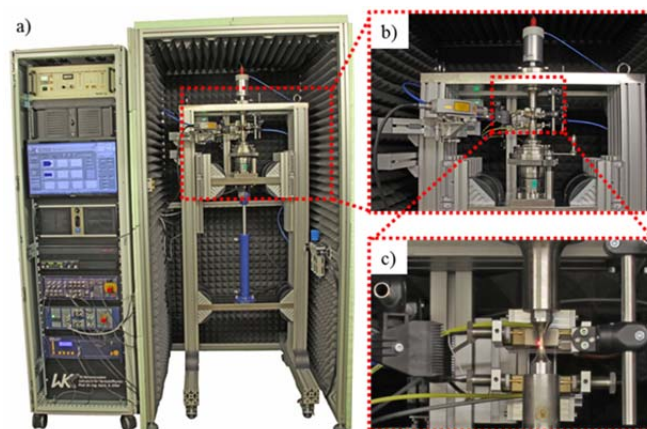


Fig. 2: Ultrasonic testing facility of the type “UltraFAST-WKK-Kaiserslautern” (a), ultrasonic resonance system (b) and specimen mounting (c)



To apply cyclic loads with superimposed mean stresses in the range  $-1 \leq R \leq 0.3$ , a servo-hydraulic cylinder in closed-loop control was used. A central part of the testing facility is the ultrasonic resonance system, consisting of an ultrasonic generator, a piezo-electrical converter and two boosters. The specimens did oscillate with a frequency of 20 kHz. The tests were performed in pulse pause mode to avoid a temperature increase of the specimens of more than 10 K due to cyclic micro-plastic deformation. The measuring unit represents the interface to the external measuring equipment like e.g. a Laser Doppler Vibrometer (LDV) or the infrared sensor for temperature measurement. Furthermore, it records the process parameters of the digital generator and the specimen temperature with a recording rate of 1 kHz. The displacement of the specimens is measured by the LDV and recorded with a rate of 500 kHz. These parameters are well suited to control the loading process and to characterize the fatigue behavior [3, 5]. The used digital ultrasonic generator allows a well defined onset and decay of the oscillation with very short transients.

## RESULTS

### S, $N_f$ – curves

Results of the tests at  $R=-1$  are summarized in Fig. 3. The observed multi slope S,  $N_f$  -curve can be divided into four ranges according to the findings of Kanazawa and Oguma [1, 6]. Range I is the High Cycle Fatigue (HCF) regime, which is characterized by decreasing stress amplitudes until  $\sigma_a = 645$  MPa and a maximum number of cycles to failure ( $N_f$ ) of  $2 \times 10^6$  followed by an almost horizontal portion of the S,  $N_f$  -curve until  $N_f = 4 \times 10^7$  cycles (range II in Fig. 3). Ranges III and IV represent the VHCF regime. Range III is characterized by a considerable decrease of the stress amplitude of about 200 MPa. In range IV a second plateau is observed at about 410 MPa until  $10^9$  cycles and beyond.

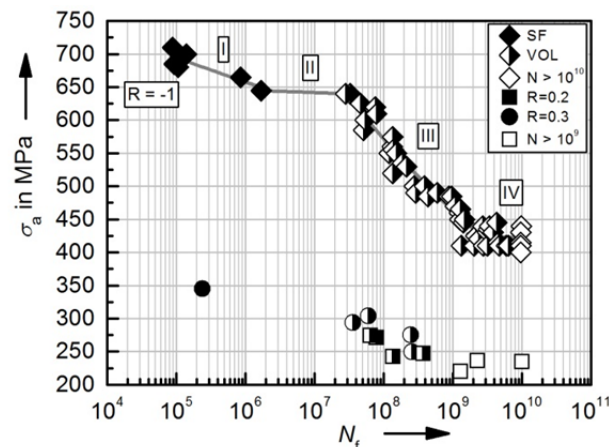


Fig. 3: S,  $N_f$  -curves of Ti6Al4V at  $R = -1, 0.2$  and  $0.3$

At this stress amplitude all specimens exceeded  $10^9$  cycles, some specimens failed between  $10^9$  and  $10^{10}$  cycles, and some reached  $10^{10}$  cycles without failure. At  $\sigma_a = 400$  MPa four specimens ( $\diamond$ ) were tested until  $10^{10}$  cycles without failure. But also in these specimens fatigue cracks were observed. In comparison to range III, the scatter of the data increases significantly in range IV. At the transition from the HCF (range I and II) to the VHCF regime (range III and IV) a change of the failure mechanisms occurs: At stress amplitudes above 645 MPa surface crack initiation was observed, below 645 MPa subsurface cracks dominate. The influence of a raising stress ratio from  $R=-1$  to  $R=0.2$  and  $0.3$  is also shown in Fig. 3. The fatigue strength significantly decreases with increasing  $R$ -value from about 400 MPa at  $R=-1$  to 250 MPa at  $R=0.2$ . As already shown for  $R=-1$  also in the case of positive  $R$ -values a tendency to multi slope S,  $N_f$  -curves is observed at the transition from HCF to VHCF.

Furthermore already the slight increase in R from 0.2 to 0.3 shifts the S, N<sub>f</sub>-data to smaller numbers of cycles to failure. Specimens which exceed 10<sup>9</sup> cycles are marked with open squares □. VHCF crack initiation and growth are very sensitive to a variation in R and the maximum stress, respectively [1, 8, 9]. There is some evidence that crack closure effects are responsible for this behavior [1, 4].

### Microscopic investigations of the fracture surfaces

The fracture surfaces of the specimens tested in the VHCF-regime were investigated by light and scanning electron microscopy. The fracture surfaces are characterized by a fish eye structure with a rough optical dark area (ODA) in their center surrounded by a smoother, circular area, which in some cases reached to the surface of the specimens. Characteristic optical dark areas of specimens tested at R=-1 are shown in Fig. 4. There exists a clear correlation between the stress amplitude, the number of cycles to failure and the size of the ODA, i.e. at the highest stress amplitude the lowest N<sub>f</sub> and the smallest ODA diameter is observed.

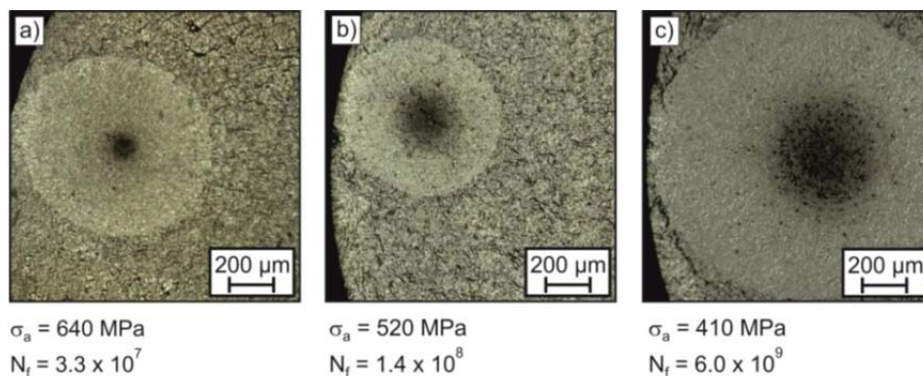


Fig. 4: Influence of  $\sigma_a$  and N<sub>f</sub> on the size of the ODA at R=-1

A characteristic example of an ODA for R=0.3 is shown in the SEM micrographs of Fig. 5 a) and b). In the center of the ODA the surface structure is significantly rougher compared to the surrounding black area.

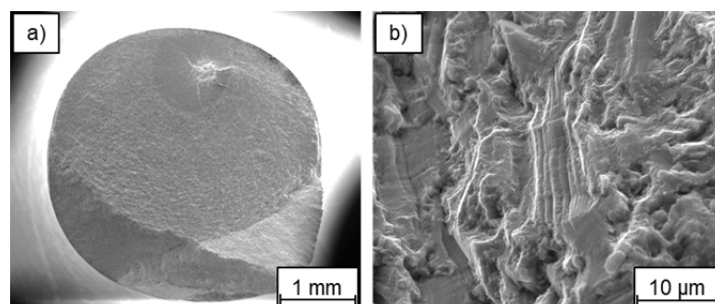


Fig. 5: Characteristic ODA at R=0.3 and  $\sigma_a$  =247 MPa and b) Characteristic facets in the center of an ODA at R=0.3 and  $\sigma_a$  =247 MPa

Furthermore planar facets are a typical feature at positive R-values and seem to be the crack origins. A systematic dependency between the stress amplitude and the location of the subsurface crack initiation site could not be found. Hence, it was assumed that differences in the local microstructure of the Ti6Al4V alloy determine the individual crack initiation site [3]. Light microscopy was used to quantify the radii r<sub>ODA</sub> of the circular ODA. Figure 6a shows the dependency between r<sub>ODA</sub> and the stress amplitude. The size of the ODA nearly linearly

decreases with increasing stress amplitude following the equation  $r_{\text{ODA}} = 459 \mu\text{m} - 0,6 \mu\text{m}/\text{MPa} \times \sigma_a$  (Fig. 6a). Plotting  $r_{\text{ODA}}$  vs.  $\lg N_f$  and linear fitting reveals that  $r_{\text{ODA}}$  increases in an exponential manner with  $r_{\text{ODA}} = 1.4 \mu\text{m} \times N_f^{0.226}$  as shown in Fig. 6b (circles:  $R=0.3$ ; black squares:  $R=0.2$ ; grey diamonds:  $R=-1$ ). The values of  $r_{\text{ODA}}$  were used to calculate the stress intensity factor  $\Delta K_{\text{ODA}}$  by equation (1)

$$\Delta K_{\text{ODA}} = 0.5 \Delta\sigma (\pi (\pi r_{\text{ODA}}^2)^{1/2})^{1/2} \quad (1)$$

according to [7]. The average value of  $\Delta K_{\text{ODA}}$  is  $6.76 \pm 0.39 \text{ MPa m}^{1/2}$  which is in good agreement with Ti6Al4V data in literature [9].

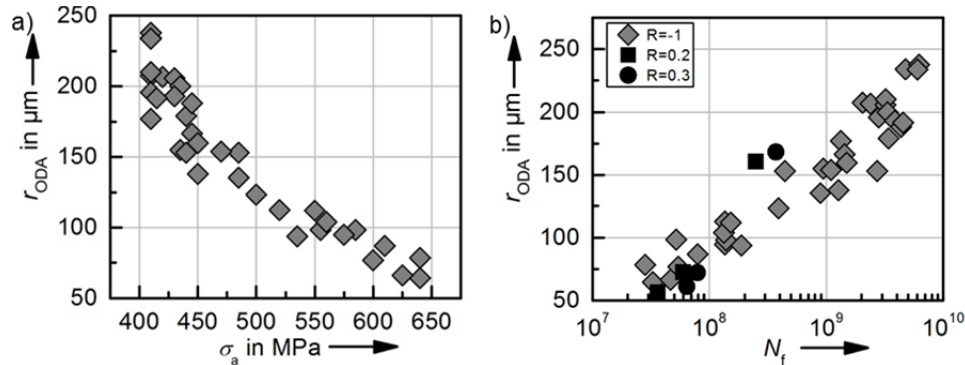


Fig. 6: a) Radius of the ODA versus  $\sigma_a$ , b) Radius of the ODA versus  $N_f$  at  $R=-1, 0,2$  and  $0,3$

Micro crack formation as well as deformation induced twinning was mainly observed in the primary  $\alpha$ -phase and at interfaces between  $\alpha$ - and  $\beta$ -phase. Fig. 7 shows a SEM micrograph of a longitudinal-section through the center of an ODA of a specimen which failed at  $\sigma_a = 460 \text{ MPa}$  at  $R=-1$  after  $1.2 \times 10^9$  cycles. Close to the fracture surface micro cracks were found in larger grains of the primary  $\alpha$ -phase parallel to the ODA surface sections (Fig. 7b). Furthermore, near to the ODAs grain refinement was observed in the VHCF regime in specimen areas with very high plastic deformation. The formation process of nanocrystalline regions seems to be similar to the mechanisms activated in the production of ultrafine grain via severe plastic deformation [9]. Grain refinement was only detected after tests at  $R=-1$  by EBSD analysis of longitudinal sections in different fatigue states and distances from the ODA [3].

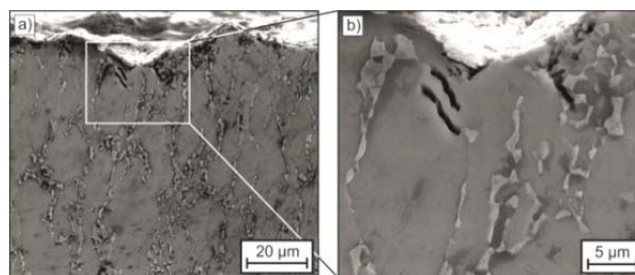


Fig. 7: a) SEM micrograph of a longitudinal-section through the center of an ODA, b) detail

The grain refinement increases with proceeding cyclic loading and decreasing distance to the ODA surface, especially close to growing internal micro cracks. The existence of nanograins additionally could be proven in FIB cross-sections taken just below the ODA surface until a depth of about  $2.6 \mu\text{m}$  (Fig. 8). In a greater depth the original grain size of Ti6Al4V was observed. After raising the  $R$ -value to  $0.2$  and  $0.3$  nanograins were not observed in the FIB section. These results prove that the crucial condition for VHCF grain refinement in Ti6Al4V is a very high local plastic deformation independent if there cracks already exist or not [8].

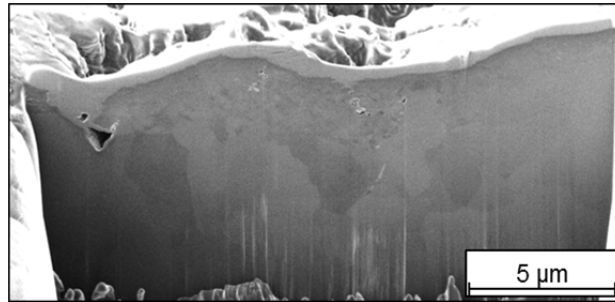


Fig. 8: FIB cross-section near to the ODA of a specimen tested at  $\sigma_a = 430$  MPa and  $R = -1$

With EBSD analysis and FIB cross sections it was proven that under VHCF loading conditions microstructural changes also occur in specimens running  $10^{10}$  cycles without fracture. Nevertheless fatigue induced microstructural changes like the formation of pronounced deformation twins in the hexagonal  $\alpha$ -phase and grain refinement as well as micro cracks could be clearly identified.

## REFERENCES

- [1] Oguma H., Nakamura, T.:  
The effect of microstructure on very high cycle fatigue properties in Ti-6Al-4V  
*Scripta Materialia* 63 (2010), pp. 32-34
- [2] Zuo JH, Wang ZG, Han EH.:  
Effect of microstructure on ultra-high cycles fatigue behavior of Ti-6Al-4V  
*Material Science and Engineering A* 473 (2008), pp. 147-152
- [3] Heinz, S. ; D. Eifler, D.:  
Crack initiation mechanisms of Ti6Al4V in the very high cycle fatigue regime  
*International Journal of Fatigue* 93 (2016) No. 2, pp. 307-308
- [4] McEvily AJ., Nakamura T., Oguma H., Yamashita K., Matsunaga H., Endo M..  
On the mechanism of very high cycle fatigue in Ti-6Al-4V  
*Scripta Materialia* 59 (2008), pp. 1207-1209
- [5] Koster M., Nutz H., Freeden W., Eifler D.:  
Measuring techniques for the very high cycle fatigue behaviour of high strength steel at ultrasonic frequencies  
*International Journal of Materials Research* 103 (2012), pp. 105-112
- [6] Nishijima S., Kanazawa K.:  
Stepwise S-N curve and fish-eye failure in gigacycle fatigue  
*Fatigue & Fracture of Engineering Materials and Structures* 22 (1999), pp. 601-607
- [7] Murakami Y:  
*Metal Fatigue: Effects of Small Defects and Nonmetallic Inclusions*  
Elsevier, Oxford; 2002
- [8] Hong, Y.; Liu, X.; Lei, Z.; Sun, C.:  
The formation mechanism of characteristic region at crack initiation for very-high-cycle fatigue of high –strength steels  
*International Journal of Fatigue* 98 (2016), pp. 108-118
- [9] Su, H.; Liu, X.; Sun, C.; Hong, Y.:  
Nanograin layer formation at crack initiation region for very-high-cycle fatigue of a Ti-6Al-4V alloy  
*Fatigue and Fracture of Engineering Materials and Structures* 00 (2015), pp. 1-15

**Corresponding author:** eifler@mv.uni-kl.de

# INFLUENCE OF MEAN STRESS AND NOTCHES ON THE VHCF-BEHAVIOR OF A MARTENSITIC STEEL FOR LOW-PRESSURE STEAM TURBINE BLADES

<sup>1)</sup>F. Ritz, <sup>1)</sup>T. Beck

<sup>1)</sup> Institute of Materials Science and Engineering (WKK), University of Kaiserslautern, P.O. Box 3049, 67653 Kaiserslautern, Germany

## ABSTRACT

The fatigue behavior of martensitic steel X10CrNiMoV12-2-2 has been investigated for load ratios from  $R = -1$  up to 0.5 and different stress concentration factors (1.09, 1.31 and 2.42) under ambient air conditions up to a maximum of  $2 \cdot 10^9$  load cycles using an ultrasonic fatigue testing system developed at the authors' institute. The S-N-curves for  $\alpha_k = 1.09$  show a flat slope independent on the R-value ( $R = -1$  and  $R = 0.5$ ) with a transition from surface to volume crack initiation from spherical AlCaO or AlCaMgO inclusions at about  $1 \cdot 10^7$  to  $2 \cdot 10^7$  load cycles. As observed in earlier investigations for smooth specimens [1], the maximum number of load cycles where failure occurs increases for higher R-values. With increasing stress concentration factor the fatigue strength for  $2 \cdot 10^9$  load cycles decreases and the S-N-curve's slope becomes steeper in the HCF-regime, especially for  $\alpha_k = 2.42$ . Fatigue failure of notched samples initiates at small surface defects resulting from the turning process ( $\alpha_k = 2.42$ ) or at regions with increased roughness due to formation of extrusions and intrusions at persistent slip bands or other surface defects ( $\alpha_k = 1.31$ ). The maximum number of load cycles where fatigue fracture can be observed at pure tension-compression loading ( $R = -1$ ) is about  $1 \cdot 10^6$  ( $\alpha_k = 2.42$ ) and  $5 \cdot 10^7$  ( $\alpha_k = 1.31$ ). A thin layer of nano-scaled grains below the fracture surface within the fish-eye around the crack initiating inclusion, a so called fine granular area (FGA), could only be observed for slightly notched ( $\alpha_k = 1.09$ ) samples at a load ratio of  $R = -1$ . FGA formation can be explained by the model of Grad et al. [2]. However, other mechanisms, especially cyclic pressing, can't be entirely excluded.

## KEYWORDS

VHCF-behavior, low-pressure steam turbine, mean stress, 12 % Cr-steel

## INTRODUCTION

The development of ultrasonic fatigue testing systems enabled investigations of materials behavior under cyclic loadings beyond the classic fatigue limit at about  $1 \cdot 10^7$  load cycles in acceptable time. It has been shown that the fatigue strength might decrease in the VHCF-regime, often associated with a change in the fracture mechanism especially for Type II materials according to the definition given by Mughrabi [3]. The martensitic 12 %-Cr-steel investigated in the present work is a state-of-the-art material for the last stages in low-pressure steam turbine blades in power plant applications. During decades of service, these components reach the VHCF-regime due to cyclic loads resulting from an inhomogeneous flow field, superimposed by high mean stresses from centrifugal forces. Earlier investigations at the same material showed that load ratio R significantly influences the fracture mechanism and the maximum number of load cycles where failure occurs [1]. These findings correlate well with the results by Schönbauer et al. who also investigated different low-pressure steam turbine steels in the VHCF-regime in a wide range of load ratios [4]. A change of the crack origin from the surface to the specimen's volume (fish-eye) is often reported in literature and, especially for high strength steels at pure tension-compression loading, associated with a fine granular area (FGA) in the vicinity of the inclusion. Several models for FGA formation are proposed describing on the one hand the FGA as a necessary condition for crack initiation

and propagation [2, 5] or, on the other hand, as a result of repeating contact of the fracture surfaces under inert conditions at very low crack propagation rates [6, 7].

## EXPERIMENTAL PROCEDURES

### Material and specimen design

In the present study the martensitic steel X10CrNiMoV12-2-2 was investigated. Specimens were prepared from the root section of steam turbine blades supplied by Siemens Energy. The chemical composition is given in Table 1.

Element	Fe	C	Cr	Ni	Mo	V	Mn	Si
weight %	bal.	0.10	12.02	2.64	1.59	0.34	0.75	0.18

Table 1: Chemical composition of X10CrNiMoV12-2-2

Heat treatment (hardening, tempering and stress relief annealing followed by slow furnace cooling) results in a tempered martensitic microstructure with finely distributed carbides along the former austenite grain boundaries and martensite laths. The mechanical properties (Table 2) combine relatively high strength and ductility.

yield strength [MPa]	tensile strength [MPa]	elongation at fracture [%]	Young's-Modulus [GPa]	Hardness [HV]
843	1001	17.7	213	334

Table 2: Mechanical properties of martensitic steel X10CrNiMoV12-2-2

Three specimen geometries with different stress concentration factors were designed for fatigue testing in the ultrasonic system described below at a load ratio of  $R = -1$  and with superimposed mean stress. Notches with 3.0 mm root diameter and a depth of 0.25 mm were turned for all variants. Different stress concentration factors were achieved by notch radii of 0.25 mm ( $\alpha_k = 2.42$ ), 1.5 mm ( $\alpha_k = 1.31$ ) and 7.7 mm ( $\alpha_k = 1.09$ ). The two highest factors represent a component relevant stress concentration factor ( $\alpha_k = 2.42$ ) and a component relevant stress gradient, respectively ( $\alpha_k = 1.31$ ). The stress concentration factor of 1.09 results from the ratio of Murakami's weighting factors for surface induced and internal crack initiation. The surfaces of  $\alpha_k = 1.09$  and 1.31 samples were mechanically polished which was not possible in case of  $\alpha_k = 2.42$ , due to a very small notch. Single samples of this type have been electropolished to clarify the influence of surface morphology on fatigue life. To correlate the displacement amplitude measured via laser vibrometry at the lower end of the sample with stress in the gauge length and notch root, respectively, elastic FEM-simulations were performed.

### Ultrasonic testing facility

Fatigue tests were carried out using an ultrasonic fatigue testing system, shown in Fig. 1, developed at the author's institute. The main components are the ultrasonic generator (2), converter (3) and the oscillation system including two boosters (10) and the VHCF-sample (9). For increased R-values the mean load is applied by a servohydraulic system consisting of a pump (4), a hydraulic cylinder (5), a traverse (6) and the load frame (7). Fatigue data is

collected and processed simultaneously from the US-generator (dissipated energy, frequency), laser vibrometer (8), an infrared temperature sensor (13), a load cell (14) and an inductive displacement sensor to measure sample elongation as a result of cyclic creep. To avoid temperatures above 50 °C fatigue tests were performed in pulse-pause mode resulting in an effective frequency of approximately 2500 Hz (500 ms pulse and 3500 ms pause) and additional cooling by compressed air.

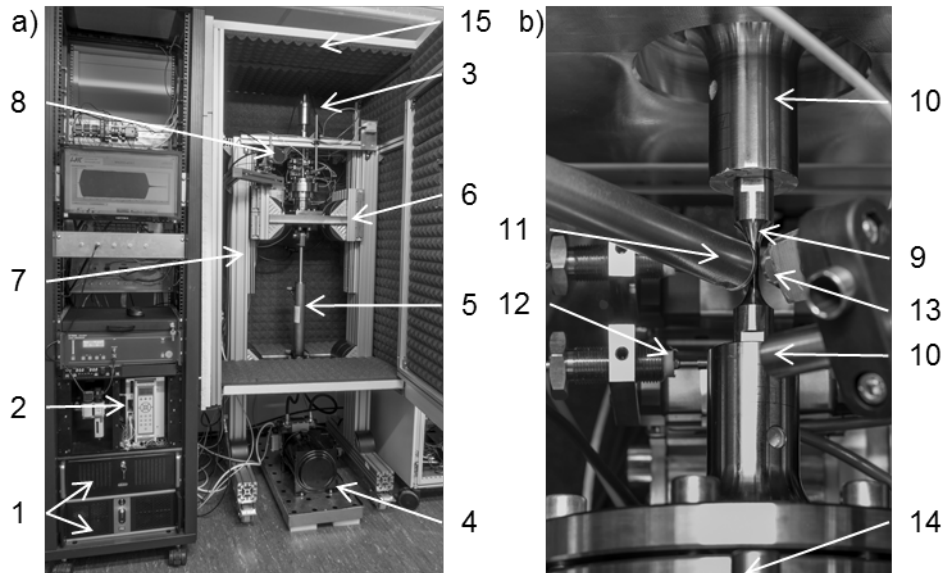


Fig. 1: a) Ultrasonic fatigue testing system b) Detailed view of oscillation system with VHCF-sample

## RESULTS

The results of fatigue tests for three different sample types and load ratios from  $-1 < R < 0.5$  are summarized in S-N-curves in Fig. 2. Failures originated at the sample's surface are plotted as open symbols. Internal crack initiation is represented by half-filled symbols and run-outs by solid symbols with added arrows. For  $\alpha_k = 1.09$  the slopes of the S-N curves plotted as black and grey squares for  $R = -1$  and  $R = 0.5$ , respectively, are rather flat, independent on the R-value. Similar to smooth specimens [1] a transition from surface to internal crack initiation at oxide inclusions of the type AlCaO or AlCaMgO is observed at  $N_f \approx 1 \cdot 10^7$  to  $N_f \approx 2 \cdot 10^7$  which does not correlate with a decrease of the fatigue strength or any change in the S-N-curve's slope. SEM images in Fig. 3 a) and b) show typical crack initiating surface and volume inclusions, respectively, as well as the fish-eye structure in case of volume cracking. Note that the number of load cycles where fracture can occur increases with increasing R-value: While for  $R = -1$  no failure was observed at  $N > 1 \cdot 10^8$ , samples failed even beyond  $2 \cdot 10^9$  load cycles for  $R = 0.5$ . The fatigue strength at  $2 \cdot 10^9$  load cycles is about 524 MPa and 251 MPa for  $R = -1$  and  $R = 0.5$ , respectively. For all samples failed in the VHCF-regime at  $R = -1$ , fish-eye fracture with a region of increased roughness around the crack initiating inclusion, indicating FGA formation, was found. For increased R-values internal crack initiation and propagation was observed without formation of a thin nanocrystalline layer below the fracture surface, as seen in Fig. 3 d) showing the fracture surface of a sample failed in the VHCF-regime at  $R = 0.5$ . Both, the presence of a FGA after fatigue tests at  $R = -1$  and preservation of the initial microstructure in case of superimposed mean stress was proved by SEM investigations of FIB-cross-sections perpendicular to the fracture surface at NSC of University of Kaiserslautern. The FGA formation can be described by the model of Grad et al. [2] where a local decrease of the fatigue crack propagation



threshold as a result of grain refinement in the plastic zone near the crack tip is postulated which enables a crack to propagate. This grain refinement continues during early crack propagation until stress intensity range exceeds the threshold value of the initial microstructure and the crack continues to grow without FGA formation. Nevertheless, other interpretations, such as a discontinuous FGA formation proposed by Sakai [5], or the NCP (= Numerous Cyclic Pressing) approach by Hong et al. can't be excluded [6, 7]. In the latter model, grain refinement is not assumed to take place in front of the crack tip. Instead, FGA formation is caused by repeating contact of the fracture surfaces under inert conditions at very low crack propagation rates. Due to reduced or entirely missing contact of the fracture surfaces at increased R-values this model might explain the absence of a FGA observed for high mean stress in the present work as well for several other materials [6, 7]. The discussed results are in good accordance with investigations by Schönbauer et al. who investigated similar steam turbine steels and also found a correlation between stress ratio and maximum number of cycles to failure [4]. In one case the S-N-curve's slope also changed with increasing R-value [8].

For increased stress concentration factors, especially  $\alpha_k = 2.42$  (plotted as black circles / see Fig. 2), the S-N-curve's slope becomes steeper in the HCF-regime. Note that for this stress concentration factor only surface crack initiation is observed and no failures occur beyond  $1 \cdot 10^6$  load cycles. Fracture is originated at small surface defects with elliptical shape (length:  $\approx 20 \mu\text{m}$  / height:  $\approx 10 \mu\text{m}$ ) resulting from the turning process as shown in a SEM image with tilted view in Fig. 3 f). Electropolishing the specimen (black triangles, Fig. 2) does, with one exception indicating a shift to higher tolerable stress amplitudes, not significantly influence the fatigue strength of sharply notched samples. The fatigue strength calculated according to the  $\arcsin\sqrt{P}$  method taking only as-turned samples into account is 213 MPa.

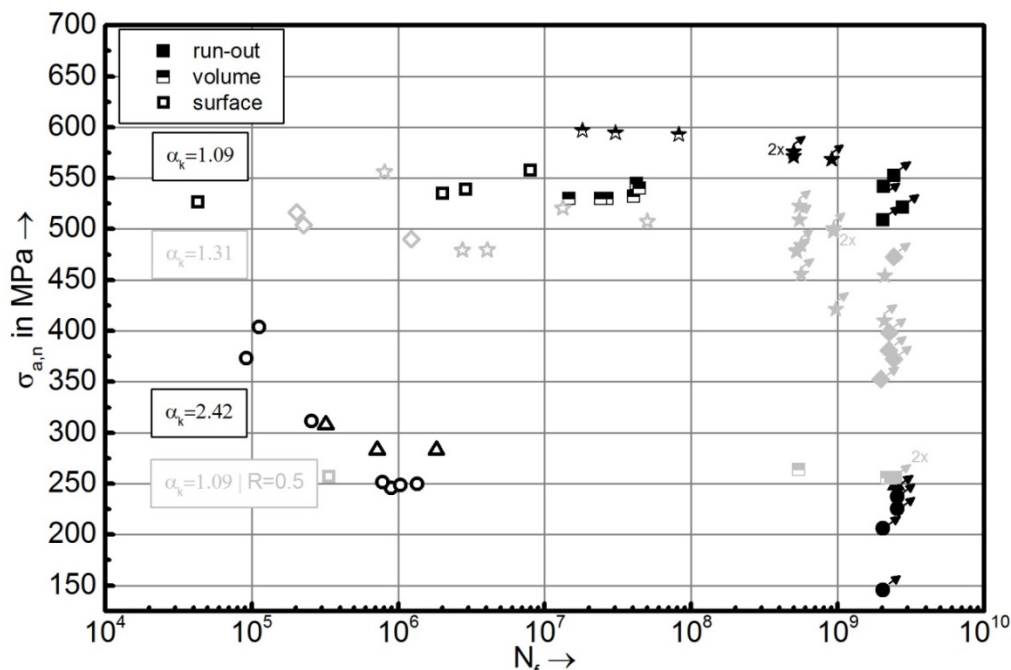


Fig. 2: S-N-curves for fatigue tests at ambient air up to a maximum number of load cycles of  $2 \cdot 10^9$  for three different stress concentration factors and R-values from -1 to 0.5

Selected run-out samples, represented by stars in Fig. 2 (black:  $\alpha_k = 1.09$  / grey  $\alpha_k = 1.31$ ), have been re-tested again at a higher stress amplitudes at least up to  $5 \cdot 10^8$  load cycles. For  $\alpha_k = 1.09$  three run-out samples have been re-tested at stepwise increased stress amplitudes and failed in the VHCF-regime at internal defects (smaller inclusions / microstructural inhomogeneities). Note that these samples still reach a very high number of load cycles and

do not fail in the LCF- or HCF-regime, despite remarkably high stress amplitudes. One possible reason might be microstructural changes during the previous run-out test. The fracture surface of a re-tested sample failed with FGA-formation at a microstructural inhomogeneity is shown in Fig. 3c).

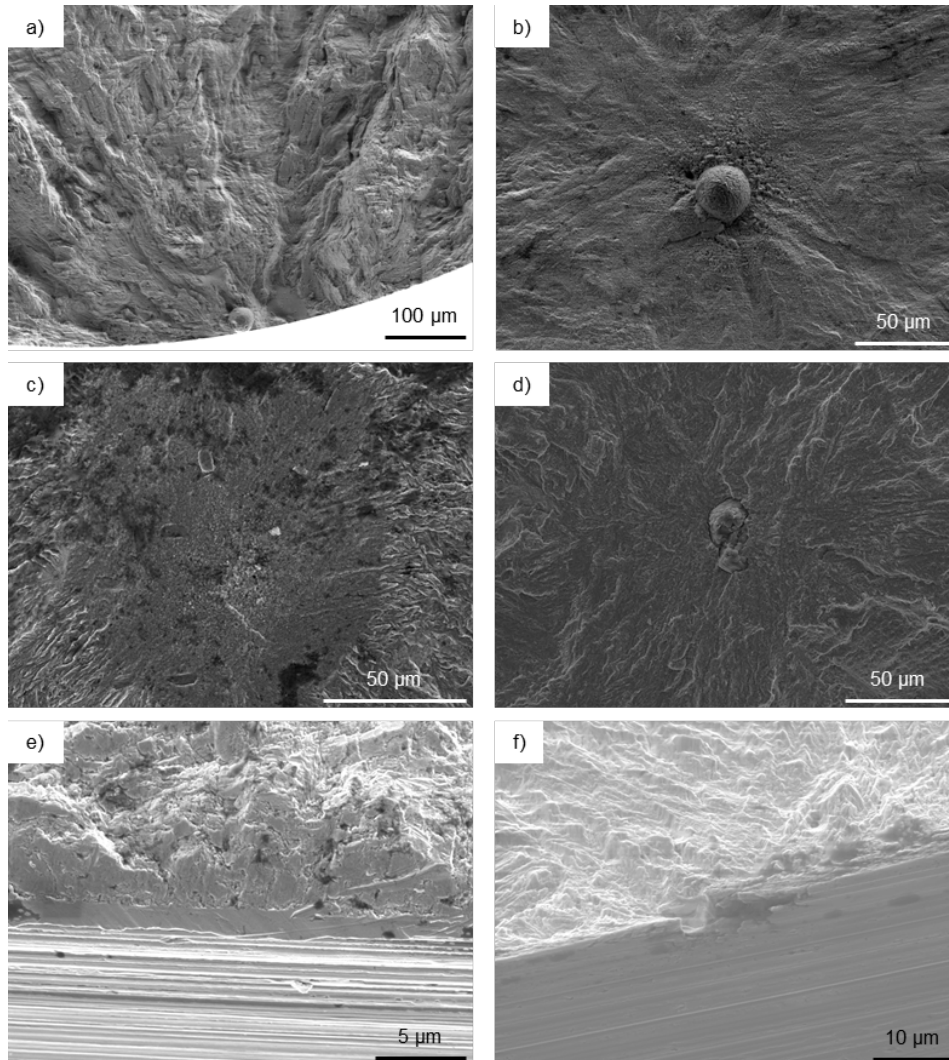


Fig. 3: SEM-analyses of fracture surfaces of: a)  $\alpha_k = 1.09$ ,  $R = -1$ ,  $\sigma_a = 527$  MPa,  $N_f = 43294$   
b)  $\alpha_k = 1.09$ ,  $R = -1$ ,  $\sigma_a = 532$  MPa,  $N_f = 4.1 \cdot 10^7$  c) re-tested sample  $\alpha_k = 1.09$ ,  $R = -1$ ,  
 $\sigma_a = 593$  MPa,  $N_f = 8.2 \cdot 10^7$  d)  $\alpha_k = 1.09$ ,  $R = 0.5$ ,  $\sigma_a = 264$  MPa,  $N_f = 5.4 \cdot 10^8$  e) re-tested  
sample  $\alpha_k = 1.31$ ,  $R = -1$ ,  $\sigma_a = 479$  MPa,  $N_f = 2.75 \cdot 10^6$  f)  $\alpha_k = 2.42$ ,  $R = -1$ ,  $\sigma_a = 246$  MPa,  
 $N_f = 900224$

For  $\alpha_k = 1.31$ , five run-out specimens were re-tested at increased stress amplitudes. Similar as for  $\alpha_k = 1.09$ , fatigue strength of these samples becomes, compared to the as-received state, shifted to higher values. Furthermore, in case of re-tested samples with  $\alpha_k = 1.31$ , VHCF-failure starting at surface defects or persistent slip bands is possible. In Fig. 3 e) crack initiation at a PSB with characteristic fracture surface tilted by  $45^\circ$  against the specimen axis near the crack origin is shown. Fatigue fracture initiated at surface or volume inclusions has not been observed so far for this stress concentration factor. The fatigue strength for  $\alpha_k = 1.31$  taking only as-received samples into account (grey diamonds in Fig. 2) calculated by the  $\arcsin\sqrt{P}$  method is 441 MPa.

## CONCLUSIONS AND OUTLOOK

The VHCF-behavior of martensitic steel X10CrNiMoV12-2-2 has been investigated under the influence of notches and R-values from -1 up to 0.5. The S-N-curves for  $\alpha_k = 1.09$  show a flat slope independent on the R-value ( $R = -1$  and  $R = 0.5$ ) with a transition from surface to volume crack initiation at about  $1 \cdot 10^7$  to  $2 \cdot 10^7$  load cycles which is not associated with a decrease of the fatigue strength or a change in the S-N-curve's slope. Run-out samples re-tested at significantly higher stress amplitudes still failed in the VHCF-regime. FGA formation was observed only for pure tension-compression loading and can be described by the model of Grad et al. [2] while other mechanisms like the NCP-model by Hong et al. [6] or discontinuous FGA / crack formation according to Sakai et al. [5] can't be excluded. Fatigue strength decreases with increasing stress concentration factor while internal crack initiation is avoided and, especially for  $\alpha_k = 2.42$ , a steeper slope of the S-N-curve is observed. Current investigations focus on further fatigue testing at increased R-values and clarification of the FGA formation mechanism as well as possible changes in the microstructure during run-out fatigue tests leading to a higher fatigue strength for re-tested samples.

## ACKNOWLEDGEMENT

The authors gratefully acknowledge funding of the present work by the German Research Association (DFG) in the framework of priority program 1466 "life $\infty$ ". The authors also thank Siemens Energy SE, Mülheim / Ruhr, Germany, for providing the test material as well as NSC, TU Kaiserslautern, for supporting the present study by FIB preparations.

## REFERENCES

1. Kovacs, S., T. Beck, and L. Singheiser, Influence of mean stresses on fatigue life and damage of a turbine blade steel in the VHCF-regime, *International Journal of Fatigue* 49 (2013), pp. 90-99
2. Grad, P., et al., Mechanism of fatigue crack initiation and propagation in the very high cycle fatigue regime of high-strength steels, *Scripta Materialia*, 67 (2012) No. 10, pp. 838-841.
3. Mughrabi, H., Specific features and mechanisms of fatigue in the ultrahigh-cycle regime, *International Journal of Fatigue*, 28 (2006) No. 11, pp. 1501-1508.
4. Schönbauer, B.M., et al., Pit-to-crack transition under cyclic loading in 12% Cr steam turbine blade steel, *International Journal of Fatigue*, 76 (2015), pp. 19-32.
5. Sakai, T., Review and Prospects for Current Studies on Very High Cycle Fatigue of Metallic Materials for Machine Structural Use, *International Journal of Fatigue*, 3 (2007 ) No. 3, pp. 425-439.
6. Hong, Y., et al., The formation mechanism of characteristic region at crack initiation for very-high-cycle fatigue of high-strength steels, *International Journal of Fatigue*, 89 (2016), pp. 108-118.
7. Su, H., et al., Nanograin layer formation at crack initiation region for very-high-cycle fatigue of a Ti-6Al-4V alloy, *Fatigue & Fracture of Engineering Materials & Structures*, 2016.
8. Schönbauer, B.M., K. Yanase, and M. Endo, VHCF properties and fatigue limit prediction of precipitation hardened 17-4PH stainless steel, *International Journal of Fatigue*, 88 (2016), pp. 205-216.

**Corresponding author:** ritz@mv.uni-kl.de

# COAXING EFFECT OF MAGNESIUM ALLOYS UNDER ROTATING BENDIGN IN VERY HIGH CYCLE REGIME

Y. Nakamura<sup>1)</sup>, T. Kasuya<sup>2)</sup>, T. Shimizu<sup>1)</sup>

<sup>1)</sup> National Institute of Technology, Toyota College,  
2-1 Eisei-cho, Toyota, Aichi, 471-8525 Japan

<sup>2)</sup> Advanced Engineering Course, National Institute of Technology, Toyota College,  
2-1 Eisei-cho, Toyota, Aichi, 471-8525 Japan

## ABSTRACT

In order to investigate the coaxing effect of magnesium alloy, stress-incremental tests were carried out on magnesium alloys, AZ31, AZ61 and AZ80 by means of cantilever-type rotating bending fatigue testing machine. Stress-incremental tests were started from 10 MPa lower stress than the fatigue strength at  $10^9$  cycles in each specimen. It was found that AZ31 and AZ61 indicated a marked coaxing effect. On the other hand, in AZ80, the noticeable coaxing effect was hardly appeared. Hardness was examined before and after the stress-incremental test and the conventional fatigue test using micro-Vickers hardness tester. Based on the hardness measurement, it was suggested that the coaxing effect in AZ31 and AZ61 was attributed to work-hardening. The stress incremental test results were analyzed by Miner's rule. In AZ31 and AZ61, the cumulative damage values in almost all stress-incremental test results are more than unity.

## KEYWORDS

Magnesium alloy, coaxing effect, miner's rule, rotary bending

## INTRODUCTION

Fatigue limit can be improved by understressing followed by a process of small step-wise increasing of stress amplitude, which is known as coaxing effect [1]. Over the past years, the coaxing effect has been studied for ferrous metals, and consequently it has been indicated that the coaxing effect was attributed to strain-aging, work hardening and the strengthening at the crack tip of non-propagating cracks [1-3]. However, the researches on the coaxing effect of non-ferrous metals are relatively few, compared to ferrous metals.

In the present study, three types of extruded magnesium alloy with different strength levels were prepared and used in stress-incremental tests. The purpose of the present work is to clarify the effect of strength level on the coaxing behavior in magnesium alloys.

## EXPERIMENTS

### Materials

The materials used in this study were extruded magnesium alloys, AZ31, AZ61 and AZ80. Their chemical compositions are given in Table 1. Fig.1 shows microstructures of materials. The average grain sizes of AZ31, AZ61 and AZ80 were  $48.5\mu\text{m}$ ,  $14.0\mu\text{m}$  and  $11.0\mu\text{m}$ ,

respectively. Table 2 indicates mechanical property of the materials. Fig.2 shows the fatigue specimen configurations, whose central part of the specimen surface was buff-finished after polishing by the emery paper with the grade of #2000.

Material	Al	Zn	Mn	Si	Fe	Cu	Ni	Mg
AZ31	3.0	1.1	0.31	0.007	0.002	0.001	0.001	Bal.
AZ61	5.9	0.6	0.280	0.010	0.002	0.002	0.002	Bal.
AZ80	8.1	0.5	0.25	0.038	0.002	0.002	0.001	Bal.

**Table 1:** Chemical composition of materials. [in mass%]

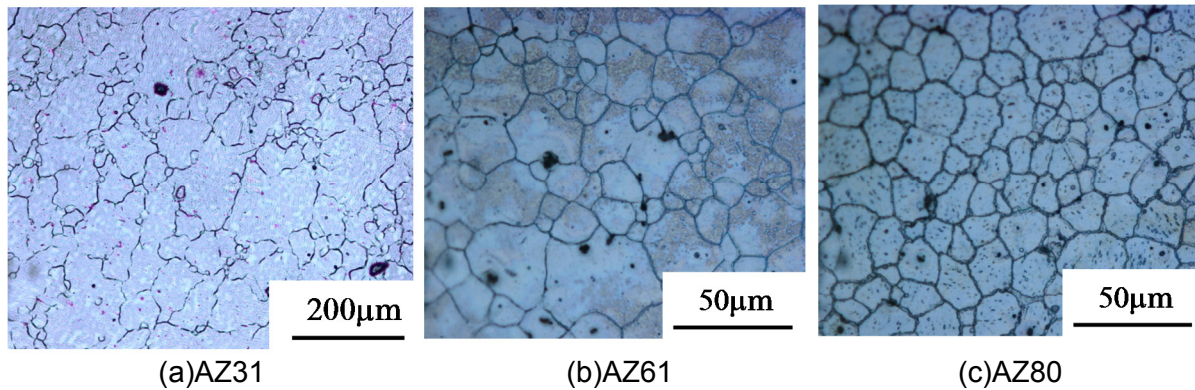


**Fig.1:** Microstructure of materials.

Material	Tensile strength (MPa)	0.2% proof stress (MPa)		Elongation (%)	Vickers hardness
		Tension	Compression		
AZ31	232	197	64	19	50
AZ61	309	221	121	13	56
AZ80	341	223	157	16	62

**Table 2:** Mechanical properties of materials.

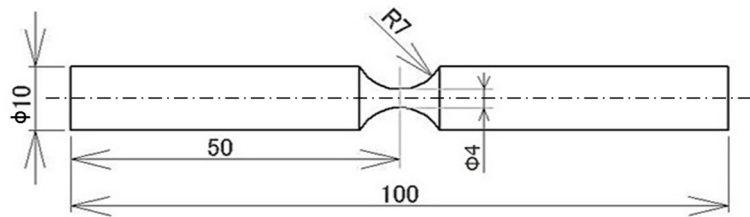


**Fig.2:** Specimen configurations.

### Procedures

Fatigue tests were performed using cantilever-type rotary bending fatigue testing machines operating at a frequency of 53Hz in laboratory air. Stress-incremental tests were started at a stress level of 10MPa below the fatigue strength at  $10^9$  cycles of each material, i.e., initial stress,  $\sigma_{ini}$ . If no failure occurred after given cycles,  $N_s$  ( $10^6$ ,  $10^7$  and  $10^8$  cycles), then the stress level was increased by a small increment of 10MPa. This procedure was repeated until fatigue failure took place.

Hardness was examined before and after the stress-incremental test using micro-Vickers hardness tester. After experiments, fracture surfaces were examined using a scanning electron microscope (SEM).

## EXPRIMENTAL RESULTS AND DISCUSSIONS

### Fatigue strength

The  $S-N$  curves of AZ31, AZ61 and AZ80 under constant stress amplitude are shown in Fig.3. As can be seen in the figure, all the  $S-N$  curves show no clear fatigue limit, with the curves decreasing continuously with an increase of the number of stress cycles to failure. As expected from tensile strength and Vickers hardness in Table 2, the fatigue strength of AZ80 is higher than that of AZ31 and AZ61. In the case of AZ80, interior-crack initiations occurred at stress levels  $\leq 190\text{MPa}$ . Fig.4 shows the SEM image of the crack initiation site of AZ80 failed at  $180\text{MPa}$  with  $N_f=11,228,660$ . Clear fish-eye was observed at the crack initiation site. However, no inclusion was found at the center of fish-eye.

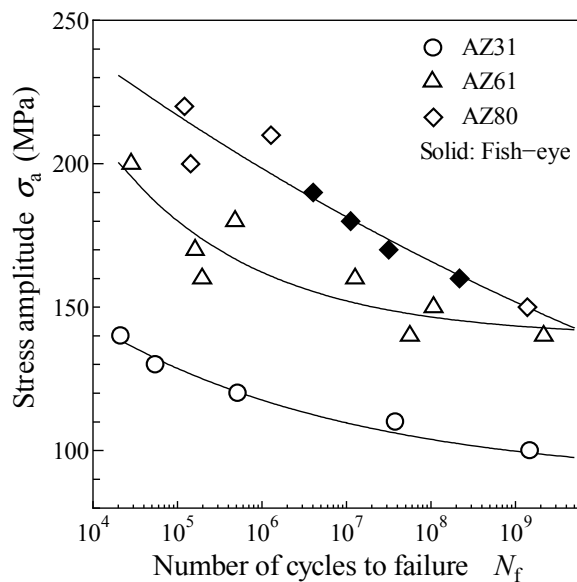


Fig.3: S-N diagram.

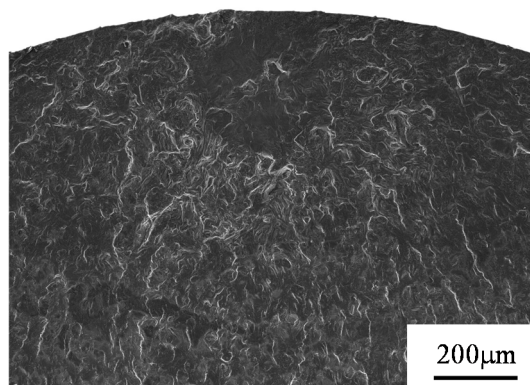


Fig.4: Appearance of fish-eye observed under stress-incremental test in AZ80.

## STRESS INCREMENTAL TEST RESULTS

The results of stress incremental test in AZ31, AZ61 and AZ80 are shown in Fig.5 with the S-N curve obtained by conventional fatigue test which is constant stress amplitude fatigue test. As can be seen in Fig.5 (a) and (b), AZ31 and AZ61 indicate a marked increase of failure stress. Therefore, the coaxing effect is quite evident in AZ31 and AZ61. On the other hand, in AZ80, the noticeable coaxing effect was hardly appeared. This means that the improvement of fatigue strength by understressing does not occur in AZ80.

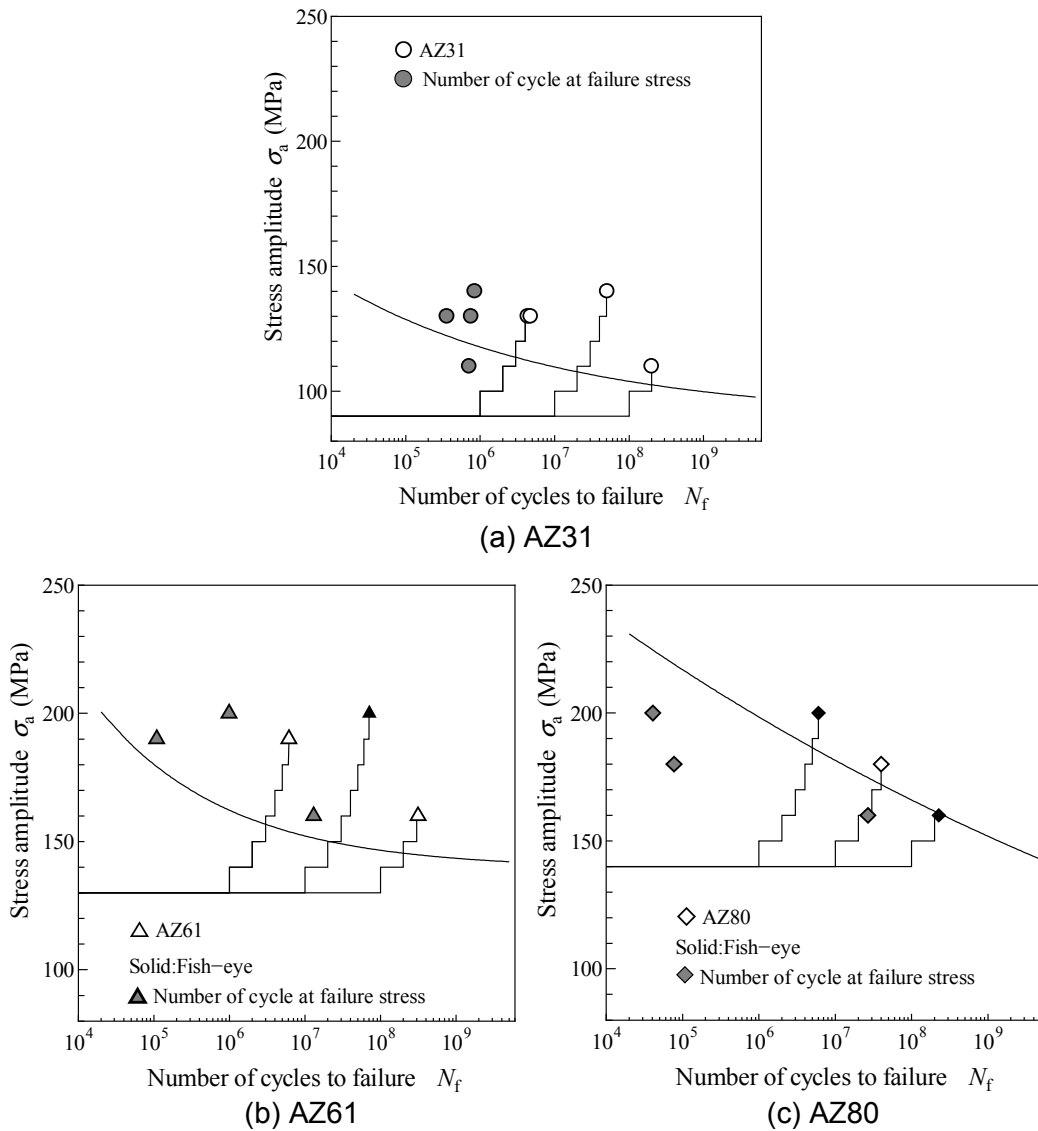


Fig.5: Stress-incremental test results.

## HARDNESS TEST RESULTS

It has been pointed out that the coaxing effect was attributed to work-hardening. Thus, after conventional and stress-incremental tests hardness near the failure site of the specimens was measured using micro-Vickers hardness tester. The results obtained are shown in Fig.6 with the hardness before test. As can be seen in Fig.6 (a) and (b), Vickers hardnesses after stress-incremental tests were higher than those of before experiments and after conventional fatigue



test, except for the case of the number of cycles in a step of  $N_s=10^6$  cycles in AZ31. On the other hand, increasing of hardness was not found in AZ80. Therefore, it is suggested that work-hardening is significant in the coxing effect observed in AZ31 and AZ61.

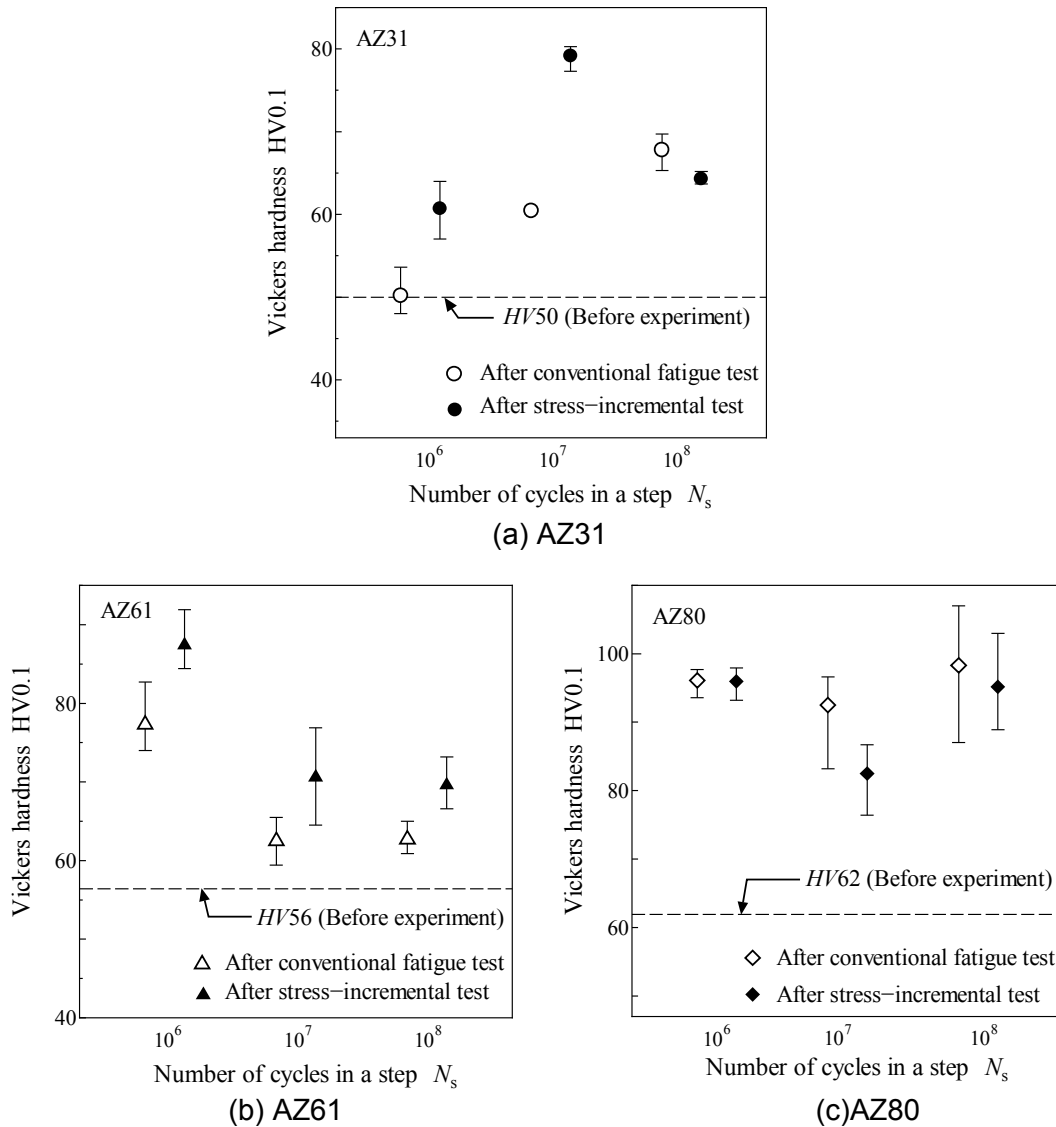
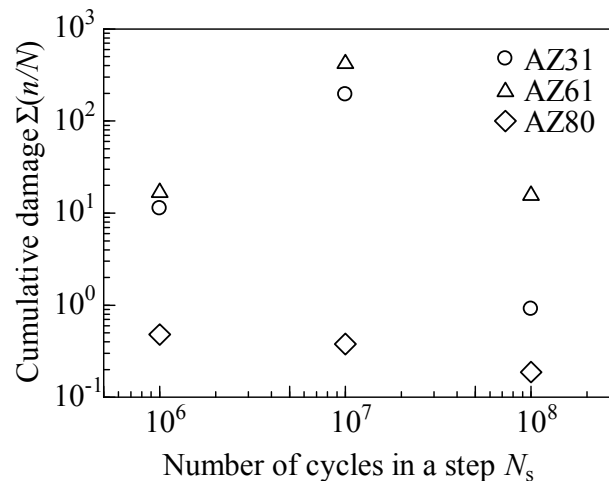


Fig.6: Vickers hardness before and after fatigue test.

### CUMULATIVE DAMAGE ANALYZED BY MINER'S RULE

The stress-incremental tests results were analyzed by Miner's rule [4]. Fig.7 indicates the result of analysis. Vertical axis of the figure indicates the cumulative damage value, whereas horizontal axis indicates the number of cycles in a step. In AZ31 and AZ61, the cumulative damage values in almost all stress-incremental test results are more than unity, indicating coxing effect was found in AZ31 and AZ61. However, the cumulative damage has no relation to the number of cycles in a step. Because the cumulative damage value for the number of cycles in a step of  $N_s=10^8$  cycles is lower than that for the number of cycles in a step of  $N_s=10^7$  cycles. The reason is not clear at the present stage of this work, and this is an important subject to be resolved in the future.



**Fig.7:** Cumulative damage as a function of number of cycles in a step  $N_s$ .

## CONCLUSIONS

In order to investigate the coaxing effect of magnesium alloy, stress-incremental tests were carried out on magnesium alloys, AZ31, AZ61 and AZ80 by means of cantilever-type rotating bending fatigue testing machine. The results obtained are as follows:

- (1) AZ31 and AZ61 indicated a marked coaxing effect. On the other hand, in AZ80, the noticeable coaxing effect was hardly appeared
- (2) Hardness was examined before and after the stress-incremental test and the conventional fatigue test using micro-Vickers hardness tester. Based on the hardness measurement, it was suggested that the coaxing effect in AZ31 and AZ61 was attributed to work-hardening.
- (3) The stress incremental test results were analyzed by Miner's rule. In AZ31 and AZ61, the cumulative damage values in almost all stress-incremental test results are more than unity.

## REFERENCES

- [ 1 ] Sinclair G.M.:  
An Investigation of the Coaxing Effect in Fatigue of Metals  
Proceedings, Am.Soc.Testing Mats Vol.52, (1952), pp.743-758
- [ 2 ] Nishitani H., Tanaka S., Todaka T.:  
Relation between micro-cracks and coaxing effect of aged 0.15% steel after quenching at low temperatures  
Journal of the Society of Materials Science, Japan, Vol.29, (1980), pp.143-149.
- [ 3 ] Nakajima M., Nakamura Y., Shimizu T., Mochizuki Y.:  
Coaxing Effect of High Strength Steels with Different Strength Levels  
Journal of the Society of Materials Science, Japan, Vol.62, (2013), pp.547-553.
- [ 4 ] Miner M.A.:  
Cumulative Damage in Fatigue  
Journal of Applied Mechanics, Vol.12, (1945), pp.A159-164.

**Corresponding author:** nakamura@toyota-ct.ac.jp

# DEVELOPMENT OF A NEW SURFACE MODIFICATION TECHNIQUE: SCANNING CYCLIC PRESS AND ITS APPLICATION FOR THE IMPROVEMENT OF FATIGUE LIFE OF MAGNESIUM ALLOY AZ31

N. Fujimura<sup>1)</sup>, T. Nakamura<sup>1)</sup>, T. Wajima<sup>2)</sup>

<sup>1)</sup> Division of Mechanical and Space Engineering, Faculty of Engineering,  
Hokkaido University, Kita 13, Nishi 8, Kita-ku, Sapporo, Hokkaido, 060-8628 Japan

<sup>2)</sup> HyBridge Co. Ltd., 2-35, Kita 23, Nishi 3, Kita-ku, Sapporo, Hokkaido,  
001-0023 Japan

## ABSTRACT

A new surface modification technique, scanning cyclic press (SCP), was developed. SCP scans a metal surface with a vibrating indenter under precise loading control based on servo fatigue testing machine and can apply a variable cyclically compressive load. This study applied SCP to magnesium alloy AZ31 to investigate the effect on fatigue properties. After applying SCP, the specimen's surfaces were observed by using a laser scanning microscope and uniaxial push-pull fatigue tests were conducted. As a result, surface roughness of SCP-treated specimens slightly increased; however, the fatigue life became longer than that of untreated specimens. To clarify the reason for the improvement effect, fracture surfaces and the microstructures of the specimens were investigated in detail on the basis of SEM and microscopic observations. SEM observation showed differences between the fracture surfaces of the untreated and SCP-treated specimens. The origin of fracture was at the surface in the untreated specimen. In the SCP-treated specimen, however, the fracture origins were sub-surface and a band-like layer just beneath the surface was observed on the fracture surface, whereas the layer did not exist on that of the untreated specimen. The layer corresponded to a mesh-patterned microstructure formed at the surface by SCP. The result suggests that SCP modified the specimen's surface layer and this layer suppressed crack initiation from surface.

## KEYWORDS

Surface modification, scanning cyclic press, magnesium alloy, improvement of fatigue life

## INTRODUCTION

Severe plastic deformation (SPD), which modifies the microstructure of metallic materials by using large plastic strain, is widely used in many fields. In SPD techniques, severe surface plastic deformation (S<sup>2</sup>PD) effectively improves hardness and fatigue strength at metal surfaces by creating a nanocrystalline layer on bulk material. The techniques used to strike workpiece surfaces by using ultrasonic vibration, such as ultrasonic nanocrystal surface modification (UNSM) [1] and ultrasonic impact treatment (UIT) [2], has attracted attention as a useful surface modification.

On the other hand, we developed a new surface modification technique, scanning cyclic press (SCP), which uses precise loading control based on servo fatigue testing machines. As shown in Fig. 1, SCP scans a metal surface with a vibrating indenter under loading control and can apply a variable cyclically compressive load with a variable frequency lower than ultrasound. Our previous study clarified that SCP created a fine microstructure, including a nanocrystalline layer, at the surface of low carbon steel S25C and improved its fatigue strength [3]. The

detailed mechanism of nanostructural refinement using SCP, including whether or not it is the same as that of UNSM or UIT, is still under investigation; however, this technique is likely to increase fatigue properties of metallic materials.

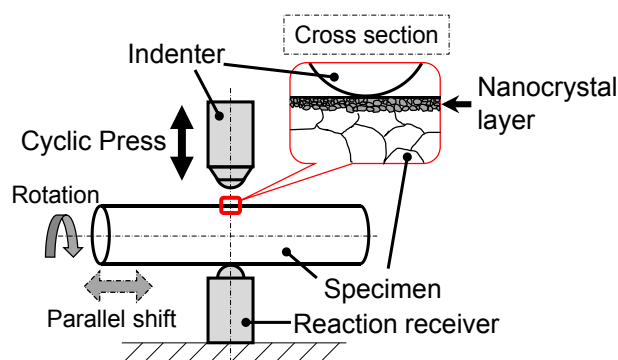


Fig. 1: Schematic drawing of scanning cyclic press

On the basis of the above background, this study applied SCP to an extruded magnesium alloy AZ31 to investigate its effect on fatigue properties. This material is light and has an excellent specific strength, but has a lower fatigue strength compared with that of steel and other light metals such as titanium and aluminum. After applying SCP, the specimen's surfaces were observed and uniaxial push-pull fatigue tests were conducted to clarify the effect on fatigue properties. Fracture surfaces and the microstructure were investigated on the basis of SEM and microscopic observations.

## EXPREMENTAL PROCEDURES

### Material and specimen

The material was an extruded magnesium alloy AZ31. The chemical components of the material were Al: 3.0, Zn: 1.1, Mn: 0.31, Si: 0.007, Fe: 0.002, Cu: 0.001, Ni: 0.001, and Mg: Bal. (wt. %). The supplied material was a 16-mm-diameter round bar extruded at a temperature of 673 K with an extrusion rate of 5 m/min. The average grain size was 45  $\mu\text{m}$ . The mechanical properties: 0.2% proof stress and tensile strength were  $\sigma_{0.2} = 197$  MPa and  $\sigma_B = 224$  MPa, respectively. An hourglass-shaped specimen with a parallel part of  $\phi 4 \times 2$  mm was used. The specimen's surface was mirror finished by polishing with emery paper (grits from 600 to 2000) followed by buffing with alumina abrasives (particle size: 1  $\mu\text{m}$ ).

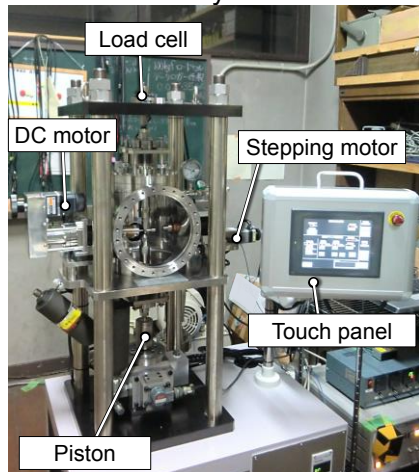
### Surface modification by scanning cyclic press

Fig. 2a shows an image of the SCP surface modification machine. This machine consists of the following parts: a hydraulic actuator to vibrate an indenter for applying cyclically compressive load to a specimen, a DC motor to rotate the specimen, a stepping motor to feed the specimen in the axial direction, and a load cell to detect the magnitude of the applied loading. Fig. 2b shows a close-up of a specimen set in the cyclically loading fixture. The specimen is supported by an indenter connected to the actuator and a reaction receiver connected to the load cell. During rotating and feeding the specimen, a cyclically compressive load is applied to the specimen's surface by the vibrating indenter.

By using the above machine, uniaxial sinusoidal compressive loading was applied to the specimen's surface in ambient air at room temperature. The maximum and minimum values of the cyclic loading were respectively 29.4 N and 0 N, and the frequency was 200 Hz. The

number of cyclic loading in SCP was  $8.0 \times 10^6$  cycles. The rotation speed and the feed rate of the specimen were respectively 2 rpm and 0.01 mm/sec. SCP scanned a range of  $\pm 4$  mm from the center of the specimen in the axial direction and the scanning range was the entire circumference of a parallel part and a part of R-parts connected to the parallel part.

a. Overview of SCP system



b. Close-up of specimen set in cyclically loading fixture

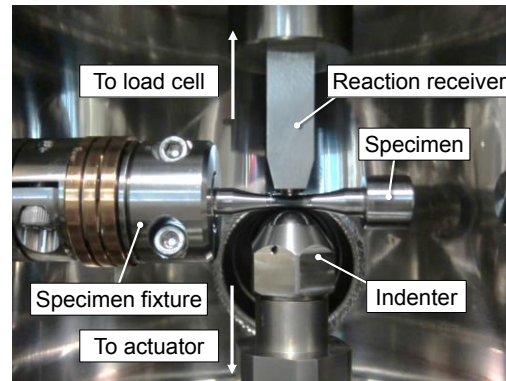


Fig. 2: SCP surface modification machine

### Fatigue test conditions

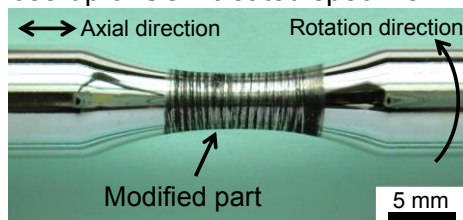
To investigate the effect on fatigue properties of AZ31 applied SCP, uniaxial push-pull fatigue tests were conducted by using a servo hydraulic fatigue testing machine. Sinusoidal loading was applied to untreated specimens and SCP-treated specimens in ambient air at room temperature. A stress ratio and a frequency of the cyclic loading were  $R = -1$  and  $f = 120$  Hz.

## EXPERIMENTAL RESULTS AND DISCUSSION

### Surface observation after applying SCP and quantitative evaluation of the change

Fig. 3 shows the surface of the SCP-treated specimen. A dark gloss was observed at the middle part of the SCP-treated specimen (Fig. 3a). Fig. 3b shows a magnified image of the modified part where streaks on the surface are aligned regularly in the axial direction. Pitches between streaks were about  $300 \mu\text{m}$ , and corresponded to a feed per revolution; calculated from the rotation speed and the feed rate condition in SCP.

a. Close-up of SCP-treated specimen



b. Magnification of modified part in 3a



Fig. 3: Surface observation of specimen after applying SCP

To quantitatively investigate the change in surface state of the modified part, the surface roughness was measured by using a color 3D laser scanning microscope (VK-9700/9710 Generation II, KEYENCE). Areal roughness parameter (arithmetic mean roughness  $R_a$ ) was

determined from the 3D image obtained from the laser microscope. Two measurement points on the circumference, measuring 820  $\mu\text{m}$  long and 60  $\mu\text{m}$  wide, were set at the specimen's center with equal angular spacing of 180 degrees.

Fig. 4 shows microscopic surface images of the middle of the specimen and the profile curves of the positions marked by the black triangles before and after applying SCP. The results of surface roughness measurement are listed in Table 1. Before applying SCP, there was no substantial asperity on the surface of a mirror-polished specimen (Fig. 4a), and the surface roughness  $R_a$  was 0.047  $\mu\text{m}$ . After applying SCP, there were fine irregularities (the profile curves in Fig. 4b), a pattern similar to that of a fish scale (the red arrow in Fig. 4b), and dark abrasion powder (the red circle in Fig. 4b) on the streaked surface of the SCP-treated specimen. The surface roughness  $R_a$  was 0.725  $\mu\text{m}$ . These results indicated that the surface roughness slightly increased after applying SCP; however, the change was small.

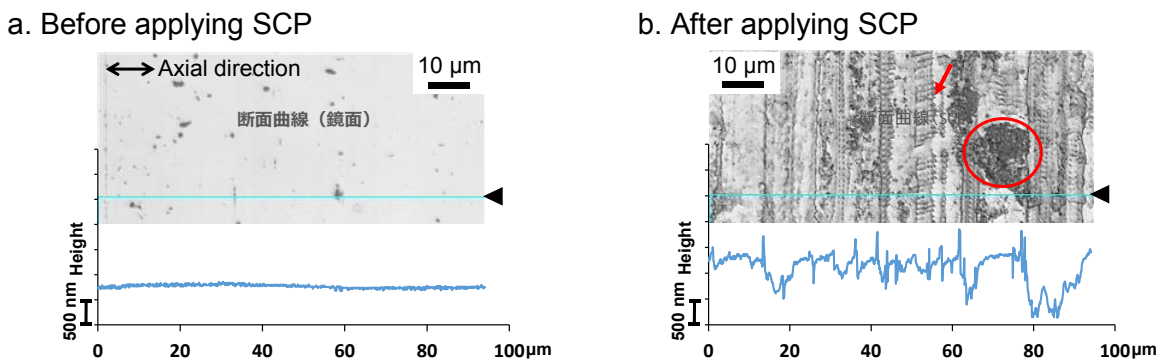


Fig. 4: Microscopic surface images of the middle of the specimens and their profile curves

	Surface roughness $R_a$ [ $\mu\text{m}$ ]	
	Mirror polished	After SCP
Average	0.047	0.725
Standard deviation	0.01467	0.19255

Table 1: Surface roughness  $R_a$  at the center of specimen

### Surface hardness and microstructure observation of SCP-treated AZ31

The Vickers hardness of the SCP-treated specimen was measured at five points on the circumference of the modified part. Table 2 lists the measurement results. The Vickers hardness increased to almost twice as much after applying SCP.

	Vickers hardness Hv	
	Mirror polished	After SCP
Average	60	117
Standard deviation	8	11

Table 2: Vickers hardness at the center of specimen (test force: 1 kg)

Fig. 5 shows the transverse structure of the SCP-treated specimen. A fine mesh-patterned region was observed beneath the surface and the depth from the surface reached about 50  $\mu\text{m}$ . Under the mesh-patterned region, twins with some lines in the crystal grains were formed. The twins did not exist at the center of the cross section of the specimen. The observation showed that the mesh-patterned region and twins were formed by SCP, and their formation might be the cause of the increase in the surface hardness of AZ31.

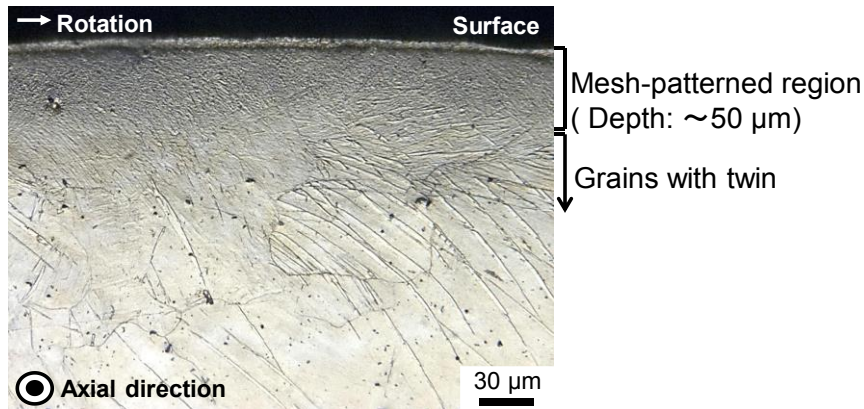


Fig. 5: Microstructure of a cross section of SCP-treated specimen

### Fatigue test results

Fig. 6 shows the  $S-N$  plots of untreated specimens and SCP-treated specimens. The fatigue life of SCP-treated specimens became longer than that of untreated specimens. Comparing the results at 120 and 100 MPa of SCP-treated specimens with those of untreated specimens, the fatigue lives were about 17 to 100 times longer.

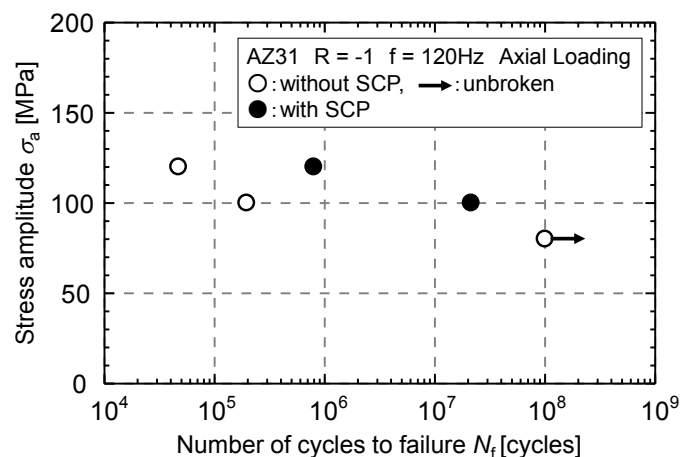


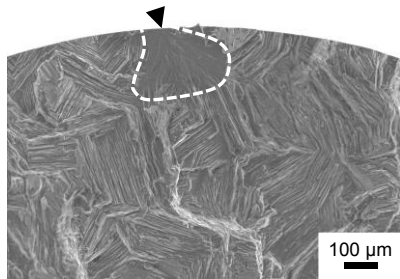
Fig. 6:  $S-N$  diagrams of AZ31 without or with SCP

### Observation of fracture surface

To clarify the reason for the improvement effect on fatigue life, fracture surfaces were investigated in detail on the basis of SEM observations. Fig. 7 shows fracture surfaces of an untreated specimen and a SCP-treated specimen fatigued at a stress amplitude of 100 MPa. A facet, outlined with a white dotted frame in Fig. 7a, was located at the surface. It showed that the origin of fatigue fracture was at the surface in the untreated specimen. On the fracture surface of the SCP-treated specimen, a band-like layer just beneath the surface (above the white dotted line shown in Fig. 7b) was observed. This layer did not exist beneath that of the untreated specimen. The depth of the layer was about 50  $\mu\text{m}$  and corresponded to the mesh-patterned region shown in Fig. 5. Some crack initiation sites were observed in the sub-surface; for example, the facet shown by the black arrow in Fig. 7b and those shown in Fig. 8. Around the facets shown in Fig. 8b, a fine granular area formed by repeating contact of fracture surfaces was observed. These fracture surface features showed that sub-surface fractures occurred in the SCP-treated specimen. Thus, the results suggest that SCP modified the surface layer of the AZ31 specimen and this layer suppressed crack initiation from the surface.



a. Untreated specimen ( $\sigma_a = 100$  MPa)



b. SCP-treated specimen ( $\sigma_a = 100$  MPa)

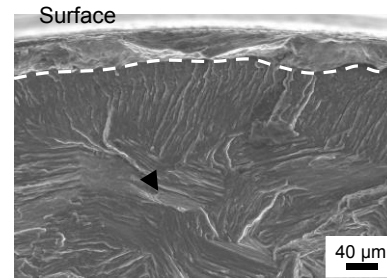
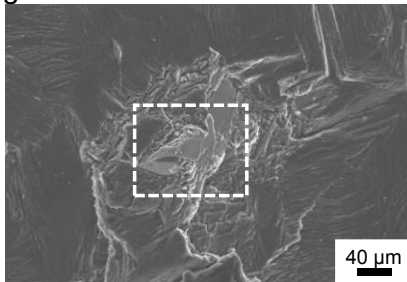


Fig. 7: SEM observations of fracture surfaces around crack initiation site of AZ31 specimens

a. Image around crack initiation site



b. Magnification of the area framed in 8a

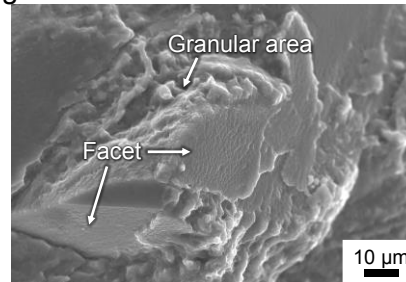


Fig. 8: SEM observations of interior crack initiation site of AZ31 with SCP ( $\sigma_a = 100$  MPa)

## SUMMARY AND CONCLUSIONS

A new surface modification technique, scanning cyclic press (SCP), was applied to magnesium alloy AZ31 to investigate the effect on fatigue properties. Uniaxial fatigue tests showed that fatigue life of a SCP-treated specimen was about 17 to 100 times longer than that of an untreated specimen. In the SCP-treated specimen, fatigue fracture origins were sub-surface and a band-like layer just beneath the surface was observed on the fracture surface, whereas the layer did not exist on that of the untreated specimen, which fractured from the surface. The result suggested that SCP modified the surface layer of the specimen and this layer suppressed crack initiation from the surface.

## ACKNOWLEDGMENT

This work was supported by the Matching Planner Program from JST.

## REFERENCES

- [1] Wu, B.; Zhang, J.; Zhang, L.; Pyoun, Y.S.; Murakami, R.: Effect of Ultrasonic Nanocrystal Surface Modification on Surface and Fatigue Properties of Quenching and Tempering S45C Steel *Applied Surface Science*, Vol. 321, (2014), pp. 318-330.
- [2] Togasaki, Y.; Tsuji, H.; Honda, T.; Sasaki, T.; Yamaguchi, A.: Effect of UIT on Fatigue Life in Web-Gusset Welded Joints *Journal of Solid Mechanics and Materials Engineering*, Vol. 4, No. 3, (2010), pp. 391-400.
- [3] Miyazaki, K.; Nakamura, T.; Fujimura, N.; Shibayama, T.; Wajima, T.: A Development of Scanning Cyclic Press Aiming for Nanostructural Surface Refinement and Its Application to Low Carbon Steel *Proceedings of Mechanical Engineering Congress, 2016 Japan, J1610203*, (2016).

**Corresponding author:** fujimura@eng.hokudai.ac.jp

# INFLUENCE OF HYBRID SURFACE MODIFICATION ON VERY HIGH CYCLE FATIGUE STRENGTH OF VARIOUS STEEL MATERIALS

**Koichiro NAMBU, Noboru EGAMI**

Toyota Institute of Technology, 12 Hisakata Tenpaku-ku, Nagoya City, Aichi, Japan  
Meijo University, 1-501 Shiogamaguchi, Tenpaku-ku Nagoya-city, Aichi, Japan

## **Abstract**

It is the purpose of this study to clarify influence of the hybrid surface modification process on very high cycles fatigue strength of steel materials. The hybrid surface modification process is the surface modification process that combined fine particle peening process with gas carburizing process. High-strength gears steel DSG2 and chrome molybdenum steel ASTM4118 were used for specimen. 3 kinds specimen (quenching tempering specimen (QT), gas carburizing (C) and hybrid surface modification process (CP)) were prepared. Fatigue experiment were performed using ultrasonic fatigue testing machine. Fatigue strength of C and CP specimens were higher than QT specimens. It was not different in C and CP specimens. As result of fracture observation, the fracture origin of C and CP specimens was destruction in 0.5mm from surface. In very high cycle region, nonmetallic inclusion was observed in the fish-eyes center.

## **Keywords**

Fatigue, Fine particle peening, fish-eye, surface treatment

## **1. Introduction**

In recent years, machinery and structures have been required to be safe and have a long service life. An indispensable part of doing so is increasing the strength of materials. Hybrid surface modification, which combines gas carburizing treatment and fine particle peening (FPP), is a method that should help further improve the fatigue strength. As the first stage, gas carburizing treatment produces high toughness, excellent wear resistance, and fatigue resistance. As the second stage, FPP treatment improves the fatigue strength by imparting a high compressive residual stress to the material surface.

Conventionally, the fatigue strength of high-strength steel and surface-modified material is assumed to be almost constant at  $10^7$  cycles. However, recent studies on very long service lives exceeding  $10^7$  times have reported fatigue failure originating not from the surface but from inclusions inside the material. In addition, the phenomenon of two-step bending in the S–N curve has been reported. Thus, a service life of up to  $10^7$  cycles is insufficient for evaluating the fatigue strength in the very long life domain. However, low-speed fatigue tests have so far required enormous amounts of testing time and labor and thus are difficult to perform. Therefore, the use of a high-speed fatigue testing machine is being studied as a method of evaluating these fatigue characteristics. The ultrasonic fatigue testing machine makes it possible to perform a high-speed fatigue test at a cycle frequency of 20 kHz by utilizing the resonance action of the test piece.

In this study, an ultrasonic fatigue testing machine was used to evaluate the fatigue strength of a hybrid surface modified material in the gigacycle domain and the influence of this treatment on the fatigue strength characteristics.

## 2. Specimens and experiment method

### 2-1. Test materials

For the test material, steel for high-strength gears (DSG 2) and chromium molybdenum steel for machine structures (SCM 420) were used. Table 1 presents the chemical components, and Fig. 1 shows the shape and dimensions of the test pieces. Because the ultrasonic fatigue testing machine uses resonance action to perform the fatigue test, the resonance dimensions of the test piece were calculated by the wave equation. However, the resonating dimension is somewhat different from the actual size. Therefore, an onsite test was conducted to determine the optimum specimen shape.

### 2-2. Specimens

Three types of specimens were used: qualified material (QT material), gas carburized material (C material), and hybrid surface modified material (CP material). After the base material was heat-treated (primary quenching at 1163 K for 1 h, secondary hardening at 1113 K for 1 h, tempering at 463 K for 1 h), it was machined to a predetermined shape with emery paper (#180–#2000) and mirror-finished with buffing (6  $\mu\text{m}$ , 1  $\mu\text{m}$ ). In order to remove residual stress, vacuum annealing was performed at 873 K for 1 h. The C material was carburized with C 4 H 10 gas. The CP material was subjected to two-stage peening in the order of steel and ceramics for FPP after gas carburization, as given in Table 2.

Table 1 Chemical compositions (mass%)

	C	Si	Mn	Cu	Ni	Cr	Mo
DSG2	0.21	0.19	0.72	0.12	0.06	0.99	0.16
SCM420	0.21	0.04	0.56	0.06	0.86	1.00	0.28

Table 2 FPP conditions

Material of particles	Diameter of shot ( $\mu\text{m}$ )	Air press (MPa)	Coverage (%)	time (s)
FSS	50	0.49	<100	40
FHB	50	0.39	<100	40

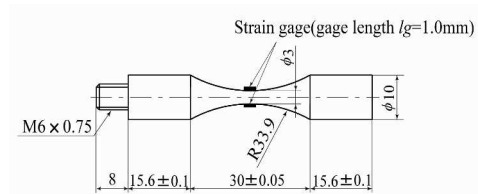


Fig. 1 Fatigue specimens

### 2-3. Fatigue experiment method

For the ultrasonic fatigue test, an ultrasonic fatigue testing apparatus (USF-2000) manufactured by Shimadzu Seisakusho was used. The fatigue test was performed at room temperature in atmosphere with a sine wave having the stress ratio  $R = -1$  and an operating frequency of 20 kHz. Because the ultrasonic fatigue testing machine operates at high speed, it generates heat near the resonance point. Therefore, in order to prevent the influence of heat, the machine was operated intermittently by alternating the execution period ( $t_e = 110$  ms) and the stop period ( $t_p = 500$  ms) with forced cooling by compressed air.

## 3. Results and discussion

### 3-1. Result of hardness measurement

Fig. 2 shows the hardness distribution for each treated material. Both the DSG 2 and SCM 420 materials had low hardness of around HV 660 near the surface. This may have been due to the influence of the carburized abnormal layer. On the other hand, the hardness around the surface of the CP material was about HV 860 for the DSG 2 material and about HV 840 for the SCM 420 material. However, the increase in hardness was limited to the vicinity of the surface. Therefore, the effect of the FPP treatment was assumed to be limited to a depth of 10  $\mu\text{m}$ , which was considered to be a hardened layer. The extremely high hardness obtained with the CP material was considered to be due to martensite in the retained austenite and refinement of the structure. In addition, the

effective hardened layer of the C material was confirmed to have a depth of about 0.25 mm for both the DSG 2 and SCM 420 materials.

### 3-2 Result of the fatigue experiment

Fig. 3 shows the fatigue test results for the QT, C, and CP materials of (a) DSG 2 and (b) SCM 420. For the C and CP materials, the first horizontal part of the S–N curve increased by about 400 MPa compared with the QT material. This may be because a high compressive residual stress was imparted to the vicinity of the surface by gas carburizing and the hybrid surface reforming treatment, which greatly increased the hardness near the surface. The fatigue limit of the QT material (Fig. 3(b)) could not be determined because it was below the set stress width of the ultrasonic fatigue test. For high strength materials, the two-step bending phenomenon of the S–N curve has been reported at the gigacycle scale <sup>1–12</sup>. Even in this study, fisheye-type internal fracture was confirmed around  $10^6$  times and is presumed to be a two-step bending phenomenon, but it seemed to be influenced by heat on the high-stress side. Thus, it could not be concluded that the failure was due to fatigue. In addition, there was not much difference between the C and CP materials, and FPP was not observed to improve the fatigue strength. The FPP treatment may not have had an effect because the high-cycle area failed internally. However, no difference was found between the C and CP materials even on the short-life side without internal failure. When a high stress of 800 MPa or more was applied to DSG 2 and 700 MPa or more was applied to in SCM 420, heat was generated in the central portion of the test piece. Heat may have had a strong influence because the central part of the test piece had a diameter as thin as 3 mm. Furuya et al. (13) reported that data could not be obtained when high stress of more than 900 MPa was applied to SNCM 439 material with an ultrasonic fatigue testing machine because the specimen generated heat. Therefore, the heat-generating stress must be considered, especially as it differs depending on the material and shape. All low-speed fatigue tests were destroyed by fisheye-type failure. After  $10^6$  times, the same tendency as that in the ultrasonic fatigue test was observed.

### 3-3 Fracture surface observation

The cross-section of the broken test piece was observed using field-emission scanning electron microscopy (FE-SEM). All fracture modes of the QT material were confirmed to be fatigue fractures originating from the surface. Fig. 4 shows representative examples of fracture photographs of the DSG 2-C material after the ultrasonic fatigue test. A fisheye was observed at  $N \geq 2 \times 10^6$  times. Clear inclusions were also found in the center of the fisheye. At (a)  $N = 3.20 \times 10^6$  times with a short lifetime, an optically dark area (ODA) was not observed around the starting inclusion. At (b)  $N = 2.28 \times 10^8$  times with a long life span, the surface condition around the inclusion ODA appeared white because of its roughness

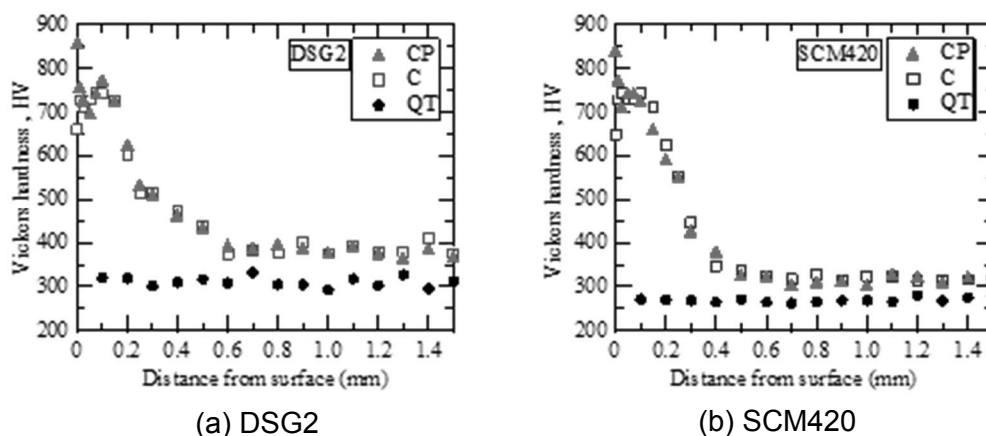


Fig. 2 Distribution of the Vickers hardness

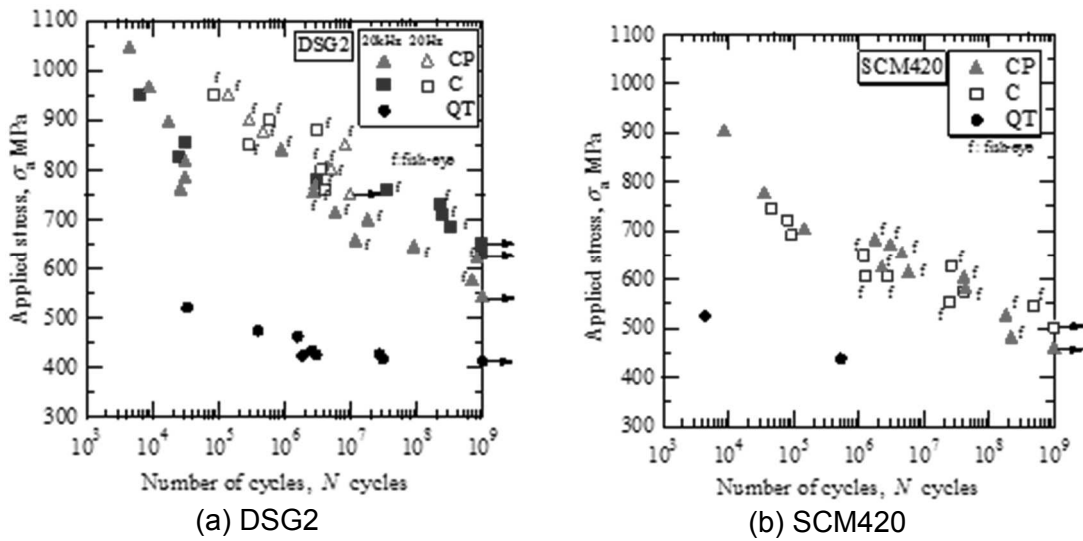
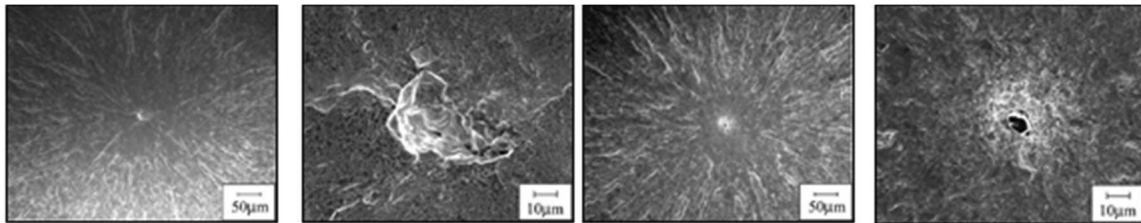


Fig. 3 Result of the fatigue experiment

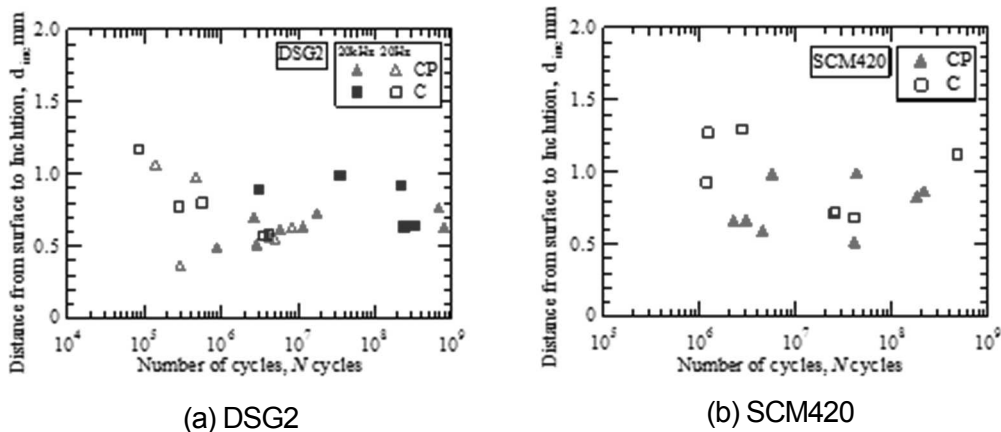
### 3-4 Fracture origin of fisheyes

Fig. 5 shows the relationship between the depth from the surface to the center of the inclusion and the number of cycles. In addition, Fig. 5(a) shows the results of the low-speed test conducted for comparison. The effective carburization depth of the gas carburized material in this study was 0.25 mm, but the figure shows that fracture in both the ultrasonic fatigue test and low-speed fatigue test originated internally. These tests use tension and compression; because there is no stress gradient, the whole specimen becomes a hazardous volume. Therefore, the FPP treatment was not observed to have an effect on the extreme surface hardness layer because the specimen was destroyed from the inside, which had lower strength.



(a) DSG2 C  $\sigma_a = 780$  MPa,  $N = 3.20 \times 10^6$  (b) DSG2 C  $\sigma_a = 729$  MPa,  $N = 2.28 \times 10^8$

Fig. 4 SEM images of fracture surface on DSG2-C



(a) DSG2 (b) SCM420  
Fig. 5 Relation between distance from surface to inclusion and number of cycles

### 3-5 Quantitative consideration of fish-eye

Fig. 6 shows the relationship between the defect size of the fracture starting point and the cycle number. The square root of the area of the inclusion is denoted by  $\sqrt{area}_{inc}$ , and the square root of the area of the ODA is denoted by  $\sqrt{area}_{ODA}$ . Fig. 6(a) is for DSG 2;  $\sqrt{area}_{ODA}$  tended to increase with the number of cycles for both the C and CP materials. As mentioned above, the ODA was not observed in the CP material at  $N \leq 4 \times 10^6$ . In both the ultrasonic fatigue test and low-speed fatigue test,  $b$  was about 10–20  $\mu\text{m}$ . Fig. 6(b) is for SCM 420; although there was some variation in  $\sqrt{area}_{ODA}$ , the tendency was similar to that of DSG 2. The ODA was not observed in the C material for  $N \leq 1 \times 10^6$  and in the CP material for  $N \leq 4 \times 10^6$ .  $\sqrt{area}_{inc}$  was about 30–40  $\mu\text{m}$  which is larger than that for DSG 2. Murakami et al. (14) pointed out that the ODA tends to increase with the number of cycles, and the results of this study also showed a similar trend. In other words, an ODA is formed by crack propagation due to a fatigue mechanism different from the normal fatigue mechanism, and an ODA is largely related to fatigue fracture at cycles of  $10^6$  times or more.

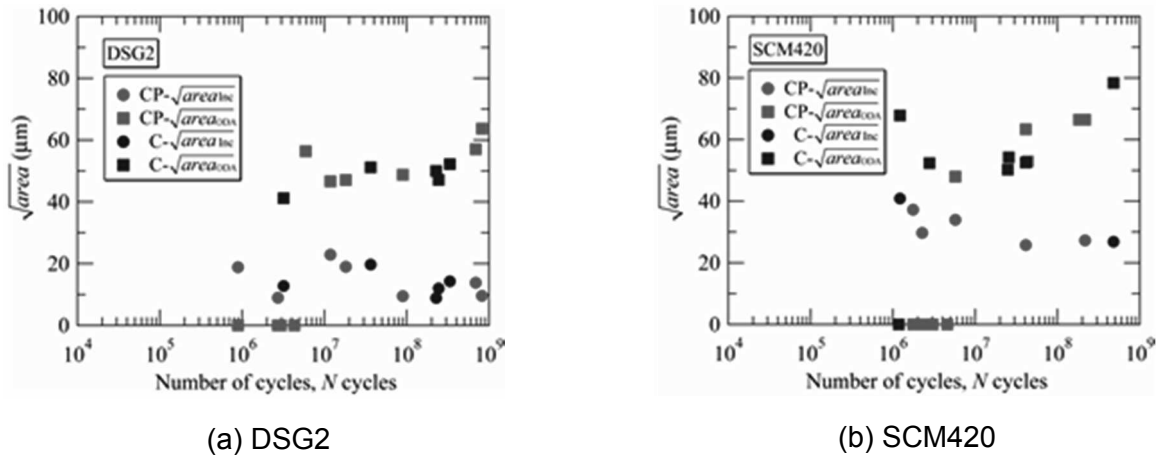


Fig. 6 Relation between  $\sqrt{area}$  and the number of cycles

### 3-6 Study on the stress intensity factor range

The stress intensity factor  $\Delta K$  when the inclusion that becomes the internal crack initiation point is regarded as the initial defect can be obtained with the following equation of Murakami et al. (15):

$$\Delta K = 0.5\sigma\sqrt{\pi\sqrt{area}} \quad (1)$$

When the value of  $\sqrt{area}_{inc}$  is substituted for  $\sqrt{area}$  in equation (1),  $\Delta K$  is set as  $\Delta K_{inc}$ . When the value of  $\sqrt{area}_{ODA}$  is substituted in, it is set as  $\Delta K_{ODA}$ . Fig. 7 shows the relationship between each  $\Delta K$  and the number of cycles. Although the amount of data for  $\Delta K_{ODA}$  in the low-speed fatigue test was small, both the C and CP materials appeared to show almost constant values of about 3.5–4.6  $\text{MPa}\cdot\text{m}^{1/2}$  regardless of the number of cycles, similar to the ultrasonic fatigue test. This means that an ODA is formed by repetitive stress; if  $\Delta K_{ODA}$  reaches a certain value, ordinary fish-eye type cracks will be assumed to grow and lead to failure.

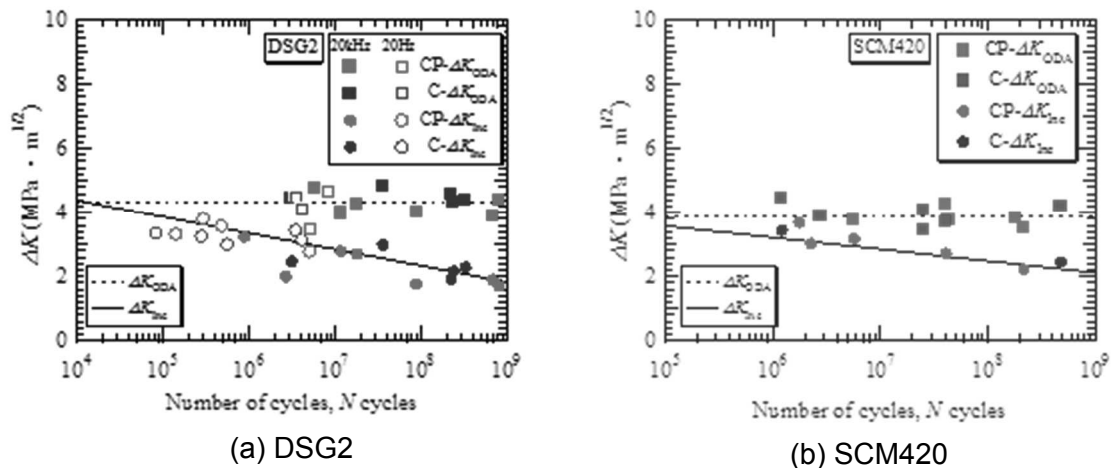


Fig. 7 Relation between  $\Delta K$  and the number of cycles

#### 4 Conclusion

In this study, the fatigue strength of steel for high-strength gears (DSG 2) and chromium molybdenum steel for machine structures (SCM 420) was evaluated by using an ultrasonic fatigue testing machine capable of operating at a high cycle frequency of 20 kHz. The conclusions are summarized below.

(1) Both the materials with gas carburizing and hybrid surface modification showed a monotonic downward slope on the S–N curve, and no definite fatigue limit could be confirmed. In addition, the hybrid surface modification was not observed to have an effect. The specimens failed from the inside rather than on the effective carburized hardened layer (0.25 mm). Therefore, hybrid surface modification does not seem to have an effect on the extreme surface hardness layer.

(2) The stress intensity factor range  $\Delta K_{ODA}$  was almost constant. For ODAs, the stress intensity factor range  $\Delta K_{ODA}$  may be an effective parameter for determining the fatigue limit in the very long life domain.

#### References

1. Y. Murakami, Proc. Int. Conf. on Fatigue in the Very High Cycle Regime, Vienna (2001), pp. 11-21.
2. K. Tanaka and Y. Akiniwa, Proc. Int. Conf. on Fatigue in the Very High Cycle Regime, Vienna (2001), pp. 61-72.
3. T. Sakai, M. Takeda, K. Shiozawa, Y. Ochi, M. Nakajima, Y. Nakamura, and N. Oguma, J. Soci. Mat. Sci., Japan, 49 (2000), pp. 779-785 (in Japanese).
4. H. Ishii, T. Yagasaki, and H. Akagi, Fatigue Fract. Eng. Mater. Struct., 25 (200), pp. 1-5.
5. C. Bathias, Fatigue Fract. Eng. Mater. Struct., 22 (1999), p. 559.
6. C. Bathias, K. El Akanu, and T. Y. Wu, Eng. Fract. Mech., 56-2 (1997), pp. 255-264.
7. Y. Wang, C. Bathias, N. Kawagoishi, and Q. Chen, Int. J. Fatigue, 24-12 (2002), pp. 1269-1274.
8. S. E. Stanzl-Tchegg and H. Mayer, Int. J. Fatigue, 23 (2001), pp. S231-S237.
9. H. Mayer and C. Laird, Mater. Sci. Eng., 187 (1994), pp. 23-35.
10. H. Mayer and C. Laird, Mater. Sci. Eng., 194 (1995), pp. 137-145.
11. H. Mayer, M. Papakyriacou, R. Pippan, and S. Stanzl-Tschegg, Mater. Sci. Eng., A314 (2001), pp. 48-54.
12. J. Ni and Z. Zhang, Eng. Fract. Mech., 52-6 (1995), pp. 1079-1086.
13. Y. Furuya, S. Matuoka, and T. Abe, Electric Furnace Steel, 75-1 (2004), p. 57.
14. Y. Murakami, T. Ueda, and T. Nomoto, Sci. Eng. 66-642 (2000), pp. 319-331.
15. Y. Murakami, S. Kodama, and S. Konuma, Sci. Eng. 54-500 (1988), p. 688.



# EXPERIMENTAL INVESTIGATION OF FREQUENCY EFFECT ON FATIGUE CRACK PROPAGATION ON 3 STEELS: DUAL PHASE (DP1180), COMPLEX PHASE (CP1000) AND MULTI-PHASE (M800HY).

M. Ouarabi<sup>1</sup>), K. Gillner<sup>2</sup>), T. Palin-Luc<sup>3</sup>), S. Muenstermann<sup>2</sup>), O. Polit <sup>1</sup>)

<sup>1</sup>Université Paris Nanterre, LEME, 50 rue de Sèvres, Ville d'Avray, France

<sup>2</sup>Steel Institute of RWTH Aachen University, Intzestraße 1, Aachen, Germany

<sup>3</sup>Arts et Metiers Paris Tech, I2M, CNRS, Esplanade des Arts et Metiers, Talence, France

## ABSTRACT

Determining the crack propagation curve is a key point for designing safe components with a damage tolerance objective. Carrying out crack propagation tests are long, especially for determining the bottom part of the  $da/dN=f(\Delta K)$  curves close to the threshold of the stress intensity factor range. In this paper fatigue crack growth tests in mode I have been carried out under two loading ratios ( $R = -1$  and  $0.1$ ), on 3 steels used in automotive industry (DP1180, CP1000 et M800HY), at 30 Hz and 20 kHz in order to study the effect of the loading frequency on the Paris curve. No significant effect of the loading frequency on the  $da/dn=f(\Delta K_{eff})$  curves was observed for the CP1000 and M800HY steels but a small effect was observed in the case of the DP1180 steel. The temperature increase during the crack propagation is very low. No striation was observed on the fracture surface at the two frequencies.

## KEYWORDS

Ultrasonic, Fatigue, Flat carbon steel, Fatigue crack growth.

## INTRODUCTION

In many modern transportation systems (cars, trains and aircrafts) the durability of some components is between  $10^8$  and  $10^9$  cycles; this is the gigacycle fatigue regime. Since in this case the fatigue tests are long at usual testing frequency, typically lower than 100 Hz, some laboratories use ultrasonic fatigue tests between 20 and 30 kHz. However, at these very high loading frequencies the question of a possible frequency effect on both the crack initiation and the crack growth arises. This paper is focused on the crack propagation only. The experimentation is focused on the Paris curve and the threshold. Several works on this subject have been published in the literature. A first study about the effect of the loading frequency was carried out by Doquet et al. [1] on a very low carbon steel (0.13%) tested at two frequencies: 10 Hz and 20 kHz. The main result is that, the decrease of the frequency generates an increase of the crack propagation rate. Sato et al. [2] have studied the effect of frequency on the fatigue crack propagation rate on two materials: aluminum alloy 2024-T3 and steel SM-50 under tension-tension loading at three frequencies (120Hz, 0.1Hz and 0.0166Hz). Again, for these two materials, the conclusion is the same: the frequency decrease generates an increase of the crack growth rate. A third study about the frequency effect (0.25 Hz and 30 Hz) was carry out by Radon et al. [3] on steel BS 4360-50C at loading ratios equal to 0.08 and 0.7. The conclusion for this study is that the effect of frequency depends of the loading ratio. At  $R=0.08$  there is no effect, but under the loading ratio 0.7, there is a frequency effect. One possible explanation of this effect is related to the presence of hydrogen with very high quantity inside the fracture surface under  $R=0.7$  because the crack is open most of the duration of each loading cycle. On the contrary at the lower  $R$  ratio the crack is partially closed. Consequently, in this case the frequency effect is related to environment. The effect, on the fatigue crack propagation, of the loading frequency under different environments has been studied by Liaw [4] on an austenitic steel at the loading ratio  $R=0.1$  and two frequencies (0.1 and 10 Hz). Three environments have been used (air,  $H_2$  and water). No effect of environment was observed at 10 Hz, but at 0.1 Hz there was an effect. Jones [5] has published an article about the effect of both the loading frequency and the temperature on the fatigue crack propagation of a ferritic steel under a loading ratio of  $R=0.1$  within a frequency range from 0.01 to 100 Hz and at different temperatures

(room temperature, 500 °C, 600°C and 700°C). A pronounced effect of the loading frequency was observed below 1 Hz, but no frequency effect beyond 1 Hz for the different temperatures. It seems that the effect of frequency is related to the material (sensitivity to the strain rate) and it is more influenced by the environment and the temperature. In this work, the effect of the loading frequency on the fatigue crack propagation rate is investigated by using two frequencies (20 kHz and 30 Hz) and two loading ratios ( $R=0.1$  and  $R=-1$ ). The investigated materials are three Advanced High Strength Steels (AHSS). According to Kuziak [6] this type of steels has the following characteristics [6]: high stiffness, strength, fatigue properties, impact resistance, and good formability. There are very few results only in the literature about the crack propagation on this family of steel. Li et al. [7] have studied the fatigue crack propagation of three different steels: FP (Ferrite - perlite 16 %), FM (Ferrite - martensite 19 %) and FM-820 (ferrite - martensite 30 %) at room temperature. The specimens were tested using a constant amplitude sinusoidal load. At a loading ratio  $R=0.1$ , at a frequency of 10 Hz. Among the three grades, the FP grade exhibits the higher fatigue crack propagation velocity with respect to the two martensite grades. Whenever the martensite content increases, the crack propagation rate decreases at the same the stress intensity factor range. At ultrasonic loading frequency, a single study has been found in the literature on AHSS. It concerns the dual phase steel DP600 [8]. Its purpose is to measure the intrinsic dissipation at a loading frequency of 20 kHz, but no paper has been found about a possible frequency effect on the crack growth rate at ultrasonic frequency.

## EXPERIMENTAL PROCEDURES

### Materials

Three different steels for automotive industry were studied: (i) DP1180, a dual phase steel with ferrite (9 %) and martensite (91 %) containing refined carbide precipitates; (ii) CP1000, a complex phase steel with ferrite (18 %) and martensite (82%) with refined carbide precipitates. These two steels are produced in sheet form by cold rolling and are zinc coated. The specimens were machined, without removing this coating, and with their longitudinal axis parallel to the rolling direction. (iii) The third steel is a multi-phase one (M800HY) with bainitic microstructure containing very few perlite and martensite and some carbides. It is produced by hot rolling in 3.2 mm thickness and it has no coating. The microstructure of these materials is illustrated in Fig. 1. Their mechanical properties under monotonic quasi-static tension in rolling direction are:  $R_m=1136$  MPa,  $R_{p0.2}=818$  MPa for CP1000,  $R_m=1245$  MPa,  $R_{p0.2}=1056$  MPa for DP1180 and  $R_m=880$  MPa,  $R_{p0.2}=826$  MPa for M800HY.

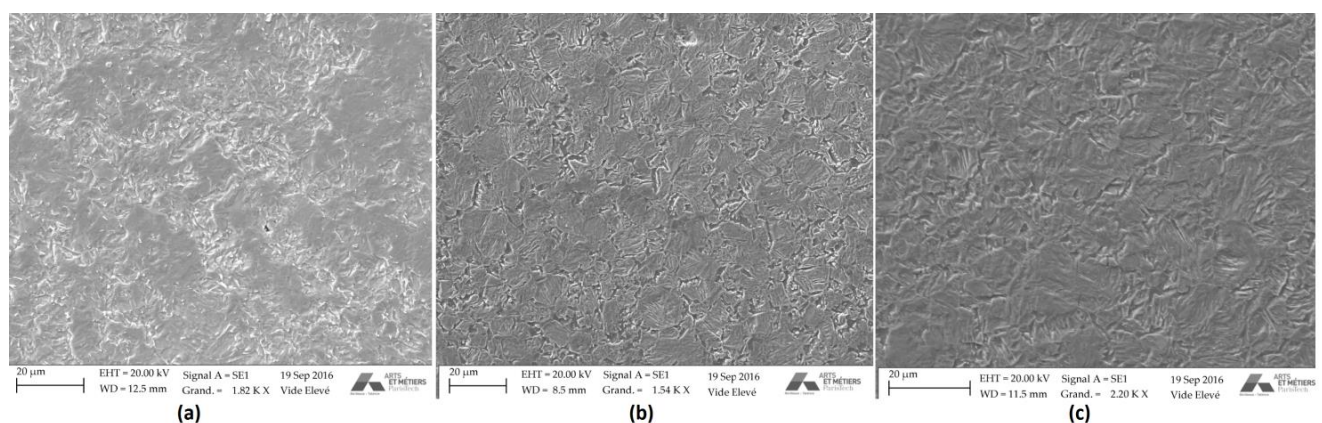


**Fig 1** :Microstructure of : (a) M800HY, (b) CP1000, (c) DP1180 after etching

### Testing conditions

The fatigue crack growth tests were carried out according to ASTM E647 standard at 30 Hz with a servo-hydraulic machine and at 20 kHz with an ultrasonic resonant one. For each frequency two loading ratios were considered:  $R= -1$  and  $R=0.1$ . The specimens' geometry is illustrated in Fig. 2. The tests were carried on long natural cracks emanating from notches. The procedure for carrying

out fatigue crack growth tests at ultrasonic frequency has some particularities described in [9], some generalities are also given in ref. [10]. In our experiments, because of the low specimen thickness a plane stress state has been assumed and the equation proposed by Wu [10] was used to compute the stress intensity factor range,  $\Delta K$ . Because of the high loading frequency, the opening loading could not be measured, consequently the effective value of  $\Delta K$  is assumed to be  $\Delta K_{\text{eff}}=K_{\text{max}}$  for  $R=-1$  and  $\Delta K_{\text{eff}}=K_{\text{max}}-K_{\text{min}}$  for  $R=0.1$ . Furthermore, all the specimens tested at 20 kHz were cooled with dry compressed air passing through an air gun (input pressure 2 bars).

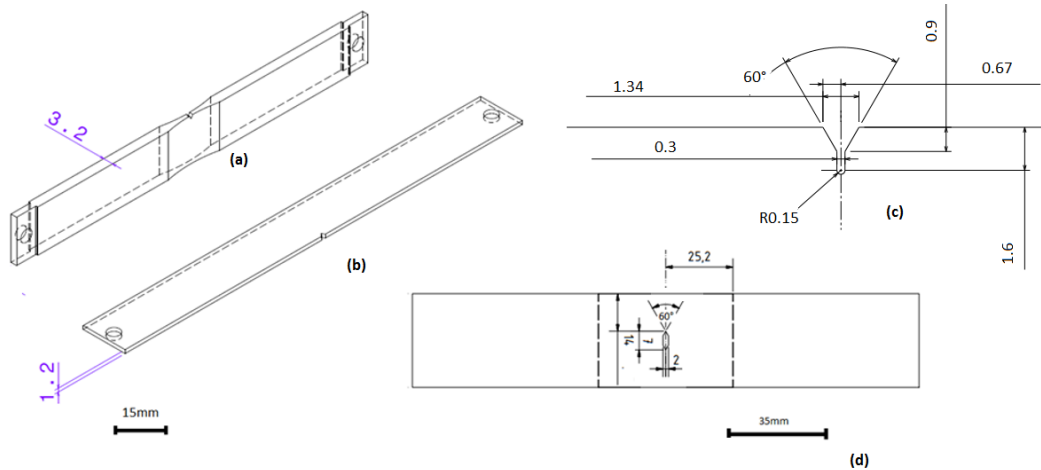


**Fig 2** :Geometry of the specimens: a, b) specimen tested at 20 kHz, c) zoom on the notch, and d) M(T)-specimen after ASTM E647 tested at 30 Hz

Since at high loading frequency the specimen heating may be high, the temperature profile at the fatigue crack tip was measured with an infrared camera on some specimens having a mat black paint surface but without any air cooling. This condition (no cooling) allows us to check the maximum possible temperature. For the tests at 20 kHz a FLIR camera SC 7000 was used with the following characteristics : (i) temperature measuring range:  $+5^{\circ}\text{C}$  to  $+300^{\circ}\text{C}$ , (ii) manual focus (ii) 25 Hz frame rate and a sub-sampling of 5Hz to reduce the size of the IR film. The other face of the specimen has been used to monitor the crack propagation with an optical camera. For the test at 30 Hz, the crack propagation was measured with the potential drop technique and the temperature field around the crack was measured with an IR camera from InfraTec with the following characteristics: (i) temperature measuring range  $+5^{\circ}\text{C}$  to  $+300^{\circ}\text{C}$ , (ii) manual focus (ii) frame rate 1 Hz. After fatigue testing the specimens were observed by SEM. To do that the specimens were broken in two parts by applying a monotonic loading after immersion in liquid nitrogen during 10 mn.

## EXPERIMENTAL RESULTS AND DISCUSSION

### Comparison of the Paris curves at 30Hz and 20kHz

The results at 30 Hz and 20 kHz in the Paris regime are in good agreement for the M800HY steel under the two investigated loading ratios  $R=-1$  and  $R=0.1$  (Fig. 3). This is the same for the CP1000 (Fig. 4): there is no effect of the loading frequency at  $R=0.1$  but a small difference at  $R=-1$ . However, for the DP1180 a significant difference between the Paris curve at 20 kHz and at 30 Hz can be observed for the two-loading ratio ( $R=0.1$  and  $R=-1$ ) on Fig. 5.

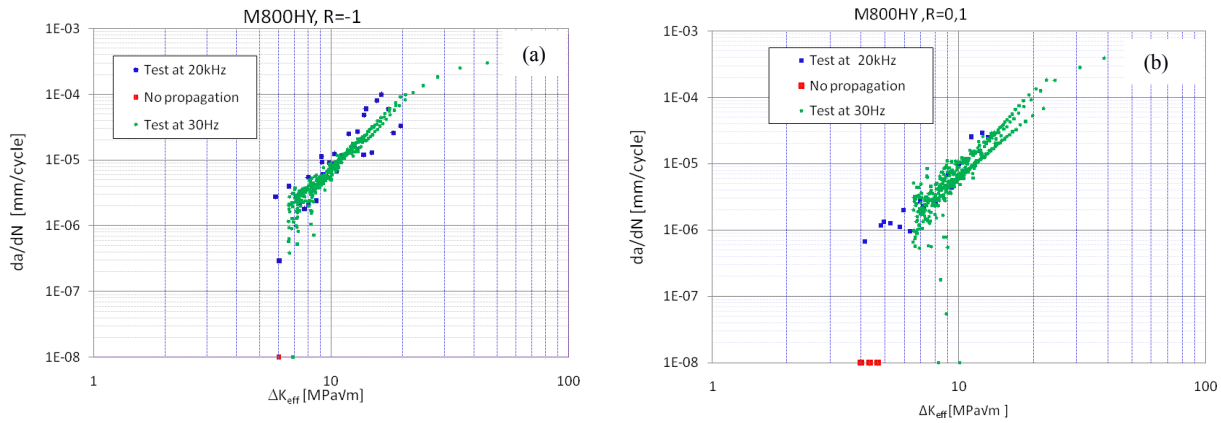


**Fig. 3** : Crack growth curves for M800HY at 30 Hz and 20 kHz for a) R=-1 and b) R=0.1.

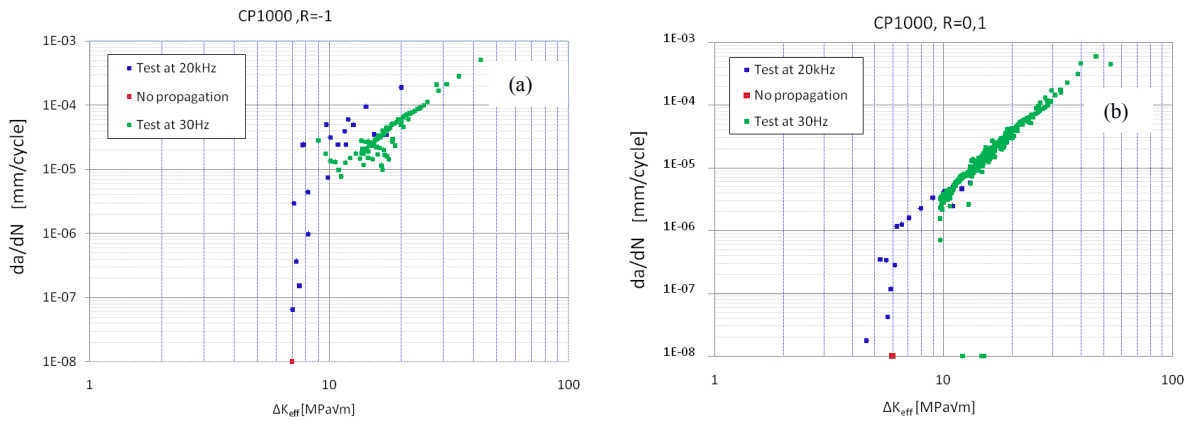


**Fig. 4** : Crack growth curves for CP1000 at 30 Hz and 20 kHz for a) R=-1 and b) R=0.1.

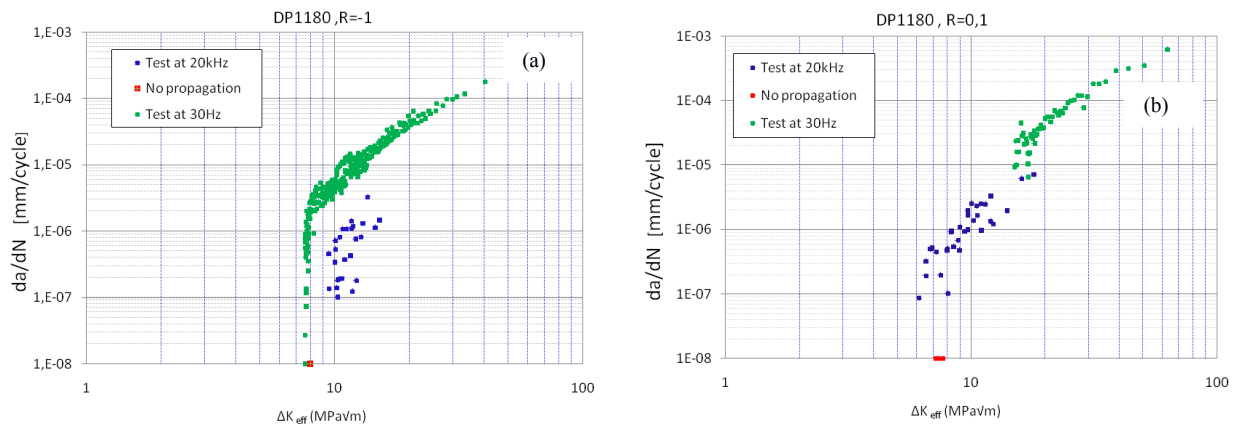


**Fig. 5** : Crack growth curves for DP1180 at 30 Hz and 20 kHz for a) R=-1 and b) R=0.1.

### Temperature measurement

Temperature analyses presented hereafter are focus on the evolution of the current temperature ( $T$ ) by reference to the initial and homogeneous temperature of the specimen ( $T_0$ ). That is why the temperature variation ( $\Delta T = T - T_0$ ) is considered. On the tests at 20 kHz, the temperature was measured by block because the crack growth experiments were done by block for having a quasi-constant  $\Delta K$  [9]. Furthermore, the duration of each block was short because of the high loading frequency ( $10^7$  cycles correspond to 8 min). But, since the tests at low frequency were long and done without stopping the propagation, the temperature variation  $\Delta T$  was defined with reference to temperature at point P8 (Fig. 6b). That is the reference measurement point which takes into account the temperature evolution of the specimen due to temperature changement of the surrounding during the test. In this example, P2 to P7 are the left-hand side measurement points. P10 to P15 are the right-hand side ones. One can see in Fig. 6 that  $\Delta T$  is small for all the tested



$\Delta K_{eff}$  values. For the higher  $\Delta K$  value a higher increase of the temperature variation is observed. This is due to the higher dissipation at the crack tip since the heat source at the crack tip is proportional to  $\Delta K^4$ . [11, 12]. Fig. 6 shows also that the temperature increase was small at the two-tested frequency. Consequently, there was no loading frequency-induced temperature effect on the crack growth curves. However, even if the temperature variations were small (a few Celsius degrees only) ahead of the crack tip, one can note that this was approximately 10 times greater at 20 kHz than at 30 Hz. The same conclusion is valid for the three steels of this study.

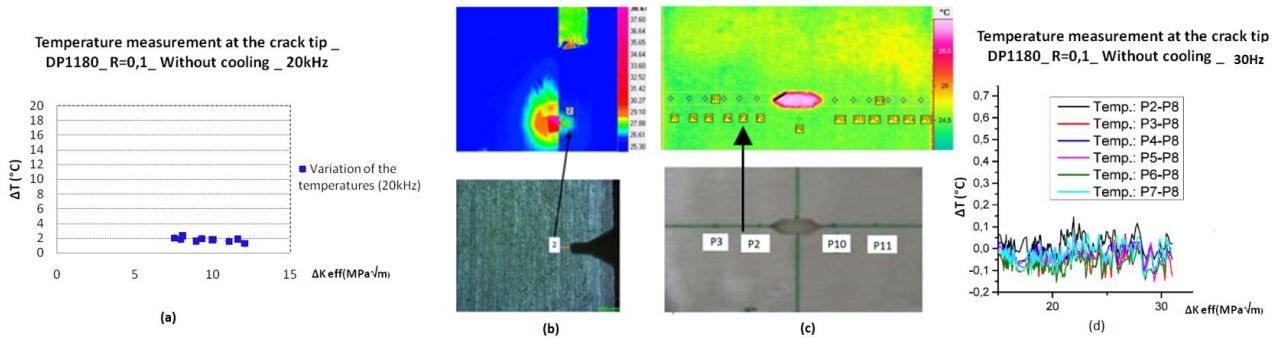


**Fig.6:** Temperature measurement on DP1180 under R=0.1: a,b) Temperature measurement at the crack tip at under loading at 20 kHz, c) M (T) specimen and the path to measure the temperature during the crack propagation at 30 Hz, d)  $\Delta T$  vs. stress intensity factor range.

### Discussion

In this study, different AHSS were tested at very high loading frequency and usual frequency to quantify if there is an effect of the loading frequency on fatigue crack propagation. To do so we have determined the Paris curves and compared them. It seems that depending of the material and the loading ratio (R=-1 or 0.1) the frequency effect on the fatigue crack growth (FCG) rate changes. Three cases are observed. No effect in the case of M800HY steel for the two loading ratios. A small effect of the frequency for CP1000 but just at R=-1. But a clear effect under the two R ratios: R=-1 and R=0.1 for DP1180. Among the three tested steels at different frequencies, it is clear that the effect of frequency is much higher in the case of DP1180. This effect could be related to the presence of martensite. Indeed, according to our results, the FCG rate of DP1180 steel was the slowest among the three investigated steels under the same  $\Delta K$ , proving a decreasing effect of martensite on the FCG rate. Furthermore,  $\Delta K_{th}$  increases with an increase in martensite content. This result was observed by other authors too [13]. This delay could be related to the formation of very high quantity of dislocations between the borders of martensite induced by the transformation of residual austenite to martensite [14], but in our case the amount of residual austenite was very low. The increase of temperature was measured too. This is very low for the two tested frequencies. The comparison by SEM of fracture surfaces obtained after low and very high loading frequencies were done. No striation was observed on the studied steels, probably because they are not ductile enough. Furthermore, it is difficult to compare these fracture surfaces because according to [7], at low frequency depending of the crack length the morphology of crack changes whereas this is not the case for the fatigue crack propagation at very high loading frequency. However, one can say that the morphologies of the fracture surfaces are quite similar.

### CONCLUSION

According to the results obtained on the three steels investigated in this work at 20 kHz and 30 Hz the conclusions are the following. (1) at the two frequencies, the fatigue crack growth rate on DP1180 is the slowest. (2) The higher threshold of  $\Delta K$  is for the steel with the higher martensite content (DP1180). (3) No striation has been observed on the fracture surface whatever the loading frequency and the steel. (4) The temperature variation ahead of the crack tip during the crack propagation tests at 20 kHz and 30 Hz is small (a few degrees Celsius). (5) There is no frequency effect in the Paris regime for M800HY whatever R. On CP1000, there is no frequency effect under R=0.1 but a small effect at R=-1. But on DP1180, there is a significant difference in the Paris regime between tests at 20 kHz and at 30Hz for both loading ratios R=0.1 and R=-1.

## ACKNOWLEDGEMENTS

The research leading to these results has received funding from the European Union's Research Fund for Coal and Steel (RFCS) research program under grant agreement no. [RFS-CT-2013-00015 (FREQTIGUE)].

## REFERENCES

- [1] Doquet.V.; Tsutsumi.N.; Murakami.Y.:  
Effect of test frequency on fatigue strength of low carbon steel.  
Fatigue and Fracture of Engineering Materials and Structures, 2009.
- [2] Sato,K; Yokobori.T.:  
The effect of the frequency loading on fatigue crack propagation rate and striation spacing in 2024-T3 aluminum alloy and SM-50 steel.  
Engineering Fracture Mechanics, 1976.
- [3] Radon, J.C.; Musuva, J.K.:  
The effect of the stress ratio and frequency on fatigue crack growth.  
Fatigue of Engineering Materials and Structures, 1979.
- [4] Leax, T.R.; Fabis, T.R.; Donald-J, K.; Liaw, P.K.:  
Fatigue crack growth behavior in a Mn-Cr austenitic steel.  
Engineering Fracture Mechanics, pages 1-13, 1987.
- [5] Jones, J.W.; Makhoulouf, K.:  
Effects of frequency and temperature on short fatigue growth in aqueous environment.  
International journal of fatigue, pages 163-171, 2012.
- [6] Kuziak, R.; Kawall, R, and Waengler, S.:  
Advanced high strength steel for automotive industry.  
Archive of Civil and Mechanical Engineering, 2008.
- [7] Li, S. ; Kang, Y.; Kuang, S.:  
Effects of microstructure on fatigue crack growth behavior in cold-rolled dual phase steels.  
Materials Science & Engineering A. Materials Science&EngineeringA612(2014)153–161
- [8] Torabian, N.; Favier, V., Ziaei-Rad, S.; Adamski, F.; Dirrenberger, J.; Ranc, N.:  
Self-Heating Measurements for a Dual-Phase Steel under Ultrasonic Fatigue Loading for stress amplitudes below the conventional fatigue limit.  
Procedia Structural Integrity, Volume 2, 2016, Pages 1191-1198,2016
- [9] Perez-Mora R. ; Palin-Luc T. ; Bathias C. ; Paris, P.C. :  
Very high cycle fatigue of high strength steel under sea water corrosion: a strong corrosion and mechanical damage coupling.  
Int. J. Fatigue, 74 (2015) 156-165.
- [10] Wu, T.Y. :  
Modelisation de la fissuration en fatigue vibratoire à haute température ; applications aux alliages à base de nickel.  
PhD Thesis Ecole Centrale de Paris, (1992).
- [11] Ranc,N.; Palin-Luc,T.; P.C. Paris,P.C. :  
Thermal effect of plastic dissipation at the crack tip on the stress intensity factor under cyclic loading.  
Engineering Fracture Mechanics, 78 (2011) 961–972
- [12] Ranc N., Palin-LucT., Paris P.C. and Saintier N.:  
About the effect of plastic dissipation in heat at the crack tip on the stress intensity factor under cyclic loading.  
International Journal of Fatigue, 58 (2014) 56-65,
- [13] Sudhakar, K.V.; Dwarakadasa,E.S.:  
A study on fatigue crack growth in dual phase martensitic steel in air environment.  
Bulletin of Materials science, 23 (2000) 193–199
- [14] Raabe,D.; Ziaei-Rad,S.; Weber, U.; Calcagnotto, M.; Kadkhodapour, J.; Schmauder,S.:  
Experimental and numerical study on geometrically necessary dislocations and non-homogeneous mechanical properties of the ferrite phase in dual phase steels.  
Acta Materialia, pp. 4387-4394., 2011.

**Corresponding author:** thierry.palin-luc@ensam.eu

## **Experimental methods**



## **INVITED**



### **Manuel José Moreira de Freitas**

Dipl. Eng. (1972) Instituto Superior Técnico, Universidade Técnica de Lisboa, Portugal

Doctor (1982) Université de Technologie Compiègne, France

From 1982 to 2013, Assistant, Associate (1987) and Full Professor (1998). Retired since 2013, Mechanical Engineering Department, Instituto Superior Técnico, Universidade Técnica de Lisboa;

Since January 2015, Professor and Dean of the Engineering Department, UATlântica, University Higher Institution, Barcarena.

Research activities:

Fatigue testing under multiaxial loading (LCF, HCF and VHCF)

Materials and Aeronautic Engineering, Light alloys and Laminated Composite materials.

Affiliation:

IDMEC, Instituto Superior Técnico, Universidade de Lisboa

Professor (retired), IDMEC, Instituto Superior Técnico, Universidade de Lisboa, Lisboa, Portugal; [manuel.freitas@tecnico.ulisboa.pt](mailto:manuel.freitas@tecnico.ulisboa.pt)

Engineering Department, UATlântica, University Higher Institution, Barcarena, Portugal; [mfreitas@uatlantica.pt](mailto:mfreitas@uatlantica.pt)

### **DESIGN AND INSTRUMENTATION OF AN AXIAL/TORSION DEVICE WORKING AT ULTRASONIC FREQUENCIES FOR VHCF TESTING**

**M. Freitas**<sup>1</sup>, L. Reis<sup>1</sup>, A. Ribeiro<sup>1</sup>, M. Vieira<sup>1</sup>, M. Fonte<sup>1,2</sup>

<sup>1</sup>IDMEC Instituto Superior Técnico, Universidade Lisboa, Lisboa, Portugal

<sup>2</sup>Escola Nautica Infante D. Henrique Máquina Marítimas, Paço de Arcos, Portugal

Fatigue damage has special relevance on the life span of mechanical components and structures, as it takes responsibility for the majority of the registered structural failures. Although its mechanisms have been the subject of continuous research, the growing need for greater lifespans forced the understanding of the behavior of materials under very high cycle loadings, also known as Very High Cycle Fatigue. On the other hand the behavior of materials under multiaxial fatigue has been the subject of research and development, but not in the region of very high cycles, due to the inexistence of appropriate machinery to perform these tests. The authors of this work have already a large experience on the performance of multiaxial fatigue tests under axial/torsion loading under servo-hydraulic fatigue testing machines and on very high cycle fatigue tests.

In this context, and in order to understand the behavior of materials on the very high cycle region of the S-N curves and remarking the absence, for some materials, of the fatigue limit that used to be considered on mechanical design, a comparison must be carried out between the loading conditions determined in lower frequencies (servo-hydraulic testing) and very high frequencies (piezoelectric ultrasonic testing machines).

In this paper, a device designed to produce biaxial, axial/torsional loading fatigue testing using a single piezoelectric axial exciter is presented, as well as the instrumentation used on the preliminary testing of this device. The device is comprised of a horn and a specimen, which are both attached to the piezoelectric exciter. The steps taken towards the final geometry of the device, including special designed horn and specimen are presented. Experimental testing of the developed device is carried out using thermographic imaging, strain measurements and vibration speeds and indicates good behaviour of the tested specimen. Results of stress and strain measurements on specimens tested under biaxial loading conditions, at static loading, lower frequencies and very high frequencies are discussed and analyzed. Measurement techniques such as electric strain gages and digital image correlation were used. Results show that it is possible to carry out multiaxial (axial/torsion loading) fatigue tests at very high frequencies with comparable results with tests at lower frequencies which allow the development of faster and reliable very high cycle multiaxial fatigue tests.

## DESIGN AND INSTRUMENTATION OF AN AXIAL/TORSION DEVICE WORKING AT ULTRASONIC FREQUENCIES FOR VHCF TESTING

P. Costa<sup>1)</sup>, M. Vieira<sup>1)</sup>, A.M.R. Ribeiro<sup>1)</sup>, L. Reis<sup>1)</sup>, M. de Freitas<sup>1)</sup>

<sup>1)</sup> IDMEC, Instituto Superior Técnico, Universidade de Lisboa, 1049-001 Lisboa, Portugal

### ABSTRACT

Fatigue damage has special relevance on the life span of mechanical components and structures, as it takes responsibility for the majority of the registered structural failures. The growing need for greater lifespans in components and structures forced the understanding of the behavior of materials under very high cycle loadings, known as Very High Cycle Fatigue. In order to understand the behavior of materials on the very high cycle region of S-N curves and remarking the absence, for some materials, of the fatigue limit that used to be considered on mechanical design, updated fatigue tests must be carried out for lives above  $10^7$  up to  $10^{10}$  cycles. Classical fatigue testing machines are not able to perform such tests in a reasonable time and very high frequencies must be used. In recent years, fatigue testing machines working at ultrasonic frequencies became more performant and allowing fatigue tests at the frequency of 20 kHz. The behavior of materials under multiaxial fatigue has been the subject of research and development, but not in the region of very high cycles, due to the inexistence of appropriate machinery to perform these tests. In this paper, a device designed to produce biaxial (axial/torsional) loading fatigue testing using a single piezoelectric axial actuator is presented, as well as the instrumentation used for monitoring and control during the fatigue testing at very high cycle loadings.

### KEYWORDS

Multiaxial fatigue, ultrasonic frequencies, specimen design, very high cycle fatigue

### INTRODUCTION

Fatigue damage has special relevance on the life span of mechanical components and structures, as it takes responsibility for the majority of the registered structural failures. Although its mechanisms have been the subject of continuous research, the growing need for greater lifespans, due to the need of both weight reduction and energy saving, forced the understanding of the behavior of materials under very high cycle loadings, also known as Giga Cycle Fatigue [1] or more recently Very High Cycle Fatigue. On the other hand the behavior of materials under multiaxial fatigue has been the subject of research and development [2], but not in the region of very high cycles, due to the inexistence of appropriate machinery to perform these tests. The authors of this work have already a large experience on the performance of multiaxial fatigue tests under axial/torsion loading under servo-hydraulic fatigue testing machines [3] and on very high cycle fatigue tests [4]. In this context, and in order to understand the behavior of materials on the very high cycle region of the S-N curves and remarking the absence,

for some materials, of the fatigue limit that used to be considered on mechanical design [5, 6], updated fatigue tests must be carried out for lives above  $10^7$  up to  $10^{10}$  cycles. Classical fatigue testing machines are not able to perform such tests in a reasonable time and very high frequencies must be used. Also, comparison must be carried out between the loading conditions determined in lower frequencies (servo-hydraulic testing) and very high frequencies (piezoelectric ultrasonic testing machines).

The behavior of materials under multiaxial fatigue has been the subject of research and development, but not in the region of very high cycles, due to the inexistence of appropriate machinery to perform these tests in a reasonable time. In this paper, a device designed to produce axial and axial/torsional loading fatigue testing using a single piezoelectric axial exciter is briefly presented [7], as well as the instrumentation used on the preliminary testing of this device [8]. The device is comprised of a horn and a specimen, which are both attached to the piezoelectric actuator. The steps taken towards the final geometry of the device, including special designed horn and specimen are presented. Experimental testing of the developed device is carried out using thermographic imaging, strain measurements and vibration speeds and indicates good behaviour of the tested specimen. Results of stress and strain measurements on specimens tested under biaxial loading conditions, at static loading, lower frequencies and very high frequencies are discussed and analyzed. Results show that it is possible to carry out multiaxial (axial/torsion loading) fatigue tests at very high frequencies with comparable results with tests at lower frequencies which allow the development of faster and reliable very high cycle multiaxial fatigue tests.

## **ULTRASONIC FATIGUE TESTING**

An ultrasonic fatigue test differs from the conventional fatigue in the nature of vibration. An ultrasonic fatigue test seeks to reproduce free vibration with the specimen vibrating at its own fundamental frequency [7]. In conventional testing the working frequency is set away from the fundamental frequencies and the specimen is subjected to forced vibration. In order to perform ultrasonic tests, it is necessary to design a specimen with a fundamental frequency tuned up to match the machine's working frequency.

### **Tension and Torsion Fatigue Testing**

The description of the processes of the development of a VHCF testing device for biaxial conditions, using a single axial piezoelectric exciter, is presented [8, 9]. The device is comprised of a horn and a specimen, being the latter the component to be tested on biaxial conditions, with a loading that was predefined to have in-phase sinusoidal components of axial and shear stress at stress ratio  $R=-1$ .

Since the horn receives a sinusoidal axial displacement from the piezoelectric actuator, and it is intended to induce also torsional loadings on the specimen, the horn has to be responsible for the generation of the rotational movement which will be imposed on the specimen and will promote shear stresses in it. This implies that the horn takes special importance on the behavior of the device, specifically on the relationship between axial and torsional loadings imposed on the specimen.

The computational modal analysis made to this geometry, proved that a certain dynamic vibrational mode could be achieved in which the horn would vibrate in a hybrid mode composed by axial and torsional modes, where axial and rotational displacements are amplified on the smaller free end. Still, there was a need for a horn that would possess this specific mode on the frequency at which the actuator operates (20 kHz). The iterative process to obtain the final geometry was produced using finite element model [8, 9], and a schematic representation is shown on Fig. 1. The final horn

geometry consists of a conical shaped part with two groups of oblique slits responsible for the generation of the rotational character of the horn, which in turn will promote sinusoidal rotations on the specimen that will add to the already existent sinusoidal axial excitation.

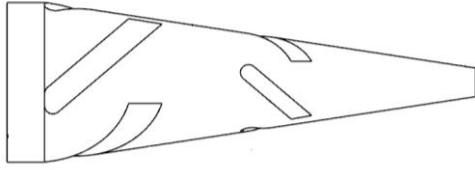


Fig. 1: Schematic 2D representation of the developed biaxial horn

Before introducing the final geometry of the used specimen, it might be interesting to analyze the dynamic equations (1) and (2) for a generic bar for both axial and torsional modes.

$$\frac{\partial^2 u}{\partial t^2} = \frac{E_d}{\rho} \frac{\partial^2 u}{\partial x^2} \quad (1)$$

$$\frac{\partial^2 \theta}{\partial t^2} = \frac{G_d}{\rho} \frac{\partial^2 \theta}{\partial x^2} \quad (2)$$

where  $E_d$  and  $G_d$ , are respectively the Young and shear torsional modulus,  $t$  is time,  $u$  and  $\theta$  are the axial and rotational displacements,  $x$  is the associated coordinate system and  $\rho$  the density of the material. The dynamic equation for axial and torsional frequency of generic cylindrical bar of length  $l$ , are respectively, Equations (1) and (2):

$$\omega_n = \frac{n\pi}{l} \sqrt{\frac{E_d}{\rho}} \quad (3)$$

$$\omega_n = \frac{n\pi}{l} \sqrt{\frac{G_d}{\rho}} \quad (4)$$

Obviously, and due to the differences found between the Young and Shear Modulus, the results of the frequencies  $\omega_n$  are lagged by a certain ratio. This implies that, for a cylindrical shape, the first axial mode will have a significant different frequency value from the respective first torsional mode. If a cylindrical shaped specimen is pretended, this raises a relevant problem to the specimen design. Other combinations of modes were considered, but the final design consisted of a specimen that possesses its first axial mode ( $n=1$ ) and its third torsional mode ( $n=3$ ) at the same frequency. This is achieved by designing a cylindrical specimen with three throats (instead of a classical one throat specimen), as seen in Fig. 2.



Fig. 2: Schematic 2D representation of the developed specimen.

A 3-dimensional view of the developed device, specimen and horn, for axial/torsion fatigue testing at ultrasonic frequencies was designed and it became mandatory to produce computational analyses to understand the dynamic behavior of the coupled system, formed by the booster, horn and specimen, which can be found in [8].

Having achieved the final geometry for the three elements coupled with the piezoelectric actuator, the ultrasonic fatigue testing device is ready for working, remembering that for each elastic material, having different elasticity properties and specific weight, will lead to different dimensions but similar shape for the specimen. But, for any geometry the loading characteristics present on the specimen will be similar and can be represented schematically in Fig. 3, for the axial displacement and axial stress and rotation and shear stress along the longitudinal axis.

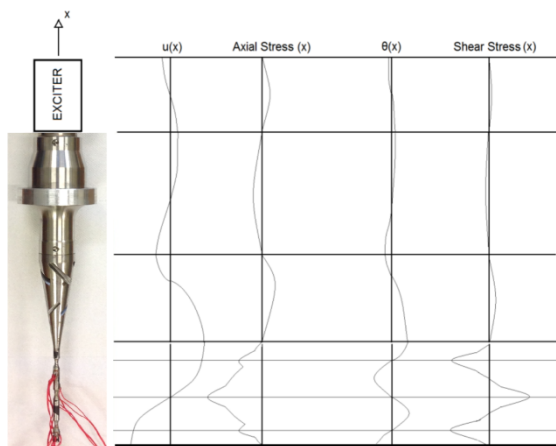


Fig. 3: Representation of axial displacement, rotation, axial and shear stress

## RESULTS AND DISCUSSION

### Thermographic imaging

Because of the high frequencies used on this type of specimen testing, material temperature control represents a challenge on the completion of such tests [1, 5, 7]. Still, because of the fact that the specimen heats up faster on regions where stresses are higher, thermographic imaging may be used to evaluate an approximation of the stress profile on the specimen. First, the specimen was tested using an axial horn, which means that no rotation was being imposed to it. The results of this test are shown in Fig. 4, and axial testing of the specimen confirmed that it is correctly synchronized at the exciter excitation frequency and higher temperature is only observed in the middle throat.

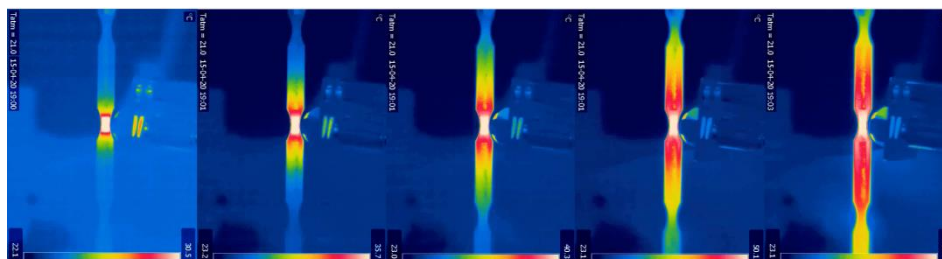


Fig. 4: Thermographic images of the axial tests performed on the specimen.

Second testing was produced with the developed horn (for tension/torsion tests), showing also higher temperatures occurring at the three throats, but with the highest temperature occurring at the middle throat, as expected and is shown in Fig. 5.

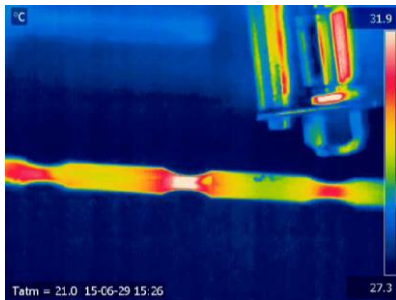


Fig. 5: Thermographic image of specimen testing in tension/torsion.

Therefore, thermographic imaging of the developed specimen and horn indicates that the specimen heats up on the three throats, but much more on the middle one, due to the higher stresses on this region due to the combination of axial and shear stresses, as it was designed to behave.

### Strain Results

To evaluate strains and stresses on the specimen middle throat, a rosette-type strain gauge with three gauges from TML, reference FRA-1-11, was used. Data from the strain gauges during test was measured with a NI 6216 DAQ with the capability of acquiring signals with a 200 kHz sampling frequency. Testing was produced at 20 kHz, using the biaxial horn and the three gorges specimen and the results obtained from the three-way strain gage installed at the middle throat of the specimen are presented on Fig. 6.

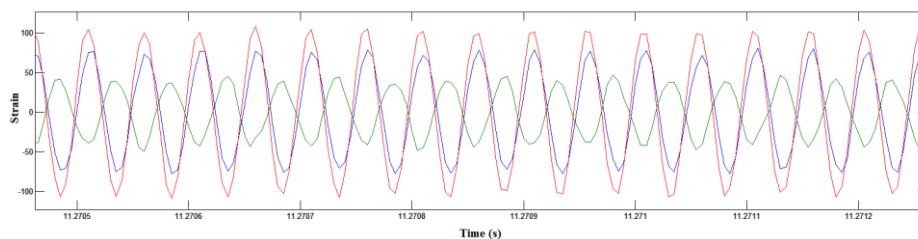


Fig. 6: Signals from the rosette strain gage at the specimen middle throat.

Further stress calculations of the strain data presented in Fig. 6 are shown in Fig. 7. Results confirm the existence of a tension/torsion stress field in the specimen middle throat where for a maximum von Mises stress of 27 MPa a stress ratio  $(\tau_{xy}/\sigma_{yy})=(2/3)$  was determined, therefore a tension/torsion fatigue test at 20 kHz was achieved.

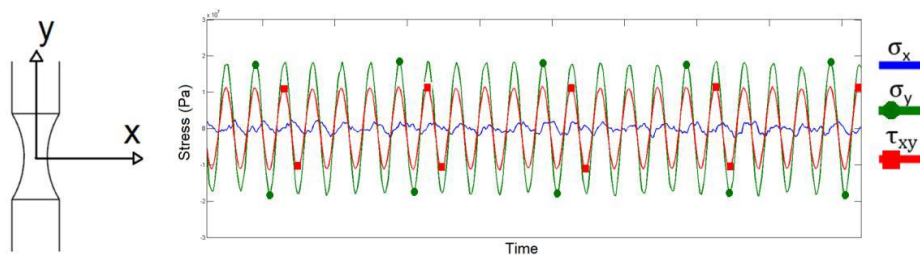


Fig. 7: Central throat axial and shear stresses calculated from experimental tests

## CONCLUSIONS

A device to produce biaxial (axial/torsion) fatigue testing at the VHCF regime, using a single axial ultrasonic actuator, has been developed. Extensive analytical and experimental analyses were produced in order to qualitatively evaluate the dynamic behaviour of the device, specifically on the specimen. Thermographic imaging proved that maximum stresses are registered at the middle throat. A three-way rosette type strain gage was installed on the middle throat in order to acquire strains and evaluate the stresses present on this region, confirming the existence of a biaxial stress state.

Further research is strongly suggested on this field, specifically on specimen control and behaviour, horn geometry influence on the axial/torsional stress ratio and final specimen dimension.

## ACKNOWLEDGEMENTS

Financial support from Portuguese Fundação para a Ciência e Tecnologia (FCT) is acknowledged through Project PTDC/EMS-PRO/5760/2014.

## REFERENCES

- [1] Bathias, C., Paris, P.  
Gigacycle Fatigue in Mechanical Practice,  
Marcel Dekker, New York (2005)
- [2] Socie, D.F. and Marquis, G.B.  
Multiaxial Fatigue  
SAE International, (2000)
- [3] Anes, V., Reis, L., Li, B., de Freitas, M.  
New approach to evaluate non-proportionality in multiaxial loading conditions  
Fatigue and Fracture of Engineering Materials and Structures, (2014) 37, 1338–1354.
- [4] Y. Lage, Y., Cachão, H., Reis, L., Fonte, M., de Freitas, M., Ribeiro, A.  
A damage parameter for HCF and VHCF based on hysteretic damping,  
International Journal of Fatigue, (2014) 62, 2 – 9
- [5] Bathias C.  
There is no infinite fatigue life in metallic materials  
Fatigue & Fracture of Engineering Materials & Structures, (1999) 07; 22(7): 559-65
- [6] B. Pyttel, B., Schwerdt, D., Berger, C.  
Very high cycle fatigue – Is there a fatigue limit?  
International Journal of Fatigue, (2011) 33 49-58.
- [7] Y. Lage, Y., Ribeiro, A., Montalvão, D., Reis, L., de Freitas, M.  
Automation in strain and temperature control on VHCF with an ultrasonic testing facility  
Application of Automation Technology in Fatigue and Fracture Testing and Analysis, STP 1571, P. McKeighan and A. Braun, Eds., (2014) 80-100.
- [8] Vieira, M., Reis, L., Freitas, M., Ribeiro, A.  
Strain measurements on specimens subjected to biaxial ultrasonic fatigue testing  
Theoretical and Applied Fracture Mechanics (2016) 85, 2-8.
- [9] Vieira, M., de Freitas, M., Reis, L., Ribeiro, A.  
Development of a Very High Cycle Fatigue (VHCF) multiaxial testing device,  
Frattura ed Integrità Strutturale, (2016) 37, 131-137

**Corresponding author:** manuel.freitas@tecnico.ulisboa.pt



# METHODOLOGY FOR SPECIMEN DESIGN AT ULTRASONIC FREQUENCIES IN AXIAL/TORSION FATIGUE LOADINGS FOR VHCF

P. Rodrigues da Costa, M. Vieira, M. Freitas, A. Ribeiro, L. Reis\*  
IDMEC, IST, Universidade de Lisboa, Lisboa, Portugal

## ABSTRACT

The procedure to achieve the design of the specimen to fulfill the required axial/torsion loading in a piezoelectric actuator running in resonance at 20 kHz is carried out. The methodology uses a numerical simulation of the specimen under a dynamical modal analysis, carried out in commercial Abaqus software. A previous mesh convergence study was carried out in order to achieve the required accuracy in accordance with experimental results. The main issue in this device and specimen dimensioning are the vibration modes in axial and torsion: in order to achieve the correct vibrational results and specimen dimension, the first axial vibration mode must be achieved at 20 kHz and the same frequency must be achieved in torsional mode. Therefore, and due to the difference in elasticity modulus in axial and torsional modes, the 20 kHz in torsional mode is achieved at the third mode, in steels. In order to validate the created numerical analyses, the obtained values of the stress relations in each throat are then compared with the experimental ones.

## KEYWORDS

Very High Cycle Fatigue, Multiaxial Fatigue, Specimen Design, Experimental tests, Numeric simulations

## INTRODUCTION

From  $1E07$  to  $1E10$  cycles it is considered to be in the very high cycle fatigue regime (VHCF). VHCF became only reliable with the introduction of piezoelectric transducers and with data acquisition equipment capable of acquiring data at a reasonable rate under ultrasonic frequencies. These piezoelectric ultrasonic machines are capable of imposing a controlled vibration to a set of components but only if the attached components are designed with a resonance frequency in the range of the transducer capabilities. The way the components are designed and attached to the transducer is not only important for the experiment to work but it also defines what type of stresses are being applied and studied. Many different test machines were already created to apply different types of loading in different conditions, as shown for example in [1, 2]. In VHCF regime, results have been published either in axial [1,3] or torsion loading [3,4]. The machine used in this paper was developed in the laboratories of DEM in IST by M. Freitas and collaborators [5]. This machine imposes two types of loading simultaneously. This is achieved by inducing the specimen in two different resonance modes, thus creating a biaxial stress condition. The components set is represented in figure 1 where it can be observed the transducer (1), booster (2), horn (3), specimen (4) and the ring (5) where the set will be in contact with the support.

To run the test all components attached to the transducer need to have their natural frequency of the intended mode of around 20kHz, which is the transducer frequency work. This means that all components will be in resonance when the transducer is vibrating. When a component is in resonance the point where the stresses tend to be the highest are on the points where the displacement is null and vice versa. This points are called nodes of displacement for the null

displacement points, and nodes of stress in the null stress points. The resting ring is located in boosters' nodes of displacement so not to disturb the sets resonance.

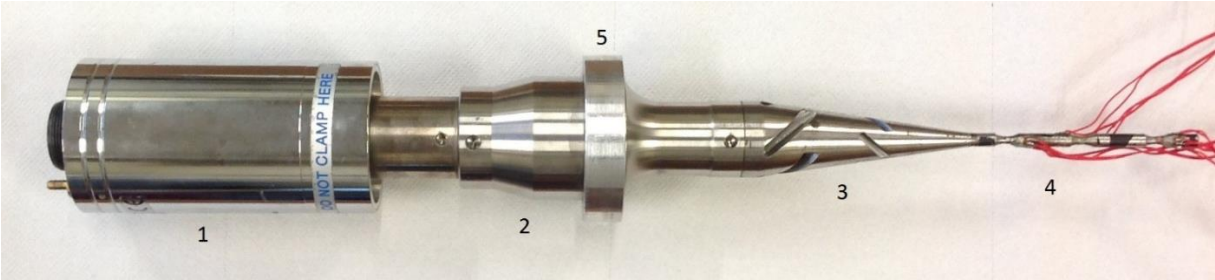


Fig. 1: Set – Transducer (1); Booster (2); Horn (3); Specimen (4); Resting ring (5)

**MACHINE MAIN COMPONENTS**

**The Booster and the horn**

Both booster and horn serve the same purpose, to amplify the displacements derived by the transducer. The amplification occurs due to the reduction of the cross-section area along the length of the booster and horn. Regarding the machine in study the horn has a new and vital purpose to create the rotation movement need it in order to induce the second resonance mode to the specimen. In order to create such rotation, the horn was design in a way where his first axial mode would create a rotation on the smallest radius base. The rotation was achieved by applying two sets of grooves. An iterative process was carried out using finite element software to obtain the final geometry with the correct resonance mode at 20kHz.

**The specimen**

The specimen is the crucial component of the machine. It needs to be well designed and manufactured in order to be able to be induced in two simultaneous resonance modes and to have the higher stresses applied in only one area of study. To achieve two resonance modes simultaneously both modes have to have similar natural frequencies. This happens because the axial and rotational displacements coming from the horn have the same working frequency, the frequency of the working transducer. In order to have a rotational mode with similar frequency to an axial mode the specimen is design with three throats that make it possible to have the third rotational mode alongside with the first axial mode. Comparing the frequencies of the rotational modes with the axial ones for a regular one throat specimen, it is easily concluded that the rotational modes have lower frequencies, as it is shown in table 1.

Frequency	Resonance mode
4807	1° Rotational
20000	1° Axial
64207	2° Rotational
64784	3° Rotational
95281	2° Axial

Table 1: Natural frequency of some of the resonance modes of a one throat ultrasonic tension-compression fatigue test specimen

With the introduction of two other throats the third rotational mode will decrease in frequency, and so it becomes possible to achieve, through an interpolation process with a finite element software, a geometry where both of these modes have similar frequencies. With the introduction of the three throats the two referred modes have now relatively similar natural frequencies as it is possible to observe through table 2.

Frequency	Resonance mode
17735	2° Rotational
20270	1° Axial
20294	3° Rotational

**Table 2:** Natural frequency of some of resonance modes of the new specimen with three throats

It is important to understand how the specimen will deform and subsequently how the stresses will develop in the peak of deformation. The first axial mode has the highest displacement on the bases and the lowest in the center where it has the highest normal stress. The third rotational mode has in each throat a node point where there is no displacement and the shear stress is maximum. The shear stress of the central throat is symmetrical to the remaining throats due to the direction of the applied torsion. Figure 2 a) and b) shows the specimen deformed as well as a graph of the displacement  $u_z$  along its length for each mode.

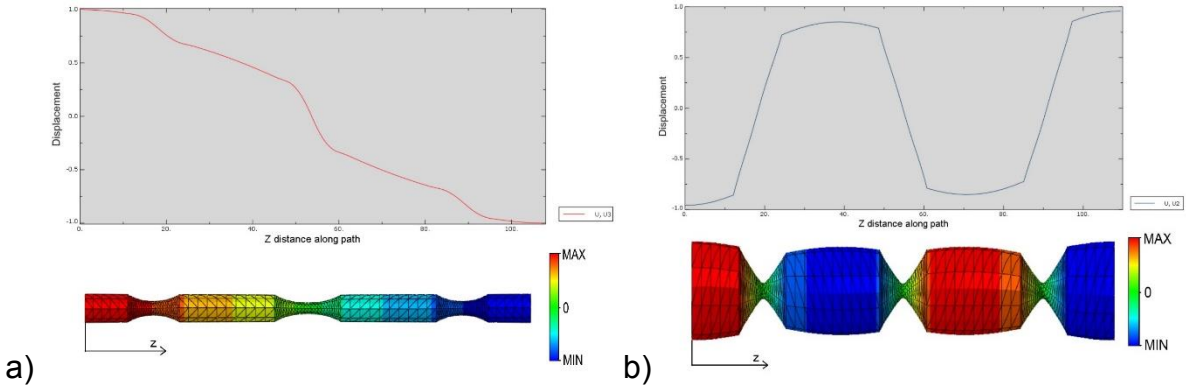


**Fig. 2:** Modal analysis simulation representing the displacements a) first axial mode b) Third rotational mode

**METHODOLOGY**

To fully understand and evaluate the specimen behavior under an induced vibration at 20kHz, strain gauges were applied in the three throats at the smallest cross section, and a numerical analysis was performed. Both methods are compared in order to validate the numerical analysis. Because each throat has its own behavior and results all the three will be analyzed, and therefore each throat is distinguished as represented in figure 3.

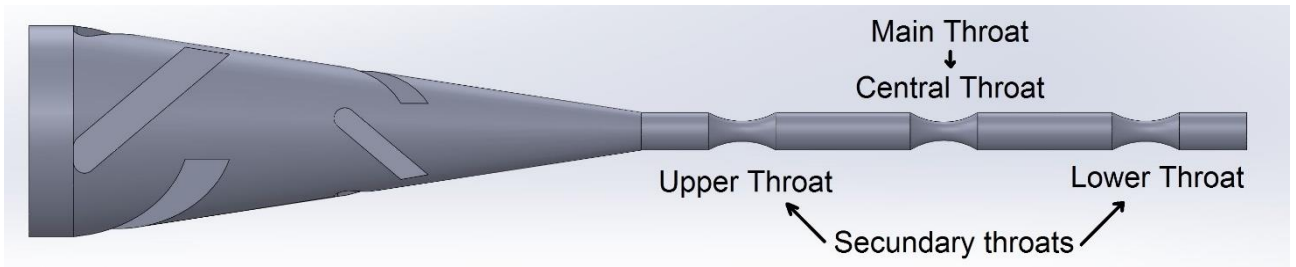


Fig. 3: Throat designations with the horn as reference

### Strain measurements

In order to measure the stress values in each throat at their smallest cross section strain gages were applied. The strain gages installed are rosette-type strain gages with three gages with a 45-degree angle between each other. The data from each strain sensor was obtained separately in order to obtain the biggest number of points in each test. Some preliminary tests were also performed, registering results from pairs of the same rosette-type strain gage to understand how the three signals were related to each other. With the information obtained by the strain gages and with the knowledge of the material properties, it is possible to obtain a good estimation of the stresses applied to the specimen surface. Since all the tests were carried out in elastic deformation conditions, it was only required to know the Young modulus, the Poisson ratio and the density of the used material. An example of the obtained results in the throats is presented in figure 4 for the Upper throat.

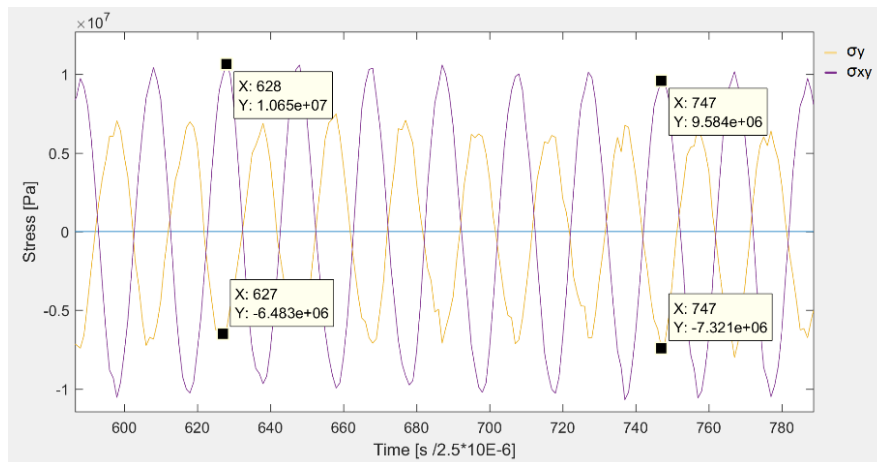


Fig. 4: Normal and shear stresses calculated from data of the strain gage in the Upper throat

With the stress results, obtained through the measured strain values, it's possible to obtain the relation between the maximum amplitude of the shear and normal stress in each throat of the specimen, as presented next:

Upper Throat:  $\tau/\sigma = 1.45$ ; Central Throat:  $\tau/\sigma = -0.66$  [6]; Lower Throat:  $\tau/\sigma = 1.93$

Regarding the results, it is possible to conclude that the stress relation of the secondary throats is different between each other. Theoretically the normal and shear stress should be relatively similar between the secondary throats. The reasons for the unexpected values in the Lower Throat will require further research in order to fully understand its appearance.

**Numerical analysis**

Regarding the finite element analysis of the components set the commercial software Abaqus 6.14-1 was used. All three main components were modelled in the analysis, booster, horn and specimen, with the correspondent materials with the respective elastic, density and Poisson ratio properties. In order to obtain stress values for the resonance mode of interest from a dynamic modal analysis, a modal analysis was initially performed. Through the modal analysis of the set components, it is possible to obtain all the resonance frequencies for all the modes. With the known frequency of the interest mode, a sinusoidal function was created. This function was then used in the dynamic modal analysis for the varying force, applied at the top of the booster, as the transducer carries on in the experiment. The total force applied will vary sinusoidal between the loads of 1.0N and -1.0N. The absolute value of the force is not important for the research since the applied method on the experiment is through power control and always under elastic loading, meaning that the force may vary along the forced vibration in order to maintain the resonance of the set, and in the finite element method is consider to be always on steady state conditions. It is required, in both analyses, to explicitly give the interactions between all the components. It was considered that the components will never slip in the contact area and will never separate. For the dynamic modal analysis, and to have a good resolution of the stress variation in each cycle, the chosen step time was calculated by the following method:

$$\text{Step time} = 1 / (\text{resonance frequency} * \text{number of points in each cycle})$$

If the number of points chosen for each cycle is too low, the results will be compromised due to the bad resolution of the force. The obtained shear stress (S23) and normal stress (S33) at a node in the smallest cross section area of the Upper throat is presented in figure 5 as an example.

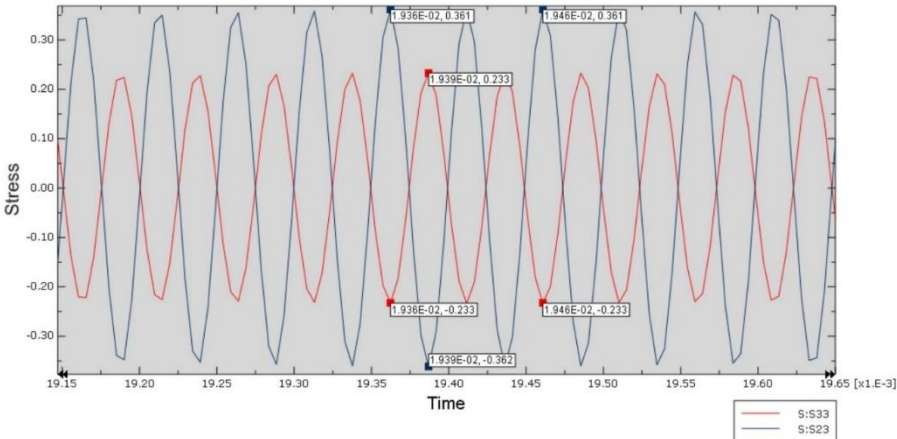


**Fig. 5:** Upper throat: Normal (S33) and shear (S23) stresses calculated by the FEM

**COMPARISON OF RESULTS**

In order to validate the created numerical analyses, the obtained values of the stress relations in each throat need to be compared with the experimental ones. Table 3 shows each of the stress relations obtained and the error between the finite method compared to the experimental one. Through table 3 it is possible to conclude that the created finite element method has a good representation of the experiments with the exception of the lower throat result. This big error in the lower throat is due to an unpredictably higher than expected normal stress obtained in the strain gauge.

Throats	Exp. (Strain Gauges) ( $\tau/\sigma$ )	FEM (Abaqus) ( $\tau/\sigma$ )	Error (%) (Exp-FEM)*100/FEM
Lower	1.14	1.93	40.9
Central	-0.66	-0.71	7.2
Upper	1.45	1.54	5.8

Table 3: Analysis of stress relation in all throats

## REMARKS

The designed specimen worked as intended and estimated, having both resonance modes, torsional and longitudinal, induced at the transducer frequency of around 20kHz. Finite element method showed a good correlation with the experimental results with the exception of the lower throat; at all the three throats the torsional stress is relatively similar, increasing slightly towards the lower throat. Higher than estimated normal stress in the lower throat was the cause of the deviation of the experimental results to the numerical ones. This phenomenon will require further research to fully understand its origin.

## ACKNOWLEDGEMENTS

This work was supported by FCT, through IDMEC, under LAETA, project UID/EMS/50022/2013. Financial support from Portuguese Fundação para a Ciência e Tecnologia (FCT) is acknowledged through Project PTDC/EMS-PRO/5760/2014.

## REFERENCES

- [1] Bathias C:  
There is no infinite fatigue life in metallic materials.  
Fatigue & Fracture of Engineering Materials & Structures 1999 07;22(7):559-65.
- [2] Bathias C:  
Piezoelectric fatigue testing machines and devices,  
International Journal of Fatigue 28, (2006) 1438–1445.
- [3] H. Mayer:  
Ultrasonic torsion and tension–compression fatigue testing: measuring principles and investigations on 2024-T351 aluminium alloy,  
International Journal of Fatigue 28 (2006) 1446–1455.
- [4] H.Q. Xue, C. Bathias:  
Crack path in torsion loading in very high cycle fatigue regime,  
Engineering Fracture Mechanics 77 (2010) 1866–1873.
- [5] Vieira, M., Freitas, M., Reis, L., Ribeiro, A. M., & Fonte, M. d. (2016):  
Development of a very high cycle fatigue (VHCF) multiaxial testing device.  
International Conference on Multiaxial Fatigue & Fracture, 37, 131-137.
- [6] M. Vieira, L. Reis, M. Freitas, A. Ribeiro:  
Strain measurements on specimens subjected to biaxial ultrasonic fatigue testing,  
Theoretical and Applied Fracture Mechanics 85 (2016) 2–8.

\*Corresponding author: [luis.g.reis@ist.utl.pt](mailto:luis.g.reis@ist.utl.pt)

# HIGH-FREQUENCY RESONANCE-REGULATED TESTING DEVICE FOR VERY HIGH CYCLE AXIAL FATIGUE TESTING OF LARGE-SCALE CAST IRON AND STEEL SPECIMENS

**Schaumann P.<sup>1)</sup>, Alt A.<sup>2)</sup>, Kulikowski J.<sup>1)</sup>, Radulovic L.<sup>1)</sup>, Steppeler S.<sup>1) 3)</sup>**

<sup>1)</sup> Leibniz Universitaet Hannover, Institute for Steel Construction, ForWind, Appelstrasse 9A, 30167 Hannover, Germany

<sup>2)</sup> Attila Alt, sole proprietorship, Droste-Huelshoff-Weg 38, 88709 Meersburg, Germany

<sup>3)</sup> now working for TÜV NORD EnSys GmbH & Co. KG, Am TÜV 1, 30519 Hannover, Germany

## ABSTRACT

A new testing device for VHCF tests on large samples has been developed. This device is able to perform tests on axial loaded plate specimens with a thickness of up to 20 mm and a width of up to 50 mm, reaching test frequencies between 400 - 500 Hz. The development is based on a previous device able to perform tests on samples with a thickness of up to 5 mm. The improvements and adjustments of the new testing device in order to enable the fatigue tests on large-scale specimens are presented. The preliminary tests show promising results. With testing frequencies reaching up to 440 Hz, tests with up to  $10^9$  load cycles can be performed in a reasonable time frame.

**keywords:** Fatigue testing device, Very high cycle fatigue, Welded steel joints, Cast iron

## INTRODUCTION

Wind turbines are expected to undergo about  $10^9$  load cycles during their service life [1]. Thus, the fatigue limit state represents a crucial factor in design. The fatigue design in current standards and guidelines is based on S-N curves, which are mostly based on fatigue tests up to  $10^7$  load cycles. The range beyond  $10^7$  load cycles and the question of the existence of an endurance limit is of particular interest of ongoing research [3, 4]. The investigation of this range requires testing facilities able to perform a high number of cycles (between  $10^7$  and  $10^9$ ) within a reasonable time frame, allowing simultaneously tests on relatively large scale specimens to limit possible scale effects. An enlarged experimental basis of fatigue tests is vital for future optimization of this kind of structures. For this reason a new optimized testing device operating at a frequency of up to 500 Hz has been developed. This device is able to perform tests on axial loaded plate specimens with a thickness of up to 20 mm and a width of up to 50 mm. It allows testing with a maximum stress amplitude of 140 MPa and a maximum stress level of 560 MPa with a stress ratio of  $0.1 \leq R \leq 0.5$ . The operating principle of the device is based on the resonance at the level of the first natural frequency of the system composed of the testing device and the specimen. The oscillation at this frequency is induced in the system via electromagnets according to [2]. Fatigue tests with a comparable testing device based on the same principle but limited to specimens with a thickness of 5 mm had already been carried out on butt welds [3-5]. The introduced new



testing device represents an optimized version of the one shown in [3-5] and will be used for fatigue tests of butt welded steel specimens and ductile cast iron specimens with and without notch effects in the range of  $10^7$  to  $10^9$  load cycles.

## TESTING DEVICE

The testing device is not a universal testing machine. It is shaped and designed for predefined geometry of specimens. The operational principle of the testing device is based on the German patent DE 10204258 [2] and illustrated in Figure 1. The device is composed of a resonance test frame and a control system. The resonance test frame has the shape of a closed rectangular frame with cantilever arms at its long sides. The system consisting of resonance test frame and specimen oscillates at its first natural frequency. The nodal points of the first mode are in the corners of the frame. The specimen is fixed between the long sides in the centre of the frame. Due to the symmetry of the first shape mode, the specimen is subjected to purely axial load. The extended ends of the resonance test frame are used as lever arms for the application of the load induced via AC magnets. The specimen is preloaded in tension until reaching the level of the mean stress of a particular test. The bending deformation of the frame caused by the preload of the specimen is neglected in Figure 1 for the sake of simplicity.

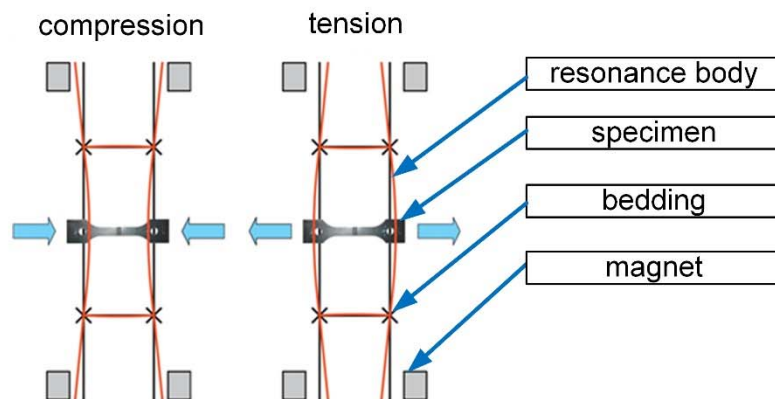


Figure 1: Operational principle of the testing device [4]

The entire control loop of the testing device consists of the test frame, alternating current magnets, strain gauges / accelerometers, measurement amplifier, control unit and power amplifier. Strain gauges are applied at the outer and inner face of the test frame. The measuring signal is then amplified and sent to the control unit. The control unit adjusts the measured signal with the set point and actuates the alternating current magnets with the power amplifier. Hence, the electromagnetic excitation of the resonance body results from the feedback of the signal of oscillation, which is proportional to the loading of the specimen. The calibration of the signal is conducted with test specimens equipped with strain gauges. For more details on the testing device and the control loop refer to [3] and [5].

The previous version of the device is shown in Figure 2 (left). This device was able to perform tests on specimens with a thickness of up to 5 mm. An overview of the performed tests and a summary of the main results are stated in the next section. The accumulated experience is used to identify the main points, which require further development. The design of the new device aims at improving these main points, which are described in the following.

As shown in Figure 2 (left), the specimen is fixed via clamping blocks composed of eccentric shafts and clamping jaws. The specimens and the clamping jaws are provided with holes in

which the eccentric shafts are placed. The preload force is induced in the system by manually screwing the eccentric shafts. This loads the specimen in tension whereas the clamping jaws exert compression load on the test frame. The surface of the clamping jaws was milled, which increased the friction between the jaws and the specimen by means of micro-scale interlock. The clamping blocks are additionally fastened with locknuts to prevent any loosening during the test. With this kind of redundant, overconstrained bearing system accurate preloading is time consuming. Also parasitic dynamic bending load are introduced, because due to the eccentricity of the shaft the sample is slightly shifted out of the frame's centre. Additionally, the contact surface between the clamping jaws and the test frame would corrode during the test, leading to an increase of the preload of the specimen. Considering the bedding, the test frame including the armatures was placed on a support plate. The AC magnets were also fixed on the support plate. From these fixed positions they were maintaining the excitation of the resonating test frame. In order to prevent short-circuit caused by a contact between the AC magnets and the armature oscillating with the frame, the entire frame was also fixed to the plate. In regard to AC magnets, their core was made of ferrite sheets which prevented sufficient current drain by high frequencies. The maximum output voltage of  $73 V_{\text{eff}}$  from 1.2 kW power amplifier had to be transformed to  $486 V_{\text{eff}}$  leading to considerable losses. A separate microcontroller controlled the dependence of the calibration factors on frequency through a set point correction. This was an electronically complex setup which allowed only a reduced insight into the control process.

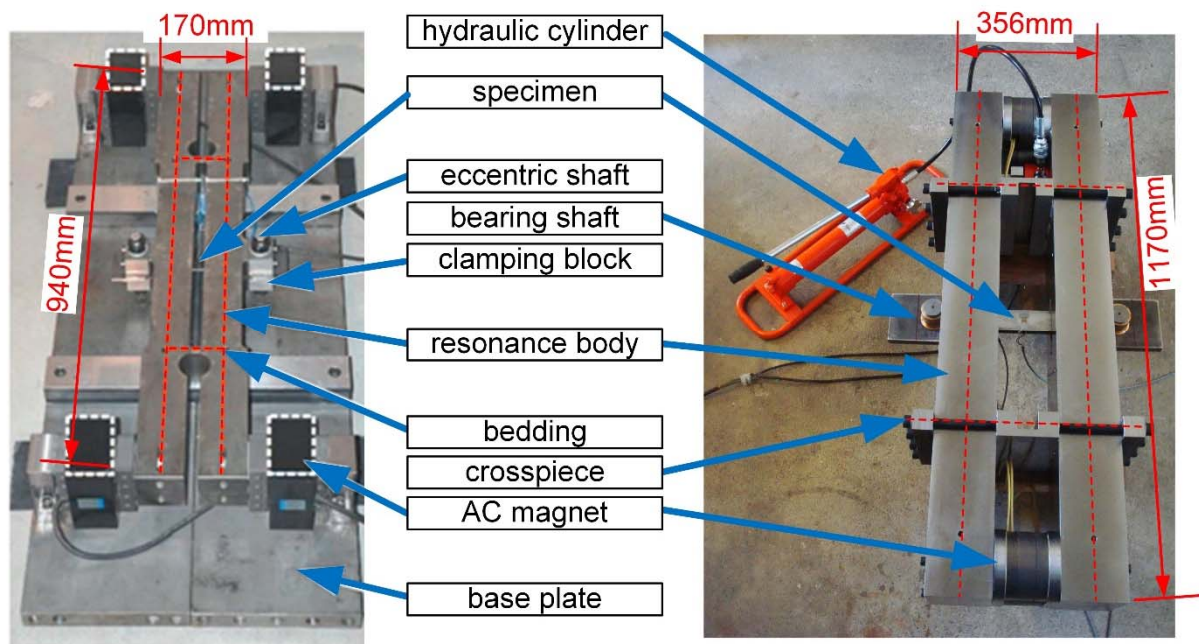


Figure 2: Previous (left) and new (right) design of the testing device

The testing frame of the new device is composed of two steel rectangular beams connected with two crosspieces (see Figure 2 (right)). The specimens are held by two bearing shafts. The hole tolerance H7 of the specimen holes ensures tight fit. With this kind of bearing system of the specimen only axial loads can be induced into the specimen. The preload force is induced via a hydraulic cylinder piston and maintained by inserting of thin plates between the steel beams and the crosspieces. Hence the preload force can be introduced only in a discrete way. More specifically, the additional thickness of the plate of 0.1 mm causes an increase of the preload force by 12 kN. The positioning of the specimen with bearing shafts ensure that there is no parasitic bending moment in the specimen even if it is not positioned in exact centre of the frame. In the new device the magnets are attached to

the levers and oscillate together with the frame. Therefore no support plate is necessary and the entire frame is supported by four rubber feet placed in the frame corners. A new powder metallurgy core of the magnets and a different coiling enable fully use of the power amplifier capacities without necessity for the conversion of voltage. Currently the dependence of the calibration factors on frequency is controlled directly by control unit. The coefficients of the calibration curve can be reset for each test.

**TESTING RESULTS WITH THE PREVIOUS VERSION OF THE TESTING DEVICE**

Test specimens of steel grade S355J2+N with a thickness of 4 mm joined by MAG welding were investigated in [3] and [4]. A total of 89 fatigue test on axially loaded butt welds were conducted in three test series (TS). As a reference, 35 fatigue test were performed in a servo-hydraulic testing machine with a conventional test frequency of 20 Hz and a stress ratio of  $R = 0.1$  (TS 1). With the previous version of the testing device 54 fatigue tests were carried out with approximately 390 Hz and stress ratio of  $R = 0.1$  (TS 2) and  $R = 0.5$  (TS 3). Run outs were stopped at  $5 \cdot 10^8$  load cycles. Thus, a single fatigue test with a run out specimen required 15 days of testing.

The results of all test series (TS 1, TS 2 and TS 3) are shown in Figure 3. The fatigue data show a fatigue limit. In the high cycle regime no significant influence of the test frequency is observed; whereas the fatigue limit of TS 2 with 390 Hz is little lower than of TS 1 with 20 Hz. Both curves show a good agreement, which demonstrates that the testing devise was qualified for the fatigue tests. The influence of increased mean stress is evident in high cycle regime, resulting in a shallower fatigue strength curve. For more details on the experimental agenda and the results of the fatigue test refer to [3] and [4].

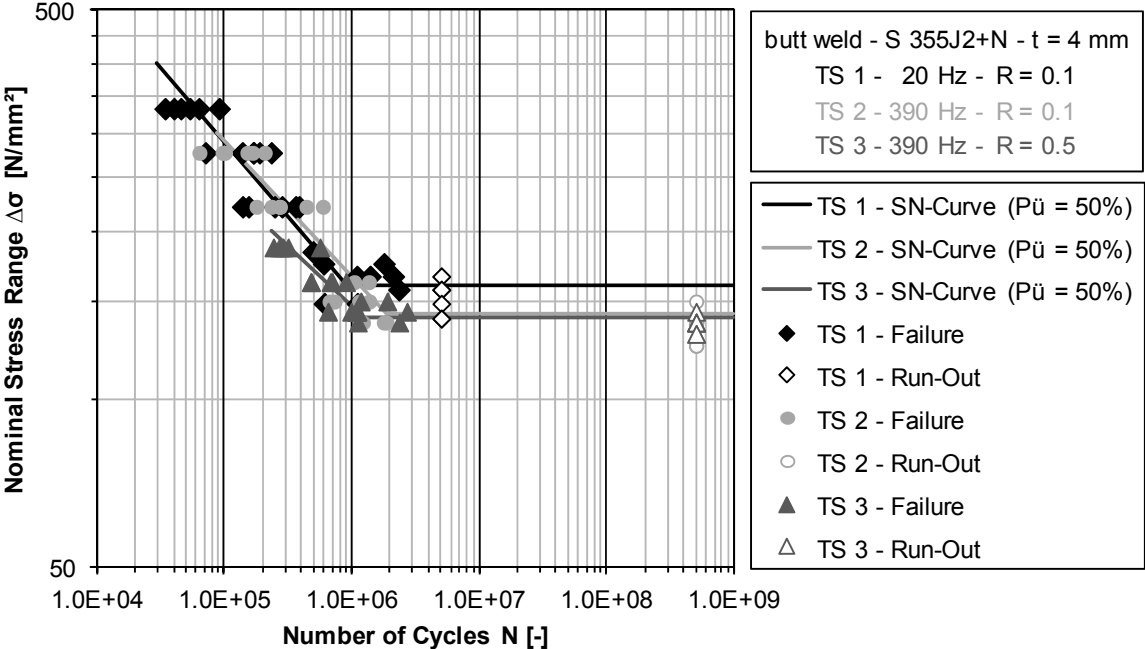


Figure 3: Test results of TS 1, TS 2 and TS 3

**TEST PLAN AND PRELIMINARY RESULTS**

The new testing device is developed for tests on two different types of specimens, both having a thickness of 20 mm. The first type represents the ductile cast iron specimen with

and without notch effect. The notch effect is obtained creating a trapezoidal shear key with a notch radius of 15 mm. This radius is chosen as it represents the minimum radius that can be casted and thus the most unfavourable geometrical configuration. The second type represents butt welded steel specimens.

The geometry of the samples is influenced by different level of expected notch stress. Another limiting factor is the way in which the specimens are loaded. As the load is induced via two shafts, the specimens have to be manufactured with two lateral holes (see Figure 4). The presence of the hole creates notch stresses. The samples have to be designed in such a way that a crack is initiated in the nominal cross-section rather than in the holes. Considering these limitations, the ductile cast iron specimen may have a maximum width of 20 mm, whereas the specimens with shear key can be designed with a width of up to 30 mm. In order to allow the comparison of the results, both configuration of the ductile cast iron specimen are designed to have a width of 20 mm. Due to higher notch stresses of the weld, steel samples can be designed with a thickness of up to 50 mm.

The final design of specimens is featured by a rectangular nominal cross section with tangential transitional fillets between the testing region and the load introduction regions on the sample's ends (see Figure 4). Recommendations according to [6] have been taken into account. The goal is to obtain a stress distribution along the specimen as constant and uniform as possible. The optimization of transitional fillets has been performed based on [7] and [8]. Instead of a traditional solution with constant radius, a set of potential functions of type  $f(x) = (x/a)^b$  describing the geometry of the fillet has been studied. In this way, the stress concentration in the transition region can be smoothed almost completely. For example, in case of specimens with a thickness of 20 mm, by designing the fillets with potential function  $f(x) = (x/28.5)^3$  the stress concentration factor was reduced to  $K_t = 1.01$ . The comparison of stress distribution along the fillets defined on one hand with constant radius and on the other with optimized potential function is shown in Figure 4 (right).

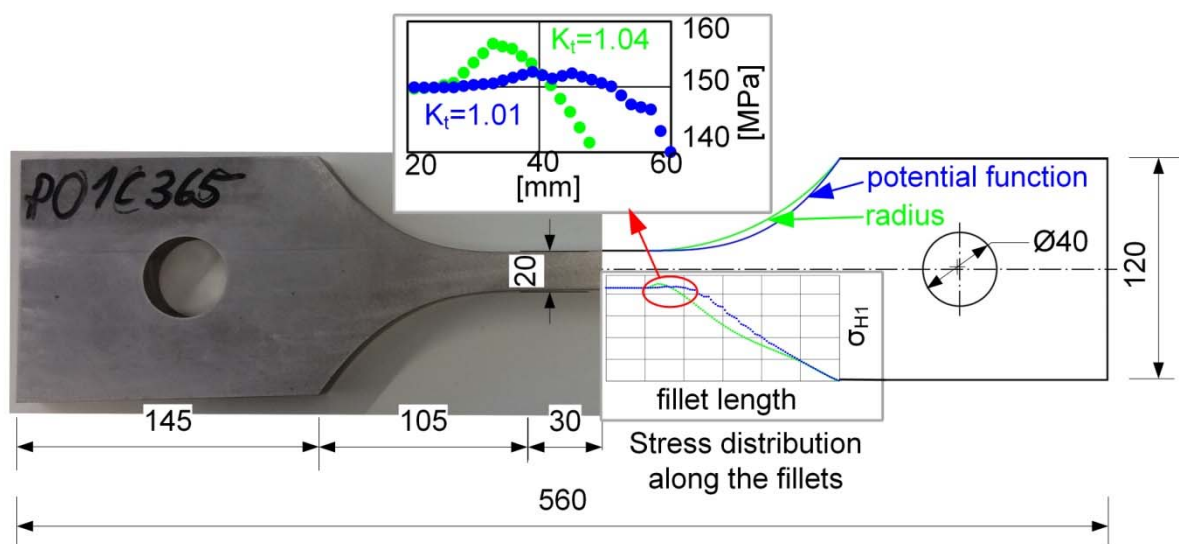


Figure 4: Ductile cast iron specimen without notch effect (left); comparison of distribution of 1<sup>st</sup> principal stress along the fillets defined via constant radius and via potential function (right)

At actual level of development, the first pre-experimental tests with the newly developed resonance test frame allow for the following results. The ductile cast iron specimens run at a frequency of 420 Hz. Furthermore, the welded steel samples with a nominal cross section of 1000 mm<sup>2</sup> ( $b \times t = 50 \text{ mm} \times 20 \text{ mm}$ ) run at 440 Hz. The mentioned results for both types of

specimens are obtained under a mean stress of 200 MPa. However, with the currently used 1.2 kW power amplifier, too low stress amplitudes can be reached. Those are 30.5 MPa for the ductile cast iron specimen and 18 MPa for the steel specimens. It is planned to run the device with a 6 kW power amplifier. By applying linear interpolation this would lead to a stress amplitude of 132 MPa for the ductile cast iron specimens and 90 MPa for the steel samples. Possibly, the nominal cross section of the welded steel samples must be reduced in order to achieve adequate stress amplitudes.

## ACKNOWLEDGMENTS

Both presented versions of the testing device have been developed by Attila Alt. The development of the new device as well as the presented new studies have been carried out within the ForWind joint research project "ventus efficiens – Joint research for the efficiency of wind energy converters within the energy supply system", financially supported by the Ministry for Science and Culture in Lower Saxony, Germany as well as within the research project "HyConCast - Hybrid substructure of high strength concrete and ductile iron castings", which is funded by the German Federal Ministry for Economic Affairs and Energy. The authors thank the Ministry for Science and Culture in Lower Saxony and the Federal Ministry for Economic Affairs and Energy for funding and all project partners for the cooperation.

## REFERENCES

- [ 1 ] Seidel M.:  
Load characterization of axially loaded jacket piles supporting offshore wind turbines  
Workshop Proceedings "Gründung von Offshore-Windenergieanlagen" (2014)  
Karlsruhe
- [ 2 ] Alt A.:  
Patent DE 10204258 B4: Prüfvorrichtung zur Dauerschwingprüfung von Prüflingen  
2007
- [ 3 ] Steppeler S.:  
Zum Ermüdungsverhalten von Stumpfnahtverbindungen bei sehr hohen  
Lastwechselzahlen  
Doctoral Thesis Leibniz Universität Hannover, 2014; Publication series of the  
Institute for Steel Construction, Vol. 32, Shaker Verlag, Hannover, 2014
- [ 4 ] Schaumann S.; Steppeler S.:  
Fatigue tests of axially loaded butt welds up to very high cycles  
Procedia Engineering 66 (2013), pp. 88-97
- [ 5 ] Schaumann S.; Keindorf C.; Alt A.:  
Hochfrequente Ermüdungstests an Schweißverbindungen mit einem neu entwickelten  
Magnetresonanzprüfrahmen  
Conference Proceedings „Große Schweißtechnische Tagung“, Dresden, 2008
- [ 6 ] ISO 1099: Metallic materials – Fatigue testing – Axial force-controlled method, 2006
- [ 7 ] Zenner H.; Buschermöhle H.:  
Vereinheitlichung von Proben für Schwingversuche  
FKM Vorhaben Nr.: 198, Heft 217 (1996)
- [ 8 ] Shirani M.; Härkegård G.:  
Large scale axial fatigue testing of ductile iron for heavy section wind turbine  
components  
Engineering Failure Analysis 18 (2011), pp. 1496-1510

**Corresponding author:** radulovic@stahl.uni-hannover.de

# ON THE USE OF THERMOGRAPHIC TECHNIQUE TO DETERMINE THE FATIGUE LIMIT OF A COLD DRAWN CARBON STEEL

**Bandeira C.F.C.<sup>(1)</sup>, Kenedi P.P.<sup>(2)</sup>, Castro J.T.P.<sup>(3)</sup>, Meggiolaro M.A.<sup>(4)</sup>**

<sup>(1,2)</sup> Programa de Pós Graduação em Eng. Mecânica e Tecnologia de Materiais CEFET - Rio de Janeiro - Brazil, <sup>(1)</sup> fillypebandeira@hotmail.com, <sup>(2)</sup> paulo.kenedi@cefet-rj.br

<sup>(3,4)</sup> Departamento de Engenharia Mecânica PUC - Rio de Janeiro - Brazil

<sup>(3)</sup> jtcatro@puc-rj.br, <sup>(4)</sup> meggi@puc-rj.br

## ABSTRACT

An accelerated thermographic technique and classic procedures are used to measure the fatigue limit of a cold drawn SAE 1020 carbon steel, using a rotating bending machine. Material temperature variations for different stress amplitude levels are accessed using an infrared camera. To validate the fatigue limit obtained by thermography, it is compared to the limit obtained by the traditional Nixon's up-and-down technique. Experimental results confirm that the fast thermographic approach yields fatigue limits quite close to the much slower staircase technique, indicating that it can be really a major asset for practical applications.

## KEYWORDS

Fatigue, Fatigue limit, Thermography, Staircase.

## INTRODUCTION

The fatigue or endurance limit  $S_L$  is an important parameter for design purposes, since it establishes a material strength that supposedly can be used to avoid fatigue failures in practice. The fatigue limit obtained by testing small polished specimens can be modified to be used in the design or analysis of real structural components, considering modifying factors to account for the effects of surface finish and similar parameters that typically reduce it [1]. However other factors like compressive residual stresses or even coxing (fatigue strengthening due cycling loading close to  $S_L$ ) can increase the fatigue limit [2-5].

Classic methods to obtain the fatigue limit require a large number of specimens, are laborious, time consuming, and quite expensive. Fortunately, new thermographic techniques have been recently developed to obtain fatigue limits in a much cheaper and fast way [6-13]. This method can be much more efficient than the standard up-and-down (or staircase) method, which has been traditionally used as a so-called accelerated method to determine the fatigue limit of materials, albeit it does not deserves this name. Thermography, on the other hand, is a really fast method to determine fatigue limits. The idea is to correlate the stress amplitude  $\sigma_a$  with the heat it generates on the specimen surface, since it can be used to determine the fatigue limit of materials through the location abrupt temperature variations induced by the transition between elastic and cyclic plastic strains, the cause for fatigue damage.

## THE THERMOGRAPHIC TECHNIQUE

The thermographic technique is characterized by the use of thermo-elasticity principles to determine the fatigue limit. It assumes that fatigue failures in materials occur when the



plastic deformation energy reaches a constant value, characteristic of each material [7, 8]. This physically reasonable hypothesis allowed a rapid correlation between temperature increments and the number of loading cycles, since fatigue damage clearly is an energy dissipation process [9]. Figure 1 shows a typical temperature versus number of cycles curve obtained by thermographic techniques during a fatigue test.

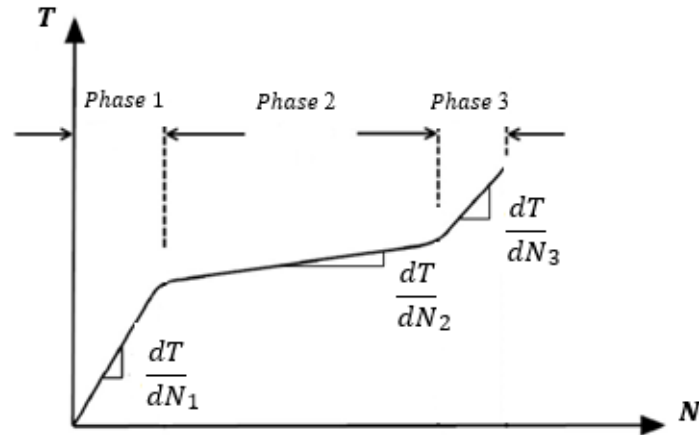


Figure 1: Typical  $N$  vs  $T$  relation observed at a critical point during a fatigue test.

Phases 1, 2, and 3 in Figure 1 represent the three thermal stages observed on the surface of a fatigue specimen during a typical thermographic fatigue test. These stages can be associated to the fatigue process, with phase 1 representing the crack nucleation, phase 2 the crack propagation, and phase 3 the imminent sudden failure. Depending on the stress level, the  $T \times N$  curves typically translate on both the  $T$  and  $N$  axes, reducing the temperature variations and increasing the number of cycles to failure as  $\sigma_a$  approaches  $S_L$ . If  $\sigma_a < S_L$ , the temperature does not change or changes very little, generating  $dT/dN_1 = dT/dN_2 = dT/dN_3 \sim 0$ , indicating no fatigue damage generation.

From the typical behavior of  $T \times N$  curves, Risitano et al. [7-8, 10] proposed to determine the fatigue limit in a very fast way by evaluating only their phase 1 for several stress amplitudes, using a single specimen to plot  $\sigma_a \times \Delta T_1$  or  $\sigma_a \times dT/dN_1$ , where  $\Delta T_1$  is the temperature variation at the end of phase 1. The behavior of  $\sigma_a \times \Delta T_1$  or  $\sigma_a \times dT/dN_1$  curves typically has a bilinear trend with different slopes, and the fatigue limit is determined by the intersection between the curve with highest slope with the  $\sigma_a$ -axis, when  $\Delta T_1 = 0$  or  $dT/dN_1 = 0$ .

## EXPERIMENTAL RESULTS

The material characterization was done by its chemical composition and by tensile tests. The specimen geometry was defined according to ASTM E466-15 [14]. The fatigue tests were performed in a rotating bending machine RBF 200 with a test frequency around 8500rpm ( $\approx 141\text{Hz}$ ). The traditional up-and-down sequential tests considered  $5 \cdot 10^6$  cycles as a suitable life to characterize the classic fatigue limit of steels, and the thermography tests were performed using the temperature increasing rate of phase 1 to determine the fatigue limit.

### Material Characterization and Specimen Definition

The material used in this research is a carbon steel SAE 1020, obtained by a cold drawn manufacturing process. Table 1 shows this material chemical composition and Table 2 its tensile mechanical properties.



Table 1: Chemical Composition

C	Si	Mn	P	S	Cr	Ni	Mo	Al	Cu	Ti	Nb	V
0,226	0,114	0,510	0,020	0,0028	0,024	0,011	0,003	0,017	0,026	<0,001	<0,003	0,001

Table 2: Tensile Mechanical Properties

Specimen number	$S_y$ (MPa)	$S_{UT}$ (MPa)	$EL$ (%)	$AR$ (%)
1	590	680	14,5	48,50
2	535	635	-	51,50
3	605	685	-	50,50

$S_y$  is the yield strength,  $S_{ut}$  is the ultimate strength,  $EL(\%)$  is the elongation and  $AR(\%)$  is the area reduction. The flow stress, or the mean value of  $S_y$  (575 MPa) and  $S_{ut}$  (665 MPa), was used in initial fatigue tests to adjust and calibrate the test machine. Manufacturing precautions were taken in order to guarantee the data repeatability and reliability, as recommended by ASTM E466-15 standard. The test specimens have a mean roughness  $R_a = 0.78 \mu m$ . Figure 2 shows the fatigue test specimens dimensions.

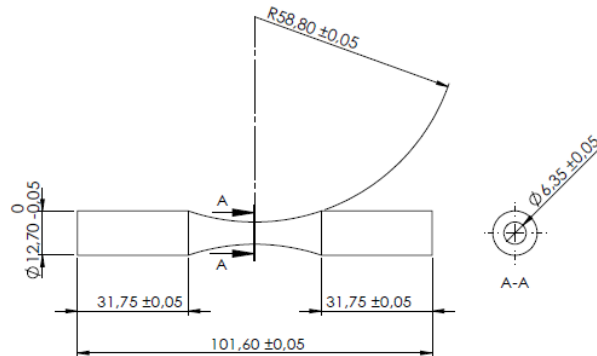


Figure 2: Specimen geometry

The stress amplitude steps used in the classic up-and-down tests (either to increase or to decrease the load in subsequent tests after a failure or a survival, respectively) was  $s = \sigma_a/S_{ut} = 2\%$ . The first value of  $\sigma_a/S_{ut}$  was an educated guess of 40%, based on the relatively high material tensile strength and on its good surface finish. Figure 3 shows results obtained with from staircase method.

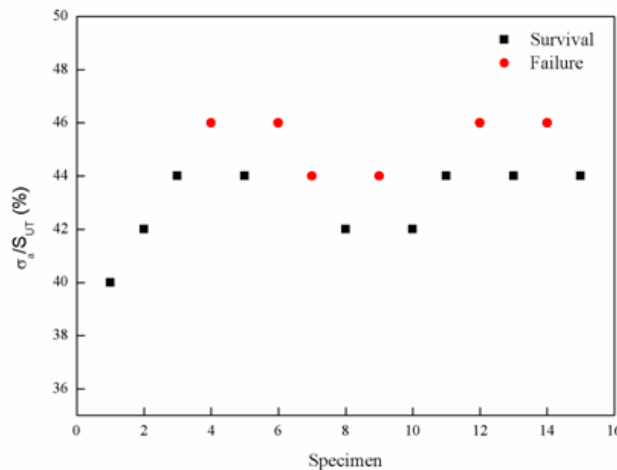


Figure 3: Staircase Results

These 15 test results have been statistically analyzed by Dixon's method [15], to determine the mean value ( $\mu$ ) and standard deviation ( $\varphi$ ) of the fatigue limit measured by staircase approach ( $S_{L_{SC}}$ ), see Equation 1.

$$S_{L_{SC}} = \mu \pm \varphi \rightarrow S_{L_{SC}} = (44,3 \pm 2,4)\% \rightarrow S_{L_{SC}} = (295,2 \pm 7,1)MPa \quad (1)$$

## Thermographic Results

The specimen surface temperature variation was recorded in real time by a FLIR A320 infrared camera, with resolution of 320 x 240 pixels, data acquiring frequency of 30Hz, and temperature sensibility of 50mK. This thermographic camera, which is not cheap, but is not as expensive as fancier models either, proved to have enough resolution and accuracy to perform the required temperature measurements. In order to improve the camera performance, the middle surface of all fatigue specimens was black painted to increase their emissivity, as shown in Figure 4. In addition, a black cloth was used to cover the test machine and the infrared camera, to minimize the effect of unavoidable noise sources induced by the variable laboratory environment.



Figure 4: Black Painted Specimen

First, the camera was used to characterize the material temperature variations until the final fatigue failure induced by  $\sigma_a/S_{ut} = 60\%$ ,  $56\%$ ,  $54\%$  and  $52\%$ , to investigate the behavior of the three temperature phases and their associated increasing rates  $dT/dN$ . In the sequence, other stress amplitude levels were tested only until the start of phase 2, using always the same specimen. Finally, the curve  $\sigma_a$  vs  $dT/dN_1$  was plotted to define the fatigue limit according to Risitano et al. method.

Figure 5 shows the curves  $T_{max} \times N$  measured for each stress amplitude and Figure 6 shows some images extracted from the ResearchIR software during the fatigue test for  $\sigma_a/S_{ut} = 60\%$ .

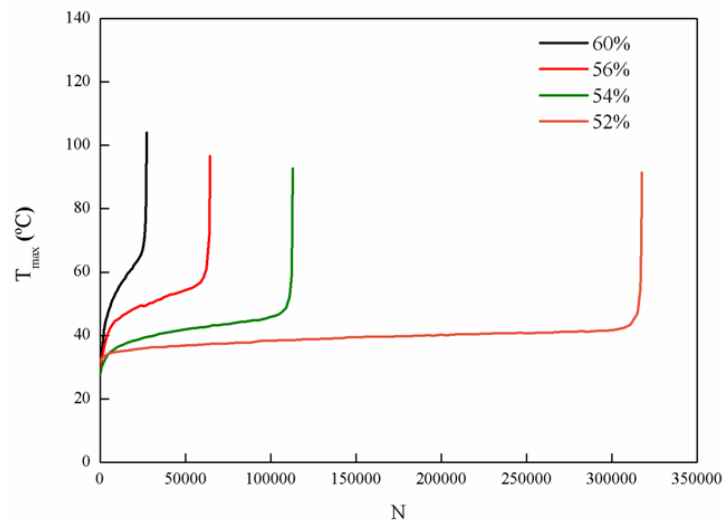


Figure 5: Relation  $N$  vs  $T_{max}$ .

Figure 5 shows that phase 1 is responsible for a small part of the total number of cycles reached for each stress amplitude until failure, as observed by *Fargione, et al* [8]. In addition, Figure 5 shows that the material behavior in phase 2 is not characterized by temperature stabilization, but by a relatively small constant temperature increase rate.

Figure 6 shows the temperature evolution for  $\sigma_a/S_{ut} = 60\%$  during the entire fatigue test with pictures extracted from the ResearchIR software used by the FLIR camera to show the temperature field on the specimen surface. To determine the fatigue limit, the curves  $\sigma_a$  vs  $dT/dN_1$  are plotted for all stress amplitude tested. Two curves are fitted to determine the fatigue transition region, with the abrupt slope changing. Figure 7 shows  $\sigma_a$  vs  $dT/dN_1$  and the fitting curves.

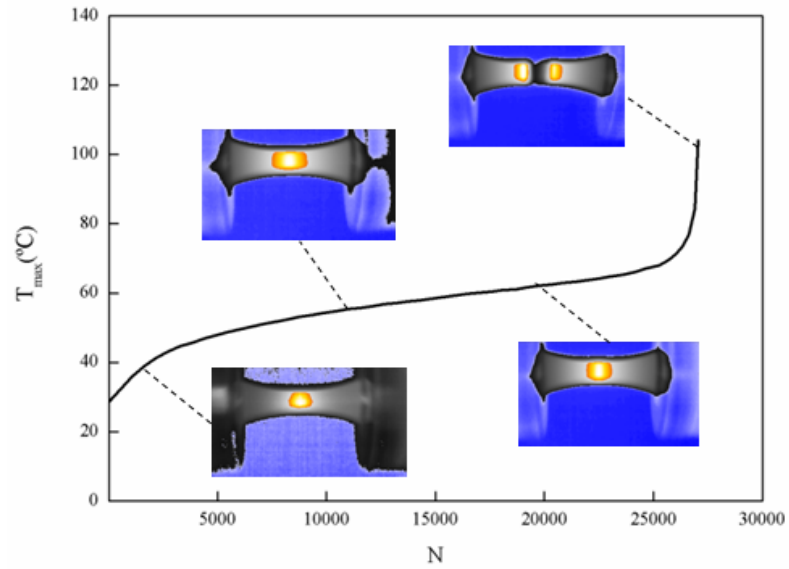


Figure 6: Relation  $N$  vs  $T_{max}$  - Temperature Evolution for  $\sigma_a/S_{UT} = 60\%$ .

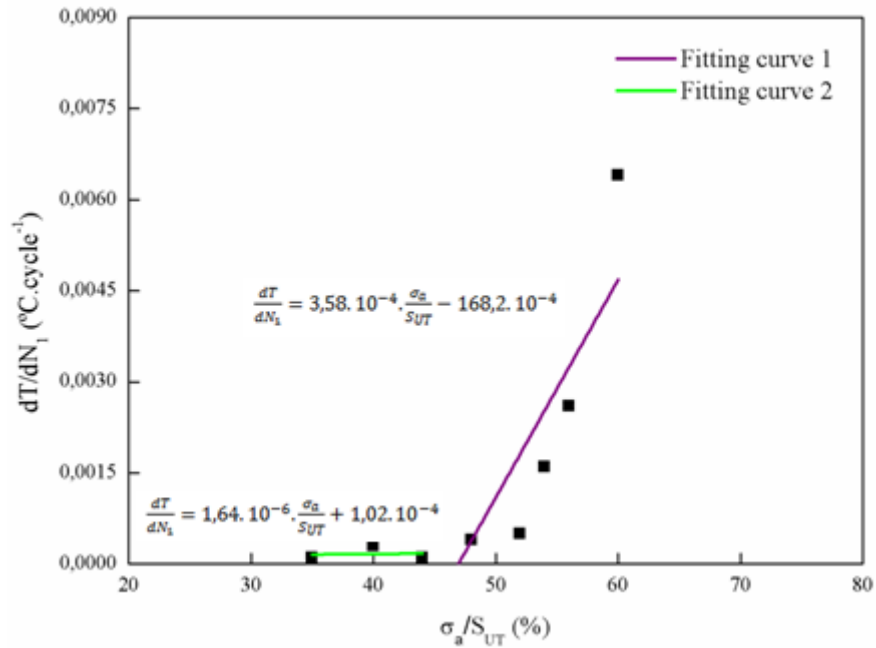


Figure 7: Fitting Curves

To determine the fatigue limit using the thermographic method ( $S_{L_{TH}}$ ), the fitting curve 1 has to be prolonged until it crosses the  $\sigma_a$ -axis, where  $dT/dN_1 = 0$ .

$$0 = 3,58.10^{-4} \cdot \frac{\sigma_a}{S_{UT}} - 168,2.10^{-4} \quad (2)$$

$$\frac{\sigma_a}{S_{UT}} = S_{L_{TH}} = 46,9\% \quad (3)$$

## DISCUSSION OF RESULTS

The fatigue limit determined by the classic up-and-down or staircase method based on fifteen specimens tested in a sequential way, following a pass or no-pass methodology, yielded a relatively small (for fatigue tests) standard deviation when compared to its mean value ( $288,1\text{MPa} \leq S_{LSC} \leq 302,3\text{MPa}$ ), as calculated by Dixon's statistical tools, indicating a relatively homogeneous sample.

The fatigue limit determined by the thermographic method  $S_{LTH} = 311,9\text{Mpa}$  was slight higher, but still close to value obtained by the much slower staircase method. The 8.3% difference between them is within the values observed by *La Rosa et al* [7].

## CONCLUSION

The thermographic approach was used to determine the fatigue limit of a cold drawn steel SAE 1020, yielding a fatigue limit slight higher than the value obtained by the much slower and laborious up-and-down methodology, indicating it can indeed be used as a practical tool to measure such an important property in practical applications.

## REFERENCES

- [1] Shigley, J.E.; Mishke, C.R.; Budynas, R.G. Mechanical Engineering Design, McGraw-Hill 2004.
- [2] Bathias, C.; Paris, P. C. Gigacycle fatigue in mechanical practice, Marcel Dekker, 2005.
- [3] Nicholas, T. High cycle fatigue – A mechanics of materials perspective, Elsevier 2006.
- [4] Pollak, R.; Palazotto, A.; Nicholas, T. A simulation-based investigation of the staircase method for fatigue strength testing. *Mech Mater* 38:1170-1181, 2006.
- [5] Castro, J.T.P.; Meggiolaro, M.A. Fatigue Design Techniques, v. 1: High-Cycle Fatigue. CreateSpace, 2016.
- [6] Luong, M. P. Fatigue limit evaluation of metals using an infrared thermographic technique. *Mech Mater* 28:155-163, 1998.
- [7] La Rosa, G.; Risitano, A. Thermographic methodology for rapid determination of the fatigue limit of materials and mechanical components. *Int J Fatigue* 22:65-73, 2000.
- [8] Fargione, G.; Geraci, A.; La Rosa, G.; Risitano, A. Rapid determination of the fatigue curve by the thermographic method. *Int J Fatigue* 24:11-19, 2002.
- [9] Curà, F.; Curti, G.; Sesana, R. A new iteration method for the thermographic determination of fatigue limit of steels. *Int J Fatigue* 27:453-459, 2005.
- [10] Risitano, A.; Risitano, G. Cumulative damage evaluation of steel using infrared thermography. *Theor Appl Fract Mech.* 54:82-90, 2010.
- [11] Hou, P.; Fan, J.; Guo, Q.; Guo, X. The application of the infrared thermography on Ti alloy for studying fatigue behavior. *Frattura ed Integrità Strutturale* 27:21-27, 2014.
- [12] Lipski, A. Thermographic method based accelerated fatigue limit calculation for steel X5CRNI18-10 subjected to rotating bending. *Polish Maritime Res* 22:64-69, 2015.
- [13] Lipski, A. Accelerated determination of the fatigue limit and the S-N curve by means of the thermographic method for X5CrNi18-10 steel. *Acta Mech Autom* 10:22-27, 2016.
- [14] ASTM E466: Standard practice for conducting force controlled constant amplitude axial fatigue tests of metallic materials, ASTM 2015.
- [15] Dixon, WJ. The up-and-down method for small samples. *Am Stat Assoc J* 60(312): 967-978, 1965.

Corresponding author [jtcastro@puc-rj.br](mailto:jtcastro@puc-rj.br)

# A first proposal of a new high frequency testing method for high strength steels under tension / compression loading in the VHCF regime

I. Milošević<sup>a</sup>, G. Winter<sup>a</sup>, F. Grün<sup>a</sup>, M. Kober<sup>b</sup>

<sup>a</sup>Chair of Mechanical Engineering, Montanuniversitaet Leoben, Franz-Josef-Strasse 18, Leoben 8700, Austria

<sup>b</sup>LEC GmbH, Inffeldgasse 19/II, Graz 8010, Austria

## ABSTRACT

In the present paper, a high frequency testing method for high strength steels is proposed through vibration-induced loadings. The setup used provides a sinusoidal excitation force by means of vibration technology in a certain frequency range up to 2kHz, as commonly used high frequency testing methods work beyond this range. Analytic and FEA calculations supported by experiments showed the applicability for specimen tests. Specimens with a diameter of  $D=2.5\text{mm}$  were tested at room temperature, different frequencies and various accelerations (load levels). Actual calculations and the experiment of the designed setup showed good correlation of the results. The analytic result proposed a resonant frequency between 732 – 1032Hz due to the calculation approach, which was highly influenced by certain boundary conditions. The FEA (782Hz) and the experiment (788Hz) showed very small differences because of the comprehensive possibilities of FEA modelling. Tests up to frequencies of 1kHz showed no self-heating of the specimen.

## KEYWORDS

High frequency testing, very high cycle regime, analytic vibration calculation, modal analysis

## INTRODUCTION

Since the early 19<sup>th</sup> century, different well-known researchers have examined metal fatigue. August Wöhler [1] described the fact that periodic macroscopic loads lower than the material's elastic properties caused failures after a certain number of repetitions. [2]

100 years ago, new requirements were outlined by the industry through progress and development of modern technologies such as automobile, railway and airplane industry. To meet these new fields of interest concerning time and economic issues testing technology had to be developed towards higher testing frequencies. Neppiras [3] proposed a testing technique for very high frequencies commonly known as ultrasound respectively ultrasonic testing devices (UST). Some of many possible comprehensive investigations regarding actual tests with UST were done by Stanzi-Tschegg [4,5], Mayer [6] and Zettl [7].

The present study focuses on a possible testing technique in a preselected frequency range up to 2 kHz. As testing specimens and components is one of the main goals, a technique besides the conventional hydraulic (...-30Hz) and resonant testing applications (...-150Hz) was developed to reach 1E9 cycles within days. Through the fact that high cycle fatigue results cannot be useful extrapolated to 1E9 cycles [8], the transfer of high frequency results (20 kHz) to low frequency results (20 Hz) is not always possible [9] and the influence of the testing frequency respectively load speed is still not clarified [10] a different testing setup was needed.

## SPECIMEN, MATERIAL and TESTING

### Material

As high strength steels were used for several applications especially for high loaded parts, a type X5CrNiCuNb16-4 (Table 1) steel is used for the tests. The content of alloying elements is given in maximum percent by weight.

	C	Cr	Ni	Cu
max.	0.07	17.0	5.0	5.0

Table 1: Composition of a high strength steel X5CrNiCuNb16-4 (wt%, DIN EN 10088)

This corrosion resistant steel is machined to the specimen shape displayed below in Figure 1. Heat treatments are shown in different data sheets and the major parameter range can be extracted from Table 2. As the material properties were adjusted individually through the heat treatment for each application, the strength range of the material is given.

	$R_m$	$R_{p0.2}$	$A_5$
	[MPa]	[MPa]	[%]
Range	$\geq 520$ to $\geq 1270$	$\geq 520$ to $\geq 1000$	$\geq 10$ to $\geq 18$

Table 2: Static strength data X5CrNiCuNb16-4 according to DIN EN 10088-3

### Specimen and testing

Results of analytic calculations regarding resonant frequency and shape lead to geometrical properties of the machined specimen in Figure 1. The cross section  $D=2.5\text{mm}$  is arranged in the centre of the specimen ensuring maximum stress in this region.

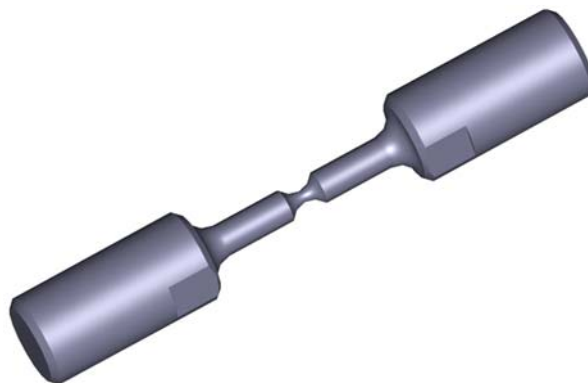


Figure 1: Shape of the used specimen, round cross section.

The testing setup was mounted on a shaker system i210 by IMV Europe Ltd., which can be seen in Figure 2. This system is an electrodynamic shaker (excitation system) providing a sinusoidal force to achieve high loads within the specimen cross section. It is possible to run the system in resonant mode or not.



Figure 2: Shaker system i210 (and components) provided by IMV Europe Ltd.

$$\omega_{res} = \sqrt{\frac{c}{m}}$$

Equation 1: Resonant frequency calculation

As mentioned above a testing setup is mounted on the shaker with M8 bolts. The principle of the test setup is shown in Figure 3. Through acceleration (Equation 2) of the whole testing cell the mass exerted a force on the specimen. The masses and the stiffness of the system determined the resonant frequency (Equation 1).

$$m\ddot{x} + b\dot{x} + cx = \hat{F} * \sin(\omega t + \varphi_0)$$

Equation 2: Harmonic vibration, external excited

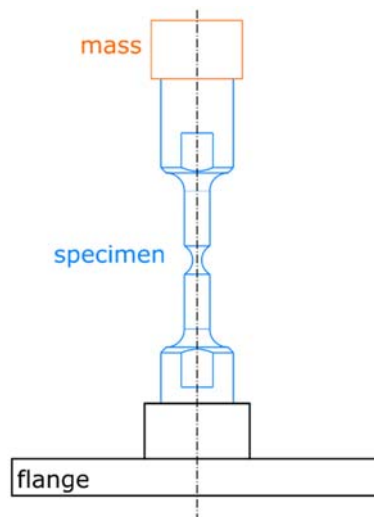


Figure 3: Schematic build off the testing setup without the shaker system below the flange.

## RESULTS

There are three different possibilities designing a high frequency testing method. In the actual case, experiments could be done after the analytic and FEA calculations. The main task is to calculate and to influence the resonant frequency, which enables high loads within the setup.

The background of the analytic approach has to be enlightened in order to rank properly the results with respect to the FEA and experiment. Figure 4 shows the stress distribution along the specimen axis. At a nominal stress of 1MPa, the peak stress is given by 1,159MPa.



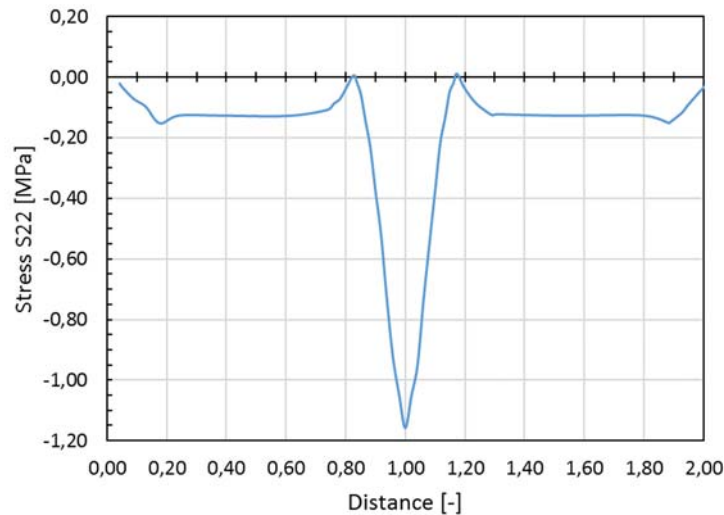


Figure 4: Stress distribution along the specimen axis (S22) at a nominal stress of 1MPa.

Table 3 presents the results according to different approaches of determining the resonant frequency. It can be seen that the FEA and experimental results fit very well considering that this is a multicomponent system with several influences.

The analytic result is considered as a resonant frequency range instead of a concrete value. In the table the extreme values of the calculations are given. The lower and upper limit of the calculation depend on the analytic approach and the definition of boundary conditions. Especially the flange's modelled vibration behaviour caused frequency differences of a few hundred Hertz as seen in the table below.

	Analytic	FEA	Experiment
Resonant frequency	732 - 1032	788	783

Table 3: Results of the different approaches of determining the resonant frequency of the system

From 700 Hz up to 1kHz tests were carried out and strain gauge measurements were performed. According to the shaker performance data, the specimen load increases linear with increasing the acceleration of the shaker. The measurements were carried out with a minimum sampling rate of 19.2kHz. The data is not satisfactory when small rates were applied (<10kHz).

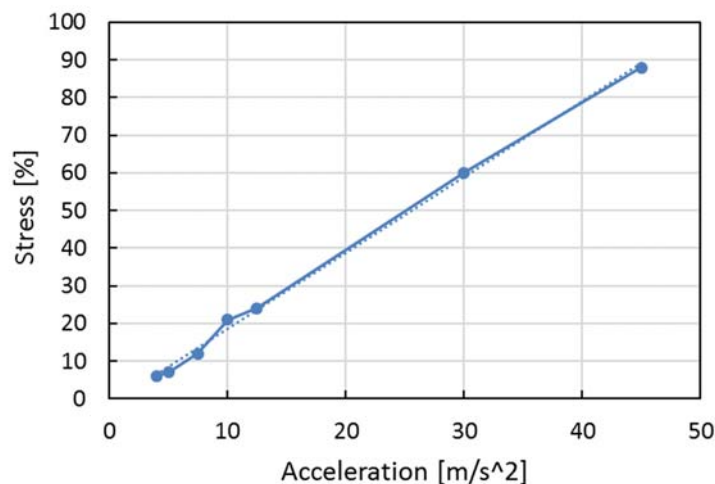


Figure 5: Correlation between shaker acceleration and measured stress in percentage.

## Outlook

Further investigations will concentrate on different influences regarding very high cycle fatigue testing. Additional tests are going to observe a possible frequency influence within a wider frequency range from 500Hz to 1kHz. Furthermore conventional HCF data and actual data will be compared in order to validate the shaker tests. Until now, no temperature increase was observed but this fact will be secured over a wide frequency and load range.

## Acknowledgements

The authors would like to acknowledge the financial support of the "COMET - Competence Centres for Excellent Technologies Programme" of the Austrian Federal Ministry for Transport, Innovation and Technology (BMVIT), the Austrian Federal Ministry of Science, Research and Economy (BWF) and the Provinces of Styria, Tyrol and Vienna for the K1-Centre LEC EvoLET. The COMET Programme is managed by the Austrian Research Promotion Agency (FFG).

## References

- [1] A. Wöhler, Ueber die Festigkeits-Versuche mit Eisen und Stahl (1866) 74–106.
- [2] C. Bathias, A. Pineau, *Fatigue of Materials and Structures*, 1st ed., Wiley-ISTE, s.l., 2013.
- [3] E.A. Neppiras, Techniques and equipment for fatigue testing at very high frequencies (59) (1959) 691–709.
- [4] S.E. Stanzl-Tschegg, Time Saving Method for Measuring VHC Fatigue and Fatigue Crack Growth Data with the Ultrasonic Fatigue Technique, *Procedia Structural Integrity* 2 (2016) 3–10.
- [5] S.E. Stanzl-Tschegg, Very high cycle fatigue measuring techniques, *International Journal of Fatigue* 60 (2014) 2–17.
- [6] H. Mayer, M. Fitzka, R. Schuller, Constant and variable amplitude ultrasonic fatigue of 2024-T351 aluminium alloy at different load ratios, *Ultrasonics* 53 (8) (2013) 1425–1432.
- [7] B. Zettl, H. Mayer, C. Ede, S.E. Stanzl-Tschegg, Very high cycle fatigue of normalized carbon steels, *Third International Conference on Very High Cycle Fatigue (VHCF-3)* Third International Conference on Very High Cycle Fatigue 28 (11) (2006) 1583–1589.
- [8] C. Bathias, L. Drouillac, P. Le François, How and why the fatigue S–N curve does not approach a horizontal asymptote, *International Journal of Fatigue* 23 (2001) 143–151.
- [9] C. Sonsino, Course of SN-curves especially in the high-cycle fatigue regime with regard to component design and safety, *International Journal of Fatigue* 29 (12) (2007) 2246–2258.
- [10] R. Ebara, The present situation and future problems in ultrasonic fatigue testing – Mainly reviewed on environmental effects and materials' screening, *International Journal of Fatigue* 28 (11) (2006) 1465–1470.

**Corresponding author:** igor.milosevic@unileoben.ac.at

# AN INNOVATIVE TESTING TECHNIQUE FOR ASSESSING THE VHCF RESPONSE OF ADHESIVELY BONDED JOINTS

D.S. Paolino<sup>1)</sup>, L. Goglio<sup>1)</sup>, A. Tridello<sup>1)</sup>, G. Chiandussi<sup>1)</sup>, M. Rossetto<sup>1)</sup>

Politecnico di Torino, Department of Mechanical and Aerospace Engineering, Corso Duca degli Abruzzi 24, 10129 Torino

## ABSTRACT

An innovative testing technique for tension-compression tests on adhesive joints is proposed. A ultrasonic testing machine commonly used for Very-High-Cycle Fatigue (VHCF) tests is used for testing adhesive butt joints in the VHCF regime. Due to the high load frequency (20 kHz), the response at very high number of cycles of the adhesive joint can be assessed in a limited testing time.

In the paper, the experimental setup is described in detail. The methodology for measuring the applied stress amplitude in the adhesive joint is also shown: the stress amplitude is calibrated through Finite Element analysis and verified through strain gage measurements before the fatigue tests. Experimental tests on a cyanoacrylate adhesive are finally carried out.

**KEYWORDS:** Ultrasonic testing machine; bonded butt joints; cyanoacrylate layer

## INTRODUCTION

Adhesive joints represent an effective alternative to conventional mechanical joints (e.g., threaded connections, rivets). The reduction of structural weight and manufacturing costs as well as the simplification of the component design are some of the advantages in the use of structural adhesives. As for other structural components, adhesives can fail according to different failure mechanisms. For instance, fatigue failures represent a common cause of damage [1,2]. Fatigue tests are generally limited to  $10^6$  cycles: however, especially in case of critical applications subjected to high frequency vibrations, the adhesively bonded joints may undergo significantly longer fatigue lives.

An innovative testing technique for performing tension-compression tests on adhesive joints is proposed in the paper. In particular, the ultrasonic testing machine [3-5] commonly used for Very-High-Cycle Fatigue (VHCF) tests is used for testing adhesive butt-joints in the VHCF regime. In the proposed application, two cylindrical bars (adherends) are butt-bonded together. The length of the two adherends is calibrated in order to obtain the desired stress amplitude in the adhesive layer; whereas, the total length of the two bonded bars is designed in order to have a resonance frequency corresponding to the resonance frequency of the horn. Due to the high load frequency (20 kHz), the response at very high number of cycles of the adhesive joint can be assessed in a limited testing time.

In the paper, the experimental setup is described in detail. The methodology for measuring the applied stress amplitude in the adhesive joint is also shown: the stress amplitude is calibrated through a Finite Element Analysis (FEA) and validated through strain gage

measurements before the fatigue tests. Experimental tests on a cyanoacrylate adhesive are finally carried out.

### SPECIMEN MATERIAL

An ultrasonic testing machine, originally designed to carry out accelerated fatigue tests on metallic structural materials, is used to perform tests on adhesively bonded butt joints. A cyanoacrylate adhesive (Loctite Ethyl-cyanoacrylate) is tested. The butt joint is made by bonding together two cylindrical bars in Ti6Al4V with a 14.6 mm diameter. The dynamic elastic modulus and the loss factor of the bars are measured through the Impulse Excitation Technique and are equal to 107.5 GPa and  $3.6 \cdot 10^{-4}$ , respectively.

Preliminary tensile tests are also carried out to assess the tensile strength of the butt-joint. Before each tensile test, the adhesion surfaces of the adherends are treated with sandpapers with increasing grit up to #600 and finally they are degreased with acetone, in order to obtain a thin layer of adhesive of 50  $\mu\text{m}$ . Three experimental tests are performed by using a servohydraulic testing machine, with 1 mm/min crosshead speed. Table 1 shows the tensile strength of the tested joints.

	Test 1	Test 2	Test 3
Tensile strength [MPa]	20.8	22.0	18.8

Table 1: tensile strength of the investigated cylindrical butt joints

An average tensile strength of 20.5 MPa is considered as a reference for the fatigue tests. Data scatter is in a limited range, typical of tensile tests on adhesives.

### TESTING EQUIPMENT DESIGN

Fig. 1 shows the testing equipment designed for carrying out the VHCF tests on the butt joints.

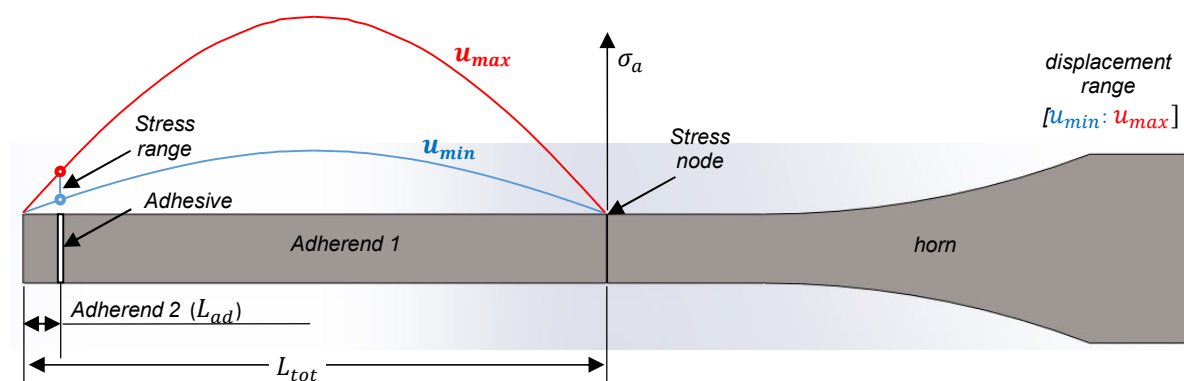


Fig. 1: Innovative testing equipment for tension-compression tests on butt-joints.

As shown in Fig. 1, two bars (adherend 1 and adherend 2) are bonded together by a butt-joint. The total length  $L_{tot}$  of the bonded bars is designed to have the first resonance frequency equal to the resonance frequency of the horn. The stress amplitude in the

adhesive layer can be set by adjusting the excitation amplitude imposed to the horn by the piezoelectric transducer. The connection between adherend 1 and horn is obtained through a second adhesive butt-joint, which is subjected to a negligible stress amplitude throughout the VHCF test (Fig.1).

### Finite Element Modelling

The length of the two adherends is designed through FEA. The design aim is to find the lengths that permit to achieve, in the tested adhesive layer, a range of the stress amplitude which is considered sufficient for the VHCF tests. In particular, it is assumed that [7-40] MPa is enough for the tests. FEAs are carried with the commercial software Ansys. Axisymmetric plane elements with 8 nodes (Ansys element Plane183) are used for the model. Material properties of adherends and horn are in agreement with the measured values.

A first modal analysis is carried out to define, for a cylindrical bar with diameter 14.6 mm, the total length  $L_{tot}$  (Fig. 1), which yields a resonance frequency equal to that of the horn.

A second modal analysis is performed on a model consisting of the horn and of the cylindrical bar with length  $L_{tot}$ . This second analysis is carried out to define the length  $L_{ad}$  (Fig. 1) that permits to achieve the desired range of the stress amplitude in the adhesive layer. Harmonic analyses are then carried out by imposing a nodal harmonic axial displacement (range [2-20]  $\mu\text{m}$ ) at the horn free end. The forcing frequency is set equal to the resonance frequency of the system horn-bar. The optimal value for  $L_{ad}$  is finally given by 7.6 mm.

In a subsequent FEA, a thin adhesive layer of 50  $\mu\text{m}$  is added at the defined distance  $L_{ad}$ . An appropriate mesh refinement is introduced in the model for accurately simulating the stress distribution within the adhesive layer. The material properties for the cyanoacrylate adhesive are assumed from the literature [6]. The complete model is shown in Fig. 2: an enlargement of the mesh refinement in the adhesive layer is also shown.

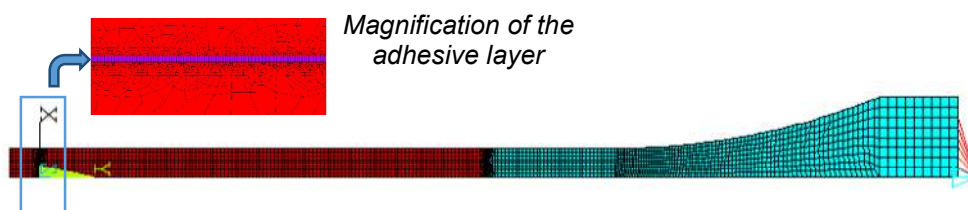


Fig. 2: FE model of the complete system with adhesive butt joints.

Firstly, a modal analysis is carried out to verify the stress range in the adhesive layer. Negligible differences are found with respect to the model without the adhesive: the variation in the stress range is found to be smaller than 0.01%.

Finally, the loss factor is introduced in the model and several harmonic analyses are performed. The loss factor of the titanium alloy is set equal to the value measured through the Impulse Excitation Technique; whereas, the loss factor of the adhesive is set equal to a reference value  $3 \cdot 10^{-3}$  taken from the literature, since it can be hardly measured. A negligible variation in the stress amplitude range is found when the harmonic analyses are carried out with the reference loss factor.

Further harmonic analyses are then carried out to verify if the uncertainty related to the loss factor can affect the stress range in the adhesive. The reference loss factor is varied by a factor of 50. The FEAs show that, due to the thin layer of adhesive, the stress amplitude range in the adhesive has a maximum negligible variation of 1.5%.

### Strain gage calibration

A strain gage calibration is finally performed in order to validate the FEA results. Two T-rossettes strain gages (HBM 1-XY31-1.5/350), each with two strain gages connected at half bridge for temperature compensation, are used for the experimental validation. The first strain gage (Gage A) is applied at half of  $L_{tot}$ , where the stress amplitude reaches its maximum value. The second strain gage (Gage B) is applied close to the adhesive layer, at the minimum distance possible. A strain gage amplifier (EL-SGA-2/B by Elsys AG) is used for the completion of the Wheatstone bridge and for the amplification of the signal. The measurement is acquired at a sample rate of 300 kHz by a National Instruments data acquisition card (PCIe-6363).

Fig. 3a shows both strain gages after the application (dimensions in mm). Fig. 3b shows a magnification of Gage B with the adhesive layer.

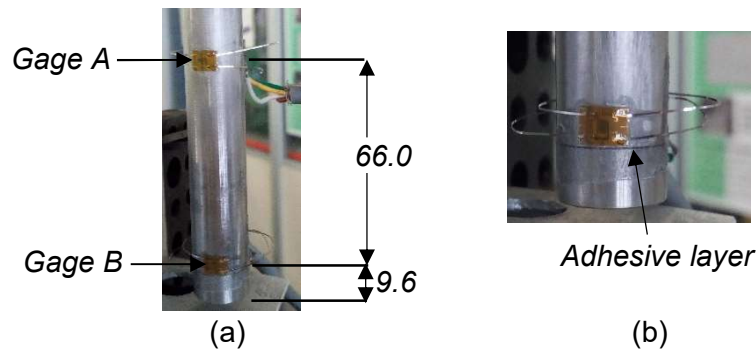


**Fig. 3:** Strain gages after application: (a) overall image with both strain gages; (b) magnification of Gage B.

The adhesive is loaded for three seconds: the applied stress amplitude at the strain gage location is obtained through a harmonic interpolation. Nine increasing load steps (from 2.2  $\mu\text{m}$  to 3  $\mu\text{m}$ , with steps of 0.1  $\mu\text{m}$ ) are subsequently applied.

Fig. 4 (Fig. 4a for Gage A and Fig. 4b for Gage B) plots the stress amplitude measured through strain gages ( $\sigma_{exp}$ ) with respect to the stress amplitude computed through FEA ( $\sigma_{FEA}$ ).  $\sigma_{FEA}$  is computed as the average stress amplitude along the gage length.

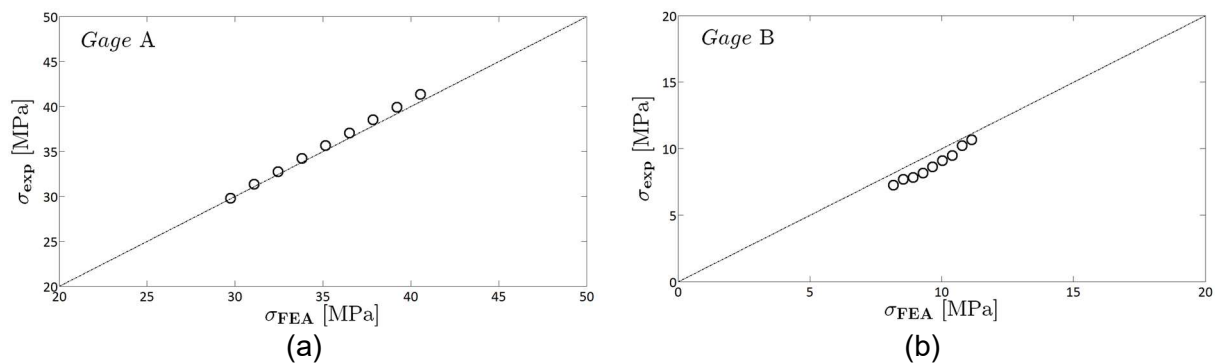


**Fig. 4:**  $\sigma_{FEA}$  with respect to  $\sigma_{exp}$ : (a) gage A; (b) gage B.

According to Fig. 4,  $\sigma_{FEA}$  and  $\sigma_{exp}$  are in good agreement (data are close to the bisector), for both gages. Therefore, FEA results can be effectively used to estimate the stress amplitude in the adhesive during the VHCF test.

## Testing setup

Experimental tests are carried out at constant stress amplitudes, up to failure or to  $10^9$  cycles. Stress amplitude in the adhesive is kept constant during the tests through a closed loop control based on the stress amplitude measured by Gage A. The correlation between the stress amplitude in the adhesive and the stress amplitude measured by Gage A is assessed through FEA.

The temperature in the vicinity of the adhesive layer is continuously measured by using an infrared sensor. Three vortex tubes are used to keep the temperature below 293 K during the test.

## EXPERIMENTAL RESULTS

Experimental tests are carried out on 15 butt-joints in a stress range between 11 and 21 MPa. Fig. 5 shows the S-N plot of the experimental data. After failure, the adherend surfaces are observed by using the optical microscope in order to investigate the mode of failure: both cohesive failures and mixed interfacial-cohesive failures [7] are experimentally observed.

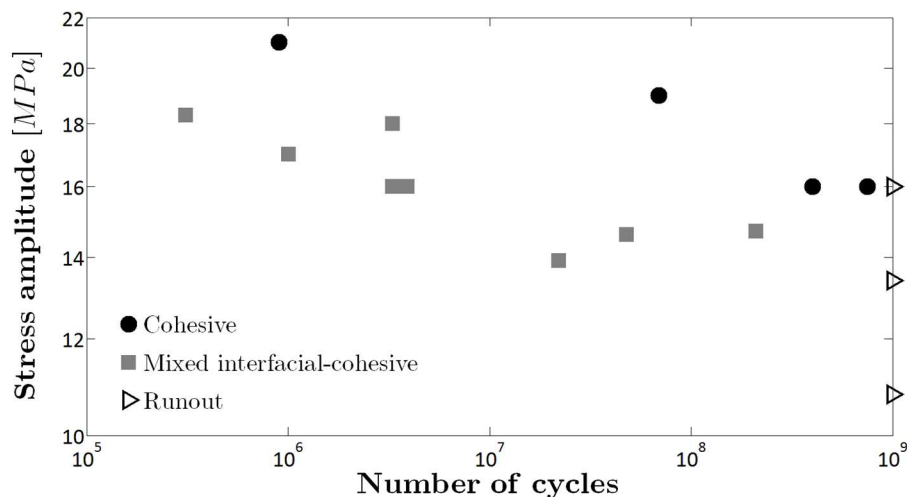


Fig. 5: S-N plot of the experimental data.

According to Fig. 5, cohesive and mixed interfacial-cohesive failures occur at stress amplitudes close to the tensile strength. According to [8,9], a significant strain rate effect can be considered as the main reason for the high fatigue strength exhibited by the adhesive. As expected, cohesive failure data are above mixed interfacial-cohesive failures. Cohesive failures do not occur below 16 MPa; whereas, mixed interfacial-cohesive failures do not occur below 14 MPa. For stress amplitude below 13 MPa, runouts at  $10^9$  cycles are experimentally found.

## CONCLUSIONS

An innovative testing technique for performing VHCF tension-compression tests on adhesive joints was proposed in the paper. The adherends forming the butt-joint were designed



through FEA for carrying out tests on a cyanoacrylate adhesive. The stress distribution in the adhesive layer was experimentally validated through strain gages.

Finally, VHCF tests on cyanoacrylate butt-joints were performed. A significant strain-rate effect was found for the tested adhesive. Cohesive failures and mixed interfacial-cohesive failures caused the failure in the VHCF region for the investigated adhesive, with the former failure mode characterized by a longer fatigue life.

## REFERENCES

- [ 1 ] Curley, A.J., Hadavinia, H., Kinloch, A.J., Taylor, A.C.:  
Predicting the service-life of adhesively-bonded joints  
Int. Journal of Fracture 103 (2000), pp. 41-69
- [ 2 ] De Barros, S., Kenedi, P.P., Ferreira, S.M., Budhe, S., Bernardino, A.J., Souza, L.F.G.:  
Influence of mechanical surface treatment on fatigue life of bonded joints  
J Adhes 2015. <http://dx.doi.org/10.1080/00218464.2015.1122531>
- [ 3 ] Bathias, C., Paris, P.C.:  
Gigacycle fatigue in mechanical practice  
CRC Dekker, New York, USA, 2005
- [ 4 ] Stanzi-Tschegg, S.:  
Very high cycle fatigue measuring techniques  
Int. Journal of Fatigue 60 (2014), pp. 2-17
- [ 5 ] Tridello, A., Paolino, D.S., Chiandussi, G., Rossetto, M.:  
VHCF Response of H13 Steels Produced with Different Manufacturing Processes  
Procedia Eng. 160 (2016), pp. 93-100
- [ 6 ] Pironi, A., Nicoletto, G.:  
Comportamento a frattura di un adesivo strutturale  
Proceedings of the 15<sup>th</sup> IGF Conference (2000), Bari (In Italian)
- [ 7 ] Da Silva, L.F.M., Öchsner, A., Adams, R.D.:  
Handbook of Adhesion Technology  
Springer, Berlin, Germany, 2011
- [ 8 ] Yokoyama, T.:  
Experimental determination of impact tensile properties of adhesive butt joints with the split  
Hopkinson bar  
J. Strain Anal. Eng. 38 (2002), 233-245
- [ 9 ] Goglio, L., Peroni, L., Peroni, M., Rossetto, M.:  
High strain-rate compression and tension behaviour of an epoxy bi-component adhesive.  
Int. J. Adhes. Adhes. 28 (2008), 329-339

**Corresponding author:** [davide.paolino@polito.it](mailto:davide.paolino@polito.it)

# ULTRASONIC FATIGUE TESTING OF THIN NITINOL SHEETS IN THE VHCF REGIME

M. Fitzka<sup>1</sup>, D. Catoor<sup>2</sup>, M. Reiterer<sup>2</sup>, H. Mayer<sup>1</sup>

<sup>1</sup>Institute of Physics and Materials Science, BOKU, Vienna, Austria

<sup>2</sup>Medtronic plc., Corporate Science and Technology, Minneapolis, USA

## ABSTRACT

The intermetallic compound NiTiNOL (composition about 50 atomic % Ni and 50 % Ti) possesses the two unique and closely related material properties of shape memory effect and superelasticity. Today, NiTiNOL is used for medical implants, notably in self-expanding stents and heart valve frames, which require excellent corrosion resistance, biocompatibility, large recoverable deformation, and high fatigue strength, in particular in the very high cycle fatigue (VHCF) regime. Fatigue testing into the VHCF regime is excessively time consuming with conventional fatigue testing methods. Several months are necessary to test a single specimen to  $10^9$  cycles, and a comprehensive characterization of a material's fatigue properties requires many specimens to be tested. Also, virtually all existing studies on the fatigue behaviour of NiTiNOL under use conditions relevant for stent and heart valve applications employ component-level testing (i.e. testing of diamond specimens rather than material level testing (e.g. testing of bulk material)). Thus, the measured lifetimes are influenced by the material properties as well as the design of the component. An accelerated testing method is necessary for the evaluation of processing and composition variations on NiTiNOL fatigue life, as well as the development and introduction of new implant materials. The ultrasonic fatigue testing method has been further developed to test thin sheets of superelastic NiTiNOL. Rather than vibrating in resonance as in conventional ultrasonic fatigue tests, the sheets are stressed with cyclic tension loads. The method is also able to simulate crimping, deployment and service loading conditions of an implant through a static pre-straining procedure prior to cycling at a constant strain amplitude.

## KEYWORDS

NiTiNOL, shape-memory alloy, medical materials, ultrasonic fatigue testing

## INTRODUCTION

Since its discovery in 1962, NiTiNOL has attracted much interest for applications in power and aerospace applications, among others. The nearly equi-atomic intermetallic Ni Ti compound NiTiNOL possesses the two unique and closely related material properties of shape memory effect and superelasticity [1, 2]. Actual applications, however, were initially rare, due to the expensive and complex melting process, along with difficulties in production and processing procedures [3, 4]. It is only by the 1990s that NiTiNOL was finally seeing widespread use, especially in medical devices, answering to the need of less invasive medical procedures and applications. Today, NiTiNOL is used for medical implants, notably in self-expanding stents and heart valve frames, which require excellent corrosion resistance, excellent biocompatibility, and high fatigue strength.

Self-expanding stents are made from wires or are laser-cut from tubes [4-8], exploiting the effect of super-elasticity at body temperature. Often these devices are required to withstand very large numbers of load cycles. Assuming a typical adult human heart rate of 72 beats per

minute, 25 years of implant deployment will roughly yield  $10^9$  cycles. Consequently, there is great interest in the fatigue properties of the material in the very high cycle fatigue (VHCF) regime, as this data is essential for the development and introduction materials and products. Several difficulties are however associated with the investigation in the VHCF regime. A limiting problem is the long testing time when using conventional testing methods, e.g. of thin wires and diamond shaped specimens [6, 9, 10]. High frequency testing techniques have not been available, as the diminutive dimensions of typical specimens place significant constraints on existing methods. In many cases samples are not tested to failure, but are taken off the test at  $10^7$  cycles, without the opportunity to investigate possible failures that may occur at greater numbers of cycles. This paper describes a novel ultrasonic testing technique for high frequency fatigue testing of thin NiTiNOL sheets. Lifetime data from tension-tension fatigue tests in the range from  $10^4$  to more than  $10^8$  cycles are presented.

## MAETRIAL AND TESTING

The investigated NiTiNOL alloy has an austenite finish temperature below room temperature i.e., the austenitic phase is stable at room and body temperature, respectively when no stress is applied [11]. The specimens (Fig. 1, left) were laser-cut from sheets and subsequently electro-polished, both to avoid preferential crack initiation from the specimen edges, and to mimic the surface conditions of actual service conditions. Applying tensile stress to the specimen causes elastic deformation in the austenitic phase as shown in a tensile curve of the investigated specimen shape (Fig. 1, right). When the maximum stress in the centre of the specimen reaches the temperature-dependent transformation stress, the austenite transforms to martensite, that allows for continued deformation without a significant increase of stress (*upper plateau stress*). When the specimen is unloaded, first the martensite unloads elastically leading to a decrease in stress. When the reverse transformation stress is reached, the martensite begins to transform back to austenite at a nearly constant stress (*lower plateau stress*) recovering the transformation strain. When the transformation is complete, the austenite unloads elastically.

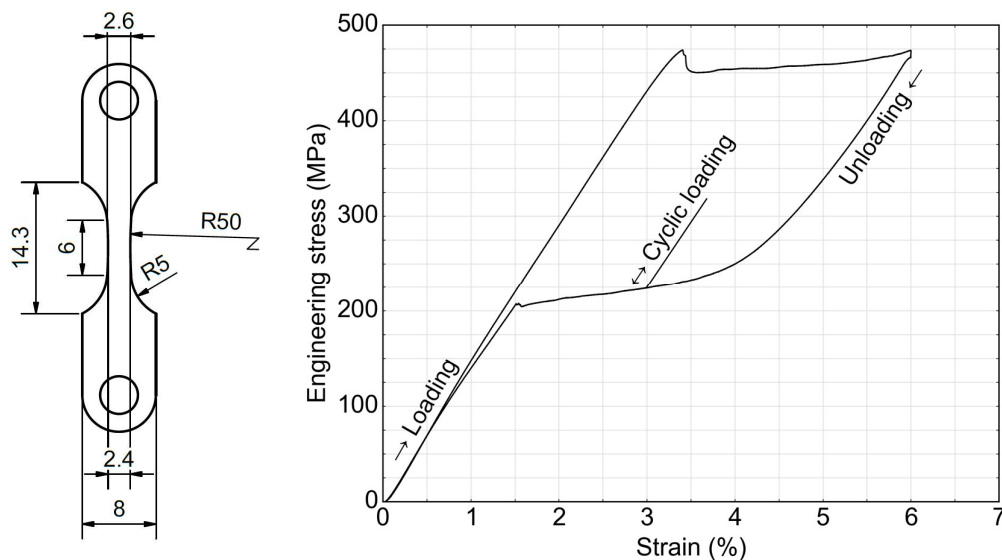


**Fig. 1:** Investigated specimen shape (all measures in mm), specimen thickness is 0.25 mm (left); stress versus strain at load frame used for ultrasonic fatigue testing (right) from DIC results

To simulate the actual application, the testing procedure should replicate the loading history during crimping, deployment and service [4]. During crimping, a strain of approximately 6 % is reached in regions at high stress; this is simulated by the loading curve in Fig. 1. Deployment i.e., releasing the device from the catheter is equivalent to partially unloading the test specimen to reach 3 % strain along the lower plateau. Subsequent cyclic loading simulates pulsatile loading within the blood vessel due to cardiac cycles. Ultrasonic fatigue testing of thin sheets, however, is not trivial, as the specifics of the specimen shape impose significant constraints on existing ultrasonic fatigue testing techniques. As specimens become very thin (typically below 1 mm thickness), the abrupt change in cross section from the load train to the thin sheet might cause a severe degradation of sound transfer i.e., the longitudinal wave might no longer propagate into the specimen, which consequently would no longer experience cyclic strain. At the same time, the tendency of the specimen to buckle increases drastically as sheet thickness decreases. A technique to test thin maraging steel sheets at ultrasonic frequency has been presented in [12], in which the sheet specimen is clamped to a so-called carrier specimen and is forced to joint vibration along the resonance vibration of the carrier specimen. This approach, however, is not directly applicable to testing thin sheets of NiTiNOL, as the carrier specimen cannot accommodate the large static strains that are required for the pre-straining procedure.

In the presented investigation, the conventional ultrasonic fatigue testing method has been adapted by removing the resonance requirement from the specimen (Fig. 2). Rather than vibrating in resonance, the upper end of the sheet specimen is screw-mounted to the lower end (*vibration antinode*) of a rod with a length of half the resonance wavelength, vibrating in resonance. The lower end is fixed to a second immovable rod. The upper end of the specimen is thus forced to move jointly with the 20 kHz resonance vibration of the upper rod and is experiencing cyclic strain at the same frequency. The pre-strain is realised by mounting the ultrasonic load train into a spindle driven load frame.



**Fig. 2:** Overview (top right corner) and detail of the ultrasonic fatigue testing setup at a spindle driven load frame with mounted NiTiNOL specimen

The cyclic displacement at close to 20 kHz cycling frequency is generated and controlled by the ultrasonic fatigue testing equipment developed at Physics BOKU Vienna [13], and applied in a pulse-pause sequence to avoid heating of both, the specimen and the fixtures. The precise displacement amplitude of the vibration antinode at the upper end of the specimen is available from integrating strain gauge readings in the centre of the rod over its full length. The corresponding strain amplitude for the specimen is derived from DIC observations during static loading of the specimen (Fig. 1). Measurements with a fibre-optic sensor were intermittently acquired during individual tests to confirm that no buckling vibrations occur. Surface temperature was monitored with an infrared thermometer to ensure that specimen temperature did not increase by more than 1 °C (i.e., above 22 °C).

## RESULTS AND DISCUSSION

Ultrasonic fatigue tests were conducted with thin NiTiNOL sheets at ultrasonic cycling frequency after applying a pre-strain procedure that mimics the loading history of the implant during crimping, deployment service. Each specimen is strained to about 6 % strain, released to 3 %, and subsequently cycled with displacement amplitudes that correspond to peak stresses that are still below the upper plateau. Specimens were tested with displacement amplitudes between 17  $\mu\text{m}$  and 30  $\mu\text{m}$  that correspond to global strain amplitudes between 0.450 % and 0.255 %. Failures were observed between  $4 \times 10^4$  and  $9 \times 10^8$  cycles. The results are presented in a strain-life diagram in Fig. 3. It can be seen that failures occur early ( $5 \times 10^4$  to  $5 \times 10^5$  cycles to failure) for the highest two investigated amplitudes. A very slight reduction amplitude subsequently yields much longer lifetimes that extend into the VHCF regime, and no failures are observed in the range between. Specimens that withstood  $10^9$  cycles are marked with arrows in Fig. 3.

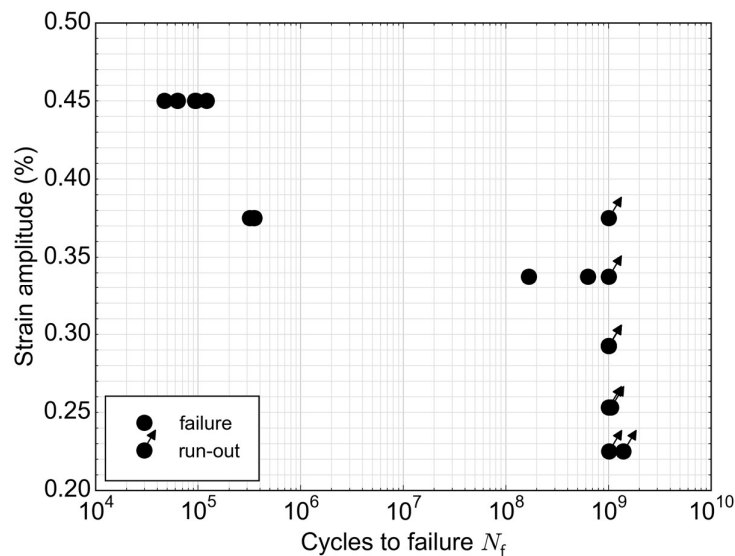
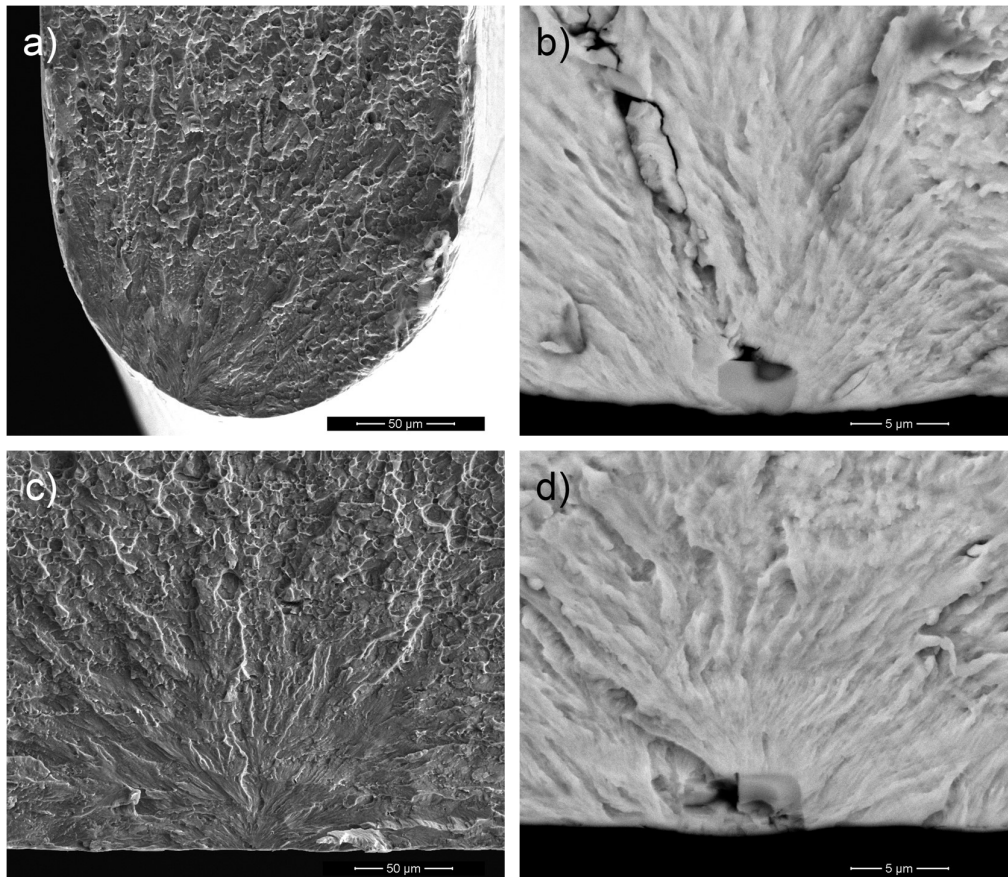


Fig. 3: Strain-life diagram of NiTiNOL tested at ultrasonic cycling frequency

Fig. 4 shows SEM micrographs of fracture surfaces of two specimens that failed after  $4.7 \times 10^4$  and  $6.3 \times 10^4$  cycles, respectively at  $\Delta\varepsilon/2 = 0.450$  %. The fatigue crack initiated at an inclusion at the surface in both cases, which are suspected to be  $\text{Ti}_2\text{Ni}$  type inclusions with some dissolved oxygen [14]. The fracture surfaces of specimens that failed in the VHCF regime (not shown) exhibit significant damage that hinders the unambiguous determination of

the crack initiation location i.e., it cannot be determined if the crack started at the surface, and if it initiated at an inclusion or elsewhere.



**Fig. 4:** SEM micrographs of fractured NiTiNOL specimens a)  $\Delta\varepsilon/2 = 0.45\%$ ,  $N_f = 4.7 \times 10^4$  cycles b) detail of crack-initiating inclusion in BSE mode c)  $\Delta\varepsilon/2 = 0.45\%$ ,  $N_f = 6.3 \times 10^4$  cycles d) detail of crack initiating inclusion in BSE mode

The damage to the fracture surfaces is suspected to result from the specimen vigorously springing back when it fails and the stored energy from elastic deformation is released, which might lead to buckling, and contact of the two newly formed surfaces. Further tests and analyses of fracture surfaces are necessary to investigate if a change in crack initiation occurs, leading to the large gap in the observed lifetimes.

## CONCLUSIONS AND OUTLOOK

For the first time, the application of the ultrasonic fatigue testing method to thin sheets of NiTiNOL has been demonstrated. This development addresses the need for rapid acquisition of lifetime data up to  $10^9$  cycles for the development and introduction of new materials and products. It was confirmed that no excessive heating of the specimen occurs when loaded at ultrasonic frequency below the upper plateau stress. As there is no adiabatic heating, the upper plateau stress is not affected even when a vastly increased cycling frequency is used.

Typically, NiTiNOL is tested as diamond shaped specimens representing unit cells of the laser-cut stent, rather than sheet specimens i.e., at the component level instead of the material level [9], which has certain implications for the strain distribution within the specimen. Also, the equivalence to loading at servo-hydraulic frequency needs to be proven.

## REFERENCES

- [1] Robertson, S.W., Pelton, A.R., Ritchie, R.O.: Mechanical fatigue and fracture of Nitinol, *Int. Materials Reviews* 57(1) (2012) pp. 1-36
- [2] Robertson, S.W., Stankiewicz, J.M., Gong, X.Y., Ritchie, R.O.: Cyclic Fatigue of NiTiNOL, International Conference on Shape Memory and Superelastic Technologies, ASM International, Baden-Baden, Germany, 2003, pp. 79-88
- [3] Stöckel, D.: Umformung von NiTi-Legierungen, in: Siegert, K. (Ed.) Internationale Konferenz Neuere Entwicklungen in der Massivumformung, Stuttgart, Germany, 2001,
- [4] Duerig, T., Pelton, A., Stöckel, D.: An overview of nitinol medical applications, *Materials Science Eng. A* 273-275 (1999) pp. 149-160
- [5] Duerig, T.W., Tolomeo, D.E., Wholey, M.: An overview of superelastic stent design, *Minim Invasive Ther Allied Technol* 9(3-4) (2000) pp. 235-46
- [6] Lin, Z., Pike, K., Zipse, A., Schlun, M.: Nitinol Fatigue Investigation on Stent-Finish Specimens Using Tension-Tension Method, *Journal of Materials Engineering and Performance* 20(4-5) (2010) pp. 591-596
- [7] Pelton, A.R., Schroeder, V., Mitchell, M.R., Gong, X.Y., Barney, M., Robertson, S.W.: Fatigue and durability of Nitinol stents, *Journal of the Mechanical Behavior of Biomedical Materials* 1(2) (2008) pp. 153-64
- [8] Scirè Mammano, G., Dragoni, E.: Functional fatigue of Ni–Ti shape memory wires under various loading conditions, *Int. Journal of Fatigue* 69 (2014) pp. 71-83
- [9] Pelton, A., Duerig, T.W., Gong, X.Y.: Fatigue Testing of Diamond-Shaped Specimens, International Conference on Shape Memory and Superelastic Technologies, ASM International, Monterey, US, 2003, pp. 1-8
- [10] Pelton, A.R., Fino-Decker, J., Vien, L., Bonsignore, C., Saffari, P., Launey, M., Mitchell, M.R.: Rotary-bending fatigue characteristics of medical-grade Nitinol wire, *Journal of the Mechanical Behavior of Biomedical Materials* 27 (2013) pp. 19-32
- [11] McKelvey, A.L., Ritchie, R.O.: Fatigue-crack propagation in Nitinol, a shape-memory and superelastic endovascular stent material, *Journal of Biomedical Materials Research* 47(3) (1999) pp. 301-308
- [12] Schuller, R., Fitzka, M., Irrasch, D., Tran, D., Pennings, B., Mayer, H.: VHCF properties of nitrided 18Ni maraging steel thin sheets with different Co and Ti content, *Fatigue & Fracture Eng. Mater. Struct.* 38(5) (2015) pp. 518-527
- [13] Mayer, H.: Recent developments in ultrasonic fatigue, *Fatigue & Fracture Eng. Mater. Struct.* 39(1) (2016) pp. 3-29
- [14] Frenzel, J., George, E.P., Dlouhy, A., Somsen, C., Wagner, M.F.X., Eggeler, G.: Influence of Ni on martensitic phase transformations in NiTi shape memory alloys, *Acta Materialia* 58(9) (2010) pp. 3444-3458

**Corresponding author:** michael.fitzka@boku.ac.at



# ACCELERATED FRETTING FATIGUE TESTING BY USING ULTRASONIC FATIGUE TESTING MACHINE WITH A CLAMPING CONTACT PAD

Y. Shimamura<sup>1)</sup>, T. Izumikawa<sup>2)</sup>, H. Ishii<sup>1)</sup>, K. Tohgo<sup>1)</sup>, T. Fujii<sup>1)</sup>,  
T. Yagasaki<sup>3)</sup>, S. Sumida<sup>3)</sup>

<sup>1)</sup> Shizuoka University, 3-5-1 Johoku, Naka-ku, Hamamatsu, Shizuoka 432-8561, Japan

<sup>2)</sup> Kawasaki Heavy Industries, Ltd., Gifu Works, 1 Kawasaki, Kakamigahara, Gifu 504-8710, Japan

<sup>3)</sup> Honda R&D Co., Ltd., Automobile R&D Center, 4630 Shimotakanezawa, Haga-machi, Haga-gun, Tochigi 321-3393, Japan

## ABSTRACT

Fretting is a phenomena that microscopic relative slips are repeated at a contact part, and fretting fatigue results from cyclic stress applied to a part with fretting. In fretting fatigue, cracks are likely to occur from a fretting part by friction force and cyclic stress. It is well known that fretting fatigue strength is much lower than the fatigue strength of smooth specimens and the fatigue limit disappears. Many studies on fretting fatigue have been reported but most of the studies have not cover fatigue properties in the very high cycle regime more than  $10^7$  cycles. In this study, an accelerated fretting fatigue testing method was developed by using an ultrasonic torsional fatigue testing machine with a clamping fretting pad. Fretting fatigue tests of carburized and non-carburized CrMo steel were conducted by using the developed method. For reference, fatigue tests for smooth specimens without fretting were also conducted. Test results showed that fatigue strength of specimens with fretting in the very high cycle regime was considerably lower than that of specimens without fretting. In each fretting fatigue specimens, fatigue cracks initiated from the fretting part.

## KEYWORDS

Fretting fatigue, carburized steel, very high cycle fatigue, ultrasonic torsional fatigue testing machine

## INTRODUCTION

Accelerated fatigue testing machines are required in order to investigate fatigue properties in the very high cycle regime within practical testing periods, and an ultrasonic fatigue testing method using a piezoelectric oscillator is prospective one. Using an ultrasonic fatigue testing method enables us to reduce required time for fatigue tests to  $1/100 \sim 1/1000$  compared with conventional fatigue test methods.

Authors have developed an ultrasonic torsional fatigue testing machine and investigated fatigue properties of carburized steels without internal fracture [1]. A fatigue crack initiated from the surface of a specimen during a torsional fatigue test because the maximum shear stress was applied to the surface. Thus, torsional loading is more suitable than axial loading for investigating fatigue properties of case hardening materials such as carburized steels.

Fretting is a phenomena that microscopic relative slips are repeated at a contact part. When cyclic stress is applied to a fretting part, the fatigue strength considerably decreases and the fatigue limit disappears. The phenomena is called fretting fatigue. Many studies on fretting fatigue have been reported but most of the studies did not cover fatigue properties in the very

high cycle regime more than  $10^7$  cycles. Sun et al. proposed an accelerated fretting fatigue testing method by using an ultrasonic tension compression fatigue testing machine [2]. However, as mentioned above, it is unsuitable for surface hardening materials. In this study, a new accelerated fretting fatigue testing method was developed by using an ultrasonic torsional fatigue testing machine with a clamping fretting pad. Fretting fatigue tests of CrMo steel were conducted by using the developed method.

## FRETTING FATIGUE TESTING METHOD

A schematic of an ultrasonic torsional fatigue testing machine is presented in Fig.1. Torsional vibration was generated by applying voltage to a piezoelectric oscillator. The resonance frequency was 20kHz and the torsional displacement amplitude was only a few  $\mu\text{m}$ . The generated torsional amplitude of the oscillator was amplified using an amplifying horn. Further amplification of stress was achieved in a specimen. In this study, dumbbell shape specimens were used. The shape and shear stress/torsional angle distributions of a specimen is presented in Fig.2.

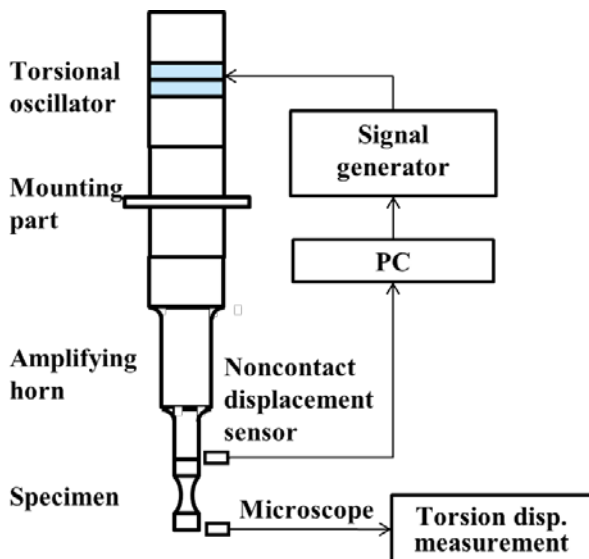


Fig.1: Ultrasonic torsional fatigue testing machine

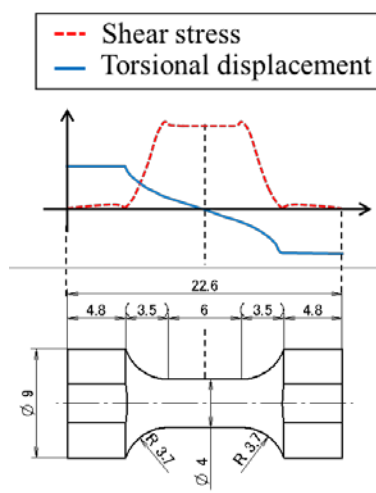


Fig.2: Specimen shape and shear stress/torsional angle distributions

Material used in this study was SCM420H. Table 1 shows the chemical composition. Carburized and non-carburized specimens were prepared. The Vickers hardness of specimen surface of carburized specimen was 780Hv and of non-carburized specimen was 480Hv. The stress ratio R was -1. Intermittent loading and compressed air cooling were simultaneously used to keep the temperature below 100°C. Fatigue test was stopped when the resonance frequency decreased by 50Hz, or when the number of cycles exceeded 10<sup>9</sup> cycles.

The torsional displacement at the end of a specimen was measured by using a microscope during fatigue testing, and the shear stress distribution of a specimen was estimated by substituting the torsional displacement at the end of the specimen into FEA solution.

Figure 3 shows a fretting fatigue specimen with a clamping fretting pad. Bridge-shaped contactors made of SKH51 were used. The Vickers hardness of the contactor was 730Hv. A contact load was provided by tightening bolts between two plate springs. An initial contact load can be measured by using a strain gage attached to one fretting pad, and was set to be 800N in this study.

Table 1: Chemical composition of SCM420H (in weight %)

C	Si	Mn	P	S	Cu	Cr	Ni	Mo
0.21	0.21	0.77	0.02	0.02	0.11	1.02	0.06	0.18

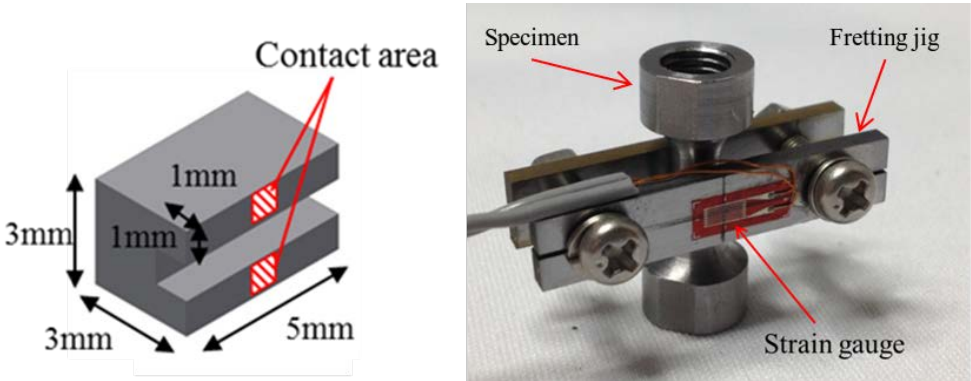


Fig.3: Contactor and a specimen with a clamping fretting pad

**RESULTS AND DISCUSSION**

S-N diagrams with and without fretting are shown in Fig.4. In the figure, symbols represent failure, where specimens have fatigue cracks long enough to decrease the natural frequency, while symbols with an arrow indicate run-outs. Fretting fatigue strengths of carburized and non-carburized specimens were much smaller than fatigue strengths of smooth specimens. For non-carburized specimens, the fatigue strength without fretting at 10<sup>9</sup> cycles was about 600MPa but that with fretting was about 150MPa. For carburized specimens, the fatigue strength without fretting at 10<sup>9</sup> cycles was about 730 MPa but that with fretting was about 430MPa.

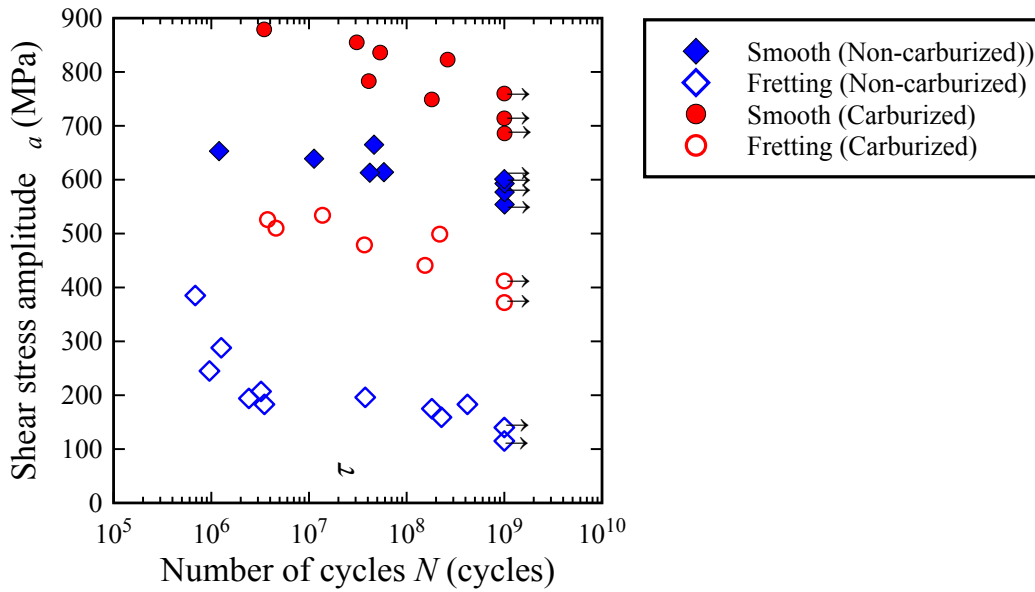


Fig.4: S-N diagram

A typical specimen surface after a fretting fatigue test is shown in Fig.5. Stick and slip areas were observed in the fretting region. In other words, a partial slip condition was successfully achieved. Many cracks were observed in the fretting region, and most of the fatigue cracks propagated to outward direction of the fretting region. Several small non-propagating cracks were also observed in the slip part. Fatigue cracks in a cross section of a specimen ( $\tau_a = 245$  MPa,  $N_f = 9.6 \times 10^5$ ) are shown in Fig.6. As seen in Fig.6, multiple fretting fatigue cracks nucleated in the fretting region and propagated in the  $45^\circ$  direction.

Figure 8 shows a fracture surface of the specimen. The figure indicated that the fatigue crack was originated from the surface and, the origin was near the boundary between slip and stick parts.

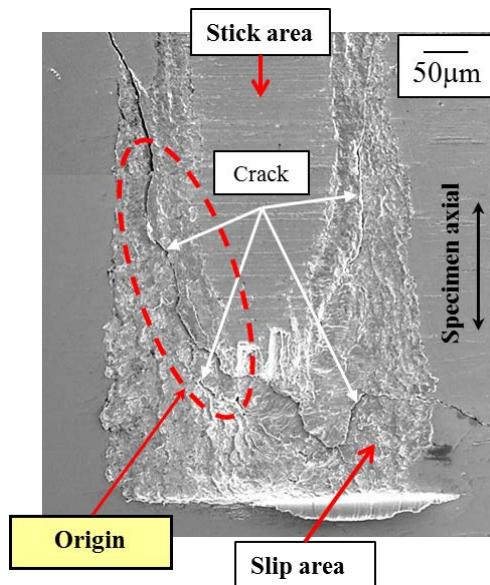
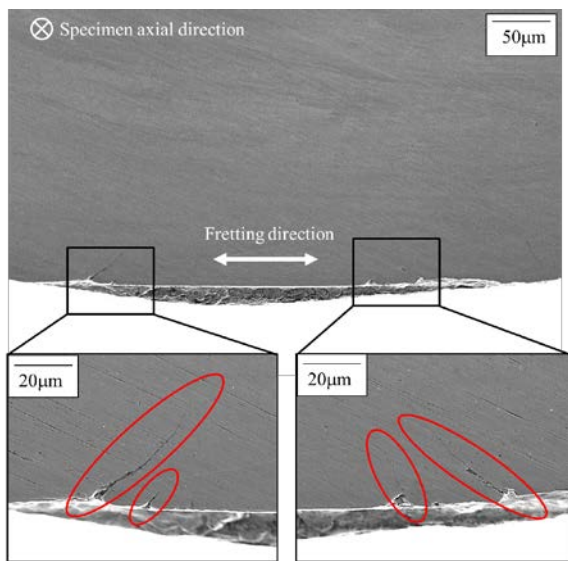
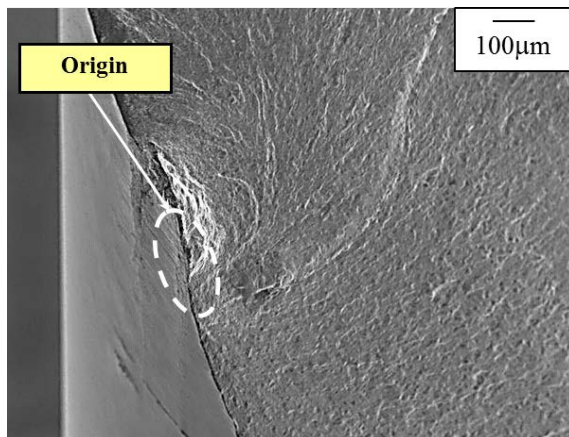


Fig.5: Typical specimen surface (non-carburized specimen)



**Fig.6:** Cross section of a fretting fatigue specimen (non-carburized specimen)



**Fig.7:** Fracture surface (non-carburized specimen)

## CONCLUSIONS

Fretting fatigue tests under a partial slip condition were successfully conducted by using an ultrasonic torsional fatigue testing machine and a clamping type fretting pad. The fatigue strength of carburized and non-carburized SCM420H in the very high cycle regime considerably decreased as a result of fretting.

## REFERENCES

- [1] Shimamura, Y.; Narita, K.; Ishii, H.; Tohgo, K.; Fujii, T.; Yagasaki, T.; Harada, M.: Fatigue Properties of Carburized Alloy Steel in Very High Cycle Regime Under Torsional Loading  
Int. Journal of Fatigue, 60(2014), pp.57-62
- [2] Sun, Z. D.; Bathias, C.; Baudry, G.: Fretting Fatigue of 42CrMo4 Steel at Ultrasonic Frequency  
Int. Journal of Fatigue, 23(2001), pp.449-453

# INFINITE LIFE OF FIBRE REINFORCED PLASTICS (FRP) INVESTIGATED WITH X-RAY-REFRACTION-TOPOGRAPHY FOR NON-DESTRUCTIVE EVALUATION OF MICRO-STRUCTURAL DEGRADATION PROCESSES IN-SITU CYCLIC FATIGUE LOADING

V. Trappe, A. Müller, S. Hickmann  
Bundesanstalt für Materialforschung und -prüfung (BAM), Unter den Eichen 87,  
12205 Berlin, Germany

## ABSTRACT

The described investigation of carbon-fibre-reinforced plastics (CFRP) documents that damage evolution can be observed by means of X-ray refractography [1]. Comparative investigations with synchrotron technique on CFRP and grey-scale analysis on glass fibre-reinforced-plastics (GFRP) confirm these results [2, 3, 4]. Moreover it was found that the fracture mechanical properties of the matrix system influence damage nucleation and propagation in the laminate during static and fatigue loads [5]. Single-step fatigue tests were carried out on laminates with RIM135 and LY556 matrix systems made from non-crimped fabric (NCF) or twill weave in different fibre orientations. The damage to the LY556 laminates was characterized by laminate cracks growing rapidly over the whole specimen width, whereas the damage on the RIM135 laminates was characterized by an earlier onset of micro-cracking followed by laminate cracks. The specimens were fatigued up to  $10^8$  (very high cycle fatigue (VHCF) regime) load cycles. S-N-curves of damage initiation were drawn and boundaries were identified for technical infinite life within the VHCF regime. A phenomenologically based model focusing on matrix stress was applied to reproduce the first inter-fibre failure (IFF) under static and fatigue loads.

## KEYWORDS

Carbon fibre-reinforced-plastics (CFRP), Fatigue, Damage evolution, X-ray refractography, Very high cycle fatigue (VHCF)

## INTRODUCTION

Carbon fibre-reinforced-plastics (CFRP) are typically used under high-cycle- (HCF) and very-high-cycle-fatigue (VHCF) at relatively low loads in the aerospace industry, but also in other sectors like wind energy and increasingly in the automotive industry as well. Nowadays the static strength of CFRP is satisfyingly predictable through layer-wise strength analysis and material data from single layers. In contrast it is becoming increasingly uncertain to predict the lifetime of such materials as the design lifetime increases. Previous studies showed that local minor cracks and inter-fibre fractures originate long before the total failure of single layers [3]. At present no reliable fatigue estimations are available for fibre-reinforced-plastics (FRP). Hence safety-related primary structures made out of FRP are over-dimensioned.

The aim of this research project is to understand damage evolution in FRP subjected to high and very high cycle fatigue. This is done by performing single-step fatigue tests combined with non-destructive testing in order to enable the monitoring and characterisation of damage evolution. The X-ray refraction topography developed at BAM [1] offers a possibility for non-destructive, quantitative and spatially-resolved determination of the internal surfaces. Thereby it is possible to identify micro-damage in the  $\mu\text{m}$ -scale (fibre-matrix debonding and matrix fracture) even in complex laminates. The objective is to monitor damage

evolution in woven textiles and non-crimp fabrics to determine the boundary to “infinite life”. The purpose is to enable a lifetime prediction for the VHCF regime (up to  $10^8$  load cycles) based on fatigue behaviour during the HCF regime ( $10^6$  load cycles). The basic idea of the investigation is represented in figure 1.

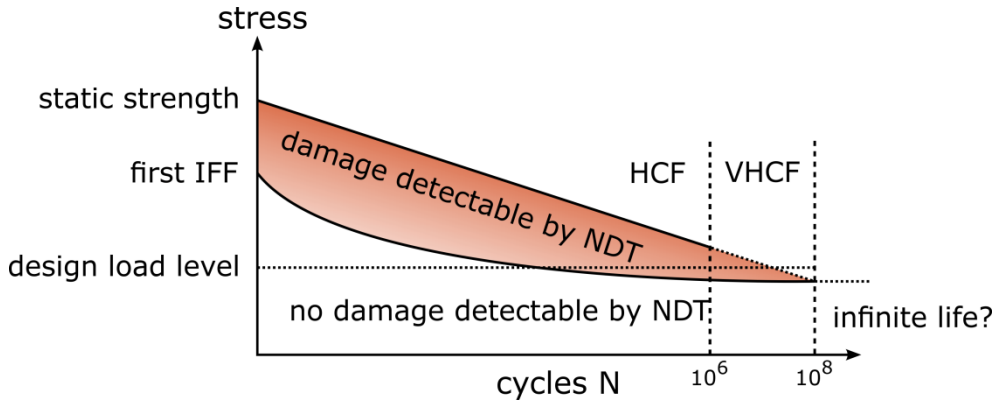


Fig. 1: Basic concept shows that damage initiation starts before failure

## EXPERIMENTAL

### X-ray refraction technique

X-ray refraction [1] is caused by the effect of refraction at the interface of materials with different refractive indexes. For X-rays the refraction angle is below half a degree and in the opposite direction. Hence Small Angle X-ray Scattering (SAXS) is used. In the experimental set-up (fig. 2) a collimated X-ray beam passes through the sample. At a fixed angle the refracted signal is measured. A signal proportional to the absorption is measured as well. A characteristic refraction value  $C$  is determined, which is proportional to the surface per unit of volume. This can be calculated from the scattering intensity  $I_R$ , the transmitted intensity  $I_A$  and the thickness  $d$  of the sample in relation to the zero values ( $I_{R0}$ ,  $I_{A0}$  - without the sample):

$$C = \left[ \frac{I_R/I_{R0}}{I_A/I_{A0}} - 1 \right] \cdot \frac{1}{d} \quad (\text{eq. 1})$$

$$I_A = I_{A0} \cdot e^{-\mu \cdot d} \quad (\text{eq. 2})$$

The intensity of the refracted beam will increase if the refractive index differs at the observed interfaces. Hence, the intensity will be higher for materials with de-bonded fibres, IFF or pores than without (fig. 3). The relative increase of the inner surface's refractive value  $C$  is measured and used in the investigations. Scanning an area of a sample yields a topographic map of the inner surfaces (fig. 3 and 5). According to the Lambert-Beer law, the absorption is a function of the density-proportional linear absorption coefficient  $\mu$  and the thickness  $d$  of the sample (s. eq. 2). For several applications it is practical to normalize equation 1 to  $\ln(I_A/I_{A0})$ , resulting in the relative specific surface  $C_m/\mu$ , independent of the variation in the number of fibre filaments due to non-perfect production of the fabrics. In this paper  $C_m/\mu$  is referred to as relative refraction (intensity).

In the experimental setup of the refraction technique the absorption and the refraction signals are measured independently in one shot (s. fig. 2). In figure 3 the absorption and refraction mapping of a CFRP sample made of UD-weave in  $0/90^\circ$  direction are compared. The absorption (fig. 3, left) maps only slight differences in the density (the glass weft yarn becomes visible). As there is no significant change of the density based on damage it is impossible to detect any fibre matrix de-bonding with classical X-ray radiography, which only



uses the absorption proportional to mass. Instead, the refraction signal (fig. 3, right) maps the cracks caused by the previous loading due to inter-fibre failure.

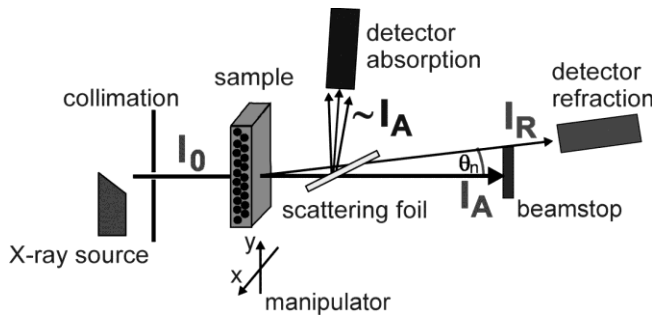


Fig. 2: Experimental set-up for the X-ray refraction method

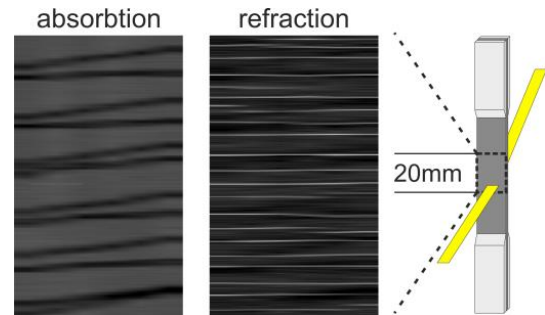


Fig. 3: Comparison between absorption and refraction signal

To obtain the proper characterization of the damage and the shape of the cracks, a comparative investigation on the fractured specimen was done at the synchrotron in Berlin (BESSY) with diffraction-enhanced imaging (DEI) [2, 6, 7]. In DEI the light refracted by the inner surfaces is differentiated with a single crystal. For this a parallel beam of monochromatic X-ray light is necessary and can be generated with synchrotron radiation. By rotating the single crystal the Bragg angle can be adjusted to the maximum intensity (peak in the rocking curve) or to the edge of the rocking curve. In so doing either the un-refracted light (cracks are imaged dark) or the refracted light (cracks are imaged bright) complies with the Bragg condition and gets displayed.

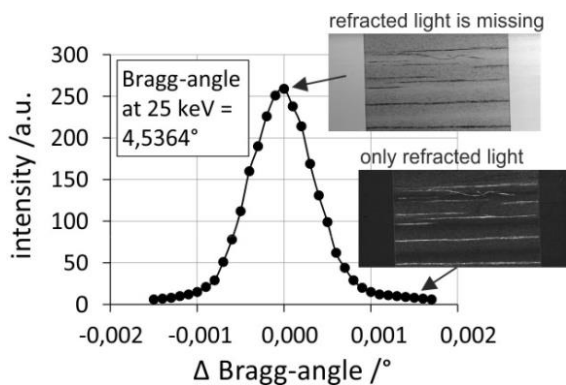


Fig. 4: Principle of Diffraction Enhanced Imaging (DEI) – refracted light is discriminated with the rocking curve of an analyser crystal



Fig. 5: Comparison of imaging techniques from left to right: fractured NCF-0/90° specimen, DEI at the peak of the rocking curve, SAXS-technique (raster method)

The DEI images show the entire width of the area and contain pixels  $28.8\mu\text{m} \times 28.8\mu\text{m}$  in size. Thus the DEI images have a much higher resolution and render a good overall picture of the damage state. It is apparent that on the fractured specimen most of the inter-fibre cracks cross the entire width in the  $90^\circ$  direction perpendicular to the load direction due to the fibre orientation in  $0/90^\circ$ . What is more the cracks are not entirely straight but follow the  $90^\circ$ -fibre bundles. The damage indicator crack density calculated by the DEI equals to approximately  $1/\text{mm}$ . Using this findings the scanning grid of the SAXS-technique was optimized. Finally, the scanning grid for the raster method was set to 400 steps of  $0.05\text{ mm}$  each in the vertical direction and 6 – 7 steps of  $1\text{mm}$  each in the horizontal direction, resulting in the same crack density of  $1/\text{mm}$  as measured with the DEI. The DEI image is shown in comparison with the SAXS topography and the fractured CFRP specimen in fig. 5.

## Materials and test specimen

The CFRP specimens were made from a 200g/m<sup>2</sup> non-crimp fabric and 400g/m<sup>2</sup> twill style textile each made with Tenax-E HTA40 E13, 6K yarn. Flat specimens with a length of 150mm, a width of 15mm or 10mm, a thickness of 1mm and tab reinforcement for clamping were used. 0°/90°- and +/-45°-laminates of each textile reinforcement were investigated. The mean fibre volume fraction was approximately 43-45%. Previous investigations showed a strong influence of the fracture mechanical properties of the matrix on damage behaviour in terms of IFF and the lifetime of a laminate [2]. The most crucial criteria of this selection were the location of the Paris line and the fracture toughness. The Matrix systems Huntsman LY556 (fracture toughness 17.94 N/mm<sup>3/2</sup>) and Hexion RIM135 (fracture toughness 33.24 N/mm<sup>3/2</sup>) were chosen as a more and less brittle epoxy system. Comparative tests on GFRP specimens of the same size were done. However this paper focuses on the CFRP results on 0/90°-laminate.

## Damage evaluation in-situ tensile strength test and tensile fatigue loading

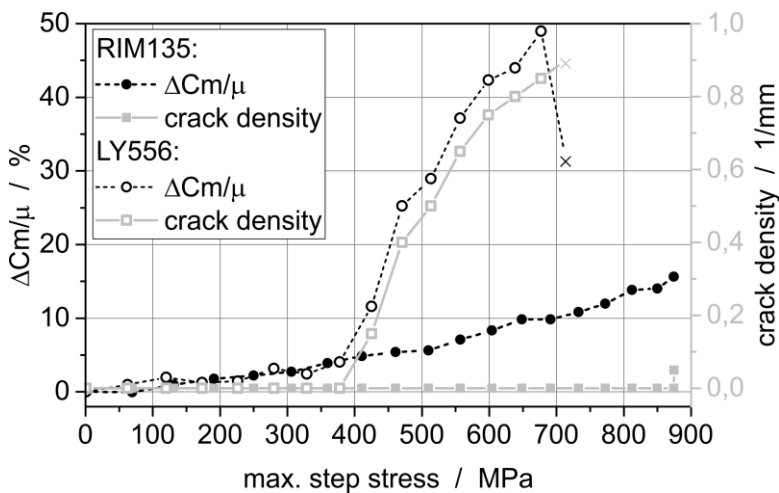


Fig. 6: Damage evolution in tensile strength test on CFRP UD 0/90 specimens.

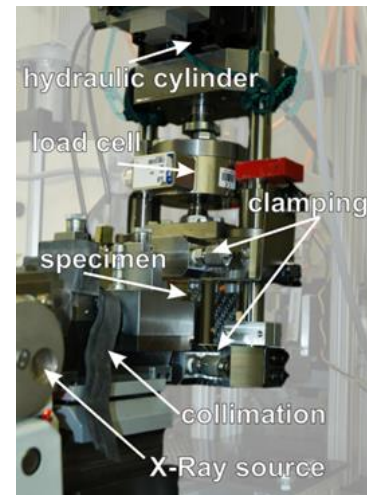


Fig. 7: 10kN testing machine integrated in SAXS-scanner

A servo-hydraulic 10kN testing machine was integrated in a SAXS setup (fig. 7). While the CFRP-samples were tensile loaded X-ray refraction topography [1, 4] was performed in situ. This non-destructive technique enables the detection of micro-cracking and inter-fibre failure especially important for CFRP. The increase of inner surface area due to inter-fibre failure was represented in terms of the increase in crack density and the increase in relative refraction intensity. Both are displayed as a function of the incremental stress state reached in figure 6.

For the 0°/90°-laminate made of UD-weave fabric and LY556 epoxy system the first inter-fibre failure is indicated by a sudden increase in the relative refraction intensity as well as a rise in crack density. This occurs between the stress steps of 375 and 425 MPa. The same laminate with epoxy system RIM135 shows a steadily rising relative refraction intensity with no discrete cracks detected resulting in a crack density of zero until final failure (fig. 6). This fact alone illustrates different damage accumulation behaviour in the static load case between the two epoxy systems. Regarding the UD 0/90° specimens with the RIM 135 system, only the relative refraction intensity is an appropriate indicator of the damage state. The same is valid for all SAXS investigations on +/-45°-laminates. In contrast discrete cracks were detected for both epoxy systems in the tensile step test on 0°/90°-laminates made of twill weave at a stress level of about 10% less.

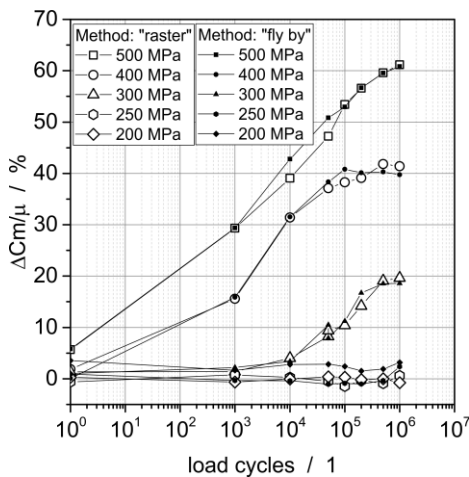


Fig. 8: Damage evolution of CFRP-0/90°-UD with LY556 matrix, fatigue tests and in situ X-ray refraction.

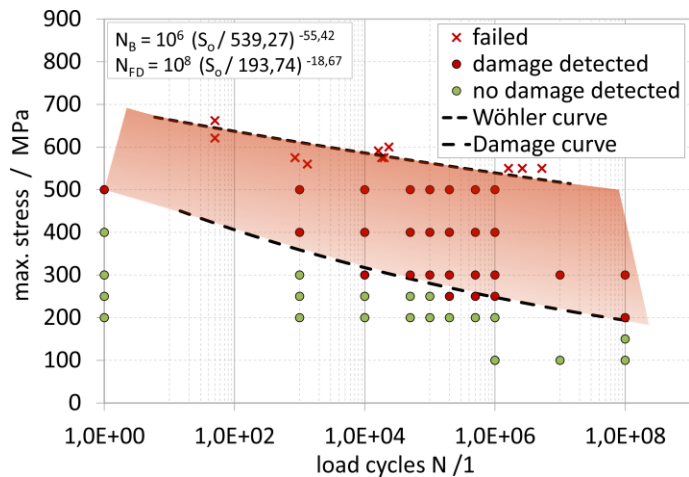


Fig. 9: SAXS-accompanied fatigue test at R=0.1 on twill 0/90° CFRP specimens made with LY556 matrix.

Fatigue tests were done in servo-hydraulic tensile testing machines at 5 up to 100 Hz. All tests were done under air conditioning at 23°C and 50% RH. The intrinsic heating at low load levels is insignificant and hence the recorded surface temperature rise is moderate until shortly before failure. Even for  $\pm 45^\circ$ -laminate the increase in the surface temperature is below 5°K at the lowest load of 50MPa and a frequency of 100Hz. The surface temperature was recorded with an infrared sensor during all fatigue tests.

The single-step fatigue tests were conducted in the two custom-made 10-kN test apparatus. The test apparatus that was integrated into the SAXS scanner was used to carry out the fatigue test, applying up to  $10^6$  load cycles at different load levels and in situ SAXS measurements (fig. 8). After a certain number of load cycles the specimens were scanned on each load level, while a static load equivalent to the mean stress was applied to open the cracks slightly. With the recorded damage evolution (fig. 6, 8), it was possible to distinguish between the damaged and undamaged state of the specimens. These data were transferred to S-N diagrams (fig. 9) to visualize the different regions defined in figure 1.

The 0°/90°-CFRP specimen of UD-weave (fig. 9) did not fail at and below a stress level of 500MPa up to  $10^6$  load cycles, even though at 500MPa the first inter-fibre failure occurred during the first load cycle. Starting at a load level of 200MPa downwards, no micro-cracking was detected up to  $10^6$  load cycles. At this load level, no total failure occurred within the VHCF regime up to  $10^8$  load cycles. Below 200MPa there was no micro-cracking detected up to  $10^8$  load cycles. Thus technically infinite life can be assumed below 200MPa. This value of 200 MPa is equal to approximately 47% to 53 % of the IFF.

## DISCUSSION AND CONCLUSION

From the literature it is already known that inter-fibre failure can be visualised with classical radiography at low X-ray energies [8]. Because this method is based on differences in density, contrast agent has to be used to highlight the cracks, and even then only those cracks connected to the specimen surface can be coated and hence detected. In [1] thin micro-cracks and inter-fibre failure averaged over the volume were visualized without a contrast agent, using X-ray refraction technique. Hence an in situ investigation of increasing micro-damages parallel to static [4] and fatigue load [3] is possible. In this paper the investigations on laminates with different fabrics and different matrix systems showed that a

stress level of approximately 40% to 50% of static inter-fibre failure seems to be the limit for the technically infinite life of CFRP, for either transverse or shear loading.

In addition, this project aims to examine the influence of the matrix properties. Thereby it could be shown, that the matrix has an influence on the kind of damage nucleation and propagation as well as on the limit to infinite life. Further investigations on different laminates with the second matrix system are in progress.

Calculations with the phenomenology-based approach have already shown good results between the maximum equivalent stress and the stress level of the first IFF. These investigations will be continued in order to prove adaptability for normalised Wöhler curves.

To conclude, it can be stated that a technically infinite life was found for cyclic fatigued CFRP-samples under transverse (0°/90° laminates) and shear (+/-45° laminates) loading, investigated up to 10<sup>8</sup> load cycles. Accompanying non-destructive X-ray refraction measurements reflect the damage state even when sample failures did not occur. This result and investigation technique is highly relevant to provide a guide value in component design for infinite life, which is often practically achieved according to the knock-down factors stipulated in certification standards. But with better knowledge of fatigue behaviour, knock-down factors or safety margins can be reduced in order to benefit more from the lightweight design potential of FRP.

## ACKNOWLEDGEMENTS

The authors would like to thank Deutsche Forschungsgemeinschaft for its financial support of this study in the framework of the priority program “Life<sup>∞</sup>” (SPP 1466 TR499/3-1,2).

## REFERENCES

- [1] M. P. Hentschel, K.-W. Harbich and A. Lange: ‘Non-destructive evaluation of single fibre de-bonding in composites by X-ray refraction’, *NDT&E Int.*, 1994, 27, 5, 275–280.
- [2] B. R. Mueller, A. Lange, M. Harwardt and M. P. Hentschel: ‘Synchrotron-Based Micro-CT and Refraction-Enhanced Micro-CT for Non-Destructive Materials Characterisation’, *Adv. Eng. Mater.*, 2009, 11, 6, 435–440.
- [3] V. Trappe and K.-W. Harbich: ‘Intralaminar fatigue behaviour of carbon fibre reinforced plastics’, *Int. J. Fatigue*, 2006, 28, 10, 1187–1196.
- [4] V. Trappe, S. Hickmann and H. Sturm: ‘Evaluation of inter fibre fracture in textile glass fibre composites by X-ray refraction topography’, *Mater. Test.-Mater. Comp. Techn. Appl.*, 2008, 50, 10, 615–622.
- [5] V. Trappe, S. Guenzel and M. Jaunich: ‘Correlation between crack propagation rate and cure process of epoxy resins’, *Polym. Test*, 2012, 31, 5, 654–659.
- [6] A. Kupsch, A. Lange, M. P. Hentschel, Y. Onel, T. Wolk, A. Staude, K. Ehrig, B. R. Müller and G. Bruno: ‘Evaluating Porosity in Cordierite Diesel Particulate Filter Materials, Part 1 X-ray Refraction’, *J. Ceram. Sci. Technol.*, 2013, 4, 4, 169–175.
- [7] D. Chapman, W. Thomlinson, R. E. Johnston, D. Washburn, E. Pisono, N. Gmür, Z. Zhong, R. Menk, F. Arfelli and D. Sayers: ‘Diffraction enhanced X-ray imaging’, *Phys. Med. Biol.*, 1997, 42, 11, 2015–2025.
- [8] F. Gao, L. Boniface, S. L. Ogin, P. A. Smith and R. P. Greaves: ‘Damage accumulation in woven-fabric CFRP laminates under tensile loading: Part 1. Observations of damage accumulation’, *Comp. Sci. Technol.*, 1999, 59, 1, 123–136.

Corresponding author: [volker.trappe@bam.de](mailto:volker.trappe@bam.de)

# INVESTIGATION OF THE RESPONSE OF DUAL-PHASE STEELS SUBMITTED TO 20 KHZ AND LOW FREQUENCY FATIGUE LOADINGS

**Noushin Torabian<sup>1,2)</sup>, Véronique Favier<sup>1)</sup>, Justin Dirrenberger<sup>1)</sup>, Frédéric Adamski<sup>1)</sup>, Saeed Ziaei-Rad<sup>2)</sup>, Nicolas Ranc<sup>1)</sup>**

<sup>1)</sup> Laboratoire PIMM, Arts et Métiers Paris Tech, CNAM, CNRS, 151 Boulevard de l'Hôpital, 75013 Paris, France

<sup>2)</sup> Department of Mechanical Engineering, Isfahan University of Technology, Isfahan 84156-83111, Iran

## ABSTRACT

Application of piezoelectric fatigue systems working at ultrasonic frequencies has enabled efficient testing in the desired Very-High-Cycle (VHC) ranges. However, the controversy is over whether the high- loading frequency affects the fatigue response of the materials or not. In this work a ferritic-martensitic dual-phase steel was investigated under ultrasonic 20 kHz loading as well as conventional low frequency fatigue tests. The objective was to study the possible effect of frequency on high and very-high-cycle fatigue behavior, thermal response of the material as well as the deformation and fracture mechanisms. The S-N curves were obtained and compared for 20 kHz and 30 Hz cycling. In addition, fractography studies were conducted to reveal the crack initiation and fracture mechanisms for ultrasonic and conventional fatigue loadings.

**keywords:** Fatigue response, Frequency effect, Dual-phase steel

## INTRODUCTION

Ultrasonic fatigue testing is an effective tool to carry out VHCF tests. Due to the extremely high loading frequency of 20 kHz, ultrasonic fatigue machine makes it possible to investigate the VHCF properties of different high strength steels in a reasonable time. However, this accelerated testing method has been always accompanied by a main question: what are the effects of such a high frequency on fatigue response of the material? Generally for high ductility and strain rate sensitive materials like low-carbon steels the influence of frequency stems from the strain rate effects [1]. Low- and medium-carbon ferritic steels exhibit clear discrepancy between fatigue life and fatigue strength, obtained from ultrasonic loading and those measured from conventional fatigue tests [1]. In this case, as a general trend, ultrasonic loadings produce higher fatigue lives than low frequency tests. The elevated fatigue life and fatigue limit under ultrasonic loading has been mostly attributed to the increase of yield strength due to increasing the strain rate [2,3]. On the contrary, high alloy and high strength steels (e.g. martensitic stainless steels) are less susceptible to frequency effects and often there is a good agreement between their fatigue life obtained from ultrasonic loadings and that measured from low frequency fatigue tests [4].

The present work aims at explaining the differences between ultrasonic and conventional fatigue accounting for strain rate and temperature effects. DP600 dual-phase steel which consists of a ferrite matrix containing martensite islands was investigated under 20-kHz ultrasonic loading as well as conventional low frequency fatigue tests. In both cases, the S-N

curves were obtained and the effect of frequency on fatigue life and fatigue limit was studied. Fractography studies were conducted and effect of frequency on crack initiation and material failure was investigated. Moreover, thermographic measurements were performed and mechanisms were proposed to explain the observed abnormal thermal response of the material under ultrasonic loading and correlate it to the fatigue and deformation behaviors.

## MATERIAL AND EXPERIMENTS

The material studied in this research was a commercial DP600 dual-phase steel. This ferritic-martensitic steel which contains 15 wt. % martensite was received as sheets of 3.6 mm thickness from ArcelorMittal. The chemical composition of the material is (%wt) Mn 0.933, Ni 0.020, Si 0.213, Cr 0.727, C 0.075, Nb 0.042. The mechanical properties of the material are presented in Table 1. Ultrasonic and conventional low frequency fatigue tests were carried out by using a piezoelectric 20-kHz system and a 10-kN servo-hydraulic MTS machine, respectively. All fatigue tests were performed under fully reverse tension-compression ( $R=-1$ ). Hourglass-shaped specimens with rectangular cross section were used. In both cases loading amplitude was low so that the specimen deformed elastically from macroscopic point of view. All specimens were electropolished after mechanical polishing in order to remove the residual stresses. Moreover, in situ infrared thermography was employed to record the mean temperature on the specimen surface under fatigue loadings. The details of temperature measurement method can be found in Ref. [5].

Young's Modulus (GPa)	Yield strength (MPa)	Ultimate tensile strength (MPa)	Elongation (%)
210	440	650	20

Table 1: Mechanical properties of DP600 steel [6]

## EXPERIMENTAL RESULTS

### S-N CURVES

The S-N curves were obtained by 20-kHz ultrasonic loadings along with cooling the specimen with compressed air, and also by 30-Hz conventional fatigue tests. The obtained S-N data are presented in Fig. 1. According to this figure, for a given stress amplitude,  $\sigma_a$ , the fatigue lifetime measured by ultrasonic loading was higher than that obtained from conventional tests. The number of cycles at the knee point obtained at 30 Hz was  $\sim 2 \times 10^6$  cycles, whereas the corresponding value at 20 kHz was  $\sim 3 \times 10^8$  cycles. For a given number of cycles ranging from  $10^6$  to  $10^7$ , where the data exist for both loading techniques, the fatigue strength is higher at 20 kHz than at 30 Hz. However, both frequencies have resulted in the same fatigue limit of  $\sim 260$  MPa.

Based on infrared thermography measurements in the case of ultrasonic loadings at stress amplitudes, above the fatigue limit (all points in the S-N diagram excluding the run-out points), strong heating occurred in the early stages of cycling, leading to significant temperature increases up to  $\sim 350^\circ\text{C}$ . However, at stress amplitudes below the fatigue limit temperature remained less than  $100^\circ\text{C}$ . The high temperature increases at high stress amplitudes could not be avoided even by using air-cooling systems. This kind of S-N data have been already reported for other bcc materials, for which intermittent loading and cooling systems could not prevent the strong heating and significant temperature rises during ultrasonic loadings (see



for example [7,8]). In the case of 30-Hz frequency, temperature increase was ignorable ( $\Delta T < 15^\circ\text{C}$ ) and no cooling system was required.

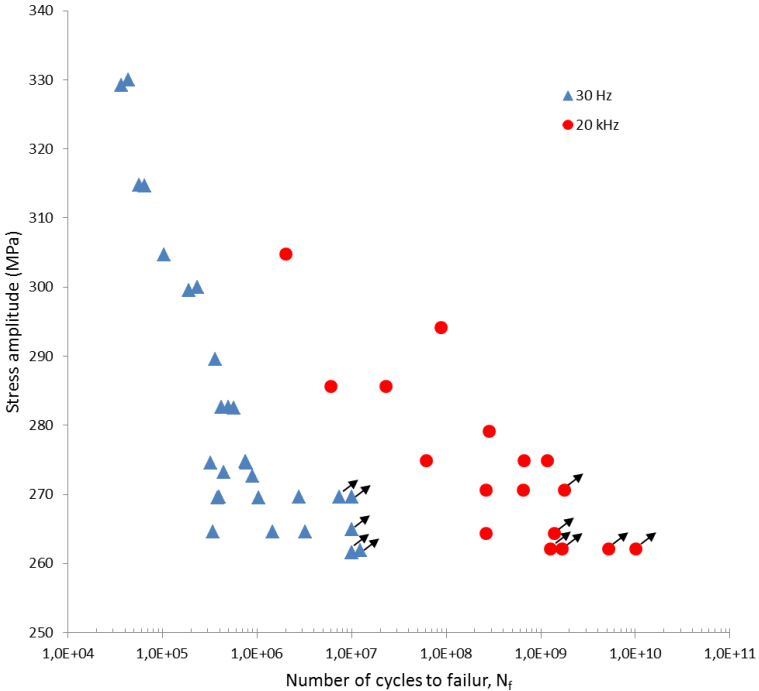


Fig.1: S-N data of DP600 steel, obtained from 20-kHz and 30-Hz fatigue loadings

### Fractography studies

Fracture surfaces of conventional and ultrasonic ruptured specimens were investigated by Scanning Electron Microscopy (SEM). For all specimens ruptured under 30-Hz frequency loading, fatigue crack initiated from slip bands on the specimen surface. For instance, Fig. 2(a) shows a surface initiation from slip bands under 30-Hz frequency loading. In the case of VHCF ruptures under ultrasonic fatigue tests, crack initiation was mainly internal however some cases of surface crack initiation were also observed. In this case, crack initiation was always inclusion-induced for both internal and surface crack initiations. An internal inclusion-induced crack initiation leading to fish-eye fracture under ultrasonic loading is presented in Fig. 2(b).

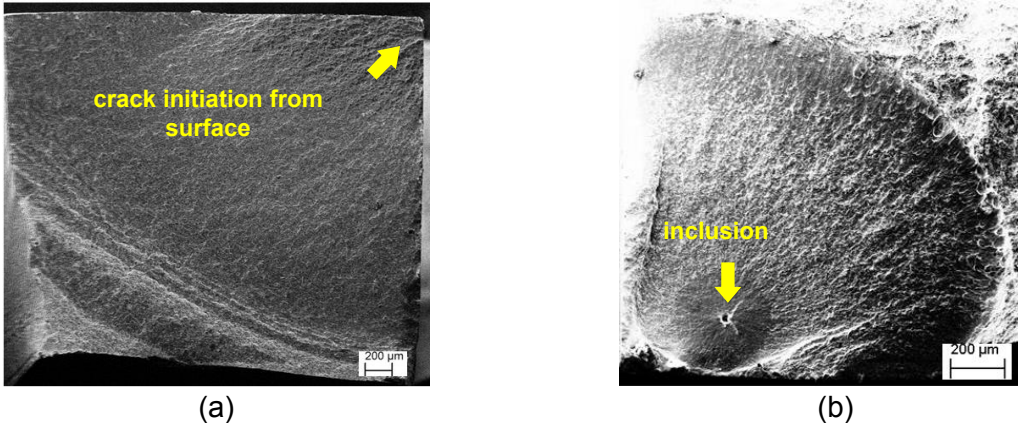


Fig. 2: Fracture surface of fatigue specimens:(a) conventional sample ( $N_f = 7.7 \times 10^5$  cycles and  $\sigma_a = 275$  MPa) (b) ultrasonic sample ( $N_f = 6 \times 10^7$  cycles and  $\sigma_a = 275$  MPa)



## Surface observations

Interrupted fatigue tests were conducted and the surface of the specimens was observed by SEM at different loading stages. All observations were made along the central axis of the specimen around the center of the gauge part. For all specimen loaded by 20-kHz frequency at low stress amplitudes ( $\sigma_a < 260$  MPa), for which no strong heating occurred ( $T < 100^\circ\text{C}$ ), no slip band (SB) was observed on the specimen surface even after  $10^9$  cycles. The same observations were carried out for a specimen loaded by 30-Hz frequency at  $\sigma_a = 250$  MPa, up to  $N=10^7$  cycles and the observation results are presented in Fig. 3(a). In this case, SBs formed in ferrite grains on the specimen surface in the early stages of loading ( $N \sim 10^5$  cycles) and were developed by increasing the number of cycles. The slip bands are indicated by arrows in the graphs. Although no slip band formation occurred under ultrasonic loading at low stress amplitudes (below the fatigue limit), for loadings at stress amplitudes above the fatigue limit, which were accompanied by high temperature increases, SEM observations of the specimen surface revealed formation of many slip bands as well as microvoids and microcracks along the slip bands in ferrite grains, as shown in Fig. 3(b).

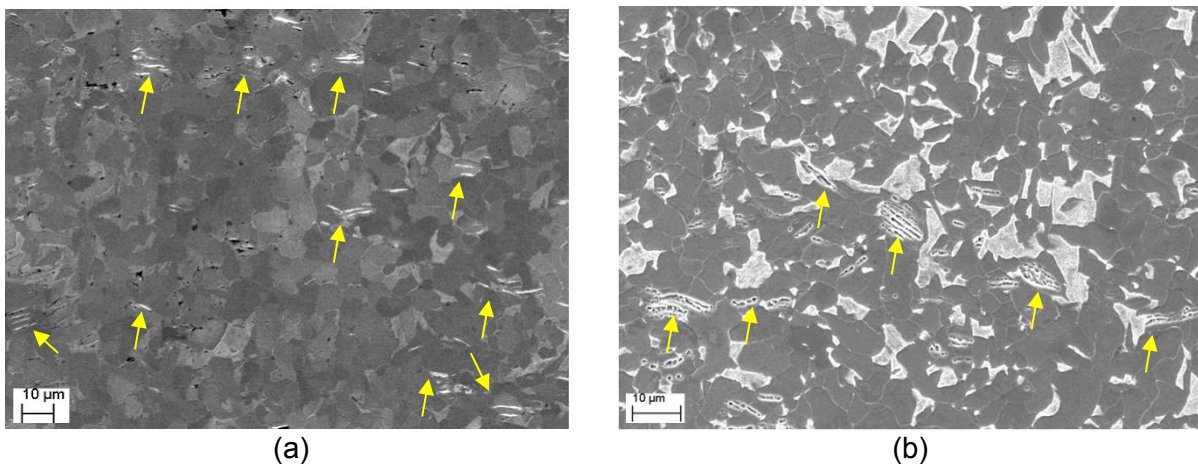


Fig. 3: SEM observations on specimen surface (a) conventional fatigue sample ( $N=10^7$  cycles and  $\sigma_a=250$  MPa) (b) ultrasonic sample ( $N=10^6$  cycles and  $\sigma_a=286$  MPa)

## DISCUSSION

### Effect of frequency on deformation mechanisms

In dual-phase steel, since the hardness of martensite is much higher than ferrite, it can be assumed that dislocation motions and plastic deformation occur in ferrite grains, as the ductile phase with a bcc structure. Mughrabi et al. [9] described the temperature and rate dependent behavior of bcc metals by defining two deformation regimes based on the transition temperature: (1) the thermally-activated mode ( $T < T_0$ ) where the screw dislocations are immobile and edge dislocations move to-and-fro in a non-hardening quasi-recoverable manner (2) the athermal regime ( $T > T_0$ ) where the mobilities of screw and edge dislocations are equivalent and screw dislocations can cross slip. In this regime, rearrangement of dislocations can take place and strain localization can occur in slip bands. The transition temperature,  $T_0$ , is highly strain rate dependent and can be shifted to higher values by increasing the strain rate. The transition strain rate of low-carbon steel should lie in the range of  $1 \text{ s}^{-1}$  to  $10 \text{ s}^{-1}$  [3]. In our case, for conventional 30-Hz frequency fatigue tests with the stress amplitudes in the range of 260 to 330 MPa (according to Fig. 1) the maximum

strain rate was estimated to range from  $0.233 \text{ s}^{-1}$  to  $0.296 \text{ s}^{-1}$ , considering elastic macroscopic behavior. Thus for conventional fatigue tests at room temperature the strain rate is much smaller than the transition strain rate and material deformation occurs in athermal regime.

For ultrasonic testing with 20-kHz frequency, the deformation regime depends on stress amplitude, as discussed in Ref. [5]. In this case, the temperature increase under high stress amplitudes plays an important role in the material deformation regime. For the stress amplitudes below the fatigue limit ( $60 \text{ MPa} < \sigma_a < 260 \text{ MPa}$ ) the maximum strain rate ranges from  $36 \text{ s}^{-1}$  to  $156 \text{ s}^{-1}$ . At these stress amplitude ranges, no strong heating occurred and specimen temperature did not significantly increase ( $T < 100^\circ\text{C}$ ). In this case, the transition temperature should be higher than room temperature for these high strain rates, therefore material deforms at thermally-activated mode under ultrasonic loadings at low stress amplitudes. Nonetheless, for ultrasonic loading at high stress amplitudes the specimen temperature increased to some hundreds of degree, which is higher than the transition temperature at the corresponding high strain rate ( $\sim 100^\circ\text{C}$ ), and material deforms in the athermal regime [5]. The aforementioned deformation modes under different loading conditions can be confirmed by the SEM observations on the surface of specimens which show slip band formations for conventional fatigue tests and ultrasonic loading at high stress amplitudes, while for ultrasonic loading at low stress amplitudes no slip band was observed.

### **Effect of frequency on fatigue life**

In the case of dual-phase steel under high temperature cycling, dynamic strain aging is known to occur [5], which results in increasing the yield and tensile strengths of the material. The higher fatigue life in the case of ultrasonic loading can be attributed to the dynamic strain aging which resulted from the high temperature increases at high stress amplitudes. In other words, in spite of the high mobility of screw dislocations in the athermal deformation regime, because of the high temperature, interstitial carbon atoms diffuse around the dislocations and restrict their movements temporarily. Subsequently, the occurrence of slip and crack initiation would be delayed, leading to an increase in the fatigue life for a given stress amplitude. The effect of strain ageing on increasing the fatigue life of low-carbon steels at high temperatures have been already reported in the literature [10].

### **Effect of frequency on fatigue limit**

the fatigue limit of materials with BCC structure can be considered as the stress necessary for activation of screw dislocations [11]. Considering this physical aspect of fatigue limit, for DP600 steel, because both conventional fatigue tests and ultrasonic loadings at high stress amplitudes lead to athermal deformation mode, from the screw dislocation activation stress viewpoint, no large difference is expected to exist between ultrasonic and low frequency tests. In other words, the stress required for the screw dislocations to have the same mobilities as edge dislocations is equivalent for ultrasonic loading and conventional low frequency tests and it can explain the similar fatigue strength of two cases.

## **CONCLUSIONS**

The effect of frequency on fatigue behavior of ferritic-martensitic dual-phase steel was studied by carrying out ultrasonic and conventional low frequency tension-compression fatigue tests along with temperature measurements and microscopic observations. A clear discrepancy was observed in the S-N curves obtained from conventional 30-Hz fatigue tests and that measured from ultrasonic 20-kHz loadings. The rate and temperature dependent

flow behavior of the ferrite phase, as a BCC structure, was found to be a decisive parameter explaining the effects of frequency on fatigue and thermal response of the material. Moreover, the significant temperature increase under ultrasonic fatigue loading at high stress amplitudes was found to play an important role in the observed phenomena.

## REFERENCES

- [1] Mayer, H.:  
Recent developments in ultrasonic fatigue  
Fatigue and Fracture of Engineering Materials and Structures 39 (2016) pp. 3-29
- [2] Tsutsumi, N.; Murakami, Y.; Doquet, V.:  
Effect of test frequency on fatigue strength of low carbon steel  
Fatigue and Fracture of Engineering Materials and Structures 32 (2009) pp. 473-483
- [3] Guennec, B.; Ueno, A.; Sakai, T.; Takanashi, M.; Itabashi, Y.; Ota, M.:  
Dislocation-based interpretation on the effect of the loading frequency on the fatigue properties of JIS S15C low carbon steel  
Int. Journal of Fatigue 70 (2015) pp. 328-341
- [4] Bathias, C.:  
Coupling effect of plasticity, thermal dissipation and metallurgical stability in ultrasonic fatigue  
Int. Journal of Fatigue 60 (2014) pp. 18-22
- [5] Torabian, N.; Favier, V.; Ziaei-Rad, S.; Dirrenberger, J.; Adamski, F.; Ranc, R.:  
Thermal response of DP600 dual-phase steel under ultrasonic fatigue loading  
Materials Science and Engineering A 677 (2016) pp. 97-105.
- [6] Munier, R.; Doudard, C.; Calloch, S.; Weber, B.:  
Determination of high cycle fatigue properties of a wide range of steel sheet grades from self-heating measurements  
Int. Journal of Fatigue 63 (2014) pp. 46-61
- [7] Yu, Y.; Gu, J.L.; Xu, L.; Shou, F.L.; Bai, B.Z.; Liu, Y.B.:  
Very high cycle fatigue behaviors of Mn-Si-Cr series Bainite/Martensite dual phase steels  
Materials and Design 31 (2010) pp. 3067-3072
- [8] Ranc, N.; Favier, V.; Munier, B.; Vales, F.; Thoquenne, G.; Lefebvre, F.:  
Thermal Response of C45 Steel in High and Very High Cycle Fatigue  
Procedia Engineering 133 (2015) pp. 265-271
- [9] Mughrabi, H.; Herz, K.; Stark, X.:  
Cyclic deformation and fatigue behaviour of alpha-iron mono- and polycrystals  
Int. Journal of Fracture 17 (1981) pp. 193-220
- [10] Thompson, N.; Wadsworth, N.J.:  
Metal fatigue  
Advances in Physics 7 (1958) pp.72-169
- [11] Shevelya, V.V.; Gladchenko, A.N.:  
Microyield and nature of the physical fatigue limit of body-centered-cubic metals  
Materials Science 11 (1976) pp. 530-535

**Corresponding author:** noushin.torabian@gmail.com

# INVESTIGATION OF THE FATIGUE BEHAVIOR OF CARBON FIBER REINFORCED PLASTICS DUE TO MICRO-DAMAGE AND EFFECTS OF THE MICRO-DAMAGE ON THE PLY STRENGTHS IN THE VERY HIGH CYCLE FATIGUE REGIME

Ch. Hopmann<sup>1)</sup>, J. Marder<sup>1)</sup>, F. Becker<sup>1)</sup>

<sup>1)</sup>Institut für Kunststoffverarbeitung in Industrie und Handwerk an der RWTH Aachen, 52074 Aachen, Germany

## ABSTRACT

The investigations discussed in this section focus on the micromechanical fatigue mechanisms in transversally loaded unidirectional plies of carbon fiber reinforced epoxy. The damage process by the formation of matrix and interface cracks and filament failures has been determined by non-destructive acoustic emission (AE) measurements. In order to extract physically interpretable results a novel clustering methodology has been developed and implemented. AE measurements show that micromechanical damage occurs very late in the fatigue life of unidirectional (UD) plies under swelling transverse loads. It is concluded that the fatigue process of transversely loaded carbon fibre reinforced plastic (CFRP) plies is dominated by the viscous properties of the matrix material.

## KEYWORDS

Fibre/matrix interface failure, Acoustic emission, Very high cycle fatigue, Micro-damage of transverse plies, Clustering of acoustic emission data

## INTRODUCTION

A fundamental and initial damage mechanism in FRP is the micro damage. Micro damage is commonly referred to as the formation of cracks at the fiber/matrix interface. In the case of cyclical loading, *Correa et al.* and *Trappe* [1-2] have shown that the damage process is initiated equivalently to the damage process under quasi-static load by micro cracking at the fiber/matrix interface and in the matrix. Micro damage primarily manifests in a strength and stiffness degradation of the transverse properties of the respective ply. Investigations of *Mannigel* [3] have revealed that combined transverse shear and longitudinal compressive loading yields in a significant reduction of the longitudinal compressive strength. The effect was attributed to the formation of micro cracks and the resulting micromechanical loss of matrix support for the filaments against buckling. However, besides investigations of *Trappe et al.* [4] who studied the formation of micro cracking under cyclical shear loads using X-ray refraction, few studies on the phenomenology of micro damage evolution under cyclical loads exist. Since the nature and the evolution of micro damage is considered a key to modelling fatigue of FRP the objective of this investigation was the determination of mechanisms of cyclically induced micro damage via the acoustic emission method. To extract information on the damage mechanisms from the AE data a novel clustering algorithm was developed and implemented and has been applied to the fatigue tests allowing for on-line monitoring of the damage.

## CLUSTERING OF ACOUSTIC EMISSION SIGNALS AND DAMAGE EVOLUTION

The damage evolution was measured by an acoustic emission (AE) system by iNDTact Measurement Systems GmbH, Würzburg, Germany. The system consists of a sensor, a pre-amplifier and a digital data acquisition system. The sensor Impact XS features a frequency range of 1 mHz to 1 MHz with a low change in sensitivity over the frequency range. The signal is pre-amplified (0 dB) by a preamplifier champ 1.1 and an analog band pass filter is applied (lower cutoff 160 Hz, upper cutoff >1 MHz). The signal is further digitalized by the DAQ system NI 9181/9223, National Instruments, Austin, USA. The basic principle of AE is that a specific damaging event – such as fiber filament failure, matrix failure or interface failure – can be considered as a characteristic AE source yielding in a characteristic measurable AE signal. Single parameter or multivariate analysis for the classification of AE signals are used [5-6]. Algorithms widely applied are the k-means algorithm and its variations as well as neuronal network based self-organizing maps (SOM). In the present study an SOM based approach was used due to the better suitability to the problem since single.

Clustering data using SOM based approaches requires multi-step approaches. The weight vectors of the neurons have to be arranged to clusters in a second step after training and association of input data to specific neurons. Clustering approaches like the k-mean algorithm yield to physically incorrect clusters in many cases. In contrast the U-matrix approach depends on the subjectivity of a visual interpretation of the topology of the SOM. To overcome the inconvenience of the U-matrix approach, another step is conducted to obtain the cluster boundaries. It was found in image processing using the watershed transformation [7]. The transformation as proposed e.g. by *Vincent* treat image data as digital elevation models (DEM). The transformation finds watershed lines by successively increasing the water level in a DEM. Object or cluster separation lines are identified where the catchment basins merge. The approach of using the U-matrix together with the watershed transformation finds clusters based on relative changes in the weight density and is hence able to detect clusters regardless of the number of elements in the cluster even if within a cluster the distance of the data points is comparatively high. For the developed methodology the AE data is preprocessed as proposed by *Sause et al.* [8]. In an initial step obvious outliers and noise data are manually removed from the datasets. In a second step the AE data is normalized by a fixed set of reference values intending to scale each feature to the interval ]0,1[. The SOM algorithm as implemented in the Software package Matlab® was applied to a dataset using a grid-type net topology and a batch training algorithm. Since watershed transformations are prone to over-segmentation [7] the SOM training process is adapted to the problem. Instead of separating the training process into an ordering and a tuning phase only the ordering phase is performed where the neighborhood radius decreases to 1. The weight distribution is hence adapted to the global input distribution only avoiding the “noise” being generated during the tuning phase. The weight vectors resulting from the training process are subsequently used to calculate the U-matrix based on the average distance of the neighboring weights as proposed by *Ultsch* [9]. Although only the ordering phase is considered during learning, areas of the SOM with small deviations in the weight vectors and a high hit count are still prone to noisy weight distances and hence over-clustering. As remedy against over-clustering *Ohser et al.* propose preprocessing the data before it will be watershed transformed. In the algorithm presented here a strategy related to the h-minima transformation has been used [10]. Values falling below a threshold will be assigned a constant value which is equal to the threshold value. Result of the watershed transformation is the regions of the clusters identified on the SOM.

During the clustering process, the choice of the features used for clustering was found to have a decisive effect on the validity and the performance of the clustering. A wide variety of parameters has been proposed for partitioning of AE datasets and correlation with damage mechanisms in FRP ranging from energy or amplitude based criteria to frequency based concepts [11]. *Sause et al.* presented an outstanding numerical study investigating on the

measurable signal caused by typical failure mechanisms in fiber reinforced composites and compared their results with experimental investigations [12]. Based on these findings in this study the weighted peak frequency and the partial powers have been used for clustering. The parameters are defined in table 1.

Weighted Peak Frequency	$\sqrt{f_{peak} \frac{\int f \tilde{U}(f) df}{\int \tilde{U}(f) df}}$
Partial Power	$\frac{\int_{f_1}^{f_2} \tilde{U}^2(f) df}{\int_0^{1MHz} \tilde{U}^2(f) df}$
Partial Power Limits	Range 1: 0-100kHz Range 2: 100kHz-200kHz

Table 1: Frequency parameters used for clustering.

### Damage evolution and effect of testing conditions

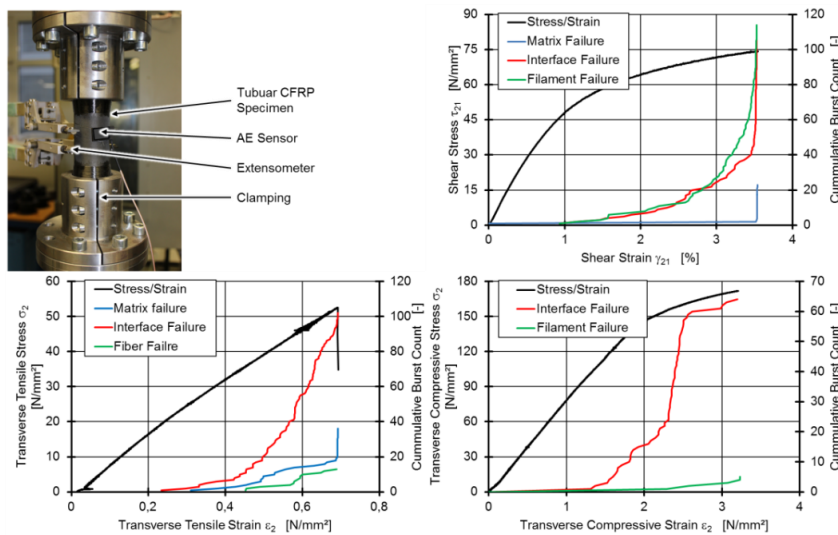


Fig. 1: Test setup and damage mode with AE algorithm under transverse basic loads.

Hoop wound tubular specimens from the material HTA40/LY556 (Toho Tenax Co., Tokio, Japan/ Huntsman A.M. BVBA Everberg, Belgium) of orientation  $89^\circ$  were manufactured. Specimen dimensions were chosen to have an inner diameter of 40 mm and a wall thickness of 1 mm. AE activity was measured during the determination of the transverse strengths  $R_{\perp}^+$ ,  $R_{\perp}^-$ ,  $R_{\perp}^+$ . Reference conditions were set to a strain rate of 1.3 %/min and room temperature of  $23^\circ\text{C}$ . Three clusters could be identified and damage evolution under quasi static loads can be summarized as described subsequently: Interfacial failure is the dominant damage mechanism under transverse loading. While under transverse tensile stresses material varies between failure by a dominant single crack and cumulative failure, the behavior under shear and transverse compressive stresses are found to be very reproducible. Detectable damage initiates comparatively late at effort factors of  $f_E > 0.8$  (calculated with *Pucks* criteria) under shear and  $f_E > 0.5$  under transverse compression (figure 1). Under shear loading significant AE activity was observed after damage onset, the detected signals were not only associated with interfacial damage but also a significant amount of signals associated with fibre filament failure could be observed. Under transverse compressive loads, AE activity was low and the signals were exclusively associated with interfacial damage (figure 1).

For reducing the time of fatigue tests, the strain rate was chosen to be factor 1000 higher than the quasi static strain rate and temperature was chosen to be  $60^\circ\text{C}$  ( $T_G$  of the resin measured via DSC for all specimens  $> 130^\circ\text{C}$ ). The damage phenomenology determined by

AE measurements is found to be significantly influenced by this testing conditions; the results are summarized in table 2.

	Damage onset		Strength		Failure
	$\sigma_2$ [MPa]	$\tau_{21}$ [MPa]	$\sigma_2$ [MPa]	$\tau_{21}$ [MPa]	
RT, 1.3%/min	15.17	0	53.89	0	Interface
	0	65.165	0	76.09	Interface
	-87.31	0	-176.84	0	Interface
60°C 1.3%/min	40.64	0	66.66	0	Interface
	0	27.7	0	65.41	Interface
	-56.00	0	-120.79	0	Interface
RT 1300%/min	9.32	0	9,32	0	None
	0	64.3	0	80.98	Interface
	-127.6	0	-152.61	0	Interface
60°C 1300%/min	8.57	0	10.05	0	Matrix
	0	82.08	0	84.6	Matrix
	-151.52	0	-163.85	0	Matrix

**Table 2:** Damage initiation and strength at elevated strain rate and temperature

## FATIGUE DAMAGE OF FRP

The fatigue behavior of CRFP under transverse loads was characterized and the change of the material state as well as the damage evolution was analyzed with the novel clustering approach. As well as for the quasi-static investigations the same specimens have been used for the fatigue investigations. Load is introduced by hoop-wound sections on the tubes which are made of the same CFRP material as the test ply. Tests have been primarily carried out on a 500 Nm torsion test rig by DynaMess Pruefssysteme GmbH, Stolberg, Germany and on a 1000 Nm torsion module of a 3-axis test rig by Instron/Schenck GmbH, Darmstadt, Germany. Tests have been carried out at a constant maximum strain rate of 50 %/s. Strain was measured using strain gauges together with a 3-D optical measurement system by Limes GmbH, Krefeld, Germany to realise strain measurement if the strain gauges fail. All tests have been carried out under load (torque) control; torque was measured in both torsion tests rigs by high precision TB2 torque transducer by Hottinger Baldwin Messtechnik GmbH, Darmstadt, Germany. Since temperature rises during testing the temperature was monitored for all specimens using an infrared pyrometer CT by optris GmbH, Germany.

### Fatigue behavior under transversal loads

The fatigue data for the three basic transversal stress states under a swelling constant amplitude load at  $R = 0.1$  and  $R=10$  for compression are depicted in figure 2. The fatigue data under shear stress has been determined using hoop wound  $89^\circ$  specimens resulting in a pure shear stress state. The transverse tension as well as transverse compression investigations has been performed using  $45^\circ$  wound specimens loaded in either positive or negative torque direction. The resulting stress state is therefore not uniaxial but a biaxial transverse  $\sigma_2 / -\sigma_1$  stress state. However fiber longitudinal stresses are comparatively small, resulting in an effort factor of  $f_{E,\sigma1(-)}=50/1800 < 0.1$  for transverse tension and  $f_{E,\sigma1(+)}= 150/2200 < 0.1$  for transverse compression. Longitudinal stresses were hence assumed to have a negligible effect on the fatigue behavior. It is evident that in all directions the material exhibits pronounced fatigue degradation. In all transversally tested specimens mean stress creep could be observed. Creep was most pronounced in the specimen



exhibited to shear while being less pronounced for the specimens being loaded in transverse tension. In contrast to the expectations none of the specimens tested exhibited measureable AE activity during most of the fatigue loading but detectable damage only occurred shortly before the specimen failed. Exemplary test data on the mean stress creep and the corresponding damage evolution are presented in figure 3.

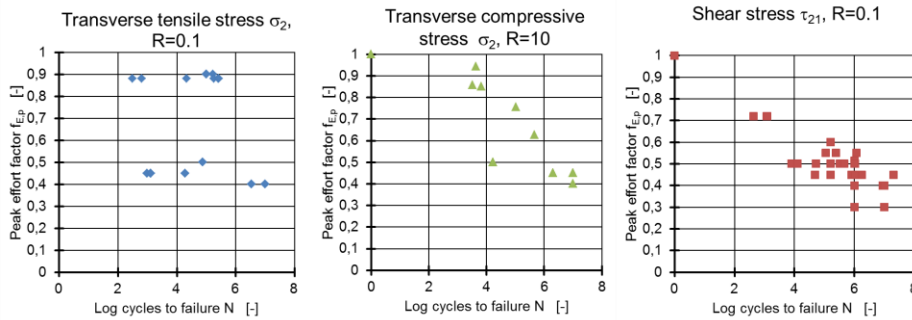


**Fig. 2:** Fatigue data for transverse swelling fatigue load at  $R=0.1$  and  $R=10$  determined using tubular specimen

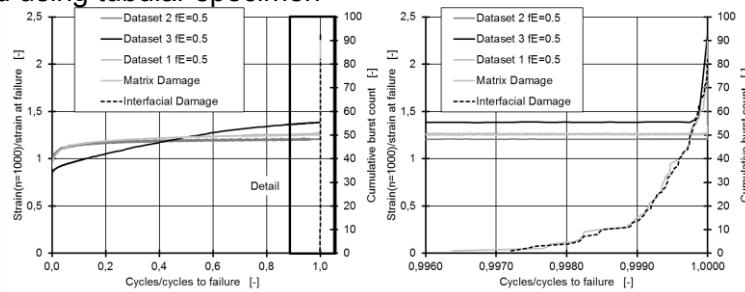


**Fig. 3:** Representative example of mean stress creep at  $f_E=0.5$  and damage detected by AE measurements at the end of the specimen's fatigue life

## CONCLUSION AND SUMMARY

The presented study presents a new clustering approach for the use of AE measurements during fatigue experiments. Due to application of the watershed algorithm after SOM and the U-matrix approach subjective identification of clusters could be minimized. With this method it could be shown that interface debonding is the primary micro damage mechanism in the material under quasi static loads. Results of the investigation on the dependency of damage initiation on variable temperature and strain rate revealed that the viscoelastic properties of the matrix resin dominate the damage initiation. These findings could be translated to the fatigue regime where the results on damage initiation indicate that mean stress creep is the major mechanism of state change in the material. Damage in the form of cumulative micro cracks could not be detected by AE measurements during fatigue loading for most of the material's fatigue life. Micro damage in the form of interface and matrix damage was only initiated in the final stage of the fatigue life of the transversely loaded material.

## ACKNOWLEDGEMENTS

The depicted research was funded by the Deutsche Forschungsgemeinschaft (DFG) as part of the priority program "Life<sup>∞</sup>" (SPP 1466). We would like to extend our thanks to the DFG

## REFERENCES

- [ 1 ] Correa, E.; Gamstedt, E.K.; Paris, F.; Mantic, V.:  
Effects of the presence of compression in transverse cyclic loading on fibre-matrix debonding in unidirectional composite plies  
Composites Part A 38 (2007) No. 11, pp. 2260-2269
- [ 2 ] Trappe, V.:  
Beschreibung des intralaminaren Ermüdungsverhaltens von CFK mit Hilfe innerer Zustandsvariablen  
Diss. TU Braunschweig, 2002;  
Braunschweig (2002)
- [ 3 ] Mannigel, M.:  
Einfluss von Schubspannungen auf das Faserbruchgeschehen in Kohlenstoffaserverstärkten Kunststoffen (CFK)  
Diss. RWTH Aachen, 2007; Institut für Kunststoffverarbeitung an der RWTH Aachen, Aachen (2007)
- [ 4 ] Trappe, V.; Harbich, K.W.:  
Intralaminar fatigue behaviour of carbon fibre reinforced plastics  
Int. Journal of Fatigue 28 (2006) No. 10, pp. 1187-1196
- [ 5 ] Berthelot, J.M.; Rhazi, J.:  
Acoustic emission in carbon fibre composites  
Composites Science and Technology 37 (1990) No. 4, pp. 411-428
- [ 6 ] Gutkin, R.; Green, C.J.; Vangrattanachai, S.; Pinho, S.T.; Robinson, P.; Curtis, P.T.:  
On acoustic emission for failure investigation in CFRP: Pattern recognition and peak frequency analyses  
Mechanical Systems and Signal Processing 25 (2011) No. 4, pp. 1393-1407
- [ 7 ] Ohser, J.; Schladitz, K.:  
3D Images of materials structures: processing and analysis  
John Wiley & Sons, 2009
- [ 8 ] Sause, M.G.R.:  
In Situ Monitoring of Fiber-Reinforced Composites  
Springer International Publishing, Berlin, 2016
- [ 9 ] Ultsch, A.:  
Self-organizing neural networks for visualisation and classification  
Information and classification, 1993
- [ 10 ] N.N., 'Matlab Documentation Matlab R2016a', The Mathworks Inc. Natick, MA, USA, June 2016 available at <http://de.mathworks.com/help/matlab/> (last accessed at 27.07.2016).
- [ 11 ] Ramirez-Jimenez, C. R.; Papadakis, N.; Reynolds, N., Gan, T.H.; Purnell, P.; Pharaoh, M.:  
Identification of failure modes in glass/polypropylene composites by means of the primary frequency content of the acoustic emission event  
Composites Science and Technology 64 (2004) No. 12, pp. 1819-1827
- [ 12 ] Sause, M.G.R.; Horn, S.:  
Simulation of Acoustic Emission in Planar Carbon Fiber Reinforced Plastic Specimens  
Journal of Nondestructive Evaluation 29 (2010) 2, pp. 123-142

**Corresponding author:** [fabian.becker@ikv.rwth-aachen.de](mailto:fabian.becker@ikv.rwth-aachen.de)

# Application

## INVITED



### **Alfonso Fernández-Canteli**

born in Oviedo (Spain), 17/04/45

Professor emeritus of Structural Engineering, Department: Construction and Manufacturing Engineering, Polytechnic School of Engineering, University of Oviedo, Spain E-mail: [afc@uniovi.es](mailto:afc@uniovi.es)

Academic Background: Mech. Engineer from the University of the Basque Country 1970

PhD. in Mech. Engineering from the Polytechnic University Madrid, 1981

#### Current research interest

1. Probabilistic fatigue modelling of metallic materials, glass, concrete and composites, including VHCF
2. Scale effect and test data evaluation based on the generalized local model
3. Three-dimensional fracture mechanics modelling applied to structural design.

#### Academic and professional career

ETH Zürich, Dep. of Civil Engineering (Swiss federal scholarship holder 1970-72, Lecture assistant 1972-75, Research Assistant 1979-81), Practicing Design Engineer SENER, EICESA, Bilbao, Spain 1975-78) Eng. Faculty, University of Oviedo, Spain (Lecturer 1981-84, Assistant Professor 1984-88, Professor 1988-15, Emeritus professor 2015- till now)

### **PROBABILISTIC MODEL FOR VHCF DATA ASSESSMENT**

**M. Muniz Calvente**<sup>1</sup>, P. Brita<sup>2</sup>, A. Fernández Canteli<sup>1</sup>, E. Castillo<sup>3</sup>

<sup>1</sup>University of Oviedo Department of Construction and Manufacturing Engineering, Gijón, Spain

<sup>2</sup>University of Applied Sciences Faculty of Mechanical and Plastics Engineering, Darmstadt, Germany

<sup>3</sup>University of Cantabria Dep. of Applied Mathematics and Computational Sciences, Santander, Spain

The Weibull regression model proposed by Castillo and Canteli for assessing fatigue results represents four relevant characteristics to proceed to successful VHCF data assessment. First, it fulfils the necessary compatibility between the statistical distributions  $F(\Delta\sigma;N)$  and  $F(N;\Delta\sigma)$ . Second, it demonstrates the necessity of existence of a fatigue limit as one of the model parameters, which differing from the arbitrary “classical fatigue limit” may adopt the zero value when prescribed by the fatigue data. Third, it allows a data normalization in the sense of reducing the whole Wöhler field to a unique 3-parameter Weibull distribution using the normalized variable  $V=(\log N-B)/(\log \Delta\sigma)$ . And fourth, it offers the possibility of including runouts besides failures in the model parameter assessment though up to an admissible rate of the failures number. In this way, the VHCF data can be adequately interpreted and treated as independent distributions arising from a dual fracture mechanism origin representing a concurrent flaw population problem [1,2], known statistically as “confounded data”, where both distributions intersect. Once the model parameters of both normalized cumulative distribution functions are estimated, the probability of failure for any of both failure mechanisms at any stress range can be determined applying a back normalization to the original Wöhler field. Joint assessment of the two-origin data, implying some correlation among the results from both flaw populations, may be eventually performed by accepting coincidence of some of the parameters. Finally, an example of application to former results from an external experimental VHCF program is presented.

#### **References**

[1] Przybilla C., Fernández Canteli A., Castillo E.

Maximum likelihood estimation for the three-parameter Weibull cdf of strength in presence of concurrent flaw populations  
Journal of European Ceramic Society, 33,1721-1727, 2013.

[2] M. Muñoz-Calvente, A. Fernández Canteli, V. Shlyannikov, and E. Castillo,

Probabilistic Weibull Methodology for Fracture Prediction of Brittle and Ductile Materials  
Appl. Mech. Mater., vol. 784, pp. 443–451, Aug. 2015.

[3] D.S. Paolino, A. Tridello, H.S. Geng, G. Chiandussi, M. Rossetto

Duplex S-N fatigue curves: statistical distribution of the transition fatigue life  
Frattura ed Integrità Strutturale, 30, 4217-423, 2015.

# STOCHASTIC MODELS FOR THE FATIGUE LIFETIME OF PARTICLE- OR FIBRE-REINFORCED METAL MATRIX COMPOSITES IN THE VHCF REGIME AND RELATED STATISTICAL METHODS

M. Baaske, F. Ballani

Institute for Stochastics, TU Bergakademie Freiberg, 09596 Freiberg, Germany

## ABSTRACT

With a particular emphasis on metal matrix composites reinforced by ceramic particles or fibres both a stochastic model for the random non-overlapping spatial arrangement of the non-metallic reinforcements as well as a stochastic model for the overall random fatigue lifetime of the composite is introduced and suitable statistical methods for the estimation of the respective model parameters are proposed. Especially for estimating the parameters of the spatial model in case data is available only as a planar section (typically from a metallographic analysis) with the stereological "unfolding" procedure as implemented in [1] and the quasi-likelihood parameter estimation method [2] two competitive methods are discussed in more detail. The stochastic model for the random fatigue lifetime as implemented in [3] allows for any spatial arrangement of spheroidal reinforcements as well as applied stress and material constants such as Vickers hardness as input and is substantially based on the " $\sqrt{\text{area}}$ "-criterion [4] relating inclusion size to fatigue strength as well as the idea of damage accumulation in the sense that a relevant portion of reinforcements with an individually non-critical projected area could be near to each other such that their surrounding damage zones interact.

## KEYWORDS

Stochastic modelling, Metal matrix composite, Ceramic reinforcements, Very high cycle fatigue, Parameter estimation

## INTRODUCTION

The present talk aims to introduce a stochastic model for the very high cycle fatigue (VHCF) behaviour of metal matrix composites. In particular this model is thought for two kinds of (AA6061) aluminium matrix composites reinforced with either alumina particles ( $\text{Al}_2\text{O}_3$ , ca. 15% volume fraction), or, short fibres (Saffil, ca. 20% volume fraction), as in [5] where experimental investigations are discussed; see Fig. 1 for planar sections. The idea to pursue such a kind of approach is based on the general finding that endurance in the VHCF regime is a random phenomenon which appears to be, to some extent, the result of the composition of the material at different scales. In case of ceramic reinforced MMCs in particular the arrangement of the reinforcements is random. The fundamental approach in building up such a stochastic model is to include explicitly the random spatial arrangement of the

reinforcements since often they are sources for fatigue failure or they are at least conducive to it, and not only sizes might matter but also orientations and the reinforcements' relative positions to each other.

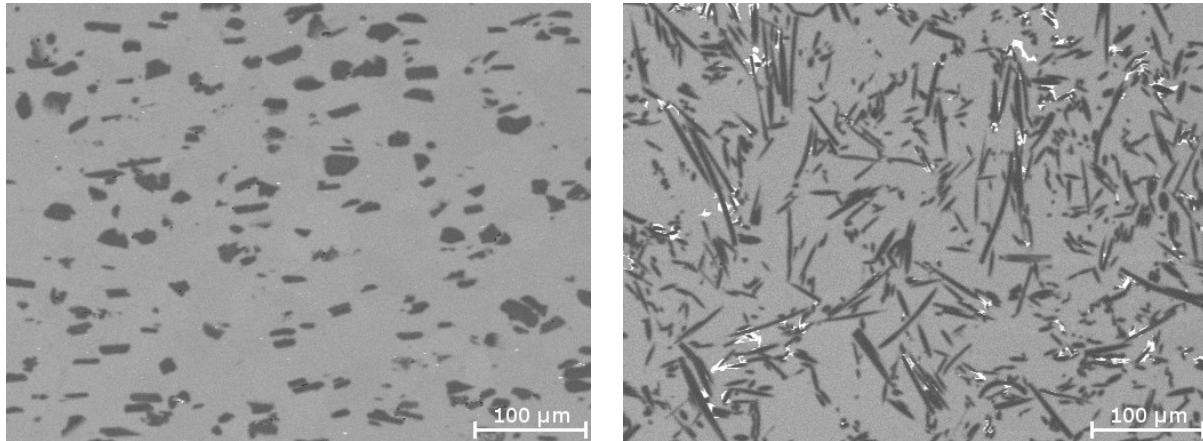


Fig. 1: SEM images of the particle (left) and short fibre (right) reinforced MMC

## MODELLING THE SPATIAL CONFIGURATION OF CERAMIC INCLUSIONS

The spatial modelling comprises both modelling the size-shape-orientation distribution of a typical reinforcement as well as modelling the whole random configuration of the non-overlapping reinforcements. The ceramic particles are modelled as prolate spheroids (ellipsoids of revolution) with one long semi-axis of length  $a$  and two short semi-axes of equal length  $c \leq a$ , whereas, similarly, the short fibres are modelled as spherocylinders. Both the production process as well as a previous statistical investigation of orientations justify the assumption that the orientation distribution of both types of reinforcements is invariant with respect to rotations about some fixed axis and may thus be well described by a Schlödlitz distribution [6] (controlled by an anisotropy parameter  $\beta > 0$ ), which has – in terms of spherical coordinates  $(\vartheta, \varphi)$  with respect to the fixed direction with polar angle  $\vartheta$  ( $0 \leq \vartheta < \pi$ ) and azimuthal angle  $\varphi$  ( $0 \leq \varphi < 2\pi$ ) – probability density function

$$h_{\beta}(\vartheta, \varphi) = \frac{1}{2\pi} \cdot \frac{\beta \sin \vartheta}{2(1 + (\beta^2 - 1)\cos^2 \vartheta)^{3/2}}.$$

It is further assumed that the size, represented by the length  $a$  of the long semi-axis, and the shape  $s=c/a$  may depend on each other but are independent of orientation by choosing  $a = \exp(\xi)$  and  $s = 1/(1 + \exp(-\eta))$  where  $(\xi, \eta)$  is a bivariate (possibly correlated) normally distributed random vector, that is, in particular, the size  $a$  is assumed to have a lognormal distribution, which is one of the established models for particle sizes.

From several possibilities to spatially arrange a system of non-overlapping spheroids or spherocylinders with a given size-shape-orientation distribution and a prescribed volume fraction the force-biased algorithm (FBA) model [6,7] was chosen. The basic idea of generating a configuration of spheroids/spherocylinders according to this model is to gradually change an initially overlapping configuration essentially by pushing-away shifts and

possibly rotations such that the amount of overlaps is reduced until the non-overlapping condition is satisfied. In the particular situation, however, pushing-away rotations were not allowed so as to keep the initial orientation distribution within the system of spheroids/sphero-cylinders fixed. See Fig. 2 for simulated configurations with volume fraction 15% in case of spheroids and 20% in case of sphero-cylinders.

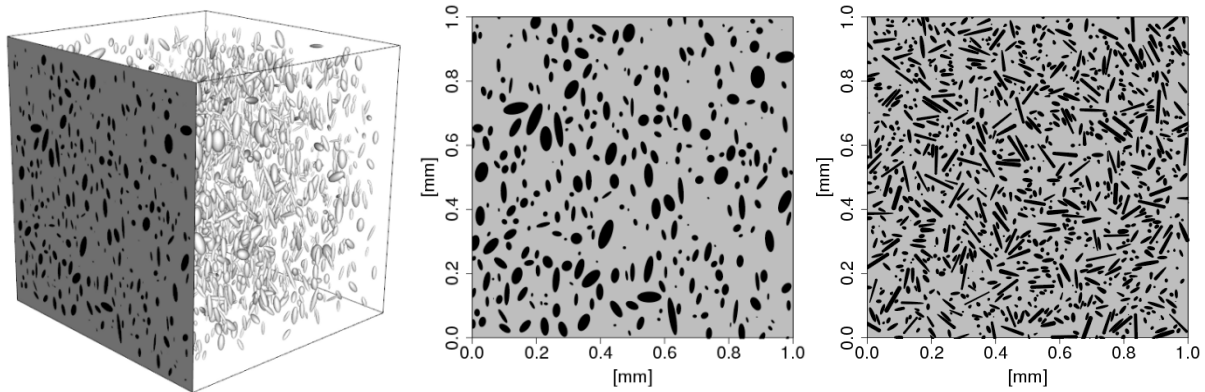


**Fig. 2:** Simulations of the FBA model with spheroids (left, middle) and sphero-cylinders (right)

Fitting a spatial model to the data is, however, quite involved since only planar data in terms of cross sections as in Fig. 1 is available, which, in particular, makes fitting the distribution of the spatial particles or fibres more complicated. Although the latter kind of problem is typically solved with the help of methods from stereology, it turned out to be beneficial to apply with the quasi-likelihood estimation approach [2] an alternative fitting method.

## MODELLING THE FATIGUE LIFETIME

### General assumptions

The first basic assumption for the modelling is that the specimen contains certain modes of failure which can happen at certain locations and to which an individual fatigue lifetime can be assigned. These cover (see [5])

- initially or during the fatigue experiment broken fibres/particles causing a crack,
- fibres/particles as inclusions with relatively low bonding within the metal matrix,
- matrix failure,
- non-infiltrated regions,

where non-infiltrated regions inside clusters of fibres are accounted for implicitly by the following approach.

Broken as well as debonded reinforcements imply each a projected area perpendicular to the direction of the maximum applied stress  $\sigma_a$ , see Fig. 3. As a second assumption it is assumed that this projected area is 'initiated' at a respective individual fatigue lifetime. Typically a singular such projected area is not critical for fatigue of the whole specimen.



However, some defects which are close to each other might imply a sufficiently large projected area.

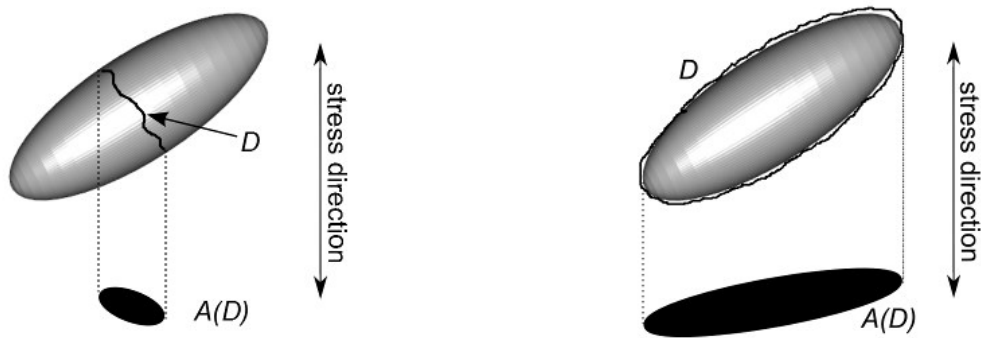


**Fig. 3:** Schematic representation of inclusion fracture (left), inclusion debonding (right), as used in modelling, each with respective projected areas

Therefore, the third assumption is that the projected areas of close defects accumulate and inherit as related individual fatigue lifetime the largest one assigned to the involved defects. Then, with progressing time (or cycles), at different locations within the specimen agglomerates of projected areas grow until the first reaches a critical size and the whole specimen fractures instantly. The critical size of an agglomerated projected area is derived from the equation for the minimum stress  $\sigma_w(A, j)$ ,

$$\sigma_w(A, j) = c_j \frac{H_V + 120}{A^{1/12}} \quad (c_1 = 1.56, c_2 = 1.43),$$

originally related to a non-metallic inclusion with projection area  $A$  and lying either in the interior ( $j=1$ ) or at the surface ( $j=2$ ) of a specimen (see [4, p. 90]), where “critical” is in the sense that if the applied stress  $\sigma_a$  is below  $\sigma_w(A, j)$  then a crack possibly initiated at this inclusion will not propagate and thus not cause failure of the whole specimen.

Finally, it is assumed that independently from the lifetimes associated with reinforcement failure or interface debonding also fatigue failure initiated by matrix failure may happen. The overall fatigue lifetime of a specimen is then given by the minimum of the fatigue lifetime associated with failure due to the reinforcements and of the (Weibull-distributed) fatigue lifetime due to matrix failure.

### Individual lifetimes

A widely accepted model for the number of cycles to failure of a ceramic specimen is the two-parameter Weibull distribution. Because of that such a law is assumed also for the random lifetime of an initially unbroken reinforcement until it potentially fractures. Since the microstructural investigations [5] show that some of the reinforcements (typically short fibres rather than particles) are broken before starting the fatigue testing, a small portion of reinforcements already broken in the beginning is assumed in the model, too, that is, they are assigned individual lifetime 0.

For the second mode of local damage it is assumed that the maximum stress intensity factor  $K_{max}$  near the boundary of a reinforcement is large enough to initiate a crack, the space of which is assumed to coincide with the respective reinforcement, and, hence, one may

associate this kind of building damage with debonding. The associated individual random lifetime  $T$  for a projected area  $A$  of a reinforcement lying either in the interior ( $j=1$ ) or at the surface ( $j=2$ ) of a specimen is modelled as

$$\log(T) = b_0 + b_1 \log(K_{\max}(A, j, \sigma_a)) + b_2 Z$$

where  $Z$  is a standardized normally distributed random number,  $b_0$  is a shift parameter,  $b_1$  is a slope parameter,  $b_2$  is a parameter (in the sense of a standard deviation) controlling for the amount of randomness in the model, and (see [4])

$$K_{\max}(A, j, \sigma_a) = k_j \sigma_a \sqrt{\pi \sqrt{A}} \quad (k_1 = 0.5, k_2 = 0.65).$$

### Accumulating initiated projected areas

Picking up the finding that nearby inclusions or cracks behave like one large inclusion or crack [4] and the projected areas of single inclusions are too small, the model allows for accumulation of projected areas. Associated with each kind of local damage is both an individual lifetime  $T_i$  and a spatial domain  $D_i$  with projected area  $A(D_i)$ . At time  $T_i$  the local damage is initiated, that is, either an inclusion is detached from the surrounding matrix or it breaks. At a later time  $T_j$  another local damage with spatial domain  $D_j$  and respective projected area  $A(D_j)$  is initiated. In case the domains  $D_i$  and  $D_j$  are close in a certain sense they are merged into a cluster  $C$  which is then considered as a new and larger local damage. The individual lifetime associated with this cluster  $C$  is then  $T_j$ , that is, the minimum of  $T_i$  and  $T_j$ , whereas the projected area assigned to  $C$  is the projected area of the convex hull of the set-theoretic union of the spatial domains  $D_i$  and  $D_j$ . Over time clusters may grow by adding further initiated domains, or even other clusters, until the projected area of one cluster is above the critical area. The corresponding process of accumulation events for  $\sigma_a=140$  MPa is illustrated in Fig. 4,

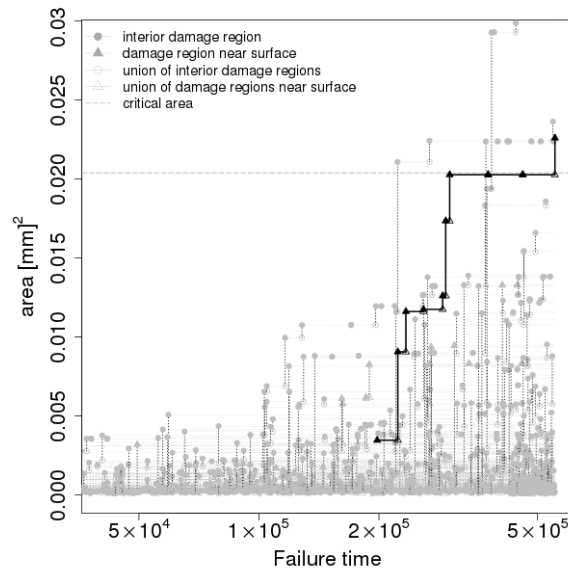


**Fig. 4:** Example for failure times associated with the individual agglomerates at  $\sigma_a=140$  MPa. The thick line shows the process of accumulating local damages which finally leads to the overall failure of the specimen.

even showing that overall fatigue failure is caused by a damage region near to surface although some projected areas related to interior damage are already above the critical area for damage regions near surface.

## STATISTICAL APPROACH

A general problem in the statistics of very high cycle fatigue data is that the data size is relatively small due to the long experimental times even when a modern high frequency testing device is used. Besides small sample sizes parameter estimation in the given situation is relatively involved for the following two reasons. Firstly, all information on the parameters has to be extracted from the observed overall fatigue lifetimes. Secondly, there is no closed form expression which relates the distribution of the overall fatigue lifetimes to the employed model parameters such that estimation can be solely based on simulation. The latter problem also arises when fitting the spatial model. Because of that in either case the simulation based quasi-likelihood estimation approach [2], which can explicitly deal with both kinds of problems, is proposed for parameter estimation.

## REFERENCES

- [ 1 ] Baaske, M.:  
unfoldr: Stereological unfolding for spheroidal particles  
R package version 0.6 (2016), <https://CRAN.R-project.org/package=unfoldr>
- [ 2 ] Baaske, M.; Ballani, F.; van den Boogaart, K. G.:  
A quasi-likelihood approach to parameter estimation for simulatable statistical models  
Image Anal. Stereol., 33 (2014), pp. 107–119
- [ 3 ] Baaske, M.; Ballani, F.:  
simLife: Simulation of fatigue lifetimes  
R package version 0.3 (2016), <https://CRAN.R-project.org/package=simLife>
- [ 4 ] Murakami, Y.:  
Effects of Small Defects and Nonmetallic Inclusions  
Elsevier Science, Amsterdam, 2002
- [ 5 ] Müller, A.; Weidner, A.; Biermann, H.:  
Influence of reinforcement geometry on the very high-cycle fatigue behavior of  
aluminum-matrix-composites  
Materials Science Forum, 825/826 (2015), pp. 150–157
- [ 6 ] Ohser, J.; Schladitz, K.:  
3D Images of Material Structures  
WILEY-VCH, Weinheim, 2009
- [ 7 ] Bezrukov, A.; Stoyan, D.:  
Simulation and statistical analysis of random packings of ellipsoids  
Part. Part. Systems Char., 23 (2006), pp. 388–398

**Corresponding author:** ballani@math.tu-freiberg.de

# EVALUATION OF MULTIPLE-FLAW FAILURE OF BEARING STEEL 52100 IN THE VHCF REGIME AND DESCRIPTION OF THE SINGLE-FLAW BEHAVIOUR

K. Burkart, B. Clausen, H.-W. Zoch

Stiftung Institut für Werkstofftechnik (IWT), Badgasteiner Str. 3, 28359 Bremen, Germany

## ABSTRACT

The demand for knowledge about fatigue behaviour of structural materials in the VHCF regime steadily grows. In the case of high strength steels, fatigue tests mostly reveal that multiple failure mechanisms occur. However, the common statistical analysis of constant amplitude tests generates summarized multiple-flaw S-N curves which neglect the differentiation according to the type of the failure cause, e.g. oxides or sulphides as non-metallic inclusions. To improve the fatigue life of materials it is essential to determine single-flaw S-N curves for the assessment of the harmfulness of each failure type. Within the evaluation it has to be taken into account that some mechanisms occur less frequently because they are covered by others. Furthermore, it has to be considered that the probability of the occurrence of different failure types depends not only on the stress amplitude but also on the applied mean stress. In this investigation specimens made of different heats of the bearing steel 52100 were tested uniaxially at two stress ratios up to  $2 \cdot 10^9$  load cycles using two ultrasonic testing devices. The tests exhibited crack initiation at different types of inclusions and at the surface. A mathematical solution is given to calculate single-flaw S-N curves including the regime of the fatigue limit from these results.

## KEYWORDS

Competing risks, 52100, very high cycle fatigue, single-flaw failure, multiple-flaw failure, inclusions

## INTRODUCTION

Fatigue tests of high strength steels mostly reveal that multiple failure mechanisms occur [1]. However, the common statistical analysis of constant amplitude tests generates summarized multiple-flaw S-N curves which neglect the differentiation between the type of failure origin, e.g. oxides or sulphides as non-metallic inclusions. The improvement of the fatigue life of materials requires the determination of single-flaw S-N curves in order to assess the harmfulness of each failure type. Since some failure types are covered by more dominant ones it is necessary to test a large number of specimens to get statistically firm information on the more seldom occurring types. The tested specimens were made of four heats of the bearing steel 52100 (100Cr6) differing in the chemical composition and in the processing route. The tests were carried out uniaxially up to  $2 \cdot 10^9$  load cycles on two piezo-electric ultrasonic testing devices. Since additionally applied mean stresses can have an effect on the occurring failure types [2, 3] two stress ratios were tested. A description of the fatigue test equipment can be found in [4]. The single-flaw S-N curves are based on the fatigue test results by adaption of the competing risks theory [5] to multiple-flaw fatigue tests.

## SPECIMENS, MATERIAL AND TESTING

Table 1 shows the chemical composition of the tested variants. The not listed titanium content of all variants is below 10 ppm. Variant A is a standard processing heat using aluminium in the deoxidation process. Since variant B is deoxidized by silicon its aluminium content is very low and this corresponds to a very high oxidic cleanliness. No sulphides were found in the metallographic investigations for variants C and D which matches with the low sulphur contents compared to that of variant A and B. Variant C is made of an ingot cast with highly improved isotropic properties and the heat for variant D was melted and remelted under vacuum (VIM-VAR).

Variant	mass %								ppm	
	C	Cr	Si	Mn	Cu	Al	S	P	O	N
A	0.95	1.33	0.24	0.41	0.10	0.010	0.005	0.013	4	77
B	0.95	1.43	0.35	0.33	0.07	0.003	0.006	0.011	5	83
C	0.94	1.50	0.29	0.26	0.04	0.027	0.001	0.003	2	67
D	1.00	1.49	0.29	0.33	0.06	0.022	0.002	0.020	2	28

**Table 1:** Chemical composition of the four steel heats

All specimens were heat treated in the following way: Austenitizing at 840 °C for 20 min, oil quenching at 60 °C and tempering at 180 °C for 2 h which led to martensitic structure with an amount of retained austenite of between 12 and 13 percent. The hardness is between 740 HV1 and 776 HV1 which means that all variants show a similar microstructure regarding the composition of phases. After grinding, the maximum compressive residual stresses at the surfaces are about 500 MPa. All variants show a similar residual stress depth profile where the stresses decrease to a negligible amount in a depth of about 12 microns.

The fatigue tests were performed under the stress ratios  $R = 0$  and  $R = -1$  at 18 °C in an air-conditioned room. In both cases, the specimens were stimulated to resonance frequencies of about 20,000 Hz by a piezo-electric ultrasonic testing device. During the tests the specimens were loaded in pulse-pause sequences and cooled via compressed air. By adapting the duration of the pause sequence this setup ensured that the temperature of the specimens surface stayed below 30 °C. Due to the necessity of pause sequences, effective test frequencies of between 2,000 and 12,000 Hz could be achieved depending on the tested stress amplitude, stress ratio and steel variant.

## EXPERIMENTAL RESULTS

The results of the fatigue tests at stress ratio  $R = 0$  are presented in Fig. 1. The test results are differentiated according to failure initiated at the surface and in the test volume. The missing information of specimens without rupture up to  $2 \cdot 10^9$  load cycles can be found in [6]. Surface failure occurs at an early stage of the test and there is mostly a gap of fatigue life between surface failure and volume failure except for variant C where the fatigue life scatter is very large. However, below a certain stress level surface failure does not occur anymore whereby this respective stress level depends on the variant. In the regions of these stress levels, it is possible that surface failure also occurs at a later stage of the test, since this is the transition zone of the single-flaw fatigue limit of surface failure as it can be seen exemplarily for variant A at  $S_a = 600$  MPa. Variant A and B show the highest fatigue strength and a similar fatigue behaviour at stress ratio  $R = 0$ . It's obvious for all variants that a real fatigue limit does not exist under the tested conditions.

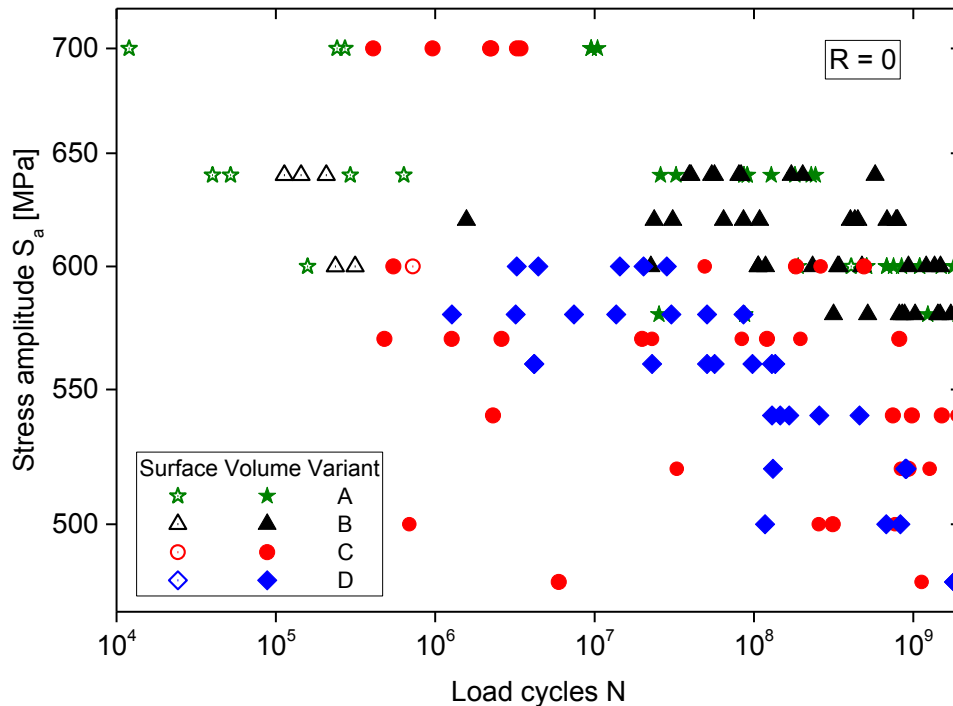


Fig. 1: Failed specimens at stress ratio R = 0 differentiated according to surface and volume failure

## MODELLING

The determination of the single-flaw fatigue behaviour of multiple-flaw failing materials is possible with the base approach given by Eq. 1 where  $P_f$  is the failure probability of a specimen in total in dependence of the number of load cycles  $N$  and  $n$  is the number of all failure mechanisms which can possibly occur.

$$P_f(N) = 1 - \prod_{i=1}^n (1 - F_{fi}(N)) \quad (1)$$

For the survival of the specimen, all possible failure mechanisms  $i$ , which are described by the single-flaw failure distribution functions  $F_{fi}$ , must survive. This means that the product of  $(1 - F_{fi})$ , where  $i$  represents all possible failure mechanisms, describes the survival probability of the specimen. Therefore, the determination of the parameters of the single-flaw distribution functions  $F_{fi}$  is needed. In the following, it is assumed that all single-flaw failure distributions can be described sufficiently by Weibull functions [7].

### Modelling of single-flaw finite fatigue life

First, all specimens of the stress level have to be sorted according to their number of load cycles at failure. Afterwards, a failure probability is assigned to each specimen calculated from an estimator. Since the early occurring failure mechanism "surface" is clearly separated from the other occurring ones, the maximal possible probability of surface failures can be derived from the values of the estimator. For all other mechanisms it is assumed that they would lead to failure some time if no other failure mechanism would be present. Therefore,

the maximum failure probability of each inclusion type equals one, which means that no fatigue limit exists.

It is assumed that surviving samples would have failed later if the test would have been continued. These data are called right hand censored data. In these cases the failure distribution function  $F$  will be regarded in form of the survival function  $(1 - F)$  in a system of terms where one term belongs to one sample test. In the case that a sample fails the failure density function  $f$  will be regarded. The most likely parameters of the distribution function can be derived out of this system of terms by the use of the Maximum-Likelihood-Method [8].

In the multiple-flaw case there is more than one possible failure mechanism. Each test leads to a more complex expression (Eq. 2). If a specimen fails by the mechanism  $i$ , the term with the failure distribution function of mechanism  $i$  is described by the failure density function  $f_i$ . Additionally, this means that all other possible failure mechanisms must be regarded with the terms of the failure distribution functions  $F_j$  in the form of the survival function  $(1 - F_j)$  of the respective (not failed) mechanisms. This indicates that all these possible failure mechanisms  $j$  are covered by mechanism  $i$ . If a specimen does not fail until the end of a test, which depends on  $N_{max}$ , each mechanism will be regarded in the same way whereby Eq. 2 simplifies to an expression without a failure density function.

$$L_i = f_i \cdot \prod_{j=1}^n [(1 - F_j)^{\delta_{ij}}] \quad , \delta_{ij} = 1 \text{ for } i \neq j \text{ and } 0 \text{ for } i = j \quad (2)$$

This system of expressions is solved in the same way as mentioned above. As an example, Fig. 2 shows the resulting single-flaw failure distribution functions of variant B at  $S_a = 600$  MPa,  $R = 0$  as dashed lines. The solid black line which represents the failure probability of the specimen in total was calculated according to Eq. 1 from these single-flaw failure distribution functions. This procedure can be performed for each stress level of the fatigue tests which leads to single-flaw S-N curves.

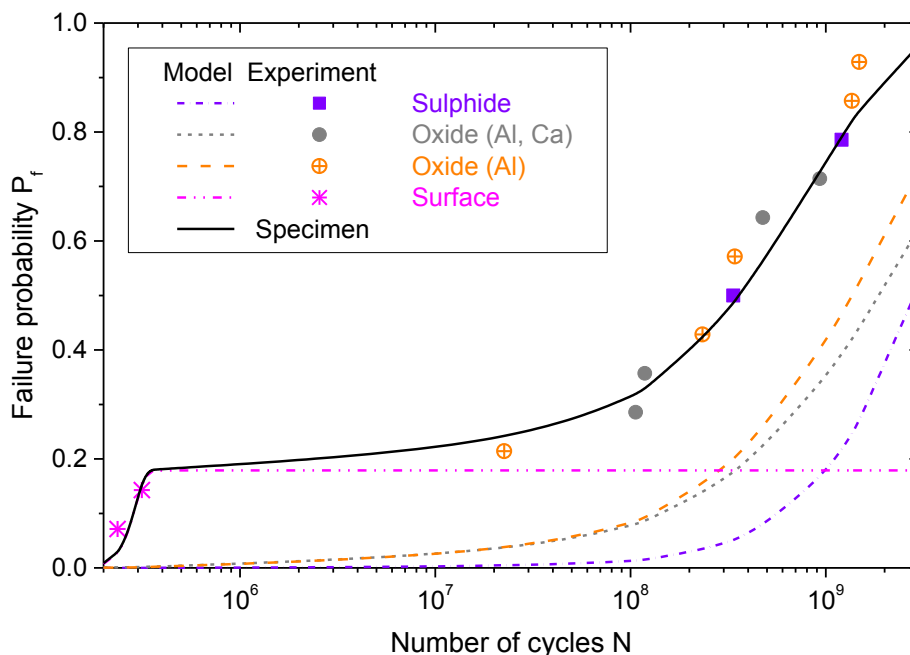


**Fig. 2:** Distribution of failure probabilities according to failure mechanisms, variant B,  $S_a = 600$  MPa,  $R = 0$



## Modelling of single-flaw fatigue limits

For the evaluation of the description of infinite life, an additional parameter  $q_i$  is necessary to describe the general failure potential of a specific failure mechanism  $i$  in dependence of the stress level  $S_a$ . At high stress levels  $q$  can normally be assumed to be 1 for failure initiated at different types of inclusions, provided that the respective type is present. At lower stress levels,  $q_i$  decreases to zero where no failure can be initiated by the respective mechanism  $i$  anymore. The stress level corresponds with the single-flaw fatigue limit when  $q$  equals 0.5 in the “normal” case where  $q_{i,max}$  is 1. This parameter has to be determined for each stress level and each mechanism together with the parameters of the respective distribution functions. The parameter  $q_i$  weights the respective failure function  $F_i$  and failure density function  $f_i$  in dependence of the stress amplitude in the region of the transition to the respective single-flaw fatigue limit. This means that not all specimens could fail from mechanism  $i$  anymore below a certain stress amplitude. However, if a specimen fails by mechanism  $i$  there are two possibilities why the other mechanisms  $j$  did not occur. Either this event is covered by the occurrence of mechanism  $i$  as it was described in the case of finite life or it is generally not possible to fail from these not occurring mechanisms in that specific test which could be the case if  $q_j$  is less than one. The latter case has to be regarded additionally in cases where real infinite life is possible. Then, the modified expression appears as follows (Eq. 3).

$$L_i = f_i \cdot q_i \cdot \prod_{j=1}^n \left[ \left( (1 - q_j) + q_j (1 - F_j) \right)^{\delta_{ij}} \right] \quad (3)$$

,  $\delta_{ij} = 1$  for  $i \neq j$  and 0 for  $i = j$

If no rupture occurs up to a defined number of load cycles, this expression simplifies to one without the failure density distribution function. Then, the remaining two terms inside the brackets represent the two possibilities why the specimen did not fail. Either it was not possible because of real infinite life at this stress level or the test did not last long enough.

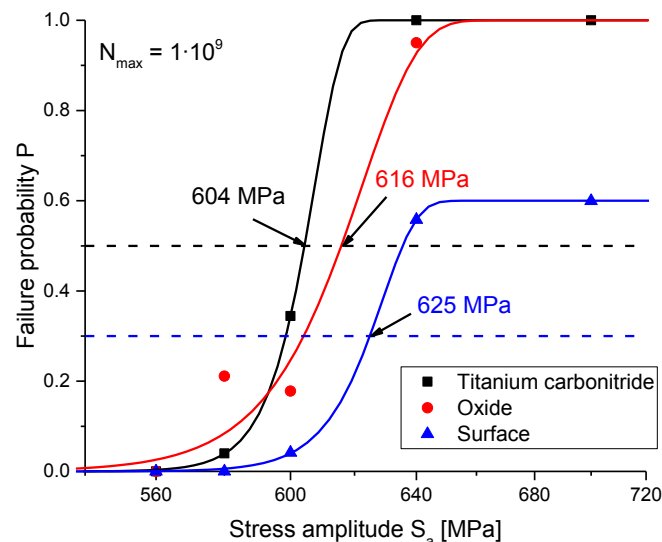


**Fig. 3:** Calculated single-flaw fatigue limits of variant A at  $R = 0$  based on a Weibull distribution for a defined maximal number of  $10^9$  load cycles.

Having all parameters of the distribution functions determined, the calculation of the failure probability for a defined number of load cycles is possible for each failure mechanism. If this is done for each stress level, it is possible to describe the failure probability of a single-flaw mechanism continuously in dependence of the stress level by adapting a distribution

function. This procedure makes it possible to calculate a “technical” fatigue limit for the single-flaw failure mechanism for an arbitrary number of load cycles. Since the parameter  $q$  is available for all stress levels it’s also possible to describe it in dependence of the stress level. This leads to the calculation of an “intrinsic” fatigue limit which, however, depends on the sample size and the test conditions. An example for the calculation of single-flaw “technical” fatigue limits of variant A and a defined maximal number of  $10^9$  load cycles is shown in Fig. 3. The distribution curve of the oxides does not fit as good as for the titanium carbonitrides to the basic data points because the fatigue tests delivered unfavourable results at stress amplitude  $S_a = 580$  MPa. This indicates an insufficient sample size for an accurate calculation of the single-flaw failure distribution function contributed by oxides.

## CONCLUDING REMARKS

Under the tested conditions, the steel variants showed no real fatigue limit. A mathematical description of the single-flaw fatigue behaviour is possible if a sufficient number of failures occur from each mechanism. The calculation of “technical” single-flaw fatigue limits can be derived here from for an arbitrary number of load cycles.

## REFERENCES

- [1] Heritier, R.; Cogne, J. Y.: Relationship of melting practice, inclusion type, and size with fatigue resistance of bearing steels  
Effect of Steel Manufacturing Processes on the Quality of Bearing Steels, ASTM STP 987, Philadelphia, 1988, pp. 149-165
- [2] Bomas, H.; Bacher-Hoehst, M.; Kienzler, R.; Kunow, S.; Loewisch, G.; Muehleder, F.; Schroeder, R: Crack initiation and endurance limit of a hard steel under multiaxial cyclic loads  
Fatigue Fract. Eng. Mater. Struct. 33 (2009), pp. 126–139
- [3] Shiozawa, K.; Hasegawa, T.; Kashiwagi, Y.; Lu, L.: Very high cycle fatigue properties of bearing steel under axial loading condition  
Int. J. Fatigue 31 (2009), pp. 880–888
- [4] Mayer, H.: Ultrasonic torsion and tension-compression fatigue testing: measuring principles and investigation on 2024-T351 aluminum alloy  
Int. J. Fatigue 28 (2006), pp. 1446–55
- [5] David, H. A.; Moeschberger, M. L.: The theory of competing risks  
Charles Griffin & Company, London and High Wycombe, 1978
- [6] Burkart, K; Bomas, H; Clausen, B.; Zoch, H.-W.: Evaluation of multiple-flaw failure of bearing steel 52100 in the VHCF regime  
Proceedings of the 6th International Conference on Very High Cycle Fatigue, Chengdu 2014, PSM11
- [7] Weibull, W.: A statistical distribution function of wide applicability  
J. Appl. Mech.-Trans. 18 (1951), pp. 293–297
- [8] Fisher, R. A.: On an absolute criterion for fitting frequency curves  
Messenger of Mathematics 41 (1912), pp. 155-160

## Acknowledgements

The presented work was carried out within the “Schwerpunktprogramm 1466”. The authors gratefully acknowledge the financial support of the “Deutsche Forschungsgemeinschaft” (DFG) under contract number ZO140/7.

**Corresponding author:** burkart@iwt-bremen.de

# DEVELOPMENT OF A PROBABILISTIC MODEL FOR THE PREDICTION OF FATIGUE LIFE IN THE VERY HIGH CYCLE FATIGUE (VHCF) RANGE BASED ON MICROSTRUCTURAL PROPERTIES

Martina Zimmermann<sup>1)</sup>, Anton Kolyshkin<sup>2)</sup>, Edgar Kaufmann<sup>3)</sup>, Hans-Jürgen Christ<sup>4)</sup>

<sup>1)</sup> Institut für Werkstoffwissenschaft, TU Dresden, 01069 Dresden, Germany

<sup>2)</sup> Robert Bosch GmbH, Renningen, 70465 Stuttgart, Germany

<sup>3)</sup> Department Mathematik, Universität Siegen, 57068 Siegen, Germany

<sup>4)</sup> Institut für Werkstofftechnik, Universität Siegen, 57068 Siegen, Germany

## ABSTRACT

Numerous investigations indicate a strong influence of microstructural inhomogeneities on the fatigue life of components subjected to more than 10 Mio loading cycles. This influence has a probabilistic character and increases the scatter band width up to three decades for the SN-curve. Thus, the application of a reliable fatigue life prediction concept by means of traditional statistical approaches is impeded and a detailed investigation of the relevant fatigue damage mechanisms is required. The aim of the present work is the development of a prediction model taking microstructural properties of failure-relevant defects or inhomogeneities and corresponding fatigue behaviour into account. For this purpose the fatigue behaviour of different metallic materials showing crack initiation at different defect types was investigated and modelled based on metallographic observations. In case of the nickel-based superalloy Nimonic 80A twin boundaries as well as regular grain boundaries with high misorientation factors were identified as crack initiation sites. In the case of the metastable austenitic stainless steel AISI 304 cracks initiated primarily from non-metallic inclusions provided the deformation-induced martensite volume fraction exceeded 30%. Based on a comprehensive experimental database, the observed correlation between failure-relevant parameters and corresponding numbers of cycles until failure or crack initiation was modelled.

## KEYWORDS

Probabilistic modelling, very high cycle fatigue, extreme value statistics, crack initiation, defects, microstructural properties

## INTRODUCTION

Since the fatigue behaviour in the VHCF range is strongly influenced by microstructural inhomogeneities such as non-metallic inclusions, pores and other local stress raisers [1], the approach of classical fatigue life prediction concepts is not applicable. Although classical prediction models consider the influence of the microstructure insofar as in some design guidelines SN curves have to be related to the particular microstructural condition (e.g. peak-aged, overaged [2]), this does not yet consider any information about failure-relevant inhomogeneities or defects and their statistical distribution in the critically loaded volume of a structure or component. However, this is in most cases the fatigue life dominating factor in the VHCF regime. Hence, two major challenges for the prediction of fatigue life in the VHCF regime have to be overcome, the identification of the failure-relevant microstructural feature and a reliable prediction of the statistical distribution of any such feature in the material given

while the measured distribution underlying the statistic database can be much smaller. Research work by Murakami 2002 [3], Beretta and Anderson 2002 [4] proved that fatigue properties of a given material volume with randomly distributed small defects are not related to the average defect size but rather to the size of the maximum inclusion in the material volume. On the basis of extreme value statistics Murakami and co-workers developed a rating method for clean steels based on the observation of the largest inclusions in a defined volume. On the basis of this method the size of the failure-relevant maximum defect can be predicted. But which approach is reasonable for quasi defect free materials? With this still open question in mind, the study presented focused on two different material groups. According to the early proposal by Mughrabi [5] to discuss VHCF damage mechanisms by making a distinction between quasi defect free and defect afflicted materials, a nickel-based superalloy assigned to the quasi defect free material group and a metastable austenitic stainless steel with defects in the form of non-metallic inclusions were investigated. Details on the VHCF failure of Nimonic 80A can be found in [6] and for AISI 304 in [7].

## **SPECIMEN, MATERIAL AND TESTING**

The materials investigated are the precipitation hardening nickel-based superalloy Nimonic 80A in the peak-aged condition consisting of  $\gamma$  matrix phase and the  $\gamma'$  phase and the metastable austenitic stainless steel AISI 304 with high martensite volume fraction. Since both materials were heat-treated prior to fatigue testing, any texture effects were assumed to be negligible. However, in the case of the AISI 304, the sampling direction relative to the original rolling direction played a significant role due to the size and shape of the inclusions, however this topic will not be covered in this paper. All tests were executed under symmetrical push-pull condition ( $R = -1$ ). In case of Nimonic 80A an ultrasonic fatigue testing system and a servo-hydraulic high-frequency fatigue testing system were used. Fatigue testing of AISI 304 was executed by means of a resonance pulsation test system of type Testronic. In each case undesirable heating of the specimens was avoided by test stand specific strategies and controlled by means of an infrared camera. All fatigue specimens (hourglass shape samples with a shallow notch in case of Nimonic 80A, flat samples for AISI 304) were machined by milling, were grinded and mechanically as well as electrochemically polished. Further information on the initial microstructure, the specimens' geometries and the test strategies can be found in [6,7].

## **INVESTIGATIONS ON THE CRACK INITIATING MICROSTRUCTURAL PARAMETER**

### *Nimonic 80A*

In most cases, only one single crack was initiated at random sites on the shallow-notched surface. Results of electron backscatter diffraction (EBSD) analysis showed that cracks initiate either at twin boundaries or at regular grain boundaries with high misorientation factor acc. to Blochwitz et al. [8]. In this concept of the misorientation factor the combination of the misorientation angle between two adjacent grains and the orientation of their boundary trace with respect to the external load characterizes the stress concentration at grain boundaries. Fig.1 depicts SEM images of both crack initiation types for load amplitudes that resulted in failure both in the transition range between HCF and VHCF as well as in the true VHCF range. While in Fig. 1a crack initiated near twin boundaries of relatively large grains, intercrystalline crack initiation at regular boundaries of arbitrary grains accompanied by moderate slip band formation is depicted in Fig. 1b. For an average grain size of 20 micron EBSD analyses of all tested specimens could prove, that Nimonic 80A in the peak-aged condition tends to show crack initiation at twin boundaries in the transition range between HCF and VHCF while in the true VHCF regime cracks primarily initiate at regular grain

boundaries with high misorientation factor. Investigations for samples with an average grain size of 32 micron showed, however, that crack solely initiated at twin boundaries. Simulations of the stress concentration at twin boundaries as well as at regular grain boundaries revealed that in the case of the twin boundaries the elastic anisotropy results in incompatibility stresses causing crack initiation. In case of the regular grain boundaries crack initiation got effective at even lower stress amplitudes which can be explained on the basis of the plastic anisotropy of adjacent grains as was already described by the extended Essmann-Gösele-Mughrabi (EGM)-model [9], where stress concentrations due to cyclic deformation are caused by dislocation pile-ups at grain boundaries.

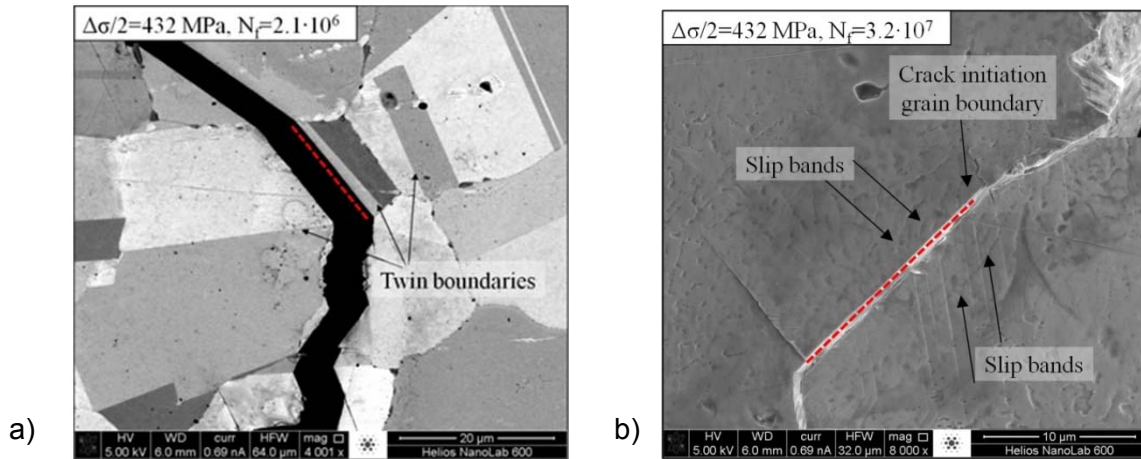


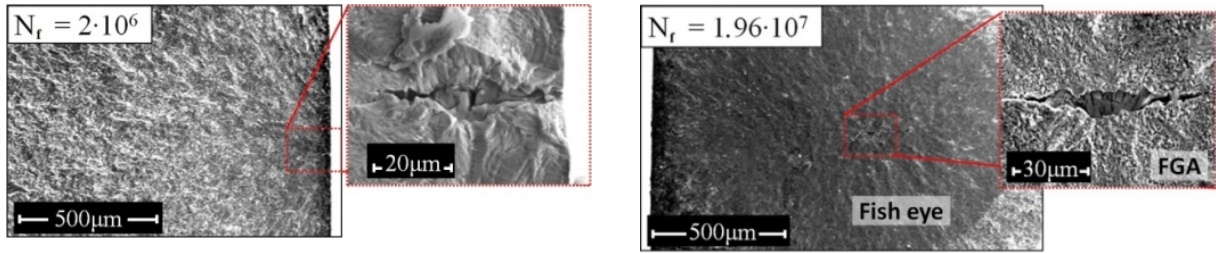
**Fig. 1:** SEM images showing the crack initiation at a) twin boundary and b) regular grain boundary (dashed lines show the crack initiating grain boundaries)

### AISI 304

The VHCF behaviour of the pre-deformed metastable austenitic stainless steel AISI 304 with a deformation induced  $\alpha'$  martensite volume of around 60% was determined by crack initiation around non-metallic inclusions, corresponding fracture surfaces are depicted in Fig. 2. In the transition range between HCF and VHCF crack initiation occurred at surface inclusions (Fig. 2a), while in the VHCF regime crack initiation took place at intrinsic inclusions in the specimens' interior. The latter is accompanied by the formation of a fine granular area (FGA) which is well known as "fish eye" formation in the context of VHCF behaviour (Fig. 2b). The failure-relevant inclusions have a disintegrated and elongated form with an average aspect ratio of  $\approx 10$ . A statistical evaluation of the fractographic analyses could prove that the percentage of interior crack initiation increases with decreasing load amplitude and hence increasing number of cycles. An assessment of the failure-relevant inclusions according to the stress intensity factor range (SIF,  $\Delta K_I$ ) calculated on the basis of the  $\sqrt{\text{area}}$ -concept by Murakami [10]

$$\Delta K_I = Y \cdot \sigma_{a,l} \cdot \sqrt{\pi \cdot \sqrt{\text{area}}} \quad (1)$$

with  $\sigma_{a,l}$  denoting the nominal stress amplitude at the inclusion and Y being the geometry function - revealed, that a clear correlation between  $\Delta K_I$  and the number of cycles to failure is given. The influence of the inclusion position (surface or interior) was taken into account by the geometry factor Y from the  $\sqrt{\text{area}}$ -concept with the value 0.5 for internal inclusions and 0.65 for surface inclusions.



a) b)  
**Fig. 1:** SEM images of the typical crack initiation a) at the surface and b) in the interior of a fatigue specimen with typical “fish-eye” fracture morphology.

## PROBABILISTIC EVALUATION OF THE FATIGUE LIFE

With the failure-relevant microstructural features that cause crack initiation in the VHCF regime identified, a comprehensive database for a statistical fatigue life prediction was created by means of extensive metallographic and electron microscopy analyses regarding the statistical distribution of each of these microstructural parameters for the given sample record. Critical values for the failure-relevant parameters were identified.

### *Nimonic 80A*

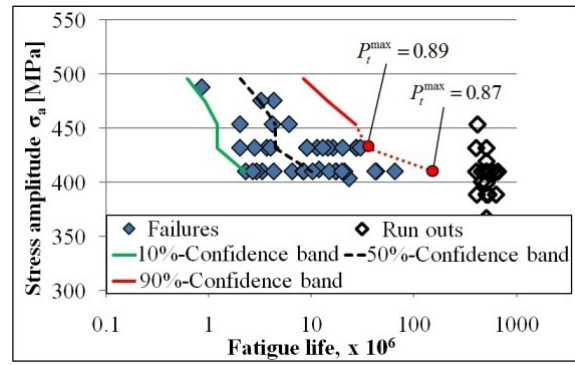
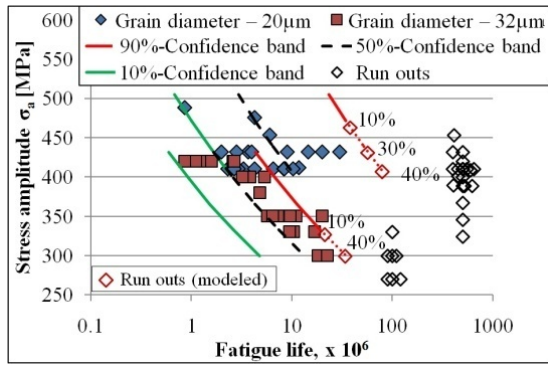
The statistical distribution of the crack initiating parameter (CIP) for twin boundaries and the misorientation factor (MOF) for regular grain boundaries was modelled by means of extreme value statistics. CIP was modelled in frames of probabilistic Monte Carlo simulations with a total of 100 simulations for each of the different stress amplitudes tested. For the statistical modelling of the MOF the distribution known from the fatigue test results alone was used. More details regarding the statistical approaches can be found in [6]. Finally the possibility of crack initiation for both microstructural features can be calculated in one single approach:

$$P_i(N | \sigma_a) = 1 - \exp \left\{ - \left[ 1 + \gamma_R \cdot \left( \frac{b_R \cdot N^{n_R} - \mu_R}{\delta_R} \right)^{\frac{1}{\gamma_R}} \right] \right\} \cdot P_{IR} - \exp \left\{ - \left[ 1 + \gamma_M \cdot \left( \frac{b_M \cdot N^{n_M} - \gamma_M}{\delta_M} \right)^{\frac{1}{\lambda_M}} \right] \right\} \cdot P_{IM} \quad (2)$$

Here  $\lambda_R$ ,  $\delta_R$ ,  $k_R$  and  $\lambda_M$ ,  $\delta_M$ ,  $k_M$  are parameters from the database describing the distribution of CIP and MOF, respectively.  $b_R$ ,  $n_R$  and  $b_M$ ,  $n_M$  are prefactors and powers of the power function describing the fatigue life and the maximum values of CIP and MOF, respectively.  $P_{IR}$  and  $P_{IM}$  represent the indicator functions defining the ratio of the fatal crack initiation at twin and regular grain boundaries to the whole number of the failures.  $P_{IR}$  and  $P_{IM}$  can be found experimentally or calculated by means of MC simulations. In case of the crack initiation at twin boundaries  $P_{IR} = 1$  and  $P_{IM} = 0$  is valid.

The 10%, 50% and 90% confidence bands calculated using Equation 1 for both grain sizes are plotted in Figure 3a. The 10%, 50% and 90% confidence bands calculated for the microstructure with the average grain diameter of 20 μm, in which the crack initiation at twin boundaries and regular grain boundaries took place are presented in Figure 3b. Figure 3 shows that the majority of fatigue results is situated within the calculated 10% and 90% confidence bands.





a)

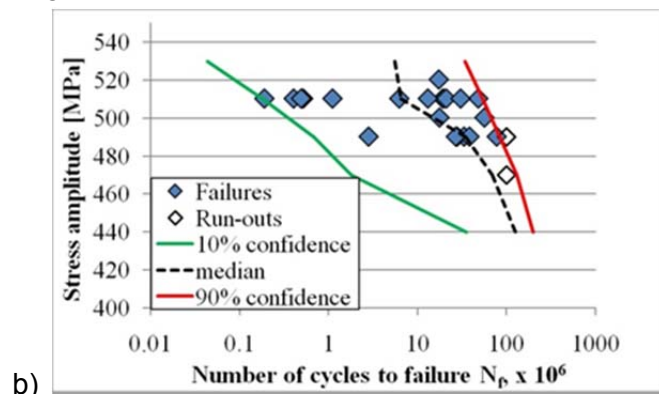
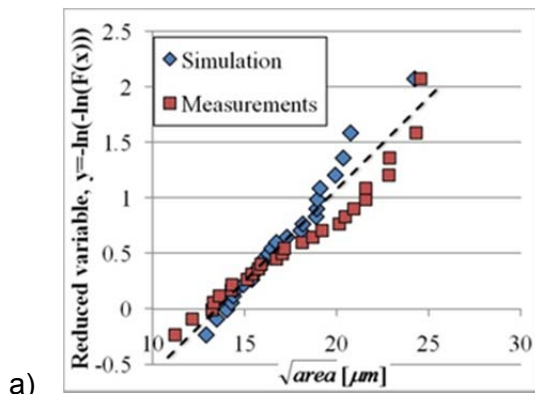
b)

**Fig. 3** Calculated confidence bands for Nimonic- 80A-specimens a) failed due to crack initiation solely at twin boundaries with an average grain size of 32  $\mu\text{m}$ ; b) with average grain diameter of 20  $\mu\text{m}$  and crack initiation at twin and regular grain boundaries.

### AISI 304

Extensive metallographic analyses and a subsequent statistical evaluation of the measured values for small representative volume fractions were used as database for the prediction of inclusion population, size and location for a defined volume in the middle of the fatigue specimen. According to the stress distribution in the fatigue specimen and the  $\sqrt{\text{area}}$ -concept by Murakami the SIF for each inclusion could be calculated. Subsequently, the fatigue life was predicted for the volume analysed assuming that crack initiation starts simultaneously at all modelled inclusions. Finally, the inclusion with predicted minimum number of loading cycles is assumed to be relevant for failure.

On this basis 100 Monte Carlo simulations for all stress amplitudes tested within the sample record were carried out. Figure 4a shows a reasonable agreement between simulation and experimental results. The size distributions of the modelled and measured crack initiating inclusions have a similar slope and belong to the same statistical population in the Gumbel probability paper. Since the influence of variance of inclusion size and location on fatigue life cannot be expressed explicitly, the confidence intervals for the tested samples were calculated on the basis of the executed simulations. The fatigue lives, which were obtained after 100 simulations at certain stress amplitudes, were arranged in ascending order. The values of 10%, 50% (median) and 90% confidence bands at each stress amplitude were assigned to the 10th, 50th and 90th values of modelled fatigue lives, respectively. The calculated confidence bands are plotted in Fig. 4b.



a)

b)

**Fig. 4:** Results for AISI 304: a) Size of simulated and measured failure-relevant inclusions; b) S-N curve with calculated confidence bands.



## CONCLUSION

In the present investigations experimental data obtained in the VHCF range for a quasi defect free and a defect afflicted material were analysed accompanied by extensive metallographic and electron microscopic analyses to identify the failure-relevant microstructural parameters for each material group. In case of the nickel-based superalloy Nimonic 80A, regular grain boundaries with the highest misorientation factors were identified as crack initiating feature in the VHCF regime, while in the transition range between HCF and VHCF cracks primarily initiated at twin boundaries. For the metastable austenitic stainless steel AISI 304, nonmetallic inclusions were the major reason for crack initiation with a shift from surface to interior crack initiation with increasing fatigue life. The microstructural parameter was described by means of its stress intensity factor. On the basis of extreme value statistics analysis a database was created that in a first step allows to predict the expected distribution of the failure relevant parameter for a given sample volume. In a second step on the basis of Monte Carlo simulations for the stress amplitudes experimentally carried out, confidence bands could be calculated for 10, 50 and 90% probability of failure which are in reasonable agreement with the experimental results.

## ACKNOWLEDGEMENT

The authors gratefully acknowledge financial support by the German Research Foundation in the framework of the priority program SPP 1466.

## REFERENCES

- [1] Proceedings of VHCF-6, Editors: Wang Q, Hong Y. Chengdu: 2014, CD-ROM.
- [2] Boller, C.; Seeger, T.: Materials Data for Cyclic Loading (Vol. A-E), Elsevier, 1987.
- [3] Murakami, Y.: Metal fatigue: effects of small defects and nonmetallic inclusions: effects of small defects and nonmetallic inclusions, Elsevier, New York, 2002.
- [4] Beretta, S.; Anderson, C. W.: Extreme value statistics in metal fatigue. In: Proc. XLI SIS Meeting, Milan (2002), pp. 251-260.
- [5] Mughrabi, H.: Specific features and mechanisms of fatigue in the ultrahigh-cycle regime, *Int. J. of Fatigue* 28 (2006) No. 11, pp. 1501-1508.
- [6] Kolyshkin, A.; Zimmermann, M.; Kaufmann, E.; Christ, H.-J.: Experimental investigation and analytical description of the damage evolution in a Ni-based superalloy beyond  $10^6$  loading cycles, *Int. J. of Fatigue*, 93 (2016) No. 2, pp. 272–280.
- [7] Grigorescu, A.C.; Hilgendorff, P. M.; Zimmermann, M.; Fritzen, C.-P.; Christ, H.-J.: Cyclic deformation behavior of austenitic Cr–Ni-steels in the VHCF regime: Part I – Experimental study, *Int. J. of Fatigue*, 93 (2016) No. 2, pp. 250-260.
- [8] Blochwitz, C.; Richter, R.; Tirschler, W.; Obtrlik, K.: The effect of local textures on microcrack propagation in fatigued fcc metals. *Mater. Sc. & Eng. A*: 234 (1997), pp. 563-566.
- [9] Essmann, U.; Gösele, U.; Mughrabi, H.: A model of extrusions and intrusions in fatigued metals. Part I: Point defect production and the growth of extrusions. *Phil Mag A*: 44 (1981), pp. 405-426.
- [10] Murakami, Y.: Inclusion rating by statistics of extreme values and its application to fatigue strength prediction and quality control of materials. *Journal of Research. National Institute of Standards and Technology* 99 (1994), pp. 345-345.

**Corresponding author:** [martina.zimmermann@tu-dresden.de](mailto:martina.zimmermann@tu-dresden.de)

# INCREMENTAL DAMAGE CALCULATION FOR VHCF UNDER NON-PROPORTIONAL MULTIAXIAL LOADING

M.A. Meggiolaro<sup>1)</sup>, J.T.P. Castro<sup>1)</sup>, H. Wu<sup>2)</sup>

<sup>1)</sup> Department of Mechanical Engineering, Pontifical Catholic University of Rio de Janeiro  
Rua Marquês de São Vicente 225 – Gávea, Rio de Janeiro, RJ, 22453-900, Brazil

<sup>2)</sup> School of Aerospace Engineering and Applied Mechanics, Tongji University  
Siping Road 1239, 200092, Shanghai, P.R. China

## ABSTRACT

In this work, the novel concept of nested damage surfaces, introduced by the authors, is used to predict fatigue damage under high-cycle fatigue. The proposed Incremental Fatigue Damage (IFD) model follows Miner's rule, integrating differentials of fatigue damage until reaching unity or any other user-defined critical value. Since damage is continuously integrated as the loading is applied, the method does not require cycle identification and counting, which are challenging and ill-defined tasks under non-proportional multiaxial loadings. Damage memory is stored through internal material variables and nested "damage surfaces" in stress space. Such surfaces can be calibrated according to any traditional high-cycle fatigue damage rule, such as multiaxial generalizations of Wöhler's curves, Findley's equation, or elastic versions of Fatemi-Socie's or Smith-Watson-Topper's models. The IFD predictions are validated for uniaxial variable amplitude loading histories.

## KEYWORDS

Incremental fatigue damage; Damage integration; Multiaxial fatigue; Non-proportional loading.

## INTRODUCTION

Wetzel and Topper proposed the first uniaxial Incremental Fatigue Damage (IFD) model a long time ago [1]. IFD models aim to calculate damage as a continuous variable, without the need to define or count cycles, and outside the framework of Continuum Damage Mechanics (CDM). Wetzel used each element of a discretized stress-strain model not only to evaluate plastic strains, but also the consequent fatigue damage, storing in this way the damage memory required for a correct damage integration in cyclic histories. Fatigue damage integration is continuously carried out without waiting for each hysteresis loop to close. Chu [2] outlined the generalization of Wetzel's model to multiaxial NP loadings, however indirectly requiring cycle detection, thus limiting its advantages. Stefanov proposed other IFD methods [3], however they do not properly take into account the "damage memory" effect without the need for heuristic calibration routines. Instead of integrating fatigue damage itself, other methods integrate strain energy or energy-based damage parameters [4], eventually giving good results under low-cycle fatigue; however, such elastoplastic energy methods are limited to ductile materials that display measurable plastic deformation, preventing their use in most high-cycle applications where damage results from elastic cycles.

Instead of integrating strain energy or energy-based damage parameters, the IFD approach integrates fatigue damage itself. As a result, it follows Miner's rule, integrating differentials of fatigue damage until reaching the 1.0 (or any other) critical value. No cycle detection or

counting is required, since damage is continuously integrated as the loading is applied. This approach is based on the derivative of the normal stress  $\sigma$  with respect to damage  $D$ , called here *generalized damage modulus*  $\mathcal{D}_\sigma$ , which for uniaxial histories can be defined as

$$\mathcal{D}_\sigma \equiv d\sigma/dD \Rightarrow D = \int dD = \int (1/\mathcal{D}_\sigma) \cdot d\sigma \quad (1)$$

From Eq. (1), damage  $D$  can be continuously integrated as long as the instantaneous value of  $\mathcal{D}_\sigma$  is known along a stress path with infinitesimal increments  $d\sigma$ . But this is not a trivial task for multiaxial non-proportional (NP) variable-amplitude loading (VAL) histories (which require damage integration along a general multiaxial load path), because  $\mathcal{D}_\sigma$  depends not only on the current stress state but also on the previous loading history. So, IFD models need to allow  $\mathcal{D}_\sigma$  to vary as a function of the stress level and of the existing state of damage [5].

### IFD APPROACH WITH NESTED DAMAGE SURFACES

Alternatively to rheological models, a direct analogy between IFD and incremental plasticity has been proposed by the authors [6] to store damage memory, using internal material variables. In this IFD model, the current damage state is stored as a five-dimensional (5D) vector  $\vec{D}' \equiv [D_1 \ D_2 \ D_3 \ D_4 \ D_5]^T$ , a purely mathematical internal variable that allows 5D *damage* increments  $d\vec{D}'$  to be more easily represented as a function of the 5D deviatoric stress increments  $d\vec{s}'$  and the current  $\mathcal{D}_\sigma$ , in a multiaxial generalization of Eq. (1) called *damage evolution rule*. The scalars  $D_1$  through  $D_5$  are signed damage quantities associated with each of the directions of the 5D deviatoric stress vector  $\vec{s}'$ .

A field of  $(M + 1)$  nested iso-damage (or damage) surfaces is then defined in the 5D deviatoric space, see Fig. 1, in a framework to provide internal material variables that can store damage memory. Each damage surface has a *constant* user-defined radius  $r_{\sigma i}$ , while the radius differences between consecutive surfaces are defined as  $\Delta r_{\sigma i} = r_{\sigma i+1} - r_{\sigma i}$ . The innermost damage surface is called the *fatigue limit surface*, while the outermost is the *failure surface*, defined respectively for  $i = 1$  and  $i = M + 1$ . The radius  $r_{\sigma 1}$  of the fatigue limit surface can be calibrated to become arbitrarily small, in case the studied material does not present a fatigue limit. These radii  $r_{\sigma i}$  are user-defined stress levels used in the discretization and non-linear interpolation of the damage curve, calibrated e.g. from the component's Wöhler/Basquin's curve, Findley's equation, or elastic versions of Fatemi-Socie's or Smith-Watson-Topper's models. More complex stress-life equations can be used in the  $r_{\sigma i}$ -based calibration, e.g. using Haibach's slope correction for very high cycle lives [7].

The *damage backstress* vector  $\vec{\beta}'_\sigma$  is here defined as the location of the center of the current fatigue limit surface, which can be decomposed as the sum of  $M$  *damage backstresses*  $\vec{\beta}'_{\sigma 1}$ ,  $\vec{\beta}'_{\sigma 2}$ , ...,  $\vec{\beta}'_{\sigma M}$  that describe the relative positions between centers of consecutive damage surfaces, as illustrated in Fig. 1 for a 2D deviatoric stress space. *Damage memory* is stored here by the current arrangement among these *damage surfaces*. No *damage* occurs if the 5D stress increment  $d\vec{s}'$  happens inside the *fatigue limit surface*. The *accumulated damage*  $D$  is then equal to the integral of the scalar norm  $|d\vec{D}'|$  of the 5D damage increments, i.e.

$$D = \int dD = \int |d\vec{D}'| \quad (2)$$

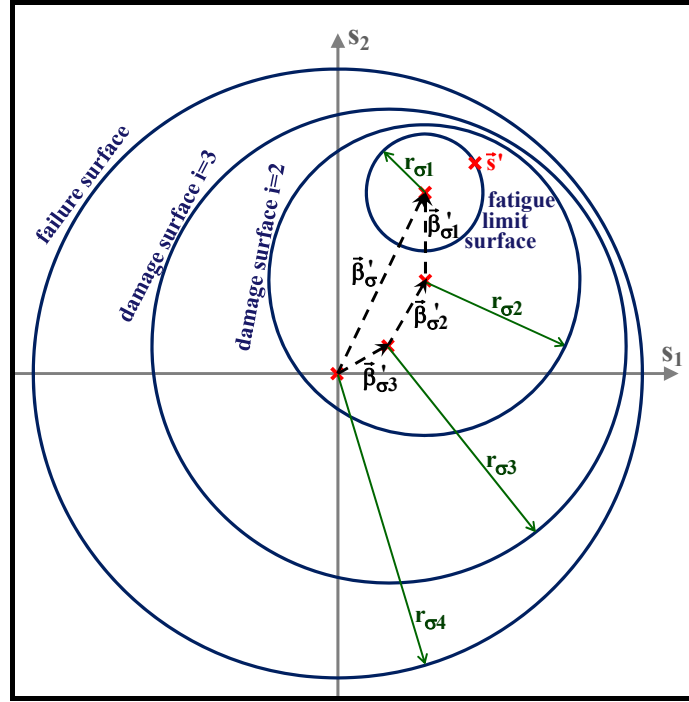


Fig. 1: Fatigue limit, damage, and failure surfaces in the  $s_1 \times s_2$  deviatoric space for  $M = 3$ , showing the damage backstress vector  $\vec{\beta}'_{\sigma}$  that defines the location of the fatigue limit surface center, and its components  $\vec{\beta}'_{\sigma 1}$ ,  $\vec{\beta}'_{\sigma 2}$ , and  $\vec{\beta}'_{\sigma 3}$  that describe the relative positions between the centers of consecutive surfaces.

If a given stress state  $\vec{s}'$  is on the fatigue limit surface with a normal unit vector  $\vec{n}'_{\sigma}$ , and if its infinitesimal increment  $d\vec{s}'$  is in the outward direction, then  $d\vec{s}'^T \cdot \vec{n}'_{\sigma} > 0$  and a fatigue damage increment is obtained from a *damage evolution rule*:

$$d\vec{D}' = (1/D_{\sigma}) \cdot (d\vec{s}'^T \cdot \vec{n}'_{\sigma}) \cdot \vec{n}'_{\sigma} \cdot f_{MS}(\vec{\sigma}) \cdot f_{NP}(\vec{\beta}'_{\sigma}, \vec{n}'_{\sigma}) \quad (3)$$

where  $f_{MS}(\vec{\sigma})$  is a scalar *mean stress function* of the current 6D stress  $\vec{\sigma}$  to account for mean/maximum-stress effects, which can be defined e.g. from Goodman's or Gerber's  $\sigma_a \sigma_m$  relations; and  $f_{NP}(\vec{\beta}'_{\sigma}, \vec{n}'_{\sigma})$  is an optional *NP function* to account for the influence of the non-proportionality of the load path on the resulting damage. Depending on the material, the mean stress function  $f_{MS}(\vec{\sigma})$  could be based on the current hydrostatic stress  $\sigma_h$  or on the normal stress perpendicular to the critical plane where the microcrack should initiate. Except for the failure surface (which never translates), during this damage process the fatigue limit and all damage surfaces suffer translations calculated from the increments

$$d\vec{\beta}'_{\sigma i} = \begin{cases} \mathcal{d}_{\sigma i} \cdot \vec{v}'_{\sigma i} \cdot dD, & \text{if } |\vec{\beta}'_{\sigma i}| < \Delta r_{\sigma i} \\ 0, & \text{if } |\vec{\beta}'_{\sigma i}| = \Delta r_{\sigma i} \end{cases} \quad (4)$$

where  $\mathcal{d}_{\sigma i}$  are material coefficients calibrated for each surface, and  $\vec{v}'_{\sigma i}$  are the *damage surface translation directions* adapted e.g. from Jiang-Sehitoglu's translation rule [8] used in plasticity, resulting in the adapted expression

$$\vec{v}'_{\sigma i} = \vec{n}'_{\sigma} \cdot \Delta r_{\sigma i} - (|\vec{\beta}'_{\sigma i}| / \Delta r_{\sigma i})^{\chi_{\sigma i}} \cdot \vec{\beta}'_{\sigma i} \quad (5)$$

where  $\chi_{\sigma i}$  are fitting exponents for each surface. The current generalized damage modulus  $\mathcal{D}_{\sigma}$  is then obtained from the consistency condition that guarantees that the current stress state is never outside the fatigue limit surface:

$$\mathcal{D}_{\sigma} = \left( \sum_{i=1}^M \mathcal{d}'_{\sigma i} \cdot \vec{v}'_{\sigma i} \cdot \vec{n}'_{\sigma} \right) \cdot \vec{n}'_{\sigma} \quad (6)$$

allowing the calculation of the evolution of the damage vector  $\vec{D}'$  from Eq. (3). The (scalar) accumulated damage  $D$  is then obtained from Eq. (2). This formulation can deal with any multiaxial stress history, proportional or NP, and eliminates the need to define or count cycles and find equivalent ranges. If Jiang-Sehitoglu's translation rule is used in the IFD formulation, then a procedure analogous to the one in [8] could be adopted to calibrate the radius  $r_{\sigma i}$  and the coefficient  $\mathcal{d}'_{\sigma i}$  from each damage surface  $i$ .

Finally, to account for mean-stress effects, a simple function inspired on Fatemi-Socie's damage parameter could be adopted in Eq. (3), which in a uniaxial case would simply become

$$f_{MS}(\vec{\sigma}) \equiv (1 + \alpha_{MS} \cdot \sigma_x / S_{Yc})^{BMS} \quad (7)$$

where  $\alpha_{MS}$  and  $B_{MS}$  are material-dependent parameters and  $\sigma_x$  is the current (instantaneous) normal stress. But since the IFD approach does not involve cycle detection or counting, the mean or peak stress values during a cycle (which require the definition of cycles and knowledge of future stress values) cannot be used in  $f_{MS}(\vec{\sigma})$ . Thus, only current/instantaneous stress values such as  $\sigma_x$  can be used in  $f_{MS}(\vec{\sigma})$ .

## NUMERICAL EVALUATION

To evaluate the prediction capabilities of the proposed IFD model, traditional cycle-based fatigue damage calculations are compared with continuous IFD predictions on a material with Basquin's equation constant 772.5MPa and exponent  $-0.09$ , subjected to the uniaxial history  $\sigma_x = \{0 \rightarrow 300 \rightarrow -300 \rightarrow 300 \rightarrow -300 \rightarrow 300\}$ MPa. To consider mean stress effects, Eq. (7) is adopted using  $\alpha_{MS} = 0.4$  and  $B_{MS} = 1$ . The IFD calculations assume Jiang-Sehitoglu's translation rule with  $M = 16$  damage surfaces, calibrated from the same Basquin equation used in the cycle-based calculations following an analogous procedure from [8].

Figure 2(left) shows the hysteresis loops  $\sigma_x \times D_1$ , where  $D_1$  is the first component of the 5D damage vector  $\vec{D}'$ . Notice in this figure that damage components such as  $D_1$  can become negative, as a result of an unloading process. This is not an issue, since  $\vec{D}'$  is just an internal variable used to calculate the actual fatigue damage. Indeed, the accumulated damage  $D$  is obtained from the integral of the norm of the infinitesimal increments  $|d\vec{D}'|$ , see Eq. (2). It is important to note that this loading example is linear elastic, without any significant macroscopic plasticity; the non-linear shape of the stress  $\times$  damage hysteresis loops is just a consequence of the non-linearity of Basquin's (or Wöhler's) damage equation.

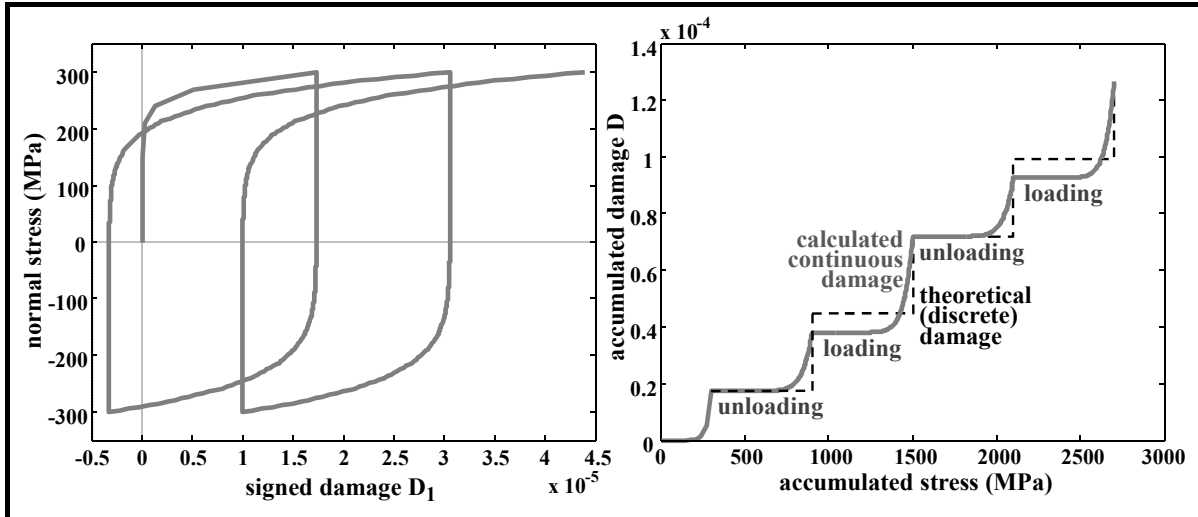


Fig. 2: Stress × damage hysteresis loops (left) and resulting accumulated damage (right) for a mean stress function based on Fatemi-Socie's damage parameter.

Figure 2(right) shows the resulting accumulated damage  $D$  as a function of an accumulated stress, defined as the integral of the norm of the infinitesimal deviatoric increments  $d\vec{s}'$ . The depicted *theoretical damage* is calculated in the traditional (discrete) way after each of the three rainflow-counted half-cycles  $\{0 \rightarrow 300\}$ ,  $\{300 \rightarrow -300\}$  and  $\{-300 \rightarrow 300\}$ MPa. Notice how the continuous IFD calculations almost exactly reproduce, at the end of each full cycle, the discrete predictions. Nevertheless, a larger damage increment is predicted by the IFD during the loading half-cycle than during unloading, see Fig. 2(right). This prediction is not physically unsound, since most of the microplasticity happens towards the end of each half-cycle, where  $\sigma_x \rightarrow 300$ MPa during loading and  $\sigma_x \rightarrow -300$ MPa during unloading in this example. Such a difference in damage increment causes the stress × damage hysteresis loops from Fig. 2(left) to remain open, which resembles but has nothing to do with a ratcheting problem, and has no physical inconsistency since  $\vec{D}'$  is just an internal variable.

The damage memory provided by the fatigue limit and damage surfaces is able to deal with VAL, exactly reproducing rainflow-based uniaxial calculations, but without the need for any cycle detection or counting. Figure 3 shows, for a VAL history with zero mean stress, the agreement between the proposed IFD approach (using e.g.  $f_{MS}(\vec{\sigma}) \equiv 1 + 0.4 \cdot \sigma_x / S_{Yc}$ ) and traditional SN calculations, which is almost exact after every full loading-unloading cycle (but not at every half-cycle, as discussed before regarding Fig. 2). The agreement is as good as the quality of the calibration of the damage surface parameters to the adopted damage model. For VAL under high mean stress levels, higher order  $f_{MS}(\vec{\sigma})$  equations need to be adopted for an accurate damage prediction, as mentioned before.

## CONCLUSIONS

In this work, an Incremental Fatigue Damage model based on nested damage surfaces was reviewed and applied to high-cycle fatigue. The method does not require cycle identification and counting, a major advantage for multiaxial problems. The proposed method is not a Continuum Damage Mechanics approach, since it does not rely on macroscopic properties such as the progressive loss of elastic stiffness. The IFD predictions were validated for selected uniaxial variable amplitude loading histories.

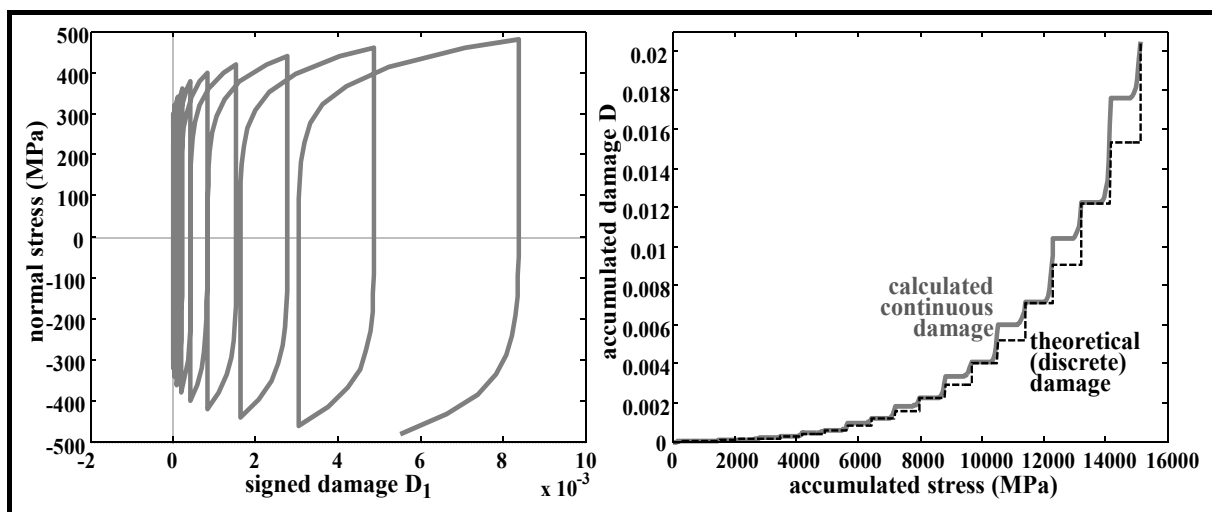


Fig. 3: Stress  $\times$  damage hysteresis loops (left) and resulting accumulated damage (right) for a VAL history with zero mean stress.

## REFERENCES

- [1] Wetzel, R.M.:  
A Method of fatigue damage analysis  
Ph.D. Thesis, U Waterloo (1971)
- [2] Chu, C.C.:  
A new incremental fatigue method  
ASTM STP 1389 (2000), pp. 67-78
- [3] Stefanov, S.H.  
A curvilinear integral method for multiaxial fatigue life computing under non-proportional, arbitrary or random stressing  
Int J Fatigue 15 (1993), pp. 467-472
- [4] Nowack, H.; Baum, C.; Ott, W.; Buczynski, A.; Glinka, G.:  
Achievements of the incremental multiaxial fatigue prediction method EVICD  
Proc. 5th Int Conf Low Cycle Fatigue, Germany (2003), pp. 277-282
- [5] Kreiser, D.; Jia, S.X.; Han, J.J.; Dhanasekar, M.:  
A nonlinear damage accumulation model for shakedown failure  
Int J Fatigue 29 (2007), pp. 1523-1530
- [6] Meggiolaro, M.A.; Castro, J.T.P.; Wu, H.:  
A Multiaxial Incremental Fatigue Damage Formulation using Nested Damage Surfaces  
Frattura e Integrità Strutturale 37 (2016), pp. 138-145
- [7] Haibach, E.:  
Modified linear damage accumulation hypothesis accounting for a decreasing fatigue strength during increasing fatigue damage  
LBF TM Nr.50, Darmstadt, Germany (1970)
- [8] Jiang, Y.; Sehitoglu, H.:  
Modeling of Cyclic Ratchetting Plasticity  
J Appl Mech 63 (1996), pp. 726-733

**Corresponding author:** meggi@puc-rio.br



# ULTRASONIC VHCF TESTS ON AISI H13 STEEL WITH TWO DIFFERENT INCLUSION CONTENT: ASSESSMENT OF SIZE EFFECTS WITH GAUSSIAN SPECIMENS

A. Tridello<sup>1)</sup>, D.S. Paolino<sup>1)</sup>, G. Chiandussi<sup>1)</sup>, M. Rossetto<sup>1)</sup>

Politecnico di Torino, Department of Mechanical and Aerospace Engineering, Corso Duca degli Abruzzi 24, 10129 Torino

## ABSTRACT

The present paper investigates the effect of the manufacturing process on the VHCF response of an AISI H13 steel. Experimental tests are carried out on a conventional AISI H13 steel and on a cleaner AISI H13 steel subjected to Electroslag Remelting (ESR). Fully reversed tension-compression tests are performed by using hourglass and Gaussian specimens with significantly different loaded volumes (risk-volume) in order to quantify the detrimental effect of the risk-volume on the VHCF response of the unrefined and the refined H13 steels.

**KEYWORDS:** Electroslag Remelting (ESR), Gaussian specimen, Risk-volume, Ultrasonic fatigue testing

## INTRODUCTION

High-strength steels are commonly used for critical structural components (e.g., railway axles, turbine palettes, aerospace bearings) subjected to Very High Cycle Fatigue (VHCF) failures, with cracks generally originating from defects formed during the manufacturing process [1]. The fatigue crack originates from the largest defect present within the loaded region of material (risk-volume): the defect population (quantity and, in particular, size) therefore strongly affects the VHCF response of high-strength steels.

The present paper investigates the effect of the manufacturing process on the VHCF response of an AISI H13 steel. Experimental tests are carried out on a conventional AISI H13 steel and a cleaner AISI H13 steel subjected to Electroslag Remelting (ESR) characterized by different inclusion content. Fully reversed tension-compression tests are performed on hourglass and Gaussian specimens with significantly different risk-volumes, in order to quantify the detrimental effect of risk-volume on the VHCF response [2] of the investigated H13 steels.

The enhancement of VHCF response attained with the ESR process and the detrimental effect of risk-volume are discussed in the paper by comparing the VHCF strength at  $10^9$  cycles and the P-S-N curves, estimated according to a statistical model recently proposed by the authors [3]. Experimental results show that size-effect significantly affects the VHCF response of the tested H13 steels, in particular for the unrefined H13 steel characterized by largest inclusions.

## SPECIMEN, MATERIAL and TESTING

### Material

AISI H13 steel is classified as a hot work tool steel, but it is also employed in applications where VHCF failures are possible (i.e., e.g., fuel injectors for naval engines and aerospace components). The chemical composition of the investigated material, as provided by the steel manufacturer (Böhler Uddeholm Company), is reported in Table 1.

Element	C	Si	Mn	Cr	Mo	V
%	0.39	1	0.4	0.4	5.3	0.9

**Table 1:** Chemical composition of the investigated AISI H13 steel.

Two different H13 steels, H13 and H13-ESR, are experimentally tested. Both the H13 and the H13-ESR are obtained by conventional casting. After the production process, the H13-ESR is subjected to an ESR process, which involves a second remelting of the steel in a protective atmosphere and a subsequent fine and controlled solidification. With the ESR process, micro and macro segregation and large defects are eliminated and the Sulphur content is reduced [4]. The steel cleanliness is therefore significantly enhanced.

### Specimens

Experimental tests are carried out on hourglass specimens ( $V_{90} = 194 \text{ mm}^3$ ) and on Gaussian specimens ( $V_{90} = 2300 \text{ mm}^3$ ) in order to assess the size-effect for the investigated steels. According to [2], the  $V_{90}$  is defined as the volume of material subjected to a stress amplitude larger than the 90% of the maximum stress. Hourglass and Gaussian specimens are analytically designed according to [2] and verified through Finite Element Analysis (FEA). Figs. 1a and 1b respectively show the hourglass specimen and the Gaussian specimen used for the experimental tests.

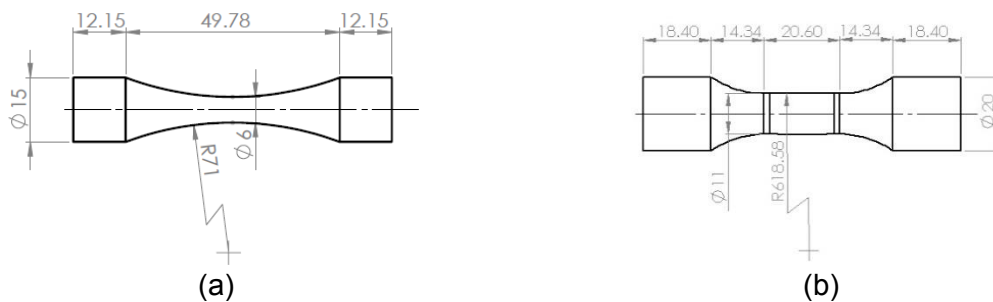


**Fig. 1:** Specimens experimentally tested: (a) hourglass specimen; (b) Gaussian specimen.

Specimens are obtained through a CNC machining process starting from rectangular bars with dimensions 32 x 32 x 115 mm. After the production process, specimens are quenched and tempered in an ordinary industrial cycle to obtain a tempered martensite microstructure. The heat treatment involves preheating at 1023 K, austenitizing at 1030 K, gas quenching and three tempering cycles: first tempering at 793 K, second and third tempering at 813 K. Specimens are finally fine polished with sandpapers with increasing grit in order to remove superficial defects formed during the machining process and to enhance internal nucleation of cracks. The hardness and tensile properties of the two investigated H13 steels after the heat treatment are found to be similar. In particular, the dynamic elastic modulus (211.8 GPa for the H13 and

212.9 GPa for the H13-ESR) and the tensile strength (2000 GPa for the H13 and 2100 GPa for the H13-ESR) are slightly larger for the H13-ESR. The Vickers hardness, equal to 560 HV, is the same for the two H13 steels.

## Testing

Fully reversed tension-compression tests are carried out up to failure or up to  $10^{10}$  cycles by using the ultrasonic testing machines developed at the Politecnico di Torino. Displacement amplitude at the specimen free end, measured by using a laser displacement sensor, is kept constant during the test. Therefore, by assuming a macroscopic linear elasticity of the material, the stress amplitude at the specimen mid-section is considered constant during the test. The correlation between the displacement amplitude and the stress amplitude is obtained through an accurate strain gage calibration.

Specimen temperature is monitored during the test by using an infrared sensor. Intermittent tests are carried out [5] in order to keep the specimen temperature between 298 K and 323 K. Vortex tubes are also employed to limit the temperature increment and speed up the cooling phase. Temperature variation within the risk-volume is verified to be smaller than 1%.

## EXPERIMENTAL RESULTS

The aim of the experimental tests is to obtain a large number of failures in the range between  $10^8$ -  $10^{10}$  cycles, in order to properly estimate and compare the P-S-N curves in the VHCF regime. The local stress amplitude at the defect location,  $\sigma_{local}$ , assessed through FEA, is considered as the applied stress during the test in the following. By considering the H13 steel, the applied stress amplitude range is [552-683] MPa for the hourglass specimens and [487-635] MPa for the Gaussian specimens. Regarding the H13-ESR, the applied stress amplitude range is [622-773] MPa for the hourglass, whereas it is [571-779] MPa for the Gaussian specimens. Fig. 2 shows the S-N plot of the experimental results.

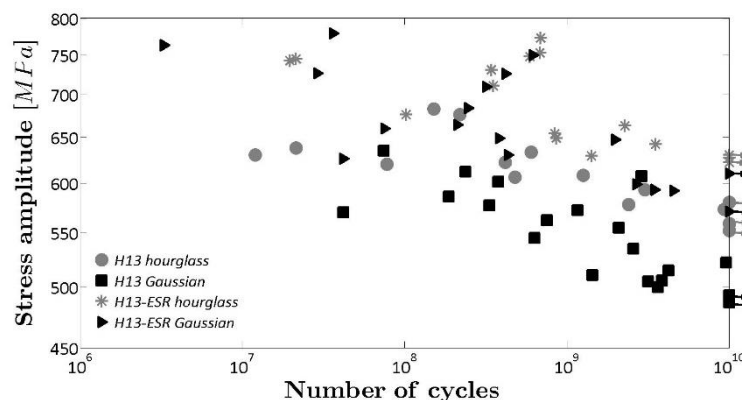


Fig. 2: S-N plot of the experimental results.

All fracture surfaces were observed by using the Scanning Electron Microscope (SEM) and the optical microscope, in order to determine the crack origin. All failures originated from inclusions present within the material, with a fish-eye morphology [1]. In particular, spherical oxide type inclusions, with high percentage of Aluminium, Calcium and Manganese are at the origin of the fatigue failure in 56 out of 59 failures. In three cases the crack originated from clusters of small inclusions (H13-ESR). According to Murakami [1], the square root of the projected area of the defect is considered as the characteristic inclusion size,  $\sqrt{a_{d,0}}$ . Table 2 reports the smallest and the largest inclusion sizes for the tested specimens.

Material	Specimen	$\sqrt{a_{d,0_{min}}}$ μm	$\sqrt{a_{d,0_{max}}}$ μm
H13	<i>hourglass</i>	21	41
H13	<i>Gaussian</i>	19	56
H13-ESR	<i>hourglass</i>	10	23
H13-ESR	<i>Gaussian</i>	15	31

**Table 2:** Inclusion originating failures: smallest and largest values.

According to Table 2, inclusion originating failures are significantly larger in Gaussian specimens.  $\sqrt{a_{d,0_{max}}}$  in Gaussian specimens is about 35% larger than  $\sqrt{a_{d,0_{max}}}$  in hourglass specimens (37% for the H13 and 35% for the H13-ESR). The effect of the ESR process on the inclusion size is also significant:  $\sqrt{a_{d,0_{max}}}$  in H13-ESR Gaussian specimens is about half of  $\sqrt{a_{d,0_{max}}}$  in Gaussian H13. Moreover, inclusion size in H13-ESR is included in a smaller range ([10-31] μm for the H13-ESR and [21-56] μm for the H13), confirming the enhancement of the steel cleanliness attainable through ESR.

### SIZE-EFFECT AND ESR PROCESS: INFLUENCE ON THE VHCF STRENGTH.

The influence of size-effect and of ESR on the VHCF strength is investigated in this Section. Following a typical procedure adopted in the literature [6], data are gathered together at a reference fatigue life ( $N_{f,ref} = 10^9$ ) by considering the power relationship between mean fatigue life and stress amplitude ( $\log_{10}[N_f] = c_Y + m_Y \log[\sigma_{local}] + n_Y \log_{10}[\sqrt{a_{d,0}}]$ , being  $N_f$  the number of cycles to failure and  $c_Y$ ,  $m_Y$  and  $n_Y$  constant coefficients). Through easy passages, the VHCF strength (corrected VHCF strength,  $\sigma_{corr}$ ) at the reference number of cycles can be expressed by:

$$\log_{10}[\sigma_{corr}] = \log_{10}[\sigma_{local}] + \frac{\log_{10}[N_f]}{-m_Y} - \frac{\log_{10}[N_{f,ref}]}{-m_Y} = \left( \frac{c_Y}{-m_Y} - \frac{\log_{10}[N_{f,ref}]}{-m_Y} + \frac{n_Y}{-m_Y} \log_{10}[\sqrt{a_{d,0}}] \right) \quad (1)$$

According to Eq. 1,  $\sigma_{corr}$  depends only on the inclusion size and therefore permits to assess the influence of the different inclusion size on the VHCF strength. Fig. 3 shows the estimated probability density function  $p(x_{corr})$  of  $x_{corr}$ , being  $x_{corr} = \log[\sigma_{corr}]$ .

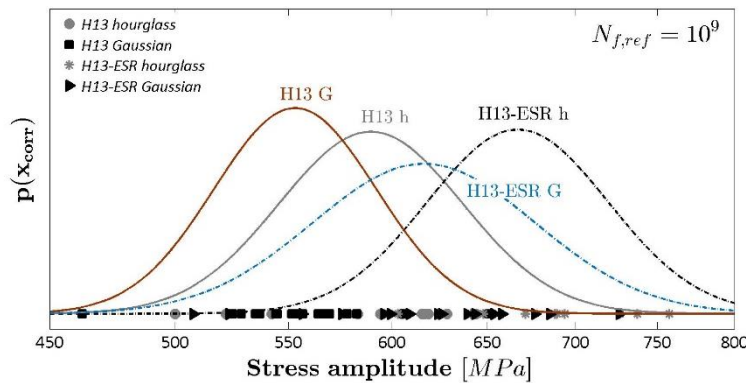


**Fig. 3:** corrected VHCF strength and probability density function for the tested specimens.

The Analysis of Variance (ANOVA) is used to statistically compare the data. A 95% significance level is considered in the analysis. The resulting ANOVA is reported Table 3. Sum of Squares (SS), Degrees of Freedom (DOF), Mean Squares (MS) and the estimated P-Value are reported in the Table. The applicability of ANOVA (variance heterogeneity) is verified through Lavene's tests.

Source	SS	DOF	MS	P-value
Material	0.0363	1	0.0363	0.000
Risk-volume	0.0137	1	0.0137	0.002
Interaction	0.0002	1	0.0002	0.727
Error	0.0697	55	0.0013	
Total	0.1224	58		

Table 3: ANOVA analysis to assess the influence of risk-volume and manufacturing process on VHCF strength.

According to the ANOVA results, the tested risk-volume and the manufacturing process significantly influence the VHCF strength, whereas the interaction is not statistically significant (both the H13 and the H13-ESR shows a significant reduction of the VHCF response due to size-effect). The different inclusion size (due to size-effect and to ESR) therefore significantly affects the VHCF strength for the investigated H13 steels.

**P-S-N curves**

P-S-N curves are estimated according to the model proposed in [3]: in particular the 0.01.th P-S-N curves (99% reliability), which ensure a safety margin with respect to failures [7], are considered for the comparison. Fig. 4 shows the 0.01-th P-S-N curves for the investigated H13 and H13-ESR steel: in Fig. 4, h refers to hourglass specimens, whereas G refers to Gaussian specimens.

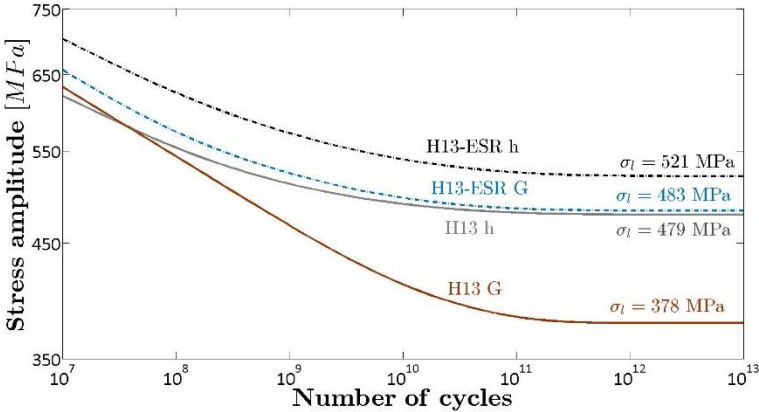


Fig. 4: 0.01 P-S-N curves for the tested H13 steels.

According to Fig. 4, size-effect is relevant for the H13 and the H13-ESR. Larger size-effect is found by testing the unrefined H13. The fatigue limit reduces by about 21% by testing Gaussian H13, whereas it reduces by about 7% by testing Gaussian H13-ESR. The difference is quite constant for the H13-ESR, while it tends to increase with the number of cycles for the H13.

The enhancement of the steel cleanliness through the ESR process therefore permits to limit size-effect.

ESR process enhances significantly the VHCF response. By testing the hourglass specimens, the difference is quite constant and equal to 40 MPa, whereas it increases with the number of cycles by considering the Gaussian specimens, with a maximum equal to 105 MPa for the fatigue limit. To conclude, the ESR process permits to significantly enhance VHCF response and to limit size-effect, due to a significantly smaller inclusion size range (Table 2).

## CONCLUSIONS

Ultrasonic tension-compression tests were carried out on specimens with significantly different risk-volumes (hourglass and Gaussian specimens) made of an unrefined H13 steel and of a very clean H13 steel subjected to an ESR process (H13-ESR). VHCF strength at  $10^9$  cycles was statistically compared: risk-volume and manufacturing process were found to significantly affect the VHCF response. The 0.01 P-S-N curves were also compared. Size-effect was found to significantly affect the VHCF response of both the H13 and the H13-ESR. However the enhancement of the steel cleanliness attained through the ESR process was found to limit size-effect. The ESR process also significantly affects the VHCF response, with larger differences found at VHCF number of cycles (larger than  $10^9$ ) by testing the Gaussian specimens.

## REFERENCES

- [ 1 ] Murakami, Y.:  
Metal Fatigue: Effects Of Small Defects And Nonmetallic Inclusions  
Elsevier Ltd, Oxford, UK, 2002
- [ 2 ] Paolino, D.S., Tridello, A., Chiandussi, G., Rossetto, M.:  
On specimen design for size effect evaluation in ultrasonic gigacycle fatigue testing  
Fatigue & Fracture of Eng. Mat. & Structures 37 (2014), pp. 570-579
- [ 3 ] Paolino, D.S., Tridello, A., Chiandussi, G. and Rossetto, M.:  
S-N curves in the very-high-cycle fatigue regime: statistical modeling based on the hydrogen embrittlement consideration  
Fatigue & Fracture of Eng. Mat. & Structures 39 (2016), pp. 1319-1336
- [ 4 ] Totten, G. E., Xie, L., Funatani, K.:  
Handbook of Mechanical Alloy Design  
CRC Press, New York, USA, 2003
- [ 5 ] Stanzl-Tschegg, S.:  
Very high cycle fatigue measuring techniques  
Int. Journal of Fatigue 60 (2014), pp. 2-17
- [ 6 ] Schuller , R., Fitzka, M., Irrasch, D., Tran, D., Pennings, B., Mayer, H.:  
VHCF properties of nitrided 18Ni maraging steel thin sheets with different Co and Ti content  
Fatigue & Fracture of Eng. Mat. & Structures 38 (2015), pp. 518-525
- [ 7 ] Tridello, A., Paolino, D.S., Chiandussi, G., Rossetto, M.:  
VHCF Response of H13 Steels Produced with Different Manufacturing Processes  
Procedia Eng. 160 (2016), pp. 93-100

Corresponding author: [andrea.tridello@polito.it](mailto:andrea.tridello@polito.it)

# INTRINSIC DISSIPATION ASSESSMENT DURING VERY HIGH CYCLE FATIGUE TESTS ON PURE COPPER

S. Yang<sup>1</sup>, N. Ranc<sup>1</sup>, E. Monteiro<sup>1</sup>, J. Dirrenberger<sup>1</sup>

<sup>1</sup>) Laboratoire Procédés et Ingénierie en Mécanique et Matériaux (PIMM), UMR CNRS 8006, Arts et Métiers Paristech - Paris, France

## ABSTRACT

In this work, a self-heating method was introduced to study the fatigue behavior of polycrystalline pure copper sheets in gigacycle fatigue regime with lifespan much longer than  $10^{10}$  cycles. A large range of stress amplitudes from 9 MPa to 82 MPa was applied on the copper plate specimen on ultrasonic fatigue system. The thermal response was recorded by infrared camera and analyzed on the basis of the heat diffusion equations. The curve of intrinsic dissipation versus stress amplitude represent a dual linear tendency. The dissipation energy caused by slipping in type II was found twice larger than that in type III.

## KEYWORDS

Damage assessment, Infrared thermography, Intrinsic dissipation, Thermomechanical coupling, VHCF

## INTRODUCTION

Nowadays, fatigue strength has become an important component of estimating material properties. With the industrial pressing requirement and the promotion of ultrasonic fatigue machine, many researchers and groups focused on very high cycle fatigue (VHCF) tests, even over  $10^{10}$  cycles. Under such conditions, traditional assessment methods can no longer fulfil the growing demand, due to huge human and financial consumption for drawing S-N curves, and experimental limit for some prediction models based on hysteresis loop characteristics, such as Miner-Wohler's law and Dang-Van, etc. [1, 2]

Recently, an alternative method named self-heating tests was proposed in several papers [3, 4], mainly based on the thermal response of material subjected to fatigue loadings. Generally, the energy of heat dissipation comes from micro-plastic deformation, i.e. dislocation slip within crystal-specific slip systems. Before the accumulation of micro-plastic deformation to rupture, the dissipation rate, the stress amplitude and the number of cycles (fatigue life) are directly correlated. Therefore, they conduct self-heating tests with stepwise loading fatigue tests in a cycle block sequence, in order to obtain a clear change in the heating regime related to the fatigue limit, which is the main application direction of this method.

N. L. Phung et al [5] and Stanzi Tschegg et al [6] drew a traditional S-N curve of polycrystalline pure copper plate and obtained its fatigue limit, 92 MPa at  $10^{10}$  cycles, shown in Fig. 1(a). N. L.



Phung [5] revealed three types of persistent slipping bands (PSB) during fatigue loadings, shown in Fig. 1(b). However, the study on the estimation of fatigue property of polycrystalline pure copper with lifespan  $> 10^{10}$  cycles is still blank.

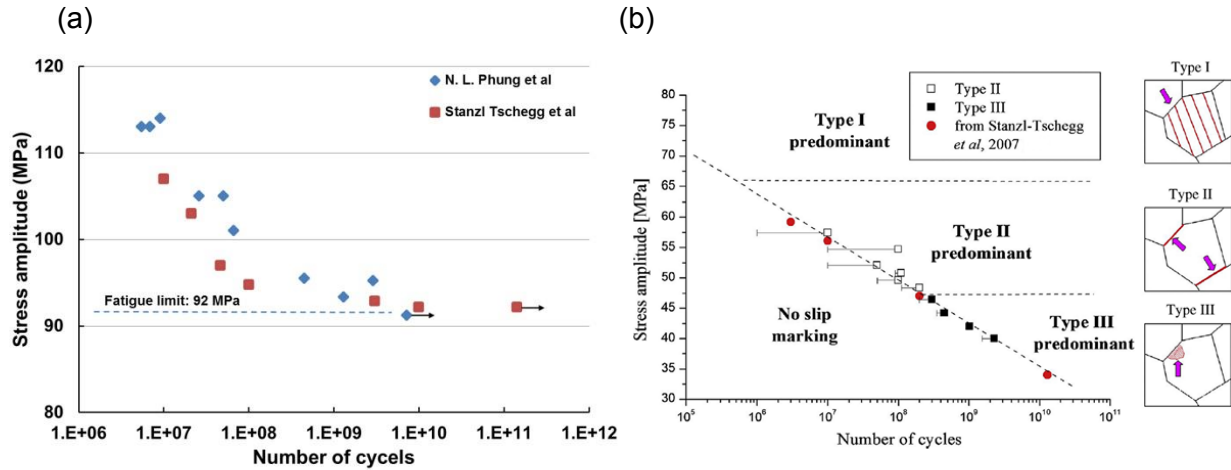


**Figure 1.** (a) S-N data of polycrystalline pure copper plate by N. L. Phung et al [5] and Stanzi Tschegg et al [6]; (b) Stress amplitude needed to form the early slip markings of type I, II and III and scheme of their location as a function of the number of cycles. (by N. L. Phung et al [5])

In this paper, the self-heating method was used to investigate this research subject. Meanwhile, the relationship of intrinsic dissipation and three types of PSB was analyzed in quantity.

## MATERIAL AND EXPERIMENTAL PROCEDURE

The material employed in the self-heating test is polycrystalline pure copper. The plate specimen is designed with a specific eigen-frequency of 20 kHz for the piezoelectric fatigue machine and its geometries are specified in Fig. 2(a).

The plate specimen was subjected to a tension-compression load with stress ratio  $R=-1$ , on ultrasonic fatigue system, without cooling air. A high-precision infrared camera was used to record synchronously the temperature evolution on the specimen surface during each self-heating test. A black material with very low light reflection was painted on the specimen to reduce the errors associated with surface emissivity. The frame rate of the camera was set as 3 Hz.

The self-heating tests were carried out on one specimen with a series of increasing stress amplitudes and a certain cycle block. In this paper, a large range of stress amplitude was set up from 9 MPa to 82 MPa, as shown in Fig. 2(b). For each block, the infrared camera will record the whole loading procedure ( $5 \times 10^7$  cycles) and a period of natural cooling process, about 1 min.

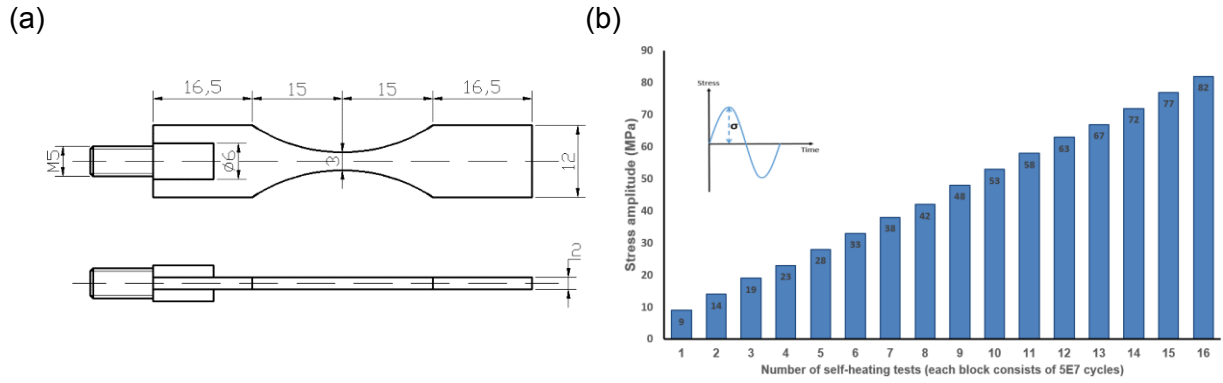


**Figure 2.** (a) The dimensions of fatigue specimen with a screw (the unit is mm); (b) The loading sequence in self-heating tests.

### Heat equations

As deduced from both principles of thermodynamics, by A. Chrysochoos and H. Louche [7], the link between the temperature and the heat source fields is provided by the heat diffusion equation:

$$\rho C_{\alpha} \dot{T} - \text{div}(k \overrightarrow{\text{grad}} T) = d_1 + S_{thm} + r_e \quad (1)$$

Where  $\rho = 8920 \text{ kg/m}^3$ ,  $C_{\alpha} = 385 \text{ J/kg} \cdot \text{K}$  and  $k = 360 \text{ W/m} \cdot \text{K}$  denote respectively the mass density, the specific heat state variable coupling the mechanical and microstructural state, and the heat conduction tensor.  $T$  is the absolute temperature. The right hand member of equation (1) consists of three heat sources,  $d_1$  the intrinsic dissipation,  $S_{thm}$  the thermo-mechanical coupling sources and  $r_e$  the volume external heat source.

Although ultrasonic fatigue tests are dynamic mechanical processes, they can still be regarded as quasi-static processes in one or a few constant cycles during stabilization period. In this paper,  $r_e$  can be reduced by introducing the relative temperature  $\theta$ . As suggested by Boulanger et al [8], the sum of the thermo-elastic power in one cycle  $S_{thm}$  can be zero, and the heat diffusion equation in zero dimension is specified finally as:

$$\dot{\theta} + \frac{\tilde{\theta}}{\tau_{th}^{0D}} = \frac{\tilde{d}_1}{\rho C_{\alpha}} \quad (2)$$

Where  $\tau_{th}^{0D}$  is a time constant characterizing heat losses perpendicular to the specimen surface through a specific region, like A in Fig. 4. This latter can be determined at the end of the test, as illustrated in Fig. 3, when the dissipation heat source is zero. Thus, the heat equation is reduced as:

$$\dot{\theta} + \frac{\theta}{\tau_{th}^{0D}} = 0 \quad (3)$$

so

$$\tau_{th}^{0D} = - \frac{\theta_{end}}{\dot{\theta}_{end}} \quad (4)$$

Where  $\theta_{end}$  is the relative temperature at the point, when the power off and vibration ends.

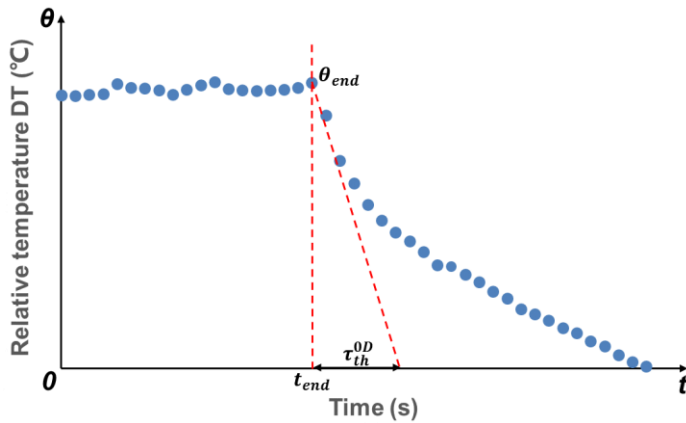


Figure 3. The schematic diagram of the calculation of  $\tau_{th}^{0D}$ .

## RESULTS AND DISCUSSION

Fig. 4 presents the evolution of relative temperature at a series of stress amplitude, ranging from 9 MPa to 77 MPa, which are much lower than the traditional fatigue limit of polycrystalline pure copper plate, 92 MPa, as shown in Fig. 1(a). At  $5 \times 10^7$  cycles, the relative stabilization occurred, neglecting the limited growth rate, lower than  $3 \times 10^{-8} \text{ }^\circ\text{C}/\text{cycle}$ . At 9 MPa, the surface temperature grows little, approaching zero. With the addition of stress amplitude, the relative temperature increases gradually before the stress reaches 53 MPa. After that, the amplification expands rapidly. In order to analyze and explain the tendency in physics, the intrinsic dissipation values at each stress amplitude was calculated by the equation (2) and (4). The final results are shown in Fig. 5.

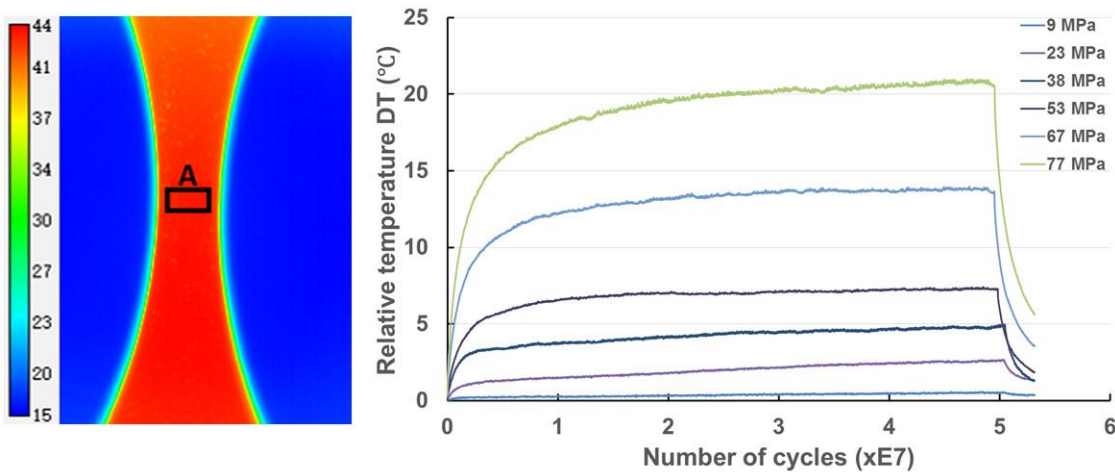


Figure 4. The evolution of relative temperature in average of region A at each stress amplitude.

To magnify and quantify the change of rising tendency in Fig. 5, the relation between  $d1$  and  $\sigma$  was well fitted as a bilinear curve, with an interaction at about 55 MPa. The slop value of

the fitting curve with stress amplitude higher than 55 MPa is four times larger than that with lower stress level. In the investigation of N.L. Phung et al [6], shown in Fig. 1(b), three types of persistent slipping bands (PSB) will occur in fatigue tests with a large range of stress amplitudes: type I. long and intergranular PSB under low and high cycle fatigue; type II. slipping bands in the grain boundary; and type III. short and intragranular PSB. These metallurgical investigations demonstrate indirectly the variation trend of intrinsic dissipation in self-heating tests here, neglecting the difference of stress on turning points. Below the fatigue limit threshold, the micro-plastic deformation appears as the competition of slipping in type II and III. Meanwhile, the energy dissipated by the slipping in type II doubles as that in type III, comparing the increment rates of the areas under two fitting lines.

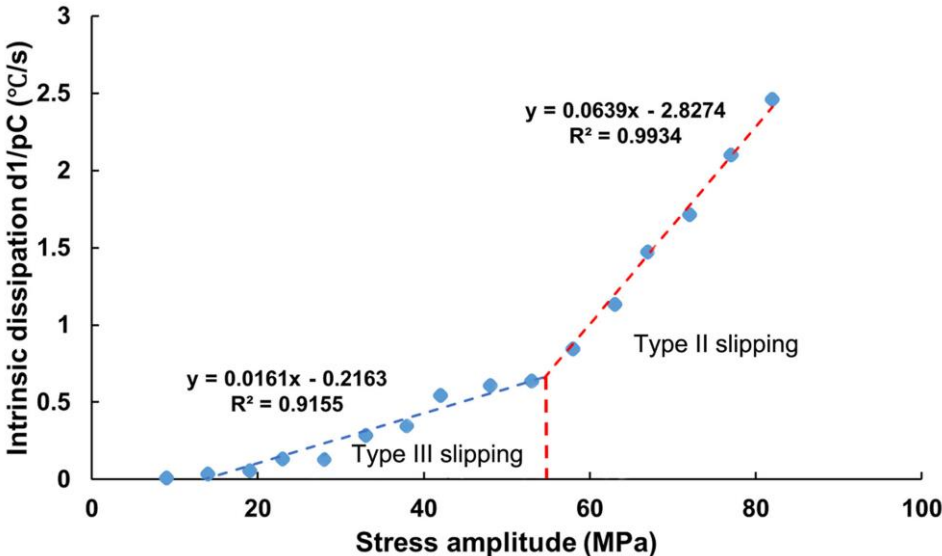


Figure 5. The intrinsic dissipation vs. stress amplitudes.

**CONCLUSION AND PROSPECTION**

In this work, the gigacycle fatigue property of polycrystalline pure copper was fast estimated by self-heating method. It is found that the intrinsic dissipation is linked to the type of PSB, and the dissipation energy caused by slipping in type II is twice larger than that in type III.

Previously, people divided simply the material behavior in fatigue into plastic deformation and elastic deformation, with a set apart at fatigue limit. C. Mareau et al [9] started to propose an anelastic (dislocation oscillations) and inelastic (plastic slip) models to subdivide the micro-plasticity of steels in gigacycle fatigue regime. While, in this aspect, few papers can be found for pure copper material. However, the comparison of intrinsic dissipation caused by two slipping types can support a theoretical foundation for establishing material behavior models in crystal plasticity simulation work.

## REFERENCES

- [ 1 ] Fatemi A, Yang L  
Cumulative fatigue damage and life prediction theories: a survey of the state of the art for homogeneous materials.  
Int J Fatigue 20(1):9–34 (1998)
- [ 2 ] Ozaltun H., Shen M. H., George T., Cross C.  
An energy based fatigue life prediction framework for in-service structural components  
Exp Mech 51(5):707–718 (2011)
- [ 3 ] N. Torabian, V. Favier, S. Ziaei-Rad, J. Dirrenberger, F. Adamski, N. Ranc  
Thermal response of DP600 dual-phase steel under ultrasonic fatigue loading  
Materials Science & Engineering A 677:97-105 (2016)
- [ 4 ] A. Blanche, A. Chrysochoos, N. Ranc, and V. Favier  
Dissipation assessments during dynamic very high cycle fatigue tests  
Experimental Mechanics 55:699–709 (2015)
- [ 5 ] N.L. Phung, V. Favier, N. Ranc, F. Vales, H. Mughrabi  
Very high cycle fatigue of copper: Evolution, morphology and locations of surface slip markings  
International Journal of Fatigue 63 68-77 (2014)
- [ 6 ] Stanzl-Tschegg S, Schönbauer B.  
PSB threshold and fatigue limit of polycrystalline copper in the VHCF-regime  
Proceedings of fourth international conference on very high cycle fatigue (VHCF-4).  
USA: TMS; 2007. p. 15–22.
- [ 7 ] A. Chrysochoos, H. Louche  
An infrared image processing to analyze the calorific effects accompanying strain localization  
International Journal of Engineering Science 38 1759-1788 (2000)
- [ 8 ] T. Boulanger, A. Chrysochoos, A. Mabru, A. Galtier  
Calorimetric analysis of dissipative and thermoelastic effects associated with fatigue behavior of steels  
Int. J. Fatigue 26, 219-221 (2004)
- [ 9 ] C. Mareau, V. Favier, B. Weber, A. Galtier, M. Berveiller  
Micromechanical modeling of the interactions between the microstructure and the dissipative mechanisms in steels under cyclic loading.  
Int. J. Plasticity 32-33, 106-120 (2012)

**Corresponding author:** YANG.SHAOBO@ensam.eu

# SIMULATION OF DAMAGE BEHAVIOR IN GFRPS IN THE VERY HIGH CYCLE REGIME

**H. Madhusoodanan, E.L. Jansen, R. Rolfes**

Institute of Structural Analysis, Leibniz Universität Hannover,  
Appelstr. 9a, D-30167 Hanover, Germany

## ABSTRACT

In the last decades there has been an intensive research activity in the field of modeling the fatigue behavior of fibre-reinforced plastic (FRPs). Recently, the potential of a physically based layer-wise, two-dimensional fatigue damage model to predict the fatigue damage in FRPs effectively was illustrated. Originally, the FDM was based on a two-dimensional (2D) formulation. In the present paper, an extended version of the FDM is presented. The methods of extension as well as formulations required for incorporating three-dimensional (3D) stress states are explained here. The extended FDM is used for the numerical simulations of the very high cycle fatigue behaviour of laminates for specific reference cases such as a four-point bending based on cyclic loading. As a result of the damage accumulation arising due to transverse cracking as well as delaminations, a variation in deflection amplitude and a consequent variation in bending modulus were observed in these tests. The bending modulus variation obtained from the original (2D FDM) and the present work (3D FDM) are compared and in a final step compared with the results obtained from the four-point bending tests.

**KEYWORDS:** Fibre reinforced plastics, Fatigue, Degradation, Damage model, 3D stress state, Very high cycle fatigue

## INTRODUCTION

The fatigue damage model (FDM) [1-2] is based on a classical laminate theory (CLT) and as a result five degradation factors are required for the definition of both strength and stiffness at different layers. These degradation factors also take into account the material orientation (longitudinal or transverse to fibre direction) as well as the type of loading (tension, compression or shear). The FDM has two main parts, the discontinuous degradation analysis, which takes into account the degradation due to quasi-static loading and the continuous degradation analysis resulting in the degradation due to the repetitive loading. The FDM has been implemented in the commercial finite element code ABAQUS through a user written material routine 'UMAT' and used together with the standard shell elements.

However in complex situation such as delaminations or complex loading conditions like bending or twisting as well as in cases where the thermal and hygrothermal effects have to be taken into account, the CLT cannot be used. Also in cases where the effects of transverse shear deformations have to be taken into account, the CLT is no longer effective. In order to analyse such complex load cases, the existing FDM has to be modified to take into account the stresses and degradation in all directions. The extension process can be divided into two parts. The first part is the extension of the stiffness matrix to take into account the three

dimensional stress states and the second part is the extension of the Puck [3] failure criteria to the 3D framework.

## EXTENSION OF THE 2D FATIGUE DAMAGE MODEL TO 3D

### Extension of the stiffness tensor to 3D stress state

Using Hooke's law for relating the stress and strain, one can produce the overall general equations for a lamina of a fibre reinforced composite material in terms of all 3 principal directions as shown in Eq. (1). As represented in Fig. 1 corresponding changes in the constitutive relations are made in order to transform the plane stress state to the 3D stress state.

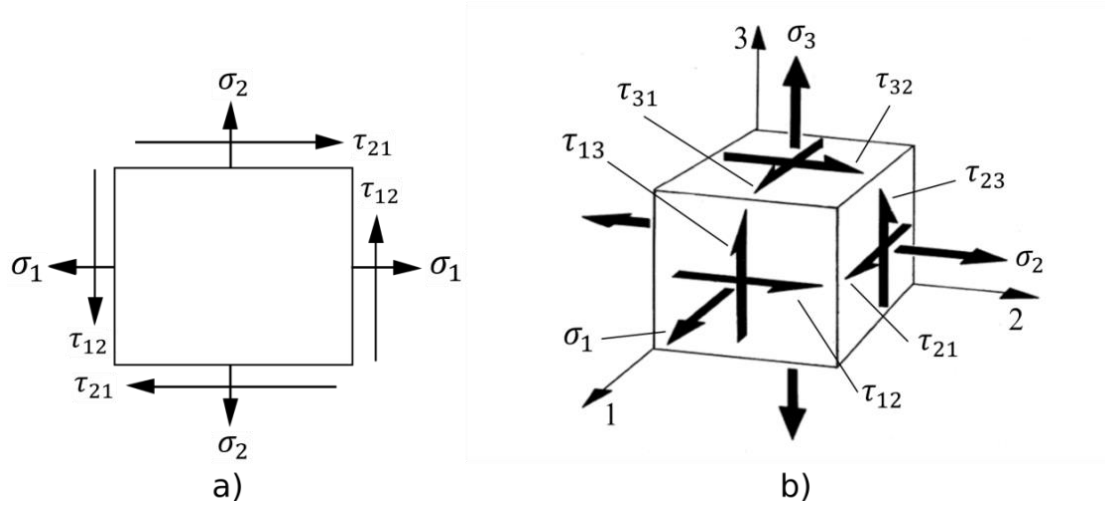


Fig 1: Schematic representations of stresses in a) Plane stress state b) 3D stress state. Here the indices 1: Longitudinal to fibre direction, 2 & 3: Transverse to fibre direction and 12,13,21,31 and 23 are the corresponding shears.

$$\begin{Bmatrix} \sigma_1 \\ \sigma_2 \\ \sigma_3 \\ \tau_{23} \\ \tau_{13} \\ \tau_{12} \end{Bmatrix} = \begin{bmatrix} Q_{11} & Q_{12} & Q_{13} & 0 & 0 & 0 \\ Q_{12} & Q_{22} & Q_{23} & 0 & 0 & 0 \\ Q_{13} & Q_{23} & Q_{33} & 0 & 0 & 0 \\ 0 & 0 & 0 & 2Q_{44} & 0 & 0 \\ 0 & 0 & 0 & 0 & 2Q_{55} & 0 \\ 0 & 0 & 0 & 0 & 0 & 2Q_{66} \end{bmatrix} \begin{Bmatrix} \epsilon_1 \\ \epsilon_2 \\ \epsilon_3 \\ \epsilon_{23} \\ \epsilon_{13} \\ \epsilon_{12} \end{Bmatrix} \quad (1)$$

In Eq. (1), the terms  $\sigma_1, \sigma_2, \sigma_3$ , etc. are the stresses,  $\epsilon_1, \epsilon_2, \epsilon_3$ , etc. are the strains and the quantities  $Q_{11}, Q_{12}, Q_{13}$ , etc. are the corresponding relations in the stiffness matrix. Taking the residual stiffnesses and transverse isotropy material property into account, the  $Q_{ij}$  quantities seen in the above stiffness matrix can be further expanded as in Eq. (2-3).

$$\begin{aligned} Q_{11} &= E_{aa,1}^k \left( 1 - (v_{23}^k)^2 \right) / \Delta^k \\ Q_{12} &= E_{aa,1}^k (v_{12} + v_{23}^k v_{12}) / \Delta^k \\ Q_{13} &= Q_{12} \\ Q_{21} &= Q_{12} \\ Q_{22} &= E_{aa,2}^k \left( 1 - v_{12}^2 \frac{E_{aa,2}^k}{E_{aa,1}^k} \right) / \Delta^k \end{aligned} \quad (2)$$



$$\begin{aligned}
Q_{23} &= E_{da,2}^k \left( \nu_{23}^k - \nu_{12}^2 \frac{E_{da,2}^k}{E_{da,1}^k} \right) / \Delta^k \\
Q_{31} &= Q_{12} \\
Q_{32} &= Q_{23} \\
Q_{33} &= Q_{22} \\
Q_{44} &= \left( 1 - \nu_{23}^k - 2 \nu_{12}^2 \frac{E_{da,2}^k}{E_{da,1}^k} \right) \frac{E_{da,2}^k}{2 \Delta^k} \\
Q_{55} &= E_{da,12} \\
Q_{66} &= E_{da,12}
\end{aligned} \tag{3}$$

with the additional terms,

$$\begin{aligned}
\Delta^k &= \left( 1 + \nu_{23}^k \right) \left( 1 - \nu_{23}^k - 2 \nu_{12}^2 \frac{E_{da,2}^k}{E_{da,1}^k} \right) \\
\nu_{23}^k &= \frac{\nu_{12} \left( 1 - \nu_{12} \frac{E_{da,2}^k}{E_{da,1}^k} \right)}{1 - \nu_{12}}
\end{aligned}$$

In Eq. (2-3), the component  $k$  represents the type of loading (tension, compression or shear). The terms  $E_{da,1}^k$ ,  $E_{da,2}^k$  and  $E_{da,12}$  are the degraded stiffnesses and  $\nu_{12}$  is the major Poisson's ratio. The input properties required for the calculation of the 3d stress state are: Stiffness parameters in the longitudinal, transverse and shear directions ( $E_{11}, E_{22}, E_{12}$ ) and the major Poisson's ratio ( $\nu_{12}$ ). The out-of-plane Poisson's ratio  $\nu_{23}$  is obtained by the Christensen's equation.

### Extension of Puck's failure criteria to the 3D framework

The residual strength analysis and the following discontinuous degradation used within the FDM is based on the well-known theory of Puck [3], which describes failure modes for fibre-failure (FF) and inter-fibre-failure (IFF). The criterion indicates failure if the value of the exposure  $f_{E_1}$  exceeds one or  $\eta_{W1}$ . Originally the Puck criterion does not take into account the strength degradation. Apart from static degradation, the fatigue loading also causes continuous degradation. Therefore the strength degradation factors  $\eta_R$  are also included in the Puck criterion. For the extension of FDM to 3D framework, the static failure criteria of Puck should also be modified to take into account the 3D stress states. The FF-criteria according to Puck can be expressed as,

$$f_{E,FF}' = \sigma_1 - \left( \nu_{\perp \parallel} - \nu_{\perp \parallel f} m_{\sigma f} \frac{E_{\parallel}}{E_{\parallel f}} \right) (\sigma_2 + \sigma_3),$$

with the condition:

$$\begin{aligned}
f_{E,FF} &= \frac{f_{E,FF}'}{\eta_{R_1}^t \cdot R_{\parallel}^t} \quad \text{for } f_{E,FF}' \geq 0 \quad \text{and} \\
f_{E,FF} &= \frac{f_{E,FF}'}{-(\eta_{R_1}^c \cdot R_{\parallel}^c)} \quad \text{for } f_{E,FF}' < 0
\end{aligned} \tag{4}$$

According to Puck's [3] modified nomenclature for 3D stress states, subscripts || and  $\perp$  are used instead of 1 (longitudinal to fibre direction) and 2 (transverse to fibre direction). In Eq. (3), the term  $f_{E,FF}'$  is the FF-condition of the UD-lamina and  $f_{E,FF}$  is the FF- stress exposure of the UD-lamina. The degradation terms  $\eta_{R_1^t}$  and  $\eta_{R_1^c}$  represents the degradations. For the consideration of the IFF-criteria, a fracture plane inclined with respect to the plane parallel to the fibres is taken into account. This transformation [3], yields stress components  $\sigma_n$ ,  $\tau_{nt}$  and  $\tau_{n1}$  which are calculated on the basis of the fracture angle  $\theta$ . The IFF criteria along with the degradation factors can be expressed as,

$$\begin{aligned}
 &\text{For } \sigma_n \geq 0 \\
 &f_E(\theta) = \sqrt{\left[ \left( \frac{1}{\eta_{R_2^t} \cdot R_{\perp 1}^t} - \frac{p_{\perp 1\psi}^t}{R_{\perp 1\psi}^A} \right) \cdot \sigma_n(\theta) \right]^2 + \left( \frac{\tau_{nt}(\theta)}{R_{\perp 1\perp}^A} \right)^2 + \left( \frac{\tau_{n1}(\theta)}{\eta_{R_{21}} \cdot R_{\perp ||}} \right)^2 + \frac{p_{\perp 1\psi}^t}{R_{\perp 1\psi}^A} \sigma_n(\theta)} \\
 &\text{For } \sigma_n < 0 \\
 &f_E(\theta) = \sqrt{\left( \frac{\tau_{nt}(\theta)}{R_{\perp 1\perp}^A} \right)^2 + \left( \frac{\tau_{n1}(\theta)}{\eta_{R_{21}} \cdot R_{\perp ||}} \right)^2 + \left( \frac{p_{\perp 1\psi}^c}{R_{\perp 1\psi}^A} \sigma_n(\theta) \right)^2 + \frac{p_{\perp 1\psi}^c}{R_{\perp 1\psi}^A} \sigma_n(\theta)}
 \end{aligned} \tag{5}$$

The weakening factor  $\eta_{W1}$  for the 3D framework can be expressed as shown in Eq. (6), where the term  $f_{E_1}$  corresponds to the effort due to the influence of  $\sigma_1$ ,  $f_{E_0}$  corresponds to the original effort and the terms  $m$  and  $s$  are the parameters used for calculation of fracture curve.

$$\begin{aligned}
 &f_{E_1} = \frac{f_{E_0}}{\eta_{W1}} \\
 &\text{with the expansion,} \\
 &\eta_{W1} = \frac{c \left( a \sqrt{c^2(a^2 - s^2) + 1} + s \right)}{(ca)^2 + 1} \\
 &c = \frac{f_{E_0}}{f_{E,FF}} \quad \text{and} \quad a = \frac{1 - s}{\sqrt{1 - m^2}}
 \end{aligned} \tag{6}$$

Another important aspect required for the fatigue based degradation or the cyclic based degradation is the strain evolution under fatigue loading,  $\varepsilon_k^{fat}$  [1-2]. As represented in Eqn. (7), considering transverse isotropy no additional strain evolutions are required for the extension to the 3D framework.

$$\begin{aligned}
 &\varepsilon_3^{fat} = \varepsilon_2^{fat} \\
 &\varepsilon_{13}^{fat} = \varepsilon_{12}^{fat}
 \end{aligned} \tag{7}$$

## COMPARISON WITH EXPERIMENTAL RESULTS

Recently, experimental investigations for the VHCF behavior of GFRP specimens have been carried out using a four-point bending setup [4]. The coupons used for this experiment are a four layered  $[90/0]_s$  as shown in Fig. 2a. The coupons are subjected to force amplitude  $f_a$  and the deflection  $d_a$  is calculated continuously throughout the test. The effective bending stiffness  $\bar{E}_{xb}$  can be calculated according to the four-point bending equation as shown Eq. (8).

$$\bar{E}_{xb} = \frac{f_a}{d_a} \frac{6}{w_{spec} t_{spec}^3} \left( \frac{1}{3} a^3 + \frac{1}{2} b a^2 + \frac{1}{8} a b^2 \right) \quad (8)$$

In Eq. (8) the parameters  $a$  and  $b$  are the relative distances and the terms  $w_{spec}$  and  $t_{spec}$  are the width and thickness of the specimen. Due to damage accumulation arising due to transverse cracking as well as delaminations, a variation in deflection amplitude and as a result the consequent variation in  $\bar{E}_{xb}$  is seen in the VHCF regime.

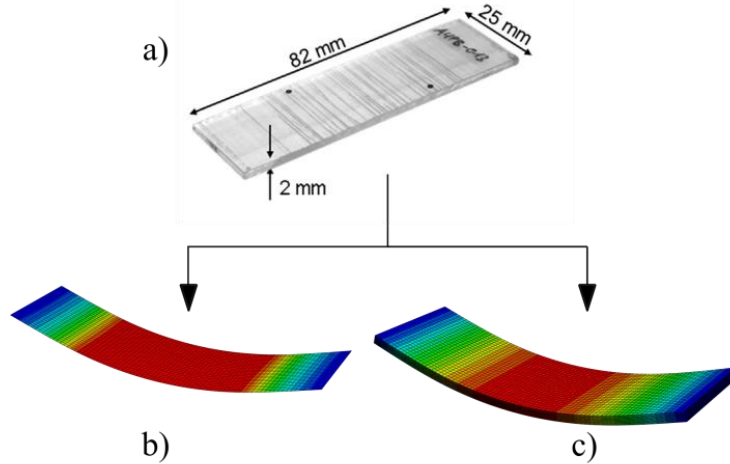


Fig 2: a) GFRP specimen used in the four-point bending test in VHCF regime [4] b) Modelling of the specimen in ABAQUS using shell elements (S4R) and c) Modelling of the specimen in ABAQUS using solid elements (C3D8).

For the purpose of fatigue simulation, the coupon is modeled according to its specifications in ABAQUS. Here two models are created, a shell based model for the 2D FDM and a solid based model for 3D FDM as shown in Fig. 2b and Fig. 2c. The six different load cases (*LL1* to *LL6*) provided in [4], are taken into account for the validation process. The force-deflection relation for a representative undamaged specimen described in [4] is used for calculating the forces and their corresponding deflection for a particular load level. For the fatigue strain evolution [1-2] in the cyclic routine, several parameters,  $\Delta \varepsilon_2^t$ ,  $f_{\Delta \varepsilon_{22}^c}$ ,  $G_{fr,2}^c$ ,  $\Delta n_2^t$ ,  $\Delta n_2^c$  and  $\Delta n_3^c$ , crucial for the tension-based and compression-based damage evolution, require to be fit according to the response observed in the VHCF regime. In order to achieve a good fit, these parameters are optimized using a non-linear least square method based on a trust region algorithm in MATLAB [5]. This process enables calibrating the 2D FDM parameters for the specific test carried out. The parameters obtained are used in the extended 3D version.

As per the fatigue test results obtained, Fig. 3 compares the numerically determined bending modulus variation to experimentally obtained results. It can be seen that for *LL1* and *LL2*, the results tend to overlap. Particularly the results of *LL1* Test data, *LL1* 3D FEM and *LL2* Test data tend to overlap each other. It can be seen that only for the load level *LL2* the results calculated by both 2D and 3D FDM are not in agreement with the experimental results. However comparing the two, it can be seen that the deviation in results remain within acceptable bounds. For the lower load levels *LL5* and *LL6*, there is less or no degradation in bending modulus occurring within the prescribed load cycles [4].

## CONCLUSION

In order to include complex stress states in laminates under cyclic loading, the fatigue damage model (FDM), originally developed for classical laminate theory, has been extended to the analysis of 3D stress states. A first validation of the extension of the 2D FDM to the 3D

FDM has been performed by the comparison of the 2D and 3D results with respect to the experimental results of a GFRP laminate subjected to four-point bending in the VHCF regime. Using a careful calibration of the relevant FDM parameters on the basis of the available experimental data, a reasonable agreement with the experimental results was obtained for nearly the full range of load cycles. It is noted that in view of the calibration process involved, the results presented can be seen as a contribution to a more complete validation of the ESM based on measured data of the relevant parameters of this model.

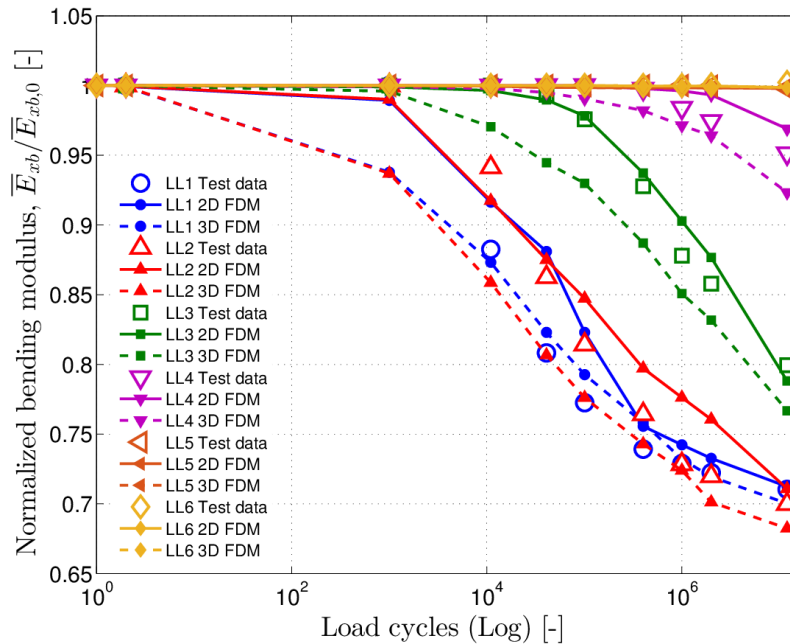


Fig 3: Comparison of bending modulus obtained from simulations to the experimental results for various load levels up to  $1.2 \times 10^7$  load cycles for a four-point bending test.

#### REFERENCES:

- [1] H. Krüger:  
Ein physikalisch basiertes Ermüdungsschädigungsmodell zur Degradationsberechnung von Faser-Kunststoff-Verbunden  
PhD thesis, University of Hannover, 2012; Institute of Structural Analysis, Hannover.
- [2] Heiko Krüger; Raimund Rolfes:  
A physically based fatigue damage model for fibre-reinforced plastics under plane loading  
Int. Journal of Fatigue, 70 (2015), pp. 241-251
- [3] A. Puck:  
Festigkeitsanalyse von Faser-Matrix-Laminaten – Modelle für die Praxis  
Carl Hanser Verlag, Munich, Germany. (ISBN 3-446-18194-6)
- [4] T.J. Adam, P. Horst:  
Experimental investigation of the very high cycle fatigue of GFRP [90/0]s cross-ply specimens subjected to high-frequency four-point bending  
Composite Science and Technology, 101 (2014), pp. 62-70
- [5] Rose Rogin Gilbert, Stefan Hartmann, Laszlo Kudela, Ernst Rank, Gideon Sahar, Zohar Yosibash, Ofry Yossef :  
Parameter identification of the passive response in arteries  
Technical Report Series No. Fac3-16-01, Clausthal University of Technology, Germany

**Corresponding author:** h.madhusoodanan@isd.uni-hannover.de

# MODELLING STRATEGY FOR MICROCRACKING IN OFF-AXIS PLYS IN CFRP-LAMINATES UNDER MONOTONIC AND FATIGUE LOADING UP TO THE VHCF-REGIME

G. Just<sup>1)</sup>, I. Koch<sup>1)</sup>, C. Leopold<sup>2)</sup>, M. Gude<sup>1)</sup>, B. Fiedler<sup>2)</sup>

<sup>1)</sup> TU Dresden, Institute of Lightweight Engineering and Polymer Technology, Holbeinstr. 3, 01307 Dresden, Germany

<sup>2)</sup> TU Hamburg, Institut für Kunststoffe und Verbundwerkstoffe, Denickestr. 15, 21073 Hamburg, Germany

## ABSTRACT

A physically based damage modelling methodology to predict the onset and evolution of inter fibre microcracking in unidirectional reinforced CF/EP-laminates under static and cyclic loading up to the very high cycle fatigue (VHCF) regime is presented. It incorporates principles of fracture mechanics in a convenient way to satisfy challenges particularly arising in composite laminates, e.g. multiple cracking and constraining. Data from fatigue experiments is used in conjunction with analytically and numerically derived strain energy release rate (SERR) to deduce fatigue crack growth curves, commonly known as Paris-like curves. Combining a static and a fatigue model leads to a comprehensive description of the fatigue behaviour of laminates containing off-axis plies capable of predicting the crack density after the first load cycle and its evolution during cyclic testing.

## KEYWORDS

VHCF, CFRP, bending, crack density

## INTRODUCTION

The demand for a steadily increasing operating life of technical applications in the energy, aeronautics or automotive industries and the growing application of fibre reinforced composites requires new experimental and modelling approaches within the very high cycle fatigue (VHCF) regime. Due to the inhomogeneous nature of continuous fibre reinforced composites, fatigue damage is initiated in various failure modes. Generalised multi-axial loads occurring during service life initiate inter fibre failure as primary failure mechanisms which may further on spread in form of delaminations. These cracks are known to significantly influence the stiffness and, in case of combination of delaminations and compression stresses, also the residual strength of the structure [1-6].

Therefore it is essential to describe and predict the fatigue behaviour with the help of suitable models, which account for micro cracking in the off-axis plies, considering crack growth and stress redistribution. Here energy based damage models for predicting the onset and evolution of inter fibre microcracking in polymer composites under static and cyclic loading up to the very high cycle fatigue (VHCF) come into focus.

Mainly due to unacceptable long test durations and expensive testing, only few fatigue experiments for fibre reinforced composites were performed above  $10^7$  cycles. Recently significant achievements into the direction of ultrasonic and accelerated fatigue testing into the VHCF-regime have been published [1, 5, 6, 8, 9]. Besides classic tension/compression tests with

single layered or laminated strip specimens also bending experiments are promising. Due to the comparably smaller loaded volume which is additionally concentrated at the specimen surface, minor concern has to be given to internal heating during high-frequency testing [1, 6].

## MATERIAL AND TESTING PROCEDURES

### Material

The tested cross-ply specimens were built from uni-directional plies consisting of T700S carbon fibre reinforcement as non-twisted 12k roving and a standard prepreg epoxy resin system Araldite LY556 enriched with multi-wall carbon nanotubes (MWCNT). The single layers were manufactured at Technical University Hamburg-Harburg by an in-house filament winding and fibre impregnation machine with an nominal ply thickness of  $d_{ply} = 0.3$  mm. Cross-ply laminates with  $[90/0_{3,5}]_s$  stacking sequence and a total thickness of  $d = 2.7$  mm were cut to size by abrasive cutting, yielding bending specimens with length  $l = 100$  mm and width  $b = 15$  mm. Further detail on the manufacturing process is given in [7].

### Testing procedures

Two sets of specimens were tested. The first set of specimens was used in four-point bending experiments with quasi-static loading and unloading to several load steps. By the incremental testing procedure the onset of matrix microcracking has been determined accurately. The maximum bending strain at the specimen surface was  $\epsilon_{max} \approx 1.7$  %. The tests were performed in accordance to DIN EN ISO 14125 and accompanied by counting the transverse cracks of the outer tension loaded  $90^\circ$ -ply by means of optical microscopy. The length of observation is equal to the distance of  $L = 27$  mm between the two loading pins. Therefore the crack density can be calculated in terms of

$$c_i = \frac{n_i}{L} \quad (1)$$

were  $n_i$  is the total number of cracks observed after load step  $i$ . The observed area is loaded with a constant bending moment, according to linear elastic beam theory.

The second set of specimens was tested in fatigue loading with a load ratio  $R = -1$  and constant strain amplitudes. The key to shorten the high testing times of the experiments lies within the shaker based bending test rig, which allows for high frequency testing at different load levels. The specimen is clamped eccentrically from the axis of rotation and therefore axially guided to avoid the introduction of axial strains into the specimens. Furthermore the whole specimen is loaded by a shear force free constant bending moment. Depending on the specimen stiffness and the use of additional masses a wide range of testing frequencies can be exploited. By testing near the setup's eigenfrequency, the inherent strain magnification is used to achieve suitable load levels. The specimens were tested at six different load levels with the maximum bending strains at the specimen surface  $\epsilon_o = \{0.2, 0.25, 0.3, 0.35, 0.4, 0.45\}$  %, respectively. Online monitoring of the maximum specimen strain enables an automatic stop of the experiment in case of specimen failure or malfunction. A more detailed description of the VHCF bending test rig can be found in [8] and [9]. The quasi-static as well as the fatigue testing setups are shown in Fig. 1.

The fatigue specimens were unmounted from the test rig several times within the experiments and the crack densities in both  $90^\circ$ -layers were determined by optical microscopy. Due to the constant bending moment along the specimen, the whole gauge length of the specimen  $L = 65$  mm can be used for crack counting. The crack density is further averaged about both  $90^\circ$ -plies per specimen.

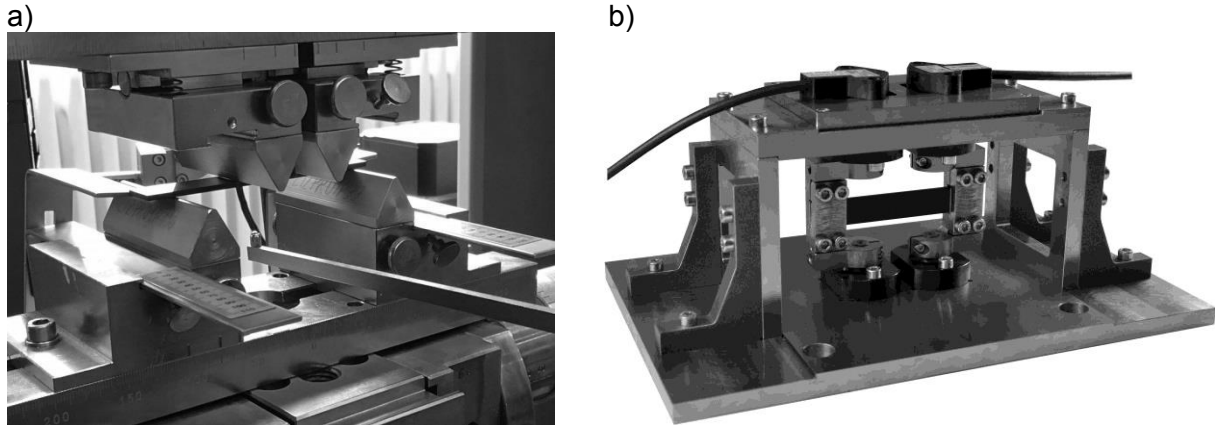


Fig. 1 a) Experimental setup used for quasi-static four-point bending and b) VHCF bending test rig for high frequency fatigue experiments.

## EXPERIMENTAL RESULTS AND PARAMETER IDENTIFICATION

### Static tests

The results of the four-point bending experiments under quasi-static monotonic loading are presented in Fig. 2. First cracks were observed for a bending strain at the specimen surface of  $\varepsilon_b = 0.587\%$ . The number of cracks then quickly increased up to  $c \approx 0.6 \text{ mm}^{-1}$ . Within the further course of the experiment, the crack growth slowed down and the maximum crack density obtained was  $c_{max} = 1 \text{ mm}^{-1}$  at the end of the test.

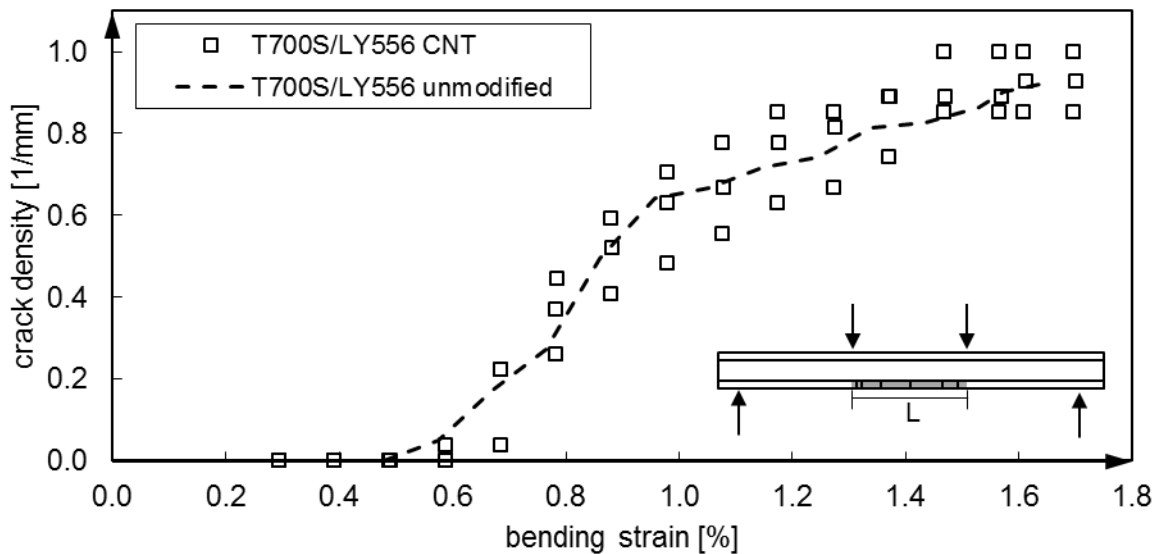


Fig. 2 Crack density growth in  $[90/0_4]_s$ -CF/EP laminates under quasi-static four-point bending. For reference the mean values of the crack growth without CNT resin modification is represented by the dashed line.

Using the model presented in [10] or suitable FEM simulations the progressive cracking under quasi-static loading can be modelled. Fitting the FE model to the experimental data leads to a critical energy release rate  $Y_c = 0.167 \text{ kJ/m}^2$ .

The reduced crack growth at the end of the experiments can be explained by the microcrack-induced growth of delaminations. Apparently, they reduce the stress transfer into the  $90^\circ$ -ply

and virtually decrease the crack distance. This behaviour has also been observed by other authors for specimens under axial tension loading [11]. Hence, it is likely that the influence of delaminations on the microcracking behaviour is even more pronounced in case of bending loads.

### Fatigue tests

Due to the thick 0°-supporting layer in the middle of the specimens, which remains undamaged throughout the whole experiments, no final failure can be observed. Therefore the SN-curve shown in Fig. 3 a) represents a specimen damage  $D = 1 - E_b/E_{b,0} = 1\%$ , corresponding to an averaged crack density of  $c \approx 0.2 \text{ mm}^{-1}$ . The SN-curve has been determined in analogy to the guideline VDI2014 [12] and is given by

$$\varepsilon_a = \varepsilon^* \left( \frac{1 - V_g}{n - V_g} \right)^{N_g} \quad (2)$$

with  $\varepsilon^* = \varepsilon_b = 0.587\%$ , the number of load cycles  $n$  and the two fitting parameters  $N_g = 0.1055$  and  $V_g = -320.7$ .

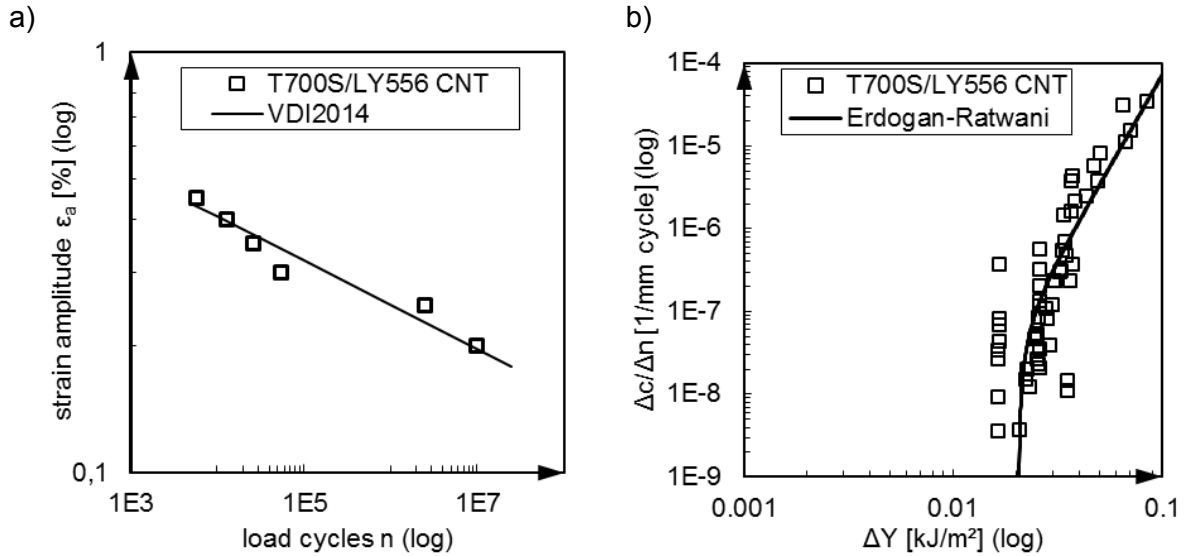


Fig. 3 a) SN-curve of  $[90/0_{3,5}]_s$ -CF/EP laminates under fatigue loading. Squares depict an averaged crack density of  $0.2 \text{ mm}^{-1}$  at each load level, respectively and b) the crack density growth rate vs. strain energy release rate.

From the evolution of the crack densities determined throughout the fatigue experiments the crack density growth rates for the tested specimens were determined. Therefore the maximum strain energy release rates  $Y$  have been calculated by means of FE simulations. By using the fluctuating part of the stored strain energy, the energy release rate is finally evaluated to

$$\Delta Y = \frac{(1 - R)^2}{2} Y. \quad (3)$$

An ERDOGAN-RATWANI like equation has been used to fit the crack density growth rate curve, which takes the form



$$\frac{\Delta c}{\Delta n} = \frac{C(\Delta Y^m - \Delta Y_{th}^m)}{\Delta Y_c - \Delta Y}, \quad (4)$$

with the fitting parameters  $C = 1.888 \text{ mm}^{-1} \text{ cycle}^{-1}$ ,  $m = 5.42$ , the critical strain energy release rate  $Y_c = 0.169 \text{ kJ/m}^2$  and fatigue threshold  $Y_{th} = 0.0207 \text{ kJ/m}^2$ . The data points below the fatigue threshold are considered as weak areas within the ply having the lowest fracture toughness, which may result from certain geometrical and rheological issues or premature cracking due to residual thermal stresses.

## MODELL APPLICATION

Combining the findings and modelling approaches for quasi-static and fatigue loading enables a comprehensive modelling strategy for arbitrary loading scenarios. Two possible use cases are presented in the following and shown in Fig. 4.

By defining an acceptable amount of crack density, the modelling approach can be used to derive the SN-curves under bending load for a constant amount of microcracks, which represent a certain stiffness drop within the laminate. It is therefore possible to calculate the SN-curves for a constant residual stiffness, as shown in Fig. 4 a).

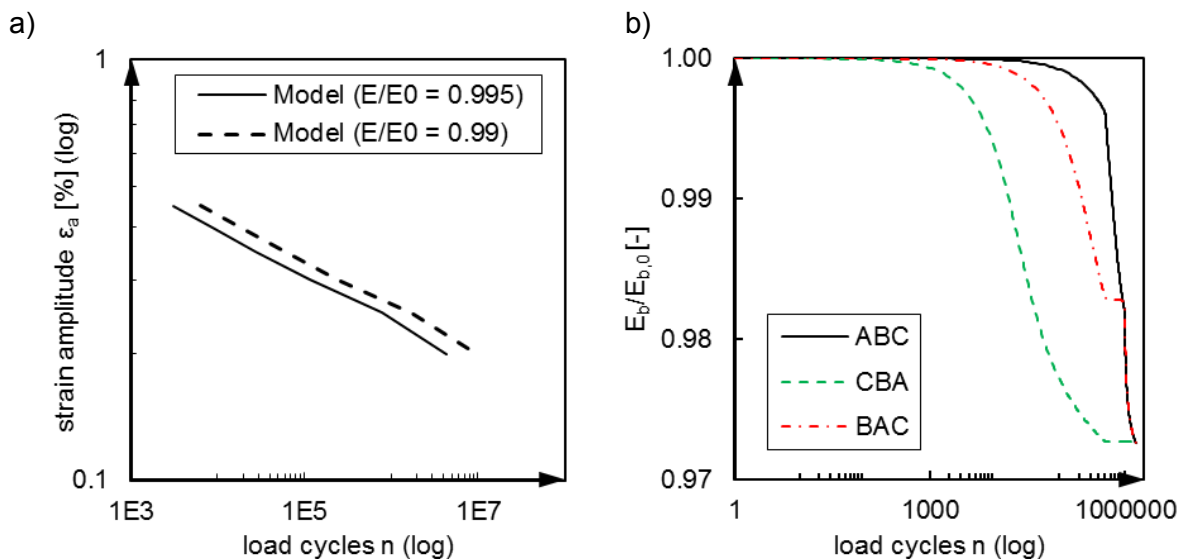


Fig. 4 a) SN-curves for constant residual stiffness and b) evolution of stiffness decrease in fatigue experiments with different block loading sequences.

The second use case deals with the sequence effect in case of block loading. Therefore, three blocks with maximum strains of  $\epsilon_o = 0.25 \%$  (A),  $\epsilon_o = 0.3 \%$  (B) and  $\epsilon_o = 0.4 \%$  (C) were defined, each having a block length of  $n = 500000$  load cycles. The model was used to calculate the stiffness evolution for the sequences ABC (increasing load), CBA (decreasing load) and BAC where the second load block has the lowest amplitude.

As seen from Fig. 4 b), the decreasing load sequence leads to an early stiffness drop and the whole amount of stiffness change occurs in the first load block whereas the other sequences show a delayed stiffness decrease. It can further be seen, that a lower load block following a higher load block has negligible influence on the stiffness decrease. It should further be mentioned that the occurrence of delaminations, which were not modelled here, could change the degradation behaviour significantly.

## CONCLUSION

The initiation and evolution of inter fibre cracks in static and fatigue loading up to the VHCF-regime of CFRP with and without nanoparticle modified matrix has been experimentally and analytically analysed.

Despite of small differences in the YOUNG's modulus, the cracking behaviour in quasistatic loading was not substantially altered by the nanoparticle modification, except for scatter.

Shear force free bending fatigue tests at  $R = -1$ , performed on a specifically designed test stand, reveal a cyclic SERR threshold for regular cracking at  $\Delta Y_{th} = 0.0207 \text{ kJ/m}^2$ . Below this threshold weak link cracking may appear already beginning at  $\Delta Y_{th, WL} = 0.0167 \text{ kJ/m}^2$ . The developed finite fracture mechanics approach exemplary facilitates the prediction of damage specific SN-curves and the influence of load sequences on the residual stiffness.

## ACKNOWLEDGEMENTS

The authors would like to thank Deutsche Forschungsgemeinschaft for financial support of this study in the framework of the priority programme "Life $\infty$ " (SPP 1466) and all the project partners for the inspiring discussions.

## REFERENCES

- [1] Adden, S.; Horst, P.: Stiffness degradation under fatigue in multiaxially loaded non-crimped-fabrics, *International Journal of Fatigue*, 32 (2010), pp. 108-122
- [2] Ellyin, F.; Martens, M.: Biaxial fatigue behaviour of unidirectional filament-wound glass-fiber/epoxy pipe, *Composite Science and Technology*, 61 (2001), pp. 491-502
- [3] Mertiny, P.; Gold, A.: Quantification of the leakage damage in high-pressure fibre-reinforced polymer composite tubular vessels, *Polymer Testing*, 26 (2007), pp. 172-179
- [4] Ogihara, S.; Takeda, N.: Interaction between transverse cracks and delamination during damage progress in CFRP cross-ply laminates, *Composites Science and Technology*, 54 (1995), pp. 395-404
- [5] Flore, D. et al.: Investigation of the high and very high cycle fatigue behaviour of continuous fibre reinforced plastics by conventional and ultrasonic fatigue testing, *Composites Science and Technology*, 141 (2017), pp. 130-136
- [6] Backe, D. et al.: Fatigue testing of CFRP in the Very High Cycle Fatigue (VHCF) regime at ultrasonic frequencies, *Composites Science and Technology*, 106 (2015), pp. 93-99
- [7] Knoll, J.B. et al.: The effect of carbon nanoparticles on the fatigue performance of carbon fibre reinforced epoxy, *Composites Part A: Applied Science and Manufacturing*, 67 (2014), pp. 233-240
- [8] Gude, M. et al.: Fatigue Testing of Carbon Fibre Reinforced Polymers under VHCF Loading, *Procedia Materials Science*, 2 (2013), pp. 18-24
- [9] Koch, I. et al.: Guided bending experiment for the characterisation of CFRP in VHCF-loading, *Polymer Testing*, 54 (2016), pp. 12-18
- [10] Kim, S.R.; Nairn, J.A.: Fracture mechanics analysis of coating/substrate systems Part I: Analysis of tensile and bending experiments, *Engineering Fracture Mechanics*, 65 (2000), pp. 573-593
- [11] Tong, J. et al.: On matrix crack growth in quasi-isotropic laminates-I. Experimental investigation, *Composites Science and Technology*, 57 (1997), pp. 1527-1535
- [12] Verein Deutscher Ingenieure (VDI): Entwicklung von Bauteilen aus Faser-Kunststoff-Verbund Blatt 3 – Berechnungen, 2006

## STRESS LEVEL INFLUENCE ON VHCF REGIME FOR IN-SERVICE FAILED TITANIUM BLADES

A.A. Shanyavskiy<sup>1</sup>, A. Nikitin<sup>1</sup>, M. Soldatenkova<sup>1</sup>

<sup>1</sup>Aviation Register of Russia Federation, Airport Sheremetievo-1, PO Box 54, Moscow region, Chimkinskiy State, 141426, Russia

### ABSTRACT

Nature of fatigue crack origination in a blade of engine TA12-60 fan-disk of VT8 titanium alloy has been considered. Crack origination has taken place subsurface in Very-High-Cycle-Fatigue regime by facets of  $\alpha$ - phase. This mechanism is the same that was seen for fatigued specimens in VHCF regime manufactured from titanium alloys of Ti-6Al-4Mo system. Experimental results attested they-self that disk blades subjected to multiaxial tension-bending-torsion cyclic loading and experienced resonance vibrations from the acting air stream with frequency 1950 Hz. In this condition stress level for blades is enough for their in-service failure for the design service goal at the durability  $10^9 - 10^{10}$  cycles.

### KEYWORDS

Titanium alloy, compressor disk, blades, multiaxial, very-high-cycle-fatigue, resonance

### INTRODUCTION

In-service aircraft structures experienced wide range of stresses and can be damaged in different regimes of fatigue due to variation of frequency and stress level in-flight operated systems [1]. Fatigue fracture process in metals usually taken into consideration applicably to different scale levels: micro- or nano- (Very-High-Cycle-Fatigue or VHCF-regime), meso- (High-Cycle-Fatigue or HCF-regime), and macro-scale level (Low-Cycle-Fatigue or LCF-regime) [2] - [7]. Transitions from one to another scale levels strongly expressed in accordance with introduced bifurcation diagram for fatigued metals [3] – [4].

Applicably to titanium compressor disks there is fatigue in-service cracking which has taken place in LCF regime [6]. Contrary, titanium compressor blades have in-service fatigue cracking in HCF or VHCF regime [7, 8]. Therefore for these two types of aircraft structures different criteria used for estimating their critical in-service lifetime for operated gas-turbine engines.

Aircraft blades in-flight subjected to bending-torsion-tension being complicated external loading which influenced their stress-state in dependence on the reached engine rotor speed for different in-flight aircraft operations. Blades can have experience of resonance by one of the main cyclic loading axis (torsion or bending) but this situation can be realized during short time only for the transition period from one to another operation. Main designer idea is to exclude for blades in-flight possible resonance during long time of operated engines.

Contemporary technology, introduced for the new generation of engine structures, realized possibility manufacturing titanium disk and their blades as one structure. For example, this technology was performed for fan stage of the engine TA12-60 which has in-service very rare

events with blade fatigue cracking before design service goal. It is clear that the question grows up: what kind of criterion has to be used for estimating this complicated structure in-service lifetime excluding the structure fatigue cracking.

Below this problem has consideration applicably to titanium disk of fan stage manufactured from VT8 (Ti-6Al-3Mo) alloy of aircraft engine TA12-60 being of "Accessory Power Plant" with design service goal 1000 hours or 2000 cycles of operated system.

## **MATERIAL AND TESTS PROCEDURE**

### **Material**

One of the in-service cracked titanium fans of the engine № 3460214363 was used in the present investigation with in-service time 435.33 hours. View of the failed disk is presented in Fig. 1.

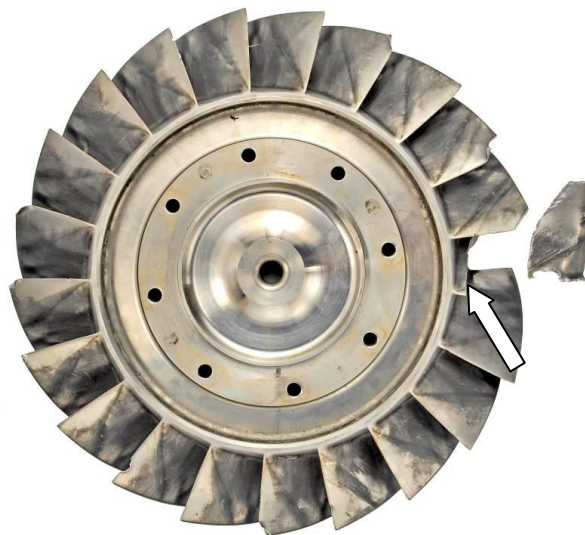


**Fig.1** View of the in-service fatigued titanium fan disk TA12.001.032.08 № 103020 with failed blade. White arrow pointed out area of crack propagation

Disk was manufactured from titanium alloy Ti-6Al-3Mo (VT8). Round bar specimens were manufactured from the disk and standard tension tests were performed for estimating material mechanical properties. Then, quantitative spectroscopic analysis was performed applicably to different areas of the investigated fan-disk. Metallographic analyses were performed for estimate material structure, which has to be two-phases ( $\alpha+\beta$ ) with dominantly globular shape of  $\alpha$ -phase.

Results of all tests have shown that titanium alloy VT8 of the investigated fan-disk has mechanical properties, two-phase structure, and chemical composition in accordance with order of certificate given by manufacturer and in accordance with order of standards.

### **Fractographic and X-ray analyses**

Fracture surface of failed fan-disk was investigated on the scanning electron microscope of Karl Zeiss with using special device "Inca" for local spectroscopic estimation material

composition. It was considered material composition by the fracture surface, and by the section prepared in the perpendicular direction to the fracture surface in area of crack origination.

**Blades resonance monitoring**

A segment of the fan-disk with three blades was prepared for estimating blades resonance characteristics in the range of 500-20000 Hz. Blades were polished by the concave surface. This segment was fixed in a special facility by the rim plane.

Piezoelectric oscillator was used for influencing in the segment one of the blades vibration from the metallic needle. On the small distance from the vibrating blade was placed detector which had not contact with the tested blade during registration the blade frequency. On the blade concave surface was placed sand to register area with its high density under different influenced external frequency. It was discovered for this type of blades many simultaneously appeared resonances in the investigated range of external frequencies, Fig.2.

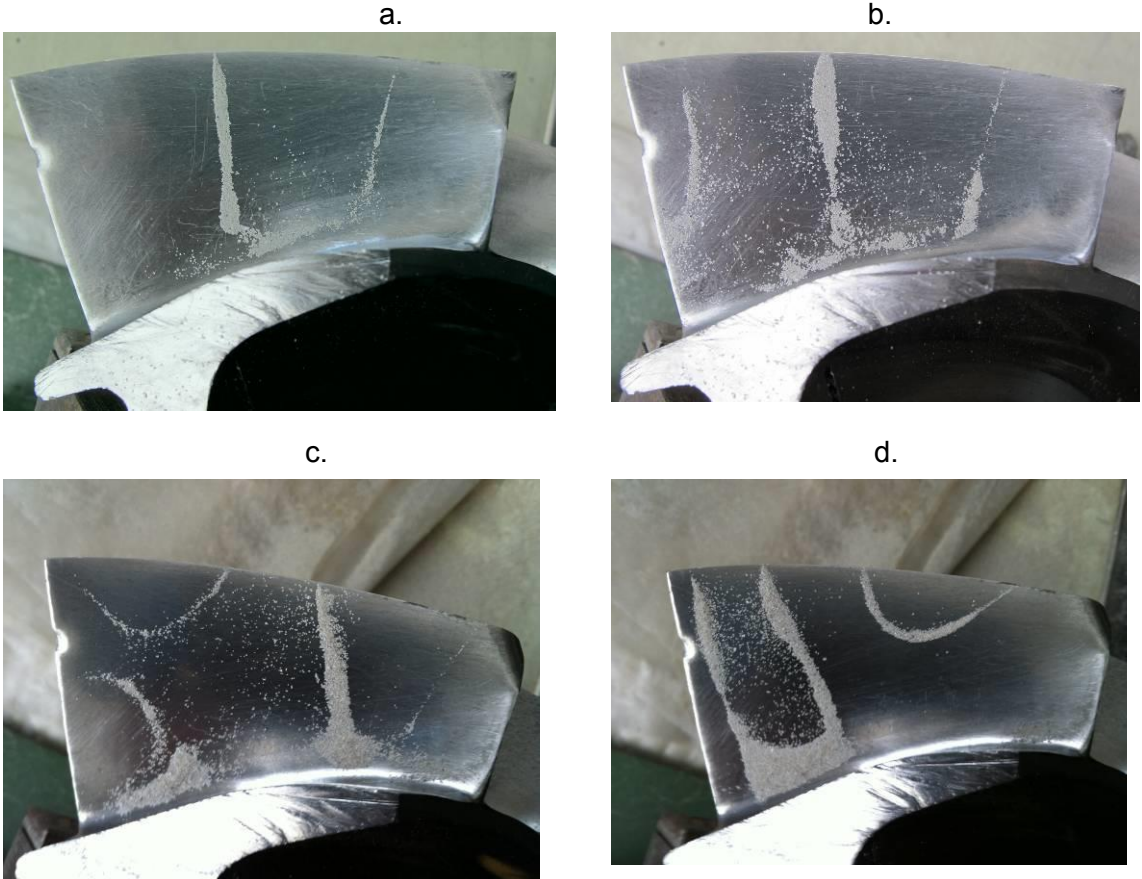


Fig.2 Types (a) - (d) of complicated resonances by the three simultaneously different forms for the same blade but for various influencing of external frequency.

**RESULTS OF INVESTIGATION**

Fractographic analyses have shown in area of crack origination the fracture surface plane of cracked material offset from the main plane, Fig.3.





**Fig.3** The fatigued blade fracture surface face. Crack origination area indicated arrow.

Crack origin area located in some distance from the concave surface as is reproduced in Fig. 3. The origin area has multiple smooth facets in the border of metal cracking through the  $\alpha$ -phase.

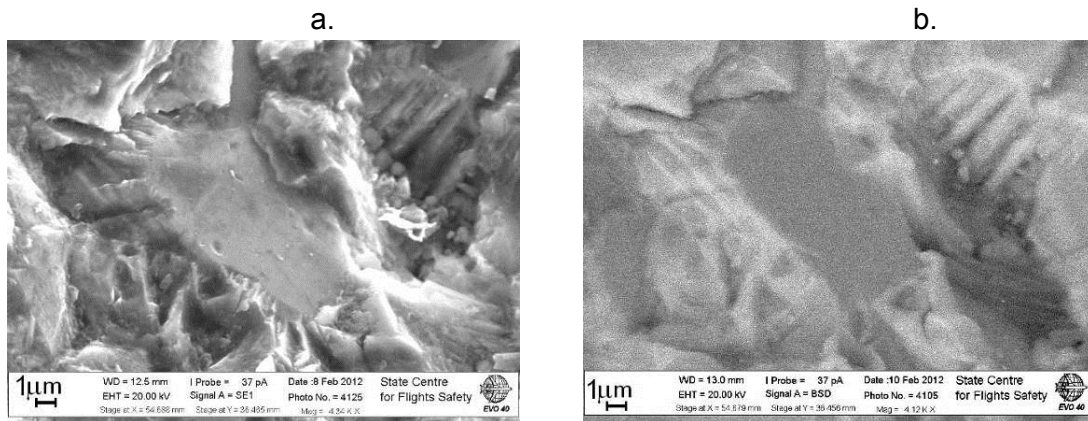


**Fig.3** View one of the smooth facets in area of subsurface crack origination (a) in the secondary electron and (b) in the back scatter regime

Material chemical composition by the all smooth facets of cracked  $\alpha$  - phase was analyzed with using X-ray spectroscopy. In all facets there were not discovered “Mo”. In neighbored  $\beta$ -phases there were discovered “Mo” in the accordance with certificate and standard. These data were compared in the slice plane prepared in the perpendicular direction through the area of origin not far from the concave surface. The same chemical composition was discovered in the slice plane that reflected material state in both phases in accordance with certificate and standard.

The blade of designed shape (large chord) has different types of resonance as was discovered during performed investigation. In some rare cases there was only one type of resonance with blade bending. But in many cases there were two and three neighbored resonance by the bending and torsion Modes. In other cases there were discovered not depended blades vibrations by two forms. For example, there is can be simultaneously large vibration with less bending stiffness for one part of blade but in another blade part there is another Mode of vibration with more intensive torsional stiffness. It can be seen gradually transition from one type of resonance to another. Therefore, material subjected to multiaxial in-flight loading with simultaneously tension (because of disk rotation), bending and torsion. It can be seen that one of the resonance, for example, is reproduced in Fig. 2, takes place in area of crack origination. The minimum frequency for the blade bending resonance in area of crack origination related to 1950 Hz.

Consequently, fatigue cracking of the in-service blade took place subsurface in area of material without or with very less percent of “Mo” under possible resonance in multiaxial condition of cyclic loading (bending and torsion).

## DISCUSSION

Discovered subsurface material cracking in the blade of VT8 titanium alloy is typical case for of VHCF. The same features of subsurface crack origination were earlier considered in VHCF regime with specimens test under frequency 20 kHz for titanium alloy VT3-1 of the same system Ti-6Al-3Mo-2Cr but having “Cr” [9]. Smooth facets by the  $\alpha$  - phases fatigue cracking were performed in the globular ( $\alpha+\beta$ ) two-phase structure. There was not revealed “Mo” by the smooth facets in area of crack origination. Therefore, it is titanium alloy chemical inhomogeneity that influenced fatigue in VHCF regime.

But in the case of specimens uniaxial tension-compression of VT3-1 titanium alloy there was minimum stress level 350MPa when cracking took place subsurface at  $5 \times 10^9$  cycles. That is why it is not only chemical inhomogeneity that can have influence on subsurface crack origination in VHCF regime. In the discussed case, there the blade fatigue cracking of VT8 titanium alloy was appeared at 435.33 hours since the disk was new. Operating period for the fan-disk with blades experienced one of the discovered resonance forms can be estimated based on the test results (see Fig. 2). If will be considered minimum frequency of 1950 Hz, is  $3600 \times 1950 \times 435.33 = 3.06 \times 10^9$  cycles.

In-flight the blade experienced influence of the air-stream with frequency by the fourth and fifth blades harmonic respectively in the range of (1599-1664) Hz and (1998-2080) Hz. Measurements accuracy has not less than 2% for estimated blade resonance and air-stream frequency. Consequently, there resonance for blades can takes place with different frequency but not only in the case of one resonance.

Performed investigations have shown that in blades can be realized different types of complicated multiaxial loading with independent vibration by the bending and torsion Modes.

It is clear that at the in-service time 453.33 hours there will be random resonance in blades under multiaxial cyclic loads with frequency more that minimum 1950 Hz. Various fan-disk operations will have more or less intensive influence on the blades damage accumulation. It is especially evident that there was revealed situation with transition from one to another resonance frequency without small interval without resonance. Different blades in fan-disk have various weight and geometry in the range of standard that influenced difference in resonance frequency and possibility to realize more or less complicated case of resonance. In the case of multiaxial resonance with highest stress level there will be only one blade that experienced this influence up to fatigue cracking in the design service goal 1000 hours. In one case it can be critical state before 1000 hours (or less than  $10^{10}$  cycles), but for many blades it can be in-service time more than 1000 hours (or more than  $10^{10}$  cycles). That is why in service there were very rear cases of blades fatigue cracking, and for one fan-disk only one blade had failure.

Consequently, in-service blades fatigue cracking takes place under resonance in the case of multiaxial loading. Their in-service time before fatigue cracking depended on the type of resonance and in the realized operating condition for fan-disk can be seen since they were new up to critical state at 400 hours and less. This state of blade can be seen in rare cases that depended on blades geometry.

## CONCLUSION

1. Fan-disk blades of engine TA12-60 have appearance in VHCF regime because of resonance by the different Modes of in-service multiaxial cyclic loading.
2. Manufacturing procedure of titanium alloys Ti-6Al-4Mo system influenced the blades cracking in VHCF regime because of in material there can be chemical inhomogeneity. It influenced material local stress-state and promotes durability variations in VHCF regime.
3. Large chord blades of fan-disks can experienced various form of vibrations by the different simultaneously acting independent Modes of stressing when one of them can be resonant. During engine operation one resonance form can have gradual transition to another form with another frequency under influenced air-stream that influence VHCF regime for short in-service time.

## REFERENCE

1. Shanyavskiy, A.A.:  
Tolerance fatigue cracking of aircraft components. Synergetics in engineering applications  
Monograph, Ufa, Russia, (2003)
2. Bathias C.; Paris P.C.:  
Gigacycle fatigue in mechanical practice  
Marcel Dekker, NY, USA, (2005)
3. Shanyavskiy A.A.:  
Modeling of metals fatigue cracking. Monograph, Ufa, Russia, (2007)
4. Shanyavskiy A.A.:  
Bifurcation diagram for in-service fatigued metals  
Procedia Engng, 2 (2010) No1, pp. 241-254
5. Shanyavskiy A.A.:  
Scales of metal fatigue cracking  
Physical Mesomech, 18 (2015) No2, pp. 87-98
6. Shanyavskiy A.A.; Losev A.I.:  
Fatigue crack growth in aeroengine compressor disks made from titanium alloys  
Fatigue & Fract of Eng. Mat. & Structures, 22 (1999), No6, pp. 949-966
7. Shanyavskiy A.A.:  
Fatigue limit – Material property as an opened or closed system? Practical view on the aircraft components failures in GCF area  
Int. Journal of Fatigue, 28 (2006), No11, pp. 1647-1657
8. Shanyavskiy A.A.; Potapenko Yu.A.:  
In-service very-high-cycle-fatigue of titanium alloy compressor blades of aircraft engines.  
Proc. 4-th Int. Conf. VHCF-4, 19-22 August, (2007), pp. 163-168
9. Nikitin A.; Palin-Luc T.; Shanyavskiy A.A.:  
Crack initiation in VHCF regime on forged titanium alloy under tensile and torsion loading modes  
Int. Journal of Fatigue, 93 (2016), No4, pp. 318-325.

**Corresponding author:** 106otdel@mail.ru



# **Materials databases and its application and numerical modelling**

## **INVITED**



**Tatsuo SAKAI**

Senior Fellow  
Research Organization of Science and Technology  
Ritsumeikan University  
1-1-1 Nojihigashi, Kusatsu, Shiga  
525-8577 JAPAN  
Phone: +81-77-561-2745  
Fax: +81-77-561-2665  
E-mail: [sakai@se.ritsumei.ac.jp](mailto:sakai@se.ritsumei.ac.jp)

Tatsuo SAKAI is currently a professor-emeritus of Ritsumeikan University, and a senior fellow of the Research Organization of Science and Technology, Ritsumeikan University, Japan. He has been teaching at Ritsumeikan University longer than 45 years, and has received several research and teaching awards. He has been played the role of chairman of many domestic and international committees such as organizing committee of the international conference of VHCF-3 and the Committee on Reliability Engineering in the Society of Materials Science, Japan(JSMS). Dr. T. SAKAI has published over 250 papers in refereed journals and 70 papers in conference proceedings in the areas of fatigue, reliability engineering, fracture mechanics and mechanical design. Some of his papers were well cited in International Journals. His current research interests are in fatigue properties of structural materials in the very high cycle regime, mechanisms of fatigue crack initiation and propagation, effects of microstructure and environments, databases of material properties and reliability engineering for the mechanical structures. Another subject of his research is the development of active use of various clean energies such as wind power, water power and solar energy. He has a couple of patents related to the fatigue testing machine and to the wind power generation system.

### **Expansion of JSMS Database on Fatigue Strength of Metallic Materials as to Include VHCF Data**

**Prof. Dr. T. Sakai**<sup>1</sup>, Prof. Dr. A. Sakaida<sup>2</sup>, Prof. Dr. A. Ueno<sup>3</sup>, Prof. Dr. K. Okada<sup>4</sup>, Prof. Dr. Y. Nakamura<sup>5</sup>, Prof. Dr. K. Hanaki<sup>6</sup>, K. Mukoyama<sup>7</sup>, Prof. Dr. N. Oguma<sup>8</sup>, Prof. Dr. T. Nakamura<sup>9</sup>, Prof. Dr. T. Matsumura<sup>10</sup>, Dr. H. Oguma<sup>11</sup>, Prof. Dr. Y. Shimamura<sup>12</sup>

<sup>1</sup>Ritsumeikan University, Research Organization of Science and Engineering - Kusatsu, Japan

<sup>2</sup>National Institute of Technology, Akashi College - Akashi, Japan

<sup>3</sup>Ritsumeikan University, Department of Mechanical Engineering - Kusatsu, Japan

<sup>4</sup>National Institute of Technology, Kagawa College - Takamatsu, Japan

<sup>5</sup>National Institute of Technology, Toyota College - Toyota, Japan

<sup>6</sup>Osaka University, Graduate School of Engineering - Suita, Japan

<sup>7</sup>Osaka University, Graduate School of Engineering - Suita, Japan

<sup>8</sup>University of Toyama, Faculty of Engineering - Toyama, Japan

<sup>9</sup>Hokkaido University, Graduate School of Engineering - Sapporo, Japan

<sup>10</sup>The University of Electro-Communications, Faculty of Informatics and Engineering - Chofu, Japan

<sup>11</sup>National Institute for Materials Science - Tsukuba, Japan

<sup>12</sup>Shizuoka University, Graduate School of Science and Technology - Hamamatsu, Japan

As a joint project of Committees on Fatigue and Reliability Engineering in the Society of Materials Science, Japan (JSMS), an electronic database on fatigue strength of metallic materials fabricated in Japan had been constructed and published in 1996. Book style of the same data compilation had been published at the same time by the JSMS and Elsevier. About twenty years have passed since the above publications of database and databook. Thus, a lot of new fatigue test data have been obtained during such a long period including many data on the very high cycle fatigue such as gigacycle regime. Based on such a circumstance, the JSMS have organized a new project to construct an electronic database on very high cycle fatigue. A lot of numerical data obtained by such fatigue tests were compiled together with many photographs of fracture surfaces. At the present conference of VHCF-7, fundamental view of the database and the first stage database constructed from domestic data in Japan are briefly introduced. In addition, some examples of useful applications of this database are also introduced to facilitate the academic and engineering applications in the wide variety of science and industries.

## EXPANSION OF JSMS DATABASE ON FATIGUE STRENGTH OF METALLIC MATERIALS AS TO INCLUDE VHCF DATA

T. Sakai<sup>1)</sup>, A. Sakaida<sup>2)</sup>, A. Ueno<sup>3)</sup>, K. Okada<sup>4)</sup>, Y. Nakamura<sup>5)</sup>, K. Hanaki<sup>6)</sup>, K. Mukoyama<sup>6)</sup>, N. Oguma<sup>7)</sup>, T. Nakamura<sup>8)</sup>, T. Matsumura<sup>9)</sup>, M. Nakagawa<sup>10)</sup>, H. Oguma<sup>11)</sup>, Y. Shimamura<sup>12)</sup>

<sup>1)</sup> Research Organization of Science and Engineering, Ritsumeikan University, 1-1-1 Noji-higashi, Kusatsu, Shiga, 525-8577 Japan

<sup>2)</sup> National Institute of Technology, Akashi College, 679-3 Nishioka, Uozumi, Akashi, Hyogo, 674-8501 Japan

<sup>3)</sup> College of Science and Engineering, Ritsumeikan University, 1-1-1 Noji-higashi, Kusatsu, Shiga, 525-8577 Japan

<sup>4)</sup> National Institute of Technology, Kagawa College, 355 Chokushi-cho, Takamatsu, Kagawa, 761-8058 Japan

<sup>5)</sup> National Institute of Technology, Toyota College, 2-1 Eisei-cho, Toyota, Aichi, 471-8525 Japan

<sup>6)</sup> Graduate School of Engineering, Osaka University, 2-1 Yamadaoka, Suita, Osaka 565-0871 Japan

<sup>7)</sup> Faculty of Engineering, University of Toyama, 3190 Gofuku, Toyama, 930-8555 Japan

<sup>8)</sup> Graduate School of Engineering, Hokkaido University, Kita 8, Nishi 5, Kita-ku, Sapporo, Hokkaido, 060-8628 Japan

<sup>9)</sup> The University of Electro-Communications, 1-5-1 Chofugaoka, Chofu, Tokyo, 182-8585 Japan

<sup>10)</sup> The Center for Information Processing, Shiga University, 1-1-1 Banba, Hikone, Shiga, 522-8522 Japan

<sup>11)</sup> National Institute for Materials Science, 1-2-1 Sengen, Tsukuba, Ibaraki, 305-0047 Japan

<sup>12)</sup> Graduate School of Science and Technology, Shizuoka University, 3-5-1 Johoku, Naka-ku, Hamamatsu, Shizuoka, 432-8561 Japan

### ABSTRACT

An electronic database on fatigue strength of metallic materials fabricated in Japan had been constructed and published in 1996, as a joint project of Committees on Fatigue and Reliability Engineering in the Society of Materials Science, Japan (JSMS). Book style of the same data compilation had been published at the same time by the JSMS and Elsevier. About twenty years have passed since the above publications of database and databook. Thus, a lot of new fatigue test data have been obtained during such a long period including many data on the very high cycle fatigue such as gigacycle regime. Based on such a circumstance, the JSMS has organized a new project to construct an electronic database including very high cycle fatigue data together with many photographs of fracture surfaces.

### KEYWORDS

Very high cycle fatigue, metallic materials, fracture surface, *S-N* data, mechanical properties, electronic database

## INTRODUCTION

In the design of machines and structures, fatigue strength of metallic materials is one of the most important design data to ensure the sufficient durability and safety of actual products [1]. Therefore, the Society of Materials Science, Japan (JSMS) had organized a joint project of Committees on Fatigue and Reliability Engineering in the JSMS to collect a number of fatigue test data of metallic materials. Thus, an electronic factual database on fatigue strength of metallic materials fabricated in Japan had been constructed and published in 1996 [2].

After the above database was published, almost two decades have passed and a lot of new fatigue test data have been obtained in the various activities such as universities and institutes. In order to collect those new data in nationwide scale of Japan, the society of the JSMS has again organized a new project in 2012. Fundamental format of the database is same as that in the former project, but some new concepts are also introduced in the present database construction system.

On the other hand, fatigue properties of metallic materials in very high cycle regime are in the active subject in the area of *Fatigue of Metals*, and a number of fatigue test data have been reported in such a research area [3-7]. Accordingly, experimental data in very high cycle fatigue are also collected together with new data in the conventional life region. Since fracture surface of the failed specimen provides an important information, photographs of fracture surfaces are also compiled in the present database.

## SCOPE OF THE DATABASE COMPILATION

A number of fatigue test data have been accumulated for various metallic materials in a wide variety of academic and engineering applications. Scope of the present project is given as follows;

**Materials:** Ferrous and nonferrous metals, exclusive of welded joints and clad metals.

**Types of fatigue tests:** Load and displacement controlled tension-compression, ultrasonic fatigue, rotating bending, plane bending and torsional fatigue tests with constant stress amplitude and mean stress are included in this database. Experimental results under combined stress, varying stress amplitude and impact, or strain-controlled low cycle fatigue, rolling contact fatigue and fretting fatigue are not included.

**Test environments:** Usual atmospheric environment at room temperature, similar environments at controlled temperature, humidity and pressure (vacuum), and inert and hydrogen gas environments are focused to collect except for corrosive environments.

**Date of the tests:** The date are those of fatigue tests completed after 1990.

In addition to the above restrictions, definitions and classifications were made concerning the fatigue test data together with the related information as follows;

**SN test data:** Fatigue test data based on ordinary testing method to obtain a conventional S-N relation or a fatigue limit or a strength at the given life, with no intention of statistical analysis.

**ST test data (Staircase data):** Fatigue test data obtained by the staircase method with an intention to determine the mean and variance (standard deviation) of the fatigue limit or the fatigue strength at the given life.

**PN test data:** Fatigue test data obtained by using a large number of specimens at one or more stress levels with an intention of statistical analysis on the fatigue life distribution or of knowing the mean and variance (standard deviation) of the fatigue strength by means of the Probit method.

**Reference data:** Information on material specifications and processing, lists of chemical compositions, records of heat treatments, data on mechanical properties, size and dimensions of the fatigue specimen together with its preparation and finishing conditions and fatigue testing conditions including the load and environment.

**Photographs of fracture surfaces:** Fracture surface of the failed specimen provides an important information to analyze the fatigue mechanism of the material. Thus, photographs of fracture surfaces are collected and compiled in the database.

**Literature:** Bibliographic citations for published data are also compiled.

All the data in the present database are compiled depending upon the individual test series for each kind of material under the definite testing condition. A unique coding system was accepted to compile the fatigue test data. This coding system is a combination of two basic codes; a contributor's code of four digits and a test series code of four digits (series number). The former is assigned to each contributor, and the series number is assigned to each fundamental set of data by each contributor. In addition, photographs of fracture surfaces for the respective failed specimens can be accessed with reference to a specially designed code number to link the numerical test results and the fracture surfaces.

## FUNDAMENTAL STRUCTURE OF THE DATABASE

All the data for each test series contributed by each person are input by using a set of twelve datasheets including the comment sheet as follows;

**Datasheet of Basic Data (I):** Contributor, conductor of experiment, corresponding person of data-input, Journal information etc. are entered in this datasheet.

**Datasheet of Basic Data (II):** Material, forming process, heat treatment, surface treatment etc. are entered in this datasheet.

**Datasheet of Basic Data (III):** Grain size/grain size No., cleanliness, chemical composition etc. should be entered in this datasheet.

**Datasheet of Basic Data (IV):** Hardness test conditions and the experimental results are entered in this datasheet.

**Datasheet of Basic Data (V):** Tensile test conditions and corresponding experimental results are entered in this datasheet.

**Datasheet of Basic Data (VI):** Impact test conditions and corresponding experimental results are entered in this datasheet.

**Datasheet of Basic Data (VII):** Fatigue test conditions including the specimen preparation are entered in this datasheet.

**Fatigue Test Results:** SN data / ST data / PN data are entered by using this datasheet.

**Photographs of Fracture Surface:** Photographs of fracture surfaces are compiled in this datasheet.

**Mapping Photographs for Element Analysis:** Mapping photographs for inclusions are compiled here.

**Datasheet for File Name of Figure:** File names of additional figures are input in this datasheet.

**Comments Sheet:** Comments to facilitate further understandings are entered in this datasheet.

## EXAMPLES OF THE ENTERED FATIGUE DATA

Based on the coding system explained above, fatigue data for a number of test series have been entered in the present database. Among them, a typical example of an entire test series for the bearing steel [JIS:SUJ2] contributed by T. Sakai is introduced here. Full information

required as basic data for a series of fatigue test is entered in the datasheets from (I) to (VII). Especially, the detailed information of the fatigue testing conditions is entered in the Datasheet of Basic Data (VII). In the following example, code of the contributor is “0161”, and the test number is “0010”. Material code is SUJ2 standardized as JIS G4805 in 1999, and type of specimen is “round bar”, respectively. Size of specimen, stress concentration factor, surface treatment, etc. are entered in the corresponding columns designated in the respective datasheets. However, only the limited part of left-hand and upper corner in each datasheet is indicated in this paper due to the page limitation.

Code of Contributor (4 digits)	Test No. (4 digits)	Database on Fatigue Strength of Metallic Materials: Datasheet of Basic Data (I) (Contributor of Data, Conductor of Experiment, Conductor of Data-Input, Journal Information)	
0161	0010		
Record No. (4 digits)	Contributor	Name of Contributor (Ex. Taro ZAIRYOU)	Affiliation of Contributor (Ex. Department of Mechanical Engineering, Zairyou University)
0010	XC	Tatsuo SAKAI	Research Organization of Science and Engineering, Ritsumeikan University
Record No. (4 digits)	Conductor	Name of Experiment Conductor (Ex. Taro ZAIRYOU)	Affiliation of Experiment Conductor (Ex. Department of Mechanical Engineering, Zairyou University)
0020	XT	Mitsuhiro TAKEDA	Graduate School of Science and Engineering, Ritsumeikan University
Record No. (4 digits)	Conductor	Name of Data-input Conductor (Ex. Taro ZAIRYOU)	Affiliation of Data-input Conductor (Ex. Department of Mechanical Engineering, Zairyou University)
0030	XW	Tatsuo SAKAI	Research Organization of Science and Engineering, Ritsumeikan University

Code of Contributor (4 digits)	Test No. (4 digits)	Database on Fatigue Strength of Metallic Materials: Datasheet of Basic Data (II) (Material, Forming Process, Heat Treatment, Surface Treatment)								
0161	0010									
Record No. (4 digits)	Material	Code of Material								
		Category of Standard	Name of Standard	Describe the Standard (if other is selected)	Code of Standard	Year	Code of Material	Input "equivalent" (if equivalent material is used)	Category of Metal	
0100	GA	standard specification number	JIS				SUJ2		high carbon chromi	
Record No. (4 digits)	Material	Melting Method			Oxygen Removing Method	Describe the Method (if other is selected)	Material Situation	Describe the Situation (if other is selected)	Shape of Material	Desc (if ot
		Name of Method	Describe the method (if other is selected)	Atmos-phere	Describe Atmosphere (if other is selected)					
0110	GB							as manufactured		round bar

Code of Contributor (4 digits)	Test No. (4 digits)	Database on Fatigue Strength of Metallic Materials: Datasheet of Basic Data (III) (Grain Size, Grain Size No., Cleanliness, Chemical Composition)												
0161	0010													
Record No. (4 digits)	Grain Size	Grain Size/Grain Size No.	Measuring Method	Describe the Method (if other is selected)	Standard of Measuring Method					Grain Size or G				
					Name of Standard	Describe the Standard (if other is selected)	Code of Standard	Year	Number of Data Points	Grain Size or Grain Size No.	Standard Deviation	Unit	Coefficient of Variation	Maxi
0140	GS													
Record No. (4 digits)	Cleanliness	Standard of Measuring Method (JIS)			Cleanliness % (JIS)						Source of Data		Describe the Sc (if other is selected)	
		Name of Standard	Code of Standard	Year	Number of Data Points	Magnifica-tion of Microscope	Series A	Series A+B	Series A+B+C	Total	In Case of High Carbon Chromium Bearing Steel (JIS G 4805)			
											Ser. A	Ser.(B+D)	Ser.(A+B+D)	
0150	GP	JIS									0.012	0.008	0.020	experimental data

In every datasheet in the present data-coding system, all the data columns are classified into five different colors depending on the respective categories as follows;

**Green columns:** If the code of contributor and the test number are entered in the columns in the datasheet of basic data (I), the pair of these data such as 0161-0010 are automatically entered in the corresponding columns in all the datasheet.

**Yellow columns:** Codes of data records such as XC, XT, XW, AU, GA, GB, GC, GS, GP, FE,

HP, TS, TP, IS, IP, FS, FP and PG are entered in advance. Thus, contributor does not need to input any data in these columns. But, only in the column of SN/ST/PN in the sheet of Fatigue Test Results, the kind of data record should be entered among SN, ST and PN.

**Light blue columns:** Contributors have to enter the corresponding information by selecting each of numerical data or alphabetical characters together with some comments if necessary.

**Thick blue columns:** If contributors move the mouse-cursor into the columns and give a left-hand click, a menu screen indicating respective items prepared in advance can be pull down. Then, if the contributors select the appropriate item, the required data can be entered automatically in the corresponding columns.


Code of Contributor (4 digits)		Test No. (4 digits)		Database on Fatigue Strength of Metallic Materials: Datasheet of Basic Data (IV) (Hardness Test)											
0161		0010													
Record No. (4 digits)	Post-treatment, Hardness	Kind of Post-treatment Input Data following the Respective Treatments, if Several Treatments was performed.	Describe the Actual Treatment (if other is selected)	Surface Treatment		Surface Roughness		Pre-strain or Hydrogen Charge							
				Kind of Surface Treatment	Describe the Surface Treatment (if other is selected)	Kind of Surface Roughness	Describe the Kind of Roughness (if other is selected)	Roughness $\mu\text{m}$	Pre-strain or Hydrogen Charge	Unit Describe the Unit (if other unit was selected)	Atmosphere	Describe Atmosp (if other select)			
	HP														


Code of Contributor (4 digits)		Test No. (4 digits)		Database on Fatigue Strength of Metallic Materials: Datasheet of Basic Data (V) (Tensile Test)											
0161		0010													
Record No. (4 digits)	Tensile Specimen	Standard of Specimen						Describe the Direction (if other is selected)	Shape of Specimen						
		Name of Standard	Describe the Standard (if other is selected)	Code of Standard	Year	Code of Shape	Direction extracted from Material		Shape of Specimen	Describe the Shape (if other is selected)	Type of Specimen	Describe l (if other l selec)			
0180	TS	JIS				14A	LL		round bar			smooth			
Record No. (4 digits)	Post-treatment, Surface Roughness	Kind of Post Treatment	Describe the Kind (if other is selected)	Surface Treatment		Surface Roughness		Pre-strain/Hydrogen Charge							
				Kind of Surface Treatment	Describe the Surface Treatment (if other is selected)	Kind of Surface Roughness	Describe the Roughness (if other is selected)	Roughness $\mu\text{m}$	Pre-strain or Hydrogen Charge	Unit Describe the Unit (if other is selected)	Atmosphere				
	TP														

Code of Contributor (4 digits)		Test No. (4 digits)		Database on Fatigue Strength of Metallic Materials: Datasheet of Basic Data (VI) (Impact Test)											
0161		0010													
Record No. (4 digits)	Impact Specimen	Standard of Specimen						Direction extracted from Material	Describe the Direction (if other is selected)						
		Name of Standard	Describe the Standard (if other is selected)	Code of Standard	Year	Code of Shape	Shape of Notch			Describe the Notch Shape (if other is selected)	Height of Specimen	Wt Spe			
	IS														
Record No. (4 digits)	Post-treatment / Surface Roughness	Kind of Post Treatment	Describe the Post Treatment (if other is selected)	Surface Treatment		Surface Roughness		Pre-strain/Hydrogen Charge							
				Kind of Treatment	Describe the Surface Treatment (if other is selected)	Kind of Surface Roughness	Describe the Roughness (if other is selected)	Roughness $\mu\text{m}$	Pre-strain or Hydrogen Charge	Unit Describe the Unit (if other is selected)					

**Beige columns:** If contributors selected the item of “other” in the thick blue columns, the contributors have to enter the information to explain the actual situation into the next column of beige color.

Significant advantage of the present database is the fact that a lot of photographs of fracture surfaces have been stored to facilitate the research on the very high cycle fatigue of metallic materials. Electronic data size of photographs is extremely higher comparing with the size of numerical data and character data. The data property of the photographs is quite differ from that of numerical and character data. In such a circumstance, the committee has developed a special method to compile many photographs of the fracture surfaces in the present database. This system is designated such that each photograph is linked to the corresponding specimen. For example, if a photograph for the specimen of No.2 is provided in the previous datasheet, the linking code is given as “0161-0010-0002-a-01.jpg”. The character of “a” in the linking code indicates one side of a pair of failed specimen. If another photograph for the fracture surface of the opposite side is also stored in the database, the character of “b” is entered instead of “a”. When another observation at different site of the same fracture surface is filed in the database, only the end code of two digits should be changed as “0161-0010-0002-a-02.jpg”. If a definite site inside the certain photograph was observed with some higher magnification, the observation site should be indicated. In such a case, an additional photograph is inserted to identify the observation site of the original photograph. In order to show this situation, the character of “Z” is attached at the linkage code such as “0161-0010-0003- a-02-Z.jpg”.

Code of Contributor (4 digits)		Test No. (4 digits)		Database on Fatigue Strength of Metallic Materials: Datasheet of Basic Data (VII) (Fatigue Test)									
0161		0010											
Record No. (4 digits)	Fatigue Specimen	Standard of Specimen					Direction extracted from Material	Describe the Direction (if other is selected)	Type of Specimen	Describe the Specimen Type (if other is selected)	Kind of Specimen		
		Name of Standard	Describe the Standard (if other is selected)	Code of Standard	Year	Code of Shape							
0200	FS	other	Research Group for Statistical Aspects of Material Strength				LL		round bar		hourglass		
Record No. (4 digits)	Fatigue Specimen	Dimensions of Tested Portion						Chuckling Portion		Stress Concentration Factor	Method to determine the Value	Describe the Method (if other is selected)	Finishing Method of Tested Portion
		Width(Plate /Square Bar) Outer Dia. (Pipe)	Thickness (Plate/Sq. Bar/Pipe) Diameter (Round Bar/Wire)	Notch Radius	Unit	Notch Angle	Unit	Width(Plate /Square Bar) Diameter (Pipe)	Unit				
0210	FF		3	7	mm			10	mm	1.06	diagram		grinder

Code of Contributor (4 digits)		Test No. (4 digits)		Database on Fatigue Strength of Metallic Materials: Datasheet of Fatigue Test Results of SN, ST, PN Data)									
0161		0010		 <p>SN and PN data should be input in order of higher stress level. These data at the same stress level should be input in order of shorte life. ST data should be input in order of the fatigue test.</p>									
Record No. (4 digits)	SN or ST or PN	Specimen No.	Stress Amplitude (MPa)	Number of Stress Cycles (Input such as 3.574E+05)	Input Failure or Runout	Category of Failure							
						Crack Initiation Site	Describe the Initiation Site (if other is selected)						
1	0250	SN	1-301	1800	3.070E+03	failure	surface						
2	0251	SN	1-281	1800	4.510E+03	failure	surface						
3	0252	SN	1-302	1700	4.370E+03	failure	surface						
4	0253	SN	1-282	1700	7.930E+03	failure	surface						

Fracture surfaces of the specimen of No.7 in the interior fracture mode is indicated in Fig.1. It is well known that a clear mark of “fish-eye” is observed in the interior fracture mode and an inclusion can be often found at the central portion of the fish-eye. In order to link the respective photographs, some additional technique is required here. If one observes the central portion



of the fish-eye in the left hand fracture surface, the observation site at higher magnification should be identified by indicating a square frame of “A” in the middle photograph. Then, the high magnification photograph of the specific frame of “A” is provided as the right hand photograph. Thus, the middle photograph is only an additional photograph to identify the observation site. In such a case, the specific character of “Z” is attached to the coding system as “0161-0010-0007- a-01-Z.jpg”. In order to indicate the observation site at the high magnification, a character assigned to the square frame “A” is also attached to the coding system as “0161-0010- 0007- a-01-Z-[A].jpg”. Of course, the code of [A] in the right hand photograph means that this photograph was taken at the site of the square frame “A” in the middle photograph of “0161-0010-0007-a-01-Z.jpg”.

In some cases, various kinds of additional comments of supplementary explanations are provided for the individual items consisting the present database. In such cases, comments sheet is further prepared in the data collection system. Each comment is linked to the corresponding item in the related datasheet by using the coding system such as “0161-0010-xxxx and so on.

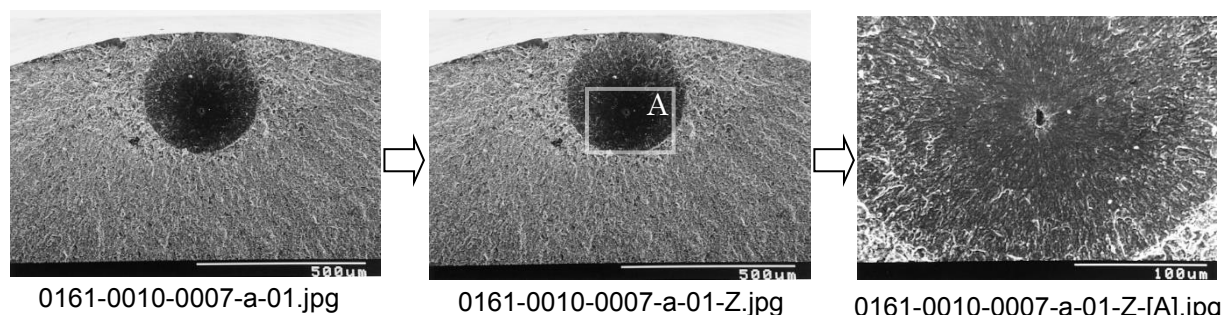


Fig. 1: SEM photographs of fracture surface for the specimen of No.7

## ADMINISTRATION OF DATA COLLECTION AND DATABASE SERVICE

In the present project of the data collection, both of numerical data and photographs should be filed in the Excel File by each contributor as explained in the previous section. Then, those data should be saved in the electronic media such as flash-memory. These electronic media saved required data should be sent to a certain key center of the society of the JSMS. Details of the data collection project and the concrete procedure to offer the fatigue data are being explained in the document attached to the e-mail asking the data submission.

Since the present project has been financially supported by the society of JSMS, the entire cost required to this project should be covered by all the users of the accomplished database. From this point of view, an appropriate payment system would be introduced carefully considering the requests from general users of the present database. As the guideline at the present stage, the amount of fee for the database service should be designated into several categories depending on the user situation such as the data contributor, the task group member and the member of the JSMS. However, the concrete prices and the payment system would be firmly discussed and established after the database construction project was accomplished and the total cost was determined.

As a parallel project in the society of the JSMS, the Database on Fatigue Strength of Metallic Materials already established is planned to open into the worldwide use through the internet website. In such a circumstance, the new database on the experimental data for the very high cycle fatigue reported in this paper would be similarly opened by using the same system

through the internet website. It is very important and difficult to keep the security of the database in the present complicated situation around the recent ICT or IoT society. Accordingly, a steady database security system is now being developed by the awful efforts of the above task group in the society of the JSMS.

## CONCLUDING REMARKS

In this paper, the fundamental scope and format of data collection organized by the society of the JSMS were firstly introduced, and some examples of the actually compiled database on the very high cycle fatigue of metallic materials were indicated in order to facilitate the better understanding of the database structure and the sophisticated coding system. However, we are now facilitating the data-input for fatigue test data on some common researches organized in Japan for metallic materials such as high strength steels of JIS:SUJ2, SCM435, SNCM439, aluminum alloy of JIS:ADC12, magnesium alloys of AZ31, AZ61, AZ80 and AMCa602, titanium alloy of Ti-22V-4Al and bulk amorphous alloy of  $Zr_{55}Al_{10}Ni_5Cu_{30}$ . At the first stage of this project, all the experimental fatigue data obtained in Japan are targeted and some refinements are expected in the format and the coding system. Then, fatigue test data obtained in overseas countries would be targeted at the second stage in the near future.

The most important point of this project is that the sufficient quantity of experimental data on the very high cycle fatigue are collected including a number of photographs for the fracture surfaces of the failed specimens. Thus, the authors are earnestly expecting that a number of researchers all over the world would join us to contribute their experimental results together with many photographs of the fracture surface. The authors hope that the present database is widely used to facilitate the research on the very high cycle fatigue of metallic materials and is applied to the fatigue design as the reference data to ensure the safety of the mechanical structures in the industrial society.

## REFERENCES

- [1] Jono M. edited: Handbook for Fatigue Design, Yokendo Ltd., Tokyo, pp.1–5, 1995
- [2] Shiozawa K.; Sakai T. Edited: Database on Fatigue Strength of Metallic Materials, The Society of Materials Science, Japan, Kyoto, 1996
- [3] Bathias C.; Paris P. C.: Gigacycle Fatigue in Mechanical Practice, Marcel Dekker, New York, 2005
- [4] Sakai T.: Review and Prospects for Current Studies on Very High Cycle Fatigue of Metallic Materials for Machine Structural Use, Journal of Solid Mechanics and Materials Engineering, Vol.3, No.3, (2009), pp.425-439
- [5] Sakai T.; Sato Y.; Oguma N.: Characteristic *S-N* Properties of High-carbon-chromium-Bearing Steel under Axial Loading in Long-life Fatigue, Fatigue and Fract. Engng. Mater. Struct., Vol.25, (2002), pp.765-773
- [6] Sakai T.; Lian B.; Takeda M.; Shiozawa K.; Oguma N.; Ochi Y.; Nakajima M; Nakamura T.: Statistical Duplex *S-N* Characteristics of High Carbon Chromium Bearing Steel in Rotating Bending in Very High Cycle Regime, International Journal of Fatigue, Vol.32, No.3, (2010), pp.497-504
- [7] Hong Y.; Lei Z.; Sun C.; Zhao A.: Propensities of Crack Interior Initiation and Early Growth for Very-High-Cycle Fatigue of High Strength Steels, International Journal of Fatigue, Vol.58, (2014), pp.144-151

**Corresponding author:** sakai@se.ritsumei.ac.jp

# **SIMULATION OF THE CYCLIC DEFORMATION BEHAVIOR OF AUSTENITIC STAINLESS STEELS BELOW THE VHCF STRENGTH**

P.-M. Hilgendorff<sup>1)</sup>, A. Grigorescu<sup>2)</sup>, M. Zimmermann<sup>3)</sup>, C.-P. Fritzen<sup>1)</sup>, H.-J. Christ<sup>2)</sup>

<sup>1)</sup> Institut für Mechanik und Regelungstechnik - Mechatronik, Universität Siegen, 57068 Siegen, Germany

<sup>2)</sup> Institut für Werkstofftechnik, Universität Siegen, 57068 Siegen, Germany

<sup>3)</sup> Institut für Werkstoffwissenschaft, Technische Universität Dresden, 01062 Dresden, Germany

Corresponding author: claus-peter.fritzen@uni-siegen.de

## **ABSTRACT**

A model describing the VHCF deformation behavior of a stable and a metastable austenitic stainless steel is presented and solved within two-dimensional (2-D) morphologies of microstructures by using a boundary element method. In case of the metastable alloy a pronounced localization of plastic deformation in shear bands followed by a deformation-induced martensitic phase transformation determines the cyclic deformation behavior. The stable alloy undergoes only a very limited local plastic deformation in shear bands with almost no phase transformation. Based on experimental observations of the cyclic deformation behavior at stress amplitudes below the VHCF strength a model was developed that can simulate the characteristic mechanisms for plastic deformation in shear bands and for deformation-induced martensitic phase transformation from the  $\gamma$ -austenite to the  $\alpha'$ -martensite. Since the deformation-induced martensitic phase transformation depends amongst others on the initial sample temperature, the effect of a moderate increase of temperature is reflected in the model. Simulation results are directly compared to the observed deformation evolution on the real specimen surfaces and a comparison based on the transient behavior (cyclic softening and hardening) is carried out. The transient behavior of the material is characterized by the change in resonant behavior during cyclic deformation, which is experimentally monitored during fatigue tests and evaluated from simulated hysteresis loops. Good agreement of results confirms the model assumptions and, finally, a more profound understanding of the VHCF deformation behavior of both austenitic stainless steels is provided.

## **KEYWORDS**

Simulation, austenitic stainless steel, very high cycle fatigue, cyclic deformation mechanisms, resonant behavior

## **INTRODUCTION**

Reliable prediction of fatigue life under VHCF condition demands a detailed knowledge and a true understanding of the basic microstructurally driven deformation processes. For that purpose the present study focuses on the investigation of cyclic deformation behavior of a metastable and a stable austenitic stainless steel (AISI 304 and AISI 316 L).

In the following paragraphs at first the results of experimental examinations are given and then the proposed mechanisms of cyclic plastic deformation are presented in the simulation model. After a short explanation of the numerical method, the results of simulation studies are demonstrated and discussed on the basis of micrographs of fatigued specimen surfaces and on the basis of the monitored resonant behavior.

## EXPERIMENTAL CHARACTERIZATION

Fatigue tests were carried out on a resonant testing machine and revealed that the metastable austenitic stainless steel AISI 304 in the initially fully austenitic condition possesses a VHCF strength of about 240 MPa and undergoes localization of plastic deformation in shear bands and a deformation-induced  $\alpha'$ -martensitic phase transformation during fatigue at the VHCF strength [1]. Emerging slip markings observed on the confocal microscopy image of the specimen surface of AISI 304 after  $2 \cdot 10^7$  cycles in Fig. 1a indicate a pronounced localization of plastic deformation in shear bands. The transmission electron microscopy (TEM) micrograph in Fig. 1c demonstrates that plastic deformation in shear bands is mainly related to stacking faults (light grey stripes) and  $\alpha'$ -martensite is generated at intersections of stacking faults (white areas). The stable austenitic stainless steel AISI 316 L, that exhibits a lower value of VHCF strength of about 190 MPa, shows clearly less and only very local plastic deformation in shear bands (marked with an arrow in Fig. 1b) [1]. In case of AISI 316 L, the martensitic phase transformation was almost not observed.

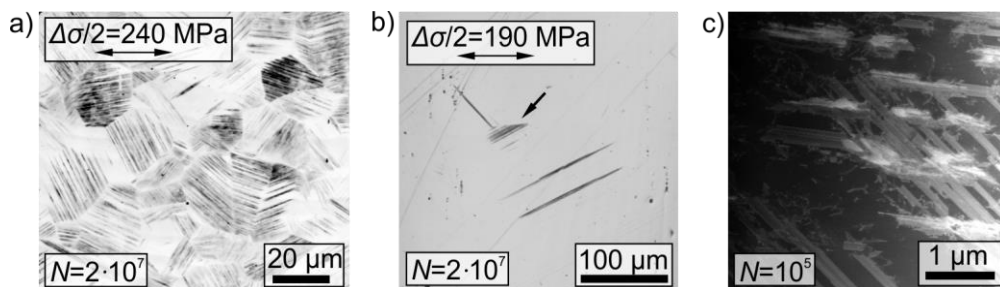


Fig. 1: a) Confocal laser microscope image of a fatigued specimen surface of AISI 304 ( $\Delta\sigma/2 = 240$  MPa,  $N=2 \cdot 10^7$  cycles) and b) of AISI 316 L ( $\Delta\sigma/2 = 190$  MPa,  $N=2 \cdot 10^7$  cycles); c) TEM micrograph of the microstructure of AISI 304 ( $\Delta\sigma/2 = 240$  MPa,  $N=10^5$  cycles) [1]

The resonant behavior of both materials was characterized in terms of the resonant frequency ratio  $\eta_{res}$ , which represents the relation of the resonant frequency  $f_{res}$  and the eigenfrequency  $f_0$  of the fatigue specimens. Both frequencies were monitored during fatigue tests on the resonant testing machine [1]. The corresponding results are given in Fig. 3 by the continuous black curves. From a mechanical point of view a decrease of  $\eta_{res}$  is equivalent to softening and, conversely, an increase of  $\eta_{res}$  corresponds to hardening. The metastable austenitic stainless steel describes a strong transient behavior over cyclic loading consisting of a beginning cyclic softening (decrease of  $\eta_{res}$ ) followed by cyclic hardening (increase of  $\eta_{res}$ ). The cyclic deformation behavior of the stable austenitic stainless steel is characterized by an increase of  $\eta_{res}$  denoting continuous slight cyclic hardening.

The aim of the present work is to give a more profound insight into the relevant deformation mechanisms of austenitic stainless steels and their effect on the resonant behavior. Therefore, in the following a simulation model is proposed.

## SIMULATION MODEL

The model focuses on plastic deformation in shear bands and on deformation-induced martensite formation as they are the predominant microstructural processes of AISI 304 and of AISI 316 L (without phase transformation) during cyclic deformation in the VHCF regime.

The localization of cyclic plastic deformation in shear bands will be considered by certain mechanisms which were proposed in [2] and are shortly summarized as follows. It is assumed that a shear band is formed in the microstructure once a critical resolved shear stress  $\tau_c$  in the most critical slip system is exceeded. Inspired by the models of Tanaka & Mura [3] and Lin [4] a shear band is represented by two closely located layers in the 2-D plane that allows considering an irreversible fraction of sliding on one of the two layers during each loading half cycle. Dislocation hardening is taken into account by increasing the flow stress  $\tau_F$  depending

on the previously evolved sliding deformation. In case of the metastable austenitic stainless steel with its planar slip character (low stacking fault energy) the flow stress  $\tau_F$  is chosen to be smaller than the critical resolved shear stress  $\tau_c$  because it is assumed that after formation of a shear band the barrier function within the corresponding shear planes is weakened by initial dislocations (here called 'short range order effect'). The effect of temperature on plastic deformation in shear bands is incorporated into the model by adjusting the critical resolved shear stress  $\tau_c$  and flow stress  $\tau_F$  depending on the yield strength measured in tensile tests as a function of temperature [5].

Apart from a surface roughening by shear bands, the material AISI 304 also undergoes deformation-induced martensitic transformation (from  $\gamma$  to  $\alpha'$ ) at intersecting shear bands in the VHCF regime [2]. According to the models of Bogers & Burgers [6] and Olsen & Cohen [7], in the present study martensite is emerging in a modeled microstructure once plastic shear deformation occurs simultaneously in two slip systems that are compatible to the two characteristic Bogers and Burgers shears. For that purpose, sliding deformation in a second slip system is determined by means of an analytical model based on the theory of dislocation pile-ups at grain boundaries (see details in [2]). Each martensite nucleus is directly included into the modeled microstructure as an independent domain. The transformation-induced volume expansion in terms of the strains  $\epsilon^M$  within the domain is characterized by calculation of the true shape deformation as a result of both participating shear deformations [8]. Following the kinetic model of Olsen & Cohen [9] the amount of generated martensite is affected by temperature-dependent parameters describing the influence of the stacking fault energy and chemical driving force. Both parameters were characterized based on investigations applying tensile tests [5].

All required modelling parameters were referred to experimental data or estimated on the basis of preliminary simulation studies and can be found in [2]. After the mechanisms of plastic deformation in shear bands and deformation-induced martensitic transformation have been shortly introduced, in the following the numerical method is presented.

## NUMERICAL METHOD

The calculation of stresses and displacements within modeled microstructures is carried out by using a 2-D elastostatic formulation of the boundary element method (BEM). The method is well suited to investigate the effect of the proposed simulation model because the representation of sliding deformation can be easily realized and the meshing is only confined to boundaries such as grain or phase boundaries and shear bands.

The BEM used in this study is based on two boundary integral equations: the displacement boundary integral equation, which is applied on the external boundary (grain and phase boundaries), and the stress boundary integral equation, which is used on the slip line faces (shear bands). Both equations are given in [2]. Due to consideration of general elastic anisotropic properties it enables computing 3-D stresses and displacements within the 2-D plane under presumption of general plane strain or stress conditions. This feature is very important for adequately representing the sliding deformation in the true spatial slip systems. Moreover, the transformation-induced strains  $\epsilon^M$  can be considered as initial strains in domains assigned to the martensite phase.

The substructure technique allows coupling individual homogeneous structures (grains, phases), so that finally a 2-D microstructure consisting of austenite grains and martensite domains can be represented.

## SIMULATION OF THE VHCF-DEFORMATION BEHAVIOR OF AUSTENITIC STAINLESS STEELS

The implementation of the simulation model into the BEM allows for simulation of the deformation evolution in shear bands and martensitic phase transformation in 2-D microstructures. The investigation was carried out on the basis of the real microstructure of

AISI 304 and AISI 316 L characterized by means of scanning electron microscopy (SEM) in combination with the electron backscattered diffraction (EBSD) technique and the orientation imaging microscopy (OIM) analysis. In this study, the simulation results are shown in terms of the distribution of simulated maximum resolved shear stresses  $\tau_{MRSS}$  in the most stressed slip systems of modeled microstructures and in terms of the resonant frequency ratio characterizing the resonant behavior.

Figs. 2a and b show the SEM image and the phase map of an examined microstructure on the specimen surface of AISI 304 fatigued at the VHCF strength of  $\Delta\sigma/2=240$  MPa up to  $2 \cdot 10^7$  loading cycles. The SEM image indicates a strong plastic deformation in shear bands, and the phase map reveals that a phase transformation from the  $\gamma$ -austenite to the  $\alpha'$ -martensite occurred. Due to computational effort, simulation of plastic deformation was only considered within the grains enclosed by the white dashed lines in Fig. 2b. In order to satisfy the true cyclic deformation of many experimental cycles within a significantly lower number of simulated cycles, in the simulations the influences of cyclic slip irreversibility, hardening and martensitic transformation rate were artificially increased. By doing so, 10 simulated cycles of AISI 304 could be referred to  $N_{exp}=10^6$  experimental cycles and 10 simulated cycles of AISI 316 L to  $N_{exp}=0.5 \cdot 10^6$  experimental cycles [2]. Figs. 2c-d show the results of simulated shear stresses  $\tau_{MRSS}$  in each case at the maximum external load (240 MPa) after 5 and 10 loading cycles  $N_{sim}$ . Modeled shear bands are emphasized by thin lines and the martensitic transformation is recognizable by distinctive shear stress peaks around the generated martensite nuclei. The comparison between the surface slip markings found in the SEM image (Fig. 2a) and the modeled shear band layers (Figs. 2c-d) illustrates that shear band formation in designated slip systems was correctly reflected in the simulation model. Also, the sites of generated martensite domains in the simulation are in good agreement with the distribution of the martensite phase presented in Fig. 2b.

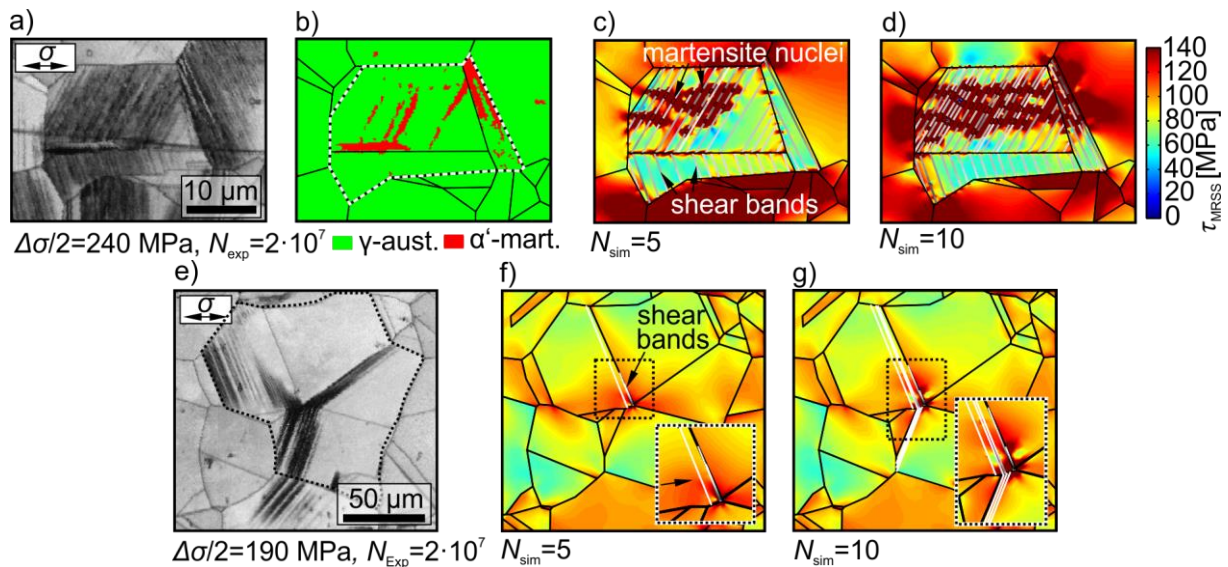


**Fig. 2:** a) SEM image, b) phase map of the examined real surface area of AISI 304 ( $\Delta\sigma/2=240$  MPa,  $N_{exp}=2 \cdot 10^7$ ), c)-d) distributions of simulated shear stresses  $\tau_{MRSS}$  at 5 and 10 simulated loading cycles  $N_{sim}$  (AISI 304, loading amplitude  $\Delta\sigma/2=240$  MPa); e) SEM image of the examined real surface area of AISI 316 L ( $\Delta\sigma/2=190$  MPa,  $N_{exp}=2 \cdot 10^7$ ), f)-g) distributions of simulated shear stresses  $\tau_{MRSS}$  at 5 and 10 simulated loading cycles  $N_{sim}$  (AISI 316 L, loading amplitude  $\Delta\sigma/2=190$  MPa).

Fig. 2e show the SEM image of the examined real surface area of the stable austenitic stainless steel AISI 316 L fatigued at the VHCF strength of  $\Delta\sigma/2=190$  MPa up to  $2 \cdot 10^7$  loading cycles. The SEM image shows that AISI 316 L undergoes a clearly lower plastic deformation in shear bands than AISI 304. The simulation of cyclic plastic deformation was confined to the grains enclosed by the black dotted lines in Fig. 2e. Figs. 2f-g show the results of simulated

shear stresses  $\tau_{\text{MRSS}}$  after 5 and 10 cycles  $N_{\text{sim}}$  at the maximum external load (here 190 MPa). Like in the previous study, modeled shear bands are emphasized by thin lines. The martensitic transformation model was disabled due to the stable condition of AISI 316 L. The simulation results confirm the reduced tendency of the stable austenitic stainless steel to undergo plastic deformation in shear bands. This observation can be referred to the higher values for the critical resolved shear stress  $\tau_c$  for shear band formation and flow stress  $\tau_f$ , along with a smaller external loading (VHCF strength). The comparison between surface slip markings found in the SEM image (Fig. 2e) and simulated shear band layers (Fig. 2f-g) illustrates that shear bands were formed in the correct slip systems.

In case of the metastable austenitic stainless steel AISI 304, shear bands were formed in all relevant grains. A gradual increase of the number of shear bands with increasing loading cycles was observed as a result of the renewed increase of shear stresses around existing shear bands allowing the new formation of shear bands in the immediate vicinity. The increase could be referred to the cyclic hardening and cyclic slip irreversibility of each shear band and to the hindrance of plastic sliding deformation by martensite domains.

For the stable austenitic stainless steel a higher cyclic slip irreversibility (due to higher stacking fault energy [2]) and the absence of blocking by martensite domains led to drastic shear stress peaks at grain boundaries, also giving rise to further shear band formation. The high shear stress peaks at grain boundaries pointed out critical sites regarding crack initiation. By contrast, the martensitic transformation in the metastable austenitic stainless steel led to a stagnating increase of plastic deformation due to the blocking of shear bands by martensite domains. Thus, it seems reasonable to suppose that this barrier to plastic deformation provides an explanation for the higher VHCF strength of AISI 304 compared to AISI 316 L.

Fig. 3 shows a qualitative comparison of the resonant frequency ratio  $\eta_{\text{res}}$  from simulation and experiment. The simulated cycles  $N_{\text{sim}}$  are shown at the top and the cycles from experiment  $N_{\text{exp}}$  at the bottom. The solid curves represent the results from experiment for AISI 304 and AISI 316 L at room temperature (RT). For AISI 304, additionally, one curve is shown for  $T=150^\circ\text{C}$  (solid grey line). In simulations, the force displacement hysteresis loops are used to determine the resonant frequency ratio  $\eta_{\text{res}}$  for each simulated cycle by applying a hysteretic and viscous damping model [2].

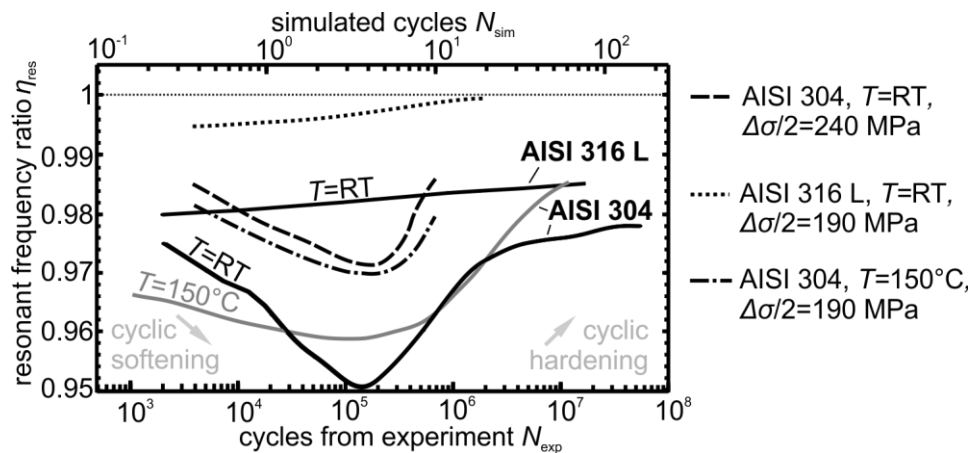


**Fig 3:** Qualitative comparison of resonant frequency ratio  $\eta_{\text{res}}$  from simulations (dashed, dotted and dash dotted curves with scale of simulated cycles at the top) and experiment (solid curves for AISI 304 and AISI 316 L with scale of cycles from experiment at the bottom) [2].

The results from simulations are indicated by non-continuous curves. The dashed curve belongs to the simulation of AISI 304 at RT and the dotted curve to the simulation of AISI 316 L at RT. In addition, the dash dotted curve belongs to the simulation of AISI 304 at  $T=150^\circ\text{C}$ . The dashed curve in Fig. 3 shows qualitatively good agreement to the experimentally measured curve of AISI 304 at RT. The beginning cyclic softening of AISI 304 could be attributed to the gradual new formation of shear bands in combination with the 'short range order effect' [2]. Once shear band saturation was reached, the local cyclic hardening and

irreversibility in each shear band dominated the global behavior resulting in global hardening. Additionally, the ongoing blocking of shear bands by martensite domains significantly enhanced the cyclic hardening.

In case of the simulated stable austenitic stainless steel the dotted curve in Fig. 3 shows a constant increase of the ratio  $\eta_{res}$  and thus continuous cyclic hardening. This is in good agreement with the experimental results obtained for AISI 316 L. In particular, the reduced tendency to form shear bands and the absence of 'short range order effect' (due to higher stacking fault energy [2]) and martensitic phase transformation prevented cyclic softening and reduced cyclic hardening.

The dash dotted curve in Fig. 3 shows that the initial cyclic softening and the subsequent cyclic hardening also revealed from the simulation of AISI 304 at an increased specimen temperature of  $T=150^{\circ}\text{C}$  and  $\Delta\sigma/2=190\text{ MPa}$ . The relevant deformation mechanisms were the same as at room temperature. Particularly, the facilitated plastic sliding deformation in shear bands due to the temperature effect led to the formation of the characteristic softening and hardening behavior also at the lower external loading of  $\Delta\sigma/2=190\text{ MPa}$ . The simulated results are consistent with the experimental observations (see grey solid curve in Fig. 3).

Finally, qualitatively good correlation of results from experiment and simulation allowed for predicting the likely course of cyclic deformation characteristics of austenitic stainless steels at low stress amplitudes in the regime of VHCF strength and certain deformation mechanisms could be assigned to the specific change of resonant behavior.

## ACKNOWLEDGEMENTS

The authors gratefully acknowledge financial support of this study by Deutsche Forschungsgemeinschaft (DFG) in the framework of the priority program Life<sup>∞</sup> (SPP 1466).

## REFERENCES

- [1] Grigorescu, A.; Hilgendorff, P.-M.; Zimmermann, M.; Christ, H.-J.; Fritzen, C.-P.; Cyclic deformation behavior of austenitic Cr–Ni-steels in the VHCF regime: Part I – Experimental study, *Int. J. Fatigue* 93 (2016), pp. 250–260.
- [2] Hilgendorff, P.-M.; Grigorescu, A.; Zimmermann, M.; Fritzen, C.-P.; Christ, H.-J.; Cyclic deformation behavior of austenitic Cr-Ni-steels in the VHCF regime: Part II - microstructure-sensitive simulation, *Int. J. Fatigue* 93 (2016), pp. 261–271.
- [3] Tanaka K.; Mura T.; A dislocation model for fatigue crack initiation, *J. Appl. Mech.* 48 (1981), No. 1, pp. 97-103.
- [4] Lin T.; *Micromechanics of crack initiation in high-cycle fatigue. Advances in applied mechanics*, Academic Press (1992), Vol. 29, pp. 1–62.
- [5] Hilgendorff, P.-M.; Grigorescu, A.; Zimmermann, M.; Fritzen, C.-P.; Christ, H.-J.; Modeling and simulation of temperature-dependent cyclic plastic deformation of austenitic stainless steels at the VHCF limit, *Structural Integrity Procedia* 2 (2016), pp. 1156–1163.
- [6] Bogers A.; Burgers W.; Partial dislocations on the {110} planes in the B.C.C. lattice and the transition of the F.C.C. into the B.C.C. lattice, *Acta Metall.* 12 (1964), pp. 255–61.
- [7] Olson G.; Cohen M.; A mechanism for the strain-induced nucleation of martensitic transformations, *J. Less Common Met.* 28 (1972), No. 1, pp. 107–118.
- [8] Hilgendorff, P. M.; Grigorescu, A.; Zimmermann, M.; Fritzen, C. P.; Christ, H. J.; Simulation of the interaction of plastic deformation in shear bands with deformation-induced martensitic phase transformation in the VHCF regime, *Key Eng. Mat.* 664 (2015), pp. 314-325.
- [9] Olson, G. B.; Cohen, M.; Kinetics of strain-induced martensitic nucleation, *Metall. Trans. A* 6 (1975), No. 4, pp. 791-795.



# ELASTIC-PLASTIC SIMULATIONS ON CRACK CLOSURE BEHAVIOR IN VHCF REGIME

C. Stäcker, M. Sander

University of Rostock, Institute of Structural Mechanics, Albert-Einstein-Str. 2,  
18059 Rostock, Germany

## ABSTRACT

In the very high cycle fatigue regime cracks usually nucleates at non-metallic inclusions with a typical fish-eye formation. Around the non-metallic inclusions many researchers observe remarkable areas, which are called “optical dark area” (ODA), “fine granular area” (FGA) or “granular bright facet” (GBF). It is commonly known that the main part of fatigue life in VHCF regime is spent on building these areas. However, the reasons for the formation of these areas has not been clarified. *Kovacs et al.* [1] found no FGA formation for positive  $R$ -ratios. But on specimens tested at negative  $R$ -ratios they detected fine granular areas. Therefore, three-dimensional finite element simulations are performed to investigate the influence of the mean stress on the crack closure behaviour. The fatigue crack is modelled as an annular crack surrounding an inclusion and cavity, respectively. For the calculations the constitutive model based on the work of *Chaboche* and *Lemaitre* [2] is used. Within the scope of this paper, two different evaluation methods to determine crack opening values are compared at selected stress ratios and their VHCF determined fatigue strengths. Moreover, the contact stresses generated at the minimum stress of the load function are evaluated at the crack flanks and the results are compared at different stress ratios.

## KEYWORDS

VHCF, mean stress, plasticity-induced crack closure behavior, crack propagation simulations, contact stresses

## INTRODUCTION

*Elber* [3] introduced the first investigations on plasticity-induced crack closure in the 1970s. Since then, additional mechanisms such as roughness-, oxid- and fluid-induced crack closure are identified. Plasticity-induced crack closure is caused by plastically deformed material along the crack flanks of the propagating crack. When a fatigue crack is exposed to a cyclic loading, large tensile plastic zones are formed near the crack tip, which are not fully reversed at the unloading state. The propagating crack front has to pass through this area and the deformed crack flanks behind the crack tip are no longer compatible into each other. Thus, a perfect elastic behaviour of the crack flanks is no longer given when the load is released. Consequently, the crack driving force is affected. In addition, the plastic deformations near the crack tip generate compressive residual stresses, which also significantly influence the crack driving force [4]. In literature, two-dimensional (2D) plasticity-induced crack propagation simulations (CPS) are primarily discussed, whereas three-dimensional (3D) simulations of crack closure are rarely performed. General reviews on 2D and 3D CPS are presented in [4–7]. In VHCF regime plasticity-induced CPS have not been carried out because in general elastic material behaviour is assumed. In previous studies [8, 9] CPS are performed at different stress ratios and amplitudes to investigate the mean stress effect in VHCF regime. Within the scope of this publication the evaluation methods to detect crack opening values are

investigated in more detail. In addition, the contact stresses of the crack flanks at the minimum load increment are evaluated at different stress ratios.

## MATERIAL

The investigated material is the high-strength steel 34CrNiMo6 with the mechanical properties listed in Table 1 and the chemical composition according to DIN EN 10083-3 from Table 2 [10]. The cyclic material behaviour of the investigated material 34CrNiMo6 has been taken into account by means of the modified *Chaboche* model based on the work of *Chaboche* and *Lemaitre* [2]. The isotropic and kinematic hardening parameters for the model have been iteratively identified using the finite element method on the basis of an incremental step test (IST) and are listed in Table 3.

**Table 1** Mechanical properties of 34CrNiMo6

$R_m$ [MPa]	$R_e$ [MPa]	$E$ -Modulus [GPa]	$A_5$ [%]	HV
1200	1000	210	9	350

**Table 2** Chemical composition of 34CrNiMo6 in weight-% [10]

C	Si	Mn	Cr	Ni	Mo
0.30 - 0.38	max. 0.40	0.50 - 0.80	1.30 – 1.70	1.30 - 1.70	0.15 - 0.30

**Table 3** Iteratively identified parameters of the *Chaboche* model

$\sigma_Y$	$\sigma_{eq}$	$Q_\infty$	$C$	$\gamma$	$b$
1000	1000	-500	60,000	100	10

## CRACK PROPAGATION SIMULATIONS

The CPS are performed by means of the parametric finite element model shown in Fig. 1. To reduce the calculation time only a section in the middle of a standardized VHCF specimen is modelled. Furthermore, the rotational symmetry in X-direction and the symmetry in load direction are exploited. To simulate the contact of the crack flanks a frictional contact option (steel-steel) is applied on the bottom side of the model between the symmetry line and the finite elements. The cyclic load is applied stress controlled on the upper side of the model. The circumferential crack initiates at the spherical imperfection and propagates alongside the uniform meshed region plotted in Fig. 1. Because the model generation is script controlled, the imperfection can either modelled as a cavity or an inclusion with different stiffnesses and contact options. Further on, amongst other parameters different initial crack lengths can be applied and the geometrical and mechanical properties can be modified. For the following investigations a spherical cavity with a radius of 15  $\mu\text{m}$  is assumed, whereby the crack initiates directly at the notch root.

In the CPS the mesh refinement is adjusted in relation to the size of the primary and reversed plastic zone. Generally, the element size in the crack propagation area is equal to the crack propagation increment. Depending on literature values [4, 11–13] and analytical assessments according to [14] for the described plastic zone sizes an appropriate crack propagation increment or element size has been calculated in [8] for the investigated stress ratios and their fatigue strengths from Table 4. Consequently, 4-node bilinear axisymmetric quadrilateral (CAX4) elements from Abaqus CAE element library with a minimum element size of 0.5  $\mu\text{m}$  are used in the crack propagation region. For the crack propagation the release node concept has been applied. Therefore, the symmetry boundary condition has been released at the maximum load of every fourth simulated cycle to realise the fatigue crack growth.

To evaluate the numerical simulations the crack opening stress  $\sigma_{op}$  is used. In literature [4, 15] different methods for analysing  $\sigma_{op}$  are presented. Within the scope of this paper, the ‘tip-tension’ (tt) approach and the ‘extrapolation first node’ (eek) technique are compared at selected stress ratios and their VHCF fatigue strengths. To determine the results for the tt-method the stress-time function  $\sigma_{22}(t)$  in load direction at the crack tip node is considered. The criterion estimates the transition from compressive to tensile stresses at the crack tip node to determine the crack opening stress  $\sigma_{op}$ . In contrast, the eek-method is a displacement controlled technique to determine crack opening values. For this, the displacement  $U_2$  in load direction at the first node behind the crack tip node is analysed. Consequently, the crack is opened if the critical limit of  $1 \cdot 10^{-6}$  mm is exceeded and the crack opening stress is determined. A more detailed description of the evaluation methods is given in [8].

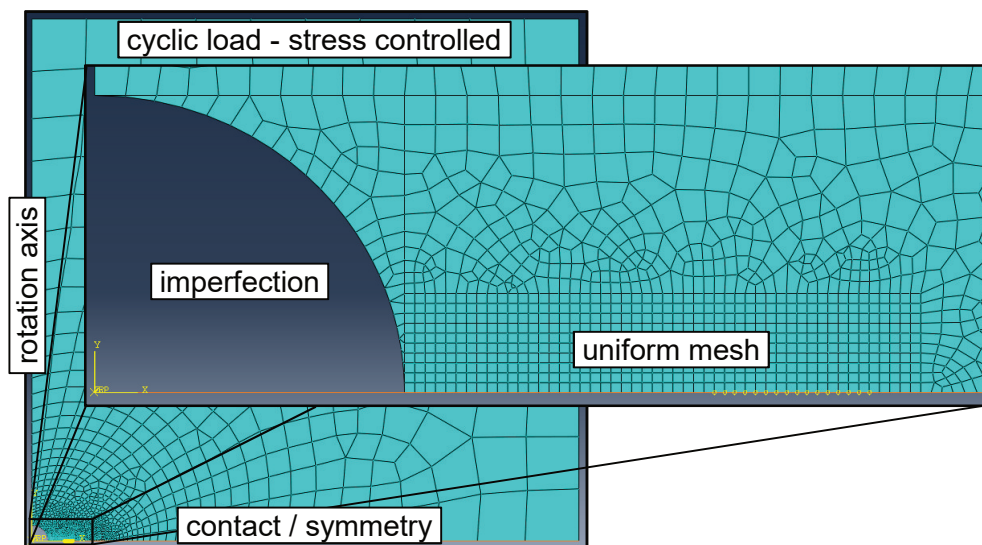


**Fig. 1.** Setup and mesh refinement of the 2D rotationally symmetric model to perform crack propagation simulations [8, 9]

**Table 4** Investigated stress ratios and respective fatigue strengths determined from VHCF experiments [8]

$R$ -ratio	-1	-0.8	-0.5	0	0.2	0.5
fatigue strength $\sigma_{a,D,VHCF}$ [MPa]	537	509	461	359	335	280

In Fig. 2 the crack opening stresses for a crack initiating at a spherical cavity evaluated by means of the tt- and the eek-method are normalised by the maximum stresses and then plotted versus the crack length  $a$  for the selected  $R$ -ratios from Table 4. Additionally, *Newman's* crack closure function [16] is plotted as dashed lines, whereby the analytical function is independent of the crack length and accordingly describes a constant value for  $\sigma_{op} / \sigma_{max}$  in the simulated range.

Independent of the stress ratio in Fig. 2 the tt-approach predicts always higher crack opening values in comparison to the eek-method. The eek-solution demonstrates a similar curve progression with slightly lower crack opening values, which are closer to the *Newman* solution. Considering the negative stress ratios in Fig. 2a) and b), the values for  $\sigma_{op} / \sigma_{max}$  using the tt-approach show a significant peak and then slowly converge, whereby the values using the eek-method converge faster. In addition, both evaluation methods show almost the same results for low crack lengths considering the negative  $R$ -ratios. But in Fig. 2c) at  $R = 0.2$  the normalised crack opening stresses are quite different in the first area. This is most likely due to the stress redistribution on the basis of the assumed cavity at higher maximum stresses, whereby the stress-based tt-values are significantly more affected than the results determined

by means of the eek-approach. At  $R = 0.5$  no opening values could be detected until a critical crack length is reached. Thus, no crack closure occurs in the first area. Whereas the tt-method firstly predict  $\sigma_{op}$  values at 0.02 mm, the eek-approach cannot determine crack opening values until a crack length of 0.04 mm is reached. The discontinuities in the curve progression especially for  $R = -1$  are caused due to a shift in the evaluation increment.

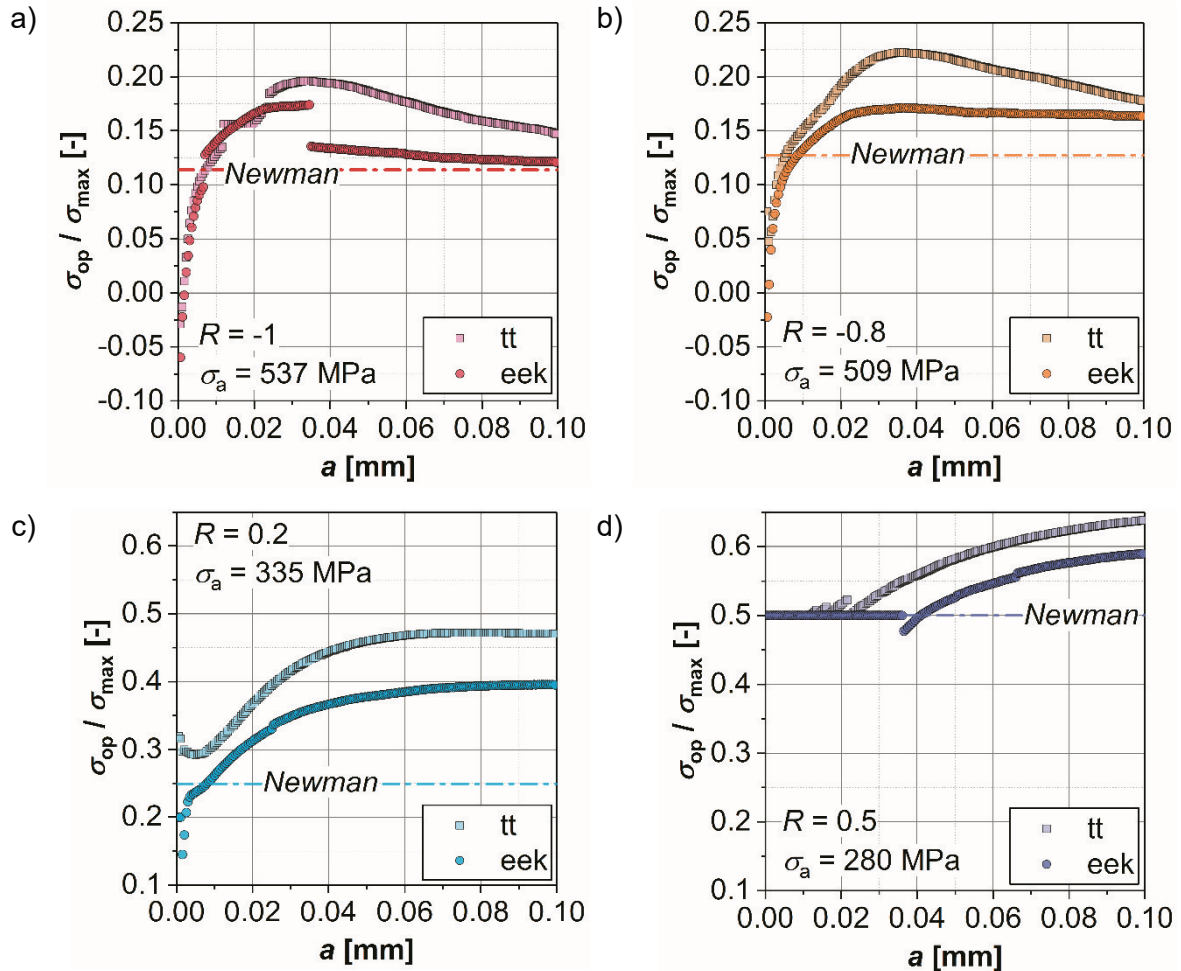


**Fig. 2.** Comparison of the crack opening values determined from numerical CPS of a spherical cavity with  $\rho = 15 \mu\text{m}$  due to the 'tip-tension' (tt) and the 'extrapolation first node' (eek) method at a)  $R = -1$  [9], b)  $R = -0.8$ , c)  $R = 0.2$  and d)  $R = 0.5$  and their corresponding fatigue strengths

For further investigations, the contact stresses between the crack flank and the contact line at the minimum load increment are evaluated. For this purpose, the elements which characterise the crack flank, are analysed for every crack length and the maximum contact stress  $\sigma_{cs,max}$  is calculated. In Fig. 3a) and b) the procedure to determine the values for  $\sigma_{cs,max}$  is illustrated using three different crack lengths for  $R = -0.5$  and  $R = 0$ , respectively. For all negative stress ratios and all crack lengths the maximum value for  $\sigma_{cs}$  is located at the initiation side, whereas for  $R = 0$   $\sigma_{cs,max}$  appears at the respective crack tip location. In Fig. 4, the calculated maximum contact stresses are plotted versus the crack length for the investigated stress ratios from Table 4. With increasing  $R$ -ratio higher maximum contact stresses could be observed. For all negative stress ratios high values for  $\sigma_{cs,max}$  are visible at the initiation side, which decrease firstly and then slightly increase with increasing the crack length. Considering the positive stress ratios, no contact stresses could be observed.

Taking into account that the maximum contact stress is located at the initiation site for all crack lengths at the negative stress ratios (Fig. 3), the material is repetitively loaded at the same location for every crack growth increment. Possibly, the repeating contact stresses cause structural changes and the formation of fine granular areas.

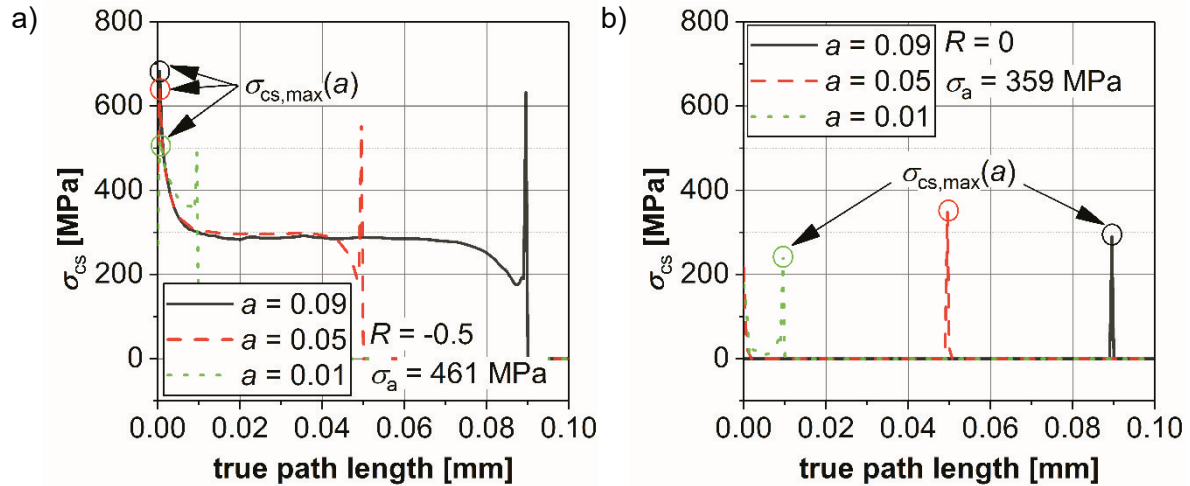


**Fig. 3.** Evaluation of the maximum contact stress  $\sigma_{cs,max}$  at the minimum load increment along the crack flank for different crack lengths at a)  $R = -0.5$  and b)  $R = 0$

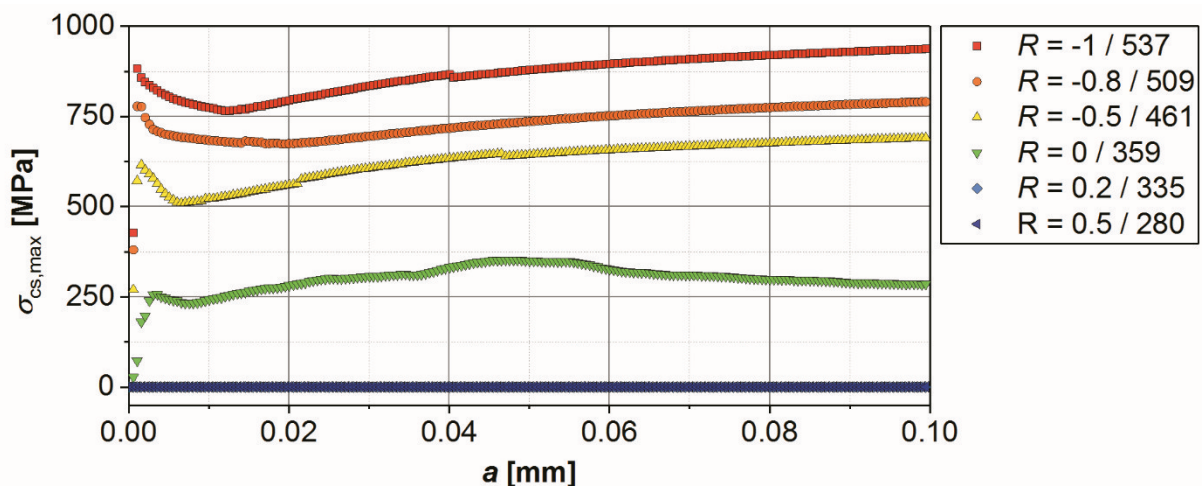


**Fig. 4.** Results for the maximum contact stress  $\sigma_{cs,max}$  versus the crack length at different stress ratios evaluated at the minimum load increment

## CONCLUSION

The following conclusions can be drawn:

1. Independent of the stress ratio both evaluation methods for detecting crack opening values predict a similar curve progression, whereby the 'extrapolation first node' (eek) method predicts smaller values, which converge and are located closer to the *Newman* solution.
2. The crack opening values obtained by the 'tip-tension' (tt) approach are more affected from the stress distribution surrounding the assumed imperfection than the eek-technique.



3. With increasing  $R$ -ratio higher maximum contact stresses could be observed, whereby the location of the maximum is found at the initiation site for all negative  $R$ -ratios and all crack lengths. In contrast, for  $R = 0$  the maximum stresses are located at the respective crack tip location.
4. Repeating contact stresses at the crack initiation site possibly cause structural changes.

## ACKNOWLEDGMENT

The authors would like to thank the German Research Foundation for the financial support of this study in the framework of the priority program “Life $\infty$ ” (SPP 1466).

## REFERENCES

- [1] S. Kovacs, T. Beck and L. Singheiser: 'Influence of mean stresses on fatigue life and damage of a turbine blade steel in the VHCF-regime', *Int. J. Fatigue*, 2013, 90–99.
- [2] V. Budaházy and L. Dunai: 'Parameter-refreshed Chaboche model for mild steel cyclic plasticity behaviour', *Per. Pol. Civil Eng.*, 2013, 2, 139.
- [3] W. Elber: 'Fatigue crack closure under cyclic tension', *Engineering Fracture Mechanics*, 1970, 1, 37–45.
- [4] K. Solanki, S. R. Daniewicz and J. C. Newman Jr.: 'Finite element analysis of plasticity-induced fatigue crack closure', *Eng. Fract. Mech.*, 2004, 2, 149–171.
- [5] McClung and R. C.: 'Finite element analysis of fatigue crack closure: a historical and critical review'. 7th Intern. Fatigue Congress. Beijing, China. 8-12 June, 1999.
- [6] J. C. Newman Jr.: 'Advances in finite element modelling of fatigue crack growth and fracture'. 8th Intern. Fatigue Congress. Stockholm, Sweden. 3-7 June, 2002.
- [7] K. D. Singh, M. R. Parry and I. Sinclair: 'A short summary on finite element modelling of fatigue crack closure', *J Mech Sci Technol*, 2011, 12, 3015–3024.
- [8] C. Stäcker and M. Sander: 'Experimental, analytical and numerical analyses of constant and variable amplitude loadings in the very high cycle fatigue regime'. Submitted for: TAFMEC, 2017.
- [9] M. Sander, C. Stäcker and T. Müller: 'Experimental and numerical investigations on crack initiation and crack growth in steels under constant and variable amplitude loadings in the VHCF regime', In: H.-J. Christ (eds.): 'Abschlussbericht SPP1466', 2017.
- [10] Deutsche Edelstahlwerke: 'Werkstoffdatenblatt - 34CrNiMo6'; available at [https://www.dew-stahl.com/fileadmin/files/dew-stahl.com/documents/Publikationen/Werkstoffdatenblaetter/Baustahl/1.6582\\_de.pdf](https://www.dew-stahl.com/fileadmin/files/dew-stahl.com/documents/Publikationen/Werkstoffdatenblaetter/Baustahl/1.6582_de.pdf) (accessed 08.02.2017).
- [11] R. C. McClung: 'Crack closure and plastic zone sizes in fatigue', *Fat Frac Eng Mat Struct*, 1991, 4, 455–468.
- [12] J. D. Dougherty, J. Padovan and T. S. Srivatsan: 'Fatigue crack propagation and closure behavior of modified 1070 steel', *Engineering Fracture Mechanics*, 1997, 2, 189–212.
- [13] S.-J. Park, Y.-Y. Earmme and J.-H. Song: 'Determination of most appropriate mesh size for a 2-D finite element analysis of fatigue crack closure behavior', *Fatigue & Fracture of Engineering Materials & Structures*, 1997, 4, 533–545.
- [14] H. A. Richard and M. Sander: 'Ermüdungsrisse', 2012. Wiesbaden, Vieweg+Teubner Verlag.
- [15] C. Benz: 'Bewertung negativer Lastanteile bei der Ermüdungsrisssausbreitung': PhD thesis. University of Rostock. Verlag Dr. Hut GmbH. Rostock, 2015.
- [16] J. C. Newman Jr.: 'Application of small-crack theory to aircraft materials', In: K. S. Ravichandran, R. O. Ritchie and Y. Murakami (eds.): 'Small fatigue cracks - Mechanics, mechanisms, and applications', 1999, Elsevier, Amsterdam, New York, 431–442.

Corresponding author: carsten.staecker@uni-rostock.de

# ASSESSMENT OF A LOCAL STRESS-STRAIN BASED FATIGUE CRACK GROWTH MODEL IN HIGH CYCLE FATIGUE

Dongjun Bang, Ayhan Ince  
Purdue Polytechnic Institute, Purdue University, West Lafayette, USA

## ABSTRACT

Recently, total fatigue life approaches are proposed for linking short and long fatigue crack propagation in high cycle fatigue (HCF) regime. As for HCF life, cracks remain short for most of the fatigue life and long crack behaviors are considered to be less important. To estimate the fatigue crack growth in HCF regime, the UniGrow model is applied by simulating the stress-strain response in the elementary material volume adjacent to the crack tip. A systematic study is performed here to assess limitations of the UniGrow model to study mechanics aspects of short crack growth behavior in HCF. A modification of the model is proposed for the unification of short and long crack propagation to account for effects of stress ratio, stress amplitude, residual stress, and initial crack size. The modified model predictions are in a good agreement with experimental fatigue data sets of 2024-T3, 7075-T561 aluminum alloys and Ti-6Al-4V titanium alloy.

## KEYWORDS

High cycle fatigue, UniGrow model, stress ratio, residual stress, initial crack size

## INTRODUCTION

There are many structures and components that are subjected to sustained loads in many machinery systems, such as automobiles, ships and aircrafts. Since continuous cyclic loads eventually lead to fatigue failure, accurately estimating the life of fatigue cracks due to cyclic loads and analyzing the crack behaviors are recognized as a very significant design and safety problem in many industries. High cycle fatigue (HCF) has long been the subject of research in many different industries, particularly in the ground vehicle and aerospace industries. Efforts to provide accurate fatigue predictions in HCF are not fully addressed by conventional crack initiation approaches [1, 2, 3]. The HCF problem can be considered as the propagation of cracks at various length scales, consisting of short crack growth and then propagation of mechanically long cracks. In particular, the behavior of short cracks is complicated and very difficult to characterize the crack behavior, requiring many controlling parameters that can schematically be considered. Miller presented [4] that as shown in Fig. 1, cracks occur in two stages, short crack and long crack, and short crack consists of microstructurally short crack and physically short crack. In the total life of the crack, the short crack plays a critical role in determining the total life of crack growth; since the life of short crack regime makes majority of the total crack life. Therefore, it is very crucial factor to predict the fatigue lives in the short crack regime. One of the most important physical properties occurring in the short crack regime is that, in the long crack, the plastic deformation at the crack tip is relatively very small and elastic stress response can be obtained by Linear Elastic Fracture Mechanics (LEFM), however, in the short crack, the plastic size is relatively large, hence an elastic-plastic based analysis should be demanded.

Under such circumstances, many efforts has been made to simulate crack growth behaviors in short crack regime. Newman at al. [5] examined the effects of small cracks on the total fatigue life using 7075-T6 and LC9cs aluminium alloys. Plasticity-induced crack-closure model was applied to predict small and large crack growth on the basis of baseline effective stress intensity factor range. Predicted small crack growth rates and fatigue lives were consistent with experimental data of surface/corner crack. Newman and Annigeri. [6] also made use of plasticity effect and crack-closure model to compute fatigue life under several loading conditions. They

used crack-closure model with a cyclic-plastic-zone-corrected effective stress intensity factor range and equivalent-initial-flaw-sizes (EIFS) for fatigue life calculations. Fatigue life predictions were well matched with test data. Caton et al. [7] conducted studies on investigation of the stress ratio effects on small cracks in titanium. The initial crack was launched at 30 to 40  $\mu\text{m}$ , and the crack propagation was examined by using standard replica technique.

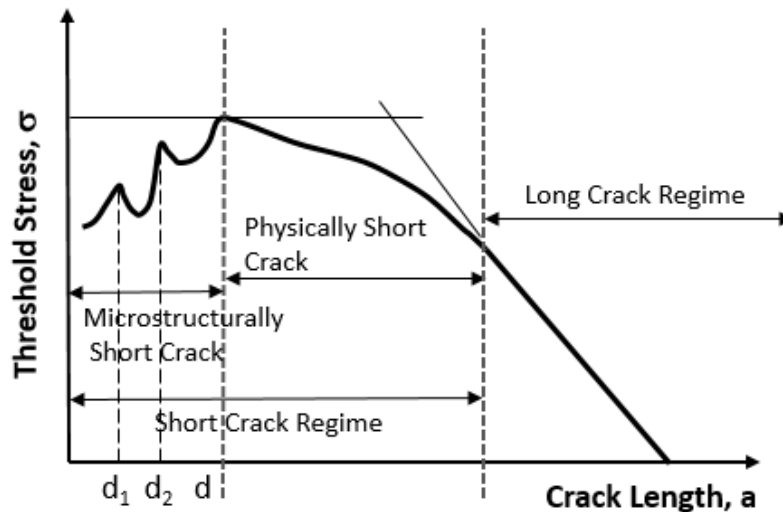


Fig. 1. Kitagawa-Takahashi type diagram representing three regimes of crack behaviors; Ref. [4].

However, these models did not account for the different response behaviors when applying loads at different R-ratios, nor could they explain stress-strain effects ahead of crack tip. To solve this problem, Noroozi, Glinka and Lambert. [8, 9] proposed a new model that can be freely applied notch theories, assuming that crack propagation is a successive crack re-initiations at the crack tip; which was later coined 'UniGrow model'; Ribeiro et al. [11] validated the UniGrow model based on the local strain approach derived from the approximate notch stress and strain approaches [21, 22]. The authors applied the model to induce fatigue crack propagation data on Al6061-T651 for different R-ratios. It was shown that their predictions were in a good agreement with experimental crack propagation data. De Jesus et al. [12, 13] assessed the UniGrow model using the P355NL1 Steel, puddle iron and construction steel, respectively. They calculated the residual stresses using the finite element method and compared them with the results obtained from Glinka's rule to identify the difference. However, all of them focused only on analyzing the behavior of long cracks using the UniGrow model.

The first attempt to apply the UniGrow model to short cracks was performed by Bogdanov et al. [14]. They carried out the fatigue life crack simulations using the modified stress intensity factor, taking into account that the crack growth rate was higher than the crack growth near the threshold, assuming that the crack initiated near the threshold. The results were shown in a good agreement with experimental data.

In this study, in order to predict the total fatigue lives in HCF, a new modeling approach is proposed for integrating short crack to long crack regimes. A small elementary block size is considered that is smaller than the initial crack size. The actual driving force for short cracks was calculated by obtaining the stress-strains and the residual stresses at the crack tip. To separate the short crack behaviors from the long cracks, three criteria, stress intensity factor range, driving force and crack growth rate of short cracks are defined. Unlike the long cracks, the short crack behaviors are very sensitive to the applied stress level; namely, the crack growth rate is determined by the applied stress amplitude as well as the stress intensity factor and the stress



intensity factor range. To estimate the fatigue lives in the short crack regime, sets of the crack growth rate are differentiated for each stress level. The total life predictions of combined short and long fatigue cracks are shown in a good agreement with experimental data for 2024-T3, 7075-T561 aluminum alloys and Ti-6Al-4V titanium alloys.

## UNIGROW MODEL

The key concept of the UniGrow model is to assume that the material is composed of elementary particles representing the elementary material block size  $\rho^*$ , the crack is considered as a notch with radius  $\rho^*$  and the fatigue crack growth is regarded as successive failure of the elementary material block, as shown in Fig. 2a.

The reason why the crack is defined as a micro notch as in the above assumptions is that the elastic-plastic analysis can be carried out at the crack tip by applying approximate notch correction theories [23, 24]. By performing the elastic-plastic analysis, the stress-strain history at the crack tip and the residual stress induced by the reverse cyclic plastic can be determined. The Neuber rule [15] can be adapted to obtain the stress-strain responses in the vicinity of the crack tip, According to this theory, the strain energy densities for elastic and elastic-plastic response under the cyclic loading are equivalent under same loadings and boundary conditions as shown in Fig 2b. Therefore, the notch correction formulation in Eq. (1) can be obtained with the correlations among the nominal stress-strain, stress intensity factor at the elementary block size,  $\rho^*$ .

$$\sigma_{y,1}^e \varepsilon_{y,1}^e = \frac{(\sigma_{y,1}^e)^2}{E} = \frac{1}{E} \left( \frac{\Psi_{y,1} K_{appl}}{\sqrt{2\pi\rho^*}} \right)^2 = \sigma_{y,1}^a \varepsilon_{y,1}^a \quad (1)$$

From Eq. (1), residual stress at the crack tip can be obtained after calculating the maximum stress and the stress range. The residual stress intensity factor,  $K_r$  can be quantified by using the residual stress [16] and the weight function.

The UniGrow crack growth model is defined in terms of two parameters  $K_{max,tot}$  and  $\Delta K_{tot}$ , which indicate actual stress maximum stress intensity factor and actual stress intensity factor range, respectively, and they are calculated by accounting for the residual stress intensity factor as

$$\begin{aligned} K_{max,tot} &= K_{max,appl} + K_r \\ \Delta K_{tot} &= \Delta K_{appl} + K_r \end{aligned} \quad (2)$$

Through the iterative computations, using Eq. (1) and Eq. (2) until  $K_{max,tot}$  and  $\Delta K_{tot}$  are iteratively computed to correlate crack growth data. The actual driving force  $\Delta\kappa$  can be obtained by combing two parameters  $K_{max,tot}$  and  $\Delta K_{tot}$ , and the UniGrow fatigue crack growth model can be expressed with the driving force  $\Delta\kappa = (K_{max,tot})^p (\Delta K_{tot})^{1-p}$  as

$$\frac{da}{dN} = C(\Delta\kappa)^y \quad (3)$$

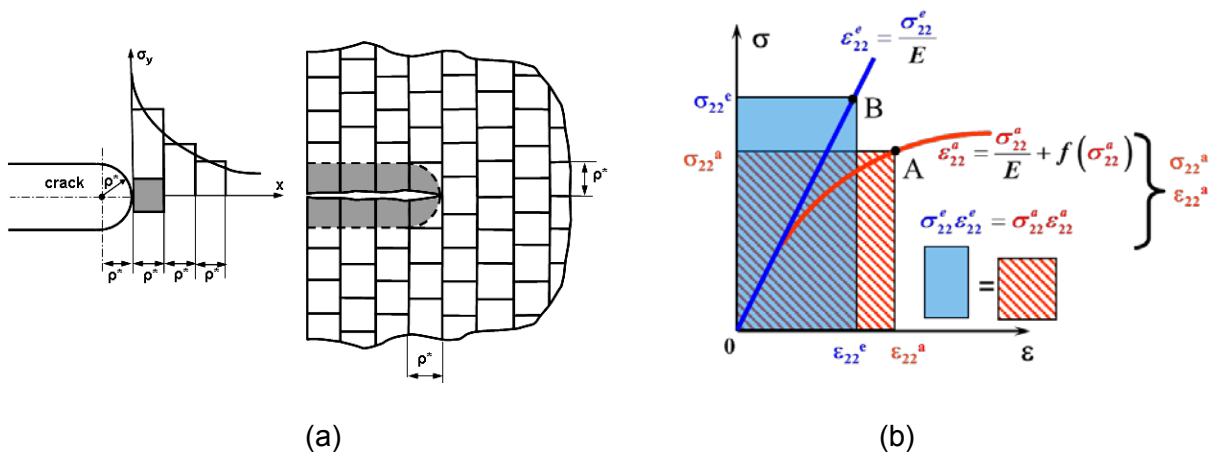
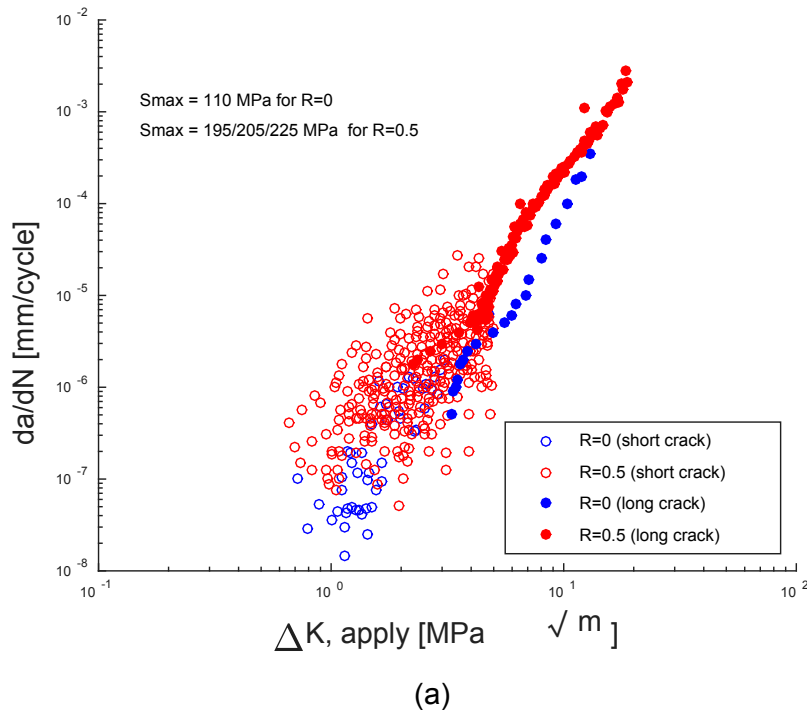
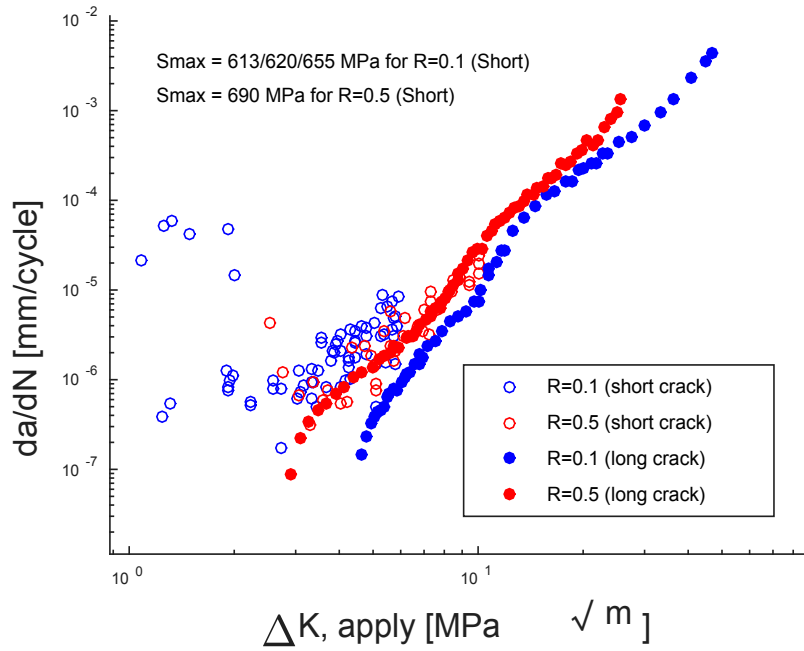


Fig. 2. (a): Crack and discrete elementary material block, (b): Graphical comparison of the equivalent strain energy densities at elastic and elastic-plastic notch tip.

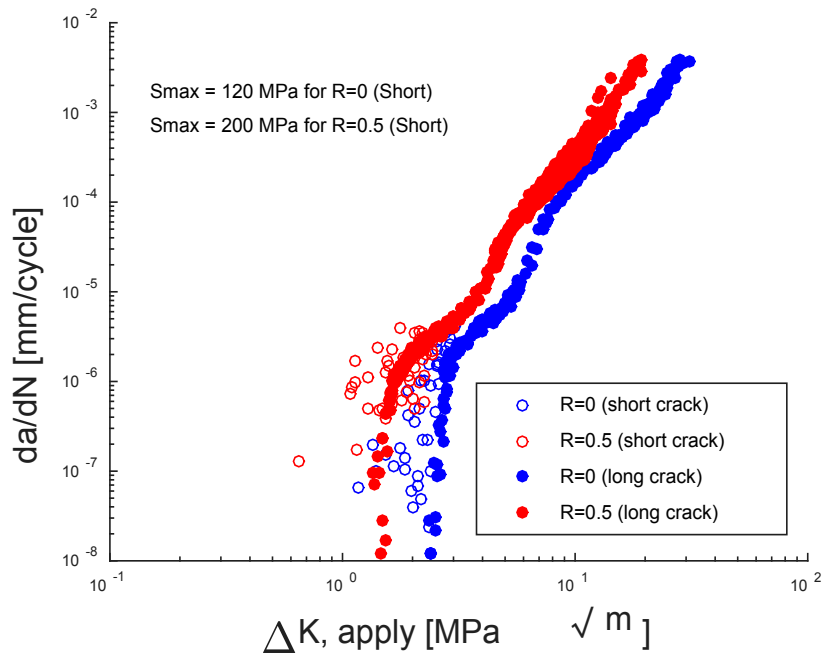
### FATIGUE CRACK GROWTH DATA

The fig. 3 shows the short and long combined fatigue crack growth data sets as a function of the applied stress intensity factor range  $\Delta K_{apply}$  for 2024-T3, 7075-T561 aluminum alloys and Ti-6Al-4V titanium alloys. Here, the crack growth data of the three materials for the two R-ratios ( $R=0, R=0.5$  or  $R=0.1, R=0.5$ ) were obtained for the short cracks at [17, 19], [19] and [20], and long cracks at [8], [9] and [10] respectively. Using these data sets, fatigue crack growth rates can be obtained after calculating the residual stress from the difference of maximum stress and stress range obtained from Eq. (1) and Eq. (2). In this case, the applied elementary material block size was determined using the iteration technique in [9].





(b)



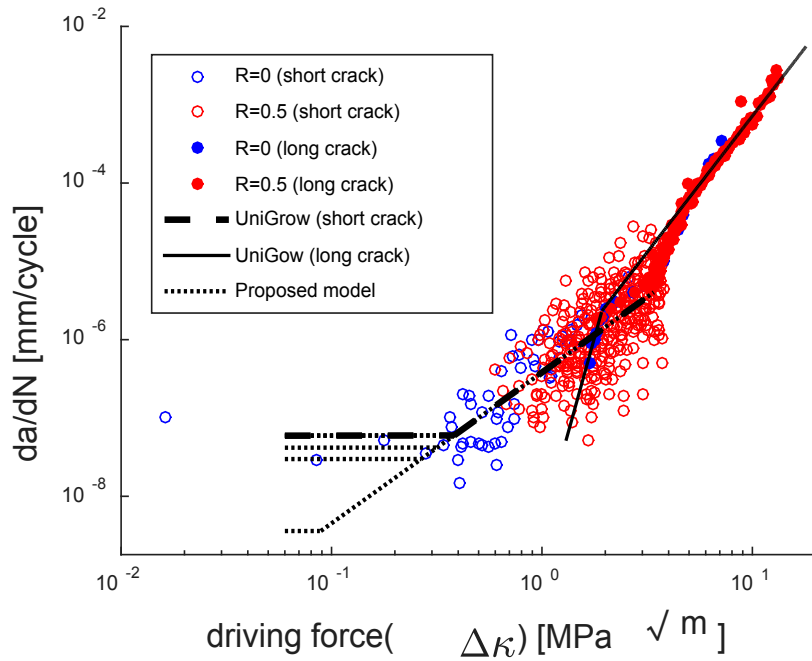
(c)

Fig. 3. Fatigue crack growth data (a): 2024-T3 aluminum, (b): Ti-6Al-4V titanium and (c): 7075-T561 aluminum alloys obtained at [9, 10, 17, 19, 20]

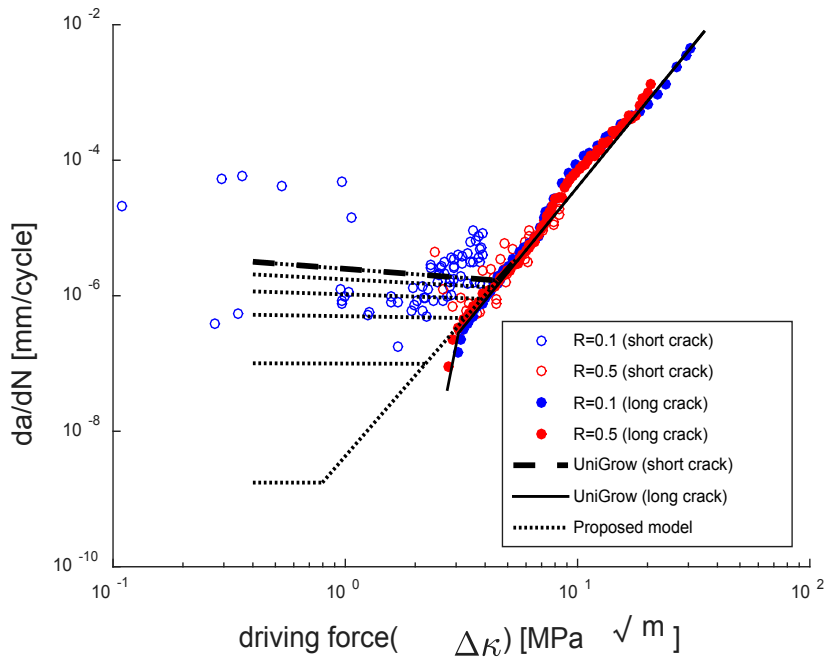
### ASSESSMENT OF THE UNIGROW MODEL

As a function of the driving force, the crack growth data sets for three materials can be plotted as shown in Fig. 4. To estimate the fatigue crack growth rate, those data sets are correlated by using the two line curve-fitting method for both short and long cracks. Here, noted that in the long crack

regime, the fatigue crack growth rate is determined by the driving force  $\Delta K$ , whereas in the short crack regime, the fatigue crack growth rate are determined by not only driving force but also stress level; i.e. each of the applied stress level has different fatigue crack growth data. Therefore, in order to define the crack behaviors in the short crack regime, the crack growth rate should be differently defined by correlating the predicted data sets for each stress level. Namely, the crack growth rate in the short crack regime should be related to different stress amplitudes for each material. This section shows a limitation of applying the UniGrow model to short cracks and will be a subject for future work.



(a)



(b)

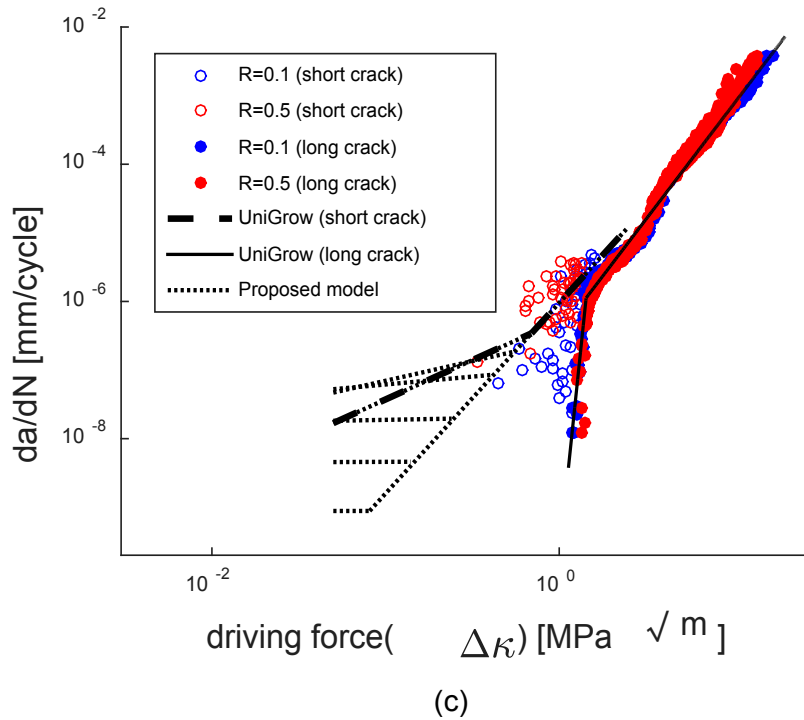
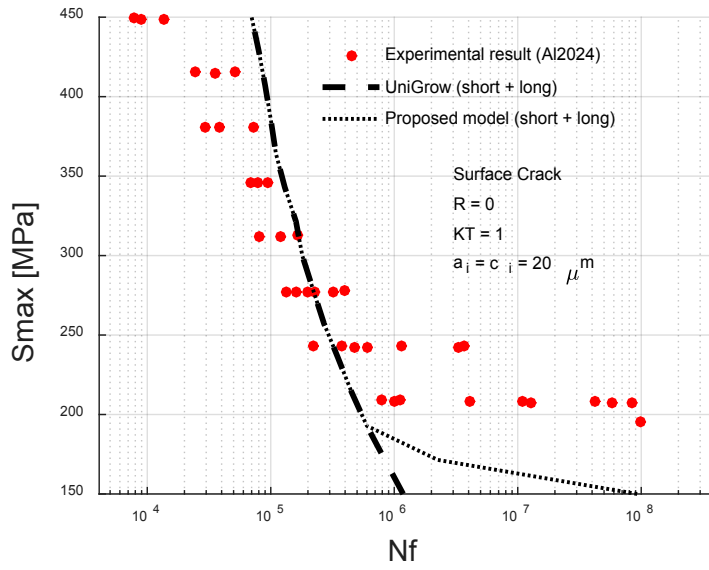


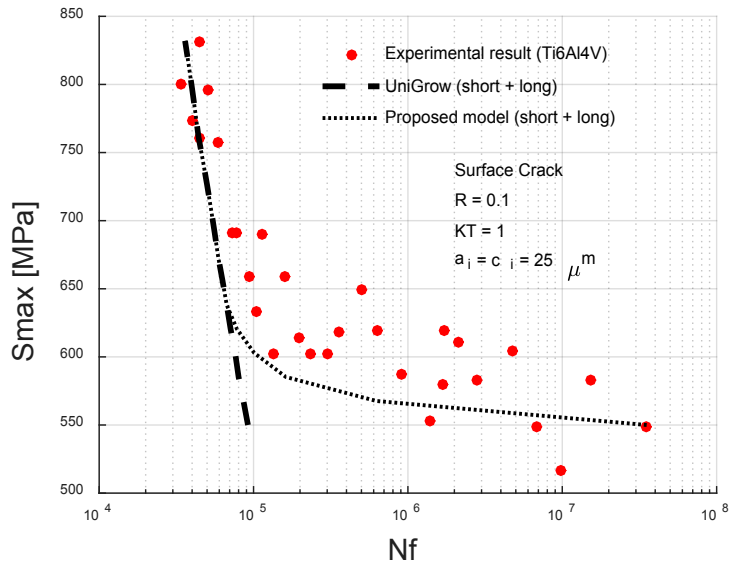
Fig. 4. Fatigue crack growth rate as a function of driving force  $\Delta K$  for (a): 2024-T3 aluminum, (b): Ti-6Al-4V titanium and (c): 7075-T561 aluminum alloys

### COMPARISON WITH EXPERIMENTAL DATA

By calculating the maximum stress intensity factor and the stress intensity factor range excluding residual stress effects and integrating the crack growth model of Eq. (3) over the number of cycle  $N_f$ , the crack growth fatigue lives can be obtained. Initial crack size was  $a_i = c_i = 20 \mu m$ ,  $a_i = 3, c_i = 9 \mu m$  and  $a_i = c_i = 25 \mu m$  for Al2024, Al7075 and Ti-6Al-4V, respectively, and cracks were assumed to be surface crack. By applying the short crack separation criteria, the life time of the short crack is determined, and the total fatigue life is determined by summing the fatigue lives of the short crack and long crack. Figure 5 shows the results of fatigue life predictions for the three materials calculated by two line and multiple line fitting methods shown in Fig. 4, which are in good agreement with the experimental data. For example, the nominal stress in Fig. 3b has a range of 610~690MPa (Ti6Al4V). The fatigue life predictions obtained by fitting the crack growth data corresponding to this range to the two lines agree well with the test data obtained at the same stress level, as shown in Fig. 6b. This is a relatively large stress level, and most fatigue life is due to the life time of the long crack. However, at a stress level lower than 610 MPa, with relatively small stress levels, most of the fatigue life is dominated by short cracks. Therefore, as mentioned in Fig. 4, in this region, the different fatigue crack growth value with each stress level should be found. In Fig. 6b, two line fitting with one stress level and multiple line fitting with different stress levels are compared for the Ti-6Al-4V titanium alloy. In the case of the multiple line fitting, the results are in good agreement with the test data for the short crack region. In the similar way, the same results are shown for aluminum alloys in Fig. 6a and Fig. 6c. The fitting way of two line or multiple line are determined at 200 MPa and 120 MPa for 2024-T3, 7075-T561 aluminum alloys, respectively. In these cases also, the crack growth rate corresponding to each stress level can be found in the short crack region. From the Fig. 5a and Fig. 5c, it can be seen that the model predictions and the experimental data are in good agreement.



(a)



(b)

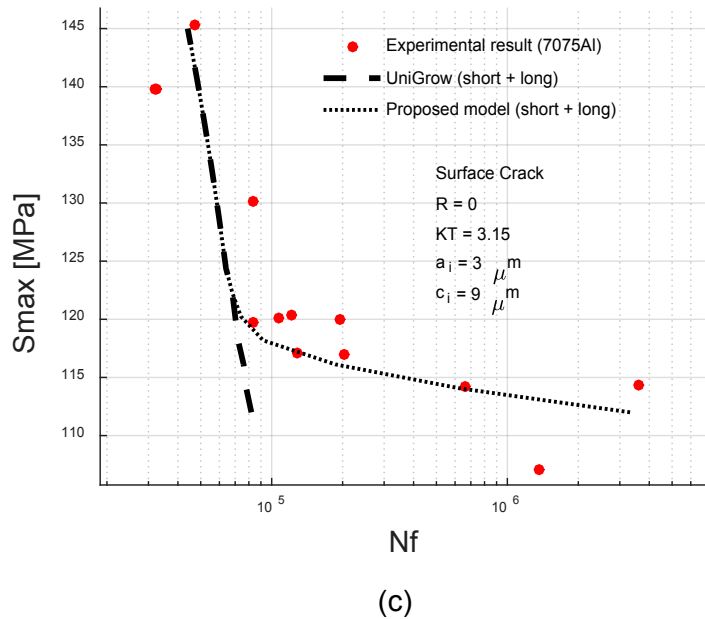


Fig. 5. Comparison of predicted fatigue lives and experimental data [5, 19, 20] for (a): 2024-T3 aluminum, (b): Ti-6Al-4V titanium and (c): 7075-T561 aluminum alloys

## CONCLUSIONS

Based on the predicted fatigue results presented, conclusions can be drawn as follows.

- Fatigue crack growth rates of short cracks are significantly higher than the growth rates of long cracks for same nominal stress intensity factor range,
- Two parameters driving force based fatigue crack growth model (UniGrow) work well for long cracks when extended short cracks lead to non-conservative life predictions.
- Short crack behavior is significantly influenced by stress amplitude.
- A new model is proposed for the unification of short and long crack propagation to account for effects of stress ratio, stress amplitude, residual stress, and initial small crack size
- Proposed fatigue crack growth model will be modified to account for controlling parameters of micro and long crack thresholds.

## References

- [1] Ince, A. and Glinka, G., A generalized damage parameter for multiaxial fatigue life prediction under proportional and non-proportional loadings, *International Journal of Fatigue*, Vol. 62, pp. 34–41, 2014, doi: 10.1016/j.ijfatigue.2013.10.007.
- [2] Ince, A., A Computational Multiaxial Model for Stress-Strain Analysis of Ground Vehicle Notched Components, *SAE Int. J. Engines* 10(2):2017, doi:10.4271/2017-01-0329
- [3] Ince, A., A mean stress correction model for tensile and compressive mean stress fatigue loadings, *Fatigue and Fracture of Engineering Materials and Structures*, 40(6) (2017): 939-948, doi:10.1111/ffe.12553.
- [4] Miller, K.J., The two Thresholds of Fatigue Behavior, *Fatigue Fract. Eng. Mater. Struct.*, Vol. 16, pp. 931-939, 1993
- [5] Newman, Jr., *Analyses of Fatigue and Fatigue-Crack Growth under Constant- and Variable-Amplitude loading*, Mechanics of Materials Branch NASA Langley Research Center Hampton, Virginia USA

- [6] Newman, Jr. and Annigeri, B.S., Fatigue-life Prediction method Based on Small-Crack Theory in an Engine Material, *J. Eng. Gas Turbines Power*, Vol. 134, 2011.
- [7] Caton, M.J., John, R., Porter, W.J. and Burba, M.E., Stress Ratio Effects on Small Fatigue Crack Growth in Ti-6Al-4V, *International Journal of Fatigue*, Vol. 38, pp. 36-45, 2012.
- [8] Noroozi, A.H, Glink G., Lambert S., A two Parameter Driving Force for Fatigue Crack Growth Analysis, *International Journal of Fatigue*, Vol. 27, pp. 1277-1296, 2005.
- [9] Noroozi, A.H, Glink G., Lambert S., A Study of the Stress Ratio Effects on Fatigue Crack Growth using the Unified Two-Parameter Fatigue Crack Growth Driving Force, *International Journal of Fatigue*, Vol. 29, pp. 1616-1633, 2007.
- [10] Ritchie, R.O., Suresh, S., Hutchinson, J.W., Milligan, W.W., Thompson, A.W., High Cycle Fatigue and Time-Dependent Failure in Metallic Alloys for Propulsion Systems, Third Progress Report, Air Force Office of Scientific Research, September, 1999.
- [11] Ribeiro, A.S., Correia, J.A.F.O., Jesus, A.M.P., Assessment of Fatigue Crack Growth Data Available for the AA6061-T651 using A Local Strain-Based Approach, In: Proceedings of 21st Brazilian Congress of Mechanical Engineering(COBEN 2011), Natal, RN, Brazil, 24-28, October, 2011.
- [12] Jesus, A.M.P. and Correia, J.A.F.O., Critical Assessment of a Local Strain-Based Fatigue Crack Growth Model Using Experimental Data Available for the P355NL1 Steel, *Journal of Pressure Vessel Technology*, Vol. 135, PVT-11-1165, 2013.
- [13] Hafezi, M.H., Jesus, A.M.P., Correia, J.A.F.O., An Assessment of a Strain-Life Approach for Fatigue Crack Growth, *International Journal of Structure Integrity*, Vol. 3, pp. 344-376, 2012.
- [14] Bogdanov, S., Mikheevskiy, S., Glinka, G., The Fatigue Life Prediction Methodology Based on the UniGrow Model, In: Proceedings of the ASME 2015 International Mechanical Engineering Congress and Exposition(IMECE 2015), Houston, Texas, November, 2015.
- [15] Moftakhar, A., Buczynski, A., Glinka, G., Calculation of Elastoplastic Strains and Stresses in Notches under Multiaxial Loading, *International Journal of Fracture*, Vol. 70, pp. 357-373, 1994.
- [16] Moftakhar, A., Glinka, G., Calculation of Stress Intensity Factors by Efficient Integration of Weight Functions, *Engineering Fracture Mechanics*, Vol. 43, pp. 749-756, 1992.
- [17] Kaynak, C., Ankara, A., Short Fatigue Crack Growth in Al2024-T3 and Al7075-T6, *Engineering Fracture Mechanics*, Vol. 43, pp.769-778, 1992.
- [18] Cook, R., The Growth of Short Fatigue Cracks in an Aluminium Alloy, Technical Report, Farnborough, Hampshire, November 1992.
- [19] Newman, J.C., Wu, X.R., Swain, M.H., Zhao, W., Phillips, E.P., Ding, C.F., Small-Crack Growth and Fatigue Life Predictions for High-strength Aluminium Alloys. Part II: Crack Closure and Fatigue Analyses, *Fatigue Fract. Eng. Mater.Struct.*, Vol. 23, pp. 59-72, 2000.
- [20] Wang, K., Wang, F., Cui, W., Hayat, T., Ahmad, B., Prediction of Short Fatigue Crack Growth of Ti-6Al-4V, *Fatigue Fract. Eng. Mater. Struct.*, Vol. 37, pp. 1075-1086, 2014.
- [21] Ince, A., and Glinka, G. A Numerical Method for Elasto-Plastic Notch-Root Stress-Strain Analysis, *Journal of Strain Analysis for Engineering Design*, Vol. 48, pp. 229-224, 2013, doi:[10.1177/0309324713477638](https://doi.org/10.1177/0309324713477638).
- [22] Ince, A., Glinka, G., and Buczynski, A., A Computational Modeling Technique of Elasto-Plastic Stress-Strain Response for Notched Components, *International Journal of Fatigue*, Vol. 62, pp. 42-52, 2014, doi:[10.1016/j.ijfatigue.2013.10.008](https://doi.org/10.1016/j.ijfatigue.2013.10.008).
- [23] Ince, A., A novel technique for multiaxial fatigue modelling of ground vehicle notched components, *International Journal of Vehicle Design*, Vol. 67, pp. 294-313, 2015, doi:[10.1504/IJVD.2015.069486](https://doi.org/10.1504/IJVD.2015.069486).
- [24] Ince A., Numerical validation of computational stress and strain analysis model for notched components subject to non-proportional loadings, *Theoretical and Applied Fracture Mechanics*, Vol. 84, pp. 26-37, 2016, doi:[10.1016/j.tafmec.2015.12.007](https://doi.org/10.1016/j.tafmec.2015.12.007).

**Corresponding author:** [aince@purdue.edu](mailto:aince@purdue.edu)



# OPTIMIZATION OF A GIGACYCLIC TORSIONAL FATIGUE SYSTEM FOR HIGH STRENGTH MATERIALS TESTING

J. Petit, Z. Jiang, O. Polit

Laboratoire Energétique Mécanique Electromagnétisme (LEME), EA4416, University of Paris Ouest Nanterre La Défense (UPOND), 92410 Ville d'Avray, France

Shear loading limit in very high cycle fatigue regime is of interest for many applications in mechanics, structures, motors, etc, when repetitive loads occur. So, this paper proposes to optimize an existing gigacyclic fatigue system developed by the Pr C. Bathias research team in order to increase the level of the shear stress in the investigated specimen and, consequently, meet the expectations from industries about fatigue life for high strength materials under shear solicitations. The system differs from other gigacyclic torsional fatigue systems, that can be found in literature, by the combination of two amplification horns, transforming a translation movement into a rotational movement. The optimization objective is to reach the maximum shear stress level in the specimen by minimizing the stress in the rest of the system. The development of the optimized system is essentially carried out by numerical simulation through modal and harmonic analysis. Numerical results are compared with experimental data from the new real device. Some experimental results on the torsional fatigue limit of high strength steels (38MnV5S, 50CrV4 and 16MnCrV5) are also presented.

**Keywords :** VHCF, Torsion, Finite Elements Simulation, Modal and Harmonic Analysis, Comparison Numerical/Experimental Results, Shear Stress Fatigue Limit.

## INTRODUCTION

For some decades, new piezoelectric fatigue testing machines were developed [1–3], working at ultrasonic test frequency. Ultrasonic fatigue testing gives access to a time saving method to investigate the fatigue behaviour of materials in the high (HCF) and very high cycle regime (VHCF). Half day becomes enough to perform tests beyond one billion cycles against three years with conventional testing methods. The common function of all piezoelectric systems is to make the specimen vibrate at one of its ultrasonic resonance modes, calculated in free-free boundary condition.

The first ultrasonic fatigue machines were designed for uni-axial tension-compression tests,  $R = -1$ , with  $R$  the loading ratio between the minimum and the maximum stress. Now, different systems can be found able to generate different fatigue solicitations in the ultrasonic regime : bending [4], fretting [1, 5], torsion [6–8].

At present, the paper is interesting in optimizing a former ultrasonic torsional fatigue testing developed about 15 years ago by Bathias et al. [6, 9], in order to largely increase the stress level in the specimen. Two kinds of ultrasonic torsion fatigue system can be found in literature. The first one, referred as "direct" system, comprises a converter, a torsional amplifier, named a torsion horn, and the specimen designed to vibrate at the resonance frequency of the system. This "direct" system, where the piezoelectric converter directly generates twist oscillations at about 20 kHz, was successfully used to realize the ultrasonic torsion experiments until 700 MPa shear stress on Si-Cr spring steel [7], 850 MPa on carburized SCM420H steel [10] and 950 MPa on high-carbon chromium bearing steel [8]. The second type of ultrasonic torsion fatigue system, referred as "indirect" system, comprises a converter providing an output linear displacement, a longitudinal horn rigidly linked to a torsion horn, and the specimen. From a technological point of view, the second system should allow reaching a higher shear stress in the specimen because the linear converters available in manufacturers are more powerful than angular converters. That is the reason why we focus on the improvement of the "indirect" system.

Although the operating of the system developed by Bathias et al. was already validated in [6, 9] to generate shear stress in material under ultrasonic regime, this system is not suitable, for example, to characterize high strength steels with endurance shear stress over than 300 MPa. Moreover, the stiff connection between the two horns turns out to be brittle and fails after some tests. Consequently, the objective of the new "indirect" system presented in this paper is double: from a classical linear converter, modify the design of the system developed by Bathias et al. in order to test very high strength materials in ultrasonic torsion fatigue, while decreasing stress in the system. For this purpose, sizing of the system was performed by numerical calculations and comparison with first experimental results is presented.

## DESCRIPTION OF THE INDIRECT TORSIONAL FATIGUE SYSTEM

In order to determine the torsion fatigue limit of the metallic alloys up to  $10^{10}$  cycles, an ultrasonic torsion fatigue system was designed [6]. The main component of the ultrasonic system is a piezoelectric transducer (Fig. 1), which converts an electrical signal at a frequency of 20 kHz into a longitudinal mechanical displacement at the same frequency. The electrical signal is provided by a generator that automatically turns to one of the natural resonant frequency of the system. Two horns are attached to the transducer. The first one (Tension-Compression horn or TC horn) is firmly connected to the converter (using a screw) and amplifies the longitudinal mechanical displacement. The second one (Torsion-Torsion horn or TT horn) is rigidly jointed at the end of the first horn by a press fitted pin going through both horns from end to end. This second horn is fixed perpendicularly to the first one, so that it transforms the linear displacement of the longitudinal horn into an angular displacement and can vibrate on its first torsional resonant mode. Thanks to its shape, the horn amplifies the angular displacement to apply to the specimen. A torsion fatigue specimen is designed to run in the same resonance as the system at a stress ratio of  $R = -1$ . This specimen is directly attached by screw at the end of the second horn. When vibrating, the displacement amplitude (rotation) inside the specimen reaches its maximum at the ends while the maximum strain occurs in the middle section, that produces the required high frequency fatigue shear stress.

In the following, several aspects of the former system are modified in order to noticeably increase the shear stress in the specimen while decreasing stress in the rest of the system. Optimization study is mainly based on the numerical calculations.

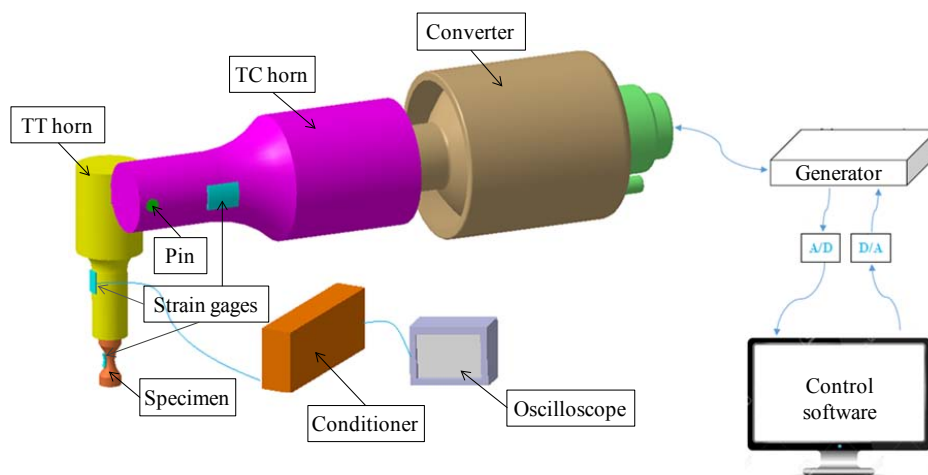


Fig. 1: Scheme of the indirect torsional fatigue system designed by Bathias et al. [6, 9] about 15 years ago

## OPTIMIZATION OF THE INDIRECT TORSIONAL FATIGUE SYSTEM

The optimization mainly concerns the modification of some geometrical characteristics of the system: pin radius, chamfers at the connection of two horns, cavity in the horns and

modification of the TT horn dimensions. All simulations were performed according to the Finite Element Method (FEM) via the ANSYS® commercial software. Initial geometry of the numerical model is based on the drawing of the Fig. 1. Materials used are TA6V titanium for the horns and 100C6 steel for the pin and the specimen. All of them are assumed isotropic. Two types of analysis are required to determine the stress in the system. First, a modal analysis gives the resonant frequency of the system. This modal frequency must be close to 20 kHz. Second, a harmonic analysis allows estimating displacement, strain and stress in the system under the resonant frequency. For this second analysis, a longitudinal input displacement of 1  $\mu\text{m}$  is imposed as boundary condition on the large face of the TC horn. Each proposed modification of the system for its optimization will be compared alone with respect to the original system to keep independency between all parameters.

### Dimensions of the TT horn

The first and the most influential parameter to increase the shear stress in the specimen while decreasing stress in the rest of the system, is the TT horn geometry. Table 1 shows several models of TT horns. They are compared function of the magnification factor of the system, i.e. the ratio between the maximum shear stress obtained into the specimen and the imposed input displacement on the TC horn. It can be observed that the higher the ratio between the large and the small radius, the higher the magnification factor and, consequently, the shear stress in the specimen. According to results from models 4 and 5, this effect is emphasized when the intermediate part of the TT horn with the progressive section is shortened. Nevertheless, a too short intermediate part would become brittle due to stress concentration. So, a compromise had to be done between the length of the intermediate part and the radius difference.

TT horn model	Large radius (mm)	Small radius (mm)	Progressive section length (mm)	Modal frequency (Hz)	Magnification factor (MPa/ $\mu\text{m}$ )
1 (original)	15	8	8.5	19765	115.4
2	16	8	8.5	19776	137.0
3	17	8	8.5	19742	170.9
4	18	8	8.5	19643	226.8
5	18	8	15	19813	175.9

**Table 1:** Comparison of five TT horn models according to their geometrical features

### Pin size

Another possibility to optimize the system by decreasing the stress level in the pin is to modify its size. Indeed, Table 2 shows the influence of the pin radius on the maximum shear stress  $\tau_s^{max}$  in the middle of the specimen and the maximum equivalent (Von Mises) stress  $\sigma_p^{max}$  in the pin. To compare the optimization level of each pin radius, a ratio  $R_\tau$  defined as the ratio between  $\tau_s^{max}$  and  $\sigma_p^{max}$  is introduced; the higher  $R_\tau$ , better the optimization. It can be observed that the higher the pin radius, the higher  $R_\tau$ . So, a bigger pin was favored.

Pin radius (mm)	Modal frequency (Hz)	$\tau_s^{max}$ (MPa)	$\sigma_p^{max}$ (MPa)	$R_\tau$
3 (original)	19765	115.4	54.1	2.13
3.5	19747	116.7	48.7	2.40
4	19738	115.7	32.8	3.53

**Table 2:** Influence of the pin radius on the  $R_\tau$  ratio

### Chamfers

In the former conception of the gigacyclic torsional fatigue system, it could be noticed that the rupture initiation of the pin was often located between the two horns and on its surface. Although the pin is press fitted in both horns and the horns are in contact, during vibrations,

there is certainly friction between the pin and the horns. This friction is intensified when the edges of the drillings into the horns are sharp, like obtained after machining, and not rectified in the previous version. So, in order to reduce the friction between the pin and the horns, chamfers were realized, making smoother the edges of the drillings. The depth of the chamfer is around 1mm.

Chamfer Angle	Modal frequency (Hz)	$R_r$
0° (without chamfer)	19765	2.13
45°	19762	3.94
60°	19762	4.44
75°	19763	4.37

**Table 3:** Effect of the chamfers along the drilling edges in the TC and TT horns on the  $R_r$  ratio

### Cavity in horns

In the aim to still reduce the stress inside the pin, cavity in each horn was made. Effect of the cavity diameter on the  $R_r$  ratio is shown Table 4. It can be observed that a large diameter would be to favor although this effect is little sensitive. Nevertheless, cavity with a large diameter provides two others significant advantages: it enables to decrease the mass of the system without changing its vibration properties and it allows a better heat evacuation around the pin.

Cavity diameter (mm)	Modal frequency (Hz)	$R_r$
0 (without hole)	19765	2.13
5	19856	2.18
8	19962	2.29

**Table 4:** Effect of the cavity diameter on the  $R_r$  ratio

### New optimized system

The parts of the torsional fatigue system to optimize were presented in the previous sections. Most of the choices for the new design results from numerical computation through modal and harmonic analysis performed with the ANSYS® FEM software. The comparison between the former system and the new optimized one is given in Table 5. The modal frequencies of the two systems are close and respect the range [19500 Hz, 20500 Hz] required by the converter. The magnification factor and the  $R_r$  ratio are largely better in the optimized version.

Torsional fatigue system	Modal frequency (Hz)	Magnification factor (MPa/μm)	$R_r$
Original	19765	115.435	2.13
Optimized	19929	232.897	9.49

**Table 5:** Comparison between the former and the new optimized gigacyclic torsional fatigue systems

## EXPERIMENTAL VALIDATIONS

### Calibration

When calibrating the system, a given value of the input voltage of the converter corresponds to a specific value of the input displacement and, furthermore, to a specific maximum shear stress value in the specimen (depending on the magnification factor). The calibration curves of the former and the optimized systems were plotted on Fig. 2. Calibration was done with steel specimen. It can be observed that the relationship between the input voltage and the maximum shear stress is linear for both systems. It is clear that the magnification factor has largely been increased in the new version of the torsional fatigue system. Moreover, since the maximum input voltage is 10 V, the optimized system should be theoretically suitable for high strength materials with torsional fatigue limit over 1000 MPa.

The magnification factor obtained by the FE model is about 233 MPa/μm. It should be equal to the slope of the calibration curve when considering the input displacement of the TC horn in abscissa. This input displacement was measured by optical fiber and the matching with the input voltage was found to be 0.387 μm/V. So, the experimental magnification factor is equal to 132 MPa/μm. This one is around 43% lower than the theoretical one. Discrepancies can be explained by several reasons:

- the material properties are not perfectly known, in particular the elastic constants and the damping properties;
- the geometry of the real system cannot be exact;
- the contact between pin and horns is not perfect, it is certainly the main source of damping in the system, this effect is not taken into account in the numerical model;
- the experimental measurement of the shear stress with strain gage presents several uncertainty sources about bonding, position, thermal effect and not perfectly local measurement;
- uncertainties can also arise during calibration of the system with optical fiber.

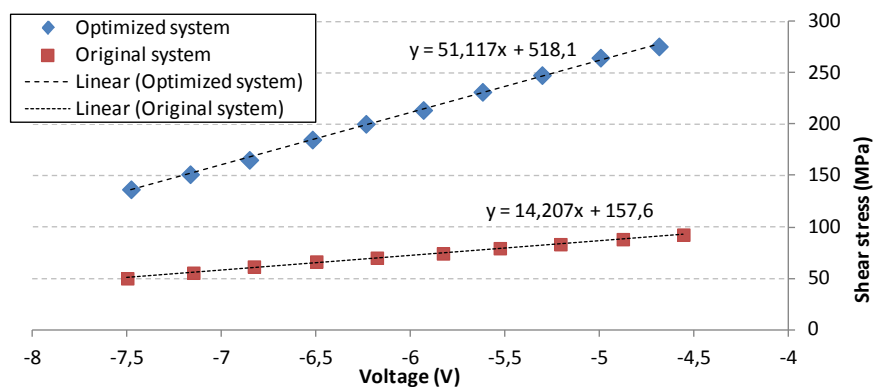


Fig. 2. Calibration of the original system and the optimized system with steel specimen

Furthermore, the three first reasons previously exposed can also explain the difference on the resonant frequency between the numerical model (19932 Hz) and the real system (20230 Hz).

### Gigacyclic fatigue tests on high strength steels

To validate the real optimized system, torsional fatigue limits at  $10^8$  cycles on high strength steels 38MnV5S, 50CrV4 and 16MnCrV5 were determined by the stair-case method. Due to the important self-heating of the specimens during ultrasonic vibrations, cooling by water with inhibitor against corrosion was installed. Fatigue limits are reported in Table 6. At the end of the tests, typical torsion fatigue cracks, as depicted in [9], occurred in the specimens. The highest torsional fatigue limit for the three kinds of steels was about 587 MPa, but the maximum imposed shear stress during tests was 645 MPa, what enables to go perceptibly higher than the original system, but does not allow confirming yet the capacity to test materials with torsional fatigue limit around 1000 MPa.

Material	Fatigue limit (MPa)
38MnV5S	260 ± 30
50CrV4	587 ± 20
16MnCrV5	513 ± 13

Table 6: Results on torsional fatigue limit of three high strength steels

### CONCLUSION

A new gigacyclic torsional fatigue system was developed. The principle of this system is based on the indirect system designed by Bathias et al. 15 years ago. The new version

proposed in this paper was numerically optimized using FEM. Four fundamental parameters were modified: TT horn dimensions, pin size, chamfers along drilling edges and cavity in horns. Each parameter was individually studied and a final geometry was chosen. The optimized system meets two objectives: increase the shear stress in the specimen during ultrasonic torsion fatigue, while decreasing stress in the system and, in particular, in the pin connecting the two horns, which was the weak point in the original version. First experimental tests were performed confirming the improved performances and robustness of the optimized system with respect to the original one. Nevertheless, very high strength materials should be tested to validate the system under the most severe conditions.

## ACKNOWLEDGMENT

Authors thank all the contributors of the "Fregtigue" project, funded by the "Research Fund for Coal and Steel" of the European Union, for the specimens manufacture.

## REFERENCES

- [ 1 ] Mason, W.P.:  
Use of high amplitude strains in studying wear and ultrasonic fatigue in metals.  
In: Well JM, Buck Roth OLD, Tien JK, editors. Ultrasonic fatigue, proceedings of the first international conference on fatigue and corrosion fatigue up to ultrasonic frequencies. (PA) USA: The Metallurgical Society of AIME (1982), pp. 87-102.
- [ 2 ] Stanzl-Tschegg, S.E.; Mayer, H.R.; Tschegg E.K.:  
High frequency method for torsion fatigue testing.  
Ultrasonic, 31 (1993) No. 4, pp. 275-80.
- [ 3 ] Bathias C.:  
Piezoelectric fatigue testing machines and devices.  
Int. Journal of Fatigue, 28 (2006), pp. 1438-1445.
- [ 4 ] Bayraktar, E.; Bathias, C.; Xue, H.Q.; Tao, H.:  
On the giga cycle fatigue behaviour of two-phase ( $\alpha_2 + \gamma$ ) TiAl alloy.  
Int. Journal of Fatigue, 26 (2004) No. 12, pp. 1263-1275.
- [ 5 ] Filgueiras, P.F.; Bathias, C.; Palma, E.S.; Wang, C.:  
Inducing very high cycle fretting-fatigue in the ultrasonic regime.  
Tribology International, 76 (2014), pp. 57-62.
- [ 6 ] Marines-Garcia, I; Doucet, J.P.; Bathias, C.:  
Development of a new device to perform torsional ultrasonic fatigue testing.  
Int. Journal of Fatigue, 29 (2007), pp. 2094-2101.
- [ 7 ] Mayer, H.; Schuller, R.; Karr, U.; Irrasch, D.; Fitzka, M.; Hahn, M.; Bacher-Höchst, M.:  
Cyclic torsion very high cycle fatigue of VDSiCr spring steel at different load ratios.  
Int. Journal of Fatigue, 70 (2015), pp. 322-327.
- [ 8 ] Sakanaka, N.; Matsubara, Y.; Shimamura, Y.; Ishii, H.:  
Rapid Evaluation of Shear Fatigue Properties of Rolling Bearing Steels. for Lifespans Up to the Gigacycle Range.  
NTN TECHNICAL REVIEW No.79 (2011).
- [ 9 ] Xue, H.Q.; Bayraktar, E.; Marines-Garcia, I.; Bathias, C.:  
Torsional fatigue behaviour in gigacycle regime and damage mechanism of the perlitic steel.  
Journal of Achievements in Materials and Manufacturing Engineering, 31 (2008) 2, pp. 391-397.
- [ 10 ] Shimamura, Y.; Narita, K.; Ishii, H.; Tohgo, K.; Fujii, T.; Yagasaki, T.; Harada, M.:  
Fatigue properties of carburized alloy steel in very high cycle regime under torsional loading.  
Int. Journal of Fatigue, 60 (2014), pp. 57-62.

**Corresponding author:** johannpetit@u-paris10.fr



**A**

Abboud A. 93  
Adamski F. 368  
Akebono H. 167; 204; 210  
Allison J. 3; 22  
Alt A. 328  
Awd M. 228

**B**

Baaske M. 382  
Bach J. 154  
Backe D. 13  
Ballani F. 382  
Balle F. 13  
Bandeira C.F.C. 334  
Bang D. 458  
Bannikov M. 57; 69  
Beck T. 248; 274; 284  
Becker F. 368  
Bergström J. 174; 192  
Bhattacharya S. 266  
Boller C. 272  
Bonnand V. 45  
Brita P. 381  
Brückner-Foit A. 119  
Bruno G. 272  
Bülbül F. 119  
Burkart K. 388  
Burman C. 174; 192

**C**

Calvente M.M. 381  
Chandran K.S.R. 113; 148  
Canteli A.F. 381  
Castillo E. 381  
Castro J.T.P. 334; 400  
Catoor D. 351  
Cervellon A. 25  
Chai G. 24; 174  
Chiandussi G. 75; 345; 406  
Christ H.J. 87; 93; 119; 160; 394;  
446  
Clausen B. 388  
Cormier J. 25  
Costa P.R. 315; 322

**D**

Daly S. 3  
Dirrenberger J. 368; 412  
Dönges B. 87; 93; 160

**E**

Egami N. 302  
Eifler D. 248; 278  
Elvira R. 192  
Endo M. 130; 136  
Escauriaza B. 193  
Ewenz L. 174

**F**

Favier V. 368  
Fiedler B. 99; 424  
Fincato R. 180  
Fitzka M. 235; 351  
Freitas M. 315; 322  
Fritzen C.P. 160; 446  
Fujii T. 357  
Fujimura N. 296

**G**

Giertler A. 87; 106  
Gillner K. 308  
Goglio L. 345  
Gohlke D. 272  
Göken M. 154  
Gotoh K. 254  
Grigorescu A. 446  
Grün F. 340  
Gude M. 99; 424  
Guha A. 266

**H**

Hallbäck H. 192  
Hanaki K. 437  
Harlow D.G. 81  
Hartmann R. 93  
He C. 260  
Heckel T. 272  
Heilemann N. 87  
Heinz S. 278  
Hervier Z. 25  
Hickmann S. 362  
Hilgendorff P.M. 446  
Hong Y. 2  
Hopmann C. 374  
Höppel H.W. 154

**I**

Ikeda Y. 136  
Ikegami T. 38  
Ince A. 458  
Ishii H. 357  
Izumikawa T. 357

**J**

Jansen E.L. 418  
Jiang Q. 2  
Jiang Z. 468  
Jones W. 3  
Just G. 99; 424



**K**

Karr U.	51; 186; 235; 242
Kakiuchi T.	167; 204; 210
Kasuya T.	290
Kaufmann E.	394
Kenedi P.P.	334
Kikuchi S.	167
Kirsten T.	119
Knorre S.	222
Kober M.	340
Koch I.	99; 424
Kolyshkin A.	394
Koschella K.	106
Kosmann J.	99
Krupp U.	87; 106; 222
Kulikowski J.	328

**L**

Leopold C.	99; 424
Li J.K.	260
Lian B.	254
Liu Y.J.	260

**M**

Madhusoodanan H.	418
Marder J.	374
Masaki K.	167; 198; 204; 210
Matsuda M.	38
Matsumura T.	167; 198; 204; 210; 437
Mauget F.	25
Mayer H.	51; 130; 186; 235; 242; 351
Meggiolaro M.A.	334; 400
Meischel M.	216
Micha J.S.	93
Michels W.	222
Milošević I.	340
Miyakawa S.	136
Miyamoto N.	136
Miyoshi T.	180
Monteiro E.	412
Muenstermann S.	308
Mukoyama K.	437
Müller A.	362
Müller B.	272

**N**

Naimark O.	57; 69; 142
Nakagawa A.	57; 81; 180
Nakagawa M.	437
Nakahashi Y.	63
Nakai Y.	125
Nakajima M.	81
Nakamura T.	125; 167; 204; 296; 437
Nakamura Y.	81; 167; 198; 204; 210; 290; 437
Nambu K.	302
Nikitin A.D.	4; 430
Nishida T.	167; 198
Nishimura Y.	136

**O**

Okada K.	437
Ogawa T.	167; 198
Oguma H.	167; 204; 437
Oguma N.	57; 63; 69; 82; 167; 180; 204; 437
Ouarabi M.	308

**P**

Palin-Luc T.	4; 45; 142; 308
Paolino D.S.	75; 180; 345; 406
Pennings B.	186
Perlega A.	216
Persson K.	174
Petit J.	31; 468
Pietsch. U	93
Polit O.	45; 308; 468
Pollock T.	3
Potluri P.	266
Pu X.	31

**R**

Radulovic L.	328
Ranc N.	368; 412
Ranc-Darbord I.	31
Reis L.	315; 322
Reiterer M.	351
Ribeiro A.M.R.	315; 322
Ritz F.	278; 284
Rolfes R.	418
Rossetto M.	75; 345; 406

**S**

Sadek M.	192
Sakai T.	38; 57; 63; 69; 81; 167; 180; 437
Sakaida A.	437
Sandaiji Y.	25; 51
Sander M.	452
Sano M.	180
Schaumann P.	328
Schetle A.	99
Schönbauer B.M.	130; 216; 235; 242
Shanyavskiy A.A.	4; 430
Shimamura Y.	167; 204; 357; 437
Shimizu T.	290
Shiozawa D.	125
Shiozawa K.	167; 198
Shokr M.	93
Siddique S.	228
Smaga M.	248
Soldatenkova M.	430
Sorich A.	248
Stäcker C.	452
Stanzl-Tschegg S.E.	216
Starke P.	272
Stein T.	119
Steppeler S.	328
Stich A.	242
Strüder L.	93
Sumida S.	357
Sun C.	2

**T**

Tohgo K.	357
Tamura E.	25; 51
Tanaka Y.	136
Tenkamp J.	222
Tewari A.	268
Torabian N.	368
Torbet C.	3
Tosson A.	93
Tran D.	186
Trappe V.	362
Tridello A.	76; 345; 406
Tsutsumi S.	57; 180

**U**

Ueno A.	38; 167; 198; 204; 437
Uematsu Y.	167; 204; 210
Uesugi K.	125

**V**

Valot E.	45
Venkat R. S.	272
Vieira M.	315; 322

**W**

Wagner D.	31
Wajima, T.	296
Walther F.	222; 228
Wang Q.Y.	260
Weibel D.	13
Wicke M.	119
Winter G.	340
Wu H.	400

**Y**

Yagasaki T.	357
Yakura R.	38
Yamamoto T.	254
Yanase K.	130; 136
Yang K.	260
Yang S.	412
Yoshinaka F.	125

**Z**

Zimmermann M.	119; 174; 394; 446
Zhang H.	260
Zhao M.X.	45
Ziaei-Rad S.	368
Zoch H.W.	388



## VHCF7

Seventh International Conference on Very High Cycle Fatigue

is supported by

The logo for DGM (Deutsche Gesellschaft für Materialkunde e. V.) consists of the letters 'DGM' in a bold, blue, sans-serif font.

Deutsche Gesellschaft für Materialkunde e. V., DE

The logo for FEMS (The Federation of European Materials Societies) features the letters 'FEMS' in a bold, black, sans-serif font, with a red swoosh underline under the 'F'.

The Federation of European Materials Societies

The logo for ESIS (European Structural Integrity Society) shows the letters 'ESIS' in a bold, black, sans-serif font, with a stylized black and white graphic element to the left.

European Structural Integrity Society



Gruppo Italiano Frattura, IT



ICF: The World Academy of Structural Integrity

The logo for SF2M (Société Française de Métallurgie et de Matériaux, FR) features the letters 'SF2M' in a bold, blue, sans-serif font, with the '2' in a lighter shade of blue.

Société Française de Métallurgie et de Matériaux, FR

The logo for TMS (The Minerals, Metals & Materials Society, US) shows the letters 'TMS' in a bold, red, sans-serif font.

The Minerals, Metals & Materials Society, US



The Society of Materials Science, JP

The logo for WAW (Wissenschaftlicher Arbeitskreis e.V. der Universitätsprofessoren der Werkstofftechnik) features the letters 'WAW' in a bold, purple, sans-serif font, with a diagonal slash through the 'W'.

Wissenschaftlicher Arbeitskreis e.V.  
der Universitätsprofessoren der Werkstofftechnik